europhysics conference abstracts

12 th European Conference on

Controlled Fusion and Plasma Physics

Budapest, 2 - 6 September 1985

Editors L. Pócs, A. Montvai

Contributed Papers
Part II

Published by: European Physical Society

Series Editor: Prof. S. Methfessel, Bochum

Managing Editor: G. Thomas, Geneva

VOLUME
9 F
PART II

Max-Planck-Institut für Plasmaphysik
14. MAI 1986
Bibliothek

12 th European Conference on

Controlled Fusion and Plasma Physics

Budapest, 2 - 6 September 1985

Editors L. Pócs, A. Montvai

Contributed Papers
Part II

0307-86

EUROPHYSICS CONFERENCE ABSTRACTS is published by the
European Physical Society, © 1985
Reproduction rights reserved

This volume is published under the copyright of the European Physical Society. We want to inform the authors that the transfer of the copyright to EPS should not prevent an author to publish an article in a journal quoting the original first publication or to use the same abstract for another conference. This copyright is just to protect EPS against using the same material in similar publications.

ISBN 963 372 376 0 (összkiadás)

ISBN 963 372 378 7

Kiadja a Központi Fizikai Kutató Intézet
Felelős kiadó: Pócs Lajos
Példányszám: 800 Törzsszám: 85-421
Készült a KFKI sokszorosító üzemében
Felelős vezető: Töreki Béláné
Budapest, 1985. julius hó

E

inertial confinement

EXPERIMENTAL STUDY OF LASER-DRIVEN IMPLOSION OF SPHERICAL MICROTARGETS

S.Denus, R.Arendzikowski, H.Fiedorowicz, K.Jeziak, B.Kaczmarczyk, S.Nagraba, P.Parys, Z.Patron, W.Pawłowicz, A.Wilczyński, J.Wołowski

Institute of Plasma Physics and Laser Microfusion
00-908 Warsaw, p.o. box 49, Poland

The results of the experimental investigation of laser - driven implosion of the spherical microtargets carried out at the IPPLM are presented in this paper.

The glass microspheres of 100-150 μm in diameter and 1-1.5 μm wall thickness, filled with deuterium or neon at a pressure of 10 atm, were irradiated by means of the four beam laser according to a tetrahedral geometry.

Investigations were carried out with the use of a measuring set-up consisting of a plasma chamber, a system for the spherical microtarget positioning and irradiation and a set of diagnostic apparatus.

The laser was the IPPLM four beam neodymium glass laser system which produced pulses of 1.5 nsec duration with energies up to 80 J.

The laser beams were focused on the microtarget surface by means of a lens focusing system.

To study the laser plasma parameters and physical processes that occur during the laser-driven implosion of the microtargets, different optical and X-ray plasma diagnostics methods were used: optical shadowgraphy and interferometry, $2\omega_o$ harmonic imaging, X-ray microphotography, X-ray line spectra measurements, X-ray continuum diagnostics and X-ray temporal measurements.

The general scheme of the measuring system, which was used for the laser-driven implosion investigations is shown in Fig.1.

Laser irradiation uniformity and implosion symmetry were studied by means of X-ray microphotography and harmonic imaging at $2\omega_o$.

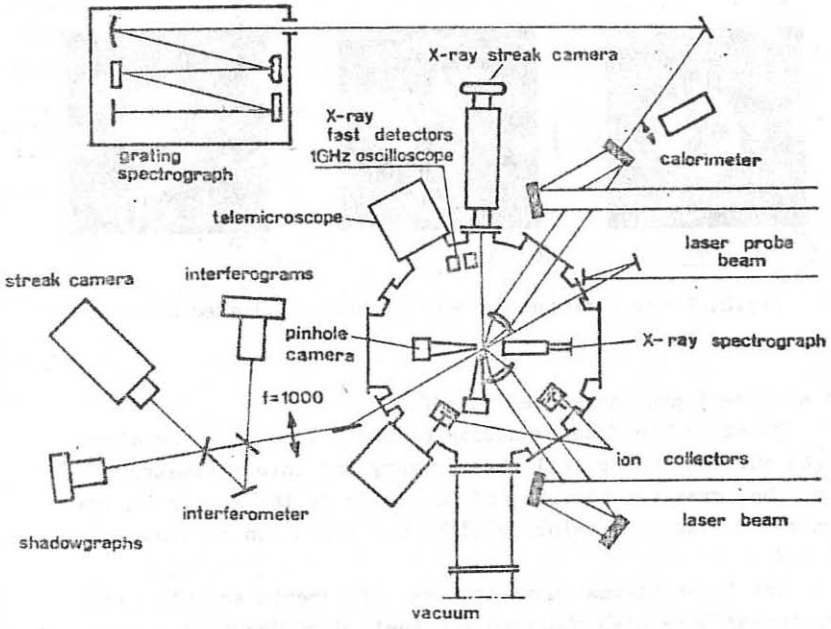


Fig.1. The scheme of the measuring system for the laser - driven implosion investigations.

To make X-ray microphotographs of the plasma two "pinhole" cameras positioned perpendicular one to the another were used. The cameras had spectral range about 1 keV and spatial resolution 20 μm.

In most cases the obtained X-ray microphotographs were of highly symmetrical shape with the characteristic bright spots on the microtarget surface. This corresponds exactly to the tetrahedral geometry of its irradiation by the laser beams /see Fig.2/.

In some X-ray microphotographs one can see bright area in the central part of the microtarget X-ray image related to X-ray emission from plasma generated in result of spherical implosion.

We also performed the harmonic imaging of plasma at $2\omega_o$. The obtained photographs allowed to estimate the irradiation uniformity of microtarget and gave information about the focusing

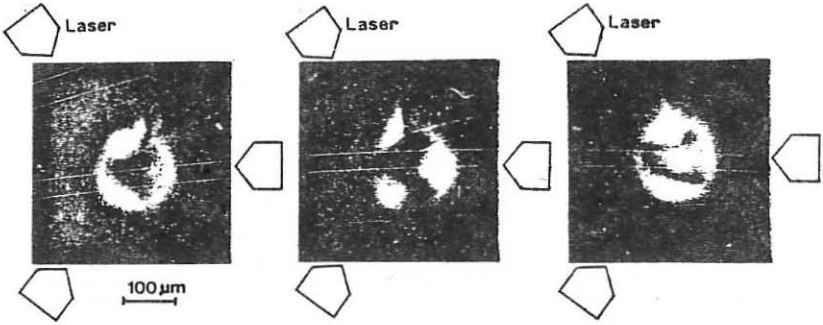


Fig.2. X-ray microphotographs of the irradiated microtargets.

and alignment procedure /see Fig.3/.

To study the free expansion of the plasma from the microtarget surface the optical shadowgraphy and interferometry were used. The frame photographs and some made by the streak camera permited to estimate velocity of plasma expansion at about 10^6 cm/s.

The laser-plasma instabilities /filaments and plasma jet structures/ were also observed and their dependence on atomic number of the microtarget material was proved.

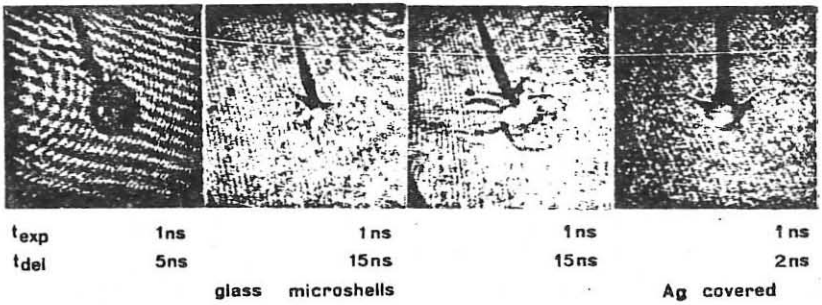


Fig.3. Shade photographs of the expanding plasma.

The parameters of the laser plasma generated in result of microtarget irradiation were measured by means of X-ray line spectra measurements and X-ray continuum diagnostics. Different

type of miniature crystal spectrographs /with ADP, KAP and mica crystals/ were used in the experiment. A typical line X-ray spectrum from a glass microtarget is shown in Fig.4.

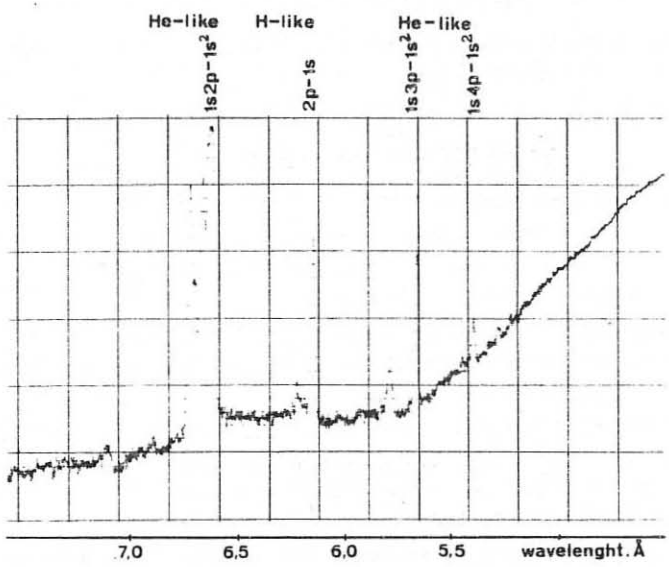


Fig.4. Microdensitometer traces of the X-ray spectrum from imploded glass microtarget.

Temporal and spectral information on X-ray emission in the continuum range were obtained from the fast X-ray silicon photodiode with the filters of different thickness. With 1 GHz oscilloscope time response of the system was about 0.5 nsec. Typical electron temperature of plasma estimated by means of the filter method was about 300 eV.

In the case when the microtarget covered with the metal layer was irradiated the X-ray streak camera was used to measure the X-ray flux with high temporal resolution.

SPECTRAL ANALYSIS OF $2\omega_o$ AND $3/2\omega_o$ HARMONIC EMISSION FROM LASER IRRADIATED SPHERICAL MICROSHELLS

S.Denus, H.Fiedorowicz, J.Kostecki, S.Nagraba, W.Pawłowicz, A.Wilczyński, J.Wołowski

Institute of Plasma Physics and Laser Microfusion
00-908 Warsaw, p.o. box 49, Poland

M.V.Osipov, A.A.Rupasov, A.S.Shikanov

P.N. Lebedev Physical Institute
Moscow V-312, Leninskij Prospekt 53

The $2\omega_o$ and $3/2\omega_o$ harmonic spectra have been studied when radiation from a neodymium glass laser has interacted with a spherical microshell.

The laser was the four-beam glass laser which produced pulses of 1.5 nsec duration with energies up to 50 J and wavelength of 1.064 μm. The spherical microshells /75-150 μm in diameter/ were irradiated in tetrahedral configuration. The laser radiation was focused by aspheric lenses f/2. Experimental layout for spectral studies is shown in Fig.1. Radiation emitted from plasma was focused on the slit of the ISP 51 spectrograph. Photographic camera provided information about the symmetry of illumination. The spectrograph was protected against the fundamental harmonic by means of optical filters.

Cardinally, the two different kinds of spectral structures have been obtained in the experiment /simple and complicated/. Examples of both simple and complicated spectral structures are shown in Fig.2. The simpliest example is shown in Fig.2a. It contains only one peak with maximum shifted 4-6 Å to the red from the exact value of $\lambda_o/2$. The red shift of maximum was caused by the Doppler effect [1,2,3]. Much more complicated structure of $2\omega_o$ is shown in Fig.2b. The component with maximum shifted to the blue about 4 Å can be explained by the Doppler effect - the motion of the critical surface out during the beginning of laser plasma interaction. The component of $2\omega_o$ shifted to the red about

4-6 Å was caused by the Doppler effect /like in the example in Fig.2a/. The occurrence of the long-wave component of the second harmonic spectrum shifted 15-30 Å means that the parametric instability took part in the process /the instability of the type of an ion decay process: $t_o \rightarrow l_s + s$, t_o - photon, l_s - plasmon, s - phonon/. Threshold character of this phenomenon attests about it as well. In the low levels of laser intensity /10^{12}-10^{13} W/cm^2/ the complicated structures were not obtained. In some shots the $3/2\omega_o$ harmonic spectra have been observed.

However, the $2\omega_o$ and $3/2\omega_o$ harmonic spectra obtained in the experiment seem promissing, they have yet to be fully explained.

The paper presents results obtained in the work carried out at the IPPLM in the co-operation with P.N. Lebedev Physical Institute, Moscow.

References:

[1] B.L.Vasin et al., Proceedings of FIAN, 133 /1983/, p.51

[2] N.G.Basov et al., Preprint FIAN No 196 /1978/, p.74

[3] N.G.Basov et al., Kvantovaya Elektronika, 6 /1979/, p.1829

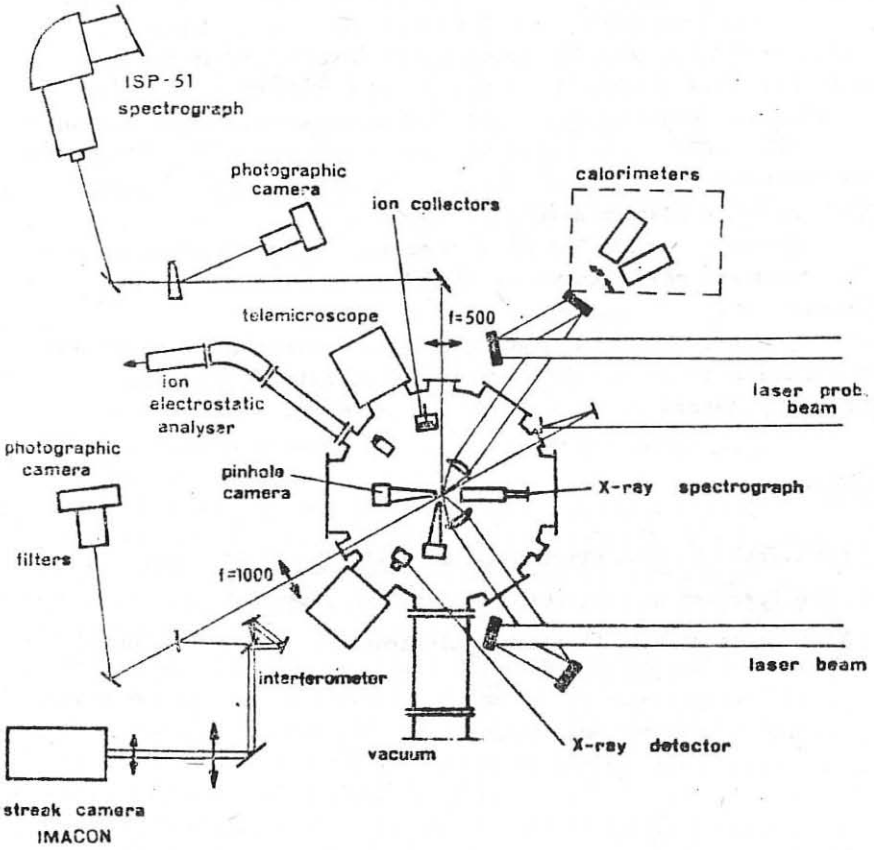


Fig.1. Experimental layout for $2\omega_0$ and $3/2\omega_0$ harmonic studies in the laser-driven implosion of the spherical microshell.

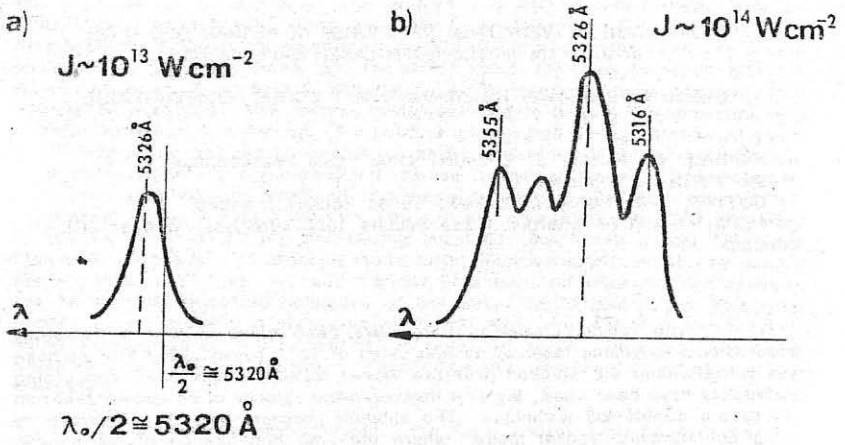


Fig.2. Typical spectral distribution of the second harmonic emission from irradiated microshells.

GENERATION OF VERY HIGH PRESSURES IN PLANAR GEOMETRY IN 0.26 μm WAVELENGTH LASER EXPERIMENTS

GRECO INTERACTION LASER-MATIERE - ECOLE POLYTECHNIQUE

R. FABBRO, B. FARAL, J. VIRMONT (PMI Ecole Polytechnique, 91128 Palaiseau France)
F. COTTET, J.P. ROMAIN (ENSMA, 86034 Poitiers France)
H. PEPIN (I.N.R.S. Energie, Case Postale 1020 Varennes, Québec JOL 2PO Canada)

The results discussed here have been obtained with a frequency quadrupled neodymium laser up to intensities of 10^{15} W/cm^2. Our first purpose was to determine the ablation pressure versus laser intensity. Two concording techniques have been used. We first measured the velocity of an accelerated thin foil by the double-foil technique. The ablation pressure was then deduced by using an improved "rocket model" where the time dependance of the applied pressure was taken into account. For this measurement, we also have determined the conditions which must be satisfied in the double foil technique, in order to give a correct measurement of the velocity. All this method has been checked by numerical simulations, using a lagrangien monodimensionnal hydrodynamic code (FILM). The second method consists in measuring the velocity of the induced shock by recording the emergence of this shock at the rear of foils of different thicknesses. A model of the formation and decay of the shock has been used to determine the maximum shock pressure. This simple and fiducial technique agrees with the first one. The experimental law :

$$P_a \text{ (Mbar)} \sim 13 \left[\frac{I \text{ (W/cm}^2\text{)}}{10^{14}} \right]^{0.55}$$

has been obtained with these two techniques. We compared this law with the numerical law obtained with our code, using "sesame" EOS. The discrepancy between the two laws (see Fig. 1) can be explained, if we take into account 2-D effects : the radial dependance of the applied pressure has been determined by measuring the radial dependance of the emergence of the shock. One can see on Fig. 2 that the effective diameter (FWHM) of the applied pressure is greater than the laser focal spot diameter (50 μm - FWHM). So, we can consider that the laser is applied on a larger spot, ie with a lower intensity, and then numerical and experimental laws are consistent. We emphasized the fact that at high intensities (~ 10^{15} W/cm^2), with this short wavelength, very high ablation pressures (~ 50 Mbar) are obtained.

The experiments described now have been conceived in order to amplify this pressure up to 100 Mbar and above. The first technique used was an impedance mismatch one, using an Al/Au layered targets. Experimentally, the measurement of the shock velocity in the Aluminium and in the Gold (by a step technique - Fig. 3a) shows that the initial shock pressure of 45-50 Mbar in Aluminium rises up to 90-100 Mbar in Gold, as predicted by shock mismatch impedance equations. The second technique used to amplify this pressure is a collision technique : a thin foil (9 μm Al) is accelerated by the ablation pressure (~ 50 Mbar) and collides an impact foil at the end of the laser pulse (0,5 ns). Simulations show, in agreement with simple analytical models, that extremely high pressures can be obtained for these conditions. These pressures are maintained during a very short time and typically decreased from 350-400 Mbar to 100-150 Mbar in 80-100 ps. During this time, the shock travels 12-15 μm inside the impact foil. In order to measure the velocity of this shock, we used a stepped impact foil (Fig. 3b) with a known high step and different thicknesses of the basis. The measured velocities of this shock at 12 and 6 μm inside the impact foil correspond to pressures of 150±60 Mbar and 440±240 respectively, using Hugoniot data from "sesame" equation of state. This high measured pressure could be overestimated if one takes into account the effect of X-ray preheating.

We then studied experimentally the X-ray emission produced during the interaction of the laser on the target. Different materials have been used (CH, Al, ...) and this X-ray emission has been spectrally resolved (Fig. 4) using an X-ray diode multi-channels detector. The heating of the target due to this X-ray emission has been determined assuming opacities of cold material. The effect of this preheating in the collision can then be numerically analysed : it appears first that the collision is softened and secondly that our step diagnostic is sensitive to this preheating. Effectively, the accelerated and impact foils are decompressed by this preheating. Therefore, the velocity of the induced shock in the step is modified, and is greater (for a given pressure) than in a non-perturbed material.

As we can see, X-ray preheating plays an important role in these high pressure experiments : but, we can easily suppress it by using a CH layer as ablated material on the Al accelerated target. This improvement will be done for future experiments.

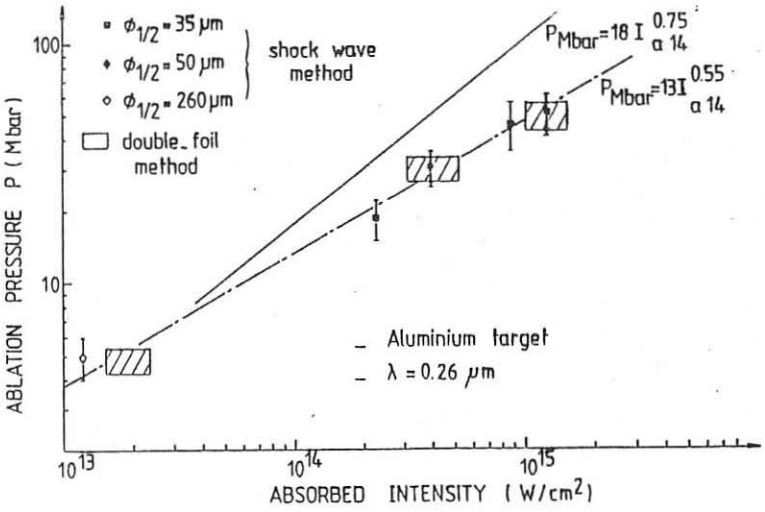


Figure 1

Variation of the experimental peak ablation pressure as a function of the absorbed irradiance. The results of the shock-wave method are given by the dots for different half-energy focal spot diameters. The rectangles represent the results of the double-foil technique. The dashed and dotted curve is a best fit of the experimental results. The continuous curve gives the result of the hydrodynamic simulations.

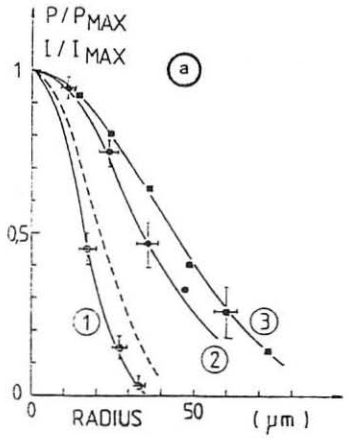


Figure 2

Visualisation of the 2-D effects leading to an increase of the diameter where the ablation pressure is applied normalized radial dependence of the laser intensity (curve 1) ; the corresponding expected ablation pressure (dashed curve) ; the experimental ablation pressure for absorbed intensity of 2.4 10^{14} W/cm (curve 2) and 1.4 10^{15}W/cm (curve 3).

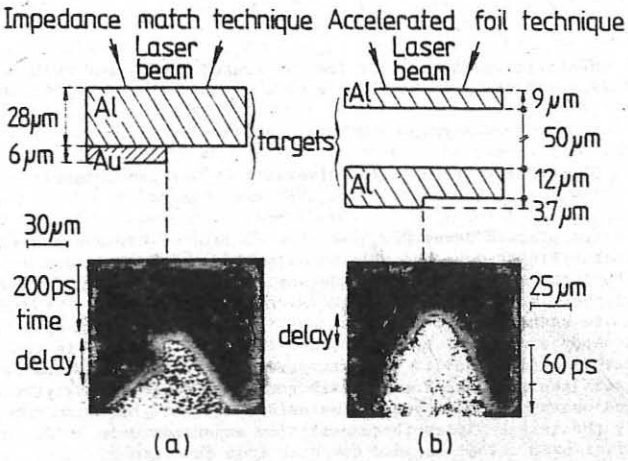


Figure 3

Design of targets used and corresponding streak recorks for impedance-match experiment (a) and accelerated foil experiment (b). Streak-camera photos show optical signals correlating with shock breakout at two surfaces on stepped target. Incident laser intensity is about 10^{15} W/cm in 0.5 ns FWHM at 0.26 μm.

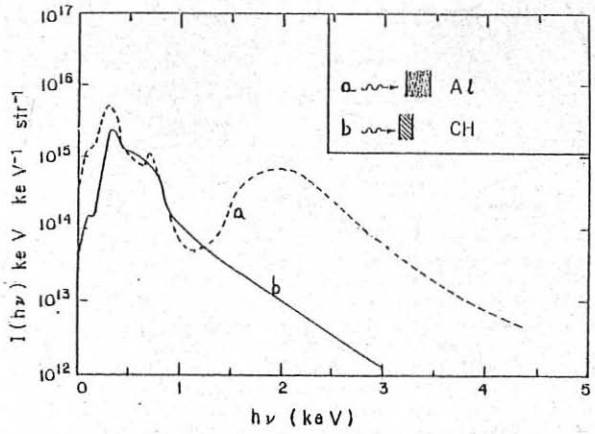


Figure 4

X-ray emission spectra for the various materials.

Experimental Investigation of the Two Plasmon Decay and Stimulated Raman Scattering Instabilities in a CO_2-Laser Produced Plasma

J. Meyer, G. McIntosh and H. Houtman

Deptartment of Physics, University of British Columbia,
Vancouver, B.C., V6T 2A6, Canada

The two plasmon decay ($2\omega_p$) and the stimulated Raman scattering (SRS) instabilities have recently received a great deal of attention since they provide potentially dangerous preheat mechanisms for laser fusion targets. Signatures of both instabilities in laser irradiated targets are usually observed in the back and side scattered spectra in the frequency range $\frac{1}{2}\omega_0 - \omega_0$ (SRS) and at $\frac{3}{2}\omega_0$ ($2\omega_p$), (ω_0 is the incident laser frequency). The interpretation of these spectra rely on quantities like thresholds and growth rates predicted by analytic theory and often on extensive computer simulations. It is therefore necessary to study the instabilities in quantitative experiments in order to test theoretical predictions and aid computer code development. The present paper reports on such measurements performed on both instabilities using Thomson scattering of probe ruby laser light as main diagnostic.

The experimental conditions are similar to those described previously[1]. A 2ns (FWHM) CO_2-laser pulse of $\leq$ 12J energy is focussed to intensities of $\leq 10^{14}$ W/cm^2 onto a laminar N_2 gas jet, producing a plasma of densities $\leq 0.4 n_c$ ($n_c = 10^{19}$ cm^{-3}). Electron plasma waves (epw.s) are probed by ps-resolution Thomson scattering.

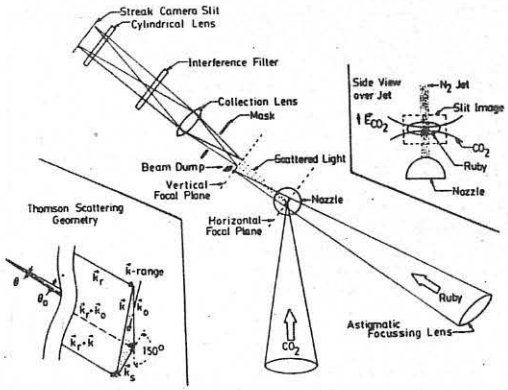


Figure 1: Experimental arrangement for Thomson Scattering

Figure 1 shows the experimental arrangement for measurements of SRS fluctuations. A 6 ns ruby laser pulse is focussed astigmatically to a line covering the CO_2-laser focal volume in the jet. The second line focus is formed 30cm beyond the jet in a plane which then contains the Fourier transform line in $\hat{k}_0$-direction of the plasma object ($\hat{k}_0$ is the CO_2-wave vector). Radiation scattered into an angular range $2° < \theta < 4.5°$ is focussed onto the slit of a ps-resolution streak camera (Hamamatsu C1370-01/III) after passing through an interference filter of 11nm pass band centered at 670nm. Either (a) the plasma for spatial measurements or (b) the Fourier transform line for wave number studies is imaged onto the slit. In case (b), shown in Fig. 1 a cyclindrical lens images the slit in perpendicular direction magnified into the plasma. The relative sizes of slit, CO_2 and ruby focus in the jet are indicated in the upper insert. The lower insert shows the scattering wave vector geometry indicating that for $k > k_0$ the case of 150° SRS side scattering is probed. The detected scattered to incident intensity ratio is absolutely calibrated against a fiducial of the probe intensity displayed at the edge of the streak records, which are digitized and stored on tape.

A similar scattering geometry was used to detect epw.s generated by the $2\omega_p$-instability, this time measuring fluctuations propagating in the CO_2-laser plane of polarization at an angle of ~ 45° against the CO_2-wave vector. This experiment has been described previously[1].

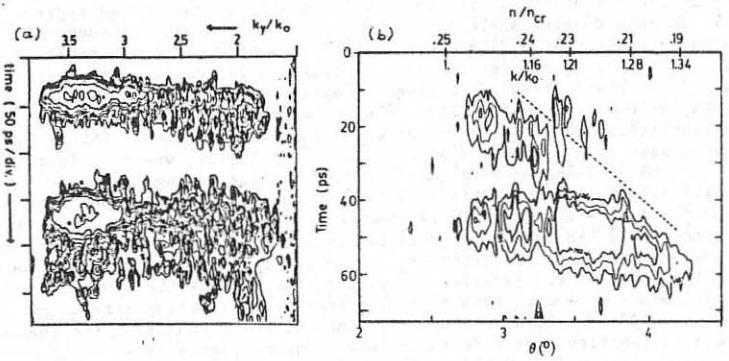


Figure 2 shows sample streak records of the wave number spectra for (a) the $2\omega_p$-instability (k_y is the wave vector component in $\hat{E}_{CO_2}$-direction) and (b) the SRS-plasma waves. Spatially resolved streak records show that the $2\omega_p$-instability is active near the quarter critical density ($n_c/4$) surface while SRS spreads continuously to lower densities. The records indicate the transient nature of both instabilites with SRS lasting for a much shorter period (~ 60ps) than the $2\omega_p$-instability. Both instabilities initially grow exponentially in time once the pump intensity surpasses 3×10^{13} W/cm^2. Then they soon saturate and decay. The $2\omega_p$-instability is frequently observed to reappear in periodic intervals of ~ 100ps. It has been shown[1] that saturation of this instability arises due to coupling of a pair of decay waves to large amplitude ion acoustic fluctuations of twice the wave number of the

fastest growing mode in the k-spectrum. The instability is quenched by profile modification resulting from the ponderomotive force of the plasma waves which have a saturated amplitude of $\delta n/n$ between 10% and 20%. Once the instability is quenched, the profile relaxes and the instability reappears.

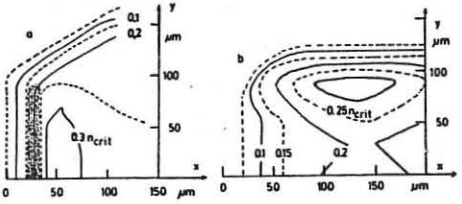
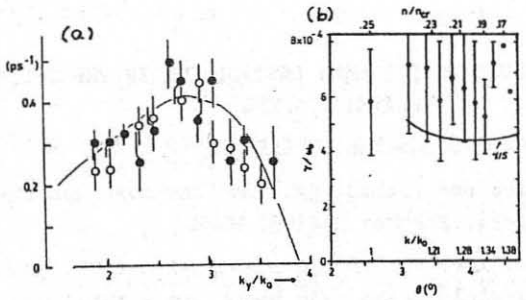


Figure 3 shows two density contour plots of the plasma derived from interferograms taken at the time of the first appearance of the $2\omega_p$ instability with (b) subsequent to (a) by about 200 ps. CO_2-laser light enters from the left. The density modifying influence of the $2\omega_p$ instability is clearly visible. The instability starts in the hashed region of Fig. 3a at a density scale length $L \equiv (dn/ndx)^{-1} \approx 30\mu m$. Subsequently the density radient at $n_c/4$ steepens until no quarter critical density remains on axis as shown in Fig. 3b. Meanwhile L increases in the region below $n_c/4$. This increase in L makes it possible for SRS to start.

SRS, shown in Fig. 2b is seen to start a few tens of ps after the $2\omega_p$ instabilities does. The wave number of the electromagnetic SRS scattered wave is $k_s = (\omega_r + \omega_p)(\theta - \theta_0)/c$ (see Fig. 1) where ω_r is the ruby-, ω_p the plasma-frequency and $\theta_0 = 2.6°$ the scattering angle for fluctuations with $k = k_0$. This wave has to satisfy both relations $\omega_s^2 = \omega_p^2 + c^2k_s^2$ and $\omega_s = \omega_0 - \omega_p$. It is thus possible to calculate ω_p for the epw probed at θ. the resulting density scale n/n_c is as well shown in Fig. 2b. The decrease in scattered instensity at $\theta > 4°$ is caused by the finite band pass of the interference filter (Fig. 1) for the scattered probe frequency $\omega_r + \omega_p$. From spatially resolved scattering streak records $L \approx 300\mu m$ at $0.2n_c$ is deduced. The threshold condition for the absolute instability near $n_c/4$ in an inhomogeneous plasma is given by Drake and Lee[2] as $v_0/c > 0.52/(k_0 L)^{2/3}$. Here v_0 is the oscillatory electron velocity in the pump electric field. At 3×10^{13} W/cm^2 the threshold scale length is then $L_{th} = 50\mu m$, by far exceeded in this experiment. At $0.2n_c$ however the inhomogeneous threshold[3] is given by $(v_0/c)^2 > 4\,(k_0 - k_0)/k^2 L$ requiring $L_{th} > 1mm$ which is much larger than that oberved in this experiment. Yet SRS is observed at these densities though it starts temporally delayed. In fact, inspection of Fig. 2b indicates that the instability spreads to lower densities at a velocity of $v = 7 \times 10^{-3}$ L ps^{-1}, which at $L = 400\mu m$ corresponds closely to the epw group velocity at wave number k_0 and the present kT = 500eV (v is indicated by the dotted line in Fig. 2b). It appears that waves generated near $n_c/4$ after reflection at their critical surface propagate down the density gradient lowering the SRS threshold here. Subsequently SRS grows exponentially in time over several e-foldings then saturates at $\delta n/n \approx 1\%$ and decays, likely due to the density modifying influence of the $2\omega_p$-instability.



At the fastest streak speeds the growth rates of both instabilities can be mesured from log I vs t plots. Figure 4 shows so determined growth rates γ as function of wave number for (a) the $2\omega_p$-and (b) the SRS-instabilities. These values can be compared to theoretical predictions. Theoretical curves calculated for the plasma parameters of this experiment are indicated as solid curves in the plots. In the case of the $2\omega_p$-instability (Fig. 4a) the agreement between experimental and theoretical values due to Simon et al.[4] is very good. For SRS the comparison to theory is more complicated due to the fact that below $n_c/4$ the instability is predicted to be convective unless the region of growth is limited[3]. The growth rates for a finite plasma as predicted by Forslund et al.[3] are five times larger than observed.

The number of hot electrons measured simultaneously with electron spectrometers scale exponentially with the duration of the generating instability and the energy distribution is seen to evolve from a 1D to a 3D (~ 100keV) Maxwellian, indicating the importance of space charge potentials. Simultaneously performed spectroscopy of back scattering CO_2-radiation in the frequency ranges of $3/2\ \omega_0$ and $> 1/2\ \omega_0$ are correclated to the fluctuation measurements.

This work was supported by the Natural Sciences and Engineering Research Council of Canada.

References

1. J. Meyer and H. Houtman, Phys. Rev. Lett. 53, 1344 (1984), and Phys. Fluids 28, 1549 (1985).
2. J.F. Drake and Y.C. Lee, Phys. Rev. Lett. 31, 1197 (1973).
3. D.W. Forslund, J.M. Kindel and E.L. Lindman, Phys. Fluids 18, 1002 (1975).
4. A. Simon, R.W. Short, E.A. Williams and T. Dewadre, Phys. Fluids 26, 3107 (1983).

ON THE HIGH-CURRENT ION BEAM INSTABILITY IN THE Z-PINCH PLASMA CHANNEL

V.I.Golota, V.I.Karas'

Institute of Physics and Technology, the Ukrainian Academy of Sciences, Kharkov 310108, USSR

In problems of inertial confinement fusion (ICF) using high-current charged particle beams, the beams are generally assumed to propagate in the Z-pinch plasma channel. To study the stability of high current beams propagating under such conditions, it is reasonable to investigate the action of the azimuthal magnetic field excited by the Z-pinch current, and the return plasma current induced by damping in a finite resistivity plasma. A total current I_Σ is supposed here to be much lower than the Alfven current I_A of the beam particles.

For simplicity, we consider a strip beam propagating along the Z-axis and bounded along the X-axis, and assume the total current density to be uniform within the range of $|x| \le a$. Then the azimuthal field is written as

$$\vec{H}^0(x) = H_y^0 \vec{e}_y , \quad H_y^0 = H^0 \begin{cases} \frac{x}{a} , & |x| \le a \\ 1 , & |x| > a \end{cases}$$

where H^0 is the peak value of the magnetic field.

The unperturbed beam distribution f_b^0 is an arbitrary function of the integrals of motion (i.e., the energy and the Z-component of the momentum) and is chosen here to be the Gibbs function with a temperature T_b

$$f_b^0 = n_b^0 (2\pi v_{Tb}^2)^{-3/2} \cdot \exp\left\{ - \frac{\omega_0^2 x^2}{2 v_{Tb}^2} - \frac{(\vec{v} - \vec{V}_b)^2}{2 v_{Tb}^2} \right\} ,$$

where n_b^0 is the beam density at $x = 0$, V_b and v_{Tb} are the directed and thermal beam particle velocities, respectively; $\Omega_b = q_b H^0 / m_b c$ and $\omega_0^2 = \Omega_b V_b / a$ are the cyclotron and betatron frequencies of the beam particles at the peak magnetic field value.

A linearized kinetic equation of the perturbed beam particle distribution f_b in the azimuthal magnetic field $\vec{H}^{\circ}(x)$ has a form

$$\frac{\partial f_b}{\partial t} + \vec{v}\frac{\partial f_b}{\partial \vec{r}} + \frac{q_b}{m_b c}\left[\vec{v},\vec{H}^{\circ}(x)\right]\frac{\partial f_b}{\partial \vec{v}} = -\frac{q_b}{m_b}\left\{\vec{E} + \frac{1}{c}\left[\vec{v},\vec{H}\right]\right\}\frac{\partial f_b^{\circ}}{\partial \vec{v}} \qquad (1)$$

The solution of (1) can be written as an integral along unperturbed trajectories

$$f_b(\vec{r},\vec{v},t) = -\frac{q_b}{m_b}\int_{-\infty}^{t} dt'\left\{\vec{E}(\vec{r}',\vec{v}',t') + \frac{1}{c}\left[\vec{v}',\vec{H}(\vec{r}',\vec{v}',t')\right]\right\}\frac{\partial f_b^{\circ}(\vec{r}',\vec{v}',t')}{\partial \vec{v}'} \qquad (2)$$

However, for the dispersion analysis of the plasma-beam system one has to know not the function (2) itself but its moments related to the perturbations of the beam current and charge densities.

The following form of space and time dependences for the perturbations of the field and distribution functions is chosen

$$\sum_{n=-\infty}^{\infty} Q_n(\kappa_y,\kappa_z,\omega)\exp\left[i\left(\frac{\pi n x}{a} + \kappa_z z + \kappa_y y - \omega t\right)\right],\quad \kappa_x = \frac{\pi n}{a}$$

Using the expressions for beam particle trajectories in the nonuniform magnetic field (e.g., see [1]) and assuming an easily satisfied condition $v_{Tb} \ll V_b$ one can reduce the expression for the perturbations of the charge and current densities to the following single integrals over τ :

$$j_{xn} = \int_0^{\infty} d\tau\,\Pi(\tau)\frac{q}{p}\left\{\frac{1}{q}\cos\omega_0\tau\left(E_{xn} - \frac{\kappa_x}{\kappa_z}E_{zn}\right) - S(\tau)\right\}, \qquad (3)$$

$$j_{yn} = \int_0^{\infty} d\tau\,\Pi(\tau)\left\{\left(E_{yn} - \frac{\kappa_y}{\kappa_z}E_{zn}\right) - i\kappa_y\tau\,S(\tau)\right\}, \qquad (4)$$

$$j_{zn} = \frac{q_b^2 n_b^{\circ} V_b}{T_b}\,\frac{\exp\left(-\frac{\omega_0^2 x^2}{2v_{Tb}^2}\right)}{i\kappa_z}E_{zn} + \int_0^{\infty} d\tau\,\Pi(\tau)\left(\frac{V_b}{v_{Tb}^2} - i\kappa_z\tau\right)S(\tau), \qquad (5)$$

$$S(\tau) = \left(x\omega_0 \sin\omega_0\tau - \frac{v_{Tb}^2}{p}q\cos\omega_0\tau\right)\left(E_{xn} - \frac{\kappa_x}{\kappa_z}E_{zn}\right) + \frac{\omega}{\kappa_z}E_{zn} -$$
$$- i\kappa_y v_{Tb}^2\tau\left(E_{yn} - \frac{\kappa_y}{\kappa_z}E_{zn}\right),$$

where

$$q = \frac{i\kappa_z x}{4V_b}\left(\cos 2\omega_0\tau - 1\right) + \frac{i\kappa_x}{\omega_0}\sin\omega_0\tau,\quad p = \left(1 + \frac{i\kappa_z v_{Tb}^2}{4V_b\omega_0}\left(2\omega_0\tau - \sin 2\omega_0\tau\right)\right),$$

$$\frac{q_e^2 n_e^0}{m_e} e^{g(\tau)} \cdot (1 - \frac{\kappa_z V_e}{\omega}) p^{-1/2} \equiv \Pi(\tau), \quad g(\tau) = -i(\kappa_z V_e - \omega)\tau - \frac{(\kappa_z^2 + \kappa_y^2) v_{Te}^2 \tau^2}{2} +$$

$$+ i\kappa_x x(\cos\omega_0\tau - 1) + \frac{v_{Te}^2 q^2}{2p} - \frac{\omega_0^2 x^2}{2v_{Te}^2} + \frac{i\kappa_z \omega_0 x^2}{8V_e}(2\omega_0\tau - \sin 2\omega_0\tau).$$

Using the expressions obtained above for the beam current density perturbations together with those for plasma charge and current density perturbations, one can write down a complete dispersion equation for the beam-plasma system in the azimuthal magnetic field.

The discussion is limited here to the study of the azimuthal magnetic field influence on the beam-plasma instability, first indicated by Akhiezer and Fainberg [2]. As to our knowledge, there is only one work [1], where the influence of the beam magnetic eigenfield or the azimuthal magnetic field of the Z-pinch on the instability near the electron plasma frequency is taken into account. However, it will be shown below that the conclusion made in [1] on the possibility of stabilizing the beam-plasma instability using the azimuthal magnetic field of the Z-pinch is not true for the parameters chosen in [1], which are typical of the ICF on light ions [3]. This is due to an error in the calculations of the integrals in the expression for the charge density perturbations.

Let the plasma density n_p be much greater than that of the nonrelativistic ion beam n_b and the electron-ion collision frequency ν_{ei} be substantial. Then, supposing the plasma electron cyclotron frequency Ω_{He} in the transverse field of the total current to be small as compared to ν_{ei}, one can obtain in the potential approximation the following dielectric constant, where the space dispersion is neglected

$$\varepsilon = 1 - \frac{\omega_{pe}^2}{\omega(\omega + i\nu_{ei})}, \quad \omega_{pe}^2 = \frac{4\pi e^2 n_p}{m} \qquad (6)$$

Supposing also that $\frac{\omega_{pe} a}{V_e} \gg 1$

which condition is very close to that of good current compensation, and considering large-scale perturbations along X and uniform ones along y, one can show from (5) at $\omega \approx \omega_{pe}$ that in case of $|\delta| = |\omega - \kappa_z V_e| \ll \kappa_z v_{Te}$ the azimuthal magnetic field can

be essential only when

$$\omega_0 \gtrsim v_{Tb} V_b^{-1} \omega_{pe} \qquad (7)$$

Note that ω_0 related to the azimuthal magnetic field of the ion beam with no current compensation is equal to $\omega_b V_b/c$. Therefore, condition (7) cannot be easily satisfied.

In the opposite limiting case $|\delta| = |\omega - \kappa_z V_b| \gg \kappa_z v_{Tb}$ the azimuthal field has to satisfy even a more rigorous condition

$$\omega_0 \gtrsim \omega_{pe} \left(\frac{\omega_b^2}{\omega_{pe}^2} \right)^{1/3} \qquad (8)$$

It is thus shown that the magnetic eigenfield of the nonrelativistic charged particle beam exerts no effect on the evolution of the plasma-beam instability in the plasma frequency range.

It is shown that at beam and plasma parameter values associated with the high-current ion beam propagation to the pellet in the Z-pinch plasma channel, the azimuthal magnetic field cannot stabilize the plasma-beam instability. This requires a rigorous restriction on the plasma temperature in the channel (to a few ten eVs) to suppress the instability considered.

The authors express their gratitude to Prof. Ya. Fainberg for useful discussions and remarks.

References

1. P.F. Ottinger et al., Phys. Fluids 22 (2), 332 (1979).
2. A.I. Akhiezer, Ya.B. Fainberg, Dokl. Akad. Nauk SSSR 69, 555 (1949).
3. R.N. Sudan et al., Nucl. Fusion 24 (7), 827 (1984).

TARGET IMPLOSION in LIB ICF

Shigeo KAWATA and Keishiro NIU
Department of Energy Sciences, Tokyo Institute of Technology,
Nagatsuta, Midori-ku, Yokohama 227, Japan.

This paper presents numerical analyses for the LIB-target implosion. The numerical results are obtained by one-dimensional(1-D) and 3-D numerical codes. In the paper the following issues are searched: LIB oblique incidence on target surface, plasma effect on LIB-stopping power, LIB particle energy, LIB time duration, target radius, LIB input energy and nonuniformity.

The problem in the computational method for description of shock phenomena in an ICF target is also described. The problem comes from numerical dissipation.

1. Target Implosion

The target structure employed in the paper is presented in Fig. 1. At first, the typical numerical results are presented. The employed parameter values are listed in Table 1. Figure 2 shows the time sequences of the peak ion temperature of the DT fuel, the target gain Q(=the output fusion energy/ the input LIB energy E_b) and the density-radius product ρR. Figure 3 presents the implosion efficiencies. In Fig.3 η_{imp} is defined by $(E_{TDT}+E_{KDT})/E_b$, η_{KDT} is defined by E_{KDT}/E_b and η_{Kin} is defined by $(E_{KDT}+E_{KALin})/E_b$. Here E_{TDT} shows the thermal energy in DT fuel, E_{KDT} the kinetic energy in DT and E_{KALin} the kinetic energy which is carried by the inward moving Al material. The implosion efficiency of η_{Kin} has a large value before the void closure time(τ_v). Before the void closure time, the DT is compressed gradually. Then the void is closed and the fuel is compressed further.

1-A. LIB oblique incidence on target surface

Usually the incident LIB has the finite radius. Some part of LIB hits the target surface obliquely. As the maximum incident angle Θ_m increases, the deposition peak becomes wide and the peak point goes outward in the target tamper. Therefore the material mass, which moves inward with DT becomes large, as the increase of Θ_m. This means that the implosion efficiency decreases as the increase of Θ_m. The relation between the implosion efficiency and Θ_m is shown in Fig. 4. On the other hand, the particle energies of LIB are scattered ia a range of Δe_b. It is clear that the broadness has the same effect as that of θ_m.

1-B. Plasma effect on LIB stopping power

During the LIB illumination on the target, the target material is partially ionized. Therefore the free electrons, the bound ones and the ions contribute to the LIB stopping power. Especially the produced plasma behaves as not only the individual single particle one but also the collective one. Therefore the total stopping power increases as the increase in the material temperature in the relaticely low temperature range, for example o to 3oo ev for the typical case. From the considerations above, it seems to be apparent that the implosionefficiency becomes low when the plasma effect on the stopping is switched on. In order to check the plasma effect on the target implosion, the numerical simulations are performed for two cases. The implosion efficiency η_{KDT} has a smaller value in the case in which the plasma effect is

switched on, than in the other case. But it should be noted that η_{Kin} and η_{imp} have larger values in the former case than those in the latter. This fact can be explained by the following considerations: In the Al layer, the retained thermal energy, which can not contribute to the implosion until the void closure time, is presented by the notation of E_{TAL}. Two values of E_{TAL} are quite different with each other. In the case which includes the plasma effect, the range shortning of the LIB stopping appears in the tamper, the narrower region is heated and expands into the target size void region. Therefore the thermalenergy of the Al layer is covered efficiently to the kinetic energy.

1-C LIB particle energy

In order to investigate the effect of the difference of LIB particle energy on the implosion, the computations for the two cases(3Mev & 5Mev) are performed. As described above, E_{TAL} has the smaller value in the case of the low e_b (3Mev) than that in the other case. This fact means that the LIB input energy into the AL layer is used more efficiently in case of 3Mev. But the implosion efficiency is small in the low e_b case, compared with the low e_b case, compared with that in the other case. This fact comes from the following point: the rapid increase of the pusher temperature leads to the appearence of the strong shock wave and the strong preheat. In the case of e_b=3Mev, T_{DT} has a larger value than that in the other.

1-D LIB duration time

As shown in the above section, it is important that the input energy is deposited during a relatively long time interval in the tamper. The comparison between two cases of τ_b=35nsec and 55 nsec is presented. As is expected, the preheat temperature is low in the case of the long time duration, compared with that in the other case. But the implosion efficiency has a low value for the case of the longer time duration. For the longer time duration, the input energy at the later stage of the LIB time duration can not contribute to the target implosion, because the only energy which is deposited far before the void closure time contributes to the implosion fficiently. The input energy which is deposited near or after the void closure time, cannot be converted to the fuel kinetic energy.

1-E Target radius

The void closure time is strongly depends on the target radius, because the implosion velocity is nearly same in many usual case and $2\text{-}3\times10^7$ cm/s. Therefore to realize the relation of $\tau_b \ll \tau_v$ (void closure time) the large void target should be chosen, except the considerations about the problems of the Rayleigh-Taylor (R-T) instability. The implosion efficiencies and the other fusion parameters have the better values for the larger target.

1-F LIB input energy

In Fig.5, the target gain is plotted for the LIB total input energy. Only the DT total mass is optimized and the other parameters are shown in Fig.5. The gain curve is not flat and increases with the increase in the input energy. This fact comes from the following: the required minimum input energy is above about several hundred kJ to 1 MJ for the fuel compression of the reactor size target. Therefore it is important that the larger input energy should be employed in a reactor system in the range of several MJ input energy except the reactor problems.

1-G Nonuniformity

The another important issue is the uniform implosion. The R-T instability prevents the target from the uniform implosion and gives the upper limit of the

target radius. The nonuniform beam illumination and the target nonuniformity itself also prevent the target from the uniform compression. The numerical analyses for the effect of the nonuniform implosion on ρR have been done by the 3-D numerical computations.[1] The results show that the restrictions for the nonuniformity of the implosion acceleration should be less than 2.7% for the volume compression ratio of 1oooo.

2. Effect of Numerical Viscosity on ICF Parameter

In numerical computations in ICF target researches, a numerical viscosity is usually employed for a shock phenomena description. The numerical dissipation strongly depends on the viscosity. The viscosity depends on the employed space mesh width. Figure 7 shows the effect on the space profiles of ion temperature, velocity and mass density in the DT fuel at the void closure time. The improved numerical method (PSM) for a shock description is presented in Fig. 8. The method is based on both the Glimm method and FDM[2].

References

1)S. Kawata and K. Niu, J. Phs. Soc. Jpn., 53(1984)3416.

2)S. Kawata and K. Niu, submitted to the proceeding of 2nd Int. Workshop on Mathematical Aspects on Fluid and Plasma Dynamics, held in Univ. Paris-orsay, June 1985.

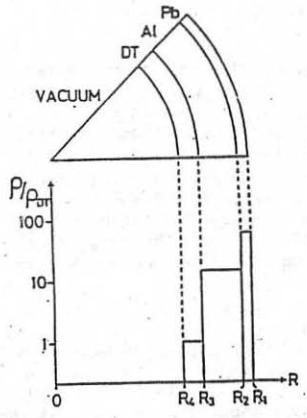


Fig.1 LIB target structure

INPUT BEAM ENERGY	E_b	5MJ
BEAM-PARTICLE ENERGY	e_b	5MeV
BEAM DURATION TIME	τ_b	35nsec
MAXIMUM BEAM INCIDENT ANGLE	θ_m	60degrees
BEAM POWER		$t^{2.5}$
TARGET RADIUS	r_t	5mm
	C_{AL}	0.8
TOTAL DT MASS	M_{DT}	1.0mg

Table 1

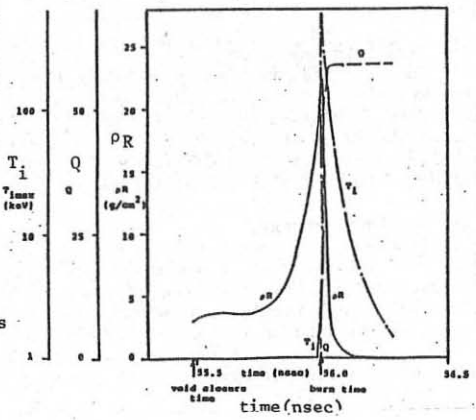


Fig. 2
Time sequences for density-radius product, target gain Q and ion Temperature T_i.

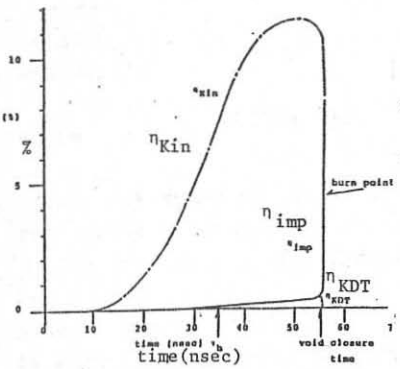
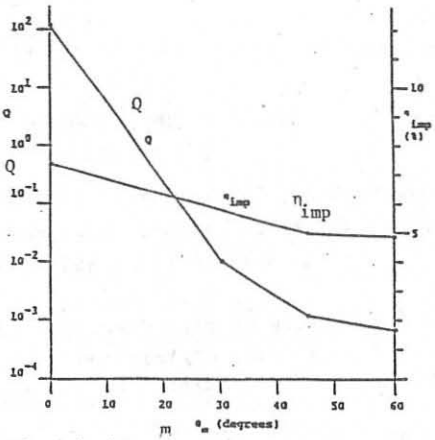
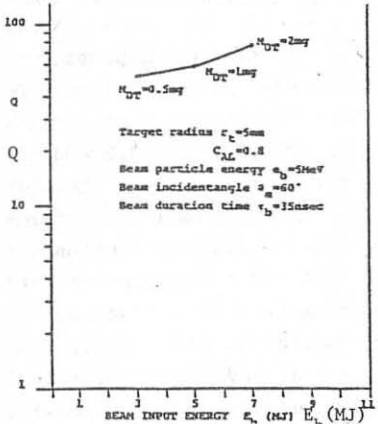


Fig.3 Implosion efficiency



Fig,4 incident angle of LIB versus implosion efficiency & target gain Q.



Fig,5 Target gain versus LIB input energy

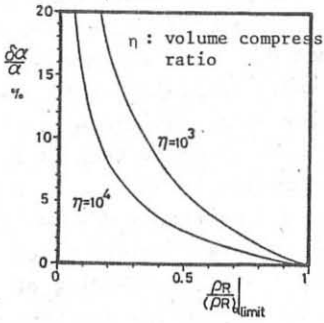
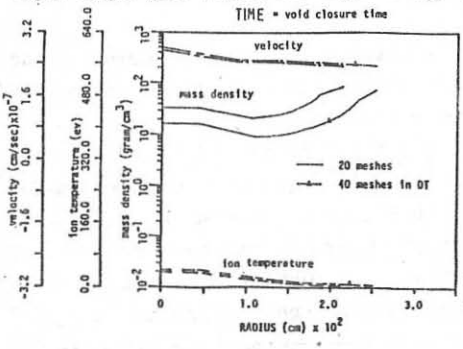


Fig.6 nonuniformity versus ρR.



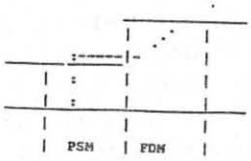


Fig.8 PSM(Mixed FDM and Glimm method).

Fig.7Effect of artificial viscosity on space profiles.

STUDY OF THE IMPLOSION OF WIRE ARRAYS AT 1 MA CURRENT PULSES

Baksht R.B., Datsko I.M., Kovsharov N.F., Loskutov V.V., Luchinsky A.V., Mesyats G.A., Ratakhin N.A., Sorokin S.A., Stas'ev V.P., and Fedusshak V.F.

Institute of High Current Electronics of the USSR
Academy of Sciences Siberian Division
634055 Tomsk, USSR

The paper reports the results of a study of fast implosion of wire arrays on "SNOP" installations [1] with the following electrical parameters: current rise time 60 ns, maximum current amplitude 0.6 - 1.5 MA, maximum generator output power 0.2 - 1 TW. In early works [2] on implosion of wire arrays it was shown that under some conditions the implosion occurred somewhat later and at lower velocity than it follows from a simple prediction of the formula $F = ma$. We supposed that one of the reasons for such a discrepancy may be "capturing" a part of current by low-density plasma layers which appear inside the wire array as a result of the spreading of the plasma of individual wires. In this case effective confinement of the individual wire plasma by the self-magnetic field will make better the implosion dynamics.

In order to understand the phenomenon of the wire array implosion, we first dwell on the experimental results we obtained for the conditions when there was no confinement of the individual-wire plasma. Figure 1 shows the current and the power of X-radiation obtained on implosion of an array of 6 glass-enclosed copper wires with total mass 34 $\mu g/cm$. Herein, a streak photo of the wire-array implosion is given. It can be seen that about 20 - 30 ns from the instant of current appearance, separate luminous columns from individual wires merge in a single luminous cylindrical column. The implosion time was cal-

culated from the formula obtained in terms of a zero-dimensio - nal model:

$$X(\theta) = 1 - 0{,}33\,\beta\theta - 0{,}024\,\beta^2\theta^2 \ldots$$

where

$$X = r/r_0;\quad \theta = (t/t_{фр.})^4;\quad \beta = 10^{-2} J_0^2 t_{фр.}^2 (N-1)/4 m r_0^2 N;$$

r_0 is the array initial radius, cm; $t_{фр.}$ and J are the current pulse rise time and amplitude, S and A, respectively; m is the array mass per unit length, $g \cdot cm^{-1}$; N is the number of wires in the array. It was assumed that the maximum im - plosion factor is equal to ten. The calculated implosion time is marked by an arrow on the oscillograms. It has been revealed that the experimental time of implosion of the wire array dif - fers from the calculated one by 10 - 15 ns. The difference be - tween calculated and experimental values of the time increases with increasing the array mass. All this suggests that the ef - fective current that accelerates the bulk of the matter is no - ticably less than the recorded one. In order that experimental velocity and time of implosion of relatively light wire arrays would fit to calculated values, it is necessary to assume that the matter accelerates at least 1.5 - 2 times slower than it follows from a simple calculation.

We suggest the following mechanism to explain the experi - mental data. After the explosion of individual wires the plasma formed expands into vacuum. As the radius of individual plasma columns increases, the opposing magnetic field inside the wire array reduces. A simple estimation predicts that in our case the field reduction is rather essential. Really, the field can be defined by the following expression

$$H \approx \frac{2I}{\rho c N} - \frac{N-1}{N}\,\frac{I}{c r},$$

where ρ is the radius of an individual plasma column. Thus, the plasma may fill in the interior of the array practically freely. In this case, as a 1-D MHD calculation shows [3], the internal plasma layers of relatively low density have higher both temperature and conductivity. As a result, these layers "capture" a significant part of current and accelerate towards the axis before than the bulk of the matter does it.

Let now consider some consequences from the mechanism sug-

gested. First of all, the above-noted decrease of the accelerating force leads to a statement that only 30 - 40 % of the total current passes through the bulk of matter. Actually, we have for the force the following expression $F \sim I_0^2 - (I_0 - I_1)^2 \approx \approx 0{,}5\, I_0^2$ from which we obtain $I_1 \approx 0{,}3\, I_0$. I_1 is the current flowing through the bulk of matter.

From the above-discussed the following conclusion can be drawn. In order to prevent the "capture" of a significant fraction of current by a small part of the matter, it is necessary to achieve the confinement of the plasma in individual columns by self-magnetic field. To be convinced of the validity of the latter suggestion we carried out the following experiment. An array of four glass-enclosed copper wires of a total mass 24 μg/cm was made. At a total current through the array of 830 kA more than 200 kA fall at each of them. Figure 2 shows typical current waveforms, an X-ray diode radiation pulse form, and a streak photo of the wire array implosion. In this regime, in contrast to the earlier experiments, individual columns remain until 60 - 70 ns after the beginning of current passage (Fig.3). It can be seen that in this regime the opaque zone forms at the axis just before the implosion. Calculated implosion time marked with arrows of the current waveforms and streak photo practically coincide to the experimental data. With this, the X-radiation pulse duration shortened down to 10 - 15 ns and its energy increased 2 - 2.5 times in the spectral range of 8 - 12Å.

Thus, increasing the current per wire up to values sufficient to confine the plasma in the column promotes the suppression of the precursor and the improvement of the implosion dynamics. It should be however noted that some part of the plasma goes out from the column, nevertheless, what can be well seen from shadowgrams, i.e. some plasma blobs separate from plasma columns as early as 30 - 40 ns after the beginning of current passage.

I. Бакшт Р.Б., Дацко И.М., Лучинский А.В. и др. Письма в ЖТФ, 1983, 9, 19, 1192-96.

2. J.Pearlman et al. Fourth Int. Conf. on Ion and Electron Beams, 1981, 1, 271-8.

3. Бакшт Р.Б., Лоскутов В.В. и др. ЖТФ, 1984, 54, 10, 1927-32.

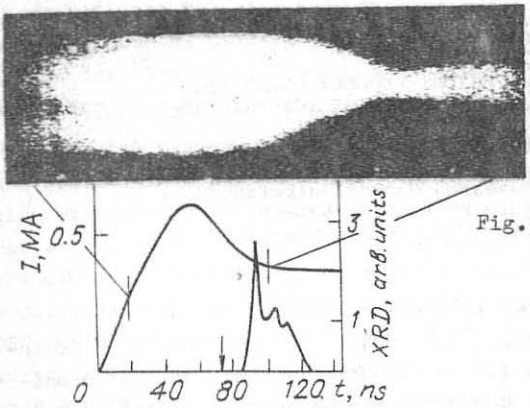


Fig.1. Load current, X-ray and visible streak photograph of a wire array. m = 34 μg/cm.

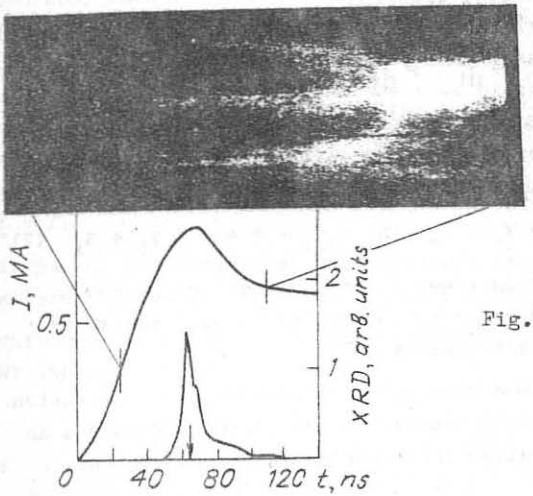
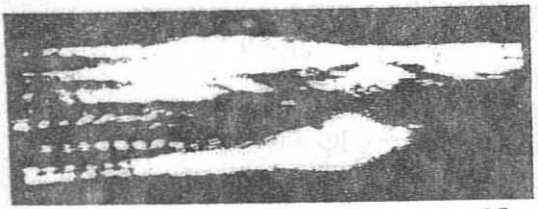


Fig.2. Load current, X-ray and visible streak photograph of a wire array. m = 24 μg/cm.

Fig.3. Laser shadow streak photograph of a wire array. m = 24 μg/cm.



EFFECTS OF FUSIONS PRODUCT TRANSPORT ON BURN CHARACTERISTICS OF ICF-PELLETS

Gerald Kamelander

Austrian Research Center Seibersdorf
Institute of Reactor Safety
Lenaugasse lo, A-lo82 Vienna

The computer program EUMOD is a new version of the well known ICF-simulation code MEDUSA [1]. EUMOD has been developed to investigate the effects of fusion product transport on the detonation of ICF-pellets. The EUMOD program bases just as Ref. [1] on the solution of the energy equation

$$C_V \frac{dT}{dt} + B_T \frac{d\rho}{dt} + p \frac{dV}{dt} = S \qquad (1)$$

where $C_V = (\frac{\partial U}{\partial T})_\rho$ and $B_T = (\frac{\partial U}{\partial \rho})_T$. U is the internal energy. Equ.(1) is solved for the ions as well as for the electrons. The source term is given by

$$S_e = H_e + K + J + Y_e + X_e \qquad S_i = H_i - K + Q + Y_i + X_i \qquad (2)$$

H means the heat conduction flow, K the ion electron exchange rate, Y the reaction energy, J the bremsstrahlung, Q the shock heating and X the externals sources.

In Ref. [1] it is assumed that the kinetic energy of the fusion products is deposited instantenously to the plasma. EUMOD has an option to solve the so-called BFP-equation (Boltzmann-Fokker-Planck) [2]

$$\frac{1}{v}\frac{\partial \varphi}{\partial t} + \Omega \nabla \varphi + (\Sigma_a + \Sigma_s)\varphi = \frac{\partial}{\partial E} S\varphi + \qquad (3)$$

$$T\left[\frac{\partial}{\partial \mu}(1-\mu^2)\frac{\partial}{\partial \mu} + \frac{1}{1-\mu^2}\frac{\partial^2}{\partial \omega^2}\right]\varphi + W(E,E')\varphi + Q$$

where S(E) and T(E) are the Fokker-Planck-coefficients, W(E,E') the inscattering operator and Q the external source. Equ. (3) allows for wide angle Coulomb scattering and nuclear elastic scattering [2,3].

Studying the transport problems in exploding dense fuel pellets the hydrodynamic plasma motion should be taken into consideration writing the BFP-equation in the modified Eulerian representation. In Ref. [4] it is shown that the transformation of the BFQ-equation into the modified Eulerian picture leads to a modification of the FP-coefficients S(E) and T(E), so that the DSN-method applied by Ref. [2] to solve equ. (3) can be used to solve the modified BFP equation. A transport modul basing on this equation has been added to EUMOD. As an example a compressed homogeneous DT-pellet with a confinement parameter (ρ.r) = 1,673 g/cm^2, a density of 418 g cm^3 and an initial pellet temperature of o,9 kev with an hot spot [8] of 5,9 kev is presented. Figure 1 shows the rise of the central ion temperature as function of the time. Figure 2 presents typical ion spectra in the center and on the edge of the pellet. The effect of application of transport theory is exhibited by figure 3 [9].

It may be concluded that the transport method [2] is a fair alternative to the tracking formalisme of Refs [5, 6, 7].

This work is supported by Austrian FONDS ZUR FÖRDERUNG DER WISSENSCHAFTLICHEN FORSCHUNG.

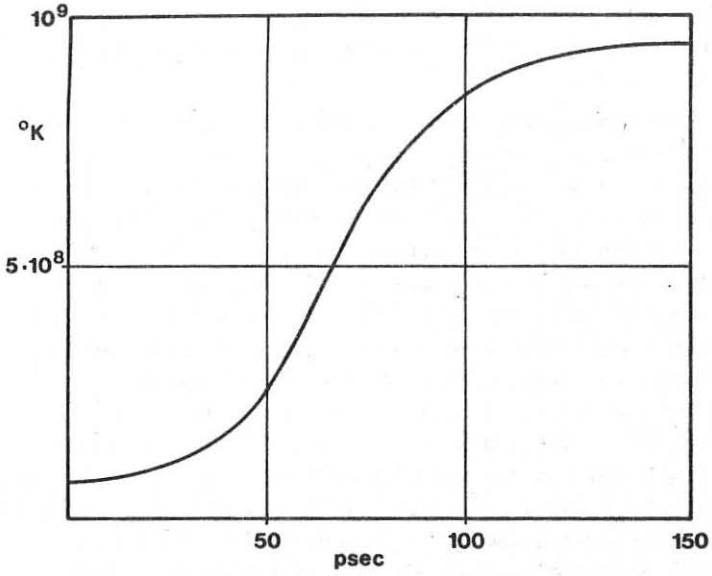


figure 1 Central ion temperature vs. time

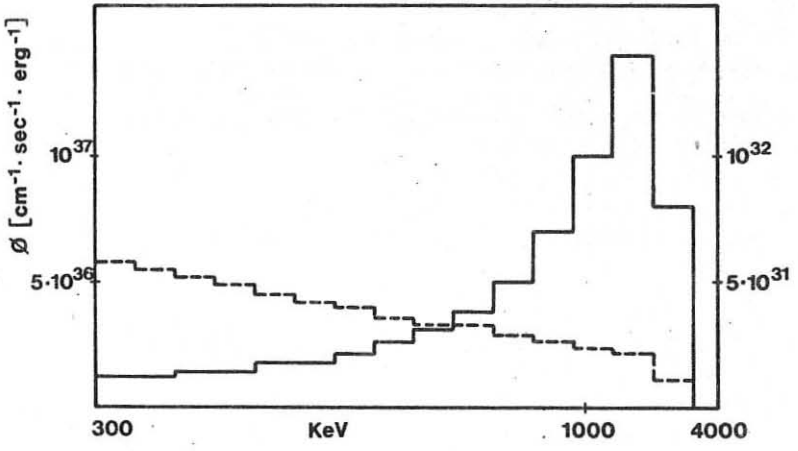


figure 2 Particle flux Ø vs. energy, (a) pellet center
(b) region near pellet surface, 1.25 psec after ignition

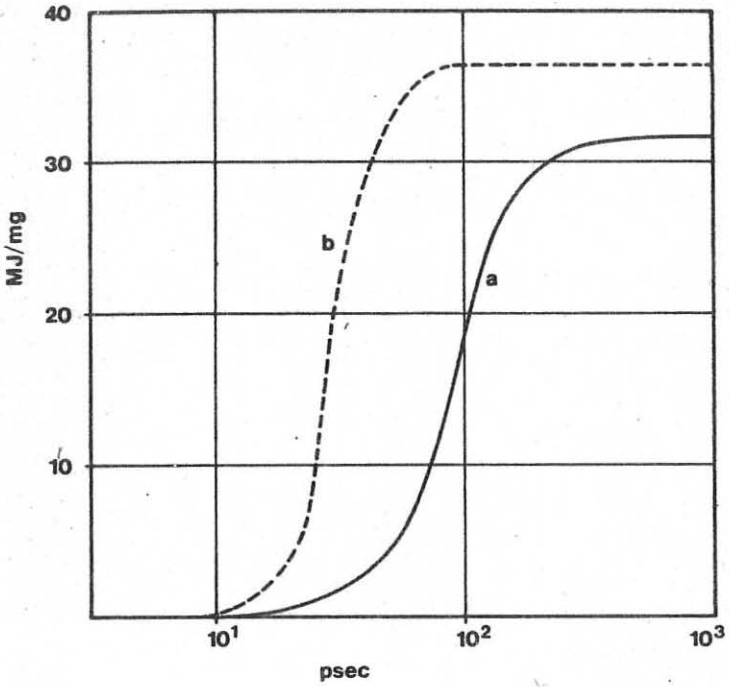


figure 3 Fusion energy versus time after ignition
a) with and b) without transport theory

REFERENCES

[1] J.P.CHRISTIANSEN et al., Computer Phys. Commun. 7, 1974
[2] K.PRZYBYLSKI, J.LIGOU, Nucl.Sc.and Eng.,81, pp.92-1o9,1982
[3] G.KAMELANDER, Nucl.Sc.and Eng.,86, 1984
[4] T.M.TRAN et al., Atomkernenergie 36, Lfg.3, 198o
[5] O.N.JARVIS, J.Phys.G., Nucl.Phys., 2, No.8
[6] G.A.MOSES, Nucl.Sc.and Eng.,64, pp.49-63, 1977
[7] G.S.FRALEY et al., Phys. Fluids, 17, 1974
[8] A.KUMAR, J.LIGOU, Trans.Am.Nucl.Soc.,47, p.143, 1984
[9] G.KAMELANDER, Trans.Am.Nucl.Soc.,48, 1985, in print

F

plasma heating and current drive

Full-Wave Calculations of the O-X Mode Conversion Process

F.R. Hansen[+], J.P. Lynov[+], C. Maroli[++], and V. Petrillo[++]

[+] Association EURATOM-Risø National Laboratory, DK-4000 Roskilde, Denmark

[++] Istituto di Fisica del Plasma, Association CNR-EURATOM. Via Bassini 15, I-20133 Milano, Italy

Abstract

A two point boundary value problem has been formulated and numerically solved for the O-X mode conversion process, which is relevant to a scheme[1] for application of ECRH in a high-density tokamak. The conversion efficiency is determined and compared to theoretical results[2] obtained in the WKB limit.

Introduction

The conversion between ordinary waves (O-waves) and extraordinary waves (X-waves) occurs in an inhomogeneous plasma near the position of the plasma cut-off ($\omega=\omega_{pe}$) if the waves propagate obliquely and near an optimal angle to the B-field. This mode conversion process is the basis of a scheme[1] to apply ECRH to a high-density tokamak, where $\omega_{peo} > \omega_{ceo}$. Theoretical calculations of the conversion efficiency of this process have previously been performed in the WKB limit (see e.g. Ref. 2). In this paper we describe how a two point boundary value problem of the conversion process can be formulated without making the WKB assumption, and we report some numerical results.

Basic equations

We consider a plasma in a Cartesian coordinate system with a density gradient in the x-direction and a homogeneous B-field orientated along the z axis. By assuming that the plasma is cold and

the wave frequency, ω, is so high that ion motions can be neglected, we find that the wave propagation is described by the equation

$$\frac{d\bar{F}}{d\zeta} = \bar{\bar{A}} \cdot \bar{F} \qquad (1)$$

where $\bar{F} = (E_y, E_z, cB_y, cB_z)^T$, $\zeta = k_o x$, $k_o = \omega/c$, and the elements in $\bar{\bar{A}}$ depend on $X(\zeta) = \omega_{pe}^2(\zeta)/\omega^2$, $Y = \omega_{ce}/\omega$, $N_y = k_y c/\omega$, and $N_z = k_z c/\omega$.

The normalized plasma density, X, is assumed to vary with ζ as

$$X = \begin{cases} X_1 , & \text{for } -\infty < \zeta < 0 \\ X_o + (X_1 - X_o)(1-(\zeta/a)^2)^3, & \text{for } 0 < \zeta < a \\ X_o , & \text{for } a < \zeta < \infty \end{cases}$$

In each of the outer regions where X is constant, the general solution to (1) can be written as a sum of four plane waves, where each wave can be identified as either an O- or an X-wave propagating or damped either to the left or to the right. We will consider the case where $X_1 < 1 < X_o$, and where the solution for $-\infty < \zeta < 0$ is a sum of an incoming O-wave and outgoing O- and X-waves, while only outgoing waves are present for $a < \zeta < \infty$. Requiring simple continuity of the components of $\bar{F}$ across $\zeta = 0$ and $\zeta = a$ results in four linear equations, two for each boundary, linking the values of the $\bar{F}$ components at $\zeta = 0$ and $\zeta = a$ together. With these boundary conditions, Eq. (1) can be solved for $0 < \zeta < a$ by use of the program[3] COLSYS which is based on a spline collacation method.

Results

After finding the solution to (1) with the appropriate boundary conditions, the actual values of $\bar{F}(0)$ and $\bar{F}(a)$ determine how much power that is carried by the various plane waves in the outer regions, so the power conversion efficiency, η, from the incoming O-wave to the outgoing X-wave is easily calculated. In Figs. 1 and 2 the crosses show some full-wave values of η versus N_z

for two different values of a, corresponding to two different values of the normalized scale length, L, determined by $(dX/d\zeta)^{-1}$ calculated at ζ_o, where $X(\zeta_o) = 1$. The theoretical value of η in the WKB limit is given by[2]

$$\eta = \exp\{-\pi L \sqrt{\tfrac{Y}{2}}[(N_z - N_{z,opt})^2 \cdot 2(1+Y) + N_y^2]\} ,$$

$$N_{z,opt} = \sqrt{\frac{Y}{Y+1}}$$

and is shown by a solid line in the figures. We see that there is good agreement for large values of L, but that the theory underestimates η for small L and non-optimal values of N_z.

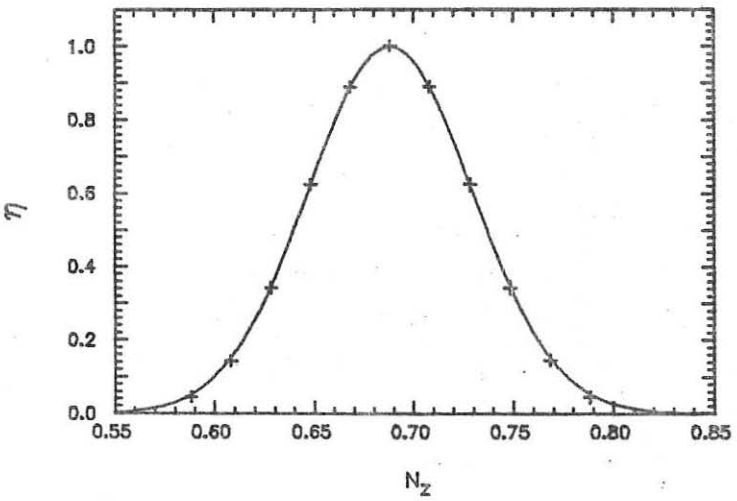


Fig. 1. Variation of the O-X mode conversion efficiency, η, for varying N_z. The crosses mark the full-wave results and the solid line shows the theoretical result in the WKB limit. The parameters are $X_o = 1.5$, X_1, $= 0.5$, $Y = 0.9$, and $a = 20\pi$, corresponding to $N_{z,opt} = 0.6882$ and $L = 36.6$.

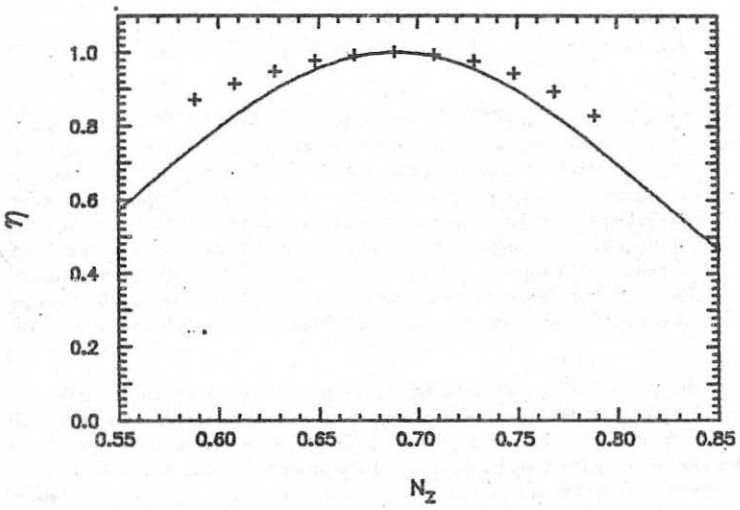


Fig. 2. Same as Fig. 1 but with a = 2π, corresponding to L = 3.66.

References

1) F.R. Hansen, J.P. Lynov, and P. Michelsen (accepted for publication in Plasma Physics and Controlled Fusion).

2) E. Mjølhus (1984). J. Plasma Phys. 31, 7.

3) U. Ascher, J. Christiansen, and R.D. Russell (1979). Math. Comp. 33, 659.

Heating and Confinement in the Doublet III Tokamak with Electron Cyclotron Heating*

by

S. Ejima, G. Jahns, S-H Lin,† C. Moeller, R. Prater, R. Snider
GA Technologies Inc., San Diego, California 92138, U.S.A.

Electron Cyclotron Heating (ECH) experiments on the Doublet III tokamak using inside launch of the extraordinary mode have shown effective bulk electron heating, with plasma stored energy increases of up to 30 kJ and central electron temperature increases up to 2.5 keV. The confinement time for discharges dominated by ECH was found to be similar in magnitude and scaling to that for discharges dominated by neutral beam injection, even though the power deposition profile for ECH discharges appears to be much narrower than for neutral beam heated discharges [1,2]. Even above the calculated extraordinary mode cutoff density, for which the observed power density profile appears to be broad, perhaps as broad as in the beam heating case, the energy confinement time does not deteriorate [1].

In this study, the ECH power incident on the plasma was between 400 kW and 700 kW, at a frequency of 60 GHz (for which the resonance corresponds to a magnetic field of 2.14 T). The power was launched from the inside wall of the tokamak, at an angle 30 degrees from the radial in the toroidal direction of the plasma current. About 70% of the generated power is launched with right-hand elliptical polarization as a pure extraordinary wave, and about 6% is in the cross polarization in the ordinary mode. Ray tracing calculations using the Toray code [3] show that for the magnetic resonance set to the plasma center the wave absorption in the plasma near the resonance is above 90% at low densities, but as the density is increased near a line-averaged density of $\bar{n}_e = 5.6 \times 10^{13}$ cm^{-3} the absorption falls rapidly due to wave refraction away from the resonance and to a decrease in wave damping with density. This characteristic density will be referred to as the cutoff density, although its exact value depends on the density profile and the launcher geometry, and the calculation neglects the effects of wave reflection at the plasma boundary.

The Doublet III tokamak was operated in the expanded boundary configuration, which under suitable conditions exhibits enhanced confinement characteristics with neutral beam heating, especially at injected power above 2 MW [4]. Plasma currents between 200 kA and 800 kA were run, with the toroidal field at the plasma center set at 2.14 T. The largest density range of the ohmic target plasma, $\bar{n}_e = 1.2 \times 10^{13}$ cm^{-3} to 10.1×10^{13} cm^{-3}, was available at a plasma current of 500 kA. The working gas was deuterium, the plasma elongation was about 1.6, and discharges were selected for those exhibiting clear sawteeth on the soft x-ray emission, since confinement in sawtoothing discharges is usually better.

Discharges with density below the cutoff and above the cutoff exhibit similar increases in plasma stored energy. Figure 1 shows data from such discharges; in both cases the total plasma stored energy, determined from an analysis of the magnetic data, shows an increase of about 21 kJ from the ohmic state. For discharge (a), the line-averaged density

* Work supported by U.S. Department of Energy contract DE-AT03-84ER51044

† Present address: Western Research Corporation, San Diego, CA

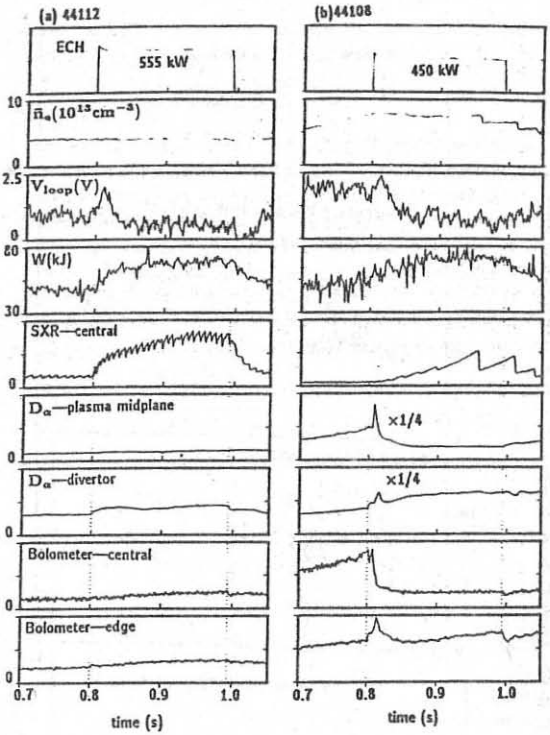


FIG. 1. Plasma reaction to ECH for density (a) $\bar{n}_e = 3.5 \times 10^{13}$ cm^{-3}, below the cutoff density and (b) $\bar{n}_e = 9.6 \times 10^{13}$ cm^{-3}, above the cutoff. The plasma current is 500 kA, and the toroidal field is 2.15 T which places the magnetic resonance near the plasma axis at $R = 143$ cm. The density shown as $\bar{n}_e$ is the signal from a chordal interferometer; determination of the actual line-averaged density requires fitting information from the three interferometer chords.

is 3.5×10^{13} cm^{-3}, and it remains constant during the heating pulse. The voltage on the plasma, which is current regulated, drops from 1 V (ohmic power 520 kW) to 0.6 V (ohmic power 280 kW) with the application of 555 kW of ECH, which implies a modest energy confinement decrease from 88 msec during the ohmic phase to 81 msec during ECH. Discharge (b) has a line-averaged density of 9.6×10^{13} cm^{-3} (central density from Thomson scattering of 14.8×10^{13} cm^{-3}), far above the cutoff density, but the energy confinement time remains about 80 msec, quite close to that in the low density discharge (a).

The ohmic phase of the discharge of Fig. 1(b) lies at the extreme high end of the density range of discharges attainable in Doublet III at this toroidal field. The strong D_α emission from the plasma midplane and the high power recorded on the bolometer which looks centrally (i.e., radially) across the plasma midplane, indicate that the plasma must be interacting strongly with the centerpost limiters, rather than being a discharge with a well developed divertor. When the ECH is applied, the plasma quickly detaches from the limiter, the midplane D_α and radiated power drop, and the energy confinement time increases. In this discharge, ECH causes the plasma energy to increase even though the total input power decreases (that is, the decrease in ohmic power when ECH is initiated is

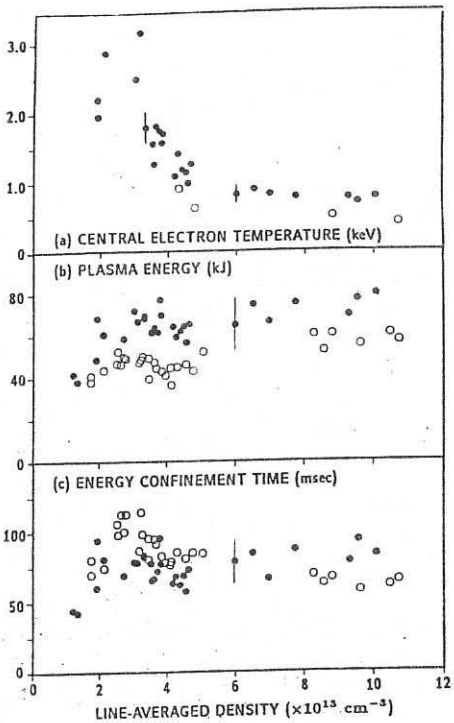


FIG. 2. Central electron temperature T_e from Thomson scattering, total plasma kinetic energy W from MHD analysis of magnetic signals, and gross energy confinement time τ_e, as a function of line-averaged density, for ohmic (open circles) and for ECH discharges (filled circles). The plasma current is 500 kA, the toroidal field is 2.15 T, and the ECH input power is 450 to 700 kW.

larger than the applied ECH power). Part of the improvement in confinement stems from the transition from what was effectively a limiter discharge to a true divertor discharge.

The central electron temperature, from Thomson scattering, is a strongly decreasing function of density for both ohmic and ECH discharges, but the plasma energy and the energy confinement time are nearly independent of density at densities above $\bar{n}_e = 2\times10^{13}$ cm^{-3}. The highest central temperatures are obtained at the lowest densities, with peak temperatures above 3 keV at this plasma current. This behavior is shown in Fig. 2a, and it suggests that the confinement time is independent of density, since ΔT_e is approximately inversely proportional to $\bar{n}_e$.

Figure 2b shows that the increase in plasma energy from the ohmic state to the ECH state is constant at about 20 to 25 kJ, from a line-averaged density of $\bar{n}_e = 2 \times 10^{13}$ cm^{-3} to $\bar{n}_e = 10 \times 10^{13}$ cm^{-3}, even though the cutoff density lies in the middle of that range at $\bar{n}_e = 5.6 \times 10^{13}$ cm^{-3}. A similar result can be seen for plasma energy confinement time, Fig. 2c. This figure indicates that the heating efficiency, which is best defined as the relative decrement in confinement time when the auxiliary power is applied, is constant over a density range that extends to about twice the cutoff density.

The scaling of the energy confinement time with parameters other than density shows a strong similarity to the scaling found for neutral beam heating in plasmas of the same divertor configuration [2]. In addition to the independence of density, both heating methods exhibit an energy confinement time which is proportional to plasma current, see Fig. 3, over a current range of 200 kA to 700 kA. Both are insensitive to the toroidal magnetic

field, although in the ECH case the toroidal field cannot be varied sufficiently to move the resonance outside the inner half of the minor radius, on either side of the plasma axis (a range of 1.7 to 2.5 T). And both heating methods show a similar decrease in confinement time as the power is increased.

The similarity of the energy confinement scaling for these heating methods implies that the advantages expected to accrue to ECH over neutral beam heating, due to the much more localized heat deposition near the plasma center of ECH, are not being realized. The determining factor for energy confinement seems to be the plasma transport properties in the outer half of the plasma. This suggests that if this effect can be understood and controlled, significant improvements in tokamak confinement may be possible; and if not, then auxiliary heating systems may not be required to heat the plasma near the center. This would ease the requirements on beam energy for neutral beam heating, or allow ECH at higher densities than theoretically expected, since wave penetration to the plasma center would not be required.

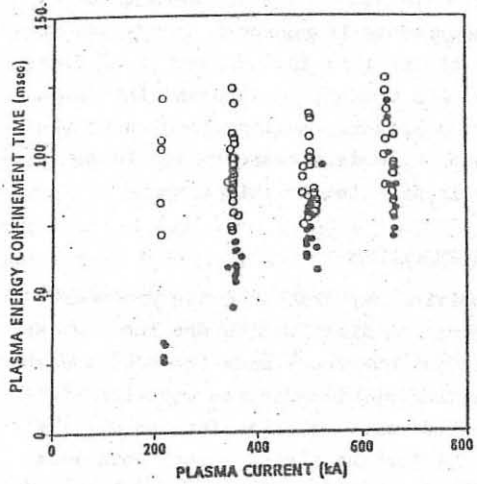


FIG. 3. Dependence of gross energy confinement time τ_e on plasma current, for ohmic discharges (open circles) and for ECH discharges (filled circles). Toroidal field is 2.15 T, plasma density is 2 to 6 $\times 10^{13}$ cm^{-3}, and the ECH power is 450 to 700 kW.

References

[1] R. Prater, K.H. Burrell, S. Ejima, G.L. Jahns, S.H. Lin, C.P. Moeller, and the Doublet III Physics Group, "Summary of Electron Cyclotron Heating Physics Results from the Doublet III Tokamak," GA Technologies report GA-A17939 (1984); submitted to Nuclear Fusion.

[2] K.H. Burrell, R. Prater, S. Ejima, et al., in *Plasma Physics and Controlled Nuclear Fusion Research*, (Proc. 10th Int. Conf., London, U.K., 1984), v. 1, p. 131 (International Atomic Energy Agency, Vienna, 1985).

[3] A.H. Kritz, H. Hsuan, A.C. Goldfinger, D.B. Batchelor, in *Heating in Toroidal Plasmas* (Proc. 3rd Joint Varenna-Grenoble Int. Symposium, Grenoble, 1982), v. 2, p. 707 (International School of Plasma Physics, Varenna, 1982).

[4] N. Ohyabu, K.H. Burrell, J. DeBoo, et al., Nucl. Fusion 25, 49 (1985).

AN ECRH RAY-TRACING STUDY WITH MULTIREFLECTION AND MODE CONVERSION

Z.X. Zhang H.Y. Jiang
Institute of Physics, Academia Sinica, P.O.Box 603
Group A41, Beijing, China

INTRODUCTION

Electron cyclotron resonance heating experiments have been carried out on many machines(1-5). We note that on small machines (such as JFT-2, TOSCA) the experimentally measured energy absorption is usually twice or even higher than that of estimated according to the optical thickness. In order to understand this difference perhaps the real antenna pattern, multireflection at the wall of vacuum chamber and possible mode conversion should be taken into account. Our work is directed to this purpose.

USED FORMULAS AND CALCULATION PROCEDURE

The used equations for solving ray trace and the procedure for calculating the energy deposition distribution are the same as that used in ref.(6). For the extraordinary mode (x-mode) and the ordinary mode (o-mode) we use the Appleton-Hartree equation (formula (1) in ref.(7))as their dispersion relation for the density range under the cut-off density, for the electron Bernstein mode we use formulas (12) and (13) in ref.(8) as its dispersion relation. The used plasma temperature distribution, density distribution, and the magnetic field are as follows:

$$D(\rho,\theta,\phi) = D_0(1-(\rho/a)^{d_1})^{d_2} \quad (1)$$

$$T(\rho,\theta,\phi) = T_0(1-(\rho/a)^{T_1})^{T_2} \quad (2)$$

$$B_\rho = 0 \quad (3)$$

$$B_\phi = B_0/(1+\rho\cos\theta/R) \quad (4)$$

$$B_\theta = B_\phi \rho/(R\, q(\rho)) \quad (5)$$

$$q(\rho) = q_0 + (q_a - q_0)(\rho^2/a^2) \quad (6)$$

where (ρ, θ, ϕ) are the quasi-cylindrical coordinates, R is the major radius, a is the radius of plasma cross-section, $q(\rho)$ is the safety factor, the subscript "0" is corresponding to the value at the plasma center, d_1, d_2, T_1, T_2, D_o, T_o, q_a and q_o are constants.

The used formulas of absorption coefficient are taken from ref.(9) and different cases, including x-mode or o-mode, oblique propagation or perpendicular propagation, are identified. For electron Bernstein mode we use formula (9) in ref.(10) for absorption coefficient.

CALCULATED RESULTS UNDER JFT-2 PARAMETERS

The parameters for the antenna system used on JFT-2 outside launch experiments(3) are used. Due to the symmetry of the antenna system we consider only two horns, which locate in the same cross-section of the torus and above the equatorial plane. We use ten rays to simulate the two radiated beams, among them every five rays form a conic with a half angle of 8° and oblique to the major radius with an angle of 10°. The power distribution ratio between the central ray and the other four symmetrically distributed periphery rays are 2:1:1:1:1. The other used parameters are: major radius R=0.90m, minor radius a=0.25 m, central magnetic field B_o=1.0 (T), wave frequency f=28 GH_z, density parameters d_1=2.0 and d_2=1.5 (see formula (1)), temperature parameters T_1=2.0 and T_2=1.5 (see formula (2)), safety factor parameters q_o=1.6 and q_a=5.0 (see formula (6)).

The ten rays are traced, averaged energy absorption and deposition profile are obtained for different cases.

(A) O-mode, single passing through plasma, without mode conversion.

The single pass energy absorption (SPEA) versus central magnetic field B_o for this case is listed below.

B_o(T)	0.9	1.0	1.1	1.3
SPEA(%)	3.3	51.4	48.2	14.0

According to ref.(3) the experimentally measured energy absorption is about 80%, the absorption at B_o=0.9 (T) is obviously

stronger than that at B_0=1.1(T). These facts are different from the calculated characterictics.

(B) O-mode, quadruple passing through plasma, without mode conversion

The calculated energy absorption (MPEA) for this case versus the central magnetic field B_0 is listed below.

B_0 (T)	0.9	1.0	1.1	1.2
MPEA (%)	82.5	92.7	73.1	16.5

Now both MPEA value and the tendency of MPEA value versus B_0 are close to the experimental result. We see that the position of the absorption layer is sensitive to the central magnetic field B_0. When B_0 changes, the relative relation between the traces and the absorption layer changes asymmetrically.

(C) O-mode, ten-fold passing through plasma, without mode conversion

The calculated energy absorption (MPEA) for this case versus central magnetic field is listed below.

B_0 (T)	0.9	1.1
MPEA(%)	98.6	98.0

This tendency is different from that experimentally obtained. This fact means that after many reflections the wave polarization may be disturbed.

(D) O-mode to X-mode and to electron Bernstein mode.

We consider that the polarization of the wave may be more or less changed when it is reflected from the wall of vacuum chamber. As an extreme case we assume that the polarization of the wave will rotate an angle of 90 during a single reflection. Thus the O-mode will be changed to the x-mode when it is reflected from the wall in the inner side of the torus. Then the x-mode propagates toward to the outside of the torus. We assume that the x-mode will be converted fully to the electron Bernstein mode at the upper-hybrid resonance layer, then the electron Bernstein mode propagates toward to the plasma center.

The ray traces and energy deposition in this process are calculated, now only two rays are traced, which are the two central rays of the two conics. The summed energy absorption (SUEA) versus central magnetic field is listed below.

B_0(T)	0.9	1.0	1.1
SUEA(%)	53	98	98

where for the case of B_0=0.9(T), the electron Bernstein mode is not deeply penetrate into its absorption region. We see that the tendency of SUEA versus B_0 is different from experimentelly obtained result. This mode conversion process may not play an important role in experiments on JFT-2.

CONCLUSION

From above comparison between calculated and experimental results we conclude that in order to understand ECRH experiments on JFT-2 it is necessary to consider a few times of wave refleetion and to average over the radiating pattern. The mode conversion at the upper hybrid resonance layer seems not occurred. After many reflections the polarization of the wave is disturbed.

CALCULATIONS UNDER TOSCA PARAMETERS

Similar calculations were carried out under TOSCA parameters (4). The typical averaged energy absorption under T_0=250 eV for the case with mullireflection and without mode conversion is about 50%, which is close to the experimentally obtained result.

REFERENCES

1 V.V. Alikaev et al., Sov. Phys. JETP Letts, Vol.15, P.27 (1972)
2 V.V. Alikaev et al., JETP Letts, Vol. 35, P.140 (1982)
3 R.Prator and C.P. Moeller, Proc. 3rd Joint Varenna-Grenoble Int. Symp. on Heating in Toroidal Plasmas, Vol. II, P.635 (1982)
4 D.C.Robinson et al., ibid, Vol. II, P.647 (1982).
5 H. Hsuan et al., Plasma Physics and Controlled Fusion, Vol. 26, P.265 (1984).
6 Z.X. Zhang, Max-Planck-Institut für Plasmaphysik Report IPP 2/264, 1982.
7 E. Ott, B. Hui, and K.R. Chu, Phys. Fluid, Vol. 23, P. 1031 (1980).
8 F.De Luca and C. Maroli, J.Plasma Physics, Vol. 20, P.299 (1978).
9 M.Bonatici, Plasma Physics, Vol. 24, P. 629 (1982).
10 M.Bonatici et al., 3rd Joint Varenna-Grenoble Int. Symp. on Heating in Toroidal Plasmas, Vol. II, P.691 (1982).

PLASMA-INDUCED TM MODE TRANSPARENCY OF ELECTROSTATIC SHIELDS USED IN RF HEATING

D.W. FAULCONER and L. BRAL

Laboratoire de Physique des Plasmas-Laboratorium voor Plasmafysica
Association"Euratom-Etat belge"-Associatie"Euratom-Belgische Staat"
Ecole Royale Militaire-B1040 Brussels-Koninklijke Militaire School

INTRODUCTION

ICRH antennas are generally surrounded by an electrostatic shield, one of the functions of which is to suppress radiation in the $TM|_z$ mode ($\vec{e}_z \| \vec{B}_o$). However, contact of a low density plasma with the shield elements can impede this function /1/, allowing passage of TM flux with attendant risk of edge heating. A theoretical basis for studying this effect has been laid in Ref. 1 where the shield elements were modeled by an infinite array of parallel metallic ribbons situated in the interface of two dissimilar homogeneous magnetized plasmas (ribbons$\| \vec{B}_o$). A cold plasma dielectric model was used. Here we present interpretation of numerical results which follow from this theoretical model.

PROCEDURE AND DISCUSSION

To simulate shield conditions we consider a wave of TM polarization to be incident from a vacuum region on the

left of the shield array located at x=0. For a given incident wave amplitude at x=0 the ratio of power transmitted with shield, P, to that with no shield, P(NS), gives an effective power transmission coefficient. This ratio is studied as a function of density and shield geometry for parameters of the TEXTOR Tokamak: f= 27 MHz, B_0= 1.55T, N_h/N_d=0.1, $k_{||}$ = 0.1cm^{-1}, ribbon spacing= u= 1.1cm, ribbon width=v=variable; nonTEXTOR value $\nu_\alpha/\omega_\alpha=10^{-10}$ is set.

Figures 1 and 2 show peaks in power transmission coefficient which occur below the lower hybrid resonance density N_{LHR}. At resonance maxima the power flux is roughly half the unshielded value for v/u = 0.6. A notable reduction in peaking behavior is seen in Figure 2 with v/u = 0.8. The power transmission peaks correspond to resonances of travelling waves (harmonics relative to ribbon spacing) which are mediated by localized surface modes undergoing bounded resonance between adjacent ribbons (see Fig. 3 where a sweep in v at N_e, u = constant shows the effect of successive bounded resonances). Since the solution employs a truncation at $|n| = n_{max}$ (n=harmonic number) /1/, resonant contributions involving waves with $|n| > n_{max}$ are eliminated from the power flux. Thus for a given plasma density, n_{max} should be chosen larger than the |n| beyond which all travelling waves suffer cutoff; appropriate augmentation in n_{max} in proceeding up to N_{res} would show this density to be an accumulation point of resonances.

The localized resonating modes become evanescent above N_{res} (see p. 235 of Ref./2/ for their description without shield). This eliminates their resonant interaction with the travelling surface waves, a fact reflected in the precipitous drop in the power transmission coefficient at N_{res}. We must strongly qualify the applicability of our method in this evanescent region between N_{res} and N_{LHR} since the absence of resonant behaviour invalidates the

aforementioned criterion for choice of n_{max}. Numerically, even the largest choices of n_{max} are not sufficient to give a transmitted power flux matching incident flux in this region in the collisioness limit. One can plausibly associate this with markedly singular behaviour of the field at one edge of each ribbon. As collisions go to zero, the increasing singularity in amplitude of this edge field could compensate loss of collisional dissipation to give a net "collisionless" absorption in the limit. This would progressively distribute the transmitted power over harmonics with $|n| > n_{max}$ as collisions vanish.

CONCLUSION

Electrostatic shields do not shield the TM field component as supposed, at densities neighboring N_{LHR}. These relatively low densities could be rendered more probable by a possible heating field ponderomotive effect which would nonlinearly hunt for a density at which resonant transmission takes place.

REFERENCES

/1/ Faulconer, D.W.; 11th European Conference on Controlled Fusion and Plasma Physics, Aachen, 1983, European Physical Society, Vol. 7D, Part II, p. 123.

/2/ Allis, W.P., Buchsbaum, S.J., Bers, A.: Waves in Anisotropic Plasmas. M.I.T. Press, Cambridge, Massachusetts, 1963.

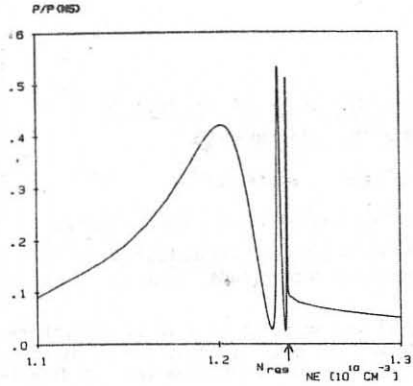


Fig. 1. Effective power transmission coefficient seen with v/u = 0.6, n_{max}=6, TEXTOR parameters; N_{LHR} is offscale at $N_{LHR}=1.75\times10^{10}$cm . Number of peaks is limited by n_{max}.

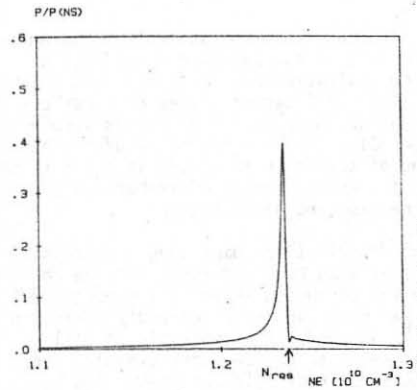


Fig. 2. Effective power transmission coefficient seen with v/u = 0.8, n_{max}=6, TEXTOR parameters; N_{LHR} is offscale at $N_{LHR}=1.75\times10^{10}$cm .

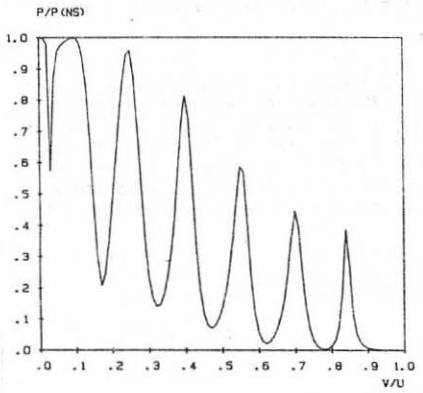


Fig. 3. Successive surface wave bounded resonances seen for varying ribbon width and fixed ribbon spacing with $N_e=1.237\times10^{10}$cm , n_{max}=6, TEXTOR parameters.

ELECTRON CYCLOTRON ABSORPTION AND EMISSION IN THE PRESENCE OF A SMALL POPULATION OF DRIFTING SUPERTHERMALS

M. Bornatici*, U. Ruffina* and E. Westerhof☆

*) Physics Department "A. Volta", University of Pavia, Pavia, Italy

☆) Association Euratom-FOM, FOM-Instituut voor Plasmafysica "Rijnhuizen", Nieuwegein, The Netherlands

The effect on electron cyclotron absorption and emission of a small superthermal population in motion relative to a Maxwellian bulk is investigated by applying the Lorentz transformation to the case in which the superthermal distribution is Maxwellian in the co-moving frame.

INTRODUCTION. It is well-known that the electron cyclotron absorption and emission can be sensitively affected by deviations of the electron distribution from the Maxwellian one[1]. At present, the evaluation of the actual form of the electron distribution for the cases of practical interest relies on numerical models which contain various approximations to the physical processes involved and whose validity remains to be assessed. Given the uncertainties of the existing self-consistent evaluations of the distribution function, it makes sense to examine the absorption (emission) for non-thermal model distributions which possess the main envisaged features of the expected distributions.

Here, we consider the case of an electron distribution comprising a superthermal population in motion relative to a Maxwellian bulk and such that the corresponding distribution is Maxwellian in the co-moving frame. The superthermal contribution to both the absorption and emission can be conveniently evaluated by applying the Lorentz transformation [2], which makes it possible to utilize the known dielectric tensor for a Maxwellian distribution, thus avoiding the complexity of the mathematics inherent to the direct calculation [3]. The absorption coefficient then is obtained from the energy balance equation [1], whereas the emissivity is evaluated from the (Lorentz-transformed) Kirchhoff law.

THE LORENTZ TRANSFORMATION OF THE DIELECTRIC TENSOR AND KIRCHHOFF LAW. We consider a group of electrons which move along the equilibrium magnetic field $\underline{B}_0 = B_0 \underline{\hat{z}}$ with uniform velocity v_0 relative to an observer in the laboratory frame, and apply the Lorentz transformation to the dielectric tensor in the co-moving frame (ε'_{ij}) to obtain the corresponding dielectric tensor in the laboratory frame (ε_{ij}). For wave propagation in the (x,z)-plane of the laboratory frame, the transverse (with respect to the streaming direction) components of ε_{ij} are given by [4,2]

$$\varepsilon_{ij} - \delta_{ij} = \gamma_0^2 (1 - N_\parallel \bar{v}_0)^2 (\varepsilon'_{ij} - \delta_{ij}) , \qquad i,j = x,y , \tag{1}$$

whereas for the longitudinal components ε_{iz}, i = x,y,z, one has [4,2]

$$\varepsilon_{xz} = \gamma_0(1 - N_\parallel \bar{v}_0)\,[\varepsilon'_{xz} + N_\perp \gamma_0 \bar{v}_0(\varepsilon'_{xx} - 1)]\,, \tag{2a}$$

$$\varepsilon_{yz} = \gamma_0(1 - N_\parallel \bar{v}_0)(\varepsilon'_{yz} + N_\perp \gamma_0 \bar{v}_0 \varepsilon'_{yx})\,, \tag{2b}$$

$$\varepsilon_{zz} = \varepsilon'_{zz} + 2N_\perp \gamma_0 \bar{v}_0 \varepsilon'_{xz} + (N_\perp \gamma_0 \bar{v}_0)^2(\varepsilon'_{xx} - 1)\,, \tag{2c}$$

with $\varepsilon_{ij} \equiv \varepsilon_{ij}(\underline{k},\omega)$ and $\varepsilon'_{ij} \equiv \varepsilon'_{ij}(\underline{k}',\omega')$, the wave frequency ω' and the refractive index $\underline{N}' \equiv \underline{k}'c/\omega' = N'_\perp \hat{\underline{x}} + N'_\parallel \hat{\underline{z}}$ in the co-moving frame are related to those corresponding quantities in the laboratory frame by [4,5]

$$\omega' = \gamma_0(1 - N_\parallel \bar{v}_0)\,\omega\,, \tag{3a}$$

$$N'_\perp = [\gamma_0(1 - N_\parallel \bar{v}_0)]^{-1} N_\perp\,, \tag{3b}$$

$$N'_\parallel = (1 - N_\parallel \bar{v}_0)^{-1}(N_\parallel - \bar{v}_0)\,, \tag{3c}$$

where $\gamma_0 \equiv (1 - \bar{v}_0^2)^{-\frac{1}{2}}$ and $\bar{v}_0 \equiv v_0/c$. As appears from (3), the streaming motion affects both the frequency and the refractive index and, hence, the dielectric tensor in a way that depends on the sign of $N_\parallel$. Therefore, information on drifting electrons can be gained from the asymmetry of the absorption and emission profile connected with the change of sign of $N_\parallel$ [3,6].

For the case of interest here, the distribution of the streaming electrons is taken to be an isotropic Maxwellian in the co-moving frame, so that the corresponding dielectric tensor ε'_{ij} is explicitly known in its fully relativistic form [7], the dielectric tensor ε_{ij} in the laboratory frame being then obtained by simply applying (1) - (3).

As for the emission of the superthermal population in the laboratory frame, this can be obtained by Lorentz-transforming Kirchhoff's law, that holds for a Maxwellian distribution in the co-moving frame. We note that the specific intensity in a non-dispersive medium (i.e., $N_r \equiv 1$, N_r being the ray refractive index) transforms as $(\omega'/\omega)^3$, as has been shown by Pomraning [5]. A straightforward generalization of Pomraning's derivation to dispersive media leads to the result that I/N_r^2 transforms as $(\omega'/\omega)^3$, where I is the specific intensity. Using this result and equation (3a) we find the transformed Kirchhoff law, relating the emissivity, η, in the laboratory frame to the corresponding absorption coefficient, α, to be given by

$$\eta = \frac{1}{\gamma_0(1 - N_\parallel \bar{v}_0)}\, N_r^2\, \frac{\omega^2 T_s}{8\pi^2 c^3}\, \alpha\,, \tag{4}$$

with the temperature T_s of the superthermal population being defined in the co-moving frame; η and α refer to the properties of the superthermal population only, while N_r incorporates the effects of both the bulk and the superthermal population.

NUMERICAL RESULTS AND DISCUSSION. The effect on the absorption profile of a small population of drifting superthermals has been investigated using the preceding relations. As an example, the numerical results for a Maxwellian bulk with $(\omega_p/\omega_c)^2 = 0.3$ and temperature $T_b = 1\,keV$, in the presence of superthermals with a relative concentration equal to $\eta = 5\,\%$, a temperature $T_s = 4\,keV$ and a streaming velocity $v_o/c = 0.2$, are shown for $N_\parallel = \pm 0.3$ in Figs. 1a and b; the normalized absorption coefficient $(c/\omega)\alpha$ is given as a function of the (bulk) profile variable $x_b \equiv (mc^2/T_b)(\omega_c/\omega - 1)$, for the first harmonic extraordinary (X) and ordinary (O) mode, respectively.

In Fig. 1a the main feature of the non-thermal profile is a double peaked structure which depends on the sign of $N_\parallel$: (i) for negative $N_\parallel$, the superthermals produce a hump far away in the low frequency wing of the thermal profile, the peak of the latter being slightly increased; (ii) for positive $N_\parallel$, the superthermal contribution to the absorption tends to pile up at frequencies just below the upper bound of the frequency range for which there is absorption $(N_\parallel^2 + (\omega_c/\omega)^2 - 1 \geq 0$, this condition being Lorentz invariant) yielding a second minor peak on the high frequency side of the absorption profile of the bulk and the peak of the latter being slightly shifted towards higher frequencies and increased by an amount somewhat larger than that corresponding to the case $N_\parallel < 0$. As it follows from (3a), for $N_\parallel < 0$, one has $\omega < \omega'$, i.e., the absorption of the superthermals occurs at frequencies lower than those for a thermal distribution; for $N_\parallel > 0$, instead, the absorption of the superthermals takes place at frequencies larger or smaller than those where the thermal absorption

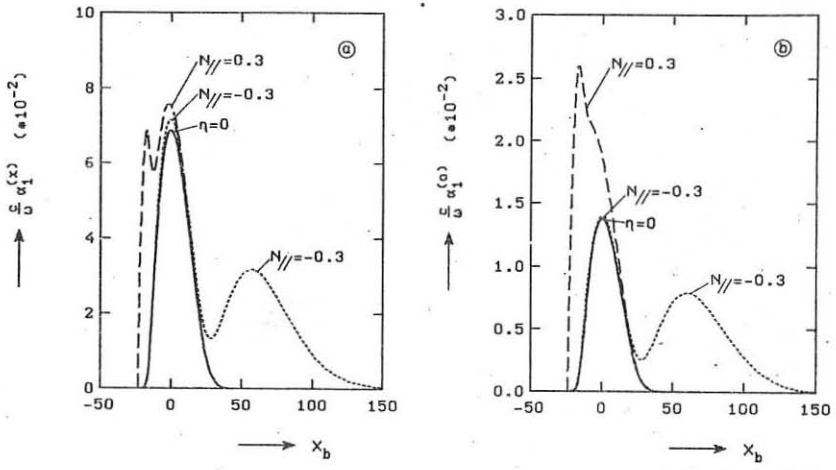


Fig. 1a: The normalized absorption coefficient $(c/\omega)\alpha_1^{(X)}$ of the first harmonic extraordinary mode vs. the profile variable $x_b \equiv (mc^2/T_b)(\omega_c/\omega - 1)$ for a Maxwellian bulk with $(\omega_p/\omega_c)^2 = 0.3$, temperature $T_b = 1\,keV$ and a superthermal population with relative density $\eta = 5\,\%$, temperature $T_s = 4\,keV$ and streaming velocity $v_o = 0.2\,c$, for $N_\parallel = \pm 0.3$.

Fig. 1b: Same as in Fig. 1a for the first harmonic ordinary mode.

occurs depending on whether $N_\parallel > \bar{v}_o/2$ (that is the case of Fig. 1a) or $0 < N_\parallel < \bar{v}_o/2$, the superthermal contribution being undistinguishable from the thermal one for $N_\parallel \approx \bar{v}_o/2$. The relative strength of the effect of the superthermals depends on the value of the effective parallel refractive index $N_\parallel^*$, given by (3c): For $N_\parallel < 0$ one has $|N_\parallel^*| > |N_\parallel|$ (i.e., one tends to be in the Doppler regime [12]) with the result that the superthermal hump is broader than the thermal profile, the corresponding height being determined by the balance between the increase of the absorption (of the X mode) due to the increase of the effective parallel refractive index and the concomitant decrease due to the lower density of the superthermals with respect to the bulk. For the case shown in Fig. 1a, the second effect prevails over the first one. For $N_\parallel > 0$, instead, $N_\parallel^*$ tends to be smaller than $N_\parallel$. For $N_\parallel \approx \bar{v}_o$, as is the case in Fig. 1a, the absorption of the superthermals is strongly affected by relativistic effects and limited to a narrow frequency range ($\Delta\omega/\omega \simeq T_s/mc^2$) on the high frequency side of the profile due to the bulk electrons and is significantly influenced by the superthermal contribution to the wave polarization.

As for the absorption profile of the first harmonic O mode, shown in Fig. 1b, a double peak structure is again present for $N_\parallel < 0$, whereas for $N_\parallel > 0$ the main feature consists of a single peak, the difference with respect to the corresponding profile of the X mode in Fig. 1a being due to the significantly different polarization of the two modes for small effective parallel refractive index.

Useful discussions with F. Engelmann are gratefully acknowledged.
This work was performed under the Euratom-FOM association agreement with financial support from ZWO, Euratom and the Ministero della Publica Istruzione of the Italian Republic.

REFERENCES.

1. M. Bornatic, R. Cano, O. DeBarbieri, and F. Engelmann, Nucl. Fusion 23, 1153 (1983).
2. S. Tamor, Nucl. Fusion 18, 229 (1978).
3. I. Fidone, G. Granata, and R.L. Meyer, Plasma Phys. 22, 261 (1980); I. Fidone et al., Phys. Fluids 23, 1336 (1980).
4. D.B. Melrose, Plasma Phys. 15, 99 (1973).
5. G.C. Pomraning, *The Equations of Radiation Hydrodynamics*, Pergamon, Oxford (1973).
6. TFR Group and I. Fidone, Phys. Rev. A 24, 2861 (1981).
7. M. Bornatici and U. Ruffina (submitted to Il Nuovo Cimento).

SCATTERING OF THE HEATING WAVE OFF ION WAVE IN ELECTRON CYCLOTRON RESONANCE HEATING

J.A. Heikkinen and S.J. Karttunen

Technical Research Centre of Finland
Nuclear Engineering Laboratory
P.O.Box 169, SF-00181 Helsinki, Finland

ABSTRACT: The problem of parametric scattering of the extraordinary and the ordinary wave near electron cyclotron frequency off ion cyclotron waves is investigated. The convective thresholds are obtained for various instabilities in an inhomogeneous plasma. The dependence of the thresholds on the plasma density, temperature and the propagation angles of the waves is described.

INTRODUCTION: Recently, the problem of scattering of electromagnetic waves in the magnetized laser fusion case has been discussed by several authors /1/. With specific application to electron cyclotron resonance heating, the problem of parametric decay is intensively studied /2/, but the thresholds of scattering processes have not been evaluated in detail. We examine analytically the parametric scattering of the extraordinary (X) or ordinary (O) pump waves off ion cyclotron (IC) waves. The ion cyclotron wave has a low group velocity (<< ion thermal velocity) and is weakly damped in a wavenumber region /3/ fulfilling well the phase matching conditions of the resonant three-wave interaction. We set no restrictions on the pump wave injection angle. Four different scattering channels, listed below, have been considered,

$$X \rightarrow X + IC, \qquad X \rightarrow O + IC,$$
$$O \rightarrow O + IC, \qquad O \rightarrow X + IC.$$

We study only the case of side-scattering, which we believe to give the lowest thresholds, provided that the gradient of the inhomogeniety in the plasma is perpendicular to the propagation direction of the side-scattered wave.

NONLINEAR DISPERSION RELATION: In the cold plasma limit the electric field of the X or O pump wave is given by

$$\bar{E}_o = \frac{1}{2}(\hat{x} + i\alpha_o\hat{y} + \beta_o\hat{z})\, E_o \exp(i\omega_o t - ik_{o\perp}x - ik_{o\parallel}z) + \text{c.c.},$$

$$\alpha_o = \frac{\Omega_e}{\omega_o}\left[(1-N^2)(\Omega_e^2 - \omega_o^2)/\omega_p^2 + 1\right]^{-1},$$

$$\beta_o = N^2\cos\theta_o\sin\theta_o(N^2\sin^2\theta_o + \omega_p^2/\omega_o^2 - 1)^{-1}, \quad N = k_o^2c^2/\omega_o^2$$

where ω_p, Ω_e and θ_o are the plasma frequency, electron cyclotron frequency and the angle between the wavenumber $\bar{k}_o$ and the external magnetic field $B\hat{z}$, respectively. For the scattered wave we have similarly

$$\bar{E}_1 = \frac{1}{2}(-i\alpha_1\hat{x} + \hat{y} + \beta_1\hat{z})E_1\exp(i\omega_1 t - ik_{1\perp}y - ik_{1\parallel}z) + \text{c.c.},$$

where α_1 and β_1 may now be obtained by replacing the subsribt "o" by "1".

For a weakly damped ion cyclotron wave (i.e., $3\omega < k_\parallel v_e$ and $k_\perp/k_\parallel \lesssim v_e/v_i$) the low-frequency nonlinearity arises mainly through the parallel ponderomotive force $ek_\parallel\hat{z}(\bar{v}_o\cdot\bar{E}_1)/\omega_o$, $\bar{v}_o = \bar{\bar{\mu}}\cdot\bar{E}_o$ where $\bar{\bar{\mu}}$ is the mobility tensor of electrons. The density perturbation at $(\omega, \bar{k})$ couples with the oscillatory velocity $\bar{v}_o$ to produce a nonlinear current at the scattered wave frequency. Following the standard methods we derive the nonlinear dispersion relation

$$D_1 D = -\delta$$

where

$$D(\omega,k) = \frac{2\omega}{\omega^2 - \Omega_i^2} I_1(b)\exp(-b) + I_o(b)\exp(-b) - 1 - T_i/T_e$$

$$D_1(\omega_1,\bar{k}_1) = 1 + (1 - \frac{\omega_p^2}{\omega_1^2})\beta_1\cot\theta_1 - (\omega_p^2 - \omega_1^2 + k_1^2c^2)\alpha_1/\Omega_e\omega_1$$

are the linear dielectric functions of the IC wave and the scattered wave, $b = k_\perp^2 v_i^2/\Omega_i^2$. I_n is the modified Bessel function, and

$$\delta = \frac{1}{3}\frac{\omega_p^2}{4\omega_o\omega_1}\frac{\Omega_e^2}{\Omega_e^2-\omega_o^2}\left\{\frac{[(1+\alpha_o\alpha_1)\Omega_e-(\alpha_o+\alpha_1)\omega_o]}{\Omega_e^2-\omega_o^2}+\beta_o^2\beta_1^2\frac{\Omega_e^2-\omega_o^2}{\omega_o^2}\right\}\frac{u^2}{v_e^2}$$

is the nonlinear coupling term where u is defined by $u = eE_o/m\Omega_e$.

The most stringent condition to the instability is set by the convective losses due to the finite extent of the pump wave and the inhomogeniety. By setting the exponential amplification factor to exceed at least unity one gets the threshold condition /4/

$$\delta L L_1 / \left|\partial D/\partial k_\perp\right| \left|\partial D_1/\partial \bar{k}_1\right| \gtrsim 1$$

where L_1 and L are the width of the pump region in the direction of the Poynting vector of the scattered wave and the spatial extent of phase matching in the direction of the inhomogeniety, respectively. The latter may be estimated by $(2L_N/k)^{1/2}$ where L_N is the gradient scale length.

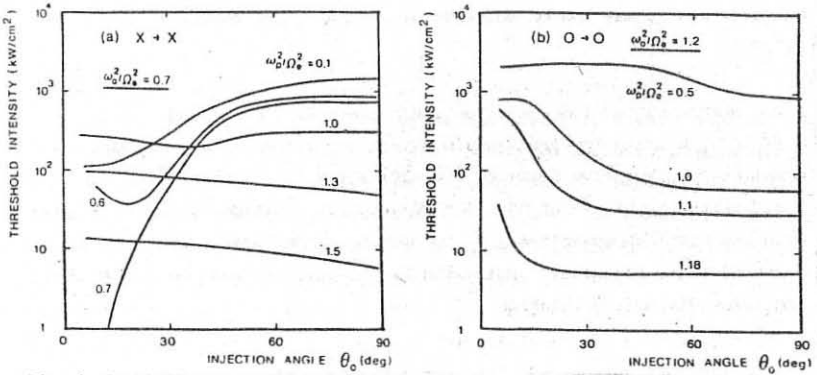


Fig. 1 Threshold intensity as a function of the pump wave injection angle with different density parameters ω_p^2/Ω_e^2 for (a) extraordinary wave scattering to another extraordinary wave with $\omega_o^2/\Omega_e^2 = 0.7$ and for (b) ordinary wave scattering to another ordinary wave with $\omega_o^2/\Omega_e^2 = 1.2$.

RESULTS: Figure 1 shows the threshold intensities as a function of the pump wave injection angle θ_o with different density parameters for (a) X → X + IC and (b) O → O + IC. We have taken $T_i \sim T_e = 1.5$ keV, B = 1T and $L_N \sim L_1 \sim 20$ cm. In (a) we have $\omega_o^2/\Omega_e^2 = 0.7$ and in (b) $\omega_o^2/\Omega_e^2 = 1.2$. The thresholds are in general fairly high ($I \gtrsim 100$ kW/cm²)

except in the vicinity of certain wave frequencies as the upper hybrid resonance or the cut-offs.

For example in (b) the threshold may be less than 10 kW/cm^2 when ω_o approaches ω_p. Similarly the threshold in (a) is low near the extraordinary cut-off ($\omega^2 = \omega_p^2 - \omega\Omega_e$) or near the upper hybrid frequency $\omega^2 = \omega_p^2 + \Omega_e^2$ for X → X + IC channel with $\omega > \Omega_e$. We find also a low threshold in (a) when the angle θ_o is reduced under 45^o, provided $\omega_o \gtrsim \omega_p$. This is due to the growth of the electrostatic nature of the extraordinary wave as θ_o becomes smaller (but not too small). Due to the phase matching condition $\theta_1 \approx \theta_0$ holds for the above mentioned channels. When we consider the channels X → O + IC or O → X + IC, θ_1 is generally different from θ_o due to the different dispersion characteristics of the X and O modes. Near perpendicular pump wave injection the coupling is very weak in these channels but is stronger for smaller injection angles. We have obtained the lowest thresholds (100 kW/cm^2 for T_e = 1.5 keV) near $\omega_o \sim \omega_p$ with $\theta_o \sim 45^o$ for X → O + IC and $\theta_o \sim 10^o$ for O → X + IC.

CONCLUSIONS: The extraordinary and ordinary waves near Ω_e may scatter off ion cyclotron waves. The intensity thresholds are larger than the power densities presently employed in ECRH experiments. The lowest obtained thresholds (1-100 kW/cm^2 at T_e = 1.5 keV) may, however, be exceeded in future high intensity experiments, in which the scale lengths may also be larger.

References:

1. H.U. Rahman et.al., Phys. Lett. 84A, 481(1981) and references therein.
2. V. Stefan and A. Bers, Phys. Fluids 27, 175(1984) and references therein.
3. A.I. Akhiezer et.al., Plasma Electrodynamics, Vol. I (Pergamon, New York, 1975), p. 267.
4. C.S. Liu, in Advances in Plasma Physics, edited by A. Simon and W.R. Thompson (Wiley, New York, 1976), Vol. 6, p. 121.

FIRST RESULTS OF THE ELECTRON CYCLOTRON EXPERIMENT ON TFR

FOM-ECRH Team*, Association Euratom-FOM
FOM-Instituut voor Plasmafysica, Rijnhuizen, Nieuwegein, The Netherlands

TFR-Group, Association Euratom-CEA sur la Fusion, D.R.F.C., C.E.N.,
Boîte Postale n°. 6, 92260 Fontenay-aux-Roses, France.

Introductory ECRH experiments were performed on TFR with one 60 GHz gyrotron. Approximately 100 kW of microwave power in 30 ms pulses was launched into the torus in the ordinary-mode polarization from the low-field side.

Heating of the (near) central region gave rise to electron-temperature increases up to 500 eV. Depending upon the initial plasma regime, the energy confinement time was either reduced or slightly increased. Preliminary experiments on control of MHD activity and on suprathermal regimes were also performed.

Introduction

The ECRH facility for use on TFR embodies three 60 GHz gyrotrons, each capable of generating in excess of 200 kW during 100 ms, in the (circular) TE_{02} mode. The power is converted, via TE_{01}, into linearly polarized TE_{11}. The system is expected to come into full operation in August 1985.

Introductory experiments were done with one gyrotron, operating at reduced power (≈ 135 kW) and limited pulse length (< 30 ms). The power (about 100 kW at the torus) was launched through an oversized open wave-guide antenna in the equatorial plane at right angles to the magnetic field. Launching was from the outboard side of the torus, in horizontal polarization, to couple to the O-mode in the plasma [1]. On the inboard side of the torus a smooth, two-sided (roof-top shaped) mirror was placed, so that the non-absorbed microwave beam is reflected symmetrically by + and - 20°, while polarization is maintained. Eventually this mirror will be replaced by a polarization-changing reflector.

Heating

TFR was operated with carbon limiters at 20 cm radius. Ohmically heated hydrogen target plasmas were used with the following characteristics:

$n_e[0] = (1:3) \times 10^{13}$ cm^{-3}	I_p = 100 : 150 kA
$T_e(0)$ ≈ 800 : 1200 eV	V_T ± 1.2 : 1.5 V
$T_i(0)$ ≈ 300 eV	ΔH ~ -2 : -4 cm
$B_t(0)$ = 19 : 23 kG (21.4 kG for center heating)	q(a) = 2.8 : 4

Depending on plasma current, two different regimes could be obtained: for $I_p \leq 110$ kA, no MHD activity was observed and the energy confinement time τ_ε was ≈ 9 ms; for $I_p \geq 110$ kA, a very strong m=2, n=1-mode developed and τ_ε was only 3.7 ms. Figs. 1a and 1b show the effects of 100 kW r.f. power during 30 ms, for the low-current and high-current cases, respectively.

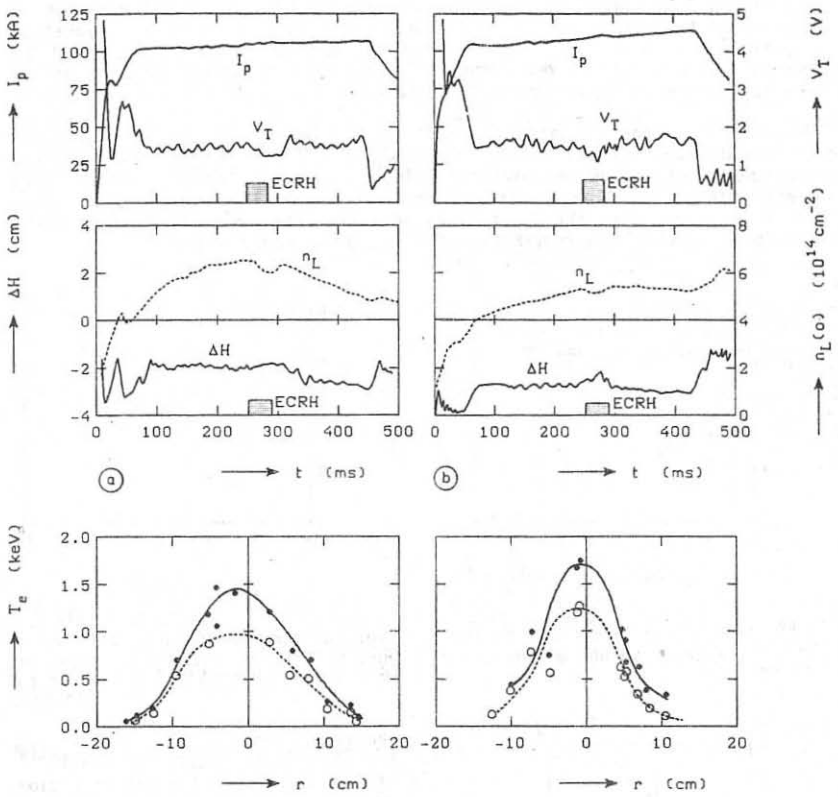


Fig. 1. Plasma current I_p, loop voltage V_T, horizontal displacement ΔH, central chord-line density $n_L(0)$ as functions of time, and electron-temperature profiles before and during ECRH, for 1a: I_p < 110 kA; for 1b: I_p > 110 kA.

For resonance in the central regions and initial temperature T_e = 1 keV, absorption in the first passage of the microwave beam is computed to be 70% initially and to rise to 80% as T_e increases with power deposition mainly within a radius of 5 cm. As the plasma current is kept constant by feed-back control, the change of resistivity is seen, with a delay due to the diffusion time, on the loop voltage V_T which decreases by about 30%. A reversible pump-out is observed on the line density: central channel about 8% in the low-current case. The electron temperature T_e, from ECE, rises by about 50% and 35% for low and high current, respectively, while energy confinement τ_E changes from 9 ms to 6 ms and 3.7 ms to 4.3 ms.

Apparently, the heat conductivity is enhanced in the low-current case but is unchanged or slightly reduced in the high-current case. A possible explanation for the latter result is that temperature profile modifications tend to decrease the size of the m=2 magnetic island [2]. No marked effects on ion temperature or impurity behaviour could be observed.

Results of a scan in density are shown in Fig. 2: for $n_e(0) \lesssim 1.5 \times 10^{13}$ cm^{-3} suprathermal effects occur; for $n_e(0) \gtrsim 4 \times 10^{13} cm^{-3}$ the high reflected power causes cut-off of the gyrotron. Fig. 3 shows the variation of ΔT_e with magnetic field, for "low-current" discharges (no MHD) but with $n_e(0)$ below that of Fig. 1a. Here, the T_e-profiles were measured with a Michelson interferometer instead of the superheterodyne detection used for Fig. 1.

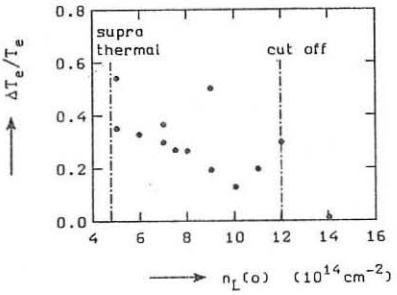


Fig. 2. Increase of T_e on axis during ECRH for different values of the central chord density.

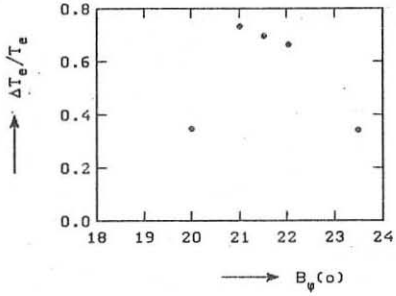


Fig. 3. Increase of T_e on axis during ECRH for different values of the toroidal magnetic field on axis.

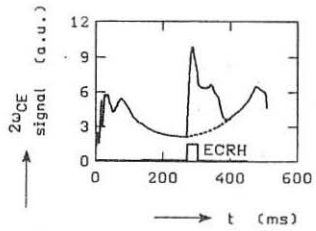


Fig. 4. Comparison of $2 \cdot \omega_{ce}$-emission with (——) and without (....) ECR heating, for $n_e(0) = 1.1 \times 10^{13}$ cm^{-3}.

Suprathermal effects

At low densities ($n_e(0) \lesssim 1.5 \times 10^{-13}$ cm^{-3}) strong suprathermal electron cyclotron emission is observed. Fig. 4 gives the $2 \cdot \omega_{ce}$ emission during a shot with $n_e(0) = 1.1 \times 10^{13}$ cm^{-3}; it is seen that a fast population stays confined for about 60 ms after the ECRH pulse.

MHD Control

Suppression of the m=2 mode has been achieved with the resonance situated slightly outside the q=2 surface: I_p = 140 kA, $B_\phi(0)$ = 24.3 kG, r(q=2) = 12.3 cm, r_ω = 13.3 cm, cf. Fig. 5. Active feedback control using the n=2 coil-signal to modulate gyrotron power was also done, cf. Fig. 6. Pulse length limitations restricted these experiments to 30 ms total time.

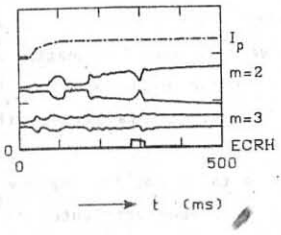


Fig. 5. The effect on the m=2 and m=3 signals of electron cyclotron heating slightly outside the q=2 surface.

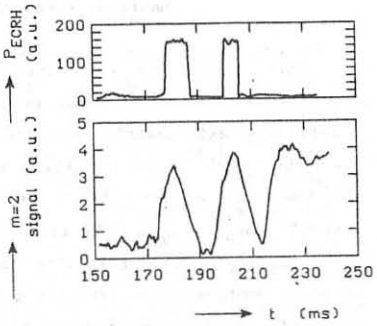


Fig. 6. Feedback control of the m=2 mode by electron cyclotron heating.

Acknowledgement

The FOM activities were performed under the Euratom-FOM association agreement with financial support from ZWO and Euratom.

* The FOM-ECRH team: J.A. Hoekzema, L.Th.M. Ornstein, R.W. Polman, T.J. Schep, W.J. Schrader, E. Westerhof, A.M.E. Winkelman, M.F. van Donselaar, C.A.J. van der Geer, A.F. van der Grift, J. de Hoop, A.M. van Ingen, M. van der Kaay, L. Kroonenburg, O.G. Kruijt, P. Manintveld, J.G. Monster, P.R. Prins, A.B. Sterk, H.L.C.J. van Strien, A.G.A. Verhoeven.

References

[1] Cano, R. et al., Proc. 4th Int. Symp. on Heating in Toroidal Plasmas, Rome (1984) Vol. II, p. 853.
[2] TFR Group, to be published.

Eigenmode Structure, ICRF Heating and Stabilization of Axially Symmetric Systems*

C. Litwin, N. Hershkowitz and J.D. Callen

Nuclear Engineering Department
University of Wisconsin-Madison
Madison, Wisconsin 53706, U.S.A.

This paper is motivated by a desire to understand recent experiments[1,2] in which radiofrequency waves have been used for heating and stabilizing axisymmetric magnetic mirrors. In these experiments it has been observed that if the fluctuating field frequency ω is greater than the the ion cyclotron frequency ω_{ci}, the plasma is stable. It becomes unstable for $\omega < \omega_{ci}$. The transition between the two stability regions is sharp ($\Delta\omega/\omega_{ci} < 1\%$). Stability and instability have been attributed [2,3,4] to ponderomotive force associated with RF field profiles whose knowledge is thus of crucial importance for understanding stability as well as heating. In this paper we examine the eigenmodes of the cold fluid plasma cylinder in a uniform magnetic field[5,6] We use obtained electric field profiles to compare the simple ponderomotive stability picture with the experiment. Coupling of the interchange modes to the ion-cyclotron sidebands[7] and finite temperature effects which may be significant — in the Phaedrus tandem mirror experiment at the University of Wisconsin, β has been as high as ten percent — are not discussed here.

To determine the RF field $\bar{E}$ it is convenient to introduce light-cone coordinates ($a_\pm = a_x \pm i a_y$, $a_\parallel = a_z$, z being the direction of the external magnetic field) in which the dielectric tensor $\bar{\bar{\varepsilon}}$ is diagonal. For the range of parameters of experimental interest ($\omega \sim \omega_{ci} \ll \omega_{pi}$), $\varepsilon_\parallel \gg \varepsilon_-$ and therefore $E_\parallel$ can be neglected to the lowest order. The remaining components are determined by Maxwell equations which, for $\bar{E} \sim e^{ik_\parallel z}$, take form

$$\partial_\pm(\partial_+ E_- - \partial_- E_+) = \pm 2K_\pm E_\pm \qquad (1)$$

Here $K_\pm = k_p^2 f^2/(1 \mp f) - k_\parallel^2$, $k_p \equiv \omega_{pi}/c$, $f = \omega/\omega_{ci}$ and $\partial_\pm \equiv \partial_x \pm i\,\partial_y$. From eq. (1) it follows that $E_+ \ll E_-$ in the vicinity of the ion cyclotron resonance as long as $k_\parallel$ is not large (i.e. fast wave). For a constant

density profile, $K_+ = \text{const}$, $K_- = \text{const}$. and in the cylindrical coordinates (r,ϕ,z) eq. (1) becomes a Bessel equation whose solution, regular at $r = 0$, is (C -- arbitrary constant)

$$E_\pm = \frac{C}{K_\pm} J_{m\pm1}(k_r r) \exp\{i[k_\parallel z - \omega t + (m\pm1)\phi]\} \tag{2a}$$

$$E_\parallel = iC \frac{\omega^2}{\omega_{pe}^2} \frac{k_\parallel}{k_r} \frac{K_+ - K_-}{K_+ + K_-} J_m(k_r r) \exp[i(k_\parallel z - \omega t + m\phi)] \tag{2b}$$

$[k_r^2 \equiv 2K_+ K_-/(K_+ + K_-)]$. Here $E_\parallel$ is given to leading order in ω_{ci}/ω_{pe}. Assuming that the plasma cylinder of radius r_p is surrounded by a vacuum region and a conducting wall at $r = r_w$ from the boundary conditions one obtains[6] a dispersion relation which determines k_r. From it one can show that $m \leq 0$ modes can propagate at $\omega = \omega_{ci}$ only if $\kappa \equiv k_p r_p > j_{0,1}$, the first zero of J_0. For the Phaedrus experiment, $\kappa = 1.$ and therefore only $m > 1$ modes can propagate in the vicinity of the cyclotron frequency. The dominant $m = 1$ mode is the surface mode[5]. For this mode $E_+ \sim J_2(k_r r)$, $E_- \sim J_0(k_r r)$ and $k_r^2 > 0$. To study effects of diffuse boundaries we observe that for $\omega \approx \omega_{ci}$, $E_+ \ll E_-$ for the fast wave unless the plasma density n is very small near the plasma edge where E_+ can have a significant value if $n(r_p)/n(0) \lesssim |1 - \omega/\omega_{ci}|$. When $E_+ \ll E_-$, eq. (1) can be solved analytically, for a variety of density profiles. In particular, for the parabolic profile[6,8] $n(r) = n_0(1 - r^2/r_p^2)$ we find a solution

$$E_- = C\, e^{-q^2 r^2/2}\, r^{m-1}\, M(\tfrac{m}{2} - \tfrac{\lambda}{4},\, m,\, q^2 r^2) \tag{3}$$

where $q^2 \equiv k_{po}/r_p$, $\lambda = (k_{po}^2 - 2k_\parallel^2)/q^2$ and $M(a,b,z)$ is the confluent hypergeometric function. As in ref. [6], one can obtain a dispersion relation whose solution differs only modestly from the step profile case. Also, the E_- profile is largely unchanged for $\kappa \lesssim 1$. Consider next the effect of an antenna. For an infinite current sheet $j_k(z) \sim e^{ikz}$ on the surface of a plasma with a constant density profile, $E_\pm \sim J_{m\pm1}(k_r r)$ with $k_r^2 \approx k_p^2 - 2k^2$ for $\omega \approx \omega_{ci}$. For the fast propagating wave $k_r^2 > 0$ and therefore $E_- \sim J_0(k_r r)$. In the present case, however, $k_r^2 < 0$ if $2k^2 > k_p^2$. Then $E_- \sim I_0(|k_r| r)$. For an antenna of width d, $kd \lesssim 1$ and if $k_p^2 d^2 \ll 1$, E_- is a monotonically increasing function of r. For the antennas used in the Phaedrus experiment $k_p^2 d^2 \approx 0.1$. Numerical studies using the XANTENNA code[9] for realistic density profiles show that E_- is monotonically increasing with r near the antenna and monotonically decreasing far from it. This is in agreement with our results and those of Byers[8].

For a cold fluid plasma the ponderomotive force due to rf fields is[10]

$$F = \sum_{s=i,e} \frac{\omega_{ps}^2}{\omega(\omega - \omega_{cs})} \nabla_\perp |E_+|^2 + \frac{\omega_{ps}^2}{\omega(\omega + \omega_{cs})} \nabla_\perp |E_-|^2 + \ldots \qquad (4)$$

The total gradient terms which do not contribute to stabillity are omitted.[3] The apparent singularity at $\omega = \omega_{ci}$ leads to the conclusion that the ponderomotive force is stabilizing at $\omega = \omega_{ci}^+$ and destabilizing at $\omega = \omega_{ci}^-$ if $|E_+|$ increases monotonically with r. The latter is indeed the case, since $E_+ \sim J_2(k_r r)$. However, the singularity at $\omega = \omega_{ci}$ is spurious[4] since $E_+ = 0$ there and in fact its contribution to the ponderomotive force vanishes. For $\omega \approx \omega_{ci}$ one thus finds

$$F \approx + \frac{\omega_{pi}^2}{2\omega_{ci}^2} \nabla_\perp |E_-|^2 \qquad (5)$$

where we have summed over both electron and ion contributions. If the electron contribution is not included, the ponderomotive force is exactly equal the negative of the value given by eq. (5). Note that while the conclusion that $E_+ = 0$ is true for strictly $\omega = \omega_{ci}$, it is not true in the vicinity of the ion cyclotron resonance at the outer radii where the density is low and E_+ can have an appreciable value, as we have mentioned before. The effect of this is to increase the stability for $\omega > \omega_{ci}$ and diminish it for $\omega < \omega_{ci}$. It is not clear however whether this alone can explain the experimental results (see later discussion).

For both sharp and parabolic density profiles $|E_-|$ is a decreasing function of r for the propagating modes. Thus the force given by eq. (10) counteracts the curvature drifts and has a stabilizing influence. This agrees with the experimental observations for $\omega > \omega_{ci}$ but not for $\omega < \omega_{ci}$. Finite temperature effects alter this conclusion since E_+ will have a nonvanishing value at $\omega = \omega_{ci}$. But they tend to smooth the transition across the ion cyclotron resonance over the range of $\Delta\omega \sim k_\parallel v_{ti}$ ($\sim 0.1\ \omega_{ci}$ for the Phaedrus parameters). Thus it appears that in order to explain the sharp stability threshold at $\omega = \omega_{ci}$ one needs a resonant effect which is not sensitive to the temperature.

It is well known[11,12,13] that the magnetosonic wave is damped for $\omega < \omega_{ci}$ due to the presence of a shear Alfvén wave resonance at the outer radii. Byers[8] have suggested that this effect may be responsible for the stability properties near $\omega = \omega_{ci}$. In the slab model Cramer and Donnelly[14] derived a dispersion relation assuming that the width Δ of the transition region is small: $\epsilon \equiv k_\parallel \Delta \ll 1$. From this dispersion relation we can

determine the evanescence length. For $\mathrm{Im}\, k_\parallel \ll |k_\parallel|$ we find that $\mathrm{Im}\, k_\parallel \sim \int_o^\Delta dx\, \mathrm{Im}\, A^{-1}$ where $A \equiv k_p^2 f^2/(1 - f^2) - k_\parallel^2$. From this it follows that $\mathrm{Im}\, k_\parallel = 0$ for $\omega = \omega_{ci}^+$ and $\mathrm{Im}\, k_\parallel \neq 0$ for $\omega = \omega_{ci}^-$. For $\kappa \lesssim 1$ we find

$$\frac{\mathrm{Im}|k_\parallel|}{|k_\parallel|} = \frac{\kappa}{4}\left(1 + \frac{1}{\sqrt{1+\kappa^2}}\right)\left(\frac{d\ \ell n\ n}{d\ \ell n\ r}\right)^{-1} \qquad (6)$$

for $\omega = \omega_{ci}^-$ and zero for $\omega < 0.8\ \omega_{ci}$. As expected, $\mathrm{Im}\, k_\parallel \to 0$ as the density gradient increases. For measured density profiles $(d\ \ell n\ n/d\ \ell n\ r)^{-1} \sim 0.2 - 0.3$ which yields the damping length comparable to the length of the plasma in the Phaedrus experiment.

It appears then that the wave damping for $\omega < \omega_{ci}$ has a destabilizing effect since it confines the wave to the vicinity of the antenna where E_- has a destabilizing profile. This agrees with the experimental observations. Also the transition from the stable region for $\omega > \omega_{ci}$ to the unstable region for $\omega < \omega_{ci}$ is sudden, since $\mathrm{Im}\, k_\parallel$ is discontinuous at $\omega = \omega_{ci}$, at least for $\mathrm{Im}\, k_\parallel \ll |k_\parallel|$. However these conclusions rely crucially on the inclusion of the electron ponderomotive force, which has been calculated in the cold collisionless limit. In the experiment, the electron collision and bounce frequencies are comparable to the ion cyclotron frequency. The role of these effects is unclear at this time.

REFERENCES

1. Ferron, J., et al. Phys. Rev. Lett. 51, 1955 (1983).
2. Yasaka, Y., Itanani, R., Nucl. Fusion 24, 445 (1984).
3. Myra, J.R., D'Ippollito, D.A., Phys. Rev. Lett. 53, 914 (1984).
4. Similon, P.L., Kaufman, A.N., Phys. Rev. Lett. 53, 1061 (1984).
5. Paoloni, F., Phys. Fluids 18, 640 (1975).
6. Apert, K. et al., Phys. Fluids 27, 432 (1984).
7. McBride, J.B. et al., Phys. Rev. Lett. 54, 42 (1985).
8. Byers, J.A., Proc. Ann. Contr. Fus. Theory Mtg., Madison, WI 1985.
9. J. Ferron priv. com.
10. Klima, R., Petrzilka, V.A., J. Phys. A 11, 1687 (1978).
11. Hasegawa, A., Chen, L., Phys. Fluids 19, 1924 (1976).
12. Tataronis, J.A., Grossman, W., Nucl. Fusion 16, 667 (1976).
13. Karney, C.F.F. et al., Phys. REv. Lett. 42, 1621 (1979).
14. Cramer, N.F., Donnelly, I.J., Plasma Phys. 25, 703 (1983).

*This work has been supported by the U.S. Depatment of Energy under Contract #DE-AC02-78ET51015 and DE-AC02-80ER53104.

Electron density profile behaviour under ECRH on T-10.

Vasin N.L., Kurchatov Institute of Atomic Energy, Moscow

The results of studies on heat conduction and energy confinement time in plasma under ECRH on T-10 are given in /1/. A detailed study of electron density profile, Ne(r), in the same regimes is made in a given paper, as the behaviour of Ne(r) under ECRH is of particular interest.

The Ne(r)-profile was determined from the measurements with a multichannel submillimetric interferometer /2/.

The work was made with variation of the plasma parameters in a wide range. The safety factor at the limiter was varied in the range 2.5 - 7; average density n_e was varied in the range 1.6 - $7 \times 10^{13} cm^{-3}$; power of auxiliary heating was varied from 200 kW to 1000 kW.

Results of measurements.

The Ne(r)-profile is noticeably changed under ECRH during the first 15-20 msec, as it is seen in Figs. 1, 2. The profiles for the regimes with different q(L) before ECRH (t=350 msec) and by the end of ECRH (t=450 msec) are given in a normalized form (by Ne max) in Fig.2 at P_{ECRH}=600 kW. One can see that the Ne(r)-profile is flattened when q 3.5 and it does not change a form at q 2.5-2.7.

The behaviour of Δ Ne(0) in time shows that the main changes in $n_e(0)$ occur in the first 15-20 msec after switching gyrotrons on. A time for 8 msec after the start-up of ECRH was chosen for a qualitative characteristics of these changes, $-\frac{dNe(0)}{dt}$.

The behaviour of Ne(0) vs. q at P_{ECRH}=600 kW and Ne(0)= $5 \times 10^{13} cm^{-3}$ is given in Fig.3. One can see that Δ Ne(0) is linearly dependent on q(L).

The dependence of Ne(0) on the electron density was considered only at q(L) =4.2 and at P_{ECRH}=900kW. As one can see in Fig.4, the behaviour of Ne(0) depends mainly on Ne(0). It is connected , most linely, with the fact that a cut-off takes

place at the densities higher than $7 \times 10^{13} cm^{-3}$, and radiation is absorbed at the external radii of plasma without reaching its centre. A change in the level of $\Delta Ne(0)$ with a rise in Ne(0) is probably connected with the increased refraction and, due to this, with a decreased localization of heating.

The behaviour of density vs. P_{ECRH} under the same initial conditions ($q_L=4.2$; $n_e(0)=4 \times 10^{13} cm^{-3}$) shows that $\Delta Ne(0)$ has a non-linear dependence on P_{ECRH} (see Fig.5) in difference from /3/.

The comparison between the behaviour of Ne(r) at two limit values of q_L ($q_L=2.4$ and $q_1=7$), $P_{ECRH}=1$ MW, is of particular interest. From Fig.1 one can see that the behaviour of $\Delta Ne(r)$ changes, i.e. $\frac{dNe(0)}{dt}$ changes its sign. However, from Fig.6, where the chord signals from the interferometer with the impact parameters of diagnostics X=6 cm and X=-3 cm, one can see that the phase of saw-tooth oscillations in density is inverse with respect to the temperature oscillations measured from the radiation at 2 Wc (Fig.6b) in the discharge with q_L 2.4 during ECRH, i.e. beginning from a certain time with a rise in Te(0), as in the regimes with high q_1, the central density drops. It supports the conclusion that the mechanism of density removal from the centre, to my mind, is the same for both limit cases and dependent on a certain limit electron pressure gradient (or, probably, the total pressure gradient) for a given current configuration. Moreover, two facts more support this idea:
1) it is impossible to explain a value of $\frac{dNe(0)}{dt}$ for the regimes with $q_L=7$ (Fig.7), even when one uses the anomalous values of Vr and De from /4/, assuming that Vr is reduced to zero for the first 8 msec of heating.
2) Changes in the total amount of particles for the first 4-6 msec of ECRH are not observed; meanwhile, $n_e(0)$ is noticeably changed, especially in the regimes with $q_L > 3.5$.

One should also note that the total amount of particles rises in the process of heating, that can be caused by an increased interaction between plasma and the walls and by the interaction between the microwave radiation and the chamber wall. By the way, this can conceal the variation in Ne(0) at the center.

Finally, one can make some conclusions on the density behaviour under ECRH on T-10:

1. The density at the centre drops at q_L 3.5 and at $Ne(0) \leq Ne_{cr}$, the density profile flattens and tends to a shape of Ne(r) at $q \approx 2.5$ (see Fig.7).
2. No change in the profile configuration is observed at $q_L < 3$, and the behaviour of saw-tooth oscillations in density (6a) can be considerably changed under higher power of ECRH.
3. Δ Ne(0) is varied non-linearly with the ECRH-power.
4. A time pattern of the total amount of particles in plasma shows that the changes in Ne(r) under ECRH are, most likely, related to the presence of a limit to the electron pressure derivative $(\frac{dPe}{dr})$ for a given current configuration.

References.

1. Alikaev V.V. et al. Electron cyclotron heating and plasma confinement in the T-10 Tokamak. 10th Int.Conf.on Plasma Phys.and Contr.Nucl.Fusion Res. (London,1984).Paper IAEA-CN-44/F-I-1.
2. Buzankin V.V., Vasin N.L., Gorbunov E.P. et al. 9-channel interferometer in submillimetric range for measuring the electron density in T-10. In 'Diagnostika plasmy', issue 4 (1),Moscow,Energoizdat,1981,p.141-146. (In Russian).
3. Bondarenko I.S., Bugarya V.I. et al. ECRH in TM-4. Study of transport coefficients. Preprint IAE-3630/7, 1982.(In Russian).
4. Bagdasarov A.A., Vasin N.L. et al. Plasma and impurity transport study on T-10 with the low level injections. 10th Int. Conf.on Plasma Phys.and Contr.Nucl.Fusion Res. (London,1984) Paper IAEA-CN-44/A-III-4.

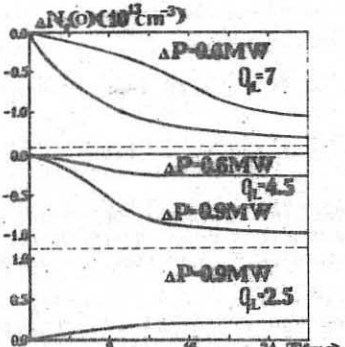


Fig.1

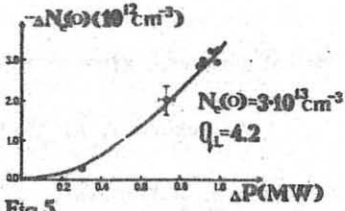


Fig.5

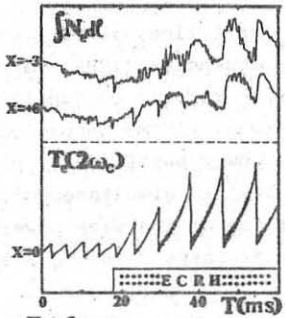


Fig.6

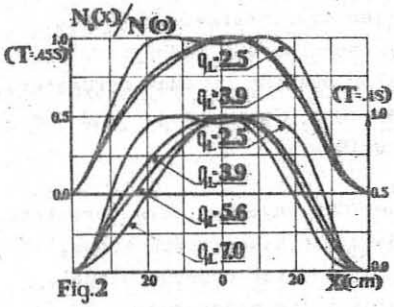


Fig.2

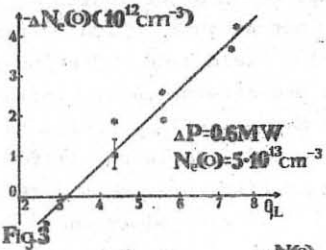


Fig.3

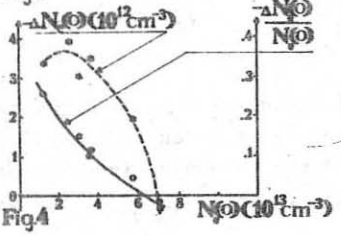


Fig.4

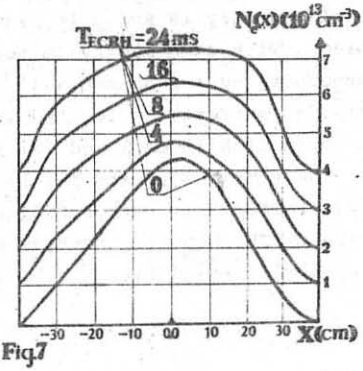


Fig.7

$\Delta P \equiv P_{ECRH}$

TWO-DIMENSIONAL KINETIC ANALYSIS OF ICRF WAVES IN A TOKAMAK

A. Fukuyama, A. Goto, K. Itoh* and S.-I. Itoh†

Department of Electronics, Okayama University, Okayama 700, JAPAN
*Japan Atomic Energy Research Institute, Tokai, Ibaraki 319-11, JAPAN
†Institute for Fusion Theory, Hiroshima University, Hiroshima 730, JAPAN

Abstract Excitation, propagation and absorption of ion cyclotron range of frequencies (ICRF) waves in tokamaks are obtained. Wave equation with kinetic conductivity tensor is solved numerically. Two dimensional plasma inhomogeneities are retained. Antenna impedance, power partition by plasma species and deposition profile are obtained simultaneously. For present tokamak parameters, the deposition of the wave power near the plasma center and the good antenna/plasma coupling are possible.

The linear wave equation of the ICRF wave has been formulated as a boundary value problem, including the kinetic processes. The model geometry is shown in Fig.1c. A circular crosssectional tokamak with axisymmetry (minor radius a and major radius R) is surrounded by a D-shaped wall. The loop antenna, which carries a poloidal current, is located in the low field side. The low-β approximation is employed (β: plasma pressure/magnetic pressure), for the simplicity, and the toroidal magnetic field varies as $B_\phi = B_0/(1+r\cos\theta/R)$ (r: minor radius, θ: poloidal angle and ϕ: toroidal angle). The density and temperature profiles are assumed as $n(r) = n_0(1-r^2/a^2)$ and $T(r) = T_0(1-r^2/a^2)$. The wave equation is

$$\nabla\times\nabla\times\vec{E} - \frac{\omega^2}{c^2}\vec{E} = i\omega\mu_0\left(\sum_s \vec{J}_s + \vec{J}_{ext}\right) \qquad (1)$$

where ω is the angular frequency of the wave, $\vec{J}_{ext}$ is the current on the antenna. The explicit form of $\vec{J}_s$ is given in Refs.[1,2]. We keep corrections up to $(k_\perp\rho)^2$ and the inhomogeneities across the magnetic field. The boundary condition is given on the wall

which is assumed to be a perfect conductor. $\vec{J}_{ext}$ is simply taken to be constant on the antenna. Each k_ϕ component is treated independently, because the plasma has a ϕ-symmetry. For an antenna which has a finite width in toroidal direction, we Fourier compose $\vec{E}(r,\theta,k_\phi)$ to construct $\vec{E}(r,\theta,\phi)$. The local power absorption is given as $P_s(\vec{r}) = \langle \vec{J}_s \cdot \vec{E} \rangle$ ($\langle\rangle$ being the average over the oscillation phase) and the integrated pwer $\bar{P}_s$ is defined by $\int d\vec{r}\, P_s(\vec{r})$.

The equation (1) is solved by use of the finite element method[3]. Parameters are chosen according to the JFT-2M tokamak ($R = 1.31m$, $a = 0.35m$, $B_\phi(0) = 1.3T$, wall radii $= 0.415 \times 0.59m$). The case of the two-ion hybrid resonance heating (majority deuterium and minority hydrogen) is shown in Fig.1. The parameters are $n_{e0} = 10^{20}/m^3$, $n_H/n_D = 0.1$, $T_0 = 3keV$, $\omega/2\pi = 18MHz$ and $k_\phi R = 12$ (low field side (LFS) excitation). The poloidal magnetic field is neglected in this report. The fast wave is excited by the poloidal loop antenna. This wave is converted to the ion-Bernstein wave near the mode conversion surface. The short wave length mode is dominant in the high-field side of the mode-conversion layer. For this parameter, the total impedance of the antenna is given as $Z = 0.22 + i\ 1.18$ (Ωm) and the division of the absorbed power is $\bar{P}_H : \bar{P}_D : \bar{P}_e = 1 : 0.37 : 0.18$.

The figure 1 illustrates that the power deposition is localized near the central region of the plasma column. The vertical localization is caused because the excited fast wave

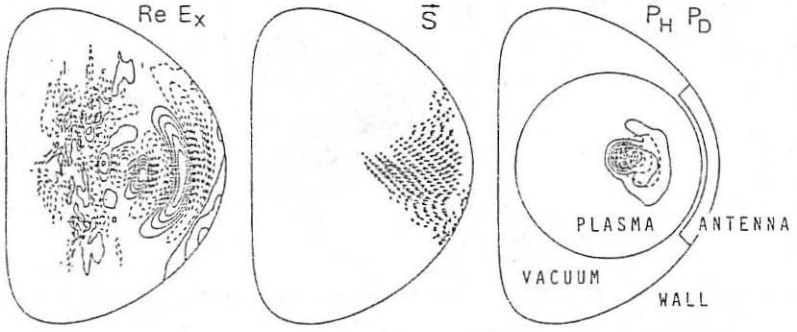


Fig.1 Poloidal structures of ReE_x (a), Poynting flux (b) and power deposition (c). Solid and dashed lines in (a) for positive and negative contours, respectively. P_H (solid lines) and P_D (dashed lines) are given in (c).

propagates to the high density region (i.e., the region with large refractive index). The Poynting vector indicates this focusing of the fast wave.

The figure 2 shows the absorbed power as a function of the plasma temperature. The power partition depends on the plasma temperature. This is because the ratio P_D/P_H is proportional to $k_\perp^2\rho^2$ where $k_\perp^2$ is approximated by ω^2/v_A^2 (v_A: Alfven velocity). This dependence agrees with the one found in the one-dimensional model calculations.[4)]

The figure 3 shows the case of the second cyclotron resonance heating of the hydrogen plasma. The parameters are $n_0 = 3\times 10^{19}$ /m^3, T_0 = 5keV, $\omega/2\pi$ = 40MHz (other parameters are the same as in Fig.1). This figure shows ReE_y (a) and P_H (solid line) / P_e (dashed line) (b) ($x = r\cos\theta$, $y = r\sin\theta$). The mode conversion is also shown in the short wave length component of the wave, which exists in the high field side of the cyclotron resonance surface ($\omega = 2\Omega_H$ holds near the magnetic axis). The cavity mode of the fast wave exist in the vicinity of this parameter, and the antenna has high resistance as $Z = 1.01 - 2.7i$ (Ωm). The division of the power is $\bar{P}_H : \bar{P}_e = 1 : 0.27$. The wave energy is also deposited near the center of the plasma column.

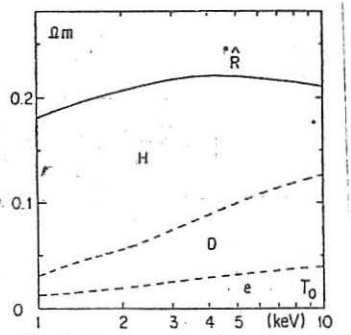


Fig.2 Temperature dependence on $\bar{P}_H$, $\bar{P}_D$ and $\bar{P}_e$. Total absorption weakly depends on temperature.

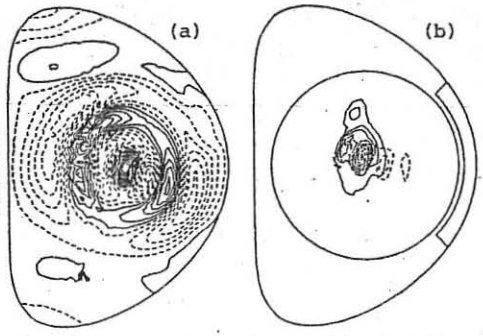


Fig.3 Contour lines of ReE_y (a) and P_H/P_e (solid lines for P_H, dashed lines for P_e) (b).

In summary, we have exploited a new and powerful method to study the excitation, propagation and absorption of the ICRF wave in tokamaks with arbitrary shapes. Power deposition profile, partition of the absorbed power and the total loading impedance of the antenna are obtained in a consistent manner. The results show an advantageous nature of ICRF waves for injecting the energy in the central region of the high temperature plasma. It is found that the values of global quantities obtained in this calculation, i.e., the loading impedance, the power partition and so on, are in good agreement with those obtained by the simple one-dimensional calculations so long as the wave damping rate is high.

References

[1] S.-I. Itoh, A. Fukuyama and K. Itoh, J. Phys. Soc. Jpn. 54 (1985) 1808.

[2] A. Fukuyama, A. Goto, S.-I. Itoh and K. Itoh, "Two-Dimensional Kinetic Description of ICRF Wave in Tokamak" Research Report HIFT-108 (Hiroshima Univ., 1985).

[3] A. Fukuyama, A. Goto, S.-I. Itoh and K. Itoh, "Finite Element Analysis of ICRF Waves in a Noncircular Tokamak", paper in preparation.

[4] A. Fukuyama, S. Nishiyama, S.-I. Itoh and K. Itoh, Nucl. Fusion 23 (1983) 1005.

Computations are performed by use of the ACOS-1000 computer of the Okayama University and the FACOM VP-100 computer of IPP Nagoya University. Work partially supported by Grant-in-Aid for Scientific Research and Grant-in-Aid for Fusion Research of MoE Japan and by Nissan Science Foundation.

NUMERICAL STUDIES OF HIGH POWER ECRH IN TOKAMAKS

M R O'Brien, M Cox and D F H Start
Culham Laboratory, Abingdon OX14 3DB, UK
(Euratom/UKAEA Fusion Association)

1. Introduction

Electron Cyclotron Resonance Heating (ECRH) has been used at powers as high as 1 MW in tokamak experiments (T10[1], DIII[2]) and will be used at even higher powers in future experiments (eg COMPASS). The localised nature of ECRH, together with the high powers used, can produce substantially non-Maxwellian electron distributions as demonstrated in low density experiments on TOSCA and CLEO[3]. These non-thermal distributions might influence the signals received by diagnostics such as soft X-ray monitors and ECE detectors and might also affect the MHD stability of plasmas by creating pressure anisotropy around a flux surface. A code has been developed to interpret and predict these effects. The code solves the bounce-averaged electron Fokker-Planck equation for tokamak magnetic field geometry to give f the electron distribution function in velocity space for one flux surface. The ECRH driving term includes the effects of finite beam width, the relativistic dependence of cyclotron frequency on electron speed, and the magnetic field variation of the tokamak.

2. The Fokker-Planck Equation

The bounce-averaged Fokker-Planck equation for the time evolution of f is:

$$\frac{\partial f}{\partial t} = \left\langle \left(\frac{\partial f}{\partial t}\right)_c \right\rangle + \left\langle \frac{-eE}{m_e} \frac{\partial f}{\partial v_\parallel} \right\rangle + \left\langle \left(\frac{\partial f}{\partial t}\right)_{ECRH} \right\rangle \qquad (1)$$

where $\langle A \rangle = \oint A v_\parallel^{-1} d\chi / \oint v_\parallel^{-1} d\chi$ with χ the poloidal angle, v the speed and $v_\parallel$ the component of velocity parallel to the magnetic field. The terms on the right hand side model collisions of f with a background electron Maxwellian and with stationary ions, the steady electric field of a tokamak, and the ECRH. This equation is written as a partial differential equation for f depending on the time t, the speed v and the pitch angle at the outside of the flux surface θ_o. It is discretized and solved numerically using an implicit method which is particularly suitable for finding steady-state solutions.

The ECRH term is calculated using a single particle approach[4] and, for uniform magnetic field geometry, is given by the quasi-linear operator

$$\left(\frac{\partial f}{\partial t}\right)_{ECRH} = \frac{1}{v_\perp} \frac{\partial}{\partial v_\perp} \left\{ \left[\frac{(\Delta v_\perp)^2}{2\Delta t} \right] v_\perp \frac{\partial f}{\partial v_\perp} \right\} \qquad (2)$$

where [ ] represents a gyrophase average and $\Delta v_\perp$ is the change in the perpendicular velocity component $v_\perp$ in time Δt. This approach is generalised to the tokamak case by considering changes in the adiabatic constants of the motion $\mu = v_\perp^2/2B$ and $J_\chi = \oint v_\parallel d\chi$ with B the tokamak magnetic field[5]. We calculate $\Delta v_\perp$ as follows. The equation for v_- ($= v_x - iv_y$) is

$$\frac{dv_-}{dt} = -eE_- - i\Omega v_-$$

with $\Omega = eB/m_e$ and $E_- = E_x - iE_y$. One can show that $[(\Delta v_\perp)^2] = \frac{1}{8}|\Delta v_-|^2$

with $\Delta v_- = e^{-i\int^t \Omega dt'} \int^t \left(\frac{-eE_-}{m_e}\right) e^{i\int^{t'} \Omega dt''} dt'$.

The form of E_-, the component of the wave field rotating with the electrons, is taken as

$$E_- = E_0 e^{-d^2/L^2} \exp[i(k_\parallel z + k_\perp x - \omega t)]$$

with L the width of the beam, d the coordinate perpendicular to the wave vector, x(z) and $k_\perp$ ($k_\parallel$) the coordinate and the component of the wave vector perpendicular (parallel) to the magnetic field. After much algebra we find

$$|\Delta v_\perp|^2 = \frac{1}{8}\left|\frac{e}{m_e v_\parallel} \frac{E_0}{(\ell-1)!} \left(\frac{k_\perp v_\perp}{2\Omega}\right)^{\ell-1} \frac{\sqrt{\pi}}{G^{1/4}} \exp\left[-\frac{\beta^2/L^2}{4G}\left(\frac{\omega-\ell\Omega}{v_\parallel} - k_\parallel\right)^2\right]\right|^2 \quad (3)$$

with $G = \beta^4/L^4 + \left(\frac{\ell\Omega'}{2v_\parallel}\right)^2$. This expression, together with equation (3), gives the ECRH term when used with the appropriate bounce time Δt. In equation (3), ℓ is the harmonic number, $\beta = k_\perp/(k_\perp^2 + k_\parallel^2)^{1/2}$, Ω is the gyrofrequency allowing for the relativistic mass shift and Ω' is the gradient of Ω along a field line. Equation (3) shows that the diffusion is proportional to the wave power and that the width of the diffusion coefficient in velocity space depends on both the beam width L and the gradient of the magnetic field via Ω'.

Equation (3) exhibits a singularity as $v_\parallel$ approaches zero which is a result of the fact that the smaller $v_\parallel$, the longer the time that the electron stays in resonance and thus the greater the heating. However there is also a tendency for the ECRH to heat the electron out of resonance by changing its mass. The resonance condition is

$$k_\parallel v_\parallel \doteq \omega - \frac{\ell eB}{m_e}(1 - v^2/2c^2) \quad (4)$$

Thus a change $\Delta v_\perp$ will change the resonant $k_\parallel$ by

$$\Delta k_\parallel = \frac{\ell eB}{m_e} \frac{v_\perp \Delta v_\perp}{v_\parallel c^2} \quad (5)$$

putting $\Delta k_\parallel \approx 1/L$ in equation (5) gives an upper bound for $\Delta v_\perp$ and hence for the diffusion coefficient $<(\Delta v_\perp)^2/2\Delta t>$.

3. Results

We have modelled the soft X-ray spectra measured by SiLi detectors

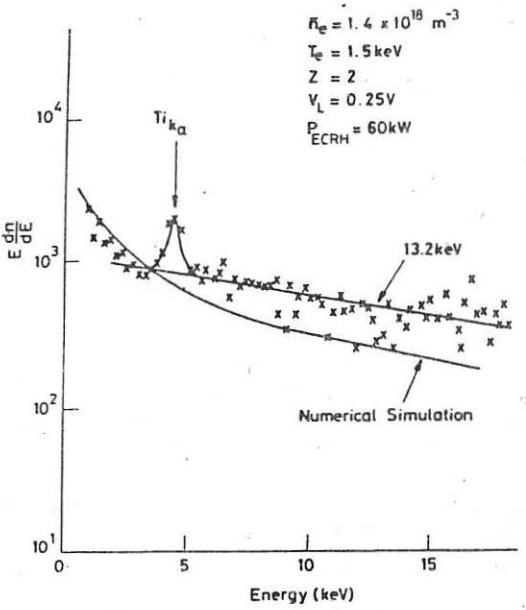


Fig 1 Soft X-ray spectrum from 28 GHz second harmonic ECRH launched perpendicularly in CLEO. In the numerical simulation L=5cm and r, the radius of the flux surface chosen, is 1.5cm.

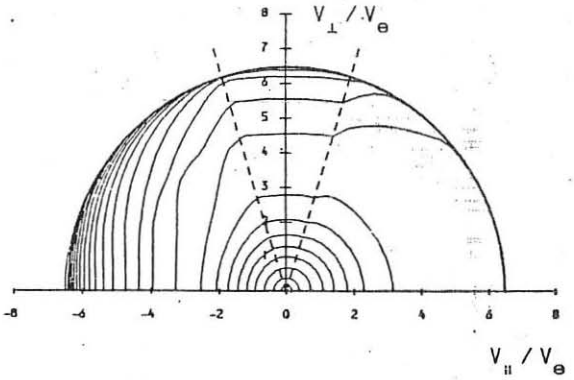


Fig 2 Contours of constant f in velocity space for the conditions of Fig 1. $v_e = (2T_e/m_e)^{\frac{1}{2}}$.

during second harmonic 28 GHz ECRH in CLEO (R/a = 90cm/13cm). The strongly distorted distribution function is reproduced reasonably well by the code (Fig 1). Figure 2 shows contours of constant electron distribution function in velocity space for the conditions of Fig 1 and shows how non-Maxwellian the distribution is. We have also modelled 60 GHz experiments in CLEO, and the SiLi spectra of the more weakly distorted distribution (due to the higher density and lower temperature) is also reproduced well.

We have also modelled the ECRH current drive experiments planned for COMPASS (R/a = 55cm/22cm). Figure 3 shows how the current J, absorbed power density P and the current drive efficiency J/P are predicted to vary with input power with and without electron trapping effects. The efficiency actually increases with increasing power due to the ECRH heating electrons to higher $v_\perp$ and hence stronger interaction with the waves.

4. Conclusions

A code has been developed which models the effect of ECRH on electron distribution functions. The code reproduces measured soft X-ray spectra from CLEO and also predicts a favourable scaling of current drive efficiency with input power.

References

[1] V V Alikaev et al, Proc 10th IAEA Conf on Plasma Phys and Cont Nuc Fus Res, 1984, Vol I, p 419.
[2] K H Burrell et al, Ibid, p 131.
[3] D C Robinson et al, Ibid, p 205.
[4] R A Cairns and C N Lashmore-Davies, to be published in Plasma Physics.
[5] M R O'Brien, M Cox and D F H Start, to be published.

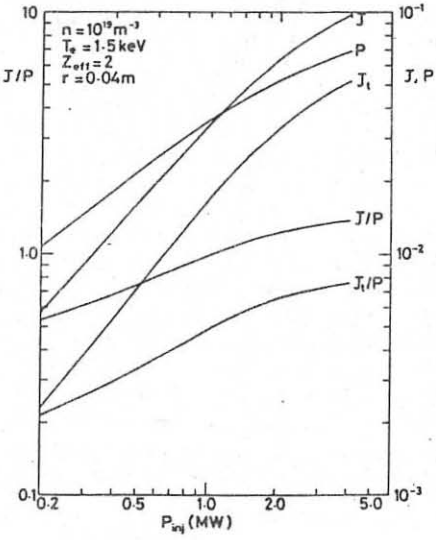


Fig 3 Graph of J, P and J/P against input power for the planned 60 GHz second harmonic experiments in COMPASS. The subscript t indicates a calculation allowing for electron trapping. The injection angle is 25° to the perpendicular and L=5cm.

FUNDAMENTAL AND 2ND HARMONIC HEATING AT THE ELECTRON CYCLOTRON RESONANCE ON CLEO TOKAMAK

T Edlington, N R Ainsworth, B Alper, D Atkinson, S G F Blewett, P R Collins, A N Dellis, B Lloyd, F Ma*, B Parham, A C Riviere, D C Robinson and T N Todd
Culham Laboratory, Abingdon OX14 3DB, UK
(Euratom/UKAEA Fusion Association)
*People's Republic of China

Introduction Initial 2nd harmonic ECRH studies on CLEO[1] were conducted at 0.5T using a single 200kW, 28GHz gyrotron. The electron density was limited to less than the low density X-mode cut-off ~ $5 \times 10^{18} m^{-3}$. Substantial increases in plasma stored energy were observed with β reaching 60% of the theoretical limit[2]. However at low density, high energy tails were observed in the soft X-ray spectra and the electron energy distribution was found to be anisotropic [3].

In this paper we describe recent experiments in which the toroidal field was ~ 1.0T. Two gyrotrons were used with frequencies of 28GHz and 60GHz each capable of generating 200kW of rf for pulse lengths of 20ms and 40ms respectively. For both cases the unpolarised TE_{01} circular mode is radiated, from the low field side of the resonant surface, through open-ended, oversized waveguide aligned along a major radius in the horizontal mid-plane. With either resonance close to the plasma centre, efficient electron heating is observed with no evidence that significant non-thermal populations are generated.

2nd harmonic heating

The scaling of 60GHz 2nd harmonic ECRH has been studied over a wide range of plasma parameters ($5kA \lesssim I_p \lesssim 30kA$, $3 \times 10^{18} m^{-3} \lesssim \bar{n}_e \lesssim 1.6 \times 10^{19} m^{-3}$, $1.0T \lesssim B_\phi \lesssim 1.15T$). Figure 1 shows the effect of injecting ~ 140kW of rf into ohmic discharges with $I_p = 17.5kA$ and $B_{\phi o} = 1.07T$. The central electron temperature increases from 425eV to 1250eV while the line

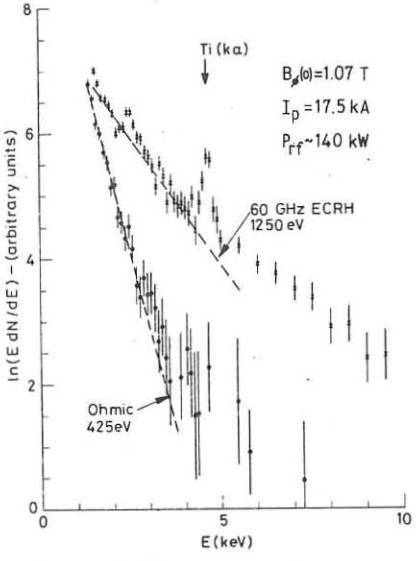


Figure 1. Si(Li) detector X-ray spectra for ohmic and 60 GHz 2nd harmonic heating

averaged electron density falls from 1 x $10^{19}m^{-3}$ to 6 x $10^{18}m^{-3}$. For these conditions $\Delta(\beta_p + \ell_i/2)$ is 0.7, in agreement with the change in β_p deduced from the diamagnetic loop. This rise in β_p would lead to a substantial outward shift of the plasma column. For optimum heating this shift was compensated by a fast change in the vertical field. The decrease in plasma resistivity leads to a substantial fall in ohmic input power which, assuming no change in confinement, accounts for ~ 40% of the absorbed rf power. For gettered discharges with a "well conditioned" vacuum vessel and constant gas injection, ECRH in CLEO invariably produces a fall in line averaged electron density. $\Delta\bar{n}_e$ can be large and increases with the ohmic target density (Fig 2(b)). The profile of soft X-ray emission from the plasma shows a slight broadening during heating (FWHM (ohmic) ~ 5.3cm, FWHM (ECRH) ~ 7.2cm) with peak emission 1→2cm outside the minor axis. Figure 2(a) shows that the increase in plasma stored energy falls off approximately linearly with increasing target density while $-\Delta n_e$ increases more rapidly. The ohmic soft X-ray profile broadens slightly as the mean electron density is reduced, but the width of this profile during the rf heating is independent of the initial target density. The heating efficiency is sensitive to the resonance position with the stored energy increase, ΔE, reduced to half its maximum value when the resonance is at r/a ~ 0.5. At low plasma current where the energy balance is dominated by the rf (P_{rf}/P_{OH}~ 10,) ΔE increases linearly with plasma current. From ~ 15 kA (q_a ~ 7) to 30kA (q_a ~ 3.5) a saturation is observed as the ohmic power becomes comparable to the absorbed rf power.

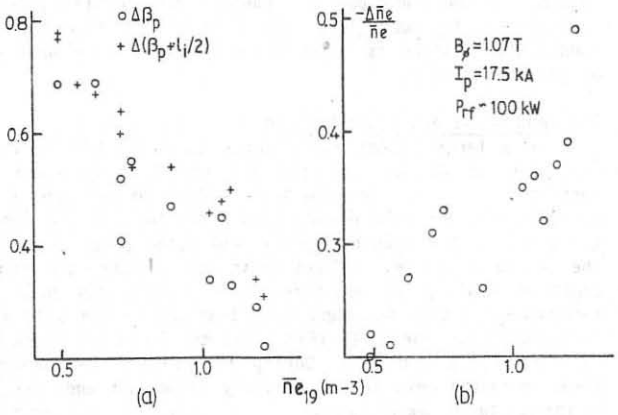


Figure 2. Density scaling of 60 GHz 2nd harmonic heating

Assuming the confinement is unchanged during 60 GHz 2nd harmonic heating up to 60% of the rf power is absorbed by the plasma. Alternatively the effectiveness of any auxiliary heating scheme can be assessed by defining a heating quality factor [4] $q_h = \frac{\Delta E_{pl}/(P_{rf}+\Delta P_{OH})}{E_{pl}/P_{OH}}$ where P_{rf} is the incident power. For these experiments values of q_h as high as 0.4→0.45 are obtained with $P_{rf}/(P_{OH} + \Delta P_{OH}) > 10$.

Fundamental Heating

Initial fundamental heating studies with the 28GHz tube have also yielded encouraging results. Injection of 70kW into target plasmas with $I_p \sim 11$kA, $\bar{n}_e \sim 3.6 \times 10^{18} m^{-3}$, $B_\phi = 1.015$T resulted in a central electron temperature increase from ~ 450eV to ~ 1keV with no significant tail production. A modest decrease in $\bar{n}_e$ (~ 7%) was observed together with a large drop in loop voltage ($V_\ell = 1.6$V to $V_\ell = 0.5$V). Equilibrium field measurements indicated an increase in $(\beta_p + \ell_i/2)$ of ~ 0.64. A modest broadening of the soft X-ray profiles was observed comparable to that measured during 60 GHz 2nd harmonic heating. On-axis 2nd harmonic heating of similar target plasmas at 60 GHz resulted in a central electron temperature increase to ~ 1.15keV for ~ 70kW of injected power. Thus for comparable target plasmas, fundamental heating can produce as large a central electron temperature increase as 2nd harmonic heating at the same power. However the initial rate of rise of electron temperature is much more rapid with 2nd harmonic heating and so far fundamental heating is found to be effective in a much more restricted region of parameter space.

Combined 60GHz and 28GHz heating

For a large aspect ratio torus such as CLEO (R/a ~ 7) the fundamental resonance at 28 GHz and the 2nd harmonic resonance at 60 GHz are well separated (~ 6cm). For combined heating either one or both of the resonant surfaces will be at a non-optimum position. If the fundamental resonance is too close to the launch antenna, reflected power causes early termination of the 28 GHz rf pulse. Nevertheless for a restricted range of toroidal fields combined heating at moderate power levels has been attempted and clear resonance position-dependent modifications to the soft X-ray emission profile demonstrated. For $B_\phi = 1$T (Fig 3(a)) the 60GHz resonance is inwardly displaced by ~ 6cm (r/a ~ 0.46). During the initial 2nd harmonic heating the soft X-ray emission profile is slightly broadened and the peak amplitude falls suggesting a loss of particles from the plasma centre. A consistent, spatially localised enhancement is observed on the low field side of the profile. Subsequent

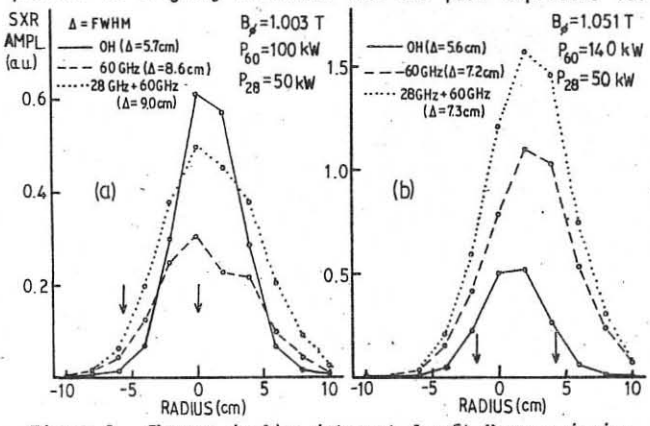


Figure 3. Changes in line integrated soft X-ray emission profiles due to 2nd harmonic (60 GHz) and combined (60 GHz + 28 GHz) heating at two different toroidal fields. The arrows indicate the resonance locations.

addition of rf at 28 GHz (resonance on axis) produced an overall increase in emission with no further broadening. In contrast for B_ϕ=1.05T (Fig 3(b)) with the two resonances either side of the machine axis the X-ray emission is increased everywhere and the profile broadens during 60 GHz injection. Addition of the 28 GHz power results in a further general increase in emission with no further broadening.

Low-voltage start-up with ECRH

Studies of ECRH-assisted start-up, using an 80kW, 20ms rf pulse at 28 GHz, have resulted in the production of well-controlled discharges with $I_p \sim$ 13kA, $\bar{n}_e \sim 5 \times 10^{18} m^{-3}$ in the presence of a loop voltage V_ℓ < 2V throughout, as illustrated in Fig 4. For the central magnetic field of $B_{\phi o}$=0.895T the cyclotron resonance was located at $(R-R_0)/a = -0.7$. The average loop voltage during the start-up phase is ~ 1.1V corresponding to an electric field E ~ 0.19V/m producing an average plasma current ramp-up rate of ~ 0.44MA/s. The initial rate of rise is ~ 0.75 MA/s.

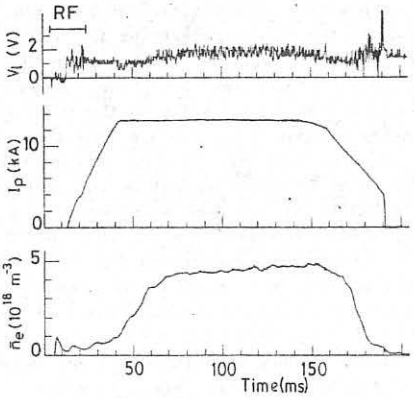


Figure 4. ECRH assisted start-up

Compared with the best ohmic discharges available in CLEO, rf-assisted start-up results in a ~ 50% reduction in the volt-second consumption and a ~ 50% increase in the fraction of the electromagnetic energy input from the poloidal field system which is converted to stored magnetic energy. The voltage required at breakdown is reduced by a factor of 5. Nevertheless it is estimated that during start-up 50-70% of the electromagnetic energy input from the poloidal field system still goes into resistive losses. This suggests that substantial further improvements may be possible by extending the rf pulse length and injected power, and optimising the start-up procedure.

References

[1] Alcock M W et al, Proc 11th EPS Conf, Vol 1, p 401 Aachen 1983
[2] Troyon F et al, (11th EPS Conf) Pl Phys & Cont Fus Vol 26, 1A, p 209, January 1984
[3] Riviere A C et al, 4th Int Symp on Heating in Toroidal plasmas, June 1984
[4] Jacquinot J, Proc 2nd European tokamak programme workshop, Paris, 1983

ACKNOWLEDGEMENT

The authors would like to acknowledge the invaluable contribution of the CLEO technical team.

ELECTRON CYCLOTRON HEATING SIMULATION IN TOKAMAKS BY COMBINED CODES

A.Airoldi(*), G.Cenacchi(+), A.Orefice(*), G.Ramponi(*)
(*) IFP, EURATOM-CNR Fusion Association, Milano (Italy)
(+) CRE "E.Clememente1", ENEA, Bologna (Italy)

The electron cyclotron resonance heating (ECRH) is currently expected to provide a very efficient heating scheme in future fusion devices |1|. Up to now, however, its utilization has been limited by technological costraints. Owing to the recent progresses in the development of gyrotrons |2|, reliable 140 GHz tubes will be available in the near future. This shall allow to couple EC frequencies to toroidal plasmas with magnetic field of the order of 50kG, so that accessibility to the ordinary mode will be possible also in high density plasmas (line average density over 10^{14} cm-3).

We present here the results of numerical simulations applied to study the effects of EC power deposition in toroidal plasmas. To this aim the transport code GETTO |3| has been combined with a suitable version of the ray tracing code ECEAIR developed for JET |4|. GETTO is used in its one-dimensional mode with circular cross-sections for the equilibrium magnetic surfaces. In these applications two impurity ion species are treated explicitly with the hypothesis of coronal equilibrium . A neoclassical resistivity (with trapped particle correction) and a neoclassical ion thermal conductivity, in the form proposed by Chang and Hinton |5|, are assumed. The electron thermal transport and particle fluxes are anomalous. The anomalous electron thermal conductivity is formulated as dependent on different plasma parameters in order to easily test any kind of transport models. An inward particle flux model |6| is also included. In the region where the safety factor q is less than one the transport is enhanced to simulate the MHD activity.

The power source for EC heating is obtained from ECEAIR according to the model described in Ref. |7|. The density, temperature and magnetic field profiles in the radial coordinate are provided by the transport code. The power deposition profile is obtained, with the usual assumption that the absorbed power is immediately distributed over the flux surface, according to the formula:

$$\frac{dP}{dV} = \frac{P_0 \sum_j w_j \alpha_j(r) \exp\left[-\tau_j(r)\right] (v_\theta/v_{gr})_j}{(2\pi)^2 r R_0}$$

where P_0 is the external power coupled to the plasma, α_j the absorption coefficient, τ_j the optical depth, $(vg/vgr)_j$ the ratio between the group velocity and its radial component, and Σ_j extends to the set of chosen rays. The power deposition term is recomputed at constant time intervals. The number of evaluations required depends on the Te profile variation during the EC power application.

Our aim was to perform different simulations relevant to an experimental scenario of ECRH on the proposed FTU device. We adopted the following basic parameters, according to the executive summary of the project |9|: R=93cm, a=31cm, B_T of the order of 5 Tesla and line average density over 10^{14} cm-3. We previously tested the combined codes by simulating the experimental results of T-10 tokamak with the model for ke proposed in Ref.|10|. In particular we reproduced the variation of $\Delta T_i(0)/T_i(0)$ with density, an important feature for a high density experiment as FTU.

Different expressions for the anomalous electron thermal conductivity χ_e were considered to predict the ECRH heating effects in FTU: T-11/10/, Neo-Alcator (N.A.)/11/ and Coppi-Mazzucato-Gruber (C.M.G.)/12/ models. All the relevant coefficients were tested by simulating experimental results of the Frascati Tokamak FT. It was found that the results were reproduced by increasing χ_e (T11) by a factor of about 1.9 and χ_e (C.M.G.) by a factor of about 1.2. No modification was required for χ_e (N.A.). In the numerical simulations for FTU the transport degradation in the presence of auxiliary heating was taken into account by multiplying χ_e by a constant factor c. The values c=2 and c=3 were chosen. Also the case without degradation was included. Moreover for the CMG model, in order to avoid the favourable effect of temperature dependence, we maintained, during the heating pulse, the initial T_e value in the χ_e computation. The impurity radiation was assumed to be about 30% of the ohmic input. A heating pulse of 800 kW lasting 200 ms was considered at 140 GHz with ordinary mode injection from the low magnetic field side.

Some of the results obtained are summarized in Table I.

Table I

Before heating	$T_e(0)$ [eV]	$T_i(0)$ [eV]	$\langle T_e \rangle$	$\langle T_i \rangle$	τ_E [ms]	P_{OH} [kW]	$\bar{n}_e \times 10^{14}$ cm^{-3}
T11	958	900	470	437	63	778	1.36
N.A.	1272	1120	423	412	57	819	1.29
C.M.G.	1546	1379	490	475	83	681	1.28
End of the heating pulse							P_{abs} [kW]
c=1							
T11	2475	1872	786	718	77	428	714
N.A.	2638	1993	759	707	76	413	700
C.M.G.	3319	2509	955	862	107	302	701
c=2							
T11	1851	1490	621	560	52	559	731
N.A.	1962	1538	593	557	48	569	732
C.M.G.	2449	1947	726	672	68	437	717
c=3							
T11	1550	1302	553	495	42	640	733
N.A.	1646	1326	530	498	39	661	736
C.M.G.	2032	1655	624	581	52	533	720

All these cases refer to a magnetic field B_T = 53kG and a plasma current I=600kA. We observe that the results obtained with T11 and Neo-Alcator models are quite similar.

The time evolution of average temperatures for the T11 model are shown in Fig.1 where (a) refer to the case with c=2 and (b) to the case with c=3. The power deposition profiles, relevant to the case (a) in Fig.1, are shown in Fig.2 at the beginning (1) and at the end (2) of the heating pulse: the broadening in the power deposition is due to T_e increasing as shown in Fig.3.

Simulations performed with an enhanced ion thermal conductivity (by a factor 3) showed that a stationary temperature state is not completely reached at the end of the heating pulse considered.

Acknowledgements

We are indebted to dr. A. Taroni for his useful suggestions.

References

| 1| F. Engelmann and NET Team: Proc. 4th Int. Symp. on Heating in Toroidal Plasmas. Roma (1984) Vol.II, p. 1408.
| 2| H. Jory: Proc. 4th Int. Symp. on Heating in Toroidal Plasmas. Roma (1984) Vol.II, p.1425.
| 3| G. Cenacchi and A.Taroni: GETTO: a one-and-a-half-dimensional transport code for a multispecies free-boundary plasma (report to be published).
| 4| A.Airoldi, A. Orefice, G. Ramponi: Electron Cyclotron Emission Simulation Code for JET. Istituto di Fisica del Plasma CNR Report FP 83/15 (1983).
| 5| C.S. Chang and F.L. Hinton, Phys. Fluids 25 (1982) p.1493.
| 6| B. Coppi and N. Sharky, Nucl. Fusion 21, 1363 (1981).
| 7| A. Airoldi, A. Orefice, G.Ramponi: To be published in 'Lettere al Nuovo Cimento'.
| 8| V. Krivenski, A. Orefice: J.Plasma Physics 30,125 (1982).
| 9| Frascati Tokamak Upgrade + ENEA Report 82.49 (1982).
|10| V.V. Alikaev et al.: Xth Conf. Plasma Physics and Controlled Nuclear Fusion Research, London 1984, Vol. 1, p.419. (IAEA, Vienna, 1985)
|11| R.J. Goldston, Plasma Phys. and Contr. Fus. 1A, 87 (1984).
|12| O. Gruber, Nuclear Fusion 22, 1349 (1982).

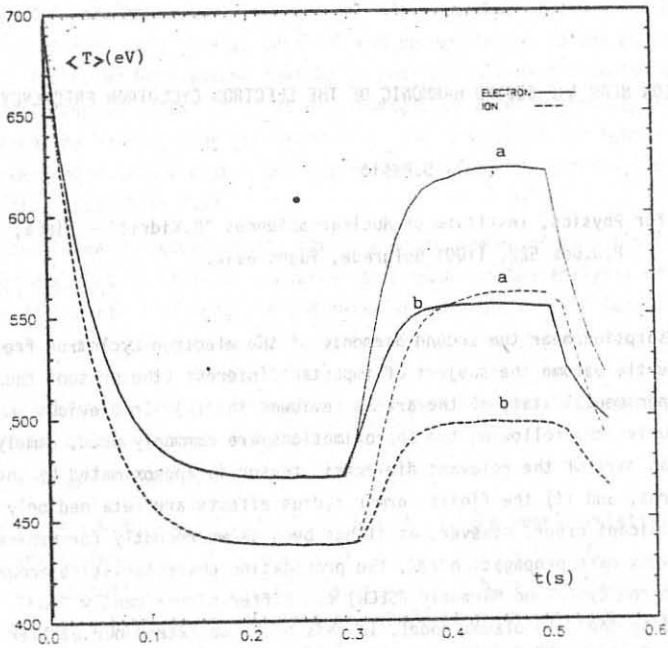


Fig.1

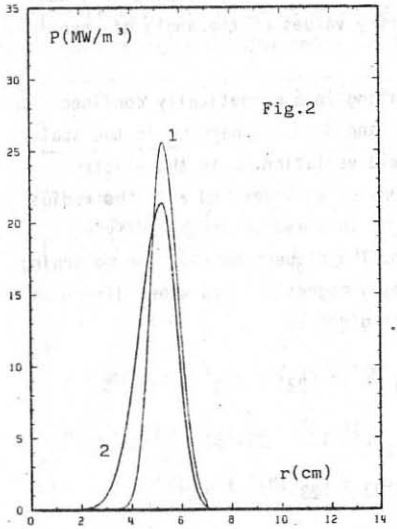


Fig.2

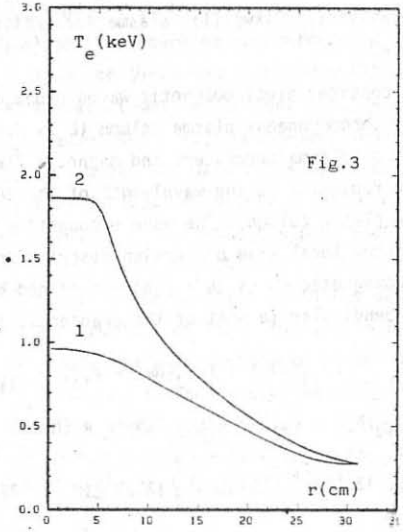


Fig.3

WAVE ABSORPTION NEAR THE SECOND HARMONIC OF THE ELECTRON CYCLOTRON FREQUENCY

S.Pešić

Laboratory for Physics, Institute of Nuclear Sciences "B.Kidrič" - Vinča,
P.O.Box 522, 11001 Belgrade, Yugoslavia.

The wave absorption near the second harmonic of the electron cyclotron frequency has recently become the subject of important interest (the present theoretical and experimental state of the art is reviewed in /1/). In previous theoretical studies the following two approximations are commonly used, namely, i) the Hermitian part of the relevant dielectric tensor is approximated by the cold plasma terms, and ii) the finite Larmor radius effects are retained only to lowest significant order. However, as it has been shown recently for non-relativistic oblique wave propagation /2/, the propagation characteristics around the second electron cyclotron harmonic (SECH) can differ significantly from those predicted by the cold plasma model. In this paper we extend our earlier work and investigate the linear wave propagation and spatial damping in a weakly-relativistic Maxwellian plasma for arbitrary values of the angle of wave incidence.

We consider electromagnetic waves propagating in a magnetically confined weakly-inhomogeneous plasma column ($L_\alpha >> \rho, \lambda$ and $\rho << a$, where L_α is the scale length of plasma parameters and magnetic field variation, ρ is the electron Larmor radius, λ is the wavelength of the considered waves and a is the radius of the plasma column). The wave propagation in this medium can be analysed within the local wave dispersion description. The dispersion equation governing electromagnetic waves in a plasma confined by a magnetic field whose direction is perpendicular to that of the gradients, is given by

$$\varepsilon_{11}N_\perp^4 + 2\varepsilon_{13}N_{/\!/}N_\perp^3 + \{\varepsilon_{33}(N_{/\!/}^2 - \varepsilon_{11}) + \varepsilon_{11}(N_{/\!/}^2 - \varepsilon_{22}) + \varepsilon_{13}^2 - \varepsilon_{12}^2\}N_\perp^2 +$$

$$+ \{\varepsilon_{13}(N_{/\!/}^2 - \varepsilon_{22}) + \varepsilon_{12}\varepsilon_{23}\}2N_{/\!/}N_\perp + (N_{/\!/}^2 - \varepsilon_{22})(\varepsilon_{13}^2 - \varepsilon_{11}\varepsilon_{33}) + (\varepsilon_{11}\varepsilon_{23} +$$

$$+ \varepsilon_{12}\varepsilon_{13})\varepsilon_{23} + (\varepsilon_{33}\varepsilon_{12} + \varepsilon_{13}\varepsilon_{23})\varepsilon_{12} - (\varepsilon_{22}\varepsilon_{33} + \varepsilon_{23}^2)N_{/\!/}^2 + \varepsilon_{33}N_{/\!/}^4 = 0, \qquad (1)$$

where $\vec{N} = \vec{k}c/\omega$ is the wave refractive index and the indices $\parallel$ and $\perp$ refer to the direction respectively, parallel and perpendicular to the equilibrium magnetic field. We here assume that $N_\parallel$ is real and determined by the direction of the wave vector of the incident electromagnetic waves at the plasma-vacuum interface, $N_\parallel = \cos\theta_i$. For the elements ε_{ij} of the dielectric tensor we use the expressions obtained within the weakly-relativistic ($\mu \equiv 2(c/v_t)^2 >> 1$) approximation (eq.(4) in /3/).

The dispersion equation (1) admits a large number of linearly independent solutions. Let us restrict ourselves at present to the analysis of this equation in the range of long perpendicular wavelengths ($\lambda \equiv N_\perp^2(\omega/\omega_c)^2/\mu << 1$) where it is amenable to analytic solution; later we present numerical solutions of equation (1). By neglecting the terms in the elements of the dielectric tensor which for n=2 are of higher order than λ, we obtain a complete algebraic equation of third order in $N_\perp^2$,

$$\alpha N_\perp^6 + a N_\perp^4 - b N_\perp^2 + c_0 = 0, \qquad (2)$$

where $\alpha = -0.5(\omega_p/\omega_c)^2 F_{7/2}(\mu, 2\omega_c/\omega, N_\parallel)$, F_q is the weakly-relativistic plasma dispersion function /3/, $a \equiv a_0 + \alpha a_1 + \beta a_2$, $a_1 = N_\parallel^2 - 2(\varepsilon_1 - \varepsilon_2) - \varepsilon_3$, $\beta = (\varepsilon_1 - 1)/\mu Y^2$, $Y = \omega_c/\omega$, $a_2 = N_\parallel^2 - \varepsilon_1$, $b \equiv b_0 + \alpha b_1 + \beta b_2$, $b_1 = 2\varepsilon_3(N_\parallel^2 - \varepsilon_1 + \varepsilon_2)$, $b_2 = -c_0/\varepsilon_1$, ε_i are the elements of the dielectric tensor of cold magnetized plasma, and a_0, b_0 and c_0 are the coefficients of the cold plasma dispersion equation to which equation (2) reduces in the limit of vanishingly small thermal effects. The roots of equation (2) determine the refractive indices of three modes: two characteristic electromagnetic modes (the X- and O-mode) and a fast quasi-longitudinal (QL) mode. The wave behaviour around the SECH depends mainly on the complex quantity α. In fact, the parameter $\alpha_r \equiv (\omega_p/\omega_c)^2(v_t/cN_\parallel)$ weighs the importance of the function F_q in the damping and coupling of these modes. For low α_r values the afore mentioned three modes propagate independently. We note that the QL-mode starts off as a highly damped low-frequency ($\omega < 2\omega_c$) mode. As the coupling parameter α_r is increased

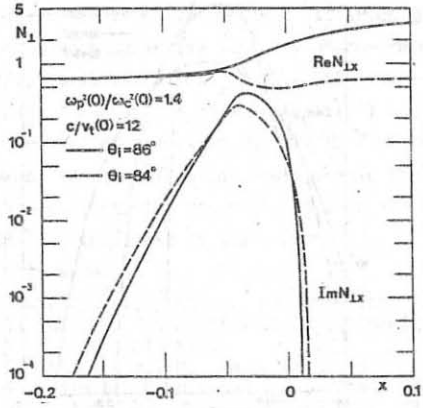


Fig. 1. $ReN_{\perp x}$ and $ImN_{\perp x}$ versus x.

the X-mode gradually deviates from the cold plasma solution and approaches the solution trajectory of the QL-mode. Finally, at some value of $\alpha_r (\alpha_r = \alpha_{rc})$ the real and imaginary part of the discriminant of equation (2) vanish simultaneously and the roots describing the X- and QL-mode coincide. For $\alpha_r \gtrsim \alpha_{rc}$ mode splitting and coupling occurs. The described wave behaviour is similar to that obtained for perpendicular wave propagation /4,5/. However, the evaluation of α_{rc} indicates that mode coupling occurs in a range of the parameter plane $\{(\omega_p/\omega_c)^2, c/v_t\}$ which is much larger than that predicted in /4,5/. Namely, it is easy to find conditions of physical interest for which the X-mode is converted to a fast QL-mode. This process enhances substantially the collisionless damping of the extraordinary mode. Futhermore, it causes the absorption line profiles for both, the X- and O-mode to be assymetric about the resonance (even in the non-relativistic range of wave propagation /2/). This assymetry is the stronger the larger the coupling parameter α_r is.

Having analysed the simplified dispersion equation (2) we proceed to examine the solutions of the complete dispersion equation (1). In the numerical analysis of equation (1) terms up to the order λ^2 are retained in ε_{ij}. The toroidal magnetic field variation is simulated by taking $\vec{B} = B_0 \vec{e}_z/(1 + x/A)$ with $x = r\cos\phi/a$, $\phi = 0$ or $\phi = \pi$ and an aspect ratio $A = 3$. Furthermore, the

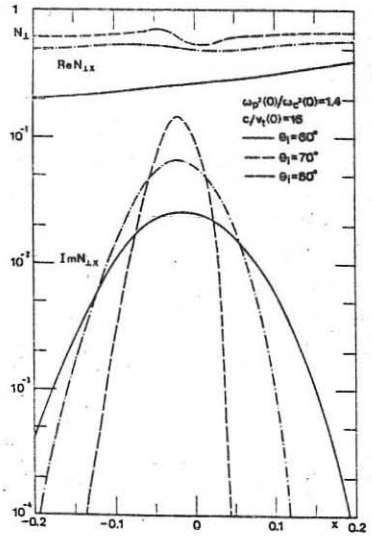


Fig. 2. $ReN_{\perp x}$ and $ImN_{\perp x}$ versus x.

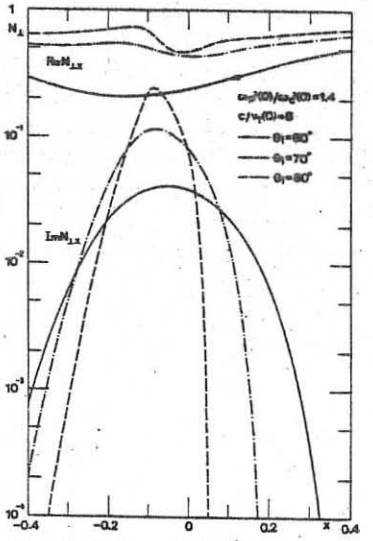


Fig. 3. $ReN_{\perp x}$ and $ImN_{\perp x}$ versus x.

electron density and temperature are allowed to have a parabolic radial profile. To illustrate the mode coupling we present in Fig.1 the solutions of the complete dispersion equation (1) which describe the X-mode for values of the angle of wave incidence just below (θ_i=86°) and above (θ_i=84°) the critical one, $\omega_p^2(0)/\omega_c^2(0)$=1.4 and $c/v_t(0)$=12. Here and in Figs. 2-3 we took a driving frequency equal to the second harmonic of the "central" electron cyclotron frequency. As expected the solution trajectories of the X-mode differ considerably in these two cases. In the mode coupling range (θ_i=86°) the X-mode propagating in the direction of decreasing magnetic field, slows down and in the immediate neighbourhood of the resonance converts to a fast forward QL-mode. This linearly converted QL-mode slows down futher and at the linear turning point, transforms into a slow backward QL-mode /6/. On the other side, the X-mode launched from the low magnetic field side, matches smoothly with the low-frequency ($\omega < 2\omega_c$) QL-mode (this solution trajectory is not represented).

In Figs. 2 and 3 we show the variation of the real and imaginary part of $N_{\perp x}$ with the dimensionless space coordinate x for $\omega_p^2(0)/\omega_c^2(0)$=1.4, θ_i=60°, θ_i=70° and θ_i=80°, $c/v_t(0)$=16 and $c/v_t(0)$=8, respectively. We see that for increasing $v_t(0)/cN_{//}$ the deviation of $ReN_{\perp x}$ from the cold plasma values and the maximum of $ImN_{\perp x}$ increase. Simultaneously, the damping region displaces towards the high-magnetic field side and becomes narrower. It should be pointed out that the assymetry of the absorption line profile about the resonance is caused by relativistic and (for relatively large values of α_r) mode coupling effects. We find that the normalized optical depth $\eta/k_0a = \int dx' ImN_{\perp x}(x')$ reaches relatively large values that is, values which are significant for the wave absorption, only in the vicinity of the resonance position (for instance, for i) $c/v_t(0)$=16 and ii) $c/v_t(0)$=8, θ_i>65° one has $\eta/k_0a \cong 10^{-3}$ at x<0.05). This implies that in large-size plasmas ($k_0a \geq 10^3$) the interaction between the X-mode and energetic electrons on the far tail of the absorption line profile is weak for wave launching from the low-magnetic field side. On the other hand, in the considered parameter range (θ_i>60°, c/v_t>4) the damping of the O-mode is much smaller than that of the X-mode.

References

1. Bornatici, M. et al., Nucl. Fusion 23, 1153(1983).
2. Pešić, S., Proc. XII SPIG '84, Šibenik, Yugoslavia, 572(1984) and Pešić, S., (to be published).
3. Shkarofsky, I.P., Phys. Fluids 9, 561(1966).
4. Lazzaro, E. and Ramponi, G., Plasma Phys. 23, 53(1981).
5. Bornatici, M. et al., Plasma Phys. 23, 89(1981).
6. Pešić, S., Physica 125C, 118(1984).

CURRENT DRIVE AND PLASMA HEATING BY LONGITUDINAL E.C.R WAVES

T. CONSOLI

COMMISSION OF THE EUROPEAN COMMUNITY - D.G XII - FUSION PROGRAMME

200 Rue de la Loi Brussels 1049 Belgium

ABSTRACT :

The aim of this paper is to investigate in whatever conditions low frequency. Heating and Current drive processes as R.F. Ohmic pumping /1/, T.T.M.P /2,3,4,5,6 / might be excited by the modulation of the diamagnetism of a hot electron toroidal plasma sheath generated by E.C.R longitudinal waves.

Introduction.

R.F. plasma heating and the curren drive in toroidal devices at any frequencies except for E.C. waves, need coupling structures located in the region between the wall and the dense plasma core. This region of thickness d(usually $3\% < \frac{d}{a} < 10\%$, where a is the plasma radius) is a "lost volume" where the launched waves may be absorbed unavailingly if the wall desorption and sputtering due to fast particles bombardement, plasma radiation and instabilities, creates an undesirable plasma target. This effect does not occurs with E.C. waves (transverse O and X modes or longitudinal whistler mode propagation).

Indeed even if an undesirable plasma target is generated, it is transparent to these high frequency waves. A more advantageous strategy is to generate round the hot plasma core a hot electron plasma shell by using longitudinal right hand R_H circularily polarized E.C.R waves. The launching system shown on fig 1.is constituted by a periodic array of guides located from the low field side. They supplie the microwave power and the neutral gaz puffing. Waves launching from the high field side is also possible with a similar bended system or with a special "slit coupled T junction", The guides are oriented along the toroidal magnetic flux tubes. The microwave sources (gyrotrons) frequency is chosen so as to excite E.C.R just in the border region. The delivered R.F. power is modulated at a low frequency fm and adequately phased.

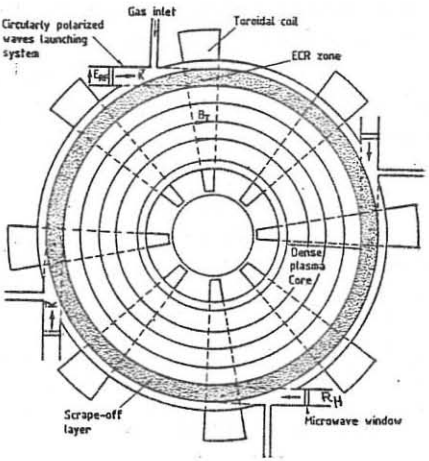


Fig 1

$$(P_{RF})_\nu = P_o \sin(\omega t + \varphi_\nu).$$

$\sin \omega_{ce} t$ where $\nu = 1,2,3...$ is the order of the gyrotrons and φ_ν the phase of the modulation of the ν^{th} RF source. According to the researched objective: heating or current drive the phase φ_ν is chosen so as to

excite a stationary or a travelling wave. The modulation frequency fm is : fm < 10 KHz for Ohmic pumping and 30 KHz < fm <150 KHz for T.T.M.P ions heating. In the case of current drive by electron TTMP, fm < 2 MHz.
With an electronic feed back system, fm and Q_v can be changed in a broad band domain so as to follow the evolution of plasma parameters (n,Te,Ti).
The hot electrons plasma jets generated along the flux tubes, create after diffusion an external toroidal plasma mantle. The density and the transverse energy $W_{\perp e}$ of the electrons of this sheath are controlled through the injected R.F. power and the neutral gaz pressure. The amplitude of the diamagnetic field of this external plasma $B_{RF)r.m.s}$ can easily be changed from few tens to few hundreds gauss, so as to get the needed field modulation rate,

$$b = \frac{|B_{RF}|_{rms}}{|B_T|} \quad , \qquad 10^{-3} < b < 10^{-2}$$

This kind of excitation suppresses the use of resistive coils, the formation of an uncontrollable plasma in the "lost volume" of the toroidal vessel and improves the efficiency of the R.F. methode. The created hot electron plasma mantle plays also a beneficial role against the pollution; because heavy atoms coming from the walls are ionized and their inward diffusion is slow down by the ambipolar potential of this external hot electron plasma.

Working scheme - Characteristics of the external mantle

The experimental feasibility of ions heating and current drive by T.T.M.P using resistive coils encircling the plasma, is well established /7,8,9/.
Let us examine the conditions for getting a modulation rate $4.10^{-3} < b < 10^{-2}$ and a wave phase velocity v_φ, $10^7 < v_\varphi < 10^8$ cm/s that is to say $v_{\varphi i} \simeq v_{thi}$ or $v_{\perp e} \simeq v_{the}$, by means of the space and time modulation of the diamagnetic field of a hot electrons plasma.
A rigourous calculations requires a numerical simulation which is in course. This paper is a preliminary rough estimation of the parameters of the external mantle. Neglecting the parallele velocity of the hot electrons because $v_{\perp e} \gg v_{\parallel e}$ in the external shell; the stored energy can be approximated by $1/2 . m_e . n_{sh} \langle v_{\perp e}^2 \rangle V_{sh}$ where $\langle v_{\perp e}^2 \rangle$ is the averaged energy value and V_{sh} the volume of the sheath.

We can also write $n_{sh} \langle W_{\perp e} \rangle . V_{sh} \simeq b^2 . B_T^2 . V_{sh} / 4\mu_0$ (1)

Considering as for example a TOKAMAK device with the following parameters: R = 5 m, a = 1 m, d = 0,1 m (B_T)$_o$ = 5 T, $\bar{n}_e = 10^{20} m^{-3}$ we get :

$$5.10^{17} < (n_{sh} . \langle W_{\perp e} \rangle) < 3.10^{18} \text{ in } (e . m^{-3} . KeV) \quad (2)$$

and $$V_{sh} = 2\pi^2 r^2 dR \simeq 9,87 \, m^3$$

The toroidal magnetic field at the edge being 4 T, the local f_{ce} is 112 GHz. and the cut off density of the ordinary wave is $1,5 \times 10^{20} e . m^{-3}$: noting that the longitudinal right hand wave has no cut off. Therefore the parameters in the product $n_{sh} . \langle W_{\perp sh} \rangle$ are mainly determined by equations (1) and by RF power balance considerations.
The estimation of the microwave power needed for sustaining the hot electrons sheath is obtained with the same procedure as that used by N.A. UCKAN /10/.

$$(Mw/m^3) \quad P_{RF}/V_{sh} = \sum_{losses} P_{(synch + bremst + scatt + drag)} \quad (3)$$

The calculation shows that the dominant loss is the drag of the hot electrons on the TOKAMAK'S plasma core :

$$P_{drag}(MW/m^3) \simeq 2,5 \times 10^{-39} \cdot n_{sh} \cdot \bar{n}_{edge} \times \frac{\gamma \ln \Lambda}{(\gamma^2-1)^{1/2}} \quad (4)$$

The table below gives this loss in MW/m³ for a density on the edge of $10^{19} m^{-3}$

$\langle W_{\perp e} \rangle$ \ n_{sh}	10^{19}	5×10^{18}	10^{18}
0,5	34	17	3,4
1	23,8	11,9	2,38
5	10,6	5,3	1,06

We see from this table that it is more convenient to choose a low density $n_{sh} \simeq 5.10^{18} e.m^{-3}$ and a higher energy $\langle W_{\perp e} \rangle \simeq 5$ keV . In this case the total losses are of the order 10 MW , and the chosen $\bar{n}_{sh} \cdot \langle W_{\perp e} \rangle$ satisfie also condition (1). This estimation does not takes into account the R.F. power needed for the low frequency modulation.

Ionizing and trapping role of the hot electron plasma mantle.

In 1958 H.DREICER has proposed the concept of the isolation of a magnetically confined hot electron plasma from wall emitted impurities by an auxiliary "intervening plasma" /11/. A same role is played in our case by the hot electron plasma mantle.

Indeed any neutral particle released by the wall and crossing the external sheath is ionized if the ionization mean free path $\ell = \frac{V_{imp}}{n_{sh} \langle \sigma_{imp} v_e \rangle}$

is smaller than d, $\ell_i < d$ where

V_{imp} is the speed of the impurity and $\langle \sigma_{imp} \rangle$ the ionization cross section.

In our case $n_{sh} \simeq 5\ 10^{13}$ e/m³ , $\langle \sigma_{imp} . v_e \rangle \simeq 10^{-9}$ cm³/sec

$V_{imp} \gtrsim 10^3$ m/sec and accordingly $\ell_i \sim 2$ cm $< d$

In addition the ionized impurity motion is restricted by its diffusion accross the sheath and also by its collisions with the deuterium atoms and neutrals.

The diffusion and elastic collision times are :

$$\tau_{diff} = \frac{d^2 B_T^2 \langle V_{dif} \rangle}{2 \times 10^3 \times n_i} \text{ sec} \quad (4) \qquad \tau_{coll} = \frac{3 d^2 B_T^2 \cdot 10^8}{V_{imp} V_{neutr} \sigma_e A^2} \text{ sec} \quad (4)$$

where V_{diff} is the averaged diffusion speed, σ_e the elastic collision cross section in cm² with deuterium ions and neutrals and A the atomic weight of the impurity.

With the parameters mentionned above, both times τ_{diff} and τ_{coll} are > 1 sec, therefore the penetration of impurities in the plasma core is slow down. Finally the hot electron plasma sheath has another active effect against the pollution.

The ambipolar potential Φ of the hot electron plasma sheath

$\Phi \simeq \langle W_{ie} \rangle \cdot \ln \frac{n_{sh}}{n_{core}}$ creates an electrostatic E_s electric field. From one side the effect of the electrostatic potential is again to slow down the penetration of any ionized neutral atom, from another side if the electrostatic field E_s is in some conditions sufficiently high $E_s > 10^2$ V/cm the resulting centrifugal force $\vec{F}_c \simeq \vec{E}_s \times \vec{B}_T$ can expel preferentially the heavy particles /12/.

Conclusion :

It is necessary for a further step to show experimentally that it is possible to modulate in space and time the main toroidal magnetic field by means of the diamagnetism of a hot electron external plasma flow created by a local E.C.R.. The R.F. power needed for a modulation rate $\delta < 10^{-2}$ on a JET's size device is of the order of 30 MW. The suppression of resistive coils and the filling of the "lost volume" by an ionizing and impurity trapping hot electrons plasma mantle seems very attractive.

References :

/1/ M. Bonnedal and E. Canobbio - Proc. of the VIIth Intern.Conf.Pl. Phys. and Cont.Nucl.Fus. Innsbruck 23-30 August 1978 Vol.II page 535

/2/ K.N. Stepanov - Sov.Phys.JETP (18). 1964 p. 826

/3/ J.M Dawson and Uman N.F. 1965. Nucl.Fusion 5 p. 242

/4/ E. Canobbio. Proc. of the IVth Intern.Conf.Pl. Phys.and Contr. Nucl. Fusion - Madison 17-23 June 1971 Vol III p. 491
E.Canobbio, Nucl. Fusion - 12 (1972) p. 561

/5/ D. J.H. Wort Proc.Nuc.Fus.Reactor Conf. U.K.E.A. 1970 p 517
C.L.M p 236 June 1970

/6/ D.A. Ehst. I.A.E.A.-Meeting on R.F. Heating in Large Fusion Experiments. Princeton Univ. P.P.L. - Oct. 1981

/7/ R.Bardet and Petula group.Proc. of the VIIth Inter.Conf.Pl.Phys. and Contr. Nucl. Fusion. Innsbruck 23-30 August. 1978 Vol II p. 545

/8/ K. Matsuura et Proc. on RF Heating Symposium Austin 1978- C_6-1.

/9/ T.Yamamoto et al. Phys. Rev. Lett. US (1980) p. 716

/10/ N.A. UCKAN. ONRL/TM. 7302 - May 1980

/11/ H. Dreicer. Los ALAMOS internal Rep. LASL. April 1958 New-Mexico.

/12/ T. Consoli et al. Proc. of the Vth Inter. Conf. on Contr. Nucl. Fusion and Pl. Physic. TOKYO Nov. 1974 Vol I p. 571.

ELECTRON CYCLOTRON HEATING OF A TOKAMAK PLASMA AT DOWN-SHIFTED FREQUENCIES

G. Giruzzi, V. Krivenski and L.F. Ziebell [a)]

Association Euratom-CEA sur la Fusion
Centre d'Etudes Nucléaires
92260 Fontenay-aux-Roses (France)

Abstract

Electron cyclotron resonance absorption at frequency significantly below the central electron gyrofrequency is investigated in the case of the extraordinary wave for oblique propagation. It is shown that strong absorption can occur for a Maxwellian plasma at temperature $T_e > 3$ keV in existing tokamak devices.

High power Electron Cyclotron Resonance Heating (ECRH) experiments in tokamaks have demonstrated the potential use of this form of plasma heating in a fusion reactor. So far, ECRH with outside launching of ordinary waves has been considered the most attractive method applicable to tokamak reactors. It has, however, some serious drawbacks. Since the rf energy is deposited in the narrow plasma region where $f \approx f_c$ (f and f_c being the wave and the EC frequencies, respectively), this type of ECRH requires the use of high frequency microwave sources. For an INTOR-type reactor, with a toroidal magnetic field B(0) =55 kG, the required frequency is $f \approx 150$ GHz. Moreover, a density limit is given by the ordinary mode cutoff at the plasma frequency f_p. An alternative way of ECRH in which those difficulties are minimized was recently proposed [1]. The basic idea can be stated as follows: in hot and dense Maxwellian plasmas, the number of energetic electrons is sufficient for a strong absorption of EC waves at down-shifted frequencies, i.e. $f \ll f_c$. In this case, ECRH can be applied to a plasma

which has been pre-heated to electron temperatures $T_e > 3$ keV, which is already a range of operations of some existing tokamaks.

We first present some numerical results for EC absorption in a high-density, INTOR-type tokamak. The appropriate theoretical framework for studying this kind of problems is the relativistic dispersion relation, which is solved along the wave trajectories, computed by a ray-tracing code.[2] We consider two launching positions, i.e. near the equatorial plane and near the vertical direction. The injection angle with respect to the normal of the magnetic field in the toroidal section is denoted by ψ. The launching position is defined from the poloidal angle ϑ and the angle $\Delta\vartheta$ between the wave direction in the poloidal section and the inner normal. For the plasma density n_e and the safety factor q we assume parabolic profiles (q(0) = 1, q(a) = 3, total current I = 3 MA), whereas $T_e(r) = T_e(0)\,(1-r^2/a^2)^{3/2}$. We show the fraction $\eta(r)$ of the wave power deposited between the plasma edge and the radial location r, for an extraordinary wave at f = 110 GHz. Fig. 1 refers to top launching ($\vartheta = 80°$, $\Delta\vartheta = 10°$, $\psi = -30°$, B(0) = 52 kG), for a) $n_e(0) = 10^{14}$ cm^{-3}, $T_e(0) = 5$ keV; b) 2×10^{14} cm^{-3}, 5 keV; c) 3×10^{14} cm^{-3}, 7 keV. Good absorption is obtained even at very high densities, midway between the edge and the plasma axis, if T_e is sufficiently large. Note that this property contrasts to the usual n_e^{-1} scaling law of the extraordinary mode absorption, which is valid at $f \approx f_c$ [1,2]. In the case of wave launching near the equatorial plane the absorption is also good, but more shifted towards the plasma edge, as shown in Fig. 2 for $\vartheta = 10°$, $\Delta\vartheta = 10°$, $\psi = -30°$, B(0) = 53 kG and a) $n_e(0) = 2.5 \times 10^{14}$ cm^{-3}, $T_e(0) = 5.5$ keV; b) 3×10^{14} cm^{-3}, 6 keV; c) 3.5×10^{14} cm^{-3}, 7 keV.

ECRH at down-shifted frequencies can be tested in present day tokamaks with the existing microwave sources (f = 60 GHz) or those under development (100 GHz), by using large values of ψ. For instance, in the PLT tokamak at f = 60 GHz, B(0) = 28.5 kG, $T_e(0) = 3$ keV, $\psi = 60°$ and top launching, we obtain

wave absorption between 60% and 95% for densities $3 \times 10^{13} < n_e(0) < 5 \times 10^{13}$ cm^{-3}; power deposition is midway between plasma edge and axis. For the TFTR tokamak at f = 100 GHz, B(0) = 47.5 kG, $T_e(0) = 3$ keV, $\psi = 60°$, top launching, full wave absorption is achieved near the central region at densities $8 \times 10^{13} < n_e(0) < 1.4 \times 10^{14}$ cm^{-3}. Note that for both tokamaks, in the same launching configuration, large absorption can be obtained at lower temperatures by slightly lowering the magnetic field. For instance, in PLT at $T_e(0) = 1.5$ keV, $n_e(0) = 5 \times 10^{13}$ cm^{-3}, total absorption is achieved by using $\psi = 50°$, B(0) = 26 kG. Thus, the principle of ECRH at down-shifted frequencies could be proved even in present-day, ohmically heated tokamak devices.

a) Permanent address: Instituto de Física , Universidade Federal do Rio Grande do Sul, 90000 Porto Alegre, RS, Brazil.

1) I. Fidone, G. Giruzzi, E. Mazzucato, Phys. Fluids 28, 1224 (1985).

2) I. Fidone, G. Giruzzi, V. Krivenski, L.F. Ziebell, E. Mazzucato, Report EUR-CEA-FC-1259 (1985), submitted to Phys. Fluids.

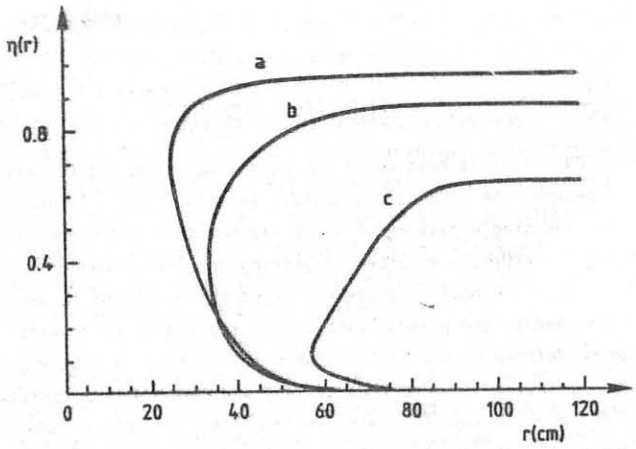

η(r)
0.8
0.4
a
b
c
0
20
40
60
80
100
120
r(cm)

Fig. 1

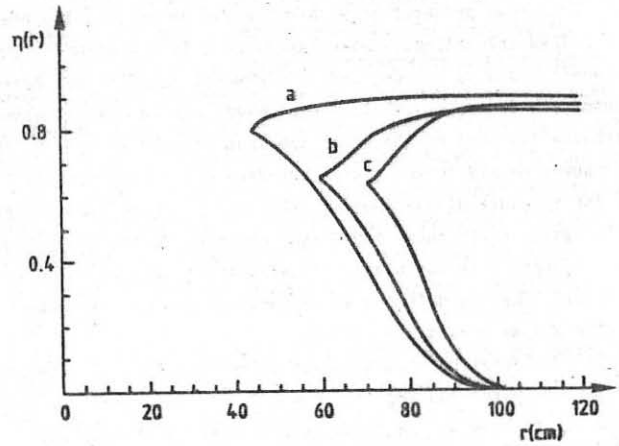

η(r)
0.8
0.4
a
b
c
0
20
40
60
80
100
120
r(cm)

Fig. 2

OPTIMIZATION OF ICRH ANTENNAS BASED ON COUPLING AND ABSORPTION

M. Söll, J.-M. Noterdaeme

Max-Planck-Institut für Plasmaphysik
EURATOM-Association, D-8046 Garching

Introduction: ICRH antennas have up to now mainly be optimized for maximum power coupling between the antenna and plasma. In this cases the coupling is calculated using the single pass model which assumes that the power radiated from the antenna is completely absorbed by passing one time through the plasma. In this idealized model the power coupled to the plasma is set equal to the power absorbed in the plasma. Within this framework, an antenna efficiency can be defined by the ratio between the maximum voltage V_{max} occuring in the rf system (antenna + coax line) and the power P_c radiated from the antenna. Minimum $V_{max}/\sqrt{P_c}$-value would define an optimum ICRH antenna system. But there exist two hints that this definitions may be not sufficient to describe a suitable antenna efficiency with respect to the aim of an rf system - namely the heating of the plasma. The first one follows from theoretical work /1/about wave propagation within the vacuum vessel. The power radiated from an ICRH 1x2 antenna (the notation used is explained in the Appendix), generally used up to now, can induce waves which travel between the plasma boundary and vacuum vessel. These waves, called coaxial waves, could be excited by the part of the power spectrum located at $k_{\parallel} \approx 0$. They deposite their power mainly in the plasma boundary and vacuum vessel; this power is lost for the bulk plasma heating. The second argument comes from ray tracing calculations. It was shown for plasma machines of the present generation that the absorption in the plasma is below the idealized value used for "single pass model". Thus by defining an antenna efficiency the power P_a absorption in the plasma should be involved.

Taking into consideration that the maximum voltage V_{max} is often the limitation in the rf system and that the power P_a absorbed in first transit calculated from ray tracing can be taken as a measure of the quality of the total power (since it is unclear what happens to the power not absorbed in the first transit) we propose to use $V_{max}/\sqrt{P_a}$ as an efficiency parameter for an ICRH antenna system.

The application of our definition $V_{max}/\sqrt{P_a}$ is especially then advantageous if antenna systems with different $k_{\parallel}$-spectra are compared. Coupling and absorption depend on a different way on $k_{\parallel}$. Whereas coupling improves for small $k_{\parallel}$-values, the absorption increases with increasing $k_{\parallel}$. A spectrum that is peaked at $k_{\parallel} \approx 0$ is produced by a 1x2 or 2x2 antenna with zero-phasing in the toroidal direction. A spectrum peaking at $k_{\parallel} \neq 0$ can be produced by a 2x2 antenna with π-phasing in the toroidal direction. As far as the coupling only is considered, the latter antennas are disadvantageous in comparison to the former antennas because large V_{max} are often necessary to radiate equal amounts of power. But if the absorption is taken into account the quadrupole antennas gain as a consequence of improved absorption. In this study a comparison between both types of antenna configurations including coupling and absorption is carried out. The model calculations are done using the parameters of ASDEX UPGRADE /2/.

Description of the calculation model: The antenna coupling calculations for antennas with different $k_{\parallel}$-spectrum were carried out with a 2-D model /3/; the ratio between absorbed power and coupled power was found with the ray tracing program RAYIC /4/. The flux surface pattern, the density and temperature profiles used for the calcultions are shown in Fig. 1. The heating scheme is the first harmonic heating of hydrogen at a frequency of 76 MHz. A schematic view of the antenna given by a poloidal cross section through the antenna is shown in Fig. 2. Figure 2a represents a 1x2 antenna and Fig. 2b a 2x2 antenna. In the figures 2a, 2b the width ($2w_z$) of the central conductor(s) the distance central conductor-return conductor d is defined. For a given total width W the geometrical constraint $2w_z+2d = W$ resp. $2d+4w_z+\varepsilon = W$ follows from thumb rule that the distance between the conductor edge and the lateral (not slotted) boundary is equal to d. The antenna parameters were calculated for the maximum width W = 70 cm available for ASDEX-UPGRADE between protection limiters; the distance d was kept constant at 14 cm.

Results: The $k_{\parallel}$-spectra for the active radiated power are shown in Fig. 3 for three 2x2, (π,π) arrays and for the 1x2 array of width $2w_z$ = 42 cm. The location of the maximum lies for the 2x2 array in the range of $k_{\parallel} = 8\ m^{-1}$. The differences in $k_{\parallel}$ at the maximum for various gap distances ε are small and in the range of $k_{\parallel} \approx 1\ m^{-1}$. Larger differences are found with respect to the maximum voltage V_{max} in a 30 Ω coax line (see curve $V_{max}/\sqrt{1MW/P_c}$ of

Fig. 4). The dependence of V_{max} on ε follows from the superposition of two opposing tendencies, an increase with increasing ε at constant $2w_z$ and a decrease with decreasing $2w_z$ at constant ε. In our case (W = const.) $2w_z$ decreases when ε increases. The decrease of V_{max} with increasing ε is essentially dominated by the variation of the conductor width $2w_z$. The V_{max} value normalized with respect to the P_a are about 30 % higher as shown in Fig. 4 because the single pass absorption for the 2x2,(π,π) arrays is about 55%. The variation of P_a/P_c with ε is small, which is in accordance to the small variations of the $k_\parallel$-spectrum with ε.

The corresponding values for the 1x2 antenna are shown in Fig. 4 at the left hand side. There is only a modest difference in the V_{max}-values between the 1x2,(0) and 2x2,(π,π) arrays as a consequence of the relatively large total width of 70 cm. However, the single pass absorption for the 1x2 antenna is, with 30 % considerably smaller than that for the 2x2,(π,π) array. Thus if one compares the voltages per MW absorbed it is possible to find 2x2,(π,π) configurations which have lower voltages than the 1x2 antenna which would fit into the same space. For smaller W values (for instance 40 cm) the difference in the coupling voltage can be much higher so that in those cases the increased absorption of a 2x2,(π,π) array can not compensate for the decreased coupling.

References

/1/ A.M. Messiaen, R. Koch, V.P. Bhatnagar, P.E. Vandenplas, R.R. Weynants: Proc. 4th Int. Symp. on Heat. in Tor. Plas. Vol.I, Rome 1984, pp 315-329
/2/ ASDEX-UG team: MPI für Plasmaphysik, Garching; Report IPP 1/217, 1983
/3/ M. Söll, E. Springmann: MPI für Plasmaphysik, Garching; Report IPP 4/215, 1984
/4/ M. Brambilla: MPI für Plasmaphysik, Garching; Report IPP 4/216, 1984

Appendix: Nomenclature for ICRH antennas

To define the geometrical arrangement, the number of loops in the array in the toroidal direction (ν) and in the poloidal direction (μ) are counted. The notation is then an $\nu \times \mu$ array.

To define the electrical connection (and therefore the direction of the currents) two numbers are sufficient if the change in phase between adjacent loops in the toroidal ($\Delta\alpha$) and poloidal direction ($\Delta\beta$) is periodic. We write them down as ($\Delta\alpha$, $\Delta\beta$).

The complete definition includes then both the geometry and the electrical connection in the form $\nu \times \mu$,($\Delta\alpha$, $\Delta\beta$). Some examples are shown in Fig. A1.

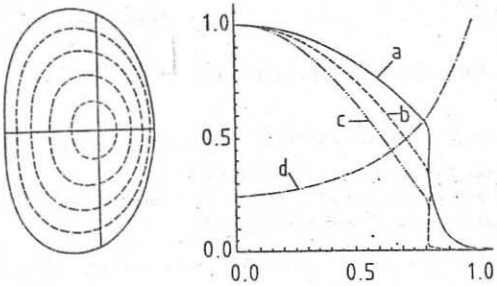
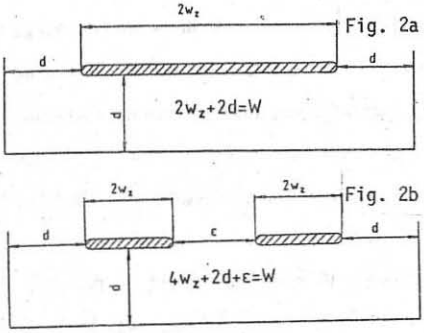


Fig.1 Flux surface plot and profiles of (a) n_e, (b) T_e, (c) T_i and (d) q used for the program RAYIC. The curves are normalized to the maximum values $n_{eo}=10^{20}m^{-3}$, $T_{eo}=T_{io}=5keV$, $q_a=4.22$



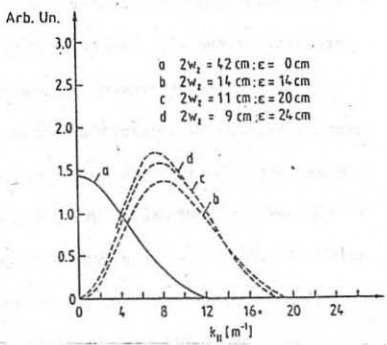


Fig.3 k_H spectra for a 1x2,(0) and three 2x2,(π,π) arrays

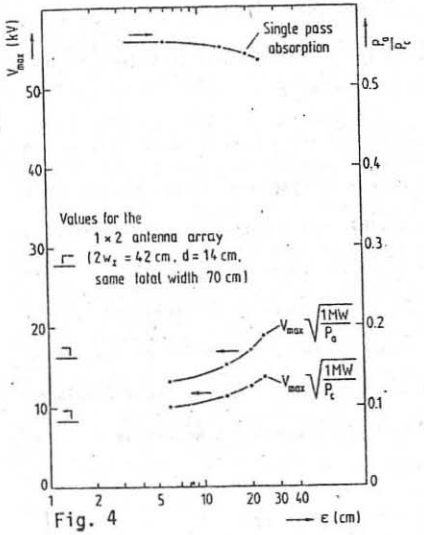
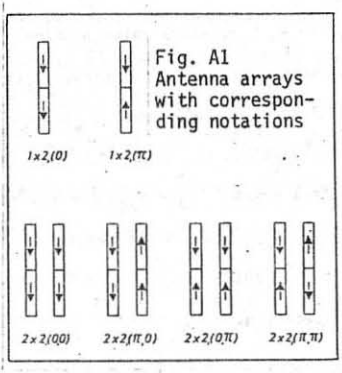


Fig. 4



CONTROL OF ENERGY EXCHANGE RATE BY I C R F CATALYST

Sanae-Inoue ITOH, Kimitaka ITOH[+] , Atsushi FUKUYAMA[-] and Kyoji NISHIKAWA
Institute for Fusion Theory, Hiroshima Univ. HIROSHIMA 730
[+] Fusion Research Center, Japan Atomic Energy Research Institute, Tokai, 319-11
[-] School of Engineering, Okayama Univ. OKAYAMA 700, JAPAN.

A concept of RF catalyst by use of ion cyclotron wave is presented. Recently, theoretical and experimental progress on RF waves have shown that RF wave becomes a strong candidate for heating, current-drive and so on. When we apply a large power input of the wave, we call it RF heating. RF catalyst is the case where we activate the plasma eigenmode by a small amount of power input. Even if the input power is small, the energy/momentum transfer rate between plasma species through wave-particle interaction can be enlarged. We consider a plasma which contains the high energy beam component. In the presence of RF waves, the beam component can amplify RF wave energy which is then absorbed by back ground ions. The stimulated energy flow from high energy beam to ions are induced by launched RF waves. The induced energy flow is proportional to the small input power, but is much larger than the latter. The case without an input corresponds to a spontaneous instability eigenmode of plasmas.

We analyze the concept of ICRF catalyst by solving a kinetic wave equation in the form of boundary value problem. Bulk plasma is immersed in an inhomogeneous magnetic field in z-direction, $B_z(x) = B/(1+x/R)$ and has the spatial profiles as $n_s(x) = n_{s_0}(1-x^2/a^2)$ and $T_s(x) = T_{s_0}\exp(-3x^2/a^2)$. The high energy beam of uniform velocity, u_b , and the temperature, T_b , is assumed to be localized in the central region $n_b = n_{b_0}(1-(4x/3a)^2)$. The plasma is surrounded by the vacuum region, $a<|x|<b$, and the resistive wall is located $x=\pm b$. The antenna is placed $x=-d$ in this case ($a<d<b$). We assume that the plasma is homogeneous in y and z directions.

The basic equation is,

$$\nabla\times\vec{E}=-i\omega\vec{B},\quad \nabla\times\vec{B}=-\frac{i\omega}{c^2}\vec{E}+\mu_0(\sum_s\vec{J}_s+\vec{J}_{ext}),$$

where $\vec{J}_s$ is the perturbed current of s-th species. Taking into account of the inhomogeneity of conductivity tensor, $\overleftrightarrow{\sigma}_s$, $\vec{J}_s$ is written

$$\vec{J}(\vec{r})=(\overleftrightarrow{\sigma}-\frac{i}{2}\overleftrightarrow{\sigma}_1'-\frac{1}{8}\overleftrightarrow{\sigma}_2''-i\overleftrightarrow{\sigma}',\frac{\partial}{\partial x}-\frac{1}{2}\frac{\partial}{\partial x}\overleftrightarrow{\sigma}''\frac{\partial}{\partial x})_{k_x-0}\vec{E}(\vec{r})$$

where $\sigma_1=\partial\sigma/\partial x$, $\sigma_2=\partial^2\sigma/\partial x^2$ and prime denotes $\partial/\partial k_x$. We retain terms up to the 2nd order of $k_x\rho$ (ρ : ion gyroradius). The kinetic effect parallel to magnetic field is included via plasma dispersion function, Z. The power absorption density is given by $P_s=\langle\vec{J}_s\cdot\vec{E}\rangle$, which satisfy the conservation law in the total system, i.e., $\Sigma\overline{P}_s+\overline{P}_w=\overline{P}_A$. ($\overline{P}_A$: input power from the antenna, $\overline{P}_w$: loss on the wall and $\overline{P}_s=\int 2\pi R\cdot P_s dx$.)

We here examine the case of proton injection into deuteron plasma. The slowed-down protons are in general confined in the plasma. We therefore consider the situation that the bulk ions of T_i consist of majority deuteron and minority proton. We take $n_{D_0}/n_{e_0}=0.9$, $n_{H_0}/n_{e_0}=0.08$ and $n_{b_0}/n_{e_0}=0.02$.

We solve the basic equation for the parameters of JET-2M grade plasma, i.e., $R=1.31m$, $a=0.35m$, $b=0.45m$, $B_z=1.4T$, $T_e(0)=T_i(0)=1keV$, $n_e(0)=5\times10^{13}/cc$ and $\eta_w=10^{-5}\Omega m$ (η_w: wall resistivity). The proton beam of $T_b(0)\cong10keV$, $E_b\cong50keV$, and $u_b\cong4.9\times10^6m/s$ is considered in this case.

The figure 1 illustrates the wave field, energy flux and power deposition profile for the parameters of $k_nR=16$ and $\omega/2\pi=21.58MHz$ (near the stable cavity resonance). The graph of the energy flux density shows the fact that the wave is emitted from the antenna, amplified by the beam in the region $-20cm\lesssim x\lesssim -10cm$ and is absorbed by cold ions in the region $-10cm\lesssim x\lesssim 0cm$. The amplification factor of the energy flux is about 8. The energy loss from the beam ions $P_b=-2.10\ W/m^2$ while the antenna radiates the power $P_A=2.6\times10^{-1}\ W/m^2$.

The injection of the small amount of the fast wave gives rise to the large energy exchange between beam component and bulk plasmas. The ion-Bernstein wave becomes unstable owing to the fast beam component, and the fast wave excited by the antenna supplies the source of the ion-Bernstein wave via the mode conversion.

In an actual application of this ICRF catalyst scheme, wide range of $k_{\parallel}$ components is radiated from the antenna for given value of ω, when the antenna area is limited in the toroidal direction. Among the excited components, there are several cavity resonances at which the large amplification of the injected fast wave is possible. We have performed the parameter survey in ($k_{\parallel}$-ω) space to find out the region where this ICRF catalyst scheme works. We find that the enhanced emission of ICRF wave from the beam ions occurs in the wide range of parameter space. As an example, Fig.2 shows the k_z

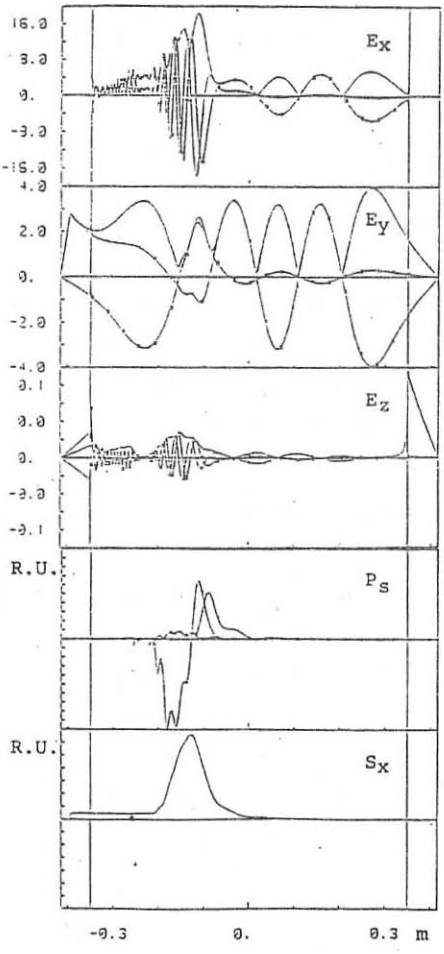


Fig.1

dependence of $-P_b$ for the fixed value of $\omega/2\pi = 21.58$MHz. We observe two cavity resonances in the regime where this scheme works.

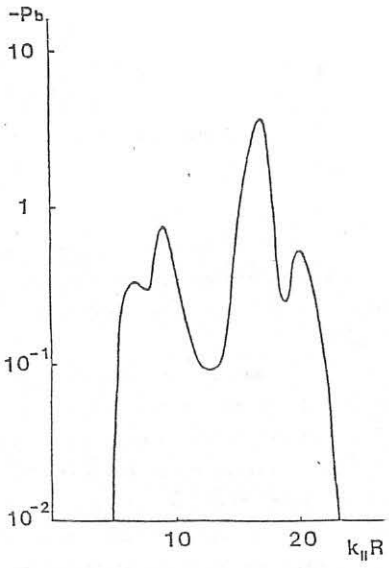


Fig.2

Acknowledgement

Work partially supported by Grant in Aid for Fusion Research and for Scientific Research of MoE Japan and by Nissan Science Foundation.

References

[1] A. Fukuyama, S. Nishiyama, K. Itoh and S.-I. Itoh, Nucl. Fusion (1983) 23 1005.

[2] S.-I. Itoh, K.Itoh and A. Fukuyama, Plasma Phys. Cont. Fusion 26 (1984) 1311.

[3] S.-I. Itoh, A. Fukuyama, K. Itoh and K. Nishikawa, J. Phys. Soc. Jpn., 55 (1985) 1808.

[4] S.-I. Itoh, K. Itoh and A. Fukuyama, paper in preparation.

COMPARAISON OF TWO $K_{\parallel}$ ANTENNA CONFIGURATIONS FOR ICRH EXPERIMENTS IN TFR

EQUIPE TFR *

ASSOCIATION EURATOM-CEA SUR LA FUSION
Département de Recherches sur la Fusion Contrôlée
Centre d'Etudes Nucléaires
Boîte Postale n°6, 92260 FONTENAY-AUX-ROSES (FRANCE)

INTRODUCTION

ICRF heating theory predicts that a low field side antenna made of 2 coils with antiparallel RF currents should lead to better performances that the same structure with parallel currents, or the single coil. This for two reasons :

i) Radial RF currents, necessarily present in the feeders if the electrical length of the antenna in the poloidal direction is different from $n\pi$, will excite TEM coaxial modes propagating between wall and plasma [1]. Although no experimental evidence for the actual existence of those modes has been reported, they may appear as a potential source of impurity production in the scrape off layer. Since their dispersion relation is $K_z^2 + K_y^2 = \omega^2/c^2$, their amplitude will be strongly reduced by the asymmetrical configuration characterized by a small spectral amplitude near $K = 0$ ($\omega/c \simeq 1 m^{-1}$ in TFR)

ii) Efficient ion cyclotron damping of the magnetosonic wave generated from the low magnetic field side of the torus requires high values of $K_{\parallel}$ (typically 10 m^{-1}).

Accordingly, a large fraction of the RF power radiated by a broad single coil antenna with a $K_{\parallel}$ spectrum peaked at $K_{\parallel} = 0$, will be weakly absorbed when crossing the ω_{ci} layer, and would require a large number of transits across that layer before complete absorption. This, again, appears as a possible source of impurity production if unexpected damping processes do exist in the plasma edge regions.

On the other hand RF coupling theory predicts that radiation resistance of the asymmetrical antenna will be appreciably lower than for the symmetrical one.

EXPERIMENTS

Comparison between the effects of the 2 configurations on TFR plasma was done using an antenna made of 2 centerfed coils located on the low field side of the torus and shown schematically in Fig.1. With the 2 coils supplied

* and H. Matsumoto. JFT - 2M, Tokai Mura - Japan.

in phase, RF currents in the upper (or lower) branches are parallel. Supplied in opposite phase, the currents are antiparallel.
The length of the 4 parallel branches is 25 cm, measured from the feeder connection. Their width is 5 cm, the 2 coils are separated by 7 cm and the antenna is protected on both sides by carbon tiles.

Experiments in the following conditions : $B\varphi$ = 40 kG ; f = 60 MHz ; n_{eo} = 1-1.5 10^{14} cm^{-3} ; deuterium plasma ; n_H/n_D = 0.05 led to the following observations :

i) Radiation resistance R, as defined in other TFR reports [2], is 1.2 Ω for the symmetrical structure, 0.5 Ω for the other one. Such reduction in the coupling efficiency was expected from the numerical calculations. However, the absolute values are lower than the ones derived from a 3-D code taking into account the RF current in the feeder and in the lateral protections (respectively 1.9 and 0.9 Ω). The low value of R for the asymmetrical configuration imposed the comparison to be made at low RF power level, between 100 and 250 kW coupled to the plasma, this corresponding for the asymmetrical antenna to peak voltages equal or lower than 25 kV.

ii) For equal total RF power coupled to the plasma, the rate of increase of T_D, derived from the slopes of the neutron rate at the time RF is applied, is systematically different for the 2 configurations : Fig. 2a compares e.g. the evolutions of the neutron flux φ_N observed in 2 experiments made at a power level of 200 kW coupled to the plasma. While φ_N is slowly growing in the case of the symmetrical configuration with an initial slope limited to 2.2 eV/ms, the abrupt change in φ_N slope in the 2^d case corresponds to a dT_D/dt of 6.5 eV/ms. Fig. 2b, comparing the initial values of dT_D/dt for the 2 modes of operation at different power levels shows that the difference apparent in Fig. 2a has been systematically observed. Although the initial heating power of the ions is clearly larger in the case of the asymmetrical configuration, no significant difference appears in the peak ΔT_D levels. As in the other TFR experiments using a low field side antenna [3], no appreciable increase of T_e has been detected here.

iii) Fig. 3a compares, for the 2 cases, the increase of radiation losses measured by fish eye bolometer within the first 10 ms of the RF pulse. The difference observed cannot be attributed to a difference in heavy impu-

rities radiation : spectroscopic analysis of Cr, Fe, and Ni lines shows that radiation emitted by those elements is negligible during the first ms of the RF pulse and remains comparable during the whole pulse for the 2 situations (Fig. 4), in contrast with the observations reported from the JFT2M experiments [4] On the contrary the amplitudes of OVI lines, emitted from a plasma radius of 15 cm, are obviously different : increasing rapidly during the first ms with the in phase configuration (Fig. 3b), OVI radiation grows at a much slower rate if the coils are supplied out of phase. This suggests a different power deposition profile leading in the second situation to a reduced interaction with the peripheral layers of the plasma. However, as for ΔT_D, the levels of radiation reach comparable values in the 2 conditions after 50 ms RF.

CONCLUSIONS

Experimental comparison between in phase and out of phase excitation of a double coil antenna indicates 2 major differences in the plasma wave interaction : at the time RF is applied on the out of phase configuration, the rate of ion heating is larger and the increase of oxygen radiation is slower by a significant factor than in the opposite situation. These observations tend to confirm the prediction from theory : more efficient cyclotron damping and hence weaker interaction with the peripheral layers if the wave spectrum amplitude is small around $K_{//} = 0$. The fact that the peak values of T_D and radiation reach comparable levels during the RF pulse does incite however to consider those observations as incomplete. Deeper investigation in this comparison would require more detailed measurements, in particular accurate comparisons between the proton distribution functions, and between the radiation profiles. Those were hardly accessible in TFR due to the low power level imposed by RF voltage limitation on the asymmetrical antenna.

REFERENCES

[1] A.M. MESSIAEN et al., Proc. 3^{d} Varenna Grenoble Symp. I, 243, (1982)

[2] Equipe TFR, Plasma Physics 24, 615 (1982).

[3] Equipe TFR, Rapport EUR-CEA-FC-1219 (1984)

[4] S. MORI et al., 10th Conf. on Plasma Physics and Cont. Nucl. Fusion Research (London) I, 445, 1984.

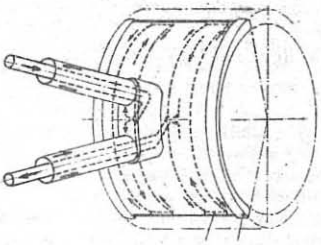
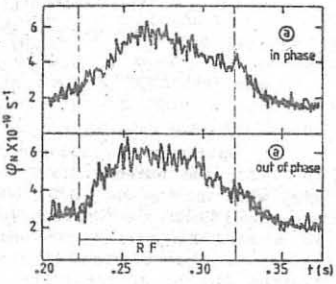


Fig.1 Schematic view of the double coil antenna



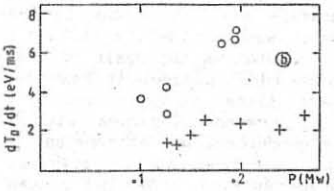
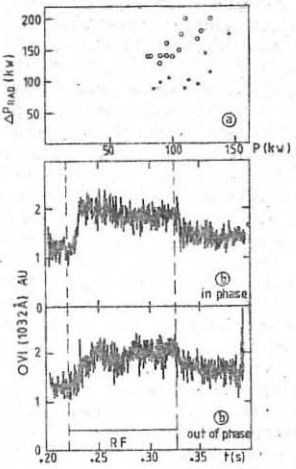


Fig.2 Ion heating rates for in phase and out of phase excitation

a) neutron rate vs time for P_{RF} = 200 KW

b) dT_D/dt vs P_{RF} at the time RF is applied (+ in phase ; 0 out of phase)



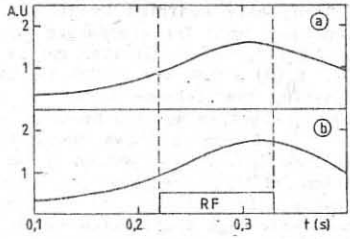


Fig.4 Ni XVIII (λ = 292 A) radiation out of phase (a) ; in phase (b)
P_{RF} = 100 kW

Fig.3a Increase of total radiation during the first 10 ms (0 in phase ; ♯out of phase)
3b OVI radiation in the 2 conditions.

INFLUENCE OF LASER-BLOW-OFF INJECTED VANADIUM IONS ON THE DEUTERON HEATING DURING ICRH IN TFR

TFR GROUP (Presented by B. SAOUTIC)

ASSOCIATION EURATOM-CEA SUR LA FUSION
Département de Recherches sur la Fusion Contrôlée
Centre d'Etudes Nucléaires
Boîte Postale n° 6. 92260 FONTENAY-AUX-ROSES (FRANCE)

Optimum ion-cyclotron resonance heating (ICRH) for excitation with a high-field side antenna (HFSA) is obtained in the so-called mode conversion regime when the two-ion (H/D) hybrid layer is located on the magnetic axis. In these conditions the antenna generated fast magnetosonic wave is converted into a slow Bernstein wave which can be absorbed by electrons (by Landau damping in the two-ion hybrid layer neighbourhood) and by protons (by cyclotron damping at the proton cyclotron resonance layer located on the low field side of the magnetic axis). TFR experiments [1] have shown important ion heating even when (due to the increased n_H/n_D ratio) the proton cyclotron layer was outside the limiter radius. It was difficult to justify this large absorption on the basis of a simple wave propagation theory for a two-component (H/D) plasma. It has been suggested [1] that energy absorption could take place through impurity ions. They act as supplementary ions in a multi-component plasma with possible second harmonic resonances in the neighbourhood of the two-ion hybrid layer, where the interaction with the wave can be strong. Acceleration and expulsion of resonating He-like Ar ions have been reported on TFR [2], when their resonant layer was coincident with the two-ion hybrid layer at 4 cm from the center towards outside. Moreover, on TFR, when using carbon instead of inconel as limiter material (i.e., at lower metallic impurity content both prior to and during the ICRH), the rate of increase of the majority deuteron temperature T_D was smaller [3].

To clarify these experimental observations, the heavy ion content was purposely modified by injection of vanadium ions (by the laser blow-off technique) into TFR discharges having the following parameters: I_p = 250 kA, B_T = 4.5 T, carbon limiter radius a = 19 cm, $n_e(0) = 10^{14}$ cm^{-3}, $T_e(0)$ = 1.5 keV, $T_D(0)$ = 0.9 keV. ICRH in the wave conversion regime was possible by adjusting the isotope ratio to $n_H/n_D \sim 0.2$. For injected powers of 600-800 kW, electron and ion heatings of $\sim$ 200-300 eV are currently measured [3].

Figure 1 shows the results obtained on the central deuteron temperature T_D for V injection 20 ms prior to ICRH application ; numerical simulation of the spectroscopic signals has indicated a central total V ion density of $\sim 5 \times 10^{10}$ cm^{-3} when ICRH is applied. On both neutron and charge-exchange diagnostics curves 3 show a larger T_D rate of increase but the asymptotic T_D values (during the second half of the ICRH pulse) are practically unaffected. When injecting 20 ms after the ICRH application (but before the attainment of the unmodified asymptotic T_D value) only a small deuteron extra-heating is observed. It has to be stressed that in any case the coupled ICRH power is unaffected by the V injection.

The simplest quantitative analysis of the observed results can be obtained by a zero-dimensional code describing the behaviour of the central plasma [3]. Considering 5 species (electrons, protons, deuterons, a light and a heavy impurity), absorbing and losing energy independently, but coupled through Coulomb collisions, it has been possible to simulate curves 2 taking ICRH power density depositions of $\sim$ 1.2 W/cm^3 and $\sim$ 0.4 W/cm^3, respectively,

An extended study has indicated that important absorption on V^{21+} ions is always possible, provided electron absorption has not become the dominant loss process leading to wave energy depletion before the impurity resonance layer (this is the case when $k_{||}$ is in the 10-20 m^{-1} range or when $y \neq 0$).

Finally we have considered the experimental situation reported in [1] by analysing the Ni ion absorption by varying η_H between 0.2 and 0.5 at B_T constant (4.9 T). For this atomic species, the most abundant TFR intrinsic element, He-like to N-like iso-electronic sequences exist in the central plasma region where $T_e \sim 1.5$ keV. Calculations similar to the one discussed above have indicated that important absorption is possible when $\alpha >> 1$ provided the resonance layer is near the two-ion hybrid layer on the HFS of the turning point. For $B_T = 4.9$ T, Li-, Be-, and B-like ions absorb ICRH power successively by varying η_H between 0.3 and 0.5.

To conclude, the observed enhanced rate of increase of T_D with V injection is accounted for by wave energy deposition on V ions. It is possible to justify this absorption by second harmonic cyclotron resonances in the frame of the WKB approximation provided a fraction (of the order of 1/10) of resonating V^{21+} ions ($n_{V21+} \sim 4.10^{10}$ cm^{-3}) is accelerated into the tens of keV range.

- REFERENCES -

[1] *Equipe TFR, in Heating in Toroidal Plasmas (Proc. 3rd Int. Conf. Grenoble, 1982) 1, 225 (1982).*

[2] *TFR Group, Nuclear Fusion 22, 956 (1982).*

[3] *Equipe TFR, in Plasma Physics and Controlled Nuclear Fusion (Proc. 10th Int. Conf. London, 1984) 1, 103 (1985).*

[4] *Lapierre Y., Thèse d'Etat Paris and Report EUR-CEA-FC-1149 (1982).*

[5] *Gagey B., Lapierre Y. and Marty D., same as 1, 1, 361 (1982).*

EFFECT OF CURRENT DRIVE ON ICRF HEATING*

Jose L. Milovich, George J. Morales, and Burton D. Fried
University of California at Los Angeles, Department of Physics
405 Hilgard Avenue, Los Angeles, California 90024 USA

ABSTRACT

Motivated by an interest in the effects of current drive on ICRF heating, we examine the modifications in the properties of ion Bernstein waves (IBW) arising from a current-carrying tail in the electron distribution function. We find that new, stable modes arising from the tail can couple to the usual IBW, resulting in detuning near harmonics of the ion cyclotron frequency and enhanced wave damping. The tail also allows normally evanescent waves to propagate, thus changing the topology and character of mode coupling and mode conversion amongst the IBW, fast wave, and "evanescent" wave.

Both experiments[1] and computer simulations[2] show that current drive (for example, by lower hybrid waves) produces an electron distribution function f_e consisting of a bulk Maxwellian plus a long, flat tail. We use an analytic model to represent a stable distribution of that character, $f_e = g_e(v_\parallel)[\exp(-v_\perp^2/a_e^2)]/\pi a_e^2$ where $g_e(v_\parallel) = N\{\exp(-v_\parallel^2/a_e^2) + \varepsilon[1+d\cosh\{v_\parallel - v_{\parallel o})/fa_e\}]^{-1}\}$, shown in Fig. 1, contains a hot tail distribution of relative magnitude ε, mean velocity $v_{\parallel o}$, and "thermal" spread $v_T = fa_e \ln(2/d)$. The normalization factor $N = (1+2\varepsilon v_T/\pi^{1/2}a_e)^{-1}$; f is a shape parameter which determines the rate of fall-off at the high velocity end of the tail; and, typically, $d \ll 1$. For ω_{pe}/ω_{ce} of order 1; $k \ll k_{Di}$, k_{De} (Debye wave-numbers); and $k_\perp \rho_e \ll 1$, the dispersion relation for electrostatic waves (appropriate when $\beta_i = 8\pi n T_i/B^2 \ll m/M$) may be written $D = D_e + D_i = 0$ where $D_i = (k_{Di}/k)^2 \sum_{\ell=-\infty}^{\infty} \Lambda_\ell(b_i)[1+\varepsilon_o Z(s_\ell)]$ and $D_e = -(\omega_{pe}k_\parallel/k)^2 \int dv_\parallel g_e(v_\parallel)(\omega - k_\parallel v_\parallel)^{-2} = D_M + \chi_T$. Here $D_M = -(k_{De}/k)^2 NZ'(\xi s)/2$ is the usual term arising from the bulk

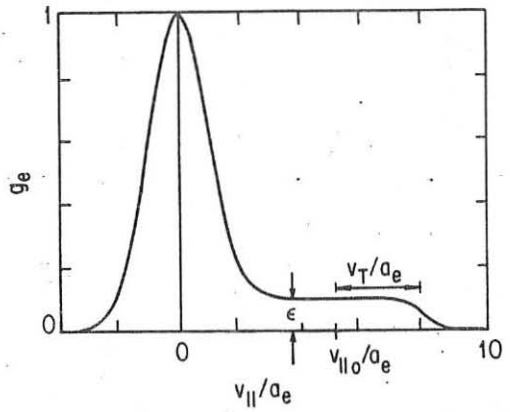


Fig. 1 Parallel electron distribution function $g_e(v_\parallel)$ for $v_{\parallel o}/a_e = 5$, $f = 0.3$, $\Delta v/fa_e = v_T/fa_e \ln 2 = 10$ and $\varepsilon = 0.1$.

Maxwellian while the tail contributes $\chi_T = -[ik_{De}^2 N/4\pi f k^2(\pi-\pi d^2)^{1/2}]\cdot$ $\cdot[\psi'(\delta_+ + \frac{1}{2}) - \psi'(\delta_- + \frac{1}{2})]$ where $\xi = \omega_{ci}/k_\parallel a_e$, $s_\ell = (\omega-\ell\omega_{ci})/k_\parallel a_i$, $\delta_\pm = [(\omega/k_\parallel - v_{\parallel 0} \pm v_T)/fa_e](2\pi i)^{-1}$, $s = \omega/\omega_{ci}$, $\Psi'(z) = d^2\ln\Gamma(z)/dz^2 = \sum_0^\infty (n+z)^{-2}$ is the trigamma function[3], and $\Lambda_\ell(b)=I_\ell(b)\exp(-b)$, I_ℓ being the modified Bessel function.

The effects of the "tail modes" are most pronounced when the phase velocity $\omega/k_\parallel$ is near the upper end of the tail, i.e., when $\delta_- \approx 0$. (The tail mode arises from a balancing of D_i and χ_T. D_i and D_M are both negative and so is χ_T when $\omega/k_\parallel$ exceeds v_o, the point of maximum tail slope. For $\omega/k_\parallel$ a little below v_o, χ_T becomes positive but, as would be expected in a region of large negative slope, there is considerable Landau damping.)

We consider first "initial value" problems, i.e., $k_\parallel$, $k_\perp$ real and ω complex. For frequencies in the range $\omega_{ci} < Re\omega < 2\omega_{ci}$, the behavior of the tail mode is as illustrated in Fig. 2, with $\epsilon = 0.1$ and the other parameters

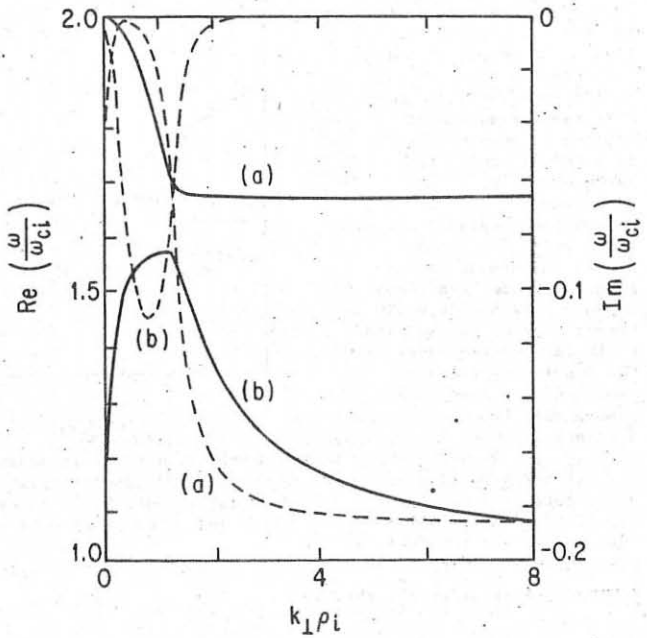


Fig. 2 Real (solid) and imaginary (dotted) parts of ω vs. $k_\perp$ for electrostatic waves with $T_e=T_i$, $\xi=4$, $f=4/\sqrt{2}$, $\Delta v/fa_e=1$, $v_{\parallel o}/a_e=5/\sqrt{2}$, $\epsilon=0.1$.

in g_e chosen so that $\delta_- \approx .32$ for $\omega = 2\omega_{ci}$. The coupling seen here between the IBW and the tail mode disappears for $\epsilon = .05$; each mode retains its own identity, the curves of $Re\omega$ simply crossing one another while $Im(\omega/\omega_{ci})$ remains small (less than .04) for the IBW and is relatively large for the tail mode. For "boundary value" problems, i.e., $k_\parallel$, ω real and $k_\perp$ complex,

the tail manifests itself through enhanced Landau damping of the IBW: the curve of $\mathrm{Re}(k_\perp\rho_i)$ vs. ω is essentially unchanged but $\mathrm{Im}(k_\perp\rho_i)$ has a bell-shaped form whose location and shape depend fairly sensitively on the parameters. This may peak either above or below $2\omega_{ci}$. In the latter case, a wave propagating towards the $2\omega_{ci}$ resonance would be damped, giving energy to electrons, before reaching the resonance.

The behavior of $k_\perp\rho_i$ near $\omega = 2\omega_{ci}$ can be examined by using the approximation $|k_\perp\rho_i|<<1$ to expand the Bessel functions in D_i. Keeping terms of order $(k_\perp\rho_i)^4$ and neglecting ion cyclotron damping (justified when $|\omega-2\omega_{ci}|>>(a_i/a_e)\xi$, which is a small number) gives

$$(k_\perp\rho_i)^2=[(4-s^2)/3]\cdot\{1\pm[1+6NX_e(s^2-1)/\tau(4-s^2)]^{1/2}\}$$

where $X_e = Z'(\xi s) - (k^2/2\ k\rho_e^2)X_T$ and $\tau = T_e/T_i$. With no tail ($\varepsilon = 0$) and $\xi s = \omega/k_\parallel a_e >> 1$, we have $X_e>0$, so in the regime $s < 2$, there are two roots for $(k_\perp\rho_i)^2$, one positive, the IBW, and one negative, an evanescent mode, as shown by the dotted curves in Fig. 3. However, if $\omega/k_\parallel$ falls on the flat portion of the tail, $\mathrm{Re}X_T$ is positive (as for adiabatic electrons, when $\omega/k_\parallel a_e<<1$ in a Maxwellian). For large enough ε, X_e may then change sign, yielding one or two propagating modes below $2\omega_{ci}$, one above, and a mode conversion region between them, as indicated by the solid curves in Fig. 3. We find a similar behavior near the ion-ion hybrid frequency in the case of a plasma with two ion species.

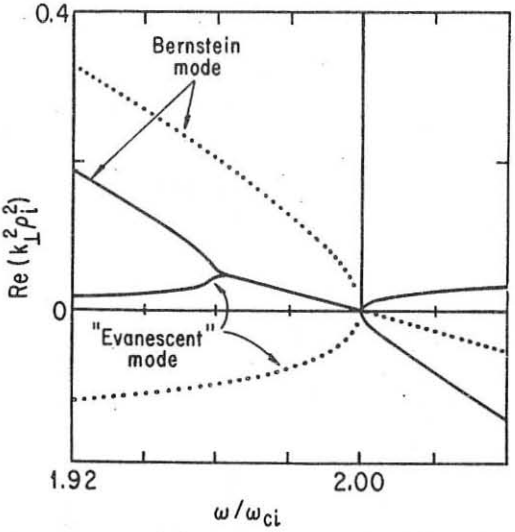


Fig. 3 Solutions of electrostatic dispersion relation in the $k_\perp\rho_i<<1$ approximation with tail (solid) and without tail (dotted) for $\xi = 2.1$, $\varepsilon = 0.2$, and other parameters as in Fig. 1.

If $m/M \lesssim \beta_i << 1$, the electrostatic approximation is no longer valid and we must use the full electromagnetic dispersion relation. Expanding again in $k_\perp\rho_i$ and neglecting corrections of order β_i^2, this is

$$D_{EM}=[3/2(s^2-4)(s-1)](k_\perp\rho_i)^6+(s^2-1)^{-1}(k_\perp\rho_i)^4+NX_e\{[3M\beta_i\xi^2s^2/2m(s^2-4)](k_\perp\rho_i)^4+$$
$$+[\tau^{-1}+\beta_i(\xi s)^2\ M/m(s^2-1)](k_\perp\rho_i)^2+\beta_i s^2/\tau(s^2-1)-$$
$$[\beta_i{}^2M/m(\xi s)^2][(NW)^2+(2NW-1)(s^2-1)^{-1}]\}=0$$

where $W = 1 + [2\varepsilon v_T/a_e(\pi-\pi d^2)^{1/2}]\ (\omega - k_\parallel v_\parallel)/\omega$. For $\varepsilon = 0$, the three roots of this cubic in $(k_\perp\rho_i)^2$ correspond to an IBW, a fast wave (FW) and an evanescent mode. The IBW and FW are shown as dotted curves in Fig. 4, along with the mode conversion region located in the range $1.94<s<2$. (The evanescent mode falls below the lower bound of this plot.) Addition of the tail changes the topology significantly: the formerly evanescent mode couples to the fast wave and in the range $1.95\lesssim s\lesssim 1.98$ there are three propagating modes. In a WKB sense, with ω/ω_{ci} a function of some spatial coordinate, the closed loop centered near ω/ω_{ci} =1.94 represents trapped waves.

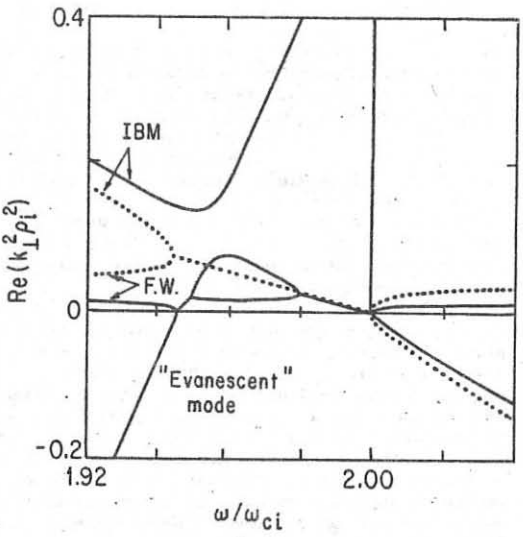


Fig. 4 Solutions of full electromagnetic dispersion relation for $k_\perp\rho_i \ll 1$ and $\beta_i \ll 1$ with tail (solid) and without tail (dotted) for $\xi = 1.85$, $\beta_i = 10^{-2}$, and other parameters as in Fig. 3.

In conclusion, we note that many of the effects we have discussed here occur only for values of $\varepsilon = (n_T/n_0)\pi^{1/2}a_e/2v_T$ much greater than those expected in large tokamaks, where n_T/n_0, the fraction of tail particles relative to the bulk Maxwellian, may be of order 10^{-4}. Moreover, we have assumed that the plasma density and temperature, the driven current density and the toroidal magnetic field are all homogeneous and we have neglected the poloidal field produced by the current. Consideration of all of these effects, together with a proper treatment of the mode conversion phenomena, will be required to assess adequately the effect of current drive on ICRF heating in large tokamaks.

REFERENCES

1. Hooke, W., Plasma Phys. and Cont. Fusion (GB), 26, 133 (1984)
2. Karney, C.F.F., and N. Fisch, Phys. Fluids, 22, 1817 (1979)
3. Morse, P.M., and H. Feshback, Methods of Theoretical Physics (McGraw-Hill, New York, 1953), Vol. 1, p. 422

*Work supported by USDOE.

HEATING, CONFINEMENT, AND STABILITY DURING HIGH POWER ICRF EXPERIMENTS ON PLT*

J. Hosea, R. Bell, M. Bitter, A. Cavallo, S. Cohen, P. Colestock, G. Greene, G. Hammett, E. Hinnov, H. Hsuan, D. Hwang, R. Kaita, E. Mazzucato, D. McNeill, M. Ono, D. Schuresko,+ C. Skinner, S. Suckewer, and J. Wilson
Princeton Plasma Physics Laboratory
Princeton, NJ 08544, USA
+Oak Ridge National Laboratory, Oak Ridge, Tenn.

ABSTRACT

The PLT ICRF program is directed toward understanding the wave physics and confinement properties for intensely heated plasmas to permit realistic extrapolation to the ignition regime. RF power delivered to the antennas in the D-^{3}He regime has been increased to 5 MW, 4.25 MW coupled to the plasma, resulting in substantial heating: $T_d(o) = 5$ keV, $T_e(o) = 4$ keV (at sawtooth peak), $\bar{n}_e = 3.7 \times 10^{13}$ cm^{-3}, E > 100 kJ, and neutron flux $\approx 10^{13}$ sec^{-1}. These results have been obtained without major disruptive effects and without m = 2 oscillations being observed. However, the electron temperature, which exhibits very large amplitude sawteeth oscillations, (~ 1.3 keV) has been limited by the m = 1 MHD mode. Total energy confinement has been observed to decrease for powers up to 2 MW but to remain essentially constant at powers in excess of 2 MW. Some improvement of confinement at the lower powers has been observed with pellet injection fueling.

Finally, two important ICRF physics issues have begun to be addressed: the properties of the transition from minority ion fundamental heating to majority ion second harmonic heating and the properties of ion Bernstein wave (IBW) heating. It is essential that these processes be understood to optimize ICRF reactor heating scenarios.

Minority Heating Regime

The high power ICRF heating experiments in the D-^{3}He (majority ion-minority ion) regime have been extended from the power levels reported earlier[1] to a net power level of 5 MW delivered to six antennas on PLT under good operating conditions (I_p = 600 kA, B_ϕ = 32.5 kG). For these conditions, the power coupled to plasma waves by the antennas, phased to peak the spectrum at $k_\parallel \sim 7$ m^{-1}, was ~ 4.25 MW. The central ion temperature achieved at a line average density of $\bar{n}_e = 3.7 \times 10^{13}$ cm^{-3} was 5 keV and the central electron temperature reached 4 keV at the peak of the sawtooth relaxations whose amplitude continued to increase (to ~ 1.3 keV) with the increase in rf power (Fig. 1). The neutron flux reached 10^{13} sec^{-1} and the total plasma stored energy exceeded 100 kJ for the first time using ICRF auxiliary heating alone on PLT. Heating rates for the deuterium ions and the electrons continued at ~ 3.3×10^{13} eV/kW cm^3 and ~ 1.7×10^{13} eV/kW cm^{-3}, respectively and the ^{3}He ions contribution to the stored energy increased to ~ 20-25%.

These high power results were obtained without major disruptions and in the absence of m = 2 oscillations as indicated in Fig. 1. As before, the impurity radiation remained at ~ 1/3 of the total power and did not affect the central electron power balance.[1,2] Furthermore, analysis with a multi-ion species one-dimensional confinement code (MICADO)[3] demonstrated that the power producing the very large T_e sawteeth came primarily from the direct deposition of energy into the electrons by the energetic ^{3}He distribution rather than from coulomb drag on the deuterium ions as illustrated in Fig. 2. (Direct wave heating of electrons was calculated to be unimportant at the relatively low level of ^{3}He concentration used.) Thus, the mode of electron heating is representative of that which might be expected to result for α particles in the ignited plasma.[4]

Upon combining the above heating results with those of Ref. 1, we obtain the energy confinement plot of Fig. 3.[5] Even though the data indicate the confinement to be consistent with the L-mode as embodied in the statistical neutral beam scaling of Kaye-Goldston,[6] it is noteworthy that above 2 MW the ICRF confinement does not continue to degrade with power.

We have begun pellet injection fueling in hopes of improving the energy confinement time during ICRF heating. Application of ~ 1 MW of ICRF power shortly after bringing the plasma density to ~ 3.7-4 x 10^{13} cm^{-3} with a deuterium pellet has resulted in a ~ 30% improvement in confinement as indicated in Fig. 3.

Additional improvement can also be expected with operation at high plasma density and current. Studies of the confinement scaling for these parameters are being extended to the higher power regimes. Current continues to be a decisive factor as indicated in Fig. 4 for the 1 MW power level.

Second Harmonic Deuterium Heating

In order to optimize heating of reactor species with fast ICRF waves it is desirable to transition from minority ion heating to second harmonic majority ion heating. Significant heating has been observed for both the minority regime (e.g. the ^{3}He minority regime in this paper) and for the hydrogen second harmonic regime[7] (for which the minority fundamental resonance is absent) but little is known of the characteristics of the transition from minority to second harmonic heating in the D-H (and T-^{3}He) regime(s) in a good confinement device.

The beginning of the transition has been achieved on PLT with the reduction of the H concentration to a level below 1.5%. Under this condition the deuterium energy distribution has been observed to be non-Maxwellian as evidenced by charge exchange measurements (Fig. 5) and an enhanced neutron production rate. Deuterium tails with energies to 70 keV and "temperatures" of 18.5 keV have been produced at rf powers of ~ 1 MW. The modeling of the D and H distributions indicate that ~ 15% of the rf power is delivered directly to the deuterons at the megawatt power level. This fraction increases with total rf power (Fig. 5). Furthermore, the time evolutions of the D and H distributions indicate that more power shifts directly to the deuterium as the deuterium distribution becomes more energetic as expected.[8]

Ion Bernstein Wave Heating

Heating by launched ion Bernstein waves (IBW) at both linear and non-linear resonances in the plasma cross section must be considered for optimizing fast wave heating of the plasma core. Furthermore, selection of IBW heating in lieu of fast wave heating could prove desirable,[9] since higher harmonic (higher frequency) heating is possible and Maxwellian distributions are maintained. To determine the possible effects of ion Bernstein waves, generated as a small component of the spectrum from fast wave launchers or for purposefully heating the plasma, an IBW launcher has been employed at modest power on PLT. Excitation with a toroidally directed quadrapole (driven as a dipole) has resulted in significant heating at both the fifth harmonic[4] and three-halves subharmonic[2] of deuterium: 5 ω_{CD} minority heating in hydrogen - 100 kW at 90 MHz, $\bar{n}_e = 7 \times 10^{12}$ cm^{-3}, $\Delta T_{d\perp} \sim 700$ eV, $\Delta T_{d\parallel} \approx \Delta T_H \approx 350$ keV; 3/2 ω_{CD} majority heating - 150 kW at 30 MHz, $\bar{n}_e = 1.7 \times 10^{13}$ cm^{-3}, $\Delta T_d \sim 450$ eV. All the heated ion species were observed to maintain Maxwellian distributions.

These results are important in that they demonstrate the potential of IBW heating and the feasibility of such heating occurring at a modest level even for fast wave launchers in which case care must be taken to avoid surface heating.

Acknowledgments

The support of Dr. H. Furth, Dr. P. Rutherford, Dr. D. Meade and of the PLT Project personnel is gratefully acknowledged.

This work supported by DOE Contract No. DE-AC02-76-CHO-3073.

References

1. E. Mazzucato, et. al., in Proceedings of the Tenth Int. Conf. on Plasma Physics and Controlled Nuclear Fusion Research, Vol. I, 443 (1985), IAEA-CN-44/F-1-2.
2. J.C. Hosea, et. al., in Proceedings of the 4th Int. Symp. on Heating in Toroidal Plasmas, Vol. I, 261 (1984).
3. M. Ono, et. al., in Proceedings of the Sixth Topical Conf. on Radio Frequency Plasma Heating, Pine Mt. GA (1985) (to be published).
4. First suggested by B. Coppi.
5. J.R. Wilson, et. al., in Proceedings of the Sixth Topical Conf. on Radio Frequency Plasma Heating, Pine Mt. GA (1985) (to be published).
6. S.M. Kaye, R.J. Goldston, NF, 25, 1, 65 (1985).
7. D.Q. Hwang, et. al., in Proceedings of the Ninth Int. Conf. on Plasma Physics and Controlled Nuclear Fusion Research, Vol. II, 3 (1983).
8. F.W. Perkins, NF, 17, 6, 1197 (1977).
9. M. Ono, et. al., in Proceedings of 2nd Joint Grenoble-Varenna Int. Symp. on Heating in Toroidal Plasmas, Vol. I, 593, (1980).

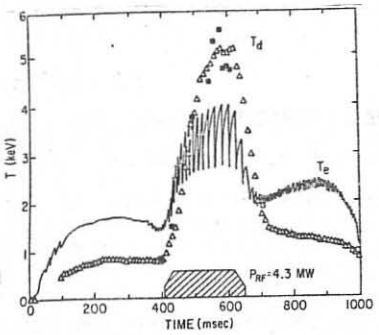


FIG. 1. T_d and T_e versus time for D-^{3}He discharge (I_p = 600 kA, B_ϕ = 32.5 kG, $\bar{n}_e$ = 3.7 x 10^{13} cm^{-3}). Δ charge exchange, ■ neutrons (30% depletion), —ECE.

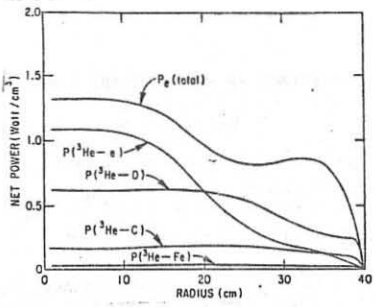


FIG. 2. Power deposition analysis.

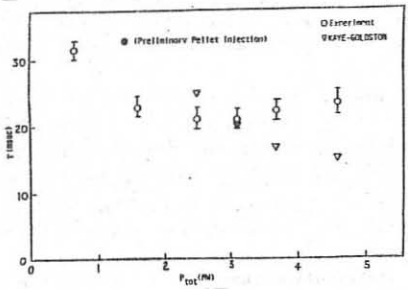


FIG. 3. Energy confinement time versus total power (o). Calculated Kaye-Goldston statistical beam injection scaling (∇). Pellet injection effect (●).

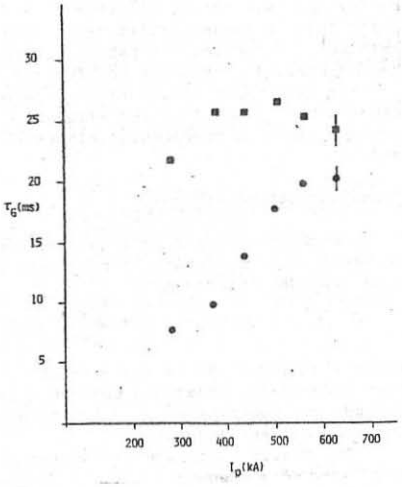


FIG: 4. Unoptimized scan of confinement times for OH (■) and OH plus ICRF (●) discharges versus I_p ($\bar{n}_e$ ~ 2.8 x 10^{13}, B_ϕ ~ 33 kG, P_{RF} ≈ 1.25 MW).

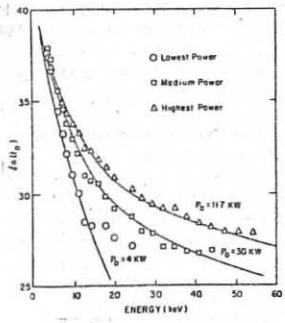


FIG. 5. Deuterium distributions at low hydrogen concentration power ($\bar{n}_e$ ≈ 1.5-2 x 10^{13}, B_ϕ ≈ 20 kG, n_H ≈ 1.5%, O - P_{RF} = 0.15 MW, □ - 0.6 MW, Δ - 1.0 MW).

EFFECT OF PARTICLE TRAPPING IN ICRF-BEAM HEATED TOKAMAK PLASMAS

T. Hellsten, K. Appert*, W. Core, H. Hamnén, S. Succi*

JET Joint Undertaking, Abingdon, Oxon., OX14 3EA, UK.

* CRPP, Lausanne, Switzerland.

Introduction

As is well known, the combined effects of resonant ion interaction with a magnetoacoustic wave and the Coulomb scattering processes leads to the development of anisotropic distributions with the most energetic particles in deeply trapped orbits [1]. However, in an actual tokamak, trapped particle effects modify the tail formation process, and hollow distributions with the most energetic ions in banana orbits with their tips on or near the resonance layer are obtained. The effect of particle trapping in the tail formation process during second harmonic frequency heating are shown in Figs. 1 and 2.

In this paper we report the results of a numerical study of trapped particle effects on the tail formation process, heating efficiency, and thermonuclear yield in fundamental minority/second harmonic, and RF/beam-plasma hybrid systems.

Computational Considerations

The Fokker-Planck code used in the investigation is the BAFIC code which is based upon the finite element code BACCHUS [2] which numerically solves the time dependent equation:

$$\frac{\partial f}{\partial t} = C(f) + Q(f) + S,$$

where $f = f(v_{\parallel}, v_{\perp}, t)$ is the resonant ion distribution function; C, Q, are the bounce-averaged linearised Coulomb scattering and quasi-linear RF operator in cylindrical coordinates in velocity space $(v_{\parallel}, v_{\perp})$, S is a source term describing neutral beam injection.

The fusion rates are calculated using the Asher-Peres cross sections [3] and takes into account the finite temperature of the bulk plasma ions.

For the fundamental minority systems, we have examined the configurations: (i) minority ^{3}He(5%) in a deuterium plasma, with $n_e = 3\times10^{13}cm^{-3}$, and $T_e = T_D = 5keV$; (ii) the beam/RF-plasma hybrid systems of 125keV ^{3}He injection into ^{3}He (5%)/deuterium admixture. These configurations give rise to the important thermonuclear reaction $^3He+D\rightarrow{}^4He+H$. The contribution to the total fusion yield due to the bulk plasma D/D reactions are not included in these particular calculations.

For the second harmonic heating configurations, we have directed our investigation towards systems based upon a deuterium plasma with 125keV D-injection, $n_e = 3.5\times10^{13}cm^{-3}$, and initial species temperatures $T_e = T_D = 5keV$. For these systems the fusion yield is restricted to the reaction $D+D\rightarrow{}^3He+n$, and the D/^{3}He reactions are not included in the calculations done.

Finally, in each RF/beam-plasma hybrid system examined, a co/counter injection beam configuration at angles 45° and 135° to the main toroidal magnetic field and a beam current corresponding to a power density of $0.1W/cm^3$ is assumed.

Conf. on Contr. Fus. & Plasma Phys., Aachen (Sept.1983), paper B29.
[3] ASHER-PERES J. Appl. Phys., 5 (1979).

Figure Captions

Fig.1: Contour plot of the velocity distribution formed during second harmonic heating of deuterium for $\varepsilon=0$. Configuration parameters $n_e = 3.5\times10^{13}cm^{-3}$, $T_i=T_e=5keV$, $P_{RF}=0.26W/cm^3$, $V_o^2=kT_i/m_i$.

Fig.2: The distortion of the velocity distribution due to trapping effects. The full line indicates the separation between the regions of trapped and passing particles. The broken line separates the heated particles from the non-heated particles. For this case $P_{RF} = 0.38W/cm^3$ and $\varepsilon = 0.1$ the other parameters are as in Fig.1.

Fig.3: The absorbed power for second harmonic heating as a function of $|E_+|^2$. The full line indicates the absorption by a Maxwellian velocity distribution and the broken line RF-absorption by the plasma beam distribution neglecting RF-modifications.

Fig.4: The logarithm of the velocity distribution along the perpendicular axis in the absence of trapping effects for second harmonic heating with and without neutral beam injection. Neutral beam injection alone is also shown. The beam injection angle 90°, power $0.23W/cm^3$, and the RF electric field is the same for the two cases and corresponds to absorption $0.53W/cm^2$ and $0.95W/cm^3$, respectively.

Fig.5: The effect of particle trapping on the fusion yield during fundamental ICRF heating of a $^3He/D$ plasma is shown. The beam injection angles are 45° and 135°; injection energy 125keV, and the power corresponds to $0.1W/cm^3$.

Fig.6: The effect of particle trapping on the fusion yield during second harmonic heating of deuterium. The effect of energy clamping of the injected deuterium beam is also shown. The injection parameters are those of Fig.5.

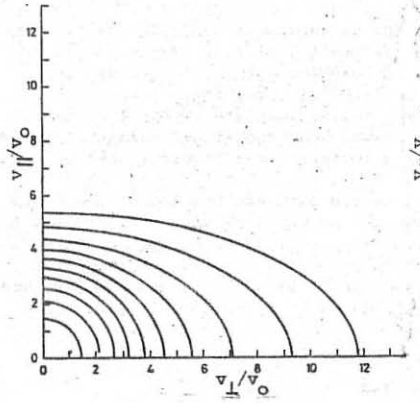


Fig.1

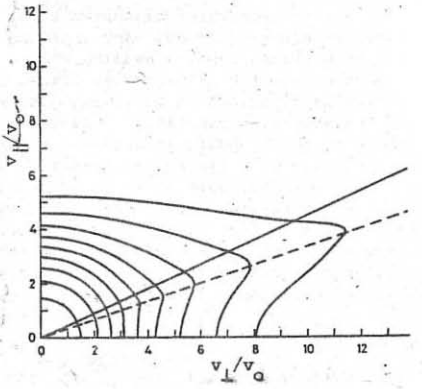


Fig.2

Numerical Results and Discussion

Since cyclotron absorption at the second harmonic resonance is proportional to $J_1^2(k_\perp v_\perp/\omega_{ci})$, a build up of the tail leads to a stronger absorption of the wave energy for a given value of E_+. In Fig.3 we have compared the power absorbed by a Maxwellian velocity distribution and that reached by steady state second harmonic heating, versus $|E_+|^2$. The square of the electric field is here normalised to the corresponding power absorption due to second harmonic heating for a Maxwellian velocity distribution. The deviation from the 45° line is a measure of how the dielectric tensor obtained using the actual velocity distribution deviates from that calculated using a Maxwellian velocity distribution.

The presence of neutral beam heating leads to a further enhancement of the tail and power absorption, Figs.3,4. The absorbed power for a given electric field increases linearly with the beam current. In Fig.3 the power absorption due to second harmonic heating for a constant beam power and having $\varepsilon=0$, where ε is the inverse aspect ratio, is shown. The dashed line in Fig.3 is the power absorption for second harmonic heating due to the increase of the $\beta_\perp$ due to the beam alone.

For heating at the fundamental and second harmonic frequencies the fusion rates have been calculated, and are shown with those obtained in the beam systems, Figs.5,6. The effect of trapping is not very important for the reaction rates. A slightly higher rate is obtained for a finite aspect ratio. This can be understood by the fact that in the case of finite trapping the power is being distributed over fewer particles than for $\varepsilon=0$. Since a fraction of the order of $\sqrt{\varepsilon}$ of the total number of particles does not interact with the wave field, these fewer heated particles will then acquire greater energy. Due to the rapid increase of the cross-section with energy a further enhancement of the thermonuclear yield is obtained.

When varying the injection angle, it is found that the fusion rate is not too sensitive a function of the injection angle. The highest rates are achieved for injection in the parts of the velocity space where $v_{\parallel}/v_\perp > \sqrt{\varepsilon}$. The lowest fusion yields are obtained for parallel injection. In the finite aspect ratio situation, direct injection into the region of velocity space where no RF interaction occurs is also ineffective.

Conclusions

For the scenarios discussed here, the calculations indicate that trapped particle effects are not very important in the calculation of the fusion yield and bulk plasma species heating rates. Second harmonic heating leads to important modifications of the plasma's dielectric properties through the change in distribution function. These modifications are strongly dependent on the wave electric field. Combined neutral beam and second harmonic further enhances these modifications, which for practical power levels cannot be represented by a linear treatment.

We may note here that in order for second harmonic heating of deuterium to be successful, the β-value of the plasma has to be large, and the level of the hydrogen impurities low. A small amount of hydrogen will change the polarisation of the electric field near the second harmonic cyclotron resonance of deuterium, so that the E_+ component diminishes. This will then reduce second harmonic heating. Instead, fundamental heating of hydrogen will occur.

References

[1] STIX, T.H. Nucl. Fusion, 15, 737 (1975).
[2] APPERT, K., KRITZ, A.H., SUCCI, S. and VACLAVIK, J. Proc. of 11th EPS

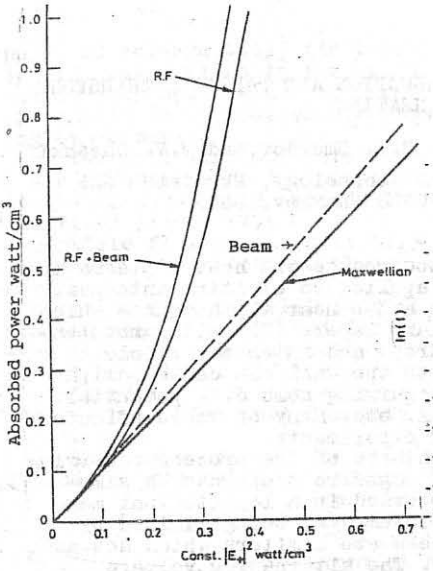


Fig. 3

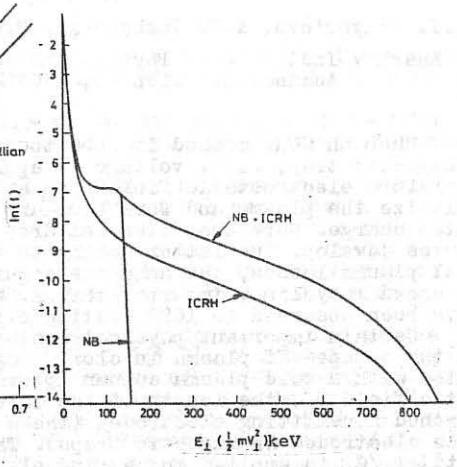


Fig. 4

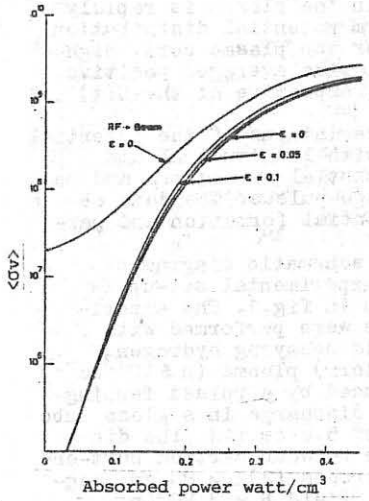


Fig. 5

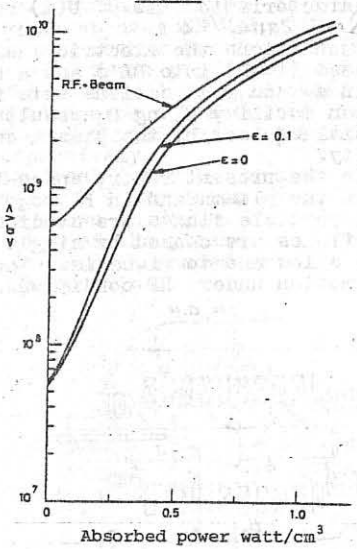


Fig. 6

SIMULATION OF PLASMA POTENTIAL INDUCTION AND PARTICLE TRANSPORT DURING ICRF HEATING

L.I. Grigor'eva, A.V. Pashchenko, B.I. Smerdov, and V.V. Chechkin

Kharkov Institute of Physics and Technology, Ukrainian SSR Academy of Sciences, 310108 Kharkov, USSR

When an ICRF method is used to produce and heat a plasma in a magnetic trap, a.c. voltage is applied to exciting antennae. Therefore electrostatic fields can arise near the antennae which polarize the plasma and form boundary layers (BL) with uncompensated charge. Here the potential drops and intense particle fluxes develop. The latter coming to the wall can cause peripheral plasma losses, the antennae acquiring some d.c. potential, enhanced recycling, impurity influx, etc. Many of these effects have been observed in ICRF heating experiments.

Certain important physical features of the process occurring in the scrape-off plasma in closed magnetic traps can be simulated with a cold plasma column immersed in a longitudinal magnetic field B_z, the length of the column, L, being limited by earthed nonemitting electrodes (these are limiters which act as such electrodes in magnetic traps). The alternating voltage $U(t) \gg T_e/e$ is applied to a ring electrode embracing the column and acting as antenna (in its electrostatic effect on the plasma). The characteristic time of U(t) variation is $\tau \gg \omega_{pe}^{-1}, \omega_{He}^{-1}$, and $\delta \sim (U/2\pi ne)^{1/2} \ll L$ where n is the plasma density. Under these conditions the electric field E in the plasma is rapidly displaced ($t \ll \tau$) into BL's and a uniform potential distribution both in z- and r-directions sets in over the plasma core. High electron mobility along B_z results in a time averaged positive potential acquired by the plasma core irrespective of the U(t) polarity.

In the present report space-time variations of the potential both in the plasma and in BL together with longitudinal and radial particle fluxes are studied. Potential variations and particle fluxes are caused by single voltage pulses. The data obtained allow one to visualize the potential formation and particle motion under RF conditions.

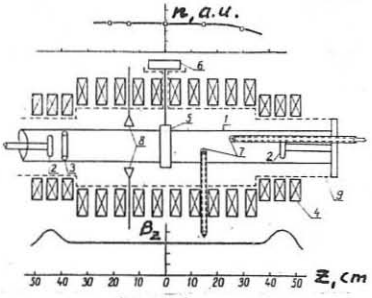


fig. 1

A schematic diagram of the experimental set-up is shown in fig.1. The experiments were performed with a cold decaying hydrogen (10^{-5} torr) plasma ($n \lesssim 10^{13}$ cm^{-3}) produced by a pulsed Penning-type discharge in a glass tube (1) of 5.6 cm i.d.; the distance between earthed butt-end electrodes (2) L = 88 cm; magnetic field B_z = 3 kG in the uniform region; a ring anode (3) was installed near one of the electrodes. A single

pulse of voltage U(t), its length τ = 0.6 μs, the amplitude U_o = 4.5 kV, was applied to the exciting electrode (EE) (5) when the density was $n = 2 \times 10^{12}$ cm^{-3}. Such a combination of U_o and n values is typical of a scrape-off plasma in some ICRF heating experiments.

The following parameters were measured :

- the potential inside the plasma (Φ_o) and in BL (Φ), the latter at the distance of 3 mm from the wall : with single electric (capacitive) probes (7);
- particle flux to the wall ($I_\perp$) at the distance z = 15 cm from EE: with a two-electrode electrostatic analyzer ("near-wall analyzer");
- particle flux parallel to B_z ($I_\parallel$): with a similar analyzer installed near the wall and facing EE ("parallel analyzer");
- particle flux to the butt-end electrode (I_T) along the radius of 1.5 cm: with a similar analyzer mounted in the electrode.

In addition to the above measurements the density n was controlled by a 8 mm interferometer; its horns (8) are shown in fig.1.

The shape of the potential time variation inside the plasma depends on the relation between U_o and n [1-3]. For $U > 0$ the potential Φ_o varies as shown in figs. 2b and 5b, its maximum value being ~1 kV. Corresponding oscillograms of the BL potential at different distances $z \neq 0$ from EE are shown in fig.2c-g and under EE (i.e. at z=0) in fig.5c.

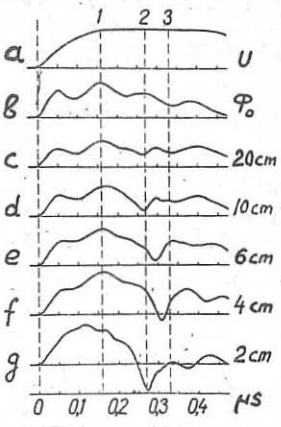


fig.2

In fig.3 radial profiles of the potential are shown near EE (fig.3-I: z = 1.5 cm) and rather far from EE (fig. 3-II: z = 6 cm). These profiles are fixed at different moments 1,2,3 indicated in fig.2. A shaded area and a dotted line in fig.3 show the position of the wall and EE, respectively.

Longitudinal distributions of the BL potential $\Phi(z)$ taken at different moments are shown in fig.4. Here $\Phi(z)$ in the absence of the plasma is shown by a dotted line and a shaded area indicates the EE position.

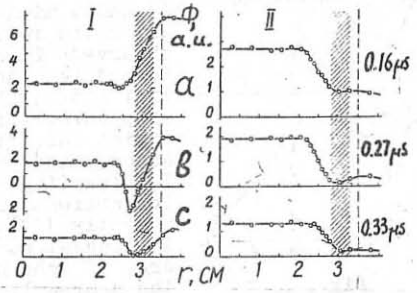


fig.3

Max-Planck-Institut für Plasmaphysik
8046 Garching bei München

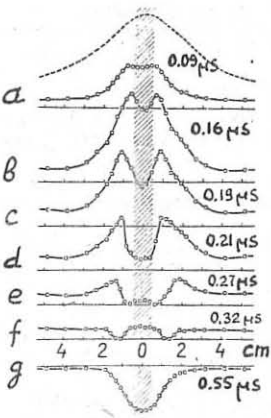


fig.4

The oscillograms of I_r, $I_\parallel$ and $I_\perp$ currents together with U, Φ_0 and $\Phi|_{z=0}$ oscillograms are shown in fig.5. Similar oscillograms for U<0 are presented in fig.6.

The experimental data (figs.2 to 6) indicate that the processes in BL affected by an external electrostatic perturbation U(t) proceed as follows.

With U(t)>0 switched on polarization of the plasma starts. The electrons provide a uniform r- and z-distribution of the potential in the plasma core while in BL the potential would be matched with the uniform potential in the core, the voltage U across EE and zero potential across the metal screen (9) and the butt-end electrodes (2) (fig.1). This results in the electrostatic field component E_z in BL being directed to the axis near EE at the very start of the process (fig.3-Ia) and consequently in ions moving to the axis with respect to magnetized electrons. In the BL region remote from EE, E_z is directed outwards (fig.3-II). A corresponding peak of the ion current $I_\perp$ is detected by the near-wall analyzer immediately after U(t) has been turned on (fig.5f). The electrons in BL at the start of the process are trapped into the potential well and oscillate therein around the EE position (z=0). As U increases with time, the potential in BL (fig.5c) and the width of BL increase too. Therefore the effective negative charge in the BL region near EE grows and the region expands. The negative charge influences the $\Phi(z,\bar{z})$ dependence where three extrema in the longitudinal distribution (figs.4a-d) and a minimum near EE in the radial profile (fig.3-Ib) are observed. Thus a space potential trap is formed for the ions near EE. This potential redistribution causes a potential drop across BL in the vicinity of the z=0 region (cf. fig.5c at $t \geqslant 0.2$ μs). This is accompanied by the first electron current $I_\parallel$ peak (fig.5e) and resumption of the $I_\perp$ ion current (fig.5f). As has been shown recently [1,3], the latter is caused by the radial motion of the plasma. The energy of ions hitting the collector of the near-wall analyzer amounts to hundreds

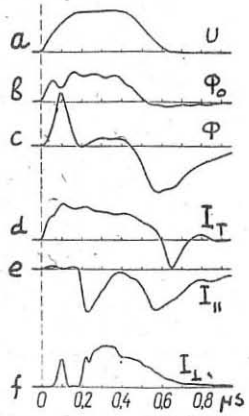


fig.5

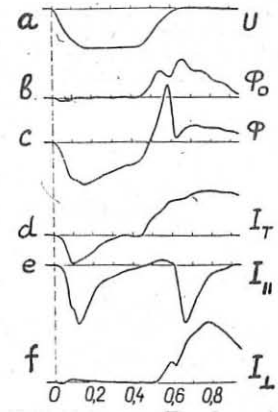


fig.6

of eV. Later on, in the U(t) plateau phase the z-distribution with five extrema is formed (figs.4e,f). A reverse evolution of the BL potential takes place during the U(t)decrease, its final stage being shown in fig.4g. In the previous phase the plasma lost ions (figs.5d,f) with resultant excess of electrons at the end of the U(t) pulse. This influences the potential distribution (fig.4g) and current characteristics (figs.5d,e at $t \gtrsim 0.4 \mu s$).

For $U < 0$ the potential in the plasma is nearly zero (figs.6a,b) and starts to rise with decreasing U(t) . The rise of the potential from U across EE to zero in the core takes place in BL under EE. Here some negative potential $\Phi < 0$ is detected (fig.6c). The zero potential inside the plasma is maintained due to electrons leaving the plasma (figs.6d,e). The ions which remain uncompensated raise the plasma core potential to some positive value as U(t) decreases (fig.6b at $t > 0.45 \mu s$).

It follows from comparison between figs.5 and 6 that similar regularities are observed in the particle fluxes and potential behavior during the $|U(t)|$ decrease at $U < 0$ and the U(t) increase at $U > 0$. Hence one can have a general idea of the potential behavior and particle motion during the oscillation period in the RF case by merely "matching" figs.5 and 6.

REFERENCES

1. Grigor'eva L.I. et al. Preprint KFTI 84-8. Moscow:TsNIIAtominform, 1984, 37 p.
2. Grigor'eva L.I. et al. ZhTF, 1984, v.54, N 3, p.470-476.
3. Grigor'eva L.I. et al. J. Nucl. Mat., 1984, v.128/129, p. 317-318.

THE USE OF HEAVY ADMIXTURE IONS FOR ENHANCING THE ICRF PLASMA HEATING EFFICIENCY

A.V.Longinov, S.S.Pavlov, K.N.Stepanov

Institute of Physics and Technology, the Ukrainian Academy of Sciences, Kharkov 310108, USSR

The ICRF heating in toroidal plasmas using fast magnetosonic waves (FW) has proved to be highly efficient. However, as demonstrated in this report, these methods of RF heating have some disadvantages, namely: i) in the regime of a FW conversion to a weakly damped short wavelength slow wave (SW), which is possible even in the FW excitation from the low magnetic-field side (LFS), the SW energy can be absorbed only by electrons and rather far from the centre of the plasma, which reduces the efficiency of heating; ii) the SW may heat the near-wall plasma thus enhancing the plasma-wall interaction and the impurity influx into the plasma. These disadvantages can be eliminated by introducing a heavy ion minority with the charge $Z' < m_{Z'}/m_D$ (Li^7, C^{13}, O^{18}, F^{19}, Ne^{22}, Fe^{56}, etc.) into the plasma. The SW propagating from the conversion region towards a high magnetic-field side (HFS) is essentially absorbed in the second-harmonic resonance region $\omega \approx 2\omega_c' = 2Z'eB/m_{Z'}c$. Because $Z' \gg 1$, heavy ions quickly transfer the energy taken from the RF field to the plasma particles. In the report presented we study the heavy ion minority method of ICRF heating (HIMH) in the D+H [1,2] and D plasmas. As an example, we consider the T-10 tokamak parameters.

The excitation of separate harmonics, $E_{R,Z} \sim f(R) \cdot \exp i(m\varphi - \omega t)$ in an annular cylinder ($R_o - a \ll R \ll R_o + a$) was calculated with and without heavy admixture ions with $Z' \gg 1$. The profiles of $n_e(R)$, $T_{e,i}(R)$ and $T'(R)$ are parabolic, $B_\varphi = B_o(R_o/R)$, $B_o = 3$ T, $R_o = 150$ cm, $a = 35$cm, the chamber radius is 39 cm, the external RF current radius is 36.5 cm, the RF current amplitude is 10A/cm, $n_o = n_e(R) \lesssim 7 \cdot 10^{13} cm^{-3}$, $T_i(R_o) = 0.5\ T_e(R_o) = 1$ keV. Fig. 1 shows the E_Z and E_R profiles (principal FW and SW components, respectively), the total power flux P and the powers absorbed by ions,

D_i, and electrons, D_e, due to the resonances $\omega = 2\omega_{cD} = \omega_{CH}$ and the electron Cherenkov damping. As is seen from fig. 1, the FW is scarcely absorbed by deuterons and protons and is almost completely converted into the SW for both the HFS-excitation (fig.1b) and LFS-excitation (fig.1a). At $n_{z'} = 0$ the SW carries away the RF power to the periphery and the electron absorption profile is not optimum, because the appreciable fraction of the RF energy is absorbed not in the central region of the plasma. The energy portion carried away by the SW, P_S/P_{in}, appears to be large even in the case of the LFS-excitation and even at large $m \ll 20$ both in the D+H and D plasmas (fig.2). The addition of heavy ions results in the total SW absorption in the plasma central region (fig. 1a,b).

It is important to know how the SW energy absorbed by heavy ions is distributed among other particles. A stationary solution of the kinetic equation has been found for the heavy-ion distribution function that takes into account heavy ion collisions with deuterons and electrons neglecting the angular scattering, and quasilinear diffusion under the action of the SW field with a diffusion coefficient $D_{QL} \sim E_R^2 \cdot J_2^2(x)/x$, where $x = k_\perp v_\perp / \omega_c'$, $J_2(x)$ is the Bessel function. Fig. 3 shows the parameter $\sum_\alpha P_\alpha$ that defines the magnetic surface average of the plasma absorbed power $\langle p \rangle = (9\sqrt{\pi}/8)^{1/2} (n' T_i / \tau_i) \cdot (m_i/m_{z'}) \cdot z'^2 \cdot \sum_{e,i} P_\alpha (k\rho_D, E^2)$, the portion of heavy ion energy transferred to deuterons $\langle p_D \rangle / \langle p \rangle$, and the SW damping factor $\mathrm{Im}\, k_\perp / (\mathrm{Im}\, k_\perp)_{max}$ (Ne^{22} admixture, $k^2 \rho_D^2 = 0.125$, $\rho_D = V_{TD}/\omega_{cD}$) versus the normalized E_R^2 value. The heavy-ion distribution function versus the transverse ion energy $\mathcal{E}_\perp = (1/2) m_{z'} V_\perp^2$ is shown in fig.4 at $E_R^2 = 175$ (curve 1) and $E_R^2 = 400$ (curve 2), the critical E_R^2 value, for which $\langle p_D \rangle / \langle p \rangle = 0.5$, is $E_{cr}^2 = 250$. For $E_R < E_{cr}$ the preferential heating of deuterons is realized, the SW damping weakly depends on E_R^2 and corresponds to its value at $T' = T_D$, the number of particles in the high energy tail is small. At $E_R > E_{cr}$ it is the electrons that are preferentially heated, $\langle p \rangle$ weakly depends on E_R^2, $\mathrm{Im}\, k_\perp$ decreases as E_R^2 increases and at high E_R^2 becomes below its value for $E_R \ll E_{cr}$. At $E_R \sim E_{cr}$, $\mathrm{Im}\, k_\perp$ reaches its maximum value. In the interaction of resonance particles with the SW field and other particles note the important role of the tail cutoff

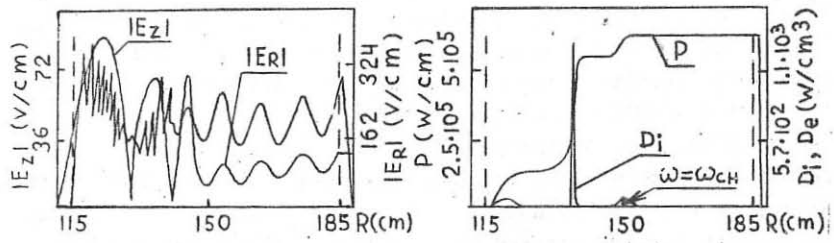


fig.1 (a) $n_H/n_D = 2\%$, $n_{C13}/n_D = 0.5\%$, $n_0 = 3\cdot10^{13}$, $m = 4$

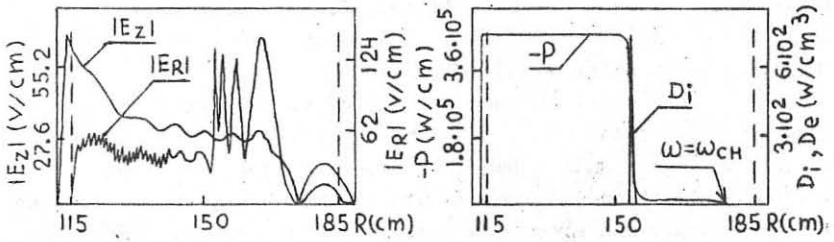


fig.1 (b) $n_H/n_D = 4\%$, $n_{Li7}/n_D = 3\%$, $n_0 = 7\cdot10^{13}$, $m = 7$

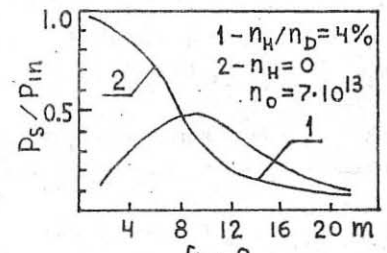


fig.2

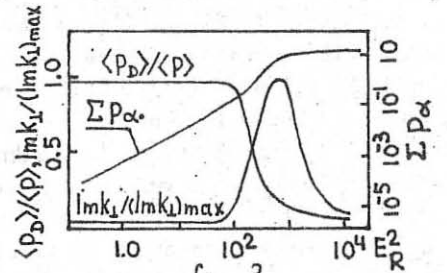


fig.3

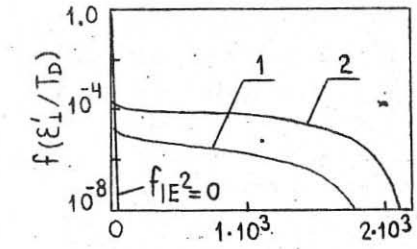


fig.4

effect occurring due to SW short wavelength ($D_{QL} \to 0$ for $X \to 5.1$).

The studies performed lead to the following conclusions.

(i) The use of heavy, high Z'admixture ions provides the energy absorption in the centre of the plasma and the heating of majority ions or electrons. In this case the maximum heating rate of the majority ions can be higher by more than order of magnitude as compared with its value for the hydrogen-minority ICRF heating.

(ii) The total cutoff effect in the heavy-ion distribution function is important in the HIMH (the interaction with majority ions is enhanced, fast particle losses are reduced due to finite orbits and a weak angular scattering of fast ions leads to the decrease of their superbanana losses if the resonance region $\omega = 2\omega_c$ lies in the region which has no locally trapped particles).

(iii) If the cyclotron resonance region for heavy admixtures is located in the region comprising locally trapped ions, a weak angular scattering of ions during their heating can provide a quick removal of heavy particles from the trap. The latter can be used to clean the plasma from impurities or to produce multi-charged ion fluxes with energies between $10^2\ T_i$ and $10^4\ T_i$.

(iv) The advantages of the HIMH become particularly prominent in the regimes with a low plasma density, in the HFS-excitation, and also in small- and medium-sized traps, where at moderate RF power levels regimes with $T_i \gg T_e$ can be attained.

References

1. A.V. Longinov, K.N. Stepanov, In: Vysokochastotnyj nagrev plazmy, Gorky, Applied Physics Institute, USSR Academy of Sciences (1983) 105-210.
2. A.V. Longinov, K.N. Stepanov, Proc. IV Intern. Symposium on Plasma Heating in Toroidal Systems (Rome, 22-28 March, 1984) v.1, p.486.

ION HEAT TRANSFER UNDER CYCLOTRON HEATING IN TOKAMAK

R.V.Shurygin, P.N.Yushmanov

I.V.Kurchatov Institute of Atomic Energy,
Moscow, USSR

An analysis of experimental data /1,2/ shows that RF-waves, besides the heating of plasma, change the confinement parameters: heat conduction and diffusion. The role of an additional transfer induced by RF-waves will be more important with a rise in the power of heating and, probably, decisive, when the thermonuclear parameters are reached.

Besides the direct effect of quasi-linear collisions of RF-waves with particles /3/, the cyclotron waves result in a horizontal polarization of plasma /4/. An additional poloidal electric field changes the drift velocity of particles and can affect the radial transfer. The additional transfer should change a sign, as the electric field, in case of ECRH or ICRH, has an opposite direction. A similar difference in the plasma confinement parameters is also observed in the experiments: typically, plasma density rises under ICRH and drops under ECRH.

The effects of quasilinear collisions and plasma polarization on the radial transport processes under the cyclotron heating are studied in this paper on the basis of a solution to the drift kinetic equation. An ion component only is under consideration, as the electron transfer cannot be calculated within the frames of the drift kinetic equation due to anomality. Let us consider, for definiteness, ICRH in tokamak plasma. ECRH differs only by a sign of a poloidal potential polarization and by the lack of a quasi-linear collision operator. Let a plasma, consisting of the same variety of ions and electrons, be in the toroidal magnetic field $\vec{B} = (B_0\vec{e}_\varphi + B_\vartheta\vec{e}_\vartheta)/h$, where $h = 1 + \epsilon\cos\alpha$, $\epsilon = r/R$ is the ratio between the minor radius and the major radius of the torus, r, α, Φ are the toroidal coordinates. Let us also consider the poloidal polarization $\varphi_1\cos\alpha$ $(\varphi_1 \sim \epsilon v_{QL}/v_c)$ to be set due to the RF-field effect /4/ so that the total electrostatic potential can be represented as $\varphi(r,\alpha) = \varphi_0(r) + \varphi_1\cos\alpha$.

The ion distribution function in the regime of rare colli-

sions $\left(\nu_{ii}/\epsilon, \nu_{QL} \ll v_{Ti}\sqrt{\epsilon}/qR\right)$ is found from a linearized drift kinetic equation

$$\frac{v_\parallel}{r}\frac{B_J}{B_0}\frac{\partial f_1}{\partial \alpha} = C_{ii}(f_0) + C_{QL}(f_0) \qquad (I)$$

where $f_0 = \left(g - \frac{v_\parallel}{\Omega_J}\right)\frac{dF_0}{dr}$, $\mu = \frac{mv_\perp^2}{2B}$, $E = \frac{mv^2}{2} + Ze\varphi(r,\alpha)$, $F_0 = F_0(E,\mu)$ is the equilibrium disribution function dependent on the integrals of motion, E and μ. The operator of quasi-linear collisions has a form /3/

$$C_{QL} = \frac{1}{v_\perp}\frac{\partial}{\partial v_\perp} D v_\perp \frac{\partial f}{\partial v_\perp}$$

where $D = D_{QL}\delta(\alpha - \frac{\pi}{2})$, $D_{QL} = \nu_{QL} v_{Ti}^2$, $\nu_{QL} = (v_E/v_{Ti})^2 \Omega_c/\epsilon$, $v_E = c\tilde{E}/B_0$. An unknown function $g = g(E,\mu)$ is found from the solvability condition for Eq. (I):

$$\oint \left[C_{ii}(f_0) + C_{QL}(f_0)\right]\frac{d\alpha}{v_\parallel} = 0 \qquad (2)$$

Usinf the variables $S = (\epsilon\mu B_0 - Ze\varphi_1)/(E - \mu B_0(1-\epsilon) - Ze(\varphi_1 + \varphi_0))$, $W = E - Ze\varphi_0$, let us simplify the kinetic equation, taking account of the inequality $\partial/\partial S \gg \partial/\partial W$ which is true in the vicinity of a separatrix:

$$\frac{v_\parallel}{qR}\frac{\partial f_1}{\partial \alpha} = \frac{v_\parallel p^2}{h\left(2(\epsilon W - Ze\varphi_1)/m\right)^{1/2}}\frac{\partial J_S}{\partial S} \qquad (3)$$

where the flux normal to the separatrix, J_S, is determined as:

$$J_S(f_0) = 2\sqrt{\frac{Q}{p}}\left\{(S+\gamma p)\left[\frac{D}{W_0}\left(Q\frac{\partial f_0}{\partial S} + L\frac{\partial f_0}{\partial W}\right) + \frac{2\nu_2}{\epsilon}p\frac{\partial f_0}{\partial S}\right] + \right.$$
$$\left. + \nu_2\gamma h\left[f_0 + T\left(\frac{\partial f_0}{\partial W} + K f_0\right)\right]\right\}$$

$p = \epsilon + S(1-\epsilon)$, $Q = 1 - 2S\sin^2\frac{\alpha}{2}$, $\gamma = \frac{Ze\varphi_1}{\epsilon W_0}$, $W_0 = W - \frac{Ze\varphi_1}{\epsilon}$, $L = \frac{hW_0}{p}$, $K = \frac{\gamma p Q}{\epsilon(W - Ze\varphi_1\cos\alpha)}$

The solution of Eq. (3), taking account of the solvability condition (2) for two limit cases, $\nu_2/\epsilon \gg \nu_{QL}$ and $\nu_2/\epsilon \ll \nu_{QL}$, has a form:

$$g_t = 0, \quad g_u = \frac{\sigma}{\Omega_J}\sqrt{\frac{2\epsilon W_0}{m}}\int_{1/2}^{S}\frac{\sqrt{Q_0}}{I}\frac{\partial}{\partial S}\sqrt{\frac{Q_0}{p}}\,dS \qquad (4)$$

$$g_t = 0, \quad g_u = \sigma\sqrt{\frac{Q_0}{p}}\sqrt{\frac{2\epsilon W_0}{m}}\left[1 - \sqrt{\frac{p}{(1+\epsilon)Q_0}}\exp\left(-\frac{W_0}{Y}\frac{\partial Y}{\partial W_0}\int_{1/2}^{S}\frac{dS}{PQ_0}\right)\right]$$

where $I = \oint Q \frac{d\vartheta}{2\pi}$, $Y = \sqrt{\epsilon w_0}\frac{dr_0}{dr}$, $Q_0 = 1 - S$

The radial fluxes of particles and heat, according to Eq. (3), are expressed as the collision integral of a function:

$$\left\{\Gamma_i, Q_i/T\right\} = -\frac{1}{\Omega_3}\oint_0^{2\pi}\frac{d\vartheta}{2\pi}\int U_{ii}\left\{1, \frac{mv^2}{2T}\right\}\left[C_{ii}(f_0) + C_{QL}(f_0)\right]d^3v \qquad (12)$$

Integration of C_{QL} with respect to a longitudinal velocity gives zero, therefore quasi-linear collisions, in difference from the results in /3/, do no introduce the direct contribution into radial fluxes.

It is qualitatively illustrated in Fig.1, where one can see that a deformation of the orbit due to quasi-linear collisions occurs so that a particle always passes through the fixed resonance points. The role of a poloidal plasma polarization is reduced to a change in the velocity space regions occupied by ions with different trajectories. Regions in the velocity space within the coordinates w, S , corresponding to the passing and trapped particles at $\varphi_1 > 0$, are depicted in Fig. 2. One can see that the separatrix, $S = 1/2$, from the vicinity of which ions introduce the main contribution into the transfer, is shifted to the high energy range $w > ze\varphi_1/\epsilon$ (region I). The region 2 is occupied by passing ions. The region 3 is occupied by trapped ions, which are trapped under strong magnetic field (reflection from the inhomogeneities in the electrical potential occurs). The case $\varphi_1 < 0$ (ECRH) is depicted in Fig.3. The region of trapped ions increases in this case. The separatrix is shifted towards the high energy range, as in the case of $\varphi_1 > 0$, but the shift is ϵ - times less. Such a change in the regions naturally results in a change in the radial fluxes.

The results of numerical calculations for a ratio $\chi_i^{\pm}/\chi_i^{neo}$ vs. a parameter $x = ze\varphi_1/T$ at $\epsilon = 0.05$ are given in Fig.4 At $\varphi_1 > 0$, a considerable decrease in the heat conduction coefficients, $\chi_i^{\pm}$ is observed; at $\varphi_1 < 0$ an insignificant rise in χ_i^{-} with a rise in x is also observed. A change in the ion heat conduction under the cyclo-

tron heating is caused by a redistribution of passing and trapped particles in the phase space due to a poloidal polarization. The magnitude of an additional flux doesn't exceed $\nu_{\varphi L}/\nu_{ii}\ \chi^{neo}$ at a relatively weak quasi-linear collisions.

References

1. R.M.Gilgenbach et al., Phys. Rev. Lett., 44, 647 (1980).
2. R.J.La Haye et al., Nucl. Fusion 21, 1426 (1981).
3. R.V.Shurygin, P.N.Yushmanov. Preprint Institute of Atomic Energy N 3630/7 (1985).
4. M.N.Rosenbluth, R.D.Hazeltine. Phys. Fluids, 15, 116 (1978).

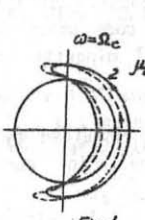


Fig.1

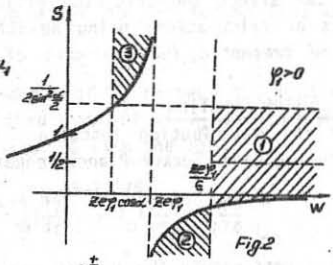


Fig.2

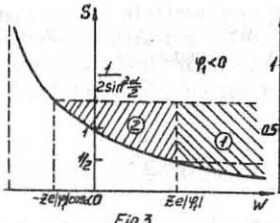


Fig.3

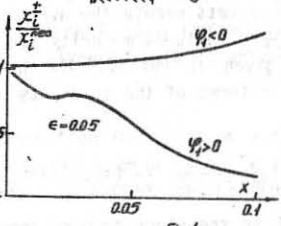


Fig.4

FOKKER PLANCK CALCULATIONS OF ICRF CURRENT DRIVE ON JET

M Cox, R O Dendy, H Hamnén*, J Jacquinot*, P Lallia*, M R O'Brien and D F H Start
Culham Laboratory, Abingdon, OX14 3BD, UK
(Euratom/UKAEA Fusion Association)
*JET Joint Undertaking Euratom

INTRODUCTION

Travelling ICRH waves can drive currents in plasmas either through cyclotron damping on a minority species (the current-drive arising from the asymmetric collisionality mechanism explored by Fisch[1]) or by absorption of the wave power by the plasma electrons through Landau damping or TTMP[2]. In this paper only the minority-ion current-drive scheme will be considered. Previous work [1-3] has indicated that the efficiency of ICRH minority-ion current-drive is sufficient to generate substantial currents in JET. However, these studies have treated the ICRH only as a perturbation to the plasma and have also used simple models for the distribution of the wave interaction in velocity space. It is known from studies of ECRH current-drive that both of these assumptions can affect the predicted efficiency[4]. In this paper the preliminary results of calculations using an ICRH code which removes these assumptions will be presented for the case of H^+ minority ions in a D^+ plasma.

MINORITY ION DISTRIBUTION FUNCTION

The minority ion distribution function f is obtained by numerically solving the bounce-averaged Fokker-Planck equation which can be written symbolically as

$$\frac{\partial f}{\partial t} = \langle\left(\frac{\partial f}{\partial t}\right)_C\rangle + \langle\left(\frac{\partial f}{\partial t}\right)_{RF}\rangle \qquad (1)$$

where the angular brackets denote the average over particle bounce phase. The collision term $\left(\frac{\partial f}{\partial t}\right)_C$ includes minority ion collisions with majority ions and electrons and is given in ref.3. The quasi-linear ICRF term for tokamak geometry is given in terms of the constants of motion $\mu = v_\perp^2/2B(\chi)$ and $K = \oint v_\parallel d\chi$ by[5]

$$\langle\left(\frac{\partial f}{\partial t}\right)_{RF}\rangle = \frac{1}{2\Delta t}\frac{\partial}{\partial \mu}\left\{\langle[(\Delta\mu)^2]\rangle\frac{\partial f}{\partial \mu} + \langle[\Delta\mu\Delta K]\rangle\frac{\partial f}{\partial K}\right\} + T_2 \qquad (2)$$

where T_2 is equal to the first term on the rhs with μ and K interchanged, $v_\perp$ and $v_\parallel$ are the perpendicular and parallel velocities respectively, $B(\chi)$ is the magnetic field as a function of the poloidal angle, and Δt is the average time between resonant interactions. The square brackets in eq(2) denote gyrophase averages and the increments $\Delta\mu$ and ΔK are related to the increment $\Delta v_\perp$ in $v_\perp$ as specified in ref.4. The increment $\Delta v_\perp$ is calculated using the single particle model of Cairns and Lashmore-Davies[6] and takes account of the finite toroidal extent of the RF field and the resonance broadening due to the

tokamak rotational transform. For the particular case of fundamental ion cyclotron waves injected on the median plane from the low field side we find

$$|\Delta v_\perp|^2 = \frac{\pi}{8} \left| \frac{Z_h e E_+}{m_h v_\parallel} \right|^2 I \qquad (3)$$

where $I = G^{-\frac{1}{2}} \exp\{-(\frac{\omega-\Omega}{v_\parallel}) - k_\parallel)^2/(2L^2G)\}$, $G = L^{-4} + (\Omega'/2v_\parallel)^2$, m_h, Z_h and Ω are the minority ion mass, atomic number and gyrofrequency respectively, E_+ is the component of the wave field rotating with the ions, ω is the wave frequency and $k_\parallel$ is the parallel component of the wavevector. From eq(3) it can be seen that the width of the resonance in velocity space depends on the toroidal extent, L, of the RF field and the parallel gradient of the gyrofrequency, Ω', due to the rotational transform. The derivation of eq(3) assumes that the parallel velocity of the ion remains constant as it passes through resonance. This is a poor assumption for trapped particles which resonate at the turning point of their orbit or, more generally, for particles close to the so called 'tangent resonance' line in velocity space[7]. For these particles we follow the procedure given in ref.7 and obtain

$$I = 4\pi^2 (\frac{2}{\ddot{\Omega}})^{2/3} [\mathrm{Ai}\{(\omega-\Omega-k_\parallel v_\parallel)(2/\ddot{\Omega})^{1/3}\}]^2 \qquad (4)$$

where Ai is the Airy function and $\ddot{\Omega}$ is the second time derivative of the gyrofrequency.

The strong radial dependence of E_+ between the proton-deuteron hybrid resonance at R_h, its associated cut-off at R_c and the proton fundamental cyclotron resonance at R_r is modelled with the form

$$|E_+|^2/|E|^2 = \begin{cases} A + (1-A)e^{-|R-R_c|/S} & \text{for } R_h < R < R_r \\ 0 & \text{for } R < R_h,\ R > R_r \end{cases}$$

where $A = 0.6$ for $R_h<R<R_c$, $A=0$ for $R_c<R<R_r$ and the scale length S in each region is chosen to reproduce the form given by Chiu et al[3]. Values of R_h and R_c were obtained from ref.8.

Steady state minority ion distribution functions on a given flux surface are calculated by numerically solving eq(1) on a (v,θ_0) grid where v is the ion speed and θ_0 is the pitch angle on the outside of the flux surface.

RESULTS

The current drive efficiency for the minority hydrogen ions expressed as the ratio of current density J to absorbed power density P_d, as normalised by Cordey et al[9], is shown in Fig.1 as a function of $k_\parallel$. The solid curve is for the form of $|E_+|^2$ given above; the dotted curve is for $|E_+|^2$ proportional to the fifth power of the distance from R_r in the region $R_c<R<R_r$ which was chosen to check the dependence on the form of $|E_+|^2$. Thus the optimum value of $k_\parallel$

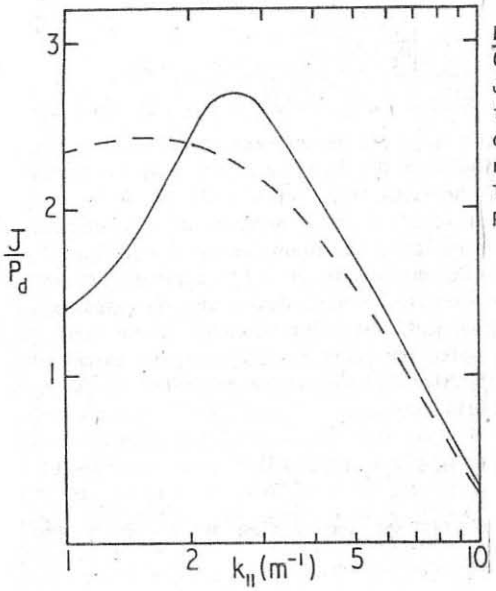


Figure 1
Current drive efficiency, J/P, versus $k_{\parallel}$ for the two forms of $|E_+|^2/|E|^2$ described in the text. $n_e=3\times10^{19}m^{-3}$, $n_h/n_i=0.05$, $T_e=T_i=5keV$, r = 0.1 m, $R_r=R_o=2.96$ m.

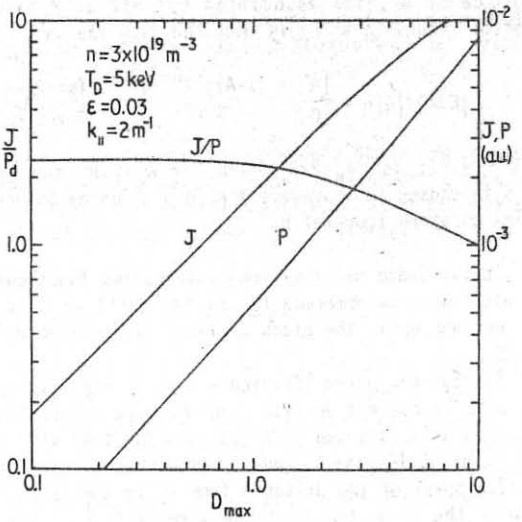


Figure 2
Current drive (J), power absorbed (P) and current drive efficiency versus D_{max} for the $k_{\parallel}$ = 2 m^{-1} case of Fig.1. J and P are in arbitrary units and J/P is normalised as for Fig.1.

and the width of the maximum depends sensitively on the details of E_+ between cyclotron resonance and cut-off. The maximum in Fig.1, corresponding to 90A/kW in JET, arises because the effective resonant velocity first increases and then decreases as $k_\parallel$ is reduced.

In Fig.2 the current density, power density and efficiency are plotted against the maximum value of the diffusion coefficient normalised to the minority ion collision frequency and deuteron thermal velocity squared, i.e. $D=\frac{1}{2}<[(\Delta v_\perp)^2]>/\Delta t \nu_i v_D^2$. Nonlinear effects such as the reduction of J/P_d are seen to occur close to $D_{max} \sim 1$. In Fig.3 the decrease in efficiency due to trapping of the minority ions is shown versus the inverse aspect ratio ε.

CONCLUSIONS

The present calculations indicate that minority ion currents of the order of 1MA appear to be feasible on JET with 15 MW of ICRF power. There appears to be an optimum $k_\parallel$ which is determined by the spatial dependence of E_+ which is presently being investigated.

REFERENCES

1. Fisch N J, Nuclear Fusion 21 (1981) 15.
2. Karney C F F and Fisch N J, Phys Fluids 22 (1979) 1817.
3. Chiu S C et al, General Atomic Company Report, GA-A16353.
4. O'Brien M R, Cox M and Start D F H, to be submitted for publication in Plasma Physics and paper 332 of this conference.
5. Laval G and R Pellat, in Physique des Plasmas, Les Houches 1972, p219. Edited by C de Witt and published by Gordon and Breach.
6. Cairns R A and Lashmore-Davies C N. To be published in Plasma Physics.
7. Kerbel G D and McCoy M G, Lawrence Livermore National Laboratory Preprint UCRL - 92062. To be published in Phys Fluids.
8. Perkins F W, Nuclear Fusion 17 (1977) 1197.
9. Cordey J G, Edlington T and Start D F H, Plasma Physics 24 (1982) 73.

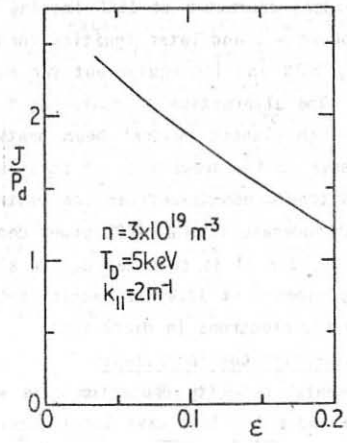


Figure 3
Current-drive efficiency, J/P, versus inverse aspect ratio, $\varepsilon=r/R_0$, for the $k_\parallel=2$ case of Fig.1.

FOKKER-PLANCK CALCULATIONS FOR JET ICRF HEATING SCENARIOS

J. Scharer

University of Wisconsin, Department of Electrical & Computer Engineering
1415 Johnson Drive, Madison, Wisconsin 53706 U.S.A.

J. Jacquinot, P. Lallia and F. Sand

JET Joint Undertaking, Abingdon, Oxfordshire OX14 3EA, England

Flux-averaged ICRF heating of the JET tokamak is considered utilizing an anisotropic, time-dependent Fokker-Planck code. Minority fundamental deuterium and tritium and second harmonic tritium and deuterium cases are considered for wave accessibility, strong single pass damping and enhanced ion tail produced fusions. It is found that enhanced fusions resulting from heated minority deuterium fundamental ion tails yielding fusion enhancement of 1.6 to 1.9 times an equivalent Maxwellian with local Q = 1 values can be achieved near the plasma core with moderate absorbed power levels, pulse widths and energy confinement times. Simulations are also presented corresponding to current D-(He_3) experiments being carried out on JET at multimegawatt levels.

1. Introduction

In this paper we examine the scaling of ICRF heating for larger tokamaks such as JET, in which active deuterium-tritium plasma experiments will be carried out in the future. The time-dependent character of ICRF heating to obtain a fusion Q = fusion power/heating power = 1 and later ignition conditions is of considerable interest for JET, TFTR and its equivalent for non-active fusion tokamaks (JT-60 and D-IIID). The alternative of achieving this by ICRF heating alone or in conjunction with planned neutral beam heating experiments can provide flexibility in tokamak fusion scenarios. A consideration of the time-dependent nature of anisotropic non-Maxwellian ion distributions for optimized mixes of D-T ions with moderate (15 MW) ICRF power deposition and energy confinement times (τ_E = 0.5-1.5 s) is considered. We also carry out computations for current 3 MW experiments at 33.4 MHz heating 5-10% concentrations of minority fundamental He-3 and electrons in deuterium.

2. 2-D Ray Focusing and 1-D Single Pass Absorption Considerations

Single pass absorption for the fundamental minority deuterium case was examined using the ray tracing FREMIR code and a 1-D fast wave local absorp-

tion code. The single pass absorption resulting from the FREMIR code for a wide range of $k_\parallel$ values for JET parameters was made for $n_D = 0.1\ n_e = 5 \times 10^{12}/cm^3$, R = 3.0 m, a = 1.25 m, T_D = 30 keV, $T_e = T_T$ = 2 keV and low field side launch. Strong single pass absorption (> 50%) is found for a major portion of the launched $k_\parallel$ spectrum 0.03 $cm^{-1} < k_\parallel < 0.10\ cm^{-1}$. A corresponding study of the second harmonic tritium case with 10% tritium (T_T = 30 keV, T_D = 2 keV) of $k_\parallel = 0.06\ cm^{-1}$ yields only 9.2% single pass absorption.

We have examined the local fast wave absorption profile by considering the power dissipation expression[1] $P_j = \omega\varepsilon_0(\bar{E}\cdot\bar{\bar{K}}_j^A\cdot\bar{E}^*)/2$ where $K_j(r)^A$ is the anti-Hermitian part of the local full hot plasma dielectric tensor for species j and the magnetic field is allowed to vary in the radial direction. We assume a hot plasma condition with substantial $k_\parallel = 0.06\ cm^{-1}$ values indicative of the antenna spectrum so that mode conversion processes are neglected. The magnetic field is scanned to simulate the relative ion absorbtivity for the resonance region. The relative drop in the peak single pass absorption for second harmonic tritium vs. deuterium is ten at the same temperatures and plasma parameters (50% D/50% T, T = 1.7 keV) but shifted frequencies to maintain resonance on axis. This is due to the lower left-hand electric field polarization and its transverse gradient for the tritium case. If the tritium concentration is lowered to 10% the local absorption near resonance decreased still further and very weak single pass absorption is obtained.

3. ICRF Tokamak Heating Physics Model

Blackfield and Scharer,[2] and Scharer, Jacquinot, Lallia and Sand[3] have presented a formulation of the ICRF Fokker-Planck equation and applied it for the cases of PLT experimental results, a full scale reactor scenario and JET. To model radial conduction and convection losses, finite energy (τ_E) confinement times are introduced for different species.

The code also includes ohmic heating via a Spitzer resistivity, D-T and D-D fusions and alpha particle production in the overall energy balance and particle source terms. The initial conditions for the RF turn on for the JET "active" high power cases are taken to be $n_e = \sum n_i = 5 \times 10^{13}/cm^3$ and $T_i = T_e$ = 1.7 keV (E_j = 1.5 x T_j = 2.55 keV) so that the local ohmic heating is weak compared to the RF power for the cases studied and decreases further as the electrons are heated. For fusion reactions for D-T the hybrid II code[4] computes the fusion energy according to the expression

$$E_F(\text{keV}) = \int_0^t n_D n_T (\overline{\sigma v})_{DT} \cdot 17{,}600\ d\tilde{t}$$

where the cross section is determined for non-Maxwellian ion components. To simulate wave focusing in the central plasma region we assume that the absorbed power density is four times that for uniform power absorption.

The plasma conditions for the current multimegawatt heating experiments in He-3 are taken to be as follows for the ohmic equilibrium which was checked to be self-consistent with the code: RF power = 3 MW at a frequency of 33.4 MHz at B_0 = 3.3 T with R = 3.0 m and a = 1.15 m. The electron density was taken to be $n_e = 3 \times 10^{13}/cm^3$ with 5-10% concentrations of He-3 and a 4% concentration of residual hydrogen. The ohmic equilibrium is taken to be T_e = 3.2 keV with $T_D = T_i$ = 2.75 keV with energy confinement times of τ_E = 0.5 s. The initial electron temperature was raised to 3.5 keV for some runs to correspond to some experimentally observed conditions.

4. Deuterium/Tritium Heating Scenarios With Alpha Production

A. Second Harmonic Tritium and Deuterium. We first consider a tritium concentration of 50/50 D-T at an electron density of $n_e = 5 \times 10^{13}/cm^3$. An energy confinement time τ_E = 0.5 second is imposed for all species. The input power level for a three second pulse is 15 MW (a 0.65 watt/cm^3 power density) near second harmonic tritium resonance (f = 33 MHz) with a 10 cm flux average. The tritium energy rises asymptotically to T_{eff} = 20 keV with a thermal anisotropy of $E_\perp/E_\parallel$ = 4.7 at the end of the pulse. The tritium produces a substantial tail which slows down on the electrons and produces a relatively low background deuterium temperature T_D = 5 keV. Note that the electron power absorption competes slightly at early times with the tritium absorption and after the tritium is heated it totally dominates the flux average power absorption. The fusion Q = 0.072 is reached at the end of RF pulse. The high concentration of tritium and weak single pass absorption make it difficult to obtain Q = 1 with the moderate 15 MW absorbed power levels unless the frequency is changed so that the fundamental deuterium resonance is also located in the core of the machine.

We consider raising the frequency to 50 MHz to correspond to second harmonic deuterium on the axis. The power levels and initial conditions corresponding to the previous second harmonic tritium case yield T_D = 23.3 keV with $T_T = T_e$ = 10.7 keV with a lower energy deuterium tail formation and negligible Q enhancement over a Maxwellian. The maximum Q value at the end of the three second pulse rises to Q = 0.68. Better alpha particle power production and deuterium tail coupling to the tritium distribution make the second harmonic deuterium heating preferable to tritium for these cases.

B. Fundamental Minority Deuterium. We consider a case with a 5% deuterium concentration (n_e = 5 x $10^{13}/cm^3$) operating at 25 MHz with a 3.29 T field on axis, a 4.8 MA current and 11.25 MW of power absorbed. The flux average is obtained at r = 10 cm with τ_E = 1.5 sec. The deuterium temperature rises to T_{effD} = 42 keV with a fusion Q = 0.88 at the end of a one second pulse. The fusion Q is about 1.5 times an equivalent Maxwellian for this case.

We now consider a longer three second RF pulse at 11.25 MW with a flux average taken at 62.5 cm. To gain full advantage of the minority heating regime, the resonant deuterium concentration starts at 5% and is increased (such as that obtained by gas puffing) to 26% in a linear fashion with a corresponding increase in electron temperature to satisfy charge neutrality. This concentration increase keeps the average deuterium energy from running away and flattens the deuterium temperature at T_D = 66 keV towards the end of the pulse which peaks the fusion Q at 1.4.

We finally consider conditions comparable to current experiments at 3 MW coupled power levels at 33.4 MHz in He-3 minority. It is not possible to simulate the sawtooth activity operating on the electrons inside the q = 1 surface with our code. We will try to model preliminary averaged temperature qualities over a 50 cm flux surface using the Fokker-Planck code. We utilize the code with 10% He^3, n_e = 3 x $10^{13}/cm^3$ and T_{eo} = 3.5 keV with $T_{Do} = T_{io}$ = 2.75 keV and τ_{Eo} = 0.5 seconds. A rise in the averaged electron temperature to 5 keV with a 1 keV rise in the deuterium temperature can be obtained in 150 ms with reduced energy confinement times. Possible causes for the required partial electron heating, He-3 absorption and the associated nature of the wave dispersion near the core will be discussed.

ACKNOWLEDGEMENTS

This research was supported in part by NSF Grant ECS-8212173, DOE Contract DE-AC02-83ER53104, and EURATOM.

REFERENCES

1. J.E. Scharer, B.D. McVey and T.K. Mau, Nucl. Fusion 17 (1977) 297.
2. D.T. Blackfield and J.E. Scharer, Nucl. Fusion 22 (1982) 255.
3. J.E. Scharer, J. Jacquinot, P. Lallia and F. Sand, Nuclear Fusion 25 (1985) 435.
4. A.A. Mirin, "Hybrid-II, A Two-Dimensional Multispecies Fokker-Planck Computer Code," Lawrence Livermore Report UCRL-51615 Rev. 1 (1975).

PLASMA-ANTENNA COUPLING AND THE RELATED SCRAPE-OFF LAYER STUDIES ON JET

M. Bureš, M.P. Evrard*, J. Jacquinot, P.P. Lallia and F. Sand

JET Joint Undertaking
Abingdon
Oxon, OX14 3EA, UK

* ERM/KMS, Brussels, Belgium

Introduction

During the first six months of 1985 the four types of different RF antenna configurations [1] were tested on JET. The antenna preformance in terms of coupling efficiency and plasma heating was investigated. In this paper we present the results on plasma-antenna coupling and also discuss the modification of scrape-off layer by RF power. The coupling resistance was measured as a function of plasma-antenna distance at different plasma densities, magnetic fields, frequencies and power levels. The experiments were performed in a deuterium plasma with Helium and Hydrogen gas as minority species. The resonances of RF field in the toroidal cavity were observed when the minority concentration was varied. The maximum power delivered to the transmission line, when operating both antennae was 5.5 MW.

Coupling Efficiency

To assess the overall efficiency of the antenna performance, two antennae were investigated. First antenna with two conductors can be phased either in monopole or dipole configuration (AØ1M, AØ1D) while the second one, having four conductors, can be phased either as dipole or quadrupole, i.e,. AØ2D and

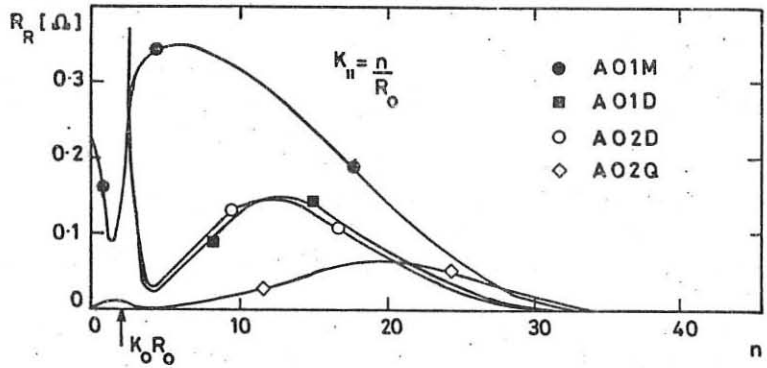


Fig. 1 Radiation resistance spectra for the AØ1 monopole, AØ1 dipole, AØ2 dipole and AØ2 quadrupole antenna configurations. The spectra are symmetric about n = 0.

AØ2Q. The radiation resistance spectra corresponding to the four antenna configurations are shown in Fig.1 as function of the toroidal mode number n. The variation of R_R at low n values are due to the coaxial modes. At present there is no evidence that these modes are excited in JET and when comparing with experimental data, these modes are excluded from model. The coupling resistance was measured by the directional couplers on the transmission line and includes the line and antenna losses $R_s = R_L + R_A \simeq 0.6\ \Omega$ (at 33 MHz). The resistance of the 80 m long transmission line is $R_L \simeq 0.35\ \Omega$. The power coupling efficiency becomes $\eta = P_{Pl}/P_{Gen} = 1 - R_s/R_c$, where $R_c = 2\,P_{Gen}\,(Z_o/\hat{V}_L)^2$. Here $Z_o = 30\ \Omega$ is the characteristic impedance of the line and $\hat{V}_L$ is the maximum voltage. Each antenna is powered by two generators and thus the power

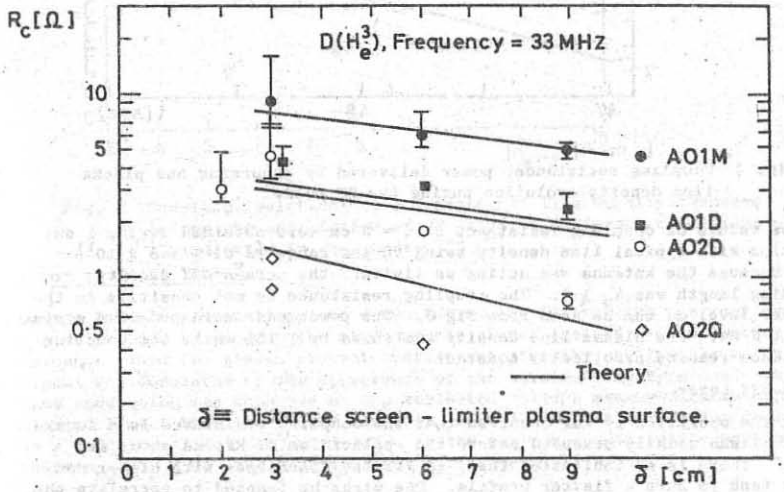


Fig. 2 Coupling resistance as a function of distance antenna screen-limiter plasma surface.

delivered per unit becomes $P_{TOT}(MW) = R_c\ (\Omega)$ when the maximum voltage on the line is $\hat{V}_L = 30$ kV. The coupling efficiency at $\delta = 3$ cm ranges from $\eta =$ 40-60% for quadrupole, 80-92% for dipole and 92-96% for monopole configuration. The tuning is performed close to the generator. The coupling resistance as function of distance screen-limiter plasma surface is plotted in Fig 2. The measured resistances are averaged over the duration of RF pulse (typically 1-2 secs). The indicated range of values reflects the variation of plasma densities over the whole period of operation, i.e., the average density being in range $\langle n_e \rangle \simeq 1.3 - 3.4 \times 10^{19}\ m^{-3}$. The inverse dependence of coupling resistance on δ is clearly seen. The plotted values apply to the D(H_e^3) operation at frequency f = 33 MHz. The 3D theoretical coupling model [2] predicts the measured values with a fair accuracy. The low coupling achieved by the quadrupole antenna could be attributed to the uncertainty about the current distribution in the antenna conductors. Using the prematching stubs close to the antenna, which lower the voltage and therefore the losses of the line, allow for 2 MW of RF power delivered to the quadrupole antenna system. The coupling efficiency in this case becomes $\eta = 0.75\%$.

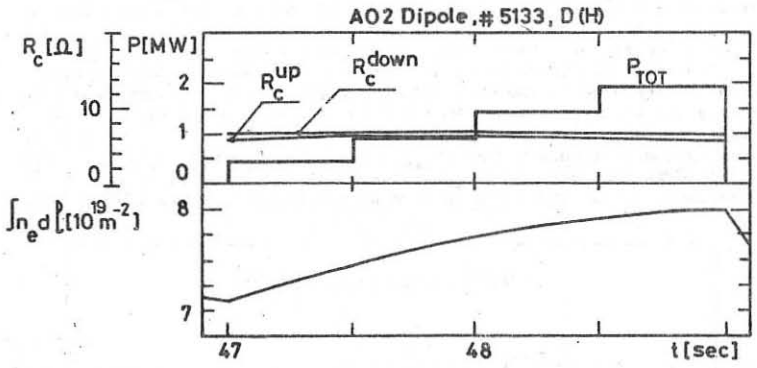


Fig. 3 Coupling resistance, power delivered by generator and plasma line density evolution during the RF pulse.

The low values of coupling resistance at δ = 2 cm were obtained during 1 day operation with typical line density being in the range $\int n_e dl \approx 4\text{-}5 \times 10^{19}$ m^{-2}. Because the antenna was acting as limiter, the scrape-off density e-folding length was $\lambda_n \cong 0$. The coupling resistance is not sensitive to the RF power level as can be seen from Fig 3. The power was increased in 4 steps up to $\approx$ 2 MW. The plasma line density increases by $\approx$ 15% while the coupling resistance remains practically constant.

Scrape-off Layer

During the operation it was observed that the coupling resistance is a function of plasma density measured before the application of RF, as shown in Fig 4. There is an indication that, in JET the discharges with higher densities tend to have a flatter profile. One might be tempted to correlate the coupling resistance to the average density and/or to the flatness of the density profile. However, the calculations indicate that the most important parameters are the density at the plasma surface defined by limiter and the density e-folding length λ_n in the scrape-off. Indeed a typical scrape-off density in JET being $n(a) = 3 \times 10^{18}$ m^{-3} is the cut-off density for the $k_\parallel$ = 6 m^{-1} implying that the $n \leq 25$ modes (Fig. 1) have its cut-off within the scrape-off. The resistance increase $\approx$ 0.7 Ω per 10^{19} m^{-2} of the line density (measured at the central chord) should be attributed to the corresponding increase of n(a). During the RF pulse the density increase is a function of RF power and can become $\Delta\int n_e dl / \int n_e dl \approx 40\%$ with $\Delta\int n_e dl \cong 2.3 \times 10^{19}$ m^{-2} in the discharges with carbonized wall. The remarkable result is that the coupling resistance during the RF pulse is not correlated to this density increase. We suggest that n(a) is not increased correspondingly which could be explained by the locally Rf enhanced particle diffusion due to the increased fluctuation level or by the recycling due to the fast neutrals. The difference between the resistances observed during the D(H) and D(He^3) operations at 33 MHz cannot be explained only by the change of the magnetic field which is required to maintain the resonance zone in the centre of the plasma cross section. The low values of R_c at the frequencies 26 MHz and 47 MHz illustrate the increased mismatch between the antenna and transmission line when going away from the antenna resonance.

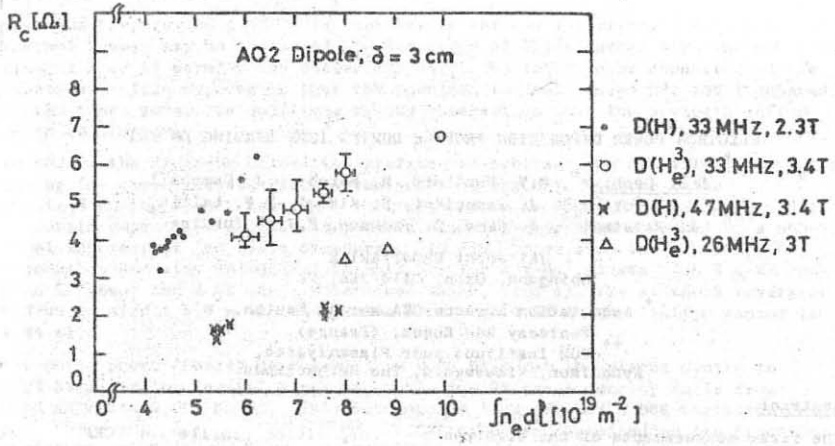


Fig. 4 Coupling resistance as a function of line density measured before the application of RF pulse at different conditions as indicated in the inset.

Toroidal Cavity Modes

During the early operation, one conductor of the AØ2 antenna was used as magnetic probe to pick up the magnetosonic signal excited by the second antenna. When the plasma did not contain the minority species the measured signal was modulated by the appearance of the toroidal cavity modes. The same modulation was observed on the reflected voltage measured on the transmission line. When the Helium minority was injected the modulation decreased as a function of He^3 concentration. At the optimum concentration estimated to be $n_{He^3}/n_e \cong 8\%$, the cavity fields were completely damped.

Conclusions

The coupling resistances measured on the AØ1 and AØ2 antennae allow for the efficient coupling of RF power. The efficiencies $\eta \gtrsim 95\%$ were readily achieved and practically all the RF power which is generated can be coupled to plasma. The measured values show a reasonable agreement with the predictions based on present coupling theories. The dependence of coupling on the scrape-off conditions is observed. The antenna loading conditions allowed for long RF pulses 1 sec $\leq \Delta t \leq$ 4 sec.

Acknowledgments

We thank Dr V.P. Bhatnagar for providing us with the computer program [2] developed at ERM, Brussels.

References

[1] Jacquinot J., Arbez J., Beaumont B., Hanley E., Kaye A.S., Lallia P.P. Plancoulaine J., Sand F., Walker C.I., in Proceedings of the 4th Inter. Symp. on Heating in Toroidal Plasmas (Rome 1984) II, 1244.

[2] Bhatnagar V.P. et al, Nuclear Fusion, Vo. 22, No. 2 (1982) 280.

ELECTRON POWER DEPOSITION PROFILE DURING ICRF HEATING ON JET

D.J. Gambier[+], D.V. Bartlett, M. Bureš, D.J. Campbell,
G.A. Cottrell, J. Jacquinot, S. Kissel, P.P. Lallia,
R. Niestadt[++], F. Sand, K. Thomsen, B.J.D. Tubbing[++]

JET Joint Undertaking
Abingdon, Oxon, OX14 3EA, UK

[+] Association Euratom CEA sur la Fusion,
[++] Fontenay aux Roses, (France)
FOM Instituut voor Plasmafysica,
Rynhuizen, Nieuwegein, The Netherlands

Abstract

The first measurements of the electron power deposition profile for ICRF heating on JET [1] are presented. In the two-ion regime (H or He^3 in D-H or D-He^3 plasmas), it is found that the power deposited directly to the electrons is strongly peaked within the volume limited by q = 1. Indeed, 'giant' sawteeth have been induced by application of RF at megawatt power levels. The sawtooth amplitude and period appear dependent on both the location of the cyclotron resonance layer and $k_{//}$ spectrum of the antenna.

Introduction

For the minority heating scenario on JET, theoretical models of ICRF [2] predict that when the wave is launched from the low field side, a large fraction of the energy is absorbed in a single transit. As the absorption occurs within the cyclotron resonance layer, it is expected that the power absorbed by the electrons is strongly peaked at the location of the cyclotron layer. Moreover, k-shaping appears crucial for the energy deposited on the electrons [maximum at $k_{//} = 0\ m^{-1}$ for a standard JET ICRF plasma].

The results presented here were obtained during experiments at multi-megawatt ICRF power levels [1]. The main objectives of these experiments were to: (i) study the power deposition profile on the electrons and compare it with a computed ohmic case, (ii) study the effect of the location of the cyclotron resonance layer on sawtooth oscillations, (iii) observe the effect of k shaping on the power deposition profile.

The electron temperature T_e was measured by electron cyclotron emission (ECE) in the second harmonic extraordinary mode, using three different instruments: a 12-channel grating polychromator [3], a Michelson interferometer and a Fabry-Perot interferometer. The Fabry-Perot and the polychromator are cross-calibrated against the Michelson which is absolutely calibrated [4].

A variety of sawtooth behaviour is observed in ohmic plasmas [5]. During ICRF heating at the plasma centre, both the sawtooth amplitude and period may increase by a factor of two or more. The sawtooth oscillation is observed on most of the diagnostic signals, including the line-integrated density, the bolometer signal and (less markedly) the magnetic β.

Power deposition profile

The spatial distribution of the absorbed RF power is determined from the change in $dT_e(r,t)/dt$ measured at the beginning of the sawtooth. As the

electron temperature profile is flat inside the q = 1 surface at this time, the thermal losses may be neglected and the slope of T_e, together with the evolution of $n_e(r,t)$ permits the determination of the total power deposited on the electrons. This hypothesis that the electron thermal losses are low (compared to the input power) is confirmed by the observation that the sawteeth seldom reach saturation.

To deduce the RF power deposition profile, we subtract the quantity $\frac{3}{2}\, d(n_e T_e)/dt$ during the ohmic plateau (before the onset of the RF) from the value obtained during the RF heating. This difference is $P_{RF} + \Delta(P_{ei} - P_{rad} - P_\Omega)$. The ohmic deposition profile is deduced from the q-profile obtained by a numerical analysis of the ohmic discharge. In Fig. 1, we show the ohmic and RF deposition profiles calculated in this way for a D-He^3 plasma with 2.4 MW coupled RF power and 2 MW ohmic power (see Table, case a). The sawtooth inversion radius is at R = 3.6 m and the plasma centre at 3.07 m (the limiter radius is 4.24 m).

The ohmic power density decreases from 0.08 MW/m^3 at the plasma centre to 0.07 MW/m^3 at the inversion radius, while the RF power density falls from 0.09 MW/m^3 to 0.001 MW/m^3. This corresponds to a 15% and a 98% variation respectively, and implies that 0.5 MW of ICRF power is deposited on the electrons within the inversion radius, ie. 20% of the coupled RF power. Assuming a deuterium plasma with 10% He^3, is in fair agreement with the predictions of ray tracing codes [2].

Assuming the ohmic deposition profile is known, it is possible to compute [6] the local confinement time during a sawtooth ($\tau_{st}(r)$) and the average confinement time (after sawtooth averaging) $\bar{\tau}(r)$. Considering the power balance representing the electron temperature during a sawtooth, as well as for T_e averaged at the same radial position, it is possible to derive both the confinement time and the power deposited on electron assuming a simple conservation of (τ_{st}, $\bar{\tau}$) in both ohmic and RF discharges. We supposed $\tau_{st}(\Omega) = \tau_{st}(\Omega + RF)$, which is equivalent to the statement that the losses inside the q = 1 surface are independent of the T_e profile outside q = 1. It then appears (Fig. 1) that this approximation is in agreement with the method of slope subtraction, suggesting that the central confinement time is not strongly affected in the presence of ICRF power, in accordance with plots of the overall increase of T_{eo} with ICRF power [7].

Effect of resonance location on sawtooth activity

The radius of the hydrogen cyclotron resonance, R_{CH}, in a D-H plasma was varied by changing the toroidal magnetic field. Three different radii were used (R_{CH} = 3.25, 3.5 and 3.7 m) at constant RF power (≃ 1.0 MW) and central density (2×10^{19} m^{-3}). The time derivative of the magnetic beta was similar in the three cases ($d\beta/dt$ = constant), as was the change in total energy content ($\Delta\beta \simeq 2 \times 10^{-4}$).

The ion temperature increase, deduced from the neutron ratio, is maximum when the cyclotron layer is located close to the centre of the plasma and smoothly decreases as R_{CH} increases (0.4, 0.3 and 0.2 keV). On the other hand, the electron behaviour is dramatically affected when R_{CH} is increased (Fig. 2).

The central electron temperature (measured by the Fabry-Perot) shows a decreasing sawtooth amplitude and period as R_{CH} moves towards the q = 1 surface. This is shown in Fig. 2. At the largest RF heating radius, the sawteeth are comparable to those observed in the ohmic heating case. However, the bottom of the small RF heating sawteeth is higher than for the large sawteeth, the two effects cancelling so as to give the same volume average temperature in the three cases.

Effect of the antenna k-spectrum on the electron power deposition profile

Using two sets of antennae [1], a monopole (M) and a quadrupole (Q), we were able to shape the $k_{//}$ spectrum emitted by the antenna [$k_{//}$ spectrum centred on 0 (M) and peaked around 7 m^{-1} (Q)]. In the same D-H plasma (see Table, case c), we compared the effect of the two antennae at the same power coupled to the plasma (P_{RF} = 0.8 MW).

Concerning the power deposition profile on electrons (Fig. 3), we expect, from the theoretical point of view, to observe the profile peak for the Q-antenna to be closer to the cyclotron layer and to be wider ($\omega - \omega_{ci} = k_{//} v_{th}$). Indeed, we observe that the power deposition profile in the quadrupole case is shifted towards the resonant layer (R = 3.24 m) by 15 cm while the width at half profile is 20 cm and 25 cm for the M and Q-antennae respectively. The power deposited on the electrons can be roughly estimated as 300 kW in the monopole case and 600 kW in the quadrupole case. Finally the amplitude and period of the sawteeth reach the values [M : 1.1 keV, 130 ms; Q : 0.75 keV, 110 ms].

Although a general observation is that the slope of T_{i_0} at the onset of the RF power and $T_{i\ max}$ are comparable for both the M and Q-antennae, the evolution of the magnetic beta is noticeably different. The slope $d\beta/dt$ at the onset of RF in both D-H and D-He^3 plasmas is higher in the Q-case than in the M-case at the same power [$\dot{\beta}Q/\dot{\beta}M \simeq 1.2 - 2.0$] while $\Delta\beta Q/\Delta\beta M \simeq 1.4$ (case c). This observation indicates that the efficiency of the Q-antenna is greater than the M-antenna.

Conclusions

The RF power deposition profile on the electrons is strongly peaked on JET and appears to be affected both by the localisation of the minority cyclotron resonance layer and the value of the $k_{//}$ spectrum of the antenna. Further experiments, including RF amplitude modulation, will be carried out, and are currently being investigated.

Table : JET ICRF Discharges

case	min	B_T(T)	ν(MHz)	R_{CH}(m)	I_p(MA)	V_L(V)	$T_{eo\Omega}$(keV)	$T_{io\Omega}$(keV)
a	He^3	3.4	33	3.23	2.8	0.7	4	2.2
b	H 5%	2.3	33	3.28	2.0	0.8	2	1.7-1.8
c	H 5%	2.0	29	3.24	2.0	0.75	1.8	1.8

References: [1] J. Jacquinot et al., invited paper, this conference.
[2] M. Brambilla, IPP JET rep. 22 Garching 1984.
[3] B.J.D. Tubbing et al., paper 142, this conference.
[4] A.E. Costley et al, paper 186, this conference.
[5] D.J. Campbell et al, paper 182, this conference.
[6] D.J. Gambier, Thèse d'état 1985.
[7] P.P. Lallia, private communication.

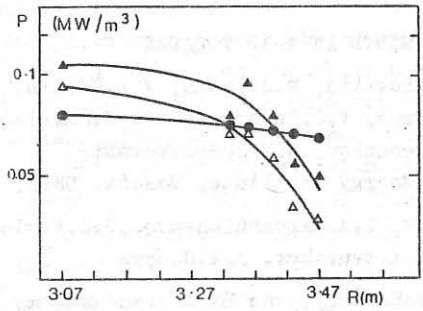


Fig.1. Power deposition profile on electrons

D–He³ P_{RF} = 2·4 MW

- ● ohmic
- △ slope subtraction
- ▲ $\bar{z}_{st}$ = const

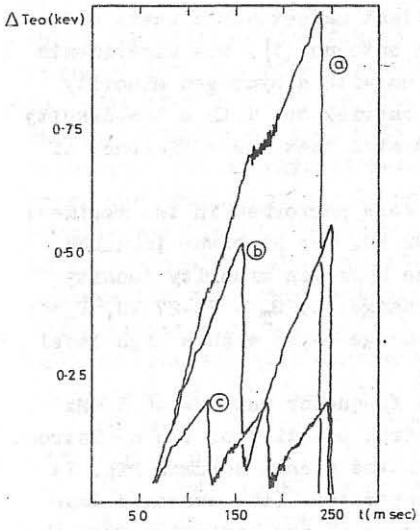


Fig. 2 : Sawtooth evolution vs. time (P_{RF} = 1 MW)
a- B_T = 2.3T (R_{CH} = 3.3 m)
b- B_T = 2.45T (R_{CH} = 3.5 m)
c- B_T = 2.6T (R_{CH} = 3.7 m).

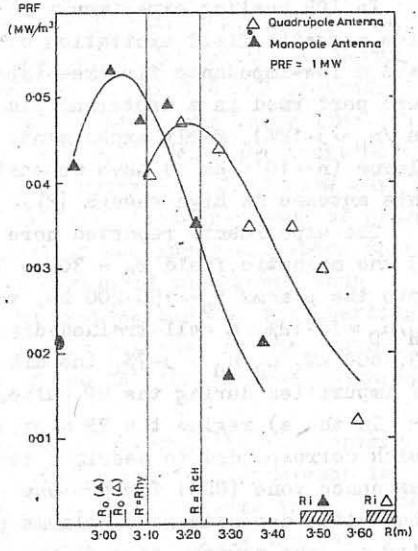


Fig. 3 : Power deposition profile for two $k_{//}$-spectrum [$k_{//}$ centred on 0 m^{-1} (▲) and 7m^{-1} (△)]

ICRH EXPERIMENTS IN T-10 TOKAMAK

V.V.Alikaev, E.L.Berezovskij, N.A.Vasin, V.L.Vdovin, A.N.Vertiporokh, S.L.Efremov, V.S.Zaveryaev, Yu.S.Maksimov, G.E.Notkin, A.V.Chesnokov, N.V.Shapotkovskij
I.V.Kurchatov Atomic Energy Institute, Moscow, USSR,

E.D.Kramskoj, A.V.Longinov, G.A.Miroshnichenko, S.S.Pavlov, K.N.Stepanov, V.A.Tsurikov, A.A.Chmyga
Institute of Physics and Technology, the Ukrainian Academy of Sciences, Kharkov 310108, USSR

In ICR heating experiments in the T-10 tokamak with the low-side magnetic field excitation of fast magnetosonic waves we used a low-impedance fir-tree-type antenna [1]. The experiments were performed in a deuterium plasma with a hydrogen minority ($n_H/n_D \sim 3$-12%). Early experiments carried out with a low-density plasma ($\bar{n} \sim 10^{13}$ cm^{-3}) have demonstrated that the efficiency of this antenna is high enough [2].

The experiments reported here were performed in two regimes: a) the magnetic field B_T = 30 to 32 kG, the RF power launched into the plasma $P_p \sim 150$-200 kW, the hydrogen minority density n_H/n_D = 10-12%, a well-trained discharge; b) B_T = 23-27 kG, $P_p \sim$ 150-600 kW, n_H/n_D = 3-7%, the discharge being with a high level of impurities during the RF pulse.

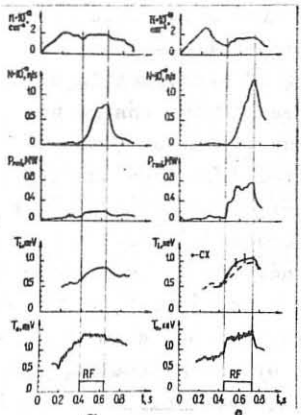
In the a) regime the RF source frequency was f = 46.5 MHz which corresponded to nearly a central position of the cyclotron resonance zone (CRZ) for protons in the plasma column. Fig. 1a shows time dependences of plasma parameters (the averaged density n_e, the neutron flux N, the power of the radiation from the plasma P_{rad}, the plasma temperature $T_i(0)$ and $T_e(0)$) for a typical discharge in this regime at P_p = 200 kW. The characteristic property here is a rather low level of the increase of the radiation losses ($\Delta P_{rad}/P_p \sim 0.5$). In such regimes the ion heating efficiency ($\eta_i = \bar{n} \cdot \Delta T_i(0)/P_p$) was about 4.5 eV/kW.

More detailed studies were made in the b) regime (fig. 1b).

This regime is characterized by an appreciable increase of the radiation from the plasma and by some loop voltage increase. Besides the heating of ions, the heating of electrons is also essential here ($\Delta T_{iD} \leq 0.5$ keV as measured by the charge exchange (solid curve) and the neutron flux technique (dashed curve), $\Delta T_e \leq 0.5$ keV). The ions are heated even when the CRZ for protons is shifted to the plasma periphery (see fig. 2a which shows ΔT_i, ΔT_e, $\eta_{i,e}$ for pulses with different B_T values or different shifts of the CRZ, ΔR_{CH}). This fact may be attributed to an RF power absorption by heavy impurity ions [3]. Fig. 3 presents the results of the calculations for the pulse at ΔR_{CH} = 25.5 cm illustrating the possibility of efficient heating due to the slow wave - heavy ion minority interaction. Here, the RF field components $E_Z(R)$ and $E_R(R)$, the specific powers absorbed by ions D_i and electrons D_e, and the RF power flux, P(R), are shown. As is seen from fig. 3, only about 30% of the RF power launched into the plasma is absorbed in the CRZ for protons. The rest of the energy is absorbed by admixture heavy ions (in the calculations we took 0.3% C^{V} and 0.1% Fe^{XXII} as heavy admixtures). The energy absorption by heavy ion admixtures may cause the heating of electrons as well. Another reason of plasma heating may lie in the development of nonlinear processes due to a high proton velocity in the region of the plasma wave propagation which may probably be responsible for the characteristic property of the $T_{i,H}(R)$ profile obtained in the regime with an essential displacement of the CRZ for protons outwards (ΔR_{CH} = + 12 cm) (fig. 2b).

The recent experiments have been performed in the regimes with higher powers (the RF power delivered to the antenna is $P_{a\,max} \simeq 900$ kW, the RF power launched to the plasma is $P_{p\,max} \simeq$ 700 kW) for a programmed RF power increase during the pulse. In the regimes with B_T = 28.6 kG, I_p = 312 kA, $Z_{eff} \simeq 2$, $\bar{n}$ = $2 \cdot 10^{13}$ cm^{-3}, $n_H/n_D \simeq 5$-7%, $\bar{P}_p \simeq 500$ kW, the deuterium temperature determined from the neutron flux measurements was T_D = 1350 eV (fig. 4a, $\Delta T_D(0) \sim 800$ eV).

Test experiments were made to clarify the possibility of increasing the efficiency of heating by adding heavy ion admixtures into the plasma thus ensuring the absorption of a small-



a б

Fig.1.

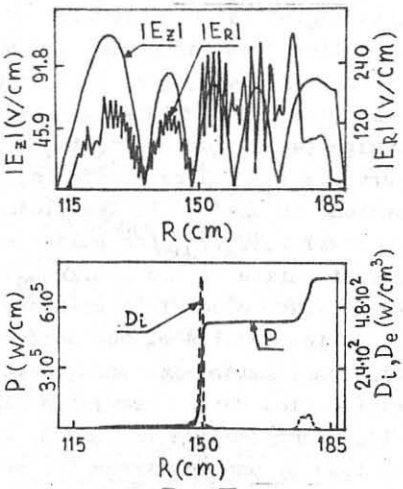
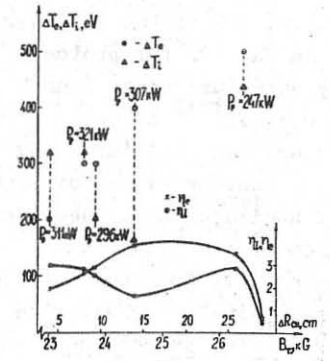
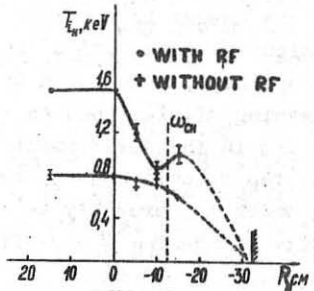


Fig.3.

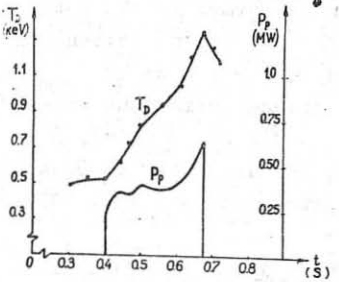


a

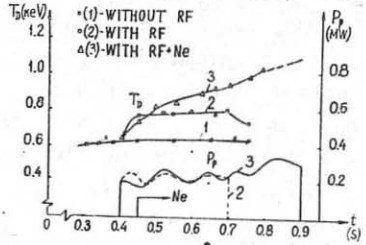


б

Fig.2.



a



б

Fig.4.

scale plasma wave [3]. As a minority heavy species we used the Ne^{22} isotope which was admitted during the RF pulse in 50-80 ms after switching on the RF pulse. Fig. 4b shows the time dependences of T_D and P_p for three pulses having the same initial parameters (B_T = 28.3 kG, n_H/n_D = 3-5%, $n'/n_D \sim 0.1\%$, I_p = 400kA, $\bar{n}_e = 4 \cdot 10^{13}$ cm^{-3}, ΔR_{CH} = + 3 cm). As is seen from fig. 4b, the heating efficiency for deuterons with neon injection (curves 3) is essentially higher than without the injection (curves 2) and progressively increases with the Ne^{22} concentration in the discharge ($\eta_i > 7$), though the heating conditions are not optimum because of the appreciable displacement of the CRZ for Ne^{22} relative to the plasma centre ($\Delta R_{CNe^{22}} = -12$ cm). A similar effect of an enhanced heating is also observed in the high-density regime ($\bar{n}_e = 6 \cdot 10^{13}$ cm^{-3}, $\bar{P}_p$ = 270 kW, $\Delta T_D \geqslant 300$ eV, $\eta_i > 6.5$).

The experiments presented lead us to the following conclusions:

1) the value of the increment $\Delta T_i = 0.85$keV at $\bar{P}_p$ = 500 kW and $\bar{n}_e = 2 \cdot 10^{13}$ cm^{-3} has been obtained;

2) regimes (inparticular, b) regime) have been found for heating both deuterium and electrons ($\Delta T_D \sim \Delta T_e \sim 0.5$ keV at $\bar{n}_e \sim 2 \cdot 10^{13}$ cm^{-3} and $P_p \leqslant 300$ kW) with a high efficiency $\eta \sim 4$-5 eV/kW (a high efficiency of heating in this regime may be attributed to the presence of highly-ionized heavy impurity ions);

3) the Ne^{22} minority admixture increases the efficiency of heating η_i and the magnitude of ΔT_i at the same P_p values.

References

1. A.V. Longinov et al. In: II Vsesoyuznaya konferentsiya po inzhenernym problemam termoyadernykh reaktorov (Leningrad, 23-25 June, 1981) v.1, p.381.
2. A.V. Longinov et al. In: Tenth European Conference on Contr. Fusion and Plasma Physics (Moscow, 14-19 September, 1981) v. 2, H-25, p.163.
3. A.V. Longinov, K.N. Stepanov. In: Vysokochastotnyj nagrev plazmy (Institute of Applied Physics, USSR Academy of Sciences, Gorkij, 1983) p.105.

ICRF HEATING EXPERIMENTS ON T–10 TOKAMAK AT THE ION–ION HYBRID RESONANCE CONDITIONS

V.V. Alikaev, A.A. Bagdasarov, E.L. Berezovsky, V.V. Buzankin, N.A. Vasin, V.L. Vdovin, A.N. Vertiporokh, N.M. Gegechkory, A.V. Gorshkov, E.P. Gorbunov, Yu.V. Esypchuk, S.L. Efremov, V.S. Zaveryaev, A.Yu. Kislov, S.Yu. Lukjanov, Yu.S. Maximov, A.A. Medvedev, G.E. Notkin, A.B. Pimenov, V.A. Rantzev–Kartinov, M.M. Stepanenko, V.S. Strelkov, V.M. Trukhin, N.V. Shapotkovskij, D.A. Scheglov

I.V. KURCHATOV INSTITUTE OF ATOMIC ENERGY, MOSCOW, USSR

E.D. Kramskoij, A.V. Longinov, G,A, Miroshnichenko, K.N. Stepanov, A.A. Chmyga

KHARKOV PHYSICO–TECHNICAL INSTITUTE, USSR

The experiments on ICRF plasma heating on T–10 tokamak with practically full loop antenna has been performed for a regime of launching fast waves from inside of the torus. The antenna has double electrostatic screen (with slots along total magnetic field $B=\sqrt{B_0^2+B_\varphi^2}$) and lateral carbon protectors. Up to 500 kW of RF power was injected by half of that antenna into plasma at the frequency f=42 MHz ($\omega \sim \omega_{CH}$).

1. The experiments at two ion hybrid resonance conditions in hydrogen–deuterium plasma were performed in the regime: $n_{eo}=7–8\cdot10^{13}cm^{-3}$, $n_h/n_d=12–15\%$, $B_o=30{,}4$ kGs, I=310 kA, $T_{eo}=900$ eV, $U_l=1.5$ V, $Z_{eff}=1.3–1.5$, $\tau_{rf}=0.15–0.2$ sec, $P_{rf}=350–450$ kW. The radial profiles of $T_e(r)$ ($T_e(2\omega)$, laser and PHA) before and after of RF pulse are shown on fig. 1. The temperature increments are: $\Delta T_e(0)=300$ eV, $\Delta T_d=100–150$ eV. The loop voltage decreases from 1.5 to 1 V, the plasma density rises to 10–15%. The temperature increment $\Delta T_e(0)$ is proportional to RF power (fig. 2) with the efficiency 4.5–5 eV/kW$\cdot10^{13}cm^{-3}$. The time evolution of T_e (fig.3) discovers the constant power deposition to electrons at plasma center (constant rising slope of the sawteeth) and stationary sustainment of the temperature rise up to $\tau_{rf}=0.3$ sec. The RF power deposition profile to electrons $P_e(r)$ ($P_e(r)=1.5n_e(r)\frac{dT_e(r)}{dt}_{t=t_e}$) is given on fig.4. At the plasma center $P_e(0)\sim1$ W/cm^3 and it is to 1.5–2 times larger than that inohmic regime. The deposition into ions is significantly lower (0.05 W/cm^3) as predicted from wave conversion theory [2,3]. The plasma radiation profiles (fig.5, bolometric measurements) show that emission in such regime arises mainly from plasma periphery. Total radiation losses from the plasma center (~0.05 W/cm^3) are unimportant in the power balance. The total (ΔP_R) and local (P_R) radiations increase with decreasing of n_h/n_d (fig.5). The ratio of line bolometer signal P_{ant} near of the antenna to that displaced over 90° along the torus P_w is tended to unit as n_h/n_d is decreased – in agreement with fast wave attenuation decreasing.

In the table 1 the powers and total thermal energies are given. It is seen the global confinment time τ_E during RF does not change significantly (τ_E^* takes into account the radiation losses). The electron central transport time τ_{Ee} (table 2) is decreased during RF by ~ 20% in regime under consideration.

2. The experiments with hydrogen minority were performed in the regime: $\bar{n}_e=2.5–3\cdot10^{13}cm^{-3}$, $B_o=29$ kGs, I=300 kA, q=3, $T_{eo}=1200$ eV, $T_{io}=600$ eV, $U_l=1.2$ V, $Z_{eff}=1.5$, $n_h/n_d=2–4\%$ $P_{rf}\leq400$ kW, $\tau_{rf}=0.15–0.2$ sec. After RF switching on the energetic tail to distribution function of protons is created (fig.6, CX measurements and theory) with $T_{eff}\simeq1.75$ keV, the deuteron temperature rises from 600 to 900 eV (fig.7), its radial profiles on fig.8 are given. Also density $\bar{n}_e$ rises from 2.5 to $3.5\cdot10^{13}cm^{-3}$

at the end of RF pulse.

Table 1

Time	t=370 ms	t=490 ms
P_{oh}, kW	450	300
P_{rf}, kW	0	350
$P_{2\omega_{ce}}$, kW	–	300
W_e+W_i, kJ	22	34
τ_E, msec	49	52
τ_E^*, msec	57	69

Table 2

Time	t=370 ms	t=490 ms
$\frac{3}{2}n_e(0)T(0)$, J/cm^3	1.51 10^{-2}	2.3 10^{-2}
Z_{eff}	1.3	1.3
P_{oh}, W/cm^3	0.64	0.43
P_{rf},	–	0.6
P_{ei},	0.6	0.6
P_{rad},	0.01	0.06
τ_{Ee}, msec	75	62

Power deposition into deuterons during RF ($P_d=1.5n_e(0)\frac{dT_N(o)}{dt}$) was $\simeq 0.12$ W/cm^3. The ion heating efficiency in the regime is 3 eV/kW$\cdot 10^{13}$cm^{-3}, as on $PLT[1]$. $^{t=t_o}$ The part of RF power ($\simeq 0.3$ W/cm^3) again deposits into electrons ($\Delta T_e \sim 150$ eV), but after ~ 50 msec of RF start T_e recovers to ohmic level. It may be partly connected with increased radiation losses from plasma center (fig.5, left curves) $P_R(0) \simeq 0.3$ W/cm^3. For a comparison with experiment 2–dimensional Fokker–Plank equation with specific 0.25 W/cm^3 RF power and T–10 ripple $\delta=0.01$ has been numerically solved. The results well agree with experiments (table 3):

Table 3

P^p_{rf}, W/cm^3	P_d	P^p_e	P^p_{ripple}	P^p_{cx}	P_d–exper	n_h/n_d
0.25	0.135	0.05	0.025	0.04	0.12	4%

Here P_d, P^p_e, P^p_{ripl}, P^p_{cx} are respectively powers to deuterons, electrons, ripple losses, CX–losses, W/cm^3. The experiments with intermediate hydrogen percentage 6–8% in deuterium plasma were conducted in the regime: $\bar{n}_e=3\cdot 10^{13}$cm^{-3}, $B_o=28.8$ kGs, I=310 kA, $q\simeq 3$, $U_l=1.5$ V, $T_{eo}\simeq 1200$ eV, $T_{io}\simeq 600$ eV, $Z_{eff}=1.5$, $P_{rf}\simeq 400$–500 kW, $\tau_{rf}=0.2$ sec. The soft RF start was provided. The neutron flux was raised by factor 35. The density n_e rised from $3.1\div 4.1\cdot 10^{13}$cm^{-3} at the stationary stage. The new result was the electron heating with $\Delta T_e \simeq 300$ eV (fig.9). The plasma radiation was approximatly doubled. The rise of deuteron temperature (fig.10) was $\simeq 350$ eV. The heating efficiency is $(\Delta T_e+\Delta T_i)\bar{n}/P_{rf} \simeq 6$ eV/kW $\cdot 10^{13}$cm^{-3}.

REFERENCES

1. J. Hosea et al, 3d International Symposium on Plasma Heating in Toroidal Syst. (Grenoble, 82), Vol. I, p. 213
2. J. Adam, Equipe TFR, 4th Intern. Symposium on Plasma Heating in Toroidal Syst. (Roma, 84), Vol. I, p. 277
3. JFT–2 Group, 3d International Symposium on Plasma Heating in Toroidal Syst. (Grenoble, 82) Vol. I, p. 259

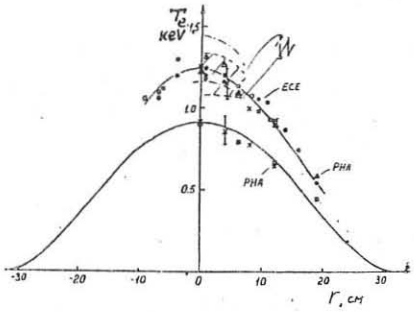


Fig. 1

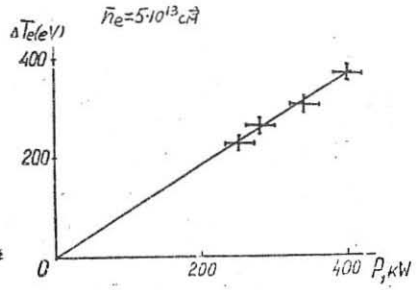


Fig. 2

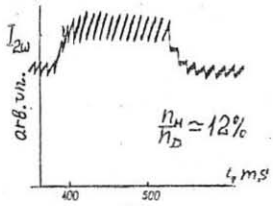


Fig. 3a

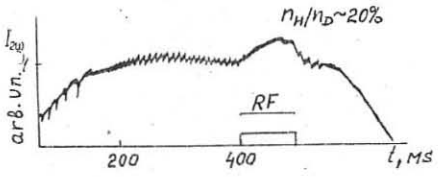


Fig. 3b

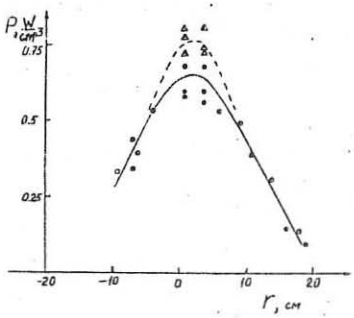


Fig. 4

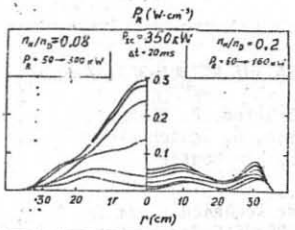


Fig. 5a

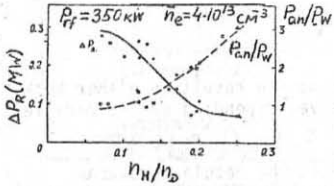


Fig. 5b

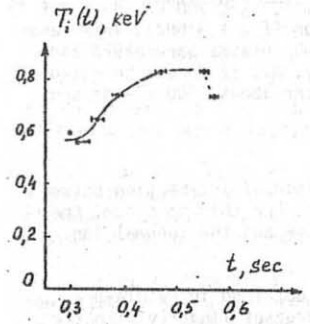


Fig. 7

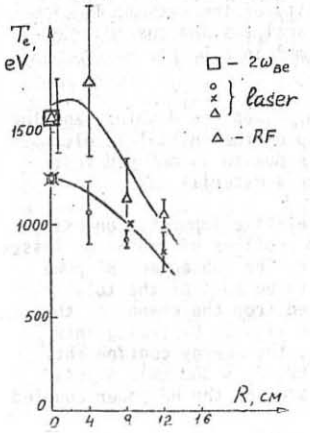


Fig. 9

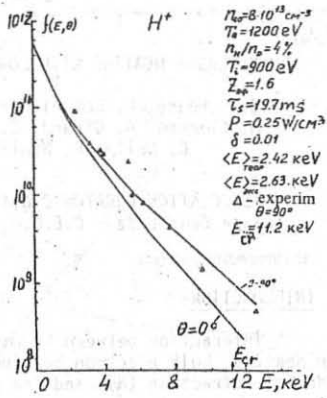


Fig. 6

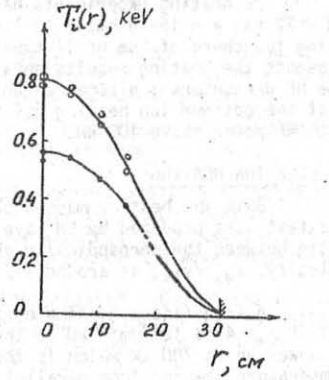


Fig. 8

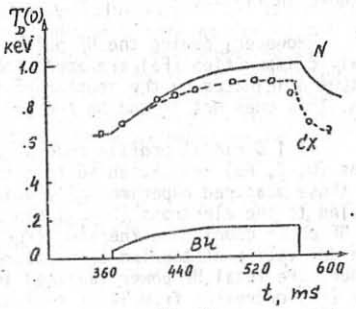


Fig. 10

BULK PLASMA HEATING WITH LOWER HYBRID WAVES IN THE PETULA-B TOKAMAK

G.T. Hoang, H. Bottollier, P. Briand, G. Briffod, P. Chabert, M. Clement, A. Girard, C. Gormezano, W. Hess, G. Ichtchenko, G. Melin, B. Moulin, F. Parlange, D. Van Houtte

ASSOCIATION EURATOM-C.E.A. - Département de Recherches sur la Fusion Contrôlée - C.E.N.G. - 85 X - 38041 GRENOBLE Cedex (France)

1. INTRODUCTION

Interaction between LH waves and the plasma can result in either bulk ion heating, bulk electron heating or current drive, depending on the parallel index of refraction ($N_{//}$) and the plasma parameters.

LH heating experiments have been studied in the Petula-B tokamak ($R = 72$ cm, $a = 16$-18 cm, $6.10^{12}cm^{-3} \leqslant n_e \leqslant 10^{14}cm^{-3}$, $I_p \leqslant 200$ kA, $B_T \leqslant 2.8$ T) using launchers of the grill type fed by a klystron ($f = 1.3$ GHz). This paper presents the heating results obtained in varying the plasma parameters and the HF parameters : plasma current, plasma density, $N_{//}$. It should be noted that the optimum ion heating has been obtained after about 1000 plasma shots with HF power above 100 kW.

2. BULK ION HEATING

Bulk ion heating may be obtained via collisional interaction between the fast ions produced by LH wave and thermal ions. For this to occur, the ratio between the perpendicular velocity of the wave and the thermal ion velocity, $v_{\varphi\perp}/v_{ti}$, is around 3 /1/.

A significant heating efficiency has been obtained in Petula-B : $\bar{n}\Delta T_i/P_{HF} \sim 4$ eV $10^{13}cm^{-3}$ kW^{-1}. The ion heating increases linearly with the HF power up to 700 kW which is the maximum capability of the system. The ion temperature deduced from parallel charge exchange analysis and the neutron flux rises from .45 keV to .9 keV at $\bar{n}_e \sim 6.10^{13}$ cm^{-3} in a D_2 plasma ($N_{//} \sim 5$), as shown in fig. 1.

However, during the HF pulse the radiation losses are doubled, and the metallic impurities (Fe) are approximately 200 % up on the initial level, most of them originated by the sputtering from the walls due to unconfined fast ions. This does not depend on the grill and limiter's material /2/.

A 1 D radial profile code is used, where relative impurity concentrations (O, C, Fe) are chosen so that the calculated profiles of radiation losses fit those measured experimentally using a bolometer. The subsequent HF power coupled to the electrons ($P_{HF,e}$) can be estimated to be 15 % of the total. The HF power coupled to the ions ($P_{HF,i}$), calculated from the change in the time derivative of the ion temperature, is shown in fig. 2. By taking into account the total HF power launched into the torus, the energy confinement time (τ_E) decreases from 11 ms to 4 ms ($P_{HF} = 700$ kW, $P_\Omega \sim 300$ kW). A less pessimistic estimation is obtained by taking into account the HF power coupled

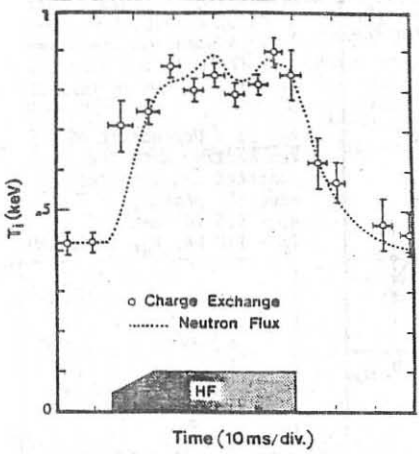


Fig. 1 : Time variation of the ion temperature.

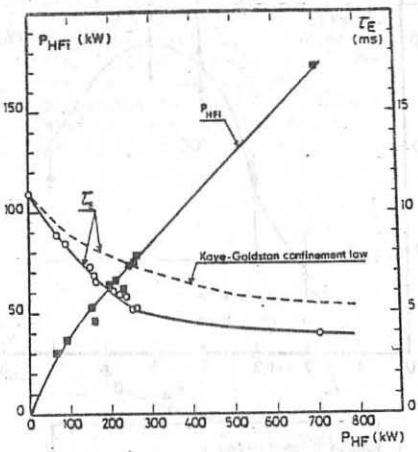


Fig. 2 : HF power coupled to the ions and energy confinement time versus HF power.

to the plasma. In this case ($P_{HF,e} + P_{HF,i} \sim 260$ kW), there is a good agreement with the Kaye-Goldston confinement time /3/, as shown in fig. 2.

The efficiency of ion heating augments approximately by a factor of 4 when the current rises from 100 to 150 kA. Above 150 kA, the heating efficiency saturates. This can be explained by a change in the scrape-off plasma parameters (increase of T_e), which may influence the wave propagation.

The dependence of ion heating with the parallel index of the wave has been studied using different phase arrangements in the two grills installed in Petula-B (4 and 8 wave guide grills with $N_{//}$'s for $\Delta\phi = \pi$ of 5 and 9, respectively). Fig. 3 shows that efficiency increases with parallel index up to $N_{//} = 5$. However, the heating efficiency calculated with the effective HF power (i.e. the power in the main lobe of the $N_{//}$ spectrum) is approximately constant for $N_{//} = 4$-7 (Table I). For higher $N_{//}$ values ($N_{//} > 7$), ion heating decreases, presumably because the wave does not penetrate as far as the plasma center. Indeed, an efficient heating may be only obtained when the wave penetrates to the central part of the plasma with a $N_\perp$ value high enough. The warm plasma dispersion relation predicts $N_\perp$ of 600 in the plasma center for $N_{//} = 7$-9. The coupling of the wave in the plasma periphery is confirmed by the appearance of fast ions observed by parallel charge exchange analysis. Therefore an anomalous propagation of the wave takes place for $N_{//} > 7$.

As shown in fig. 4, above $\bar{n}_e = 6.10^{13}$cm^{-3} the efficiency decreases. Once again, an anomalous propagation of the wave takes place for $\bar{n}_e > 6.10^{13}$cm^{-3}. For $\bar{n}_e \leqslant 5.10^{13}$cm^{-3} the energy transfer to the bulk ions is reduced. It seems as though the density limits do not depend on the value of $N_{//}$. This contradicts the ray tracing calculations /4/.

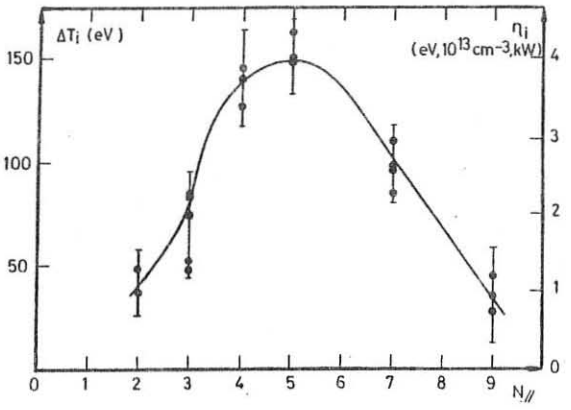
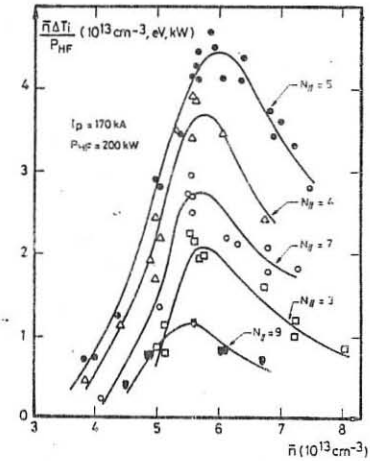


Fig. 3 : Dependence of ion heating with the parallel index of the wave (D_2 plasma, $n_e \sim 5.5\ 10^{13} cm^{-3}$, I_p = 170 kA, P_{HF} = 200 kW).



$N_{//}$	$P_{effective}/P_{HF}$	$n\Delta T_i/P_{eff}$ (10^{13} cm³eV./kW)
2	.52	2.5
3	.56	3
4	.54	7
5	.58	7
7	.44	6.4
9	.63	2

TABLE I

Fig. 4 : Ion Heating efficiency versus density for various $N_{//}$ values.

3. BULK ELECTRON HEATING

Landau damping theory indicates that bulk electron heating may be expected to occur when the ratio of the parallel phase velocity of the wave to the thermal electron velocity, $v_{\varphi //}/v_{te}$, is also around 3 (i.e. $N_{//} \geqslant 6.4\ Te^{-1/2}$ (keV)).

Therefore, since the electron temperature in Petula-B is about 1-1.2 keV, electron heating can be obtained with $N_{//} > 6$. In fact, no significant electron heating has been observed even with $N_{//} = 9$ for which $v_{\varphi//}/v_{te} \sim 2.5$

is expected. A weak increase of Te at the start of the HF is offset by a rapid increase of metallic impurities (fig. 5). For $n_e > 4.10^{13}$ cm^{-3} the electron temperature is often observed, after HF start-up, to increase slightly for about 15 ms and decrease continuously from thereon. From Thomson scattering measurements an increase of about 150 eV is observed for $\bar{n}_e \sim 10^{13}$cm^{-3} (fig. 6), where a fast electron population exists /5/. With a low value of $N_{//}$ ($N_{//} \sim 2$), bulk electron heating has been obtained for $\bar{n}_e \sim 8\ 10^{12}$cm^{-3}. The electron temperature rises by about 300 eV.

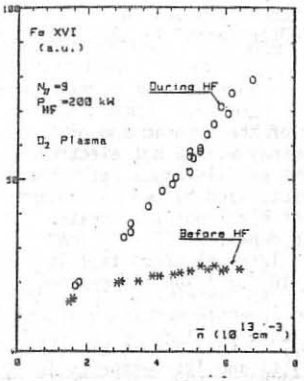


Fig. 5 : Variation of the metallic impurities versus density (carbon limiter, I_p=170 kA).

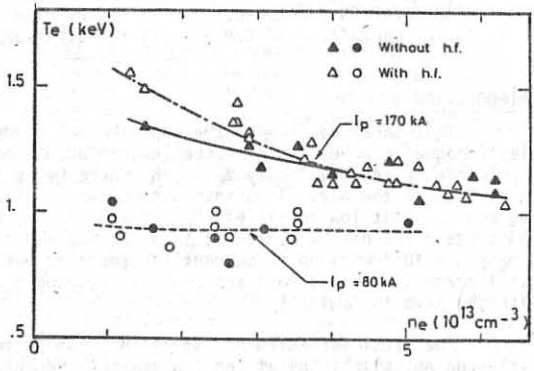


Fig. 6 : Variation of the central electron temperature with density ($N_{//}$ = 9, $P_{HF} \sim 200$ kW).

4. CONCLUSIONS

Efficient bulk ion heating may be obtained when the wave penetrates to the plasma center ($n\Delta T_i/P_{HF} \sim 4$ eV 10^{13}cm^{-3} kW^{-1}). Heating efficiency is enhanced when the plasma current is increased. Ion heating is reduced for high value of $N_{//}$ ($N_{//} > 7$) and for high plasma densities ($\bar{n}_e > 6\ 10^{13}$cm^{-3}), owing to the fact that the wave does not penetrate to the central part of the plasma.

No direct bulk electron heating via electron Landau damping is obtained. An electron heating is only obtained for low densities $\bar{n}_e \leqslant 10^{13}$cm^{-3} ($\Delta T_e \sim 300$ eV for $P_{HF} \sim 200$ kW and a progressive wave which $N_{//} \sim 2$).

REFERENCES

/1/ KARNEY, C.F.F., Phys. FLuids 22 (1979) 2188.
/2/ VAN HOUTTE, D., et al., 4th Int. Symp. Heat. Tor. Plasmas, Roma (1984).
/3/ KAYE, S.M., GOLDSTON, R.J., Nucl. Fusion, Vol. 25, N° 1 (1985).
/4/ GORMEZANO, C., et al., 3rd Int. Symp. Heat. Tor. Plasmas, Grenoble (1982).
/5/ GIRARD, A., et al., this conference (1985).

HOT ELECTRON STUDIES IN PETULA-B DISCHARGES DURING LH WAVE APPLICATION

A. Girard, G. Melin, G. Agarici, P. Blanc, H. Bottollier, P. Briand, G. Briffod, P. Chabert, M. Clement, C. Gormezano, P. Grelot, W. Hess, G.T. Hoang, G. Ichtchenko, B. Moulin, A. Panzarella, F. Parlange, J.C. Vallet, D. Van Houtte

ASSOCIATION EURATOM-C.E.A. - Département de Recherches sur la Fusion Contrôlée - C.E.N.G. - 85 X - 38041 GRENOBLE Cedex (France)

INTRODUCTION

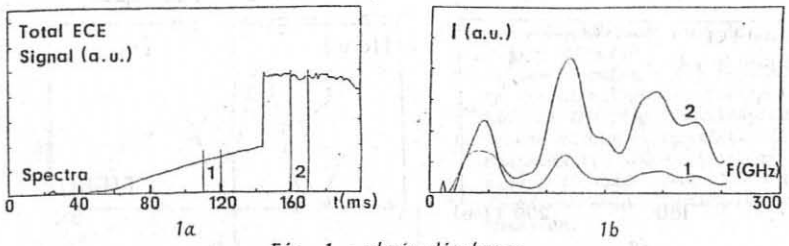
This paper deals with the experimental study of the interaction of electromagnetic waves close to the lower-hybrid frequency with a hot electron population having a velocity $V_e \simeq C/N_{//}$, where $N_{//}$ is the parallel index of refraction of the wave. This interaction can be characterized by two distinct regimes : (i) at low densities ($\bar{n}_e \lesssim 2 \times 10^{13} cm^{-3}$) hot electrons are created and sustain the plasma current ; (ii) at intermediate densities ($2 \times 10^{13} cm^{-3} \lesssim \bar{n}_e \lesssim 5 \times 10^{13} cm^{-3}$) no HF current is generated but a large electron tail is still present and fast ions are observed. Beyond $5 \times 10^{13} cm^{-3}$ ion interaction with the wave is dominant.

The total far-infrared radiation (from 30 to 1000 GHz) due to electron cyclotron emission (ECE) at the fundamental frequency ω_c and its harmonics is measured by a liquid helium cooled InSb detector via a wedged quartz window and an oversized waveguide. ECE spectra are given by a two grid polarization Michelson interferometer /1/.

1. LOW-DENSITY REGIME $\bar{n}_e \lesssim 2 \times 10^{13} cm^{-3}$

(i) ohmic discharges (no HF) : in this range of densities ECE signals generally show runaway electrons : total ECE signal is about ten times greater than for thermal shots i.e. without decoupled electrons. Moreover, the plasma can sometimes spontaneously evoluate to a different state via an instability, with the total ECE signal rising suddenly (fig. 1a) and an almost simultaneous drop in loop voltage therein. ECE spectra before and after this transition are very different (fig. 1b) : in the first state radiation at the fundamental is higher than in the second state, thus suggesting a strong modification of the pitch angle in the electron distribution. Moreover, second state spectra are very similar to current drive spectra.

(ii) Current-drive discharges : as previously reported /2//3/ the total integrated ECE signal increases after the HF pulse is turned on and reaches a level of about fifty times the thermal one (fig. 2a). When the HF power is turned off a spike or burst is always observed on the ECE signal, due to a very fast change in the parallel and perpendicular momenta of the electrons in the tail. This burst, which has also been observed on other LH-current drive experiments, has yet to be fully understood. Classical superthermal spectra are obtained (fig. 2b), emission being displaced towards lower frequencies and higher harmonics being enhanced. We concentrated our attention on the second harmonic emission in the range 100-200 GHz ($\omega_c \simeq 75$ GHz). The



1a 1b

Fig. 1 : ohmic discharge
1a) total integrated ECE signal 1b) corresponding spectra

maximum intensity (at about 120 GHz) is, in fact, greatly enhanced by reflections from the walls of the vacuum vessel. In addition, superthermal emission at higher frequencies (between 120 and 200 GHz) is strongly absorbed by the thermal layer at 2 ω_c. In order to derive the intensity of superthermal emission ($I_{ST}(\omega)$), thermal absorption and reflections are taken into account via the second harmonic X-mode optical depth ($\tau_2(\omega)$) and a reflection coefficient, R. The detected intensity, $I(\omega)$, is a function of $I_{ST}(\omega)$, $\tau_2(\omega)$ and R :

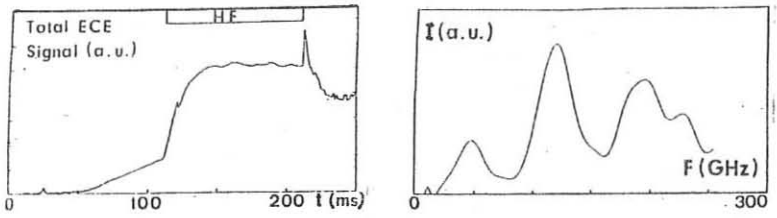
$$I(\omega) \cong I_{ST}(\omega) \frac{e^{-\tau_2(\omega)}}{1 - Re^{-\tau_2(\omega)}}$$

where thermal emission is neglected. Such a derivation shows (fig. 3) that the strongest superthermal emission takes place at about 2 ω_c, but the slight frequency downshift of this maximum cannot be rigorously used to calculate the factor $\gamma = (1 - v^2/c^2)^{-1/2}$ of the corresponding superthermal electrons, due to assumptions made on temperature and density profiles in order to calculate $\tau_2(\omega)$. However this method does show that both mildly ($\sim$ 20 keV) and highly ($\gtrsim$ 100 keV) superthermal electrons are excited by the waves. In order to have a better estimation of the parallel energy of fast electrons a periscope-type antenna has been installed to measure ECE at different angles of sight with respect to the toroidal magnetic field. Doppler-shifted emission should be observed according to parallel impulsion ($p_{//}$) of fast electrons at a frequency $\omega = 2\,\omega_c\,(1 - \frac{p_{//}\cos\theta}{\gamma mc})^{-1}/\gamma$. Preliminary studies have shown slight differences in spectra which still need to be better analyzed.

2. INTERMEDIATE DENSITY REGIME ($2 \times 10^{13}\text{cm}^{-3} \lesssim \bar{n}_e \lesssim 5 \times 10^{13}\text{cm}^{-3}$)

(i) ohmic discharges : in this range of densities ECE signals show there are no runaway electrons so that the second harmonic emission may, in fact, be used to give electron temperature profiles.

(ii) After HF application: the total ECE signal increases, but it saturates at a level lower than that of the first regime, while the loop voltage hardly decays. Fig. 4 shows the dependence of the ECE signal on the density when HF is turned on : fast electrons are still observed ; ECE spectra look similar to those of the first regime. Temperature profiles are modified so much by superthermal emission (Fig. 5) that it is no longer possible to differentiate between a rise in T_e at the center of the plasma or an overlapping of third harmonic superthermal emission. Anyway the change in intensity at the center is so small that it confirms the absence of electron bulk heating at these densities as reported by Thomson scattering /4//5/.



2a 2b

Fig. 2 : Current-drive discharge (P_{HF} = 220 kW)
a) total integrated ECE signal
b) spectrum during HF pulse.

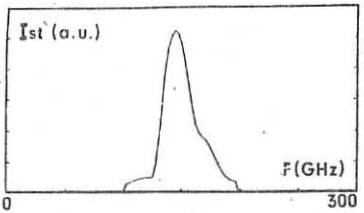


Fig. 3 : Electron cyclotron superthermal emission $I_{ST}(\omega)$ deduced from fig. 2b (same scales) $\bar{n}_e = 9 \times 10^{12} cm^{-3}$, $T_e = 1$ keV, $R = 0,9$.

CONCLUSION

Measurements of ECE radiation signify the presence of a hot electron population during LH wave launching. At low densities analysis of the data shows that the HF current may be driven by an electron distribution with both mildly and highly superthermal electrons whilst for intermediate densities a high energy tail is still excited without any current drive or electron bulk heating.

REFERENCES

/1/ HOW, J.A., and WHITBOURN, L.B., Int. J. Infr. Mill. W., 4, 335 (1983).

/2/ HOW, J.A., MELIN, G., GIRARD, A., Proc. 4th Int. Work. ECE and ECRH, 173 (1984).

/3/ MELIN, G., et al., Proc. 4th Int. Symp. Heat. Tor. Plasm., Vol. I, 628 (1984).

/4/ GORMEZANO, C., et al., 6th Top. Conf. R.F. Plasm. Heat., Pine Mountain (Georgia), paper IT 3 (1985).

/5/ PARLANGE, F., et al., this conference (1985).

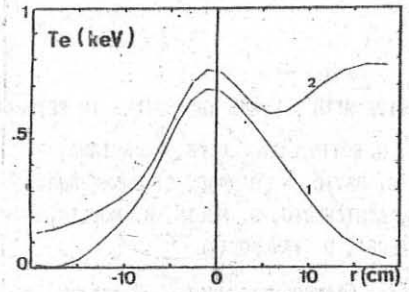


Fig. 4 : Temperature profiles
1) Before HF pulse
2) During HF pulse : the increase in the signal on the low field side of the plasma corresponds to second harmonic superthermal emission and the increase on the high-field side corresponds to third harmonic superthermal emission.

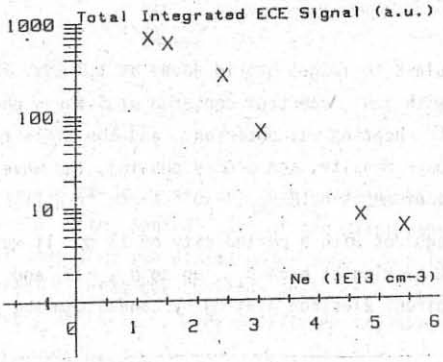


Fig. 5 : Total integrated ECE signal during HF pulse versus plasma density (Log scales). P_{HF} = 110 kW. The signal at 5,5 x $10^{13}cm^{-3}$ does not show any fast electrons and thus corresponds to thermal level.

LOWER HYBRID ION HEATING AND CURRENT DRIVE WITH ONE AND TWO GRILLS IN PETULA-B

F. PARLANGE, G. AGARICI, P. BLANC, H. BOTTOLLIER-CURTET, P. BRIAND, G. BRIFFOD, P. CHABERT, M. CLEMENT, C. DAVID, A. GIRARD, C. GORMEZANO, P. GRELOT, W. HESS, G.T. HOANG, G. ICHTCHENKO, G. MELIN, B. MOULIN, A. PANZARELLA, J.C. VALLET, D. VAN HOUTTE.

ASSOCIATION EURATOM-CEA - Grenoble, France.

---

1 - CONDITIONS FOR PLASMA HEATING. -

Two grills are used in Petula-B to launch hybrid waves at 1.3 GHz. The first one is a 4-waveguide grill with a $N_{//}$ spectrum centered at 5 for π phasing. With that grill, significant heating was observed and the efficiency is up to 4.4 10^{13} eV/kW cm^3. At lower density, and proper phasing, the wave drives an RF current with a figure of merit $n\ IR/P_{HF} \simeq 10^{15}$ kA cm^{-2}/kW [1].

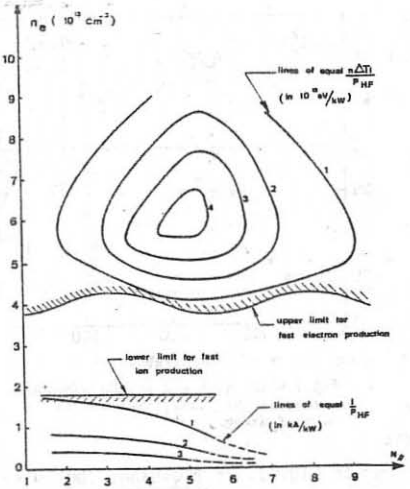
The second grill has 8 waveguides with a periodicity of 13 mm. It was designed to extend the study of LH heating at high $N_{//}$, up to $N_{//} = 9$, and particularly find conditions for direct electron heating by Landau damping at thermal velocity.

By proper phasing of one or the other grill, a large variety of $N_{//}$ spectrum can be excited with the maximum power located anywhere between 1.8 and 9.

A summary of the results obtained at different $N_{//}$ is presented in Fig. 1 in the density - $N_{//}$ plane for discharges with $B_T \simeq 2.7$ T and plasma current 130 < Ip < 170 kAmp.

Ion heating. -

Interaction with ions takes places only for densities $n_e > 1.8\ 10^{13}$ resulting in a high perpendicular energy ion tail which is detected by charge exchange diagnostic and neutron emission. Under favorable conditions : fast ion production well inside the plasma, high enough current for containement of these fast ions and high enough collision frequency, these ions can loose their energy on the bulk polulation and give true ion heating. Best conditions for it are $N_{//} \simeq 5$ and density in the 5-6 10^{13} cm^{-3} range, with an efficiency >4 10^{13} eV/kW. Lines of equal efficiency $\frac{n\ \Delta\ Ti}{P_{HF}}$ are sketched on



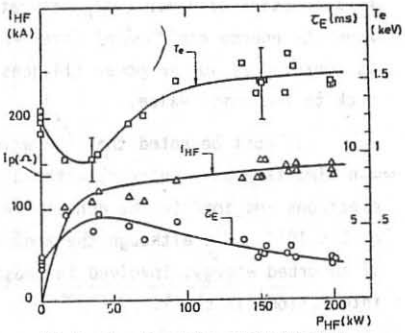


Fig.2 : I_{HF}, T_{e_0} and τ_E versus HF power (I_p = 140 kA, $\bar{n}_e$ = 9 10^{12} cm^{-3} carbon limiter)

Fig. 1 : Lines of equi n Δ T_i/P_{HF} and equi I/P_{HF} in the $N_{//}$. n_e plane (units are eV, cm, kA, kW).

Fig. 1. At densities or $N_{//}$ higher than the optimum, the waves does not penetrate in the central part of the plasma and the detected fast particules originates from the plasma outer zone. This is in contradiction with theory which predicts effective heating even at densities higher than 8 10^{13} cm^{-3}, particularly at low $N_{//}$. More details on ion heating is to be found in [2].

Electron heating. -

Interaction with electrons can lead to electron heating or current drive. Bulk electron heating through Landau damping is expected when $N_{//} \simeq 6.4/\sqrt{Te}$, i.e. $5.5 < N_{//} < 9$ for Petula plasmas.

Actually no direct heating was observed at any $N_{//}$, plasma current or density, even at $P_{HF} > 2\ P_{ohm}$ and $n_e \simeq 4\ 10^{13}$ cm^{-3} where wave absorption by ion is negligeable. Oppositely, even with that low phase velocity, the formation of a high energy electron tail is observed through a distortion of the ECE emission spectrum at densities up to 4÷ 5 10^{13} cm^{-3}. This electron tail indeed exists in that density range for any $N_{//}$ [3].

By collisions, these electrons can heat the plasma. However the efficiency of that process is quite poor in Petula. For $N_{//} = 9$, the maximum temperature increase is at most 150 eV at $n_e = 10^{13}$ cm^{-3} and this is attributed to the low confinement time. Similarly, at low values of $N_{//}$, in the current drive regime, when enough power is applied, Te can increase by 300 eV over the ohmic value, due to energy losses from current carrying electrons (Fig.2).

As a function of power , ΔT_e saturates when the energy confinement time, which is improved at low RF power [1],goes back to the ohmic value.

It must be noted that the wave can simultaneously interact with both electrons and ions in the density range 2-5 10^{13} cm^{-3}, although the amount of absorbed energy, involved in these interactions is small.

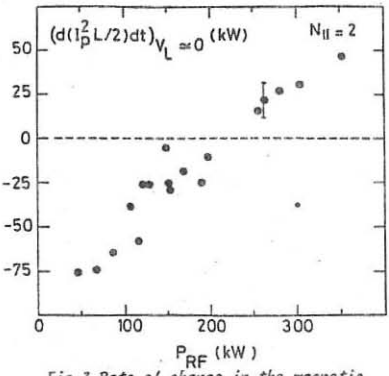


Fig.3 Rate of change in the magnetic energy of the transformer during current drive.

2 - CURRENT DRIVE STUDIES. -

At low density and low $N_{//}$, the interaction of the wave leads to current drive. Lines of equal I/P value are shown on Fig. 1. On one hand, they reflect a well documented $1/n_e$ dependance ; on the other hand the efficiency clearly increases when the spectrum is concentrated in the vicinity of $N_{//} < 2$, although $N_{//} = 9$ is quite as efficient as $N_{//} = 5$.

Effeciency $\frac{nI}{P}$ can reach 1.5 10^{13} kA/kW cm^3 at zero loop voltage. If the power is further increased and the loop voltage set to zero, the plasma current is ramped up and RF energy is converted in magnetic energy (Fig. 3). A maximum ramping rate of 250 kA/s was obtained.

MHD behaviour of a current driven discharge. -

A constant feature of current driven discharges is the triggering by the RF of an m = 2 mode, which however saturates at low level, generally well below the level corresponding to the onset of a disruption [3]. This occurs in a large variety of situation, even if the RF power is quite low and the discharge current still partially supported by ohmic heating. It has been observed when the limiter q is up to 8 (Fig. 4). In fact, if an m = 2 oscillation is already present prior to RF application, it's amplitude is damped, hence the stabilizing effect of the wave. If an m > 2 mode is present, it's structure is changed to m = 2 within a few millisecond .

Conversely, the sawtooth activity, when present, is stopped in a short time (Fig. 5). Flattening of the current profile, indicated by a decrease of the internal inductance after a short transition phase, is a general tendancy and may expell the q = 1 zone from the plasma, even at $q_a = 2.5$.

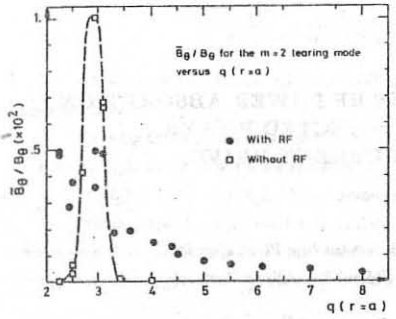


Fig. 4 - Amplitude of the m = 2 mode versus q(a)

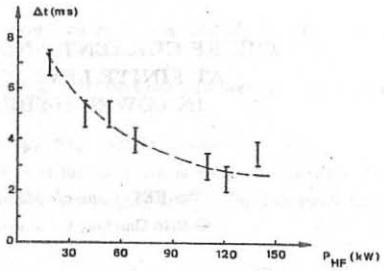


Fig. 5 - Delay between the application of RF and the end of sawtooth activity versus RF power

Association of two grills. -

The exact shape of the $N_{//}$ spectrum is supposed to play a key role in the current drive mechanism [4]. This can be studied by powering two grills with different $N_{//}$ simultaneously. Actually adding a small amount of power at $N_{//} = 5$ has a benefic effect on the efficiency of a $N_{//} = 2$ grill : the same loop voltage drop (> 90 %) can be obtained either with 72 kW on grill $N_{//} = 2$ alone or 27 kW only if 7 kW is launched at $N_{//} = 5$ simultaneously.

A possible explanation is that the high parallel index wave helps building a plateau at a higher level by interacting with a larger number of (slower) electrons.

1 - C. GORMEZANO, G. AGARICI et al. Plasma Physics and ControlledNuclear Fusion Research 1984 (Proc. 10th Int. Conf., London 1984) Vol.2 IAEA, Vienna (1985) 503.
C. GORMEZANO, P. BLANC et al. Proc. 6th Topical Conf. on Radio Frequency Plasma Heating, Pine Mountain, Georgia (USA) 1985
2 - G.T. HOANG, H.BOTTOLLIER et al., Paper 57, this conference.
3 - A. GIRARD, G. MELIN et al., paper 58, this conference
4 - S. SUCCI, K. APPERT, J. VACLAVIK, D. MOREAU Plasma Physics and Controlled Nuclear Fusion Research 1984 (Proc. 10th Int. Conf., London 1984) Vol. 2, IAEA, Vienna (1985) 549.

ON THE RF CURRENT AND THE RF POWER ABSORPTION AT FINITE LEVELS OF INJECTED POWER IN LOWER-HYBRID CURRENT DRIVE.

J-G. Wégrowe

The NET Team, c/o Max-Planck-Institut fuer Plasmaphysik,
D-8046 Garching bei Muenchen, Federal Republic of Germany

Abstract:

Theoretical estimates of the RF current driven by lower hybrid waves, I_{LH} , and of the absorbed RF power, P_{LH} , have been given under the assumption of 'strong' RF fields, for a simple wave spectrum, in the absence /1/ and in the presence /2,3/ of a quasi-static toroidal electric field. However, current drive efficiency of the lower hybrid waves, loop voltage, and power absorption vary rapidly, according to recent experimental results /4,5,6/ already at very low levels of injected power. It is thus desirable, to interpret these results to develop a model for 'weak' RF fields including the effect of the electric field.

In this paper, such a model is proposed. We first estimate the quasi linear diffusion coefficient as a function of the RF and plasma parameters, then using this estimate, we compute I_{LH} and P_{LH} as a function of the injected power P_{inj} for a simply shaped wave spectrum. Several features of the experimental results are well reflected by the results of this model, in particular an increased efficiency at low power levels when a residual co-acting electric field is present, and a saturation of the absorbed power at higher levels of injected power which depends strongly on the electric field.

I - Estimate of the quasi-linear diffusion coefficient as a function of the RF and plasma parameters.

The quasi-linear diffusion coefficient for electrons in presence of an RF electric field $E_{//}$ is given by /7/:

$$D_{\parallel}(v_{\parallel}) = \frac{\pi e^2}{2m_e^2 k_0 v_{\parallel}} \frac{d(|E_{\parallel}|^2)}{dN_{\parallel}}\bigg|_{N_{\parallel}=\omega/k_0 v_{\parallel}} \qquad (1)$$

An estimate of the spectral density of the electric field strenght in the plasma: $\frac{d(|E_{\parallel}|^2)}{dN_{\parallel}}$ is obtained using the cold electrostatic dispersion equation and the corresponding dielectric tensor to obtain the group velocity and the electrostatic energy density. The local electric field is then related to the field at the plasma edge by computing the total radial power flux Φ_r through a magnetic surface to the next taking account of the power absorption at outer radii. Strictly speaking, the area of the magnetic surface to be considered is the intersection of the latter with the propagation cone. However, as the effect of the RF field on circulating electrons has to be averaged over the torus length in order to obtain the effective diffusion coefficient, the actual toroidal length of this intersection is not relevant, and one may write $\Phi_r \simeq P_{av}/\Sigma$, where Σ is the lateral area of the magnetic surface, and $P_{av} < P_{inj}$ is the accessible power still available impinging on the considered surface.

Using this device, we obtain :

$$\frac{d(|E_{\parallel}|^2)}{dN_{\parallel}} = \frac{1}{c\varepsilon_0}\frac{P_{av}}{\Sigma}\frac{N_{\parallel}F(N_{\parallel})}{\omega_{pe}/\omega[1+\omega_{pe}^2/\omega_{ce}^2-\Sigma_i(\omega_{pi}^2/\omega^2)]^{1/2}} \tag{2}$$

II - Special form of the diffusion coefficient for a simply shaped wave spectrum.

In order to obtain estimates of the driven current I_{LH} and of the absorbed power P_{LH} , we specialise now to a simple shape of the wave spectrum:

$F(N_{\parallel}) = 1/N_{\parallel}\ Log(N_{\parallel M}/N_{\parallel m})$ for $N_{\parallel m} \geq N_{\parallel} \geq N_{\parallel M}$, and zero outside ;

which might be considered as a realistic envelope of the main lobe of actual wave spectra if one remembers that the plasma impedance at the edge behaves very roughly as $N_{//}^{-1}$ /8/.This yields finally: $\tilde{D}(v_{\parallel}) = D_{\parallel}/(\nu_e v_{eth}^2) = D_0(v_{\parallel}/v_{eth})^{-1} = D_0/u$, with:

$$D_0 = \frac{2\pi^2}{m_e Log\Lambda}\frac{P_{av}}{\Sigma}\frac{1}{Log(N_{\parallel M}/N_{\parallel m})}\frac{1}{\omega_{pe}^3[1+\omega_{pe}^2/\omega_{ce}^2-\Sigma_i(\omega_{pi}^2/\omega^2)]^{1/2}} \tag{3}$$

A numerical evaluation of Equ. (3) shows that $D_0 = 1$ is reached for P_{inj} of the order of a few tens of kW (Petula) to a few hundreds of kW (Asdex) in cases pertaining to recent experiments.

III - Electron distribution function, RF Driven current and absorbed power

We seek for a steady-state solution of the Fokker-Planck equation with a static electric field :

$$\frac{1}{\nu_e}\frac{\partial f}{\partial t} = \frac{\partial}{\partial u}\tilde{D}\frac{\partial f}{\partial u} + \frac{\partial}{\partial u}\left[\frac{f}{u^2} + \frac{1}{u^3}\frac{\partial f}{\partial u}\right] + \tilde{E}\frac{\partial f}{\partial u} \tag{4}$$

$$where: \quad \begin{cases} \tilde{E} = E/E_{Dr} & eE_{Dr}v_{eth}\nu_e = m_e v_{eth}^2 \\ \tilde{D} = D_{\parallel}/\nu_e v_{eth}^2 & \nu_e = \omega_{pe}^4 Log\Lambda/4\pi n_e v_{eth}^3 \\ u = v_{\parallel}/v_{eth} & v_{eth} = \sqrt{T_e/m_e} \end{cases}$$

integrating Equ. 4 with $\partial/\partial t = 0$:

$$f(u) = Cexp - \int_0^u \frac{1+\tilde{E}v^2}{1+\tilde{D}v^3}vdv \tag{5}$$

The resulting distribution function reads :

$$f = f_1(u) = A\ exp[(-u^2)/2 - \tilde{E}u^4/4] \tag{6a}$$

for $u \leq u_m = c/(N_{//M}v_{eth})$

$$f = f_2(u) = f_1(u_m)\ exp[\tilde{E}(u_m^2 - u^2)/2\ D_0]\left(\frac{1+D_0u^2}{1+D_0u_m^2}\right)^{-(D_0-\tilde{E})/2D_0^2} \tag{6b}$$

for $u_m < u < u_M = c/(N_{//m}v_{eth})$

$$f = f_3(u) = f_2(u_M)\ exp[(-u^2+u_M^2)/2 - \tilde{E}(u^4 - u_M^4)/4] \tag{6c}$$

for $u > u_M$

where, for simplicity we considered here a unidirectional wave spectrum ($u_m, u_M > 0$). These functions are not monotonous but increase for $u > u_c = -1/\tilde{E}$ (runaway range) when the electric field

accelerates electrons in the direction of the wave phase-velocity (co-acting E field : $E > 0$). These formulas are thus valid for counteracting E field, or for moderate co-acting fields. In the cases when integrations of the distribution function are required beyond u_c, we extend the function in the co-acting direction by a flat plateau up to some arbitrary and large 'cut-off' velocity u_0.

The RF current and the absorbed power are then obtained by:

$$j_{RF} = ev_{eth}\int_{-\infty}^{+\infty}[f(u) - f_{D=0}(u)]u\,du \tag{7}$$

$$p_{RF} = \frac{1}{2}m_e v_{eth}^2\nu_e\int_{-\infty}^{+\infty}\left.\frac{\partial f}{\partial t}\right|_{RF}u^2\,du = \frac{1}{2}m_e v_{eth}^2\nu_e\int_{-\infty}^{+\infty}u^2\frac{\partial}{\partial u}\tilde{D}\frac{\partial f}{\partial u}du \tag{8}$$

The absorbed RF power can thus be written in an analytic form:

$$p_{RF} = m_e v_{eth}^2\nu_e D_0\left\{f_1(u_m) - f_2(u_M)\right\} \tag{9}$$

whereas the current is given by an integral (easily approximated by analytical forms in different cases of interest. For easy comparison with previous works, the integrals in Equs. 7 and 10 b have been taken in the following only on the support of the wave spectrum). The behaviour of I_{LH} and P_{LH} resulting from this model is characterized by the following features as examplified in Fig. 1.

• For strong RF fields, ($D_0 \gg 1/u_m^2$), these quantities tend towards the limits:

$$p_{RF\infty} = p_F\ exp(-\tilde{E}u_m^4/4)\left\{1 + \tilde{E}[(u_M^2 - u_m^2)/Log(u_M^2/u_m^2)]\right\} \tag{10a}$$

$$j_{RF\infty} = j_F\ exp(-\tilde{E}u_m^4/4) - j_\Omega \tag{10b}$$

(see Fig. 1 a and b) where p_F and j_F are the values obtained by Fisch and Karney /1/ for D large and $E = 0$; and j_Ω corresponds to the second term of Equ. 7

We recover the expressions given in /2/ for D large: both I_{LH} and P_{LH} thus display a strong dependency on the electric field .

The current drive efficiency, measured as the ratio of the absorbed power , normalised to (10 a); to the RF current,normalised to (10 b) increases up to unity for sufficient injected power, the more slowly, the highest the counteracting field. (see fig 3).

• The ratio of the RF current to the injected power is seen to peak at very low values of the injected power and decreases monotonically beyond. This ratio , normalised to the Fisch value p_F can reach several units at very low power levels. (see Fig. 4)

/1/ N.J. Fisch, Phys. Rev. Letters 41, (1978), 13; and Ch.F.F. Karney and N.J. Fisch, Phys. Fluids 22 (9), (1979).

/2/ K. Borrass and A. Nocentini - Plasma Physics and Controlled Fusion 26, (1984), 11

/3/ N.J. Fisch, Phys. of Fluids 26, (1985), 245

/4/ D. Van Houtte et al., 4th. Int. Symp. on Heating in toroidal plasmas, Roma, It., March 1984, p 554.

/5/ T. K. Chu et al., 4th. Int. Symp. on Heating in toroidal plasmas, Roma, It., March 1984, p 571.

/6/ F. Soeldner et al. , this conference

/7/ Kennel and F. Engelmann , Phys. of Fluids, 9 ,12, dec. 1966, p 2377

/8/ M. Brambilla ,Nucl. Fusion 16, No 1 (1976)

I wish to express my gratitude for fruitfull discussions to F. Engelmann, A. Nocentini and M. Brambilla.

Figure Caption:

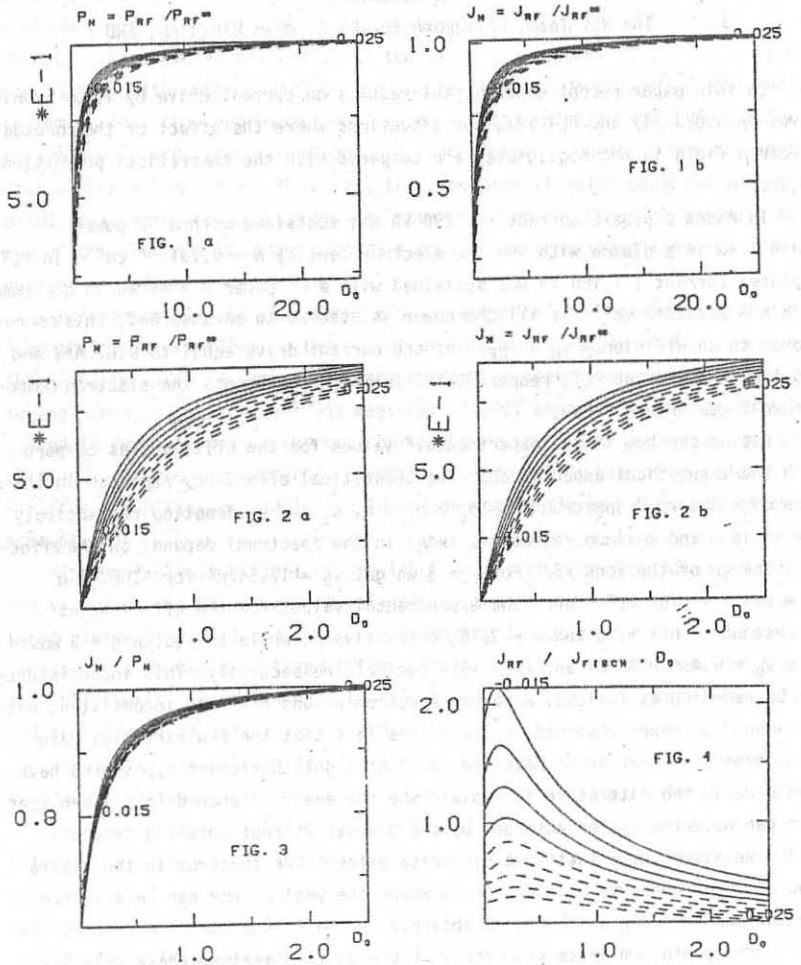
The curves are drawn for equidistant values of $\bar{E}$ (full lines for $\bar{E} < 0$: co-acting field.) ranging from -0.015 to 0.025, increment 0.005 ; and $u_m = 3.2$, $u_M = 6.4$

Fig 1 and 2 : normalized absorbed RF power and driven RF current.

Fig. 3 Ratio of the normalized absorbed power to the normalized driven current.

Fig. 4 RF driven current reported to D_0 (proportional to the injected power) and to j_F

j_F and P_F refer to the values of ref /1/ (E = 0, D_0 large), $j_{RF\infty}$ and $p_{RF\infty}$ refer to the values of Equ. (10).



COMPARISON BETWEEN THEORY AND EXPERIMENTS ON LOWER HYBRID CURRENT DRIVE

A. Nocentini
The NET Team, Boltzmannstrasse 2, 8046 Garching, BRD

In this paper recent experimental results on current drive by lower hybrid waves in ASDEX /1/ and PLT /2/, for situations where the effect of the toroidal electric field is not negligible, are compared with the theoretical predictions /3,4/.

In Asdex a plasma current I = 290 kA was sustained with a RF power P = 435 kW in a plasma with average electron density $N = 0.7 \times 10^{13}$ cm^{-3}. In PLT a plasma current I = 180 kA was sustained with a RF power P = 40 kW in a plasma with $N = 2.2 \times 10^{12}$ cm^{-3}. If all the power is assumed to be absorbed, this corresponds to an efficiency $\gamma_0 = I_{RF}/P$ of the current drive equal to 0.67 A/W and 4.5 A/W in ASDEX and PLT, respectively. In both experiments the electron temperature T was around 1 keV.

Let us see how these "experimental" values for the efficiencies compare with the theoretical expectations. The theoretical efficiency reported in the case of a "narrow" spectrum ($n_2 - n_1 \ll n_1 = n$, n_1 and n_2 denoting respectively the minimum and maximum refractive index in the spectrum) depends on the effective charge of the ions /5/. For Z = 3 we get $\gamma_0 = 17.54/n^2$ for ASDEX and $\gamma_0 = 63.51/n^2$ for PLT. Hence the experimental values for the efficiencies correspond to n = 5.12 and n = 3.76, respectively, while the value n = 2 would give $\gamma_0 = 4.4$ for ASDEX and $\gamma_0 = 15.9$ for PLT, respectively. This inconsistency can be remedied as follows. A narrow spectrum around n = 2 is inconsistent with the amount of power absorbed, owing to the fact that too few particles have velocities of the order of half the speed of light. Different hypotheses have been made in the literature to explain why the energy launched in a low-n spectrum can nevertheless be absorbed by the plasma. Without entering into details, we assume here that some mechanism extends the spectrum in the plasma towards lower phase velocities, up to where the whole power can be absorbed. The maximum power P_m which can be absorbed by the plasma when the spectrum extends from a minimum phase velocity $v_1 = c/n$ up to a maximum phase velocity $v_2 = c/2$ is that calculated for a saturated plateau and reads /4/

$$P_m = k \exp\left\{-v_1^2/2u^2\right\} \ln\left\{c/2v_1\right\} \; /\sqrt{T} \qquad (1)$$

where $u = \sqrt{T/m}$ is the electron thermal speed and k a coefficient depending on the density and the dimensions of the torus. Hence, to explain the power absorption, the spectrum in the plasma should extend from $n_1 = 2$ up to at least $n_2 = 6.65$ ($v_1 = 3.4u$, $v_2 = 11.3u$) both for ASDEX and PLT. Note that the value of v_1/u is almost independent of T. The efficiency corresponding to these wide spectra (in the case of a saturated plateau) is /4/ $\gamma_0 = 1.6$ for ASDEX, $\gamma_0 = 6$ for PLT. These two values are still too large (by factors of 2.3 and 1.3, respectively) with respect to the experimental values. On the other hand, we have to remark that they represent ideal upper limits, and they would be smaller in the case of a non-saturated plateau, or with larger impurity concentrations, or with larger values of n_1. Moreover, the experimental value could be underestimated as a consequence of incomplete absorption of the RF power by the plasma, and of the presence of a spurious part of the spectrum travelling and driving current in the wrong direction.

References /1/ and /2/ report also on a series of experiments differing from that just described in the amount of RF power used. In ASDEX powers lower than that required to keep the plasma current constant were used, and the consequent decay of the current was measured. In PLT powers higher than that required to keep the plasma current constant were used, and the consequent ramp-up of the current was measured. In both cases the influence of the electric field on the efficiency /3,4/ should not be negligible and should be taken into account.

In the first four lines of the TABLE we report, for four ASDEX experiments, the values of the RF power P (first column) and, at a given instant, the measured plasma current I and its time derivative $\dot{I}$ (second and third column, respectively). In the last three columns of the TABLE we do the same for three PLT experiments. The datas have been obtained from Fig. 3 of Ref. 1 for ASDEX, and from Fig. 1 of Ref. 2 for PLT /6/.

To compare these results with theory, we assume T, N and L (plasma inductance) constant. In the ASDEX case we take L = 4 μH (the value 3.62 holds for a uniform current distribution); from Fig. 3 of Ref. 1 we get for the resistence R the value 4 μohm (I = 240 kA/s at I = 240 kA for the P = 0 case) and for γ_0 the value 0.58 A/W (P = 500 kW is needed to drive a current of 290 kA in the absence of an E-field). In the PLT case we take L = 3 μH (2.33 is the value corresponding to a uniform current distribution), R = 3 μohm and $\gamma_0 = 4.5$ A/W.

Max-Planck-Institut für Plasmaphysik
8046 Garching bei München

If we apply the theory of current drive in the presence of an E-field developed in Ref. 3, i.e. we use $I_{RF} = \gamma_0 P/(1-\gamma_0 V)$, where V denotes the loop voltage, from Ohm's law $V = R(I-I_{RF})$ and the circuit equation $L\dot{I}+V = 0$ we obtain

$$\dot{I} = -\frac{1}{L}\left\{\frac{1}{2}\left(\frac{1}{\gamma_0} + RI\right) - \sqrt{\frac{1}{4}\left(\frac{1}{\gamma_0} - RI\right)^2 + RP}\right\}. \qquad (2)$$

which gives the values in the fifth column of the Table. In the fourth column the values of $\dot{I}$ are reported, which result from the theory not taking into account the effect of the electric field on the current drive efficiency.

Note that run-aways are not taken into account in the theory to which we are referring. In the ASDEX experiments in the absence of RF, at the density and current under consideration, run-aways indeed seem to play only a minor role in the discharge. The RF can, on the other hand, appreciably enhance the run-away production rate. In this respect the important parameter is η, the ratio of the larger phase velocity in the spectrum, v_2, to the Dreicer speed relative to the loop voltage (note that η is independent of the value assumed for the electron temperature). The value of this parameter, calculated by taking for the loop voltage the experimental value $L\dot{I}$, is reported in the last column in the Table. It should be smaller than 1, to justify the use of a theory in which run-aways are not taken into account. In the case of ASDEX, the fact that, towards lower values of the RF power, the decay time of the current increases more rapidly than foreseen by the theory (compare the third and fifth colums in the Table), could be explained by the increase of η and the consequent increase of the role played by suprathermal electrons in the ohmic part of the current. To take this effect into account in a euristic way, we could consider for the first two discharges of the Table a reduced resistence. To fit the experimental value of $\dot{I}$ of the first discharge, we would have to use for the resistence the value 2.5 μohm in place of 4, which amounts to a reduction of almost 40 %, i.e. to 40 % of the current being carried by run-aways.

In case of PLT the waves and the E-field accelerate electrons in opposite directions, hence the condition $\eta < 1$ is less critical than in ASDEX. In fact, the high-energy electrons produced by the waves have to be collisionally deflected by an angle of the order of 180^0, without losing too much momentum, to enter the run-away region. Nevertheless, we expect that with increasing η, the enhanced production of run-aways will increase the ramp-up time. If we again describe this effect by a reduction of the plasma resistence, we find that the experimental value of $\dot{I}$ for the last case of the Table could be explained by choosing R = 1.9 μohm in place of R = 3, which amounts to a reduction of the resistence by almost 40 %.

In conclusion, we see that a theory of LH current drive in the presence of an E-field not taking run-aways into account /4,5/ correctly predicts the positive influence on the CD efficiency ($\gamma = I_{RF}/P$) of an electric field pushing the current parallel to the CD current, and the negative influence of an electric field pushing the current antiparallel to the CD current, insofar as run-aways do not start to dominate. Actually, the theory seems to be valid up to the very end of its range of applicability (i.e. up to $\eta \lesssim 1$).

Note, that a theory linear in the electric field, thus requiring $V\gamma_0 \ll 1$, is certainly not applicable to the last case of the TABLE.

Useful discussions with F. Engelmann and J.-G. Wegrowe are gratefully acknowledged.

T A B L E

P(kW)	I(kA)	$\dot{I}$(kA/sec)			η
100	220	-110	-162	-135	0.80
190	230	-83	-120	-90	0.69
280	240	-54	-78	-54	0.56
380	260	-28	-40	-26	0.40
65	190	31	102	26	0.8
125	200	75	362	77	1.2
260	210	132	960	160	1.6

References

/1/ Leuterer F. er al, Tenth International Conference on Plasma Physics and Controlled Nuclear Fusion Research, London 1984, paper CN-44/F-IV-3.

/2/ Motley R. et al, Tenth International Conference on Plasma Physics and Controlled Nuclear Fusion Research, London 1984, paper CN-44/F-II-2.

/3/ Borrass K., Nocentini A., Plasma Phys. Contr. Fus. 26, 1299 (1984) .

/4/ De Barbieri O., Engelmann F., Nocentini A., Wegrowe J.-G., INTOR Europ. Contr. to the 10th Workshop Meeting, Oct 84, Vol I, paper 2.2.1.2.a.

/5/ Fisch N.J., Boozer A.H., Phys. Rev. Lett. 45, 720 (1980).

/6/ Nocentini A., NET int. rep., EUR XII - 324/36.

RF CURRENT-DRIVE(LHH+ECH) AND ELECTRON CYCLOTRON HEATING EXPERIMENTS ON JFT-2M TOKAMAK

K.Hoshino, T.Yamamoto, N.Suzuki, Y.Uesugi, H.Kawashima, T.Matoba, S.Kasai, T.Kawakami, M.Maeno, T.Matsuda, H.Matsumoto, Y.Miura, M.Mori, K.Odajima, H.Ogawa, T.Ogawa, H.Ohtsuka, S.Sengoku, T.Shoji, H.Tamai, T.Yamauchi, S.Yamamoto, I.Ochiai[+], M.Hasegawa[++], K.Ohta[++], S.Takada[+++], I.Yanagisawa[++++], A.Funahashi and Y.Tanaka
Department of Thermonuclear Fusion Research, Naka Fusion Research Establishment
Japan Atomic Energy Research Institute, Tokaimura, Nakagun, Ibarakiken, Japan

ABSTRACT

RF current-drive/ramp-up by the simultaneous injection of the lower hybrid wave(LHW) and the electromagnetic wave of the frequency near the second harmonic electron cyclotron frequency(ECW) is investigated in the JFT-2M tokamak. A significant ramp-up of the toroidal current of 48kA/sec is observed by the electron cyclotron heating(ECH) of the LH sustained tokamak plasma. Further, the local bulk electron heating by the second harmonic extraordinary mode(X-mode) ECH is observed.

INTRODUCTION

The rf current drive using the ECW seems to have several attractive features. First, it is possible to place the antenna far away from the plasma without the coupling problem. Second, the penetration of the ECW in the high density plasma is possible by choosing the frequency above the cutoff frequency. Third, as the resonant coupling of the ECW to the electrons occurs in the parameter space in which the electron cyclotron resonance(ECR) condition is satisfied, the power deposition(or the current) can be controlled by choosing the ECR condition appropriately. Fourth, the theoretical current drive efficiency by the ECW is as large as 3/4 of that by the LHW[1]. Fifth, the threshold power of the ECW parametric decay instability is relatively large, which means that high power density can be transmitted to the plasma core region to maintain the current.

The difficulty hitherto encountered to obtain the ECH driven current by the bulk heating of the plasma lies in that the large single path absorption sufficient for the energy absorption to occur in one side of the ECR layer[2] is needed. And there is a possibility that the drive efficiency may deteriorate by the trapped particle effect by the bulk heating.

But by using the relativistically down shifted ECR of the high energy electrons, these difficulties are avoided. The reflection at the vessel wall may increase the power deposition at the shifted ECR layer even if the absorption in single path is not large. Moreover, it was revealed that the current drive efficiency J/Pd is improved by the wave coupling to the high energy electrons[1),2)].

Thus the scheme of the coupling of the ECW to the LHW sustained tail electrons arises to investigate the ECH effect because the stable well defined tail is produced by the LHW. The theoretical calculation of the coupling of ECW to the LHW tail electrons shows the marked damping of ECW and improvement of the current drive efficiency[3)].

The combined effects of LHH+ECH are studied on the JFT-2M tokamak(R=1.31m,

---

On leave from + the Univ. of Tokyo, ++ Mitsubishi Electric Co., +++ Mitsubishi Electric Computer Systems Tokyo Co., ++++ Mitsubishi Atomic Power Industries Inc.

a=0.35m) experimentally. The frequency of the LHW is 750MHz, and the spectrum of the parallel refractive index is controlled by four waveguides[4]. The launcher spectrum concentrates dominantly around $n_{//}$=1~3 when the phase difference is -90^{o}. The frequency of the ECW is 60GHz. The second harmonic X-mode with $n_{//}$=-0.17 of the narrow beam divergence is launched in almost linear TE_{11} mode from the low field side of the torus.

LHH+ECH CURRENT DRIVE

Time evolutions are depicted in Fig.1(a). The toroidal electric field is applied by the primary OH circuit in the initial 100ms for the production of the target plasma, and then the primary voltage is shut down and held zero (AVR operation). The application of the LHW of pulse length ~400ms and power 70kW starts before the shut down of the primary voltage. In this way, the quick ramp-up of the plasma current I_p by the LHW is obtained. Ramp-up only by the LHW without the initial OH field takes longer time with less stability to reach 10kA level of the driven current.

A saturation of the LHW driven current around I_p≃18kA with the efficiency 0.26A/W is observed. The ECH pulse is applied for 100ms during the saturation phase. A significant ramp-up of the current occurs almost linearly in time as shown in the figure. During the ECH pulse, the loop voltage drops and the plasma density changes. In this case, the 2nd harmonic ECR layer locates at r_0 =0.1m outside and the plasma displacement is held inside of the center of the vacuum vessel with B_{t0}=1.15T.

The time rate of the current rise $(d/dt)I_p$ as a function of B_{t0} is given in Fig.1(b). $\dot{I}_p$ has two peaks. A peak around B_{t0}=1.0T corresponds to the location of the ECR layer around the plasma core which is shifted inside, and indicates the contribution of the bulk ECH to the current rise. The second peak in B_{t0}=1.15~1.30T seems to be due to the coupling of the ECW to the LH sustained tail electrons. The drive mechanisms are different between the two cases, namely, the coupling to the bulk electrons causes an increase in the bulk electron temperature which enhances the damping of the LHW and then the plasma current. The drive efficiency, however, stays constant. On the other hand, the second case is due to the coupling of the ECW to the LH sustained tail. There are marked different results between the two cases. In the former case, the increased current does not decrease after the ECH pulse, which implies that a new saturation level is set for the LHW current drive by the effect of bulk ECH, for instance, by increase in the bulk electron temperature. On the other hand, in the latter case, the current decreases after the end of the ECH pulse, indicating that the increased current is attributed to the ECW. The time behaviour of the density is also different between the two cases as shown in the figure. The density drop of B_{t0}=1.0T case is larger than that of B_{t0}>1.1T case in which a gradual increase in density occurs after the small density drop at the beginning of the ECW pulse. The ECW coupling to the trapped electrons at the ECR layer in the low field side may affect the particle transport.

The resonant energy of an electron is obtained as shown in Fig.1(c) by the relativistic ECR condition

$$1-s\omega_{ce}/\omega - n_{//}v_{//}/c = 0 \qquad (s= 1, 2, 3, \ldots).$$

A divergence of the microwave beam from the horn antenna gives a spread of $-0.26<n_{//}<-0.09$. Owing to the 2nd harmonic resonance (s=2), ECW couples to the tail electrons at the center of the vessel which have the energy of 12~27keV in B_{t0}=1.15T(r_0=.10m) case, 20~45keV in B_{t0}=1.20T(r_0=.16m) case and 45~85keV in B_{t0}=1.30T(r_0=.28m) case. The resonant energy of the plasma core shifted inside is even higher. The energy spectrum analysis of the soft X-ray radiation shows that an increase of the photon counts of energy up to 80keV occurs and the increment is a few times as large as the radiation from the LH sustained plasma. The contribution from the s=3 resonance seems to be small which is derived from the negligible $\dot{I}_p$ in $B_{t0}<0.8$T cases. The soft X-ray measurement

shows also that the emission region is highly localized inside of the center of the chamber during the ECH pulse, implying that the current channel is localized inside. In the B_{to}=1.40T case in which no bulk ECR layer exists in the plasma column, the coupling to the tail electrons is detected by the ECE measurement in spite of no increase in the current. The increase in I_p decreases as the plasma density increases because of the decrease of the LH tail.

These observations show the coupling of the ECW to the high energy tail electrons satisfying the resonance condition, and resulting localized current channel. It brings the possibility of the formation of the hot electron channel in the high temperature tokamak plasmas which is proposed to stabilize the high beta tokamak plasmas[5].

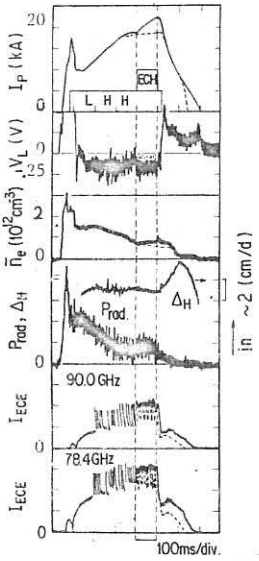


Fig.1(a) Time evolutions. B_{to}=1.15T, P_{LH}=P_{ECH}=70kW Δ_H denotes the displacement of the plasma column.

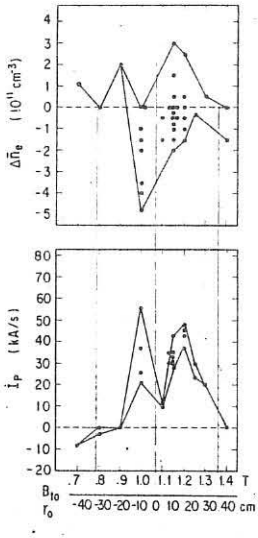


Fig.1(b) $\dot{I}_p$ and $\Delta\bar{n}_e$ during the ECH pulse. r_o denotes the minor position of the bulk ECR layer(s=2).

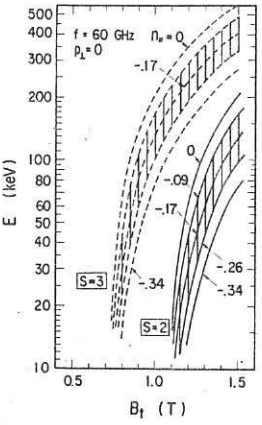


Fig.1(c) Resonant energy v.s. the local magnetic field B_t. s denotes the harmonic number of the ECR.

BULK ELECTRON HEATING BY THE SECOND HARMONIC X-MODE ECH

Bulk ECH by a 28GHz fundamental(s=1) wave was investigated on the JFT-2 tokamak by launching three different modes[6]. In the JFT-2M, the bulk ECH by the 60GHz 2nd harmonic(s=2) X-mode is studied. The calculated absorption in single path is given in Fig.2(a). The absorption rate increases with plasma density n_e and electron temperature T_e of the ECR layer. More than 80% of the wave power is absorbed in the parameter region of T_e>500eV and n_e>1.0x10^{19}m^{-3}. Therefore the local core heating by ECH is expected in the JFT-2M.

The experimental result of the density dependence of the increase of the center electron temperature ΔT_{eo} and the value $\Delta\Lambda\equiv\Delta(\beta_p+l_i/2)$, where β_p denotes poloidal beta value and l_i denotes the internal inductance, are plotted in

Fig.2(b). Calculated cutoff density of X-mode and O-mode is expressed by arrows in the abscissa. It is shown that the wave cutoff occurs above the right hand cutoff density. The ΔT_{eo} which is linear in rf power in r_o=0m case, depends much on r_o as shown in Fig.2(c). In the off-center heating in which r_o=-0.13m, +0.18m, no increase in T_{eo} is observed. However, a drop in the loop voltage and increase of the laser electron temperature around the ECR layer are obtained. Namely, the temperature profile becomes broad. The change in l_i affects $\Delta\Lambda$ and the effect is not negligible, because the increase in β_p is small due to the decrease of the joule power during the ECH pulse the power of which is less than the joule power. The density drop by ECH was large in the off-center heating and was proportional to the plasma density as were observed in the 28 GHz ECH on the JFT-2. A comparison with the fundamental ECH shows almost the same core heating efficiency $\eta \equiv \Delta T_{eo}\, \bar{n}_e / P_{rf}/R \simeq 5\times10^{19}$eV/kW/m^4.

These observations show the local heating and the possibility of the profile control by the 2nd harmonic X-mode ECH. No impurity problem is observed up to the power level of 80kW, which is one of the advantages of ECH.

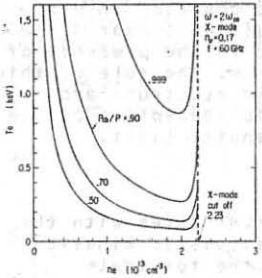


Fig.2(a) Calculated power absorption rate P_{ab}/P_{rf} at the 2nd harmonic ECR layer. f=60GHz, $n_{//}$=0.17. Cutoff of the X-mode occurs at n_e=2.23x10^{19} m^{-3} which is the right hand cutoff density.

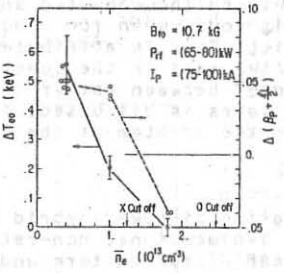


Fig.2(b) Density dependence of the increase in the center electron temperature ΔT_{eo} and the value $\Delta\Lambda \equiv \Delta(\beta_p + l_i/2)$. Position of the ECR layer is at the center of the chamber r_o=0m. Base $T_{eo}\simeq$700eV (low density case) and $T_{eo}\simeq$600 eV(higher density cases).

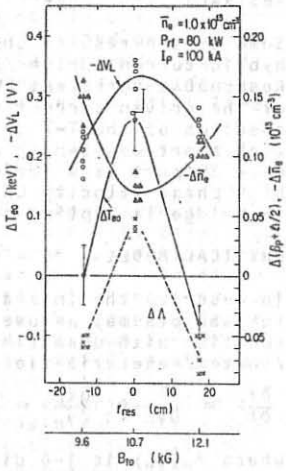


Fig.2(c) Dependence on the minor position of the ECR layer. $\bar{n}_e$=1.0x10^{19}m^{-3}, P_{rf}=80kW, I_p=100kA.

ACKNOWLEDGEMENT

The authors are grateful to Messrs. T.Shibata, T.Shibuya and the members of the operations group. They greatly acknowledge the continued encouragements of Mr. K.Suzuki, Drs. M.Tanaka, Y.Obata, Y.Iso and S.Mori.

REFERENCES

1) N.J.Fisch and A.H.Boozer, Phys. Rev. Lett., 45, 720 (1980).
2) O.C.Eldridge, ORNL/TM-7503 (1980).
3) I.Fidone, G.Giruzzi, G.Granata et al., Phys. Fluids, 27, 2468 (1984).
4) Y.Uesugi, K.Hoshino, T.Yamamoto et al., submitted to Nucl. Fusion.
5) J.Y.Hsu, C.S.Liu, R.Prater et al., GA-A 17731 (1984).
6) K.Hoshino, T.Yamamoto, A.Funahashi et al., J .Phys.Soc.Jpn., 54, 2507(1985).

COMPUTER SIMULATION OF LOWER HYBRID CURRENT DRIVE IN T-7 TOKAMAK

P. Pavlo and R. Klima

Institute of Plasma Physics, Czechoslovak Academy of Sciences,
Pod vodárenskou věží 4, 182 00 Praha 8, Czechoslovakia

ABSTRACT

Some of the results obtained on computer simulations of lower hybrid current drive /LHCD/ in T-7 tokamak are presented. Reasonable agreement between the computed and observed values of the driven current is found even for unmodified linear spectrum of the T-7 grill. This is attributed to the presence of weak short wavelength /SW/ part in the spectrum. The role of this weak SW part as a "bridge" between rather cold electrons and high phase velocity LH waves is discussed. The conception of the SW bridge is applied to the problem of the density limit.

PHYSICAL MODEL

To describe the interaction of lower hybrid /LH/ waves with the tokamak plasma, we use 1-dimensional non-relativistic kinetic equation with quasilinear diffusion term and the toroidal /vortex/ electric field term /1/

$$\frac{\partial f_{\parallel}}{\partial t} = \frac{\partial}{\partial v_{\parallel}} D_q \frac{\partial f_{\parallel}}{\partial v_{\parallel}} + \frac{e}{m_e} E_{\parallel} \frac{\partial f_{\parallel}}{\partial v_{\parallel}} + a(Z_{eff}) \frac{\partial}{\partial v_{\parallel}} \nu_r \left(v_{\parallel} f_{\parallel} + \frac{T_e}{m_e} \frac{\partial f_{\parallel}}{\partial v_{\parallel}} \right) \qquad /1/$$

where $f_{\parallel}(v_{\parallel})$ is 1-D distribution function of electrons, $v_{\parallel}$ is the velocity parallel to the toroidal magnetic field, D_q is the quasilinear diffusion coefficient

$$D_q = \frac{e^2}{\varepsilon_o m_e^2} \frac{\omega^2}{\omega_{pe}^2} \frac{1}{|v_{\parallel}|} W_k \Big/ k_{\parallel} = \frac{\omega}{v_{\parallel}} \qquad /2/$$

ν_r is the collision frequency of resonant electrons adjusted via $a(Z_{eff})$ to the value inferred from 2-D calculations, ω is the frequency and W_k the spectral energy density of the applied rf field. The remaining symbols have their usual meaning.

Equation /1/ is solved in steady state approximation. Runaway of electrons is permitted, the loss being compensated for by a source imposed through the boundary condition at $v_{\parallel}=0$. Discretizing the LH spectrum in a number of modes allows for a tractable solution of /1/. The value of $f_{\parallel}$ at chosen mesh points can be then simply evaluated, and the damping rate $2\gamma_k$ and the driven current determined. This is performed in each space mesh point. The spatial dependence of W_k is given by

$$\frac{1}{r}\frac{\partial}{\partial r}(r\, v_{gr}\, W_k) = 2\gamma_k W_k \qquad /3/$$

v_{gr} being the group velocity of the mode k. At the boundary /r = a/, $W_k(a)$ is given by the shape of the input spectrum.

The code based upon the above equations has been either coupled to a standard 1-D tokamak transport code to obtain temporal evolution of plasma parameters at LHCD, or used independently with radial profiles of plasma parameters prescribed and fixed.

T-7 RESULTS

The use of LH spectra computed for the T-7 grill on the basis of the linear theory /2/ led to better than order-of-magnitude agreement between the computed values of the driven current I_{rf} and those observed in experiments. In the simulations, the transport code was first run without rf to obtain steady-state profiles of plasma parameters; then rf was switched on. The details will be given elsewhere; here, for lack of space, only an illustrative example is given. Fig. 1 shows the dependence of I_{rf} /stationary value/ as obtained in simulation /full line/ and in experiment /3/ /dots/.

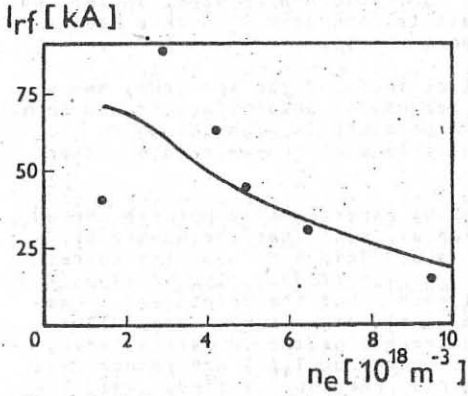


Fig. 1. The driven current I_{rf} vs. density. Effective ion charge Z_{eff}= 1.5, total plasma current kept fixed at I_p=125 kA, input power P_{rf}=40 kW. In simulations, linear spectrum for grill phasing φ=120° was used, $a(Z_{eff})$=0,7 was chosen to fit the experimental data at n_e=5x$10^{18}$$m^{-3}$. From 2-D calculations, follows the value $a(Z_{eff})$ = 1.25.

The T-7 /three-waveguide/ grill produces rather broad spectrum, which for 120° phasing extends /in the useful branch/ up to $N_{\parallel}$=8, with roughly 3.5% of the total power residing above $N_{\parallel}$=6. It was found that the driven current critically depends on this short wavelength part to the extent that if the same spectrum is cut off at $N_{\parallel}$=6, the resulting Irf is practically zero. This led to an extensive study of the role of SW part of spectra main conclusions of which are formulated in /4/. Note that the value $N_{\parallel}$=6 is valid for $T_{e,max}$ 0,9 keV.

The fact that higher values of $N_{\parallel}$ are necessary to explain the electron heating and LHCD effect is known as notoriously as that the linear theory does not, as a rule, provide them. Much effort has been spent to explain what causes the broadening of the spectra. However, strong effects were searched for. In /5/, it

it was shown for the first time that a small rf power residing in the SW range can efficiently raise the quasilinear plateau up to the level requiredto explain the observed values of the driven current. In /4/, we have shown, with the inclusion of the space dependences that if a spectrum given at the plasma boundary decreases with $N_{\parallel}$ fast enough toward the SW end, small power contained in the SW part can last /in space/ long enough to grant absorption profiles observed in experiments. It is therefore possible that weak effects, such as nonlinear generation of higher spatial harmonics due to ponderomotive density modulations at the edge of plasma /6/, may be sufficient to explain the necessary upshift of $N_{\parallel}$.

DENSITY LIMIT

Suppose an LH spectrum composed of large long-wavelength main lobe and weak SW complement /either launched or produced in the boundary region/ is propagating toward the plasma centre. The SW part of the spectrum /a few percent of the total power/ provides the bridge between the rather cold electrons and the high phase velocity waves of the main lobe. Because in regimes at which the density limit occurs $N_{\perp}$ is roughly proportional to $N_{\parallel}$, the SW part is the first to get absorbed by ions. In /4/, we suggested that the density limit is connected with this fact. Here, the idea is pursued in more detail.

Denote $N_{\parallel max}$ the highest parallel index of the spectrum, and suppose it can be altered only because of absorption. At a certain space point r_o, the electron temperature is high enough to satisfy the condition for observable electron-wave interaction

$$N^2_{\parallel max}(a) \cdot T_e(r_o) \approx 32. \qquad /4/$$

The onset of ion absorption can be expected at a point r where $w_i = v_{ph\perp min}/v_{Ti}$ reaches the value w_{io} such that the number of resonant ions $\sim n_i \cdot \exp(-w_{io}^2)$ is sufficient to damp the corresponding mode $N_{\parallel max}$ /note that $v_{ph\perp min} = c\omega/(N_{\parallel max}\omega_{pe})$/. The situation $w_i = w_{io}$ can happen at each r but the point $r = r_o$ seems to be the most probable. In fact, starting from r_o toward the plasma centre, $N_{\parallel max}(r)$ fast decreases as the SW part is weak; on the contrary, the profiles of $n(r)$ and $T_i(r)$ are rather flat for $r < r_o$ /from x-ray measurements, one usually finds $r_o = (0.7 - 0.75) \cdot a$, a being the small radius/. This assumption is consistent with experiments /10/, /11/ where fast ions originate near to the plasma boundary; moreover, if $r_c < r_o$, both electron and ion tails would have to be present. Such case was observed in PETULA B /7/ but seems to be rather rare; in most experiments, the electron tails disappear abruptly. This indicates that the whole bridge is being absorbed, with the ions allways one step ahead of the electrons.

The condition $w_i = w_{io}$, with inclusion of /4/ then leads to

$$n_c(r_o) = \frac{59}{w_{io}^2} \frac{f^2 A}{N_{\parallel max}^2 (a) T_i(r_o)} = \frac{1.8}{w_{io}^2} f^2 A \frac{T_e(r_o)}{T_i(r_o)} \left[10^{20} m^{-3}\right] \qquad /5/$$

where f is in GHz and A is the ion mass number; taking $T_e(r_o) \approx T_i(r_o)$ in the boundary region, and $\overline{n_c} \approx n_c(r_o)$ for flat density profiles and $r_o \approx 0.7a$, the formula considerably simplifies. For

$w_{io}=4$, $\bar{n}_c=0.11f^2$ for hydrogen yields in most cases, considering the simplifications used, acceptable values. The value of w_{io}, higher than would follow from /8/, may be justified because, unlike the electrons, the perpendicularly accelerated ions are poorly confined /11/ and the rf field works on less disturbed distribution function while a quasilinear plateau is formed in the case of electrons.

The dependence of the density limit on the ion mass given by /5/ holds only for very pure discharges. H minority ion absorption was shown to be responsible for experimentally observed little sensitivity of $\bar{n}_c$ on A /9/. To clear the point, consider a pure H discharge and a D discharge with H minority, $\bar{n}_H=p.\bar{n}_e$, $p \ll 1$. We demant that, in both discharges /i=H or D/ at their respective density limits the same number of resonant ions be present. The resulting relation, complicated because of spatial dependences, can be simplfied assuming that T_e r and T_i r profiles, the threshold point r_0 and $n(r)/\bar{n}$ are the same in both cases; then it can be approximated for $p \gtrsim 0.005$ as

$$\bar{n}_c^H/\bar{n}_c^D = 1 + \ln p \,/\, (1 + w_{H_0}^2) \qquad /6/$$

For 3% H minority and $w_{H_0} = 4$, we have $\bar{n}_c^D/\bar{n}_c^H = 1.25$. To have the density upshift 1.5, $p = 0.3\%$ is required.

Relation similar to /6/ can be derived for the density limit upshift with increasing SW power, demanding that the energy per resonant ion be the same at n_c. It leads e.g. to $\Delta\bar{n}_c/\bar{n}_c \sim 15\%$ at 10-fold increase of the applied power, cf. /9/. However, the possible dependence of w_{io} on the energy density should also be considered here.

The formulae given in this section, despite of the severe simplifications used, yield reasonable results, confirming the viability of the conception of the "SW bridge".

REFERENCES

/ 1/ Parail, V.V., Pereverzjev, G.V., Fiz. plazmy 9 /1983/ 585.
/ 2/ Preinhaelter, J., Proc. Coll. on Plasma Phys., ICTP Trieste Italy, ed B. McNamara 1983, Vol. II, 813.
/ 3/ Alikaev, V.V. et al., Fiz. plazmy /U.S.S.R./ 11 /1985/ 53.
/ 4/ Pavlo, P., Klima, R., to appear in Phys. Lett. A.
/ 5/ Succi, S. et al., IAEA Int. Conf. Plasma Phys., Contr. Nucl. Fusion, 10th, London 1984, p. CN-44/F-III-5-1.
/ 6/ Petržilka, V.A., Klima, R., Pavlo, P., Czech. J. Phys. B33 /1983/ 1002.
/ 7/ Van Houte, D. et al., Rep. EUR-CEA-FC-1218, 1984.
/ 8/ Tonon, G., Plasma Phys. and Contr. Fus. 26, 1A /1984/ 145.
/ 9/ Alladio, F. et al., IAEA Int. Conf. Plas. Phys. and Contr. Nucl. Fusion, 10th, London 1984, p. CN-44/F-II-3.
/10/ Leuterer, F. et al., ibid., p. CN-44/F-IV-3.
/11/ Porkolab, M. et al., ibid., p. CN-44/F-II-1.

LOWER HYBRID EXPERIMENTS AT 2.45 GHz ON PLT*

J.E. Stevens, R. Bell, S. Bernabei, A. Cavallo, T.K. Chu,
S. Cohen, P. Colestock, G. Gammel, S. Guharay+, G.W. Hammett,
W. Hooke, J. Hosea, F. Jobes, E. Mazzucato, R. Motley,
E. Meservey, S. von Goeler, and J.R. Wilson
Princeton Plasma Physics Laboratory
Princeton, NJ 08544, U.S.A.

ABSTRACT

A 2.45 GHz, 1.2 MW lower hybrid system was installed on PLT to extend lower hybrid operation to the normal PLT density range of 1-5 x 10^{13} cm^{-3}. The present system consists of three identical grills, two on top ports and one on an outside equatorial port. Experiments with the new system will explore current drive, heating, current profile modification and confinement at values of $\omega_{pe}^2/\omega_{ce}^2$ approaching 1. Initial experiments have focused on understanding several lower hybrid wave related topics; especially

1) the density limit for 2.45 GHz lower hybrid waves,
2) the validity of ray tracing theory, and
3) the effect of lower hybrid current drive on plasma MHD behavior.

*Supported by DOE Contract No. DE-AC02-76-CHO-3073
+University of Maryland

Coupling and Current Drive

The PLT 2.45 GHz lower hybrid system has three identical grills, each with 8 waveguides of dimension 10 cm x 1 cm. Measurements of grill reflection versus phase show agreement with Brambilla theory. The current drive figure of merit is observed to be $I\bar{n}_{13}R_o/P_{rf} \gtrsim 1$ A 10^{13} cm^{-3} m/W, which is comparable to that of the previous 800 MHz system. So far, flattop currents of $I_p \sim 500$ kA have been maintained for densities up to 8 x 10^{12} cm^{-3}, $V_L = 0$, and $P_{rf} \sim 600$ kW from two grills.

Density Limit and Ray Tracing

A measure of the effectiveness of LH current drive is its ability to increase the slope ($\dot{I}_p$) of the plasma current from that of the no-rf case. With no rf, the plasma current was maintained approximately constant at I_p = 400-500 kA. The change in plasma current slope, $\Delta\dot{I}_p$, during a 200 ms rf pulse is plotted in Fig. 1 for top and side antenna phasings of (a) $\Delta\phi$ = 90° & 90°, and (b) $\Delta\phi$ = 60° & 90°. The 2.45 GHz system was able to affect the slope of the plasma current at densities above 3 x 10^{13} cm^{-3}, well beyond the density limit of 0.7 x 10^{13} cm^{-3} for the old 800 MHz system. A surface ion tail begins to appear above $\bar{n}_e \sim 2.5 \times 10^{13}$ cm^{-3} for side launch but not for top launch as measured by a horizontally scanning charge exchange analyzer. No parametric decay waves were observed for $\bar{n}_e < 4 \times 10^{13}$ cm^{-3}. The disappearance of current drive effects above ~ 3.5 x 10^{13} cm^{-3} may be due to a decreasing electron tail energy or it may simply be due to a lack of rf power.

The comparison of top and side launching in Fig. 1 shows that outside launch is more effective in case (a) where the launched spectra are identical, while the top and side couplers are equally effective in case (b) where the top grill launches faster waves ($n_{\parallel o}$ (top) ≈ 1.8, $n_{\parallel o}$ (side) ≈ 2.7). This feature is explained by ray tracing theory which predicts that the $n_\parallel$ spectrum for top launch should be significantly upshifted as the wave propagates from the edge to the center of the plasma. Figure 1(c) shows the launched spectra for $\Delta\phi$ = 60° and 90°. At $\bar{n}_e \simeq 1.3 \times 10^{13}$ cm^{-3} and $\Delta\phi$ = 90°, for each coupler, the launched wave spectra are transformed into the spectra in Fig. 1(d) by the time they are near the center of the plasma (r ≈ 10 cm). It is assumed that the damping takes place inside r ≈ 10 cm because the hard X-ray emission (20 < hν < 750 keV) is concentrated there (see Fig. 3). The spectrum for side launch in Fig. 1(d) contains more power in the faster, low $n_\parallel$ waves and thus produces more efficient current drive, as shown in Fig. 1(a). In the case where the top coupler has $\Delta\phi$ = 60° and the outside coupler has $\Delta\phi$ = 90°, the spectra at the plasma center are virtually identical [Fig. 1(e)] and the effects on the plasma current slope are also identical [Fig. 1(b)]. Thus, ray tracing with primarily single pass absorption appears qualitatively to explain these results.

Hard X-ray emission, Hx, integrated over all energies (20 < hν ≲ 1000 keV) is plotted in Fig. 2 for a density scan with $\Delta\phi$ = 60°. The hard X-ray emission and 2 Ω_{ce} emission behave similarly to Figs. 1(a)-(b) for top versus side launch. If the electron tail distribution is assumed to be the same function of energy at all densities, then we would expect Hx to be independent of density. This is because Hx ∝ $n_e n_t$ while for rf current drive $n_t \propto P_{rf}/n_e$. Since Hx decreases strongly with n_e, the energy of the tail must be a decreasing function of density.

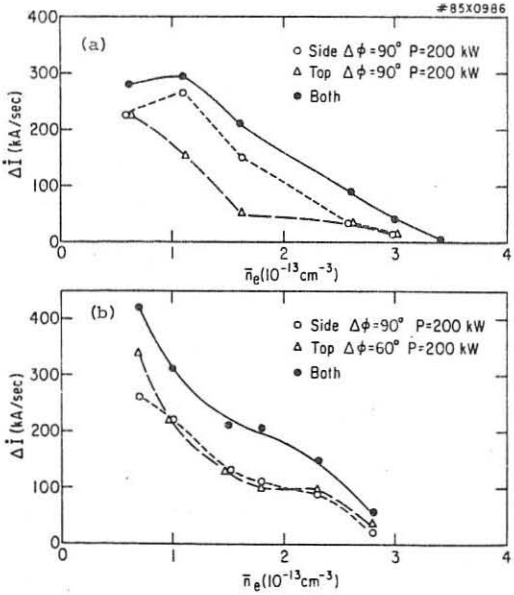
Because electric fields, which distort the tail distribution, are present in all of our experiments above 10^{13} cm^{-3}, we have not yet been able to determine directly the maximum extent of the rf produced tail expected from the LH wave accessibility condition.

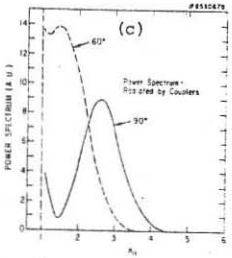
Current Profiles, Heating, and Confinement

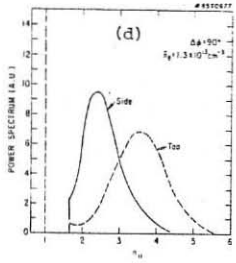
A five channel vertical hard X-ray array was used to infer the radial location of the rf-driven component of the plasma current. In general, the hard X-ray emission is sharply peaked in the inner 10-15 cm of the 40 cm minor radius plasma (Fig. 3). The profiles broaden slightly for lower q, lower B_T, lower $\bar{n}_e$, and higher rf power. However, in general, the X-ray profile widths cannot be changed by more than a few cm. Slower waves were also tried ($\Delta\phi$ = 120°) in an attempt to have the waves damp further out. However, the X-ray profiles were unchanged although the overall emission decreased.

Evidence that rf current drive affects the plasma MHD behavior was obtained during an rf power scan with $\bar{n}_e \sim 10^{13}$ cm^{-3}, $I_p \sim 500$ kA, $\Delta\phi$ = 60°, and B_T = 29 kG. Sawteeth, initially present in the ohmic discharge, were observed to increase in amplitude and period for powers up to ~ 200 kW. As the power was raised further, the sawteeth became smaller. No sawteeth were detectable for powers above 400 kW. The diameter of the sawtooth inversion surface as inferred from 2 Ω_{ce} emission measured by a grating polychromator remained approximately constant as a function of rf power until it was no longer observable.

Measurements of electron heating for the conditions described above show that the electron energy confinement time $\tau_{Ee} \equiv$ (electron thermal energy)/ (total input power) = E/ ($P_{OH} + P_{rf}$) is approximately constant for rf powers between 0 and 500 kW (Fig. 4). The total input power remained approximately constant as the rf power essentially replaced the ohmic power. At LH power levels above ~ 300 kW the central (r < 15 cm) electron temperature measured by TVTS and confirmed by soft X-rays can be increased from ~ 2 to ~ 4 keV at $\bar{n}_e \sim 8 \times 10^{12}$ cm^{-3} although the total electron energy content increases only slightly (Fig. 5). The best conditions for electron heating coincide with the conditions for optimum current drive. Scaling studies of electron heating and confinement for different density and other parameters are yet to be carried out.







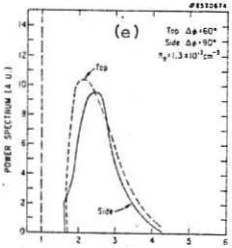


Fig. 1(a) Change in plasma current slope for identical launched spectra from top and side, and (b) faster spectrum launched from the top. (c) Power spectra radiated for $\Delta\phi$ = 60° and 90°. (d) Power spectra at 10 cm minor radius for conditions in part (a). (e) Power spectra at 10 cm minor radius for conditions in part (b).

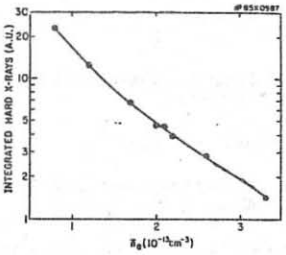


Fig. 2 Integrated hard X-ray intensity versus density for $\Delta\phi = 60°$ and $P_{rf} = 280$ kW from side and one top coupler.

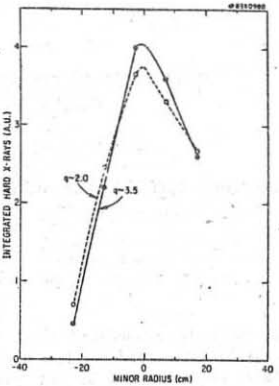


Fig. 3 Integrated hard X-ray intensity versus minor radius for $q = 2.0$ and $q = 3.5$.

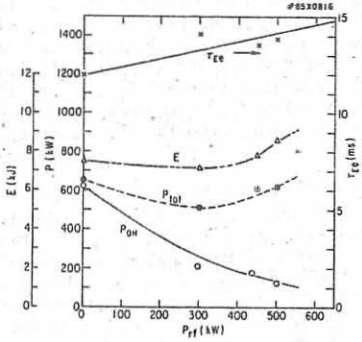


Fig. 4 Bulk electron energy, input power, and bulk electron confinement time versus rf power for $\bar{n}_e = 10^{13}$ cm^{-3} and $I_p = 500$ kA.

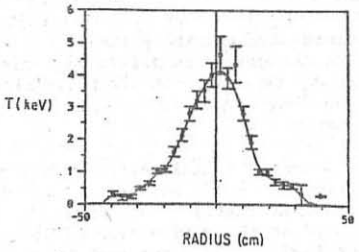


Fig. 5 Electron temperature for 500 kW of rf at $\bar{n}_e = 0.8 \times 10^{13}$ cm^{-3}.

SIMULATION OF NEUTRAL EMISSION IN THE ION INTERACTION REGIME DURING LH EXPERIMENT IN FT

E. Barbato, G. Bracco, S. Podda, V. Zanza

Associazione EURATOM-ENEA sulla Fusione, Centro Ricerche Energia Frascati, C.P. 65 - 00044 Frascati, Rome, Italy

INTRODUCTION

In many lower hybrid heating experiments a strong interaction with the electrons is observed at low density, while above the so called critical density this interaction is not present any more. In FT this occours at 5×10^{13} cm^{-3} and has been shown as due to the wave interaction with ions, and mainly with the protons which are present as a minority also in D_2 discharges ($n_H/n_D = 0.021$) [1]. In this density region, during the RF pulse, both H and D perpendicular tails are observed in D_2 discharges, together with a neutron flux enhancement, while no parametric decay instabilities (PDI) are observed. At higher densities, above 1.5×10^{14} cm^{-3}, a strong PDI activity is observed without neutron enhancement and H tails. The D tails. The D tails are present up to 1.6×10^{14} cm^{-3}.

In order to get informations about both the wave propagation into the plasma and the wave ion interaction the ion tails generation profile should be known. To this end radial resolved charge exchange measurements has been performed. Unfortunately the interpretation of the results is very difficult because the perpendicular tails, which are generally ripple trapped, are affected by the vertical drift velocity which makes the ions whose mean free path is long enough to be seen in regions different from the one where they are born.

In order to analyse the radial resolved CX measurements during the LHH experiment on FT a simulation code has been produced which, given the ion distribution function, computes the neutral emission from a plasma taking into account the ripple trapped ions. The model has been applied to two different D discharges, the first one in the intermediate regime at density of 10^{14} cm^{-3}, and the other one at $n = 1.4\times10^{14}$ cm^{-3} that is in the PDI regime. In both cases a peripherical deposition profile seems to be more consistent with the experimental data.

THEORY

Let g be the distribution function of the ripple trapped ions and f the one of the bulk ions. If v is the drift velocity which is supposed downward, we can write

$$V_D = \partial g/\partial y = - g/\tau_D + f/\tau_T \qquad (1)$$

where τ_D is the detrapping time due to collisions ($\tau_D \sim \tau_i \frac{\Delta B}{B}$) and τ_T is the trapping rate which is connected to τ_D by: $\tau_T = \tau_D \sqrt{\Delta B/B/\pi}$. Equation (1) can be easily solved and the result is:

$$g(\varepsilon,y) = \int_y^a f/V_D\tau_T \, e^{-\int_y^{y'} dt/V_D\tau_D} \, dy' \qquad (2)$$

The neutral emission can be computed by:

$$\Gamma(\varepsilon) = \int_{-a}^{a} g \, n_o n_i \, \langle\sigma_{cx} v\rangle \, \eta(x) \, d\xi \qquad (3)$$

where n_i and n_o are the ion and neutral density respectively, $\langle\sigma_{cx} v\rangle$ is the charge exchange reaction rate and η is the plasma transparency. If the ion distribution function is known, Eqs (2) and (3) allows to calculate the neutral flux. The distribution function is supposed to be maxwellian during the ohmic phase while, during the RF phase a distorted distribution function of the type $f(V_{\parallel})\, F(V_{\perp})$

$$\begin{aligned} F(V_\perp) &= N \, e^{-E_\perp/T_T} \qquad \text{if} \qquad E_\perp > E_m \\ F(v_\perp) &= e^{-E_\perp/T_i} \qquad \text{if} \qquad E_\perp < E_m \end{aligned} \qquad (4)$$

is assumed in the region between R_1 and R_2. The parameters T_T E_m R_1, and R_2, are choosen in such a way to make the computed neutral emission fit the experimental one.

From Eq. (4) both the neutron emission and the energy stored in the tails can be calculated.

RESULTS

The described model has been applied to two different deuterium discharges with RF power of 300 kW. The first one with $n = 10^{14}$ cm^{-3} and T_i = = 1.2 keV, where both H, D tails and neutron enhancement are observed (see Fig. 1). The results of the simulation are reported in Fig. 2a and 2b respectively for H and D. In both cases the deposition profile which reproduces the experimental data, full line, is outside 15 cm (the minor radius is 20 cm). For E_m, which is the minimum ion energy interacting with waves, we find the values 2.5 and 6 keV respectively for H and D. Inside the errors the condition $E_{mD} = 2E_{mH}$ is fulfilled. From E_m and from the dispersion relation we get for $n_\parallel$ a value in the range from 5 to 10. The tail temperature, T_T is 30 keV for H and 15 keV for D, this is in agreement with the quasi linear theory. The neutron emission computed from the ion distribution function is in agreement with the observed one. Almost the total tail energy, 400 J, is stored on the minority H. The obtained tail energy confinement time 1 ms, is consistent with a ripple drift loss. A broader deposition profile reaching the plasma center, dashed lines in Fig. 2a and 2b is inconsistent with experimental data mainly as far as H data are concerned. In fact the short mean free path does not allow a ion of few keV to drift in order to be detected at a radius of 18 cm.

The second case refers to a discharge with $n = 1.4\times10^{14}$ cm^{-3} and T_i = 1 keV. In this regime a PDI activity and D tails are observed, while no neutron enhancement nor H tails are present. The simulation of D emission is reported in Fig. 3. Also in this case the neutral flux is consistent with a peripherical deposition profile, $r > 17$ cm. The tail temperature is, in this case,

about 3.5 keV. The computed neutron emission and the tail stored energy are negligible.

Then, from the analysis on neutral emission in FT during LH experiment the ion wave seems to occur at radius greater then 15 cm. Moreover an up shift of n (from 2 to 5-10) seems to be present. The same up shift is required to explain the electron wave interaction occouring at lower densities.

REFERENCES

[1] F. Alladio et al., Nucl. Fusion 24 (1984) 725.

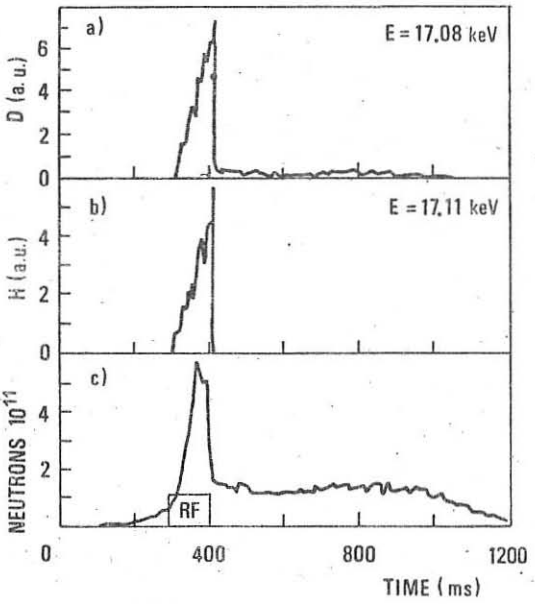


Fig. 1 - Fast neutral emission and neutrons enhancement during RF at $\bar{n} = 10^{14}$ cm^{-3}.

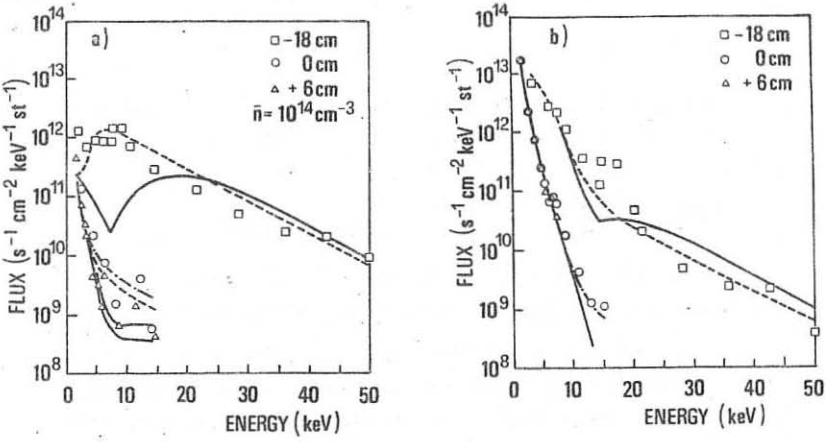


Fig. 2 - H(a) and D (b). Emission simulation results compared with the experimental data at .3 different radius. The full line is obtained with a broad deposition profile $0 < r < 20$ cm, the dashed line with a peripherical one $r > 15$ cm.

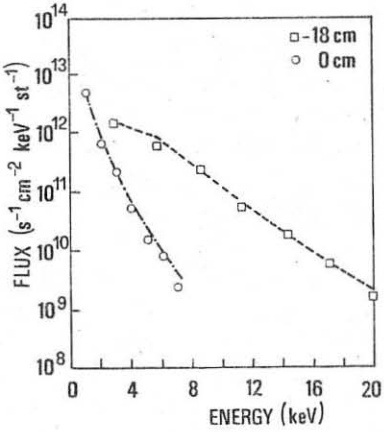


Fig. 3 - Simulation of D emission at $\bar{n} = 1.4 \times 10^{14}$ cm^{-3}.

TOROIDAL AND ELECTRICAL FIELD EFFECTS ON CURRENT DRIVE IN TOKAMAK BY LH-WAVES AND BY ECR-WAVES

Yu.N.Dnestrovskij, V.V.Parail
I.V.Kurchatov Institute of Atomic Energy, Moscow, USSR

D.P.Kostomarov, A.A.Luk'yanitsa, A.P.Smirnov
M.V.Lomonosov Moscow State University, Moscow, USSR

1. The current drive by LH-waves and by ECR-waves has been studied theoretically in some papers /1-5/. In a given paper we consider some new effects. A two-dimensional kinetic equation for the electron distribution function in a range of high velocities, $v \gg v_e = (2T/m)^{1/2}$, serves as the basis for a model.

$$\frac{\partial f}{\partial t} - \frac{eE}{m}\frac{\partial f}{\partial v_\parallel} = L_{st}[f] + L_{HF}[f] + L_{tr}[f] \qquad (1)$$

where, L_{st} is the linearized Landau-Fokker-Planck operator, $L_{HF} = L_{LH} + L_{EC}$,

$$L_{LH}[f] = \frac{\partial}{\partial v_\parallel}\left(D_{LH}\frac{\partial f}{\partial v_\parallel}\right), \quad L_{EC}[f] = \frac{1}{v_\perp}\frac{\partial}{\partial v_\perp}\left(v_\perp D_{EC}\frac{\partial f}{\partial v_\perp}\right), \qquad (2)$$

E is the external electric field, $e > 0$. The operator L_{tr} describes (in averaged form) the trapped particles in the toroidal trap.

$$L_{tr}[f] = \frac{1}{\sin\theta}\frac{\partial}{\partial\theta}\left(\gamma(\theta)\sin\theta\frac{\partial f}{\partial\theta}\right), \quad \gamma(\theta) = \begin{cases} 1/\tau_B & |\pi/2-\theta| < \theta_0 \\ 0 & |\pi/2-\theta| > \theta_0 \end{cases} \qquad (3)$$

θ is the pitch angle, $\tau_B \sim qR/v_e\sqrt{\varepsilon}$ is the electron bounce period, $\varepsilon = a/R$, $\theta_0 \sim \sqrt{\varepsilon}$ is a parameter characterizing the region occupied by trapped particles. We assume the quantities env_e, nT/τ, $ev_e\tau/T = 4/E_{cr}$ and v_e^2/τ as the units for a current j, power P, efficiency $\zeta = j_{HF}/P_{HF}$ and for a diffusion coefficient D_{HF} respectively, where $\tau = m^2v_e^3/4\pi ne^4L$. The problem (1)-(3) was solved numerically within the reference frames (v, θ) and $(v_\perp, v_\parallel)$ with a boundary condition f=0, at $v = v_{max} \sim (7-10)v_e$
The "reference" spectra were used for the waves
$D_{HF} = const$ at $u_1 < u < u_2$, $D_{HF} = 0$ at $u < u_1$ and $u > u_2$

where $U = v_{\parallel}/v_e$.

2. Toroidal effects. They are important for ECR-waves, resulting in an increase in the transversal energy of electrons and in the transition of particles to the banana orbits. As a result, the efficiency of current drive, $S = j_{EC}/P_{EC}$, decreases. The dependences of S on $\mathcal{D}_{EC}$ at different θ_0 for $U_1=2.8$; $U_2=3.5$; $Z=Z_{eff}=1$ are given in Fig.1. The curve for $\theta_0=0$ is in agreement with the results from /2/. The values of S at low $\mathcal{D}_{EC} \lesssim 10^{-2}$ in the dependence on U_1, are given in Fig.2. The results from /3/ are shown as a dashed line obtained on the assumption that a uniform heating across the whole magnetic surface takes place. Until now, it was considered /2/ that with a rise in $\mathcal{D}_{EC}$, the efficiency S also noticeably rose. One can see in Fig.1 that this effect is absent at $\theta_0 \gtrsim 15^\circ$ (that corresponds to $\varepsilon \gtrsim 0.1$ under heating from the low-field side of the torus).

3. Induced conductivity. Let $\gamma = E/E_{cr}$, $j = j(\gamma, \mathcal{D}_{HF})$ be the total plasma current, $j_{SP} = j(\gamma, 0)$, $j_{HF} = j(0, \mathcal{D}_{HF})$, $j = j_{SP} + j^0_{HF} + j_1$. The current drive efficiency is a quantity $S = (j - j_{SP})/P_{HF}$, where P_{HF} is the absorbed power of the waves. Let the parameter $\hat{u}$ characterize the position of resonance region. Let us introduce a variable $\xi = \hat{v}/v_R$ where $\hat{v} = \hat{u} v_e$, $v_R = -\gamma v_e/|\gamma|\sqrt{2|\gamma|}$ is the run-away velocity. The current j_1 exponentially depends on γ: $j_1 = j^0_{HF}[\exp(\alpha\gamma) - 1]$. The parameter α has a weak dependence on $\mathcal{D}_{HF}$. At $\alpha\gamma \ll 1$, $j_1 \approx \alpha\gamma j^0_{HF} = \sigma_1 E$. The value σ_1 referred as an "induced conductivity", is determined by the effect of waves on the electron distribution function: $\sigma_1 \to 0$ at $\mathcal{D}_{HF} \to 0$. The dependence of α on U_1, at $\mathcal{D}_{HF} = 0.1$ for LH-waves and for ECR-waves is shown in Fig,3. Using the ideas from /4/, one can obtain asymptotic relationships, valid at $U_1 \gg 1$. In particular,

$$\alpha_{LH} = \left(1 + \frac{2}{Z+3}\right) U_1^2 + \frac{4}{Z+5}\left(U_1^4 + \frac{15}{4} U_1^2\right) \qquad (4)$$

The dependences (4) for LH-waves and for ECR-waves are given

as dashed lines in Fig.3. Note that the main terms proportional to $4/Z+5$ are omitted in /4/ by mistake.

4. Current ramp up. Kirchhoff's equation and Ohm's law for a plasma column in the presence of LH-waves and at short-circuited primary winding have a form: $L\frac{dI}{dt}+U=0, U=I_{SP}R=(I-I_{LH})R$. Hence

$$\bar{\chi}=\frac{\frac{1}{2}L\frac{dI^2}{dt}+U^2/R}{P_{LH}}=-\frac{I_{LH}U}{P_{LH}}=-4\gamma\bar{S} \qquad (5)$$

where $\bar{S}$ is the efficiency averaged over the plasma cross-section. Let us consider the behaviour of a function $\chi=-4\gamma S=-\frac{\gamma}{|\gamma|}\xi^2\varphi$ where $\varphi=\frac{2S}{\hat{u}^2}=\varphi(\xi,\hat{U},\mathcal{D}_{LH},Z)$. The calculations show that the function φ has a weak dependence on $\hat{U}$; $\varphi\approx\varphi_0(\xi,\mathcal{D}_{LH},Z)=\lim_{\hat{u}\to\infty}\varphi(\xi,\hat{U},\mathcal{D}_{LH},Z)$, at rather high $\hat{U}$ in a range $|\xi|\le 1-1.5$. The curves for a function $\chi^0=-\gamma\xi^2\varphi_0/|\gamma|$ at $\mathcal{D}_{LH}=0.1$ and 5; Z = 1 and 5 are given in Fig.4. The results of calculations from /5/ are shown as dashed lines for Z=5, they are valid at $\mathcal{D}_{LH}\ll 1$. At the transition to a higher level of power ($\mathcal{D}_{LH}>1$), the efficiency rises. With a rise in $\mathcal{D}_{LH}$, the type of a dependence S on Z is changed. The efficiency decreases as $1/Z+5$ with a rise in Z at $\mathcal{D}_{LH}\ll 1$. The efficiency is almost constant or slightly rises with a rise in Z, at $\mathcal{D}_{LH}>1$. As a result, the efficiency at $\mathcal{D}_{LH}=5$, Z=5 more than two times exceeds that at $\mathcal{D}_{LH}\ll 1$, Z=5, with which the experiments on PLT have been analyzed in /5/.

References

1. C.F.F.Karney, N.J.Fisch, Phys. Fluids, 22 (1979) 1817.
2. C.F.F.Karney, N.J.Fisch, Nucl.Fusion, 21 (1981) 1549.
3. J.G.Cordey, T.Edlington, Plasma Phys., 24 (1982) 73.
4. N.J.Fisch, Preprint PPPL-2108 (1984).
5. C.F.F.Karney, N.J.Fisch, F.C.Jobes. Preprint PPPL-2152 (1984).

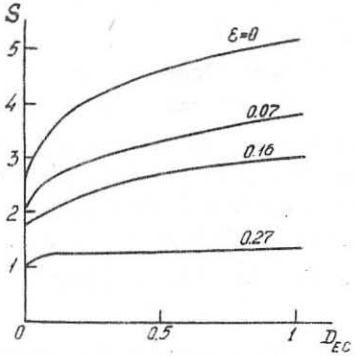


Fig 1

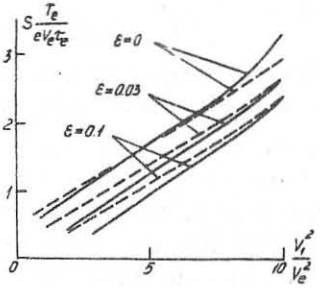


Fig 2

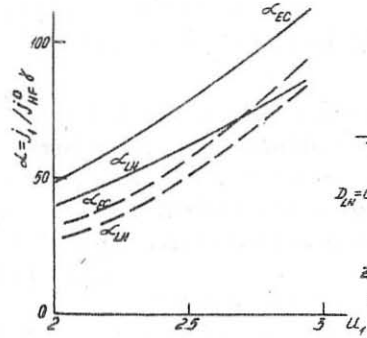


Fig 3

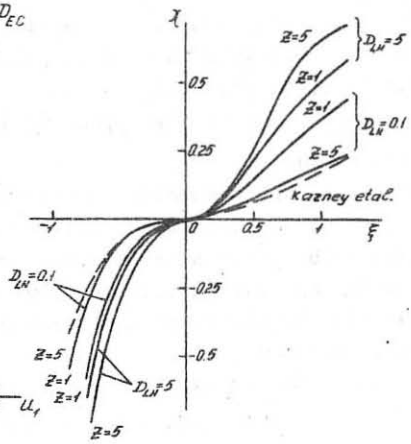


Fig 4

CURRENT DRIVE BY NONUNIFORM EXTERNAL FORCES

K.N.Stepanov, V.D.Yegorenkov

Kharkov Institute of physics and Technology of the Ukrainian Academy of Sciences, 310108 Kharkov, USSR

Abstract. The current drive by damping waves travelling along the discharge axis is considered. For the case of frequent collisions the current flow is shown to involve the longitudinal electric field. The expressions for the current driven and the electric field as functions of the power absorbed by electrons are obtained.

If the damping length of a wave travelling along the torus is less than $2\pi R$ than in a collisional regime ($l_{coll} \ll R$) the current drive in the region where the wave is damped is shown to be accomplished by the appearing longitudinal potential electric field.

In the report presented the current density and the potential electric field distribution are obtained for the plasma cylinder with identical ends when the force acting on electrons and causing the current is distributed nonuniformly. The plasma is described by the two-fluid hydrodynamic equations (α= e,i)

$$d(nV_\alpha)/dz = 0, \quad (1)$$

$$m_e n V_e dV_e/dz = -dp_e/dz - enE + R + f(z), \quad (2)$$

$$m_i n V_i dV_i/dz = -dp_i/dz + enE - R - \nu_i n m_i V_i, \quad (3)$$

$$\frac{3}{2} nV_\alpha \frac{dT_\alpha}{dz} + p_\alpha \frac{dV_\alpha}{dz} = -\frac{dq_\alpha}{dz} + Q_\alpha + P_\alpha(z) - \nu_E^\alpha nT_\alpha, \quad (4)$$

$$p_\alpha = nT_\alpha, \quad R = -m_e n \nu_e (V_e - V_i) - 0{,}71\, n\, dT_e/dz,$$

$$q_e = 0{,}71\, nT_e (V_e - V_i) - \varkappa_\parallel^e dT_e/dz, \quad \nu_e = 0{,}51/\tau_e,$$

$$q_i = -\varkappa_\parallel^i dT_i/dz, \quad Q_i = \nu_E n (T_e - T_i), \quad \nu_E = (3m_e/m_i)/\tau_e,$$

$$Q_e = -R(V_e - V_i) - \nu_E n (T_e - T_i)$$

The force $f(z) = \sum_k (k/\omega) P(k_\parallel, z)$ where $P(k_\parallel, z)$ is the power absorbed by the unit volume electrons, ν_i describes the momentum loss rate by ions due to e.g. viscosity. P_e and P_i are the heating

powers, $1/\nu_E^\alpha$ is the energy lifetime of α species, other notations are given elsewhere [1].

One should add to these equations the relations for the transverse momentum components for electrons and ions which in line with Eqs.(1)-(4) determine the heat and particle fluxes across magnetic surfaces. The force f(z) is determined by the rate with which the electromagnetic waves are absorbed. Therefore one should add Maxwell equations to basic equations. Even when the field amplitudes are small and linear approach is valid the absorbed power distribution over radius may essentially depend on the rotational transform and the toroidal displacement of the column which in the case considered are in turn determined by the RF field distribution. Thus the problem of stationary equilibrium in a tokamak with RF current drive in a self consistent approach involves a strongly nonlinear system of transport equations for the electron and ion momenta, heat and particles and Maxwell equations in which the RF current density (Dielectric tensor components) are in their turn functions of the RF field amplitudes through their dependence on density and temperature.

We restrict ourselves to that part of the stationary distribution problem which deals with the current flow along the magnetic lines considering the radial dependences of all magnitudes as if they were known.

The simple formula for the current driven may be obtained if the following condition holds

$$\gamma^{-1} \equiv \frac{2\pi R f}{n T_e} \sim \frac{u}{v_{Te}} \frac{L}{l_e} \ll 1 . \qquad (5)$$

Here l_e is the mean free path of electrons, v_{Te} is their thermal velosity, u is the current velocity, L is the characteristic length of change of f(z). For simplicity we consider the heating sources which do not drive the current to be uniformly distributed along z . The presence of the f force leads to small deviations δT_α, δn from average (not depending on z) values $T_{\alpha o}$, n_o, to the electric field E and the driven current density. In the zeroth approximation we obtain

$$n_o T_{eo} = \frac{\nu_\varepsilon + \nu_E^i}{\nu_\varepsilon (\nu_E^e + \nu_E^i) + \nu_E^e \nu_E^i} \left(\frac{\nu_\varepsilon}{\nu_\varepsilon + \nu_E^i} P_i + P_e \right), \qquad (6)$$

$$n_0 T_{i0} = (P_i + \nu_\varepsilon n_0 T_{e0}) / (\nu_\varepsilon + \nu_E^i). \quad (6)$$

In the first approximation we obtain from Eqs.(2) and (3) the current density, the density perturbation and the electric field:

$$j = -(\sigma_0 / e n_0) \bar{f}, \quad \bar{f} \equiv \oint f(z) dz / (2\pi R), \quad \sigma_0 = e^2 n_0 / m_e \nu_e, \quad (7)$$

$$\delta n = \Big[\int_0^z (f - \bar{f}) dz - n_0 (\delta T_e + \delta T_i) \Big] / (T_{e0} + T_{i0}^-), \quad T_{i0}^- = T_{i0} - m_i V_{i0}^2, \quad (8)$$

$$E = \Big[T_{e0} \frac{d\delta T_i}{dz} - (0{,}71 T_{e0} + 1{,}71 T_{i0}^-) \frac{d\delta T_e}{dz} + T_{i0}^- \frac{(f - \bar{f})}{n_0} \Big] / e (T_{e0} + T_{i0}^-). \quad (9)$$

If the current is driven by LH waves damped due to electron -ion collisions then the f force becomes

$$f(z) = \sum_{\vec{\kappa}} \frac{\kappa_\parallel}{\omega_0 \tau_e} \left(\frac{\omega_{pe}^2}{\omega_{ce}^2} + \frac{\kappa_\parallel^2}{\kappa^2} \frac{\omega_{pe}^2}{\omega_0^2} \right) \frac{|\vec{E}^{\sim}|^2}{8\pi}, \quad (10)$$

where $\omega_0^2 = (\omega_{pe}^2 \kappa_\parallel^2 / \kappa^2 + \omega_{pi}^2) / (1 + \omega_{pe}^2 / \omega_{ce}^2)$. $\vec{E}^{\sim}$ is the amplitude of the wave electric field. For $\omega_{pe} \ll \omega_{ce}$ the formula (7) coincides with the result obtained in [2] aside from a numerical factor.

To find δT_e and δT_i we obtain on neglecting the convection terms the equations

$$\varkappa_\parallel^e \frac{d^2 \delta T_e}{dz^2} + a_{11} \delta T_e + a_{12} \delta T_i + F_e = 0, \quad (11)$$

$$\varkappa_\parallel^i \frac{d^2 \delta T_i}{dz^2} + a_{21} \delta T_e + a_{22} \delta T_i + F_i = 0, \quad (12)$$

$$a_{11} = a_e S_e, \quad a_{12} = a_i S_e, \quad a_{21} = a_e S_i, \quad a_{22} = a_i S_i,$$

$$a_\alpha = \Big(\frac{n_0}{T_{e0} + T_{i0}} \frac{\partial}{\partial n} - \frac{\partial}{\partial T_\alpha} \Big), \quad S_\alpha = \pm \nu_\varepsilon n (T_e - T_i) + \nu_E^\alpha n T_\alpha,$$

$$F_e = \delta P_e(z) - \int_0^z (f - \bar{f}) dz \, (\partial S_e / \partial n) / (T_{e0} + T_{i0}^-),$$

$$F_i = \int_0^z (f - \bar{f}) dz \, (\partial S_i / \partial n) / (T_{e0} + T_{i0}^-).$$

If $l^2 / L^2 \ll \nu_E^\alpha / \nu_e$, $\nu_E^\alpha \sim \nu_\varepsilon$, then the heat transfer along the magnetic field due to thermoconductivity is negligible and

$$\delta T_e = (F_i a_{12} - F_e a_{22}) / (a_{11} a_{22} - a_{12} a_{21}), \quad (13)$$

$$\delta T_i = (F_e a_{21} - F_i a_{11}) / (a_{11} a_{22} - a_{12} a_{21}). \quad (14)$$

To the order of magnitude, $T_e \sim T_i$,

$$\delta n/n \sim \delta T_e/T_e \sim \delta T_i/T_i \sim \gamma^{-1}. \qquad (15)$$

Thus neglecting the thermoconductivity gives us E described by Eq.(9) in which all three terms are equal to the order of magnitude.

If $\sqrt{m_i/m_e}\,\nu_E^{\alpha}/\nu_e \gg \ell^2/L^2 \gg \nu_E^{\alpha}/\nu_e$ then one must account for the electron thermoconductivity only and the ion thermoconductivity may be neglected. Then

$$\delta T_i = -F_i/a_{22}, \qquad (16)$$

$$\delta T_e = -(\varkappa_{\parallel}^e/a_{11})\overline{F(z)} + z\overline{[F(z)(z-2\pi R)]} + \int_0^z F(z_1)(z-z_1)\,dz_1, \quad F(z) = (F_e a_{22} - F_i a_{12})/(\varkappa_{\parallel}^e a_{22}). \qquad (17)$$

In this case $d\delta T_e/dz \ll d\delta T_i/dz$ and we may omit the term $\sim\delta T_e$ in the formula (9).

If $\sqrt{m_i/m_e}\,\nu_E^{\alpha}/\nu_e \ll \ell^2/L^2$ then the temperature gradienta of electrons and ions are small due to large thermoconductivity and the electric field is determined from Eq.(9) in which one should put $\delta T_e = \delta T_i = 0$. In the region where the wave field is damped $E \sim j/\sigma_0$. This value has the same order of magnitude as the solenoidal electric field required to sustain the configuration given. If the f force is localized in the narrow region $\Delta z \ll 2\pi R$ then $E \sim (j/\sigma_0)(2\pi R/\Delta z) \gg j/\sigma_0$ in it. Besides in this region the E field is directed opposite to the E field direction on the main part of the torus.

The results obtained are applicable to the current drive in the low temperature plasma, e.g. for the data from [2] $j \sim 1$ mA/cm^2, $n \sim 10^{11}$ cm^{-3}, $T_e \sim 1$ eV, $E \sim 3\cdot 10^{-5}$ V/cm.

References

1. Braginskii S.I. in Rev. of Plasma Phys.(Consultants Bureau, New York, 1965). vol.1.
2. McWilliams R. et al. Phys. Rev. Lett. 14 n.4 (1980) p.245.

EFFECT OF THE TOROIDAL MAGNETIC FIELD ON THE CURRENT DRIVE IN TOKAMAKS WITH TRAVELING WAVES

V.S.Belikov, Ya.I.Kolesnichenko, I.S.Plotnik

Institute for Nuclear Research, Ukrainian SSR
Academy of Sciences, Kiev, USSR

Abstract: Equations describing the trapped particle-wave interaction in a tokamak are obtained. The influence of the trapped electrons on the current drive with Alfven waves is discussed.

Derivation of the equations (outline). It was concluded in Ref. [1] that the quasi-linear theory does not describe absorption of the RF field energy by the trapped particles in tokamaks because of the specific resonant condition $\omega = s\omega_b$ (ω is a wave frequency, s is an integer, ω_b is a bounce frequency). Hence, the problem of derivation of equations which suitable for studying the RF heating of the trapped particles exists. Such equations are obtained in a present work.

The equation of the electron motion in a superposition of the tokamak magnetic field, $\vec{B} = B_0(1-\epsilon\cos\theta)(0, \epsilon/q, 1)$ and the wave electric field $\tilde{E}_\parallel = E_0 \cos(k_\parallel q R - \omega t)$ can be presented as follows:

$$\ddot{\theta} + \sin\theta = \alpha \cos(\lambda\theta - \nu\tau) \qquad (1)$$

Here we used the notations: $\epsilon = r/R$, r and θ are the radial and poloidal coordinates of the torus, q is the tokamak safety factor, $k_\parallel = (\vec{k}\cdot\vec{B})/B$, $\ddot{\theta} = d^2\theta/d\tau^2$, $\tau = \omega_{b0}t$, $\mu = v_\perp^2/2B$, $\omega_{b0}^2 = \epsilon\mu B_0/q^2R^2$, $\alpha = \omega_w^2/\lambda\omega_{b0}^2$, $\omega_w^2 = e k_\parallel E_0/m_e$, $\lambda = k_\parallel q R$, $\nu = \omega/\omega_b$.

Let us consider the case of $\alpha \ll 1$ and $\lambda \gg 1$. Then we can assume that the wave weakly perturbs the electron motion in the toroidal field and that perturbation takes place only in

points where $\dot{\theta}=\nu/\lambda$ (i.e. $\omega = K_{\parallel} V_{\parallel}$). It makes it possible to replace Eq.(1) by the following set of the difference equations:

$$\rho_{j+1}=\rho_j + \delta(\rho_j)\cos\left(\Psi_j+\frac{1}{2}\Omega(\rho_j)\right)\cos\left(\rho_j-\frac{1}{2}\Omega(\rho_j)\right) \quad (2)$$

$$\Psi_{j+1} = \Psi_j + \Omega(\rho_j) \quad (3)$$

where ρ is connected with the particle velocity, $\Psi=\nu\tau-\lambda\theta$ is the wave phase, δ is proportional to α , the subscript j characterizes time, the time interval between $j+1$ and j is equal to the bounce period. Eq.(3) yields the resonant condition $\Omega(\rho_s)=2\pi s$ (i.e. $\omega=s\omega_b$) which determines the resonant values of ρ_s . Near ρ_s the particle motion is characterized by the closed orbits in the phase plane (ρ , Ψ). The width of the region with closed orbits, $\delta\rho$, is proportional to $\sqrt{\delta}$, i.e. it raises when the wave amplitude increases. When $\delta\rho > \rho_{s+1} - \rho_s$ then the resonances overlap. The corresponding condition has the form:

$$\mathcal{K} \equiv \frac{\pi^2}{2}\,\frac{s^2\omega_w^2}{\lambda^2\omega_{bo}^2}\,J_s'(r) > 1 \quad (4)$$

where $J_s(r)$ is the Bessel function, $r=2\varkappa\lambda$, $\varkappa^2=\frac{\mathcal{E}-\mu B_0(1-\epsilon)}{2\epsilon\mu B_0}$. The overlap of neighboring resonances results in the dynamic randomization of the electron motion ensuring the electron heating. When $\mathcal{K} < 1$ Eq.(1) describes the periodic change of the particle energy.

It should be noted that Eq.(1) does not take into account the influence of the Coulomb collisions on the particle motion. But collisions are essential because they lead to a stochastic motion in the case of $\mathcal{K} < 1$, depending on the ratio τ_c/τ_ρ the various regimes being possible (τ_c is the time of the collisional randomization, $\tau_\rho \sim \tau_b \mathcal{K}^{-1/2}$ is the period of the wave phase change). To include collisions into analysis we use the approach developed in Ref.[2] for studying the plasma heating by cyclotron waces. The diffusion coefficient we find by means of the following expression:

$$D(\mathcal{E}) = \lim_{t \to \infty} \frac{\langle (\mathcal{E}_t - \mathcal{E}_0)^2 \rangle}{2t} \qquad (5)$$

where the brackets denote ensemble average. Calculations yield results given below.

The rules for getting the diffusion coefficient. When $\mathcal{K} < 1$ one can obtain $D(\mathcal{E})$ from equations of the quasi-linear theory [3] replacing $\delta(\omega - S\omega_b)$ by the following function:

$$\frac{\nu_* / \pi}{\nu_*^2 + (\omega - S\omega_b)^2} \quad \text{for} \quad \mathcal{K}^{3/2} \ll \nu_* \tau_b \ll 1 \qquad (6)$$

$$\frac{\nu_* \tau_b}{\mathcal{K}^{3/2}} \frac{\omega_p / \pi}{\omega_p^2 + (\omega - S\omega_b)^2} \quad \text{for} \quad \nu_* \tau_b \ll \mathcal{K}^{3/2}$$

where $\nu_* = S^2 \nu_c / \epsilon$, $\omega_p = \mathcal{K}^{1/2} / \tau_b$ is the frequency of the particle energy change, ν_c is the collisional frequency, $\tau_b = 2\pi / \omega_b$.

When $\mathcal{K} \gg 1$ a summation over the bounce-harmonics in the quasi-linear diffusion coefficient should be replaced by integration with approximation of the Bessel function by $J_S^2(r) = \frac{2}{\pi} (r^2 - S^2)^{-1/2} \cos^2(\ldots)$ (the similar rule takes place in the theory of the plasma heating by a lower hybrid wave [4]).

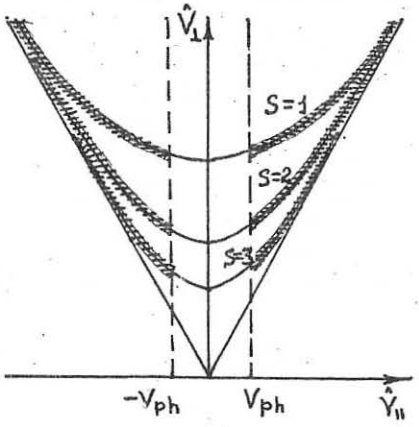


Fig.1. The curves which follow from the resonant condition $\omega = S\omega_b(\hat{V}_\perp, \hat{V}_\parallel)$ where $\hat{V}_\parallel = V_\parallel(\theta = 0)$, $\hat{V}_\perp = V_\perp(\theta = \pi/2)$. The hatched regions indicate the particles interacting with a wave in the case of $\mathcal{K} < 1$. $V_{ph} = \omega / K_\parallel$.

Role of the trapped electrons in a current drive with Alfven waves. The emergence of the trapped electrons during transition of a plasma to the banana regime may dramatically affect the RF current drive in a tokamak. Actually, it results in the necessity to increase strongly the amplitudes of an electromagnetic field (in order to keep a plasma current unchanged). This is explained by that circumstance that in the regime without trapped particles the Alfven wave driven current is carried mainly by the thermal electrons with small longitudinal velocities. In the case when distribution function of the circulating electrons is essentially disturbed in the resonant region ($\frac{\partial f}{\partial v_{\parallel}} \ll \frac{v_{\parallel}}{v_e^2} f$) the wave amplitudes should be increased by a factor of ($\frac{1}{A}\frac{r}{a}\frac{v_e^2}{v_A^2}$)^2 where $v_e = \sqrt{T_e/m_e}$, is the Alfven velocity, a is the plasma radius.

In addition, the presence of the trapped particles leads to decreasing the efficiency of driving current because of the curving of the boundaries of the resonant region [1] and the absorption of an energy of the RF fields. To find the power absorbed by the trapped electrons one can use the obtained above equations. It is clear that a value of decreasing efficiency depends on the parameters of a tokamak and system of the RF power input.

References.

1. V.S.Belikov, Ya.I.Kolesnichenko, I.S.Plotnik. Nucl. Fusion, 22,1559(1982).
2. A.V.Timofeev. Fizika Plazmy, 1,88(1975).
3. V.S.Belikov, Ya.I.Kolesnichenko. Plasma Physics, 24,61(1982)
4. C.F.F.Karney. Phys. Fluids, 22,2188(1979).

INFLUENCE OF TOROIDAL EFFECTS ON PROPAGATION OF LOWER-HYBRID WAVES IN PLASMA

S.V.Neudachin, V.V.Parail, G.V.Pereverzev, R.V.Shurygin

I.V.Kurchatov Institute of Atomic Energy,
Moscow, USSR

The important feature of the lower-hybrid wave propagation in a toroidal plasma is a deformation of the wave spectrum launched by a moderating wave-guide set. A ray-tracing technique (approximation of geometrical optics) is widely used /1,2/ at present to study this effect. However, this approach describes only the motion of a maximum in the wave envelope and does not allow to take the account of such effects as the envelope spread, interference of the waves, excitation of natural oscillations etc. Moreover, the ray-tracing technique is inapplicable to the waves with low poloidal wave number, and therefore it cannot describe the RF-energy penetration into the plasma column centre. A wave approach to the problem of lower-hybrid wave propagation is free from the drawbacks mentioned. However, the direct solution of a wave equation /3/ is a rather time-consuming problem, as the wave length in the frequency range under consideration is less than the plasma size by two-three orders of magnitude. A simplified equation which allows, on one hand, to reduce considerably the number of calculations in comparison with the full wave problem and, on the other hand, to provide an analytical description of some important peculiar features of the wave propagation has been obtained in a given work.

A wave equation for rather-moderated lower-hybrid waves ($N_\parallel^2 \gg 1$) can be written in a potential approximation, $div(\varepsilon\, grad\,\Phi)=0$. Expanding the solution into a Fourier series in terms of the toroidal angle φ and the poloidal angle θ, $\Phi(r,\theta,\varphi) = \sum_m \Phi_m(r) \exp(im\theta - in\varphi)$ and assuming that the plasma density and the safety factor depend on a minor radius only, one obtains a set of ordinary differential equations for separate poloidal harmonics /3/. There is a large parameter, $\omega_{pe}/\omega\, k_\parallel r \gg 1$, in this set, that allows to use a quasi-classical approximation with respect

to r . Seperating a fast-oscillating part of the solution,

$$\Phi_m(r) = A_m(r)\exp\left(i\int k_m dr\right)$$ where

$$k_m r = \pm\sqrt{\alpha^2\epsilon^2(n+m/q)^2 - m^2} \qquad (1)$$

$\alpha = \omega_{pe}/\omega$, $\epsilon = r/R_0$ is the inverse aspect ratio, one obtains a set of equations for slowly-varying functions

$$i\left(2k_m r^2\frac{dA_m}{dr} + A_m r\frac{d(rk_m)}{dr}\right) = \epsilon\left(F_{m+1}A_{m+1} + F_{m-1}A_{m-1}\right) \qquad (2)$$

Here $$F_{m\pm1} = \left[\frac{i}{2}k_{m\pm1}r - \alpha^2\epsilon^2\left(n+\frac{m\pm1}{q}\right)n + \left(1-\frac{\alpha^2\epsilon^2}{q^2}\right)\frac{1\pm m}{2}\right]e^{i\int(k_{m\pm1}-k_m)dr}$$

In the derivation of (2), it is taken into account that

$$\alpha \gg 1\,,\quad n \gg 1\,,\quad \epsilon \ll 1\,,\quad k_m r \gg 1.$$

The further simplifications in the set (2) one can make for a case when $m \gg 1$. The right-hand side of Eq.2 can be considered for this limit as a difference derivative with respect to m . Substituting the finite differences by their differential analogues, let us write the equation of the lower-hybrid wave propagation as the Schrödinger equation:

$$2ik r^2\frac{\partial A}{\partial r} = \epsilon\left\{-\alpha^2\epsilon^2\left(n+\frac{m}{q}\right)n\cos\chi\,\frac{d^2A}{dm^2} - 2i\alpha^2\epsilon^2 n\left(n+\frac{m}{q}\right)\sin\chi\,\frac{\partial A}{\partial m}\right\} \qquad (3)$$

Here, $\chi = \int\frac{dk}{dm}dr$, $K = K_m(r)$, $A = A_m(r)$ are the functions of two variables. In the derivation of (3), it is taken into account that $\partial^2(kr)/\partial m^2 \ll 1$. One should remember that Eq.(3) is valid for a wide (with respect to m) wave envelope, as $A_m = A_m(r)e^{i\chi}$ and an inequality $A_{m+1} - A_{m-1} \simeq 2\frac{\partial A}{\partial m}$ is violated, when the phases of adjacent harmonics differ by a value of the order of π . Nevertheless, one can conclude from (3) that the diffusion of a spectrum with respect to m not taken into account in the ray-tracing technique, can be as much important as convection. Let us now analyze Eq. (1) more attentively. An area of propagation for strongly-moderated lower-hybrid waves vs. the parameters m/nq and $\beta = \alpha\epsilon/q$ is shown in Fig.1. The inaccessability area, where $k_m^2 < 0$, is shown as a shaded one. It follows from the Figure that two principally-different situations take place, dependent on the β -value (which reaches its maximum at about a half of the plasma radius, $\beta_0 = \beta(a/2)$ under real conditions).

Namely, only a slight broadening in the spectrum with respect to $K_{\parallel}$ is possible at $\beta_0 < 1$, as only the waves with $-\alpha\varepsilon/(\alpha\varepsilon+q) \leq m/nq \leq \alpha\varepsilon/(\alpha\varepsilon+q)$ or $|\Delta K_{\parallel}/K_{\parallel}| \leq \beta_0$ are found to be in the accessability area. In the opposite limit case $\beta_0 > 1$, an unlimited broadening in the spectrum with respect to m $m/nq \geq -\alpha\varepsilon/(\alpha\varepsilon+q)$ toward a rise in m is possible.

For a detailed analysis of the influence of toroidal effects on the wave propagation, the set (1)-(2) was numerically solved. The results of calculations for both cases are shown in Fig.2 ($\beta_0 < 1$) and in Fig.3 ($\beta_0 > 1$). The incident and reflected waves were matched by the asymptotics of Bessel functions, the presence of a superconducting surface at the boundary was assumed. In both cases, a narrow (with respect to m) spectrum corresponding to a wide (with respect to Θ) radiator at the low-field side of the torus was preset at the input into plasma. From Figures it follows that the deformation of lower-hybrid wave spectrum with respect to m is saturated for a few passages of the waves along the radius at $\beta_0 < 1$. In the opposite limit case, a strong transformation of the spectrum with respect to m takes places, that results not only in the redistribution of the lower-hybrid wave energy with respect to $K_{\parallel}$, but in a considerable increase in the fraction of RF-energy which does not penetrate into the plasma core. The further analysis requires the inclusion of damping mechanisms into the dispersion law for lower-hybrid waves. It is expected to be done in future. The calculations made allow to conclude that the suggested technique of calculation adequately represents the dynamics of the lower-hybrid wave propagation in the toroidal plasma, it is time-saving in the use of computers and free of the ray-tracing technique drawbacks.

References

1. Yu.F.Baranov, V.I.Fedorov, Pis'ma Zh. Tekh. Fiz., 800 (1978).
2. P.Bonoli, E. Ott, Phys. Fluids, 25, 359 (1982).
3. J.J.Schuss, PFC/JA-84-21, 1984.

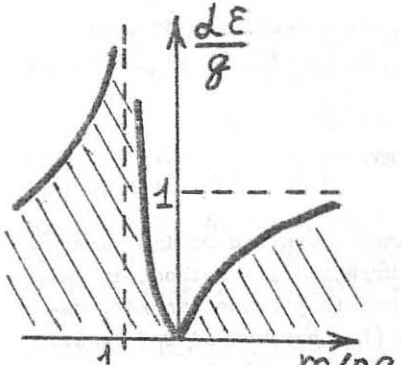


Fig.1

Fig.1. Area of propagation of LH waves.

Fig.2..Wave spectrum $|\Phi_m(r=a/2)|$ evolution for both the inward (solid curves) and outward (dashed curves) propagating waves. (K is the number of radial reflection at the plasma edge.) β =0.5.

Fig.3. Same as Fig.2, except that here β =2.5.

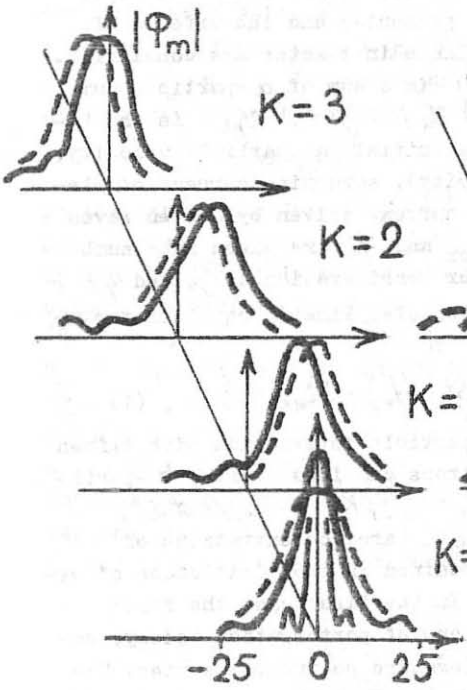


Fig.2

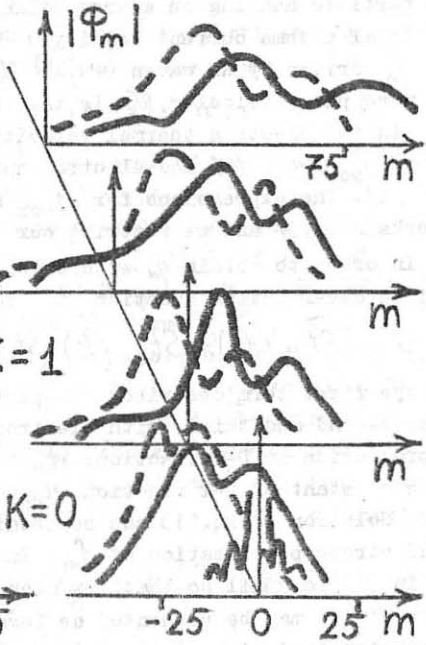


Fig.3

CURRENT DRIVE IN TOKAMAK-REACTOR DUE TO RF-HEATING OF α-PARTICLES

S.I.Krasheninnikov, T.K.Soboleva
I.V.Kurchatov Institute of Atomic Energy,
Moscow, USSR

Evident advantages of steady tokamak operation regime cause increasing interest in non-inductive current drive methods, in particular RF-methods /1-3/. One more method is proposed in /4/, making use of RF-heating of α-particles (the product of D-T reaction) by low frequency Alfven waves, and simple estimate of current drive efficiency $\eta_\alpha = |j_\alpha| / P_\alpha$ (j_α - current density, P_α - RF power needed to sustain this current), is made. In this paper more precise expression for η_α is presented and the effects of α - particle heating on energy balance in reactor are considered.

Total plasma current density j is a sum of α-particle current j_α driven by RF waves ($v_{ph} < v_\alpha \ll v_{Te}$, v_{ph} is the Alfven wave phase velocity, v_α is the initial α -particle velocity, v_{Te} is the electron thermal velocity), screening current of electrons $j_{scr} \sim j_\alpha$ /5/ and electron current driven by Alfven waves j_e /2/. The expressions for j_{scr} and j_e are given in a number of works /1,2,5/ and we restrict our consideration to j_α and η_α .

In order to obtain η_α we are to solve kinetic equation for α-particle distribution function f_α :

$$St_{\alpha h}(f_\alpha) + St_{\alpha,e}(f_\alpha) + St_{\alpha,i}(f_\alpha) + St_{\alpha R} = 0 \qquad (1)$$

Here the first term describes α-particle interaction with Alfven waves, second and third, with electrons and ions, forth, α-particle production in D-T reaction: $St_{\alpha R} = n_D n_T K \delta(v - v_\alpha)/4\pi v_\alpha^2$, K-rate constant of D-T reaction, n_D, n_T are concentrations of D and T. Solution of Eq.(1) can be obtained in two limit cases of weak and strong perturbation of f_α . In the first case the first term in (1) is small so that, by means of perturbation theory, solution of (1) may be presented as Legandre polinomial series. Under reactor conditions ($v_{Ti} \ll v_\alpha \ll v_{Te}$), $St_{\alpha,e}$ and $St_{\alpha,i}$ are considerably simplified and small correction to f_α can be obtain by means of the Green function found in /3/.

Thus the expression for η_α in the regime of magnetic pumping ($St_{\alpha,h}(f_\alpha) = \frac{\partial}{\partial v_\parallel} v_\perp^4 \mathcal{D}(v_\parallel) \frac{\partial f_\alpha}{\partial v_\parallel}$) takes the form:

$$\eta_\alpha = \eta_0 \tilde{\eta}_\alpha(w_{\alpha c}, u_0) \qquad (2)$$

To avoid effects of RF waves spectrum on η_α it was assumed that $\mathcal{D}(v_\parallel) \sim \delta(v_\parallel - v_0)$; $\eta_0 = v_\alpha^2 M_i / 4\pi\Lambda Z_\alpha Z_i n_e e^3$, $u_0 = v_0/v_\alpha$, $w_{\alpha c} = v_\alpha^3/v_c^3$, $v_c^3 = 3\sqrt{\pi}\, m\, v_{Te}^3 Z_i / 4 M_i$. When $w_{\alpha c} \gg 1$, $\tilde{\eta}_\alpha \sim 1/w_{\alpha c} u_0$. Numerical values of $\tilde{\eta}_\alpha(w_{\alpha c}, u_0)$ are given in Table 1. It can be shown that $\eta_\alpha \simeq \eta_e^{tor}$ (η_e^{tor} - current drive efficiency due to electron heating by low frequency Alfven waves /2/ with account for trapped electrons /1/).

In the second limit case (strong perturbation of f_α), it can be assumed that $\mathcal{D}(v_\parallel) \to \infty$ in the region $v_1 < v_\parallel < v_2$.

Then in this region $f_\alpha(\vec{v}) = \bar{f}_\alpha(v_\perp) + \delta f_\alpha$, where $|\delta f_\alpha| \ll \bar{f}_\alpha(v_\perp)$. In case when $v_1^3 \gtrsim v_c^3$ α- particle scattering on ions can be neglected and Eq.(1) takes the form:

$$\frac{\partial}{\partial v_\parallel} v_\perp^4 \mathcal{D}(v_\parallel) \frac{\partial f_\alpha}{\partial v_\parallel} + \nu_{\alpha e} \nabla_{\vec{v}} (\vec{v} f_\alpha) + St_{\alpha,R} = 0 \qquad (3)$$

In the expression for $St_{\alpha e}(f_\alpha)$ the terms of the order $T/\varepsilon_\alpha \ll 1$ are omitted; $\nu_{\alpha e} = 16\sqrt{\pi}\Lambda e^4 Z_\alpha^2 n_e^4 / 3 M_\alpha m v_{Te}^3$.
In what follows it is convenient to consider four regions in the velocity space: 1) $D - v_\perp \le v_\parallel \le v_2$ 2) $\tilde{D} - v_\perp/v_\parallel \le \sqrt{v_2^2 - v_1^2}/v_1, v_\parallel < v_1$; 3) $D_{(+)} - v_\parallel > v_2$; 4) $D_{(-)} - v_\perp/v_\parallel > \sqrt{v_2^2/v_1^2 - 1}$, $v_\parallel < v_1$. Since $St_{\alpha e}$ in (3) has the form $\nabla_v \vec{\Phi}_c$, where $\vec{\Phi}_c \sim \vec{v}$, then perturbation of f_α are carried by the flux $\vec{\Phi}_c$ towards coordinate origin. Therefore f_α is not affected by RF-waves in the regions $D_{(+)}$ and $D_{(-)}$, whereas in $\tilde{D}$-region f_α is totally defined by its value at the boundary between D and $\tilde{D}$-regions, i.e. at $v_\parallel = v_1$. Integrating (3) over $dv_\parallel$ from v_1 to v_2 and taking into account that $|\delta f_\alpha| \ll f_\alpha$, we obtain:

$$\Phi_{QL}\Big|_{v_\parallel = v_2} - \Phi_{QL}\Big|_{v_\parallel = v_1} = \frac{\Delta v}{v_\perp^2} \frac{d}{dv_\perp} v_\perp^3 \bar{f}_\alpha(v_\perp) + \int_{v_1}^{v_2} St_{\alpha R}\, dv_\parallel \qquad (4)$$

where $\Phi_{QL} = v_\perp^4 \mathcal{D}(v_\parallel) \frac{\partial \delta f_\alpha}{\partial v_\parallel}$, $\Delta v = v_2 - v_1$.
Taking into account continuity of f_α at $v_\parallel = v_1$ and particle flow conservation along $v_\parallel$ coordinate at $v_\parallel = v_1$, $v_\parallel = v_2$,

we obtain:

$$\Phi_{QL}\big|_{v_{\parallel}=v_1}=0\,;\quad \Phi\big|_{v_{\parallel}=v_2}=v_2\left(\bar{f}_\alpha(v_\perp)-f_\alpha(\bar{v}_\perp, v_2+0)\right), \tag{5}$$

where $f_\alpha(\bar{v}_\perp, v_2+0)$ is defined by undisturbed f_α in $D_{(+)}$ - region. Substituting (5) in (4) and solving differential equation, we obtain $\bar{f}_\alpha(v_\perp)$:

$$\bar{f}_\alpha(v_\perp)=\frac{\varkappa}{\Delta v\, v_\perp^{3-\ell}}\int_{v_\perp}^{\hat{v}_1}\frac{v_\perp'^{2-\ell}\,dv_\perp'}{\sqrt{1-(v_\perp'/v_\alpha)^2}}\quad,\ \hat{v}_2<v_\perp<\hat{v}_1 \tag{6}$$

$$\bar{f}_\alpha(v_\perp)=\frac{\varkappa}{\Delta v\, v_\perp^{3-\ell}}\int_{\hat{v}_2}^{\hat{v}_1}\frac{v_\perp'^{2-\ell}\,dv_\perp'}{\sqrt{1-(v_\perp'/v_\alpha)^2}}+\frac{\varkappa v_\alpha^{\ell}}{v_\perp^{3-\ell}}\int_{v_\perp}^{\hat{v}_2}\frac{v_\perp'^{2-\ell}\,dv_\perp'}{\left(v_2^2+v_\perp'^2\right)^{3/2}},\quad v_\perp<\hat{v}_2 \tag{7}$$

where $\ell=v_2/\Delta v$, $\hat{v}_\kappa=\sqrt{v_\alpha^2-v_\kappa^2}$, $\varkappa=\kappa n_{\mathcal{D}} n_T/4\pi v_\alpha^2\gamma_{\alpha e}$.
When f in D-region is known, it is easy to obtain distribution function in D-region and thus expressions for j_α and P_α -(RF-power, needed to sustain this current):

$$j_\alpha=j_*\frac{\Delta u^2}{2u_1}\quad,\ P_\alpha=P_*\frac{\Delta u^2}{2}\left(1+\frac{2}{3}\frac{\Delta u}{u_1}\right), \tag{8}$$

where $j_*=e v_\alpha P_*/\gamma_{\alpha e}\varepsilon_\alpha$, $u_\kappa=v_\kappa/v_\alpha$, $\Delta u=\Delta v/v_\alpha$,
$P_*=\kappa n_{\mathcal{D}} n_T \varepsilon_\alpha$ - thermonuclear power deposited in α-particles. Efficiency of current drive for $\Delta u/u_1$ in this case is about 3,5 times lower than η_e /2/, so that $\eta_e^{tor}/\eta_\alpha\simeq 3{,}5\,\eta_e^{tor}/\eta_e\le 1$ /1/.

Thus the efficiency obtained is rather high, however it must not be forgotten that RF heating of α-particles results in a considerable increase of their pressure and in an appropriate increase of $\beta=\beta_{\mathcal{D}+T}+\beta_\alpha$, where β_κ is the main plasma and α - particle contribution to the total β. Since β in tokamak is strongly limited, an increase in β_α results in a decrease of β_{D+T} and therefore in a considerable decrease of the reactor power. It can be easily shown that the change in β_α due to RF-heating is: $\delta\beta_\alpha=\beta_\alpha P_\alpha/P_*$. To drive the current in the tokamak with the INTOR parameters j_α is to be about the mean current density $j_0\simeq 200\,A/cm^2$. It can be seen from (8) that under optimal reactor conditions ($\bar{T}\simeq 10$ keV,

$n_e \simeq 10^{14}\,cm^{-3}$), $j_* \simeq 20 A/cm^2 \ll j_o$. To satisfy the consideration $j_\alpha \simeq j_o$ is is necessary to increase P_α , so that $P_\alpha \gg P_*$, which results in an increase of β_α and a decrease in the reactor output power.

Thus despite of high η_α , the method of current drive by means of RF-heating of α-particles seems to be not advisable due to sharp increase in β_α . It is to be noted that effects of β_α increase must also be taken into account in all cases, when current drive by means of RF-waves with low phase velocities $v_{ph} \ll v_{Te}$ /2,6/ in tokamak reactor is considered.

Table I

U_o	0,1	0,2	0,3	0,4	0,5	0,6	0,7	0,8
W_{dc} =5	$3,310^{-1}$	$1,810^{-1}$	$1,310^{-1}$	$1,110^{-1}$	$9,410^{-2}$	$8,610^{-2}$	$8,210^{-2}$	$9,710^{-2}$
W_{dc} =10	$1,710^{-1}$	$9,110^{-2}$	$6,610^{-2}$	$5,310^{-1}$	$4,610^{-2}$	$4,110^{-2}$	$3,810^{-2}$	$3,510^{-2}$
W_{dc} =30	$5,410^{-2}$	$2,910^{-2}$	$2,010^{-2}$	$1,610^{-2}$	$1,310^{-2}$	$1,110^{-2}$	$9,710^{-3}$	$8,910^{-3}$

REFERENCES

1. V.S.Belikov, Ya.I.Kolesnichenko, I.S.Plotnik. Nucl.Fus.22, 1982, 1559.
2. N.J.Fisch, C.F.F.Karney. Phys.Fluids, 24, (1981), 27.
3. S.I.Krasheninnikov, Fizika Plasmy, 9, (1983), 1201.
4. D.K.Bhadra, C.Chu. Phys.Rev.Lett., 48 (1982), 1824.
5. D.F.H.Start, J.G.Cordey, E.M.Jones. Plasma Phys., 22, (1980), 303.
6. T.Okazaki et al. Nucl.Fus. 24 (1984), 1451.

PARAMETRIC INSTABILITIES DURING THE LOWER HYBRID POWER INJECTION IN THE HIGH DENSITY REGIME OF THE FT TOKAMAK

R. Cesario, V. Pericoli-Ridolfini

Associazione EURATOM-ENEA sulla Fusione, Centro Ricerche Energia Frascati, C.P. 65 - 00044 Frascati, Rome, Italy

The electromagnetic emission from the FT deuterium plasma, during the lower hybrid heating experiments [1], in the range 0 ÷ 2.6 GHz has been studied. Regimes with different line average density ($\bar{n} = 0.3 \div 2.4 \times 10^{14} cm^{-3}$), toroidal field ($B_T$ = 60 kG and 80 kG), plasma current (I_p = 220 ÷ 600 kA) and RF power injected (f = 2.45 GHz; P_{RF} = 6 ÷ 300 kW) has been explored. The high frequency ($\gtrsim$ 1 GHz) portion of the spectrum was detected by means of four equal loop antennas placed outside the vacuum vessel at the end of two top and two bottom 1.2 m long vertical ports (Fig. 1). The low frequency portion was detected using a floating half limiter as an antenna. Typical high density spectra are reported in Fig. 2. The satellites (Fig. 2a) are rather regularly spaced by the ion cyclotron frequency relative to the outer plasma edge in agreement with previous measurements with an internal probe [2] . The main spectral characteristics studied are the pump broadening and intensity, the near (to the pump) and far satellites intensity at different plasma regimes. The distinction between near and far satellites comes from the typical spectrum (Fig. 2a) at the point where the convolution of the peaks intensities has a minimum. The importance of the far satellites has already been emphasized [2,4]. The principal results are summarized in Figs 3,4,5. Figure 3a shows the effects of varying the plasma density $\bar{n}$, at fixed plasma current and RF power. The main characteristics, found for each antenna, are the strong decrease of the pump signal with $\bar{n}$ and the different threshold densities for the near and far satellites. The pump intensity decrease, as seen also in Alcator C [3], can be attributed to worse penetration of the lower hybrid waves. The appearance at the same density value of strong pump broadening and far satellites suggests that a sudden change in the plasma periphery must occur. Moreover an abrupt variation of the far satellites RF power threshold at densities around $\bar{n}_{th}$ was found. In a very short range of density P_{th} changes from 10 kW for $\bar{n} > \bar{n}_{th}$ to values greater than 300 kW for $\bar{n} < \bar{n}_{th}$. The near satellites, instead, show a much milder behaviour, not in contrast with existing scaling laws [5], [6].

Measurements performed at different RF powers (P_{RF} down to 6 kW up to 300 kW) for $\bar{n} > \bar{n}_{th}$ suggest that pump depletion is likely to occur and that both pump broadening and low frequency spectrum broadening are quite independent of P_{RF}. It is an open question how much of these broadenings are due to scattering or to decay process into ion-sound quasi modes [3].

The increase of the plasma current at $\bar{n}$ = cost is observed to produce the same effects on all the above phenomena as the reduction of the plasma density at I_p = cost. This is believed to be connected [7] to modifications of the FT plasma edge with I_p. As an example Fig. 4 reports the variation of the threshold density $\bar{n}_{th}$ with I_p.

The importance the far satellites with regard to the RF induced effects on the FT plasma is stressed in Fig. 5. It is seen how any enhancement of neutron or fast neutrals fluxes disappears as they occur. In the case shown the perpendicular neutral analyzer is looking at the plasma edge in direction of the trapped ions drift. It is excluded therefore that fast ion tails are produced when the far satellites occur, even at the plasma border. By contrast the presence of the near satellites alone does not appreciably affect the interaction of the lower waves either with bulk electrons or ions.

In conclusion substantial differences are found between far and near satellites both in their properties, such as threshold densities and powers, and in the effects on the bulk plasma. It is yet to understand what so suddenly occurs at $\bar{n} = \bar{n}_{th}$ (far satellites) changing dramatically the RF propagation characteristics.

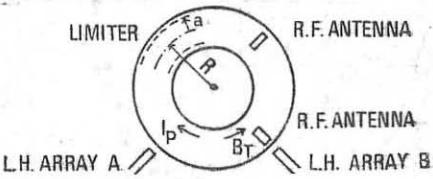


Fig. 1 - The FT Tokamak viewed from the top.

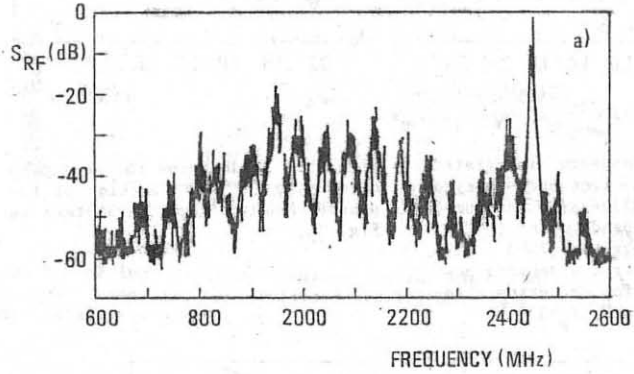


Fig. 2a - The frequency spectra of the ion-cyclotron sidebands in deuterium plasma at: $\bar{n} = 1.5\times10^{14}$ cm^{-3}, I_p =330 kA, B= 8 T, P^p_{RF} = 100 kW.

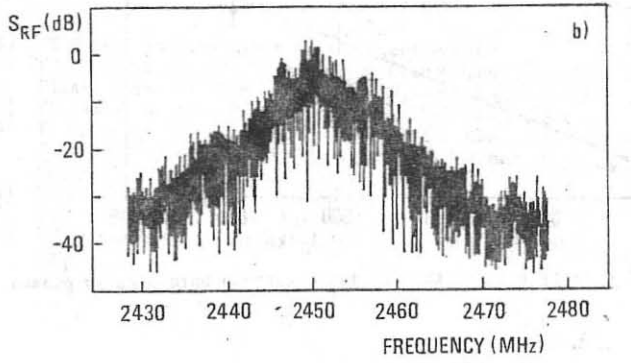


Fig. 2b - The pump frequency spectra. Same parameters as Fig. 2a.

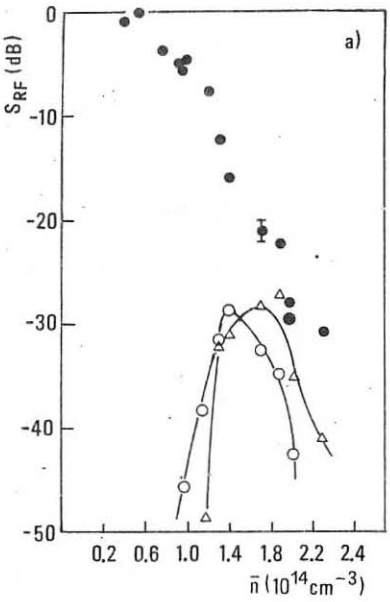


Fig. 3a - The frequency integrated pump power (●), the frequency integrated (2300÷2430 MHz) near(to the pump) ion-cyclotron sidebands power (○) and the frequency integrated (1600 ÷ 2295 MHz) far ion-cyclotron sidebands power (Δ) vs density for deuterium plasma, B=8 T, P_{RF}=100 kW, I_p=330 kA.

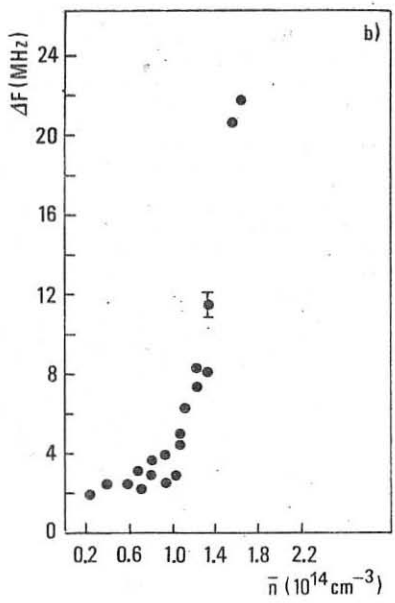


Fig. 3b - 10 dB below the peak pump broadening (ΔF) as function of the plasma density. Same parameters as Fig. 3a.

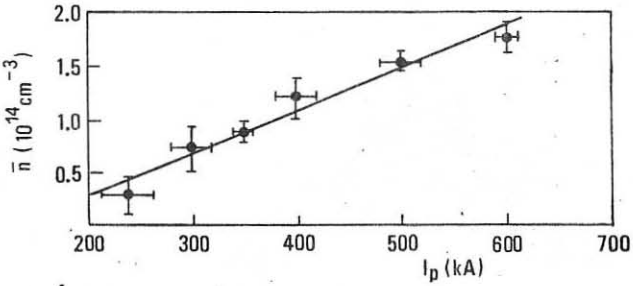


Fig. 4 - Threshold density $\bar{n}_{th}$ for the far ion cyclotron harmonics vs plasma current I_p.

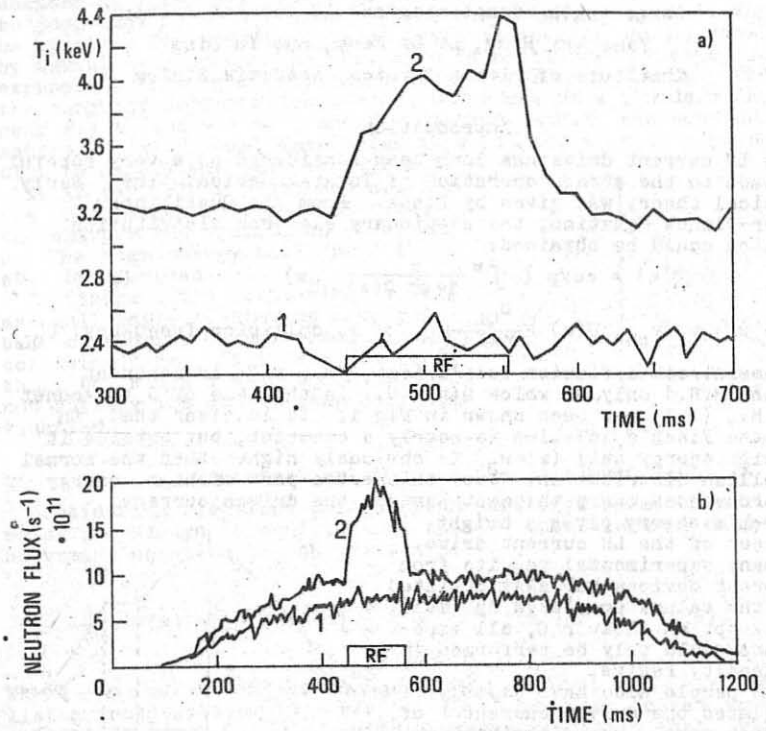


Fig. 5 - RF induced effects on: a) nuetral edge temperature; b) neutron flux. Curve 1: strong far ion cyclotron satellites present ($n > n_{th}$). Curve 2: only near satellited present ($n < n_{th}$).

REFERENCES

[1] FT Group, Invited Paper at this Conference
[2] F. Alladio et al., Proc. 11th Europ. Conf. on Controlled Fusion and Plasma Phys. (Aachen 1983) Vol. 7D, part I (1984) 281
[3] Y. Takase et al., Phys. Fluids 28 (1985) 983
[4] F. Alladio et al., Proc. 11th Europ. Conf. on Controlled Fusion and Controlled Fusion and Plasma Phys. (Aachen 1983), Plasma Phys. and Controlled Nucl. Fusion. 26 1a (1984) 157
[5] M. Porkolab, Phys. Fluids 20 (1977) 2058
[6] C.S. Liu et al., Phys. Fluids 27 (1984) 1709
[7] V. Pericoli-Ridolfini, Plasma Phys. and Controlled Fusion 27 (1985) 493.

Large Angle Scattering and LH Current Drive

Yang Wei Hong, Li Da Feng, Huo Yu Ping
Institute of Plasma Physics, Academia Sinica

Introduction

The LH current drive has long been considered as a very hopeful approach to the steady operation of Tokamak device. The early classical theory was given by Fisch. From the Quasilinear Fokker-Planck equation, the stationary electron distribution function could be obtained:

$$f(w) = c\exp\left(-\int^{w} \frac{x}{1+x^3 D(x)}\, dx\right) \qquad (1.1)$$

where $w = v_z/v_{th}$, $D(w) = \frac{D_{QL}}{\gamma w^3 v_{th}^2}$, γ is collision frequency, D_{QL} is quasilinear diffusion coefficient, $[w_1, w_2]$ is resonant region (R.R.) only in which $D(w) \neq 0$. In the case of $D_0 = Dw = \text{const}$ in R.R., (1.1) has been shown in Fig 1. It is clear that, in R.R. the Fisch's solution is nearly a constant, but outside it the high energy tail ($w > w_2$) is obviously higher than the normal Maxwellian distribution. Just this extra-part of high energy electrons does carry the most part of the driven current.

Fisch's theory gives a bright prospect of the LH current drive. But many experimental results from different devices far away deviated from the values predicted by (1.1), and except on Alcator C, all experiments could only be performed in low density regime.

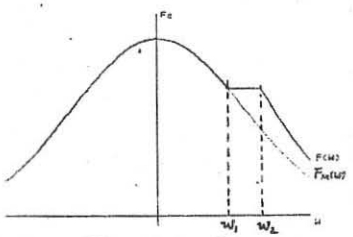


Fig 1.

Some people also have exactly calculated the driven current of coherent wave. The distribution obtained has a plateau in R.R., but the high energy tail doesn't be elevated. Thus, the current is very small and proportional to $E_{wav}^{3/2}$. It is very difficulty to believe that, non-coherent wave with a narrow band spectrum could lift all of the high energy tail of distribution, but a intensive monochromatic wave couldn't. Thus, the possibility of elevation of the high energy tail is the crux to understand the machanism of the current drive.

The large angle scattering

In Coulomb collision case, due to the smallness of the cross-section, the large angle scattering could usually be thought as negligible. The Fokker-Planck equation, which is the lowest order term of the expansion of Boltzmann equation in term of momentum exchange, describs the diffusion process in velocity space.

The quasilinear term makes the distribution in R.R. flatten, due to the requirement of continuity of distribution at w_1 and w_2, the Gauss-type distribution in region w w_2 should be elevated. This is the elevated high energy tail.

But though the cross-section is very small, the large angle scattering makes all electrons with $w > w_2$ to have the possibility to jump back to $w < w_1$ region, thus, the high energy tail should be spread. The effect of large angle scattering can be considered by taking into acount the next term in small angle scattering expansion. This is a small third order differential term. From the singular perturbation theory, there may be a boundary layer near $w = w_1$ and $w = w_2$, and the plateau in R.R. can continuously matche with nomal Maxwellian in $w < w_1$ and $w > w_2$. The solution is nearly the same as in Fig 2.

It is very clear that, the smaller the third order differential term, the sharper the tramsition at w_1 and w_2. The high energy tail doesn't ever be elevated.

The large angle scattering as well as small angle scattering have all been considered by Boltzmann integral collision term. It is easy to prove that, the Fisch's solution(1.1) does not satisfy the quasilinear Boltzmann equation.

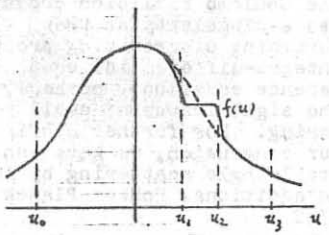


Fig 2.

Numerical solution of the Boltzmann equation

Considering electrons collide with particles of another kind, which are always in equilibrium, the 1-D quasilinear steady-state Boltzmann equation can be written as :

$$\frac{d}{dw} D(w) \frac{d}{dw} f(w) + \int_{-\infty}^{\infty} \left[e^{-w^2/2} f(w') - e^{-w'^2/2} f(w) \right] W(v_{e\beta})\, dw' = 0 \qquad (3.1)$$

Where $-\infty < u < \infty$, $W(V_{e\beta}) = a V_{e\beta} \sigma_{e\beta}$, $V_{e\beta} = |w' - w|$, $\sigma_{e\beta}$ is the collision cross-section, $w = v/v_{th}$. (3.1) has been solved numerically in region $[w_0, w_3]$ with boundary condition that, outside $[w_0, w_3]$ f(w) is Maxwellian:

$$f(w) = \begin{cases} a\, e^{-w^2/2} & w < w_0 \\ b\, e^{-w^2/2} & w > w_3 \end{cases} \qquad (3.2)$$

here $w_0 = w_1 - d$, $w_3 = w_2 + d$, d is large enough. A special wave spectrum $D(w) = \begin{cases} D & w_1 \le w \le w_2 \\ 0 & w < w_1 \text{ or } w > w_2 \end{cases}$ has been selected for the simplicity of calculation. Limiting the momentum exchange $v_{e\beta}$ smaller than a large value v_m, it could be proved that, the difference calculation is convergent and the solution is independent of d if d is large enough.

The solution has been shown in Fig 2. It is clear that, the distribution in R.R., similar to the Fisch's discussion, is nearly a plateau, but just outside the R.R. the two parts of distribution ($w < w_1$ and $w > w_2$) all restore quickly to a unique Maxwellian. The most attractive feature of Fig 3 is that, even we introduce different Maxwellian in regions $w < w_0$ and $w > w_3$ (b≠a in(3.2)), the solution of equation(3.1) in regions $(w_0 + \delta, w_1 - \delta)$ and $(w_2 + \delta, w_3 - \delta)$ still belong to the same Maxwellian, as shown in Fig 3,

here δ is a small number. Only very near w_0 and w_3, the solution jumps back to the values given by the boundary conditions. Thus, let $w_0 \to -\infty$, $w_3 \to \infty$ $(d \to \infty)$, the whole distribution will be determined uniquely without any elevated high energy tail. The driven current calculated from(3.1) is one or two order of magnitude smaller than the Fisch's value. For example, $w_1 = 10$, $w_2 = 11$ the ratio: J/JF = 0.0169.

It has been argued that, because the Coulomb collision cross-section has a singularty at $|w-w'| = 0$, the foregoing discretizing process (from integro-differential equation to difference equation), perhaps, plays down the significance of small angle scattering. For further confirming of our conclusion, we have enhanced the small angle scattering by introducing an additional Fokker-Planck term into (3.1)

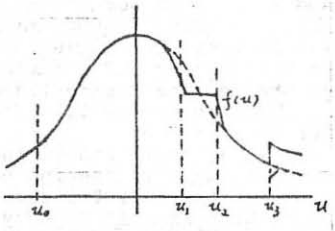


Fig 3.

$$\frac{d}{dw} D(w) \frac{d}{dw} f(w) + c \int_{w-v_m}^{w+v_m} \left[e^{-w'^2/2} f(w') - e^{-w^2/2} f(w) \right] \frac{dw'}{v_{e\beta}^3} + \alpha L_F f(w) = 0 \qquad (3.3)$$

where $L_F f(w) = C \frac{d}{dw} \left(\frac{1}{w^3} \frac{d}{dw} \frac{1}{w^2} \right) f(w)$ is the lowest order term of small angle scattering of Boltzmann integral term. Varying α from 1 to 10^4 , all the solutions of (3.3), except in small regions round u_1 and u_2 , are nearly the same as shown in Fig 2. Therefore, the effect of large angle scattering is similar a singular perturbation and, thus, can suppress the whole high energy tail of distribution.

We also have changed the wave spectrum (D(w)) and the numerical method of integration, except near u_1 and u_2 , the results remain the same.

All the above 1-D calculations show that, the LH wave can't elevate the high energy tail of distribution.

3-D case

The 3-D stationary Boltzmann equation is:

$$\frac{d}{d\vec{u_e}} D(u_e) \frac{d}{d\vec{u_e}} f_e(\vec{u_e}) + C \int [f_e(\vec{u_e}) f_\beta(\vec{u_\beta}) - f_e(\vec{u_e}) f_\beta(\vec{u_\beta})] v_{e\beta} \sigma_{e\beta} \, d\Omega \, d\vec{u_\beta} = 0 \qquad (4.1)$$

where $f_\beta(\vec{u_\beta})$ is assumed as Maxwellian, the integration is in a sphere of radius v_m centred at $\vec{u_e}$. Because the whole problem is axisymmetric, only two dimensions have to be calculated. Defining $g = f/f_{ae} - u_e^2/2$, the boundary conditions are:

$$\begin{cases} g(\vec{u}) = 1 & u_x \leq u_0 \text{ or } u_0 < u_x < u_3, |u_y| \geq r_0 \\ g(u) = k & u \geq u_3 \end{cases} \qquad (4.2)$$

The numerical solution of (4.1) and (4.2) has been obtained by the same method as in 1-D case, but of course, it is very

tedious. The final result has been shown in Fig 4. It is very similar to the solution in 1-D case qualitatively. Therefore the 3-D study doesn't change the conclusions from the 1-D calculation.

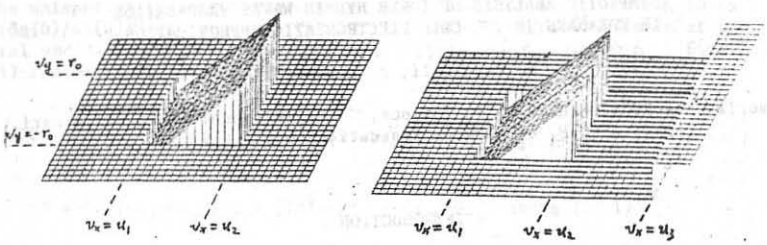


Fig 4.

Discussion

From the foregoing studies, it has been concluded that, considering the large angle scattering, the LH wave couldn't elevate the high energy tail of electron distribution, the plateau in resonant region is also lower than the value obtained by Fisch. Therefore, the driven current and efficiency obtained by quasi-linear theory are lower than the Fisch's results by one or two order of magnitude. This is the reason why the current drive couldn't be observed in high density discharges on most of the Tokamaks. Even on strong magnetic field device Alcator C, the high density driven current still was too low compared with the Fisch's prediction. The current drive observed in low density discharges is, perhaps, due to some other mechanisms such as, the toroidal effect, some instabilities and run-away electrons.

It is also very interesting that, the large angle scattering, though its cross-section is very small, plays a significant role in momentum transport processes.

Refferences

(1) N.J.Fisch, Phys. Rev. Lett., 41 (1978), 873
(2) S.Y.Yuen, et al., Nuclear Fusion 20 (1980), 159
(3) C.F.F. Karney, N.J.Fisch, Phys. Fluids 22 (1979)
(4) Z.G.An, C.S.Liu, Y.C.Lee, and D.A.Boyol, Phys. Fluids 25 (1982)

ASYMPTOTIC ANALYSIS OF LOWER HYBRID WAVES PROPAGATION IN TOKAMAKS IN THE COLD ELECTROSTATIC APPROXIMATION

A. Cardinali, F. Romanelli

Associazione EURATOM-ENEA sulla Fusione, Centro Ricerche Energia Frascati, C.P. 65 - 00044 Frascati, Rome, Italy

INTRODUCTION

The WKBJ analysis of the lower hybrid wave propagation [1-4] in thermonuclear plasmas has gained in the last years a widespread interest owing to the understanding of the experimental results on this field [5]. Two equations, for the phase S and for the amplitude A are deduced by applying the WKBJ approximation to the wave equation $\nabla\cdot\underline{\underline{\varepsilon}}\cdot\nabla\phi=0$ which describes the propagation of the electrostatic potential $\phi=A\exp(iS)$ in a cold low-β plasma. Expanding the quantities S and A in terms of the small parameter $\delta_o=(ak_o)^{-1}$, to the lowest order the following equations are deduced:

$$\vec{\nabla}S \cdot \underline{\underline{\varepsilon}} \cdot \vec{\nabla}S = 0 \tag{1}$$

$$2\vec{\nabla}S \cdot \underline{\underline{\varepsilon}} \cdot \vec{\nabla}A + A\vec{\nabla} \cdot (\underline{\underline{\varepsilon}} \cdot \vec{\nabla}S) = 0 \tag{2}$$

respectively for the phase and the amplitude. The equation for the phase S is a non-linear first order partial differential equation while that for the amplitude is a linear one. Both equations can be solved by the method of characteristics which are the well-known ray equations of the geometric optics. In the case of lower hybrid waves where $\Omega_i \ll \omega \ll \Omega_e$ the ray equations are:

$$\frac{d\hat{r}}{d\theta} = -\frac{\delta^2 q n_r}{\varepsilon \nu n_{\parallel}}\left[1 - (n_{\parallel} - \frac{n_{\parallel_o}}{h})\frac{\delta^2 q^2}{\varepsilon^2 \hat{r}^2 \nu n_{\parallel}}\right]^{-1} \tag{3}$$

$$\frac{d\phi}{d\theta} = \frac{q}{h}\left[1 - (n_{\parallel} - \frac{n_{\parallel_o}}{h})\frac{\delta^2 q^2}{2\hat{r}^2 \nu n_{\parallel}}\right]^{-1} \tag{4}$$

$$\frac{dn_{\parallel}}{d\theta} = -\frac{d\hat{r}}{d\theta}\left[\frac{q'}{q}(n_{\parallel} - \frac{n_{\parallel_o}}{h}) + \frac{\varepsilon n_{\parallel_o}\cos\theta}{h^2} - \frac{n_{\parallel_o} q \sin\theta}{\hat{r}\, n_r\, h^2}(n_{\parallel} - \frac{n_{\parallel_o}}{h})\right] \tag{5}$$

In writing eqs (3-5) we have assumed a pseudotoroidal geometry. $\hat{r}$ and ϕ are the radial and toroidal position of the ray while $n_{\parallel}$ is the wavenumber parallel to the magnetic field and n_r is the radial wavenumber and its value is deduced from the cold electrostatic dispersion relation. The radial dependence of q and ν (respectively the safety-factor and the plasma density) is assumed parabolic.

Analytical solutions of Eqs (3-5) ar obtained taking advantage of the difference in magnitude between the parallel and perpendicular wavevector, the former being smaller that the latter by the quantity $\delta=(m_e/m_i)^{\frac{1}{2}}$.

I. SOLUTION OF THE RAY-EQUATIONS

The radial and toroidal position equations can be analitycally solved by the method of matched asymptotic expansion by observing that the toroidal correction are almost irrelevant everywhere but near the point $n_r \cong 0$, where the whispering gallery phenomenon occurs. The radius $\hat{r}_{wg}$ where $n_r \cong 0$ is $\hat{r}_{wg} = (\delta q(0)/\varepsilon v(0)^{1/2})|n_{//}-n_{//_c}|/n_{//}$. Upon dividing the integration domain of the radial and toroidal variables into two regions $\hat{r} \gg \hat{r}_{wg}$ and $\hat{r} \sim \hat{r}_{wg}$; Eqs (3) and (4) can be integrated to yield:

$$\theta = \theta_o - \frac{\varepsilon v_{(o)}^{1/2}}{\delta(q(a)-q(0))} \left[\left(\frac{q(a)}{q(0)}\right)^{1/2} \operatorname{arctg}\left(\left(\frac{q(a)}{q(0)}\right)^{1/2} \frac{\hat{r}}{(1-\hat{r}^2)^{1/2}}\right) - \arcsin \hat{r}\right]\Bigg|_{\hat{r}_o}^{\hat{r}} \quad (6)$$

$$\theta = \bar{\theta} \left(|n_{//_c}-n_{//_o}|/n_{//_c}\right) \left[(z^2-1)^{1/2} - (n_{//_c}-n_{//_o}) \operatorname{arctg} (z^2-1)^{1/2}\right] \quad (7)$$

respectively for $\hat{r} \gg \hat{r}_{wg}$ and $\hat{r} \sim \hat{r}_{wg}$ and

$$\phi = \phi_o + \varepsilon\phi_1 + (\varepsilon v_{(o)}^{1/2}/2\delta) \left[\arcsin \hat{r} + \hat{r}(1-\hat{r}^2)^{1/2}\right]\Big|_{\hat{r}_o}^{\hat{r}} + \varepsilon\, \hat{r}\, q \sin\theta \quad (8)$$

$$\phi = \phi_o + \varepsilon\phi_1 - (\varepsilon v_{(o)}^{1/2}/2\delta) \left[\arcsin \hat{r}_o + \hat{r}_o(1-\hat{r}_o^2)^{1/2}\right] + q(0)\left(|n_{//_c}-n_{//_o}|/n_{//_c}\right)(z^2-1)^{1/2} \quad (9)$$

where θ_o, ϕ_o, $\hat{r}_o$ are respectively the starting poloidal and toroidal angles and the radial position of the ray. The constant $\bar{\theta}$ is obtained asymptotically matching Eqs (6) and (7) in the limit $\hat{r} \sim \hat{r}_o$, while ϕ_1 is a constant obtained by the matching Eqs (14) to the solution in the outer region (where the assumptions on the ordering of the various parameters breaks down). Note that near the whispering gallery v, q and $n_{//}$ are taken constant. In Eqs (7) and (9) $z = \hat{r}/\hat{r}_{wg}$.

In Figures 1 and 2 a comparison between the analytical (solid line) and a numerical (dashed) solution of Eqs (3) and (4) is presented for a typical situation $n_{//}(\hat{r}_o)=5$, $v(0)=0.95$, $q(a)=3$, $q(0)=1$, $\hat{r}_o=0.95$. A very good agreement is found.

Coming to Eq. (5) that for $n_{//}$, an anlytical solution is obtained observing that, since the rate of change of $n_{//}$ on the poloidal scale is small, a multiple scale analysis [6] can be applied. A straightforward application of this method leads to the following solution for the average part of $n_{//}$

$$\bar{n}_{//} = n_{//_o} + (\bar{n}_{//}(\hat{r}_o)-n_{//_o})q(a)/q - (\varepsilon^2 n_{//_o}/2q)\,(\hat{r}_o^2\, q(a) - \hat{r}^2 q) \quad (10)$$

At the next order an explicit expression for the fluctuating part of $n_{//}$ is obtained

$$\tilde{n}_{//} = n_{//_o}(\delta/v^{1/2})\,(q+\hat{r}q')\sin\theta \quad (11)$$

In Figure 3 a comparison between the analytical and numerical solution (Eqs (10)) is presented and again it can be noted a good agreement within order ε^2 consistently with the approximation used to evaluate the analytical solution.

II. SOLUTION OF THE PHASE-EQUATIONS

The variation of the phase along the characteristics is obtained from the following equation

$$dS/d\theta = - n_\phi \, d\phi/d\theta \tag{12}$$

The equation for the phase is hence reduced to the toroidal position equation whose integral in the two regions above defined is given by Eqs (8) and (9). The plot of the phase S as function of the trajectory is given in Fig. 4.

III. SOLUTION OF THE AMPLITUDE EQUATION

From Eqs (2) it is possible to derive an equation for the amplitude A_o of the electrostatic potential Φ along the trajectory

$$d\ell n \, [A_o(\hat{r}nrh)]/d\hat{r} = - \frac{1}{2} \frac{qV}{\delta^2 \varepsilon \hat{r}^2} \frac{1}{n_r^3} \frac{n_{\parallel o}^2}{h^3} \frac{\partial(n_\parallel h)}{\partial\theta} \tag{13}$$

Again the solution of Eq (14) is obtained considering separately the two regions $\hat{r} \gg \hat{r}_{wg}$ and $\hat{r} \sim \hat{r}_{wg}$. In the first case the following result is obtained

$$A_o = A_o(\hat{r}_o,\theta_o) \, (\hat{r}_o \, n_r \, (\hat{r}_o) \, h(\hat{r}_o,\theta_o)/(\hat{r} \, n_r \, h))^{\frac{1}{2}} \tag{14}$$

while in the whispering gallery region we have

$$A_o = A_o(\hat{r}_o,\theta_o) \, (\hat{r}_o \, n_r \, (\hat{r}_o) \, h(\hat{r}_o,\theta_o)/(\hat{r} \, n_r \, h))^{\frac{1}{2}} \, (1-\alpha/(z^2-1)^{\frac{1}{2}})^{-\frac{1}{2}} \tag{15}$$

where $\alpha=(n_{\parallel o}/n_{\parallel c})^2 |n_{\parallel c}-n_{\parallel o}|^{-1} \, \partial n_\parallel/\partial\theta_o$. In Fig. 5 the amplitude A_o is plotted along the trajectory (solid line). In the same figure the parallel (dotted) and perpendicular (dashed) electric field are shown.

CONCLUSION

The method presented here for studying asymptotically the propagation of the lower hybrid waves is limited to situations where the cold resonance $1+\omega_{pe}^2/\Omega_{ce}^2-\omega^2/\Omega_{ci}^2=0$ is not inside the plasma, this signifies that the range of central density we are considering is such that $\omega_{pi}^2 < \omega^2(1-\omega^2/\Omega_e \Omega_i)^{-1}$. Further the neglecting of the e.m. effects impose values of $n_\parallel$ above the critical value for confluence between the slow and the fast branches of the cold dispersion relation. Within these limits our analysis can be an useful tool for future investigation on this field.

REFERENCES

[1] K.L. Wong, M. Ono, Nucl. Fusion, 23, (1983) 805
[2] P.T. Bonoli, E. Ott, Phys. Fluids, 25 (1982) 359
[3] S. Bernabei, D.W. Ignat, Nucl. Fusion, 22 (1982) 735
[4] Yu.F. Baranov, V.I. Fedorov, Nucl. Fusion 20 (1980) 1111
[5] F. Alladio et al., Proc. of the 4th Joint Varenna-Grenoble Int. Symp. on "Heating in Toroidal Plasmas", ed. by H. Knoepfel and E. Sindoni, Rome (1984), vol. 1, 546
[6] R.C. Davidson "Methods in Nonlinear Plasma Theory" Academic Press, New York (1982).

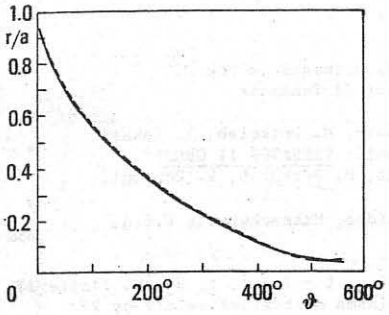


Fig. 1

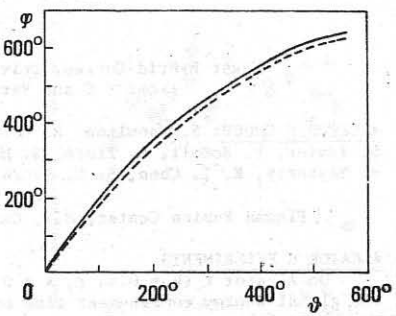


Fig. 2

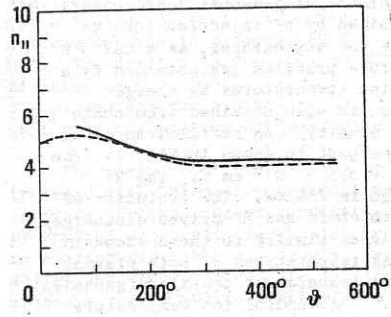


Fig. 2

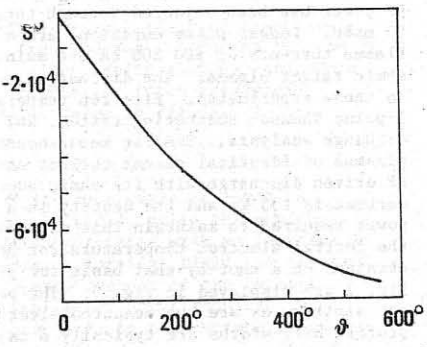


Fig. 4

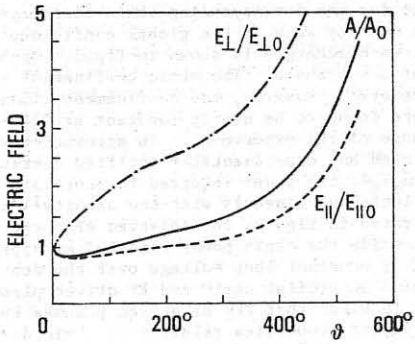


Fig. 5

Lower Hybrid Current Drive Experiments on the MIT Alcator C and Versator II Tokamaks

ALCATOR C GROUP: S. Knowlton, S. McDermott, M. Porkolab, Y. Takase, S. Texter, P. Bonoli, C. Fiore, S. McCool†; VERSATOR II GROUP: M. Mayberry, K. I. Chen, S. C. Luckhardt, M. Porkolab, R. Rohatgi.

Plasma Fusion Center, MIT, Cambridge, Massachusetts U.S.A.

ALCATOR C EXPERIMENTS

On Alcator C ($\bar{R}$ = 0.64 m, a = 0.165 m, B = 7 - 11 T, H_2, Mo limiters), the global energy confinement time of plasma maintained solely by RF current drive is being measured and compared with values obtained from similar ohmic discharges. Current drive experiments are performed at 4.6 GHz over the density range $\bar{n}_e = 3\text{-}7 \times 10^{13}$ cm^{-3}. Up to 1.4 MW net RF power has been injected through three sixteen waveguide arrays for 90 msec. Longer pulse durations are achieved at somewhat lower powers. Plasma currents of 100 200 kA are maintained by RF injection into an ohmic target plasma. The discharges are not sawtoothing, as q (a) > 8 in these experiments. Electron temperature profiles are obtained by a 5-point Thomson scattering system, and ion temperatures by charge exchange analysis. Similar measurements are also obtained from ohmic plasmas of identical plasma current and density. An oscillogram of an RF driven discharge with its ohmic counterpart is shown in Fig. 1. The current is 135 kA and the density is $\bar{n}_e = 5.5 \times 10^{13}$ cm^{-3}. The RF power required to maintain this discharge is 750 kW. The evolution of the central electron temperature for both ohmic and RF driven discharges obtained on a shot-by-shot basis for plasmas similar to those shown in Fig. 1 are displayed in Fig. 2. The peak temperatures of both plasmas are similar, as are the measured electron temperature profiles (gaussian profile half-widths are typically 6 cm). The central ion temperature is 0.6 keV in both cases. Thus, the thermal energy content of the RF driven and ohmic plasmas are nearly the same. The global energy confinement time is defined as $\tau_E = 3/2 \int (n_e T_e + n_i T_i)\, dV/P_{in}$, where P_{in} is the total input power, RF or ohmic. For the RF driven case, τ_E = 2.3 msec. The confinement time for the corresponding ohmic discharge ($P_{in} \simeq 200$ kW) is $\tau_E \simeq 10$ msec. A density scan of the global confinement time for 140 kA ohmic and RF driven discharges is shown in Fig.3. Each point represents the average of 5 - 6 shots. The ohmic confinement times increase with density, as expected. However, the confinement times in the RF driven discharges are found to be nearly constant at 2.4 - 3.0 msec over the density range of the experiment. In accordance with the theoretically predicted and experimentally verified current drive scaling law ($P_{RF} \propto \bar{n}_e I_p$), the power required to sustain a discharge of a given current increases linearly with the density[1,2]. For the density scan illustrated in Fig. 3, the injected RF power was varied from 325 to 900 kW, while the ohmic power remained at approximately 200 kW due to a nearly constant loop voltage over the density range. Since the temperatures of similar ohmic and RF driven plasmas are nearly the same, it is clear that the RF driven plasmas exhibit reduced global energy confinement properties relative to ohmic discharges.

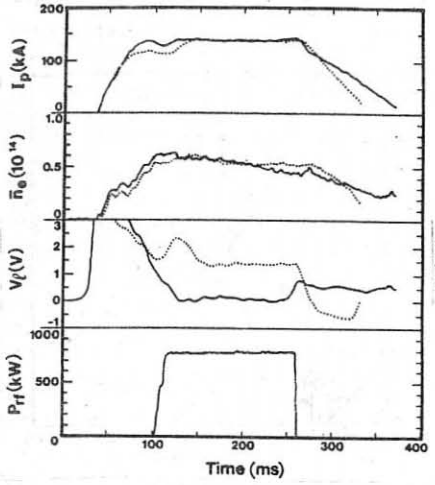


Fig.1 Evolution of I_p, $\bar{n}_e$, and V_ℓ for a typical Alcator C LH current drive discharge in hydrogen at B = 8 T. The density during the 750 kW Rf pulse is $\bar{n}_e = 5.5 \times 10^{13}cm^{-3}$. The parameters for a similar ohmic shot are indicated by dotted lines.

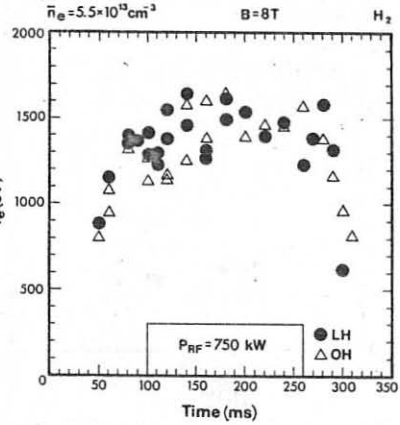


Fig.2 Central electron temperature from Thomson scattering for the RF driven (solid circles) and ohmic discharges (open triangles) illustrated in Fig. 1.

The energy confinement time of RF driven plasmas is found to increase with increasing toroidal magnetic field, while the ohmic confinement times remain constant. This correlates with an increase in RF current drive efficiency with increasing toroidal field, as observed in earlier experiments.[2] Again, the energy content of the current driven and ohmic plasmas are similar, while the power required to maintain the RF driven discharge is determined by the current drive efficiency. For both density and magnetic field scans, the ratio of the confinement times of RF driven discharges to those of ohmic ones is inversely proportional to the RF power, as shown in Fig. 4. The confinement times of both RF and ohmic discharges decrease weakly with increasing plasma current over the range I_p = 100-200 kA.[3] The similar behavior of the confinement times of the two types of discharges may result from the input power increasing nearly linearly with current in both cases.

Although initial bolometric and impurity radiation measurements indicate that the radiated power and metallic content (mainly molybdemum) of the plasma is strongly enhanced in the RF driven discharges relative to the ohmic ones, the inclusion of radiation in the power balance does not appear to explain the difference in the confinement times. The total radiated power increases very weakly with density, while the increase in net injected RF power is roughly linear. Thus, the fraction of radiated to input power decreases with increasing density. At $\bar{n}_e = 3 \times 10^{13}cm^{-3}$, all of the net injected RF power can be accounted for by radiation, while at $\bar{n}_e = 6 \times 10^{13}cm^{-3}$ approximately 60% of the input power of 750 kW is radiated. Moreover, the power radiated from the volume $r/a \leq 1/3$ represents 20% of the total input power at $\bar{n}_e = 3 \times 10^{13}\ cm^{-3}$,

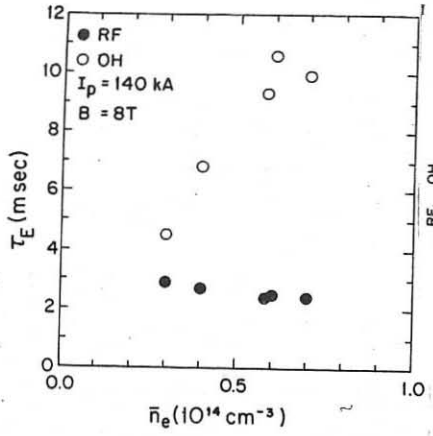


Fig.3 Global energy confinement times of 130 - 140 kA RF driven (solid circles) and ohmic discharges (open circles) vs. density.

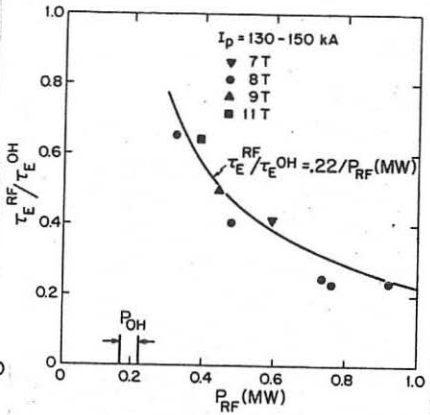


Fig.4 Ratio of energy confinement time in RF driven discharges to those in ohmic ones. The range of power needed to sustain the ohmic discharges is indicated by the arrow.

but only 10% of the total injected power at the higher density.

In order to understand the marked difference in energy confinement scaling between ohmic and RF driven discharges, we have simulated the plasmas with a numerical model incorporating a toroidal ray tracing code, Fokker Planck calculation and a 1-D radial transport code.[4] Approximately 85% of the injected RF power was calculated to be absorbed via quasi-linear electron Landau damping in the inner half of the plasma column. At $\bar{n}_e = 3 \times 10^{13} cm^{-3}$ and $P_{RF} = 320$ kW, $\chi_e^{RF} = 1.25\ \chi_e^{OH}$ and τ_E was found to decrease from $\tau_E(OH) = 4.9$ msec to $\tau_E(RF) = 3.6$ msec. At $\bar{n}_e = 5.5 \times 10^{13} cm^{-3}$ and $P_{RF} = 750$ kW, $\chi_e^{RF} = 2.5\ \chi_e^{OH}$ and τ_E decreased from $\tau_E(OH) = 8.5$ msec to $\tau_E(RF) = 3.0$ msec. In both cases χ_e^{RF} was chosen to keep the electron temperature at its ohmic value [$T_{eo}(RF) \approx T_{eo}(OH) \approx 1500$ eV]. The numerical value of $\chi_e^{(RF)}(r)$ remains nearly constant in this range since $\chi_e^{(OH)} \propto n_e^{-0.8}$ and T_e was not changing.

VERSATOR II EXPERIMENTS

A noticeable density "limit" above which RF current drive cannot be obtained is a commmon feature observed in a number of experiments, especially those employing a relatively low frequency. In recent experiments on the Versator II tokamak (R = 40 cm, a = 13 cm, B ≤ 1.5 T), a new 100 kW RF system at 2.45 GHz is being used to study the frequency dependence of the density limit. In previous 800 MHz studies this limit occurred at a line-average density of $\bar{n}_e \approx 6 \times 10^{12} cm^{-3}$.[5] Up to 95 kW of 2.45 GHz RF power has been coupled to the tokamak plasma through a 4-waveguide array (waveguide dimensions are 1.0 cm × 8.64 cm). The Brambilla RF power spectrum for this 2.45 GHz antenna is nearly identical to that of the 800 MHz 4-waveguide side-launch antenna used earlier ($1 \leq n_\parallel \leq 5$ for + 90° phasing, where $n_\parallel = ck_\parallel/\omega$). Fully RF driven discharges with the ohmic heating primary open circuited have been achieved at densities up to $\bar{n}_e = 1.0 \times 10^{13}\ cm^{-3}$ at 2.45 GHz.

driven discharges with the ohmic heating primary open circuited have been achieved at densities up to $\bar{n}_e = 1.0 \times 10^{13}$ cm^{-3} at 2.45 GHz. The toroidal magnetic field has not been raised above the levels used in the 800 MHz experiments ($B \lesssim 1.3$ T). Therefore, in the present experiment the parameter $\omega_{pe}^2/\omega_{ce}^2$ has exceeded unity, and the previous density limit has been exceeded by 70%. Because the accessibility for a given $n_\parallel$ spectrum is expected to be worse at 2.45 GHz than at 800 MHz, we believe that the 800 MHz density limit is not due to inaccessibility of low $n_\parallel$ waves to the plasma center. The current drive figure of merit, $\eta = nIR/P$, has been determined for 2.45 GHz "flat-top" discharges in which the OH primary was open circuited and inductive contributions were negligible. A plot of I/P versus $\bar{n}_e$ is shown in Fig. 5 for the following parameters: $\bar{n}_e = 0.2 - 1.0 \times 10^{13}$ cm^{-3}, $I = 15 - 24$ kA, $B = 1.0 - 1.2$ T, $P_{RF} = 30 - 95$ kW, $\Delta\phi = 90°$, H_2 gas. The data is consistent with the efficiency scaling of Fisch[1], with $\eta = .0072\ (10^{20})\ (kA)(m)/(kW)$ (shown by the solid curve). Although flat-top current drive has been limited to densities $\bar{n}_e \lesssim 1.0 \times 10^{13}$cm^{-3}, superthermal electron effects have been observed during RF injection into ohmic plasmas at densities up to $\bar{n}_e = 2.5 \times 10^{13}$cm^{-3}, representing a factor of four improvement over the 800 MHz limit. At present we do not know whether the maximum density represents a 2.45 GHz density limit, or whether we are limited by the RF power available.

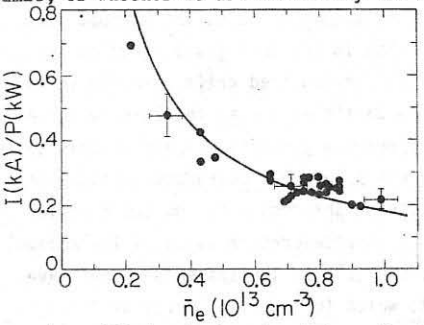


Fig. 5 Efficiency data from fully RF driven discharges on the Versator II tokamak with 2.45 GHz RF. The solid curve is $\eta = nIR/P = 0.0072\ (10^{20}\ m^{-3})\ (kA)\ (m)/(kW)$. The 800 MHz density limit occurs at $\bar{n}_e \approx 6 \times 10^{12}$cm^{-3}.

At sufficiently low densities, $\bar{n}_e \lesssim 7 \times 10^{12}$cm^{-3}, it has been possible to ramp up the plasma current with the loop voltage negative. Ramp-up rates as high as 190 kA/s have been recorded at $\bar{n}_e = 7 \times 10^{12}$ cm^{-3}, with an efficiency of converting RF energy to poloidal field energy of $\eta = 0.06 \pm 0.02$, where $\eta \equiv \Delta(1/2\ LI^2)/P_{rf}\Delta t$).

REFERENCES

1. N. J. Fisch, Phys. Rev. Lett. 41, (1978) 873.
2. M. Porkolab et al., Proc. 5th Top. Conf. on RF Plasma Heating, Madison, Wisc. (1983) 88; Phys. Rev. Lett 53 (1984) 450.
3. S. Knowlton et al., Proc. 6th Top. Conf. on RF Plasma Heating, Pine Mountain, GA (1985).
4. P. T. Bonoli, R. Englade, M. Porkolab, Proc. 4th Int. Symp. on Heating in Tor. Plasmas, Rome, Vol. II (1984) 1311.
5. S. C. Luckhardt et al., Phys. Rev. Lett. 48 (1982) 152.

ACKNOWLEDGEMENTS

We are grateful for the continual support of D. Griffin and his RF engineering group, and of the Alcator and Versator II technical staff.

Work supported by U.S. D.O.E. under contract DE-AC02-78-ET-51013.

†Present address: University of Texas, Austin, Texas.

ION TAIL FORMATION BY CASCADE TRAPPING IN LOWER-HYBRID H. EXPERIMENTS

Y. Gell and R. Nakach

Association Euratom-CEA , DPhPFC Service Ign- CENG B. P. 85
Centre de tri - 38041 Grenoble cedex (France)

Lately, there has been a renewed interest in a wave damping mechanism based on trapped particles dynamics resulting in a drift acceleration of these particles [1-3]. The impetus for this activity stems from the observation in numerical simulations[3] as well as in laboratory experiments[4] of the high efficiency of this drift acceleration mechanism in the damping of waves for a rather large variety of processes. In the simulations, the waves were set to propagate perpendicularly or nearly perpendicularly to a uniform magnetic field. The trapped particles in these waves execute bouncing motion in the wave frame, getting an acceleration parallel to the wave front until the acquired drift velocity in this direction allows for the detrapping of the particles due to the Lorentz force. The detrapped particle then, generally performs a gyromotion which is only slightly perturbed by the wave. The kinetic energy of this detrapped particle which remains essentially constant in the nonresonant region is now too high for the wave to be able to capture it again at an acceleration phase of the motion. However, a new trapping can occur if there exists in the system an other wave with a higher phase velocity, relative to which the kinetic energy of the particle is consistent with the trapping conditions. In this way the existence of many waves with appropriate phase velocities allows for an acceleration cascading process via trappings and detrappings of the particle to take place. Such a cascade process is thus to be expected in lower-hybrid waves heating experiments in which a wave spectrum in the parallel index ($n_{//}$) is inherently generated by the launching structure. This spectrum leads to a spectrum in the perpendicular wavevector $k_\perp$ via the dispersion relation for lower-hybrid waves and consequently to a distribution in phase velodities $\omega/k_\perp$.

For the purpose of demonstrating the possibility of a drift acceleration in a cascading sequence, we will restrict our analysis to consider a configuration consisting of a discrete limited series of lower-hybrid waves with different phase velocities. Assuming first the existence of a second electrostatic lower hybrid wave propagating also in the perpendicular direction with a phase velo-

city about equal to the absolute value of the velocity of the particle at detrapping, the conditions for a possible occurence of trapping in this wave can be fulfilled. Indeed, for a wave with such a phase velocity, when the particle arrives at a position in its gyroorbit for which v_y is small, its kinetic energy (which is then mainly concentrated in the x component) relative to the wave will also be small, and a wave having even a smaller amplitude than the slower phase velocity wave might be able to trap the particle. One should note that these velocity conditions still do not insure the actual trapping of the particle which depends also on the phase of the wave at this preferential position of the particle in its orbit. The particle might have to complete few gyrations in order for the wave to have the right phase for the capturing process to take place. Moreover, even though the conditions for a next trapping are fulfilled, the fact that the particle enters, at this stage of its gyromotion, into the resonance region, might cause an abrupt change in its v_x component, the size of which depends on its phase relation with the wave and on the amplitude of the wave, thus disturbing the trapping process or reducing considerably its effectiveness. Once the particle has been trapped, it will be accelerated and detrapped again, in the same way as by the lower phase velocity wave. Obviously, this mechanism might be operating in a repetitive manner as long as appropriate waves are present in the system. In order to exhibit this cascading process in a trasparent manner, we have considered the motion of an ion in a sequence of configurations having an increasing number of waves with appropriate parameters.Since no preferential frame is available for such a problem, it is most convenient to analyze the motion of the particle in the laboratory frame in which the equation of motion reads :

$$\frac{d^2x}{dt^2} = \frac{qE_1}{M}\sin(k_1x+\omega t)+\frac{qE_2}{M}\sin(k_2x+\omega t)+\frac{qE_3}{M}\sin(k_3x+\omega t)+\omega_c(v_{y_0}-\omega_c x) \qquad (1)$$

where $E_{1,2,3}$ and $k_{1,2,3}$ are respectively the amplitudes and wavenumbers of three electrostatic waves, and where the frequency ω is fixed by the launching structure. Starting with a single wave (setting $E_2 = E_3 = 0$) and considering a deeply trapped particle, we solve numerically the equation of motion and recover the results of references1-3, see Fig. I. In order to insure the possibility of a next trapping, we fix k_2 so that $\omega / k_2 \simeq v_{1detrap.}$ where $v_{1detrap.}$ is the velocity of the particle at detrapping from the first trapping wave and set $E_2 = 0$. These successive trappings and detrappings are clearly exhibited in Fig. II. In this case, the particle after getting detrapped for the first time completes two gyrations before finding the proper trapping conditions. Once being trapped in the second wave, its x velocity component remains almost constant

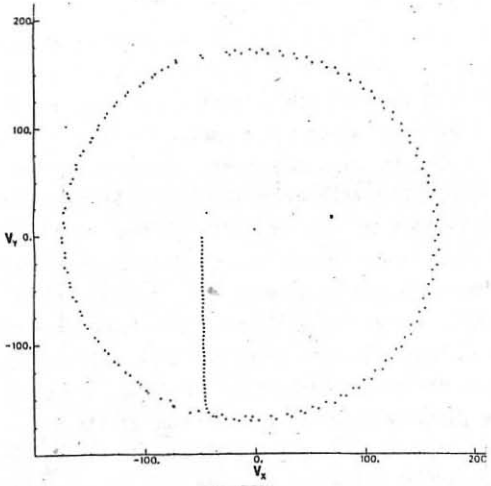


Fig. I

Velocity space orbits of a particle in the laboratory frame, normalized to $\omega_c/k_1 = c/\nu n_{\perp 1}$, as a solution of Eq.(1) with: $\omega = 1.5 \times \pi_x 10^9$ rad/s, $\nu = \omega/\omega_c = 47$, $n_{\perp 1} = 800$, $E_1 = 12.5$ kV/cm, $E_2 = E_3 = 0$, $(k_1 x)_{t=0} = 3.1416$, $u_0 = k_1 v_{y0}/\omega_c = 3.1416$, $(k_1 v_x/\omega_c)_{t=0} = -47$.

though oscillating slightly, similarly to what happened in the first pronounced trapping seen in the center of the figure, till it gets detrapped due to the Lorentz force. As the amplitude of this wave is smaller than the one of the first wave the velocity gained during this last acceleration is accordingly smaller. By superimposing additional waves having finite amplitudes and wavenumbers k_i determined by requiring $\omega/k_i \simeq v_{(i-1)\text{detrap.}}$, the sequence

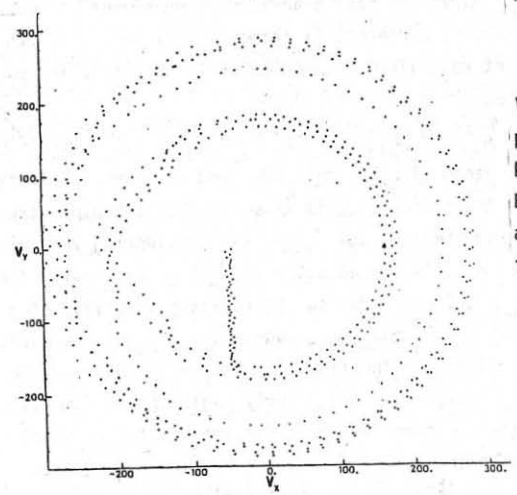


Fig. II

Velocity space orbits of a particle as in Fig. I, with $k_2 = 0.2668\ k_1$, $E_2 = 2/3\ E_1$, $E_3 = 0$, other parameters and initial conditions as in Fig. I.

of trappings and detrappings, thus described, can be extended. To illustrate this process we show in Fig. III three steps of the drift acceleration mechanism. Note that in this case, we have fixed the parameters of the system in such a way that successive trappings occur within only one gyration of the particle, showing thus that favorable conditions for trapping could be realized at the first possible opportunity.

In conclusion, it seems reasonable to assume that this cascading drift acceleration mechanism is operating in the plasma and is manifested in the generation of ion tails observed in lower-hybrid heating experiments.

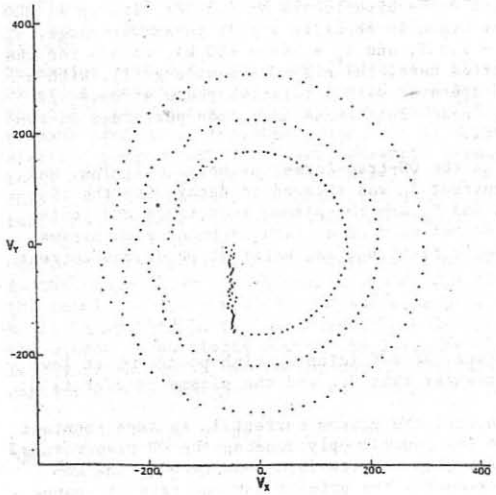


Fig. III

Velocity space orbits of a particle as in Fig. I, with $k_2 = 0.267\ k_1$, $k_3 \doteq 0.199 k_1$ $E_2 = E_3 = 2/3\ E_1$, other parameters and initial conditions as in Fig. I.

References

1. R. Z. Sagdeev and V. D. Shapiro, Pis'ma Zh. Eksp. Teor. Fiz. 17, 389 (1973) JETP Lett. 17, 279 (1973).

2. R. Sugihara and Y. Midzuno, J. Phys. Soc. Jpn., 47, 1290 (1979).

3. J. M. Dawson et al., Phys. Rev. Lett. 50, 1455 (1983).

4. Y. Nishida, M. Yoshizumi and R. Sugihara, Institute of Plasma Physics Report No. IPPJ - 648 , (1983) (unpublished).

LOWER HYBRID CURRENT DRIVE IN THE ASDEX TOKAMAK

F. Leuterer, D. Eckhartt, F. Söldner and R. Bartiromo[1], G. Becker, K. Bernhardi, H.S. Bosch, M. Brambilla, H. Brocken, H. Derfler, A. Eberhagen, G. Fußmann, O. Gehre, J. Gernhardt, G. v. Gierke, A. Giuliana[1], E. Glock, O. Gruber, G. Haas, M. Hesse[2], G. Janeschitz, F. Karger, M. Keilhacker, O. Klüber, M. Kornherr, P.B. Kotzé[3], M. Lenoci[1], G. Lisitano, H.M. Mayer, K. McCormick, D. Meisel, V. Mertens, E.R. Müller, M. Münich, H. Murmann, H. Niedermeyer, W. Poschenrieder, H. Rapp, F. Ryter[2], K. H.Schmitter, F. Schneider, G. Siller, P. Smeulders, K.H. Steuer, T. Vien, G. Vlases[4], F. Wagner, F. v. Woyna, M. Zouhar,

Max-Planck-Institut für Plasmaphysik
EURATOM Association, D-8046 Garching

Lower hybrid heating and current drive experiments at 1.3 GHz with up to 800 kW/1.5 sec pulses have been performed in ASDEX in a wide parameter range, $\bar{n}_e = 0.2 - 5 \times 10^{13}$ cm^{-3}, $B_t = 2 - 2.5$ T, and $I_p = 140 - 400$ kA, /1,4/. For the current drive experiments reported here, the eight waveguide grill, with a nominal $\langle N_{\parallel} \rangle = 4$ at $\Delta\varphi = \pi$, is operated with a relative phase of $\Delta\varphi = \pi/2$ between successive waveguides. These experiments have been performed in two different modes of operation /2/.

In the first mode the current in the OH-transformer primary coil, I_{OH}, was kept constant and the plasma current I_p was allowed to decay with the characteristic time $\tau_p = L_p/R_p$. L_p and R_p are the plasma inductance and resistance. RF-current drive then reduced this decay rate, depending on plasma density $\bar{n}_e$, RF-power P_{RF}, magnetic field B_o, and original OH-driven current I_{po}. The decay rate then is

$$\dot{I}_p = -(I_{po} - I_{RF})/\tau_p, \qquad (1)$$

where I_{RF} is the RF-driven current. At sufficiently high powers or at low enough densities, I_{RF} becomes greater than I_{po} and the plasma current is ramped up.
In the second mode of operation /3/, the plasma current I_p is kept constant by a feedback control acting on the power supply feeding the OH-transformer. Switching on an RF-driven current then results in a reduction of the OH-power input into the plasma by reducing the primary current rate of change $\dot{I}_{OH}$. At low enough densities or high enough powers, when $I_{RF} > I_{po}$, this primary current rate of change must be reversed to induce an opposing dc electric field in the plasma in order to prevent ramping-up the plasma current. In this way the OH-transformer is recharged without loosing the plasma, as is required for a quasistationary tokamak operation.

Due to the reciprocal nature of the air core transformer both modes of operation are equivalent, and for the same plasma parameters we have the proportionality

---

[1] CNEN Frascati, Italy
[2] CEN Grenoble, France
[3] Nuclear Development corp. of South Africa, Pretoria
[4] University of Washington, Seattle, USA

$$\dot{I}_{p,I_{OH}=\text{const}} = \dot{I}_{OH,I_p=\text{const}} \cdot M/L_p, \qquad (2)$$

M is the mutual inductance between primary coil and the plasma ring /3/.

In Fig. 1 and 2 we show the result of power and density scans of $\dot{I}_{OH}$ with a constant plasma current of I_p = 290 kA. Similar curves are obtained for $\dot{I}_p$ when I_{OH} is kept constant /2,4/. From the points where $\dot{I}_p = \dot{I}_{OH} = 0$, i.e. where a stationary plasma current is maintained by RF alone, we obtain the relation between the RF-driven current and the launched RF-power,

$$I_{RF} = a \cdot \mu \cdot g \cdot P_{RF}/\bar{n}_e \qquad (3)$$

which is in rather good agreement with theoretical estimates /5,6/. Here g is a factor describing the absorbed wavenumber spectrum. μ is the fraction of the total RF-power which can be absorbed by the current carrying electrons and which is determined by the accessibility and directivity of the launched spectrum as obtained from spectrum and raytracing codes /11/. A current of 400 kA has been maintained for 1 sec at $\bar{n}_e = 5 \times 10^{12}$ cm^{-3} with a power of 450 kW.
Examining such a discharge we find strong suprathermal electron cyclotron emission, an enhancement of soft and hard X-ray signals extending up to about 400 keV (but not showing any runaway electrons). The density profile remains similar to the Ohmic case, and $T_i(0)$ stays roughly constant. The electron temperature increases somewhat, depending on density. Thus we find these RF-sustained plasmas very similar to the Ohmic suprathermal discharges found in ASDEX at very low densities, which have a very low plasma resistance and operate at a very low loop voltage /7/.

Our measurements can be understood in terms of theories for LH-current drive in the presence of a dc-electric field /8,9,10/. In our comparison we use the results of N. Fisch /9/ for the case of a small electric field which may still be applicable for our experiment. In this theory the enhancement of the plasma conductivity due to the RF-generated suprathermal electron velocity distribution is calculated and yields, when combined with equ. (2), a current rate of change

$$\dot{I}_{OH} = \frac{-1}{\tau_{po}} \cdot \frac{I_{po} - I_{RF}}{1 + b \cdot I_{RF}/\bar{n}_e} \cdot \frac{L_p}{M} \qquad (4)$$

Here τ_{po} is the characteristic time without RF, I_{RF} is taken from equ. (3) and $b = \alpha w^2/(qe\, v_{the}\, \bar{n}_e)$ where α is a function of Z_{eff}, q is the plasma cross-section and $w^2 = v^2/v_{the}^2$. In the experiment τ_{po} is found to depend on density and for the calculation we approximate it by $\tau_{po} = 60/(30 + \bar{n}_e)$ [sec, 10^{12} cm^{-3}]. With the plausible value of $b = 0.03 \times 10^{12}$ cm^{-3} kA^{-1} we get a reasonable fit to the experimental data as shown in Figs. 3 and 4. To obtain these curves, we did assume a constant electron temperature. However, in recent current drive experiments we observed the electron temperature to rise linearly with rf-power, reaching $\Delta T_e \approx 300$ eV at $P_{RF} \approx 400$ kW and $\bar{n}_e \approx 1 \cdot 10^{13}$ cm^{-3}. Taking such an electron heating into account reduces the fitted factor b by up to a factor of 2, resulting in an even more plausible value.
Both, the experimental and theoretical curves show remarkable features already predicted in /9/: there is a saturation of $\dot{I}_{OH}$ with power and there is a maximum for $\dot{I}_{OH}$ as a function of density. Towards higher densities the degrading accessibility diminishes the power available for electron

interaction. This is further corroborated by experiments and calculations for different magnetic fields, as shown in Fig. 5, since it affects only the accessibility. In hydrogen plasmas we observe that, in addition to the accessibility, the onset of an interaction with fast ions near $\bar{n}_e \simeq 2 \times 10^{13}$ cm^{-3} reduces the power available for current drive even more, imposing a density limit /12/.

Exciting the grill with $\Delta\varphi = -\pi/2$ we drive the rf-current in a direction opposite to I_{po}. In this case we find that the current decay becomes also slower than without RF as shown in Fig. 6. There is no theory to describe this situation but in order to simulate it, we intuitively take equ. (4) and change the sign of I_{RF} in the numerator but not in the denominator, the latter describing the modification of the conductivity. The result, also shown in Fig. 6, suggests that the concept of RF-enhanced conductivity would also apply in this case.

The essential point which we learn from these comparisons is, that the achievable ramp-up or recharging rates and the corresponding efficiencies are considerably reduced by the enhancement of the electrical coductivity of the plasma due to the RF-power. For a given frequency and wavenumber spectrum accessibility and beginning ion interaction limit the operational density regime.

References

/1/ D. Eckhartt, et al., 4th Int. Symp. Heating in Toroidal Plasmas, Rome, Vol. I, 501 (1984);
D. Eckhartt, et al., this meeting; F. Söldner, et al., this meeting;
F. Söldner, et al., IPP-Report IPP-3/77 (1984)

/2/ F. Leuterer, et al., IPP-Report IPP-4/233 (1985)

/3/ F. Leuterer, et al., Phys. Rev. Lett. to be published

/4/ F. Leuterer, et al., 10th. Int. Conf. Plasma Phys. and Contr. Fusion, London, paper IAEA-CN-44/F-IV-3 (1984)

/5/ F. Karney, N. Fisch, Phys. Fluids 22, 1817 (1979)

/6/ G. Tonon, D. Moulin, 4th Int. Symp. Heating in Toroidal Plasmas, Rome, Vol. II, 1343 (1984)

/7/ G. Fußmann, et al., Phys. Rev. Let. 47 (1981)

/8/ K. Borrass, A. Nocentini, Plasma Phys. and Contr. Fus., 26, 1299, 1984

/9/ N. Fisch. Phys. Fluids 28, 245 (1985)

/10/ N. Fisch, F. Karney, Phys. Rev. Lett. 54, 897 (1985)

/11/ M. Brambilla, 3rd Symp. Heating in Toroidal Plasmas, Greenoble, Vol. II, 439 (1982)

/12/ G. Wegrowe, et al., 4th Symp. Heating in Toroidal Plasmas, Rome, Vol. I., 593 (1984)

Figure Captions

Fig. 1: Primary current rate of change, $\dot{I}_{OH}$, as a function of net RF-power.

Fig. 2: Primary current rate of change, $\dot{I}_{OH}$, as a function of density

Fig. 3: $\dot{I}_{OH}$ vs. P_{RF} calculated with equ. (4)

Fig. 4: $\dot{I}_{OH}$ vs. $\bar{n}_e$ calculated with equ. (4)

Fig. 5: $\dot{I}_p$ vs. $\bar{n}_e$ for different magnetic fields and constant $P_{RF} \simeq 400$ kW

Fig. 6: $\dot{I}_p$ vs. P_{RF} for $\Delta\varphi = \pi/2$ and $\Delta\varphi = -\pi/2$
a) experiment, b) calculation

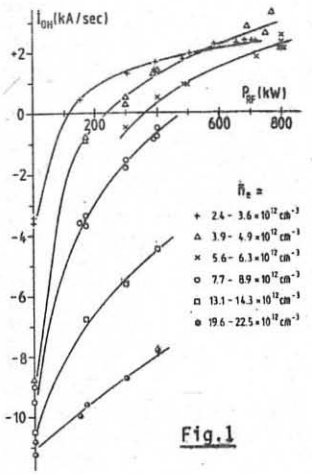


Fig.1

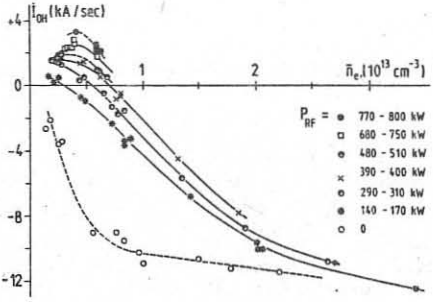


Fig.2

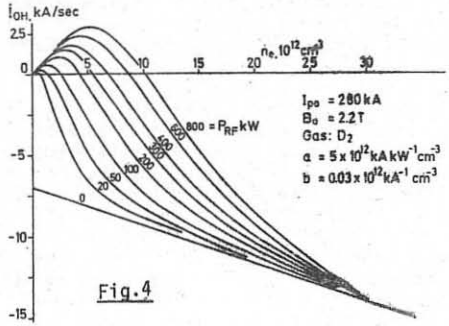


Fig.4

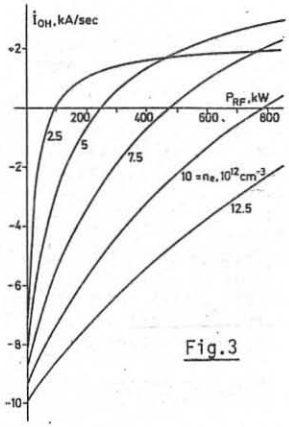


Fig.3

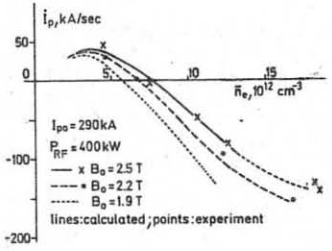


Fig.5

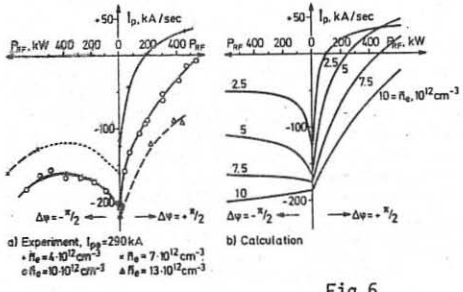


Fig.6

POWER ABSORPTION STUDIES FOR LOWER HYBRID HEATING AND CURRENT DRIVE IN ASDEX

F. Söldner, D. Eckhartt, F. Leuterer, A. Eberhagen, A. Giuliana, E. R. Müller, H. Murmann, F. Ryter[1], R. Bartiromo[2], G. Becker, H. S. Bosch, M. Brambilla, H. Brocken, R. Burhenn, H. Derfler, G. Fußmann, O. Gehre, J. Gernhardt, G. v. Gierke, E. Glock, O. Gruber, G. Haas, M. Hesse[1], G. Janeschitz, F. Karger, M. Keilhacker, O. Klüber, M. Kornherr, P. B. Kotzé[3], M. Lenoci[2], G. Lisitano, H.M. Mayer, K. McCormick, D. Meisel, V. Mertens, M. Münich, H. Niedermeyer, W. Poschenrieder, H. Rapp, H. Röhr, N. Ruhs, K.H. Schmitter, F. Schneider, G. Siller, P. Smeulders, K.-H. Steuer, T. Vien, G. Vlases[4], F. Wagner, F. v. Woyna, M. Zouhar

Max-Planck-Institut für Plasmaphysik
EURATOM Association, D-8046 Garching

Introduction: The absorption of Lower Hybrid waves has been investigated on ASDEX in the density range 2×10^{12} cm^{-3} - 4×10^{13} cm^{-3}. For most of the experiments the radiated rf power exceeded largely the Ohmic power input. The parallel refractive index $N_{\parallel}$ was altered between 4 and nearly 1. Heating and current drive, respectively, were studied with stationary or propagating waves. Several figures of merit may by used for the different schemes of Lower Hybrid application: A current drive efficiency for stationary rf-current drive /1/, a recharging efficiency for power transfer into the primary circuit of the OH transformer by an rf-driven current /2/ and a heating efficiency for the increase of the central plasma energy density by rf-heating. In order to obtain a more general criterion which applies to all modes of LH operation we derived a total absorption coefficient of rf-power from the global power balance at the begin of the rf pulse. Using this absorption coefficient, the energy confinement time is then determined during the stationary phase.

2. Operation regimes: Three different regimes of coupling of LH waves have been identified: At low density suprathermal electron tails are generated by the rf. Above a density threshold ($\bar{n}_e \approx 2 \times 10^{13}$ cm^{-3}) fast ions are produced whereas the electron distribution stays thermal. In both regimes bulk plasma heating is observed /3/. When $\bar{n}_e \geq 4 \times 10^{13}$ cm^{-3} only fast ion tails are formed near the plasma edge without any energy transferred to the bulk /4/.

Current drive: The efficiency of stationary LH-current drive has been investigated in the density range $\bar{n}_e = 0.2 - 1 \times 10^{13}$ cm^{-3} /5,6/. The rf-power was varied such that the plasma current stayed just constant (I_p = 290 kA, $\dot{I}_p = 0$) without any Ohmic induction ($\dot{I}_{OH} = 0$). At low densities the power necessary for inductive and rf-current-drive, respectively, is about the same and it increases linearly with density. Above $\bar{n}_e \approx 6 \times 10^{12}$ cm^{-3} the power required for Ohmic current drive stays nearly constant for a rather wide range of density while the power for LH-current-drive continues to

[1]CEN Grenoble, France, [2]ENEA Frascati, Italy
[3]Nuclear Development Corporation of South Africa, Pretoria
[4]University of Washington, Seattle, USA

increase with $\bar{n}_e$. The rate of rf current drive therefore drops with density: $I_p/P_{RF} = \eta_I/\bar{n}_e$, where η_I is the current drive efficiency. It should be noted that the power scaling for inductive and rf-current-drive begins to diverge at a density which is the upper limit for Ohmic suprathermal discharges in ASDEX /7/. The rf seems to extend the suprathermal regime above this limit.

The plasma energy content in stationary rf-driven discharges is higher than in Ohmic discharges. Figure 1 shows the time evolution of β_p, as determined from diamagnetic measurements, for a current drive shot in comparison with an Ohmic discharge. The injected rf-power in this case was higher than necessary for stationary rf-current-drive. A global power balance has been established for stationary rf-driven discharges ($\dot{I}_p = 0$, $\dot{I}_{OH} = 0$, $I_p = I_{RF}$). The energy confinement time then is calculated from the relation $\tau_E^{(LH)} = W_p/P_{RF}$, where the total plasma energy is determined from the diamagnetic beta and P_{RF} is the total rf-power transmitted by the antenna. For $\bar{n}_e \lesssim 0.6 \times 10^{13}$ cm^{-3} the confinement during LH is improved with respect to Ohmic discharges (Fig. 2) while at higher densities a degradation appears. This, however, could be also due to a deterioration of rf absorption or due to a power dependence because the rf-power was varied in this series in order to have full stationary LH-current-drive for all densities.

Plasma Heating: Density scans with constant rf-power have been made in the range $\bar{n}_e = 0.2 - 4 \times 10^{13}$ cm^{-3} in hydrogen and deuterium discharges. Strong thermal electron heating is observed at low densities with $\Delta T_e(0) \lesssim 600$ eV for $P_{RF} \approx 400$ kW. The usual heating efficiency $\eta_h = \bar{n}_e\,(\Delta T_e(0) + \Delta T_i(0))/P_{RF,t}$ is plotted in Fig. 3 for two different wave spectra ($\bar{N}_{\parallel} = 2$ and 4). At densities $\bar{n}_e \lesssim 2 \times 10^{13}$ cm^{-3} faster waves (low $\bar{N}_{\parallel}$) lead to better heating. At densities $\bar{n}_e \gtrsim 2 \times 10^{13}$ cm^{-3}, the heating is better in deuterium than in hydrogen and it depends only weakly on the wave spectrum /3/. The increase of the beta as determined from magnetic measurements agrees with the thermal measurements at higher densities. Below $\bar{n}_e \approx 2 \times 10^{13}$ cm^{-3} the increment of the beta values is larger than the increase of thermal energy and the equilibrium beta rises more than the diamagnetic beta (l_i = const was assumed according to poloidal field measurements /8/). These differences are attributed to an anisotropic suprathermal electron distribution with larger energy parallel than perpendicular to the magnetic field.

The magnetic measurements were used for the power balance during Lower Hybrid heating. The change of the energy content $\dot{W}_p$ at the begin of additional rf-heating is described by the equation

$$(1) \quad \dot{W}_p = P_{OH}^{(RF)} + \alpha P_{RF,t} - P_{rad}^{(RF)} - P_c^{(RF)}$$

The heat conduction losses $P_c^{(RF)}$ can be determined from the power balance in the Ohmic phase before the RF under the assumption that they do not change at the begin of the rf pulse:

$$(2) \quad P_c^{(RF)} = P_c^{(OH)} = P_{OH}^{(OH)} - P_{rad}^{(OH)}$$

The loop voltage drops suddenly after start of the rf at low density and a rapid increase of the radiation is observed at high density with application of the rf. Therefore the changes of Ohmic power input P_{OH} and of radiation losses P_{rad} have to be taken into account in the power balance. The absorption coefficient of rf power can then be determined from equation (1) and (2):

(3) $\alpha = (\dot{W}_p - \Delta P_{OH} + \Delta P_{rad})/P_{RF,t}$,

with $-\Delta P_{OH} = P_{OH}^{(OH)} - P_{OH}^{(RF)}$; $\Delta P_{rad} = P_{rad}^{(RF)} - P_{rad}^{(OH)}$

The various terms are plotted in Fig. 4 for LH heating with $\bar{N}_{\parallel} = 2$ in deuterium. The reduction of Ohmic power input due to the drop in resisitvity during LH injection /6/ dominates the power balance at low density. At higher densities radiation losses become important. In this regime fast ions are produced by the RF.

The absorption coefficient α is shown in Fig. 5, including increase of parallel energy (β_p^{equ}) or not (β_p). The decrease of α with $\bar{n}_e$ may be partly due to an increase of nonaccessible rf-power. With this absorption coefficient the energy confinement time $\tau_E^{(RF)}$ is then calculated during the stationary phase of LH heating from:

(4) $P_{OH}^{(RF)} + \alpha P_{RF,t} = W_p^{(RF)}/\tau_E^{(RF)}$

A lower limit for $\tau_E^{(RF)}$ is obtained when assuming that the total rf power is absorbed ($\alpha = 1$). The confinement times calculated in both ways are compared with the Ohmic values in Fig. 6. At low density in the suprathermal regime the confinement during LH heating is improved with respect to the thermal Ohmic phase. At densities $\bar{n}_e \geq 2 \times 10^{13}$ cm^{-3} the confinement seems to be degraded. The absorption coefficient α was derived under the assumption that the heat conduction losses do not change at the begin of the rf. This is justified at least for low densities and therefore the $\tau_E^{(RF)}$ determined with $P_{RF,abs} = \alpha P_{RF,t}$ should be taken here. At higher densities, where the losses seem to increase, the confinement times might be between the values obtained with $P_{RF,abs} = \alpha P_{RF,t}$ and those with $P_{RF,abs} = P_{RF,t}$.

Conclusion: In LH heating and current drive experiments similar results are obtained for the absorption of rf power. At low density ($\bar{n}_e \lesssim 2 \times 10^{13}$ cm^{-3}) a suprathermal electron distribution is formed and a large fraction of the rf power is coupled to fast electrons. The rf absorption coefficient in this regime is of order 0.5. The energy confinement is improved above the Ohmic values. At higher densities where fast ions are produced the rf absorption is poor ($\alpha \approx 0.2$) and the confinement is degraded. The electron regime therefore is preferable for LH heating. The best results may be obtained if current drive and heating are present simultaneously.

References:

/1/ F. Leuterer et al., 10th Int. Conf. Plasma Phys. and Contr. Fusion, London, IAEA, Vienna (1985), Vol. I, p. 597.
/2/ F. Leuterer et al., Phys. Rev. Lett., 55, 75 (1985)
/3/ D. Eckhartt et al., this conference
/4/ D. Eckhartt et al., 4th Int. Symp. Heating in Toroidal Plasmas, Rome, Vol. I, 501 (1984)
/5/ F. Söldner et al., IPP-Report IPP-3/77, to be published
/6/ F. Leuterer et al., this conference, and IPP-Report IPP-4/223
/7/ G. Fußmann et al., Phys. Rev. Lett. 47, 1004 (1981)
/8/ K. McCormick, this conference.

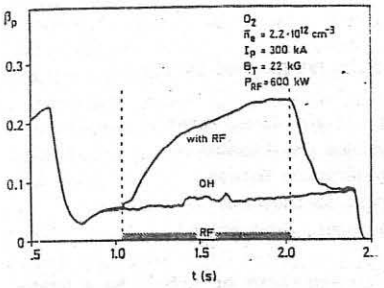


Fig. 1: β_p with LH-current-drive

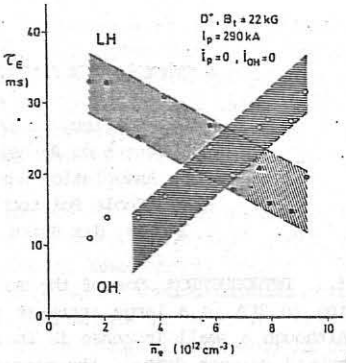


Fig. 2: τ_E with LH-current drive

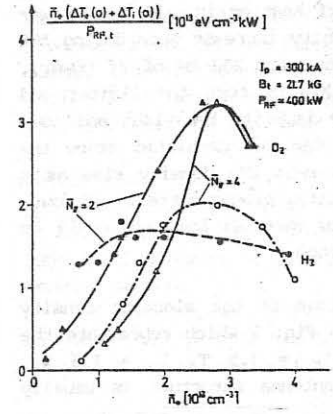


Fig. 3: LH-heating efficiency

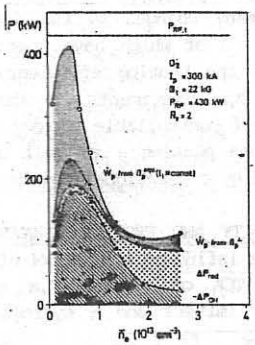


Fig. 4: Power balance for LH-heating

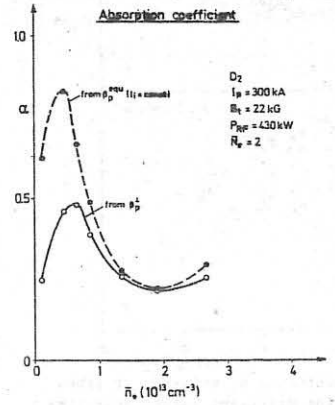


Fig. 5: Absorption coefficient of LH-power

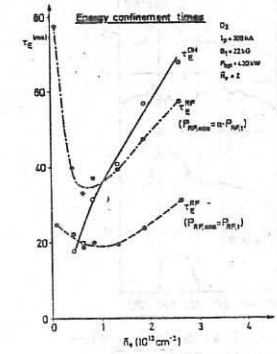


Fig. 5: τ_E with LH-heating

A STUDY OF THE DENSITY RISE OBSERVED DURING AWH IN TCA

G.A. Collins, B. Joye, J.B. Lister and J.-M. Moret
Centre de Recherches en Physique des Plasmas
Association Euratom - Confédération Suisse
Ecole Polytechnique Fédérale de Lausanne
21, Av. des Bains, CH-1007 Lausanne, Switzerland

I. INTRODUCTION. One of the most striking consequences of Alfvén Wave Heating in TCA is a large increase in the electron density during the rf pulse. Although a small increase is characteristic of rf heating in ICRF[1] and lower hybrid current drive[2], the magnitude of the density increase seen during AWH is astonishing (up to 300% of the target density with 200 kW of rf power). Despite many changes to the design and materials of both the limiter and antenna, all of which have greatly modified the impurity behaviour and consequently the heating efficiency, the density rise has persisted since the earliest TCA experiments. In this paper, we document the density rise as a function of controllable parameters - target density, plasma current, rf power and antenna phasing - as well as discussing how such an increase could be explained by conventional models of particle balance.

II. DENSITY AND PROFILE BEHAVIOUR. The behaviour of the electron density under the influence of 100 kW of rf is shown in Fig. 1 which represents the standard TCA conditions: R,a = 0.61,0.18 m, B_ϕ = 1.5 T, I_p = 130 kA, graphite limiters and a hydrogen plasma. The antenna structure is usually

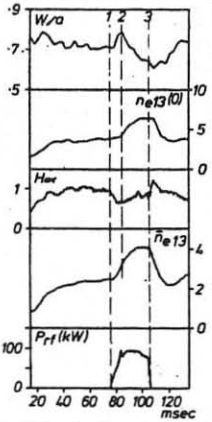


Fig.1 Typical hydrogen discharge with 100kW of rf

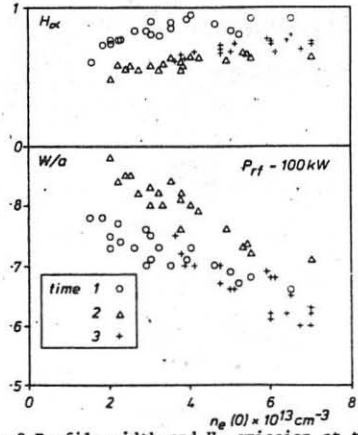


Fig.2 Profile width and H_α emission at times shown in Fig.1 for different target densities

phased to excite waves with dominant toroidal wavenumbers n = ±2 and poloidal wavenumbers m = ±1, at a frequency of 2.5 MHz. The target density is set up using feedback control of the gas valve and the rf power is applied when a stationary state has been reached. During the rf pulse the gas valve voltage is clamped at its pre-rf value, although little difference is observed in the qualitative effects of the high rf power on the density if the gas feed is cut to zero.

The evolution of the electron density profile is indicated in Fig. 1 by both the central electron density $n_e(0)$ and W, the profile half width at half maximum. Even though $n_e(0)$ begins rising immediately, the profile flattens during the first 7 ms, but then peaks to have a form typical of ohmic conditions. This is also shown in Fig. 2 for discharges at different target densities. Associated with the onset of the rf is a significant drop in the line-integrated H_α emission which then increases slowly, reflecting the overall rise in electron density but never reaching the equivalent ohmic level (Fig. 2). A qualitatively similar H_α signal is obtained at all observable toroidal positions even when viewing the limiter and antennae.

The temporal evolution shown in Figs. 1 and 2 is qualitatively similar to purely ohmic discharges in which the density is increased either by strong puffing of deuterium or by the injection of light impurities. The initial dip in the line-integrated H_α emission in all three cases (rf, puffing, impurity injection) seems to be associated with the initial broadening of the electron density profile.

At lower values of I_p, the density increase is smaller and even appears to vanish if $I_p \sim 20$ kA. However, an overall decrease in particle confinement at these low currents makes interpretation of the results difficult.

III. INFLUENCE OF ALFVEN WAVE SPECTRUM. In Fig. 3 we show the final electron density as a function of the target density for both hydrogen and deuterium discharges with 100 kW of rf power. The curves show regions of apparent re-

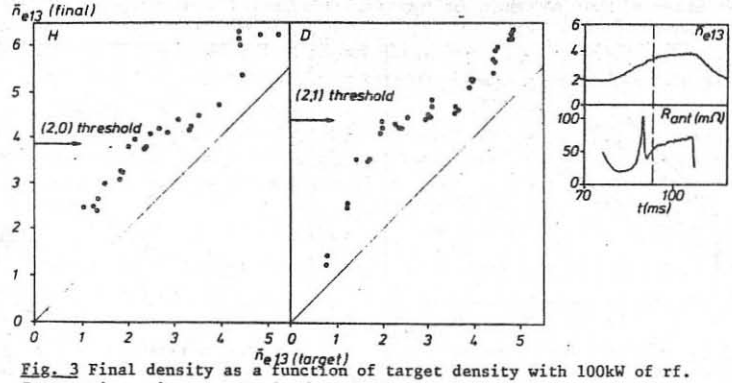


Fig. 3 Final density as a function of target density with 100kW of rf. Inset: Discontinuous behaviour at (2,0) threshold in hydrogen

duced increase ($\bar{n}_e$(final) ~ 4 x 10^{13} cm^{-3} in hydrogen and 4.5 x 10^{13} cm^{-3} in deuterium). This corresponds to discharges which display a discontinuity in the density rise[3] when a new resonance surface appears in the centre of the plasma as shown as an inset in Fig. 3. Apart from these discontinuities, the density rise is normally linear with rf power. This has been verified by using subsets of our 8 antennae to couple equivalent powers with different antenna currents giving the same density increase.

Further evidence of the effect of the Alfvén wave spectrum is given in Fig. 4 where we have varied the antenna phasings to change the dominant toroidal wavenumbers in the excited spectrum. For the same power delivered the density increase is greatest for the N = 4 phasing which is known to couple poorly to central resonant surfaces at this density. Similarly the n = 2 surfaces tend to be more central than the n = 1 yet the N = 1 phasing produces the greater rise in density. It is tempting to link the density rise with a phenomenon that is reduced in importance when central power deposition increases.

IV. PARTICLE CONFINEMENT RECYCLING AND IMPURITIES. We can write the global particle balance equation as:

$$dN/dt = S_H + S_Z - N/\tau_p \qquad (1)$$

where N is the total number of electrons in the discharge, τ_p is the global particle confinement time, and S_H, S_Z represent the ionisation of hydrogen and impurity atoms respectively. In general $S_H = \psi + RN/\tau_p$ where ψ is the additional source of neutrals from the gas valve and R is the recycling coefficient (representing both back-scattering and de-trapping). Under conditions where ψ is zero or constant there are three possible causes for a rise in electron density, each of which will be considered in turn.

(a) An increase in S_H due to greater recycling. Integration of the H_α profile suggests that any increase in S_H is commensurate with the overall rise in electron density. Unlike ICRF heating experiments[1] we have never observed any significant increase in neutral efflux. A deuterium discharge fired after a long sequence of hydrogen discharges (and vice-versa) has been

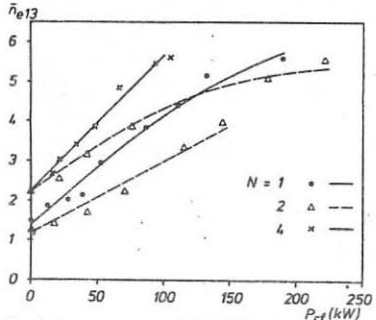


Fig.4 Power scans with different antenna phasings in deuterium discharges

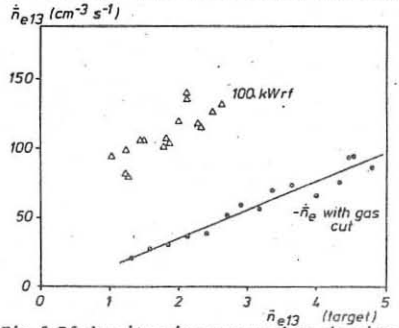


Fig.5 Rf density rise compared to density decrease obtained with gas cut and no rf

used to elucidate further the recycling processes[4]. The ratio of the line-integrated emissions of H_α and D_α measured by a Fabry-Perot spectrometer did not change significantly during the rf pulse, indicating that recycling is not substantially modified.

(b) An increase in S_Z due to either a greater flux of impurities or a change in the profiles of temperature and density. As the plasma purity has been improved by successive modifications to limiter design and material and antenna design and materials the density rise has persisted and even seems to be greatest under the cleanest conditions. This argues against the ionisation of impurities as the source of the density rise. Radiated power profiles and simulations indicate that for the discharge shown in Fig. 1 the low-Z and metal impurity concentrations increase from 2.5% and 0.1% to 3.2% and 0.18% respectively. The central Z_{eff} and A_{eff} rise from 2.7 and 1.2 to 3.3 and 1.3 respectively in agreement with measured values (the effective mass A_{eff} can be estimated from the frequencies of the global eigenmodes that appear in the antenna spectrum). The increase in impurity concentration can at most account for 20% of the observed central density rise.

(c) Improved particle confinement. If τ_p becomes infinite, equation (1) gives an upper limit to $\dot{N}$/dt. In Fig. 5 we plot the initial value of $\dot{\bar{n}}_e$ against the target density for the series of discharges shown in Fig. 2. Also shown in Fig. 5 are the results of an experiment without rf in which we cut the external source ϕ. Equation (1) shows that the instantaneous decrease in $\dot{N}$/dt will be equal to the above limit. Even with 100 kW of rf the discharges in Fig. 5 exceed this limit by a considerable factor, pointing to the limitations of a simplistic model.

V. CONCLUSION. It seems that neither improved recycling nor increased impurity concentrations can explain the observed increases in density. If the particle balance is represented as the difference between an inward and outward flux, as is suggested by many experimental results, then the limit on $\dot{N}$/dt is much greater than that predicted by eqn (1). The rf power could act to perturb the balance by either suppressing one of the loss terms contributing to the outward flux or by increasing the inward pinch velocity. In this model it is easier to envisage the spectrum related effects as discussed in section 3.

Acknowledgements. We recognize the assistance of the whole TCA team in this work and the support of Professor F. Troyon and A. Heym. The work was partially supported by the Fonds National Suisse.

References

[1] J. Hosea et al., in Heating in Toroidal Plasmas (Proc. 4th Int. Symp., Rome, 1984) Vol. I, 261.
[2] K.-I. Chen et al., ibid, 680.
[3] K. Appert et al., ibid, 171.
[4] G.M. McCracken et al., Nucl. Fusion 18 (1978) 35.

KINETIC THEORY OF ALFVEN WAVE HEATING IN FINITE BETA TOKAMAK PLASMA

Huang Lin Qiu Xiaoming Ding Ning
Southwestern Institute of Physics, Leshan, P.O.Box 15,
Sichuan, the People's Republic of China

Abstract

In the present paper, a kinetic theory on Alfven wave heating in finite beta tokamak plasma is developed. In cylindrical geometry, we have derived three differentail equations of the second order in r for the radial component E_r of the perturbed electric field and its $E_\perp$ and $E_\parallel$, perpendicular and parallel to magnetic field $\underset{\sim}{B}_0$, and the corresponding boundary conditions in plasma region. Our system of the equations not only includes the main characteristics of tokamak configuration--magnetic shear and equilibrium current, and some conventional kinetic effects, but also the ones associated with the finite beta, such as transit time magnetic pump(TTMP), ion sound, and ion Landau damping.

1. Introduction

Alfven wave, in view of its low frequency and longer wavelength is taken to be most suitable for heating the plasmas in large-size tokamak and future fusion reactor. At least, one need not worry about skin effect. Moreover, coupling of Alfven wave energy to plasma is easier than RF waves. Hence, last decade the theoretical investigations on heating of Alfven wave are quite active. In particular, the development of MHD theory[1-3] is more systematic. But, kinetic theory[4] only begins. However, all of those is restricted to the case of low beta limit.

The paper is aimed at developing a kinetic theory on heating of Alfven wave to finite beta tokamak plasmas. Difficulty in analysing wave heating of tokamak plasma by means of kinetic method consists in that up to now, no strict method allows one to derive an explicit expression of susceptibility tensor for the tokamak

plasma. One usually employs so called heuristic method to transform the susceptibility tensor of homogeneous plasma into the inhomogeneous case. Employing the method and shear coordinate system ($\hat{e}_r$, $\hat{e}_\parallel = \underline{B}_0/B_0$, $\hat{e}_\perp = \hat{e}_\parallel \times \hat{e}_r$) introduced by Ross[4] et al at first, we can obtain tokamak plasma susceptibility tensor which contains magnetic shear, the equilibrium current, and almost kinetic effects. In particular, the kinetic effects associated with the finite beta, such as TTMP, ion sound, and ion Landau damping, are clearly reflected in our expression of susceptibility tensor. In cylindrical geometry, we derive a system of the differential equations of the second order for the components(E_r, $E_\perp$, $E_\parallel$) of the perturbed electric field. Since the parallel component $E_\parallel$ appears in the set of equations, it suggests that a set of new boundary conditions (by contrast with the case of low beta) is necessary to make the solution of the equations uniquely determined. Although the equations and the boundary conditions are formally complicated, they could be widely used to analyse Alfven wave heating of tokamak plasma.

2. Equations of perturbed electric field and boundary conditions

The tokamak plasma under consideration is geometrically same as the one in Ref[4]. As Alfven wave frequency is very low, the inequality $\omega\gamma_p/c \ll 1$ always is valid. Therefore, the displacement current can be neglected. Maxewell's equation becomes

$$\nabla \times \nabla \times \underline{E} = i\frac{4\pi\omega}{c}\underline{J} = \frac{\omega^2}{c^2}\underline{\underline{\chi}} \cdot \underline{E} \,, \qquad (1)$$

where $\underline{\underline{\chi}}$ is the plasma susceptibility tensor, whose expression in uniform magnetic field has been already given by linear Vlasov theory.[5] The heuristic method means that we rotate the susceptibility tensor given in Ref.[5] for an angle, i.e, from the x-y plane to x'-y', and replace(k_x', k_y', k_z) by ($-i\,d/dr, k_\perp, k_\parallel$) or ($-ir'(d/dr)r, k_\perp, k_\parallel$)

in accordance with the operator's self-adjointness. In addition, by the aid of the shear coordinate system, we finally get the susceptibility tensor for finite beta tokamak plasma. On the other hand, three components on the left-hand side of Eq.(1) are easily written. Thus the equations of the perturbed electric field are as follows

$$\left[\frac{\omega^2}{c^2}(A_1^e + A_1^i) - k_\parallel^2 - k_\perp^2 - \frac{\omega^2}{c^2}\frac{d}{dr}(A_2^e + A_2^i)k_\perp^{-2}\frac{1}{r}\frac{d}{dr}r\right] E_r - i\left[\frac{\omega^2}{c^2}(A_3^e + A_3^i) + \frac{\omega^2}{c^2}\frac{d}{dr}k_\perp^{-1}(A_2^e + A_2^i)\right.$$

$$-\frac{\omega^2}{c^2}(A_1^e+A_1^i)k_1^{-1}\frac{1}{\gamma}\frac{d}{d\gamma}\gamma+k_1\frac{1}{\gamma}\frac{d}{d\gamma}\gamma+\frac{\omega\Omega_e}{\omega_{pe}^2}k_\alpha A_3^e\frac{1}{\gamma}\frac{(\delta'\gamma)'}{1+\delta^2}-\frac{k_\alpha^2(\delta'\gamma-\delta\gamma+k_\alpha\delta^2}{\gamma(1+\delta^2)}]E_1-i[\frac{\omega^2}{c^2}k_\alpha(\rho_e A_4^e+\rho_i A_4^i)$$
$$+\frac{\omega^2}{c^2}\frac{d}{d\gamma}(\rho_e A_5^e+\rho_i A_5^i)+k_\alpha\frac{d}{d\gamma}+\frac{k_\alpha\delta^2+k_\alpha(\delta\gamma)'}{\gamma(1+\delta^2)}]E_\alpha=0\ , \qquad (2\text{-}a)$$
$$i[\frac{\omega^2}{c^2}(A_3^e+A_3^i)-\frac{\omega^2}{c^2}(A_2^e+A_2^i)k_1^{-1}\frac{1}{\gamma}\frac{d}{d\gamma}\gamma+\frac{\omega^2}{c^2}\frac{d}{d\gamma}k_1^{-1}(A_1^e+A_1^i)-\frac{d}{d\gamma}k_1+\frac{\omega\Omega_e}{\omega_{pe}^2}k_\alpha A_3^e\frac{(\delta'\gamma)'}{\gamma(1+\delta^2)}-\frac{k_\alpha(\delta'\gamma-\delta\gamma+k_\alpha\delta^2}{\gamma(1+\delta^2)}]E_\gamma$$
$$+[\frac{\omega^2}{c^2}(A_1^e+A_1^i)-k_1-\frac{\omega^2}{c^2}\frac{d}{d\gamma}k_1^{-2}(A_1^e+A_1^i)\frac{1}{\gamma}\frac{d}{d\gamma}\gamma+\frac{d}{d\gamma}\frac{1}{\gamma}\frac{d}{d\gamma}\gamma+\frac{(\delta'\gamma)'(\delta\gamma)'}{1+\delta^2}-\frac{[\delta'\gamma^2-(1+\delta^2)(\delta\gamma)\gamma]^2}{(1+\delta^2)^2}]E_\perp$$
$$+[\frac{\omega^2}{c^2}k_1(\rho_e A_5^e+\rho_i A_5^i)+k_\alpha k_\perp+\frac{\omega^2}{c^2}\frac{d}{d\gamma}(\rho_e A_6^e+\rho_i A_6^i)+\frac{2\delta'}{1+\delta^2}\frac{d}{d\gamma}+\gamma^{-1}(\frac{\delta'\gamma}{1+\delta^2})'-\frac{\delta}{\gamma^2(1+\delta^2)}]E_{11}=0, \qquad (2\text{-}b)$$
$$i[\frac{\omega^2}{c^2}k_\perp(\rho_e A_4^e+\rho_i A_4^i)-\frac{d}{d\gamma}k_\perp-\frac{\omega^2}{c^2}(\rho_e A_5^e+\rho_i A_5^i)\frac{1}{\gamma}\frac{d}{d\gamma}\gamma-\frac{k_\alpha-k_1(\delta\gamma)'}{\gamma(1+\delta^2)}]E_\gamma+[\frac{\omega^2}{c^2}k_\perp(\rho_e A_5^e+\rho_i A_5^i)+k_\alpha k_\perp-\frac{\omega^2}{c^2}(\rho_e A_6^e+\rho_i A_6^i)$$
$$\times\frac{1}{\gamma}\frac{d}{d\gamma}\gamma-\frac{2\delta'}{(1+\delta^2)}\frac{d}{d\gamma}-\frac{1}{\gamma}(\frac{\delta'\gamma}{1+\delta^2})'-\frac{\delta'}{\gamma^2(1+\delta^2)}]E_\perp+[\frac{d}{d\gamma}\frac{1}{\gamma}\frac{d}{d\gamma}\gamma+2\frac{\omega^2}{c^2}(A_6^e+A_6^i)-k_\perp^2-(\frac{\delta'}{1+\delta^2})'+\frac{1}{\gamma^2(1+\delta^2)}]E_{11}=0, \qquad (2\text{-}c)$$

where

$$A_1^\alpha=\sum_{\ell=-\infty}^{\infty}G_{\alpha\ell}Z_{\alpha\ell}(\eta_{\alpha\ell}^{-1}I_\ell^{\alpha\alpha}+2\eta_{\alpha\ell}I_\ell^\alpha-2\eta_{\alpha\ell}I_\ell^{\alpha\prime}), \qquad A_2^\alpha=\sum_{\ell=-\infty}^{\infty}\ell^2G_{\alpha\ell}\eta_{\alpha\ell}^{-1}Z_{\alpha\ell}I_\ell^\alpha\ ,$$
$$A_3^\alpha=\sum_{\ell=-\infty}^{\infty}\ell G_{\alpha\ell}Z_{\alpha\ell}(I_\ell^\alpha-I_\ell^{\alpha\prime})\ , \qquad A_4^\alpha=\sum_{\ell=-\infty}^{\infty}G_{\alpha\ell}(1+S_{\alpha\ell}Z_{\alpha\ell})(I_\ell^\alpha-I_\ell^{\alpha\prime})\ ,$$
$$A_5^\alpha=\sum_{\ell=-\infty}^{\infty}\ell G_{\alpha\ell}(1+S_{\alpha\ell}Z_{\alpha\ell})\eta_{\alpha\ell}^{-1}I_\ell^\alpha, \qquad A_6^\alpha=\sum_{\ell=-\infty}^{\infty}G_{\alpha\ell}S_{\alpha\ell}(1+S_{\alpha\ell}Z_{\alpha\ell})I_\ell^\alpha\ .$$

Z_α is the plasma dispersion function, $G_{\alpha\ell}=(\omega_{p\alpha}/k_z v_{t\alpha}\omega)\exp(-\eta_\alpha)$, $I_\ell^\alpha=dI_\ell^\alpha(\eta_\alpha)/d\eta_\alpha$, $\eta_\alpha=k_1^2v_\alpha^2/2\Omega_\alpha^2=k_1^2\rho_\alpha^2/2$, $S_{\alpha\ell}=(\omega-\ell\Omega_\alpha)/(k_z v_{t\alpha})$. Eqs.(2) include the various kinetic effects in the case of low beta limit, while $2G_{i\ell}\eta_{i\ell}(I_\ell^{i\prime}-I_\ell^{i\prime\prime})Z_{i\ell}$ and $G_{i\ell}(1+S_{i\ell}Z_{i\ell})k_\perp\rho_{i\ell}(I_\ell^{i\prime}-I_\ell^{i\prime\prime})$ terms describe the ion sound and TTMP, respectively, and $G_{i\ell}S_{i\ell}(1+S_{i\ell}Z_{i\ell})I_\ell^i$ represents ion Landau damping. The latter kinetic effects associated with the finite beta are clearly reflected in our equations. It is a main result of this paper.

In order to uniquely determine the solution of Eqs.(2), we derive the corresponding boundary conditions. They are, at the origin, either

$$E_\gamma(0)=E_\perp(0)=E_{11}(0)\ , \qquad |m|\neq 1 \qquad (3\text{-}a)$$

or

$$E_\gamma'(0)=E_\perp'(0)=E_{11}'(0)\ , \qquad |m|=1 \qquad (3\text{-}b)$$

at the plasma-vacuum interface

$$[A_2^e(\gamma_p)+A_2^i(\gamma_p)]E_\gamma(\gamma_p)-i[A_3^e(\gamma_p)+A_3^i(\gamma_p)]E_\perp(\gamma_p)-i(k_\perp\rho_i A_4^e+k_\alpha\rho_i A_4^i)_{\gamma_p}E_{11}(\gamma_p)=0\ , \qquad (4\text{-}a)$$
$$f_1E_\gamma(\gamma_p)+f_2E_\perp(\gamma_p)+f_3E_{11}(\gamma_p)+f_4E_\perp'(\gamma_p)+f_5E_{11}'(\gamma_p)=0\ , \qquad (4\text{-}b)$$
$$g_1E_\gamma(\gamma_p)+g_2E_\perp(\gamma_p)+g_3E_{11}(\gamma_p)+g_4E_{11}'(\gamma_p)=g_5J_3\ , \qquad (4\text{-}c)$$

where

$$f_1=[\frac{1}{\gamma}(A_2^e+A_2^i)-k_\perp(A_3^e+A_3^i)-k_\alpha k_\perp(\rho_e A_6^e+\rho_i A_6^i)+k_{11}\frac{1}{\gamma}(\rho_e A_5^e+\rho_i A_5^i)]_{\gamma_p}\ ,$$
$$f_2=[-i\frac{d}{d\gamma}(A_3^e+A_3^i)+ik_1(A_4^e+A_4^i)-ik_\alpha\frac{1}{\gamma}(\rho_e A_6^e+\rho_i A_6^i)+ik_\alpha k_\perp(\rho_e A_5^e+\rho_i A_5^i)+ik_\perp\sum_{\omega^2}\frac{(\delta\gamma)(\delta\gamma)'}{(1+\delta^2)^2\gamma^2}]_{\gamma_p}\ ,$$
$$f_3=[ik_1^2(\rho_e A_5^e+\rho_i A_5^i)+2k_{11}(A_6^e+A_6^i)]_{\gamma_p}\ , \qquad f_4=[A_4^e+A_4^i+k_\alpha(\rho_e A_5^e+\rho_i A_5^i)]_{\gamma_p}\ ,$$
$$f_5=-i[A_5^e+A_5^i+k_{11}(\rho_e A_6^e+\rho_i A_6^i)]_{\gamma_p}\ , \qquad g_1=i[(1+\delta^2)^{-1/2}ik_\alpha/k_z)(F_3/F_2)]_{\gamma_p}\ ,$$
$$g_2=[(1+\delta^2)^{-1/2}(\delta'-\delta/\gamma)(F_3/k_zF_2)-(1+\delta^2)^{-3/2}(m\delta+k_z\gamma)(m-\delta k_z\gamma)/(k_z^2\gamma^2)]_{\gamma_p}\ ,$$
$$g_3=[(1+\delta^2)^{-1/2}(\delta^2/k_z\gamma)(F_3/F_2)+(1+\delta^2)^{-3/2}(m\delta^2+k_z\gamma)^2/(k_z^2\gamma^2)]_{\gamma_p}\ , \qquad g_4=-[(1+\delta^2)^{-1/2}(F_3/k_zF_2)]_{\gamma_p}\ ,$$
$$g_5=i[\frac{4\pi\omega}{c}(k_\alpha^2+k_z^2)^{-1/2}(1+\delta^2)^{-1}(m-\delta k_z\gamma)(\gamma_c/\gamma)(\frac{F_3}{F_2}g_1-g_3)]_{\gamma_p}\ ,$$

$F_1 = I_m(|k_z|r) - K_m(|k_z|r) I_m(|k_z|\gamma) / K_m(|k_z|\gamma)$, $F_2 = I_m(|k_z|r) - K_m(|k_z|r) I_m(|k_z|\gamma_w) / K_m(|k_z|\gamma_w)$,
$F_3 = I_m'(|k_z|r) - K_m'(|k_z|r) I_m'(|k_z|\gamma_w) / K_m'(|k_z|\gamma_w)$, $g_1 = I_m'(|k_z|\gamma_c) K_m(|k_z|r) - K_m'(|k_z|\gamma_c) I_m(|k_z|r)$,
$g_2 = I_m'(|k_z|\gamma_c) K_m'(|k_z|r) - I_m'(|k_z|r) K_m'(|k_z|\gamma_c)$.

3. Discussion

(1) In the present paper, the finite beta refers to an average meaning, namely, the beta value in the bulk plasma region is higher, while the condition of low beta in the narrow edge is still valid. Thus, there is no surface current. This is of the prerequisite for deriving the boundary conditions in the paper.

(2) We can solve the Eqs.(2), by the aid of numerical method, and obtain the distribution of the perturbed electric field, as soon as J_S in the antenna, the profiles for plasma density and temperature, and the safety factor q have been given. Furthermore, we can compute the energy deposition, the heating efficiency, and so on. The numerical results will be published in our upcoming paper.

References

1. A. Hasegawa and L. Chen, Phys. Fluids, 19, 1924(1976).
2. K. Appert et al, presented at the Second International symposium on heating in Toroidal Plasmas, Como, Italy (1980).
3. A.A. Galeev, R.N. Suodan, Basic Plasma Physics I, North-Holland Publishing Company Amsterdam, New York, Oxford (1983).
4. Davidw Ross, et al, Phys. Fluids, 25, 652 (1982).
5. A.I. Akhiezer, et al, Collective Oscillations in a Plasma (Pergamon, Oxford, 1967), Chap.2.

DOUBLE ALFVEN WAVE RESONANCE - IS THE POSSIBLE HEATING SCHEME OF A LARGE TOKAMAK PLASMA.

Elfimov A.G. (I.N. Vekua Inst. of Phys. and Tech., Sukhumi, USSR)

INTRODUCTION. During the plasma heating in large tokamaks we need to place RF-circuit in the recess [1] - a special hole in a chamber wall - to cover one from the hot plasma flux. Such a recess can not be great, hence, RF-circuit should be modular and its square S_c would be more less than the chamber wall square S_w. In this case, spatial harmonics of RF-field appear and their number is determined by the value of S_w/S_c. Since during Alfven wave heating not more than two harmonics can satisfy the conversion conditions simalteniously, the circuit-plasma coupling will be significant only in the resonance regimes. In Alfven wave range the kink-resonance [2] and the global resonance [3,4] have been investigated. In the conditions of large tokamaks, when the chamber wall is close to the plasma boundary it's impossible to create kink-resonance conditions with the conversion poit close to the plasma centre. So it's hard to support the global resonance in the non-steady state plasma because of its high Q-factor.

Here, we offer to use for the plasma heating "double" Alfven wave resonance, which means the resonance of the fast Alfven wave in the region $[r_A\, a]$ from the plasma boundary till the conversion point and local resonance, providing Landau-damped electron absorption of the shortwave mode, appearing because of the fast mode conversion. This resonance needs the field of the fast magnetosonic wave in the region $r<r_A$. Such a resonance can be realized in plasma with the magnetic field shear and the RF-field Q-factor ~ 15 when the conversion point r_A is close to the plasma centre.

SOLUTIONS. We shall demonstrate the possibility of various resonances in terms of a model of a trapezoidal density profile plasma. A homogeneous axial current flows through a homogeneous region of density ($r<a_t$) and generates a falling down magnetic field ($B_\varphi = B_t a_t/z \ll B$) in an inhomogeneous region of density ($a_t < z < a$). Following Ref. [2], linear solutions can be found for a binormal component of the electric field in an inhomogeneous region, within the MHD-approximation for $(na)^2 \ll (mR)^2$; $(a-a_t)^2 \ll a^2$:

$$2E_\rho = \pi a_t E_0 \left\{ \left[\frac{k_z^2 J_m}{J_m'(k_z z)} \right]_{z=a_t} \cdot (z_A/a_t - 1) \left[N_0(x_t) J_0(x) - N_0(x) J_0(x_t) \right] - \frac{x_t}{2} \left[N_1(x_t) J_0(x) - N_0(x) J_1(x_t) \right] \right\};$$

$$x = 2\sqrt{A(1-z/z_A)}\,; \qquad A = \frac{m\left[\Omega^3/\omega_{ci} c_{A0}^2 - 4 k_\parallel (a-a_t)(1-\Omega^2/\omega_{ci}^2)/R a_t q_t\right]}{\Omega^2/c_{A0}^2 - 4m k_\parallel (a-a_t)(1-\Omega^2/\omega_{ci}^2)/R a_t q_t}\,; \tag{1}$$

$$k_z^2 = \frac{\Omega^2}{c^2}\varepsilon_1 - k_\rho^2 + \frac{G^2 - \frac{1}{2}\frac{d}{dz}(z k_\rho G)}{k_\parallel^2 - \varepsilon_1 \Omega^2/c^2}\,; \qquad G = 2k_\parallel B_\varphi/z\beta - k_\rho B_\varphi^2/B^2 - \varepsilon_1 \Omega^3/c^2\omega_{ci}\,. \tag{1a}$$

J_0 and N_0 are Bessel functions of zero indexes. Matching solution for plasma with those for vacuum and using an expression for a radial component of Umov-Pointing vector, we obtain 2 the absorbed power value for a plasma cylinder $2\pi R$ in length, deducing it via a surface impedance, Z_{mn}, for Fourrier harmonics of surface current $J_{\varphi,z} = J^{\varphi,z}_{mn} \exp i(m\varphi + nz/R - \Omega t)$:

$$\bar{W} = 2\pi^2 R b \sum_{mn} \mathrm{Re}\, Z_{mn} |J^{\varphi}_{mn}|^2; \qquad (2)$$

$$Z_{mn} = 4\pi i \frac{\Omega b}{c^2} (K_m)^2_b \left[\left(\frac{I'_m}{K'_m}\right)_d - \left(\frac{I'_m}{K'_m}\right)_b\right]\left[\left(\frac{I'_m}{K'_m}\right)_b + \Psi_{mn}\right] \Big/ \left[\left(\frac{I'_m}{K'_m}\right)_d + \Psi_{mn}\right];$$

$$\Psi_{mn} = -\left[\frac{I'_m}{K'_m} \cdot \frac{\frac{d}{dz}(zE_\theta)/E_\theta - \frac{2}{1+nq/m} - \frac{(mR)^2+(na)^2}{|m|aR} \cdot \frac{I_m}{I'_m}}{\frac{d}{dz}(zE_\theta)/E_\theta - \frac{2}{1+qn/m} - \frac{(mR)^2+(na)^2}{|m|aR} \cdot \frac{K_m}{K'_m}}\right]_{z=a} \qquad (3)$$

and $I'_m(nz/R)$; $K'_m(nz/R)$ are derivatives from modified Bessel functions; b -circuit radius; d - conducting wall radius.

As it is seen from Exp.(3), due to the clousely spaced conducting wall, the circuit resonance [2] is reduced by a factor of $(1-b/d)^2 \ll 1$. This fact implies that the resistance will be significant only in resonance conditions, other wise , the reactanc will be greater than the resistance. The resonance conditions are established when the denominator is minimal in the expression for plasma impedance; then for $d-b \ll d$, one has:

$$\mathrm{Re}\left[\frac{d}{dz}(zE_\theta)/E_\theta\right] - 2(1+nq_a/m)^{-1} + (1-a/d)^{-1} \simeq 0. \qquad (4)$$

Then, the maximum resistance of a single mode will be:

$$\mathrm{Re}\, Z_{max} \simeq -4\pi\Omega m^4 R^4 (d-b)^2 \Big/ \left[b c^2 n^4 a^4 (K'_m)^2_b \, \mathrm{Im}\, \Psi_{res}\right]. \qquad (4a)$$

The resonance condition (4) can be easily analysed for the trapezoidal density profile in three cases:

1. If $|A(a-a_t)| \ll a$,it leads to the kink- resonance [2]:

$$\Omega^2 = k^2_{\parallel 0} c^2_{A0} \frac{1-\Omega^2/\omega_{ci}}{|m|-A}\left[\frac{1}{1-a/d} - \frac{2}{1+nq_a/m}\right].$$

In order to get optimum plasma heating for the kink-resonance mode, it is necessary to have the energy input region r_A close to the plasma centre (or close to a_t in the trapezoidal density profile). This condition and that of the kink-resonance, due to (d-b) d, may be simulteneously met only for near-cyclotron frequencies ($\Omega < \omega_{ci}$) with $m < 0$.

2. If there is no conversion point in plasma and $0 < k^2_{\parallel} - \varepsilon_1 \Omega^2/c^2 \ll k^2_{\parallel}$

in a homogeneous density region, then Exp.(4) gives rise to a global Alfven resonance [3,4].

$$(a-a_t)\,k_z\,J_m'(k_z a) \simeq J_m(k_z a_t) \quad . \qquad (6)$$

Hence, it follows that $k_z a_t$ should be close to the Bessel function (J_m) root where k_z is defined by Exp.(1a) for $m\,k_{||} > 0$. In a collisionless hydrodynamic model, the RF-field is not absorbed and the resonance is infinitely narrow and of high Q-quality.

3. For $4A(z_A-a) = \varkappa^2 z_A$, Exp.(3) gives the "double" Alfven resonance mode where $\varkappa$ is the first root of the Bessel function J_o

$$\Omega^2 = \frac{4m\,k_{||}(a-a_t)\,c_{A0}^2}{R\,a_t\,q_t} \cdot \frac{\varkappa^2 z_A + 4(a-z_A)}{\varkappa^2 z_A + 4m(a-z_A)\,\Omega/\omega_{ci}} \quad . \qquad (7)$$

In order to have the conversion point close to the homogeneous density region ($z_A \simeq a_t$), or $\Omega \simeq (k_{||}c_A)_{z=a_t}$; with $a-z_A = a/3$ it is necessary that $nq(a_t) \simeq 1.7\,m$. Calculation performed in accodance with Ref. [5] for parabolic density and axial current profiles, with the conversion point close to the plasma centre, for m=2, gives fast mode resonance condition at $nq(o) \simeq 3.6$ These conditions are well met for main spatial modes ($n = \pm 3; \pm 6$; $m = \pm 2; \pm 3$) with the presumed value of $q(o) = 0.9 \div 1.2$ in INTOR.

RECESS SOLUTIONS. We estimate the impedance Z_{mn} of a semiloop-shaped poloidal circuit which drives a RF field with M=0 and N=$\pi R/L$ modes within the recess: d_1-recess bottom, b-radius conducting wall and circuit current $J_\varphi = 0.5\,\pi (I_c/L)\cos(\pi z/L)\exp(-i\Omega t)$ at $\frac{L}{2} < z < \frac{L}{2}$; $\varphi_o/2 < \varphi < \varphi_o/2$ (L- recess dimension in axis z):

$$Z_{mn} = -4\pi i \frac{\Omega}{c^2}(d_1-b)\left|\frac{N}{n}\right| \cdot \frac{(I_m' + \Psi_{mn} K_m')_{z=b}}{\left[I_m' + \Psi_{mn} K_m' + |N|\,\frac{d_1-b}{R}(I_m + \Psi_{mn} K_m)\right]_b} \quad . \qquad (9)$$

This surface impedance will be highest when the real part of the denominator in Exp.(9) is smallest for $(b-a) \ll b$.

$$\left[1 - \frac{a}{b} + \left(\frac{d_1}{b} - 1\right)\frac{N^2 a^2}{m^2 R^2 + n^2 a^2}\right]\left\{\mathrm{Re}\left[\frac{d}{dz}(zE_b)/E_b - \frac{2}{1+nq/m}\right]_{z=a}\right\} + 1 \simeq 0 \quad . \qquad (10)$$

Without disclosing details about resonances in Exp.(5-7), the resistance of (m,n) mode can be found for the frequency given by Cond.(10) while the impedance value will be expressed via Form. (4a). The reactence of this mode will change its sign while frequency passing through Cond.(10). The remaining modes will be nonresonant, contributing to the circuit reactence, their contribution to the resistance being small.

We shall assme that there are three recesses along the whole length of the torus and these recesses are equally spaced with

the period $2\pi R/3$ and the currents in them are in phase. With such feeding, the principal harmonics will be $m=0;\pm1;\pm3;$ and $n=\pm3;\pm6;\pm9$ with approximatly equal amplitudes $J^{\varphi}_{mn} \simeq 0.5\,\pi I_c S_c / L S_w$

Since the resonance in Exp.(6) can have only a couple of harmonics ($m/n = 2/3$), the total absorption due to a single circuit will be:

$$W = 0.5\, X\, I_c^2 = 0.5\, \frac{b}{R}\, Z_{res}\, I_c^2$$

where $L = \pi R/6$; $\varphi_0 = \pi/2$; $m = \pm 2$; $n = \pm 3$.

Hence, the circuit impedance in a single recess circuit is :

$$X = 4\pi\Omega\, \frac{(d_1-b)^2}{Rc^2} \cdot \frac{N^2 a^2}{m^2R^2+n^2a^2} \left| Re^2\left[\frac{d}{d\tilde{r}}(\tilde{r}E_\theta)/E_\theta\right] \Big/ Im\left[\frac{d}{d\tilde{r}}(\tilde{r}E_\theta)/E_\theta\right]\right|_a$$

Estimating $|ReE_\theta / ImE_\theta| \simeq 3$ for a mildly peaked resonance in Exp.(6) for the INTOR parameters (a=120; b=130; d=140 cm) we obtain X=1.5 Ohm for the resistance of the circuit and this value is quite enough for feeding 20 MW of power via a single recess. The reactence of the circuit ~5 Ohm, can be estimated from Exp(9) via the impedance of idle harmonics; since $\Psi_{idl} \simeq 0$, one has

$$Z_{idl} \simeq -4\pi i\, \frac{\Omega}{c^2}\,(d_1-b)\left|\frac{N}{n}\right|$$

In order to diminish the reactence of RF-circuit, the number of idle harmonics should be decreased, this requires to increase the radiating surface of RF-circuit; the reactence of idle harmonics should be compensated also against the negative reactence (capacitance) of resonant harmonics for the frequencies somewhat exceeding the resonance frequency within the halfwidth of the resonance.

CONCLUSION. Using the magnetic field shear, $q\frac{d}{d\tilde{r}}\left(\frac{1}{q}\right) > 0$ for $\frac{4}{1+nq/m} > k_z^2 a^2$ conditions can be obtained for a double Alfven resonance which is represented by a local resonance in the combination with a fast mode one over the region extending from the plasma bounary up to the conversion point. The RF-field absorption takes place due to the fast mode conversion into the short wavelength Alfven mode which is absorbed by Landau-damped plasma electrons.

The double Alfven wave resonance may be applied to heat plasmas in large tokamaks over the frequency range from 1 to 3 MC. In thiscase, the spectrum of spatial harmonics arising due to a modular (piecewise) shape of the RF-circuit in the recess can be used and absorption of 20 MW of a power can be ensured via a single recess.

1. VDOVIN V.L. Nuclear Fusion, 1983, v.23, 1435.
2. ELFIMOV A.G. Fizika plazmy, 1984, v.10, 700.
3. ROSS D.W., MAHAJAN S.M., CHEN G.L. Phys. Fluids, 1982, v.25, 652.
4. APPERT K., GRUBER R., TROYON F., VACLAVIK J. Plasma Physics, 1982, v.24, 1147.
5. ELFIMOV A.G. Fizika Plazmy, 1985, v.11, 550.

RF POWER INPUT IN THE TOKAMAK REACTOR WITH ALFVEN HEATING.

A.G.Kirov, V.P.Sidorov, S.N.Lozovskij, A.G.Elfimov, L.F.Ruchko, K.G.Komoshvili, V.V.Dorokhov.

I.N.Vekua Institute of Physics and Technology, Sukhumi, USSR.

Alfvén wave heating of plasma has been intensively studied recently both experimentally [1,2] and theoretically [3,4] and the results obtained allow to consider this method as an alternative for using in thermonuclear reactors. The peculiarity of RF power input in a device of Intor type is the necessity for antenna to be placed in special recesses in the first wall [5]. In the present paper the question of efficiency of Alfvén wave heating by means of an antenna which is located in such a recess and excites waves with $M,N \neq 0$ is investigated. It is shown that in such a case the maximum amplitude takes place for harmonics with $N = 10$, $M = 1 \div 3$, which have the most effective coupling with plasma.

For calculating the optimal conditions of RF heating in the Alfvén frequency range a onedimensional kinetic code EPSI has been developed [6] . It describes the processes of propagation and absorption of RF fields excited by a helical antenna with a surface current $I = I_0 \exp i(\pm N/R + M\varphi - \Omega t)$. The tensor-operator of dielectric permittivity involves the Landau electron damping, magnetic field shear and drift effects. For Intor parameters (minor radius a =120 cm, major radius R =500 cm, density profile $n = n_0(1-x^2)$, $x = r/a$; $n_0 = 2 \cdot 10^{14} cm^{-3}$; $B_0 = 5.5$ T; current profile $j = j_0(1 - x^2)^2$; $q_0 = 0.74$; $T_0 = 8$ KeV) the resistance of helical antenna has been calculated for various values of toroidal (N) and poloidal (M) mode numbers and for various positions of the wall (d) and antenna (b). (In Figs.1,2 b = 125 cm, d = 130 cm).Fig.1 shows a smooth increase of resistance when the conversion point x_A is shifted towards the plas-

ma boundary and sharp resonance peaks when x_A is placed in the central region of the plasma column which are presumably connected with the resonance excitation of combination of the fast and slow (kinetic) Alfvén modes. The modes with M = ±2, N = ±10 experience the maximum absorption and the differencies between positive and negative modes are insignificant which is connected with the small value of gyrotropy factor Ω/ω_{ci} for INTOR. Note that for $|M| > 2$ the resistance decreases. Decreasing q_o in the centre leads to absorption increasing for all modes and shifting the resistance maximum towards the plasma centre. Temperature variation within the range T_o = 2 ÷ 8 KeV leads to small variations of sharp resonance absorption peaks and does not change the principal picture of the resistance curves. Fig. 2 shows the radial distributions of electric fields at the conversion point positions X_A = 0.5 and 0.7 for M = -2, N = -10 and for parameters values as in Fig.1. The RF field distribution has a localized character which corresponds to the local character of the RF power absoption.

Analytical calculations of RF field excitation in plasma by means of antenna placed in the recess of the first wall have been carried out. We consider here the case of one window (recess); if several windows are present, the solution is found by the same way. Then the following simple estimate of RF power absorbed due to mode conversion is obtained:

$$W = \frac{S_w}{S_{tot}} W_1 \qquad (1)$$

where S_w and S_{tot} are the window area and the total area of the first wall, resp., W_1 is the value of power absorbed in the system where the wall (at r = d) is replaced by the recess bottom (r=h). In particular, if the recess bottom is situated close enough to the antenna, the efficiency of excitation is reduced proportionally to $(h-b)^2$. Formula (1) allows us to use the one-dimensional cylindrical code described above for estimating the power absorption level.

The above calculations show that modes with N = 10, M=1÷3 which may be excited by antenna with current $I_\varphi \sim \sin \frac{\pi z}{l}$ (where l is the window size along Z) are optimal for plasma heating.

Fig.3 shows one variant of the antenna schematic design. In order to reduce the voltage at the leads and to form the wave spectrum, the current sheet is divided into 6 elements with separate coaxial leads. The antenna elements may be made in the form of modules allowing the independent assembling. Estimates show that at $q(a)=2.1$; $T_{e,i} \simeq 2$ KeV, $\langle n_i \rangle = 1.4 \cdot 10^{20} m^{-3}$ and for the RF power input region $r < 0.4\,a$, the antenna has the resistance $Z_a \sim 1 \div 2.5$ Ohm, quality factor $Q \simeq 3$, and in order to put in plasma the power $\simeq 20$ MW with help of one antenna, it is necessary to apply the voltage $\lesssim 20$ kV.

The Alfvén wave heating method, thanks to the fact that it uses the low frequency range ($f \sim 1$ MHz) with the wavelengths much greater than the blanket thickness, allows to reduce considerably the window area necessary for RF power input.

The generators may be situated at practically any distance from the reactor. The power losses in the transmission line would be less than 200 kW if its length is ~ 100 m.

Conclusions. The above analysis shows that Alfvén wave heating can be used in systems of the INTOR type rather effectively, the antenna design being relatively simple and the electric parameters (antenna voltage etc.) being close to those accepted for other RF heating schemes.

REFERENCES.

1. De Chambrier A., Cheetham A.D., et al. Proc. 9-th Int. Conf. on Plasma Phys.and Contr.Nucl.Fusion Res.(Baltimore, 1982). IAEA, Vienna, v.2 (1983) p.301.
2. Demirkhanov R.A., Kirov A.G. et al. Proc.9-th Int.Conf. on Plasma Phys. and Contr.Nucl.Fusion Res.(Baltimore, 1982). IAEA, Vienna, v.2 (1983) p.91.
3. Appert K., Balet B., Gruber R., et al. Proc.8-th Int. Conf.on Plasma Phys.and Contr.Nucl.Fusion Res.(Brussels, 1980). IAEA, Vienna, v.2 (1981) p.43.
4. Elfimov A.G., Lozovskij S.N., Dorokhov V.V.(Jr.).Nucl. Fusion 24, (1984) p.609.
5. Vdovin V.L. Nucl.Fusion 23 (1983) p.1435.

6. Dmitrieva M.V., Elfimov A.G.,Komoshvili K.G., et al. Preprint of the M.V.Keldysh Institute of Applied Mathematics IPM-4 (Moscow,1984).

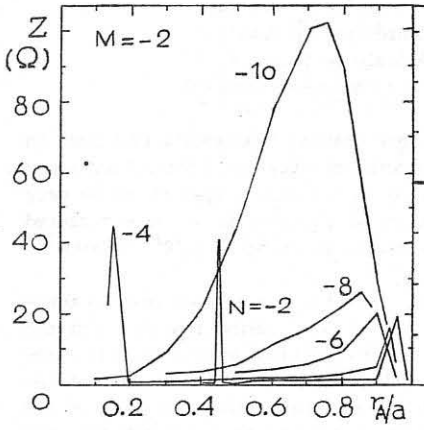


FIG.1

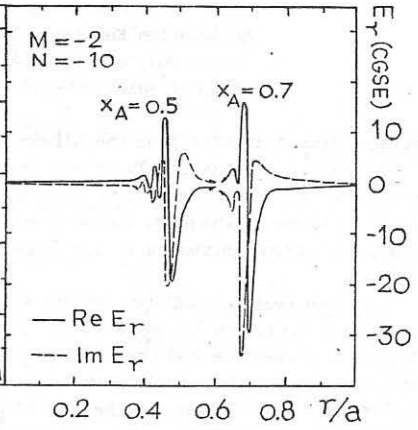


FIG.2

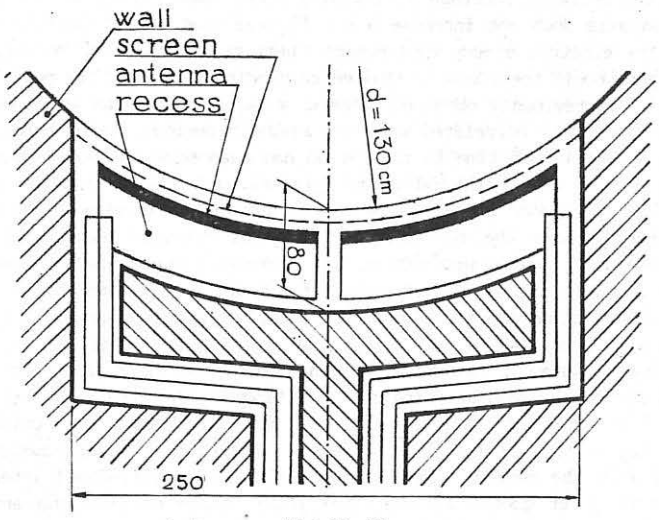


FIG.3

STRONG ELECTRON AND ION HEATING IN CLEAN CONDITIONS IN TCA

A. de Chambrier, G.A. Collins, B. Joye, A. Lietti, J.B. Lister and J.-M. Moret
Centre de Recherches en Physique des Plasmas
Association Euratom - Confédération Suisse
Ecole Polytechnique Fédérale de Lausanne
21, Av. des Bains, CH-1007 Lausanne, Switzerland

Abstract. Recent results from the Alfvén Wave Heating experiments (2.5 MHz) on the TCA Tokamak show extremely strong sawtooth activity above the AW continuum thresholds. The power deposition profile to the electrons appears to be very peaked in these conditions. Below dominant AW thresholds, we have measured anomalously strong increases in ion temperature, reaching 17 x 10^{13} eV/kWcm^3.

I. Electron Heating. AWH experiments are currently underway on the TCA tokamak (R,a = 0.61,0.18 m, B_ϕ = 1.5T, I_p ~ 130 kA). Using new SiC limiters and lateral screens we had obtained very clean conditions with sustained electron heating and a drop in loop voltage during the rf pulse[1]. The cost of installing side screens was a reduction of the antenna loading and hence of the available rf power. We therefore removed these screens to carry out the work described at 200-230 kW, greater than the ohmic power in the target plasma. Even with the measured increase in radiated power loss during the rf pulse, the loss on axis does not increase until 13 msec into the rf pulse[2], representing a few electron energy confinement times at low density. The electron energy balance could therefore be studied convincingly during this period. The increase in T_e previously obtained[1] showed a large dispersion which we subsequently found to be correlated with the sawtooth period. The electron temperature as a function of time in the period has been measured and repeated in three conditions, namely the OH target plasma, with the rf applied in the (n,m) = (2,0) continuum[3] and with the rf applied in the (n,m) = (2,1) continuum. Figure 1 shows the representative results obtained using a 1 pulse - 1 position Ruby scattering system. The central temperature was measured 7 msec after the start of the rf pulse, about 1-2 x τ_{Ee} under these conditions, so the electron energy balance was probably quasi-stationary. The electron temperature ramp (solid line) is the result of a linear fit to the data. These discharges were, in two cases, obtained only three days after the vessel was opened up to air, demonstrating the resiliance of the effect; no gettering is used in TCA. In Table I, we have in addition calculated $3/2\ e \times n_{eo} \times \Delta\tilde{T}_{eo}/\Delta\tilde{t}$ where $\Delta\tilde{T}_{eo}$ is the amplitude of the sawtooth of period $\Delta\tilde{t}$, with the central density measured using a multi-chord interferometer. The rf power quoted is the total power delivered from the antenna,

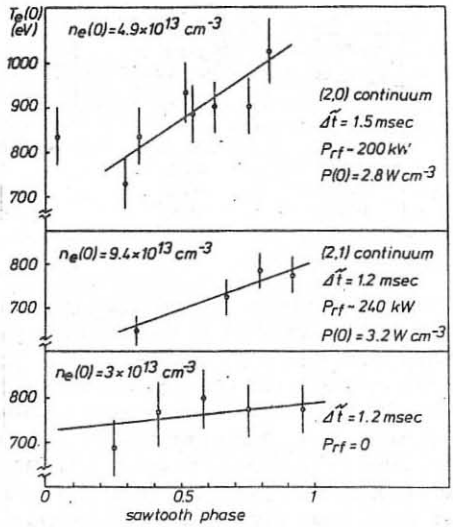


Fig. 1: Electron temperature increase measured during a sawtooth period, for different conditions.

uncorrected for coupling efficiency. The greatest increase is in the (2,0) continuum, with the (2,1) continuum almost as good. We have not included the term 3/2 e x T_{eo} x dn_{eo}/dt in the calculation of the electron energy increase, although the magnitude of the term is similar. The value of $\dot{W}_{eo}$ is conventionally[4-6] related to the central power deposition $P_{rf}(0)$, and we have compared our values of $P_{rf}(0)/\langle P_{rf}\rangle$ with these available references in Table II. The power deposition is clearly inferior to that obtained with ECRH[4] on PDX whose authors quote the major part of the incident power as being deposited within the q = 1 surface. The central deposition analysed according to these accepted, but not necessarily correct, assumptions is higher for AWH than for ICRH and NBI.

TABLE I

Case	n_{eo}(pre-rf) (x 10^{13} cm^{-3})	$\tilde{\Delta t}$ (msec)	$\tilde{\Delta T}_{eo}$ (eV)	P_{rf} (kW)	$P_{rf}(0)/\langle P_{rf}\rangle$
a - OH	3.0	1.2	60	-	-
b - (2,0)	4.7	1.2	420	195	8.0
c - (2,0)	4.9	1.5	360	200	5.5
d - (2,0)	5.2	1.5	300	195	5.0
e - (2,1)	9.4	1.2	202	265	5.6

TABLE II

Case	$\dot{W}(0)$ (W cm^{-3})	P_{rf}(kW)	$P_{rf}(0)/\langle P_{rf}\rangle$
ECRH-PDX[4]	0.65	75	37
AWH-TCA	2.5-3.8	200-265	5.0-8.0
ICRH-PLT[6]	2.00	4300	1.94
ICRH-TEXTOR[5]	0.2	1000	1.46
NBI-DIII[7]	0.75	2100	2.16

In addition to these measurements we have also integrated the electron power balance equation in the presence of rf assuming both $n_e(r)\chi_e(r)$ and the temperature profiles to be unchanged from their ohmic values. This analysis showed that the missing power was greater than the delivered rf power, which translates to the deposition profile being more peaked than the divergence of the conducted energy flow. This is roughly the ohmic power deposition profile which has a value $P_{OH}(0)/\langle P_{OH}\rangle \sim q_a \sim 3.2$. The two approaches therefore support each other. The reasons for the strong core heating are not yet elucidated but it seems clear that the power deposition is not local to the (2,0) resonance layer, estimated to be at $r_s/a \sim 0.5$. The results suggest that the kinetic Alfvén wave which propagates inwards from the appropriate resonance surface, is able to deposit appreciable energy within the $q = 1$ surface at $r/a \sim 0.2$. The local kinetic Alfvén wavelength is roughly 2.5 cm for the lower density case.

II. Ion Heating. The first heating results[8] on TCA showed considerable ion heating, but not under the same conditions as the strongest electron heating quoted. This has now been very clearly shown by varying the conditions of plasma density, filling gas and applied AW "mode". A typical result is shown in Fig. 2 in which the ion temperature rate of increase stops at the AW threshold $(n_\parallel m) = (2,0)$. This behaviour repeats itself below several AW thresholds. Fig. 2 shows the calculated value of $P_{ei}(0)$, assuming $Z_{eff} \sim 2.0$, and assuming $T_i \sim T_z$; the value of $\dot{W}_i(0)/P_{ei}(0)$ exceeds unity and this is a much more direct proof of ion heating than was available before[9]. The value of $\bar{n}\Delta T_i/P_{rf}$ is not particularly useful since the temperature increase is discontinuous and the density increases strongly, nonetheless the value measured reaches 17×10^{13} eV/kW cm^3. The results obtained at higher density are particularly relevant since the Neutral Particle Analyser is more reliable than at the low densities at which the signal is weaker. Two interpretations are open to us. Firstly, there can be direct ion heating from an rf wave and secondly there could still be an anomalous electron-ion equilibration rate. Until we reach $T_i > T_e$ we cannot exclude the latter, but it is clear that the anomaly factor would have to be of the order of 2-3 for the rf power used, and it would have to be sensitive to the Alfvén Wave Spectrum excited. The

mechanism which could lead to direct ion heating is unclear, although ion heating has already been observed in particle simulations of AWH[10]. Since the ion temperature increase stops abruptly above a AW resonance threshold, the heating may well be unrelated to the excitation of Shear Alfvén Waves.

Acknowledgements: We thank the whole TCA team for their assistance in this work, and are grateful to Professor F. Troyon and A. Heym for their support. The work was partly funded by the Fonds National Suisse.

References

[1] A. de Chambrier et al., F-III-3, X Int. Conf. IAEA, London (1984)
[2] B. Joye et al., paper presented at this conference
[3] K. Appert et al., Phys, Rev. Lett. 54 (1985) 1671.
[4] A. Cavallo et al., Nucl. Fusion 25, (1985) 335.
[5] R.R. Weynants et al., 6th Topical Conf. on Radio Frequency Plasma Heating, Georgia, USA (1985).
[6] A. Cavallo et al., ibid.
[7] F.B. Marcus et al., GA Technologies Report GA-A16960 (1983)
[8] A. de Chambrier et al., Plasma Physics 25 (1983) 1021.
[9] A. de Chambrier et al., Plasma Physics 26 (1984) 173.
[10] J.L. Geary et al., Bull. Am. Phys. Soc., 29, (1984) 1401.

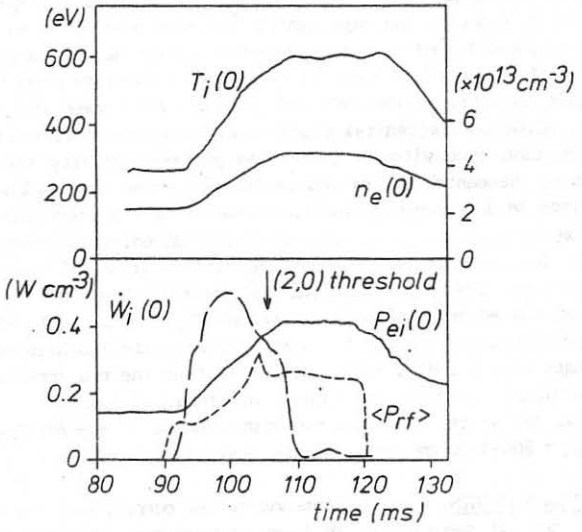


Fig. 2: Time evolution of the ion temperature, electron density, and central ion energy balance during the rf pulse.

TOWARDS A BETTER UNDERSTANDING OF IMPURITIES IN TCA

B. Joye, J.B. Lister, F.B. Marcus and S. Nowak*
Centre de Recherches en Physique des Plasmas
Association Euratom - Confédération Suisse
Ecole Polytechnique Fédérale de Lausanne
21, Av. des Bains, CH-1007 Lausanne, Switzerland

* Institut de Physique, Université de Fribourg, Switzerland

Abstract. The behaviour of impurities during the Alfvén Wave Heating pulse is still being studied. We show that the impurity increase is independent of the number of active antennae, and depends only on the rf power delivered. The time development of the radiated power profile is discussed, and indicates propagation delay and a final stationary state. Finally, we discuss spectroscopic measurements apparently incompatible with these other data.

I. THE RADIATED POWER PROFILE. The behaviour of the radiated power profile in ohmically heated discharges has been discussed[1]. The initial rf experiments on TCA showed a large impurity increase, which has been reduced to an acceptably low level[2]. We present in Fig. 1 the time-development of the local radiated power loss as a function of radius. The outer radii increase promptly when the 180 kW rf pulse is applied. The radiated power on axis does not increase for some 13 msec, although the central electron density starts rising promptly. This indicates that even with an increasing electron density the highly radiating species in the centre are extremely dilute in the target plasma, and their radiative loss is immeasurably small. The delay is therefore attributed to the propagation time of new heavy impurities, which enter the plasma when the rf is applied. The accumulation of heavy impurities already present before the rf pulse would not therefore be indicated by this temporal behaviour. Towards the end of the 40 msec rf pulse shown in Fig. 1 the radiated power loss on axis stops increasing and for the last 5-10 msec the radiated power is virtually stationary at all radii. This again shows that the new impurities do not increase indefinitely, but a new balance is established after an initial transient rise. If we write the impurity transport as $\Gamma = -D\nabla n + V_{in}\, nr/a$, then we obtain $V_{in} \sim 800\text{-}1200$ cm sec^{-1} for the heavy impurities.

II. DIFFERENT ANTENNA GROUPS. The TCA antenna system comprises eight antenna groups which can be fed separately. We have carried out experiments using different numbers of antennae, as a function of power. Figure 2 shows the increases of total and central radiated power, plasma resistance and the intensity of the SiIII line (1206.5 Å) as the rf power is increased.

Silicon carbide is used as the limiter coating. The relative antenna currents are shown in the figure and we see that over a large range of antenna currents/voltages the impurity increase depends only on the total delivered rf power, for a given target plasma. As a result of these indications, we do not relate the impurity production to effects which are local to the antenna structure, but rather to a change brought about by the total delivered rf power. At present the metallic pollution of the limiters coupled with a change in the scrape-off layer during rf[3] is considered to be one of the most likely origins.

III. SPECTROSCOPIC MEASUREMENTS. The waveform of the SiIII line intensity during one discharge is shown in Fig. 3, together with the antenna loading curve which it accurately reflects. The mechanism relating the two is not yet identified. However, it is not directly proportional to the total rf power or to the antenna current, also shown in Fig. 3. Nor is it one of the rf wavefields measured at the plasma edge, or the total rf wavefield. The increase in the SiIII line is not considered to be only an influx measurement. This "peak reflection" exhibits itself in most low-Z edge lines observed in the VUV part of the spectrum, but less so in the visible spectrum in which few data were taken. It is not considered to be a temperature effect at the emitting radius, as no indication of this effect is seen on the Soft X-ray signals near the plasma edge. We hypothesise that the edge line intensities at the plasma edge may be altered by a non-Maxwellian electron velocity distribution in the outer region of the plasma, similar to that measured in the edge plasma[3].

A study of the core-line intensities has also been carried out, and Fig. 4 shows the intensities of the lines FEXVIII, FEXIX, FEXXI and TiXIX. Apart from their strong increase, the most noticeable feature is their prompt response to the rf, starting to rise in less than 1 msec. The density rise cannot explain this since the sensitivity of these core lines to an increasing density is generally much weaker than linear[4], and the density only increases by a factor of 40% in the discharge shown. The increase cannot be attributed to the time variation of the temperature which is not much higher at the end of the full 30 msec rf pulse. New impurities cannot be the cause since these lines radiate near the plasma centre, and firstly there is the inward propagation delay, shown in the first section, and secondly there is the burn-through delay to the higher ionised states. A further observation is the appearance of a weak "peak reflection" similar to the edge lines on the TiXIX waveform. None of the mentioned effects (except Te, already discounted) could produce such a temporally sharp response. We note that the observation of the spectroscopic line intensities, without detailed bolometric measurements, would have led us to an imcompatible conclusion, namely strong axial accumulation of the impurities already in the plasma.

Acknowledgements. We recognize the help of the whole TCA team and the support of Professor F. Troyon and A. Heym. The work was partly funded by the Fonds National Suisse.

References

[1] B. Joye et al., paper presented at this conference.
[2] A. de Chambrier et al., Proc. X Int. Conf. IAEA, London (1985) 531.
[3] A. de Chambrier et al., J. Nucl. Mater. 128 (1984) 310.
[4] J.D. Lawson et al., J. Phys. B14 (1981) 929.

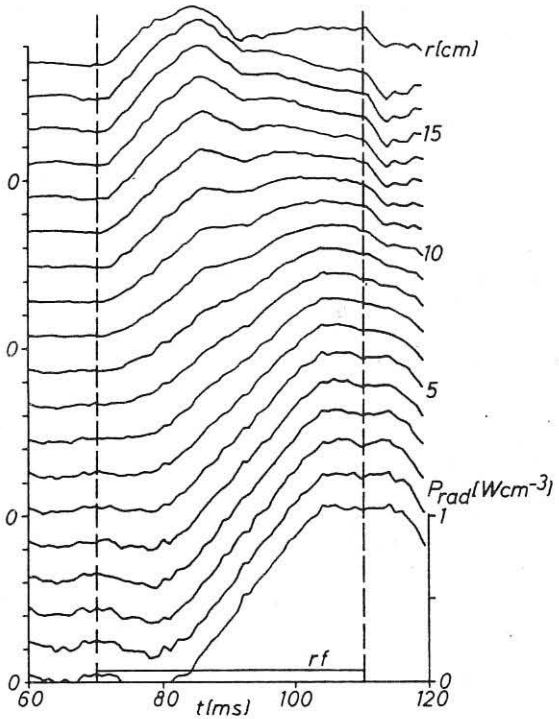


Fig. 1: The temporal evolution of the radiated power loss at different radii during the rf pulse.

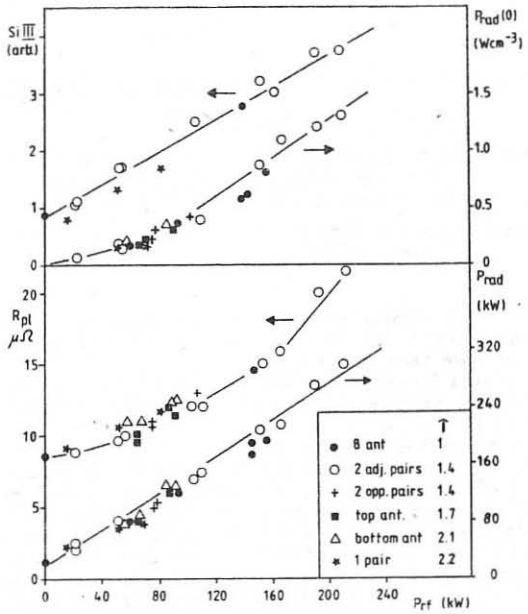


Fig. 2: The increase in the radiated power loss for different groups of antennae.

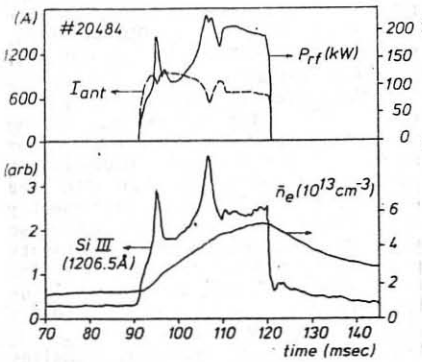


Fig. 3: Time dependence of the SiIII intensity during the rf pulse.

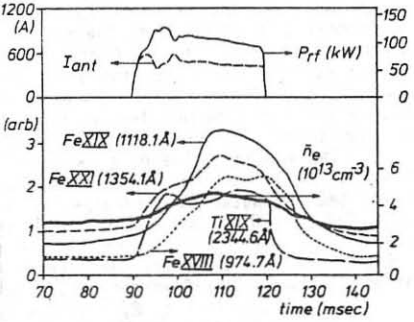


Fig. 4: Time dependence of the core-line intensities during the rf pulse.

PLASMA HEATING IN THE TORTUR TOKAMAK BY LOW-FREQUENCY TOROIDAL CURRENT PULSES

TORTUR Team: H. de Kluiver, N. Yousef, B. de Groot, C.J. Barth, H.A. van der Laan, N.J. Lopes Cardozo, H.J. van der Meiden, W. van Toledo, W.A. de Zeeuw, E.J. Puik

Association Euratom-FOM, FOM-Instituut voor Plasmafysica, Rijnhuizen, Nieuwegein, The Netherlands.

In the TORTUR tokamak ($R = 0.46$ m; $a = 0.085$ m; $B_{max} = 3.0$ T) the turbulent heating effects due to fast toroidal current pulses on top of the plateau current have been investigated.

After plasma formation ($t = 0$: $T_e = 10$ eV; $T_i \ll T_e$; $n_p = (2\text{-}10)\times10^{19}$ m^{-3}) the plasma is rapidly heated to plateau values by the discharge current of capacitor C_1 (1 mF; 5000 V; $I_{1max} \leq 70$ kA; $E_1 \leq 25$ V/m $E_{max}/f \leq 0.15$ Vs/m), which is coupled to the primary of the 0.25 Vs iron core transformer. The plateau lasts up to 50 ms by discharging an electrolytical bank C_2 (0.4 F; 500 V; $I_{2max} \leq 45$ kA). In Fig. 1, the evolution of several parameters vs time are shown. Three periods of different strengths of "Current-Driven Turbulence" ("CDT") can be identified. The first turbulent period, up to about 5 ms, is due to the very fast increase of the plasma current ($dI/dt = 3.3\times10^7$ A/s). This stage can be characterized by parameters indicating the possiblility of CDT: $E_1/E_{cr} > 0.1$ (E_{cr} the runaway fieldstrength); $(\omega_{ce}/\omega_{pe})^2 = 4$ (magnetized plasma); $T_e/T_i \gg 1$ (ion-acoustic turbulence); drift parameter $\alpha \equiv$ from 0.05,.. ..,0.5 (excitation of CDT). The first 300 μs, a non-thermal radiation is registred by ECE-spectroscopy (down-shifted $2\omega_{ce}$) together with X-ray electron tails of several tens of keV's. Evidence exists for a skin-current layer δ from time lag in the increases of T_e at the centre as compared to the edge of the plasma. The maximum dissipation occurs near $t_1 = 1.5$ ms. Surprisingly, T_e keeps increasing to almost its triple value about 2 ms later ($t_1 \approx 3.5$ ms). Increases of T_e at r=0 are from 300 eV up to 950 eV. Then, T_e decreases in about 3 ms, toward the plateau values (600 eV for $I_p = 30$ kA). During this period the ions are heated by thermalization: $T_i \approx 0.7\ T_e$. The rising current stage and the 2 ms period thereafter is interpreted by ion-acoustic turbulence [1,2]. The persistence of CDT after the maximum of the energy input may be due to the diffusive broadening of the skin, while α decreases towards the lowest possible value for CDT: $\alpha \approx (m_e/m_i)^{\frac{1}{2}} = 0.029$ [3].

The initial value of δ is calculated to be 0.02-0.03 m. When after the broadening of δ up to the plasma radius (a), α and E/E_{cr} are sufficiently high, the CDT state is maintained in a quasi-stationary manner. For TORTUR we have $E/E_{cr} > 0.05$ and $\omega_{ce}/\omega_{pe} > 1$ and we find an anomaly of conductivity σ: $\sigma_{cl}/\sigma \gg Z_{eff}$, where Z_{eff} is the real averaged impurity value < 2 for TORTUR. Broad T- and n-profiles are found (T-edge $\approx$ 150 eV), with high fluctuation levels for low-frequency drift waves. Also a broad spectrum up to 50 MHz (ω_{ci}) is present. In Fig. 2, σ_{cl}/σ vs E/E_{cr} is given for several devices. In Fig. 3, the collective scattering spectrum under 80° [4] is shown. Anomalies in the Thomson-scattering spectra indicate magnetosonic turbulence (Fig.4).

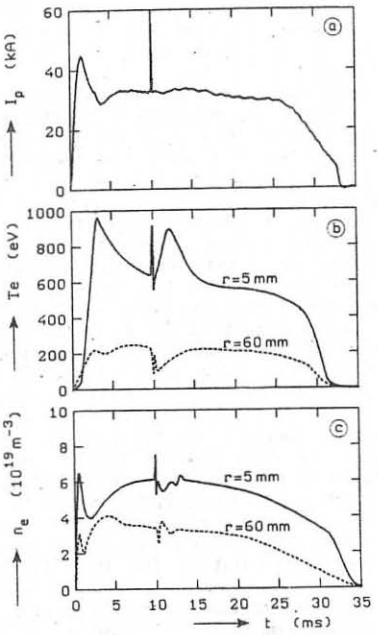


Fig. 1.

Time evolution of I_p, and Thomson-scattering values of T_e and n_e.

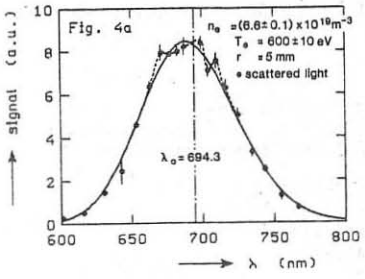


Fig. 4a.

Thomson-scattering spectrum showing significant deviations from a gaussian.

Fig. 4b.

Time behaviour of these deviations (δ): I with, II without fast pulse.

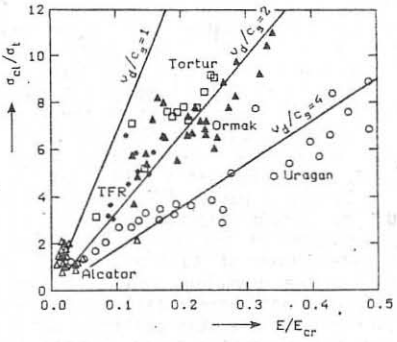


Fig. 2.

Anomalous conductivity of different devices as a function of E/E_{cr} (E_{cr} = runaway field).

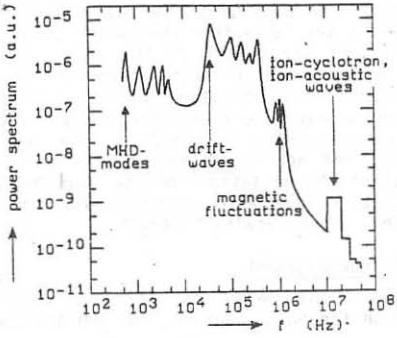
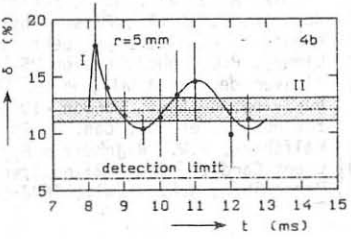


Fig. 3.

Power spectrum S(k) of density fluctuations from collective scattering (λ_o = 4 mm, ϑ = 80°, k = 20 cm^{-1}). Analysis performed with FFT up to 10 MHz; above this with filters.



The anomalous quasi-stationary resistivity in TORTUR is not yet explained. A candidate could be the ion-cyclotron waves coupling with low-frequency electrostatic drift waves (near the edge) and fast Alfvèn branches (near centre) [5,6]. The optimal β varies in accordance with the Troyon scaling. Above 55 kA (q_a = 3) internal disruptions occur. τ_ε = 1.5-2.2 ms.

The third CDT-phenomena are due to short duration-high voltage-current pulse (Fig. 1) superimposed on the plateau. The pulses obtained by discharge of capacitors C_3 (2 μF; 50 kV), coupled to a break in a 2 cm thick copper shield around the liner, have τ_{rise} = 5 μs; $E_3 \lesssim 1$ kV/m (on plasma); $\Delta I_{pmax} < 60$ kA; $E_{3max}/f < 2\times10^{-2}$ V/m [7]. Up to 4 pulses are possible.

During a pulse: $E/E_{cr} \lesssim 40$. Dissipation is initially in a skin, $\delta \approx 2\times10^{-2}$ m. Strong reduction of conductivity: $\sigma/\sigma_{cl} = 2.4\times10^{-3}$. Current-driven unstable modes of the ion-cyclotron and ion-acoustic types can exist together with interaction of tail-accelerated electrons ($v \gg v_{Te}$) with bulk plasma modes via the anomalous Doppler effect. In Figs. 5 and 6 the formation of considerable non-thermal tail populations are shown (see also [8]). As observed earlier [9], the skin collapses already during current build-up. This leads to the experimentally found rapid electron- and ion-heating throughout the entire plasma [10]. Also the density increases near the centre ($\Delta n/n < 20\%$) and decreases at the edge. This implosion is shown in Fig. 7. During a fast decompression (10 microseconds) the increases disappear. However, T_e and T_i increasing again are reaching a maximum in about 2 ms, followed by the usual decay in $\tau_\varepsilon \approx 2$ ms. The delayed heating is explained for a major part as L/R-relaxation of the magnetic energy stored in the peaked current profile, which was left after the skin implosion and after the strong reduction of the current (reversal) in the outer plasma zone caused by the removal of the current pulse. (A skin region for the second time.) Model calculations of this effect in combination with a simple transport calculation for the plasma energy gives very satisfactory agreement with the experimentally found delayed plasma heating at $\tau \approx 2$ ms. The initial strong enhancement of magnetic fluctuations near 1 MHz and in the low-frequency spectrum (see Fig. 7c,d) as well as in the deviations on the Thomson-scattering spectra (Fig. 4b) support this picture (see also magnetic fluctuations in [11]). The pressure increase by this method scales $\sim (\Delta I_p)^2$.

Acknowledgement

This work was performed under the Euratom-FOM association agreement with financial support from ZWO and Euratom.

References

[1] Collective phenomena in current-carrying plasmas; Volkov, E.D., Perepelkin, N.F., Suprunenko, V.A. and Sukhomlin, E.A.; Kiev: Naukova Dumka 1978. English translation: Gordon and Breach Companies, 1985.
[2] Kluiver de, H. et al., Phys. Lett. 94A (1983) 156.
[3] Hirose, A. et al., Nucl. Fusion 16 (1976) 963.
[4] Huussen, F. et al., Plasma Phys. 27 (1985) 447.
[5] Kando, M. et al., Phys. Lett. 101A (1984) 204.
[6] Liewer, P.C., Nucl. Fusion 25 (1985) 543.
[7] Kluiver de, H. et al., Proc. 10th Int. Conf. on Plasma Phys. and Contr. Nucl. Fusion Res., London (1984) Vol. 1, p. 375.
[8] Boucher, C. et al., Can. J. Phys. 61 (1983) 147.
[9] Kalfsbeek, H.W., Rijnhuizen Report 78-114 (1978).
[10] Lopes Cardozo, N.J., Rijnhuizen Report 85-160 (1985).
[11] Perepelkin, N.F. et al., IPPJ-548 Nagoya, October 1981.

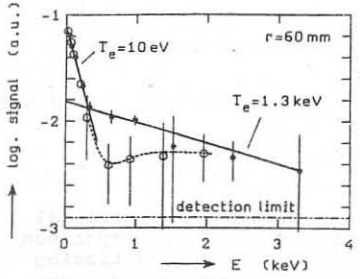


Fig. 5.

Non-thermal electrons at r = 60 mm, Δt = 4 µs after the puls; • blue wing and o red wing of the spectrum.

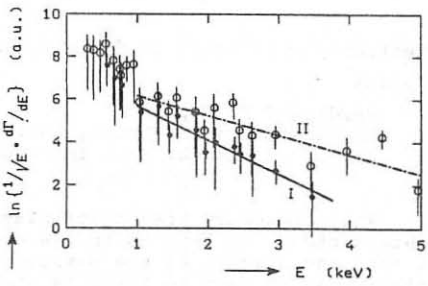


Fig. 6.

Non-thermal ions at the centre during a 100 µs interval:
I: before, II: after the pulse.

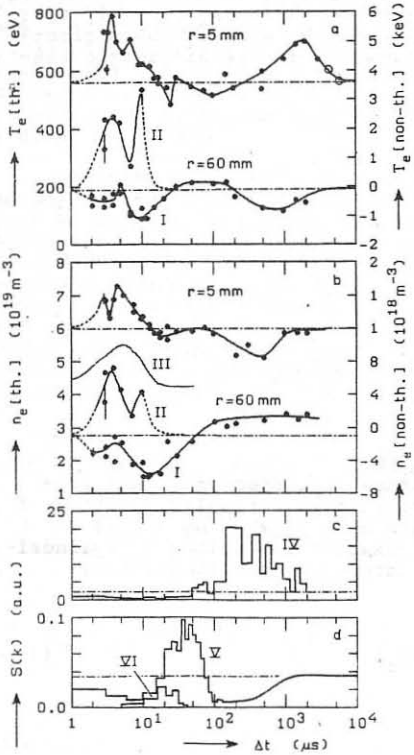


Fig. 7.

Time development of T_e (a), n_e (b) and $\tilde{n}_e$ (c and d) on log-time scale Δt (µs) after the pulse.
-•-•-•-: plateau values.
I: thermal distribution
II: non-thermal distribution
III: plasma current, ΔI_p = 28 kA
IV: density fluctuations $\tilde{n}_e$ in the frequency interval 1-50 kHz
V: $\tilde{n}_e$ in interval 0.7 - 3 MHz
VI: $\tilde{n}_e$ in interval 3.5 - 4.5 MHz.

Electromagnetic Waves in Toroidal Anisotropic Inhomogeneous Plasmas

Ferdinand F. Cap
University of Innsbruck, Austria
A 6020 Innsbruck, Karl Innerebnerstr. 40, Austria

Radiofrequency heating of plasmas is used in many toroidal installations. As long as the wave-length is small in comparison to the length scale of the device geometric-optical ray tracing methods may be used to describe the waves. If however the wave-length is of the order of the dimensions of the device wave optical methods are needed for the description. Three difficulties appear when one tries to solve Maxwell's equations: 1. the plasma is inhomogeneous. 2. the plasma is anisotropic. 3. Maxwell and Helmholtz wave equations are unseparable for toroidal surfaces. Using a superposition of degenerate eigenfunctions in cylindrical coordinates r, ϕ, z it is however possible to satisfy the electromagnetic boundary conditions on toroidal surfaces of nearly arbitrary meridional cross section. Assuming $\vec{B}_0 = B_{0\phi}\vec{e}_\phi$ and neglecting the influence of the magnetic wave-field the dielectric tensor reads

$$\overleftrightarrow{\varepsilon} = \begin{pmatrix} \varepsilon_r & 0 & \varepsilon_z \\ 0 & \varepsilon_\phi & 0 \\ -\varepsilon_z & 0 & \varepsilon_r \end{pmatrix}, \text{ where}$$

$$\varepsilon_r = 1 + \sum_s \omega_{Ps}^2/(\Omega_s^2 - \omega^2)$$

$$\varepsilon_\phi = 1 - \sum_s \omega_{Ps}^2/\omega^2$$

$$\varepsilon_z = i\sum_s \Omega_s \omega_{Ps}^2/\omega(\Omega_s^2 - \omega^2)$$

and where $\Omega_s = \Omega_{0s}R/r$, $\Omega_{0s} = e_sB_{0\phi}/m_s$, R major torus radius, s species index, ω_{Ps} species plasma frequency. Assuming a density distribution as parabolic function of the distance from the magnetic axis as $n_0(r,z) = n_1 - \bar{n}_0 z^2 - \bar{n}_0(r - R)^2$ one may derive from Maxwell's equations in cylindrical coordinates for axisymmetric harmonic modes ($\sim\exp(i\omega t)$, $\partial/\partial\phi = 0$) the equations

$$B_r = -\frac{i}{\omega}\frac{\partial E_\phi}{\partial z}, \quad B_z = \frac{i}{\omega}\frac{1}{r}\frac{\partial}{\partial r}(rE_\phi) \qquad (1)$$

$$\frac{\partial^2 E_\phi}{\partial z^2} + \frac{\partial^2 E_\phi}{\partial r^2} + \frac{1}{r}\frac{\partial E_\phi}{\partial r} - \frac{1}{r^2}E_\phi + \omega^2 \varepsilon_o \mu_o \varepsilon_\phi E_\phi = 0 \qquad (2)$$

for the TM mode and

$$\frac{1}{r}\frac{\partial E_r}{\partial z} - \frac{1}{r}\frac{\partial E_z}{\partial r} + \frac{\partial^2 E_r}{\partial z \partial r} - \frac{\partial^2 E_r}{\partial r^2} + \omega^2 \varepsilon_o \mu_o (\varepsilon_z E_r - \varepsilon_r E_z) = 0, \qquad (3)$$

$$-\frac{\partial^2 E_r}{\partial z^2} + \frac{\partial^2 E_z}{\partial r \partial z} - \omega^2 \varepsilon_o \mu_o (\varepsilon_r E_r - \varepsilon_z E_z) = 0,$$

$$-i\omega B_\phi = \frac{\partial E_r}{\partial z} - \frac{\partial E_z}{\partial r} \qquad (4)$$

for the TE mode. These equations have to be solved together with the boundary conditions valid on a given meridional cross section $z^* = z(r)$ of the toroidal vessel. Since the equations (2) - (4) are linear, partial solutions belonging to different initial values $A_1 E_r^{(1)}$, $A_2 E_r^{(2)}$ etc may be superposed to form a general solution. Partial solutions belonging to the same eigenvalue ω are called degenerate. Their partial amplitudes A_i may be determined in such a way that the boundary conditions can be satisfied along a given curve $z^*(r)$.

In order to explain the new method let me deviate from plasma physics for a moment and consider a circular membrane of radius R. Oscillations $w(x,y)\exp(i\omega t)$ may be described in Cartesian coordinates by the Helmholtz equation $w_{xx} + w_{yy} + k^2 w = 0$, where $k = \omega/c$, c phase velocity of elastic waves. A solution of the Helmholtz equation is given by $w(x,y) = A\cos kx + B\cos(\sqrt{k^2 - \alpha^2}x) \cdot \cos \alpha y$. Here α plays the role of a separation constant if we would like to satisfy the boundary conditions $w(x = a, y) = w(x, y = a)$ for a square membrane so that $\alpha = n\pi/a$ etc. We would like, however, to satisfy the boundary condition $w(r = R, \phi) = 0$ on a circle given by $x^2 + a^2 = R^2$. Thus the function y(x) defined by

$$A\cos kx + B\cos(\sqrt{k^2 - \alpha^2}x)\cos \alpha y = 0$$

must describe the circle $x^2 + y^2 = R^2$. With $R = 1$ $\alpha = 2{,}0780$, $k = 2{,}4019$ this is possible within some $^0/_{00}$ accuracy /1/.

Returning to plasma physics we have to satisfy $E_t = 0$ and $B_n = 0$ on the curve $z^*(r)$. Since $B_n = -B_r \sin\gamma + B_z \cos\gamma$, $\tan\gamma = dz^*/dr$ etc we have

$$E_r + E_z \frac{dz^*}{dr} = 0, \quad \frac{dr}{B_r} = \frac{dz^*}{B_z} \quad \text{or} \quad rE_\phi = \text{const} \qquad (5)$$

due to (1), where $E_r(r,z) = \sum_{i=1}^{N} A_i E_r^{(i)}(r,z)$ etc. The larger N the more exact

is the satisfaction of the boundary conditions on a given arbitrary cross section $z^*(r)$. Using only two partial solutions for the TM mode

$$E_\phi(r,z) = (AR_1(r) + BR_2(r))(CU_1(z) + DU_2(z)) \qquad (6)$$

solving (2), we are able to describe the circular cross section of a Tokamak R = 0,95, a = 0,35 given by $z^*(r) = \sqrt{a^2-(r-R^2)}$ by (5) (for const = 0) /1/

r	z from (5)	exact
0,66580	0,21156	0,20428
1.09478	0,31946	0,31865
1,18058	0,26668	0,26331

Choosing $n_1 = 1{,}225 \cdot 10^{15}$ m^{-3}, B_o = 0,1 Tesla we obtain the eigenfrequency ω by inserting (6) into (5) for const = 0. Thus (5) becomes a system of 4 homogeneous linear equations for A, B, C, D. Vanishing of the determinant $D(\omega)$ gives ω. In order to integrate the ordinary differential equations for R(r) and U(z) stemming from (2) we need an approximate value for ω. This value can be obtained from isotropic plasma where the equations for R(r) and U(z) can be solved analytically /2/. Improving ω by a regula falsi method applied on $D(\omega)$ and repeated integration of the differential equation for R(r) and U(z) yields $\omega/2\pi$ = 0,42969 Mcycles for the TM mode.

For the TE-mode equations (2), (3) have to be solved. The ansatz $\varepsilon_z = i\bar{\varepsilon}_z$ and $E_r(r,z) = v(r)\cos lz$, $E_z(r,z) = if(r)\cos lz$ yields v(r) and a differential equation for f(r). The same procedure as for the TM mode yields /1/ $\omega/2\pi$ = 5,2331 MHz for the TE mode if the plasma is assumed to be homogeneous. For inhomogeneous plasmas $\varepsilon_r(r,z)$, $\varepsilon_\phi(r,z)$, $\varepsilon_z(r,z)$, calculations are being made during summer 1985. In Fig. 1 the TE mode is shown for an ovaloid cross section and in Fig. 2 the TM mode is presented.

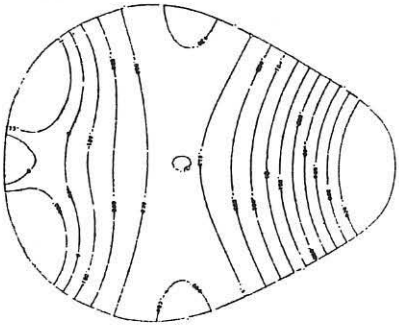


Fig. 1. TE mode

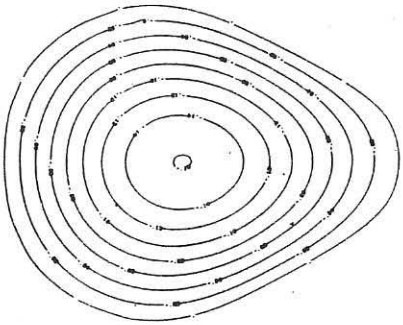


Fig. 2. TM mode

If non-axisymmetric modes ($\partial/\partial\phi \neq 0$) are considered in an inhomogeneous, anisotropic plasma, the solutions of equations (3),

(4) have to be supplemented by solutions of equations with ϕ-dependence. Using $\partial/\partial z = 0$ these equations read

$$\bar{E}_z'' + \frac{1}{r}\bar{E}_z' + \bar{E}_z H - \frac{\bar{\varepsilon}_z \omega^2 \varepsilon_o \mu_o}{H}\left(\omega^2 \varepsilon_o \mu_o \bar{\varepsilon}_z \bar{E}_z + \frac{m}{r}\bar{E}_\phi' + \frac{m}{r^2}\bar{E}_\phi\right) = 0 \quad (7)$$

$$E_z(r,\phi) = i\bar{E}_z(r)\cos m\phi; \qquad E_\phi(r,\phi) = \bar{E}_\phi(r)\sin m\phi;$$

$$E_r(r,z) = \bar{E}_r(r)\cos m\phi\ ; \qquad H = \omega^2 \varepsilon_o \mu_o \varepsilon_r - m^2/r^2; \quad \varepsilon_z = i\bar{\varepsilon}_z \quad (8)$$

$$\bar{E}_r = \left(\bar{E}_z'' + \frac{1}{r}\bar{E}_z' + \omega^2 \varepsilon_o \mu_o \varepsilon_r \bar{E}_z - \frac{m^2}{r^2}\bar{E}_z\right)/\omega^2 \varepsilon_o \mu_o \bar{\varepsilon}_z$$

$$\bar{E}_\phi''\left(1 + \frac{m^2}{r^2 H}\right) + \bar{E}_\phi'\left(\frac{1}{r} - \frac{m^2}{r^3}\cdot\frac{1}{H} + \frac{m^2}{r^2}\frac{d}{dr}\left(\frac{1}{H}\right)\right) +$$

$$+ \bar{E}_\phi\left(-\frac{1}{r^2} + \omega^2 \varepsilon_o \mu_o \varepsilon_\phi - \frac{3m^2}{r^4}\cdot\frac{1}{H} + \frac{m^2}{r^3}\frac{d}{dr}\left(\frac{1}{H}\right)\right) + \quad (9)$$

$$+ \frac{m}{r}\frac{1}{H}\omega^2 \varepsilon_o \mu_o \bar{\varepsilon}_z \bar{E}_z' - \frac{m}{r^2}\frac{1}{H}\omega^2 \varepsilon_o \mu_o \bar{\varepsilon}_z \bar{E}_z +$$

$$+ \frac{m}{r}\frac{1}{H}\omega^2 \varepsilon_o \mu_o \bar{E}_z + \frac{m}{r}\frac{d}{dr}\left(\frac{1}{H}\right)\omega^2 \varepsilon_o \mu_o \bar{\varepsilon}_z \bar{E}_z = 0.$$

In this case separate TE and TM modes no longer exist. The solution of (7) - (9) has to be superposed on the solution of (3), (4) to form a function $E_z(r,z,\phi)$ etc. The electric field lines are now given by solutions of

$$\frac{dz}{d\phi} = \frac{rE_z(r,\phi,z)}{E_\phi(r,\phi,z)}, \qquad \frac{dr}{d\phi} = \frac{rE_r(r,\phi,z)}{E_\phi(r,\phi,z)} \quad (10)$$

integrated around the torus ($0 \le \phi \le 2\pi$). For a meridional cut $\phi = \phi_o$ = const, $E_r(r,\phi_o,z)$ and $E_z(r,\phi_o,z)$ have to satisfy $E_t = 0$ or (5) which delivers the eigenvalue.

References

/1/ F. Cap, Physics of Fluids, issue May 1985
/2/ F. Cap, IEEE Trans.Microwave Theory Tech.MTT 32, October 1984, 1336-1341

Further Heating of a High Beta Plasma by the Compressional Alfven Wave

K.Saito, N.Inaba, Y.Osanai, Y.Nogi and S.Shiina

Atomic Energy Research Institute and Department of Physics,
College of Science and Tecnology NIHON UNIVERSITY
Kanda-Surugadai, Chiyoda-ku,TOKYO 101, JAPAN

Abstract

The compressional Alfven wave excited in 2m theta-pinch is investigated. The wave which propagates in the radial direction of the plasma column is excited by using of a dischage of a LC circuit. The exponential dumping factor of the rf current is observed by a magnetic probe. Three peaks of it are observed and two peaks of it are explained as a result of resonant absorption of the wave energy. But another large absorption must be explained by other effect. An attempt to explain the fact is made.

Introduction

A plasma column which is made by a theta-pinch includes an axial magnetic field and is surrounded coaxially by vacuum magnetic field and one turn theta-pinch coil. When a high frequency magnetic field is imposed upon the plasma surface, the plasma column begins to oscillate and the compressional Alfven wave is excited in it. This wave is diminished in time by the viscosity and the resistivity of the plasma and its energy is converted into the heat energy. We can excite the compressional Alfven wave having m=0, n=0 mode without exciting any other modes in a toroidal plasma. This gives only small oscillating perturbation to the aspect ratio.

Experimental arrangement

A high beta plasma is produced in a 14cm i.d. quartz tube inserted in a 16cm i. d. , one-turn theta-pinch coil 2m long. The sequence begins with the ringing Z-discharge preionization, followed by the rapidly rising theta-pinch crowbarred with 60 μs decay time, and then rf (∿560kHz) circuit is operated to excite the compressional Alfven wave. The schematic diagram of the experimental arrangement is shown in Fig.1. The time sequence of the operation is shown in Fig. 2. The Z-discharge current (C=4 μF, V=20 kV) decays sufficiently in the time of 50 μs. The theta-pinch (C=72 μF,V=35 kV, filling pressure of 50mTorr ∿ 300mTorr D_2) is operated on its time. The peak axial magnetic field, B_0 , of 1T is obtained 2 μs after discherge initiation. The crowbar system is operated to extend the equilibrium time and to obtain the required field strength of the pinch. The plasma column produced by the theta-pinch oscillates radially with the natural frequency around the equilibrium point. The radial oscillation decreases about 10 μs after discharge initiation. Then rf energy (C=0.6 μF,V=30 kV) is supplied to the same coil used for the theta-pinch. The e-holding time and the muximum field strength are 5 μs and 300 gauss, respectively. The period of the rf circuit in connected to the plasma becomes slightly small in comparison with in the vacuum shot, but these do not deppend on the filling pressure as shown with a dotted line in Fig. 3. The period of the radial oscillation of the plasma column is also observed as a function of the initial filling pressure, P_0, by a magnetic probe inserted between the theta-pinch coil and the discharge tube, as shown in Fig. 3. The broken line shows the theoretically calculated dependency of the period on P_0, $T \propto \sqrt{P_0}/B_0$, where B_0 is fixed.

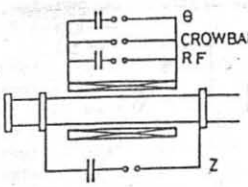


Fig.1 Schematic diagram of the experimental arrengement.

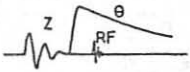


Fig.2 Time sequency of the discharge currents of each circuit.

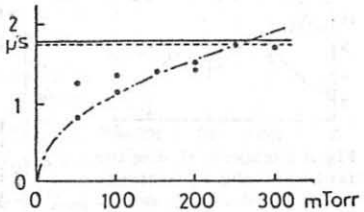


Fig.3 Period of the radial oscillation of the plasma column and the rf circuit.

Experimental results

RF current is lightly dumped and oscillatory, $I=I_0\exp(-\alpha t)\sin(\omega t)$. The exponential dumping factor, α, is observed by a magnetic probe set near the rf discharge bank. When B_0 is fixed at 1T and P_0 is swept between 50mTorr and 300mTorr, two peaks of α are observed as shown in Fig. 4. The value of α in the vacuum shot is about 3×10^5/s. As the wave is excited transiently from the outer region of the plasma column, α becomes large gradually in time. The muximum value of α is plotted in Fig. 4. Four magnetic probes at the radial interval of 9mm are inserted into the plasma column to observe the propagation of the wave. The magnetic field included in the plasma column is compressed and expanded alternatively with the plasma and the maximum amplitude of the rf component at each point is plotted in Fig. 5. The amplitudes become large for each filling pressure on the axis, depending on the geometry of the plasma column. If we assume a sharp boundary model, the profile calculated from MHD theory is zero order Bessel function, J_0. Another peaks of the amplitudes are also observed in the outer region of the plasma column clearly in the case of 100mTorr filling pressure. The velocity of the wave observed by using of the probes gives that the plasma temperature is about 20 eV. The radial profiles of the beta value are also observed by the probes and the typical profiles of 50mTorr, 100mTorr and 250mTorr are plotted in Fig. 6. These profiles show that a hump of the wave amplitude shown in Fig. 4 appears in the outerside of the plasma column where the gradient of the beta value becomes large. When P_0 is fixed at 100mTorr filling pressure and B_0 is swept by the control of the crowbar time, a sharp peak of α appears at the point of $B_0\simeq 0.6$T as shown in Fig. 7, where the interval between the Z-discharge and the theta-pinch is changed from 50 μs to 60 μs.So the peak of α does not appear at the point of P_0=100mTorr and B_0=1T.But we can find again the peak of α at the point of P_0=100mTorr and B_0=1T, when we put back the inteval, as shown in Fig. 9. The natural frequencies of the radial oscillation of the plasma column are plotted as a function of B_0 in Fig. 8. The dotted line shows the frequency of the rf circuit.

To clear up the effect of the gradient of the beta value for the appearance of the hump in the outer region of the plasma, the beta profile is controlled by changing the interval between Z-dicharge and the initiation of the theta-pinch, where P_0 and B_0 is fixed to 100mTorr and 1T, respectively. When the interval becomes long, the beta profile comes to broad. The gradient of the beta value comes to large gradually when the interval is growing shorter. The beta profiles at 12 μs after the initiation of the theta-pinch are shown in Fig. 9. The amplitude of the wave is large on the axis of the plasma column and decreases monotonously toward the outerside of the plasma, when the beta profile is broad. We can see that a hump appears in the outerside of the plasma when the gradient of the beta value becomes large.

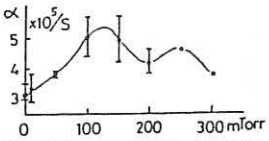


Fig.4 Exponential dumping factor of the rf current. B_0 is fixed and P_0 swept.

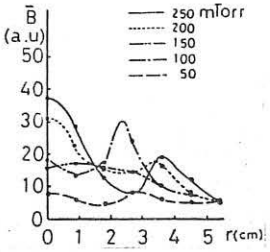


Fig.5 Radial distributions of the maximum wave amplitude.

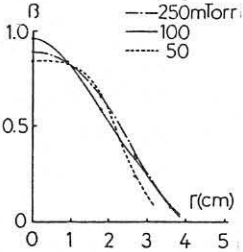


Fig.6 Beta profiles at 12 μs after the theta-pinch initiation.

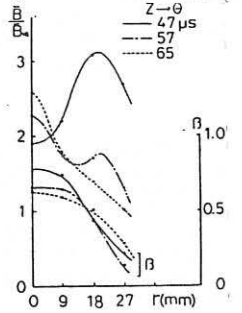


Fig.9 Relation of the radial beta gradient and the wave amplitude.

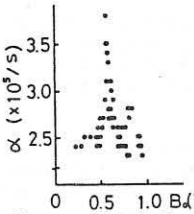


Fig.7 Exponential dumping factor of the rf current. P_0 is fixed and B_0 swept.

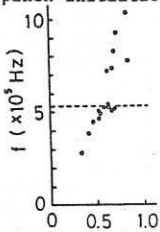


Fig.8 Natural frequencies of the plasma column. P_0 is fixed and B_0 swept.

Discussions

The compressional Alfven wave travelling to the radial direction makes a radial gradient of the internal magnetic field. This gradient induces the azimuthally oscillating current in the plasma column which diminishes in time by resistivity of the plasma and is converted into the heat energy. The frequency of the radial oscillation of the plasma column depends on the field strength and the initial filling pressure (which nearly equals the plasma pressure because the ionization rate is high in theta-pinch) as follows,

$$\omega_0 = C\, B_0/\sqrt{P_0} \qquad (1)$$

where C is a function of the beta value but it does not depend strongly on its value. When B_0 is fixed at 1T and P_0 is swept, we can see a resonant point at P_0=250mTorr in Fig. 3, and the large amplitude of the wave is excited near the plasma axis as shown in Fig. 5. This makes a large gradient of the field and induces a large azimuthal current. A peak of α is observed at this point as shown in Fig. 4. We can see also a resonant point at B_0≃0.6T as shown in Fig. 7 and Fig. 8, when P_0 is fixed to 100mtorr and B_0 is swept. The width of the resonance is very narrow in comparison with the former, because the natural frequency of the plasma column depends on B_0 linearly and $1/\sqrt{P_0}$ as shown in equation (1). These peaks of α are plotted in Fig. 10, where y axis is P_0 and x axis is B_0. The curve is drawn by using of the eq. (1), where $\omega_0$is fixed to the frequency of the rf circuit and constant C is chosen to be coincident with the resonant point at P_0=250mTorr and B_0=1T. The peak of α at P_0=100mTorr and B_0≃ 0. 6T plotted in double circle is on the curve, so we conclude that two peaks of α described by double circles are due to the effect of the resonant absorption of the wave energy. Another peak of α labeled by x in Fig. 10, which corresponds to the peak of α at P_0=100mTorr and B_0=1T in Fig. 4, is far from the curve expressing the resonant absorption. This fact sets the cause of the absorption of the wave energy apart from the resonant absorption.

An attempt to explain the fact is made here. The velocity of the

compressional wave depends on the beta value as follows,[1]

$$V_A = V_S\sqrt{(1+6/(5\beta))}, \qquad (2)$$

where V_S is the sound velocity. When plasma has an approprate gradient of the beta value, the velocity of the wave in the outer region of the plasma column is faster than the velocity of the wave in the inner region. The compressional wave propagating toward the axis will catch the inner wave up and overlap to it. So the amplitude of the copressional wave becomes large at the adequate gradient of the beta value. We can see the large amplitude of the wave in the outer region of the plasma columun in Fig. 5, especially in the case of P =100mTorr, B =1T. The hump does not appear when the beta value has small gradient in the plasma region and the sharp profile at the plasma boundary. These are crearly confirmed by changing the radial beta profile in the plasma column, as shown in Fig. 9, where the gradient of the beta value will behave shuch a beach. This hump of the amplitude induces the azimuthal current flowing to the opposite direction in the both slopes of the hump, and makes the absorption large.

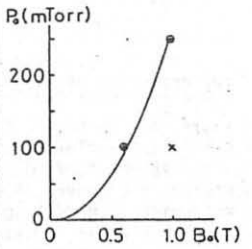


Fig.10 Map of the peak points of the dumping factor α for P_0 and B_0.

The efficiency of the energy transfer can not measure directly from the rising of the plasma temperature, because the source energy of the wave exciter is comparable to the internal energy of the plasma. The efficiency is estimated from the variation of the dumping factors obtained in the cases of the vacuum shot and the shot wiht plasma. Most fraction of the rf source energy is consumed by the resistance of the circuit, because the wave is excited transiently in this experiment. The dumpig factor becomes large gradually and the maximum α is plotted in Fig. 4. The efficiency estimated on these peaks of α are about 30%.

Conclusion

The compressional Alfven wave is excited by using of the discharge of the LC circuit. Its amplitude makes a hump at the center of the plasma column because the waves concentrate on the axis by the resultant of the plasma geometry. This hump becomes large when the resonance occur between the radial oscillation of the plasma column and the LC oscillation of the rf circuit. We find another hump of the amplitude in the outer region of the plasma column, which appears in the region of the large gradient of the beta value. These humps make the radial gradient of the axial magnetic field and induce the azimuthally oscillating current. The latter hump induces especially the current flowing to the opposite directions in the both slopes of the hump. The exponential dumping fuctor, α , of the rf current becomes large when the big hump appear in the plasma column. Three peaks of α are observed in our experiment. Two peaks of α are explained as a result of the resonant absorption of the rf circuit energy between the natural oscilletion of the plasma column and the rf oscillation of the LC circuit. Another peak of α may be explained by the result of the concentration of the wave in the region of the large gradient of the beta value. The efficiency of the further heating of the plasma is about 30% at the peak points of α.

Acknowlegement

The authors wish to devout this study to Professor Dr. Hisamitu Yoshimura who was a collaborator and leaved this world April 1984.

Referrence

Edward Teller; FUSION. Vol 1 Part A, P 19 (1981).

THE EFFECT OF NEUTRAL BEAM DEPOSITION ON HEATING AND CONFINEMENT IN ASDEX

E.Speth, A. Eberhagen, O.Gehre, I.Gernhardt, G. Janeschitz, E.R.Müller, A.Stäbler, O.Vollmer, F.Wagner, R.Bartiromo, G.Becker, H.S. Bosch, G.Fußmann, G.v.Gierke, E.Glock, O.Gruber, G.Haas, F.Karger, M.Keilhacker, A.Kislyakov, O.Klüber, M.Kornherr, P.B.Kotzé, K.Lackner, M.Lenoci, G.Lisitano, H.M.Mayer, K.McCormick, D.Meisel, U.Mertens, H.Murmann, H.Niedermeyer, W.Poschenrieder, H.Rapp, H.Riedler, F.Ryter, J.Roth, J. Schneider, G.Siller, P.Smeulders, F.Söldner, K.Steinmetz, K.H.Steuer

Max-Planck-Institut für Plasmaphysik
EURATOM-Association, D-8046 Garching

Abstract: The effect of the beam deposition profile on heating and confinement in ASDEX has been studied by comparing plasmas with center-peaked and hollow beam deposition profiles. There is no significant difference in global energy confinement time and central electron energy density. A hollow deposition profile reduces the central electron heat transport at least by a factor of two. A beam energy of 75 keV/nucleon would be sufficient in order to generate the same (a/λ =const.) deposition profile for a full-density, full-bore scenario in NET.

Introduction: The degradation of confinement properties of neutral injection heated Tokamak plasmas (L-regime) is a common feature also observed in divertor plasmas at low beam power /1/. In this paper we study the effect of the neutral beam power deposition profile on confinement and transport properties in the L-regime by applying different beam deposition profiles to identical ohmic target plasmas. Apart from the physics interest for this question there is also some technological relevance, which forms the second motivation for this work: since the shape of the deposition profile is essentially determined by beam energy which in turn governs the efficiency of the neutral beam system /2/, we attempt an experimental assessment of neutral beam penetration requirements for large toroidal plasmas.

Experiments and results: Three different beam voltages as well as H_2 and D_2 in the beam sources were used (40 kV H_2, 45 kV D_2, 29 kV D_2) in order to vary the deposition profiles, while the injected neutral power, the plasma density, the plasma current and the divertor configuration were kept constant. Since the extracted ion beams of the ASDEX injectors contain a large fraction of molecular ions ($H^+ : H_2^+ : H_3^+ = 40 : 50 : 10$), the penetration characteristics of the beams are more adequately described by a species-averaged beam energy $\langle E \rangle$ rather than by the beam voltage E_0. For a line-averaged density of about 6×10^{13} cm^{-3}, a plasma current of 420 kA, a neutral power of 1.1 ÷ 1.3 MW, and a single-null configuration the global energy confinement τ_E^* (deduced from the diamagnetic β_p) is independent of the beam energy (Fig.1) and therefore independent of the details of the heating power distibution. (The power deposition profiles computed with the code FREYA /3/ for the two extreme cases 40 keV H°, 29 keV D° are shown in Fig.2a and 2b). Also the electron temperature and density profiles (Fig.3a,b) are about the same for the two extreme cases with the n_e-profiles even somewhat more peaked in the hollow deposition profile case.

Discussion: Though the global confinement is not affected by the shape of the deposition profile, the central electron confinement is clearly changed. The central electron energy density is about the same in the two extreme cases whereas the beam power to electrons in the range $r \leq a/3$ is different by about a factor 3 ÷ 4 (Fig.2). Since the power transferred from the ions to the electrons is not known, the electron heating power has been determined separately by analysing the rise of the central electron energy density $W_e(0)$ after a sawtooth drop. The results agree fairly well with the calculated ones and are given in table 1. The improvement of central electron energy confinement (by about a factor 2) for the hollow deposition profile matches the observation of increased central electron density, suggesting improved central particle confinement as well.

TABLE 1
electron power densities on axis [W/cm³]

	SAWTOOTH $P_{S.T.}$	FREYA P_b^e	OHMIC P_Ω	$P_b^e+P_\Omega$	$W_e(0)/P_{S.T.}$ [msec]
40 keV H_2	0.32	0.28	0.14	0.42	73
29 keV D_2	0.18	0.04	0.14	0.18	150

The improved central confinement provides favourable aspects for ignition scenarios and the fact that this can be achieved with a hollow deposition profile can be used to extrapolate the penetration requirements for a larger toroidal plasma like NET. We postulate that a/λ = const. (a= minor plasma radius, λ = mean free path of the injected fast neutrals), because the shape of the deposition profile is essentially determined by a/λ . Taking into account the energy and temperature dependence of the trapping cross section /4/ and allowing for an injection angle of $\theta = 20°$ w.r.t. perpendicular at $R = R_0 + a$ (for ASDEX $\bar{\theta} = 45°$), a relation between plasma opacity $\bar{n}_e a$ and species-averaged beams energy $\langle E \rangle$ can be obtained as shown in Fig.4. For a full-bore, full-density scenario of $\bar{n}_e = 1.25 \cdot 10^{14} cm^{-3}$ in NET (a = 1.2 m) a beam energy $\langle E \rangle$ of 75 keV/nucleon will produce the same relative deposition profile as the most extreme case realised in ASDEX, i.e. 29 keV D° at $\bar{n}_e = 6 \cdot 10^{13} cm^{-3}$.

References

/1/ F.Wagner et al., this conference
/2/ D.R.Sweetman et al., CLM-R 112 (1971)
/3/ G.G.Lister et.al., Proc. 3rd Symp. Pl.Heatg., Varenna (1976), 303
/4/ S.Rehker and E.Speth, IPP 2/217 (1974)

Figure captions

Fig.1 Global confinement time τ_E^* vs. species-averaged beam energy $\langle E \rangle$ and beam voltage E_0 respectively.

Fig.2 Power deposition profiles for electrons (p_e) amd ions (p_i), P_N = neutral power
a) for 40 keV H°
b) for 29 keV D°

Fig.3 Electron temperature and density profiles
a) for 40 keV H°
b) for 29 keV D°

Fig.4 Opacity $\bar{n}_e \cdot a$ vs. species-averaged beam energy $\langle E \rangle$;
σ_{tot} = total trapping cross section, T = plasma temperature

$I_p = 420$ kA
$\bar{n}_e = 6 \cdot 10^{13}$ cm^{-3}
$P_N = 1.1 - 1.3$ MW

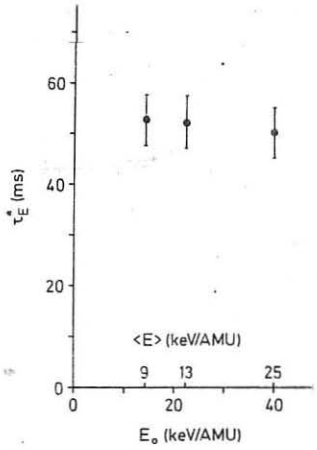


Fig.1

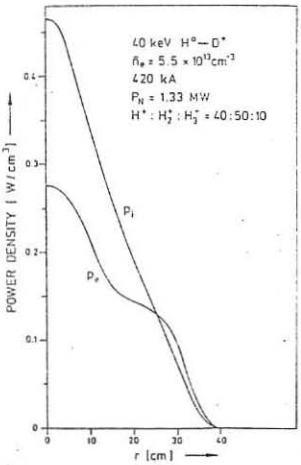


Fig.2a

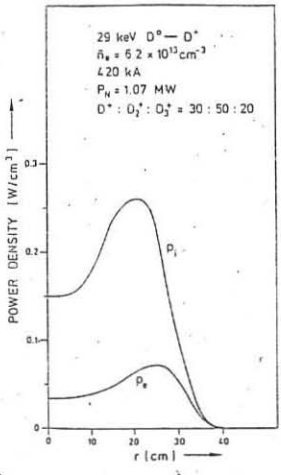


Fig.2b

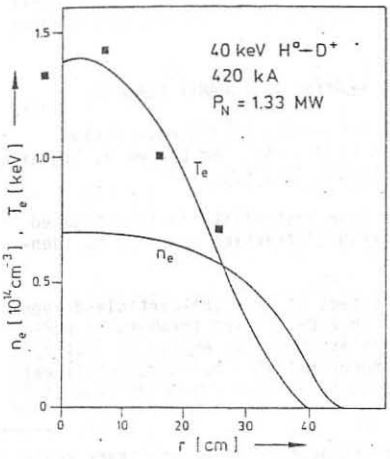


Fig.3a

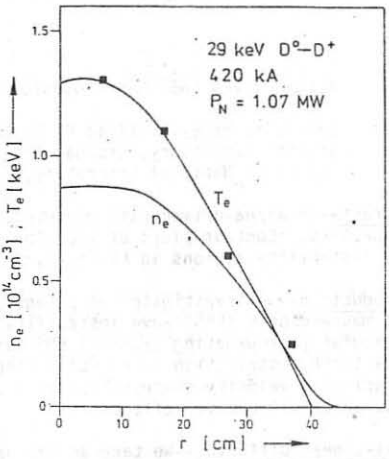


Fig.3b

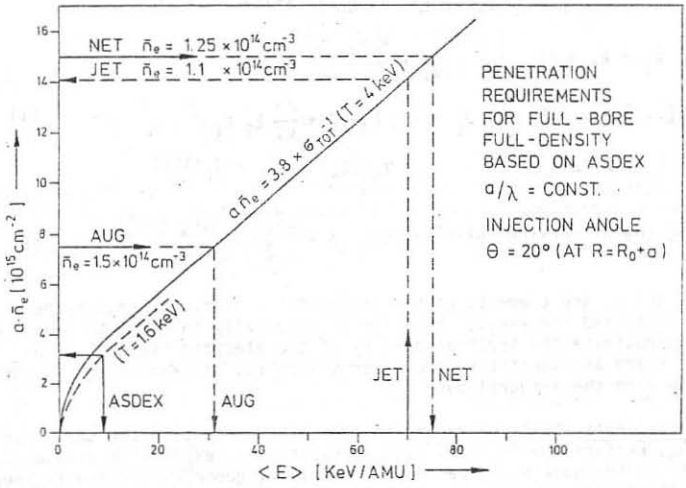


Fig.4

ALPHA-DRIVEN FAST MAGNETOSONIC WAVE HEATING IN TOKAMAK PLASMAS

George H. Miley, William R. Sutton, University of Illinois Fusion Studies Laboratory, Urbana, Illinois 61801, USA, and Dieter J. Sigmar, Oak Ridge National Laboratory, Oak Ridge, TN 37830, USA

Abstract--An alpha-driven fast magnetosonic wave instability is investigated in tokamaks. Contour plots of the alpha threshold fraction are used to identify instability regions in the n_e-T_i plane.

Introduction--We investigate the potential effect of an alpha-particle-driven fast magnetosonic (FMS) wave instability[1-4] in a D-T fueled tokamak. A perpendicularly propagating ($k_\parallel \ll k_\perp$) FMS wave is assumed. We employ an isotropic alpha birth distribution to calculate the energy released during quasi-linear diffusion in velocity space. Results are used in a 1½-D transport code to scope potential reactor effects.

Quasi-Linear Diffusion--We take an FMS wave propagating at an arbitrary angle to the applied toroidal magnetic field, and employ circular cylindrical $v_\perp$-$v_\parallel$ coordinates. We approximate a cylindrical tokamak with Cartesian geometry ($r \gg 1/\kappa 1$). With $\hat{x} = \hat{r}$, $\hat{y} = \hat{\theta}$, and $\hat{z} = \hat{z}$, the general quasi-linear diffusion equation is:[5] (nomenclature follows Ref 4)

$$\frac{\partial f_\alpha}{\partial \tau} = \frac{\pi q_\alpha^2}{m_\alpha} \sum_L \int d\vec{k} \, \frac{1}{v_\perp} \, \hat{R}_1 \{[\ldots](\hat{R}_2 f_\alpha) \, \delta(\omega(\vec{k}) - L\Omega_\alpha - k_\parallel v_\parallel)\}$$

$$\hat{R}_1 = \hat{R}_2 = (1 - \frac{k_\parallel v_\parallel}{\omega}) \frac{\partial}{\partial v_\perp} + \frac{k_\parallel v_\perp}{\omega} \frac{\partial}{\partial v_\parallel}$$

$$[\ldots] = v_\perp \left| E_r \frac{L}{|\lambda|} J_L + i\eta_\alpha E_\theta J_L' + \frac{v_\parallel}{v_\perp} E_z J_L \right|^2 \qquad (1)$$

$$\lambda = k_\perp v_\perp / \Omega_\alpha \qquad \eta_\alpha = q_\alpha / |q_\alpha| \qquad J_L = J_L(|\lambda|)$$

With $k_\parallel = 0$ the dispersion relation is: $\Delta = \frac{c^2 k^2}{\omega^2} - \frac{\varepsilon_1 \varepsilon_2 - \varepsilon_x^2}{\varepsilon_1}$ (2)

where ε_1, ε_2, and ε_x are elements of the dielectric tensor. (We reject the second solution to $\Delta = 0$ for $\vec{k} = k_\perp$.) Equation 2 is formally inverted to give $\omega = \omega(k)$. We approximate the spectral density of the electric field by a box function in k space and substitute these forms into Eq. (1) and associate the delta function with the integral over $k_\perp$.

Diffusion Coefficients--Next, we expand the Bessel functions in the small parameter $k_\parallel v_\parallel / L\Omega_\alpha$, perform the integral over $k_\parallel$ exactly and expand the evaluated integral again in the same small parameter. In $v_\perp$-$v_\parallel$ geometry the quasi-linear diffusion coefficients are dependent on $v_\parallel$ only to first order in $k_\parallel / k_\perp$. Physically this occurs because the instability ($\omega - L\Omega_\alpha = k_\perp v_A$ and $k_\parallel \ll k_\perp$) acts on the perpendicular energy.

The instability is favored at $r \to 0$ where the fusion rate is maximum. Then

unstable harmonic numbers permitted in a tokamak magnetic field collapse to a single integer[6]; therefore, the diffusion coefficients are restricted to the same harmonics, and to zero order in $k_\parallel/k_\perp$:

$$D_\perp \simeq k_\parallel v_\perp \, L\Omega_\alpha \{\ldots\} \; ; \; D_X \simeq \frac{1}{2} k_\parallel^2 v_\perp^2 \{\ldots\} \; ; D_\parallel \simeq \frac{1}{3} \frac{k_\parallel^3 v_\perp^3}{L\Omega_\alpha} \{\ldots\} \quad (3)$$

with

$$\{\ldots\} = \frac{v_A^2}{v_\perp^2} E_r^2 J_L^2 + E_\theta^2 (J_L')^2$$

The ordering of the diffusion coefficients is found to be:

$$D_\perp : D_X : D_\parallel \simeq 1 : \frac{1}{2} O\left(\frac{k_\parallel}{k_\perp}\right) : \frac{1}{3} O\left(\frac{k_\parallel^2}{k_\perp^2}\right) \quad (4)$$

FMS Wave Growth and Damping--Next we require an expression for the alpha growth rate, γ_α, and plasma damping of the wave. Our derivation generalizes prior results[3] for propagation in the $k_\perp$ plane at an arbitrary angle to the radial vector, and also includes the effect of relative polarization between the radial and poloidal electric fields vs. ω. Neglecting terms proportional to $k_\parallel$ we obtain:

$$\gamma_\alpha = \frac{-1}{\Delta'\left(1 + p_{r\theta}^2\right)} \frac{\omega_{p\alpha}^2}{k_\perp^2} \int d\vec{v} \, \frac{1}{v_\perp} \frac{\partial \hat{f}_\alpha}{\partial v_\perp} R(v_\perp, \omega) \quad (5a)$$

and

$$R(v_\perp, \omega) = \sum_L \frac{L\Omega_{\alpha 0}}{\omega} \frac{\left[J_L^2 + p_{r\theta}^2 \frac{v_\perp^2}{v_A^2} (J_L')^2\right]}{\sqrt{\varepsilon^2 - \left[1 - \frac{L\Omega_{\alpha 0}}{\omega}\right]^2}} \quad (5b)$$

with

$$\frac{\omega}{\Omega_\alpha}(1 - \varepsilon) < L < \frac{\omega}{\Omega_\alpha}(1 + \varepsilon) \quad (5c)$$

Dependence on $v_\parallel$ in Eqs. (5) appears only in the normalized alpha distribution function $\hat{f} \equiv f_\alpha / n_\alpha$. If the instability operates predominantly along $v_\perp$, we may integrate out the $v_\parallel$ dependence. Such a condition exists for the isotropic alpha source without loss cones, which to a first approximation is assumed here.

Threshold Studies--We define threshold fraction, n_τ, as the ratio of alpha-to-electron density at marginal stability, i.e., when the sum of the alpha-driven growth and damping rates equal zero. We assume the device parameters (major and minor radii and magnetic field), radial position and wave frequency are fixed and n_τ is computed vs. density and ion temperature, giving threshold contours in the n_e-T_i plane. Typical results for a demonstration-sized reactor (FED[7]) are presented in Fig. 1. The threshold contours are incremented by units of -1 since we have plotted $\log_{10}(n_\tau)$. The heavy outer boundary labeled "0.0" is defined as the limit outside of which the FMS wave is stable. At a fixed n_e, n_τ increases with an increased T_i due to Doppler broadening of the alpha source function. Strong variations in n_τ along the n_e axis at fixed T_i arise from successive tuning and detuning due to the dependence of the growth and damping rates (γ_α) on the Alfvén speed. We find that the instability

heating is strongest where the threshold fraction is a minimum (~10 keV in Fig. 5). Thus, the effect will be strongest for a low <β> device, where the magnetic field remains relatively strong on axis.

One-Dimensional Quasi-Linear Approximation--Another objective is to assess reactor level effects. We reduce the 2-D quasi-linear diffusion to 1-D with mild restrictions. The final set of 1-D quasi-linear equations is solved using a code package described elsewhere.[6] We use representative reactor parameters:[7] a toroidal magnetic field of 42 kG on axis, $n_e \sim 4.75 \times 10^{13}$ cm^{-3} at 5 cm and $T_e \sim T_i \sim 10$ keV. Then $\eta_T \sim 3.55 \times 10^{-6}$ for $\omega = 6\Omega_\alpha$ and the total wave damping rate is $\gamma_d = 437$ sec^{-1}. The enhancement factor, p_{iv}, is the ratio of the time averaged alpha ion heating rate in the presence of the instability vs. that with classical slowing. For present plasma conditions the maximum p_{iv} is ~1.3.

A typical time history is shown in Fig. 2. The total growth rate γ_T is plotted along with the wave energy density and the response of p_{iv}. At time $\tau = 0$, $\gamma_T = 0$ and the wave electric field E_1 is set arbitrarily low so that quasi-linear diffusion is negligible. As the alpha densities increases, γ_T increases since the damping rate (dependent on the background plasma conditions) remains constant. Then, E_1 grows exponentially until $D_\perp$, which depends on E_1, becomes large enough to change the alpha profile. As the profile flattens, the growth rate which depends on the slope in $f_\alpha(v_\perp)$ drops. As the instability continues into saturation, $f_\alpha(v_\perp)$ diffuses sufficiently that $\gamma_\alpha < -\gamma_d$ and the wave decays via cyclotron and collisional damping. After the distribution collapses, the process begins anew and repeats itself after ~15 ms.

Reactor Simulation--We use data from the lowest "lobes" of the contours in Fig. 1 (i.e., at $n_e \gtrsim 5 \times 10^{13}$ cm^{-3}) to examine effects in a demonstration-type reactor.[7] The data were incorporated in 1½-D tokamak transport code and a typical result is shown in Fig. 3. Contours of the auxiliary power (P_{aux}) required to hold a given <T> are plotted. The instability occurs in the shaded region, i.e., during the startup phase at moderate density-temperature. The rather restricted instability region is encouraging from a control point of view and could be avoided with an appropriate startup trajectory.

Summary and Conclusion--Generally the threshold is smallest for relatively low electron density, ion temperature, and β, although values do extend over a fairly wide range of parameters (Fig. 1). Furthermore, cf Fig. 2, when the instability is triggered, a significant collapse of the alpha distribution occurs. A repeated buildup and collapse is observed with a period of ~15 ms. Since the energy fluctuation is <1% of the background plasma energy, this is not viewed as disruptive. In fact, the increase in alpha energy transferred to background ions (versus electrons) is desirable. Also, the reduction in the time-averaged alpha pressure would be beneficial. However, cf Fig. 3, the region where the instability occurs is quite isolated.

Acknowledgments--Work sponsored by the U.S. DOE contract DEAC02 76ET52040. Contributions by S. K. Ho, Univ. of Illinois, are recognized.

References--[1] A. B. Mikhailovskii, Proc. of the 1979 Intern. School of Plasma Physics, Varenna, Italy, Aug.27-Sept. 8, 1979. [2] A. B. Mikhailovskii, et al., Soviet J. of Plasma Phys., 5:2, 173 (1979). [3] D. J. Sigmar, Workshop on Physics of Plasmas Near Thermonuclear Conditions; Varenna, Italy, Aug. 27-Sept. 7, 1979. [4] W. R. Sutton, D. J. Sigmar, and G. H. Miley, Fusion Technology, 7, 374 (1985). [5] A. I. Akhiezer, et al., Plasma Electro-dynamics, Pergamon Press, New York, 1975, Vol. 2, 67. [6] V. M. Bardakov, A. B.

Mikhailovskii, Soviet J. of Plasma Phys., 3:2, 121 (1977). [7] C. A. Flanagan, et al., Report ORNL/TM-7777, Oak Ridge National Laboratory, Oak Ridge, TN, May 1981. [8] W. R. Sutton, Report COO-2218-251, Fusion Studies Laboratory, Univ. of Illinois, Urbana, IL, June 1982.

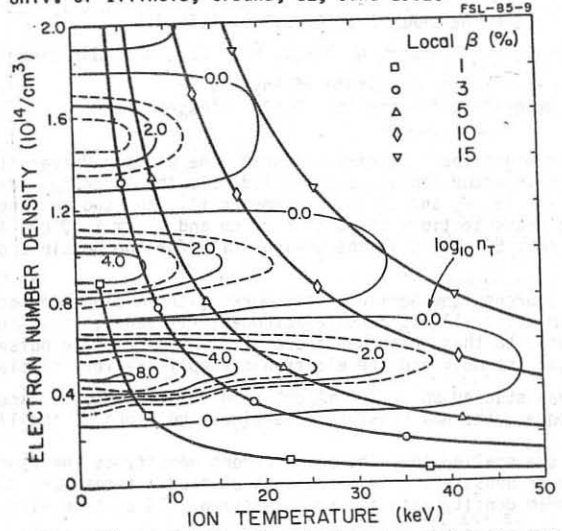


Fig. 1. Alpha threshold fraction (n_T) contours for the FMS wave in the FED: $\omega=6\Omega_\alpha=k_\perp v_A$, $k_\parallel << k_\perp$, B_o = 42 kG, r=10cm.

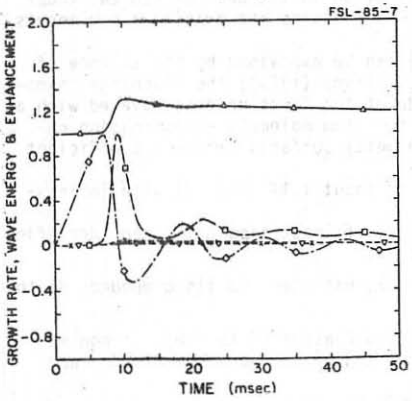


Fig. 2. Time histories of instabiity, [○]=total growth rate $\gamma_T=\gamma_\alpha+\gamma_D$, [□] =wave energy $W_{E(\tau)}$, ∇=density, X=relative error in system energy, Δ=enhancement factor p_{iv}. The normalizations are $\log_{10}(\text{max. } W_E)$ = 1.992 and $\log_{10}(\text{max. } \gamma_T)$ = 3.022

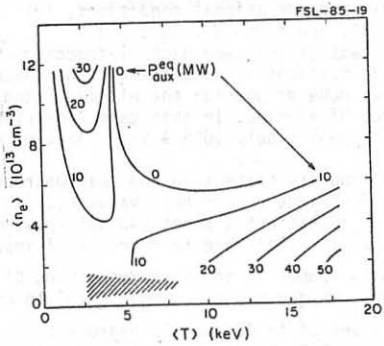


Fig. 3. External power P^{eq}_{aux} required to hold a given <n>-<T> operating point using Alcator scaling and B_o = 42 kG. Alpha instability occurs in the shaded region.

THE RF-NEUTRAL INJECTOR ION SOURCES RIG

J. Freisinger, M. Kaufmann, W. Kraus, H.W. Löb, R. Reuschling

Ist Institute of Physics
Heinrich-Buff-Ring 16, D-6300 Giessen, FRG

In the course of an eight years research program, the Giessen University developed a family of rf-injector ion sources, called RIG. The three cylindrical sources are of 10 cm, 15 cm, and 20 cm in diameter (1); the two rectangular ionizer chambers have cross sections of 10 cm x 20 cm and 10 cm x 30 cm (1)(2). A hexagonal RIG (28 cm x 59 cm) is in the design state for the possible operation at ASDEX-Upgrade.

Contrary to other sources, the German system works with an electrodeless annular rf-discharge. By omitting all discharge electrodes, filaments, etc., the lifetime problems related to these components are eliminated from the outset. - Both, the mechanical assembly and the electronic supply are very simple (Fig. 1a and 1b).
The beam density was studied up to 300 mA/cm^2 (Fig. 2); it depends linearly on the rf-discharge power; the gas pressure determines the slope of the linear increase.
By Fig. 2 we find the scaling low: The beam current density is the same for the same "discharge power density". This means that we need 4 times more power to produce the same beam density with the (double-sized) RIG 20 than with RIG 10.

The beam yield is about 1 A/kW; the rf-frequency is in the order of 1 MHz.

Mass spectrometric analyses and beam profile measurements had been carried out. Fig. 3 shows the hydrogen ion species distribution in the beam of RIG 20. Under optimized operational conditions, the ion bean contains the principal components H_1^+, H_2^+, and H_3^+ (95% : 3% : 1%).
The fact of the very high H_1^+-fraction (95%) can be explained by the absence of metal surfaces in contact with the discharge plasma (1)(3): The discharge chamber is made of quartz; the plasma-facing side of the first grid is covered with a layer of alumina. In this case, therefore, the atom-molecule-recombination coefficient is only $10^{-4} \div 10^{-3}$ compared with metal surfaces owning a coefficient of 1.
The impurity content in the beam decreases to about 1.1% (Fig. 3) with increasing discharge power (best value 0.7%).
About 60 different kinds (40 different masses) of impurities have been identified (TABLE 1). There are four groups of impurities:

- Mass number 12 to 19: hydrocarbons C^+ to CH_5^+, nitrogen and its compounds N^+ to NH_3^+, oxygen and its compounds O^+ to OH_3^+.
- Masses 24 to 33: mainly hydrocarbons with two C-atoms C_2^+ to $C_2H_6^+$, carbon monoxide CO^+, oxygen and nitrogen molecules O_2^+ and N_2^+, as well as silicon and silane ions Si^+ to SiH_4^+.
- Masses 46 to 68: metal ions in total less than 10^{-3}%.

Masses heavier than 68 have not been observed. Common with all these measurements is the rapid rise of the impurities beyond 1 Pa discharge pressure (Fig. 4).

When the discharge power is increased, the temperature of the discharge ion rises. The intensified thermal movement superposes on the velocity of the beam ions resulting in a higher beam-divergence at the same beam voltage (Fig. 5).

TABLE 1: Distribution of the impurities in the beam of the rf-discharge (X: observed only during the baking phase).

MASS No.	INTENSITY, %	IDENTIFIED ION MASSES (singly charged)				GROUP
12	0.027			C		
13	0.004			CH		
14	0.048		N	CH_2		
15	0.037		NH	CH_3		
16	0.268	O	NH_2	CH_4		I
17	0.364	OH	NH_3	CH_5		
18	0.552	OH_2				
19	0.086	OH_3				
20	0.001				Ne	
21	X					
23	0.0016				Na	
24	X			C_2		
25	X			C_2H		
26	0.0005			C_2H_2		
27	0.0016			C_2H_3	Al	
28	0.07	CO	N_2	C_2H_4	Si	
29	0.022	COH	N_2H	C_2H_5	SiH	
30	0.011	COH_2, NO		C_2H_6	SiH_2	II
31	0.002				SiH_3	
32	0.002	O_2			SiH_4	
33	X					
34	X					
35	X					
36	X			C_3H		
37	X			C_3H_2		
38	X			C_3H_3		
39	X			C_3H_4	SiC, K	
40	0.002			C_3H_5	Ca, Ar	III
41	0.001			C_3H_6		
42	X			C_3H_7		
43	X			C_3H_8		
44	0.001	CO_2, SiO, N_2O				
45	0.0002	SiOH				
46	X	NO_2				
56	X				Fe	
63	0.0001				Cu	
64	0.0001				Zn	IV
65	X				Cu	
66	X				Zn	
68	X				Zn	
	1.5	impurities (total)				I-IV

The minimum divergence angle is found in Fig. 5 to be 1.1° by asymptotic approach.
The beam voltage and the rf-discharge power are proportional (Fig. 6) at the minimum beam divergence.

REFERENCES

(1) J. Freisinger, H.W. Loeb: "The Neutral Particle Injectors RIG for Fusion Reactors" Atomkernenergie/Kerntechnik 44, 81, 1984

(2) R. Reuschling, J. Freisinger, H.W. Loeb: "Plasma Diagnostics in a Rectangular Rf-Ion Source" Proc. XIth Internat. Symp. on Discharges and Electrical Insulation in Vacuum, Berlin, Vol. 2, 437, 1984

(3) W. Kraus, J. Freisinger: "Impurity-Ion-Production in a Hydrogen Rf-Ion Source" Proc. 1984 Internat. Conf. on Plasma Physics, Lausanne, Vol. II, 252, 1984

(4) J. Freisinger, M. Kaufmann, W. Kraus: "Impurities in an Rf-Hydrogen Plasma" 7th Internat. Symp. on Plasma Chemistry, Eindhoven, July 1985 (in press)

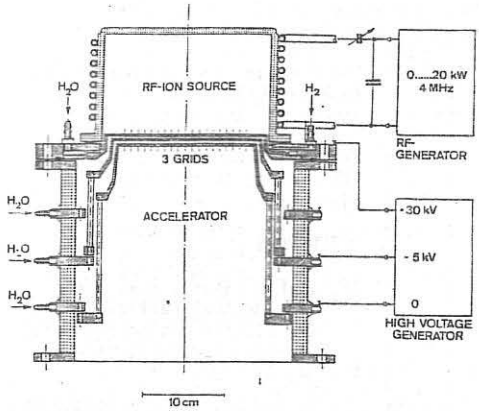


Fig. 1a:
Technical drawing of RIG 20 true to scale (diam: 20 cm) and electrical wiring.

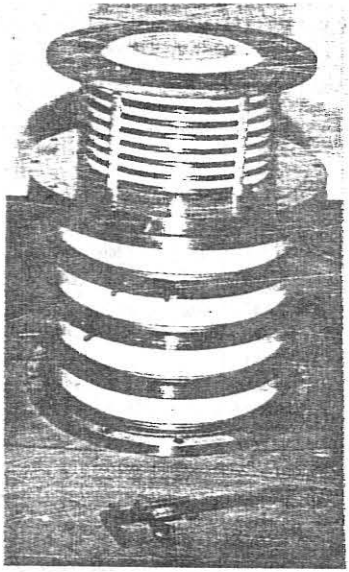


Fig. 1b:
Photograph of RIG 20. The assembly is very simple and rigid.

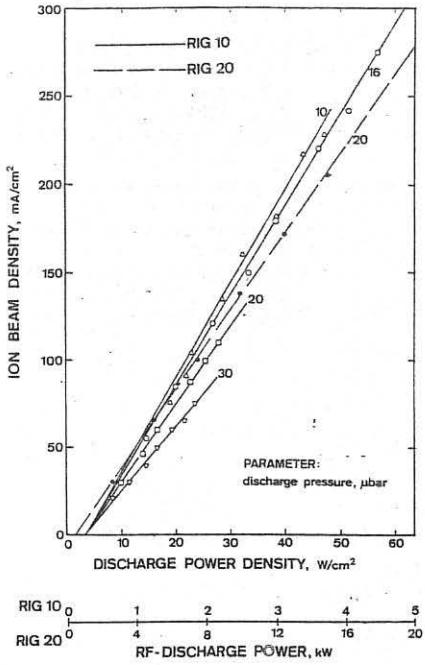


Fig. 2:
Ion beam density vs. discharge power of RIG 10 and RIG 20. The discharge pressure determines the inclination of linear increase. The "discharge power density" is defined as the rf-power per inner wall surface of the discharge chamber.

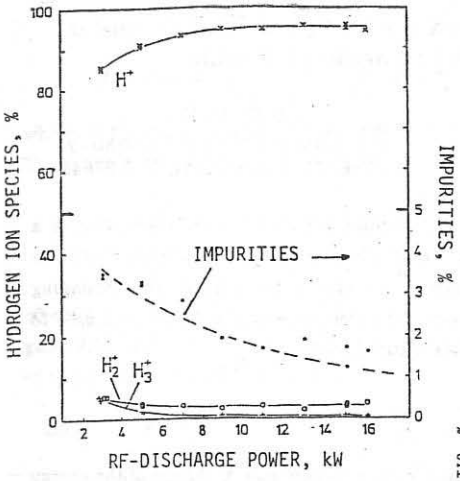


Fig. 3:
Hydrogen ion species in the beam of RIG 20 as a function of the discharge power. The impurities, 10 times enlarged (right scale) decrease to 1% (discharge pressure 0.5 Pa).

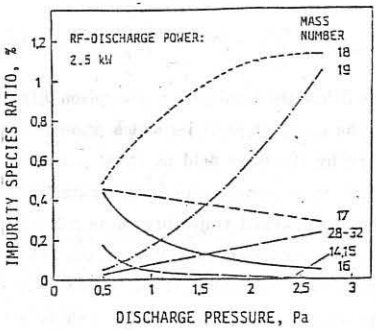


Fig. 4:
The ratio of the impurity species as a function of the discharge pressure.

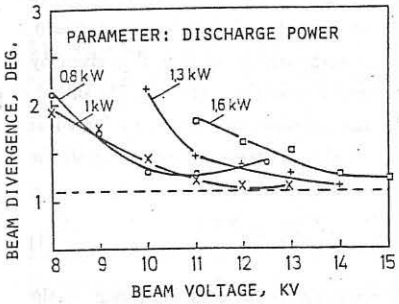


Fig. 5:
The minimum divergence angle of RIG 10 is 1.1°.

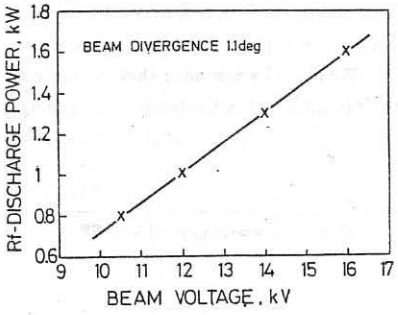


Fig. 6:
At the minimum divergence the beam voltage increases linearly with the rf-discharge power of RIG 10.

Local Power Conservation for Linear Wave Propagation in an Inhomogeneous Plasma

R.S. Sund, J.E. Scharer[1]
University of Wisconsin – Madison
Madison, WI 53706 U.S.A.

B.D. McVey
Los Alamos National Laboratory
MS E531, Los Alamos, NM 87545

Abstract : *An expression for local power absorption for linear wave propagation in a non-uniform hot magnetoplasma is derived from fundamental principles. The formalism is applied to wave propagation in the ion cyclotron range of frequencies where strong damping and mode conversion processes may be present. The power absorption definition is used to obtain a local power conservation relation for a slab model.*

We define the local power absorption $P(\mathbf{r})$ as the time-average rate of change of the energy of the group of particles which pass through $\mathbf{r}$. $P(\mathbf{r})$ must equal the average rate of work done by the wave field on these particles. Consider the subset of this group which have phase space coordinates $(\mathbf{r},\mathbf{v})$ at time t. Let $\tau = t - t'$ and let $\mathbf{r}'(\mathbf{r},\mathbf{v},\tau), \mathbf{v}'(\mathbf{r},\mathbf{v},,\tau)$ define the unperturbed trajectory these particles follow such that $\mathbf{r}' = \mathbf{r}$ and $\mathbf{v}' = \mathbf{v}$ at $\tau = 0$. The instantaneous rate of work the field does on one such particle at time t' is given by $q\mathbf{E}(\mathbf{r}',t')\cdot\mathbf{v}'$. To obtain the average rate of work performed on all the particles in the subset, the work done on the single particle is weighted by the distribution function evaluated at $(\mathbf{r}',\mathbf{v}',t')$ and the average is computed as t' varies. Finally, the power absorbed by all the particles passing through $\mathbf{r}$ is obtained by an integration over $\mathbf{v}$. Thus

$$P(\mathbf{r}) = q\int d^3v \left\langle \mathbf{E}(\mathbf{r}',t')\cdot\mathbf{v}' f_1^*(\mathbf{r}',\mathbf{v}',t') \right\rangle \qquad (1)$$

where $\langle\ \rangle$ denotes an average over t'. The above represents the complex power — the real power transfer is obtained by taking one half the real part of P. We will develop this expression explicitly in terms of the local wave field and its spatial derivatives.

We begin by assuming that the unperturbed plasma is uniform in the y and z directions and is immersed in a z-directed static magnetic field $\mathbf{B}_0$. The wave propagation is restricted to the $x - z$ plane and is allowed to have a non-sinusoidal x-dependence :

$$\mathbf{E}(\mathbf{r},t) = \mathbf{E}(x)e^{i(kz-\omega t)}$$

[1]RSS and JES were supported by NSF Grant ECS-8212173

The linearized Vlasov equation is solved as usual by the method of characteristics :

$$f_1(\mathbf{r},\mathbf{v},t) = -\frac{q}{m}e^{i(kz-\omega t)}\int_0^\infty d\tau\,[\mathbf{E}(x')+\mathbf{v}'\times\mathbf{B}(x')]\cdot\frac{\partial f_0}{\partial \mathbf{v}'}e^{i(\omega-kv_x)\tau} \qquad (2)$$

where x',z', and $\mathbf{v}'$ are the characteristics of the Vlasov equation, parameterized by t'. These are of course identical to the particle orbits which are given by

$$v_x' = v_+e^{i\omega_0\tau} + \frac{i\epsilon}{\Omega}\left[-v_xv_+e^{i\omega_0\tau} + v_+^2e^{i2\omega_0\tau}\right] + c.c. \equiv a + a^*$$

$$v_y' = -ia + \frac{\epsilon}{\Omega}v_+v_- + c.c. \qquad v_z' = v_z$$

where $\tau = t-t'$, $\epsilon = \frac{1}{B}\frac{dB}{dz}$, $\omega_0 = \Omega+\epsilon v_y$, $v_\pm = \frac{1}{2}(v_x \pm iv_y)$, and c.c. denotes complex conjugate of the entire preceeding expression. The y-coordinate is ignorable. The x-component of the particle's position is given by

$$\Delta x \equiv x'-x = \frac{iv_+}{\Omega}\left(e^{i\omega_0\tau}-1\right) + \frac{\epsilon v_+}{\Omega^2}\left[2v_-\left(e^{i\omega_0\tau}-1\right) - \frac{1}{2}v_+\left(e^{i2\omega_0\tau}-1\right)\right] + c.c. \quad (3)$$

Where we have used $\frac{1}{\omega_0} \simeq \frac{1}{\Omega}\left(1-\epsilon\frac{v_y}{\Omega}\right)$. We also need $z' = z - v_z\tau$.

There are three constants of the motion. To lowest order in ϵ they are

$$x_g = x + \frac{v_y}{\Omega} = x_g' = x' + \frac{v_y'}{\Omega} \qquad v_\perp^2 = v_\perp'^2 = v_x'^2 + v_y'^2 \qquad v_z = v_z'$$

The unperturbed distribution is a function of the constants of the motion for each particle species. For simplicity in the following development we choose f_0 to be

$$f_0(x',\mathbf{v}') = \frac{n_0(x_g)}{\pi^{3/2}u^3(x_g)}e^{-v^2/u^2(x_g)} = f_0(x_g,v^2) \qquad (4)$$

Because of the dependence of ω_0 on v_y we have the relation $\frac{\partial f_0}{\partial v'} = -2v'\frac{f_0}{u^2} + \frac{1}{\Omega}\frac{\partial f_0}{\partial x_g}$.

In order to evaluate the integral over τ in Eq. (3) we need a representation of the wave electric field along a particle's orbit. Since the waveform is allowed to be arbitrary in the x-direction, a natural choice is to represent the field as a power series expansion about some fixed x.

$$\mathbf{E}(x') = \mathbf{E}(x) + \Delta x\mathbf{E}'(x) + \frac{1}{2}(\Delta x)^2\mathbf{E}''(x) + \cdots \qquad (5)$$

Δx is given by Eq. (3). For present purposes we will truncate the expansion at second order. This corresponds to the restriction that $\rho/\lambda \ll 1$, where ρ is the thermal gyroradius and λ is the local wavelength.

Grouping terms by harmonics of $e^{i\omega_0\tau}$ provides a convenient system for computing the time-average required by Eq. (1). Thus we define the coefficients a_n, c_n, d_n by the relations

$$\mathbf{E}(x')\cdot\mathbf{v}' = \sum_{n=-\infty}^{\infty} a_ne^{in\omega_0\tau} \qquad E_y(x') = \sum c_ne^{in\omega_0\tau} \qquad \frac{v_x'}{\omega}\frac{\partial E_y(x')}{\partial x'} = \sum d_ne^{in\omega_0\tau}$$

The coefficients are functions of r, v, and x-derivatives of the components of E. To compute them up to $n = 2$ we require the following products in addition to $\dot{v}'$ and Δx : $v_x'\Delta x$, $v_y'\Delta x$, $(\Delta x)^2$, $v_x'(\Delta x)^2$, $v_y'(\Delta x)^2$ to form $\mathbf{E}\cdot\mathbf{v}$ etc. From these we identify the a_n's etc.

Collecting the pieces we find

$$f_1(\mathbf{r}',\mathbf{v}',t') = -\frac{q}{M}e^{i(kz'-\omega t')}\sum\left\{-2\left[\frac{f_0}{u^2}+\frac{v_y}{\Omega}\left(\frac{f_0}{u^2}\right)'\right]a_n \right. \tag{6}$$

$$\left. +\frac{f_0'}{\Omega}\frac{\omega-kv_z}{\omega}c_n + i\frac{f_0''}{\Omega}d_n\right\}e^{in\omega_0\tau}\int_0^\infty d\zeta e^{i(\omega-kv_z+n\omega_0)\zeta}$$

We can abbreviate the notation by defining $b_n \equiv \{\ \}$. Eq. (6) then takes the form

$$f_1(\mathbf{r}',\mathbf{v}',t') = \frac{q}{M}e^{i(kz'-\omega t')}\sum_m \frac{b_m e^{im\omega_0\tau}}{i(\omega+m\omega_0-kv_z)}$$

Inserting this result into Eq. (1) we obtain $P_r = \frac{1}{2}\Re e\left(-i\frac{q^2}{M}\int d^3v\sum\frac{a_n b_n^*}{kv_z-\omega^*-n\omega_0}\right)$

Notice that in the case of a homogeneous plasma $b_n = -2f_0 a_n/u^2$ so that the numerator inside the summation sign is pure real and P_r becomes positive definite.

To handle the terms involving $(f_0/u^2)'$ we use $\left(\frac{f_0}{u^2}\right)' = \left[\epsilon_n + \left(2\frac{v^2}{u^2}-5\right)\epsilon_T\right]f_0$, where $\epsilon_n = \frac{1}{n}\frac{dn}{dx}$ and $\epsilon_T = \frac{1}{T}\frac{dT}{dx}$. The other f_0' terms contribute nothing to P_r and are therefore dropped. After performing the velocity integrals we obtain $P(x) = i\omega\varepsilon_0\sum_S\sum_{n=-\infty}^{\infty}p_n(x)$ where

$$\begin{aligned} p_0 &= 2\Delta\left\{-\xi_0 Z_0^{*\prime}\left[2|E_z|^2+\rho^2\left(|E_z'|^2+E_zE_z^{*\prime\prime}+c.c.\right)\right]+2\rho^2Z_0^*\left|E_y'\right|^2+\rho Z_0^{*\prime}(E_zE_y^{*\prime}\right. \\ &\quad \left.+c.c.)-\epsilon\rho Z_0^{*\prime}(E_yE_z^*+c.c.)-2\epsilon\rho^2Z_0^*(|E_y|^2)'\right\}-\tfrac{d}{dx}\left[\Delta\rho^2\xi_0Z_0^{*\prime}\right](|E_z|^2)' \end{aligned}$$

$$\begin{aligned} p_1 &= \Delta\rho\left\{\rho^{-1}R_1^*|E_+|^2+iR_2^*(E_+E_z^{*\prime}-c.c.)+R_3^*(|E_+|^2)'+\rho R_4^*\left(E_+\left[2E_+''-E_-''\right.\right.\right. \\ &\quad \left.-\epsilon(8E_+'-E_-')\right]^*+c.c.)+\rho R_5^*\left[(|E_+|^2)''+2(\epsilon_n-5\epsilon_T)(|E_+|^2)'\right] \\ &\quad \left.+\epsilon_T\rho R_6^*(|E_+|)'+i\rho R_7^*\left((E_+E_z^{*\prime\prime})'-c.c.\right)+\rho R_{12}^*|E_z'|^2\right\} \end{aligned}$$

$$p_2 = \Delta\rho^2Q^*\left[|E_+'|^2+\epsilon(|E_+|^2)'\right]$$

where $\Delta = \frac{\omega_p^2}{4\omega ku}$ and $\sum_S$ designates a sum over particle species. Also

$R_1 = \mathcal{R}_{00}+2\mathcal{R}_{20}$ $\quad R_2 = \mathcal{R}_{01}+2\mathcal{R}_{21}$ $\quad R_3 = \mathcal{R}_{10}+2\mathcal{R}_{30}+\frac{\epsilon}{2}(\frac{3}{4}\mathcal{R}_{00}-\mathcal{R}_{40})$

$R_4 = \frac{1}{4}(\frac{3}{4}\mathcal{R}_{00}+\mathcal{R}_{20}+\mathcal{R}_{40})$ $\quad R_5 = \frac{1}{2}\mathcal{R}_{20}+\mathcal{R}_{40}$ $\quad R_6 = 6\mathcal{R}_{20}+4\mathcal{R}_{40}+2\mathcal{R}_{22}+15\mathcal{R}_{60}+4\mathcal{R}_{42}$

$R_7 = \mathcal{R}_{11}+2\mathcal{R}_{31}$ $\quad Q = \frac{1}{2}(\frac{3}{4}\mathcal{Q}_0+\mathcal{Q}_2+\mathcal{Q}_4)$

where $\mathcal{R}_{mn} = I_{mn}(\xi_1, \frac{\epsilon}{ku})$ and $\mathcal{Q}_m = I_{m0}(\xi_2, \frac{2\epsilon}{ku})$ and. $\xi_n = \frac{\omega-n\Omega}{ku}$ and where

$$I_{pr}(\xi,\delta) = (1+\delta^2)^{-\frac{p+r+1}{2}}\sum_{\ell=0}^{p}\sum_{n=0}^{r}\frac{p!}{\ell!(p-\ell)!}\frac{r!}{n!(r-n)!}(-1)^{r-n}\delta^{\ell+r-n}\Phi_{p-\ell+r-n}I_{\ell+n}$$

and $\Phi_m = \frac{1}{\sqrt{\pi}}\int_{-\infty}^{\infty} x^m e^{-x^2} dx$ and $I_m = \int_{-\infty}^{\infty} \frac{dv}{\sqrt{\pi}} \frac{v^m e^{-v^2}}{v - \xi/\sqrt{1+\delta^2}}$

Evaluation of I_m is facilitated by the recursion relation $I_m = \Phi_{m-1} + \frac{\xi}{\sqrt{1+\delta^2}} I_{m-1}$. The corresponding p_{-n}'s are obtained from the p_n's by the replacements:
$n \to -n$, (and hence $\xi_n \to \xi_{-n}$ and $\epsilon/k \to -\epsilon/k$), $\quad i \to -i$, (hence $E_\pm \to E_\mp$).

It can be shown that by repeated application of the differential identity $A'B = (AB)' - AB'$ to the terms in P we may write $P = \mathbf{E}\cdot\mathbf{J}^* - \nabla\cdot\mathbf{S}_K$ whence the following quadratic form from Maxwell's equations $\frac{\partial}{\partial x}\left(E_y H_z^* - E_z H_y^*\right) + i\omega(\epsilon_0|\mathbf{E}|^2 - \mu_0|\mathbf{H}|^2) = -\mathbf{E}\cdot\mathbf{J}^*$ can be written in the form $\frac{\partial}{\partial x}(S_{em} + S_{Kx}) + P = 0.$

The current density is specified by $\mathbf{E}\cdot\mathbf{J}^* = -i\omega\epsilon_0 \sum_{Species}\sum_n \mathbf{E}\cdot\mathbf{J}_n^*$ where

$$\begin{aligned}
\mathbf{E}\cdot\mathbf{J}_0^* &= E_y\left\{4(\Delta\rho^2 Z_0 E_y')' + 2(\Delta\rho Z_0' E_z)' + 2\epsilon\Delta\rho Z_0' E_z\right\}^* \\
&\quad + E_z\left\{-2\Delta\rho Z_0'(E_y' - \epsilon E_y) + 4\Delta\xi_0 Z_0' E_z + 2(\Delta\rho^2\xi_0 Z_0' E_z')'\right\}^*
\end{aligned}$$

$$\begin{aligned}
\mathbf{E}\cdot\mathbf{J}_1^* &= E_+\left\{|\Delta R_1 - (\Delta\rho R_3)' + 2(\Delta\rho^2 R_4)'' + 8(\epsilon\Delta\rho^2 R_4)' + (\Delta\rho^2 R_5)''\right. \\
&\quad -\Delta\rho^2\{2(\epsilon_n - 5\epsilon_T)R_5' - \epsilon_T R_6'\}]E_+ + \Delta\rho^2 R_4(4E_+'' - E_-'' + \epsilon E_-') \\
&\quad \left.+4(\Delta\rho^2 R_4)' E_+' - i(\Delta\rho^2 R_7)' E_z'\right\}^* - E_-\left\{(\Delta\rho^2 R_4 E_+)'' + \epsilon\Delta\rho^2(R_4 E_+)'\right\}^* \\
&\quad -E_z\left\{i(\Delta\rho R_2 E_+)' - i(\Delta\rho^2 R_7)' E_+' + (\Delta\rho^2 R_{12} E_z')'\right\}^*
\end{aligned}$$

$$\mathbf{E}\cdot\mathbf{J}_2^* = E_+\left\{(\Delta\rho^2 Q E_+')' + \epsilon\Delta\rho^2 Q' E_+\right\}^*$$

Recall that the corresponding terms arising from the p_{-n}'s are also required.
If we represent the kinetic flux as the sum $S_{Kx} = -i\omega\epsilon_0 \sum_S \sum_n S_n$ then

$$\begin{aligned}
S_0 &= -4\epsilon\Delta\rho^2 Z_0^*|E_y|^2 + 4\Delta\rho^2 Z_0^* E_y E_y^{*\prime} + 2\Delta\rho Z_0^{*\prime} E_y E_z^* \\
&\quad + (\Delta\rho^2\xi_0 Z_0^{*\prime})'|E_z|^2 - 2\Delta\rho^2\xi_0 Z_0^{*\prime} E_z' E_z^*
\end{aligned}$$

$$\begin{aligned}
S_1 &= \Delta\rho\left\{-iR_2^* E_z E_+^* + R_3^*|E_+|^2 + \rho R_4^*\left[(2E_+' - E_-') - \epsilon(8E_+ - E_-)\right]E_+^*\right. \\
&\quad + \rho R_5^*(|E_+|^2)' + \rho[2(\epsilon_n - 5\epsilon_T)R_5^* + \epsilon_T R_6^*]|E_+|^2 + i\rho R_7^*(E_+ E_z^{*\prime} - \text{c.c.}) \\
&\quad \left.+\rho R_{12}^* E_z E_z^{*\prime}\right\} - (2E_+ - E_-)(\Delta\rho^2 R_4^* E_+^*)' - (\Delta\rho^2 R_5^*)'|E_+|^2 + i(\Delta\rho^2 R_7^*)' E_z E_+^*
\end{aligned}$$

$$S_2 = \Delta\rho^2 Q^* E_+(E_+^{*\prime} + \epsilon E_+^*)$$

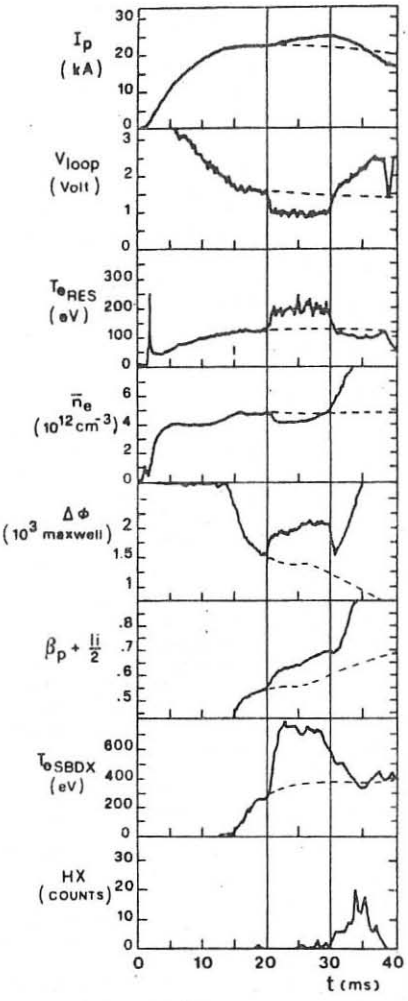
EFFECTS OF ECW INJECTION INTO THE THOR TOKAMAK PLASMA

L.Argenti, G.Cima, S. Cirant, F. De Luca*, A. Jacchia, P. Mantica, G. Ramponi, A. Simonetto*, U. Tartari
Istituto di Fisica del Plasma, CNR-EURATOM, Milano, (Italy)
*Università di Milano (Italy)

The efficiency of ECRH both at the fundamental and at the second harmonic resonance has been demonstrated in many experiments /1/. In most cases the plasma optical thickness was high enough to allow a substantial single-pass absorption of the EC wave. In these conditions, the conversion of the EM wave into Bernstein waves at the upper hybrid layer and their absorption /2/ cannot be clearly identified. Therefore, the interaction of EC waves with low density, low temperature plasmas, which are present even in large devices during the start-up phase, is still a subject of investigation.
The THOR tokamak plasma, at peak densities between .6 and 1x10E13 cm^{-3} allowing the resonant layer to be accessible by the 28 GHz wave, is characterized by electron temperatures ranging between 100 and 200 eV. By varying the plasma current between 20 KA and 50 KA, with a safety factor at plasma boundary between 9 and 3.5, regimes are produced which are increasingly suprathermal with current.
In these conditions, single-pass absorption at the resonance is only a few percent of the total injected power and the absorption via conversion at the upper hybrid, if present, should be privileged. Moreover, the low optical thickness allows the use of a simple launching set-up, consisting of a Wengenroth polarizing antenna placed at the low field side plasma edge and an opposite twist reflector inside the vacuum vessel which rotates the polarization and provides for the inside launch of an extraordinary wave, mostly perpendicular to the toroidal field. The antenna conversion efficiency into a single polarized beam is greater than 95% for TE01 illumination and its beamwidth at 3 db is $\mp$ 4°.
The transmission line delivering the microwave power to the antenna in circular electric modes comprises a rippled wall helical waveguide $5\lambda_b$ long mode converter from the TE02 mode available at the VGA-8050 gyrotron output to the TE01 mode, two 90° electroformed mitre bends and two helical waveguide mode filter sections. Overall transmission is 95%.
Heating pulse lengths between 3 and 10 ms and power levels between 80 and 130 kW have been employed in the experiment.
Fig. 1 shows diagnostic output of a typical ECH discharge characterized by a 10 ms, 80 kW RF pulse and by the resonance position placed along the plasma midplane.
Increments as high as 75% are observed in the peak resistive temperature obtained under the assumptions of classical Spitzer resistivity and constant profiles. The increase in the poloidal beta measured by the diamagnetic loop can be made consistent with the increment in the eccentricity factor $\beta_p + li/2$ deduced from equilibrium measurements assuming a slight broadening

of the current density profile. The time scale of both the resistivity and diamagnetism variations is in the order of the energy confinement time.
Many of the RF heated discharges show a pronounced density rise delayed with respect to the start of the RF pulse. Before the rise the density profile goes through a flattening, as is shown in Fig. 4, and the volume averaged density drops by about 10%.
Thermal effects in the order of Δ Te = 30 eV have been observed by Thomson scattering, even if non thermal features in the spectra are often a serious limitation to the temperature assessment.
The bulk temperature as measured in the spectral range of 2-2.5 KeV by a SiLi detector increases by about 40 eV during the RF pulse. The spectrum also shows the appearence of a flat tail extending to the high energies up to 8 KeV (Fig. 3). The electron temperature as measured by means of the "two foils absorber method" along a chord in the equatorial plane shows a pronounced rise on a time scale longer than the energy confinement time (Fig. 1). No variation of the hard x-ray activity, as measured by a NaI detector, is obeserved during RF injection while at the very end of the pulse a sudden burst appears, whose maximum energy has been measured to be 150 KeV (Fig. 1).
The main features of the 2nd harmonic ECE signals is a large increase of the radiative temperature, clearly due to suprathermal emission. The rise and fall times are longer than the energy confinement time (Fig. 5a). A second feature, with a sharp density threshold around ne = 6x10E12 cm^{-3}, is the appearence of a second emission maximum after the end of the pulse (Fig. 5b), as reported also in the ISX-B 28 GHz experiment /3/. This post-ECH effect is not revealed by electric diagnostics, indicating little relevance of the electrons responsible for this emission to the energy balance.
The diamagnetic increase of the plasma energy content can be 100% or higher, and its dependence on electron density, resonance position and injected power is illustrated in Fig. 2. For the shot in Fig. 1, assuming constant energy confinement, an RF power absorption efficiency in the order of 60-70% can be estimated. Independent microwave and bolometric measurements give an RF wall loading $\simeq$ 30%, the plasma absorbed fraction being consistent with the diamagnetic measurements.
The moderate rise in the central electron temperature can account for the measured increase in the plasma energy content only if a large broadening of the temperature profile is assumed. On the other hand, enhanced signals on those diagnostics which are sensitive to high energy tails are clearly present during and after the heating pulse. All these data suggest that cyclotron resonance bulk electron heating is acting together with coupling of the injected power with the high energy part of the distribution function, directly at the resonance or after conversion into high n Bernstein waves.
Planned modifications of the launching set-up will allow changes in the efficiency of the inside launch of the extraordinary wave. The comparison of the absorption efficiency and suprathermal tail production in different launching schemes should add information on the relative roles of the cyclotron resonance and of the upper hybrid in the absorption of EC waves.

/1/ Proc. Heating in Toroidal Plasmas, Rome, March 1984
/2/ A.Airoldi et al., P.P. and C.N.F.R. 1980, vol.II,IAEA, Vienna (1981),537
/3/ G.B.Elder et al.,Oak Ridge Nat. Lab., ORNL/TM 8403 (1983)



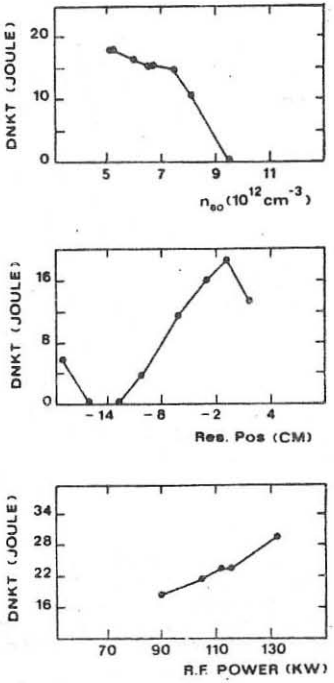


Fig.2: Energy content increase versus density,resonance position,RF power.

Fig.1: Waveforms of shot 20414. Dotted lines show the ohmic behaviour. Vertical lines represent RF duration.

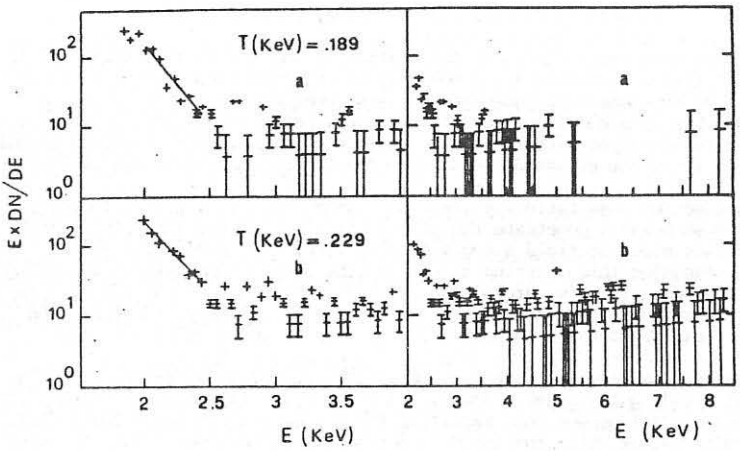


Fig.3: Soft X ray spectra with (a) and without (b) RF, plotted for two energy ranges.

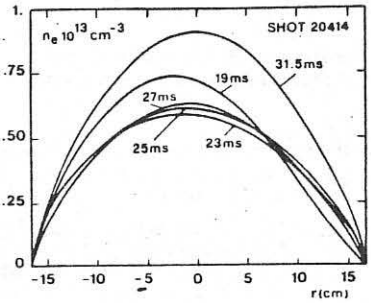


Fig.4: Density profile evolution.

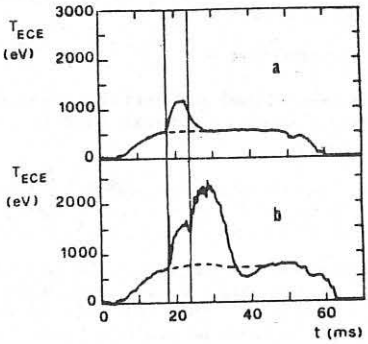


Fig.5: EC 2nd harmonic emission near plasma centre for
a) $\bar{n}_e$ = 6.5x10E12 cm-3
b) $\bar{n}_e$ = 5.5x10E12 cm-3

INJECTION AND TRAPPING OF INTENSE NEUTRALIZED ION BEAMS IN CLOSED MAGNETIC CONFIGURATION

J. Katzenstein, Renjun Li* and Norman Rostoker
University of California, Irvine, California 92717

It has been demonstrated by calculation[1] and verified by experiment[2,3] that a neutralized ion beam may be injected across magnetic field lines, that the beam will penetrate a plasma confined by the field and be trapped. The combined processes of injection, penetration, and confinement of the beam requires the satisfaction of three conditions. For injection across the field lines the plasma dielectric constant must exceed the square root of the ion-electron mass ratio i.e., $\varepsilon = (1 + 4\pi nMc^2/B^2) > (M/m)^{1/2}$. In order for the injected beam to penetrate the plasma the time for the shorting of the polarization electric field along the field lines must exceed the pulse length. Assuming this shorting time to be the propagation time of an Alfven wave whose velocity is v_A around the major circumference of the torus, this condition can be written as $2\pi R/v_A >$ pulse length. Finally, the condition that the beam be confined is just $(v_T q/\Omega_T) < (r/2)$ where v_T is the beam velocity for the case of tangential injection, Ω_T the gyro frequency in the toroidal field, q the safety factor, and r the minor radius of the torus. The first two conditions are well satisfied for the experiment described in Ref. 3 on the UCI Tokamak while the third is not satisfied because of the ion value of Ω_T and the large value of q. Thus only the lower velocity components of the beam could be observed in the Tokamak. We plan to carry out a similar experiment on the Tokamak device at the University of Texas (TEXT). The parameters of this machine are such as to satisfy these three conditions for mean ion energies exceeding about 200 kev. Furthermore, the total injected energy (5 to 10 kJ) is to be equal or greater than that of the confined plasma so the effect of the beam on the plasma temperature and toroidal current can be readily measured.

1. INTRODUCTION

A neutralized ion beam can propagate across a magnetic field if the dielectric constant perpendicular to the magnetic field satisfies the condition[1,2,3]

$$(M/m)^{1/2} < \varepsilon_\perp < (c^2/u_o^2) \qquad (1)$$

where

$$\varepsilon_\perp \simeq 4\pi nMc^2/B_\perp^2$$

M is the beam ion mass, n is the beam density, $\varepsilon_\perp$ is the dielectric constant and u_o is the beam velocity. $B_\perp$ is the magnetic field component perpendicular to the beam path. The inequality to the left is the condition for transverse charge separation; an electric field is produced so that $\underset{\sim}{u}_o = c(\underset{\sim}{E} \times \underset{\sim}{B})/B^2$ and the beam drifts across the field. If this condition is not satisfied there is charge separation parallel to the beam axis and the beam reflects instead. The inequality to the right implies that $4\pi nMu_o^2/B^2 < 1$ so that the magnetic field is not significantly altered by the beam. Applied to injecting a proton beam into a tokamak the condition is

$$42 < \varepsilon_{\perp} = \frac{2.9 \times 10^3}{B_{\perp}^2} \frac{J}{\sqrt{W}} < \frac{4 \times 10^5}{W} \tag{2}$$

$B_{\perp}$ is in kilogauss, J is the beam current density in amps/cm^2 and W is the ion energy in kev.

The ion beam can be trapped in a magnetic containment device if it contains plasma. The plasma will "short out" the polarization and then the motion of the beam particles is determined by the confining fields as it is for the plasma particles. If the plasma is a good conductor the shorting by a local conduction current will be very slow because of low conductivity across the magnetic field lines. Instead the polarization will disappear due to communication along the field lines which in a tokamak means around the major circumference. The problem is similar to a capacitor connected at t = 0 to a dissipationless transmission line; the capacitor is initially charged and the transmission line initially has no current or voltage. The characteristic velocity of the transmission line is the Alfven speed. For t > 0 the charge will spread out with the characteristic speed $V_A = B(4\pi nM)^{-1/2}$ and the charge on the capacitor which represents the transverse polarization will decay on the time scale $\tau = 2\pi R/V_A$. The condition that all of the neutralized ion beam will penetrate the plasma is that the beam pulse length T satisfy

$$T < 2\pi R/V_A . \tag{3}$$

After the beam has been trapped in the plasma the question of confinement must be reconsidered. In this paper we address the question of single particle confinement of the beam. In a cartesian coordinate system centered on the minor axis of a tokamak as illustrated in Fig. 1, the guiding center equations of motion of the ions are

$$\frac{dx}{dt} = -\omega y \tag{3}$$

$$\frac{dy}{dt} = \omega x - \frac{V_T^2}{\Omega_T R} \tag{4}$$

These equations describe the motion of ions along helical trajectories. V_T is the toroidal velocity, Ω_T is the ion cyclotron frequency in the toroidal field. $V_T^2/\Omega_T R$ is the toroidal drift. $\omega = V_T/qR$ is the rotational velocity resulting from helical field lines. $q = rB_T/RB_p$ is the safety factor. The solution is a circular orbit with the center shifted from the minor axis by

$$d = \Delta x = \frac{V_T}{\Omega_T} q = \frac{r}{R} \rho_p < r \tag{5}$$

where $\rho_p = V_T/\Omega_p$ is the gyro radius of ions in the poloidal magnetic field B_p. If we assume a uniform beam injected over the entire minor cross section, only

ions with the radius of the projected orbit less than r-d would be contained as indicated in Fig. 1. The fraction contained would be

$$F = [(r-d)/r]^2 = [1 - (\rho_p/R)]^2 \qquad (6)$$

The condition for containment of most of the injected particles is $(\rho_p/R) \ll 1$.

2. INJECTION OF A NEUTRALIZED ION BEAM INTO THE UCI TOKAMAK[3]

The parameters of the UCI tokamak were:

Major radius R = 60 cm
Minor radius r = 15 cm
Toroidal field B_T = 6 k-gauss
Plasma electron temperature T_e = 100 ev
Plasma density n = $10^{13}/cm^3$
Maximum plasma current I_p = 13 k amp.

The parameters of the neutralized ion beam were:

Current density J = 5 A/cm^2
Ion energy W = 50-150 kev
Pulse length T = .5 μsec.

For tangential injection $B_\perp = B_T/2^{1/2}$ so that $\varepsilon_\perp$ = 80 (W = 100 kev) and $2.7 \times 10^3 > \varepsilon_\perp > 42$ is well satisfied. The condition for penetration is Eq. (3) where T = .5 μsec and $2\pi R/V_A$ = .9 μsec. The condition for containment of beam particles Eq. (6) was not satisfied. Containment of 100 kev ions requires a poloidal current of about 50 kA and the largest poloidal current was only about 13 kA. In spite of this limitation pulses of energetic ions in the range 50-120 kev with transit times corresponding to the energy were detected for 3-5 transits of the major circumference. The experiment demonstrated injection and penetration but not confinement.

3. INJECTION OF A NEUTRALIZED ION BEAM INTO TEXT

The parameters of TEXT are:

Major radius R = 100 cm
Minor radius r = 27 cm
Toroidal field B_T = 28 k-Gauss
Plasma electron temperature T_e = 1 kev
Plasma density n = 4×10^{13} cm^{-3}
Maximum plasma current I = 400 kA

The parameters of the neutralized ion beam are:

Current density J = 200 A/cm^2
Pulse duration T = .5 μsec
Ion energy W = 1-300 kev.

Construction of the new ion diode and associated pulsed power has recently been completed. For an ion energy of 200 kev $\varepsilon_\perp = 105$, $2\pi R/V_\beta = .65$ sec and $\rho_p/R = .25$. Thus all of the conditions required for injection, trapping and confinement are well satisfied. The plasma energy in TEXT is about 8 kJ at $T_e = 1$ kev. The injected beam will have an energy of about 5 kJ so that the change in T_e should be easy to measure. Another quantity that can be measured and will be of considerable interest is the net beam current in the Tokamak that has been predicted to be[4]

$$I = I_B \left(\frac{V_B T}{2\pi R}\right) \left[1 - \frac{Z_B}{Z_p} + 1.46\left(\frac{r}{R}\right)^{1/2} \frac{Z_B}{Z_p}\left(1 + \frac{.68}{Z_p}\right)\right] \qquad (7)$$

I_B is the beam current of fast ions (50 kA), $V_B T$ is the beam length (225 cm) and $2\pi R = 628$ cm is the tokamak circumference. Z_B is the beam atomic number ($Z_B = 1$) and Z_p is the effective atomic number of plasma ions. The second term is the electron return current and the last term is due to electron trapping. Assuming $Z_B = Z_p = 1$, the net current predicted by Eq. (7) would be 12.5 kA.

*Permanent Address: Institute of Atomic Energy, Academia Sinica, Beijing, China.

ACKNOWLEDGEMENT

This work was supported by the Department of Energy.

REFERENCES

[1] W. Peter and N. Rostoker, Phys. Fluids 25(4), 730 (1982).
[2] S. Robertson, H. Ishizuka, W. Peter, and N. Rostoker, Phys. Rev. Lett. 47(7), 508 (1981).
[3] J. Katzenstein, S. Robertson, and N. Rostoker, Proceedings of the Fifth International Conference on High-Power Particle Beams, 264 (1983).
[4] D. F. H. Start and J. G. Corday, Phys. Fluids 23, 14 (1980).

FAST IONS BEHAVIOUR DURING N.B.I. IN TFR FROM AUXILIARY MODULATED BEAM MEASUREMENTS

TFR Group presented by T.Hutter and J.P. Roubin

ASSOCIATION EURATOM-CEA SUR LA FUSION
Département de Recherches sur la Fusion Contrôlée
Centre d'Etudes Nucléaires
Boîte Postale n°6. 92260 FONTENAY-AUX-ROSES (FRANCE)

Abstract : Local measurements of injected fast ions distribution by charge exchange with an auxiliary modulated beam are presented. The fast ions density in the center of the discharge is shown to saturate with injected power.

I - INTRODUCTION

High power neutral beam injection experiments have been performed on T.F.R. Two quasi-perpendicular (75°) co-injection lines composed of 4 sources in a vertical plane [1] deliver typically 1.5 MW neutral H° or D° beams at 35 keV, that is about three times the usual ohmic power. Heating efficiency saturation has been previously reported [2]. Fast injected ions behaviour is investigated in order to establish to what extent this phenomenon is actually due to plasma bulk confinement decrease and/or heating source deterioration related to specific beam effects.

Previous work [3] based on passive charge-exchange analysis showed a classical behaviour of injected ions. However because of the very hollow thermal neutral profile, only peripheral ions were observed. In this work, enhanced contrast for the central ions is obtained by a modulated auxiliary beam, crossing the line of sight of mass resolved multi-channel fast neutral particles analyzers. This arrangement provides a localization of the fast neutrals origin.

II - CHARGE EXCHANGE HYDROGEN FLUXES ORIGIN

Two different experimental set-up are used and are described in fig.1. Hydrogen fluxes coming from charge exchange of fast injected ions with either thermal neutrals (background signal) or with doping beam neutrals and its halo (modulated signal) are measured by a 6 channel mass resolved CX analyzer.

With the shape of neutral density and the fast ions profile computed by classical codes, it is possible to localize the origin of the fluxes. Results of simulation (see figure 2) show that, in spite of the doping effect of the halo which is larger than the beam itself, modulated fluxes do come from a central part of the plasma, whereas background fluxes originate from a more peripheral region. This is true even in experiment (b) where the geometry is less favourable.

III - EXPERIMENTAL PARAMETERS AND RESULTS

The ohmic plasma parameters are hold constant. Working gas : Deuterium, $a = 20$ cm (carbon limiters), $R_o = 98$ cm, $B_T = 4.5$ T, $I_p = 250$ kA, $n(o) = 10^{14}$ cm^{-3}, $T_i(o) = 0.9$ keV, $T_e(o) = 1.5$ keV.

The only varying parameter is the injected power. Four duopigatron sources were available during these experiments and injected hydrogen beams at a reproducible regime of 33 kV, 10 A. Powers from about 150 kW to 600 kW are injected in the plasma according to the number of

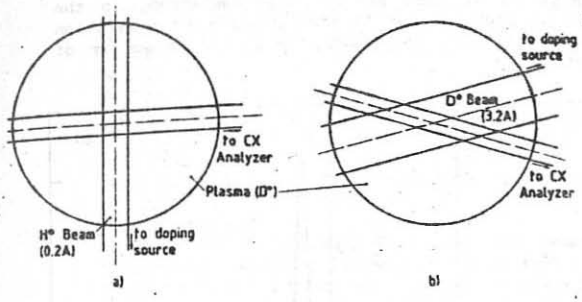


Fig. 1 Geometric configuration for (a) first experiment, (b) second experiment

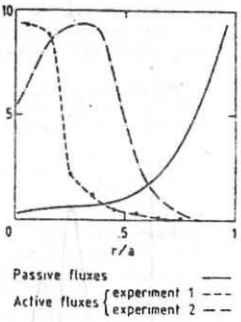


Fig. 2

operated sources. As reported in [1], the increase of D^+ ion temperature and electron temperature is small and saturates with power.

P_{inj} (kW)	150	300	600
$\Delta T_i(0)$ eV	110	165	225
$\Delta T_e(0)$ eV	30	50	60

Injected ions CX signals are shown fig.3. During the heating pulse the background and modulated components clearly appear. In the second configuration, due to the large doping current, the modulated signal is far larger than the continuous one.

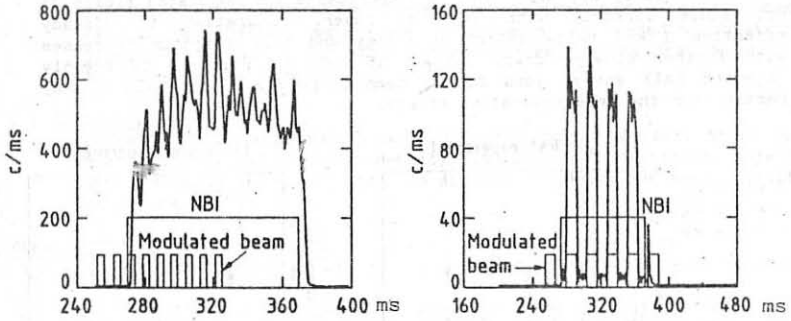


Fig. 3 - CX flux at 30 keV versus time

IV - SIGNAL ANALYSIS AND DISCUSSION

A Fourier transform algorithm is used to analyse the signals. A clear maximum is always seen at the modulation frequency, theoretically equal to the amplitude of modulation time $2/\pi$ (Fig. 4a). In the first configuration an other important peak appears at about 150 Hz, that is the sawtooth activity frequency as seen by 2 ω_{ce} and soft X-rays

measurements. This activity is also present off-modulation, in the background signal and is probably due to sawtooth-induced relaxation in the thermal neutral profile. The other peaks are harmonics of modulation and sawteeth.

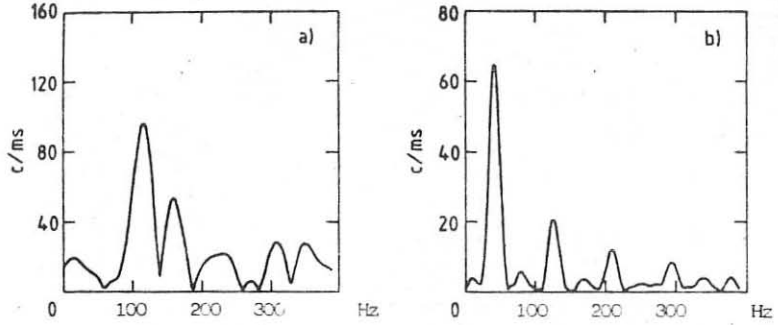


Fig. 4 - Fourier transform module of CX signals shown on fig. 3

The same method is applied for a set of shots at various power levels. Figures 5a and 5b represent the evolution of the modulated fluxes as a function of analyzed energy and injected power. For each energy the fluxes are normalized to their values at the lowest injected power. The error bars represent the shot to shot dispersion.
One fact clearly appears : in both experiments the modulated fluxes do not scale linearly with injected power. Saturation is already effective 3 keV below injection energy and only slightly increases with further slowing down. Below 16 keV the presence of freshly injected half energy ions due to beam composition (65-25-10 %) may partly mask the true saturation effect.

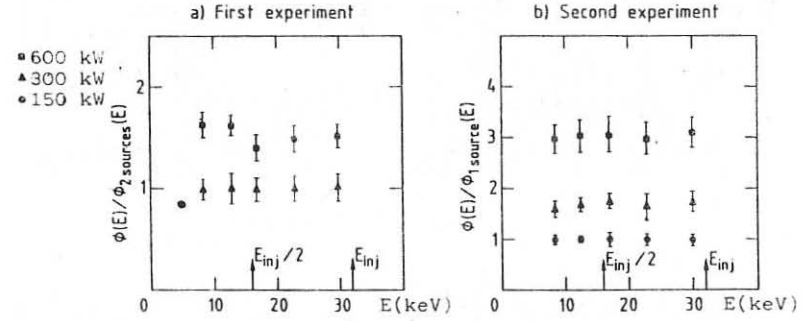


Fig. 5 - Charge exchange fluxes versus energy for different powers

In the first experiment where the signals are more central, the saturation is stronger (ϕ (4 sources)/ ϕ (2 sources) = 1.5) than in the second one (ϕ(4 sources)/ϕ(2 sources) = 1.75). In contrast, the background signal grows linearly or even more than linearly with power.

The saturation of the modulated fluxes implies that at least a part of the heating saturation during NBI is related to specific fast ions problems, that is additional heating power density problems rather than bulk confinement degradation only.

Three broad types of mechanisms have to be examined.

1) Injected power saturation due to souce or beam problems before plasma boundary.

2) Enhanced peripheral capture of the beams, for instance related to increased impurity production due to fast ions losses.

3) Confinement degradation of the central fast ions themselves for instance due to beam-enhanced charge exchange.

We think that issue 1 can be discarded : first, electrical and calorimetric beam diagnostics never show any anomaly related to multi-source operation and second, the observed heating saturations are identical when 4 sources are operated on the same line or 2 on each line (diametrically opposed) tuling out any source interaction scheme.

Concerning issue 2, calculations with spectroscopically measured impurity concentrations and published cross sections [4] give unsufficient effects.

Issue 3, with charge-exchange as a candidate, would require a central neutral density reaching 10^9 cm^{-3} in order to account for the observed saturation. Comparing measured modulated and background CX fluxes of thermal ions (as in [5]), the central neutral density can be evaluated and is found to increase only slightly from 6 to 10.10^7 cm^{-3} for 600 kW of injected power. Clearly CX cannot dominate central fast ions confinement. Moreover, with CX beams losses, saturation would be much stronger at low than at high energy, contrary to experiment. Therefore, if fast ions confinement rather than neutral capture has to explain the observed saturation, a mechanism is needed which strongly affects essentially the most energetic ions, during the beginning of the slowing-down process.

V - CONCLUSION

Central ion heating scaling with injected power has been shown to be related to central fast ion density saturation. While trivial injection line problems can be excluded, no precise mechanism has been identified inside the plasma.

REFERENCES

(1) J.Druaux, M. Fois P. Giovannoni : 13th symposium on Fusion technology Varese 1984 Vol 1 p. 625.

(2) Equipe TFR : Plasma Physics and controlled nuclear fusion research (Proc. 10th Int. Conf. London 1984) Vol 1, IAEA, Vienna 1985 (103)

(3) TFR Group, Nucl. Fusion 23, 4 (1983) 425

(4) R.E. Olson and A. Salop, Phys. Rev. A 16,2 (1977) 531

(5) W.R. Hess, B.C. Gregory, C. Gormezano Rev. Sci. Ins. 55 (5) 1984.

G

basic physics

THE PONDEROMOTIVE DECAY OF LH WAVES AS A MEANS OF FILLING THE SPECTRAL GAP AND UNDERSTANDING THE OPACITY OF HIGH-DENSITY PLASMAS TO LH WAVES

E. Canobbio and R. Croci

Max-Planck-Institut für Plasmaphysik
EURATOM Association, D-8046 Garching

Abstract. The solution of the relevant nonlinear partial differential equation for the LH wave amplitude E has been found to have a secular behaviour in space accompanied by decay of the original k-spectrum of E. This is instrumental to the solution of the spectral gap problem. Another fundamental aspect of the nonlinearity is the possible existence of an infinity surface for grad E (wave breaking). The characteristic distance of such a surface from the plasma boundary is a measure of the maximum penetration depth of a LH pump. The results are used to interpret the experiments.

Secular nonlinearity. We consider a uniform, magnetized plasma half-space which is accessible to a y-independent electrostatic LH wave launched at the x=0 surface: $E_{\parallel}(x,z,t) = E(x,z)\exp(-i\omega t) + c.c.$, $(\mathrm{Im}(\omega) = 0)$.

If thermal dispersion, dissipation and linear mode conversion are neglected, the ponderomotive density change is

$$n(x,z) = n_0 \exp(-\gamma |E(x,z)|^2),$$

where

$$\gamma = -\varepsilon_{\parallel}/\varepsilon_{\perp} 8\pi n_0 (T_e + T_i)\,, \quad \varepsilon_{\parallel} = 1 - (\omega_p/\omega)^2, \quad \varepsilon_{\perp} \simeq 1 + (\omega_{pe}/\omega_{ce})^2 - (\omega_{pi}/\omega)^2.$$

Disregarding the small region where the two types of rays - right-going and left-going - are superposed, we only consider right-going rays. Then with the sole assumption $\gamma |E|^2 \ll 1$, the wave equation reduces to the first-order equation

$$E_s + E_z = \tfrac{1}{2}\gamma (E|E|^2)_z, \qquad (1)$$

where $s = (-\varepsilon_{\parallel}/\varepsilon_{\perp})^{1/2} x$ (s/2π is the penetration distance measured in numbers of radial wavelengths) and subscript s(z) denotes the derivative with respect to s (z). Equation (1) is solved with the two conditions $E(s=0,z;\gamma) = E^{(0)}(z)$ and $E(s,z;0) = E^{(0)}(\sigma)$, $\sigma = z - s$, where $E^{(0)}(\sigma)$ is the linear solution. The equation for $M = |E|^2$ is

$$M_s + M_z = \tfrac{3}{2}\gamma M M_z. \qquad (2)$$

Thus (see, for example, Courant-Hilbert, Vol. II) M obeys the implicit equation

$$M(s,z) = M^{(0)}(z - s(1 - \tfrac{3}{2}\gamma M(s,z))), \qquad (3)$$

where $M^{(0)}$ is a given function.
Equation (3) shows that even if $M^{(0)}(\sigma)$ is periodic, M is not periodic in s, and, most important, that there is a surface D(s,z) = 0 at which wave breaking occurs, $|\mathrm{grad}\ M| \propto 1/D \to \infty$, where

$$D(s,z) \equiv 1 + \tfrac{3}{2}\gamma s\, \partial M^{(0)}(A)/\partial A\,, \quad A \equiv z - s(1 - \tfrac{3}{2}\gamma M). \qquad (4)$$

Beyond the wave breaking surface, M would be multi-valued. Inclusion of a dispersive term prevents the shock from forming and causes the LH field to have a marked decay beyond such a surface. Equations (1)-(4) can be used to describe the distortion of the wave before the wave-breaking surface. It is important to stress that according to eqs. (1)-(4) even a wave with smooth profile and arbitrarily small amplitude at s=0, with $\partial M^{(0)}/\partial\sigma \neq 0$, is nonlinearly distorted and breaks at sufficiently large s since the nonlinear effect is secular.
With $E = E(\sigma,t)$, $t = s\gamma/2$, eqs. (1) and (2) become

$$E_t = (EM)_\sigma \quad \text{and} \quad M_t = 3MM_\sigma. \qquad (5)$$

Taylor expanding

$$(E,M) = \sum_{p=0}^{\infty} t^p (E^{[p]}, M^{[p]})/p!, \qquad (6)$$

with $(E^{[p]}, M^{[p]}) \equiv (\partial^p(E,M)/\partial t^p)_{t=0}$,

one finds by induction, for $p \geq 1$,

$$M^{[p]} = (3^p/(p+1)!)\,\partial^p(M^{(0)}(\sigma))^{p+1}/\partial\sigma^p, \tag{7}$$

(by making use of $(M^\beta)_t = (3\beta/(1+\beta))(M^{\beta+1})_\sigma$, where β is any number), and

$$E^{[p]} = \sum_{s=0}^{p-1} [(p-1)!/(p-1-s)!\,s!]\,(M^{[p-1-s]}\,E^{[s]})_\sigma . \tag{8}$$

This yields

$$E^{[1]} = (M^{(0)}E^{(0)})_\sigma ; \tag{9}$$

$$E^{[2]} = (M^{(0)}E^{[1]} + M^{[1]}E^{(0)})_\sigma ; \quad M^{[1]} = \tfrac{2}{3}(M^{(0)2})_\sigma , \ldots$$

Series (6) with eqs. (7) and (8) converge for $0 \leq t < t(\sigma)$, where $t = t(\sigma)$ is the wave-breaking surface ($t(\sigma)=0(1)$). Equations (9) give the decay of the original $\vec{k}$-spectrum of the LH pump, which is instrumental in solving the spectral gap problem.

Upshift of the $\vec{k}$-spectrum. We consider a 2N waveguides grill (N=1,2,...) located in $|z|<L$. Let $E_g(z)$, the field at s=0, be zero for $|z|>L$ and constant at the mouth of each waveguide, with the relative phase φ between two adjacent waveguides. Then the module squared of the Fourier transform of $E_g(z)$ is proportional to

$$\alpha(k) = \left\{\sin\left(\frac{kL}{2N}\right)\frac{\sin[2N(\varphi/2 + kL/2N)]}{k\sin(\varphi/2 + kL/2N)}\right\}^2 . \tag{10}$$

The main peaks of $\alpha(k)$ are essentially due to the zeros of the denominator: $\varphi + kL/N = 2m\pi$ (m=0,±1,±2,...), with a correction of order 1/kL. The position k_m and the relative amplitude $|e_m|^2$ of the main peaks can be used to approximate $E_g(z)$ in $|z|<L$ as the sum of a few terms $e_m \exp(ik_m z)$. For nondirectional grills ($\varphi = \pi$), the only ones considered explicitly in the present paper, we get $k_{-m} = -k_m$ and $e_{-m} = -e_m$.

Examples: (a) N=1: $k_0 \simeq 3\pi/4L$, $k_1 \simeq 3\pi/L$, $e_1 \simeq 0.3$; (b) N=4: $k_0 \simeq (.94)4\pi/L$, $k_1 \simeq 12\pi/L$, $e_1 \simeq 1/3$.

By using radiation conditions and excluding the Fourier components of the LH pump with $k_{//} < k_a$, the accessibility value, one finds that $E^{(0)}(\sigma)$ is related to $E_g(z)$ by the equation

$$E^{(0)}(\sigma) = \tfrac{1}{2}E_g(\sigma) + \frac{1}{2\pi i}\,P\int_{-\infty}^{\infty} dz'\,\frac{E_g(z')}{z'-\sigma}\,e^{-ik_a(z'-\sigma)} \tag{11}$$

In view of the foregoing, we have, within the right-going resonance cone,

$$E^{(0)}(\sigma)/\bar{E} \simeq e^{ik_0\sigma} + e_1 e^{ik_1\sigma} + e_a e^{ik_a\sigma}, \tag{12}$$

where $e_1 \simeq 1/3$ and, provided that $|\sigma| \ll L$ and $(k_0 - k_a)L \gg 1$, $e_a \simeq 2\cos((k_0-k_a)L)/\pi(k_0-k_a)L$. Equation (12) exhibits the existence within the plasma of a travelling wave with $k_{//} = k_a$. If only the leading term of eq.(12) is considered, there is no secular effect, as eq. (3) clearly shows, since M = const. For this reason, the interaction of the leading term of the right-going ray with that of the left-going one was postulated in /1/. Here, however, we are able to show that the secondary waves $e_{1,a}$ of the same ray interact nonlinearly with its leading term and produce the required $\vec{k}$-upshift, without having to assume a questionable superposition of left and right-going rays.

We consider separately the effect of the e_1 and e_a terms by writing

$$E^{(0)}(\sigma)/\bar{E} = e^{ik_0\sigma} + b\,e^{ik_b\sigma} \tag{13}$$

and $|E^{(0)}(\sigma)/\bar{E}|^2 = 1 + 2b\cos((k_b - k_0)\sigma)$.

Thus, using eqs. (5) to (9) and keeping only the highest harmonics, which are the most effective in producing absorption, we get

$$E(\sigma, s)/\bar{E} = \sum_{p=0}^{\infty}\left(\tfrac{2}{3}b\gamma\bar{E}^2 k_0 s\Delta\right)^{2p}\left\{\alpha_p(k_0)e^{i(1+p|\Delta|)k_0\sigma} + \alpha_p(k_b)e^{i[1+p|\Delta|(-\Delta)]k_0\sigma}\right\}, \tag{14}$$

where $\Delta \equiv 1 - k_b/k_0$, $\alpha_0 = 1$,

$$\alpha_p(k) = -\frac{i}{3}\left(1 + \frac{k}{p|\Delta|}\right)\sum_{s=0}^{p-1}\frac{(p-s)^{p-1-s}}{(p-s)!}\,\alpha_s . \tag{15}$$

The last term in eq. (14) is the dominant one if $\Delta < 0$ and if the wave $e^{ik_b\sigma}$ has sufficiently small attenuation. With eq. (13), the characteristic distance of the discontinuity surface from the plasma edge, l_o, as given by eq. (4), is

$$l_o = (-\varepsilon_\perp/\varepsilon_\parallel)^{1/2}/3\, b\, \overline{E}^2 k_o \Delta . \qquad (16)$$

When 1 approaches l_o, more and more wave energy spreads over higher and higher harmonic numbers and over reflected rays.

The absorbed power density. The time average of the power absorbed by the electrons (ions) per unit volume P_e (P_i) is the sum over all harmonics of the quasilinear expressions for electron Landau damping (stochastic ion heating) /1/. For comparison with the experiments the following practical units (PU) will be used: $P_{e,i}$ in MW/m^3, U in MJ/m^3, $T_{e,i}$ in keV, n in 10^{20}/m^3, frequency f in GHz, $B \equiv B_o$ in tesla, and lengths in m; the atomic number is indicated by A. For simplicity, we only give the formulae for the case $k_b = k_a$, i.e. $\Delta > 0$ in eqs. (14) and (15). For each harmonic p we use the interpolation $P_p = P_{LP}/(1+P_{LP}/P_{NP})$, where subscript L (N) refers to the linear (nonlinear) collision (rf) dominated regime. For the electrons we have

$$P_{eLP} = \frac{2}{3}\sqrt{\pi}\, 10^{-7} N_o \phi_\sigma \frac{\omega_{pe}}{\sqrt{\varepsilon_\perp}} |\overline{E}_p(s)/\overline{E}|^2 \left(\frac{w_e}{1+p\Delta}\right)^3 \exp\left(-w_e^2/(1+p\Delta)^2\right),$$

$$P_{eNP} = (1.05)\, 10^3\, n^2\, T_e^{-1/2}\, \eta_{\parallel p} \exp\left(-w_e^2/(1+p\Delta)^2\right),$$

$w_e^2 = 255.9/N_o^2 T_e$, $N_o = 4.77 k_o/f$, $\eta_{\parallel p} = \Delta k_\parallel / k_{\parallel min}$ (taken to be of order unity),

$$|\overline{E}_p(s)/\overline{E}|^2 = |(1.32)\, 10^{-1}\, l\, N_o^2\, \phi_\sigma\, b\Delta / f \varepsilon_\perp^2 (T_e+T_i)|^{2p}\, |\alpha_p|^2,$$

$|\alpha_1|^2 = c_1^2$; $|\alpha_2|^2 = c_2^2(1+c_1^2)$; $|\alpha_3|^2 = c_3^2((c_1+c_2)^2+(1.5-c_1c_2)^2)$, ...; $c_p = (1+k_a/p\Delta)$, where ϕ_σ is the rf power input per unit plasma surface to the right-going rays; l is the penetration length. Notice that if the rays make more than one turn in the toroidal direction, l can be larger than the plasma minor radius r_p. For the ions we have

$$P_{iLP} \simeq (4.56)\, 10^{-11}\, \frac{\omega_{pe}^3\, \phi_\sigma |\overline{E}_p(s)/\overline{E}|^2 (w_i/(1+p\Delta))^2 \exp\left(-w_i^2/(1+p\Delta)^2\right)}{A\, \varepsilon_\perp^{3/2}\, \omega_{ci}^{1/3}\, \omega^{5/3}},$$

$$P_{iNP} \simeq \frac{3}{\sqrt{2}}(1.92)\, 10^2\, n^2 (T_i A)^{-1/2}\, \eta_{\parallel p} \left(w_i/(1+p\Delta)\right) \exp\left(-w_i^2/(1+p\Delta)^2\right),$$

$w_i^2 = w_e^2 \varepsilon_\perp \omega T_e/T_i \omega_{pi}^2 \simeq 58.9\, \varepsilon_\perp f^2 A/N_o^2 T_i n$.

Finally, from eq. (16),

$$l_o = 3.79\, f \varepsilon_\perp^2 (T_e+T_i)/N_o^2 \phi_\sigma\, b\Delta . \qquad (17)$$

Notice the strong dependance of l_o on $\varepsilon_\perp$.

The absorbed power density has to be compared with the time average of the reactive power density $P_R = 10\phi_\sigma/h$, where h is the depth at which the LH pump is totally damped.

Comparison with experiments. The previous results are now used for a comparison of LH heating experiments in FT /2/ and ASDEX /3/. The characteristic parameters of FT are:

f=2.45, N=1, L=1.5 cm, ϕ_σ =1.7, e_a=.3, $\Delta \simeq .7$, B=8, A=2, $T_e(0)$=1.5−1, $T_i(0)$=.8 - 1, r_p=.2

The characteristic parameters of ASDEX are:

f=1.3, N=4, L=12 cm , ϕ_σ =1.4, e_a=.1, Δ =1, B=2.2, A=1, $T_e(0)$=.75 $T_i(0)$=.6, r_p=0.4.
For FT: $.75 \lesssim n(0) \lesssim 1.5$; for ASDEX: $.3 \lesssim n(0) \lesssim .6$
An adiabatic evaluation of eq. (17) for n_o, T_e, and T_i profiles gives $l_o = l_o(s)$. At the plasma periphery the shortest l_o-values are given by the k_o-$3k_o$ interaction; we find for FT $l_o \simeq 2.24\ (T_e(s)+T_i(s))/(T_e(0)+T_i(0))$ and for ASDEX $l_o \simeq .45\ (T_e(s)+T_i(s))/(T_e(0)+T_i(0))$. Whereas the FT value is such as to allow wave penetration, the ASDEX value might explain the observed peripheral phenomena. Within the plasma l_o increases to 7 - 8 m in FT and to 1 - 1.5 m in ASDEX, in both cases owing to the $(k_o - k_a)$ interaction, which is the main cause of the $\vec{k}$-spectrum decay. In FT, rf power is absorbed almost exclusively by the electrons on the p=1 and 2 harmonics; higher harmonics do not contribute since the absorption length $h \propto (3 - 4) r_p \ll l_o$. In ASDEX, on the other side, rf power is deposited between $.5 r_p$ and r_p with P_i/P_e increasing from .5 to 1.5 in the density range considered. The harmonics involved are p=1,2 and 3, with a substantial power fraction (30%) going to high energy ($\simeq 3T_i$) ions.

References

/1/ E. Canobbio and R. Croci, in Plasma Physics and Controlled Nuclear Fusion Research, IAEA 1985, Vol1, p. 567
/2/ F.De Marco et al., in Heating in Toroidal Plasmas, Roma 1985, Vol.1, p.546
/3/ D. Eckhartt et al., ibid. p. 501.

ASYMPTOTIC THEORY OF FLUID WAVES IN RELATIVISTIC PLASMAS

F. Porcelli and F. Pegoraro
Scuola Normale Superiore, Pisa, Italy

Abstract The dispersion relation of Langmuir, ion-acoustic and transverse waves in a relativistic, homogeneous, non-magnetized plasma is derived from a fluid model. It is shown that in the collisionless limit their dispersion relation depends on a polytropic index, on a generalized specific heat and on an anisotropy factor which characterize the particle response.

An asymptotic analysis of the dispersion relation identifies four regions in the phase velocity-temperature plane. In these regions the three quantities mentioned above take simple values. In particular it is found that the equation of state for supersonic waves is isothermal for temperatures exceeding the electron rest mass.

In this paper we address the question of the fluid description of waves in a collisionless relativistic plasma. For the sake of simplicity, we consider a homogeneous non-magnetized plasma and neglect radiative processes. Since the treatment of Landau damping is beyond the scope of a fluid theory, we restrict ourselves to those situations where this damping is negligible. We show that in these cases the fluid derivation of the correct dispersion relation of longitudinal waves requires the knowledge of three generalized thermodynamic quantities which are determined using kinetic equations. These quantities are the polytropic index $\gamma(\alpha,y) = \tilde{p}/T\tilde{n}$, the generalized specific heat $c_v(\alpha,y) = \tilde{\varepsilon}/\tilde{T}$ and the anisotropy factor $\sigma(\alpha,y) = \tilde{p}_\parallel/\tilde{p}$. Subsequently, we show that in the limit of large phase velocities the same quantities also determine the dispersion relation of transverse waves. Here, $\alpha = m/T$ is the inverse temperature normalized to the particle rest mass, n is the density, ε is the average particle energy, $p = \frac{1}{3}[\mathrm{Tr}(T_{\mu\nu}) - \varepsilon n] = nT$ is the scalar pressure, $p_\parallel = T_{zz}$, $T_{\mu\nu}$ is the energy-momentum tensor, a tilde indicates perturbed quantities, z is the direction of the wave-vector in the equilibrium rest frame, and $y = (\omega/k)/(1 - \omega^2/k^2)^{1/2}$ is the "reduced phase-velocity" of the wave which is the natural variable in the Vlasov theory of relativistic waves.

Our main interest is the characterization of asymptotic regions in the α-y plane where γ, c_v and σ are given by a simple set of rules. Thus we start by determining γ, c_v and σ as function of α and y using the linearized relativistic Vlasov equation for longitudinal waves. We recall that in the equilibrium rest frame of the plasmas, γ, c_v and σ are defined by

$$\gamma = \Sigma_i \tilde{T}_{ii}/3T\tilde{n}_t \quad , \quad i = x,y,z \quad , \qquad (1)$$

$$c_v = (\tilde{T}_{tt} - \varepsilon \tilde{n}_t)/(\Sigma_i \tilde{T}_{ii}/3 - T\,\tilde{n}_t) \quad , \tag{2}$$

$$\sigma = 3\tilde{T}_{zz}/\Sigma_i \tilde{T}_{ii} \quad , \tag{3}$$

where $\tilde{T}_{\mu\nu} = \int (d^3p/p_t) p_\mu p_\nu \tilde{f}$ is the perturbed energy-momentum tensor, $\tilde{n}_\mu = \int (d^3p/p_t)\, p_\mu \tilde{f}$ the perturbed 4-velocity, $\tilde{n}_t = \tilde{n}$ the perturbed density in the equilibrium rest frame, p_μ the particle four-momentum, $\mu = t,x,y,z$, and $f = ie\ (\underline{E} \cdot \partial f_0/\partial \underline{p})(\omega - \underline{k} \cdot \underline{p}/p_t)^{-1}$ is the perturbed distribution function which we obtain from the linearized relativistic Vlasov equation. To derive Eqs. (1)-(3) we used the relationships $\tilde{T}_{tt} = \tilde{\varepsilon} n + \varepsilon \tilde{n}$ and $\tilde{p} = \tilde{n} T + n \tilde{T} = \Sigma_i \tilde{T}_{ii}/3$. Taking $f_0 = C \exp(-\alpha \sqrt{1 + p^2/m^2})$, the Jüttner-Synge (relativistic Maxwellian) distribution function, we can express $\tilde{T}_{\mu\nu}$ and $\tilde{n}_\mu$ as algebraic combinations of derivatives with respect to the variable α of the integral

$$I(\alpha,y) = \int_0^\infty dt\, \frac{\exp[-\alpha\sqrt{1+t^2}]}{\sqrt{1+t^2}} \frac{y^2}{t^2 - y^2} \quad , \quad t = p/m \quad . \tag{4}$$

An asymptotic analysis of (4) singles out four regions in the α-y plane, which are summarized in table I. For brevity, we omit the explicit expressions of γ, c_v and σ in terms of $I(\alpha,y)$, but give the leading-order term of their asymptotic expansions in regions A and B (table II).

Region	Inequalities	Type of wave	Leading term
A_1	$\alpha > 1$, $y^2\alpha < 1$	SUBSONIC	$I(\alpha,y) \sim (\pi/2\alpha)^{1/2} \alpha y^2 \exp(-\alpha)$
A_2	$\alpha < 1$, $y^2 < 1$		$I(\alpha,y) \sim y^2$
B_1	$\alpha > 1$, $\lvert y^2\alpha \rvert > 1$	SUPERSONIC	$I(\alpha,y) \sim (\pi/2\alpha)^{1/2} \exp(-\alpha)$
B_2	$\alpha < 1$, $\lvert y^2\alpha^2 \rvert < 1$		$I(\alpha,y) \sim 1$
C	$\alpha < 1$, $1 < y^2 < \alpha^{-2}$	BARELY SUBSONIC	$I(\alpha,y) \sim \ln y^{-1/2}$
D	$\alpha < 1$, $\lvert y^2\alpha^2 \rvert > 1$	BARELY SUPERSONIC	$I(\alpha,y) \sim \ln \alpha^{-1}$

Table I: the four relevant asymptotic regions in the α- y plane.

The following physical picture results. For supersonic waves (region B), the plasma obeys an adiabatic equation of state in the low temperature limit ($\alpha \gg 1$) and an isothermal one in the relativistic limit ($\alpha < 1$)[1]. In the same asymptotic region, the anisotropy factor is constant to lowest order in $k^2 v_{th}^2/\omega^2$. The

value $\sigma \simeq 9/5$ can be justified by writing $\tilde{p}_{\parallel} = \gamma_{\parallel} p\tilde{n}/n$, $\tilde{p} = \gamma p\tilde{n}/n$ with $\gamma_{\parallel} = \sigma\gamma$, and using $\gamma_{\parallel} = 3$ and $\gamma = 5/3$ for the one-dimensional and for the three-dimensional adiabatic equation of state respectively. Then $\sigma = \tilde{p}_{\parallel}/\tilde{p} = \gamma_{\parallel}/\gamma = 9/5$ at low temperatures. At higher temperatures both $\gamma_{\parallel}$ and γ change so as to mantain a constant ratio. For subsonic waves (region A) the appropriate equation of state is isothermal with $\gamma \simeq \gamma_{\parallel} \simeq 1$. Any departure from an isotropic configuration is proportional to the square of the wave frequency. Finally, for both subsonic and supersonic waves and for all values of α, it is reasonable to approximate the generalized specific heat by its thermodynamic expression, $c_v \simeq \partial\varepsilon/\partial T = (\gamma_{ad} - 1)^{-1}$. The difference between $\tilde{\varepsilon}/\tilde{T}$ and $\partial\varepsilon/\partial T$ is 5% at most and is apparent only at intermediate temperatures. The asymptotic analysis in regions (C) and (D) is more complicated, due to the logarithmic behaviour of the leading order of $I(\alpha,y)$, and lacks a direct physical interpretation.

Region	γ	c_v	σ	type of wave
A_1	1	3/2	1	SUBSONIC
A_2	1	3	1	
B_1	5/3	3/2	9/5	SUPERSONIC
B_2	1	3	9/5	

Table II: values of γ, c_v and α in regions A and B

The fluid dispersion relation of longitudinal and transverse waves are obtained by linearizing the two-fluid continuity and energy-momentum equations. We write the energy-momentum tensor in the form

$$T^{\mu\nu} = \varepsilon n u^{\mu}u^{\nu} + p(u^{\mu}u^{\nu} - g^{\mu\nu}) + \Pi^{\mu\nu} + I^{\mu}u^{\nu} + I^{\nu}u^{\mu} \quad , \qquad (5)$$

with $u^{\mu} = (n^{\nu}n_{\nu})^{-1/2}\, n^{\mu}$, $g^{\mu\nu} = \mathrm{diag}(1,-1,-1,-1)$, $\Pi^{\mu\nu} = \Pi^{\nu\mu}$ the traceless (i.e. anisotropic) part of the pressure tensor with $\Pi^{\mu}_{\mu} = \Pi^{\mu\nu}\, u_{\nu} = 0$, and I^{μ} is the heat flux with $I^{\mu}\, u_{\mu} = 0$ (sum over repeated indices is understood). The perturbed quantities are then Fourier-analyzed in the equilibrium rest frame.

For longitudinal waves the resulting dispersion relation is

$$\omega^2 = \Sigma_j \frac{4\pi n_0 e^2}{M_{\parallel j}(\alpha_j,y) - (k/\omega)^2 \gamma_{\parallel j}(\alpha_j,y) T_j} \quad , \qquad (6)$$

where the sum is over particle species,

$$M_{\|j} = \varepsilon_j + c_{vj}(\gamma_j - 1) = \varepsilon_j + (1 + \tilde{I}_z/T\tilde{n}_z)_j \, T_j \quad , \tag{7}$$

$$\gamma_{\| j} = \sigma_j \gamma_j = \frac{\omega}{k} (\tilde{T}_{zz}/T\tilde{n})_j = \frac{\omega}{k} (\tilde{T}_{zz}/T\tilde{n}_z)_j \tag{8}$$

and c_v, γ and σ are the three thermodynamic quantities discussed above. Langmuir waves are treated extensively in Ref. [1]. Here, we give the lowest order term in the dispersion relation of ion acoustic waves. We refer to region B for weakly relativistic ions ($\alpha_i > 1$) and to region A for relativistic electrons. Then, from the asymptotic expansions $M_{\|i} \simeq m_i(1 + 5/2\alpha_i) + O(\alpha_i y^2)^{-1}$ and $\gamma_{\| e} = \sigma \gamma_e \simeq 1 + O(y^2)$, we obtain

$$\omega^2 \simeq [\, c_s^2/(1 + k^2\lambda_{De}^2)\,] \, (1 - \frac{5}{2\alpha_i}) + O(\alpha_i^{-1} y^{-2}, y^2) \quad , \tag{9}$$

where $c_s^2 = T_e/m_i$ and $\lambda_{De}^2 = T_e/4\pi n_0 e^2$. The relativistic correction to the lowest-order term in the dispersion relation of ion-acustic waves in this limit is entirely due to the variation of the ion inertia. For transverse waves, the dispersion relation reads

$$\omega^2 = \Sigma_j \frac{4\pi n_0 e^2}{M_{\perp j}(\alpha_j, y) - (k/\omega)^2 \gamma_{\perp j}(\alpha_j, y) T_j} \quad , \tag{10}$$

where

$$M_{\perp j} = \varepsilon_j + (1 + \tilde{I}_x/T\tilde{n}_x)_j \, T_j = \varepsilon_j + (1 + \tilde{I}_y/T\tilde{n}_y)_j \, T_j \quad , \tag{11}$$

$$\gamma_{\perp j} = \frac{\omega}{k} (\tilde{T}_{xz}/T\tilde{n}_x)_j = \frac{\omega}{k} (\tilde{T}_{yz}/T\tilde{n}_y)_j \quad . \tag{12}$$

In region B the ratios $\tilde{I}_x/T\tilde{n}_x$ and $\tilde{T}_{xz}/T\tilde{n}_x$ can be related to the corresponding terms in the dispersion relation of longitudinal waves and the dispersion relation (10) can thus be expressed in terms of γ, c_v and σ. In fact, to lowest order in $k^2 v^2/\omega^2$, the approximate equalities hold $(\tilde{I}_z/\tilde{n}_z)_\| \simeq (\tilde{I}_x/\tilde{n}_x)_\perp$ and $(\tilde{E}_z/\tilde{n}_z)_\| \sim (\tilde{E}_x/\tilde{n}_x)_\perp$, where $\|$ and $\perp$ denote longitudinal and transverse waves respectively. From these, using the identity $(\tilde{T}_{xz}/\tilde{E}_x)_\perp = (\tilde{T}_{xx}/\tilde{E}_z)_\perp$ we obtain $M_{\|j} = M_{\perp j}$ and $\gamma_\perp/\gamma_\| \simeq \tilde{T}_{xx}/\tilde{T}_{zz}$ $\tilde{p}_\perp/\tilde{p}_\| = (3 - \sigma)/(2\sigma) = 1/3$. The above equalities can be understood in terms of symmetry considerations, as no preferential direction can be singled out in the limit $k^2 \to 0$. Similar arguments can be invoked if higher order terms are considered.

Reference: [1] F. Pegoraro and F. Porcelli, Phys. Fluid. 27, 1984, p. 1665.

MAGNETOSONIC NORMAL MODES IN INHOMOGENEOUS TOROIDAL PLASMAS

F. Pegoraro, B. Coppi and P. Detragiache
Scuola Normale Superiore, Pisa - Italy

Abstract The normal mode solutions of the dispersion equation of magnetosonic waves in inhomogeneous toroidal plasmas are studied analytically in the limit of large poloidal mode numbers. Radially localized normal modes are found which are confined by the plasma inhomogeneity. In the cylindrical limit the modes are localized within a circular annulus which, in a torus, becomes distorted. When a resonance condition, depending on the density profile, is (approximately) satisfied, this distortion is enhanced and leads to the loss of the normal modes for particular profiles. These results agree with the numerical solution of the dispersion equation in the geometrical optics limit.

Localized normal modes in inhomogeneous, toroidal plasmas, with frequencies in the ion-cyclotron range, have been investigated both in connection with the spin depolarization processes, which arise from collective modes [1,2] in magnetically confined fusing plasmas with spin-polarized nuclei [3], and in connection with the study of the high frequency modes driven unstable [4] by a superthermal anisotropic particle popolation produced by an external injection system. These localized modes are also relevant to the ion-cyclotron heating schemes and differ from those considered for homogeneous models [5].

We refer to a two-ion component plasma and consider modes propagating almost perpendicularly to the magnetic field lines with vanishing parallel electric field. In the cold plasma limit, taking first a homogeneous configuration, their dispersion relation is given by

$$4\pi\sigma_0(1 - \lambda^2) = k^2c^2 \quad , \tag{1}$$

where $\sigma_0 = -(en_e c\omega^2/B_0)[\Sigma_j \alpha_j \Omega_j/(\Omega_j^2-\omega^2)]$, the polarization factor λ is $\lambda = [\Sigma_j \alpha_j \omega/(\Omega_j^2-\omega^2)]/[\Sigma_j \alpha_j \Omega_j/(\Omega_j^2 - \omega^2)]$, the index $j = 1,2$ labels the ion species, $\alpha_j = n_j/n_e$ and Ω_j is the cyclotron frequency of the ion species j. An equivalent form of Eq. (1) is

$$K(\omega) \equiv (\omega^2/k^2v_A^2)\left[(\omega^2 - \bar{\bar{\Omega}}^2)/(\omega^2 - \Omega_h^2)\right] = 1 \quad . \tag{2}$$

Here $\bar{\bar{\Omega}} = \alpha_1\Omega_2 + \alpha_2\Omega_1$ and $\Omega_h = (\Omega_1\Omega_2\,\Omega/\bar{\Omega})^{1/2}$, with $\bar{\Omega} = \Sigma_j \alpha_j \Omega_j$, are respectively the cut-off and resonance frequencies, which modify the magnetosonic dispersion relation in a two-ion plasma, and v_A is the Alfvén velocity v_A^2

$= \Omega_e \bar{\Omega}/d_e^2$ with d_e the electron inertial skin depth. We shall consider a "high frequency" range, $\omega^2 > \Omega_j^2$, where the term inside square brackets in Eq. (2) is approximately equal to one and a "low frequency" range where the cut-off and resonance frequencies play an essential rôle.

In a toroidal inhomogeneous configuration the relevant dispersion equation can be written in terms of the perturbed parallel magnetic field $\tilde{B}_\parallel$ as [2]

$$\underline{b} \cdot \nabla \times (\underline{\sigma}^{-1} \cdot \nabla \times \underline{b}\tilde{B}_\parallel) = -(4\pi/c^2)\partial \tilde{B}_\parallel/\partial t \quad , \tag{3}$$

where $\underline{b}$ is the unit vector along the equilibrium field and $\underline{\sigma}$ is the cold plasma conductivity tensor. Taking the limit of modes with large poloidal mode numbers, referring for simplicity to a configuration with circular concentric magnetic surfaces and using polar coordinates, Eq. (3) can be brought to the hermitian form

$$8\pi \tilde{B}_\parallel \simeq -c^2 \left\{ D_R^+ [\sigma_0(1+\lambda)]^{-1} D_R + D_L^+ [\sigma_0(1-\lambda)]^{-1} D_L \right\} \tilde{B}_\parallel \quad , \tag{4}$$

where D_R is the differential operator $D_R = \partial/\partial r + (i/r)\partial/\partial\theta$, $D_R^+ = (1/r)(\partial/\partial r)r - (i/r)\partial/\partial\theta$, $D_L = D_R^*$ and L and R refer to the polarization of the perpendicular fluctuating electric field. In the low frequency range the coefficient $[\sigma_0(1+\lambda)]^{-1}$ is singular for $\omega = \bar{\Omega}$ i.e. for $\lambda = -1$. For $\omega = \Omega_h$, i.e. for $\lambda = \infty$, the two coefficients $[\sigma_0(1 \pm \lambda)]^{-1}$ are regular and equal and opposite.

First we consider the high frequency range in which case the coefficients of Eq (4) are regular and slowly varying functions of r and θ on the made scale length. Then, to leading order, Eq. (4) becomes

$$4\pi\sigma_0(1-\lambda^2)\tilde{B}_\parallel \simeq -c^2 \left[\frac{1}{r}\frac{\partial}{\partial r} r \frac{\partial}{\partial r} + \frac{1}{r^2}\frac{\partial^2}{\partial\theta^2} \right] \tilde{B}_\parallel \tag{5}$$

and can be conveniently solved in the eikonal approximation $\tilde{B}_\parallel(r,\theta) = \hat{B} \exp[iP(r,\theta)]$, where P is a fast varying phase such that $\partial P/\partial\theta \sim O(m)$, with $m >> 1$. The resulting equation for P is then expanded in inverse powers of m. The equation for the leading order term P_0 is

$$\left(\frac{\partial P_0}{\partial r}\right)^2 + \frac{1}{r^2}\left(\frac{\partial P_0}{\partial\theta}\right)^2 = \frac{\omega^2}{v_{A0}^2}\frac{n(r)}{n_0}\left[\frac{B_0}{B(r,\theta)}\right]^2 \quad , \tag{6}$$

where the r.h.s. has been written in the form of Eq. (2) with the term in square brackets equal to one. The index 0 on the Alfvén velocity v_{A0} and on the equilibrium particle density n_0 and magnetic field B_0 refer to their values at the centre of the plasma column. In the cylindrical limit the

coefficients of Eq. (6) are independent of θ and P_0 is given by

$$P_0 = m\theta + i(r - r_0)^2/(2\Delta^2), \tag{7}$$

where m is the poloidal number and r_0 and θ are defined by

$$r_0 = -2\left\{ d[\ln\ n(r)/n_0]/dr \right\}^{-1}_{r=r_0},$$
$$\Delta^{-1} = \frac{(2m)^{1/2}}{r_0}\left\{ \frac{3}{4} - \frac{1}{2}\frac{d\ \ln[-n'(r)/n_0]}{d\ \ln[\ n(r)/n_0]} \right\}^{1/4}_{r=r_0}, \tag{8}$$

with B constant over the plasma column and $n'(r) = dn(r)/dr$. These modes propagate in θ and are radially localized within an annulus of width $\Delta \propto m^{1/2}$, centred around $r = r_0$. In the toroidal case a further expansion in powers of the inverse aspect ratio ε is employed. We write $P_0 = \Sigma_k \varepsilon^k P_{0,k}$ with $P_{0,k} = P_{0,k}(r,\theta,\varepsilon)$ periodic in θ. To first order in ε, $P_{0,0}$ is given by Eq. (7) with $\theta - r\sin\theta/R_0$ substituted for θ, where R_0 is the major radius of the torus. The higher order terms $P_{0,k}$ lead to a θ-dependent shift $\delta r_0(\theta)$ of the radius around which the mode is localized proportional to $\varepsilon^k \cos k\theta$. This expansion procedure breaks down for those density profiles for which

$$m\Delta^2 = sr_0^2, \tag{9}$$

with s an integer. When condition (9) is met, the equation which determines $P_{0,s}$ leads to a secular term. For example a parabolic density profile $n(r) = n_0(1 - r^2/a^2)$, with a the minor radius of the torus, gives a secular term proportional to ε^2. If condition (9) is only approximately met, the circular annulus, obtained in the cylindrical limit, is distorted but remains well confined inside the plasma column provided

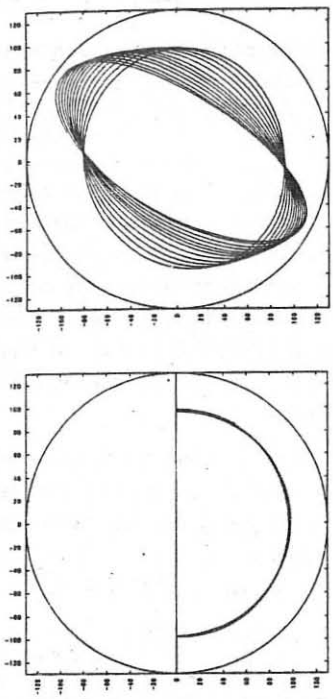
$$\left[\left\{ \frac{3}{4} - \frac{1}{2}\frac{d\ \ln[-n'(r)/n_0]}{d\ \ln[\ n(r)/n_0]} \right\}^{1/2}_{r=r_0} - \frac{s}{2} \right] >> \frac{\varepsilon^s}{2} \tag{10}$$

for all integer values of s. For a quasi-parabolic density profile $n(r) = n_0[1 - (r/a)^{2+\delta}]$, Eq. (10) gives $\delta >> 4\varepsilon^2$.

In the low frequency range the derivatives of the coefficients $[\sigma_0(1 \pm \lambda)]^{-1}$ in Eq. (4) are large and an equation similar to (6) cannot be derived. Modes on the low field side of the column are reflected at the cut-off surface $\omega = \overline{\overline{\Omega}}$ with a fraction of their energy tunneling to the ion hybrid resonance $\omega = \Omega_h$ where it is converted to short wave length modes [6]. Then, radially localized modes are possible only if the cut-off surface is approximately at the middle of the plasma column ($\theta = \pi/2$). These modes have large values of the parallel

mode number for at least one of the two components (incident and reflected) which propagate in θ in opposite directions.

These analytical results have been confirmed by solving numerically, for different density profiles and mode frequencies, the ray-path equation obtained from Eq. (4) in the geometrical optics limit. In this approach Eq. (9) reduces to the resonance condition $\omega_r = s\,\omega_\theta$, with ω_θ the transit frequency of the ray along θ and ω_r its oscillation frequency around r_0.



Numerical solution of the ray-path equation

Top left: parabolic density profile, $\omega = 5.05\,\Omega_\alpha(B_0)$.

Top right: $n(r) = n_0(1 - 0.8r^2/a^2 - 0.2r^4/a^4)$, same frequency.

Bottom: same quasi-parabolic density profile, $\omega = 5/6\,\Omega_\alpha(B_0)$.

References

[1] B. Coppi, F. Pegoraro adn J.J. Ramos, Phys. Rev. Lett. 51, 892, 1983

[2] B. Coppi, S. Cowley, P. Detragiache, R. Kulsrud and F. Pegoraro, Comments on Plasma Physics and Controlled Fusion 9, 49, 1985

[3] R. Kulsrud, H.P. Furth, E. Valeo and M. Goldhaber, Phys Rev. Lett. 19, 1248, 1982

[4] S. Yamamoto et al., 10th International Conference on Plasma Physics and Controlled Nuclear Fusion Research, London, 1984, Paper IAEA-CN-44/F-IV-10

[5] T. H. Stix, Nuclear Fusion 15, 737, 1975

[6] P. W. Perkins, Nuclear Fusion 17, 1197, 1977.

PSEUDO THREE-DIMENSIONAL INTERCHANGE-MODE TURBULENCE IN MAGNETIZED PLASMAS

P.K. Shukla and K.H. Spatschek*

Institut für Theoretische Physik, Ruhr-Universität Bochum
D-4630 Bochum 1, Federal Republic of Germany

Abstract: The role of finite parallel wavelength on electrostatic interchange mode is examined. It is shown that the pressure gradient as well as a nonuniform magnetic field can induce a new class of fluid instabilities in plasmas.

It is common belief that electrostatic interchange flute modes[1] can deteriorate the plasma confinement in magnetic fusion devices such as mirrors and tokamaks. Therefore, it is of great interest to understand the linear as well as the nonlinear behaviour of multidimensional interchange mode instability. In this paper, we have incorporated the parallel electron inertial effects and have obtained a set of nonlinear fluid equations governing the evolution of the interchange-mode instability.

Consider a nonuniform plasma in an inhomogeneous magnetic field $\vec{B}_o$. In the limit of low-frequency ($\ll \Omega_i = eB_o/Mc$, the ion gyrofrequency) electrostatic oscillations, the single particle currents are due to the drifts associated with finite ion Larmor radius, the ion polarization, and the $\vec{E}\times\vec{B}_o$ ($\vec{E} = -\nabla\phi$):

$$\vec{J}_{p\perp} = -\frac{c^2 P_i}{B_o^2 \Omega_i}\nabla\nabla^2\phi\times\hat{z} - \frac{n_i e c}{B_o \Omega_i}\left(\partial_t + \frac{c}{B_o}\hat{z}\times\nabla\phi\cdot\nabla\right)\nabla\phi - \frac{ec}{B_o}\hat{z}\times\nabla\phi\,(n_e - n_i), \tag{1}$$

together with the magnetization, the ∇B_o, and the curvature drifts:

$$\vec{J}_M = -c\sum_j \nabla\times(P_{j\perp}\vec{B}_o/B_o^2),\ \vec{J}_{\nabla B_o} + \vec{J}_c = cB_o^{-2}\sum_j (P_{j\perp}\hat{z}\times\nabla B_o + P_{j\parallel}\vec{R}\times\vec{B}_o/R^2), \tag{2}$$

respectively. Here, $P_j = n_j T_j$ is the pressure, $\vec{R}/R^2 = -\ln B_o$ represents the curvature of the magnetic field, and other notations are standard.

The nonlinear interaction of the electrostatic modes in a nonuniform magnetized plasma is governed by the conservation of

the charge density $(\nabla \cdot \vec{J}_\perp + \partial_z J_{ez} + e\partial_t (n_i - n_e) = 0)$

$$- (4\pi)^{-1}(\partial_t + \frac{c}{B_o}\hat{z}\times\nabla\phi\cdot\nabla)(\nabla^2\phi + \partial_z^2\phi) - \frac{c^2}{B_o^2\Omega_i}\nabla\cdot(P_i\nabla^2\phi\times\hat{z})$$

$$- \frac{n_o e c}{B_o\Omega_i}(\partial_t + \frac{c}{B_o}\hat{z}\times\nabla\phi\cdot\nabla)\nabla^2\phi + \frac{c}{B_o}\sum_j \nabla\cdot[P_{j\perp}\hat{z}\times\nabla B_o + P_{j\parallel}\vec{R}\times\vec{B}_o/R^2]$$

$$= e\partial_z(n_e v_{ez}), \qquad (3)$$

and the parallel component of the electron momentum equation

$$(\partial_t + \frac{c}{B_o}\hat{z}\times\nabla\phi\cdot\nabla + v_{ez}\partial_z)v_{ez} = \frac{e}{m_e}\partial_z\phi - \frac{1}{m_e n_e}\partial_z P_{ez}, \qquad (4)$$

where the $\vec{E}\times\vec{B}_o$ drift is assumed to be larger than the magnetic curvature and the $\nabla\vec{B}_o$ drifts, and the ions are taken to be two-dimensional. Equations (3) and (4) can be closed with the help of appropriate equations of state. Assuming isothermal, isotropic ($P_{e\perp} = P_{e\parallel} = P_e$) electrons, one gets

$$(\partial_t + \frac{c}{B_o}\hat{z}\times\nabla\phi\cdot\nabla + v_{ez}\partial_z)P_e = -P_e\partial_z v_{ez}. \qquad (5)$$

On the other hand, for the isotropic ($P_{i\perp} = P_{i\parallel} = P_i$), incompressible ions, one finds

$$(\partial_t + \frac{c}{B_o}\hat{z}\times\nabla\phi\cdot\nabla)P_i = 0. \qquad (6)$$

Equations (3)-(6) constitute a coupled set of nonlinear equations governing the nonlinear interaction of electrostatic fluctuations in a nonuniform magnetized plasma. For a simple curved field line ($\nabla B_o = \hat{x}\, dB_o/dx$) and isotropic pressures, one can linearize Eqs. (3)-(6) under the local approximations. Our new dispersion relation for the coupled drift-convective cell-interchange modes is given by

$$(\omega^2 - k_z^2 v_{te}^2)\left[\omega(\omega - \omega_i^*) - \frac{2\,\Omega_i\omega^* k_y}{Rk_\perp^2}\right] = \omega_o^2(\omega + \omega_e^*)(\omega + 2k_y\Omega_i\rho_s^2/R), \qquad (7)$$

where the Alfvén speed is assumed to be much smaller than the velocity of light, and we have defined $\omega^* = \omega_e^* + \omega_i^*$, $\omega_j^* = (ck_y T_j/eB_o)(d\ln P_{jo}/dx)$ is the drift frequency of particle species j, $\omega_o^2 = k_z^2 v_{te}^2/b$, and $b = k_\perp^2\rho_s^2$. Here, ρ_s is the ion Larmor radius at the electron temperature and v_{te} is the electron thermal velocity.

Several comments are in order. For $R \to \infty$ and $\omega \ll k_z v_{te}$ Eq. (7) yields the drift wave spectrum $\omega \approx -\omega_e^*/(1+b)$. In a homogeneous plasma, Eq. (7) reduces to $\omega = \omega_o (1+b)^{1/2}$, which is the Okuda-Dawson mode[2] with finite Larmor radius correction. These two modes can couple with each other and with the interchange mode. First, for $k_z = 0$, Eq. (7) gives the dispersion relation of the flute interchange modes, namely

$$\omega(\omega - \omega_i^*) = \omega_B \omega^* \quad , \tag{8}$$

where $\omega_B = 2k_y \Omega_i / k_\perp^2 R$. It follows from Eq. (8) that a pressure gradient driven oscillatory instability arises when $4|\omega_B \omega^*| > \omega_i^{*2}$. Hence, Eq. (8) becomes $\omega = \omega_i^*/2 + i|\omega_B \omega^* + \omega_i^{*2}/4|^{1/2}$.
Secondly, For $R \to \infty$ one recovers the drift-convective cell dispersion relation

$$(\omega^2 - k_z^2 v_{te}^2)(\omega - \omega_i^*) = \omega_o^2 (\omega + \omega_e^*) . \tag{9}$$

Finally, there is a new instability of the Okuda-Dawson mode due to the curved magnetic field lines. In the absence of the pressure gradient ($\omega_e^* = \omega_i^* = 0$), Eq. (7) yields

$$\omega(\omega^2 - k_z^2 v_{te}^2) = \omega_o^2 (\omega + b\omega_B) \quad , \tag{10}$$

which clearly shows that for $b^2 \omega_B^2 > 4\omega_o^2 (1+b)^3/27$ a Rayleigh-Taylor like instability occurs.

It is obvious that these results will be modified if the three effects of finite k_z, the plasma inhomogeneity, and the magnetic curvature are treated on the same footing. For example, for $\omega \ll k_z v_{te}$ one finds from Eq. (7) $\omega = \omega_r \pm [\omega_r^2 - \omega_B \omega_i^*/(1+b)]^{1/2}$, where $\omega_r^* = -(\omega_e^* + b\omega_B)/2(1+b)$. For $\omega_i^* = 0$, the mode is stable. However, for $|\omega_B \omega_i^*| > \omega_r^2 (1+b)$ an instability is possible but the growth rate is quite small. We have numerically solved Eq. (7) and have found that finite k_z reduces the growth rate. It is of interest to point out that the present fluid results are not valid for waves with $\omega \sim k_z v_{te}$. Here, one should resort to the kinetic electrons in order to include the Landau damping effects.

To summarize, we have derived a set of new nonlinear equations which governs the dynamics of low-frequency electrostatic turbulence in nonuniform plasmas. The important nonlinearities come from the $\vec{E} \times \vec{B}_o$ convection and the nonlinear ion polarization

drift. Our nonlinear system of equations is simple enough to enable a treatment of electrostatic interchange mode turbulence when the finite parallel wavelengths are included in a real geometry. In the linear limit, we find some new hydrodynamic instabilities which are primarily driven by the pressure gradient and the magnetic field curvature in a nonuniform plasma. In closing, we note that the inclusion of the electromagnetic effects in the present problem can lead to coupled drift-ballooning modes whose details appear in Ref. 3.

The authors are grateful to R. Balescu for useful discussions. This research was performed under the auspices of the SFB 162.

References:

[1] B.B. Kadomtsev, Plasma Turbulence (Academic Press, New York, 1965).

[2] H. Okuda and J.M. Dawson, Phys. Fluids 16, 408 (1973).

[3] A. Hasegawa and M. Wakatani, Phys. Fluids 26, 2777 (1983).

*Permanent address: Institut für Theoretische Physik, Universität Düsseldorf

ANALYTICAL TREATMENT OF THE ABSORPTION/EMISSION COEFFICIENT FOR SYNCHROTRON RADIATION

Ali NASSRI, Manfred HEINDLER

AEP, Institut für Theoretische Physik
Technische Universität Graz
A-8010 Graz, Petersgasse 16, Austria

ABSTRACT: The absorption coefficient for synchrotron radiation in plasmas is derived for a relativistic Maxwell distribution of electrons. An exact sum-integral-representation is found which is particularly convenient for numerical evaluation. Both for low temperatures (up to a few tens of keV) and for high temperatures analytical representations are derived without recurrence to the usual approximations. In spite of the simplicity of these analytical expressions, their accuracy is found to be superior to existing approximations.

INTRODUCTION: In D-T and other D based fusion plasmas, synchrotron radiation represents an important energy transport mechanism; in very hot plasmas, as required for advanced fusion fuels, it is one of the most important loss mechanisms. The mathematical treatment of these phenomena is based on the radiation transport equation and requires the explicite knowledge of the synchrotron absorption and emission coefficient as a function of radiation frequency, direction of propagation relative to the magnetic field vector, and plasma temperature. In such calculations, the use of any one of the usual exact integral representations of the synchrotron coefficient is prohibitively time consuming[1,2]; on the other hand, the use of tabulated values requires too extensive data storage and handling.
Much effort has therefore been devoted to the derivation of analytical formulations; however, existing ones are of limited validity and accuracy due to the underlying approximations. The best analytical representation presently available is incorporated in the computer code Syncrad [3]; however, in its derivation the approximations $\mu=m_o c^2/kT>>1$ and $\omega=\omega/\omega_b>>1$ were used (ω_b: cyclotron frequency). Therefore, in these formulations the resonant behaviour at low temperatures - of special interest for D-T fusion reactors - is lost and the application to temperatures relevant for advanced fuels is questionable. The accuracy of other analytical representations - such as the often quoted Trubnikov formula[4] is even worse.
This motivated us to derive an exact representation of the absorption coefficient which is considerably easier to evaluate numerically than the widely used presentation derived from plasma kinetic theory[1,2]. As is discussed elsewhere[5] and confirmed by our results, the difference between the single particle model and the kinetic theory, i.e. the dielectric effect is of no relevance.

BASIC IDEA: The cyclotron emission of an electron of charge e_o and mass m_o in a locally uniform magnetic field $\underline{B}_o = B_o \underline{e}_z$ is given by [5]

$$\eta(\omega,v,\theta) = \frac{e_o\omega^2}{8\pi^2\varepsilon_o c}\sum_{m=1}^{\infty}\{(\frac{\cos\theta-v_{\parallel}/c}{\sin\theta})^2 J_m^2(x) + \frac{v_{\perp}^2}{c^2} J_m'^2(x)\}\delta(y) \qquad (1)$$

where $\underline{v}=(v_\perp\cos\phi, v_\perp\sin\phi, v_\parallel)$, $x=(\omega/\omega_o)v_\perp\sin\theta/c$, $y=m\omega_o-\omega(1-v_\parallel\cos\theta/c)$, $\omega_o=\omega_b(1-v_\perp^2/c^2-v_\parallel^2/c^2)^{1/2}$, J_m and J_m' are the Bessel functions and their derivatives, θ is

the angle between $\underline{B}_o$ and direction of the propagation.
For electrons with a relativistic Maxwellian distribution $f_o(p)$, the emission coefficient is given by

$$j_\omega = \int \eta_\omega(p) f_o(p) d^3p \quad ; \quad f_o = \frac{\mu N(\underline{r})}{4\pi (m_o c)^3 K_2(\mu)} \exp\{-\mu(1+p^2/m_o^2c^2)\}$$

with η_ω from Eq.(1). Here p is the momentum, K_2 is the McDonald function and N is the electron density. After integration with respect to ϕ and $v_\perp$ we find the exact sum-integral-representation of the emission coefficient. For $\theta=\pi/2$ it is

$$j_\omega^\pm = \frac{e_o^2 \omega \mu N(\underline{r})}{8\pi^2 \varepsilon_o c^4 K_2(\mu) \bar{\omega}^3} \sum_{m=[\bar{\omega}]}^{\infty} m^3 \exp(-\mu m/\bar{\omega}) I_m^\pm \qquad (2)$$

where the bracket $[x]$ denotes the smallest integer greater or equal to x, and $v_m = c(1-\bar{\omega}^2/m^2)^{1/2}$. Furthermore

$$I_m^- = \int_o^{v_m} v_\parallel^2 J_m^2 \{m(v_m^2-v_\parallel^2)^{1/2}/c\} dv_\parallel \qquad (3)$$

and

$$I_m^+ = \int_o^{v_m} (v_m^2-v_\parallel^2) J_m'^2 \{m(v_m^2-v_\parallel^2)^{1/2}/c\} dv_\parallel \qquad (4)$$

To obtain the absorption coefficient we assume that the Kirchhoff relation $\alpha=j/I_{bb}=8\pi^3 c^2 j/\omega^2 kT$ is valid. The numerical evaluation of α from Eqs.(2) to (4) is used to check the accuracy of analytical representations derived therefrom and to compare results from single particle model and kinetic theory.

RESULTS: We consider two temperature ranges, one up to a few tens of keV and the other one beyond. For the lower range we obtain a sum representation which converges so fast that up to three terms yield already very accurate results:

$$\alpha_\omega^\pm(\theta=\pi/2, \bar{\omega}, \mu \geq 17) \approx \frac{\omega_p^2}{c\omega_b} \frac{\pi\mu^2}{30K_2(\mu)\bar{\omega}^3} \sum_{m=[\omega]}^{[\omega+3]} \kappa_m \exp(-\mu m/\bar{\omega}) J_m^2(\kappa_m) \begin{bmatrix} \frac{4\bar{\omega}}{\mu}+\mu \\ 1 \end{bmatrix} \qquad (5)$$

For the higher temperature range the mode contributions overlap sufficiently to allow the replacement of the sum by an integral which we could solve analytically:

$$\alpha_\omega^\pm(\theta=\pi/2, \bar{\omega}, \mu<17) \approx \frac{\omega_p^2}{c\omega_b} \frac{F(\mu)}{\bar{\omega}} \mu^{\bar{\omega}/9} \exp(0{,}03\bar{\omega}^{1/2}) \Gamma\left(\frac{\bar{\omega}+3}{2}\right)$$
$$\times U\left(\frac{\bar{\omega}+3}{2}, 3, 2\mu\right) \begin{bmatrix} \frac{4\bar{\omega}}{\mu}+\mu \\ 1 \end{bmatrix} \qquad (6)$$

where $F(\mu)=2\mu^{1,37-0;04\mu} e^{-\mu}/3K_2(\mu)$, $\omega_p^2=e_o^2 N/m_o\varepsilon_o$, Γ and U are the Gamma- and Kummer function, respectively.

Figures 1 to 3 show our results for three different temperatures, T=1okeV,5okeV

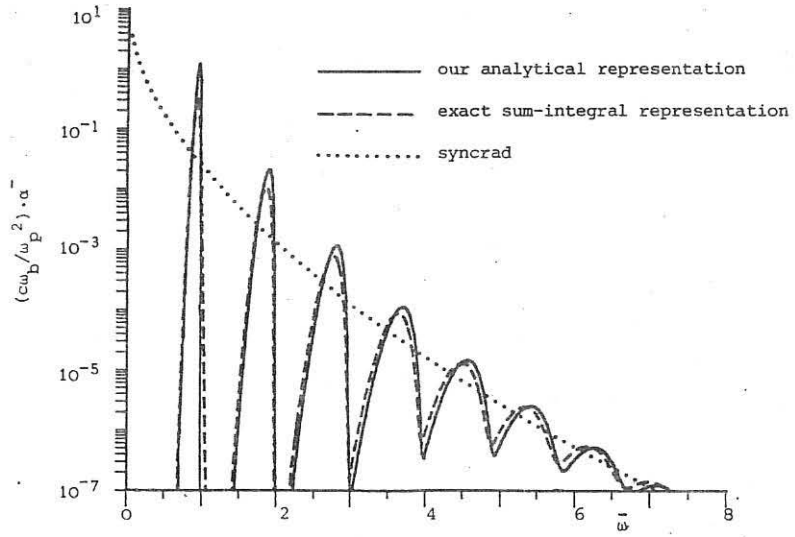


Fig.1: ordinary wave opacity vs. frequency; T= 10 keV

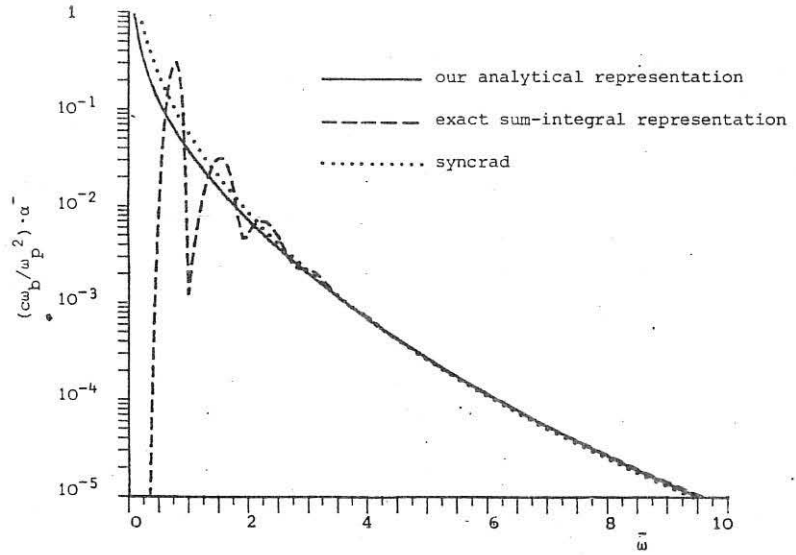


Fig.2: ordinary wave opacity vs. frequency; T= 50 keV

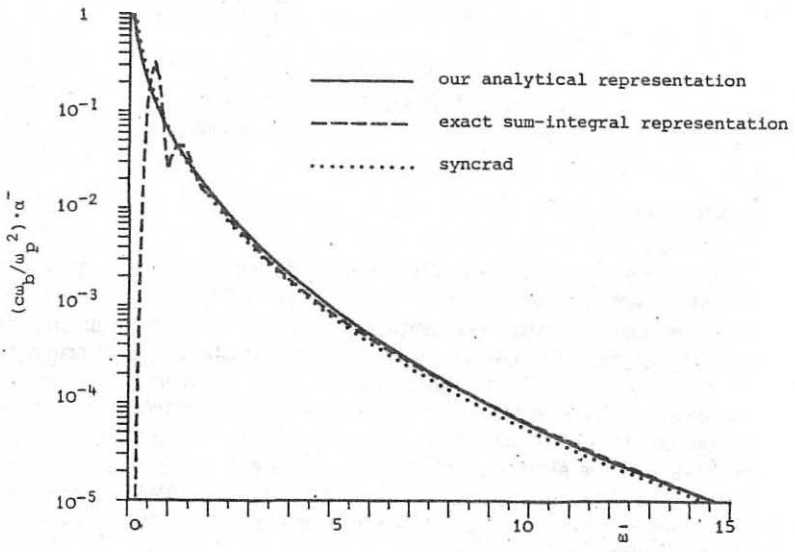


Fig.3: ordinary wave opacity vs. frequency; T= 100 keV

and 1ookeV respectively; for T=1okeV we use Eq.(5), and for the other ones Eq.(6).
For $\theta=\pi/2$ the numerical evaluation of our sum-integral-representation Eq.(2) gives the same results as that of the corresponding exact formulae derived from kinetic theory[1,2], however with considerably reduced computational effort. Our analytical representation for the lower temperature range, Eq.(5), adequately represents the resonance behaviour of the absorbtion coefficient and is thus clearly superior to the Syncrad formula. In the higher temperature range our results obtained from Eq.(6) are the same as from Syncrad. While Syncrad is based on the $\mu>>1$ approximation, our formulation involves no restrictions regarding T and $\bar{\omega}$ and can thus be trusted also above the 1ookeV range. The extension to $\theta\neq\pi/2$ of our formulae is straightforward and will be discussed.

REFERENCES:

[1] De Barbieri, O., Association Euratom-C.E.A. (1980), EUR-CEA-FC-1035

[2] Tamor, S., Nucl.Fusion 18, 229 (1978)

[3] Gordon, J.D., et al., Report TRW-FRE-007 (1981)

[4] Trubnikov, B.A., Vol.7, p 345, Consultants Bureau, New York (1979)

[5] Bekefi, G., Radiation Processes in Plasmas, John Wiley, New York (1966)

ACKNOWLEDGEMENT: Work supported by the Steiermärkische Landesregierung.

MODE CONVERSION OF LOWER HYBRID WAVES

M. Krämer, N. Sollich and J. Dietrich
Institut für Experimentalphysik II
Ruhr-Universität Bochum, W.-Germany

I. INTRODUCTION

Mode conversion of lower hybrid (LH) waves into ion plasma (IP) waves or ion Bernstein waves, predicted two decades ago /1,2/ and considered as a potential candidate for ion heating, has been verified in small scale experiments recently /3,4/. In this work we investigate the waves originating in the LHR region in the presence of ion heating: The wave dispersion is in agreement with that expected for ion plasma waves. Both frequency and wave number spectra of the high frequency (hf) signals are measured by correlation analysis of probe signals which is shown to be a suitable method to detect waves in a turbulent plasma. To study also the accompanying process of scattering at low frequency (lf) density fluctuations /5/ the lf spectra are taken with the same technique.

II. EXPERIMENT

The experiment is performed on a linear reflex discharge (length $\approx$ 2 m) with a hot cathode and a grid anode at each side of the device. Inside the rf antenna the plasma is surrounded by a glass tube with a radius of 70 mm. The discharge parameters are U = 30V, I = 2 x1A at p = 27 mPa H_2 and B_0 = 0.23T. The density and the temperatures of the target plasma are typically: $n_e \leq 10^{17} m^{-3}$, T_e = 1 -5 eV, $T_i \leq$ 1 eV. The rf power is launched to the plasma by means of a slow wave antenna (SWA) /6/ consisting of eight alternatively phased rings with a distance of 62.5 mm and a corresponding axial wave number of $k_\parallel = 50.3\ m^{-1}$. The antenna is fed by rf power pulses (P_{rf} = 80 W, $\tau \leq 500\mu s$) at frequency $\omega_0/2\pi$ = 47.5 MHz.

Different standard diagnostics are used to determine the plasma parameters: Langmuir probes are applied to measure both plasma density (in rel. units) and electron temperature. The ion temperature measurements are performed with an ion sensitive probe /7/ as well as with an energy analyzer. The absolute density is measured with an 8 mm interferometer and a resonance cone double probe /8/. The potentials of the rf wave fields excited by the launcher are determined by several electrical probes in absolute units. (In detail, this method will be reported elsewhere.)

Both high frequency (hf) and low frequency (lf) spectra are measured applying correlation analysis. In the hf case, the signals are converted into the lf range by means of a balanced mixer and a local oscillator driven 150kHz below the wave frequency. With this heterodyne technique energy density and wavelenth of the original waves are detected, too. Furthermore, eventual asymmetry of the sideband spectra can be observed. The signal functions $f_{1,2}(x\mp\chi/2,t)$ - associated with the two probes separated by a distance χ - are referred to the density fluctuation amplitude $\tilde{n}$ in the lf case and to the rf potentials $\tilde{\Phi}$ in the hf case. The signals are digitized by means of a transient recorder and transmitted to a LSI 11/23 computer. After Fourier transforming the signals $f_{1,2}(x\mp\chi/2,t)$ (FFT)→ $F_{1,2}(x\mp\chi/2,\omega)$ the auto power spectra $P_{11,22}(x\mp\chi/2,\omega)$ as well as the cross power spectrum $P_{12}(\chi,\omega)|_x = F_1^*(x-\chi/2,\omega)\,F_2(x+\chi/2,\omega) = |P_{12}(\chi,\omega)|_x|\,\exp[i\Delta\vartheta(\chi,\omega)]$ are determined. It can be shown /9/ that $\Delta\vartheta(\chi,\omega)$ can be related to the wave number k if there is a well-defined (statistical) dispersion of the waves, i.e. $k(\chi,\omega) = \Delta\vartheta(\chi,\omega)/\chi$. To get the spectral density $S(\omega,k)$, an ensemble of time series (30x1024 samples in T = 500 µs, typically) has usually been taken. The k-range has to be divided into a sufficient number of intervalls, and the power of all time series is distributed on the k-intervalls. With the normalized spectral density $\hat{S}(\omega,k) = S(\omega,k) / (1/2)(P_{11}(\omega) + P_{22}(\omega))$ the mean wave number $k(\omega)$ and the standard deviation $\sigma_k(\omega)$ (broadening caused by decorrelation and/or damping) are obtained as its first and second moment, respectively:

$$k(\omega) = \int k\,\hat{S}(\omega,k)\,dk\,, \quad \sigma_k^2(\omega) = \int (k-k(\omega))^2\,\hat{S}(\omega,k)\,dk$$

III. RESULTS

Fig. 1 shows the typical lower hybrid cones converging in the LHR region. Due to the field concentration there both electrons and ions are heated. Here,we show the more relevant ion temperature profile (fig. 2), which depicts significant ion heating in the LHR region.

For the correlation measurements, we have focussed our interest mainly on this region. In fig. 3a we plot a typical crosspower spectrum taken in the presence of rf power coupling which shows an energy maximum of the fluctuations at about 70 kHz. The azimuthal wave number spectrum belonging to it is given in fig. 3b. Both, direction and order of magnitude of the phase velocity correspond to the electron diamagnetic drift indicating drift wave turbulence. From the standard deviation σ it is evident that the modes are well coherent whereas the lf spectra of the target plasma show much less coherence. Furthermore, the energy content in the lf spectra is at least one order of magnitude smaller in this case. Thus, the LH waves cause further excitation of the drift modes.

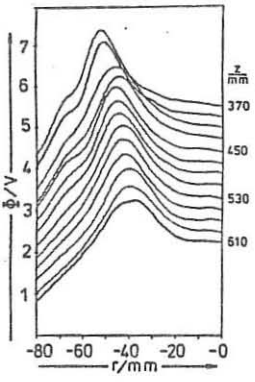


Fig. 1 RF potential profiles (center of antenna at z=0, curves shifted against each other by 0.25 V)

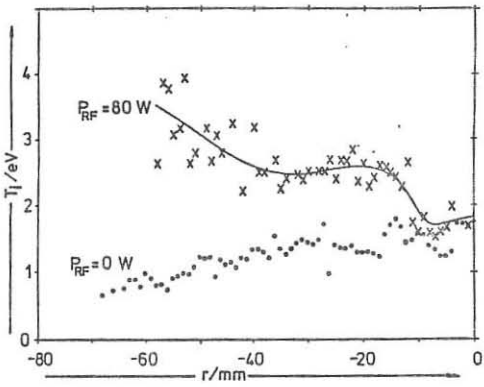
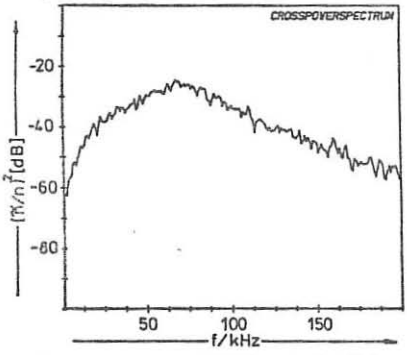


Fig. 2 Ion temperature profile as determined by Katsumata probe measurements (here, position of LH layer $r_{LH} \approx 2$ cm)



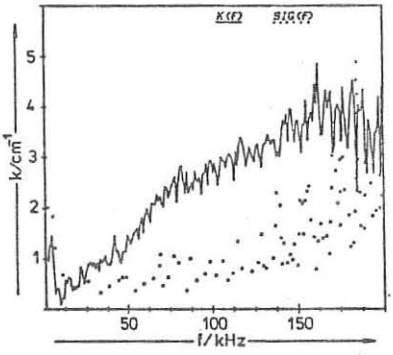


Fig. 3 LF cross power (a) and k_ϑ - spectra (b) ($r = 5$ cm, $z = 52$ cm, $\chi = 3.1$ mm)

Correlation analysis of the LH waves show that approximately the same k_ϑ-values appear in the hf wavenumber spectra thus indicating scattering at the turbulent drift waves. For the study of mode conversion, radial wave number (k_r) spectra have been taken. From fig.4b fairly coherent waves - associated with the broad cross power spectrum (fig. 4a)- can be seen obeying the IP dispersion relation (DR) $\omega^2 = \omega_{LH}^2 + 3k_r^2 T_i/m_i$, $\omega/k_r \cdot \partial\omega/\partial k_r = 3T_i/m_i$: 1.) At the frequency of the original wave (ω_0) we have $k_r \approx 6$ cm^{-1}. With the $k_\parallel$-value of the launcher one would expect larger wavenumbers (at the linear turning point: $k_r \propto k_\parallel$). However, since only the enveloppe of the antenna wave field is observed (fig. 1.), considerably smaller $k_\parallel$ -values must be assumed.

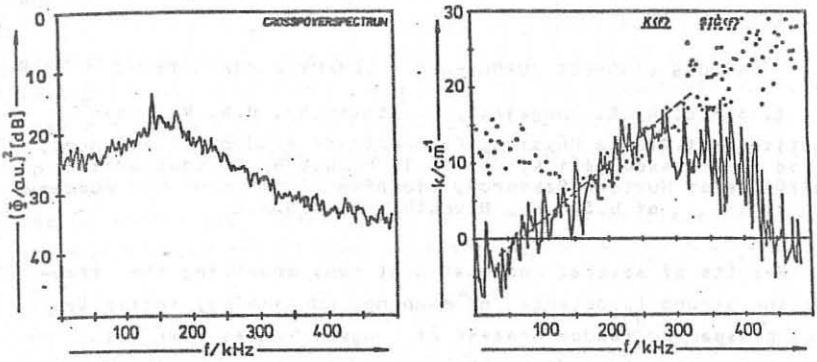


Fig. 4 HF cross power (a) and k_r-spectra (b) ($r = 4$ cm $\approx r_{LH}$, $z = 52$ cm, $\lambda = 0.2$ mm)

2.) The waves are most coherent above ω_0 according to the DR ($\omega > \omega_{LH}$). Both phase- ω/k_r and group velocity $\partial\omega/\partial k_r$, as determined by the slope of the dispersion curve, are directed outward which is in agreement with the DR, too.
3.) For the (scattered) LH waves we expect the opposite (backward) behaviour. Furthermore, radial Fourier analysis of the LH cone yield smaller wavenumber values ($k_r < 2$ cm^{-1}).
4.) From the DR (second eq.) ion temperatures of $T_i = 1.5 - 2.0$ eV are obtained with 3 different spectra (r/cm = 3.5;4.0;4.5) being in reasonable agreement with the measured values.
In conclusion, it seems to be evident that the hf waves observed in the LHR region are ion plasma waves. At present, it can not be decided if they play a role for ion heating. Estimates on the base of the energy balance equation show, however, that collisional heating - also via the heated electrons - can be excluded.

REFERENCES

/1/ STIX Th. H. (1965) *Phys. Rev Lett.* 15, 878.
/2/ PILIYA A. D. and FEDOROV V. I. (1970) *Sov. Phys. JETP* 30, 4.
/3/ KRÄMER M., LUCKS K., SCHLÜTER H. and WIESEMANN F. (1983) *Phys. Lett.* 96A, 195.
/4/ ONO M., WONG K. L., and WURDEN G. A. (1983) *Phys. Fluids* 26, 298.
/5/ OTT E. (1979) *Phys. Fluids* 22, 1732.
/6/ BELLAN P. M. and PORKOLAB M. (1976) *Phys. Fluids* 17, 995.
/7/ KATSUMATA I. (1968) *Conf. on Plasma Diagnostics*, Culham Laboratory Abingdon.
/8/ LUCKS K. and KRÄMER M. (1980) *Plasma Phys.* 22, 879.
/9/ BEALL J. M., KIM Y. C., and POWERS E. J. (1982) *J. Appl. Phys.* 53, 3933

STRONG LANGMUIR TURBULENCE - COMPUTER SIMULATIONS

Z. Sedláček, K. Jungwirth, P. Stavinoha, B.N. Breizman*

Institute of Plasma Physics, Czechoslovak Academy of Sciences, Pod vodárenskou věží 4, CS-182 11 Prague 8, Czechoslovakia
*Institute of Nuclear Research, Siberian Division of the Academy of U.S.S.R., Novosibirsk, U.S.S.R.

Results of several computational runs modelling the free-evolving strong turbulence /no pumping, no damping, initially quiet plasma and random phases/ of Langmuir waves /LW/ with group velocities exceeding those of the ion sound $v_g/k/ \gg c_s$ are presented. The dimensionless spatially one-dimensional set of Zakharov equations

$$ig\frac{\partial E}{\partial t} + \frac{\partial^2 E}{\partial x^2} = nE \quad \text{and} \quad \frac{\partial^2 n}{\partial t^2} - \frac{\partial^2 n}{\partial x^2} = \frac{\partial^2 |E|^2}{\partial x^2}$$

/time t is in $/k_o c_s/^{-1}$ units, x in k_o^{-1}, $g = 2c_s v_g^{-1}/k_o/$ and k_o is related to the initial LW spectrum/ is solved by using a pseudo-spectral computer code.

Similarly to other turbulent systems, profiles of complex E and real n fields become sooner or later strongly dependent on slight changes in the initial spectrum E_k and perturbed density n /in $3k_o^2 r_D^2 n_o$ units/ if automodulation takes place. Suitable integral characteristics are, therefore, of more practical interest. Averaged density of the Zakharov set Hamiltonian gets with V related to n by the continuity equation the form

$$W_H = \frac{1}{L}\int_0^L \left(\left| \frac{\partial E}{\partial x} \right|^2 + n|E|^2 + \frac{n^2}{2} + \frac{V^2}{2} \right) dx$$

It contains contributions due to the ion sound waves /SW/ w_s and to the freely propagating and to the trapped in bounded states /and quasistates/ LW, Δw_{pf} and Δw_{pt}, respectively. The analysis of Langmuir solitons and of SW leads to the estimates

$$\Delta w_{pt} \approx \frac{1}{4L}\int_0^L n|E|^2 dx \quad \text{and} \quad w_s \approx \frac{1}{L}\int_0^L V^2 dx$$

The averaged LW energy density

$$w_p = \frac{1}{L}\int_0^L |E|^2 dx \qquad / \text{ in } 6k_o^2 r_D^2 n_o T \text{ units/}$$

composed roughly of contributions of LW freely propagating w_{pf} and of the trapped ones w_{pt}, is another integral of motion.

The analytical theory based on averaging over random phases predicts for $g \ll 1$ the threshold $/w_p/_{th} = 0.5$ of the modulation instability of Gaussian LW spectra. All the computational runs have $g = 0.05$, $w_H/w_p = 0.25$ and $w_p = 0.4$, excepting run 1 with $w_p = 0.8$. Nevertheless, Figs. 1,2 demonstrate that rather strong and rapid LW trapping and SW excitation occurs /in two stages/. The processes are closely interconnected, as confirmed also by the numerically established relation $w_s \approx -\Delta w_{pt} \gtrsim \Delta w_{pf}$ /0/.

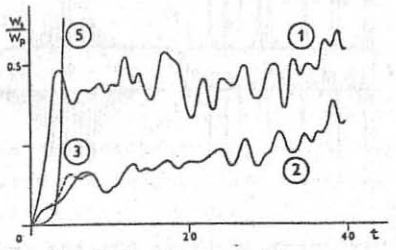


Fig.1: Evolution of SW energy

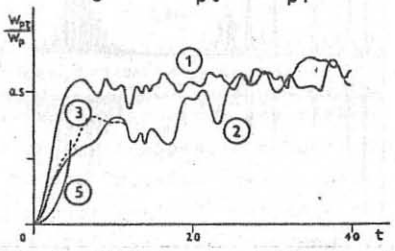


Fig.2: Efficiency of LW trapping

/Numbers in circles indicate individual numerical runs./

Fig. 3 shows initial conditions of all the runs discussed.

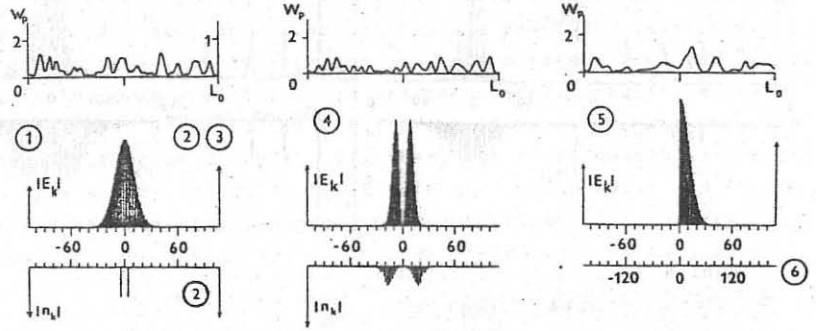
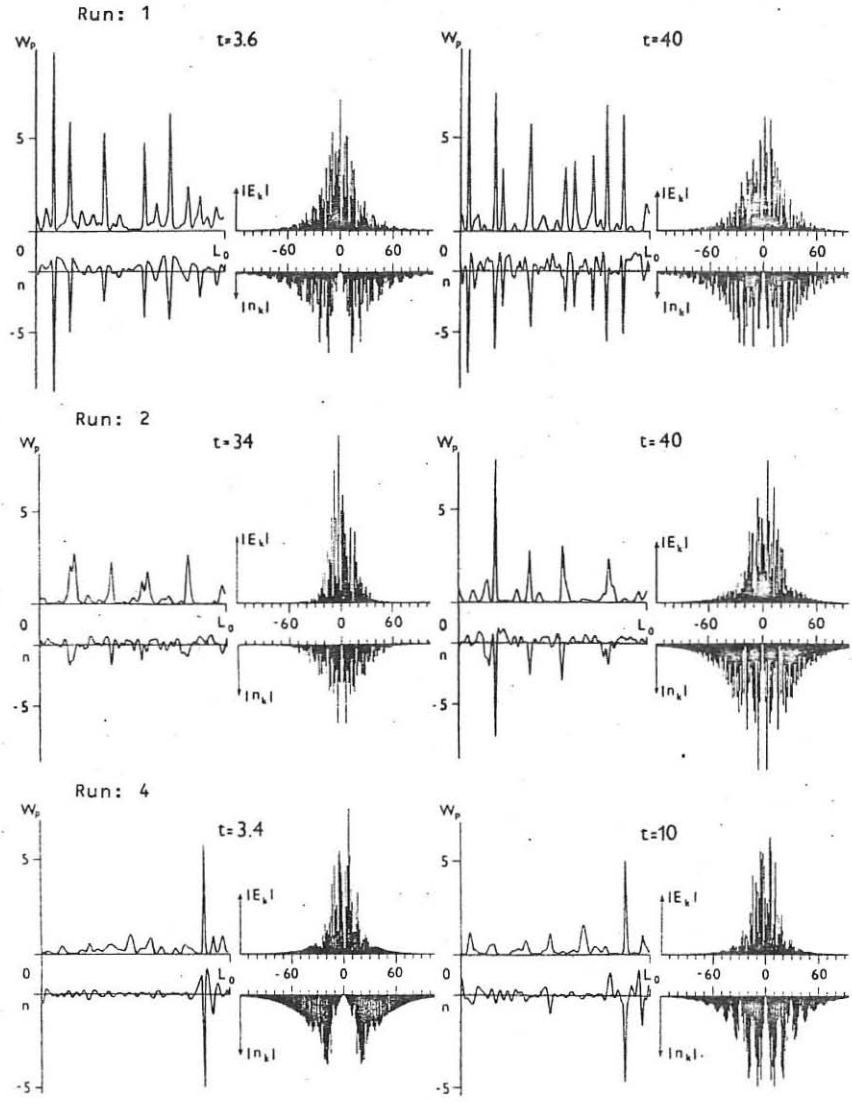


Fig.3: Initial LW energy density /upper curves/, LW electric field /middle/ and density /bottom/ spectra. /Bars - 0.1 value./

Fig. 4 presents detailed spatial $/|E|^2$, n/ and spectral $/|E_k|, |n_k|/$ profiles at two selected times. With $L = L_o = 32\pi$ /excepting 6, where $L = 2L_o$/ the $k=k_o$ wave is the 16th harmonics.

LW moving in both directions /runs 1-4/ form temporarily standing-wave-like structures in $|E|^2$ distribution. Thus, the

automodulation processes are triggered by forced generation of nuclei of possible future density wells. Variations in relative excess of the nuclei affect then the 1st stage of LW trapping.



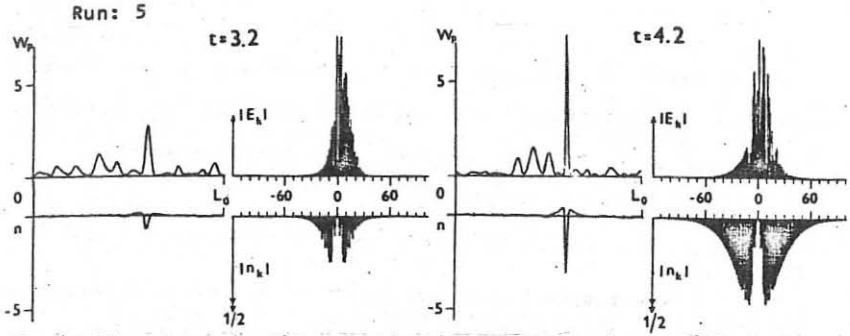


Fig.4: LW energy density and density perturbation profiles /solid curves/ and spectra of the electric field and density

In this stage nonlinear entities of two kinds are created in dependence on the amount of LW energy trapped in competition with the neighbouring cavities: 1/ The "quasisolitons", which are almost stationary long living structures narrower than the nucleus and close to exact Langmuir solitons. 2/ The "cavitons", which are less stable formations of comparable with the nucleus size, moving at roughly $c_s/2$ velocity. They are omnipresent in all processes driving the 2nd stage. Acts of caviton creation, anihilation, caviton - quasisoliton and caviton - caviton merging /leading sometimes to creation of a new quasisoliton/ and caviton stripping from a quasisoliton are then rather frequent events.

The 1st stage is quite different if LW with $v_g \gg c_s$ move in one direction only /runs 5,6/. Then, the first quasisolitons grow up from a very low noise level with the growth rates and final amplitudes strongly dependent on the spectral line density, as shown in Fig. 5. /At the right side it is twice as large./

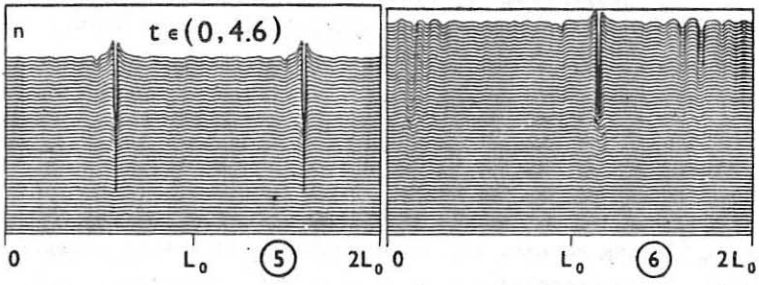


Fig.5: Temporal evolution of the perturbed density profiles.

INITIAL STAGE OF DEVELOPMENT OF NON-LINEAR EFFECTS AT OBLIQUE INCIDENCE OF ELECTROMAGNETIC WAVES ON AN INHOMOGENEOUS PLASMA

J. Preinhaelter, J. Lacina, A. Y. Omeltchenko[+/]

Institute of Plasma Physics, Czechoslovak Academy of Sciences
Pod vodárenskou věží 4, 182 11 Prague 8, Czechoslovakia

[+/] Kharkov Physical and Technical Institute, Kharkov, USSR

The incidence of a P-polarized wave on an inhomogeneous collisionles plasma is studied. In many papers devoted to this problem little attention was paid to the possibility that the highly inhomogeneous electric field with strong ponderomotive effect can arise in the plasma resonance region as a result of the transient phenomenon /a rare exception forms paper /1//. Usually the harmonic waves are studied, some averaging is used and the resulting smooth profile of electric field in the plasma resonance region is given by a phenomenologically introduced damping /see /2/ dealing with the capacitator model, /3/ using the barometric formula model or /4/ solving the Zakharov equations/. The linear theories investigating the incidence of wave on a cold plasma solve only the equation for the magnetic field of wave which is smooth in the plasma resonance region and deduce from it the absorption rate. In a warm plasma theses theories deal with harmonic wave solutions /see e.g. /5//.

In our analytical model it is supposed that the wave having a frequency ω and a wave vector $\vec{k} \equiv (k_x, 0, k_z)$ reaches at $t = 0$ the surface of an unperturbated cold plasma with the linear density profile. During a transient period, i.e. for $t \in (0, T)$, the wave amplitude is supposed to grow from 0 to a small value E_o. Linearizing the equations and using the Laplace transforms technic we have obtained an explicit formula for the time evolution of the electric and magnetic fields of wave / $\vec{E} \equiv (E_x, 0, E_z)$, $\vec{B} \equiv (0, B_y, 0)$ /. The time asymptotic behaviour of the electric field component parallel to the density gradient can be approximated in the plasma resonance region as follows

$$E_x(x,t) = \frac{\bar{E}_o \left(e^{-i\omega t} - e^{-i\omega_o(x)t} R(-i(\omega_o(x)-\omega)T)\right)}{\omega_o(x) - \omega} \quad \text{for } t > T + L/c$$

Here L is the density scale-length, $\omega_o(x)$ is a local plasma frequency, $\bar{E}_o$ is proportional to E_o and $R(x)$ is determined by the

time evolution of the incident wave amplitude during the transient period. It holds $R(0)=1$ and for the smooth growth of the amplitude R rapidly decreases for large imaginary arguments $/|R| \sim 1/|x|^2$ /. The component E_x thus has a form of a compressing standing wave packet and its amplitude grows linearly with time in the plasma resonance. The electric field of the harmonic wave /i.e. $T \to \infty$ / is singular here. The considered effects can take place in a real plasma only if $T < T_c$ where T_c is a mean collision time and if the Debay length is much smaller than the width of the resonance region, i.e. if $T < L/V_{Te}$, where V_{Te} is thermal velocity of electrons.

The incidence of a strong electromagnetic wave on a plasma slab was studied numerically using the two-fluid approximation for ions and electrons, the adiabatic pressure equation for electrons /the ions are cold/ and the full set of the Maxwell equations. This set of equations was solved for the initial and boundary conditions corresponding to the oblique incidence of a wave on the plasma with the help of a simple difference scheme /for more details see /6//. To be able to compare the numerical results with the linear theory we first computed several cases of the incidence of the waves with a small amplitude. The instantaneous values of the electric field of wave is shown in Figs. 1 and 2 for different times. The parameters in the pictures have the following meaning: $\tau = 2\pi/\omega$, $\lambda_x = 2\pi/k_x$, $\vec{E}' = e\vec{E}/(m_e c\omega)$, $T'_{oe} = T_{oe}/(m_e c^2)$ where T_{oe} is the electron temperature in the centre of the slab. It is supposed that the angle of incidence is equal to 35° and that initial plasma density profile has the shape given in Fig. 4 for $t = 12\,\tau$ with the central density equal to 1.2 times the critical one. The transient time T is equal to $10\,\tau$. The electric field depicted in Fig. 1 coincides fully with the linear theory. The component E_x grows rapidly and has highly corrugated profile in the plasma resonance region, E_z grows also here but not so conspicuously and B_y /not shown/ is smooth here having practically a time-independent amplitude. In a mildly warm plasma the electric field of wave develops in a similar way near to the plasma resonance but the generation of the Langmuir waves, their propagation and interferences, wash up the peaks in overdense region and the energy is transported to

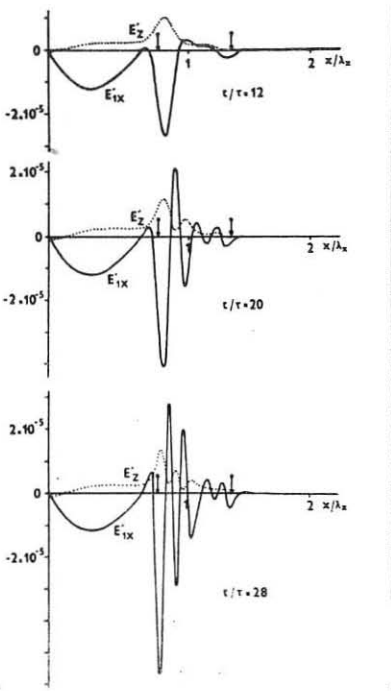


Fig. 1. Time evolution of electric field for $E_0' = 10^{-5}$, $m_i/m_e = 10^4$, $T_{oe}' = 0$.

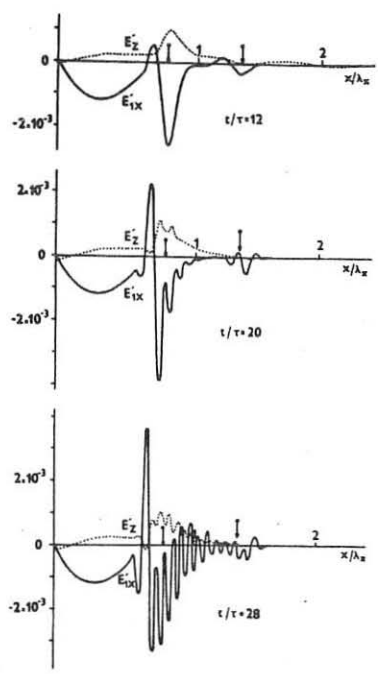


Fig. 2. Same as Fig. 1 but for $T_{oe}' = 5 \times 10^{-3}$.

the rarefied plasma.

The most important results from the numerical investigation of the incidence of a strong wave on a cold plasma are collected in Figs. 3 and 4. The time evolution of the energy balance at the wave incidence is given in Fig. 3. Here W_A represents the absorbed energy, W_{EX}, W_{EZ} and W_B are parts of energy corresponding to E_x, E_z and B_y, respectively, W_{kx} and W_{kz} are the kinetic energies corresponding to the motion along X and z, respectively. All quantities are normalized by E_0^2. The energy absorption is stopped at $t/\tau \sim 40$ and the density profile is highly deformed by the creation of the cavitons. These effects start much quickly then in case that E_x has a smooth profile in plas-

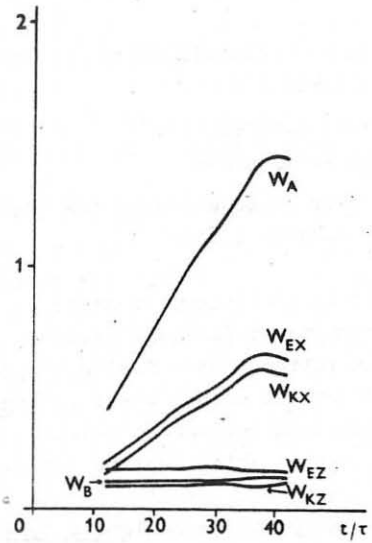


Fig. 3. Time evolution of wave absorption for $E_o' = 10^{-2}$, $m_i/m_e = 100$.

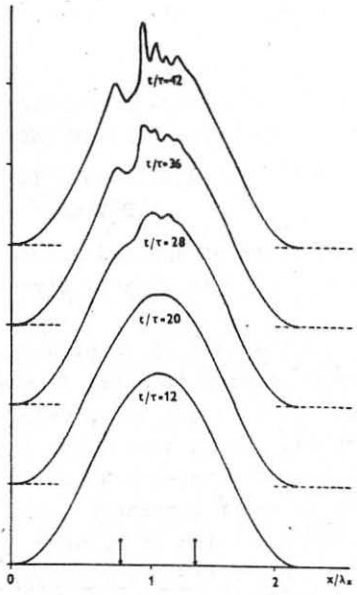


Fig. 4. Evolution of density profile for $E_o' = 10^{-2}$, $m_i/m_e = 100$.

ma resonance region /see e.g. /7/ where cavitons are formed at $t/\tau = 150$ for same parameters with except $T_{oe}' = 3 \times 10^{-3}$/.

REFERENCES

/1/ I. C. Rae, Plasma Physics 24 /1982/, 133

/2/ G. J. Morales, Y. C. Lee, Phys. Fluids 20 /1977/, 1135

/3/ T. Uenoyama, K. Mima, T. Watanabe, J. Phys. Soc. Jap. 50 /1981/, 3107

/4/ A. Gourdin, J. C. Adam, Phys. Fluids 27 /1984/, 2005

/5/ H. J. Kull, Research Rep. MPQ 50 /1981/, München

/6/ J. Lacina, J. Preinhaelter, Czech. J. Phys. B 33 /1983/,160

/7/ D. W. Forslund et al., Phys. Rev. A, 11 /1975/, 679

SELF-INTERACTION OF PLASMA OSCILLATIONS WITH ANOMALOUS DISPERSION

A.G.Litvak, T.A.Petrova, A.M.Sergeev,
A.D.Yunakovsky, and N.A.Zharova

Institute of Applied Physics, Academy of Sciences of the USSR
46 Uljanov Street, 603600 Gorky, USSR

In the case of HF plasma heating in stationary magnetic traps, energy transfer from electromagnetic fields to plasma often occurs due to conversion of electromagnetic fields to potential plasma waves. The latter dissipate either while propagating in inhomogeneous plasma to cyclotron resonance regions or due to their intrinsic nonlinear dynamics which implies effective generation of damping spatial harmonics directly in the region of conversion. The nonlinear absorption mechanism is typical of regimes with strong plasma turbulence.

Plasma waves in magnetized plasma have a number of specific features which distinguish the pattern of strong plasma turbulence in systems with magnetic confinement from similar processes in isotopic plasma. Thus, the refractive index surfaces of potential waves are hyperbolic in some cases (upper hybrid, electron and ion cyclotron oscillations), i.e. spatial dispersion is opposite in sign along and across the constant magnetic field [1-3]. This report deals with nonlinear dynamics of plasma oscillations with such an anomalous dispersion.

Under certain conditions, the self-action of these oscillations is described by a hyperbolic-parabolic nonlinear Srödinger equation for a complex amplitude of a HF electric field [1,2]

$$-i\,\partial u/\partial t + \partial^2 u/\partial r^2 + \frac{1}{r}\,\partial u/\partial r - \partial^2 u/\partial z^2 + |u|^2 u = 0 . \qquad (1)$$

When studying Eq.(1), it is essential to find out whether its solution becomes singular with time, in other words, whether plasma wave collapse [4] exists in the problem. We have failed to formulate a mathematical theorem to give a sought-for answer,

however, the considerations given below show that the solutions are not singular at any evolution time.

First of all, we can rigorously substantiate that the second momentum of the localized field distribution $\overline{\delta^2} = \int z^2 |u|^2 dv / \int |u|^2 dv$, that describes the mean-square longitudinal dimension of the envelope, increases monotonously (provided that the phase front is plane at the initial moment, $\frac{d\overline{\delta^2}}{dt}(t=0)=0$), since

$$\frac{d^2\overline{\delta^2}}{dt^2} = 4\int |u'_z|^2 dv / \int |u|^2 dv .$$

As a result, the energy W_z per unit length of the bunch of plasma waves decreases with time. Hence, a situation most favourable for collapse is realized when self-interaction of the oscillations elongated in the direction of the magnetic field takes place. The process in this case is defined by the law of two-dimensional self-focusing according to which the transverse size is $a \sim \sqrt{t_0 - t}$ and the field amplitude is $A \sim 1/\sqrt{t_0 - t}$, such that the HF energy per unit length, that removes to a singularity, is approaching a critical value [5,6] (similarly to the critical power for self-focusing of quasioptical beams). However, the energy W_z drops below the critical level due to the energy flux in the longitudinal direction, that intensifies as the singularity is approached, and, hence, compression ceases. The growth of the amplitude A lags from the self-similar one in time. As a consequence, the distribution becomes unstable with respect to the growing perturbations with a longitudinal scale $L_{\parallel} \sim a$ and the structure breaks into several secondary bunches.

The pattern of the self-action described above was substantiated by the numerical study of the dynamics of localized distributions in Eq.(1) with the initial Gaussian form of the field

$$u(r,0) = A \cdot \exp(-r^2/2a^2 - z^2/2\delta^2)$$

Figure 1 shows isolines of the function $|u|^2$ and its local maxima at successive instants of time for the parameters $A = 4$, $a = 1$, and $\delta = 3$.

When an analogous problem with periodic boundary conditions is solved, which corresponds to the excitation of a considerable number of interacting turbulence "cells" in the region where electromagnetic energy is absorbed, the process has a more com-

plicated character.

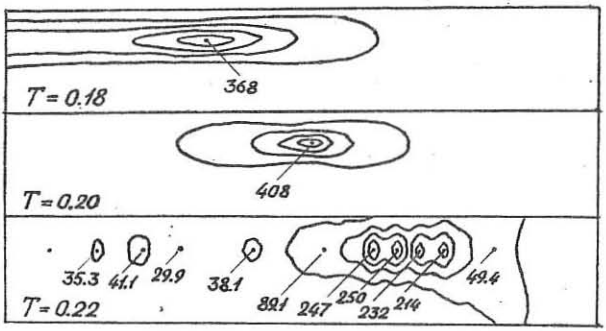


Fig. 1

The initial stage of evolution of HF field bunches is qualitatively similar to that described above for localized structures: the initial distribution is focused in a two-dimensional fashion, a waist is formed in the region with the maximum field amplitude, after which the energy is ejected in the longitudinal direction. Here the periodicity of the system affects its behaviour, such that the neighbouring cells begin to interact. This hinders the initiated defocusing of distribution, hence the processes of compression and fractioning are repeated at a higher level (with higher amplitudes and smaller characteristic scales). As a result of multiple fractioning of structures, the energy is transferred upward the wavenumber spectrum along "jets" with $K_{\perp} \sim K_{\parallel}$ (see also [7]). Note, that for a large enough ratio of initial scales of the localized distribution, a pattern intermediate between the two described can occur: the initial bunch breaks several times before compression in the transverse direction ceases. It is essential, that in spite of the defocusing character of nonlinearity in the Z-direction, the energy is effectively transferred to spatial harmonics with high K_z and, subsequently, is absorbed by plasma electrons. Thus, the self-action of plasma oscillations with anomalous space dispersion demonstrates a new, different from collapse pattern of HF energy dis-

sipation in magnetized plasma.

References

1. A.G.Litvak and V.I.Talanov, Izv. VUZov, Radiofizika, 10, 537 (1967).
2. A.G.Litvak, T.A.Petrova, A.M.Sergeev, and A.D.Yunakovsky, Fizika Plazmi, 9, 495 (1983).
3. J.R.Myra and C.S.Lin, Phys. Fluids, 23, 2258 (1980).
4. V.E.Zakharov, ZhETF, 62, 1745 (1972).
5. S.N.Vlasov, L.V.Piskunova, and V.I.Talanov, ZhETF, 75, 1602 (1978).
6. G.M.Fraiman, ZhETF, 88, 390 (1985).
7. D.V.Martin and H.C.Yuen, Phys. Fluids, 23, 881 (1980).

CONVECTION IN PLASMA DUE TO DRIFT VORTEXES (COMPUTER SIMULATION)

O.V. Batishchev, Yu.S. Sigov, I.I. Silaev

Keldysh Institute of Applied Mathematics,
Academy of Sciences of the USSR, Moscow, 125047, USSR

V.I. Petviashvili

Kurchatov Institute of Atomic Energy, Moscow, 123182, USSR

The heat and particle transport across the magnetic field in plasma appears to occur through convection with the scale of mixing which exceeds the ion cyclotron radius. The convection is due to generation of slow waves across the magnetic field. These waves are the potential drift waves, drift Alfven waves or flute like waves. Having negative energy they are liable to dissipative instability. Even at a relatively small amplitude, the oscillation velocity of particles in the wave is larger than a wave phase velocity, which results in closing the current lines followed by developing of vortexes. Thus, under the drift instability the structures evolve in the plasma, which may play a role of convective cells.

As it known, the potential drift waves as well the drift Alfven and flute waves are described by a system of the Hasegava -Mima (HM) type equations. Therefore, the first step in studying the wave convection in a plasma is to simulate numerically the HM equation and modify it subsequently by adding the terms describing instability, nonpotentiality, etc.

In this paper the HM equation involving the Landau damping is numerically integrated by using the so-called "vortex-in-cell" technique. That allows to take into account the vortex discontinuities and hence to approximate properly fine coherent effects in plasma, what is not possible by means of conventional pure finite-difference schemes.

ON THE CYCLOTRON ABSORPTION OF A FAST-WAVE

P.E.Moroz

Institute of General Physics of the
USSR Academy of Sciences, Moscow, USSR

Radio-frequency plasma heating in the ion-cyclotron frequency range (ICRF) is now one of the most powerful and promising heating methods for toroidal magnetic devices. This report is concerned with plasma heating by fast magnetosonic waves at the fundamental cyclotron resonance of main ions $\omega \simeq \Omega_i$. Recent theoretical papers considering tokamaks [1,2] and stellarators [3] show that in this regime the absorption power can be essentially higher than that previously calculated using the same value of local plasma conductivity as for homogeneous magnetic field. This effect is due to finite rotational transform in tokamaks and to helical structure of confining magnetic field in stellarators. Moreover, the effects of increased absorption in a stellarator may be much higher than in a tokamak with similar plasma parameters [3].

In the theoretical works mentioned above the only considered was the case of non-zero derivative of magnetic field module $(d\Omega_i/dt)_{t_s} \neq 0$ at the moment when an ion passes through a resonant point (where $\omega = \Omega_i$). But in tokamaks and stellarators there are magnetic surfaces where derivative of magnetic field module in the resonant point is zero. This case for a tokamak with heating at the cyclotron harmonic $\omega \simeq \ell \Omega_i$ is treated in [4], therein the absorption is concluded to be much higher near such magnetic surfaces due to expansion of the resonance-interaction region. Here the same problem is considered for the fundamental resonance case $\ell = 1$.

For the left-hand polarized component of induced ion current j_i^+ we use the expression [3]

$$j_i^+ = \frac{\omega_{pi}^2}{4\pi^{3/2} V_i} \int_{-\infty}^{\infty} e^{-v_\parallel^2/v_i^2} dv_\parallel \cdot \int_{-\infty}^{t} E^+(t') e^{i\int_{t}^{t'} (k_\parallel v_\parallel - \omega + \Omega_i) d\tau} dt' \quad (1)$$

where ω_{pi} and Ω_i are the plasma and the cyclotron ion frequencies, ω and $k_\parallel$ are the frequency and the longitudinal wavenumber of the fast wave, V_i is the ion thermal velocity.

Let us consider dimentionless parameters

$$\eta = \varepsilon\Omega_{i0}/\omega_B , \qquad \chi = \varepsilon\Omega_{i0}/k_\parallel V_i \tag{2}$$

for which the conditions $\eta \gg 1$, $\chi \gg 1$ (when the enhancement of cyclotron absorption is possible [3]) are satisfied. Here Ω_{i0} and $\varepsilon\Omega_{i0}$ are the mean value and the amplitude of the varying part of the cyclotron frequency during ion motion within a given magnetic surface, ω_B is the typical frequency with which an ion encounters similar consequtive resonances. Usually we can consider [3] that the phase of cyclotron rotation randomly varies in time of ion passing between consecutive resonances. In this case the current j_i^+ near the resonance angle $\theta=\theta_s$ (where $\omega=\Omega_i$) is determined by the E^+ field in a small vicinity of θ_s. Expanding the integrand of integral (1) in series near $t'=t$, for an average absorption power

$$P = \frac{1}{8\pi}\int_0^{2\pi} \mathrm{Re}\left\{ j_i^+ E^{+*} \right\} d\theta \tag{3}$$

we obtain

$$P = \frac{\omega_{pi}^2}{32\pi^{5/2}\omega_B}\cdot\int_{-\infty}^{\infty} e^{-u^2}du\cdot\int_0^{2\pi}|E^+(\theta)|^2\cdot\mathrm{Re}\left\{I(\theta,u)\right\}d\theta \tag{4}$$

where

$$I(\theta,u) = \int_{-\infty}^{0}\exp\left[i\eta f(\zeta)\right]d\zeta \tag{5}$$

$$f(\zeta) = \frac{\zeta}{\varepsilon\Omega_{i0}}\left[k_\parallel u V_i - \omega + \Omega_i + \frac{u}{2!}\frac{d\Omega_i}{d\theta}\zeta + \frac{u^2}{3!}\frac{d^2\Omega_i}{d\theta^2}\zeta^2\right] \tag{6}$$

$$u = V_\parallel/V_i , \qquad \zeta = \omega_B(t'-t)$$

Let us consider the case $(d\Omega_i/d\theta)_{\theta_s}=0$. Then for $I(\theta_s,u)$ we have the estimation

$$I(\theta_s,u) = \Gamma\left(\frac{4}{3}\right)\left[\frac{6i\omega_B}{u^2(d^2\Omega_i/d\theta^2)_{\theta_s}}\right]^{1/3} \tag{7}$$

The main contribution in the absorption power comes from a small vicinity of the resonance angles $\Delta\theta_s \sim \ell^{-1/3}$.

Integration in (4) gives

$$P = \frac{\Gamma^3(1/3)}{2^{7/3}\,3^{1/3}\,\pi^{5/2}} \cdot \frac{\omega_{pi}^2}{\omega_B^{1/3}} \cdot \sum_s \frac{|E^+(\theta_s)|^2}{\left|\left(d^2\Omega_i/d\theta^2\right)_{\theta_s}\right|^{2/3}} \qquad (8)$$

Here summing is performed over all resonant angles where $(d\Omega_i/d\theta)_{\theta_s}=0$. When resonances with $(d\Omega_i/d\theta)_{\theta_s}\neq 0$ take place at a given magnetic surface too, we add [3]

$$P_1 = \frac{\omega_{pi}^2}{32\,\pi} \cdot \sum_{s1} \frac{|E^+(\theta_{s1})|^2}{\left|\left(d\Omega_i/d\theta\right)_{\theta_{s1}}\right|} \qquad (9)$$

to expression (8).

To find the field $E^+(\theta_s)$ we introduce (as in [3]) the function G slightly varying in scales of $\Delta\theta_s$

$$E^+(\theta_s) = \frac{4\sqrt{2}\,\pi}{\omega} \cdot \frac{G(\theta_s)}{\varepsilon^+(\theta_s)} \qquad (10)$$

$$\varepsilon^+(\theta_s) = \frac{i}{\sqrt{\pi}} \cdot \frac{\omega_{pi}^2}{\omega\omega_B} \cdot \int_{-\infty}^{\infty} e^{-u^2} I(\theta_s, u)\, du \qquad (11)$$

$$G = \frac{c}{4\pi} \cdot \frac{1}{(2g^{11})^{1/2}} \cdot \left[g^{ij} + i\,\frac{q^{kj}}{g^{1/2}} \cdot \frac{B_o^\ell}{B_o}\left(q_{2k}q_{3\ell} - q_{3k}q_{2\ell}\right)\right] \cdot \frac{\partial B_\parallel}{\partial x^j} \qquad (12)$$

Expression for G is written in an arbitrary toroidal coordinate system (x^1, x^2, x^3) for which $x^1 = \text{const}$ is the magnetic surface equation, g_{ij} is the metric tensor, B_o^ℓ is the stellarator (or tokamak) magnetic field, $g = \mathrm{Det}\, g_{ij}$, $B_\parallel$ is the longitudinal component of the wave's magnetic field.

Then for the power P (8) we obtain

$$P \simeq \frac{\omega_B}{\omega_{pi}^2} \sum_s |G(\theta_s)|^2 \qquad (13)$$

this also corresponding to absorption power under the conditions $(d\Omega_i/d\theta)_{\theta_s}\neq 0$ [3]. We should emphasize this result to be only characteristic of the fundamental cyclotron resonance $\ell = 1$.

If we average the local power values, obtained from the theory for homogeneous magnetic field at local plasma parameters, over the magnetic surface, we find

$$\bar{P} \simeq \sqrt{\frac{8}{\pi}} \frac{(k_{\parallel} V_i)^{3/2}}{\omega_{pi}^2} \cdot \sum_s \frac{|G(\theta_s)|^2}{\left|(d^2\Omega_i/d\theta^2)_{\theta_s}\right|^{1/2}} \qquad (14)$$

Comparing the values P and $\bar{P}$ we determine the coefficient of absorption enhancement

$$\mathcal{E} \simeq \sqrt{\frac{\pi}{8}} \cdot \frac{\omega_B}{(k_{\parallel} V_i)^{3/2}} \cdot \left|\left(\frac{d^2\Omega_i}{d\theta^2}\right)_{\theta_s}\right|^{1/2} \qquad (15)$$

Hence, absorption enhancement (i.e. $\mathcal{E} \gg 1$) takes place, provided the following conditions are satisfied

$$1 \ll \eta \ll \chi^{3/2} \qquad (16)$$

Comparison the absorption powers averaged over magnetic surfaces in both stellarator and tokamak with similar plasma parameters yields a large value $P_s / P_t \simeq m_s q_t$ where m_s is the number of stellarator field periods on the major circumference, q_t is the tokamak safety factor.

References.

1. Cattanei G., Croci R. Nuclear Fusion, 1977, v.17, p.239.
2. Stepanov K.N., Kaladze T.D., Pyatak A.I. Proc. 4th Intern. Symp. on Heat. in Tor. Plasmas, Roma 1984, v.1, p.476.
3. Kovrizhnykh L.M., Moroz P.E. Proc. 10th Intern. Conf. on Plasma Phys. and Contr. Nucl. Fus. Res., London 1984, IAEA, Vienna 1985, v.1, p.633.
4. Kaladze T.D., Pyatak A.I., Stepanov K.N. Ukr. Fiz. Zh., 1983, v.28, p.995.

STOCHASTIC INSTABILITY IN HOT ELECTRON PLASMA

Wang Zhongtian
Southwestern Institute of Physics, Leshan P.O.Box 15,
Sichuan, People's Republic of China

Abstract

Secular perturbation theory is used to describe the hot electron motion in an inhomogeneous magnetic field. A group of precessional modes are investigated. A criterion for determining the stochastic instability is obtained. It is found that higher precessional frequency has more stabilizing effects.

1. Introduction

Experimental evidence[1] has shown that plasmas containing hot electrons, such as the ELMO Bumpy Torus, that would be highly unstable according to conventional MHD thoery, can be stable. The reason for this is that these electrons generate a diamagnetic well within which the colder core plasma is stabilized. An analogous mean for stabilizing plasma in an axisymmetric tandem mirror has been proposed wherein the hot electron population in symmetric cells would play anchoring function.

To investigate this problem, many studies[2] have been carried out. A ballooning formalism was used by Berk et al.[3] The compressional mode has been investigated by Rosenbluth.[4] In the present paper, an alternative picture is proposed in the view of intrinsic stochasticity. A criterion for the stochastic instability is derived. It is applied to a planned device designed for producing hot electron ring with ECRH. According to the criterion, the higher electron energy and the larger gradient of the magnetic field have more stabilizing effects. The both factors are closely related to the precessional frequency. On the other hand, stochasticity of the charged particle motion is in favour of the particle heating and current drive.[5] The latter is quite important in tokamak for steady-state operation.

2. Hamiltonian Formulation

The motion of a charged particle in the electro-magnetic field is governed by the equation of the motion

$$M \frac{d\underset{\sim}{v}}{dt} = e\underset{\sim}{E} + \frac{e}{c}\underset{\sim}{v} \times \underset{\sim}{B} \tag{1}$$

where M is the mass of the charged particle, e the charge, c the speed of high, E the electric field, B the magnetic field. Now we introduce in a straight-field-line model

$$\underset{\sim}{B} = B_0 \left(1 + \frac{x}{L}\right) \hat{z} \tag{2}$$

where B_0 is a constant, L is the gradient length of the magnetic field depending on the equlibrium configuration involved with the hot electron ring.[2] We transform the original variables to action-angle variables through the generating function

$$F_1 = M\Omega \left[\frac{1}{2}(y - y_0)^2 \cot\phi - \left(x + \frac{x^2}{2L}\right) y_0 \right] \tag{3}$$

where $\Omega = eB_0/Mc$ is the gyrofrequency, and $y_0 = y + \rho \sin\phi$, ρ is equivalent to the Larmor radius, ϕ is equivalent to the gyration angle. From Eq.(3), the new momenta are

$$P_\phi = \frac{1}{2} M\Omega \rho^2 \tag{4}$$

$$P_{y_0} = M\Omega \left(x + \frac{x^2}{2L}\right) - M\Omega\rho\cos\phi \tag{5}$$

conjugate to ϕ and y_0 respectively.

The unperturbed Hamiltonian of the charged particle is

$$H_0 = \frac{1}{2M} \left| \underset{\sim}{p} - \frac{e}{c}\underset{\sim}{A} \right|^2 \tag{6}$$

where $\underset{\sim}{A}$ is the magnetic vector potential. The transformed Hamiltonian can be written as

$$H_0 = \frac{p_z^2}{2M} + \Omega P_\phi + \frac{P_\phi}{LM} P_{y_0} + \tilde{H}_0(P_\phi, P_{y_0}, \phi) \tag{7}$$

where $\tilde{H}_0$ is a periodic function and equal to zero on integrating over a period of ϕ. Since y_0 does not appear in the Hamiltonian, P_{y_0} is a constant of the motion.

The motion of the charged particle is perturbed by electrostatic waves. The perturbed part of the Hamiltonian can be written as

$$H_1 = e \sum_m \Phi_m \cos(k_z z + m k_y y - \omega t) \tag{8}$$

In guiding center coordinates,

$$H_1 = e \sum_m \Phi_m \cos(k_z z + m k_y y_0 - m k_y \rho \sin\phi - \omega t) \tag{9}$$

To find the resonances in the nonlinear forcing function, we expand H_1 in a Bessel series, and obtain

$$H = H_0 + \sum_{m,n} e \Phi_m J_n(m k_y \rho) \cos(k_z z + m k_y y_0 - n\phi - \omega t) \tag{10}$$

where Jn is Bessel function of order n.

3. The Criterion And Its Application

Neglecting the difference between $\Phi_m J_n(m k_y \rho)$ and $\Phi_{m+1} J_n[(m+1) k_y \rho]$,

3e2-3

using the secular perturbation theory and the two-thirds rule [6], we obtain the island overlap condition

$$\left| \frac{36 F G L^2 M^2}{k_y^2 P_\phi^2} \right| > 1 \quad , \tag{11}$$

where

$$G = \frac{k_z^2}{M} - \frac{2 m n k_\eta}{L M} \quad , \qquad F = -e \Phi_m J_n (m k_y \rho) \tag{12}$$

The Eq.(11) is the criterion for the stochastic instability of the charged particle motion.

We apply the criterion to a planned device. The parameters are

$m = 5$, $L = 0.5 Cm$, $\omega = 2 \times 1.5 \times 10^{10}$ rad/sec ,

$B_0 = 5400$ Gauss for $n = 1$, $B_0 = 2700$ Gauss for $n = 2$,

$k_z = k_y = 1\ cm^{-1}$, $-m k_y \Phi_m = 40$ Volt/cm .

For simplicity, it is assumed that the electron energy E is approximately equal to ΩP_ϕ. We take E= 40kev. For n=1, the criterion (11) is satisfied. The stochasticity of the charged particle motion is expected. The momentum stochasticity can lead to the stochasticity in coordinates. For n=2, the criterion does not satisfied. The electron ring might be generated.

The model used here is simple but gives a clear picture. It is helpful in interpretation of experimental results and in designing a new machine for generating electron ring.

References

1. R.A. Dandl et al, Nuclear Fusion, 11, 411(1971).
2. H.L. Berk et al, Phys. Fluids, 25, 1349(1982).
3. D.E. Baldwin and H. L. Berk, Phys. Fluids, 26, 3595(1983).
4. M.N. Rosenbluth, Phys. Rev. Lett., 46, 1525(1981).
5. Y. Gell and R. Nakach, Proceedings of the IAEA Technical Committee Meeting On Non-Inductive Current Drive In Tokamaks, 202, Culham(1983).
6. A.J. Lichtenberg and M. A. Lieberman, Regular and Stochastic Motion, Applied Mathematical Science, 38(1983).

The q(0) < 1 Regime of the Tokamak

H.P. Furth, A.H. Glasser*, W. Park,
P. Rutherford, H. Selberg, and R.B. White

Princeton Plasma Physics Laboratory
Princeton, New Jersey 08540

*Auburn University
Auburn, Alabama 36849
(*Temporarily at Los Alamos National Laboratory
Los Alamos, New Mexico)

Introduction

An apparent anomaly of experimental tokamak research is that gross stability and confinement are found to be most favorable for $q(0) \lesssim 1$ (i.e., just below the Kruskal-Shafranov limit). This regime is characterized by the so-called "sawtooth" mechanism,[1] where the central plasma temperature, current density, and rotational transform q^{-1} exhibit a roughly linear rise on a slow (resistive) time scale, which is interrupted periodically by a dynamic process of magnetic reconnection. During the course of the sawtooth rise time τ_{ST}, the instantaneous measure of energy confinement, τ_E, tends to increase -- though the overall effect on confinement is masked in present-day tokamak regimes, where $\tau_E \gg \tau_{ST}$.

The mechanism of sawtooth reconnection can be viewed as a nonlinear m = 1, n = 1 resistive kink mode[2,3] that arises for q(0) < 1. The measure of kink-mode driving energy (which is mainly magnetic but includes a finite-β term) and the magnitude of plasma resistivity control the maximum growth rate of the m = 1 island width. Since the resistivity η scales as $T_e^{-3/2}$, one may expect to reach the condition $\tau_{ST} > \tau_E$ in the high-temperature tokamak reactor regime: A likely consequence is that ignition will be facilitated during the sawtooth rise -- possibly followed by "disignition" during the reconnection phase.

In this context, there would be obvious advantages in arresting q(0) at the lowest level for which stable operation can be maintained. One theoretical approach to the stabilization of resistive kinks is rf feedback control. Suppression of $m \geq 2$ magnetic islands by local rf-heating appears to be feasible.[4] (This is the inverse of the kink-destabilizing process described in Ref. 5.) A more efficient approach is feedback control by local current drive.[4,6] In that case, the magnetic island growth rate can be written[6] as

$dw/dt = \eta[\Delta' - (C/w)(\tilde{j}_{rf}/j_o)]$ where $C = 8(rj_z/B_\theta)/(q/rq')$. For a moderately unstable kink, where $\Delta' a \sim 5$, a fractional feedback current $\tilde{j}_{rf}/j_o$ of order 3% should be sufficient to suppress island widths up to $w = a/10$. Localized current-drive feedback using lower-hybrid waves appears to be feasible.[6] Unfortunately, the $m = 1$, $n = 1$ mode borders on ideal-MHD instability even when stabilizing contributions from toroidicity and triangularity of the plasma cross section are taken into account, so that the effective $\Delta' a$-values tend to become very large as $q(0)$ falls below unity. A number of theoretical studies are currently in progress to address this problem.[6,7] A hopeful sign on the experimental side is that stable $q(0) < 1$ regimes have been achieved in a variety of auxiliary-heated tokamak plasmas, including lower-hybrid current-drive experiments[8] -- even prior to the application of feedback.

Resistive MHD Stability of the $q(0) < 1$ Regime

The optimization of the tokamak current profile against resistive kink modes was investigated in Ref. 9, for the range $q(0) > 1$. In the absence of a conducting outer shell, a minimum stable limiter q-value of 2.6 was found for the optimum profile. The present paper extends this study to the range $q(0) < 1$: Assuming that feedback stabilization and/or other special techniques may prove capable of suppressing the family of modes that is resonant at $q(r) = 1$ (i.e., $m/n = 1/1$, $2/2$, etc.), we investigate what other kink-stability boundaries are encountered and what optimal shape should be given to the current profile.

To illustrate the nature of the kink-stability problem, we first consider the profiles shown in Fig. 1. As the central current density $J(0)$ is raised, (Fig. 2) the central q-value falls through a series of resonances $m/n \leq 1$. For a "peaked" profile of the type shown in Fig. 1, modes with $m \geq 5$ are stable ($\Delta' < 0$) and even the $m = 4$, $n = 5$ mode becomes only weakly unstable ($\Delta' a \sim 1$) when $q(0) \lesssim 4/5$. Two serious instabilities ($\Delta' a \sim 5$) are encountered at $q(0) \lesssim 3/4$ and $2/3$, respectively, and the calculation was stopped at $q(0) = 1/2$, where the $m = 1$, $n = 2$ mode first appears. Turning to the $q(r) > 1$ part of the profile, one finds that with decreasing $q(0)$ and $q(1)$, the $m = 3$, $n = 2$ and $m = 2$, $n = 1$ modes become stabilized (a beneficial aspect of the sawtooth regime that has been noted in tokamak experiments), but there is no actual "window of stability" between the $m/n > 1$ and $m/n < 1$ modes. When the width Δx_c of the central current profile is varied, as in Fig. 3, one finds that 2/1-stability improves with greater Δx_c, while 4/5-stability diminishes. (As was shown in Ref. 10, current profiles with "flat tops" tend to excite the higher-m modes.)

To create a stable configuration, it is necessary, as in the $q(0) > 1$ case,[9] to resort to more detailed profile shaping. The introduction of a small pedestal at the edge of the J(r)-profile in Fig. 3, combined with the choice $q(0) \gtrsim 0.75$, to avoid the 3/4 mode and an appropriate choice of the width Δx_c, serves to provide a range of stable cases with $q(1) \sim 2.2$, as shown in Fig. 4.

Conclusion

Reducing q(0) is clearly helpful in permitting stable tokamak operation at lower limiter safety factor q(1). Following the present techniques, one might expect even $q(1) \gtrsim 1.5$ to be achievable by detailed profile shaping in the region $q(x) \leq 1$, as q(0) is lowered towards the m = 1, n = 2 stability limit.

Work supported by DoE Contract No. DE-AC02-76CHO3073.

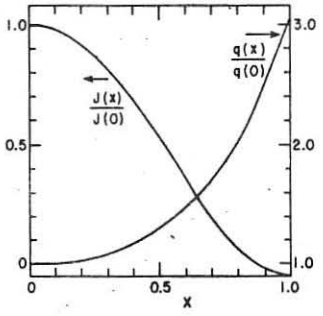


Fig. 1: Illustrative profiles of j(x) and q(x) vs. x = r/a.

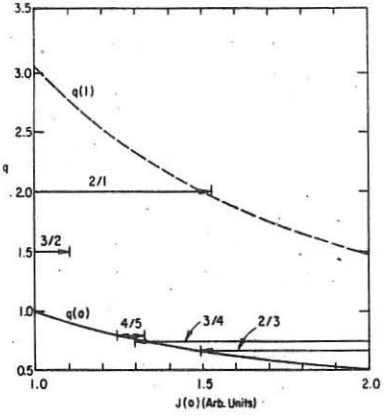


Fig. 2: For increasing central current density j(0), the q(x)-profile of Fig. 1 shifts to lower values. The unstable ranges of various modes m/n as a function of j(0) are plotted at the corresponding q-levels.

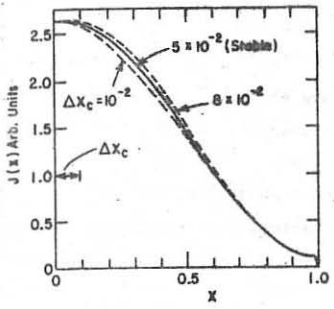


Fig. 3: Optimized j(x) profile (solid line) lies between two unstable profiles (dotted lines) with slightly different central-region widths Δx_c.

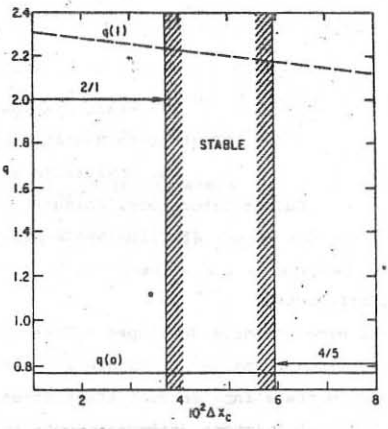


Fig. 4: For increasing width Δx_c of the j(x)-profile in Fig. 3, there is a range of stability around q(a) = 2.2.

References

1. S. Von Goeler, W. Stodiek, N. Sauthoff, Phys. Rev. Lett. 33 1201, 1974.
2. B.B. Kadomtsev, Fiz. Plazmy, 1 710, 1975.
3. R.B. White, D.R. Monticello, M.N. Rosenbluth, Phys. Rev. Lett. 39 1678, 1977.
4. Y. Yoshioka, S. Kinoshita, and T. Kaboyashi, Nucl. Fusion 24 565, 1984.
5. P. Rebut and M. Hugon, Plasma Physics and Controlled Nuclear Fusion Research (Proc. 10th International Conference, London, England, 1984) Vol. 2, IAEA, Vienna, 1985, 197.
6. P. Rutherford, Workshop on Magnetic Reconnection and Turbulence (Cargese, France) July 7-13, 1985.
7. R.B. White et al., Course and Workshop on Application of RF Waves to Tokamak Devices (Varenna, Italy) Sept. 5-14, 1985.
8. S. Bernabei et al., Course and Workshop on Application of RF Waves to Tokamak Devices (Varenna, Italy) Sept. 5-14, 1985.
9. A.H. Glasser, H.P. Furth, and P.H. Rutherford, Phys. Rev. Lett. 38 234, 1977.
10. H.P. Furth, P.H. Rutherford, and H. Selberg, Phys. Fluids 16 1054, 1973.

Test-Particle Transport Due to Fluctuating Magnetic Fields in Tokamaks

A. Thyagaraja and F. A. Haas
Culham Laboratory, Abingdon, Oxfordshire, OX14 3DB, UK
(Euratom/UKAEA Fusion Association)

1. Introduction

We have recently developed a Fokker-Planck approach[1] for investigating test electron transport in tokamaks due to magnetic fluctuations. In this approach we take into account the time-dependence of the fluctuations and collisions, but ignore drifts in comparison with the electron thermal velocity. Assuming the field fluctuation spectrum as known the density fluctuation spectrum and transport coefficients are calculated. Thus taking

$$\frac{\delta B_r}{B_o} = \int_{-\infty}^{\infty} d\omega \sum_{m,n} \bar{b}_{m,n}(r,\omega) e^{i(m\theta + \frac{nz}{R} + \omega t)}$$

we find that

$$\frac{\delta n}{n_o} = \int_{-\infty}^{\infty} d\omega \sum_{m,n} \bar{n}_{mn}(r,\omega) e^{i(m\theta + \frac{nz}{R} + \omega t)}$$

where

$$\bar{n}(r,\omega) = v_{the}\tau \bar{b}_{mn} \frac{1}{n_o}\frac{dn_o}{dr}\frac{1}{\sqrt{2\pi}}\int_{-\infty}^{\infty} \bar{W}(x,r)e^{-x^2/4}dx$$

$$+ \tau \bar{b}_{mn}(r,\omega)\frac{dv_{the}}{dr}\frac{1}{\sqrt{2\pi}}\int_{-\infty}^{\infty} \bar{Z}(x,r)e^{-x^2/4}dx$$

where $\bar{W}$ and $\bar{Z}$ are Fourier components of the perturbed distribution function δf. The complete distribution function $f = f_o(r,v_\parallel) + \delta f(r,v_\parallel,t)$ satisfies the Fokker-Planck equation

$$\frac{\partial f}{\partial t} + v_\parallel \nabla\cdot(\underline{b}\, f) = \frac{1}{\tau}\frac{\partial}{\partial v_\parallel}\left(v_{the}^2 \frac{\partial f}{\partial v_\parallel} + v_\parallel f\right) + \rho^2/4\tau\, \nabla^2 f + S(v_\parallel,\underline{r}) \text{ where}$$

$\underline{b} = \frac{\underline{B}}{B}$, S is the particle source and τ is the Braginskii collision time for electrons. The perturbative solution of this equation leads to expressions for $\bar{w}, \bar{z}$ in terms of $\bar{b}_{mn}$ and ω_{mn}, m and n. A result of this calculation is the following expression for thermal conductivity,

$\chi_{\perp e} = \frac{v_{the}^2}{2} \tau \int_{-\infty}^{\infty} d\omega \sum_{m,n} |\bar{b}_{mn}|^2 \Phi_{mn}(\omega\tau, v_{the}\tau/qR, r)$, where Φ_{mn} is a form factor involving the velocity space integral of $\bar{z}$. This theory has been applied to experiments in TFR, JET & PDX and the results are summarised below.

2. Applications

In TFR[2] high m,n density fluctuations and anomalous electron thermal conductivity have been found to be correlated. We have applied our model to the conditions of this experiment. Thus we take

$$\frac{\delta B_r}{B_o} = \frac{\varepsilon r}{2a} \sum_{m=1}^{80} \sum_{n=1}^{m} e^{-1/4(m-nq)^2} \cos(m\theta - \frac{nZ}{R} + m\omega^* t)$$

where

$q(r) = 1 + \frac{3r^2}{a^2}$, $\varepsilon = 3 \times 10^{-5}$, $\omega^* = 8$ kHz, R = 100cms, a = 20 cms. The collision time τ is taken as 10^{-6} and v_{the} as 10^9 cms^{-1}. The last two parameters are treated as uniform across the radius and represent an average value typical of the experiment. Allowing them to vary with radius in accordance with temperature and density profiles does not change the result significantly. Figs. 1 & 2 show the radial profiles of the RMS values of field and density fluctuation, respectively. Fig 3 shows the resultant $\chi_\perp$ as a function of r. The amplitude parameter ε is fixed by requiring the calculated $\chi_\perp$ at $\frac{r}{a} = 0.5$ to match the experimental value 3×10^3 cm^2 s^{-1}. It is then seen that for $r/a > 0.2$ the calculated $\chi_\perp$ agrees with the experimental $\chi_\perp$ everywhere. Furthermore, the calculated density fluctuations agree with the experiment to within the quoted errors. The region $r/a < 0.2$ is not modelled by our theory as we take no account of saw-tooth and other low m,n activity. In Fig.4 we plot the variation of $\chi_\perp$ with collision frequency at constant temperature. In obtaining this we have assumed that $\delta n/n_o$ is $\propto \tau \propto \frac{1}{n_o}$. The results show that $\chi_\perp$ also varies like $\frac{1}{n_o}$ in agreement with experiment. It is also the case that $\frac{\delta B_r}{B_o} \propto \frac{1}{n_o}$.

We have applied the same model to an Ohmic discharge in JET (Pulse no. 2523 Table II[3]). We solve the transport equation

$$\frac{1}{r}\frac{\partial}{\partial r}\left(rn_o\chi_\perp \frac{dToe}{dr}\right) P_{ohm}(r) - P_{rad}(r) = 0.$$

We take n_o to be uniform (3×10^{13} cm^{-3}). P_{rad} and P_{ohmic} are derived from JET data given in Fig.9 of the report cited. We calculate $\chi_{\perp e}$ assuming that the $\frac{\delta B}{B_o}r$ spectrum is identical with that of the TRF simulation. Values are calculated for $r/a > 0.1$. For $r/a < 0.1$ $\chi_{\perp e}$ is set equal to 10^6 cm^2 s^{-1}. Defining $\tau_{conf} = 3/2\, n_o \frac{\int T_{oe}\, dV}{\int P_{ohm}\, dV}$, we obtain $T_{oe}(o) = 3$kev and $\tau_{conf} = 160$ ms, both of which are in acceptable agreement with experiment given the many uncertainties involved.

We finally consider PDX ohmic and beam heated data[4], which apply to a 10 K Gauss rail-limiter plasma of dimensions R=140cms, a = 40cms. I_p=300 kA, $n_o = 4 \times 10^{13}$ cm^{-3}. We take the radial difference of the density and temperature profiles to be $e^{-(r/a)^2}$ and $e^{-2(r/a)^2}$ respectively. The parameters ω^* and ε are chosen to be $\omega^* = 6 \times 10^4$ rads s^{-1} and $\varepsilon = 4.5 \times 10^{-5}$ to obtain $\frac{\delta n}{n_o}$ 2.5×10^{-3} at r = a, in accordance with observation. The $\chi_{\perp e}$ profile is similar to the TFR one with a maximum value 4×10^4 cm^2 s^{-1} at the edge. Taking the ohmic input power as 0.4 MW the calculations show the electron energy confinement time to be 25 ms and the central electron temperature to be 0.5 keV. With the addition of 3 MW of beam heating and $\varepsilon = 3 \times 10^{-5}$ we obtain $\delta n/n_o = 9 \times 10^{-3}$ at the edge again in accordance with experiment. The thermal diffusivity $\chi_{\perp e}$ is equal to 1.5×10^4 at $r/a = 0.3$ and rises to 2.0×10^5 towards the edge. This corresponds to a global electron energy confinement time of 15.0 ms and a calculated central electron temperature of 3.5 keV, both in agreement with experiment. It is of interest to note that the fluctuation levels for $\delta B/B_o$ are actually slightly smaller than the ohmic case, but yet lead to higher $\delta n/n_o$ and larger χ values. The increases are essentially attributable to the higher T_{oe} and lower collisionality, n_o being the same.

The study shows that if either the field or density fluctuation spectrum for the short wave modes is known experimentally, the test-electron transport model is giving $\chi_\perp$'s (outside q = 1 surface) which are in reasonable agreement with experiment, for both ohmic and beam heated discharges.

REFERENCES

1. Thyagaraja,A., Robertson,I.L., Haas,F.A.,(1985) CLM-P 748
2. Equipe TFR (1983) Plasma Physics 25, 641
3. Cordey, J.G., et al (1984) IAEA London Conf. IAEA-CN-44/A III.3.
4. Crowley, T., (1984) Ph. D. Thesis, Princeton University.

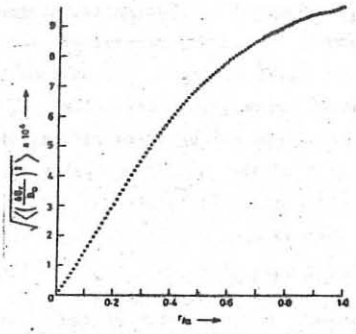


Fig. 1

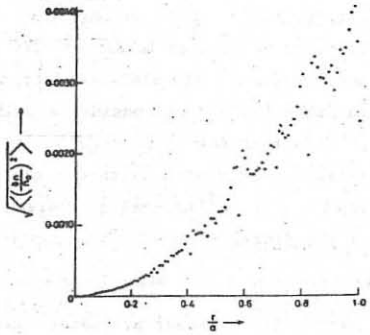


Fig. 2

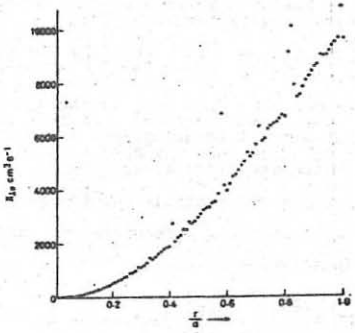


Fig. 3

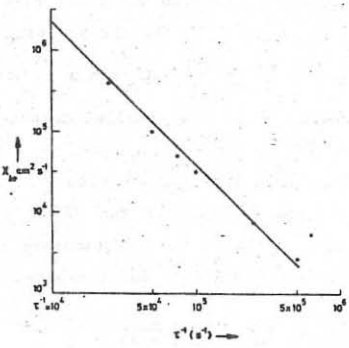


Fig. 4

LINEAR THEORY AND ENERGY INTEGRAL OF RESISTIVE MODES

T.J. Schep
FOM Instituut voor Plasmafysica
Nieuwegein, The Netherlands

and

F. Pegoraro
Scuola Normale Superiore,
Pisa, Italy

Abstract. A quadratic form is derived from the dispersion equation of current driven, collisional resistive modes. This form is presented in terms of the ballooning representation and is shown to be related to the global energy balance. The partition of the released magnetic energy between dissipation, electron compression along field lines and ion fluid motion is discussed.

Linear theory. Near the singular layer where resistive modes undergo fast variations, $r^2k_r^2 >> r^2k_\theta^2 \sim m^2$ and $|\partial/\partial\theta - im| << 1$ so that the ballooning transformation may be applied locally to low m number modes. The global properties of the mode appear as singular boundary conditions at small values of the ballooning variable [1,2]. We consider a cylindrical equilibrium with periodicity length $2\pi R$ so that the ballooning representation reduces to a Fourier transform. We refer to modes with perturbed electric potential of the form $\tilde{\Phi}(r,\theta,\phi) = \bar{\Phi}(x) \exp[-i\omega t + i(\ell\phi - m\theta)]$, where $x = (r - r_s)/r_s$ and r_s is the radial location of the singular layer. The transformed amplitude is

$$\hat{\Phi}(z) = m\hat{s}\delta\int_{-\infty}^{+\infty} d\frac{x}{\delta}\,\bar{\Phi}(\frac{x}{\delta})\exp(i\,m\,x\,z) \quad , \qquad (1)$$

where $\hat{s}$ is the shear parameter, and δ is a measure for the width of the singular layer. The behaviour of $\bar{\Phi}$ for $x/\delta \to \infty$ is determined by the external ideal MHD solution and gives rise to a singular behaviour of $\hat{\Phi}(z)$ for $\delta z \to 0$ (but $|z| >> 1$). The MHD solution in the external region for $x \to 0$, is

$$\frac{e\bar{\Phi}}{T} = \frac{C_1}{x} - C_2\,\mathrm{sgn}\,x \ , \quad \text{and} \quad \frac{c_a}{c}\frac{e\bar{A}}{T} = -\frac{im}{\lambda}[C_1 - C_2\,x\,\mathrm{sgn}\,x] \ , \qquad (2)$$

where $\bar{A}$ is the parallel component of the vector potential, c_a is the Alfvèn velocity, $\lambda = -i\omega\tau_H$ and $\tau_H = \hat{s}\,c_a/qR$. The internal solution for $x/\delta \to \infty$ must also have the behaviour (2) in order to match the external solution.

From collisional two fluid equations, using quasineutrality and Ampere's law, we obtain the relationship between the dimensionless potentials $\Phi = e\hat{\phi}/T$, and $A = c_a e\hat{A}/(cT)$ and the parallel current density $J = \hat{J}/(enc_a)$

$$\Phi = -\frac{1}{\tau b(\lambda - i\lambda_i)}\,z^{-2}\frac{d}{dz}J \ , \quad A = \frac{\lambda}{\tau b}z^{-2}J \ , \quad \frac{\varepsilon m^2}{\tau b}J = g(\lambda)E \ , \qquad (3)$$

where $\tau = T_e/T_i$, $b = (m/r_s)^2\rho_i^2$, ρ_i is the thermal ion gyroradius, $\lambda_i = \tau_H\omega_*(1+\eta_i)/\tau$, $\eta_i = d\ln T_i/d\ln n$, ω_* is the electron drift frequency, $\varepsilon = \tau_H/\tau_R$, τ_R

the resistive diffusion time, $g(\lambda) = 1 - i\lambda_e/\lambda$ and $\lambda_e = -\tau_H\omega_*[1 + (1+\alpha)\eta_e]$. The last expression in (3) is Ohm's law with $E = -d\Phi/dz - \lambda A$ the parallel electric field. The second term in $g(\lambda)$ arises from the electron pressure gradient along field lines and from the thermal electric force which has coefficient α. We have neglected thermal conductivity along field lines. The isothermal case can be recovered by formally setting $1 + \alpha \to 0$. Upon combining the expressions (3) we obtain the dispersion equation

$$\frac{d}{dz} z^{-2} \frac{d}{dz} J - (z_J^{-4} + z_a^{-2} z^{-2}) J = 0 \quad , \tag{4}$$

where $z_J^2 = (m^2\varepsilon)^{-1/2}[(\lambda - i\lambda_e)z_A^2]^{1/2}$, $z_a^2 = \lambda^{-1}(\lambda - i\lambda_1)^{-1}$. Upon combining the Fourier transform of (2) with (3), we obtain the boundary condition set by the MHD solutions in the outer region

$$J = J_0 \left[1 - \frac{1}{2} z^2 z_a^{-2} + \frac{\pi m}{6}(C_1/C_2) z^3 z_a^{-2} \operatorname{sgn} z\right] \tag{5}$$

with $J_0 = -2i\tau \hat{bs} C_2 \lambda^{-1}$. The solution of (4) which decays at Re $z^2/z_J^2 \to \infty$ is [2]

$$J = J_0 2\pi^{-1/2} \Gamma(\tfrac{1}{4} z_J^2 z_a^{-2} + \tfrac{5}{4}) \; U(\tfrac{1}{4} z_J^2 z_a^{-2} - \tfrac{1}{4}, -\tfrac{1}{2}, z^2 z_J^{-2}) \exp(-z^2/2z_J^2) \quad , \tag{6}$$

where U is the confluent hypergeometric function. The dispersion relation is obtained by matching (6) for $z^2/z_J^2 \to 0$ and (5), and reads

$$z_a^2 z_J^{-3} = \frac{\pi m}{16}(C_1/C_2)\, \Gamma(\tfrac{1}{4} z_J^2 z_a^{-2} - \tfrac{1}{4}) / \Gamma(\tfrac{1}{4} z_J^2 z_a^{-2} + \tfrac{5}{4}) \quad . \tag{7}$$

Equations (6) and (7) describe the m = 1 resistive internal kink mode for which $C_1/C_2 = 2\lambda_H/\pi$, λ_H being the ideal MHD growth rate [3], the m = 1 reconnecting and $m \geq 2$ tearing modes, for which $C_1/C_2 = -2/\Delta'$, where Δ' is the logarithmic jump in the radial magnetic field, and Alfvèn modes.

Quadratic form and energy balance. Upon multiplying (4) by the complex conjugate current density J^* and integrating over z we obtain

$$\int_0^\infty dz\, |J|^2 + z_J^4 \int_0^\infty dz\, \frac{1}{z^2}\left|\frac{dJ}{dz}\right|^2 + \frac{z_J^4}{z_a^2}\int_0^\infty dz\, \frac{|J|^2 - |J_0|^2}{z^2} + \left[\frac{z_J^4}{z_a^2}\frac{|J_0|^2}{z} + \frac{z_J^4}{z^2} J^* \frac{d}{dz} J\right]_{z\to 0} = 0. \tag{8}$$

The last two contributions are rearranged such that each is regular. Substituting the boundary condition (5) the expression between brackets becomes $\frac{\pi m}{2}(C_1/C_2) z_J^4 z_a^{-2} |J_0|^2$. The real and imaginary part of (8) are,

$$\int_0^\infty dz\, |J|^2 + \mathrm{Re}\, z_J^4 \int_0^\infty dz\, \frac{1}{z^2}\left|\frac{dJ}{dz}\right|^2 + \mathrm{Re}\, \frac{z_J^4}{z_a^2}\left[\int_0^\infty \frac{dz}{z^2}(|J|^2 - |J_0|^2) + \frac{\pi m}{2}\frac{C_1}{C_2}|J_0|^2\right] = 0, \tag{9a}$$

$$\mathrm{Im}\, z_J^4 \int_0^\infty dz\, \frac{1}{z^2}\left|\frac{dJ}{dz}\right|^2 + \mathrm{Im}\, \frac{z_J^4}{z_a^2}\left[\int_0^\infty \frac{dz}{z^2}(|J|^2 - |J_0|^2) + \frac{\pi m}{2}\frac{C_1}{C_2}|J_0|^2\right] = 0. \tag{9b}$$

The first term in (9a) is proportional to the Ohmic power dissipated by the

mode in the singular layer

$$P_r = \int dV\, \eta_s |\bar{J}|^2 = (n\, T\, V_s/\tau_H)\, [(m^2\varepsilon)/(\pi\, m\, \hat{s}^2\, \tau b)] \int_0^\infty dz\, |J(z)|^2 , \quad (10)$$

where V_s is the volume enclosed by the singular surface. The second term in (9a) is proportional to the time derivative of the total magnetic energy. To show this we need the quasilinear contribution $\bar{A}_{20}$ to the vector potential, averaged over equilibrium flux surfaces [4]. This is obtained from Ohm's law

$$r_s^2/\tau_R\, \frac{1}{r}\frac{\partial}{\partial r}\, r\, \frac{\partial}{\partial r}\, \bar{A}_{20} = 2\gamma\, \bar{A}_{20} + \mathrm{Re}\, [\, i\, g\, \frac{mc}{B_0 r}\, \frac{\partial}{\partial r}\, \bar{A}^* \bar{\Phi}\,], \quad (11)$$

where g is given below (3). In the external region the LHS of (11) is negligible, $\bar{\Phi} = (\omega/ck_\parallel)\bar{A}$ and $\bar{A}_{20}$ is given by $\bar{A}_{20} = (m/4r)\partial\, [|\bar{A}|^2/k_\parallel B_0]/\partial r$. The change W_m of the magnetic energy consists of a contribution from the singular layer and one from the external region

$$W_m = (V_s/8\pi r_s^2) \left[\int_0^a r dr + r_s^2 \delta \int_0^\infty d\, \frac{x}{\delta} \right] \left[|\nabla_\perp \bar{A}|^2 + 4\, \bar{A}_{20}\, F' \right] , \quad (12)$$

where $(c/4\pi)F'$ is the equilibrium current. Using the ideal equations in the external region it can be shown that the first integral in (12) becomes

$$-(V_s/8\pi r_s^2)\, \mathrm{Re} \left[r\, \bar{A}^*\, d\bar{A}/dr + (mF'/k_\parallel B)|\bar{A}|^2 \right]_{r_s^-}^{r_s^+} . \quad (13)$$

In the second integral F' may be taken to be constant. Applying (11), the magnetic energy in the layer is

$$(V_s/8\pi r_s^2) \left[\delta \int d\, \frac{x}{\delta} \left| \frac{d}{dx}\, \bar{A} \right|^2 + m\, \frac{|\bar{A}|^2 F'}{k_\parallel B} \Big|_{-\infty}^{+\infty} \right] . \quad (14)$$

Adding (13) and (14) the terms containing the equilibrium current cancel. Applying the boundary conditions (2) and the Fourier transform (1), we obtain

$$\dot{W}_m = [\tau_H/(2m^2\varepsilon)]\, C_r \left[\int_0^\infty dz\, z^{-2} (|J|^2 - |J_0|^2) + \frac{\pi m}{2}\, (C_1/C_2)\, |J_0|^2 \right] , \quad (15)$$

C_r is the constant in front of the integral in (10). In deriving (15) one should recall that, inside the layer, sgn x is not a distribution at the origin but at large values of x/δ so that its Fourier transform is z^{-1}. The third term in (9a) is proportional to the sum of the rate of change of the fluid ion kinetic energy $W_k = \int dV\, (nm_i/2) c^2 E_\perp^2/B^2$ and of the work W_p done against the electron pressure. It follows from $\bar{E}_\perp = -\nabla_\perp \bar{\Phi}$ and (3) that

$$\partial W_k/\partial t = C_r\, \mathrm{Re}\, [m^2\varepsilon(\lambda - i\lambda_i)]^{-1} \int_0^\infty dz\, z^{-2} \left| \frac{dJ}{dz} \right|^2 . \quad (16)$$

The work W_p is obtained by considering the time rate of change of the internal electron energy, $(3/2)\partial/\partial t \int p\, dV = \mathrm{Re} \int dV\, \bar{J}^*\, \bar{E}$. Using Ohm's law in the form $E = (\varepsilon m^2/\tau b)J + (g - 1)\, (\partial\Phi/\partial z + \lambda A)$, we obtain

$$3/2\, \partial/\partial t \int p\, dV = P_r + C_r\, \mathrm{Re}\, z_a^2 \lambda (g - 1)(m^2\varepsilon)^{-1} \int_0^\infty dz\, z^{-2} \left| \frac{dJ}{dz} \right|^2 , \quad (17)$$

where the second term on the RHS is the time derivative of W_p. From (15), (16) and (17) it is seen that the quadratic form (9a) is the conservation of energy

$$P_r + \frac{\partial}{\partial t}(W_p + W_k + W_m) = 0 \quad . \tag{18}$$

From the real and imaginary parts of the quadratic form and (15), (16) and (17) we obtain, in terms of the frequency, the ratios

$$\frac{W_k + W_p}{W_m} = -\frac{\mathrm{Im}\, z_J^4 z_a^{-2}}{\mathrm{Im}\, z_J^4}\,\frac{\mathrm{Re}\, z_J^4}{\mathrm{Re}\, z_J^4 z_a^{-2}} \quad \text{and} \quad \frac{W_p}{W_k} = \frac{\lambda_e \mathrm{Im}\, z_a^2}{\mathrm{Re}\ \lambda z_a^2} \quad . \tag{19}$$

Then, (18) gives $P_r/(2\gamma W_m) = -1 - (W_k + W_p)/W_m$. For modes that are almost purely growing and have $\lambda >> |\lambda_{e,i}|$, the first ratio in (19) can be expressed in a more convenient form. In such cases W_p/W_k becomes negligible and $z_J^4 z_a^{-2}$ and z_J^4 are almost real. The imaginary parts can be obtained from a variation of the dispersion relation (7). This gives $\mathrm{Im}\, z_J^4 z_a^{-2}/\mathrm{Im}\, z_J^4 = z_a^{-2}(2 + z_J^2 z_a^{-2}\Delta\psi)/(8 - 2\, z_J^2 z_a^{-2}\Delta\psi)$ where $\Delta\psi$ is the difference between two psi functions and equals the logarithmic derivative of the ratio of the Γ functions in (7). Thus we find

$$\frac{P_r}{2\gamma W_m} + 1 = -\frac{W_k}{W_m} = \frac{2 + z_J^2 z_a^{-2}\Delta\psi}{8 - 2z_J^2 z_a^{-2}\Delta\psi} \quad . \tag{20}$$

This relation also follows from a straightforward computation of the various integrals by using the explicit solution (6) for purely growing modes. In particular we find $\int_0^\infty dz\, z^{-2}(|J|^2 - |J_0|^2) = (m\pi/8)(C_1/C_2)|J_0|^2\, z_J^2 z_a^{-2}\Delta\psi$, so that the ratio between the two contibutions to the magnetic energy is $1/4\ z_J^2 z_a^{-2}\Delta\psi$. First we consider the ideal m = 1 internal kink mode which corresponds to $z_J^2 z_a^{-2} \to \infty$. In this limit $z_J^2 z_a^{-2}\Delta\psi = -6$ so that dissipation vanishes and $W_k + W_m = 0$. At ideal marginal stability, i.e. $C_1/2C_2 = \lambda_H = 0$, the dispersion relation (7) yields an unstable mode with a strongly localized current perturbation. For this mode $z_J^2 z_a^{-2} = 1$, $\Delta\psi$ diverges and we find $P_r/2\gamma = W_k = -1/2\ W_m$. The available magnetic energy is given by the first term in (15) and is transformed in equal amounts into heat and fluid motion. Finally, the $m \geq 1$ tearing modes are obtained for $z_J^2 z_a^{-2} \to 0$. In this limit $P_r/2\gamma = -3/4\ W_m$ and $W_k = -1/4\ W_m$. The magnetic energy is given only by the second term of (15) and is primarily dissipated. This is in contrast with the treatment of the energy balance in [4] where it is concluded that dissipation is negligible.

REFERENCES

1 F. Pegoraro, T.J. Schep and L. Klieb, in Proc. Int. Conf. Plasma Physics, Lausanne 1984, Vol. 1 p. 201.

2 F. Pegoraro and T.J. Schep, PP 85/03 Nieuwegein 1984, to be published.

3 B. Coppi, R. Galvão, R. Pellat, M.N. Rosenbluth and P.H. Rutherford, Fisika Plazmy 6, 961, 1976

4 E. A. Adler, R.M. Kulsrud and R.B. White, Phys. Fluids 23, 1375, 1980.

MINIMUM ENERGY PRINCIPLE FOR PLASMA RELAXATION TO EQUILIBRIA WITH PRESSURE AND TEMPERATURE PROFILES

J.B.M.M. Eggen and W. Schuurman

Association Euratom-FOM, FOM-Instituut voor Plasmafysica
Rijnhuizen, Nieuwegein, The Netherlands

Abstract

The paper extends Taylor's relaxation model for force-free plasmas. When the timescale of relaxation is such that the plasma is a closed system that conserves entropy and is always near to a static equilibrium state, the theory predicts pressure and temperature profiles. Special cases and numerical examples are given.

Introduction

A variational principle by Taylor [1] minimizes the magnetic energy W_B of a cylindrical plasma column enclosed by a perfect conducting metal wall, subject to the constraints of constant longitudinal flux Ψ and magnetic helicity $K = \int \vec{A}\cdot\vec{B}d\tau$. The minimizing magnetic field is a solution of the Euler equation $\nabla\times\vec{B} = \lambda\vec{B}$, and its Bessel-function solution correctly demonstrates the reversal of the longitudinal magnetic field component, observed in reversed-field pinches. The relaxation timescale is large enough to decouple the variations of $\delta\vec{B}$ and δp (final state force-free), and to loose the connection with a specific equation of state, adiabatic or otherwise (absence of density and temperature profiles).

In the underlying paper, we consider the possibility of relaxations on a shorter timescale, so that pressure, density and temperature gradients in the plasma may still be present. Two suggestions of how to couple $\delta\vec{B}$ to δp were made: the use of additional global constraints [2,3] or the restriction of the states to be compared to equilibrium states [4]. In our paper we accept the latter possibility. Also, we incorporate the global entropy $S = 1/(\gamma-1)\int k\rho\,\log(N(\gamma)p/\rho^{\gamma})d\tau$ (with γ the specific heat ratio and $N(\gamma)$ a normalization constant) as a constraint in the variational principle, together with the mass invariant leading to the adiabatic equation of state as one of the Euler equations. Together with the assumption that the systems on this contracted timescale is in good approximation closed, yielding constant total potential energy $E = \int (\vec{B}^2/2\mu_0+p/(\gamma-1))d\tau$, we arrive at the mathematical formulation as given in the next section. The resulting equilibrium equations are solved analytically for a special case and numerically in the general case.

The variational principle and its resulting equilibria

The mathematical formulation of the variational principle becomes:

$$\delta\tilde{W} \equiv \delta W_B - \alpha\delta E - \frac{\lambda}{2\mu_0}\delta K - \omega\delta M - \tau\delta S - \phi\delta\Psi - \frac{1}{\gamma-1}\delta\int \vec{\mu}(\vec{x})\cdot\{\nabla p - \vec{j}\times\vec{B}\}d\tau = 0 \qquad (1)$$

where $\alpha,\lambda,\omega,\tau,\phi$ are constant Lagrange multipliers and $\vec{\mu}(\vec{x})$ a space-dependent one. (Note: by a proper shift of parameters this formulation can be extended in order to include an entropy principle, i.e. maximizing the entropy subject to given total energy, mass, longitudinal flux, local pressure balance.) If we consider the cylindrical plasma to be of radius a with all the quantities depending only on the radial coordinate $r \in [0,a]$ the resulting Euler equations are ($B_r = 0$; primes denote differentiation to r):

$$(1-\alpha)\frac{1}{r}(rB_\vartheta)' - \lambda B_z + \frac{1}{\gamma-1}(rB_\vartheta\mu' - B_\vartheta\mu)' = 0. \quad (2) \qquad \mu' + \frac{\mu}{r} + \alpha - \tau\frac{k\rho}{p} = 0. \quad (4)$$

$$(1-\alpha)B_z' + \lambda B_\vartheta + \frac{1}{\gamma-1}\{B_z(\mu' + \frac{\mu}{r})\}' = 0. \quad (3) \qquad \omega + \frac{\tau k}{\gamma-1}\{\log(\frac{N(\gamma)p}{\rho^\gamma} - \gamma\} = 0. \quad (5)$$

As a result of partial integrations applied to obtain these equations, we have the boundary conditions:

$$\delta\vec{A}(a) = \vec{0}. \quad (6) \qquad \delta\{p(a) + \vec{B}^2(a)/(2\mu_0)\} = 0. \quad (7)$$

(6) is satisfied trivially because of the perfectly conducting metal wall; (7) - which has been derived using the formal solution to (4) - still lacks a rigorous justification. Using (5) and the values p_0 and ρ_0 of pressure and density on the magnetic axis, the density can be written as:

$$\rho(r) = \rho_0(p(r)/p_0)^{1/\gamma}, \quad (8)$$

the adiabatic equation of state, and be eliminated from (4) to give

$$\mu' + \frac{\mu}{r} + \alpha - \tilde{\tau}p^{\frac{1-\gamma}{\gamma}} = 0 . \quad (9)$$

The Euler equations (2,3) together with this equation and the pressure-balance equation

$$\mu_0 p' + B_z B_z' + B_\vartheta B_\vartheta' + \frac{B_\vartheta^2}{r} = 0 \quad (10)$$

constitute a set of four equations from which B_z, B_ϑ, μ and p are to be solved.

Once the pressure is known, the density is given by (8), and the ideal gaslaw further determines the temperature.

Special equilibria arise when we disregard the entropy conservation ($\tau=0$). The equations (2,3,9,10) can then be solved analytically to give:

$$B_z(r) = B_0 C_0(\nu r) \quad (11) \qquad p(r) = (\frac{1}{\gamma-1}\frac{\alpha}{1-\alpha}\frac{1}{\beta_0}\{C_0^2(\nu r)-1\}+1)p_0 \quad (13)$$

$$B_\vartheta(r) = \sigma(\sigma\frac{1+\kappa\alpha}{1-\alpha})^{\frac{1}{2}} B_0 C_1(\nu r) \quad (12) \qquad \mu(r) = \frac{1}{2}\alpha r , \quad (14)$$

where $\beta_0 \equiv 2\mu_0 p_0/B_0^2$, $\nu = \lambda\{\sigma(1+\kappa\alpha)(1-\alpha)\}^{-\frac{1}{2}}$, $\kappa = \frac{2-\gamma}{\gamma-1}$, (15)

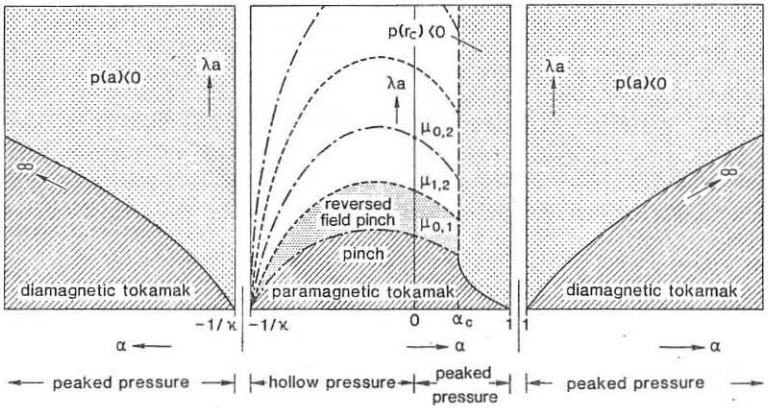
and $C_n \equiv J_n$, $\sigma = +1$ if $\kappa > 0$ and $-(1/\kappa) < \alpha < 1$
or if $\kappa < 0$ and $\alpha < 1$ or $\alpha > -(1/\kappa)$,

$C_n \equiv I_n$, $\sigma = -1$ if $\kappa > 0$ and $\alpha < -(1/\kappa)$ or $\alpha > 1$
or if $\kappa < 0$ and $1 < \alpha < -(1/\kappa)$,

with J_n the ordinary, I_n the modified Bessel functions of the first kind. ($B_0 = B_z(0)$ and $p_0 = p(0)$ are integration constants to (3), resp. (10)). The solutions (11)-(14) depend on α, λ, p_0 and B_0. To have physical acceptable solutions, the parameters must yield a positive pressure, i.e. satisfy:

$$C_0^2(\nu r) - 1 + \frac{(\gamma-1)(1-\alpha)}{\alpha}\beta_0 > 1 \qquad (r \in [0,a]) \ . \tag{16}$$

The values of the parameters distinguish different discharge regimes as is illustrated for $\kappa > 0$ in Fig. 1 ($\kappa < 0$ can be treated analogously), and they are determined by the value of E, K, Ψ and $R = p(a) + B^2/(2\mu_0)$ or another set of four quantities. However, in the case of a reversed field configuration these special solutions exhibit two unrealistic features: the pressure is extremal in the point of field reversal (Fig. 2) and the toroidal current density near the wall can be relatively large (since $p'(:)B_zB_z'$, respectively $j_z(:)B_z$). Furthermore, the density decouples from the description.



$\gamma = \frac{5}{3}$ $\quad$ -·-·-: $\lambda a = \mu_{0,i}\sqrt{(1+\kappa\alpha)(1-\alpha)}$ $\quad$ ——: $p(a) = 0$

($\kappa=\frac{1}{2}$) $\quad$ ----: $\lambda a = \mu_{1,i}\sqrt{(1+\kappa\alpha)(1-\alpha)}$ $\quad$ – –: $p(r_c) = 0 \quad r_c \in (0,a]$

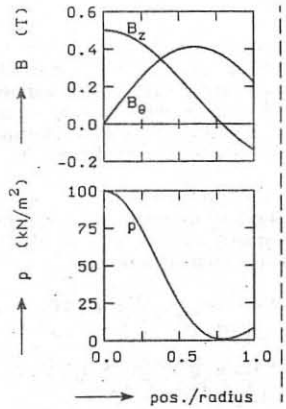
$\beta_0 = 1$ $\quad$ $J_n(\mu_{n,i}) = 0$ $\quad$ $\alpha_c = (\gamma-1)\beta_0/\{(\gamma-1)\beta_0+1\}$.

Fig.1. Existence of solutions and discharge regimes for the parameters $(\lambda a, \alpha)$.

The general case $\tau \neq 0$ unfortunately has no evident analytical solution, but numerical calculations show, that: 1) the general effect of adding the entropy as a constraint is that the equilibrium profiles are flattened, 2) field reversal and extremal pressure are no longer at the same radial position, 3) the current-density components are no longer proportional to the components of the magnetic fields, 4) the mass density is given by (8). An illustrating example, for which the profiles are obtained numerically, is given in Fig. 3.

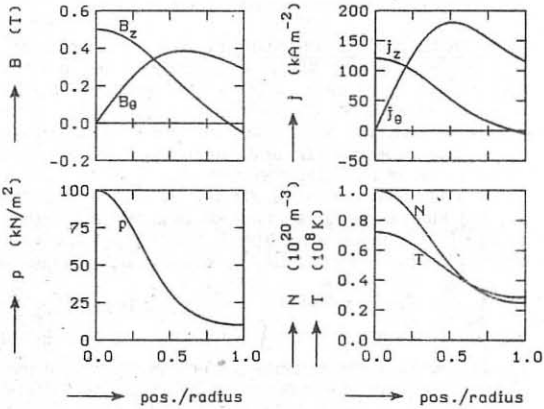
Equilibrium profiles

(α = 0.4; λa = 2.6; γ = 5/3; β_0 = 1)



τ = 0

Fig. 2. External pressure at field-reversal point.



τ = 0.1

Fig. 3. Equilibrium with monotonous pressure and field reversal.

Acknowledgement

This work was performed under the Euratom-FOM association agreement with financial support from ZWO and Euratom.

References

[1] J.B. Taylor, Phys. Rev. Lett. 33 (1974) 1139.
[2] A. Bhattacharjee and R.L. Dewar, Phys. Fluids 25 (1982) 887.
[3] E. Hameiri and J.H. Hammer, Phys. Fluids 25 (1982) 1855.
[4] J.W. Edenstrasser and W. Schuurman, Phys. Fluids 26 (1983) 500.

THE F-Θ-DIAGRAM AND OTHER CHARACTERISTICS OF A VARIATIONAL PRINCIPLE FOR STATIONARY, FINITE-β PLASMA EQUILIBRIA

J.W. Edenstrasser, University of Innsbruck, Austria
W. Schuurman, Association Euratom-FOM, FOM-Instituut voor Plasmafysica, Rijnhuizen, Nieuwegein, The Netherlands

Abstract To the familiar minimum energy principle by Taylor, extensions and modifications are given that allow the treatment of plasma equilibria with a pressure gradient in the presence of flow. The F-Θ-diagram is discussed with β and the dimensionless rotation velocity ξ as parameters.

THE VARIATIONAL PRINCIPLE: In a variational principle formulated by Taylor /1/ the magnetic energy W_B of a plasma enclosed in a cylindrical vessel is minimized subject to the constraints of conserved magnetic helicity K and longitudinal magnetic flux. We extend this minimum energy principle to finite-β plasmas with flow by incorporating, first, the local force balance constraint based on the concept of a multiple time-scale ordering /2/ and, secondly, additional global constraints applicable to a flowing plasma in a closed system.
In accordance with existing analysis of plasma relaxation /3/, the sum W of the magnetic and kinetic energy parts tends to a minimum value. We take as invariants the total energy E, the total momentum $\vec{I}$, the total angular momentum $\vec{L}$, the total mass M, the helicity K, the cross helicity H, and the local equilibrium equation $\vec{P} = 0$ where

$$E = \int \left(\frac{\vec{B}^2}{2} + \frac{p}{\gamma-1} + \varrho\frac{\vec{v}^2}{2}\right)d\tau\,, \quad \vec{I} = \int \varrho\vec{v}\cdot d\tau\,, \quad \vec{L} = \int (\vec{x}\times\varrho\vec{v})d\tau\,, \quad M = \int \varrho\, d\tau\,,$$
$$K = \int \vec{A}\cdot\vec{B}\cdot d\tau\,, \quad H = \int \vec{v}\cdot\vec{B}\, d\tau\,, \quad \vec{P} = \varrho\frac{d\vec{v}}{dt} + \nabla p - \vec{j}\times\vec{B} = 0.$$

Furthermore for these relaxation processes an equation of state $\varrho = F(p)$ is assumed. The mathematical formulation of the suggested variational approach becomes

$$\delta W + \alpha\delta E + \vec{a}\cdot\delta\vec{I} + \vec{\omega}\cdot\delta\vec{L} + m\delta M - \frac{\lambda}{2}\delta K + \nu\delta H + \delta\int \vec{\mu}\cdot\vec{P}d\tau = 0 \qquad (1)$$

where α, $\vec{a}$, $\vec{\omega}$, m, λ, ν and $\vec{\mu}(\vec{x})$ are Lagrange multipliers. With the aid of the homogeneous boundary conditions

$$\delta v\Big|_{\partial p} = 0, \qquad \delta\vec{A}\Big|_{\partial p} = 0, \qquad \delta\left(p + \frac{\vec{B}^2}{2}\right)\Big|_{\partial p} = 0 \qquad (2)$$

the stationarity condition of the first variation in (1) leads to the Euler equations

$$(\alpha+1)\nabla\times\vec{B} - \lambda\vec{B} - \nabla\times\left\{\vec{\mu}\times\vec{j} - \nabla\times(\vec{\mu}\times\vec{B})\right\} + \nu\,\nabla\times\vec{v} = 0 \qquad (3)$$

$$(\alpha+1)\vec{v} + \frac{\nu}{\varrho}\vec{B} + \nabla(\vec{\mu}\cdot\vec{v}) + (\nabla\times\vec{\mu})\times\vec{v} - 2(\vec{v}\cdot\nabla)\vec{\mu} + \vec{a} + \vec{\omega}\times\vec{x} = 0 \qquad (4)$$

$$\nabla\cdot\vec{\mu} - \frac{\alpha}{\gamma-1} - \left\{\vec{\mu}(\vec{v}\cdot\nabla)\vec{v} + \frac{1}{2}\vec{v}^2 + m + \vec{a}\cdot\vec{v} + \vec{\omega}\cdot(\vec{x}\times\vec{v})\right\} F'(p) = 0 \qquad (5)$$

ONE DIMENSIONAL SOLUTION FOR ϱ = const: We now confine ourselves to the case of a radially symmetric plasma with constant density, i.e., $F'(p) = 0$.
After replacing all multipliers λ_ν by $\lambda_\nu(\alpha+1)$ equations (4) become

$$v_\vartheta + \frac{\nu}{\varrho}B_\vartheta - 2\frac{\mu_r}{r}\cdot v_\vartheta + \omega r = 0 \qquad (6)$$

$$v_z + \frac{\nu}{\varrho} B_z + a_z = 0 \tag{7}$$

with the solution of (5) $\mu_r = \alpha r/(\gamma-1)$ leading to

$$v_\vartheta = -k(\frac{\nu}{\varrho} B_\vartheta + \omega r), \quad v_z = -(\frac{\nu}{\varrho} B_z + a_z), \quad k = \frac{1}{1-(\alpha/\gamma-1)} . \tag{8}$$

After elimination of $\vec{v}$ and $\vec{\mu}$ equations (3) become

$$-\lambda B_\vartheta + (\frac{\nu^2}{\varrho} - \frac{1}{k}) \frac{dB_z}{dr} = 0 \tag{9}$$

$$(1 - k \frac{\nu^2}{\varrho}) \frac{1}{r} \frac{d}{dr} (rB_\vartheta) - \lambda B_z - 2k\omega\nu = 0 \tag{10}$$

leading to the differential equation

$$B_z'' + \frac{1}{r} B_z' + \frac{\lambda^2 k}{(1-k \frac{\nu^2}{\varrho})^2} B_z = - \frac{2k^2\omega\nu\lambda}{(1-k \frac{\nu^2}{\varrho})^2} . \tag{11}$$

The solution of (9) and (10) thus becomes

$$B_\vartheta = \frac{SA}{\sqrt{|k|}} Z_1(\mu r), \qquad B_z = A \left[Z_o(\mu r) - \gamma \right]$$

$$\text{with } S = \text{sign} \left[\lambda(1-k\zeta^2) \right], \quad \mu = \left| \frac{\lambda}{1-k\zeta^2} \right| \sqrt{|k|} , \quad \gamma = \frac{-2k\omega\nu}{\lambda A}, \quad \zeta^2 = \frac{\nu^2}{\varrho} \tag{12}$$

and $Z_n(\mu r) = J_n(\mu r)$ for $k > 0$ and $Z_n(\mu r) = I_n(\mu r)$ for $k < 0$, where J_n and I_n are the ordinary (OBF) and modified (MFB) Besselfunctions respectively.
For the components of the current density we obtain

$$j_\vartheta = - S\sigma\mu \sqrt{|k|} B_\vartheta, \qquad j_z = \frac{S\mu}{\sqrt{|k|}} (B_z + \gamma A) \tag{13}$$

where the signfactor σ is defined as $\sigma_{(OBF)} = -1$ and $\sigma_{(MFB)} = +1$. The force free static Taylor case is obtained as the limiting case $k = 1$, $\gamma = 0$, $\zeta = 0$ /1/. For $k = 1$, $\gamma = 0$, $a_z = 0$ the equilibrium is the parallel flow solution originally obtained by Chandrasekhar /4/. For $\zeta = 0$ we have the rigid rotor equilibrium.
We obtain with the homogeneous boundary condition for the pressure

$$p(r) = \frac{A^2}{2} \left\{ (\frac{1}{k} - 1 - k\zeta^2)\left[Z_o^2(\mu r) - Z_o^2(\mu a)\right] - |k| \zeta^2 (Z_1^2(\mu r) - Z_1^2(\mu a)) \right.$$
$$\left. + 2\gamma k\zeta^2 (Z_o(\mu r) - Z_o(\mu a)) + \frac{\gamma^2\lambda^2}{4\zeta^2} (r^2 - a^2) \right\} . \tag{14}$$

Without prescribing further boundary conditions for the velocity, the equilibria obtained depend on the 6 paramters λ, k, ζ, γ, A, a_z and hence comprize a large varity of different equilibria. The mulitplier a_z only enters into the expression of the z-component of the velocity field and the integration constant A is an amplitude factor so that we are left only with four parameters.

REPRESENTATION IN F- θ-DIAGRAMS: Since those four parameters have no direct physical meaning we replace them by θ ; β , ζ and either an additional physical parameter or an additional boundary condition and construct then the corresponding F- θ-diagrams.
The attenuation F and the pinch ratio θ are defined as the toroidal and poloidal magnetic field at the plasma boundary, respectively, both normalized with respect to the volume averaged toroidal field

$$\theta := \frac{B_\vartheta(a)}{\langle B_z \rangle} = \frac{S}{\sqrt{|k|}} \frac{Z_1(x)}{2\frac{Z_1(x)}{x} - \gamma}, \quad F =: \frac{B_z(a)}{\langle B_z \rangle} = \frac{Z_0(x) - \gamma}{2\frac{Z_1(x)}{x} - \gamma}, \quad x = \mu a \qquad (16)$$

The expression for β defined as $\beta = \int p d\tau \,/\, \int (\vec{B}^2/2) d\tau$ is found to be

$$\beta = \left\{ -k\zeta^2 Z_0^2(x) - \sigma\left(\frac{1}{k} - 1 - k\zeta^2\right) Z_1^2(x) + 2k\zeta^2 \frac{Z_0(x) Z_1(x)}{x} \right.$$

$$\left. + 2\gamma k\zeta^2 \left[2\frac{Z_1(x)}{x} - Z_0(x)\right] - \frac{\gamma^2(1-k\zeta^2)x^2}{8|k|\zeta^2} \right\} \Big/$$

$$\left\{ \left(1+\frac{1}{k}\right)(Z_0^2(x) - \sigma Z_1^2(x)) + \frac{2\sigma}{|k|} \frac{Z_0(x) Z_1(x)}{x} - 4\gamma \frac{Z_1(x)}{x} + \gamma^2 \right\} \qquad (14)$$

As velocity ratio ξ we define

$$\xi = \frac{v_z(o) - v_z(a)}{v_A} =: \left|\zeta\right| \cdot \frac{Z_0(x) - 1}{\gamma - 1} \qquad (18)$$

where $v_z(o)$ and $v_z(a)$ are the toroidal velocities at the axis and at the wall and v_A is the Alfhen velocity taken at the magnetic axis.

CASE A: If during turbulent relaxation the plasma was highly viscous then the homogeneous boundary condition $\vec{v}_{tang} = 0$ is certainly justified leading to the determination of a_z and γ

$$a_z = -\zeta v_A \cdot \frac{Z_0(x) - \gamma}{1 - \gamma} \quad \text{and} \quad \gamma = -\frac{2k\zeta^2}{(1-k\zeta^2)} \cdot \frac{Z_1(x)}{x} \qquad (19)$$

In Fig. 1 we have plotted θ-reversal versus β, where the dotted lines belong to equilibria where close to the wall the pressure becomes negative. It is seen that θ_r increases with increasing β and increasing rotation ξ. In Fig. 2 we have plotted some of the corresponding F-θ diagrams.

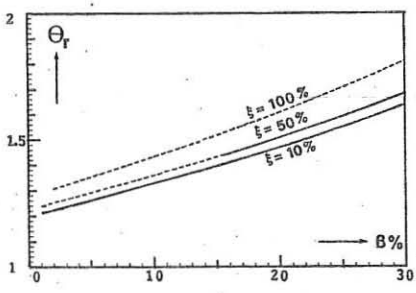


Fig.1

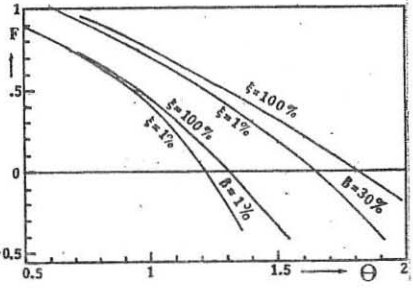


Fig.2

CASE B: To exclude the equilibria for which (in the case of homogeneous boundary condition) the pressure close to the wall becomes negative, it may be convenient to determine γ by the boundary condition of a vanishing pressure gradient. Here, only high β solutions with relatively high values of θ-reversal are found. For example, for ξ = 50% and β = 24%(50%) θ_r was found as θ_r = 1,8 (3,4).

CASE C: In /5/ the safety factor on axis q_{ax}/ε has turned out a convenient internal parameter determining the operating regimes of the various confinement experiments. In case C we hence determine the parameter γ by prescribing the value of

$$q_{ax}/\varepsilon = \frac{2\ |1-\gamma|\sqrt{|k|}}{x} \qquad (\varepsilon \text{ inverse aspect ratio}) \tag{20}$$

For RFP's typical values of q_{ax}/ε are between 0.5 and 0.8 thus we have choosen $q_{ax}/\varepsilon = 0.65$.

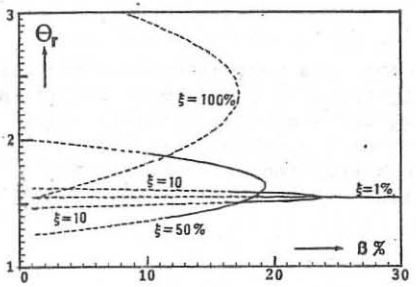


Fig.3

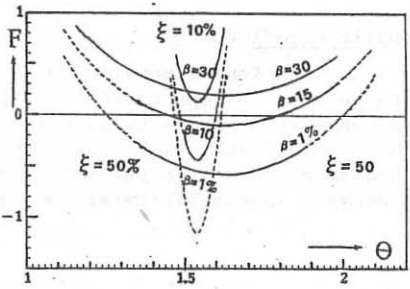


Fig.4

In Fig. 3 we have plotted θ-reversal versus β, the dotted lines again belonging to equilibria where the pressure close to the wall becomes slightly negative. It is interesting to note that reversal occurs only below a certain value of β. In the limit $\xi \longrightarrow 0$ θ-reversal occurs at $\theta_r = 1.6$, independent of β.
Finally, in Fig. 4 we have plotted the corresponding F-θ-diagram showing that for a given value of β and ξ, F reverses at two different values of θ.

Summarizing it can be stated that for $\xi \gtrsim 10\%$ θ-reversal is stronly increasing with increasing rotation ξ. Therefore, the question arises whether in a confinement experiment rotation velocities in the order of some fraction of the Alphen velocity (on axis) can appear. For case C it turns out that in the limit $\xi \longrightarrow 0$ θ_r only depends on the prescribed value q_{ax}/ε but not on β. For example, for $q_{ax}/\varepsilon = 0.65$ $\theta_r = 1.6$, a value considerably higher as in the forcefree static $\xi = 0$, $\beta = 0$ case with $\theta_r = 1.2$.

/1/ Taylor, J.B., Phys.Rev.Lett. 33 (1974) 1139
/2/ Edenstrasser, J.W., and Schuurman, W., Phys.Fluids 26 (1983) 500
/3/ Riyopoulus, S. et al, Phys.Fluids 25 (1982) 107
/4/ Chandrasekhar, S., Proc.Nat.Acad.Sci. 42 (1956) 273
/5/ Edenstrasser, J.W., Nalesso, G.F., and Schuurman, W., Nucl.Instr.Meth. 207 (1983) 75

The Authors are indepted to M. Hauser for performing the numerical calculations. This work was partly supported by the "Fonds zur Förderung der Wissenschaftlichen Forschung" (Austria) under grants No. S-1803 and P 5178. It was also partly performed under the Euratom-FOM association agreement with financial support from ZWO and Euratom.

Metastable States in Tokamaks

E. Minardi and V. Toschi
Associazione EUR-CNR sulla Fusione, Via Bassini 15, Milano, ITALY

Basic equations

A situation is considered such that the thermal conductivity of the electrons depends on the safety factor q and is much larger in an outer zone characterized by $q>q_a$ where q_a is a critical value of q, thus simulating the existence of a cold boundary region dominated by losses related to stochastic magnetic effects and to resonant instabilities around rational q-surfaces:

$$\chi_e = \begin{cases} \chi_a & \text{for } q<q_a \\ \chi_b >> \chi_a & \text{for } q>q_a \end{cases} \qquad (1)$$

We shall investigate the consequences of (1) on the transport and on the electric dissipation in the framework of a one-fluid model of the plasma with homogeneous and constant density in a one dimensional cylindrical Tokamak. As is known, the Ohm-Maxwell equations in cylindrical symmetry can be reduced to the following set of equations:

$$-\frac{1}{4\pi r}\frac{\partial}{\partial r}\left(r\frac{\partial A_o}{\partial r}\right) = j_o(r) \qquad (2)$$

$$-\frac{1}{4\pi r}\frac{\partial}{\partial r}\left(r\frac{\partial A_1}{\partial r}\right) = E_o\left(\frac{1}{\eta(T)} - \frac{1}{\eta(T_o)}\right) - \frac{1}{\eta(T)}\frac{\partial A_1}{\partial t}$$

with $j_o(r)\eta(T_o) = E_o$ and the boundary conditions $(\partial A_1/\partial r)_o = A_1(b) = 0$.

Here $A_o(r)$, $T_o(r)$, $j_o(r)$ are the axial component of the vector potential, the temperature and the current density respectively at zero order; $\eta(T)$ is the Spitzer resistivity, E_o is an externally given induced electric field, b is the plasma boundary and A_1 is the part of the vector potential related to the resistive dissipation. The condition $A_1(b)=0$ expresses the fact that the inductive electric field is fixed to the value E_o at the boundary during the dissipation inside the plasma. The temperature distribution T is determined by the transport equation in the one-fluid approximation

$$\frac{3}{2}\frac{\partial}{\partial t}(nT) - \frac{1}{r}\frac{\partial}{\partial r}\left[rn\chi_e\frac{\partial T}{\partial r}\right] = \eta(T)j^2 \qquad (3)$$

where n is the density and

$$\eta(T)j = E_o - \frac{\partial A_1}{\partial t} \tag{4}$$

with the boundary conditions $(\partial T/\partial r)_o = 0$, $T(b) = \text{const}$ and the continuity conditions of T and $\chi_e\ \partial T/\partial r$ through the interface q_a=const. An Alcator scaling $n\chi_e = \text{const}$ is assumed.

A peculiar property of the solutions of the above set of equations is that the poloidal flux and the q-conservation hold simultaneously on the interface between the two conductivity regions (1). A sufficient condition for this to hold is easily derived starting from the definition of the safety factor, which gives $B_p = -\partial A/\partial r = rB_T/Rq(r,t)$, where B_p and B_T are the poloidal and toroidal magnetic field. Partial differentiation with respect to t gives

$$\frac{\partial^2 A}{\partial r \partial t} = \frac{r\ B_T}{R}\ \frac{1}{q^2}\ \frac{\partial q}{\partial t} \tag{5}$$

Putting $d/dt = \dot{r}\partial/\partial x + \partial/\partial t$ where $\dot{r}$ is the velocity of the interface, one obtains

$$-\frac{\partial}{\partial r}\left(\frac{dA}{dt}\right) = \frac{B_T}{Rq}\ \frac{\partial}{\partial r}(\dot{r}r) - \frac{B_T r}{Rq^2}\ \frac{dq}{dt} \tag{6}$$

One sees from this relation that if $\dot{r}r$=const, then dA/dt=0 implies dq/dt=0. Fig. 1 shows an example of solution of (1.2) to (1.7) with $\dot{r}$ so chosen that dA/dt = 0. In Fig. 1c) the time behaviour of $r^2(t)/I_a(t)$ is plotted, where $I_a(t)$ is the current enclosed by the interface. This quantity is proportional to the value on the interface of the safety factor, which is then found to be practically constant in time, as shown by the figures. One has then $r\dot{r} \sim \dot{I}_a$. But $\dot{I}_a$ is practically constant, as indicated in Fig. 1d). Consequently $r\dot{r}$ is also constant, so that, in accordance with (6), the A-conservation and the q-conservation hold simultaneously on the interface.

As known from Ref.[1] the nonlinear evolution of the profiles is characterized by the ratio τ_b/τ_E where τ_b is the dissipation time at the boundary, $\tau_b = 4\pi a^2/\eta(b)$ and τ_E is the confinement time.

Taking $\tau_E = Cna^2R$ (where $C \sim 10^{-20}$s) one has the relation $\tau_b/\tau_E \sim B_T/nRqCU$ which connects τ_b/τ_E to the Hugill-Murakami parameter nRq/B. Here $U = 2\pi RE_o$ is the loop voltage (in Volt). Fig. 1 shows the case $\tau_b/\tau_E \sim 10$ and $nRq(a)/B_T \sim 0.12/CU$. The current decay, indicated in Fig. 1b, is linear and the decay time is much shorter than τ_b. The decay time depends on the magnitude of the initial cooling perturbation but it is found to be completely independent

of τ_E. Its magnitude, in the case of Fig. 1, is 5 ms for a=20 cm and T(b)=50 ev (compare with [2]).

In the previous calculations an infinite thermal conductivity was assumed in the boundary zone. Stabilization should be expected with a sufficiently low outer conductivity. This is illustrated in Fig. 2 where the time behaviour of the temperature and of the current is given for different values of χ_b/χ_a showing complete stabilization for $\chi_b/\chi_a=5$. A conductivity ratio $\chi_b/\chi_a=10$ is however enough for allowing the development of the instability.

Bifurcation Theory and Metastable States

When the outer thermal conductivity is infinite, the temperature on the interface is rigorously constant. Under these conditions the resistive instability is entirely determined by the equation (2) for the poloidal flux and by its marginal modes. The time scale of the process depends only on the rate of electric dissipation of $A_1(r,t)$ (which scales with τ_b^{-1}) and not on τ_E, and this is also true for the time behaviour of the temperature (see Fig. 2a):

$$\frac{1}{T}\left(\frac{\partial T}{\partial t}\right)_r \sim \frac{1}{A}\left(\frac{\partial A}{\partial t}\right)_r \qquad (7)$$

Expressing T in terms of A, $T(r,t)=\tilde{T}(A(r,t),t)$, one has from (7) that approximately $T(r,t)\approx\tilde{T}(A)$. Applying the Ohm law one then obtains $\tilde{T}(A)\sim j_o^{2/3}(A)$ with $j_o(A)$=const for $a+\xi\leq r\leq b$, where $T_o(0)$, $j_o(0)$ are unperturbed values ($A_1=0$) on the axis and $a+\xi$ is the position of the interface determined by the equation

$$A_o(a+\xi) + A_1(a+\xi) = A_o(a)$$

The equation (2) for A_1 then reduces to the following form [1]

$$\frac{1}{4\pi r}\frac{\partial}{\partial r}\left(r\frac{\partial A_1}{\partial r}\right)=j_o(A_o)-j_o(A_o+A_1) = \frac{j_o(A_o+A_1)}{E_o}\frac{\partial A_1}{\partial t} \qquad (8)$$

The bifurcation properties of this equation will be discussed in detail in a forthcoming paper. The results are summarized in Fig. 3 where $\Gamma=1-\eta(T_o(0))/\eta(T_o(b))$. In the so called "metastable" region the nonlinear behaviour of the system exhibits a bifurcated character. Any initial perturbation cooling the edge and shrinking the current channel gives rise to the current collapse described e.g. by Figs. 1 and 2. The situation is quite different for the heating perturbation, such that the interface is initially moved outwards, generated for instance by an outward heat pulse, widening the central warm zone. In this case the system evolves slowly towards a stable state with broader temperature and current profiles which is a stable stationary state of (8). Fig. 4 (where $\tau_{os}=4\pi a^2/\eta(T_o)$) shows an example of this transition described by a solution of the complete set of equations (1) to (4). This behaviour resembles the processes observed experimentally, in-

volving the so called L and H states and the transitions between them [3] . In the case of the figure the transition is very slow and a time of the order of 1s is needed in order to reach a complete stabilization starting from a slightly perturbed metastable state with a temperature of 0.17 kev in the region r>a=20 cm ($T_o(0)$=0.5 kev).
Further work is necessary in order to develop an accurate simulation of the experimental data from the present rather schematic picture.

References

[1] E. Minardi, Plasma Phys. Contr.Fusion 26, 1505 (1974)

[2] Equipe TFR, Rep. EUR-CEA-1151 (1982)

[3] Keilhacker et al.(Proc.10th Conf.London,1984)Paper CN-44/A-II/1.

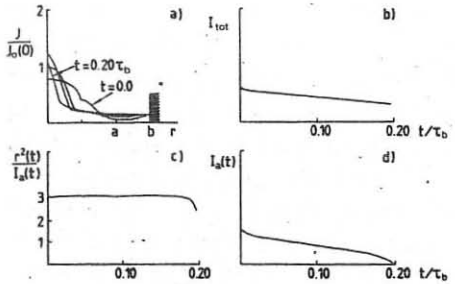


Fig. 1

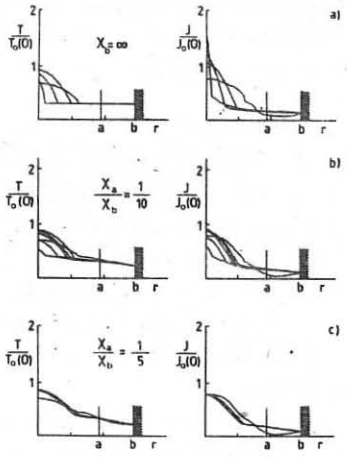


Fig. 2

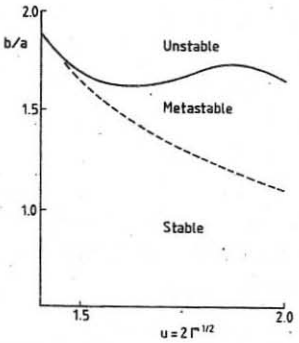


Fig. 3

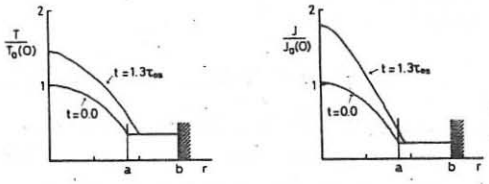


Fig. 4

On the second variation of a minimum energy principle for a force free plasma with a free boundary,

M.A. van Houten and M.P.H. Weenink, Eindhoven University of Technology, Eindhoven, The Netherlands
W. Schuurman, Association Euratom-F.O.M., FOM-Instituut voor Plasmafysica, Rijnhuizen, Nieuwegein, The Netherlands.

Abstract

A calculation is presented of the second variation of the magnetic energy in a Taylorlike variational principle for a cold cylindrical plasma separated from the wall by a vacuum layer, and with a freely movable boundary between the plasma and the vacuum.

I. Introduction

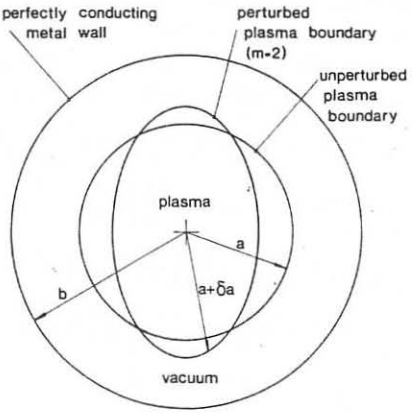
In a variational principle due to Taylor (1/) the magnetic energy of a cold cylindrical plasma, completely filling a perfectly conducting vessel, was minimized. With the helicity $K = \int \underline{A}.\underline{B}d\tau$ and the axial magnetic flux globally conserved, the resulting Euler equation is $\nabla \times \underline{B} = \lambda \underline{B}$ with λ constant. Centen et al. (2/), restricting the analysis as Taylor did to the first variation, extended the model to a plasma isolated from the wall by a vacuum layer. Edenstrasser and Schuurman (3/) derived a stability criterium for resistive modes using the second variation.

In our paper we determine, by combining the two above-mentioned extensions of Taylor's model, the second variation of the magnetic energy of a cold cylindrical plasma separated from the wall by a vacuum layer. In section 2 we describe the model and give the calculation of $\delta^2 W$. The result is briefly discussed in section 3.

2. Description of the model and calculation of $\delta^2 W$

We consider a plasma column surrounded by a vacuum layer and a perfectly conducting cylindrical metal wall (radius b). As in the Taylor model this plasma relaxes violently to a state of minimum total magnetic energy $W_B = \int_{V_p+V_v} B^2/2d\tau$, subject to conservation of the plasma helicity $K = \int_{V_p} \underline{A}.\underline{B}d\tau$. V_p and V_v denote the volumes of plasma and vacuum respectively, and the subscripts p and v keep their meaning throughout this paper(see figure). Also the

longitudinal fluxes in the plasma and in the vacuum as well as the azimuthal flux in the vacuum (the plasma surface is assumed to be perfectly conducting) are conserved quantities.



When the geometry approximates a torus with large aspect ratio the flux through the hole of the torus is taken to be zero, making $A_z(b) = 0$ (4/). At the edge of the plasma the vector potential and the magnetic pressure are continuous. Furthermore, $(n.\underline{B}) = 0$ on the metal wall and on both sides of the plasma boundary, where $\underline{n}$ is the unit vector normal to the metal wall and the plasma boundary respectively.

We wish to investigate the stability of an equilibrium which is r-dependent only. The perturbation is Fourier-analyzed ($\exp i(m\theta+kz)$), and the modes (m,k) are considered independently. For instance, the vector potential $\underline{A}(r,\theta,z) = \underline{A}_o(r) + \underline{\delta A}(r,\theta,z)$, where the components of $\underline{\delta A}$ have the exponential dependence on θ and z. Also the plasma radius has the same θ- and z-dependence in the perturbed state.

The magnetic energy difference between the perturbed and equilibrium state is

$$W_B - W_{BO} = \int_{z=0}^{2\pi R_t} \int_{\theta=0}^{2\pi} \Bigg[\underbrace{\int_o^{a+\delta a(\theta,z)} \left\{ \underline{B}_p \cdot \underline{\delta B}_p - \frac{\lambda}{2} \left(\underline{A}_p \cdot \underline{\delta B}_p + \underline{B}_p \cdot \underline{\delta A}_p \right) \right\} rdr}_{①} +$$

$$+ \underbrace{\int_a^{a+\delta a(\theta,z)} \left\{ \tfrac{1}{2} B_p^2 - \frac{\lambda}{2} \underline{A}_p \cdot \underline{B}_p \right\} rdr}_{②} + \underbrace{\int_o^a \left\{ \tfrac{1}{2} (\underline{\delta B}_p)^2 - \frac{\lambda}{2} \underline{\delta A}_p \cdot \underline{\delta B}_p \right\} rdr}_{③} + \underbrace{\int_{a+\delta a(\theta,z)}^b \left\{ \underline{B}_v \cdot \underline{\delta B}_v \right\} rdr}_{④}$$

$$- \underbrace{\int_a^{a+\delta a(\theta,z)} \left\{ \tfrac{1}{2} B_v^2 \right\} rdr}_{⑤} + \underbrace{\int_a^b \left\{ \tfrac{1}{2} (\underline{\delta B}_v)^2 \right\} rdr}_{⑥} \Bigg] d\theta dz = \delta W + \tfrac{1}{2}\delta^2 W, \qquad (1)$$

where R_t is the large radius of the torus.

The terms ① and ④ of eq. (1) are integrated partially to yield the Euler equations for the equilibrium fields in the plasma and vacuum respectively,

plus a surface term.

In order to transform this surface term we employ $\underline{B} = \nabla \times \underline{A}$, the equilibrium field solution, Taylor series expansions of the integrands in δa up to second order and the following important relations

$$\left.\begin{aligned}
\delta A_{pz}(a+\delta a) &= B_{p\theta}(a)\delta a + \left(\frac{\lambda}{2} B_{pz}(a) - \frac{1}{2a} B_{p\theta}(a)\right)\delta a^2 \\
\delta A_{p\theta}(a+\delta a) &= -B_{pz}(a)\delta a + \left(\frac{\lambda}{2} B_{p\theta}(a) + \frac{1}{2a} B_{pz}(a)\right)\delta a^2 \\
\delta A_{vz}(a+\delta a) &= B_{v\theta}(a)\delta a - \frac{1}{2a} B_{v\theta}(a)\delta a^2 \\
\delta A_{v\theta}(a+\delta a) &= -B_{vz}(a)\delta a + \frac{1}{2a} B_{vz}(a)\delta a^2
\end{aligned}\right\} . \qquad (2)$$

The surface term then becomes

$$2\pi^2 R_t \left[\left\{-\frac{1}{2}\delta a^2 B_{pz}^2 - \frac{\lambda^2}{4} a\delta a^2 A_{pz} B_{p\theta} + \frac{\lambda}{4}\delta a^2 A_{pz} B_{pz}\right\} + \right.$$
$$\left. - \left\{-\frac{1}{2}\delta a^2 B_{p\theta}^2 - \frac{\lambda^2}{4} a\delta a^2 A_{p\theta} B_{pz} + \frac{\lambda}{4}\delta a^2 A_{p\theta} B_{p\theta}\right\} + \left\{\frac{1}{2}\delta a^2 B_{vz}^2 - \frac{1}{2}\delta a^2 B_{v\theta}^2\right\}\right] . \qquad (3)$$

In the terms ② and ⑤ of eq. (1) the integration over the infinitesimal change in volume can be carried out after a Taylor series expansion of the integrands up to first order in (r-a). The result is

$$2\pi^2 R_t \left\{\frac{1}{4}\delta a^2 B_p^2(a) - \frac{1}{2}\delta a^2 B_{p\theta}^2(a) - \frac{\lambda}{4} a\delta a^2 A_{p\theta}(a) B_{pz}(a) + \frac{\lambda}{4} a\delta a^2 A_{p\theta}(a) B_{p\theta}(a) + \right.$$
$$\left. \frac{\lambda^2}{4} a\delta a^2 A_{pz}(a) B_{p\theta}(a) - \frac{\lambda}{4}\delta a^2 A_{pz}(a) B_{pz}(a) - \frac{1}{4}\delta a^2 B_v^2(a) + \frac{1}{2}\delta a^2 B_{v\theta}^2(a)\right\} . \qquad (4)$$

Assembling the various terms, leaving ③ and ⑥ as they stand, we separate the first and second order parts of eq. (1). The first order part put equal to zero again yields the Euler equations for the equilibrium (2/). The accompanying surface term vanishes due to the boundary conditions

$$\underline{\delta A}(b) = 0, \quad B_p^2(a) = B_v^2(a), \quad \underline{\delta A}_{p,v}(a) = \underline{\delta a} \times \underline{B}_{p,v}(a). \qquad (5)$$

The second order part of (1) is easily simplified to

$$\frac{1}{2}\delta^2 W = \int_{z=o}^{2\pi R_t} \int_{\theta=o}^{2\pi} \int_{r=o}^{a} \left\{\frac{1}{2}\underline{\delta B}_p^2(\underline{r}) - \frac{\lambda}{2}\underline{\delta A}_p(\underline{r}).\underline{\delta B}_p(r)\right\} r dr d\theta dz +$$
$$+ \int_{z=o}^{2\pi R_t} \int_{\theta=o}^{2\pi} \int_{r=a}^{b} \left\{\frac{1}{2}\underline{\delta B}_v^2(r)\right\} r dr d\theta dz + \pi R_t^2 \left[B_{vz}^2(a) - B_{pz}^2(a)\right]\delta a^2 \qquad (6)$$

3. Discussion

We note that the free boundary terms in eq. (6) can be stabilizing or destabilizing, depending on whether the B_z-field is increasing or decreasing outwards at the plasma boundary. This term vanishes when plasma surface currents are absent. Since the variations δA and δB in the volumes can be chosen freely, the sign of $\delta^2 W$ is determined by the accessorial problem, i.e. $\delta^2 W$ should be minimized. This is true as it stands when at least one of the mode numbers m, k is unequal to zero, because the invariance of K up to first order is guaranteed by the periodicity of the first variation δK. For the $m = k = 0$ mode, however, the constraint $\delta K = 0$ must be taken into account when solving the accessorial problem. The full stability analysis along these lines will be presented in a forthcoming paper.

Acknowledgement

This work was performed partly under the Euratom-FOM association agreement with financial support from ZWO and Euratom.

References

1/ J.B. Taylor, Phys. Rev. Letters 33 (1974), 1139.

2/ P. Centen, M.P.H. Weenink, W. Schuurman, Proc. 1984 Int. Conf. on Plasma Phys., June 27 - July 3, Lausanne 1984, Vol. 1, 116.

3/ J.W. Edenstrasser, W. Schuurman, ibid. 213.

4/ A. Reiman, Phys. Fluids 24 (1981), 956.

ION KINETIC ENERGY PRODUCTION DURING FAST RECONNECTIONS

M. DUBOIS and A. SAMAIN

Association Euratom-CEA sur la Fusion
Centre d'Etudes Nucléaires
Boite Postale n° 6, 92260 FONTENAY AUX ROSES (FRANCE)

ABSTRACT: It is shown that a fast reconnection in non viscous case converts a significant part of the liberated magnetic energy into kinetic eddies.

INTRODUCTION: A major objection to the Kadomtsev reconnection scheme for internal disruptions /1/ is that the inductive voltage during disruptions is identified to a resistive effect ηI within a singular layer at the separatrix. The very small observed ratios of the disruption time scale to the regeneration time between two successive disruptions then lead to unconsistently large values of I. An escape is to accept that during disruptions the inductive voltage is due to turbulent dynamo effects $\delta V \times \delta B$. Such a turbulence is only possible if the reconnection tends to produce a large amount of ordered kinetic energy. We will discuss this point.

SLOW AND FAST RESISTIVE RECONNECTIONS: The simplest reconnections (Fig. 1)exhibit a regular current density and proceed at a resistive time scale as a sequence of MHD equilibria. Neglecting the pressure effects, the equilibrium at time t is entirely determined by the knowledge of the function $G(\phi, t)$ relating the helical flux ψ to the toroidal flux ϕ embraced by each magnetic surface: $\psi(x,y,t) = G(\phi(x,y,t), t)$. For given $G(\phi,t)$ in each topological domain I,II,III, the shape of the magnetic surfaces minimizes the magnetic energy /2/, i.e., neglecting the toroidal effects:

$$\mathcal{E}_M = \int P(\phi,t)(\partial G(\phi,t)/\partial\phi)^2 \, d\phi/2\pi \quad (1)$$

where $P(\phi,t) = (\oint ds \cdot \delta\ell)(\oint ds/\delta\ell)$ (cf. Fig.1). The rate of the reconnection is determined by the evolution of $G(\phi,t)$ with t. The latter may be deduced from the generalized Ohm law which imposes, whatever the velocity field /2/

$$\frac{\partial G(\phi,t)}{\partial t} = \frac{\eta c^2}{4\pi} \frac{\partial \left(P(\phi,t) \, \partial G(\phi,t)/\partial\phi \right)}{\partial \phi} \quad (2)$$

The slower resistive reconnections require a rearrangement of the function $G(\phi,t)$ by the resistive equation (2) in the bulk of the domains I,II,III, in order that the energy $\mathcal{E}_M$ decreases as the reconnection proceeds. However along the process a situation may arise where a bulk rearrangement of $G(\phi,t)$ is no longer necessary for a further reconnection to be energetically possible. Then the resistive effect on $G(\phi,t)$ applies only near the separatrix. The rate of reconnection, while being still of a resistive nature, becomes much faster. The evolution of $G(\phi,t)$ tends to obey the Kadomtsev rules : $G(\phi,t)$ is independant of t in the bulk of the domains I,II,III; the lost values of G in the reconnecting shells build up by continuity in the reconnected ones. It is very plausible that this regime occurs in Tokamaks at the transition between the relatively slow growth of a precursor island and the very fast internal disruption /2,3/.

DISRUPTIVE RECONNECTIONS: The above situation of fast resistive reconnection occurs when the minimum energy $\mathcal{E}_M$ given by (1), with G deduced from the Kadomtsev rules exhibits a variation $(\delta\mathcal{E}_M)_K \simeq 0$ for a small reconnection progress. A still faster process, identified in principle as the very internal disruptions, must take place when $(\delta\mathcal{E}_M)_K < 0$. Actually, as it may shown numerically from (1), more unstable $(\delta\mathcal{E}_M)_K$ typically occur for increasing island sizes. It is of course important to understand the (helical) magnetic and kinetic fields B, V in that explosive regime. The Kadomtsev model proposes its traditional 3 domains magnetic reconnection and G continuation, and a plasma flow of the Parker type at Alfven velocity in a thin layer along the separatrix. A crucial character of the model is that no kinetic energy density $\rho V^2/2$ at the level of $B^2/8\pi$ is allowed in a finite domain outside the separatrix.

A consequence /2,4/ is that the actual magnetic field B is close to the field B_{var} which minimizes (1). At each level of reconnection the latter is completely determined and has in fact the structure /3/ shown on Fig.2, namely a discontinuity $\pm B_{var}$ across a branch of the separatrix terminating at two Syrovatskii points X', X'', where B_{var} cancels. The rest of the separatrix is regular. One has $B = B_{var} + B'_{//} + B'_{n}$ where the component $B'_{//} \sim B_{var}$ parallel to $X'X''$ cancels outside the thickness δ of the singular layer along $X'X''$, while B'_n is a small unlocalized component $\sim \delta/a\, B_{var}$ normal to $X'X''$. $B'_{//}$ accounts for the current profile I and B'_n for the inclination of the flux lines within the layer. Closed contours are forbidden within the layer by the Ohm law and the constraint that the current I reflecting the discontinuity $\pm B_{var}$ decreases from the centre X to the points X', X''. The flux lines must have the open structure shown on Fig.3.

The key of the self consistency of this model is the dynamical equation

$$\oint_R F \cdot dM + \oint_R \rho \frac{dV}{dt} \cdot dM = \oint_R (I \times B/c) \cdot dM \qquad (3)$$

written along the contour R shown on Fig.3. Neglecting first the frictional forces F, and taking into account that no values $\rho V^2/2 \sim B^2/8\pi$ occurs outside the layer $X'X''$ and that B is regular there, one finds that the L.H.S. of (3) cancels while the R.H.S. is at least equal to the finite variation of $B^2/8\pi$ from inside to outside the singular layer. The plasma experiences along R a magnetic impulsion which requires in fact that kinetic energy $\rho V^2/2$ accumulates in finite kinetic (and magnetic) eddies outside the layer $X'X''/4/$. On the other hand, the Kadomtsev model is self consistent when frictional (e.g. viscous) forces F dominate the inertial force $\rho dV/dt$. The former then balance the magnetic impulsion along R by producing ion kinetic energy in thermal form. In both inertial and frictional cases, the magnetic energy liberated by the reconnection must be in fact shared more or less equally between Joule effect and ion energy production. One may remark that the numerical simulations of the Kadomtsev scheme are possible only in frictional cases /5/.

CONCLUSION: A reconnection entering into the fast regime in the inertial case tends to produce kinetic and magnetic eddies representing equivalent amounts of energy. These eddies do not reflect a MHD instability but simply the self consistency of the plasma flow. It is however plausible that they result in a magneto-kinetic turbulence, more or less localized near $X'X''$, which may largely influence the development of the disruption.

/1/ Kadomtsev B.B., Fiz.Plasmy (1975) 1, 710.
/2/ Dubois M., Samain A., Nuclear Fusion (1980) 20, 1101.
/3/ Dubois M., Marty D., Pochelon A., Nuclear Fusion (1980) 20, 1355. and Dubois M., Pequet A.L., Reverdin C., Nuclear Fusion (1983) 23, 147.
/4/ Samain A., Spring College on Fusion Energy, may 1981, International Centre For Theoretical Physics, Trieste (1982) p. 393.
/5/ Park W., Monticello D.A., White R.B., Phys. Fluids (1984) 27, 137.

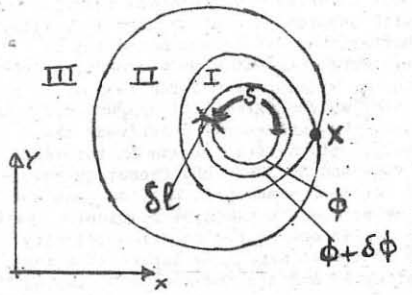


Fig. 1. Slowly reconnecting magnetic surfaces

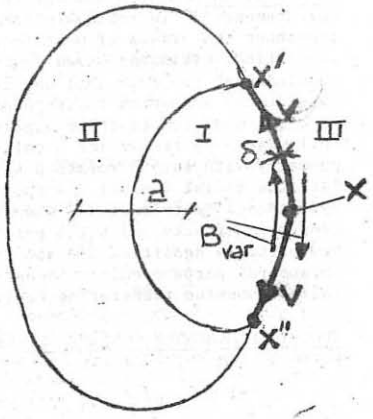


Fig. 2. Fast reconnection

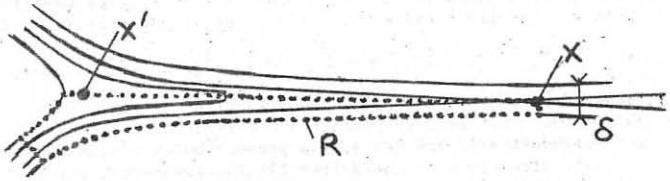


Fig. 3. Singular layer and contour R

Toroidal Momentum Confinement of Strongly Rotating Tokamak Plasma

W. M. Stacey
Department Nuclear Energy and Health Physics
Georgia Institute of Technology
Atlanta, GA 30332

D. J. Sigmar
Plasma Fusion Center
Massachusetts Institute of Technology
Cambridge, MA 02139

ABSTRACT A theoretical expression for the momentum confinement time in strongly rotating tokamak plasmas is presented, derived from neoclassical theory for gyroviscous forces, taking into account $0(\varepsilon)$ poloidal variations in the flow velocities and ion and impurity densities. Predictions for momentum confinement times in ISX-B, PLT, TFTR and PDX are in good agreement with measured values.

INTRODUCTION Momentum confinement times inferred from toroidal rotation measurements[1-4] in tokamak plasmas with unbalanced neutral beam injection are about two orders of magnitude shorter than can be accounted for by theoretical estimates based on the standard perpendicular viscosity of neoclassical theory. This has led to the widespread feeling that an "anomalous" mechanism is responsible for enhanced radial transport of toroidal momentum in these experiments. We have recently derived[5] the full viscosity tensor for a collisional, axisymmetric plasma in toroidal geometry with strong rotation ($v_\phi \simeq v_{th}$) and applied this tensor to calculate the radial viscous transport of toroidal momentum. We find that the gyroviscous contributions, when proper account is taken of toroidal geometric effects and $0(\varepsilon)$ poloidal variations in the rotation velocity and particle densities are about two orders of magnitude larger than the "standard" perpendicular viscosity effects[6] and are the dominant viscous radial momentum transfer mechanism.

THEORY OF MOMENTUM CONFINEMENT We define the momentum confinement time in terms of the toroidal viscous force as

$$\tau_\phi^{-1} \equiv \langle R^2 \nabla\phi \cdot \nabla \cdot \vec{\pi} \rangle / \langle R^2 \nabla\phi \cdot nm\vec{v} \rangle \qquad (1)$$

where $\vec{v}$ is the plasma flow velocity, m is the ion mass, n the ion density, $R\nabla\phi$ is the toroidal unit vector and $\langle\ \rangle$ denotes an average over the magnetic flux surface. The traceless symmetric viscous stress tensor, $\vec{\pi}$, is[7]

$$\pi_{\alpha\beta} = -\ \eta_0 W^0{}_{\alpha\beta} - [\ \eta_1 W^1{}_{\alpha\beta} + \eta_2 W^2{}_{\alpha\beta}] + [\eta_3 W^3{}_{\alpha\beta} + \eta_4 W^4{}_{\alpha\beta}] \qquad (2)$$

for a general tokamak flux surface geometry with magnetic field $\vec{B} = \nabla\phi\times\nabla\psi + F\nabla\phi$. The parallel viscosity coefficient (η_0) scales inversely with the self-collision frequency; the perpendicular viscosity coefficients (η_1, η_2) scale directly with the self-collision frequency; and the gyroviscosity coefficients (η_3, η_4) are independent of collision frequency, see Ref. 7.

The gyroviscous tensor (third piece on right of Eq. (2)) becomes

	ψ	θ	ϕ
ψ	$-\eta_3\left[h_\theta \frac{\partial}{\partial \ell_\psi}\left(\frac{V_p}{h_\theta}\right) - f_p R \frac{\partial}{\partial \ell_\psi}\left(\frac{V_\phi}{R}\right)\right]$	$-\eta_3 \frac{1}{RB_p}\frac{\partial}{\partial \ell_p}\left(RB_p V_p\right) - \left(\eta_4 - \eta_3\right) f_p R \frac{\partial}{\partial \ell_p}\left(\frac{V_\phi}{R}\right)$	$-\eta_4 R \frac{\partial}{\partial \ell_p}\left(\frac{V_\phi}{R}\right)$
θ	$= \pi_{\psi\theta}$	$\eta_3 h_\theta \frac{\partial}{\partial \ell_\psi}\left(\frac{V_p}{h_\theta}\right) + \left(2\eta_4 - \eta_3\right) f_p R \frac{\partial}{\partial \ell_\psi}\left(\frac{V_\phi}{R}\right)$	$\eta_4 R \frac{\partial}{\partial \ell_\psi}\left(\frac{V_\phi}{R}\right)$
ϕ	$= \pi_{\psi\phi}$	$= \pi_{\theta\phi}$	$-2\eta_4 f_p R \frac{\partial}{\partial \ell_\psi}\left(\frac{V_\phi}{R}\right)$

where $h_\theta = JB_p$, with J the Jacobian, $f_p = B_p/B$ and the metric element is $\partial\ell^2 = (RB_p)^{-2}\,\partial\psi^2 + h_\theta^2\,\partial\theta^2 + R^2\,\partial\phi^2$.

Thus, $\pi^{3,4}_{\phi\psi} = -\eta_4 R \frac{\partial}{\partial \ell_p}\frac{V_\phi}{R}$ where $(\eta_4)_j = (nmT/ZeB)_j$, with j the ionic species index (main ions or impurities) and $\langle R^2 \nabla\phi\cdot\nabla\cdot\pi^{3,4}\rangle =$

$$\frac{1}{V'}\frac{\partial}{\partial\psi} V' \langle R^2 \nabla\phi\cdot\tilde{\pi}^{3,4}\cdot\nabla\psi\rangle = -\frac{1}{r}\frac{\partial}{\partial r} r \langle \eta_4 \frac{R^2}{r}\frac{\partial}{\partial\theta}\frac{V_\phi}{R}\rangle$$

where we introduced a circular flux surface geometry in the last step.

Adopting the notation

$$X(r,\theta) = X^\circ(r)(1 + X_c \cos\theta + X_s \sin\theta) \tag{3}$$

where X stands for V_ϕ, n or η_4 one obtains

$$\langle R^2 \nabla\phi\cdot\nabla\cdot\tilde{\pi}^{3,4}\rangle = -\frac{\varepsilon^2}{2} R_o \left[\frac{1}{r}\frac{\partial}{\partial r}\eta_4^\circ V_\phi^\circ\right]\tilde{\theta} \tag{4}$$

Here the quantity

$$\tilde{\theta} \equiv \frac{V_s}{\varepsilon}\left(3 + \frac{n_c}{\varepsilon}\right) + \frac{n_s}{\varepsilon}\left(1 - \frac{V_c}{\varepsilon}\right) + 0(\varepsilon) \tag{5}$$

measures the amplitude of the poloidal variations. It has been shown elsewhere[8] that for momentum inputs such that

$$V_{\phi j} \sim V_{thj}, \; V_s/\varepsilon \sim V_c/\varepsilon \sim n_c/\varepsilon \sim n_s/\varepsilon \sim 1$$

thus making $\tilde{\theta} = 0$ (1) during steady state rotation levels at thermal speed.

This yields for the momentum confinement time defined in (1) on a given flux surface

$$\tau_\phi^{-1} \simeq \frac{T}{2 R_o^2 Z e B^\circ} G(r) \tilde{\theta} \qquad (6)$$

where

$$G(r) \equiv - \frac{r}{n^\circ T^\circ V_\phi^\circ} \frac{\partial}{\partial r} (n^\circ T^\circ V_\phi^\circ), \qquad (7)$$

a gradient scale factor of 0 (1).

INTERPRETATION OF EXPERIMENTS We have compared the prediction of Eq.(6) with two experimental values of the the momentum confinement time in ISX-B[2]. In the first case, the steady-state toroidal rotation velocity was measured for an oxygen impurity, and a momentum confinement time was inferred assuming that all the plasma ions rotate with the same velocity. The experimental confinement time thus determined was 16 ms. Applying Eq. (6) to a composite ion species with an effective charge Z = 2.5 and an average temperature $\overline{T}_i$ = 500 eV [2] results in a predicted momentum confinement time of 12 ms.

In the second ISX-B experiment, the decay of the Ne^{IX} toroidal rotation velocity after neutral beam shut off led to an experimental confinement time of 35 ms for the center of the plasma[2]. Applying Eq. (6) to an ion with charge Z = 9 and a central ion temperature of T_i (0) = 800 eV results in a predicted momentum confinement time of 28 ms.

In PLT, momentum confinement times of 10 - 30 ms were inferred[1] from measured toroidal rotation velocities at known momentum input. Applying Eq. (6) to a composite ion species with an effective charge Z = 2.5 and an average ion temperature $\overline{T}_i$ = 900 eV[9] results in a predicted momentum confinement time of 23 ms.

The decay of the toroidal rotation velocity of centrally peaked T_i^{XXI} after beam turn off in PDX showed a central momentum confinement time of 80 - 100 ms for PDX. These experiments were performed at 3.5 MW of beam power. For similar plasma parameters and 7.2 MW of beam power the central ion temperature in PDX was 6 keV[10]. Applying Eq. (6) to a titanium ion with charge Z = 21 and temperature T_i (0) = 2.5 keV results in a predicted momentum confinement time of 78 ms.

Preliminary data from TFTR[3] at R_o = 2.56 m for a steady-state rotation with $Z_{eff} \simeq 4$ show a central toroidal rotation velocity of (6-7) $\times 10^7$ cm/s at Ti = 3 keV with a measured momentum confinement time of 76 ms, vs 82 ms theoretical from Eq. (6).

Thus, there is good agreement between the experimentally determined confinement time and the prediction of Eq. (4) over a range of major radii (93 - 256 cm), magnetic field (1.4 - 4.7 T), ion charge (2.5 - 21) and ion temperature (500 - 3000 eV). These results are summarized in the Tables:

EXP	Charge	Ion Temp. (eV)	Major Radius (cm)	Magnetic Field (T)	Momentum Confinement Time Exp.	Eq. (6)
I	$\bar{Z}$ = 2.5	500	93	1.4	16 ms	12 ms
II	9	800	93	1.4	35 ms	28 ms
III	$\bar{Z}$ = 2.5	900	130	2.5	10 - 30 ms	23 ms
IV	21	2500	145	2.2	80 - 100 ms	78 ms
V	4	3000	256	4.7	76 ms	82 ms

The 5 experiments were as follows:

Experiment	Ion Species	Ion Atomic #	$(V_{th})_Z$ cm/sec	V_ϕ cm/sec	$V_\phi/(V_{th})_Z$
I ISX-B (st. st.)	Composite	20	6.9×10^6	$.8 \times 10^7$	1.2
II ISX-B (decay)	N_e^{1X}	20	8.7×10^6	1.2×10^7	1.4
III PLT (st. st.)	Composite	56	5.5×10^6	$.9 \times 10^7$	1.6
IV PDX (decay)	Ti^{XX1}	48	9.9×10^6	1×10^7	1
V TFTR (st. st.)	Composite			$(6-7) \times 10^7$	

Here, st. st. denotes steady state for which $\bar{V}_\phi$, the radial average, is quoted. Decay denotes a beam turn off experiment for which V_ϕ (0), the central value, is quoted.

SUMMARY We conclude that the neoclassical gyroviscosity can account for the experimental momentum confinement times, and there is no need to postulate an anomalous mechanism.

We thank Dr. S. Scott for making available the preliminary rotation data of TFTR. This work was supported by the U.S. D.O.E.

REFERENCES

1. S. Suckewer, et al., Phys. Rev. Ltr., 43, 207 (1979); also Nucl. Fusion, 21, 1301 (1981).
2.a R. C. Isler, et al., Nucl. Fusion, 23, 1017 (1983).
2.b R. C. Isler, et al., "Rotation Scalings and Momentum Confinement in ISX-B Plasmas", submitted to Nucl. Fusion 1985.
3. S. Scott, private communication, June 1985.
4. K. Brau, et al., Nucl. Fusion, 23, 1643 (1983).
5. W. M. Stacey, Jr., D. J. Sigmar, "Viscous Effects in a Collisional Tokamak Plasma with Strong Rotation", Phys. Fluids, (1985), in press.
6. J. T. Hogan, Phys. Fluids, 27, 2308 (1984).
7. S. I. Braginski, in Review of Plasma Physics, 1, Consultants Bureau, New York (1965), 205.
8. W. M. Stacey, Jr., D. J. Sigmar, Phys. Fluids, 27, 2076 (1984).
9. H. Eubank, et al., in Proc. Seventh Int. Conf. Plasma Physics and Cont. Nuc. Fusion, IAEA, Vienna (1978).
10. D. Johnson, et al., in Proc. Ninth Int. Conf. Plasma Physics and Cont. Nuc. Fusion, IAEA, Vienna (1982).

Analytical Theory of MHD Ballooning Modes

P. Andersson and J. Weiland

Institute for Electromagnetic Field Theory
Chalmers University of Technology
S-412 96 Göteborg, Sweden

Abstract:
A dispersion relation for MHD ballooning modes has been derived. Stability limits and growthrates obtained from the dispersion relation are in good agreement with numerical results. Average curvature and FLR effects can be included in the model.

We will start with the low β large aspect ratio eigenvalue equation for MHD ballooning modes ref. 1

$$[1+(sx-\alpha\sin x)]\Omega^2\phi+\frac{\partial}{\partial x}[1+(sx-\alpha\sin x)^2]\frac{\partial\phi}{\partial x}+\alpha g(x)\phi \qquad (1)$$

where $\Omega=\omega qR/v_A$, x is the poloidal angle in a infinite domain, ϕ is the electrostatic potential and $g=\cos x+sx\sin x-\alpha\sin^2 x$.

This eigenvalue equation can be solved analytically for small s and α by substituting an trial function into a quadratic form obtained directly from [1]ref 2. Due to the variational properties it turns out that a relatively simple trial function could be used.

We have after introducing the transformed potential $\psi=\phi\cdot(1+s^2x^2)^{1/2}$ and expanding in α

$$\psi_{trial}=\left(1+\alpha\frac{[\cos x+sx\sin x]}{1+s^2x^2}+\alpha^2\frac{[(1-2s^2x^2)\cos 2x+3sx\sin 2x]}{4(1+s^2x^2)^2}\right)\langle\psi\rangle \qquad (2)$$

where $\langle\psi\rangle = \begin{cases} 1 & \text{for } x\leq \kappa/s \\ e^{i\Omega(x-\kappa/s)} & \text{for } x>\kappa/s. \end{cases}$

The transition point κ/s between the constant $\langle\psi\rangle$ approximation and the conintumsolution is to be determined by the numerical results. It is then found that κ=0.25 gives very good agreement between numerical and analytical eigenfunctions. When we integrate the quadratic form from 0 to ∞ we find that

$\Omega^2\langle\psi\rangle$ and $\Omega^2 \frac{\partial^2}{\partial\chi^2}\langle\psi\rangle$ cancel each other from $x = \kappa/s$ to ∞ and that the change in $\frac{\partial\langle\psi\rangle}{\partial x}$ at $x = \kappa/s$ will introduce a new type of frequency dependence Ref. 3,4. We then have using a δ function for $\frac{\partial\langle\psi\rangle}{\partial x}$

$$\Omega^2 \int_0^\infty \langle\psi\rangle^2 dx + \int_0^\infty \langle\psi\rangle \frac{\partial^2\langle\psi\rangle}{dx^2} \approx \kappa/s\Omega^2 + i\Omega \qquad (3)$$

where the new Ω term is found to have a substantial impact on the growth rates.

We now have a dispersion relation

$$i\Omega(1+a)+\Omega^2(\kappa/s+b)\Omega^2 = \delta w$$

$$\text{where} \quad \delta w = \frac{\pi}{4s}\left[s^2 - \frac{3}{2}\alpha^2 s + \frac{9}{32}\alpha^4 - \frac{5}{2}\alpha e^{-\frac{1}{s}}\right] \qquad (4)$$

a and b represent the influence of Ω on the integrals giving δw for $\kappa = 0.25$ we have

$$a = \pi/4[-0.69+0.57\alpha^2/s-0.11\alpha^4/s\ ]$$

$$b = \frac{\pi}{4s}\,[0{,}3-0{,}18\alpha^2/s+0.03\alpha^4/s^2]$$

a and b are however only needed when we want a very accurate growthrate.

The dispersion equation (4) has been compared with results obtained by solving 1 numerically using a shooting method and infinite boundary conditions, stability limits growthrates and eigenfunctions have all been found to be in good (for small shear extremely good) agreement.

In order to include the average curvature and FLR we must add a term $2\alpha\varepsilon(1 - \frac{1}{q^2})$ to (4) (ε is the inverse aspect ratio and q is the safety factor) and substitute $\Omega(\Omega-\Omega_{*i})$ for Ω^2 where Ω_{*i} is theion diamagnetic drift frequency. The stability criteria is then.

$$\frac{1}{2}|\Omega_{*i}|\,(1+a_1)+\frac{1}{4}(\frac{\kappa}{s}+b_1)\Omega_{*i}^2+2\alpha\delta\,\frac{\pi}{4s}+\delta w \geq 0 \qquad (5)$$

where $a_1 = a - 3.6\alpha\ \delta) \frac{\pi}{4s^2}$

$b_1 = b + 2,4\alpha\ \delta \frac{\pi}{4s^3}$ and

$\delta = \varepsilon(1 - \frac{1}{q^2})$

We can now find a maximal overall stable shear ref. 5.

$$S_m = \left[0,20\Lambda + [0,07\Lambda^2 + 3,3\delta - \frac{\Lambda\delta}{0,20\Lambda+(0,07\Lambda^2+3,3\delta)^{1/2}}]^{1/2}\right]^{4/3} \quad (6)$$

where $\Lambda = k_\perp \rho_i \sqrt{\varepsilon_p}$ $\quad \varepsilon_p = [\frac{d\ln P}{dr}]^{-1}{}_R$

and ρ_i is the ion larmor radius.

References

1. J.W. Connor, R.J. Hastie and J.B. Taylor. Phys. Rev. Lett. 40, 396 (1978).

2. O.P. Pogutse and E.J. Yurchenko. Sov. J. Plasma Phys. 5, 441 (1979).

3. L. Chen, R.B. White and M.N. Rosenbluth. Phys. Rev. Lett. 52 1122 (1984).

4. J. Weiland and L. Chen. Phys. Fluids 28 1359 (1985).

5. W.M. Tang, J.W. Connor and R.B. White. Nucl. Fusion 21, 891 (1981).

NEOCLASSICAL MHD INSTABILITIES AND TRANSPORT IN TOKAMAKS

J.D. Callen and W.X. Qu*, Nuclear Engineering and Physics Departments
University of Wisconsin, Madison, WI 53706 USA

K.C. Shaing, Fusion Energy Division, Oak Ridge National Laboratory
Oak Ridge, TN 37830 USA

Neoclassical MHD Equations. The moment equation approach [1] to neoclassical-type processes is used to derive the flows, currents and resistive MHD-like equations for studying equilibria and instabilities [2] in axisymmetric tokamak plasmas. The resultant "neoclassical MHD" equations are valid for arbitrary collisionality $\nu_* \; (\equiv \nu/\varepsilon^{3/2}\omega_b)$ and low to medium mode number modes for which the electrons are fluidlike. The equations differ from the usual reduced equations of resistive MHD [3] primarily by the addition of the viscous relaxation effects within a magnetic flux surface, which cannot be neglected in the physically relevant banana-plateau collisionality regime ($\nu_* \sim 1$). The primary effects of the parallel and poloidal viscous relaxation are: (1) Damping of the poloidal ion flow to zero on the ion-ion collision time scale to yield only toroidal bulk plasma flows; (2) Addition of the bootstrap current [4] contribution to the Ohm's law due to the parallel viscous damping [at rate $\mu_e = 2.30\sqrt{\varepsilon}\,\nu_e/(1 + 1.02\,\nu_{*e}^{1/2} + 1.07\,\nu_{*e})$] of the poloidal electron flow; and (3) An enhanced (by B^2/B_θ^2) polarization drift type term due to parallel flow inertia, which increases the effective perpendicular dielectric constant to $1 + 4\pi c^2\rho_m/B_\theta^2$ and causes the equations to depend only on the poloidal magnetic field B_θ. Gyroviscosity (or diamagnetic viscosity) effects have been included to provide a proper treatment of diamagnetic flow effects. A nonlinear version of the neoclassical MHD equations has been derived and shown to satisfy an energy conservation equation with dissipation arising from Joule heating, bootstrap current effects, classical and neoclassical diffusion, and viscous heating.

For modes which are highly extended along the magnetic field lines and only slightly ($\sim \varepsilon$) ballooning, the Pfirsch-Schlüter flows and currents cancel the lowest order geodesic curvature effects so that the magnetic field curvature effects reduce to only their $\oint d\ell/B$ or flute average. Further, the net curvature effects are negligible compared to the viscous damping effects for the physically relevant banana-plateau collisionality regime ($\nu_* < \varepsilon^{-3/2}$).

Neoclassical MHD Instabilities. The possible neoclassical MHD instabilities are analogous to the resistive MHD ones [5] of the pressure-gradient-driven, tearing, and rippling type. For the pressure-gradient-driven neoclassical MHD instability [2] the expansion free energy is released through the viscous damping of the poloidal electron flow, which is proportional to the radial pressure gradient $dp/d\psi$. These modes [2] have growth rates $\gamma_\mu = n^{2/3} S_\theta^{-1/3} \beta_\theta^{2/3} (\mu_e/\nu_e)^{1/3}/\tau_{A\theta} = [4(m_e/m_i)\mu_e \omega_{*e}^2]^{1/3}$ in an $\underline{E} \times \underline{B}$ toroidal rest frame ($\omega = \omega_E + i\gamma_\mu$) and radial extent $\delta_\mu \sim n^{-1/3} S_\theta^{-1/3} [\beta_\theta (\mu_e/\nu_e)^2]^{1/6}$. They scale like the usual resistive-g modes [5] except that: (1) They depend only on the poloidal magnetic field -- the radial extent δ_μ is larger by a factor of $(q/\varepsilon)^{2/3}$ while the growth rate is about the same; (2) There is an extra parallel electron viscosity factor $\mu_e/\nu_e \approx 2.30\sqrt{\varepsilon}/(1 + 1.02\,\nu_{*e}^{1/2} + 1.07\,\nu_{*e})$, which replaces the dependence on magnetic field curvature; and (3) The modes are unstable for either sign of magnetic field curvature, but require $(dp/d\psi)(dq/d\psi) < 0$ for instability. For $\gamma_\mu < \omega_*$, diamagnetic drift frequency effects reduce the growth rate and radial extent by factors of $(\gamma_\mu/\omega_*)^2$ and $(\gamma_\mu/\omega_*)^{1/2}$, respectively.

Tearing type neoclassical MHD instabilities [6] are driven primarily by the bootstrap current effect within the resistive layer for $(\mu_e/\nu_e)\beta_\theta \gg S_\theta^{-2/5}$. Their growth rate and radial extent are approximately the same as the pressure-gradient-driven neoclassical MHD modes. They differ from the usual resistive MHD tearing modes [5] in that: (1) Their growth rate scales as $S_\theta^{-1/3}$ instead of $S^{-3/5}$; (2) Their radial extent scales as $S_\theta^{-1/3}$ instead of

$s^{-2/5}$; and (3) Their instability depends only weakly on Δ' -- since they are driven primarily by the pressure gradient source of free energy.

Finally, rippling type neoclassical MHD modes are possible with changes in the neoclassical parallel electrical conductivity $\sigma_{\parallel} = \sigma_{Sp}/(1 + \mu_e/\nu_e)$ due to density perturbation effects on μ_e/ν_e. However, these modes are only important for ν_{*e} fairly close to unity.

Turbulent Transport Effects. To estimate the anomalous transport induced by the pressure-gradient-driven form of the neoclassical MHD instabilities, we follow the procedures developed by Carreras and Diamond [7,8] for estimating transport from resistive ballooning instabilities. We find for the anomalous electron heat diffusivity $\chi_e \sim C_o(n/\mu_o)(\mu_e\beta_\theta/\nu_e)^2 \sqrt{m_i/m_e}\,/(1 + n_m^{2/3}\omega_{*o}^2/\gamma_{\mu o}^2)^{3/4}$ in which n_m is a typical mode number and ω_{*o}, $\gamma_{\mu o}$ are the diamagnetic drift frequency and mode growth rate for n = 1. The mass diffusion coefficient D is smaller by the factor $\sqrt{m_e/m_i}/(\mu_e\beta_\theta/\nu_e) \sim 1/5$, which increases with minor radius r.

From the ohmic heating power balance $\eta J^2 \sim \chi_e n T_e/a^2$, we find the scaling $\beta_\theta \sim (m_e/m_i)^{1/6}(\mu_e/\nu_e)^{-2/3} \sim 0.3$. In the outer confinement region the ω_* correction becomes negligible and $\mu_e/\nu_e \sim \sqrt{\varepsilon}/\nu_{*e}$. Then, utilizing the ohmic power balance to determine the scaling of T_e, we find for the scaling law $\tau_E \sim n_e^{13/14} a^{4/7} R_o^{5/7} q^{5/7} B_p^{1/7}$, which is close to the tokamak ohmic scaling law [9] $\tau_E \sim n_e a R_o^2 q^{0.5}$. For auxiliary heating the ν_{*e} decreases and the scaling becomes approximately (for $\mu_e/\nu_e \sim \sqrt{\varepsilon/\nu_{*e}}$) $\tau_E \sim P_{aux}^{-5/7} n_e^{3/7} a^{1/7} R_o^{12/7} I_p^{8/7}$, which is not too dissimilar from the L-mode scaling law [9] for auxiliary heated tokamaks. For $\nu_{*e} \ll 1$ the estimated χ_e is similar to but scales slightly differently (by $1/\sqrt{\varepsilon}$) than the Carreras-Diamond result [7,8].

Note that, in agreement with the empirical scaling laws for tokamaks [9], all the scaling laws derived from neoclassical MHD turbulence depend only on the poloidal magnetic field B_θ or current I_p, at least to the extent that diamagnetic drift (ω_*) effects are negligible. Also, while all neoclassical

MHD instabilities are purely growing modes in an $\underline{E} \times \underline{B}$ rest frame, in the lab frame they would be Doppler shifted by the $\underline{E} \times \underline{B}$ velocity. Thus neoclassical MHD turbulence would have lab frame frequencies that are of the order of the electron diamagnetic drift frequency ($ed\phi/dr \sim - dp/dr$ in tokamak plasmas).

In addition to the particle and electron heat transport, the turbulence due to neoclassical MHD instabilities can also affect the bootstrap current modification of the average Ohm's law, the toroidal momentum damping and, in transients, the neoclassical pinch effect.

Acknowledgement. The authors gratefully acknowledge many stimulating discussions of this work with B.A. Carreras and P.H. Diamond. This research was sponsored by the Office of Fusion Energy, U.S. Department of Energy under Contract No. DE-AC02-80ER53104 with the University of Wisconsin and under Contract No. DE-AC05-84OR21400 with Martin Marietta Energy Systems, Inc.

---

[1] S.P. Hirshman and D.J. Sigmar, Nuclear Fusion 21, 1079 (1981).

[2] J.D. Callen and K.C. Shaing, Phys. Fluids 28, 1845 (1985); K.C. Shaing and J.D. Callen, Phys. Fluids 28, 1859 (1985); J.W. Connor and L. Chen, Phys. Fluids (to be published).

[3] H.R. Strauss, Phys. Fluids 19, 134 (1976); B.V. Waddell, B.A. Carreras, H.R. Hicks and J.A. Holmes, Phys. Fluids 22, 896 (1979).

[4] R.J. Bickerton, J.W. Connor and J.B. Taylor, Nat. Phys. Sci. 229, 110 (1971); for an experimental confirmation of the existence of this current in an axisymmetric toroidal geometry see: M.C. Zarnstorff and S.C. Prager, Phys. Rev. Lett. 53, 454 (1984).

[5] H.P. Furth, J. Killeen and M.N. Rosenbluth, Phys. Fluids 6, 459 (1963).

[6] W.X. Qu and J.D. Callen, "Tearing Instabilities in the Banana-Plateau Collisionality Regime," U.W. Plasma Report 85-2, April 1985.

[7] B.A. Carreras, P.H. Diamond, et al., Phys. Rev. Lett. 50, 503 (1983).

[8] P.H. Diamond, P.L. Similon, T.C. Hender and B.A. Carreras, Phys. Fluids 28, 1116 (1985).

[9] R.J. Goldston, Plasma Phys. Cont. Fusion 26, 49 (1984).

---

*Permanent address: Southwestern Institute of Physics, Leshan, Sichuan, China

A CLASS OF SPECIAL TOROIDAL MHD EQUILIBRIA, INCLUDING MINIMUM-B

C. M. Bishop and J. B. Taylor
Culham Laboratory, Abingdon, Oxon. OX14 3DB, England
(Euratom/UKAEA Fusion Association)

Axisymmetric toroidal MHD equilibria are usually specified in terms of two functions such as the pressure profile $p(\psi)$ and poloidal current $f(\psi)$ (or something equivalent, such as the safety factor $q(\psi)$) together with appropriate boundary conditions. An interesting, and potentially important, question is whether an equilibrium is uniquely determined by other data. Recently, Christiansen and Taylor[1] showed that the shape of the magnetic surfaces alone can uniquely determine an axisymmetric equilibrium and described a method for constructing the current profile from the shape of the surfaces in both toroidal and linear systems. In the linear case, the construction obviously fails when the magnetic surfaces in question are concentric circular cylinders, since an infinity of different pressure and current profiles lead to equilibria with such magnetic surfaces. In this paper we show that there is an analogous configuration of <u>toroidal</u> magnetic surfaces with the corresponding property that they arise from many different plasma equilibria. These equilibria include toroidal minimum-B configurations.

In a cylindrical coordinate system R, ϕ, Z the magnetic field can be written $\underset{\sim}{RB} = \left(\underset{\sim}{e}_\phi \times \nabla\psi + \underset{\sim}{e}_\phi f(\psi)\right)$ and in MHD equilibrium $\psi(R,Z)$ satisfies the equation

$$\Delta^+(\psi) \equiv R^2\nabla\cdot\left(\frac{1}{R^2}\nabla\psi\right) = -\mu_0 R^2 p'(\psi) - ff'(\psi) \qquad (1)$$

where $p(\psi)$ is the plasma pressure. If a different magnetic field, given by $\underset{\sim}{RB} = \underset{\sim}{e}_\phi \times \nabla\chi + \underset{\sim}{e}_\phi F(\chi)$, has identical magnetic surfaces then $\chi = \chi(\psi)$ and

$$\Delta^+\chi = \frac{d\chi}{d\psi}\Delta^+\psi + \frac{d^2\chi}{d\psi^2}\left|\nabla\psi\right|^2 \qquad (2)$$

so that $\chi(\psi)$ is also an MHD equilibrium if, and only if,

$$\left|\nabla\psi\right|^2 = \alpha(\psi) + \beta(\psi) R^2 \qquad (3)$$

where α and β are arbitrary functions of ψ. Hence, if one can find a solution of Eq. (1) which also satisfies (3), then there will be a whole family of "degenerate" equilibria which have exactly the same magnetic

surfaces. To calculate these surfaces we write $\nabla\psi = R^2 g(\psi,R)\underset{\sim}{e}$ where $\underset{\sim}{e}$ is a unit vector $(e_R, 0, e_Z)$ and $g^2 = (\alpha(\psi) + \beta(\psi)R^2)/R^4$. Then the Grad-Shafranov equation (1) can be used to show that

$$e_R = h(\psi,R)/g(\psi,R) \tag{4}$$

$$\text{where} \quad h(\psi,R) = \frac{L(\psi)}{2}\,\frac{(R^2 - R_0^2)}{R} + \frac{M(\psi)}{R}\log R/R_0 \tag{5}$$

$$\text{and} \qquad L(\psi) \equiv -(p' + \beta'/2) \;, \quad M(\psi) \equiv -(ff' + \alpha'/2) \;. \tag{6}$$

These equations define a single magnetic surface in terms of the three parameters L, M and R_0 but several restrictions have to be imposed on these parameters. One is to ensure that the surface should be a smooth closed curve - but it is convenient to defer this until other conditions have been dealt with. These stem from the requirement that $\nabla\times(R^2 g\underset{\sim}{e}) = 0$. Introducing (R, ψ) as independent variables this leads to the condition

$$\frac{R^3 h}{2}\frac{\partial q^2}{\partial\psi} - R^3 g^2\frac{\partial h}{\partial\psi} + \frac{R}{2}\frac{\partial q^2}{\partial R} - \frac{R}{2}\frac{\partial h^2}{\partial R} + 2(g^2 - h^2) = 0 \;. \tag{7}$$

At this point it is convenient to introduce new quantities $P \equiv \alpha/L^2$, $Q \equiv \beta/L^2$ and $X \equiv R_0^2$. Then Eq. (7) is satisfied if, and only if, $M = 0$ and

$$\text{(i)} \quad \frac{dP}{d\lambda} = \frac{4Q^2}{P + XQ} - X \;, \quad \text{(ii)} \quad \frac{dQ}{d\lambda} = 3 \;, \quad \text{(iii)} \quad \frac{dX}{d\lambda} = \frac{-2Q}{P + XQ} \tag{8}$$

where $d\lambda = d\psi/L(\psi)$.

The result $M = 0$ implies that $f^2(\psi) + \alpha(\psi) = \text{constant}$. Hence in degenerate equilibria the total magnetic field is of the form $B^2 = f^2/R^2 + |\nabla\psi|^2/R^2 = \beta(\psi) + k/R^2$. Equilibria with $k = 0$ have been investigated by Palumbo and termed Isodynamic.

With $M = 0$ and $x = R^2$, the equation for a single magnetic surface (4) can now be written

$$\frac{dZ}{dx} = \frac{(x - X)}{4\left[P + Qx - x(x - X)^2/4\right]^{1/2}} \tag{9}$$

and the surface closure condition $\oint dZ = 0$ is given in terms of complete elliptic integrals. Note that $L(\psi)$ no longer appears explicitly in the problem and can be chosen arbitrarily. This reflects the degeneracy of the plasma equilibria we are seeking. However, the magnetic surfaces themselves

are unique, up to a scale transformation $X \to \mu X$, $P \to \mu^3 P$, $Q \to \mu^2 Q$, $\lambda \to \mu^2 \lambda$, which merely magnifies and re-labels the surfaces.

The surfaces are calculated as follows. We use the scale invariance to set $X = 1$ at the magnetic axis. Then the closure condition shows that near the axis $P \to 0$, $Q \to 0$ with $P/Q = -1/3$. Using these as starting values, $P(\lambda)$, $Q(\lambda)$ and $X(\lambda)$ are computed from the differential equations (8). [We set $\lambda = 0$ on the axis so that $Q(\lambda) = 3\lambda$ and a very good approximation to the computed results is $P(\lambda) = \lambda(10\lambda - 1)$ and $X(\lambda) = 1 - 3\lambda$.] Once $P(\lambda)$, $Q(\lambda)$ and $X(\lambda)$ are known the individual magnetic surfaces are computed from (9) and the complete configuration built-up surface by surface. The result is shown in Fig. 1. [It can be shown that if the initial values of P , Q and X correspond to a closed surface then subsequent surfaces are also closed, i.e. development of P , Q and X according to the differential equations (8) preserves closure.] The equilibrium quantities p , f , α and β can then be calculated in terms of P and Q . This method of construction can be summarised as follows. We first obtain an equation for a <u>single</u> magnetic surface; this contains three unknown parameters. The condition that this single surface be part of a global equilibrium imposes constraints in the form of differential equations for these parameters and the condition that the surfaces be closed provides the initial values for these differential equations. Their solution then determines the three parameters on each magnetic surface.

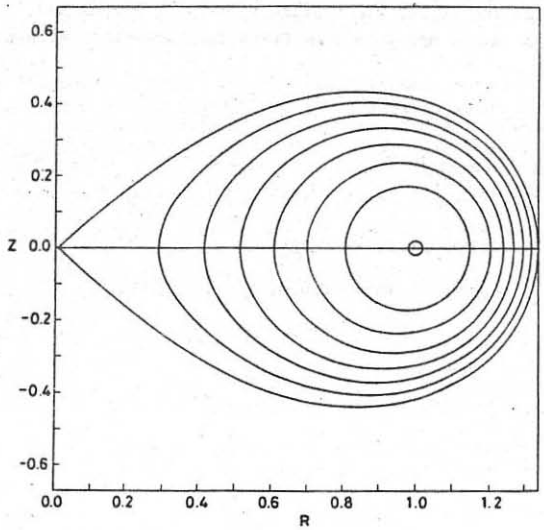


Fig. 1. The Unique Magnetic Surfaces of Degenerate Equilibria.

Among the degenerate equilibria are the isodynamic equilibria of Palumbo, in which the flux surfaces coincide with constant-B surfaces, and among these are toroidal minimum-B equilibria in which B increases and p decreases everywhere with distance from the magnetic axis. They are possible despite the well-known result[3] that there are no similar vacuum fields because they exist only at high-β and have no low-β limit. Such equilibria do not fit easily into the conventional classification of toroidal confinement systems. They differ from tokamaks in that $B_p \gtrsim B_\phi$ and from the toroidal pinch in that $q(\psi)$ is increasing with minor radius rather than decreasing, and from both in that B and q are zero on the magnetic axis. They have the property that pressure is a function only of field strength $(p = p(B))$ and that all guiding centre drifts lie in the magnetic surface, (i.e. the equilibria are omnigeneous[4,5]). Consequently, they are not subject to any neoclassically enhanced transport and are free of all trapped particles and any instabilities or anomalous transport they may cause. However, they do not possess the intrinsic MHD stability of their mirror counterparts and are unstable on axis by the Mercier-Suydam criterion. Nevertheless, their freedom from neoclassical and trapped particle effects might make them interesting if examples with gross stability could be found. In this regard, the instability to localised modes on axis need not be catastrophic - any more than it is in tokamaks with $q < 1$ or in pinches.

Acknowledgements

We are grateful for useful discussions with B. J. Braams and R. J. Hastie, and to T. J. Martin and A. Sykes for assistance with numerical computations.

References

[1] J. P. Christiansen and J. B. Taylor, Nucl. Fusion 22, 111 (1982).

[2] D. Palumbo, Il Nuovo Cimento X 53B, 507 (1968).

[3] J. D. Jukes, Plasma Physics 6, 84 (1964).

[4] L. S. Hall and B. McNamara, Phys. Fluids 18, 552 (1975).

[5] P. J. Catto and R. D. Hazeltine, Phys. Fluids 24, 1663 (1981).

Constants of the motion for inhomogeneous plasma

Erik T. Karlson
Department of Technology, Uppsala University, Box 534,
S-751 21 Uppsala, Sweden

1. Introduction. The usual way to describe motion of charged particles, and through that also the motion and behaviour of a plasma in a magnetic field that is weakly inhomogeneous and slowly varying in time, is by means of the introduction of adiabatic constants of the motion, such as the magnetic moment. Using the constants of the motion, a fluid description of the plasma becomes possible.

In many experimental and observational situations, the particle excursions are not small, and the magnetic field varies appreciably over one gyroexcursion. We will as a reference example take the Extrap configuration /1/. Other situations of this kind are reversed field pinch, multipoles, α-particles in tokamaks, etcetera. In such situations, it is not possible to use small gyroradius approximation to derive a fluid theory.

A collisionless plasma is described by the Vlasov equation, the general solution of which is an arbitrary function of the constants of the motion. The existence of a continuous symmetry implies the existence of a constant of the motion. For time-independent systems, the total energy is a constant of the motion. Unfortunately, most systems are not sufficiently symmetric for a sufficient number of constants of the motion to be found in this way. Even though systems exist, which do not have symmetries, but are still separable, in the sense that the Hamilton-Jacobi equation is separable, most systems are still non-integrable /2/.

If a sufficient number of constants of the motion can be found, it is possible, by choosing certain simple functional forms of the distribution functions, to find self-consistent solutions to the Vlasov-Maxwell system of equations /3/. In the case that systems are neither sufficiently slowly varying to possess adiabatic invariants, nor sufficiently symmetric, or otherwise separable, modifications of this method are necessary:

A. One can use the known constants of the motion, writing the distribution function as a function of these only. In this way, it is possible to derive fluid-type equations, valid e.g. for the Extrap configuration /4/. Obviously, this property of the distribution function is not generally persistent.

B. Starting with the symmetric case, one can find approximate constants of the motion for nearly symmetric systems /5/.

C. Starting with a separable potential, we find approximate constants of the motion for the case of potentials, close to a separable potential.

For may systems, a small change in the parameters might lead to a large change in the particle trajectories. As an example, compare a straight Extrap field, with $\underline{B} = \mathrm{curl}\ \underline{A}$; $\underline{A} = A(r,\theta)\ \underline{e}_z$, to the corresponding circular pinch. For the Extrap case, there are three kinds of trajectories; 'free', semi-trapped, and trapped.

For the circular case, only the first two types of trajectories exist.

If we start from the circular case, a small change in the potential might change some trajectories completely. Mathematically this would turn up in the form of resonances.

To avoid this, we suggest a completely different method of analyzing particle motion in inhomogeneous systems. The idea is to use the motion of a particle in a separable potential as the lowest order motion, where the requirement on the separable potential is that the trajectories should be topologically the same as for the real potential. The potential, corresponding to the real field is then written as the separable potential plus a disturbance, and the particle motion and constants of the motion are found by means of (secular) perturbation theory.

2. The separable potential. A convenient separable potential is /6/

$$V(x,y) = -\frac{\alpha}{2}(x^2+y^2) + \beta(x^4+y^4+6x^2y^2) \qquad (1)$$

The Hamiltonian separates by the simple variable change $X = x + y$; $Y = x - y$, into $H_o = h + k$; $h = P_X^2 - \frac{\alpha}{4}X^2 + \frac{\beta}{2}X^4$; $k = P_Y^2 - \frac{\alpha}{4}Y^2 + \frac{\beta}{2}Y^4$

Now, this defines the constants of the motion h , k and the character of the trajectories. If $h < 0$, $k < 0$, the particles are trapped near the potential minimum in both directions. If e.g. $h < 0$, $k > 0$, there is trapping in the X-direction, whereas in the Y-direction the particle can pass the potential maximum. Finally, for $h > 0$, $k > 0$, the particles are free in the potential trough. This corresponds to the three classes of trajectories in Extrap.

As the particle motion is (multiply-) periodic, it seems natural to use action-angle variables. However, we will instead use (h, k) as (momentum) variables, and find the canonically conjugate variables. This makes the inversion of the transformation much simpler, and also avoids unphysical resonances. We transform then from (P_X, X) to new variables (h, Q_X) through a generating function

$$F_2(h,X) = \int^X dx \sqrt{-\frac{\beta}{2}x^4 + \frac{\alpha}{4}x^2 + h}\,, \quad Q_X = \frac{\partial F_2}{\partial h} \qquad (2)$$

Now, if $h < 0$, Q_X is an elliptic integral of the first kind, and we can invert to get X as a function of Q_X, expressed in snoidal functions. In the same way, if $k > 0$ we get Y in terms of a cnoidal function. Obviously, if h and k are both negative, the frequencies for the X- and Y- motion are equal for $h = k$. Also, the variation of frequency with amplitude is weak, except when the particles are close to the trapping limit. Thus, we remove the resonance corresponding to $h = k$ by introducing the generating function

$$F = (Q_X - Q_Y)J_1 + (Q_X + Q_Y)J_2, \text{ or}$$

$$h = J_1 + J_2;\ k_Y = -J_1 + J_2;\ \theta_1 = Q_X - Q_Y\ ;\ \theta_2 = Q_X + Q_Y\ ;\ H_o = 2J_2 \quad (3)$$

If both h and k are positive, then again the frequencies are equal, if the energies are equal. The variation of the frequency with amplitude is slow if the particles are far from (above) the trapping limit, and thus the same transformation is used to remove the resonance.

If e.g. $h < 0$, $k > 0$ ('semi-trapped' particles), the situation is more complicated. The X-frequency ω is again slowly varying with amplitude, whereas Q defined by means of the time to move between two minima in the Y-direction, varies faster with energy, the closer we are to the trapping limit. For a range of energies, ω and Q are close to each other, and we can again remove the resonance by a generating function, similar to F.

3. The disturbed Hamiltonian. The total Hamiltonian, assuming no electric field, is given by $H = T + V$; $T = \frac{1}{2}(p_x^2 + p_y^2)$; $V = \frac{1}{2}(p_o - eA(r,\theta))^2$
The form of $A(r,\theta)$ could be chosen at will, the final intention being to get a self-consistent field. Here, we will choose a convenient magnetic field of the Extrap typ

$A(r,\theta) = \gamma r^2(1 - \frac{1}{3}\cos 4\theta)$, giving

$$H = H_o + H_1;\ H_1 = -\frac{\alpha}{4}\ \frac{(X^2 - Y^2)^2}{X^2 + Y^2} + \frac{\beta}{4}(X^2 - Y^2)^2\left(1 + \frac{(X^2 - Y^2)^2}{(X^2 + Y^2)^2}\right) \quad (5)$$

where X and Y are given in terms of elliptic functions. X, Y, h, and k are expressed in J_1, J_2, θ_1, and θ_2 for trapped particles, and in a similar way for semitrapped particles. For perturbative treatment, we write $H = H_o + \eta H_1$,
For small amplitudes, the snoidal function can be replaced by a sine-function, for larger amplitudes it can be Fourier-expanded in terms of the Nome /7/. As ω and Q are nearly equal, θ_1 is slowly varying while θ_2 varies quickly. We take the mean value over θ_2, and for small amplitude, trapped particles we get a constant of the motion to first order

$$\bar{J}_1 = \frac{1}{2}\left[\left(J_2 + \frac{\alpha^2}{32\beta}\right)^2 - J_1^2\right]^{1/2} \cos\left(\sqrt{\varepsilon\alpha}\,\theta_1\right) \quad (6)$$

with a more complicated expression for larger amplitudes. For semi-trapped particles, we make the same kind of perturbation treatment to find an expression for the constant of motion, now by an expansion of the cnoidal function. Again, for the 'free' particles, a third treatment of this kind gives a third form of the constant of the motion.

4. Higher order approximations. The computation of constants of the motion by means of perturbation theory is useful if the procedure is convergent. The KAM theorem tells us that if a system is perturbed slightly from an integrable system fulfilling certain conditions, most invariant phase spece tori survive, i.e. constants of the motion exist. Thus, ηH_1, has to be small in order to secure the existence of the tori. Now, the real system corresponds to $\eta = 1$, and the disturbance is not small. However, first order perturbation with η small gives a disturbed system, fulfilling the conditions of the KAM theorem, and we can take this as the new unperturbed system, etcetera, corresponding to computation of higher order approximations. This is carried out by means of Lie transformation methods.

References

1. Lehnert, B. (1982). Unconventional Approaches to Fusion (B. Brunelli and G. Leotta, eds.) p. 135, Plenum Press, New York
2. Poincare', H. (1892). Les Methodes Nouvelles de la Mècanique Cèleste, Gauthier-Villars, Paris
3. Sestero, A. (1966), Physics of Fluids 9, 2006, Åkerstedt, H.O., (1981), Physica Scripta 24, 775
4. Ågren, O. and Persson, H., (1984), Plasma Physics and Controlled Fusion, 26, 1177
5. Mynick, H.E. (1980). Physics of Fluids 23, 1888
" " " (1980). Physics of Fluids 23, 1897
6. Bountis, T., Segur, H., and Vivaldi, F., (1982). Phys. Rev. A25, 1257.

DEPARTURE OF RUN-AWAY ELECTRONS AND THE FAN-LIKE INSTABILITY IN TOKAMAK

V.V.Parail, O.P.Pogutse, I.A.Voitsekhovich

I.V.Kurchatov Institute of Atomic Energy,
Moscow, USSR

By the present time, a kinetic instability connected with the run-away electron beam production in plasma has got rather complete theoretical explanation (see, e.g. /1/). However, the simulation of the instability development dynamics made recently has shown /2/ that , after its first burst, a quasi-steady state operation with excited oscillations, accompanied by a slow growth of the beam energy, is reached. A possibility of explaining the periodic nature of the instability by the anomalous loss of fast particles is shown in a given paper. Two such mechanisms have been studied at present. First of them is related to a quasi-linear diffusion along the radius of resonance electrons interacting with the high $K_\perp$ -oscillations excited during the instability. The characteristic life time of particles in this interaction is equal (by the order of magnitude) to $\tau_1 \sim 1/\alpha \mathcal{D}_0$, where $\alpha = (K_\perp/K_\parallel)^2 (V_{Te}/a\omega_{pe})^2$; a is the minor plasma rdius, $\mathcal{D}_0$ is the coefficient of quasi-linear diffusion (see Eq.(1)). The second mechanism of departure is related to the stochastic diffusion of banana electrons /3/. The first mechanism will be analyzed in detail in a given paper.

Let us consider qualitatively how the presence of the resonance electron departure mechanism can affect the nature of the fan-like instability development. We shall use a one-dimensional set of quasi-linear equations for the electron distribution function, $f(x)$, and for the function of spectral energy oscillations, W_K , to describe the instability dynamics after the first burst:

$$\frac{\partial f}{\partial t} = -\varepsilon \frac{\partial f}{\partial x} + \frac{\partial}{\partial x} \frac{1}{x^2} \left(f + \frac{1}{2x} \frac{\partial f}{\partial x} \right) + \frac{\partial}{\partial x} \mathcal{D}_0 \frac{\partial f}{\partial x} - \alpha \mathcal{D}_0 f \qquad (1)$$

$$\frac{\partial W_K}{\partial t} = \left(\sqrt{\pi} \frac{\omega}{J} \frac{\omega_{pe}^2}{K^2 V_{Te}^2} \int dx\, K_\parallel \delta\left(\frac{\omega}{V_{Te}} - K_\parallel x \right) \frac{\partial f}{\partial x} - 1 \right) W_K \qquad (2)$$

Here, $\mathcal{D}_0 = \frac{2\pi\omega_{pe}^2}{\nu\omega}\int d\vec{k}\left(\frac{k_\parallel}{k}\right)^2 W_k\,\delta\left(\frac{\omega}{v_{Te}} - k_\parallel x\right)$, $f = \int d\vec{v}_\perp f$, $\varepsilon = eE/m\nu v_{Te}$. A set (1), (2) is written in dimensionless variables $x = v_\parallel/v_{Te}$, $t \to t\nu$, $f \to f\sqrt{\pi}\,v_{Te}/n$, $W_k \to W_k \frac{\omega}{nTv_{Te}}$. It is evident that Eqs. (1), (2) are not applicable in the Doppler resonance range, where isotropization, f, in the velocity space occurs. It is shown below that this range doesn't affect the nature of the instability development and can be replaced by an equivalent boundary condition of absence of the particle flux towards the Doppler resonance range at $W_k \neq 0$. As it is shown in /2/ at $\alpha = 0$ the set (1), (2) allows a stationary solution with excited oscillations; in this case, the particle flux, due to an external electric field E, is compensated by a counter-streaming quasilinear flux, due to excited oscillations, in the Cherenkov resonance range, where $x > x_c = 1/\sqrt{\varepsilon}$:

$$f(x \geq x_c) = f(x_c) + \frac{\nu}{\sqrt{\pi}\omega}\left(\frac{1}{x_c} - \frac{1}{x}\right) \qquad (3)$$

$$\mathcal{D}_0(x) = \sqrt{\pi}\,\frac{\omega}{\nu}\,(\varepsilon x^2 - 1)\,f(x_c) \qquad (4)$$

The solution (3-4) is valid in a range $x_c \leq x \leq x_c(1+\omega_{Te}/\omega_{pe})$ The Doppler resonance range starts, when $x > x_c(1+\omega_{Be}/\omega_{pe})$. Let us see how the solution (3-4) is varied with due regard for the finite life time of resonance particles ($\alpha \neq 0$).For this, we remind that the solution of Eq.(1), in the absence of instability $\mathcal{D}_0 = 0$ dependent on the particle flux Γ towards the run-away region, has a form /1/:

$$f(x) = e^{-x^2 + \frac{\varepsilon}{2}|x^3|x} - \frac{\Gamma}{\varepsilon}\,e^{-x^2+\frac{\varepsilon}{2}|x^3|x}\left(1 - e^{x^2 - \frac{\varepsilon}{2}|x^3|x}\sqrt{\frac{2}{\varepsilon}}\,J(x,\varepsilon)\,e^{\frac{1}{2\varepsilon}}\right) \qquad (5)$$

$$\sqrt{1/2}\,x - 1/\sqrt{2\varepsilon}$$

where $J(x,\varepsilon) = \int_{-1/\sqrt{2\varepsilon}} \exp(-\xi^2)\,d\xi$

It is easy to show that the solution (5) is limited at $x \to \infty$, when the condition

$$\Gamma > \Gamma_0 = \frac{\varepsilon^{3/2}}{\sqrt{2\pi}}\,e^{-1/2\varepsilon} \qquad (6)$$

is satisfied, and hence the stationary solution (4-5) cannot exist. Let us estimate now a flux Γ_α, which is provided by the departure mechanism discussed at a noise level satisfying (4):

$$\Gamma_\alpha = \int_{x_c}^{x_c(1+\omega_{Be}/\omega_{pe})} \alpha D_0(x) f \, dx \simeq \alpha \sqrt{\pi} \frac{\omega_{Be}}{\vartheta} \frac{1}{x_c} f^2(x_c) \qquad (7)$$

From (6) and (7) it follows that the stationary solution (3-4) with excited oscillations is not realized, when an inequality

$$\alpha > \alpha^* = \sqrt{2} \frac{\vartheta}{\omega_{Be}} \sqrt{\varepsilon} \, e^{1/2\varepsilon} x_c / \left(1 + 1/\varepsilon x_c^2\right)^2 \qquad (8)$$

is satisfied, and the instability should be of relaxational nature under these conditions. The inequality (8) is a sufficient condition for the relaxational nature of instability because both the analytical /1/ and numerical /2/ calculations show that the level of oscillations, after the first burst of instability, considerably exceeds the stationary distribution described by the relationship (3). Therefore, the particle departure mechanism, proportional to αD_0, should result in a relaxational nature of instability at $\alpha < \alpha^*$ also. In order to prove it, the set of equations (1-2) was integrated numerically according to the following scheme. First, Eq. (1) was numerically integrated at $D_0 = 0$, $f(t=0) = \exp(-x^2)$ and the solution obtained, $f(x,t)$, was analyzed for stability. The calculation was interrupted, when a point, at which an increment in the oscillation drive due to the Doppler resonance exceeded the Cherenkov damping decrement, appeared on the distribution function. Then, f was analytically rebuilt, according to the scheme described in /1/, and the set (1-2) was numerically integrated again.

The results of calculations are given in Figs.1-2. At $\alpha = 0$ according to /2/, the solution (1-2) reaches the steady state operation with excited oscillations. When $\alpha \simeq 5 \cdot 10^{-6}$, after the first burst of instability, the energy of oscillations drops down to a thermal noise level for $t \simeq 7$; f is considerably lower, in this case, than a level at which an instability due to the anomalous Doppler resonance emerges. Thus, from calculations it follows that the regard for a quasilinear departure of resonance particles from plasma in the real range of parameters results in a relaxational nature of the fan-like instability development.

The authors are thankful to G.V.Rereverzev for numerous useful discussions.

References

1. V.V.Parail, O.P.Pogutse. Voprosy teorii plasmy, issue II, p.5, Moscow, Energoizdat, 1982.
2. L.Muschietti, K.Appert, J.Vaclavic, Phys. Fluids, 25 (7), 1982, p.1187.
3. V.V.Parail, P.N.Yushmanov. European Conf. on Plasma Physics and Contr. Fusion, Budapest, 1986.

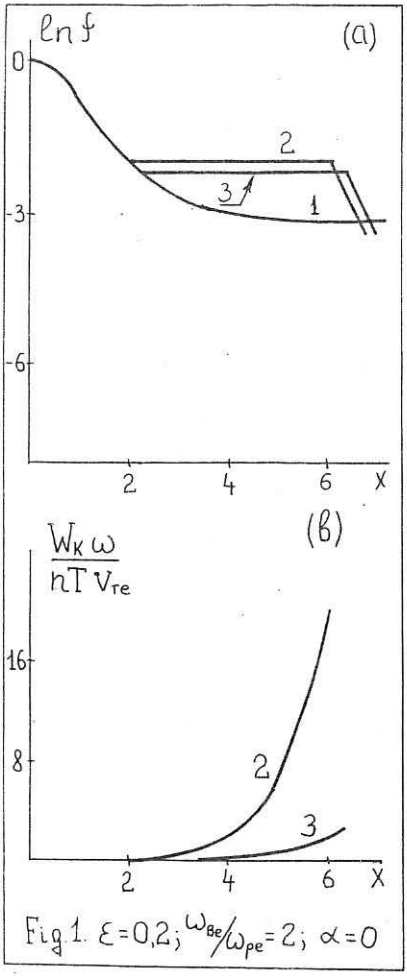


Fig.1. $\varepsilon=0{,}2;\ \omega_{Be}/\omega_{pe}=2;\ \alpha=0$

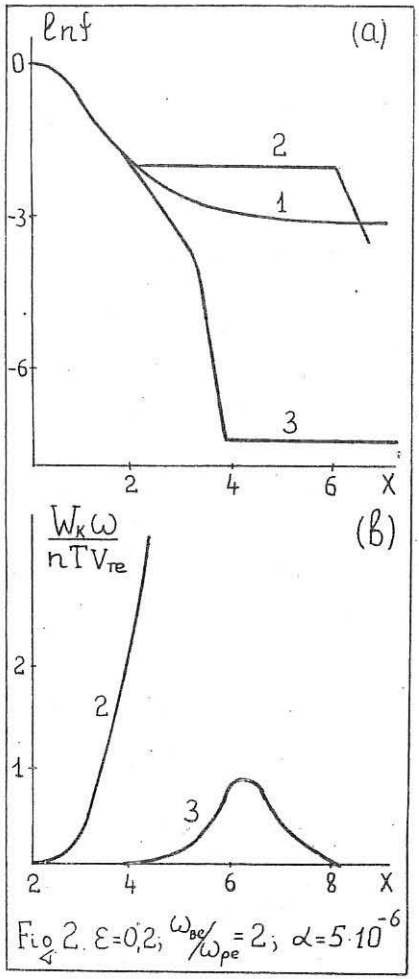


Fig.2. $\varepsilon=0{,}2;\ \omega_{Be}/\omega_{pe}=2;\ \alpha=5\cdot10^{-6}$

THEORY OF DISSIPATIVE BALLOONING MODES IN TOKAMAK AT A FINITE SOUND SPEED

A.D.Beklemishev, E.I.Yurchenko

I.V.Kurchatov Institute of Atomic Energy,
Moscow, USSR

The effect of a sound speed or plasma compressibility on the development of dissipative ballooning modes in tokamak has been studied in some papers /1-3/. The procedure developed in /1,2/ has not allowed to find a radial structure of unstable modes. A discrete variational method is being developed in this paper for description of an arbitrary radial structure at a finite sound speed.

According to the method developed in /4/, a set of equations for low-scale Alfven and ion-sonic oscillations can be written in a form:

$$\frac{c^2}{4\pi}\hat{k}_\parallel \Delta_\perp \frac{\hat{k}_\parallel}{D}\varphi + c\left[\nabla\frac{1}{B_0^2}\times\vec{B}_0\right]\nabla p - \gamma\frac{c^2}{B_0^2}\rho_0\Delta_\perp\varphi = 0 \quad , \qquad (1)$$

$$\left(1-\frac{c_s^2}{\gamma^2}\hat{k}_\parallel^2\right)p = \frac{cp_0'}{\gamma\sqrt{g}B_0^3}\frac{\partial}{\partial\theta}\left(1-\frac{c_s^2}{\gamma^2}\hat{k}_\parallel\frac{\hat{k}_\parallel}{D}\right)\varphi - \frac{\rho_0 c_s^2 c_{\omega t}}{\gamma}\frac{\vec{B}_0}{B_0^2}\nabla\varphi \quad . \qquad (2)$$

Here, $\hat{k}_\parallel = (B_0^3)^{-1}\vec{B}_0\nabla$, $D = 1 - a^2\Delta_\perp/\gamma\tau_s$, c_s is the sound speed; γ is the increment; τ_s is the skin time; p and φ are the perturbations in pressure and in potential, respectively; a, θ, ζ are the coordinates in which the field lines are straightened.

Let us expand the perturbations into a Fourier series: $\varphi(a,\theta,\zeta) = \sum_m \varphi_m(a)\exp(im\theta - in\zeta)$. For representing an eigenfunction, one should know the local radial dependence of each harmonic and the distribution of relative harmonic amplitudes along the radius, as $\varphi_m(a)$ are localized in the vicinity of resonance surfaces, $a = a_m$ ($q(a_m) = m/n$, $q(a) \equiv aB_0^\zeta/RB_0^\theta$). This distribution determines a global radial structure /5/.

Let us introduce a new radial variable, $m - nq(a)$ in each equation of a set obtained for the Fourier harmonics and then, with the Fourier transform, make a transition to a

single variable, y : $\varphi_m(a) = \int_{-\infty}^{+\infty} \varphi_m(y) \exp[-i(m-nq(a))y]\,dy$.

The second subset for harmonics $p_m(y)$ can be solved by the averaging technique for aperiodic perturbations with a rather high increment.

For a tokamak with circular magnetic surfaces, the problem is reduced to the solution of the following set of equations:

$$\Gamma^2 N^{-2}\left(1+\frac{2q^2}{1+\Gamma^2 C_0^{-2}}\right)(1+t^2)\varphi_m = \frac{d}{dy}\left[\frac{1+t^2}{1+\Gamma^{-1}(1+t^2)}\frac{d\varphi_m}{dy}\right] - \alpha V\varphi_m +$$

$$+ \frac{d}{dy}\left[(1+\Gamma^{-1}(1+t^2))^{-2}\left(\mathcal{D}\frac{d\varphi_{m+1}}{dy} + \mathcal{D}^*\frac{d\varphi_{m-1}}{dy}\right)\right] - \frac{\alpha}{2}\left(L\varphi_{m+1} +\right.$$

$$\left. + L^*\varphi_{m-1}\right) - \alpha^2(1+t^2+2S)\left[2\Gamma(1+\Gamma^2C_0^{-2})(1+\Gamma N^{-2}t^2)\right]^{-1}\varphi_m \,. \qquad (3)$$

Here, $\Gamma = N\gamma\tau_\theta$, $\tau_\theta = Rq/C_A$, $N = \tau_s/n^2q^2\tau_\theta$, $N \gg 1$; $C_0 = NC_s/C_A$. $t = Sy$, $S = q'a/q \le 1$ is the shear, $L = (1-it)e^{iy}$, $\mathcal{D} = -\frac{\alpha}{4}(1-it)^2e^{iy}$, $\alpha = -8\pi p_0' Rq^2 B_0^{-2}$, $V = \frac{\alpha}{2} - \frac{S}{4} + \varepsilon(1-q^{-2})$, V is the magnetic well.

The equations for averaged components of the Fourier harmonics $\bar{\varphi}_m$ are separated after averaging over fast oscillations included into the coefficients D and L. As a result, one can find asymptotic eigenfunction of the set (3), dependent on relative amplitudes of averaged components of the Fourier harmonics A_m. The substitution of these functions as trial ones into a functional corresponding to the set (3) results in a quadratic form with respect to A_m.

For an electromagnetic branch of the ballooning instability, when the interaction of local solutions is of importance (characteristic $t \sim 1$), the global radial structure and an increment (A_m, γ) are found from the solution to a set of algebraic equations:

$$\left\{\Gamma N^{-1}\left(\frac{2S^2}{\pi}\left[1+\frac{2q^2}{1+\Gamma^2C_0^{-2}}\right]\right)^{1/2} - \frac{S^2}{2(\Gamma+1)} + K\right\}A_m = \frac{3}{4}\alpha e^{-1/S}\left(A_{m+1}+A_{m-1}-2A_m\right), \qquad (4)$$

$$K(\alpha,S) \equiv \frac{S^2}{2} + \alpha\varepsilon(1-q^{-2}) - \frac{S\alpha^2}{2} - \frac{3}{2}\alpha e^{-1/S}.$$

The amplitudes A_m differ from zero only for those harmonics for which the resonance surfaces a_m are within the plasma column at a given n. It follows from (4) that a certain

set of poloidal harmonics possess maximal increment (Fig.1).

It has been assumed that $\Gamma^2 \gg S^2 C_0^2 / t_0^2$ in the derivation of the set (3); if an inverse relation is satisfied, a nonperiodic ballooning instability will be suppressed by the ion sound. For an electromagnetic branch (Fig.3, curve I), this results in the emergence of a threshold in the pressure gradient $\alpha_1 \simeq \alpha_K + S(2C_0)^{-1}(\partial K/\partial\alpha)^{-1}_{\alpha=\alpha_K}$ where α_K is the ideal instability threshold /4/. At a high sound speed, $\alpha_1 \to \alpha_K$ i.e. at $C_S > C_A / NS$, a slow electromagnetic mode is suppressed, and only an ideal branch remains unstable.

For an electrostatic branch, the lowest scale one along the radius, ($t \sim N^{1/3}$), the dispersion relationship follows from the set (3):

$$\Gamma^3 + C_S^2 C_A^{-2}(1+2q^2)\Gamma N^2 = \alpha^2 N^2/2 \qquad (5)$$

The dependence of an increment of α is given in the curve 2, Fig.3. In this case, a threshold connected with a sound, $\alpha_2 = C_S^2 C_A^{-2}[2S^4\varepsilon^{-1}(1+2q^2)^2]^{1/4}$, also takes place. At $\alpha > \alpha_2$ the perturbations localized at the adjacent resonance surfaces develop with their increments (5) independently (Fig.2), as their interaction is exponentially small ($\sim exp(-N^{2/3}/S)$). In this case, contrary to the electromagnetic one, a global radial structure does not emerge.

Aperiodic instability is absent for the thresholds α_1, α_2 and the branches transit into a range of complex increments.

References

1. O.P.Pogutse, E.I.Yurchenko. Pis'ma J.Ehksp. Teor. Fiz. 1978, v.28, p.344.
2. A.B.Mikhailovskii, E.I.Yurchenko. Fizika plasmy, 1983, v.9, p.707.
3. T.C.Hender, B.A.Carreras et al. Preprint Univ. of Texas, Austin , 1983, DOE/ET - 53088-108.
4. O.P.Pogutse, E.I.Yurchenko. In "Voprosy teorii plasmy" Ed.Kadomtsev B.B., Energoizdat, 1982, issue II, p.56.
5. J.W.Connor, R.J.Hastie, J.B.Taylor. Proc. Roy. Soc., London, 1979, Ser. A365, p.1.

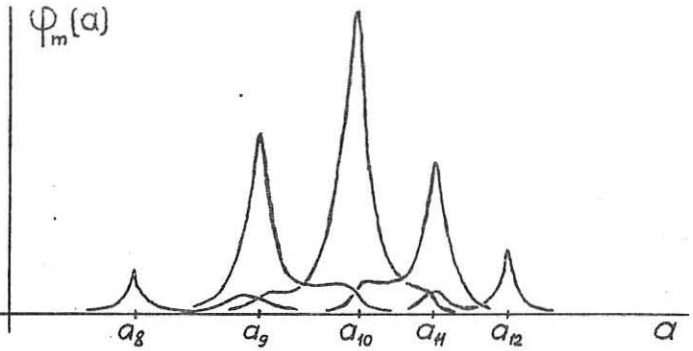


Fig 1.

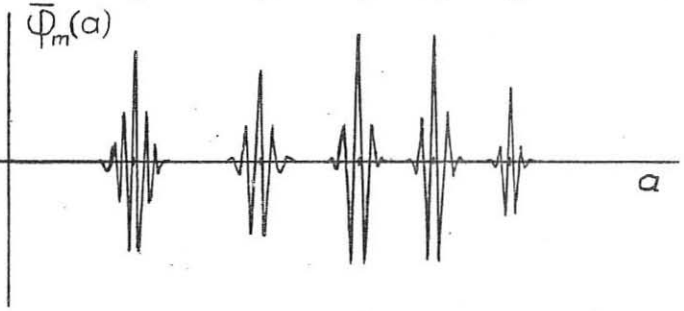


Fig 2.

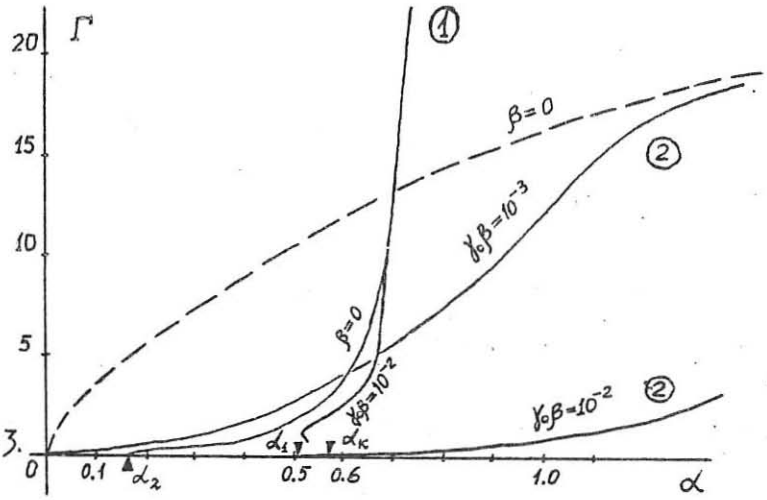


Fig 3.

ON STABILITY OF RUNAWAY ELECTRONS

N.T.Besedin, I.M.Pankratov

Institute of Physics and Technology, the Ukrainian Academy of Sciences, Kharkov 310108, USSR

Until now the theoretical analysis of the electron runaway phenomenon [1] was performed using the Landau collision integral that took into account far collisions occurring with small changes of particle momenta. The estimates made in [2] have shown that the number of runaway electrons may essentially grow due to close collisions between fast electrons of the tail and thermal electrons, as a result of which the latter ones receive the energy sufficient to become runaways.

In this report we study the beam instability of runaway electrons using the kinetic equation with the integral accounting for close collisions [3] ($f(p_\parallel, p_\perp, t)$ is the distribution function of runaways, $p_\parallel$ and $p_\perp$ being the electron momenta along and across the accelerating electric field $\vec{E}$)

$$\frac{\partial f}{\partial t} + eE\frac{\partial f}{\partial p_\parallel} = \tag{1}$$

$$= 4\pi n r_0^2 \left[\frac{p_\parallel + p_{\parallel 1}}{\sqrt{(p_\parallel + p_{\parallel 1})^2 + m^2c^2}} - \frac{p_{\parallel 1}}{\sqrt{p_1^2 + m^2c^2}}\right]^{-1} \frac{p_{\parallel 1}^4}{p_\perp^4} \frac{m^2c^2}{(p_\parallel + p_{\parallel 1})^4} \bar{f}(p_\parallel + p_{\parallel 1}, t) + St\{f\}$$

Here n is the thermal electron density, r_0 is the classical electron radius, $St\{f\}$ is the Landau collision term,

$$p_{\parallel 1} = p_\parallel \frac{p_\perp^2}{p_\parallel^2 - (\sqrt{p^2 + m^2c^2} - mc)^2}, \quad p_{\perp 1} = p_\perp, \quad p_\perp^2 < 2mcp_\parallel \tag{2}$$

Expressions (2) result from the conservation laws of colliding particle energy and momentum. For $\bar{f}(p_{\parallel 1} + p_\parallel, t)$ we have

$$\bar{f}(p_\parallel + p_{\parallel 1}, t) = \theta\left(\frac{eEt}{p_\parallel + p_{\parallel 1}} - 1\right) + 2\pi \int_0^\infty dp_\perp\, p_\perp\, f(p_\parallel + p_{\parallel 1}, p_\perp, t), \tag{3}$$

$$\theta(x) = 1, \text{ if } x \geq 0, \qquad \theta(x) = 0, \text{ if } x < 0.$$

The first term in eq.(3) describes the tail formation without close collisions and the second one takes into account the back

action of the particles, that appeared in the runaway region due to close collisions, on the runaway electron tail formation. We have calculated the relative increase of the number of accelerated electrons that does not depend on the normalizing factor of the distribution function.

Eq. (1) was solved numerically by splitting the physical processes for each time step. The first stage involves the knockout of thermal electrons to the runaway region. At the second stage the electrons move on the phase plane $(p_{\parallel}, p_{\perp})$ according to the equation ($p_{cr}^2 = 12\pi e^3 nLmE^{-1}$)

$$\frac{dp_{\parallel}}{dt} = eE\left[1 - \frac{p_{cr}^2 p_{\parallel}}{(p_{\parallel}^2 + p_{\perp}^2)^{3/2}}\right] \qquad (4)$$

We took $E = 5\cdot10^{-3}$ V/cm, the Coulomb logarithm $L = 15$, $n \approx 1.15\cdot10^{14}$ cm^{-3}, $p_{max} = 20$ mc, p_{max} being the maximum momentum of the electrons, at which the fast electrons start to leave the discharge. The second term in (4) is the friction force due to collisions of runaway electrons with the thermal particles. Electrons may run away, if the inequality $(p_{\parallel}^2 + p_{\perp}^2)^{3/2} > p_{cr}^2 \cdot p_{\parallel}$ holds. This inequality is fulfilled for the points on the phase plane (see fig.1) outside the region bounded by the curve α. The electrons knocked out from the thermal region are arranged on the elongated ellipses, some of which are shown and denoted by figures 1,2,3 in fig. 1. The electrons with $p_{\perp} > p_{\perp cr} = 0.45$ mc cannot be held by the friction force ($p_{\perp cr}$ being the maximum $p_{\perp}$ value on the curve α), and these electrons become runaways. The formation of the nonequilibrium distribution function in transverse momenta takes place ($\partial f/\partial p_{\perp} > 0$).

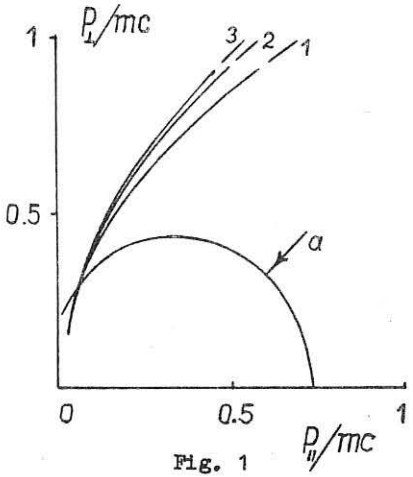


Fig. 1

The $f(p_{\parallel}, p_{\perp}, t)$ relief for the electrons knocked out to the runaway region due to

close collisions is shown (in relative units) in fig. 2a,b for two succesive moments of time. Fig. 2a corresponds to the time moment when the longitudinal momentum of the accelerated electron tail has already attained the p_{max} value. From this moment the electrons begin to leave the discharge and the break is

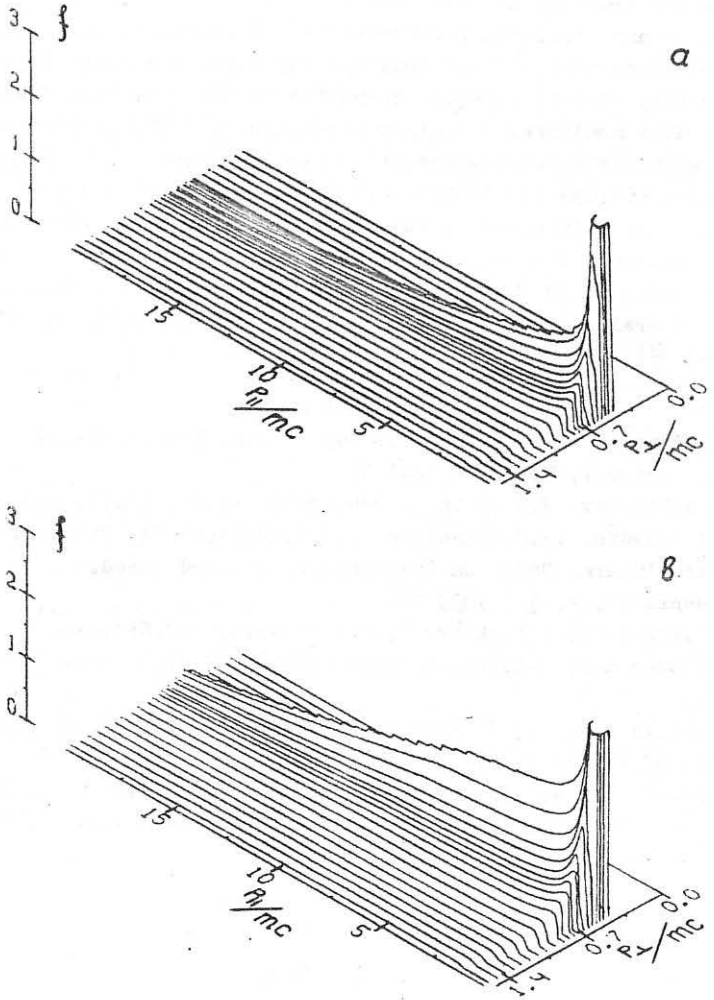


Fig. 2

formed on the distribution function relief (see fig. 2b). This break moves in the direction of larger $p_{\parallel}$ values. It is seen from fig. 2 that a nonequilibrium low-density relativistic electron beam is formed in the plasma. This beam may effectively excite electromagnetic waves under the conditions of the Cherenkov and cyclotron resonances [4]. Besides, the nonequilibrium electron distribution function may lead to a burst-like instability at semi-integral harmonics of the cyclotron frequency at a nonlinear cyclotron resonance [5]. The formation of the transverse momentum-nonequilibrium distribution function of runaway electrons due to knockout of thermal electrons to the runaway region is possible in tokamaks with good containment of fast electrons. The function of such a distribution function may be responsible for the cyclotron radiation at integral and semi-integral harmonics of the cyclotron frequency in the FT tokamak [6].

References

1. V.V.Parail, O.P.Pogutse. In: Vopr. Teor. Plazmy, is. 11, Ehnergoizdat, Moscow (1982) 3.
2. Yu.A.Sokolov. Pis'ma Zh. Ehksp. Teor. Fiz. 9 (1979) 244.
3. N.T.Besedin, Yu.K.Kuznetsov, I.M.Pankratov. In: Proc. of the XVIth Intern. Conf. on Phenomena in Ionized Gases, Dusseldorf, v. 1 (1983) 32.
4. A.I.Akhiezer, I.A.Akhiezer, R.V.Polovin, A.G.Sitenko, K.N.Stepanov. Ehlektrodinamika plazmy, Nauka, Moscow (1974) 320.
5. A.B.Kitsenko, I.M.Pankratov, K.N.Stepanov. Zh. Ehksp. Teor. Fiz. 67 (1974) 1728.
6. F.Alladio et al. In: Proc. of the 11th Europ. Conf. on Contr. Fusion and Plasma Phys., Aachen, v. 7D, part 1 (1983) 277.

A NONVARIATIONAL MHD STABILITY CODE FOR AXISYMMETRIC PLASMAS*

C.Z. Cheng and M.S. Chance
Princeton Plasma Physics Laboratory, Princeton, NJ 08544

Abstract

A Nonvariational code for determining the ideal MHD stability of axisymmetric toroidal confinement systems is presented. The code employs cubic B-spline finite elements and Fourier expansion in a general flux coordinate (ψ,θ,ζ) system. Better accuracy and faster convergence were obtained in comparison with the variational PEST and ERATO codes. The nonvariational approach can easily be extended to problems having non-Hermitian eigenmode equations.

I. Introduction

The principle motivation of the paper is to construct low-n toroidal stability codes for solving non-Hermitian eigenmode equations (eg. ideal MHD with flows, resistive MHD, and kinetic MHD, etc.) where variational energy principles can not be established. Here, we present a nonvariational ideal MHD stability code which can easily be extended to integrate non-Hermitian eigenmode equations. All the existing low-n ideal MHD stability codes[1,2] employed linear finite elements in the minor radius direction. Since they are all variational codes, the numerical errors in the eigenvalue ω^2 scale as N^{-2}, where N is the total number of the computational grid points. Therefore, our nonvariational approach requires higher order finite elements to achieve better accuracy and faster convergence. With the choice of cubic B-spline finite elements,[3] the errors in ω^2 will scale as N^{-4}.

II. Equilibrium and Flux Coordinate System

In terms of the flux coordinate system (ψ,θ,ζ), the toroidal equilibrium magnetic field can be written as $\vec{B} = \nabla\zeta \times \nabla\psi + q(\psi)\nabla\psi \times \nabla\theta$, where q is the safety factor, $2\pi\psi$ is the poloidal flux within a magnetic surface. Since $\vec{B}\cdot\nabla = \mathcal{J}^{-1}(\partial/\partial\theta + q(\partial/\partial\zeta))$, where the Jacobian is $\mathcal{J}^{-1} = \nabla\psi \times \nabla\theta \cdot \nabla\zeta$, the magnetic field line is straight. For axisymmetric equilibrium, the magnetic field can be obtained by solving the Grad-Shafranov equation and is expressed as $\vec{B} = \nabla\phi \times \nabla\psi + g(\psi)\nabla\phi$, where ϕ is the toroidal angle and $g(\psi)$ is a given function. The generalized toroidal angle ζ can then be constructed by letting $\zeta = \phi - q\delta(\theta,\psi)$, where $\delta(\psi,\theta)$ is periodic in θ and is governed by $q\,(1 + \partial\delta/\partial\theta) = g\mathcal{J}/x^2$. Note that ζ is an ignorable coordinate for axisymmetric equilibria. Once an equilibrium is constructed in terms of certain flux coordinate system, it is possible to map the equilibrium to a new flux coordinate (ψ,θ,ζ) by choosing a new Jacobian. In the paper, we choose the Jacobian in the form[4]

$$\mathcal{J}(x,z) = x^m/[\alpha(\psi)|\nabla\psi|^i B^j] \qquad (1)$$

III. Linearized Ideal MHD Eigenmode Equations

The linearized ideal MHD eigenmode equations can be written in terms of the following variables $\nabla\cdot\vec{\xi}$, ξ_s, P_1, ξ_ψ, where $\xi_s = \vec{\xi}\cdot\vec{B} \times \nabla\psi/|\nabla\psi|^2$ is the

surface displacement, $P_1 = p_1 + \vec{B}\cdot\vec{B}$ is the total perturbed pressure, $\xi_\psi = \vec{\xi}\cdot\nabla\psi$ is the radial displacement. They can be cast into the following form;

$$\nabla\psi \cdot \nabla\begin{pmatrix} P_1 \\ \xi_\psi \end{pmatrix} = C \begin{pmatrix} P_1 \\ \xi_\psi \end{pmatrix} + D \begin{pmatrix} \xi_s \\ \nabla\cdot\vec{\xi} \end{pmatrix} \quad , \tag{2}$$

$$E \begin{pmatrix} \xi_s \\ \nabla\cdot\vec{\xi} \end{pmatrix} = F \begin{pmatrix} P_1 \\ \xi_\psi \end{pmatrix} \quad , \tag{3}$$

where C, D, E, F are 2 × 2 matrix operators involving only surface operators $(\vec{B}\times\nabla\psi)\cdot\nabla$ and $\vec{B}\cdot\nabla$. Explicitly, these matrix operators are given by

$$E_{11} = \frac{2\vec{K}\cdot\vec{B}\times\nabla\psi}{B^2} \quad , \quad E_{12} = \frac{\gamma_s p_o + B^2}{B^2} + \frac{\gamma_s p_o}{\omega^2\rho}\,\vec{B}\cdot\nabla\left(\frac{\vec{B}\cdot\nabla}{B^2}\right) \quad ,$$

$$E_{21} = \frac{\omega^2\rho|\nabla\psi|^2}{B^2} + \vec{B}\cdot\nabla\left(\frac{|\nabla\psi|^2}{B^2}\vec{B}\cdot\nabla\right) \quad , \quad E_{22} = 2\gamma_s p_o \frac{\vec{K}\cdot\vec{B}\times\nabla\psi}{B^2} \quad ,$$

$$F_{11} = -\frac{1}{B^2} \quad , \quad F_{12} = -\frac{2\vec{K}\cdot\nabla\psi}{|\nabla\psi|^2} \quad , \quad F_{21} = -\frac{2\vec{K}\cdot\vec{B}\times\nabla\psi}{B^2} + \frac{\vec{B}\times\nabla\psi}{B^2}\cdot\nabla \quad ,$$

$$F_{22} = \vec{B}\cdot\nabla\left(\frac{|\nabla\psi|^2}{B^2}\hat{S}\right) - \frac{\vec{J}\cdot\vec{B}}{B^2}\vec{B}\cdot\nabla - 2p_o\frac{\vec{K}\cdot\vec{B}\times\nabla\psi}{B^2} \quad ,$$

$$C_{12} = \omega^2\rho + 2p_o'\vec{K}\cdot\nabla\psi + |\nabla\psi|^2\vec{B}\cdot\nabla\left(\frac{\vec{B}\cdot\nabla}{|\nabla\psi|^2}\right) + \left(\vec{B}\cdot\vec{J} - \hat{S}|\nabla\psi|\right)^2\frac{|\nabla\psi|^2\hat{S}}{B^2} \quad , \tag{4}$$

$$C_{11} = 2\vec{K}\cdot\nabla\psi, \quad C_{21} = 0 \quad , \quad C_{22} = -|\nabla\psi|^2\nabla\cdot\left(\frac{\nabla\psi}{|\nabla\psi|^2}\right) \quad ,$$

$$D_{11} = \left(|\nabla\psi|^2\hat{S} - \vec{B}\cdot\vec{J}\right)\frac{|\nabla\psi|^2}{B^2}\vec{B}\cdot\nabla \quad , \quad D_{12} = 2\gamma_s p_o\vec{K}\cdot\nabla\psi \quad ,$$

$$D_{21} = |\nabla\psi|^2\left(\frac{2\vec{K}\cdot\vec{B}\times\nabla\psi}{B^2} - \frac{\vec{B}\times\nabla\psi}{B^2}\cdot\nabla\right) \quad , \quad D_{22} = |\nabla\psi|^2\left[1 + \frac{\gamma_s p_o}{\omega^2\rho}\vec{B}\cdot\nabla\left(\frac{\vec{B}\cdot\nabla}{B^2}\right)\right] \quad ,$$

where $\hat{K}$ is the curvature, and $\hat{S}$ is the local shear. The boundary conditions are $\xi_\psi = 0$ at the magnetic axis, and $\xi_\psi = 0$ at plasma-wall interface for fixed boundary modes. For free boundary modes, the boundary condition at the plasma-vacuum interface is given by $\vec{b}_v\cdot\nabla\psi = \vec{B}\cdot\nabla\xi_\psi$, where $\vec{b}_v$ is the vacuum magnetic field obtained from the vacuum solution of $\nabla\cdot\vec{b}_v = 0$.

IV. Numerical Methods

To solve the linearized MHD eigenmode equations, we first represent the perturbed quantities by Fourier expansion in θ;

$$\xi(\psi,\theta,\zeta) = \sum_m \xi_m(\psi)\exp[i(m\theta - n\zeta)] \quad . \tag{5}$$

We then eliminate ξ_s and $\nabla\cdot\vec{\xi}$ in terms of P_1 and ξ_ψ. Equation (2) is then reduced to a set of L second-order differential equations in r, where L is the total number of the truncated poloidal harmonics, $r = (\psi/\psi_o)^{1/2}$. The set of

the differential equations is integrated by employing cubic B-spline[5] finite elements with

$$\xi_m(r) = \sum_{k=1}^{N+2} \xi_{mk} U_k(r) \quad , \tag{6}$$

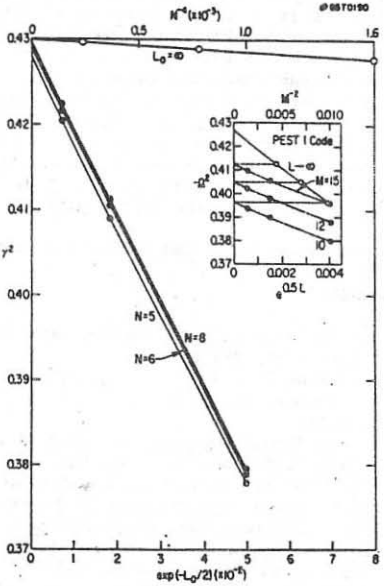
where the U's are the finite elements, N is the total number of grid points. Note that for the choice of cubic B-spline, $N \geq 5$. We can obtain a set of albegraic equations

$$\sum_{m,k}^{m'k'} M_{mk} \xi_{mk} = 0 \quad , \tag{7}$$

where $M_{mk}^{m'k'}$ is a $L(N+2) \times L(N+2)$ matrix with nonvanishing elements along its L^2 7-band-diagonals.[5] After imposing the boundary conditions to modify the matrix M, the nontrivial solutions of Eq. (7) can be obtained by requiring the determinant of the matrix M to be vanished.

V. Convergence Studies

To illustrate the convergence properties of the code, we consider the analytic Solovev equilibria[6] which have been used previously for extensive comparisons of ideal MHD stability codes. The Solovev equilibrium is characterized by three parameters; inverse aspect ratio ε, ellipticity E and safety factor at magnetic axis q(0). Numerical convergence will be shown for the small aspect ratio, elliptical case with the parameters E = 2, ε = 1/3, q(0) = 0.3, and n = 2W. We will keep the poloidal harmonics m = $(-L_o, L_o)$ and use a uniform r-mesh of N grid points. Using equal arc-length θ-coordinate the convergence curves of γ^2 scales as $\gamma^2 = \gamma_o^2 + C_1 \exp(-L_o/2)$ for fixed N and as $\gamma^2 = \gamma_0^2 + C_2 N^{-4}$ for fixed L_o. For the PEST code, γ^2 scales as $\gamma^2 = \gamma_o^2 + D_1 \exp(-L/2)$ for fixed $N(L=2L_o+1)$, and as $\gamma^2 = \gamma_o^2 + D_2 N^{-2}$ for fixed L. Convergence curves from the PEST code are also shown in Fig. 1. Detailed comparison shows that $|C_1| \sim |D_1|$ and $|C_2| \ll |D_2|$. Even with N = 5, our code converges in L_o with an error of less than 1% of its converged values. On the other hand, comparable accuracy with the PEST code would require at least 3 times as many linear finite elements. Comparison of the growth rates for different Solovev equilibria obtained from various ideal MHD stability codes [1-2,7-9] are summarized in the following table. For most of the cases, our results are roughly between those of PEST AND ERATO CODES.



COMPARISON OF γ^2 FOR DIFFERENT SOLOVEV EQUILIBRIA FROM VARIOUS IDEAL MHD STABILITY CODES

ϵ^{-1}	E	A	q(0)	q(a)	n	KERNER	PEST	ERATO	DEGTYAREV	CHENG
6	1	2	1.791	2.0	1	0.202	0.204		0.211	0.208
6	1	2	2.2387	2.5	1	0.504	0.506		0.511	0.508
3	2	1	0.3	0.5224	2	0.413	0.427	0.431	0.430	0.430
3	2	1	0.7	1.219	2	0.118	0.119	0.120	0.121	0.119
3	2	∞	1.2	2.0897	1		0.75	0.78		0.748
3	2	∞	2.0	3.4829	1		0.68	0.75		0.656
3	2	∞	0.6	1.0449	2		1.31	1.40	1.32	1.35
3	2	∞	1.0	1.7415	2		1.03	1.07	1.06	1.038

VI. Applications

We have successfully applied the code to study ballooning modes, internal kinks, external kinks, toroidal global Alfven modes and the continuum modes for various toroidal equilibria (from circular to bean-shaped and from low-β to high-β). Here, we will only show the convergence properties of different θ-coordinates when the plasma shape is far from being circular. Our numerical equilibrium is a high-β bean shaped equilibrium with $\langle\beta\rangle_{ave}$ = 8.75%, d/2a = 0.3035, b/a = 1.7385, R/a = 3.449, q(0) = 1.03, q(a) = 4.2, and n = 1F. The instability is an external kink with γ^2 = 3.5 and has maximum amplitudes near the plasma surface. The convergence in L is much more rapid for the equal arc length θ-coordinate than the PEST θ-coordinate. This is because the equal arc length θ-grids are uniformly distributed over the flux surface, but the PEST θ-grids concentrate more grid points around the tips of the bean. In this case, the equal arc length θ coordinate is rapidly convergent with an error of 2% of its converged value with $-8 \leq m \leq 8$. Comparable accuracy with the PEST θ-coordinate would require approximately 3 times as many fourier components.

*Work supported by United States DoE Contract No. DE-AC02-76-CHO-3073.

REFERENCES

1. R. C. Grimm, J. M. Greene, and J. L. Johnson, Methods in Computational Physics 16, 253 (1976).
2. R. Gruber, F. Troyon, D. Berger, L. C. Bernard, S. Rousset, R. Schreiber, W. Kerner, W. Schneider, and K. V. Roberts, Comput. Phys. Comm. 21, 323 (1981).
3. K. S. Kung, Numerical Analysis (McGraw-Hill, New York, 1957) pp. 100-103; also, C. DeBoor, J. of Approx. Theory 6, 50 (1972).
4. R. C. Grimm, R. L. Dewar, and J. Manickam, J. Comput. Phys. 49, 94 (1983).
5. J. C. Wiley, The University of Texas Report FRCR# 131 (1977).
6. L. S. Solovev, Sov. Phys. JEPT 26, 400 (1968).
7. M. S. Chance, J. M. Greene, R. C. Grimm, J. L. Johnson, J. Manickam, W. Kerner, D. Berger, L. C. Bernard, R. Gruber, and F. Troyon, J. Comput. Phys. 28, 1 (1978).
8. W. Kerner, Nucl. Fusion 16, 643 (1976).
9. L. M. Degtyarev, V. V. Drozdov, A. A. Martynov, and S. Yu. Medvedev, Proceedings of International Conference on Plasma Physics, Lausanne, Switzerland, 1985, Vol. I, pp. 157-175.

CANONICAL REPRESENTATION OF MAGNETIC FIELDS*

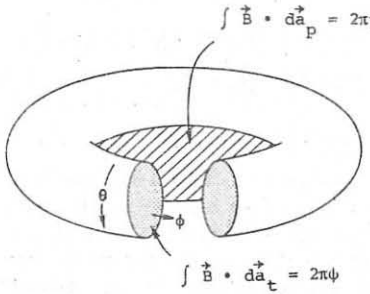
A. H. Boozer
Princeton Plasma Physics Laboratory, Princeton, NJ 08544

The canonical representation of magnetic fields[1,2] is a generalization of the magnetic coordinate representation. The existence of magnetic coordinates requires that the magnetic field lines be integrable, or form nested toroidal surfaces. The existence of canonical coordinates requires only that the field be globally divergence-free. In both magnetic and canonical coordinates, the magnetic field is represented as

$$\vec{B} = \vec{\nabla}\psi \times \vec{\nabla}\theta + \vec{\nabla}\phi \times \vec{\nabla}\chi \quad . \tag{1}$$

The toroidal flux inside a constant ψ surface is $2\pi\psi$, the poloidal flux outside a constant χ surface is $2\pi\chi$, θ is a poloidal angle, and ϕ is a toroidal angle, Fig. (1). In magnetic coordinates χ is a function of ψ alone while in canonical coordinates χ depends on ψ, θ, and ϕ. For mathematical simplicity, we assume the magnetic field has a non-zero toroidal component.

The applications of the canonical representation include the following, and efficient representation, of magnetic field lines;[1,2] toroidal equilibrium and stability calculations,[2] especially tearing modes; magnetic field evolution;[2] and particle drift orbits.[3] The canonical formulation can also be used to study other divergence-free fields such as the vorticity.



First consider the properties of magnetic coordinates. The trajectory of a field line that starts at ψ_o, θ_o is $\psi = \psi_o$ and $\theta = \theta_o + \iota\phi$ with $\iota = d\chi/d\psi$, the rotational transform [this follows from $\vec{B}\cdot\vec{\nabla}\psi = 0$ and $\vec{B}\cdot\vec{\nabla}(\theta - \iota\phi) = 0$]. The transformation equations $\vec{x}(\psi,\theta,\phi)$ from magnetic coordinates ψ,θ,ϕ to ordinary spatial coordinates give the actual location of the field lines. Once $\chi(\psi)$ and $\vec{x}(\psi,\theta,\phi)$ are evaluated in some region of space,[4] the field lines are effectively known throughout that region. The functions $\chi(\psi)$ and $\vec{x}(\psi,\theta,\phi)$ also determine the magnetic field uniquely. The dual relations of partial differentiation theory, such as $\partial\vec{x}/\partial\psi = J(\vec{\nabla}\theta\times\vec{\nabla}\phi)$ with the Jacobian $J = 1/(\vec{\nabla}\psi\times\vec{\nabla}\theta)\cdot\vec{\nabla}\phi$, imply that Eq. (1) can be written as $B = (\partial\vec{x}/\partial\phi + \iota\partial\vec{x}/\partial\theta)/J$.

The field line trajectories are more complicated to evaluate in canonical coordinates than in magnetic coordinates. Using Eq. (1), the field line equations, such as $d\psi/d\phi = \vec{B}\cdot\vec{\nabla}\psi/\vec{B}\cdot\vec{\nabla}\phi$, become

$$d\psi/d\phi = -\partial\chi/\partial\theta \text{ and } d\theta/d\phi = \partial\chi/\partial\psi \quad , \tag{2}$$

which are Hamilton's equations with one degree of freedom. The trajectories can be plotted in ordinary space using the transformation equations $\vec{x}(\psi,\theta,\phi)$. Since continuous transformations do not alter topology, the topology of the field lines is determined by the Hamiltonian $\chi(\psi,\theta,\phi)$ alone. As in magnetic coordinates, $\vec{x}(\psi,\theta,\phi)$ and $\chi(\psi,\theta,\phi)$ determine a unique magnetic field.

To prove the existence of the canonical representation, as well as to evaluate it, assume some transformation equations $\vec{x}(\rho,\theta,\phi)$ are given. The equations are arbitrary except that the Jacobian is finite, that θ and ϕ are a poloidal and a toroidal angle, and that the radial coordinate ρ is zero along the axis of the poloidal angle. The existence proof uses Poincare's theorem that a globally divergence-free field has a single-valued vector potential $\vec{A}(\vec{x})$. An arbitrary vector can be represented as

$$\vec{A} = A_\rho\vec{\nabla}\rho + A_\theta\vec{\nabla}\theta + A_\phi\vec{\nabla}\phi \quad . \tag{3}$$

By defining G so that $\partial G/\partial\rho = A_\rho$, this expression can be rewritten in the form

$$\vec{A} = \psi\vec{\nabla}\theta - \chi\vec{\nabla}\phi + \vec{\nabla}G \tag{4}$$

which has Eq. (1) as its curl.

Equations for evaluating the canonical coordinates of a given field $\vec{B}(\vec{x})$ can be derived by dotting Eq. (1) with $\vec{\nabla}\phi$ and $\vec{\nabla}\theta$ while considering ψ and χ to be functions of ρ,θ,ϕ. That is, $\partial\psi/\partial\rho = J_\rho\vec{B}\cdot\vec{\nabla}\phi$ and $\partial\chi/\partial\rho = J_\rho\vec{B}\cdot\vec{\nabla}\theta$ with J_ρ the ρ,θ,ϕ Jacobian. The dual relations of partial differentiation theory, which relate $\vec{\nabla}\theta$ and $\vec{\nabla}\phi$ to derivatives of the transformation equations $\vec{x}(\rho,\theta,\phi)$, allow one to obtain the differential equations

$$\frac{\partial\rho}{\partial\psi} = \frac{1}{\vec{B}\cdot[(\partial\vec{x}/\partial\rho)\times(\partial\vec{x}/\partial\theta)]} \quad , \quad \frac{\partial\chi}{\partial\psi} = \frac{\vec{B}\cdot[(\partial\vec{x}/\partial\phi)\times(\partial\vec{x}/\partial\rho)]}{\vec{B}\cdot[(\partial\vec{x}/\partial\rho)\times(\partial\vec{x}/\partial\theta)]} \quad . \tag{5}$$

The right-hand sides of these equations are known functions of ρ,θ,ϕ. To integrate them, one picks a value of θ and of ϕ and uses the boundary conditions, which are implied by regularity, that ρ and χ are zero at ψ equal to zero. After evaluating χ for a number of θ,ϕ values, one can use a fast Fourier transform to obtain χ in Fourier decomposed form,

$$\chi = \chi_o(\psi) + \sum\chi_{nm}(\psi)\exp[i(n\phi - m\theta)] \quad . \tag{6}$$

For an analytic field the Fourier coefficients converge exponentially; so the number of θ,ϕ values required to obtain an accurate Hamiltonian is small. In principle one should integrate $\vec{B}$ over the area enclosed by the curve $\phi = 0$ to obtain the poloidal flux $2\pi\chi_o(0)$, but this constant, which should be added to χ, is important only in time dependent problems.

There is considerable arbitrariness in the choice of canonical coordinates. This is implied by the arbitrariness of the transformation equations $\vec{x}(\rho,\theta,\phi)$, but it is more useful to consider the arbitrariness to be that of canonical transformations with the generating function $S(\theta,\bar{\psi},\phi,\bar{\chi})$. The most useful canonical coordinates are as close as possible to magnetic coordinates. This means that the Fourier coefficients χ_{nm} are zero unless $n = \iota m$ for some $\iota = d\chi_o/d\psi$ in the spatial region of interest. These resonant Fourier coefficients represent the magnetic islands or stochastic regions, which cannot be altered by canonical transformations.

An evolving magnetic field depends on a parameter t, which will be called time. Nevertheless, the parameter can be used in other ways, for example $\vec{B}(x,t) = (1-t)\vec{B}_1(x)+t\vec{B}_2(x)$ carries one magnetic field into the other as t advances from zero to one. The evolution equations[2] are simpler in terms of the vector potential $\vec{A}(\vec{x},t)$. The differentiation of Eq. (4) gives

$$\partial\vec{A}/\partial t = (\partial\psi/\partial t)\vec{\nabla}\theta - (\partial\theta/\partial t)\vec{\nabla}\psi - (\partial\chi/\partial t)\vec{\nabla}\phi + \vec{\nabla}s \qquad (7)$$

with $s \equiv (\partial G/\partial t)+\psi(\partial\theta/\partial t)$ and with $\partial\phi/\partial t$ assumed zero for simplicity. The function $s(\psi,\theta,\phi,t)$ can be chosen arbitrarily since it is the generating function for infinitesimal canonical transformations. This identification follows from dotting Eq. (7) with $\partial\vec{x}/\partial\theta$, $\partial\vec{x}/\partial\psi$, and $\partial\vec{x}/\partial\phi$ to obtain

$$\frac{\partial\psi}{\partial t} = \frac{\partial\vec{A}}{\partial t}\cdot\frac{\partial\vec{x}}{\partial\theta} - \frac{\partial s}{\partial\theta} \quad , \quad \frac{\partial\theta}{\partial t} = -\frac{\partial\vec{A}}{\partial t}\cdot\frac{\partial\vec{x}}{\partial\psi} + \frac{\partial s}{\partial\psi} \quad , \quad \frac{\partial\chi}{\partial t} = -\frac{\partial\vec{A}}{\partial t}\cdot\frac{\partial\vec{x}}{\partial\phi} + \frac{\partial s}{\partial\phi} \; . \qquad (8)$$

If $\partial\vec{A}/\partial t = 0$, these are the well-known equations for infinitesimal canonical transformations. One can use

$$\partial\vec{x}/\partial t = -(\partial\vec{x}/\partial\psi)(\partial\psi/\partial t) - (\partial\vec{x}/\partial\theta)(\partial\theta/\partial t) - (\partial\vec{x}/\partial\phi)(\partial\phi/\partial t) \qquad (9)$$

to evaluate the time evolution of the transformation equations. The most important evolution equation is

$$\frac{\partial\vec{A}}{\partial t} = -\frac{\partial\chi(\psi,\theta,\phi,t)}{\partial t}\vec{\nabla}\phi + \frac{\partial\vec{x}}{\partial t}\times\vec{B} + \vec{\nabla}s \quad . \qquad (10)$$

The dot product of this equation with $\vec{B}$ gives the time evolution of χ in canonical coordinates. The similarity of Eq. (10) and the generalized Ohm's law, $\vec{E}+\vec{v}\times\vec{B}=\eta\vec{j}$, should be noted. If the resistivity η is zero, one can choose s so that $\partial\chi(\psi,\theta,t)/\partial t$ is zero and $\partial\vec{x}/\partial t = \vec{v}$. The equation $\partial\vec{x}/\partial t = \vec{v}$ implies

that the canonical coordinates ψ,θ,ϕ and the plasma are tied together.

The canonical representation can be used with the energy principle to study not only ideal perturbations but also, by varying χ, topological changes which are tearing modes.[2] The general variation of magnetic energy can be calculated using Eq. (10) by identifying $\delta\vec{x} \equiv (\partial\vec{x}/\partial t)\delta t$ etc.,

$$\delta\int(B^2/2)d^3x = -\int\delta\vec{x}\cdot(\vec{j}\times\vec{B})d^3x - \int\vec{j}\cdot\vec{\nabla}\phi\delta\chi d^3x \ . \qquad (11)$$

If the boundary conditions of a plasma equilibrium are perturbed, then there is a relation between $\vec{j}\cdot\vec{\nabla}\phi$ and $\delta\chi$ at surfaces on which ι is a rational number. One can show that the perturbation releases energy if the well-known Δ' of tearing mode theory is positive.

*This work supported by DoE Contract No. DE-AC02-76-CHO-3073.

REFERENCES

1) A. H. Boozer, Phys. Fluids 26, 1288 (1983).
2) A. H. Boozer, Princeton Plasma Physics Laboratory Report PPPL-2094 (March 1984) and revisions.
3) A. H. Boozer, Phys. Fluids 27, 2441 (1984).
4) A. H. Boozer, Phys. Fluids 25, 520 (1982) and G. Kuo-Petravic, A. H. Boozer, J. A. Rome, and R. H. Fowler, J. Comput. Phys. 51, 737 (1983).

KINETIC THEORY OF BALLOONING-MODE IN COLLISIONAL PLASMA

Pan Chuan-Hong Ding Hou-Chang Wu Ling-Qiao
Southwestern Institute of Physics, Leshan P.O.Box 15,
Sichuan, the People's Republic of China

Abstract In this paper, the kinetic effects on ballooning-mode are systematically considered. It has been numerically shown that both gyroradius and trapped particles have stabilizing effect on ballooning-mode, whereas the collision term has the destabilizing one. In addition, kinetic theory also proves that the magnetic shear can improve the stability of ballooning-mode.

1. Linear Parturbation in Axisymmetrical Plasma

The plasma distribution function satisfies Bollzmann equation

$$\frac{d}{dt}F=\left[\frac{\partial}{\partial t}+\vec{v}\cdot\nabla+\frac{\hat{q}}{m}\left(\vec{E}+\frac{1}{c}\vec{v}\times\vec{B}\right)\cdot\frac{\partial}{\partial\vec{v}}\right]F=\left[\frac{\partial F}{\partial t}\right]_c \tag{1}$$

where we have dropped the subscript describing particle species, and $F=F_0+\tilde{f}$, $\hat{q}$ and m are the charge and the mass, respectively, $[\frac{\partial F}{\partial t}]_c$ is the collision term, explicitly

$$\left[\frac{\partial F}{\partial t}\right]_c=-\nu^*\left[F-N_t\left(\frac{m}{2\pi T}\right)^{3/2}e^{-\frac{m}{2T}(\vec{v}-\vec{\xi})^2}\right] \tag{2}$$

It conserves number of particles, energy and monentum. In Eq.(2) ν^* is the effective collision frequency, $\vec{\xi}\equiv\frac{1}{N_t}\int d\vec{v}\,\vec{v}F$, the total density $N_t=\int d\vec{v}\,F=N+\tilde{N}$, $N=\int d\vec{v}\,F_0$, $\tilde{N}=\int d\vec{v}\,\tilde{f}$.

We adopt the eikonal form to describe the high-n modes and assume the equilibrium distribution function to be Maxwellian. Under the condition $\frac{v_d}{v_t}\sim\frac{\rho_i}{L_n}\sim[\frac{\partial F}{\partial t}]_c/\Omega\ll 1$, we have $[\frac{\partial F}{\partial t}]_c\cong-\nu^*[\tilde{f}-F_m(\frac{\tilde{N}}{N}+\frac{m}{T}\vec{v}\cdot\vec{\xi})]$. The perturbed distribution function, $\tilde{f}=\hat{f}e^{i(S-\omega t)}$, is given by

$$\hat{f}=-\frac{\hat{q}}{m}\hat{\phi}F_m+\hat{h}e^{iL} \tag{3}$$

The gyrokinetic equation in ballooning space is

$$\frac{v_{t_0}}{Jq_0}\frac{\partial\hat{h}}{\partial\theta}-i(\omega+i\nu^*-\omega_d)\hat{h}=-i\frac{\hat{q}}{T}F_m(\omega-\omega_*^T)\left[J_0\left(\hat{\phi}-\frac{v_{t_0}}{c}\hat{A}_\parallel\right)+\frac{v_{t_0}}{c}\frac{v_d}{v_{t_0}}\hat{B}_\parallel\right]$$
$$+\nu^*\frac{F_m}{N}\left[J_0\int d\vec{v}\left(\frac{\hat{h}_+ + \hat{h}_-}{2}\right)J_0+\frac{m}{T}v_{t_0}J_1\int d\vec{v}\left(\frac{\hat{h}_+-\hat{h}_-}{2}\right)|v_0|\,J_0+\frac{m}{T}v_{t_0}J_1\int d\vec{v}\left(\frac{\hat{h}_++\hat{h}_-}{2}\right)v_\parallel J_1\right] \tag{4}$$

In Eqs.(3) and (4), $L=\vec{v}\times\vec{e}_{//}\cdot\vec{k}/\Omega$, $J=$ Jacobian, $J_n=J_n(\frac{k_\perp v_\perp}{\Omega})$ Bessel function, $\hat{B}_\parallel=i\vec{e}_{//}\times\vec{k}_\perp\cdot\hat{A}$, the others are conventional.

The quasineutrality condition and Ampere's law yield

$$0=-\sum_j\left(\frac{N\hat{q}^2}{T}\right)_j\hat{\phi}+\sum_j\hat{q}_j\int d\vec{v}\left(\frac{\hat{h}_++\hat{h}_-}{2}\right)_j J_{0j} \tag{5}$$

$$\hat{B}_{\parallel} = -\frac{1}{K_\perp}\frac{4\pi}{c}\sum_j \hat{\beta}_j \int d\underset{\sim}{v}\left(\frac{\hat{h}^+ + \hat{h}^-}{2}\right)_j v_\perp J_{1j} \tag{6}$$

$$\hat{\partial}_{\parallel}\hat{A}_{\parallel} = \frac{c}{4\pi}K_\perp^2 \hat{A}_{\parallel} = \sum_j \hat{\beta}_j \int d\underset{\sim}{v}\left(\frac{\hat{h}^+ - \hat{h}^-}{2}\right)_j |v_\parallel| J_{0j} \tag{7}$$

where subscript j denotes the jth species of the plasma, $J_{0j} = J_0\left(\frac{K_\perp v_\perp}{\Omega_j}\right)$, $J_{1j} = J_1\left(\frac{K_\perp v_\perp}{\Omega_j}\right)$, the perturbed current along $\underset{\sim}{B}_0$, $\tilde{\partial}_{\parallel} = \hat{\partial}_{\parallel} e^{i(S-\omega t)}$.

The " e^{iL} moment" of the gyrokinetic equation is

$$\begin{aligned}\frac{i}{\omega}\frac{1}{J}\frac{\partial}{\partial\theta}\left(\hat{\partial}_{\parallel}/B_0\right) = &-\sum_j \left(\frac{N\beta^2}{T}\right)_j \int d\underset{\sim}{v}\left(\frac{F_M}{N}\right)_j \left[\left(1 - J_{0j}^2\frac{\omega-\omega_{dj}}{\omega}\right)\hat{\phi} - J_{0j}J_{1j}\frac{\omega-\omega_{*T}}{\omega}\frac{v_\perp}{c}\frac{1}{K_\perp}\hat{B}_{\parallel}\right] \\ &+\sum_j \hat{\beta}_j \int d\underset{\sim}{v}\left(\frac{\hat{h}^+ + \hat{h}^-}{2}\right)_j \left\{J_{0j}\frac{\omega_{dj}}{\omega} - i\frac{\nu_j^{eff}}{\omega}\left[J_{0j}\left(1-\Lambda_{0j}\right) - \Lambda_{0j}'\frac{K_\perp v_\perp}{2\Omega_j}J_{1j}\right]\right\} \\ &+\frac{i}{\omega}\sum_j \hat{\beta}_j \int d\underset{\sim}{v}\left(\frac{\hat{h}^+ - \hat{h}^-}{2}\right)_j \frac{|v_\parallel|}{J B_0}\frac{\partial J_{0j}}{\partial\theta}\end{aligned} \tag{8}$$

where $\Lambda_{0j} = \Lambda_0(b_j) \equiv I_0(b_j)\, e^{-b_j}$, $\Lambda_{0j}' = \frac{d\Lambda_0(b_j)}{db_j}$, $b_j \equiv \frac{1}{2}K_\perp^2\rho_j^2 = \left(\frac{K_\perp^2 T}{m\Omega^2}\right)_j$, $I_0(b_j)$ is the modified Bessel function.

2. Kinetic Ballooning-Mode Equation

Under the weakly collision condition (banana region) we can substitute the solution to collisionless case into nonlinear term on the right hand side of Eq.(4) to make it linearized. Here, we discuss the two limit cases, $\omega \ll \omega_t, \omega_b$ and $\omega \gg \omega_t, \omega_b$, where ω_t and ω_b are the transit frequency and the bounce frequency, respectively. When $\omega \ll \omega_t, \omega_b$, we have $\left(\frac{\hat{h}^+ - \hat{h}^-}{2}\right) \approx 0$ and

$$\left.\begin{aligned}\left(\frac{\hat{h}^+ + \hat{h}^-}{2}\right)_{j\,Cir} &= \frac{\hat{\beta}_j F_{Mj}}{T_j}\frac{\omega-\omega_{*T}}{\omega}J_{0j}\,\hat{\psi}_{\parallel} \\ \left(\frac{\hat{h}^+ + \hat{h}^-}{2}\right)_{j\,Tr} &= \frac{\hat{\beta}_j F_{Mj}}{T_j}(\omega-\omega_{*T})\left[\frac{J_{0j}}{\omega}\hat{\psi}_{\parallel} + \frac{\langle \bar{X}_j\rangle}{\langle\omega+i\nu_j^{eff}-\omega_{dj}\rangle}\right]\end{aligned}\right\} \tag{9}$$

with

$$\left.\begin{aligned}\hat{\psi}_{\parallel} &\equiv \frac{i\omega}{2c}\left(\int_{-\infty}^{\theta} d\theta' J B_0 \hat{A}_{\parallel} - \int_{\theta}^{\infty} d\theta' J B_0 \hat{A}_{\parallel}\right) \\ X_j &\equiv J_{0j}\hat{\phi} - J_{0j}\frac{\omega+i\nu_j^{eff}-\omega_{dj}}{\omega}\hat{\phi}_{\parallel} + \frac{v_\perp}{c}J_{1j}\hat{B}_{\parallel} + i\frac{\nu_j^{eff}}{\omega+i\nu_j^{eff}-\omega_{dj}}\left(J_{0j}\overline{V}_j - \frac{K_\perp v_\perp}{2\Omega_j}J_{1j}\overline{V}_j'\right)\hat{\phi}_{\parallel} \\ \overline{V}_j &= \int d\underset{\sim}{v}\left(\frac{F_M}{N}\right)_j \frac{\omega-\omega_{*T}}{\omega}J_{0j}^2, \quad \overline{V}_j' = \int d\underset{\sim}{v}\frac{\omega-\omega_{*T}}{\omega}\frac{d J_{0j}^2}{d b_j}.\end{aligned}\right\} \tag{10}$$

$\langle\ldots.\rangle$ denotes averaging over the banana orbit of the trapped particles, Cir and Tr represent the circulating and the trapped particles, respectively.

When $\omega \gg \omega_t, \omega_b$, the trapped particle effect is not important and we can drop the first term on the left hand side of Eq.(4), due to $\frac{\omega_t}{\omega} \sim \frac{v_T}{L_n}/\omega \sim \frac{1}{\omega}\underset{\sim}{v}\cdot\nabla \ll 1$. We obtain, in this case, that $\left(\frac{\hat{h}^+ - \hat{h}^-}{2}\right) \approx 0$ and

$$\left(\frac{\hat{h}^+ + \hat{h}^-}{2}\right)_j = \frac{\hat{\beta}_j F_{Mj}}{T_j}\left\{\frac{\omega-\omega_{*T}}{\omega+i\nu_j^{eff}-\omega_{dj}}\left(J_{0j}\hat{\phi} + \frac{v_\perp}{c}J_{1j}\hat{B}_{\parallel}\right) + i\frac{\nu_j^{eff}}{\omega+i\nu_j^{eff}-\omega_{dj}}\left[\left(J_{0j}\overline{G}_j - \frac{K_\perp v_\perp}{2\Omega_j}J_{1j}\overline{G}_j'\right)\hat{\phi}\right.\right.$$
$$\left.\left. -\left(J_{0j}\overline{G}_j' - \frac{K_\perp v_\perp}{2\Omega_j}J_{1j}\overline{K}_j'\right)\frac{v_\perp}{c}\hat{B}_{\parallel}\right]\right\} \tag{11}$$

In which $\overline{G}_j \equiv \int d\underset{\sim}{v}\frac{F_{Mj}}{N_j}\frac{\omega-\omega_{*T}}{\omega-\omega_{dj}}J_{0j}^2$, $\overline{G}_j' \equiv \int d\underset{\sim}{v}\frac{F_{Mj}}{N_j}\frac{\omega-\omega_{*T}}{\omega-\omega_{dj}}\frac{d J_{0j}^2}{d b_j}$, $\overline{K}_j \equiv \int d\underset{\sim}{v}\frac{F_{Mj}}{N_j}\frac{\omega-\omega_{*T}}{\omega-\omega_{dj}}\left(\frac{m v_\perp^2}{2T}\right)^2 J_{1j}^2$, $\Gamma_j \equiv \frac{1}{c}\left(\frac{T}{m\Omega}\right)_j$.

(1) Low Frequency Ballooning-Mode Equation.

In the low frequency limit $\omega \ll \omega_{te}, \omega_{ti}$, both electron and ion (including background and hot ion) are governed by Eq.(9). We

substitute this into Eqs.(5), (6) and (8). The quasineutrality condition and the radial Ampere's law can be combined to express $\hat{\phi}$ and $\hat{B}_\theta$ by means of $\hat{\psi}_n$, $\hat{\phi}=A_1\hat{\psi}_n$, $i\hat{B}_\theta=B_1\hat{\psi}_n$. Making use of Eq.(8) we derive the low frequency ballooning-mode equation from the " moment", which is

$$\tau_i\frac{v_{Ai}^2}{\omega^2}\frac{1}{JB_0^2}\frac{\partial}{\partial\theta}\left(\frac{b_i}{J}\frac{\partial\hat{\psi}_n}{\partial\theta}\right)=-\sum_{j=i,e,h}\tau_j\left[A_1(1-\overline{V_j})+B_1\frac{r_i}{r_i}\overline{V_j'}-\overline{U_j}\right]\hat{\psi}_n+\sum_{j=i,e,h}\mathcal{H}_j\langle\hat{\psi}_n\rangle \tag{12}$$

where $\tau_j\equiv\frac{N_j\hat{P}_j^2}{T_j}/\frac{N_e\hat{P}_e^2}{T_e}$, the Alfven speed $v_{Ai}^2=B_0^2/4\pi N m_i$, subscript "n" represents "hot" ion component,

$$\overline{U_j}\equiv\int d\mathcal{U}\,\frac{F_{mj}}{N_j}\frac{\omega-\omega_{Dj}^*}{\omega}J_{0j}\left\{\frac{\omega_{tj}}{\omega}J_{0j}-i\frac{\nu_j^*}{\omega}\left[J_{0j}(1-\Lambda_{0j})-\Lambda_{0j}'\frac{K_\theta v_{tj}}{2\Omega_j}J_{1j}\right]\right\} \tag{13}$$

$$\mathcal{H}_j\langle\hat{\psi}_n\rangle\equiv\tau_j\int_{\mathcal{U}}d\mathcal{U}\,\frac{F_{mj}}{N_j}(\omega-\omega_{Dj}^*)\frac{\langle\hat{\chi}_j\rangle}{\langle\omega+i\nu_j^*-\omega_{Dj}\rangle}\cdot\left\{\frac{\omega_{tj}}{\omega}J_{0j}-i\frac{\nu_j^*}{\omega}\left[J_{0j}(1-\Lambda_{0j})-\Lambda_{0j}'\frac{K_\theta v_{tj}}{2\Omega_j}J_{1j}\right]\right\} \tag{14}$$

(2) Intermediate Frequency Ballooning-Mode Equation

In the frequency domain $\omega_{ti}\ll\omega\ll\omega_{te}$, only the trapped electron effect must be retained. The perturbed distributions of electrons and fusion α- particles are still given by Eq.(9), meanwhile both background ions and beam-injection ions satisfy Eq.(11). We derive the intermediate frequency ballooning-mode equation by using the same methods as the one above. The ballooning-mode equation is as follows

$$\tau_i\frac{v_{Ai}^2}{\omega^2}\frac{1}{JB_0^2}\frac{\partial}{\partial\theta}\left(\frac{b_i}{J}\frac{\partial\hat{\psi}_n}{\partial\theta}\right)=-\left\{A_2\left[\sum_{j=e,\alpha}\tau_j(1-\overline{V_j})+\sum_{j=i,b}\tau_j(1-\overline{W_j})\right]-\sum_{j=e,\alpha}\tau_j\overline{U_j}\right.$$
$$\left.+B_2\left[\sum_{j=e,\alpha}\tau_j\frac{r_i}{r_i}\overline{V_j'}+\sum_{j=i,b}\tau_j\frac{r_i}{r_i}\overline{W_j'}\right]\right\}\hat{\psi}_n+\sum_{j=e,\alpha}\mathcal{H}_j\langle\hat{\psi}_n\rangle \tag{15}$$

with

$$\overline{W_j}\equiv\int d\mathcal{U}\,\frac{F_{mj}}{N_j}\left\{\frac{\omega-\omega_{Dj}^*}{\omega+i\nu_j^*-\omega_{Dj}}J_{0j}^2+i\frac{\nu_j^*}{\omega+i\nu_j^*-\omega_{Dj}}\left(J_{0j}\overline{G_j}-\frac{K_\theta v_{tj}}{2\Omega_j}J_{1j}\overline{G_j'}\right)\left[\frac{\omega_{tj}}{\omega}J_{0j}-i\frac{\nu_j^*}{\omega}\left(J_{0j}-\Lambda_{0j}J_{0j}-\Lambda_{0j}'\frac{K_\theta v_{tj}}{2\Omega_j}J_{1j}\right)\right]\right\} \tag{16}$$

$$\overline{W_j'}\equiv\int d\mathcal{U}\,\frac{F_{mj}}{N_j}\left\{\frac{\omega-\omega_{Dj}^*}{\omega+i\nu_j^*-\omega_{Dj}}\frac{dJ_{0j}^2}{dr_j}+i\frac{\nu_j^*}{\omega+i\nu_j^*-\omega_{Dj}}\left(J_{0j}\overline{G_j'}-\frac{K_\theta v_{tj}}{2\Omega_j}J_{1j}\overline{K_j}\right)\left[\frac{\omega_{tj}}{\omega}J_{0j}-i\frac{\nu_j^*}{\omega}\left(J_{0j}-\Lambda_{0j}J_{0j}-\Lambda_{0j}'\frac{K_\theta v_{tj}}{2\Omega_j}J_{1j}\right)\right]\right\} \tag{17}$$

$\mathcal{H}_j\langle\hat{\psi}_n\rangle$ is still given by Eq.(14), and are used instead of and

3. Fluid Limit

Under the fluid limit $\frac{\omega_{ti}}{\omega}\ll1$, $K_\theta\hat{\rho}_i\ll1$, dropping the hot ion component neglecting the electron Larmor radius and taking the approximation $\langle\hat{\psi}_n\rangle\approx\hat{\psi}_n$ we can reduce Eqs.(12) and (15) to

$$\frac{v_{Ai}^2}{\omega^2}\frac{1}{JB_0^2}\frac{\partial}{\partial\theta}\left(\frac{b_i}{J}\frac{\partial\hat{\psi}_n}{\partial\theta}\right)+\left\{\frac{2\omega_{ap}\omega_{ni}}{\omega^2}+b_i\alpha_{ii}+i\frac{\nu_i^*}{\omega}b_i(\alpha_{ni}-\alpha_{ii})-T_{rap}^{(1)}\right\}\hat{\psi}_n=0 \tag{18}$$

for the low frequency mode, and

$$\frac{v_{Ai}^2}{\omega^2}\frac{1}{JB_0^2}\frac{\partial}{\partial\theta}\left(\frac{b_i}{J}\frac{\partial\hat{\psi}_n}{\partial\theta}\right)+\left\{\frac{2\omega_{ap}\omega_{ni}}{\omega^2}+b_i\alpha_{ii}+i\frac{\nu_i^*}{\omega}b_i(\alpha_{ni}-\alpha_{ii})\left(1-\tau_i\frac{\alpha_{ii}}{\alpha_{ie}}\frac{2\omega_{ni}}{\omega}\right)-\frac{\omega_{ti}^2}{\omega^2}\left(7\alpha_{ii}+4\tau_i\frac{\alpha_{ii}^2}{\alpha_{ie}}\right)-T_{rap}^{(2)}\right\}\hat{\psi}_{ii}=0 \tag{19}$$

for the intermediate. In Eqs. (18) and (19)

$$T_{rap}^{(1)}=\sum_{j=i,e}\frac{\tau_j}{\tau_i}\int_{B_m}^{B_0}d\lambda B_0(1-\lambda B_0)^{-\frac{1}{2}}\left\{\frac{3}{4}\frac{\bar{\omega}_{dj}}{\omega}(\alpha_{ij}^a-\alpha_{ij})+\frac{15}{8}\frac{\bar{\omega}_{dj}}{\omega}\frac{\langle\bar{\omega}_{dj}\rangle}{\omega+i\nu_j^a}\alpha_{ij}^a+i\frac{\nu_j^a}{\omega}\frac{\bar{\omega}_{dj}}{\omega}\alpha_{ij}^a\left(\frac{3}{4}+\frac{15}{8}\frac{\langle\bar{\omega}_{dj}\rangle}{\omega+i\nu_j^a}\right)\right\} \tag{20}$$

$$T_{rap}^{(2)}=\frac{\alpha_{ii}}{\alpha_{ie}}\frac{\omega_{ni}}{\omega}\int_{B_m}^{B_0}d\lambda B_0(1-\lambda B_0)^{-\frac{1}{2}}(\alpha_{ie}^a-\alpha_{ie})-\frac{3}{2}\tau_i\frac{\alpha_{ii}}{\alpha_{ie}}\frac{\omega_{ni}}{\omega}\int_{B_m}^{B_0}d\lambda B_0(1-\lambda B_0)^{-\frac{1}{2}}\frac{\langle\bar{\omega}_{di}\rangle}{\omega+i\nu_i^a}\alpha_{ie}^a+$$
$$+\int_{B_m}^{B_0}d\lambda B_0(1-\lambda B_0)^{-\frac{1}{2}}\left[-\frac{3}{2}\tau_i\frac{\alpha_{ii}}{\alpha_{ie}}\frac{\omega_{ni}}{\omega}\frac{\bar{\omega}_{di}}{\omega}\alpha_{ie}^a-\frac{3}{4}\frac{\bar{\omega}_{di}}{\omega}(\alpha_{ie}^a-\alpha_{ie})+\frac{15}{8}\tau_i\frac{\bar{\omega}_{di}}{\omega}\frac{\langle\bar{\omega}_{di}\rangle}{\omega+i\nu_i^a}\alpha_{ie}^a\right.$$
$$\left.-i\frac{\nu_i^a}{\omega}\frac{\bar{\omega}_{di}}{\omega}\alpha_{ie}^a\left(\frac{3}{4}-\frac{15}{8}\tau_i\frac{\langle\bar{\omega}_{di}\rangle}{\omega+i\nu_i^a}\right)\right] \tag{21}$$

$\omega_{*p} = \omega_{*i}(1+\eta_i) - \omega_{*e}(1+\eta_e)$, $\omega_{kj} = (\frac{T}{m\Omega})_j \underset{\sim}{k_\perp} \cdot \underset{\sim}{\rho_\pi} \times (\underset{\sim}{\rho_\pi} \cdot \nabla \underset{\sim}{\rho_\pi})$, $\omega_{Bj} = (\frac{T}{m\Omega})_j \underset{\sim}{k_\perp} \cdot \underset{\sim}{\rho_\pi} \times \frac{\nabla B_0}{B_0}$, $\alpha_{Bj}^2 = \frac{\omega - \omega_{kj}(1+\varepsilon\eta_j)}{\omega + (1+\varepsilon)\omega_{Bj}}$,

$d_{Bj} = \frac{\omega - \omega_{kj}(1+\varepsilon\eta_j)}{\omega}$, $\bar{\omega}_{dj} = 2(1-\lambda B_0)\omega_{kj} + \lambda B_0 \omega_{Bj}$, $\langle \bar{\omega}_{dj} \rangle \approx \langle \omega_{kj} \rangle$.

4. Result and Conclusion

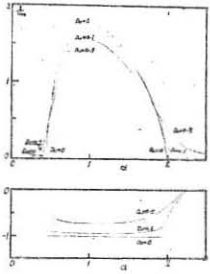
For a circular crass-section magnetic field configuration with $\frac{|\Delta|}{r} << 1$ and $r\Delta'' \approx \Delta'$ (Δ is the Shafranov shift) we botain from the result given in Ref.[3] that $\Delta' \cong r\Delta'' = -\frac{1}{2}\frac{\alpha}{2-\hat{s}}$, where $\alpha = -\frac{8\pi p' q R^2}{B_0^2} > 0$, $\hat{s} = \frac{r q'(r)}{q}$ and q is the safety factor. We express Eqs.(18) and (19) by means of magnetic-surface quantities and then solve them. It has been shown that the frequencies of two modes are near unity, i.e. and the kinetic effect on frequency is less than that an growth rate.

The results also show that both ion gyroradius and trapped particles have stabilizing effect on ballooning-mode. When $b_\theta = \frac{1}{2} k_\theta^2 \rho_i^2$ increases, for both modes the maximum growth rate, γ_M, decreases obviously and the critical , α_c, increases. The trapped particle effect on ballooning-mode is less than the ion-gyroradius one, especially when $\varepsilon = \frac{r}{R}$ is small.

The figure gives the destabilizing effect of collision. It is well-known that ballooning-mode has two stabilizing reguin, when $[\frac{\partial p}{\partial t}]_c = 0$. Now the second region disappears and the first contracts if we introduce collision effect. This indicates that there exists a dissipative ballooning-mode instability, even though the Ideal MHD theory predicts it to be stable.

The stabilizing effect of magnetic shear is still reproduced in our work.

parameters, $\hat{s} = 0.5$, $b_\theta = 0.1$, $\eta_i = \eta_e = 1$, $|\frac{d\varepsilon_n N}{dr}|^{-1}/a = 0.2$, Trap $= 0$, $\varepsilon = 1$.



References

1. W.M. Tang et al, Nul. Fus., 20, 1439(1980).
2. C.Z. Cheng, Nul. Fus., 22, 773 (1982).
3. V.D. Shafranov, 10th Europ. Conf., Moscow(1981), 269

Stability of External Kink Mode of Tokamak

Toshihide TSUNEMATSU, Shinji TOKUDA, Tatsuoki TAKEDA

Department of Thermonuclear Fusion Research, JAERI
Tokai, Naka, Ibaraki, Japan 319-11

1. Introduction

The limitation of the beta value of tokamak plasmas (β = plasma pressure/magnetic pressure) is approximately proportional to a plasma current for the n = 1 external kink mode and $n = \infty$ ballooning mode, where n is the toroidal mode number [1-3]. However, the stability of the external kink mode is sensitive to the profile of plasma current when the conducting shell is placed far from the plasma surface [4]. There appears the unstable zone, in the cylindrical model, near the rational numbers of the safety factor, q_a, even for β=0. The unstable region in q_a is wider for broad current profiles. In experiments it is very difficult due to disruption to cross q_a = 2, and sometimes q_a = 3 for well confined plasmas with a divertor. The external kink mode is considered to be one of the candidates of this disruption. In this paper by using the ideal MHD stability code ERATO we study the dependence of the beta limit of a circular tokamak due to the external kink mode on the profile of the toroidal current, especially, for $q_a \sim 3$.

2. Equilibrium

The equilibria used in our analysis are obtained by solving the Grad-Shafranov equation in a flux coordinate system. The solution is expressed as the position on the magnetic surfaces as follows :

$$R=R_0(1+\varepsilon x), \quad Z=R_0\varepsilon y, \tag{1}$$

$$x=\Delta+\rho\cos\theta+\rho\sum_{m\geq 2} X_m\cos(m\theta), \tag{2}$$

$$y=\kappa\rho\cos\theta+\rho\sum_{m\geq 2} Y_m\sin(m\theta), \tag{3}$$

where Δ, κ, and ε are the toroidal shift and the ellipticity of magnetic surfaces and the inverse aspect ratio. The "plasma radius", ρ, is taken as an independent variable. The pressure, p, and the poloidal current function, F (or safety factor, q), are given as fuctions of ρ . The partial differential equation of ρ and θ are ruduced to coupled ordinary differential equations by using the Fourier transformation in the θ direction. The detail of the numerical method is described elsewhere.

In our analysis the current profile at $\beta = 0$ is chosen as $j_t(\rho)=j_0(1-\rho^2)^\nu$ where ν specifies the width of the current channel. The coefficient j_0 is determined by q_a. The ratio of q_a and q_0 (q_0: safety factor at the magnetic axis) is given by $q_a/q_0=\nu+1$. When $q_0 < 1$, we modify the profile of the current such that q=1 within the q=1 surface of the original profile. To make the series of the equilibria the pressure is increased by fixing the initial profile $q(\rho)$ for β=0.

3. Numerical Results

We study the β limit due to the external kink mode of a circular tokamak in (ν, q_a) plane. Figure 1 shows the stability diagram in the cylindrical model. The conducting shell is placed at $a_w/a = 2$, where a_w and a are the minor radii of the shell and the plasma surface, respectively. This diagram is the same as one obtained by Hastie et al.[4] except for $q_a<2$. In our study, the current profile is flattened inside of the q=1 surface and the unstable region (hatched region) becomes wider than that in Ref.4 for $q_a < 2$ due to the weak shear in the central region of the plasma column.

Two current profiles are chosen to study their dependence on the beta limit. For one case we decrease q_a by decreasing ν with q_0=1 (curve 1 in Fig.1), where the pressure profile is optimized against the $n = \infty$ ballooning mode. For the other case we decrease q_a by fixing ν to 1.5 and the pressure profile is fixed as $p(\rho)=p_0(1-\rho^2)^2$ to avoid the change in the current profile near the plasma surface (curve 2 in Fig.1). In Fig.2 the dependence of the beta limit on q_a are shown for two cases. The numbers (I) and (II) denote the cases 1 and 2, respectively. For the broad current profile (case 2) there appears an unstable window near $q_a = 3$ even for $\beta = 0$. This region corresponds to the unstable one in the cylindrical model. For the case 1, the beta limit decreases near $q_a = 3$ but remains

finite. For a_s/a = 1.5, the beta limit is higher than or almost coincides with ballooning limit. However the shell should be very close to the plasma surface to increase the beta limit up to the ballooning limit near q_a = 3 for the case 2.

4. Discussion and Conclusions

We have shown the hard barrier to cross near q_a = 3 for broad current profile because of the external kink instability. The beta limit becomes smaller in q_a < 3 than that in q_a > 3 even for the peaked current profile when the stabilizing effect of the conducting shell is weak. It is preferable to use the region with q_a greater and nearly equal to 3 when the current profile is broad and/or the conducting shell is far from the plasma surface. When the beta limit due to the external kink mode is larger than that due to the ballooning modes for this operation, the stability of the finite n ballooning modes with free boundary condition will become important and it is now being studied.

Acknowledgement

The authors would like to acknowledge Drs. T. Tuda, T. Takizuka and K. Itoh for helpful discussions.

References

1) SYKES, A., TURNER, M.F., PATEL, S., in *Controlled Fusion and Plasma Physics* (Proc. 11th Europ. Conf., Aachen, 1983), Part II B23 (1983) 363.

2) TROYON, F., GRUBER, R., SAURENMANN, H., SEMENZATO, S., SUCCI, S., Plasma Phys. 26 (1984) 209.

3) TUDA, T., AZUMI, M., ITOH, K., KURITA, G., TAKEDA, T., TAKIZUKA, T., TOKUDA, S., TSUNEMATSU, T., ADACHI, M., TANAKA, Y., WATANABE, M., ITOH, S-I., in *Plasma Physics and Controlled Nuclear Fusion Research 1984* (Proc. 10th International Conf. on Plasma Phys. and Controlled Nucl. Fusion Research, London, 1984) (IAEA, Vienna, 1985) Vol.2, p.173.

4) HASTIE, R.J., SYKES, A, TURNER, M., WESSON, J.A., Nucl. Fusion 17 (1977) 515.

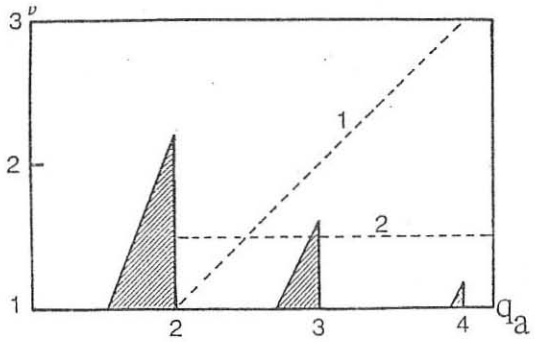


Fig.1 Stability diagram of the n=1 external kink mode in the cylindrical model. The hatched regions are the unstable ones. The lines 1 and 2 denote the cases mentioned in the text.

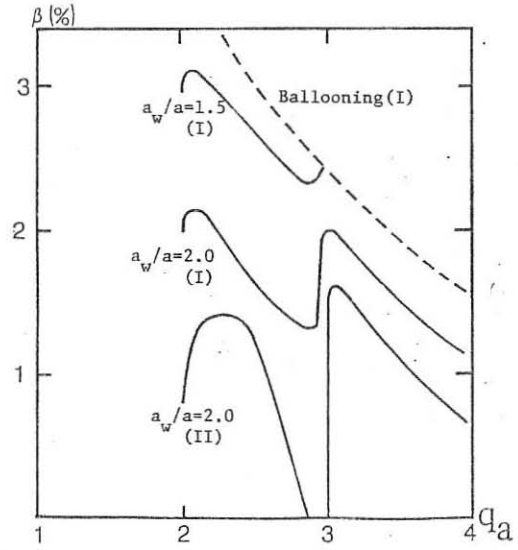


Fig.2 Beta limit versus q_a. Aspect ratio is chosen as A=3.37. The numbers I and II denote the cases 1 and 2, respectively. The lower two lines denote the cases with a_w/a=2.0 and the upper line denotes the case with a_w/a=1.5. The dashed line is the ballooning limit.

TOROIDAL ROTATION EFFECT ON THE COLLISIONAL PLASMA TRANSPORT IN A TOKAMAK .

V.S.Tsypin
I.N.Vekua Institute of Physics and Technology,
Sukhumi, USSR.

It has been shown in Paper [1] that the toroidicity contribution into a radial thermal flux of ions can be essentially diminished by involving a collisional plasma of a tokamak into a longitudinal motion. The ion thermal conductivity effect already appears when: $\alpha \gtrsim \lambda_i / qR$ ($\alpha = M_i V_{\parallel}^2 / (T_e + T_i)$, $\lambda_i = v_{Ti} / \nu_i$, $v_{Ti} = \sqrt{T_i / M_i}$, where M_i is the ion mass, T_i and T_e are ion and electron temperatures, respectively, $V_{\parallel}$ is the longitudinal plasma motion velocity, λ_i, v_{Ti} are the free path length and the thermal velocity of ions, respectively, ν_i is the ion-ion collision frequency, q is the safety factor and R is the torus major radius. The thermal conductivity effect is more notable for lower values of λ_i / qR .

This effect has been treated in Paper [1] as due to plasma compressibility influence on a toroidally perturbed ion temperature, i.e., the thermal balance equation [2] is taken as:

$$div \vec{q}_i = (n T_i U_{\theta i} / r)(\partial n / \partial \theta) \qquad (1)$$

where $\vec{q}_i$ is the ion heat flux [2], r is the minor radius of the torus, n is the ion density, $U_{\theta i}$ is the poloidal velocity of ion rotation and θ is the poloidal angle measured from the inner circumference of the torus.

However, in Paper [1] they made use of Braginsky viscosity [2] which, in general, is not applicable in describing drift movements. Thus, in Paper [1] it has been implicitly assumed that $U_{\theta i} \gg U_{dr}$, where $U_{dr} \simeq \rho_i v_{Ti} / r$, $\rho_i = v_{Ti} / \omega_{Bi}$, $\omega_{Bi} = e_i B / M_i C$ are Larmor radius and cyclotron frequency of ion rotation, respectively. The poloidal velocity, $U_{\theta i}$, in a collisional plasma moving with the longitudinal velocity, $V_{\parallel}$, has been defined in [3] using expressions for viscosity appropriate for

describing drift motions [3-6]. In Ref. [3] it has been shown that $U_{\Theta i} \gg U_{\alpha i}$ holds only close to the value of $\alpha \simeq \lambda_i / qR$ (In Ref. [3] an interesting effect of increasing $U_{\Theta i}$ for $\alpha \simeq \lambda_i / qR$ was found).

Besides, one may show that the ambipolarity condition is reduced to [3]:

$$\langle [(\tfrac{3}{2}+\alpha)\tilde{\pi}_{11} + \alpha n \tilde{T}_i] \sin\Theta \rangle_\Theta = 0 \qquad (2)$$

where $\tilde{\pi}_{11}$ and $\tilde{T}_i$ are ion longitudinal viscosity and temperature, respectively, which oscillate with Θ; $\langle \dots \rangle_\Theta$ indicates averaging over Θ. Since $\tilde{T}_i$ contains a large factor of q^2R^2/λ_i^2 while the viscosity, $\tilde{\pi}_{11}$, does not contain it, one sees that for low α the temperature ($\tilde{T}_i$) perturbations are already descreased as a result of tuning the poloidal velocity so that to compensate some part of the longitudinal heat flux of ions found in Ref. [7]. It also follows from Exp.(2) that while defining the radial heat flux $\Gamma_{Ti} = \langle q_i^r \rangle$ averaged over the magnetic surface, the ion heat flux $\vec{q}_i$ for finite values of α should be taken [5 - 6] as:

$$\vec{q}_i = q_{11}\vec{h} + [\vec{h}\vec{G}]/\omega_{Bi} - (2nT_i v_i / M_i \omega_{Bi}^2)\nabla_1 T_i \qquad (3)$$

where:

$$q_{11} = -(T_i/M_i\nu_i)\{3{,}9n(\vec{h}\nabla)T_i + \vec{h}\nabla(1{,}56\vec{\pi}_1 - 6{,}93\vec{\pi}_1^*) + (\vec{h}\nabla)(5{,}73\chi - 1{,}82\chi^*)\}.$$

$$\vec{G} = (T_i/M_i)\{\tfrac{5}{2}n\nabla T_i + \tfrac{5}{2}\nabla\chi + \nabla(\vec{\pi}_1 - \tfrac{7}{2}\vec{\pi}_1^*) - \vec{\pi}_1\nabla\ln n\}$$

$\vec{\pi}_1^*$ is some analogue for the viscosity tensor; χ and χ^* are the distribution function moments characterizing its spherically symmetric deviation from the Maxwell one in the velocity space. These moments are defined in Refs. [5 - 6]. Thus, in Ref. [1], the drift effects have been considered without sequence.

Having substituted Exp.(3) into Exp.(1) using the ambipolarity condition (2), and following the procedure described in Ref. [3], one finds K - the coefficient from $U_{\theta i} = K T_i' / M_i \omega_{Bi}$

$$K = -\frac{0{,}96(2{,}75 - 0{,}42\alpha - 0{,}95\alpha^2) - \frac{5}{3}\alpha\ell(1+\frac{\alpha}{2})}{0{,}96(1{,}5 + 0{,}57\alpha + 1{,}29\alpha^2) + \frac{1}{3}\alpha^2\ell} \qquad (4)$$

where $\ell = 3q^2R^2/3{,}9\lambda_i^2$. Exp.(4) differs from the corresponding coefficient value found in Ref. [1] by the fact that it takes into account the terms with α which do not contain ℓ . Exp.(4) differs as well from the value found in Ref.[3] where additional heat fluxes were neglected (See Exp.(3).)

Using Exp.(4) and the heat flux from Exp.(3), one finds the radial heat flux of ions averaged over the magnetic surface:

$$\Gamma_{Ti} = -(2n T_i \nu_i / M_i \omega_{Bi}^2) T_i' (1 + 1{,}6 q^2 J) \qquad (5)$$

where, for $\alpha^2\ell > 1$, one obtains:

$$J = (\lambda_i^2/\alpha^2 q^2 R^2)(5{,}6 + 11{,}9\alpha + 16{,}5\alpha^2 + 9{,}0\alpha^3 + 0{,}5\alpha^4)$$

For $\alpha^2\ell \lesssim 1$, Expression $J = (1 + 0{,}18\alpha^2 q^2 R^2/\lambda_i^2)^{-1}$ coincides in value with that of Ref.[1].

The coefficient, J , reaches its minimum for $\alpha \simeq 1{,}4$, i.e., its minimum value is $J_{min} \simeq 40\lambda_i^2/q^2R^2$. For $\alpha \gg 1$ (but $\alpha < \varepsilon^{-1}$) J grows as α^2. The minimum value of J found in Ref. [1] is approximately 30 times lower than that cited above, being reached only for $\alpha \gg 1$, while $J = J(1,4)$ is nearly 5 times smaller.

Note as well that the thermal input $\langle \overleftrightarrow{\pi} \nabla \vec{V} \rangle$ decreases together with α $\widetilde{\pi}_i$, being negligibly small for $\alpha \simeq 1{,}4$.

Moreover, heat dumping in a collisional plasma as a result of ion thermal conductivity proceeds faster than the process of relaxation of a longitudinal plasma motion[8].

REFERENCES

1. Wong S.K., Hinton F.L. Phys. Rev.Lett., 1984, 52, 10,827.

2. Braginsky S.I. "Voprosy Teorii Plazmy" edited by M.A.Leon-

tovich, Moscow, 1963, v.I, p.183.

3. Mikhailovsky A.B., Tsypin V.S. ZHETF, 1982, v.83 N 1(7), p.139.

4. Mikhailovsky A.B., Tsypin V.S. Fizika Plazmy, 1984,v.10, N 1, p.92.

5. Mikhailovsky A.B., Tsypin V.S., Preprint issued at the Institute of Atomic Energy, 3751/6, 1983.

6. Mikhailovsky A.B., Tsypin V.S. Plasma Physics, 1971, 13, 785.

7. Shafranov V.D. Plasma Physics, 1966, 8, 314.

8. Kadomtsev B.B. Morozov D.Kh. , Pogutse O.P. Pisma v ZHETF, 1984, v.40, p.80.

NEW REPRESENTATION OF THE PLASMA - MAGNETIC FIELD SYSTEM IN EQUILIBRIUM

A. Montvai
Central Research Institute for Physics
H-1525 Budapest, P.O.Box 49, Hungary

It is shown that the plasma equilibrium in magnetic field can be represented in a form:

$$x d(j \wedge B) - dp \equiv 0$$

where d - is the exterior derivation, x - is the duality transormation, j, B and p are exterior forms representing the vector fields of current distribution, magnetic field and the pressure distribution respectively.

Because of the geniune independence of the representation (and the manipulations of the exterior calculus) from the coordinate system used, important conclusions can be drawn with regard to basic properties of the physical system. These are as follows.

- The magnetic surface can be defined as integral manifold of vanishing Pfaffian form, which leads to
- new integrability criterium of existence, and
- a new geometrical invariant of the form:

$$x\, d(d \wedge B) \equiv 0$$

which in turn impose severe limitations on the vector fields of the current distribution and magnetic induction.

DIMENSIONALITY AND MHD MODE COUPLING STUDIES OF DITE

W. Arter and D.N. Edwards

Culham Laboratory, Abingdon, Oxon, OX14 3DB
(UKAEA/Euratom Fusion Association)

Abstract Concepts from dynamical systems theory are applied to studies of DITE magnetic field fluctuation data and a characteristic dimension $\nu \doteq 2.1$ is calculated. This suggests that the data results from a system where only 3 processes operate; the identities of these are inferred using bispectral analysis.

ν, the Grassberger-Procaccia exponent [1] is a measure of the dimension of the region of phase space occupied by a dynamical system's trajectory. In the presence of dissipation, such a region, after transients have decayed, is referred to as an attractor. For a time series x_j, $j = 1, \ldots, N$, where x_j are vectors sampling the attractor in an n-dimensional phase space ($n > \nu$) at time t_j, we define the correlation integral $C(r) = \lim (N \to \infty)\ N^{-2} \sum \theta(r - |x_i - x_j|)$, where θ is the Heaviside step function. ν is then defined as $\nu = \lim (r \to 0)\ d\ln C/d\ln r$, assuming the limit exists. If only one time series X is available, an n-dimensional vector can be constructed as $x_k = (X(t_k), X(t_k+\tau), \ldots, X(t_k+[n-1]\tau))$, where τ is a non-zero time interval. In practice, C is plotted against r on log-log paper and straight line sections sought.

To demonstrate the method we specialise to the current plateau phase of an ohmic, non-diverted DITE discharge (refs.[2] and [3] measure ν on JET and HBTXIA). The local $\dot{B}_\theta$ was sampled by 8 Mirnov coils at a rate of 40 kHz (time interval $\Delta t = 25$ μs). For the flat-top phase, N=1920, where N is the number of samples of each coil's signal. For coil 1, $\nu = 2.1 \pm 0.3$ is obtained: figure 1 demonstrates that the logarithmic slope of C saturates at this value as n is increased, for $\log_{10} r > -0.7$. Here $\tau/\Delta t = 6$; ν is independent of $\tau/\Delta t \lesssim 8$ [4]. At smaller r, C(r)'s logarithmic slope is $\doteq n$ for $n \lesssim 6$ and this might well be identified with experimental noise. Taking n=4 and $\tau = 6\Delta t$, we measured ν for some of the other coils (3,4 and 7) obtaining values consistent with the above estimate. We also cross-checked by using the signals at a given instant from coils 1,2,3 and 4 to construct a 4-dimensional vector; figure 2

shows that $\nu \doteq 2.2$ is thereby obtained. These results were validated [4] using a chaotic solution of the Lorenz equations that was sampled in such a way as to reflect the precision and temporal resolution of the DITE data. A value $\nu = 2.1 - 2.2$ was obtained, c.f. the published value of 2.05 [1].

Whilst our estimate of ν for DITE is consistent with a value of 2, we find that an interpretation of ν in terms of 3 processes is required. Plotting averaged oscillation frequency versus time [4] reveals a steady downward frequency drift, presumably associated with evolution of the plasma profiles; this we ascribe to one process.

Fourier analysis of the 8 coil signals for mode numbers $m \leq 4$ shows the presence of 2 modes $m = 2$ and $m = 3$ evolving essentially independently, and no $m = 4$ component. Quadratic nonlinear interactions are observed through the bispectrum [5], defined by $B(k,\ell) = M^{-1} \sum F^i_k F^i_\ell F^{*i}_{k+\ell}$ where F^i_k is the Fourier component at frequency ω_k of the time series X_i and the sum $\sum$ is over i from 1 to M: B is nonzero only if there is a phase dependence between 3 modes. A test of the coupling model is given by the bicoherence spectrum $b(k,\ell)$, defined by

$$b^2(k,\ell) = \frac{|B(k,\ell)|^2}{M^{-1}\left[\sum |F^i_k|^4 \sum |F^i_\ell|^4\right]^{\frac{1}{2}} \sum |F^i_{k+\ell}|^2} .$$

b^2 is plotted in figure 3, where a false base has been drawn at the statistically expected noise level.

Despite the absence of an $m = 4$ component, implying no $m = 2$ self-interaction, figure 3 shows that there is quadratic coupling (i.e. the modes satisfy $F_{k+\ell} = A_{k,\ell} F_k F_\ell$) between modes of the same frequency ~ 5kHZ. We infer that this is caused by the interaction of the modes $(m,n) = (2,1)$ and $(3,1)$ to produce $(5,2)$. The second peak in $b^2(k,\ell)$ is identified as due to the n=1 and n=2 modes combining to drive an n=3 mode with either m=7 or 8. Absolute values of the coupling coefficients $|A_{k,\ell}| = 0.2$ and 0.9 are obtained for the first and second peaks respectively. Modes at n=1 and n=2 are fully locked to drive the n=3, however the n=1 modes are by no means fully coupled.

We can now postulate that the 3 processes which determine the dynamics of the MHD signals in this discharge are the two modes $(m,n) = (2,1)$ and $(3,1)$, loosely coupled, driving higher harmonics, together with

a process associated with the evolution of the plasma profile. The importance of finding $\nu \doteq 2.1$ is that it suggests we do not have to seek any further processes. The fact that ν is significantly smaller than the number of processes and the absence of any evident periodicity, is consistent with the attractor being strange.

Acknowledgements: We are grateful to Messrs. K.B. Axon and W. Millar for providing the DITE data.

References

[1] P. Grassberger and I. Procaccia, Phys. Rev. Lett. 50 (1983) 346.
[2] A. Cotê, P. Haynes, A. Howling, A.W. Morris and D.C. Robinson. Proceedings of this conference.
[3] S. Gee and J.B. Taylor. Proceedings of this conference.
[4] W. Arter and D.N. Edwards submitted to Phys. Lett. A.
[5] Y.C. Kim and E.J. Powers, IEEE Trans. Plasma Science, PS-7 (1979) 120.

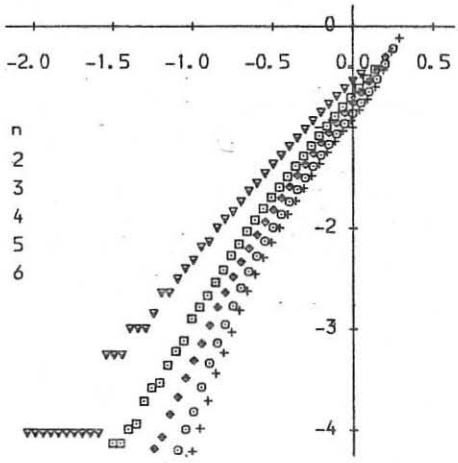


Fig.1 $\log_{10}C$ vs $\log_{10}(r/r_o)$ using data from coil 1 showing saturation of slope with n.

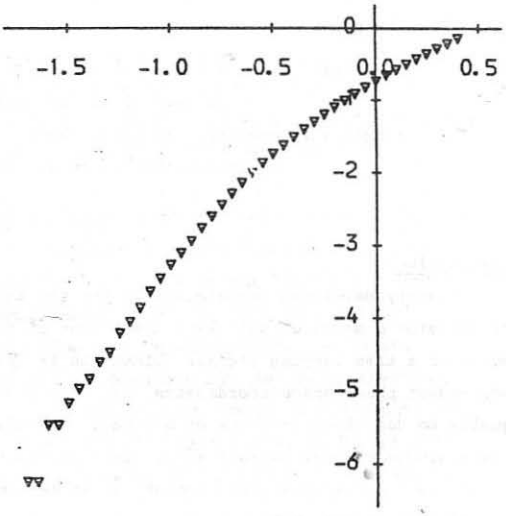


Fig.2 $\log_{10} C$ vs $\log_{10}(r/r_o)$ for 4-dimensional vectors constructed using signals from coils 1-4.

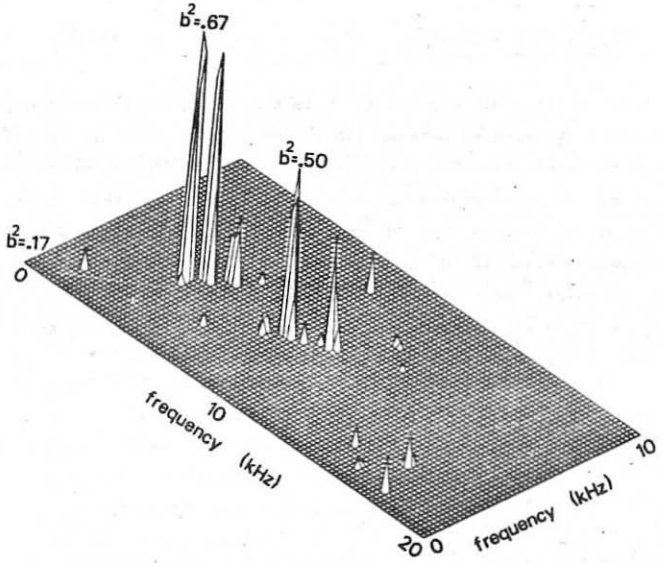


Fig.3 $b^2(k, \ell)$ for 70-85 ms into the discharge. The false base is drawn at the expected noise level (= .17).

DIMENSION MEASUREMENT OF FLUCTUATIONS IN HBTX1A

S. J. Gee[+] and J. B. Taylor
Culham Laboratory, Abingdon, Oxon. OX14 3DB, England
(Euratom/UKAEA Fusion Association)

Introduction

Recently developed techniques [1] for the analysis of 'Strange Attractors' provide a means of assessing the number of active dimensions in the source of a time varying signal. Dimension is usually associated with independent phase-space coordinates (x_i, p_i) but motion in phase space can equally be described in terms of a single coordinate and the dimension deduced from a single channel signal $X(t)$. One constructs, from the signals $X(t_i)$, an m-dimensional phase space vector $\vec{X}_i$ whose components are the signals at m different delayed times, thus

$$\vec{X}_i \equiv \{X(t_i), X(t_i + T), X(t_i + 2T), \ldots, X(t_i + (m-1)T)\} .$$

[The delay time T is arbitrary but if it is too short the information is only in the small differences between successive $\vec{X}_i$ while if it is too long it is only in the small residual correlations.] The determination of the dimension d of the underlying process is based on the fact that if the chosen dimension m is less than d then the $\vec{X}_i$ will fill the whole m-dimensional space whereas if d is less than m, the points fill only a d-dimensional sub-space. We therefore construct, for each value of m, the distance $R_{ij} \equiv |\vec{X}_i - \vec{X}_j|$ between all pairs of $\vec{X}_i$ and determine the fraction $C(\rho)$ of the R_{ij} which are less than ρ. Thus

$$C(\rho) \equiv \frac{2}{N(N-1)} \sum_{i<j} H(\rho - |X_i - X_j|)$$

where $H(x)$ is the Heaviside function.

Clearly, if the points $\vec{X}_i$ fill a space of m- or d-dimensions

$$C(\rho) \propto \rho^m \text{ or } \rho^d .$$

Hence a plot of $\log C(\rho)$ vs. $\log \rho$ should yield a straight line segment whose slope saturates at the value d as m is increased. [A strange attractor yields a dimension d which is non-integer but our first concern is not whether d is integer but whether it is small - indicating that the excitation of the plasma may be decribed by a low dimensional model.]

The signals conventionally recorded on plasma experiments are well-suited to the above analysis and we have applied it to the fluctuations recorded by magnetic coils and by Si Surface Barrier Diodes on the HBTX1A, reverse-field pinch, experiment. Similar measurements have been made on the DITE experiment*. An analysis of the same data by conventional correlation techniques was recently carried out by Malacarne [2] and by Brotherton-Ratcliffe [3] who concluded that the fluctuations could be represented by a few global modes plus a small noise-like component. Details of the HBTX1A experiment can be found in reference [4] and of the magnetic coil and SBD arrays in reference [2].

Results

As is well-known, RFP discharges are principally characterised by the value of $\theta = 2I/aB_0$, which usually lies in the range $1 < \theta < 2$. We have analysed the fluctuations in discharges at $\theta = 1.2$, 1.8 and 2.0. A typical result is shown in Fig. 1, which displays $\log C(\rho)$ vs. $\log \rho$ for various values of m computed from the signals recorded by a B_ϕ coil. The data were recorded over 1.5 ms of the quiescent phase of a $\theta = 2$ discharge and the delay T is 60 μsec. Slow drifts were eliminated using a linear regression routine so that all fluctuations are about zero mean. In Fig. 1 the dimension (i.e. the slope of the line) saturates with increasing m at a value $d = 7$. It was found that this dimension is insensitive to the choice of the time-delay T in the range $20 < T < 200$ μsec .

Fig. 1 was obtained with an unfiltered signal which includes low frequency (0-20 kHz) and high frequency (20-50 kHz) oscillations as well as noise up to > 100 kc/s. Filtering the signal to exclude frequencies > 50 kHz did not affect the dimension but a cut-off at 20 kHz reduced the dimension to ≈ 5.

A similar analysis has been made for the signals from many B_ϕ and B_θ coils and for the SBD signals. Magnetic B_θ and B_ϕ probes in different

poloidal positions and the SBDs all gave a similar dimension for discharges at the same θ-value, suggesting that all were recording the same basic excitations. For discharges at $\theta = 2$ the dimension in all cases was $\simeq 7$. For discharges at $\theta = 1.2$ the dimension decreased to $\simeq 5$. This is in accord with the general observation that RFP discharges are more unstable as θ is increased but the change in dimension is remarkably small.

Although Fig. 1 shows the typical behaviour expected for $C(\rho)$, some anomalies have also been observed. Fig. 2 shows an example from the B_θ signal at $\theta = 1.2$ in which the correlation function exhibits two distinct regions leading to a pronounced "kink" when m is increased. At large ρ the slope saturates at $d \simeq 6$ but at smaller ρ there is no saturation. This could be interpreted as a large amplitude excitation of dimension 6 plus a small additional independent noise-like process. In the presence of such noise one would expect the slope to saturate only at large ρ.

Conclusion

We have demonstrated the applicability of dimension analysis to the signals conventionally recorded from toroidal discharges. This seems a useful complement to more conventional analysis. The application to HBTX1A using several B_ϕ and B_θ magnetic edge coils and SBDs indicates that these diagnostics are recording the same basic excitations and that these can be represented by a low dimensional model, ranging from $d = 5$ for discharges at low θ to $d \simeq 7$ for discharge at high θ. These values are reduced if the signals are low-pass filtered and there is evidence for an additional low-level noise-like component. These results support the conclusions drawn from conventional analysis of similar data. It would be of great interest to apply this technique to Tokamak signals during the approach to disruption.

+ UMIST, Manchester, England.

* See Arter & Edwards, Proceedings of this Conference.

References

[1] P. GRASSBERGER, I. PROCACCIA, Physica 9D, p189-208 (1983).
[2] M. B. V. MALACARNE, D. Phil thesis (1984).
[3] D. BROTHERTON-RATCLIFFE, Ph.D. thesis (1984).
[4] H. A. B. BODIN et al, in "Plasma Physics and Controlled Nuclear Fusion Research" (Proc. 9th Conf. Baltimore) Vol. 1, IAEA Vienna, 641 (1983).

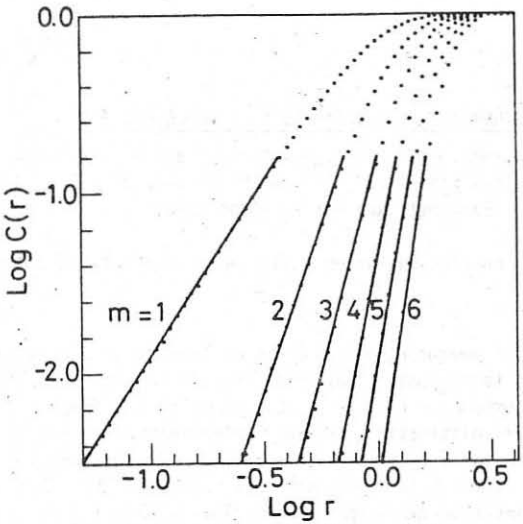


Fig. 1. B_ϕ, $\theta = 2$ no filter

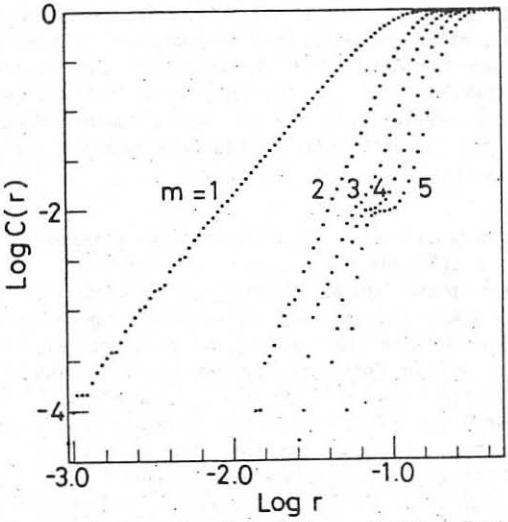


Fig. 2. B_θ, $\theta = 1.2$ filtered 20 - 50 kHz

EPS Budapest paper

DIMENSIONALITY OF FLUCTUATIONS IN TOSCA AND JET#

A Cotê*, P Haynes, A Howling*, A W Morris* and D C Robinson
Culham Laboratory, Abingdon OX14 3DB, UK
(Euratom/UKAEA Fusion Association)

*University of Oxford

#Part of the work was carried out under a Task Agreement between JET and Culham Laboratory

Introduction

The potential for measuring the degrees of freedom or dimensionality of a set of fluctuations is pointed out by Arter and Edwards and by Taylor [1,2]. A measure of the strangeness of strange attractors is the fractal dimension, d, which permits the distinction between deterministic chaos and random noise[3]. An estimate for d is given by the quantity $d\log C/d\log \rho$ in the limit that ρ becomes small where C is the correlation integral [3]. d is obtained by constructing vectors from sampling a single time series of data forming a k dimensional phase space $\underset{\sim}{x}_i = (x_i, x_{i+p}, x_{i+2p}, \cdots x_{i+(k-1)p})$. If k is greater than d then $\underset{\sim}{x}_i$ fill a subspace of d dimensions such that $C(\rho) \sim \rho^d$ in the limit $\rho \to 0$ If noise is present then a plot of $C(\rho)$ against ρ will show two regions and saturation is not achieved at small ρ.[3] Fluctuations observed on the TOSCA device using far forward CO_2 scattering which is sensitive to density fluctuations, radial magnetic field fluctuations measured with a probe inside the plasma and fluctuations in the saturation current of a Langmuir probe, have been investigated. On the JET device MHD activity has been investigated which is observed with pick up coils situated inside the vacuum vessel and in addition sawtooth activity has been examined using both soft X-ray and electron cyclotron emission diagnostics.

TOSCA results

The rate of change of radial field fluctuations measured at a radius of 7 cm when there is a coherent m=2,n=1 mode present ($\frac{\delta B}{B} < 10^{-3}$) do show saturation when the phase space variable, k, exceeds 4 indicating a dimensionality of $\sim 2.4 \pm 0.1$ (Fig 1). This value is not dependent on the number of samples used between 300 and 2000 nor on p between 3 and 10. The slope at small ρ is however influenced by the level of high frequency MHD activity ($\frac{\delta B}{B} \lesssim 10^{-5}$) seen with the internal coils. The range over which $C(\rho) \sim \rho^d$ is increased when the coil is closer to the vacuum vessel wall. For the CO_2 scattering results, which are also sensitive to the m=2 activity, the dimensionality does not appear to saturate with d being 5 for k=7. This would seem to indicate a high value for the dimensionality or that the fluctuations resemble white noise. The ion saturation current from a double Langmuir probe at the same minor radius and poloidal angle and for the same discharge as the magnetic field measurements, shows weak signs of saturation for the

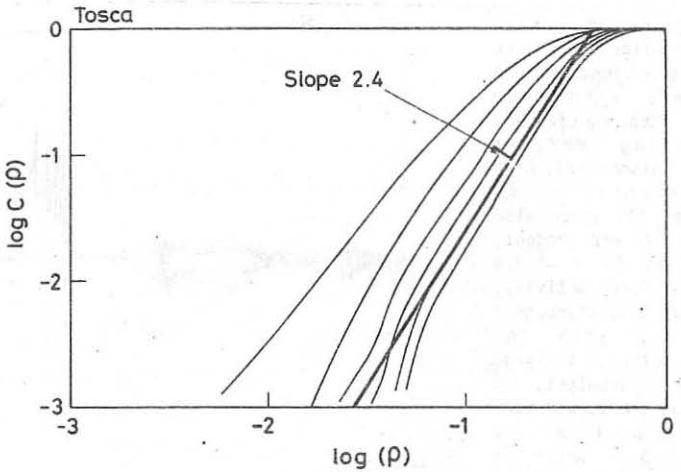


Figure 1. Log C(ρ) as a function of log(ρ) for TOSCA MHD data with k=2,→7.

dimensionality indicating ~ 5 when k=8 (Fig 2). In this case the probe is sensing primarily density fluctuations[4] present in the plasma probably associated with collisional drift wave turbulence.

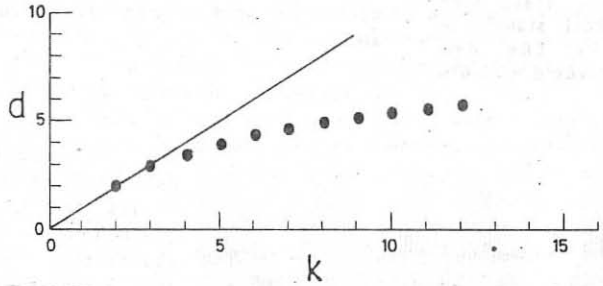


Figure 2. d as a function of k for TOSCA Langmuir probe fluctuations.

JET results

JET MHD data has been explored during the current rise, flat top, oscillating precursor phase (A on Fig 3), locked mode phase, B, and post disruption phase, C. For discharges with no coherent mode activity, but only low level turbulent fluctuations ($\frac{\delta B}{B} \sim 10^{-6}$), no obvious saturation is observed as k is varied, similar to the turbulent fluctuations observed on the TOSCA device. However for coherent mode activity with primarily m=2,n=1 or m=3,n=1 (which may be triggered by the production of a radiation dominated region at plasma edge) then saturation is observed and d is typically between 2.4 and 2.9 depending on the case. During the current rise phase when the

mode activity can be quite irregular often associated with soft disruptions and sometimes with mode locking, then d ~ 3. The oscillating m=2,n=1 activity associated with the precursors to disruption (A) which also has ~ 25% of n=2 present, give values of d ~ 2.4 amplitude of the activity. During the post disruption phase, C, when the magnetic activity is large and highly turbulent, d $\lesssim$ 4. During the locked mode phase prior to disruption,B, which is characterised by irregular activity with small mini-disruptions, d $\gtrsim$ 4. If cyclic non-linear behaviour of the m=2,n=1 mode is observed, eg that seen on Fig 4(a), then combining coil signals to give only the n=1 component gives d = 2.56 - Fig 4(b).

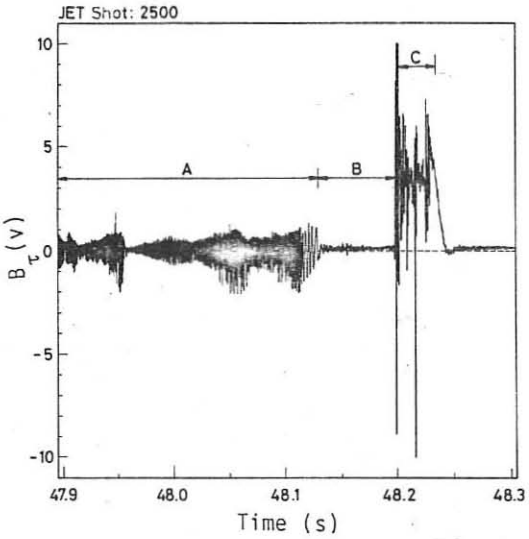


Figure 3. Rate of change of tangential component of magnetic field as a function of time on JET at disruption showing phases A, B and C.

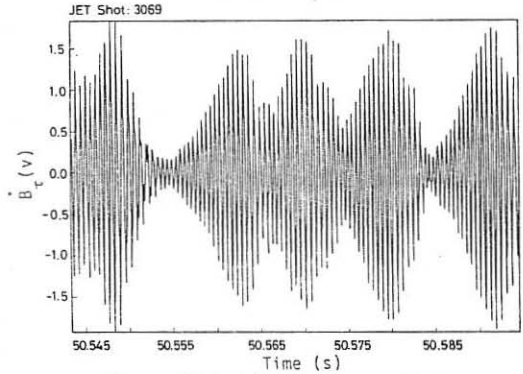


Figure 4(a) Rate of change of tangential component of magnetic field with n=1 as a function of time during period A.

If sawtooth activity exhibited on soft X-ray diodes or the electron cyclotron emission diagnostic, is examined then we obtain d =1 whether the signal is from inside or outside the q=1 surface. Higher values of d are indicated if the diagnostic is primarily looking at the reconnection region.

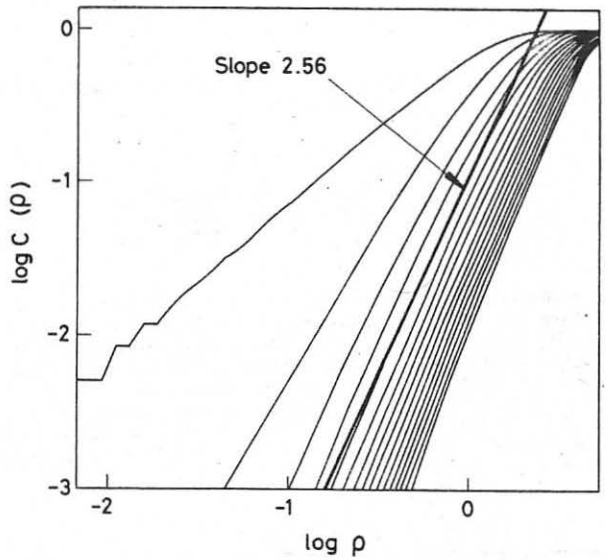


Figure 4(b) Log C(ρ) as a function of logp for Fig 4(a) with k=1,→16.

Conclusions The MHD activity associated with the coherent Mirnov oscillations present on both TOSCA and JET have the same dimensionality ~ 2.5 regardless of whether the mode is present during the current rise, flat top, current run down or oscillating precursor disruption phases. Thus the activity is characterised by fractal dimensionality associated with a strange attractor and that a minimum of three variables are involved. Fluctuations present during the flat top phase on JET, the locked mode phase or the post disruption phase indicate higher dimensionality, ie more variables are involved. Internal fluctuations either of the density or the magnetic field which are more likely to be linked to microinstabilities and confinement, indicate high dimensionality, associated with a more fully developed state of turbulence and may be more akin to white noise. The low dimensionality is in acco d with that observed on DITE[1] and the higher dimensionality associated with the post disruption phase in agreement with that observed on the reversed field pinch device HBTXIA.[2]

References

[1] W Arter and D Edwards, Paper, EPS Budapest, 1985
[2] S Gee, J B Taylor, Paper, EPS Budapest, 1985
[3] P Grassberger, I Procaccia, Physica 9D, 189 (1983)
[4] A Howling et al, Paper No 333, EPS Budapest, 1985

ANOMALOUS TRANSPORT AND UNSTABLE MODES IN NEUTRAL-BEAM-HEATED L AND H PLASMAS OF ASDEX

G. Becker

Max-Planck-Institut für Plasmaphysik
EURATOM Association, D-8046 Garching

Abstract: It is attempted to determine the type of instabilities which are probably responsible for anomalous transport in the L and H regimes. Resistive and ideal ballooning modes are found to be stable. With collisionality factors $\nu_{*e,i}<1$, dissipative trapped-electron and trapped-ion modes are unstable in the L and H discharges and should be the prevailing drift instabilities. The time evolution of $\eta_{e,i} = d \ln T_{e,i}/d \ln n$, which are important parameters for these modes, is shown to be correlated with L and H transport. The operational limits of the H regime are found to be connected with variations of $\eta_{e,i}$, which primarily result from changing the profiles of injection heating and beam fuelling.

Introduction: Usually, the fluctuation spectra and the anomalous transport observed in tokamaks are ascribed to microturbulence excited by instabilities. The fluctuation levels and spectra and the scalings of diffusivities depend on the saturation processes in non-linear growth of the instabilities. As theory fails at present to predict the fluctuation spectra for strong turbulence, reliable microinstability-based anomalous diffusivities are not available.

Results from earlier transport simulations of neutral-beam-heated L (low-confinement) and H (high-confinement) discharges in ASDEX have been reported in Refs. /1-4/. In this paper the L and H confinement is investigated with respect to the underlying unstable modes. This is done by selecting the instabilities which might be the cause of the anomalous energy and particle fluxes observed with neutral injection and by comparing the peculiarities of transport in the L and H regimes with specific features of trapped-particle instabilities /5/.

Linear stability theory is important for confinement studies insofar as it can serve to select the unstable modes underlying the anomalous particle and heat fluxes. The most important instabilities that have to be considered for ASDEX plasmas are resistive and ideal ballooning modes and drift modes.

Stable and unstable modes in L and H discharges: Owing to the high electron temperature and correspondingly large electrical conductivity in L and H plasmas of ASDEX the linear growth rates of resistive ballooning modes are only very small. Highly unstable plasmas are anticipated for $S(r=0) = \tau_{res}/\tau_A \approx 10^5$ to 10^6, where τ_{res} and τ_A are the resistive and Alfvén times, respectively, while in the L and H phases typical S values are 10^8. According to Ref. /6/ the saturation level strongly decreases as S increases. Resistive pressure-driven modes in ASDEX are thus only weakly unstable and should produce very low fluctuation levels. Moreover, recent theoretical work has shown that resistive ballooning modes may be completely stabilized if finite parallel electron heat conductivity /7/ is taken into account.

A local criterion for stability of ideal ballooning modes reads /8/

$$-\frac{2\,R_o q^2}{B_t^2}\,\frac{\partial p}{\partial r} \leq f(s), \qquad (1)$$

where $q = rB_t/(R_oB_p)$ and $f(s)$ is a known function of the dimensionless shear $s = (r/q)\partial q/\partial r$. According to this criterion the analyzed L and H plasmas are stable to ideal ballooning and pressure-driven modes. This conclusion is supported by the result that for $B_t = 2.2$ T the volume-averaged β_t values including the beam contribution do not exceed 1 %. Stability calculations with the ERATO code have shown that the free and fixed-boundary equilibria based on measured profiles are stable to ideal ballooning and kink modes /9/.

It is obvious that these instabilities cannot cause the enhanced losses, which even occur in L discharges with low poloidal beta ($\beta_p = 0.3$) and rather small injection power P_{NI} of about the ohmic input /2/. Raising P_{NI} and β_p results in a smooth increase of the electron heat diffusivity. A change in scaling due to the possible onset of pressure-driven modes is not seen. We conclude that ideal ballooning modes are stable and thus cannot contribute to the observed anomalous losses.

In order to select possible candidates from the large family of drift instabilities, the radial extent and time development of collisionality regimes in OH, L and H discharges are determined (see Fig. 1). Both dissipative trapped-electron instabilities ($\nu_{*e} < 1$) and dissipative trapped-ion instabilities (ν_{*e}, $\nu_{*i} < 1$) have to be taken into account and are possibly responsible for the L and H transport. Important parameters for trapped-electron and trapped-ion modes are

$$\eta_{e,i} = \frac{d\ln T_{e,i}}{d\ln n} = \frac{r_n}{r_{Te,i}} \qquad (2)$$

with the density scale length $r_n = -n/(\partial n/\partial r)$ and the temperature scale lengths $r_{Te,i} = -T_{e,i}/(\partial T_{e,i}/\partial r)$.

A very characteristic time development of H discharges is observed. They are found to pass through the phases OH → L → H → L → OH, i.e. the H phase always develops from an L discharge and returns to an L phase. This indicates that the same instabilities are responsible for the L and H confinement, which is consistent with the finding that the criteria for dissipative trapped-particle instabilities are satisfied both in L and H plasmas. This conclusion is also supported by the parallels in empirical scaling of the electron thermal diffusivity, i.e. $\chi_e \sim B_p^{-1}$ in the L and H regimes /2,4/. The very specific features of the L and H confinement make it promising to look for correlations with trapped-particle instabilities.

Connection between η values and operational limits: As the time developments of η_e and η_i are rather similar, it is sufficient to look for parallels between η_i and local transport. The η_i values and scale lengths r_n and r_{Ti} presented are evaluated near the middle of the confinement zone ($r_{q=1} \leq r \leq 0.9\ r_s$ with separatrix radius $r_s = 40$ cm) at $r = 2r_s/3$ from measured and computed density and temperature profiles.

The time evolution of the profile parameters $\eta_{e,i} = r_n/r_{T_{e,i}}$ is found to be correlated with L and H transport and with the sequence of phases OH → L → H → L → OH passed through in H discharges (see Fig. 2). The L and H regimes correspond to large and small $\eta_{e,i}$ values, respectively. For $\bar{n} > \bar{n}_{cr}$ small η values result, so that the H regime is accessible, whereas at low densities peaked temperature profiles corresponding to large η are obtained (L regime). The operational limits for reaching the H mode, i.e. the minimum line-averaged density and the minimum injection power, can be qualitatively explained in terms of the parameters $\eta_{e,i}$ (see Figs. 3 and 4). Limiter discharges and divertor discharges with strong influx of neutral hydrogen or light impurities exhibit more peaked temperature profiles. According to the model they persist in the L regime owing to large η values.

The variation of η_e and η_i with the plasma parameters is found to be primarily due to changing the heating profiles of neutral injection. This becomes obvious from the very sensitive dependence of the absorbed beam power profile on the target density in the range of $\bar{n}$ variation ($\bar{n}$ = 1.5 to 8 x 10^{13} cm^{-3}).

As the more sophisticated linear stability theory of dissipative trapped-particle modes does not predict sharp η_e or η_i limits, the rather abrupt L-to-H transition cannot be explained by the correlation of η values with L and H transport only. Indeed, there are experimental indications that this transition is triggered by rapid profile changes due to processes near the separatrix.

References

/1/ Becker, G., ASDEX Team, Neutral Injection Team, Nuclear Fusion 22 (1982) 1589.
/2/ Becker, G., Campbell, D., Eberhagen, A., Gehre, O., Gernhardt, J., et al., Nuclear Fusion 23 (1983) 1293.
/3/ Becker, G., et al., Proc. 11th Europ. Conf. on Contr. Fusion and Plasma Physics, Aachen 1983, Vol. II, p. 299.
/4/ Becker, G., Nuclear Fusion 24 (1984) 1364.
/5/ Becker, G., Report IPP III/100 (1985).
/6/ Carreras, B.A., Diamond, P.H., Murakami, M., Dunlap, J.L., Bell, J.D., et al., Phys. Rev. Lett. 50 (1983) 503.
/7/ Sundaram, A.K., Sen, A., and Kaw, P.K., Phys. Rev. Lett. 52 (1984) 1617.
/8/ Connor, J.W., Hastie, R.J. and Taylor, J.B., Phys. Rev. Lett. 40 (1978) 396.
/9/ Kerner, W., private communication.

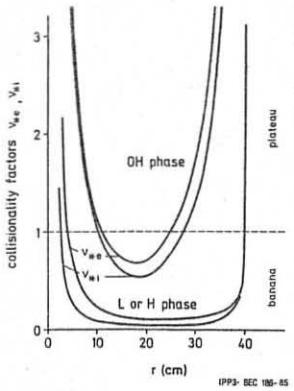


Fig. 1: Radial extent of banana and plateau regimes in the ohmic phase ($\bar{n}$ = 4.2 x 10^{13} cm^{-3}) and typical extent of banana zone in L and H phases.

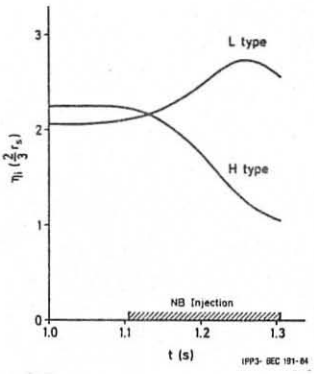


Fig. 2: Time behaviour of η_i in an L discharge with $\bar{n}$ = 2.5 x $10^{13}cm^{-3}$ (I_p = 380 kA, P_{NI} = 2.5 MW) and in an H discharge with $\bar{n}$ = 4.2 x 10^{13} cm^{-3} (I_p = 380 kA, P_{NI} = 3.2 MW).

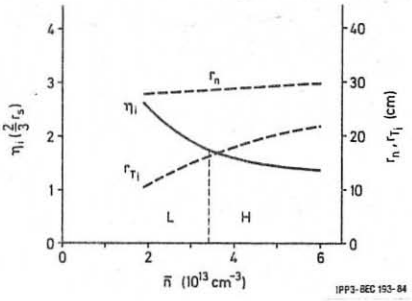


Fig. 3: η_i and scale lengths r_n and r_{Ti} vs. $\bar{n}$ for I_p = 380 kA and P_{NI} = 2.5 MW.

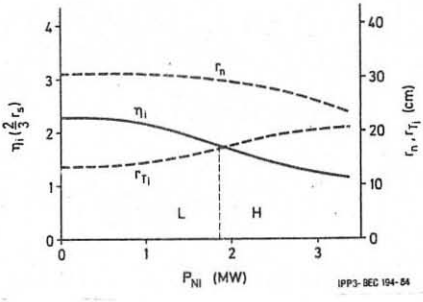


Fig. 4: η_i and scale lengths r_n and r_{Ti} vs. P_{NI} for I_p = 380 kA and $\bar{n}$ = 4.5 x 10^{13} cm^{-3}.

H

plasma edge physics

IMPURITY TRANSPORT IN THE LIMITER SHADOW DUE TO CONVECTION AND CROSS-FIELD DIFFUSION

H.A. Claaßen, H. Gerhauser
Institut für Plasmaphysik, Kernforschungsanlage Jülich GmbH,
Association EURATOM-KFA, FRG

We study the transport of impurities sputtered from a limiter by hydrogen ion bombardment using a drift-kinetic approach. The present theory accounts for convection both parallel and perpendicular to the magnetic field as well as for cross-field diffusion. We assume that the parallel-field transport is governed by collisional friction with hydrogen ions and by electrostatic acceleration [1], whereas the cross-field transport is caused by plasma turbulence rather than by neoclassical drifts.

The derivation of the underlying drift-kinetic equation and some basic features of the problem are already given in ref. [2]. The drift-kinetic equation could be solved analytically making use of Green's function for diffusion in an unbounded radially uniform plasma background. The volume and surface sources were assumed to be concentrated in a narrow boundary layer in contact with an impurity emitting limiter target.

In the present paper an extended version of this solution is given for a 'two-zone' model treating plasma core and scrape-off layer (s.o.l.) separately. The basic processes to be considered in the two plasma regions are listed in table 1.

scrape-off layer	plasma core
ion production from neutrals emitted from target and walls	
electron impact ionization	
ion injection from the target	recombination
parallel convection	
collisional friction with H^+/D^+	thermalization with H^+/D^+
electrostatic acceleration	
anomalous cross-field convection and diffusion	

table 1 : basic processes to be considered in the impurity transport problem

In order to get a tractable analytical solution, we use a slab geometry and approximate the radial density and temperature profiles of the plasma background by step functions with the steps being located at the separatrix (fig.1). Whereas the plasma core is assumed to be completely homogeneous, the s.o.l. is characterized by toroidal plasma variations (along the magnetic field lines perpendicular to the limiter surface) allowing for large plasma convection velocities and parallel electric fields. A similar model was used in ref. [3] to study the impurity transport by Monte-Carlo calculations.

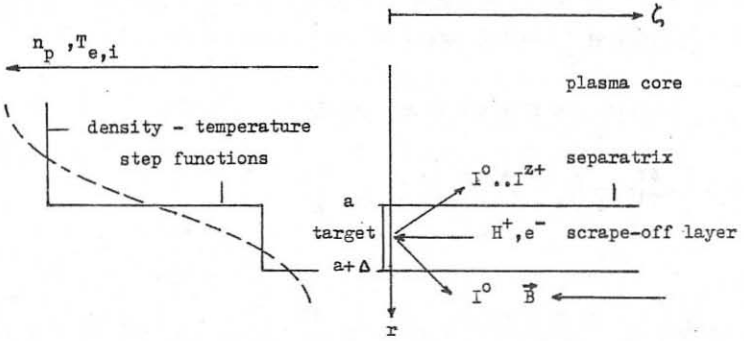


fig.1 : 'two-zone' model in slab geometry

The starting point of the analysis is the drift-kinetic equation integrated over $v_\perp$ [2]. The $v_\perp$ - integration produces a diffusion-convection equation for the guiding-centre distribution in $(r, \zeta, v_\parallel)$- space ($v_{\parallel,\perp}$= velocity components $\parallel$ resp. $\perp$ to the magnetic field). By use of a BGK (Bhatnagar-Gross-Krook) collision operator [4] to describe the thermalization between impurity and hydrogen ions in the plasma core and by application of the method of characteristics to treat the Fokker-Planck operator for collisional friction between impurity and hydrogen ions in the s.o.l. (neglecting the thermalization with respect to $v_\parallel$) [1], we arrive at a uniform representation of the diffusion-convection equation for the two separate plasma regions. For $V_\perp/D_\perp$= const. ($V_\perp$= cross-field convection velocity, $D_\perp$= diffusion coefficient assumed to be independent of the charge state of the impurity ions) and for steady-state conditions this equation can be solved by Laplace-transform methods to satisfy boundary conditions at finite radii. The impurity ion flux across the separatrix, which is taken as one of the boundary conditions for both the s.o.l. and the core solution, is determined from matching the solutions at the separatrix

and requires the inversion of an Abel integral equation. The impurity ion density, which by use of the BGK operator is still included in the solution as a space-dependent parameter, has to be calculated by successive approximation starting with the collisionless solution. To tackle the problem of ionization and recombination in the plasma core, we have to resort to linear matrix algebra.

As an example of the above mentioned solution procedure (to be published elsewhere) we give the following formula for the guiding-centre distribution function $a(\vec{\mu})$ of the phase space coordinates $\vec{\mu} = (\varrho = r-a, \zeta, v_\parallel)$ in the s.o.l. (in front of a limiter target of radial extent Δ):

impurity ion flux across the separatrix at $\varrho = 0$

$$a(\vec{\mu}) = \int_0^{\zeta} \frac{d\tau}{v_\parallel^{\pm}(\tau)} \gamma_\perp\left(0, \tau, v_\parallel^{\pm}(\tau)\right) F^{\pm}\left(\vec{\mu}, 0, \tau\right) + \tag{1}$$

surface sources — volume sources

$$+ \int_0^{\Delta} d\sigma \left[\delta\left(\sigma, \zeta^{\pm}, v_\parallel^{\pm}(\zeta^{\pm})\right) F^{\pm}\left(\vec{\mu}, \sigma, \zeta^{\pm}\right) + \int_{\zeta^{\pm}}^{\zeta} \frac{d\tau}{v_\parallel^{\pm}(\tau)} Q\left(\sigma, \tau, v_\parallel^{\pm}(\tau)\right) F^{\pm}\left(\vec{\mu}, \sigma, \tau\right) \right]$$

density of impurity ions emitted from the target at $\zeta^+ = 0$ $(v_\parallel \geq 0)$
or coming from the turning plane $\zeta^- = \zeta_T$ $(v_\parallel < 0,\ v_\parallel^-(\zeta^-) = 0)$

satisfying the boundary conditions

$$\left.\begin{aligned} a(\infty, \zeta, v_\parallel) &= 0 \\ \frac{v_\perp}{2}(\zeta)\, a(0, \zeta, v_\parallel) - D_\perp(\zeta) \frac{\partial a}{\partial \varrho}(0, \zeta, v_\parallel) &= \gamma_\perp(0, \zeta, v_\parallel) \\ a(\varrho, 0, v_\parallel \geq 0) &= \delta(\varrho, 0, v_\parallel) \end{aligned}\right\} \tag{2}$$

The integrations in eq.(1) are performed along the characteristic $v_\parallel^{\pm}(\tau)$. The latter depends on the coordinates $\zeta, v_\parallel$ of the point under consideration and includes friction and electrostatic forces. The splitting in solution branches for $v_\parallel \geq 0$ (upper index +) and $v_\parallel < 0$ (upper index -) by the method of characteristics yields automatically $\delta(\varrho, \zeta_T, 0)$ at the turning plane ζ_T as part of the solution. The fundamental solution to be used in eq.(1) for the boundary conditions, eqs.(2), reads

$$F^{\pm}\left(\vec{\mu}, \sigma, \tau\right) = \frac{1 + \exp\left(-\dfrac{\varrho\sigma}{\displaystyle\int_{\tau}^{\zeta} \frac{D_\perp(\xi)}{v_{\parallel}^{\pm}(\xi)}\, d\xi}\right)}{2\sqrt{\pi \displaystyle\int_{\tau}^{\zeta} \frac{D_\perp(\xi)}{v_{\parallel}^{\pm}(\xi)}\, d\xi}} \exp\left[-\frac{\left(\varrho - \sigma - \displaystyle\int_{\tau}^{\zeta} \frac{v_\perp(\xi)}{v_{\parallel}^{\pm}(\xi)}\, d\xi\right)^2}{4 \displaystyle\int_{\tau}^{\zeta} \frac{D_\perp(\xi)}{v_{\parallel}^{\pm}(\xi)}\, d\xi} - \int_{\tau}^{\zeta} \frac{\nu_{eff}(\xi)}{v_{\parallel}^{\pm}(\xi)}\, d\xi\right] \tag{3}$$

$\nu_{eff} = \nu_I - \alpha\nu_c$, ν_c = Coulomb collision frequency
ν_I = ionization frequency , α = collision parameter [1]

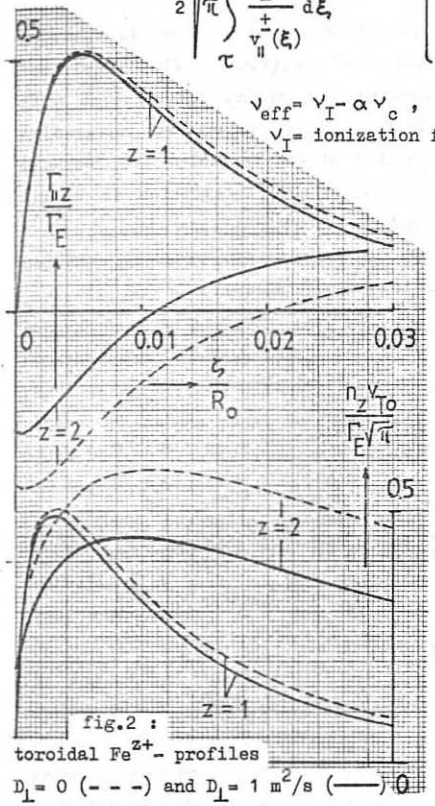


fig.2 : toroidal Fe^{z+}- profiles
$D_\perp = 0$ (- - -) and $D_\perp = 1\ m^2/s$ (——) 0

In case that volume and ζ - surface sources vanish in the plasma core the matching between s.o.l. and core solution yielding $\gamma_\perp(0, \zeta, v_\parallel)$ just cancels the term $\sim \exp(-\varrho\sigma/..)$ in $F^{\pm}(\vec{\mu}, \sigma, \tau)$. For this case toroidal particle flux and density profiles of Fe^{z+} in a deuterium plasma have been calculated in the limit $\alpha = 0$ and $v_\perp = 0$. The results for $\varrho = \frac{\Delta}{2} = 1$cm, $n_p = 2\times10^{12}\,cm^{-3}$, $kT_{e,i} = 2o$ eV are plotted in fig.2 assuming $ZeE_\parallel + m_z v_{Tz}\beta\nu_g = C(\zeta/R_o - \pi)$ with $E_\parallel(\zeta=0) = -kT_i/e\pi R_o$ [1]. The neutral particle sources and the emission flux Γ_E originating from deuteron sputtering of the limiter are given in ref. [2] assuming the emission distribution $\Gamma_E/(\pi v_{To}^3)\exp(-v_\parallel^2/v_{To}^2)\,\delta(v_\perp - v_{To})$ with $m_z v_{To}^2/2 = 2$ eV.

The authors thank Mr. G. Giesen for the numerical evaluation of eq.(1).

[1] H.A. Claaßen, H. Repp, Nucl. Fusion 23 (5), 597 (1983)
[2] H.A. Claaßen, H. Gerhauser, Report JÜL-1971, KFA Jülich (Febr. 1985)
[3] S. Sengoku et al., Nucl. Fusion 19 (1o), 1327 (1979)
[4] M.S. Grewal, Phys. Rev. 136 (5A), A1181 (1964)

A NUMERICAL STUDY OF PLASMA PROFILES IN THE LIMITER SHADOW REGION OF A TOKAMAK

H. Gerhauser, H.A. Claassen
Institut für Plasmaphysik, Kernforschungsanlage Jülich GmbH
Association EURATOM-KFA, P.O. BOX 1913, D-5170 Jülich, FRG

A 2-dimensional numerical study of a limiter scrape-off plasma in a strong magnetic field is undertaken on the basis of electron-ion fluid equations assuming local ambipolarity and accounting for plasma interactions with neutral particles recycled at the limiter. On a rectangular integration domain steady-state spatial profiles of the plasma variables are computed using a time relaxation method with explicit time integration in radial direction and an efficient implicit procedure in toroidal direction.
The basic eqs. are similar to /1/. We use continuity, parallel momentum balance, radial diffusion, electron and ion energy balance:

$$\frac{\partial n}{\partial t} + \frac{\partial}{\partial x}(nu) + \frac{\partial}{\partial y}(nv) = S_n$$

$$\frac{\partial}{\partial t}(mnu) + \frac{\partial}{\partial x}\left(mnu^2 + p_e + p_i - \frac{4}{3}\eta\frac{\partial u}{\partial x}\right) + \frac{\partial}{\partial y}(mnuv) = S_p$$

$$\Gamma^{\perp} = nv = -D^{\perp}\frac{\partial n}{\partial y}$$

$$\frac{\partial}{\partial t}\left(\frac{3}{2}nT_e\right) + \frac{\partial}{\partial x}q_e^{\parallel} + \frac{\partial}{\partial y}q_e^{\perp} = \left(u\frac{\partial}{\partial x} + v\frac{\partial}{\partial y}\right)p_e + Q_{ei} + W_e$$

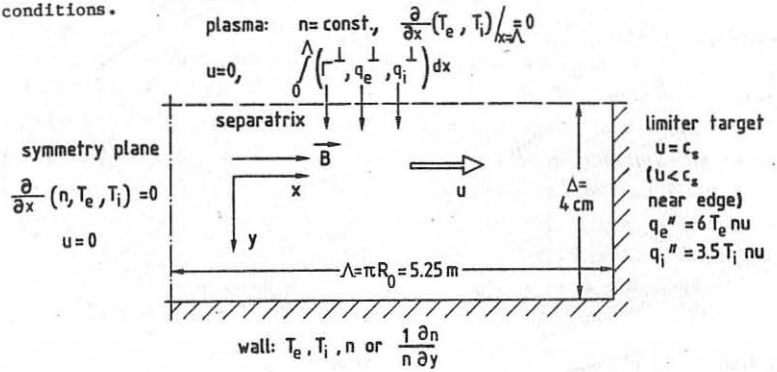
$$\frac{\partial}{\partial t}\left(\frac{3}{2}nT_i + \frac{1}{2}mnu^2\right) + \frac{\partial}{\partial x}\left(q_i^{\parallel} - \frac{4}{3}\eta u\frac{\partial u}{\partial x}\right) + \frac{\partial}{\partial y}q_i^{\perp} = -\left(u\frac{\partial}{\partial x} + v\frac{\partial}{\partial y}\right)p_e - Q_{ei} + W_i$$

$$\text{with } q_e^{\parallel} = \frac{5}{2}T_e nu - \chi_e^{\parallel}\frac{\partial}{\partial x}T_e \quad , \quad q_e^{\perp} = \frac{5}{2}T_e nv - \chi_e^{\perp}\frac{\partial}{\partial y}T_e$$

$$q_i^{\parallel} = \left(\frac{5}{2}T_i + \frac{1}{2}mu^2\right)nu - \chi_i^{\parallel}\frac{\partial}{\partial x}T_i \quad , \quad q_i^{\perp} = (\ldots)nv - \chi_i^{\perp}\frac{\partial}{\partial y}T_i$$

Here u is the toroidal convection velocity (x-axis $\parallel \vec{B}$), v the radial diffusion velocity (y-axis $\perp \vec{B}$), $p_{e,i} = nT_{e,i}$ with $T_{e,i}$ in eV, η is the viscosity, $\chi_{e,i}^{\parallel,\perp}$ are the heat conductivities, Q_{ei} is the energy exchange between species, S_n, S_p, W_e, W_i are source terms from the interaction with recycled neutrals, and $(u,v)\cdot\nabla p_e$ is volume work by electric fields for ambipolar motion. $D^{\perp}$ and $\chi_e^{\perp} = nD^{\perp}$ are assumed anomalous, the other transport coefficients are taken from classical theory /2/. The electric potential ϕ follows from $-eE_{\parallel} = e\,\partial\phi/\partial x = \partial p_e/n\,\partial x + 0.71\,\partial T_e/\partial x$.

The diagram shows the scrape-off-layer (s.o.l.) together with the boundary conditions.

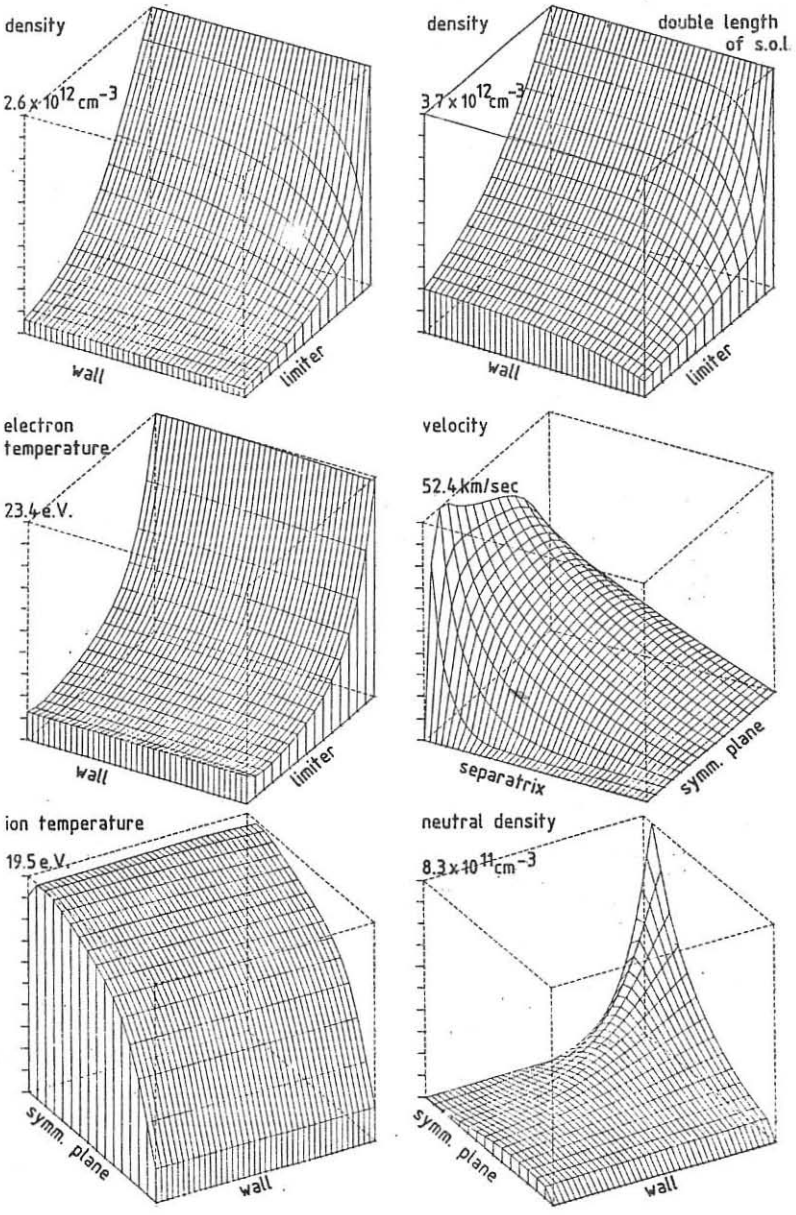


Fluxes across the symmetry plane must vanish. The temperatures and particle density (or $\partial n/n\,\partial y$) at the torus wall are prescribed, as well as the total particle and heat fluxes from the plasma core. $\Gamma^{\perp}(x)$ and $q_{e,i}^{\perp}(x)$ at the separatrix are adjusted such that n is independent of x and $\partial(T_{e,i})/\partial x$ vanish at the limiter edge. u reaches sound velocity $c_s = \sqrt{(T_e + T_i)/m_i}$ at the limiter surface and decays to 0 near the edge. $T_{e,i}$ at the limiter are determined by the usual matching between the continuum and sheath region in front of the target. Quadratic space extrapolation is used for n at limiter and u at wall.

The H^+-ions impinging on the target are nearly monoenergetic with near-normal incidence due to the acceleration in the Langmuir sheath. After neutralization part of them are reflected as H-atoms with reduced energy (fast neutrals n_o^f, u_o^f), part of them released as H_2-molecules with thermal energy. We use the particle and energy reflexion coefficients R_N, R_E from /3/ and assume the neutral atoms created from dissociation of molecules to start with ≈5 eV (slow neutrals n_o^s, u_o^s). We treat the recycled neutrals to be emitted normally ($\| \vec{B}$) from the limiter surface, those moving at an angle being rapidly lost to the wall or plasma due to the s.o.l. geometry. The neutral density $n_o = n_o^f + n_o^s$ decays according to

$$n_o^{f,s}(x) = n_o^{f,s}(\Lambda)\ \exp\left[-\int_{\Lambda}^{X} dx\ (\nu_I + \nu_{cx})/\,u_o^{f,s}\right]$$

and produces ions at the rate $S_n = \nu_I\, n_o$. The frequencies of electron impact ionization ν_I and of charge exchange collisions ν_{cx} are calculated by $\nu_{I,cx} = n\, S_{I,cx}$ with the rate coefficients $S_{I,cx}$ from /4/. The combined


density
2.6 x 10^12 cm^-3
wall
limiter
density
double length of s.o.l.
3.7 x 10^12 cm^-3
wall
limiter
electron temperature
23.4 e.V.
wall
limiter
velocity
52.4 km/sec
separatrix
symm. plane
ion temperature
19.5 e.V.
symm. plane
wall
neutral density
8.3 x 10^11 cm^-3
symm. plane
wall

momentum and energy transfer terms constitute S_p, W_e and W_i. We also include in W_e radiation losses by electron impact excitation.

The basic eqs. are transformed to give $\partial (n,u,T_e,T_i)/\partial t$ as explicit functions of the 4 variables and the sources. We discretize on a spatial grid with 40 x-steps and 15 y-steps and apply the Mc Cormack integration procedure /5/ which is second order accurate by using forward and backward spatial differencing alternately. The vectorization capabilities of the Cray X-MP give a speed-up factor of ≈ 25. The variables are relaxed in time until the profiles become stationary. Because of the very large $\chi^{\parallel}_{e,i}$ the usual CFL-criterion for numerical stability of the explicit time integration method imposes time steps $\approx 10^{-3}$ smaller along x than necessary along y. Therefore we derive an implicit modification of /5/ restricted to the x-direction and requiring only the solution of bidiagonal instead of block-tridiagonal equations. With this method a 50-fold CFL time step is enough for convergence within 1 or 2 minutes total CPU time. The particle and energy flows in the s.o.l. are analyzed and the balances checked.

We show six 3d computer plots of plasma profiles for TEXTOR-relevant parameters. The throughput of particles is $\approx 5.5 \times 10^{20}$ per sec and m along one side of the poloidal ring limiter, the throughput of energy ≈ 11 kW/m and the limiter recycling factor ≈ 0.9. The neutral particles penetrate rather deeply into the s.o.l. plasma and cause a monotonic decrease of n, T_e, T_i, ϕ towards the limiter accompanied by a slight constriction of the radial profiles. Since the segmented structure of the limiter leads to enhanced effective toroidal connexion lengths, one density plot is computed with double length of s.o.l. (10.5 m). Due to the sonic boundary condition at the limiter when keeping the radial input flux densities constant we find that the density at the separatrix and the radial decay length in the symmetry plane are both increased by $\approx \sqrt{2}$. The results are in good qualitative agreement with TEXTOR measurements (see paper No. 139 this conf.).

The authors thank Mr. G. Giesen for valuable programming assistance.

/1/ Yu.L. Igitkhanov et al., Proc. 11th EPS conf. Aachen vol. II,397 (1983)

/2/ S.I. Braginskij, Rev. Plasma Physics vol. 1, 205 (1965)

/3/ E. Cupini et al., NIMBUS report part I, 127/83-1/Fu-I/NET (1983)

/4/ R.L. Freeman, E.M. Jones, Report CLM-R 137 (1974)

/5/ R.W. Mac Cormack, AIAA Journal 20, 1275 (1982)

PLASMA SHEATH TRANSITION IN A MAGNETIC FIELD PARALLEL TO THE WALL

J. Behnel

Institut für Theoretische Physik, Ruhr Universität Bochum
D - 4630 Bochum 1, Federal Republic of Germany

Abstract: In the plasma sheath transition region the ion distribution function is calculated solving the ion-Boltzmann equation and accounting for charge exchange collisions and a magnetic field parallel to the wall. An equation for the selfconsistent electrostatic potential of the presheath is formulated.

Introduction

It is well known in plasma-wall interaction that - in order to fulfill the Bohm sheath criterion - a "pre-sheath" exists, where the ions are far away from their equilibrium and are accelerated to the ion sound speed. The investigation of this transition zone from a quasi-homogeneous plasma to the Langmuir sheath in front of a wall is a problem of great interest, since it forms the basis for calculating the selfconsistent electrostatic potential and for formulating exact boundary conditions to macroscopic transport equations.

In the unmagnetized plasma the presheath has been studied for various model assumptions, but in the presence of a magnetic field the only detailled approach to describe the transition zone is a numerical simulation method /1/, which is not jet suited to resolve the strong inhomogeneity and to allow for the correct boundary conditions. Therefore there is a strong need for an analytical treatment of the problem.

The kinetic treatment of the magnetized presheath

Due to the strong inhomogeneous situation our analysis has to be based on kinetic methods. We take the following model assumptions:

- there is plane geometry with a constant magnetic field parallel to the wall
- the Debye-length of the plasma is small compared to the ion gyro-radius calculated with the ion sound speed
- we account for charge exchange collisions with a constant collision frequency
- the density of the electrons is a prescribed function of the potential or the spatial variable.

With the last point we concentrate our investigation to the ions, which dominate the transition region.

We start from the stationary ion Boltzmann equation in cartesian coordinates

$$\omega v_z \frac{\partial f}{\partial z} + \omega (\chi'(z) - v_y) \frac{\partial f}{\partial v_z} + \omega v_z \frac{\partial f}{\partial v_y} = \left(\frac{\delta f}{\delta t}\right)_{cx} \qquad (1)$$

with the charge exchange collision term

$$\left(\frac{\delta f}{\delta t}\right)_{cx} = \nu_{cx} \, (n_+ (z) \, f_o (\underline{v}) - f (z, \underline{v})) \qquad (2)$$

where we have normalized all velocities to the ion sound speed and the only spatial coordinate z to the ion gyro-radius calculated with the ion sound speed. ω and ν_{cx} are the gyro- and collision frequency, respectively, n_+ is the ion density, f_o, f the distribution function of the neutrals and the ions and $\chi(z)$ is the negative electrical potential energy normalized to the thermal energy of the electrons. The electric field is oriented in z-direction, the magnetic field in x-direction.

To solve the Boltzmann equation we use the method of characteristics and integrate the distribution function

along the ion orbits. This is by no means a trivial task, since we neither know the ion orbit in the inhomogeneous field nor the electric field, which develops selfconsistently.

First we must classify the ion orbits into two groups: one group of "open" orbits hitting the wall and one of "closed" orbits doing periodic motions in the crossed electric and magnetic fields. Each group has a different form of boundary conditions. To formulate these conditions we devide the distribution function into its parts $f^+(z,v_y,v_z)=f(z,v_y,v_z>0)$ and $f^-(z,v_y,v_z)=f(z,v_y,v_z<0)$. We thus get with the wall located at z=0:

$$f^+(z,v_y,v_z\to 0) = f^-(z,v_y,v_z\to 0) \quad \text{for closed orbits and}$$

$$f^-(z=0,v_y,v_z) = r(v_y,v_z)$$
$$f^+(z,v_y,v_z\to 0) = f^-(z,v_y,v_z\to 0) \quad \text{for open orbits}$$

where $r(v_y,v_z)$ denotes the spectrum of reemitted ions from the wall.

In a special procedure we now can achieve a local classification of the orbits /2/, i.e. for a given potential we decide only upon z,v_y,v_z for the character of the orbits. Therefore it is now possible to integrate the distribution function for an arbitrary electric potential $\chi(z)$. The somewhat lengthy result reduces to a simpler form in the model of cold neutrals, a totally absorbing wall and in the limit $\frac{\omega}{\nu} \ll 1$:

$$f(z,v_y,v_z \gtrless 0) = 2\,\frac{\nu}{\omega}\,n_+\,(z-v_y)\,\delta\,(v_z^2+v_y^2-2\,(\chi(z)-\chi(z-v_y))$$

for open orbits (3)

$$f(z,v_y,v_z) = \frac{2}{\tau_o(z-v_y)}\,n_+(z-v_y)\,\delta\,(v_z^2+v_y^2-2(\chi(z)-\chi(z-v_y))$$

for closed orbits

With this we can formulate an equation for the selfconsistent electric potential. Since the presheath is quasineutral, the poisson equation is not suited to evaluate the potential, but it is the quasineutrality condition itself, which forms the equation for the potential. Integrating the distribution function and using $n_+ = n_-$ we get

$$n_-(z) = \int_{\bar{z}}^{z} \frac{n_-(u)}{\kappa(u)\sqrt{2(\chi(z) - \chi(u)) - (z - u)^2}}\, du \qquad (4)$$

with the function

$$\kappa(u) = \begin{cases} \frac{\omega}{\nu} & \text{for u corresponding to open orbits} \\ \frac{\tau_o(u)}{2} & \text{for u corresponding to closed orbits} \end{cases}$$

where $\tau_o(z)$ denotes the time of one gyration for an ion starting at $\bar{z}$ and z is the zero of the denominator in (4). (see /2/ for a detailled discussion)

For a given function $n_-(z)$ this is a complicated transcendental integral equation for the potential distribution $\chi(z)$, which has to be solved numerically in an iterative procedure. The calculations for this are in progress.

/1/ R. Chodura, 11th European Conf. on Contr. Fusion and Plasma Physics, Aachen 5.-9. Sept. 1983, paper C 30

/2/ J. Behnel, Report of the Sonderforschungsbereich Plasmaphysik Bochum/Jülich 85-02-118 (1985)

This work was done under the auspices of the Sonderforschungsbereich Plasmaphysik Bochum/Jülich of the Deutsche Forschungsgemeinschaft.

Electron Energy Flow in a Collisional Scrape-Off Plasma

R. Chodura
Max-Planck-Institut für Plasmaphysik, EURATOM Association,
D-8046 Garching, Fed. Rep. of Germany

Abstract

A kinetic model of particle and energy flow along the magnetic field of a scrape-off layer is described. Using a particle code with a Fokker-Planck collision term energy transport in the presheath region for arbitrary length of the mean free path as well as the transition between the collisional presheath and the collisionless sheath can be modeled. Profiles of the macroscopic quantities of a 1d flow along the magnetic field are shown.

1. Introduction

The main energy transport from the bulk plasma through the scrape-off layer to a limiter or divertor plate takes place by electron heat conduction. This heat flux is achieved in different ways whether or not the scrape-off layer is collisionless or collisional.

In the collisionless case the heat flux is strongly connected with the properties of the electrostatic sheath ahead of the wall: In the sheath electrons are reflected by the negative potential, but the most energetic ones penetrate the sheath and are absorbed at the wall. Thus the sheath establishes in the upstream region, i.e. the so-called presheath region, a velocity distribution which is mainly symmetric but has a truncated tail in the direction off the wall due to the lack of the absorbed electrons (we assume $B = o$ or B perpendicular to the wall for simplicity) (Fig. 1a). This asymmetry of the electron distribution gives rise to an electron energy flux $Q_e = \frac{m_e}{2}\int d^3v\, v^2 \underline{v} f_e$ which is a function of the truncation velocity $v_c = -\left[\frac{2}{m_e}(\phi-\phi_w)\right]^{1/2}$ and thus of the local potential $\phi(x)$ (ϕ_w is the wall potential). For truncated Maxwellian electrons with bulk temperature T_{es}, $Q_e = \delta_e T_{es}\Gamma$, with

Γ the particle flux through the sheath, and $\delta_e = 2 + e(\phi-\phi_w)/T_{es}$. If the presheath upstream of the sheath edge would be completely collisionless the truncated electron distribution would persist in this region. Temperature potential and energy flux would be uniform and equal to their values at the sheath edge.

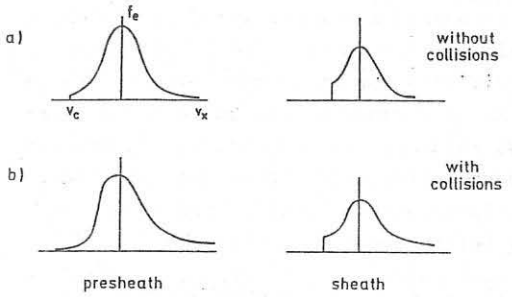


Fig. 1: Schematic electron distribution in the presheath and the sheath.

If the presheath is collisional the loss region in the electron distribution with increasing distance from the sheath will be filled up by collisional diffusion in velocity space. Electron energy flux therefore must be maintained by another asymmetric deformation of the electron velocity distribution, i.e. by a twist, such that the downstream wing of the distribution is enhanced and the upstream wing is reduced /1/ (Fig. 1b). The twist is produced as a combined effect of collisions and a spatial electron temperature gradient. Together with the elctron temperature, the potential and all other flow quantities in the collisional presheath become non-uniform.

In order to obtain a consistent description of a collisional presheath and its transition to a collisionless sheath one has to treat a kinetic model with a Fokker-Planck collision term. The numerical approach to this problem is shown in the next section.

2. Numerical method

The solution of the collisionless electrostatic kinetic (Vlasov) equation is equivalent to solving the equations of motion of several representative particles in their self-consistent electric field. This method was applied to a collisionless presheath and sheath in Ref. /2,3/. In a collisional plasma the equations of motion

have to be extended by a stochastic velocity range Δv_{coll} which represents the velocity change of an individual particle by collisions with other particles in the plasma within a time step Δt /4,5,6/.

In order to determine Δv_{coll} it is assumed that the distribution of the collision partners is nearly a Maxwellian determined by the momentary density, mean velocity and temperature at the location of the colliding particle. Under this condition the velocity change of the colliding particle is determined by the three coefficients of dynamic friction $\langle \Delta v_{\parallel} \rangle$, parallel and perpendicular diffusion $\langle (\Delta v_{\parallel})^2 \rangle$ and $\langle (\Delta v_{\perp})^2 \rangle$ respectively /7/. "Parallel" and "perpendicular" is to be understood as in respect of the direction of the particle velocity $\underline{v}$ before the collision. Thus

$$\Delta \underline{v}_{coll} = \left\{ \langle \Delta v_{\parallel} \rangle \Delta t + \xi_1 \left[\langle (\Delta v_{\parallel})^2 \rangle \Delta t \right]^{1/2} \right\} \underline{e}_{\parallel} + \xi_2 \left[\langle (\Delta v_{\perp})^2 \rangle \Delta t \right]^{1/2} \underline{e}_{\perp}$$

where $\xi_{1,2}$ are random numbers with $\langle \xi_{1,2} \rangle = 0$ and $\langle \xi_{1,2}^2 \rangle = 1$. $\underline{e}_{\parallel}$ and $\underline{e}_{\perp}$ are unit vectors parallel and arbitrarily perpendicular to $\underline{v}$. Δv_{coll} has to be summed up over the different species of colliding partners, i.e. ions and electrons.

3. Results

In order to study the qualitative behaviour of plasma flow through a collisional presheath and a collisionless sheath the numerical method was applied to a model plasma of ion mass ratio $m_i/m_e = 100$ and electron mean free path λ (as defined by the slowing down distance of an electron with thermal velocity by collisions with ions of charge Ze)

$$\lambda = m_e^2 v_{te}^3 / (4\pi Z^2 e^4 n_i \ln \Lambda) \quad , \quad v_{te} = (T_e/m_e)^{1/2}$$

of $\lambda = 5 \lambda_D$, where λ_D is the Debye length. The magnetic field is assumed to be zero or perpendicular to the wall. At $0 \leq x \leq 10$ (in units of λ_D) a source of electrons with temperature T_{eo} and of cold ions creates a steady-state 1d ambipolar plasma flux Γ. The plane at $x = 0$ reflects electrons with temperature T_{eo} and ions elastically. The wall at $x = L = 50$ is assumed to be totally absorbing.

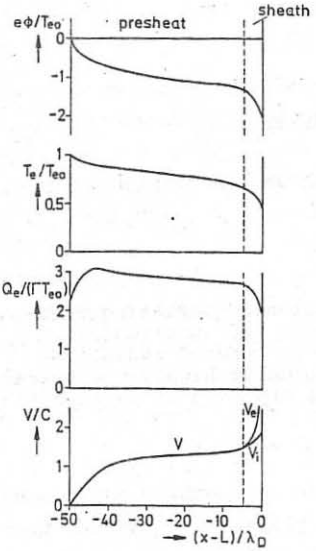


Fig. 2: Profiles of potential ϕ, electron temperature T_e, electron energy flux Q_e and mean velocity V for a mean free path length $\lambda = 5\,\lambda_D$.

Figure 2 shows profiles of potential ϕ, electron "temperature" $T_e = m_e \langle (v_{ex}-V_{ex})^2 \rangle$, electron energy flux $Q_e = \frac{m_e}{2} \langle v_e^2 v_{ex} \rangle$ and flow velocity of ions and electrons $V_{i,e} = \langle v_{i,e\,x} \rangle$ normalized by T_{eo}, particle flux Γ and sound velocity $C = (T_{eo}/m_i)^{1/2}$.

After being accelerated in the source zone a collisionless plasma would be uniform and isothermal in the presheath /3/. In the collisional case of Fig. 2 electron energy transport demands a negative gradient of electron temperature T_e which leads to a negative gradient of electron pressure p_e and potential ϕ. Ions, which have been accelerated to supersonic speed in the source zone already, feel the negative potential gradient and the oppositely directed thermal force $0.7\, n_e \nabla T_e$. In result, they are further accelerated at the expense of a decrease in electron energy flux Q_e. The plasma finally reaches the sheath region where ions are accelerated further and most of the electrons are reflected.

References

/1/ L. Spitzer, R. Härm, Phys. Rev. 89, 977 (1953).
/2/ R. Chodura, Phys. Fluids 25, 1628 (1982).
/3/ R. Chodura, Proc. 11th Europ. Conf. on Controlled Fusion and Plasma Physics, Vol. 2, p 479 (1983).
/4/ R.J. Mason, Phys. Fluids 23, 2204 (1980).
/5/ S.A. Khan, T.D. Rognlien, Phys. Fluids 24, 1442 (1981).
/6/ T. Takizuka, K. Tani, M. Azumi, K. Shimizu, J. Nucl. Mat. 128&129, 104 (1984).
/7/ L. Spitzer, Jr., "Physics of Fully Ionized Gases", (Interscience, New York, 1962).

Thermal Instabilities on Magnetic Flux Surfaces

J. Neuhauser, W. Schneider, R. Wunderlich
Max-Planck-Institut für Plasmaphysik, EURATOM Association,
D-8046 Garching, Fed. Rep. Germany

Abstract

The poloidal thermal stability of a collisional, radiating tokamak edge plasma is investigated analytically and numerically. A non-local electron heat flux model and a non-Coronal radiation model are included. Instabilities and poloidally highly asymmetric equilibria are found very similar to those observed in experiment.

1. Introduction

In many tokamaks strong poloidal asymmetries of density and temperature are sometimes observed in the edge plasma (e.g. ASDEX "predisruptive state" /1/; "marfes" in ALCATOR /2/). A poloidal thermal instability caused by impurity radiation and insufficient parallel heat conduction at low temperature was considered as the basic mechanism /1,2/. In the following we present analytical and numerical studies of this problem and we show that many of the experimentally observed features are, indeed, well reproduced.

2. Dispersion relation of a homogeneous, radiating plasma

In order to identify the basic mechanisms and their scaling, we start with an analytic treatment of the homogeneous plasma. Fluid equations along field lines are used. Perpendicular heat transport is included. Assuming a 2D perturbation of the form $T = T_o + \tilde{T} \cos(h_\parallel s) \cos(h_\perp x) \exp(\gamma t)$ etc. and using $P_{Rad} \sim n^\mu T^\nu$ in the vicinity of T_o ($\mu = 2$: const. impurity concentration; $\mu = 1$: const. impurity density) we get the following dispersion relation

$$\gamma^{*3} + \gamma^{*2}\left[(\omega_o\tau_{HC})^{-1} + \nu(\omega_o\tau_{Rad})^{-1}\right] + \frac{5}{3}\gamma^{*}(\omega_o\tau_{HC})^{-1} - (\mu-\nu)(\omega_o\tau_{Rad})^{-1} = 0$$

Here, $\gamma^* = \gamma/\omega_o$ is the growth rate normalized to the isothermal sound frequency $\omega_o^2 = 2\,kT_o\,h_\parallel^2/m$, and $\tau_{Rad} = 3\,n_o kT_o/P_{Rad}$ and $\tau_{HC} = (\tau_{HC\perp}^{-1} + \tau_{HC\parallel}^{-1})^{-1} = 3/(\chi_\perp h_\perp^2 + \chi_\parallel h_\parallel^2)$ are the radiation cooling time and the (parallel plus perpendicular) heat conduction times, resp.. Instability ($\gamma_1 > 0$) is obtained for

$$\nu \equiv \partial(\ln P_{Rad}) / \partial(\ln T) < \left[\mu - (\tau_{Rad}/\tau_{HC})\right]$$

i.e. for negative and even weakly positive ν because of pressure constancy on field lines for $\gamma \to 0$. The dispersion relation also describes correctly the sound waves and their modification by radiation ($\gamma_{2,3}$). As an example, fig. 1 shows $\gamma^* = f(\nu)$ for $\omega_o \tau_{HC} = \omega_o \tau_{Rad} = 1$, $\mu = 2$.

The validity of the fluid model is extended towards lower collisionality by applying a non-local form for the parallel electron heat flux $q_{\parallel}$ /3/, which in the limit of a small, periodic temperature perturbation reduces to a correction factor for the Spitzer-Härm heat flux q_{SH}

$$q_{\parallel} = q_{SH} / (h_{\parallel}^2 \lambda_{HC}^2 + 1)$$

where λ_{HC} is the mean free path of the heat conduction electrons ($\lambda_{HC} \approx 45 \lambda_o$, /3/). P_{Rad} is taken from non-Coronal calculations using data sets of K.Behringer /4/ with $n_o \tau_{imp}$ as parameter (fig. 2), i.e. a finite impurity residence time τ_{imp} is included. For typical edge conditions and impurities the cooling rate is roughly $L(T) = P_{Rad}/(n_o n_{imp}) \approx 10^{-25}$ [W cm^3]. Assuming carbon as impurity and $n_o = 10^{13}$ cm^{-3}, $T_o = 10$ eV, $\lambda_{\parallel} = 2\pi/h_{\parallel} = 30$ m (a field line length corresponding to one poloidal revolution, i.e. a "marfe"-type perturbation) and $\tau_{HC\perp} \gg \tau_{HC\parallel}$ we find instability, if a critical concentration $c_{crit} \approx 1$ % is exceeded, a value quite common in limiter experiments. For this example, $h_{\parallel} \lambda_{HC} \ll 1$ holds and the scaling in the vicinity is

$$c_{crit} \sim T_o^{7/2} h_{\parallel}^2 \left[(\mu - \nu)\, n_o^2\, L(T_o)\right]^{-1}$$

The scaling changes rapidly, however, if $h_{\parallel} \lambda_{HC} \gg 1$ (e.g. $\lambda_{\parallel} = 30$ m, $n_o = 10^{13}$ cm^{-3}, $T_o \gg 25$ eV) and c_{crit} becomes independent of $h_{\parallel}$ and n_o:

$$c_{crit} \sim \left[(\mu - \nu)\, \sqrt{T_o}\, L(T_o)\right]^{-1}$$

Typical c_{crit} values in this more collisionless regime, however, are around 10 percent (depending, of course, on the impurity) and are probably reached in experiment only occasionally or locally near sources (e.g. limiter sputtering, impurity puffing etc.). Altogether, instability seems to be quite likely for a variety of

plasma parameters and wave-lengths and many experimentally observed pecularities like "marfes" and high-amplitude fluctuations in the edge plasma may be driven that way.

3. Numerical simulations

Numerical solutions of the fully nonlinear 1D problem were obtained from a modified version of the hydrodynamic code SOLID /5/ coupled with a multifluid impurity code /4/. In the latter, each impurity charge state is treated as a testfluid, which is coupled to neighbouring states by ionization and recombination and to the hydrogen majority by collisions (friction and thermal forces). A finite impurity life time simulating cross field losses is included and the impurity source can be chosen arbitrarily. The only feedback from impurities onto the hydrogen plasma is assumed to occur via radiation cooling of the electrons (non-corona).

Starting with a weakly perturbed homogeneous plasma with parameters close to those mentioned in § 2, the stability criterion is clearly verified. In the unstable range, an initial instability is followed usually by a series of relaxation oscillations well below the sonic frequency, being caused by a slow redistribution of impurity charge states. The latter effect is even more important in case of inhomogeneous equilibria, obtained e.g. by assuming an in-out asymmetry of the radial heat flux in a tokamak. For infinite residence time τ_{imp} of impurities on a flux surface, a marfe-type equilibrium is relaxed on the 10 ms time scale because of thermal force effects. Stationary solutions however, are obtained, if τ_{imp} is in the ms range as appropriate for the tokamak edge.

We have also simulated a variety of experimental scenarios, e.g. a smooth electron density rise at constant impurity density and plasma pressure. These simulations have reproduced many of the experimentally observed stationary or transient pecularities in the tokamak edge, showing in turn the relevance of the model and of the basic mechanisms considered. Details must be given elsewhere.

Acknowledgement

We thank Dr. K. Behringer for providing his impurity data sets.

/1/ Niedermeyer, H., et al.; Proc. 11th Europ. Conf. Contr. Fusion and Plasma Physics, Aachen 1983, Eds. S. Methfessel, G. Thomas, EPS Geneva 1983, 7DI, 43; see also report IPP III/90, Garching (1983)

/2/ Lipschultz, B., et al.; Nucl. Fusion 24, 977 (1984)

/3/ Luciani, J.F., et al.; Phys. Rev. Lett. 51, 1664 (1983)

/4/ Neuhauser, J., et al.; J. Nucl. Mater., 121, 194 (1984)

/5/ Schneider, W., et al.; J. Nucl. Mater., 121, 178 (1984)

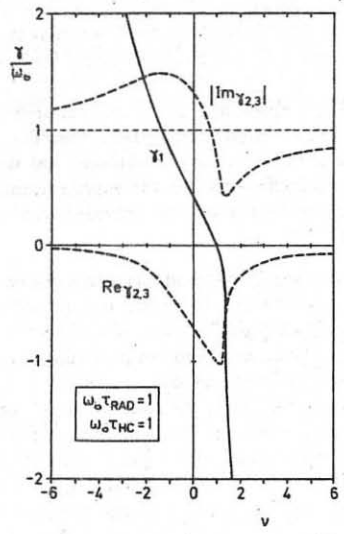


Fig. 1: $\gamma^* = f(\nu)$, $\nu = \partial(\ln P_{Rad})/\partial(\ln T)$

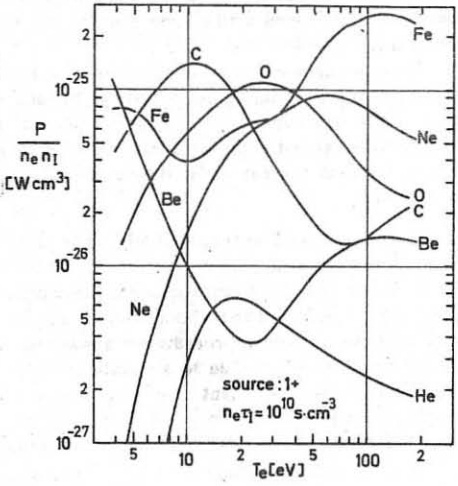


Fig. 2: Non-coronal radiation cooling rates calculated from data sets of K. Behringer (ref. /4/, chapt. 4)

TWO-DIMENSIONAL MULTISPECIES PLASMA TRANSPORT MODELLING

B.J. Braams

F.O.M. Instituut voor Plasmafysica,
Postbus 1207, 3430 BE Nieuwegein, The Netherlands.

On attachment to Max-Planck-Institut für Plasmaphysik,
D-8046 Garching bei München, Fed. Rep. Germany.

The design of a two-dimensional multifluid plasma transport code is described. The code is primarily intended for the modelling of particle and energy transport in the edge region of a tokamak, with specific interest in the study of the reactor relevant issues of helium pumping, impurity transport, and plasma-wall interaction, but it will have wider applicability. The most important enhancement with respect to the work described in [1]-[5] is the inclusion of several ion and neutral species in a multifluid model, whereas the earlier code assumed a single ion species, and employed a simple analytic model for the neutral particles.

Here, a 'canonical form' of the governing equations is given, and the numerical procedure is outlined. These equations are to be seen as the immutable core of the code. They specify the structure of the transport equations and of the boundary conditions, but do not provide explicit expressions for, e.g., the transport coefficients and the source terms. The code is at present under development, and further details will be provided at the conference.

Geometry and external fields. The physical domain of the model is a two dimensional, pseudo-rectangular region, which, for the tokamak studies, is located in a poloidal cross-section of the configuration. For the computation this region is mapped to a rectangle, $[0, N_x] \times [0, N_y]$. The mapping will usually be nonuniform, and need not be orthogonal, although the numerical procedure is allowed to deteriorate for large departures from orthogonality. It is possible to simulate internal boundaries, or to cut out parts of the rectangle, by the expedient of setting appropriate local metric coefficients or transport coefficients equal to 0 or to ∞. A finite-element style generality is not sought. All vector quantities have three components, so in this sense the code is $2\frac{1}{2}$-dimensional.

A fixed external magnetic field is assumed, and the contribution of the computed plasma currents to the magnetic field is ignored. The magnetic field need not be alligned with any coordinate. An electric field is computed as part of the solution, and this field contains both an assigned external contribution and a self-consistent part.

Unknowns. The desire to study helium pumping and impurity transport, and the rôle of the neutral particles in the important high recycling edge plasma regime, necessitates the use of a multispecies model. The temperature and velocity differences between electrons, main ions, impurities, and neutrals may also be significant, and therefore a multifluid model is chosen. For each fluid, which may be composed of several species, there will be one bulk velocity and one temperature. An additional unknown is the electric potential,

and thus, with N species grouped together into M fluids ($N \geq M \geq 1$), the primary unknowns of our model are,

n_α	$(0 \leq \alpha < N)$	$N \times$ number density,
Φ		electric potential,
$\mathbf{u}_a$	$(0 \leq a < M)$	$M \times$ bulk flow velocity,
T_a		$M \times$ temperature.

The subscript α is used as a species index and the subscript a as a fluid index, and the notation $\alpha \in a$ will be used to express that species α is included in fluid a. These primary unknowns are governed by a strongly coupled system of differential equations.

Secondary unknowns include:

$\mathbf{u}'_\alpha$	$(0 \leq \alpha < N)$	$N \times$ diffusive velocity,
Π_a	$(0 \leq a < M)$	$M \times$ viscosity tensor,
$\mathbf{q}_a$		$M \times$ heat flux.

The secondary unknowns are governed by transport relations, through which they are expressed in terms of the primary unknowns.

It is not specified here how the species are to be grouped into fluids, and it is intended that both the single fluid and the multifluid case can be treated using the same formalism and code. Furthermore, the case in which all species are neutral must also be handled correctly. In fact we hope to be able to model also the transition region between ionized plasma and neutral gas. These considerations have led to an approach in which quasi-neutrality is nowhere explicitely assumed.

Fundamental Equations. The first three moment equations for the single species α are the following.

Continuity:

$$\frac{\partial}{\partial t} n_\alpha + \nabla \cdot (n_\alpha \mathbf{u}_\alpha) = S^n_\alpha, \tag{1}$$

Momentum balance:

$$\frac{\partial}{\partial t} (m_\alpha n_\alpha \mathbf{u}_\alpha) + \nabla \cdot (p_\alpha \mathbf{I} + \Pi_\alpha + m_\alpha n_\alpha \mathbf{u}_\alpha \mathbf{u}_\alpha) = \mathbf{S}^{mu}_\alpha + \mathbf{F}_\alpha + e_\alpha n_\alpha (\mathbf{E} + \mathbf{u}_\alpha \times \mathbf{B}),$$

Energy balance:

$$\frac{\partial}{\partial t} \left(\frac{3}{2} n_\alpha T_\alpha + \frac{1}{2} m_\alpha n_\alpha u_\alpha^2\right) + \nabla \cdot \left(\left(\frac{5}{2} n_\alpha T_\alpha + \frac{1}{2} m_\alpha n_\alpha u_\alpha^2\right) \mathbf{u}_\alpha + \mathbf{q}_\alpha + \Pi_\alpha \cdot \mathbf{u}_\alpha\right) = S^E_\alpha + Q_\alpha + e_\alpha n_\alpha \mathbf{u}_\alpha \cdot \mathbf{E} + \mathbf{u}_\alpha \cdot \mathbf{F}_\alpha,$$

where S^n_α is the particle source for species α, $\mathbf{S}^{mu}_\alpha$ and S^E_α are outside sources of momentum and energy, $\mathbf{F}_\alpha$ and Q_α are sources of momentum and energy due to collisions among the species in the model, and all other quantities have their usual meaning. We define $\rho_\alpha = m_\alpha n_\alpha$ and $\sigma_\alpha = e_\alpha n_\alpha$.

Associated with the electric potential is Poisson's equation,

$$\Delta \Phi = -\frac{1}{\epsilon_0} \sum_\alpha e_\alpha n_\alpha, \tag{2}$$

More will be said about this equation in the Section on numerics.

The single particle momentum and energy equations are not solved, and the velocity $\mathbf{u}_\alpha$, occurring in the continuity equation, is represented as $\mathbf{u}_a + \mathbf{u}'_\alpha$, where $\mathbf{u}'_\alpha$ is governed by a transport equation. For the fluid a, the bulk velocity $\mathbf{u}_a$ and the temperature T_a are computed (in fact defined) through the equations,
Momentum balance:

$$\frac{\partial}{\partial t}(\rho_a \mathbf{u}_a) + \nabla \cdot (p_a \mathbf{I} + \Pi_a + \rho_a \mathbf{u}_a \mathbf{u}_a) = \mathbf{S}_a^{mu} + \mathbf{F}_a + \sigma_a(\mathbf{E} + \mathbf{u}_a \times \mathbf{B}), \tag{3}$$

Energy balance:

$$\frac{\partial}{\partial t}\left(\frac{3}{2} n_a T_a + \frac{1}{2}\rho_a u_a^2\right) + \nabla \cdot \left(\left(\frac{5}{2} n_a T_a + \frac{1}{2}\rho_a u_a^2\right)\mathbf{u}_a + \mathbf{q}_a + \Pi_a \cdot \mathbf{u}_a\right) = S_a^E + Q_a + \sigma_a \mathbf{u}_a \cdot \mathbf{E} + \mathbf{u}_a \cdot \mathbf{F}_a, \tag{4}$$

where n_a, ρ_a, σ_a, p_a, Π_a, $\mathbf{S}_a^{mu}$, and S_a^E are defined by summation of the corresponding single species quantity (the contribution of $\mathbf{u}'_\alpha$ to p_a and Π_a is ignored), and

$$\mathbf{q}_a = \sum\nolimits_{\alpha \in a}\left(\mathbf{q}_\alpha + \left(\frac{5}{2} n_\alpha T_\alpha + \frac{1}{2}\rho_\alpha u_\alpha^2\right)\mathbf{u}'_\alpha + \Pi_\alpha \cdot \mathbf{u}'_\alpha\right) \tag{5}$$

$$\simeq \sum\nolimits_{\alpha \in a}\left(\mathbf{q}_\alpha + \frac{5}{2} p_\alpha \mathbf{u}'_\alpha\right) \tag{5'}$$

$$\mathbf{F}_a = \sum\nolimits_{\alpha \in a}(\mathbf{F}_\alpha + e_\alpha n_\alpha \mathbf{u}'_\alpha \times \mathbf{B}) \tag{6}$$

$$= \sum\nolimits_{\alpha \in a} \mathbf{F}_\alpha + \mathbf{j}'_a \times \mathbf{B} \tag{6'}$$

$$Q_a = \sum\nolimits_{\alpha \in a}(Q_\alpha + \mathbf{u}'_\alpha \cdot (\mathbf{F}_\alpha + e_\alpha n_\alpha (\mathbf{E} + \mathbf{u}_a \times \mathbf{B}))) \tag{7}$$

$$= \sum\nolimits_{\alpha \in a}(Q_\alpha + \mathbf{u}'_\alpha \cdot \mathbf{F}_\alpha) + \mathbf{j}'_a \cdot (\mathbf{E} + \mathbf{u}_a \times \mathbf{B}) \tag{7'}$$

where $\mathbf{j}'_a = \sum_{\alpha \in a} e_\alpha n_\alpha \mathbf{u}'_\alpha$.

The specific transport relations are not specified here. In principle any prescription for $n_\alpha \mathbf{u}'_\alpha$ and $\mathbf{q}_a/T_a$ in terms of the primary variables of the model is allowed, including flux limited and nonlocal transport relations, although the numerical method is not expected to converge for all such cases. For the purpose of linearizing the equations as part of the numerical solution procedure, approximate local linear transport relations are given that connect the fluxes $n_\alpha \mathbf{u}'_\alpha$ and $\mathbf{q}_a/T_a$ with their conjugate forces,

$$\nabla \ln p_\alpha - e_\alpha(\mathbf{E} + \mathbf{u}_a \times \mathbf{B})/T_\alpha,$$
$$\nabla \ln T_a.$$

The source terms are also not specified here, but include the usual ionization and recombination processes, friction forces, and a model for radiation energy loss. Local linearized expressions for those terms causing strong coupling between equations are again required for the numerical solution procedure.

The use of a fluid model for the neutral "hydrogen" (H, D, or T) may seem to be only marginally justified, the requirement being that the mean free path for charge exchange is small compared to the gradient scale length, which is determined by the mean free

path for ionization. A flux limit will therefore be imposed on the neutral species diffusion rate, making the model at least qualitatively correct even in the marginal case. A further refinement that is envisaged is to treat the first generation of neutrals by analytical means, as this first generation will have a distribution function far removed from that of the bulk.

Numerical approach. In the previous work [1]–[5] a numerical procedure was employed in which for every implicit time step, each equation was relaxed in turn, using a procedure based on incomplete L*U decomposition of the five-point discretization. Thus, the spatial couplings in the system of equations were well reflected in the solution procedure, at the expense of a less satisfactory treatment of the coupling between the component equations. This approach is not tenable for the present multispecies, multifluid model with its many strong interspecies couplings, and we now employ a spatial splitting of the system of equations, solving large banded discrete equations at each implicit time step. Interest still centers on steady state solutions, and accuracy in following the time evolution is of little concern.

The treatment of the electric potential and of Poisson's equation, Eq. (2), is of some interest. It is clearly improper in plasma physics to consider Poisson's equation as governing the electric potential; instead it is usually replaced by a quasi-neutrality assumption, the electric potential then being obtained through the electron momentum equation. We have earlier given reasons for not wishing to follow that approach, to which may be added the elegance of treating all the species on an equal footing.

In fact, Eq. (2) is only part of complete system of equations, (1)–(4), solved simultaneously, and there is thus no basis for considering it specifically as an equation governing the electric potential. At each stage of the solution procedure, a system of equations is linearized, scaled, and passed to a band matrix solver. Inasmuch as the pivoting strategy of this solver allows to assign any correspondence between equations and unknowns, Eq. (2) will likely be associated with the electron density, and the electron equations will be associated with the electric potential.

Acknowledgement. The guidance of Prof. F. Engelmann is gratefully acknowledged. This work was performed under the Euratom-FOM and Euratom-IPP association agreements with financial support from ZWO and Euratom.

References.

1. B.J. Braams, *Numerical Studies of the Two-Dimensional Scrapeoff Plasma*, Paper B34, 11th European Conference on Controlled Fusion and Plasma Physics, Aachen, 1983, Europhysics Conference Abstracts **7D**–II (1983), 431–434.
2. B.J. Braams, P.J. Harbour, M.F.A. Harrison, E.S. Hotston and J.G. Morgan, *Modelling of the Boundary Plasma of Large Tokamaks*, J. Nucl. Mater. **121** (1984), 75–81.
3. B.J. Braams, *Modelling of a Transport Problem in Plasma Physics*, in "Topics in Applied Numerical Analysis", Vol 1, CWI Syllabus no 4 (J.G. Verwer, ed.), Centrum voor Wiskunde en Informatica, Amsterdam, 1984, pp. 149–164.
4. B.J. Braams, M.F.A. Harrison, E.S. Hotston and J.G. Morgan, *Application of Two-Dimensional Modelling to the Scrape-off and the Single-Null Poloidal Divertor Plasma of INTOR*, 10th International Conference on Plasma Physics and Controlled Nuclear Fusion Research, London, 1984.
5. B.J. Braams and C.E. Singer, *Low Temperature Plasma near a Tokamak Reactor Limiter*, Report PPPL–2191, Princeton Plasma Physics Laboratory, 1985; to be published in Nucl. Technol. and Fusion.

TWO DIMENSIONAL ANALYTIC AND NUMERICAL MODELS OF THE SCRAPE-OFF LAYER OF TOROIDAL LIMITERS

R. Simonini, W. Feneberg*, A. Taroni

JET Joint Undertaking, Abingdon, Oxon., OX14 3EA, UK
* On attachment from IPP, Garching

1. Introduction

From the classical system of equations describing the transport processes we derive a simplified system (one fluid, two spatial dimensions) of flow equations for the density n, the parallel velocity $v_{\|}$, the perpendicular velocity $v_{\rho cl}$ and the pressure p in the plasma boundary layer (Section 2).

A code has been written for the solution to these equations, based on a splitting technique in spatial directions (Section 3). Classical effects are taken into account and shown to be important: they lead to radial fluxes near the limiter tip of the same order (or even larger) of the anomalous ones usually adopted, resulting in a non-symmetric layer around the limiter. Another characteristic feature of this code with respect to other 2-D codes [1-3], is the avoidance of any symmetry assumption along field lines. A JET-like plasma with one toroidal limiter has been considered in the computations reported here.

2. Description of the Physical Model

We start from the moment equations for electrons and ions given in [4], assuming toroidal symmetry. We use an orthogonal coordinate system: ρ labels the magnetic surfaces, θ is a poloidal coordinate and ϕ the toroidal one. The metric is given by $ds^2 = H_\rho{}^2 d\rho^2 + H_\theta{}^2 d\theta^2 + R^2 d\phi^2$, R being the distance from the torus axis. In the electron equations we neglect the resistivity and the external toroidal electric field, which is justified in the thermal-diffusion dominated scrape-off layer. Using an expansion in the ratio ε of the toroidal Larmor radius to the layer thickness we find that in lowest order the flow is parallel to the magnetic field. From the toroidal component of the electron equations of motions we find the flow velocity $v_{\rho cl}$ perpendicular to the magnetic surfaces:

$$v_{\rho cl} = \frac{c}{enB_\phi H_\theta} \frac{\partial}{\partial \theta} (m_i n v_{\|}{}^2) - 0.71 \frac{c}{eB_\phi H_\theta} \frac{\partial T_e}{\partial \theta} \qquad \ldots (1)$$

here c is the light velocity, e the electron charge, m_i the ion mass, B_ϕ the toroidal magnetic field, T_e the electron temperature. The first term in eq (1) gives the contribution of a perpendicular electric current related to the inertial term of the ions, while the second comes from parallel thermal diffusion.

Assuming $T_e = T_i = T$ and one fluid, one is left with the system:

$$\sqrt{g} \frac{\partial n}{\partial t} = - \frac{\partial}{\partial \rho} \left[\frac{\sqrt{g}}{H_\rho} n v_\rho \right] - \frac{\partial}{\partial \theta} \left[\frac{n \sqrt{g}}{H_\theta} n v_{\|} \right] + \sqrt{g}\, S_i$$

$$\sqrt{g}\,\frac{\partial (nv_{\parallel})}{\partial t} = -\frac{\partial}{\partial \rho}\left[\frac{\sqrt{g}}{H_\rho} nv_\rho v_{\parallel}\right] - \frac{\partial}{\partial \theta}\left[\frac{h\sqrt{g}}{H_\theta} nv_{\parallel}^2\right] + H_\rho h \frac{\partial R}{\partial \theta} nv_{\parallel}^2 + \frac{2}{m_i}\frac{\partial}{\partial \theta}\left[\frac{h^2\sqrt{g}}{H_\theta^2}\eta_o \frac{\partial v_{\parallel}}{\partial \theta}\right]$$

$$- \frac{2}{3m_i}\frac{h\sqrt{g}}{H_\theta}\frac{\partial}{\partial \theta}\left[\eta_o \frac{h}{H_\theta}\frac{\partial v_{\parallel}}{\partial \theta}\right] - \frac{2}{m_i}\frac{h\sqrt{g}}{H_\theta}\frac{\partial p}{\partial \theta} + \sqrt{g}\, F_{\parallel}$$

$$3\sqrt{g}\,\frac{\partial p}{\partial t} = \frac{\partial}{\partial \rho}\left[\frac{\sqrt{g}}{H_\rho} q_\rho\right] + \frac{\partial}{\partial \theta}\left[\frac{\sqrt{g}h}{H_\theta} q_{\parallel}\right] - \frac{\partial}{\partial \theta}\left[\frac{5\sqrt{g}h}{H_\theta} v_{\parallel} p\right] + \frac{2\sqrt{g}}{H_\theta} hv_{\parallel}\frac{\partial p}{\partial \theta} + \sqrt{g}\, Q. \qquad \ldots (2)$$

Here $p = nT$, $\sqrt{g} = H_\rho H_\theta R$, $h = B_\theta/B$ is the ratio of the poloidal to the total magnetic field, while $v_\rho = v_{\rho cl} + v_{\rho an}$, $v_{\rho an}$ being an anomalous transverse diffusive velocity $v_{\rho an} = D/(nH_\rho)\,\partial n/\partial \rho$; D can be any anomalous diffusion coefficient. Here we choose for simplicity an Alcator-Intor form $D = D_{AI}/n$ with constant D_{AI}. η_o and $q_{\parallel}$ are the classical viscosity and parallel heat flux as given in [4]. q_ρ is the transverse heat flux, that we choose to be anomalous, again of the Alcator-Intor type: $q_\rho = \chi_{AI}\,\partial/\partial_\rho (p/n)$. S_i, $F_{\parallel}$ and Q are related to the neutral background and radiation losses. Here we assume $F_{\parallel} = 0$, while S_i and Q come from a simplified analytic background neutral model, relating the neutral density to their mean free path.

The model described above, with proper boundary conditions (see Sections 3 and 4), is on one side sufficient to study the effect of the classical term $v_{\rho cl}$ and on the other side contains, from the mathematical and numerical point of view, most of the features that are present in more complex boundary models. For this reason, it has been chosen as a test model for the present 2-D limiter edge code.

3. Numerical Method

The system of equations (1) and (2) requires a careful choice of the numerical scheme because it is not of the type solved by standard methods of numerical fluid dynamics. In fact, not only does it present a mixture of terms with hyperbolic and parabolic character, but the relative importance and even the presence of these terms depend on the direction considered. This must reflect on the choice of both the numerical method and the proper boundary conditions. We decided to adopt a splitting technique along directions as the one that can best treat the anisotropy due to the magnetic field. Thus, the per-se interesting sets of the 1-D parallel and perpendicular equations can be solved independently, and, moreover, the technique and the code can be easily extended to include additional equations (e.g. $T_e \neq T_i$, impurities).

A staggered finite difference grid is used for spatial discretisation to avoid unstable wriggles in the solution. Good resolution near the limiter is achieved by a non-uniform grid. Different terms can be centered in space and time in a different way by prescribing a set of parameters. Implicitness is treated by linearisation and iteration. An important feature characterising this code with respect to others (see e.g. [1-3] is the possibility to combine a periodicity condition for the plasma with given boundary conditions for the limiter, thus avoiding any assumption of symmetry along field lines. This is of course necessary to study the effects of eq. (1).

A full 2-D Monte-Carlo code is at present being interfaced to the fluid code to treat the background neutrals, with the aim to allow benchmark computations to calibrate simpler models of neutrals.

4. Numerical Results

To test the code and to study the effects of $v_{\rho cl}$ we have considered a simple configuration with a toroidal limiter that in the poloidal plane maps

as in Fig. 1. Dimensions are JET-like:

$$R_o = 300cm,\ \rho_{MP} = 110cm,\ \rho_L = 130cm,\ \rho_W = 150cm,\ \rho_L(\pi - \theta_L) = 40cm$$

These assumptions, in particular circular magnetic surfaces, are not essential to our code. Non-circular plasmas can be treated by supplying the appropriate metric coefficients (possibly tabulated). An extension to two toroidal limiters and different limiter and wall shapes is being implemented.

The following boundary conditions have been considered:

$\rho = \rho_{MP},\ \rho_W;\ -\pi \lesssim \theta \lesssim +\pi$: given n, T; $v_{||}$ advected by v_ρ or computed through $\partial v_{||}/\partial\rho = 0$.

$\theta = \pm\pi;\ \rho_{MP} \lesssim \rho < \rho_L$: periodicity.

$\rho = \rho_L,\ -\pi \lesssim \theta \lesssim -\theta_L$ or $\theta_L \lesssim \theta \lesssim \pi$: n, T are computed by interpolation from the values at $(\rho_L, \pm\theta_L)$; $v_{||}$ either advected or computed as above.

$\rho_L \lesssim \rho < \rho_W;\ \theta = \pm\theta_L$: n advected by $v_{||}$; $v_{||}$ computed by the free surface condition [1],[5] $2p = \eta_o\, h/H_\theta\ \partial v_{||}/\partial\theta$, $v_{||} \lesssim c_s$; $q_{||} = \beta n v_{||}\, T$, $\beta \simeq 1 - 5$, $T \gtrsim T_W$.

The transition of $v_{||}$ from the sound velocity c_s to zero at the limiter tip is represented by a linear decay along ρ over 2 or 3 steps ($\simeq$ 2cm). The width of this transition region influences the details of the nearby profiles, but not the general pattern. Similarly, we have found that reasonable changes in the values of T_W (2 - 10eV) and n_W (10^{10} - 10^{11} cm^{-3}) do not influence the results noticeably. More important can be the changes in the background neutral model and in particular the recycling model at the limiter. For this reason benchmark computations and/or coupling with a Monte-Carlo neutral code are required.

Within the frame of our present model and assumptions, the importance of $v_{\rho cl}$ is illustrated in Figs. 1-4. Figures 1-3 map n, $v_{||}$ and T in a typical case ($n_{MP} = 10^{13}$ cm^{-3}, $T_{MP} = 400eV$) with $v_{\rho cl}$. Here $D_{AI} = 4000cm^2/s$, $\chi_{AI} = 5 \times 10^{17}$ $cm^{-1}s^{-1}$. T near the limiter tip varies from $T_u = 32eV$ upwards to $T_d = 25eV$ downwards. More significant is the change of particle flux from $\phi_u = 4.0 \times 10^{18}$ to $\phi_d = 2.5 \times 10^{18}$ $cm^{-2}s^{-1}$. The up-down asymmetry does of course decrease as $v_{\rho an}$ increases, but it is still noticeable at D_{AI} as large as $40{,}000cm^2/s$. In this case we find T_u=32eV, T_d=29eV, $\phi_u = 2.9 \times 10^{18} cm^{-2}s^{-1}$, $\phi_d = 2.5 \times 10^{18} cm^{-2}s^{-1}$.

For comparison, Fig. 4 shows the pattern of the parallel velocity when the classical term is absent (dashed lines represent negative velocities).

In conclusion, even if these results are to be considered as preliminary only, due to the simplifying assumptions in models and geometry, they show that classical effects can indeed play a role in the boundary layer. Moreover, they illustrate the potential capabilities of the code which is at present being adapted to more realistic JET situations.

References

[1] Igitkhanov, Y.L., Kukushkin, A.S., Pigarov, A.Y., Pistunovich, V.I., Proc. 11th European Conf. on Controlled Fusion and Plasma Physics, Aachen, 5-9 September 1983.

[2] Braams, B.J., Ibidem.

[3] Petravic, M., Heifetz, D., Post, D., Proc. 10th IAEA Int. Conf. on Plasma Physics & Controlled Nucl. Fusion Research, London, 12-19 Sept. 1984.

[4] Braginskii, S.I., Rev. of Plasma Physics, edited by Leontovich, M.A., (Consultant Bureau, New York, 1965), Vol 1, p 205.
[5] Landau, L., Lifchitz, E., Mecanique des Fluides, Editions MIR, Moscow, 1971.

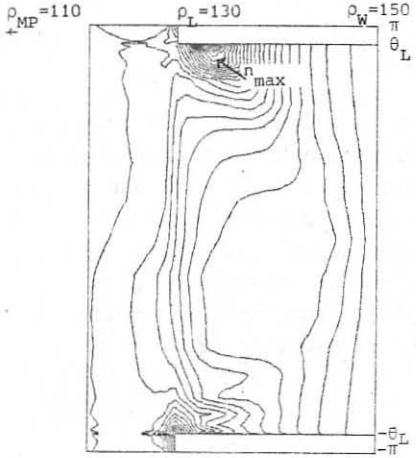


Fig 1: Density (cm^{-3})
n_{max} = 2.6 x 10^{13} Δn = 7.2 x 10^{11}

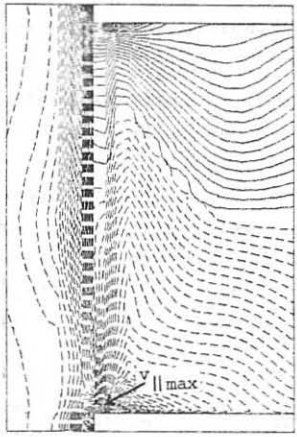


Fig 2: Parallel flow velocity (cm/s)
$v_{\parallel max}$ = 5.0x10^6 $\Delta v_{\parallel}$ = 1.6x10^5

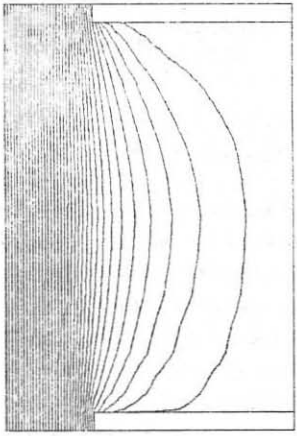


Fig 3: Temperature (eV).
T_{max} = 189, ΔT = 5.2

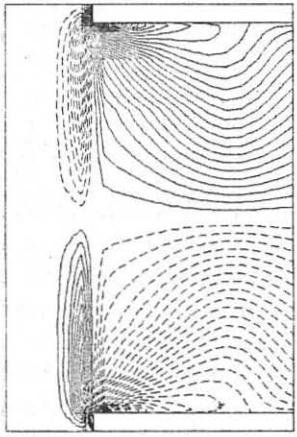


Fig 4: Parallel flow velocity (cm/s) when v_{pol} = 0
$v_{\parallel max}$ = 4.8x10^6, $\Delta v_{\parallel}$ = 1.3x10^5

IMPROVED HYDRODYNAMIC SIMULATION OF A DIVERTOR PLASMA UNDER WEAK COLLISIONS

Yu.L.Igitkhanov, A.S.Kukushkin, V.I.Pistunovich, V.A.Pozharov
I.V.Kurchatov Institute of Atomic Energy, Moscow, USSR

Simulation of the heat and particle transfer in the near-wall plasma in ASDEX within the frames of a hydrodynamical approximation results in a good quantitative agreement with the values of density and temperature experimentally measured near the divertor plates /1-3/. At the same time the calculated values of density and temperature in plasma within the scrape-off layer close to the symmetry plane noticeably differ from the experimental values. In typical regimes with a strong recycling (Q_s= 2.5 MW), the temperatures of electrons and ions at the separatrix are close to each other and equal to $\sim$ 120 eV, density $\sim 6\text{-}9\times10^{12}\,cm^{-3}$. The calculated values are $T_{es} \approx 50$ eV, $T_{is} \approx 67$ eV and $n_s \approx 3{,}5\times10^{13}\,cm^{-3}$ /1-2/. The classical expressions for the longitudinal heat conduction and viscosity coefficients, the Bohm expressions for the transversal ones are used in the model. The ratio between the input electron heat flow and the input ion heat flow is assumed to be equal to $Q_{es}/Q_{is} = 2$. This ratio is a free parameter in the model. Under the conditions of energy removal to the divertor as heat conduction, $T_{es}/T_{is} = \left(\frac{Q_{es}\chi_i}{Q_{is}\chi_e}\right)^{2/7}$. Hence, $T_{is} \approx T_{es}$, when $Q_{es} \sim \sqrt{\frac{m_i}{m_e}}\,Q_{is}$. The calculations show that a rise in the electron fraction of the input power results in a reduction in the ion temperature at the separatrix and, practically, weakly affects the electron temperature. Thus one can equalize the temperatures at the separatrix at a level of electron temperature ($\sim$ 50 eV) by the proper option of a ratio between the input heat flows. It is shown below that a difference in the calculated plasma parameters is connected with the overestimation of the longitudinal heat conduction coefficients $\chi_{i,e}$ and with that of the longitudinal viscosity coefficient η_i in the layer close to the symmetry plane, where the ranges of hot particles become comparable with the field line length. The transfer coefficients are mainly determined by the di-

stribution function tails as the longitudinal transfer of momentum and energy is performed mainly by hot particles. The tail is deteriorated with the departure of particles to the plate. This results in a reduction in the hydrodynamical heat conduction and viscosity coefficients under conditions, when a mean free path calculated with plasma temperature is much less than the characteristic length, and the condition of hydrodynamical approximation is formally satisfied /4/. A reduction in classical coefficients of longitudinal transfer can be taken into account:

$$\tilde{\chi}_{e,i} = \chi_{e,i}\left(1+\alpha_{e,i}\frac{\lambda_{e,i}}{L}\right)^{-1}, \quad \tilde{\eta}_i = \eta_i\left(1+\alpha_i\frac{\lambda_i}{L}\right)^{-1} \qquad (1)$$

where $\lambda_{e,i}(n,T)$ is the Coulomb range, L is the characteristic longitudinal length accepted in calculations as $L = \min\left\{L_0, 1/\frac{\partial \ln T}{\partial z}\right\}$, L_0 is the length of a field line from the symmetry plane to the divertor plate. The parameters $\alpha_{e,i}$, according to the above mentioned can be much higher than unity. Their magnitude is determined by a nature of the particle distribution function.

The results of calculations with coefficients (1) are given in Fig.(1-3). A longitudinal density distribution (a), velocity (b) and temperature (c) in the layer and in the divertor volume calculated for a typical regime with strong recycling (Q_s = = 2.5 MW, $Q_{es}/Q_{is} = 2$) /1,2/ are given in Fig.1. The distributions corresponding to the classical transfer coefficients (solid line) are given for comparison. One can see that the account for non-locality results in the plasma temperature rise and density drop in a layer near the symmetry plane and, at the same time, weakly affects the plasma parameters in the divertor. A drop in the plasma density is connected with a plasma velocity increase in the layer due to a decrease in the viscosity coefficient. The values of density and temperature at the separatrix, close to the experimental ones, have been obtained for the option $\alpha_i = \alpha_e \simeq 50$. Note that the ratio $\lambda_{e,i}/L \lesssim 0.1$ practically in the whole region, including that near the walls. The transversal plasma density and temperature distributions in the layer near the symmetry plane are given in Fig.(2,3). It has been noted previously that the transversal distributions peaked towards

the separatrix are found to be low sensitive to a change of transversal transfer coefficients /1,2/. This circumstance is, probably, partly connected with an overestimation of the longitudinal transfer and with a smallness of the transversal heat and particle flows. As it follows from Fig.(2,3),a plasma spread across the layer is increased with a decrease in the longitudinal removal, that results in a noticeable flattening of transversal profiles. The last circumstance results in a more uniform plasma distribution within the layer, including the zone near the plates, and can assist in a greater volumetric energy loss in the divertor.

In conclusion, we would like to note that the estimates (1) can be written more precise, if one takes the account of the highest order moments in the distribution function by Grad's method.

References

1. Yu.L.Igitkhanov, A.S.Kukushkin, A.Yu.Pigarov, V.I.Pistunovich, V.A.Pozharov. Paper IAEA-C-44/E-11-5-2 at the 10th Intern.Conf. on Plasma Physics and Controlled Fusion, London, 1984, Sept. 12-19.
2. Yu.L.Igitkhanov, A.S.Kukushkin, A.Yu.Pigarov, V.I.Pistunovich, Doklady Academii Nauk (DAN) 278, 2, 1984, p.338.
3. K.Lackner et al. 10th Int.Conf. on Plasma Physics and Contr. Nucl. Fus. Rsearch, London, UK, Sept. 1984 IAEA-CN-44/A-V-4.
4. D.Gray, J.Kilkenny, Plasma Physics, 22, p.81 (1980).

Figure captions

Fig.1 Longitudinal distributions of density (a), velocity (b) and temperature (c) in the layer and in the divertor volume. Input heat and particles flows through the separatrix: $Q_s = 2{,}5MW$, $\Phi_s = 2\cdot10^{12}s^{-1}$, $Q_{es}/Q_{is} = 2$. Solid lines correspond to the standard regimes with classical coefficients /1,2/, others are obtained with the account for a correction factor,for the dashed lines: $\alpha_i = \alpha_e = 50$, $L = min\{L_0, 1/\frac{\partial c_n T}{\partial z}\}$ for the dotted lines: $\alpha_i = \alpha_e = 50$, $L = L_0$ where L_0 is the length of a magnetic field line from the symmetry plane to the divertor plate.

Fig.2,3 Transversal plasma density and temperature distribution near the symmetry plane. Designations are the same as in Fig.1

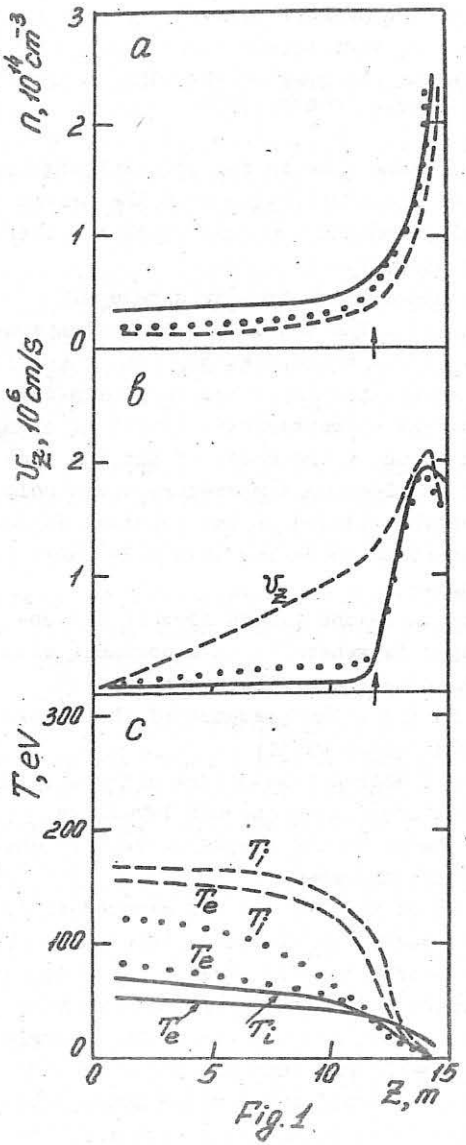


Fig.1

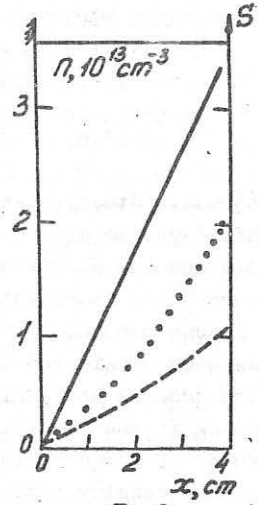


Fig.2

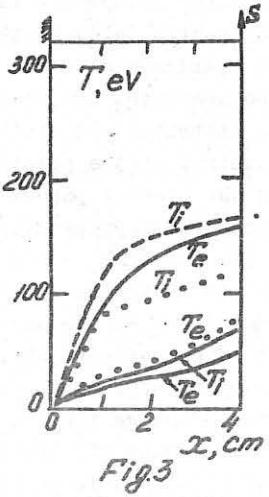


Fig.3

THERMAL FLUXES WITH PLASMA CONVECTION IN THE TOKAMAK LIMITER SCRAPE-OFF LAYER

A.V. Nedospasov, V.G. Petrov
Institute for High Temperatures of the USSR Academy of Sciences, Moscow, USSR

Abstract. Steady-state plasma flow in the poloidal limiter scrape-off layer is discussed. The distributions of the plasma parameters and the electrical potential are found with the thermal balance being taken into account.

1. Plasma convection in the tokamak limiter scrape-off layer has been considered in [1] . The ion and electron temperatures were assumed constant. It was found that poloidal electric field acting in the limiter scrape-off layer led to plasma drift along the minor torus radius. The characteristic length of change in the plasma density proved to be of the order of the ion cyclotron radius calculated for an electron temperature and a poloidal magnetic field. This length depended on the poloidal angle. The radial electric field was found to be low in a wide range of the poloidal angle meanings.

The theoretical description of the plasma flow in the poloidal limiter scrape-off layer is generally in accordance with the experimental data. On the other hand, the strong radial electric field was observed in [2] . The presence of this field cannot be accounted for in the frames of [1] .

The distributions of the electron temperature and the electric potential in the poloidal limiter scrape-off layer are found in the present paper. Change in the plasma convection due to temperature inhomogenuity is discussed.

2. All the ions impinging on the limiter are assumed to be converted to neutrals, and no secondary electron emission is present. The plasma in the scrape-off layer is assumed to be transparent to the neutrals generated in the neutralization process. The energy exchange between the ions and the electrons is neglected as the exchange time is much longer than the particle life time in the scrape-off layer. The transversal temperature conductivity of electrons is assumed to be anomalously high with the

constant coefficient $\chi_\perp$. The possible anomalous diffusion is not taken into account. The presence of such diffusion would not change the results qualitatively.

The plasma density and the ion and electron temperatures slightly vary along the magnetic field line sections the both ends of which hit the limiter. Each such section can be characterised by the minor moving radius r and the minor azimuth θ. The azimuth θ is reckoned from the external contour of the torus in the poloidal cross section opposite to the limiter cross section. θ is positive at the ion toroidal drift side and it is negative at the electron toroidal drift side.

3. The electron energy equation is integrated along the magnetic field line sections. The ratio of the plasma pressure to the magnetic pressure and the inverse aspect ratio $\frac{a}{R}$ are supposed small where a is the limiter edge radius, R is the torus major radius.

The boundary condition at the limiter necessary for the electron energy equation has the form

$$\left| -\chi_\perp n \nabla_n T_e + \frac{5}{2} T_e n V_{e\parallel} \right| = (2T_e + e\varphi) n \sqrt{\frac{T_e}{2\pi m}} \exp\left(-\frac{e\varphi}{T_e}\right)$$

where φ is the Langmuir potential drop, subscript ($_\parallel$) means the component along the magnetic field, $nV_{e\parallel}$ is the electron flux, m is the electron mass.

Electrons loose the additional energy ($\frac{T_e}{2}$) while moving to the limiter along the magnetic field in the longitudinal electric field, which brakes electrons and accelerates ions. Finally the electron energy equation integrated over the magnetic field line section and transformed with the help of equations [1] is

$$(1 + \frac{\varphi^*}{e^\tau})\left\{\sqrt{\frac{e^\tau + T_i^*}{2}} + \frac{\Lambda}{2}\sin\theta\left[(e^\tau + T_i^*)\frac{\partial u}{\partial z} + \frac{\partial(e^\tau + T_i^*)}{\partial z}\right]\right\} =$$

$$= s^2\left[\frac{\partial^2\tau}{\partial z^2} + \left(\frac{\partial\tau}{\partial z}\right)^2 + \frac{\partial u}{\partial z}\frac{\partial\tau}{\partial z}\right] + \frac{3}{2}\Lambda K\left(\frac{\partial\tau}{\partial\theta}\frac{\partial\varphi^*}{\partial z} - \frac{\partial\tau}{\partial z}\frac{\partial\varphi^*}{\partial\theta}\right) +$$

$$+ \Lambda\sin\theta\left(\frac{7}{4}e^\tau\frac{\partial\tau}{\partial z} + \frac{e^\tau}{2}\frac{\partial u}{\partial z} - \frac{1}{2}\frac{\partial\varphi^*}{\partial z}\right) \qquad (1)$$

The dimensionless variables $T_i^* = \frac{T_i}{T_a}$, $\tau = \ln \frac{T_e}{T_a}$, $\varphi^* = \frac{e\varphi}{T_a}$, $u = \ln \frac{n}{n_a}$ and the parameters $\Lambda = \frac{4T_a cq}{eB\sqrt{\frac{2T_a}{M}}} \sin\frac{\pi}{q}$, $k = \frac{\pi R}{4qq \sin\frac{\pi}{q}}$, $s^2 = \frac{\pi R \chi_\perp}{\sqrt{\frac{2T_a}{M}}}$ are introduced. Here T_a, n_a are the plasma temperature and density at the internal boundary of the scrape-off layer (r = a), respectively, q is the safety factor, B is the magnetic field, c is the speed of light, M is the ion mass.

The equation is valid in the region $-\pi + \sqrt[3]{\frac{\Lambda}{q}} \lesssim \theta \lesssim \pi - \sqrt[3]{\frac{\Lambda}{q}}$ where the poloidal variation of the plasma density proves to be insignificant in comparison with the radial variation.

The contribution of the radiative energy transport to the electron energy balance can be taken into account by decreasing s.

The ions in the scrape-off layer have no potential barrier to get to the limiter. They carry out the mean energy and the ion temperature should slightly change along the minor moving radius. $T_i^* = 1$ is set.

4. As a zero approximation ($\frac{\Lambda}{s} = 0$) the solution $\tau_0 = 0$ can be obtained. The results of [1] are valid in this case:

$$\varphi_0^* = \ln \sqrt{\frac{M}{4\pi m}} - \ln\left(1 - \frac{\Lambda}{d}\sin\theta\right) \qquad (2)$$

$$u_0 = -\frac{r-a}{d}, \quad d = \frac{\Lambda \sin\theta}{2(1 - x \pm \sqrt{x^2 - x})}, \quad x = \exp\left(\frac{1-\cos\theta}{2k}\right) \qquad (3)$$

The sighn $\pm$ refers to $\theta \gtrless 0$, respectively. As a first approximation one can obtain from (1)

$$\tau_1 = -\frac{r-a}{s^2}\left[(\varphi_0^* + 1)(d - \Lambda\sin\theta) + \frac{\Lambda}{2}\sin\theta\right] \qquad (4)$$

In the range $-\pi + \sqrt[3]{\frac{\Lambda}{q}} \lesssim \theta \lesssim \frac{\pi}{6}$ the small corrections for solutions φ_0^*, u_0 have the forms:

$$\varphi_1^* = \tau_1 \varphi_0^* \qquad (5)$$

$$u_1 = \frac{\Lambda}{d}\left\{-\varphi_0^* \frac{\partial \tau_1}{\partial r}\sin\theta\,(r-a) + \left[\frac{k}{d}\left(\frac{\varphi_0^*}{d}\frac{\partial \tau_1}{\partial r}\frac{\partial d}{\partial \theta} + \frac{\partial}{\partial \theta}\left(\varphi_0^* \frac{\partial \tau_1}{\partial r}\right)\right) - \frac{1}{4\Lambda}\frac{\partial \tau_1}{\partial r}\right]\frac{(r-a)^2}{2}\right\} \qquad (6)$$

5. The calculations have been made with B=2T, T_0=20 eV, q=3, a=35 cm, R=150 cm, $\chi_\perp = 10^4$ cm^2/c. This corresponds to Λ =0.24 cm, k=1.3, s=1.05 cm. The dependence of the characteristic length of change in the electron temperature $\left(-\Lambda \frac{\partial \tau}{\partial r}\right)^{-1}$ on the poloidal angle θ is presented in Fig.1. The length decreases

along with $\chi_\perp$. The dependence of the electric potential φ^* on the poloidal angle θ with r=a and r=a+Λ is presented in Fig.2. There is a radial electric field in the scrape-off layer. It's strength is about $\frac{T_a}{e\Lambda}$. It leads to a poloidal plasma rotation. The characteristic length of radial change in the plasma density proves to be more profound function of the poloidal angle θ than it is in the case $\tau=0$. With $\theta>0$ the characteristic length is at average much longer than with $\theta<0$. The poloidal electric field in region $|\theta|>\pi-\sqrt[3]{\frac{\Lambda}{a}}$ is opposite to the field in the region $|\theta|<\pi-\sqrt[3]{\frac{\Lambda}{a}}$. A part of the plasma outcoming into the scrape-off layer in the region $|\theta|<\pi-\sqrt[3]{\frac{\Lambda}{a}}$ drifts poloidally to the internal contour of the torus. On entering the region of the inverse poloidal electric field it returns to the main tokamak volume. In particular this can lead to impurity penetration in the main discharge. One can evaluate the returning part of the plasma outflux. It is about 10 per cent.

The thermal fluxes to the ion and electron sides of the limiter prove to be functions of the poloidal angle. The thermal flux to the ion side of the limiter element situated at the external torus contour ($\theta=\frac{\pi}{q}$) is twice the thermal flux to the electron side of this element ($\theta=-\frac{\pi}{q}$).

1. Nedospasov, A.V., Petrov, V.G., Fidel'man, G.N., Nucl.Fus. 25 (1985) 21.
2. Fidel'man, G.N., Ivanov, R.S., Stotsky, G.I., in Controlled Fusion and Plasma Physics (Proc. 11th Europ.Conf. Aachen, 1983), Part 2, European Physical Society (1983) 409.

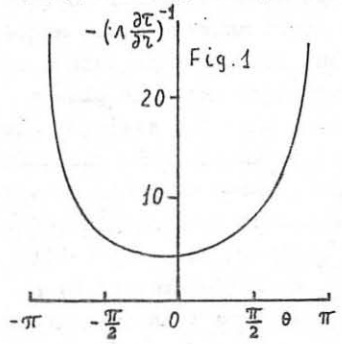


Fig.1

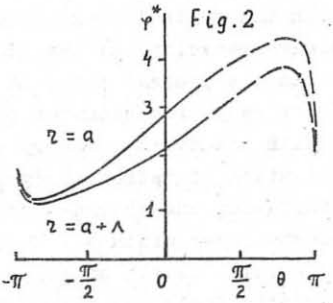


Fig.2

ON IZOTOPE COMPOSITIONS OF PLASMA AND GAS IN TOKAMAK REACTOR DIVERTOR

M.Z. Tokar'

Institute for High Temperatures of the USSR
Academy of Sciences, Moscow, USSR

In the divertor chamber of a tokamak-reactor the plasma will be in contact with the neutral gas. The difference in masses and thermal velocities of deuterium and tritium particles can result in the appearance of the difference in the izotope composition of the charged and neutral components. On the one hand, the distinction of the plasma composition from stoichiometric one will be manifest in a reduction of the intensity of thermonuclear reaction in the reactor operating volume, since the latter is proportional to the product of the izotope ion densities while the sum of those is restricted with the criterion of the plasma stability [1] . On the other hand an excess of the tritium neutrals in the divertor chamber will result in the intensification of their pumping and complicate the problems of the tritium extraction from the reactor structural elements. Therefore it is of particular interest to consider the question about relation between the deuterium and tritium neutral and charged particle densities in the divertor chamber of the tokamak reactor. For the case of the plasma recycling at the first wall of the tokamak this problem has been examined in Ref. [2] .

Geometry of the chamber of the poloidal divertor is scematically shown on Fig. 1; the magnetic field makes a small angle Ψ with the neutralizing plate surface. The neutrals born during the plasma recycling at the plate return back into the plasma layer. In the present paper it is assumed that the averaged energy of the recycling atoms of both izotopes is the same and coinsides with the average energy of the ions. Also we shall consider the situation of "strong recycling" when atom path length before the ionization and charge-exchange is small in comparison with the plasma layer width δ . In this case δ is determined by a characteristic length of the plasma temperature T change across the magnetic field [3] : $\delta \simeq \langle \varkappa_\perp T \rangle S_0 / Q_0$, where $\varkappa_\perp$ is transverse heat conductivity of the plasma, S_0 is the separatrix area,

Q_o is the total heat flux into the divertor layer and $\langle\cdots\rangle$ is averaging along the magnetic field.

In the plasma layer the atom velocity distribution functions, f_a^j, are described by two-dimensional kinetic equations:

$$v_x \frac{\partial f_a^j}{\partial x} + v_z \frac{\partial f_a^j}{\partial z} = -(k_i n + k_e^j n_j + k_e^* n_{3-j}) f_a^j + (k_e^j n_a^j + k_e^* n_a^{3-j}) f_i^j \qquad (1)$$

and the plasma - by a system of one-dimensional hidrodynamic equations (the plasma parameters are assumed to be constant across the layer and the electron and ions temperatures are the same)

$$\sin\psi \frac{dn_j V_\parallel}{dz} = (k_i n + k_e^* n_{3-j}) \bar{n}_a^j - k_e^* n_j \bar{n}_a^{3-j} \qquad (2)$$

$$\sin\psi \frac{d}{dz}(\rho V_\parallel^2 + 2nT) = V_\parallel \Big[k_i n(m_1 \bar{n}_a^{1,*} + m_2 \bar{n}_a^{2,*}) - \rho_1 (k_e^1 \bar{n}_a^{1,0} + k_e^* \bar{n}_a^{2,0}) - \rho_2 (k_e^* \bar{n}_a^{1,0} + k_e^2 \bar{n}_a^{2,0}) \qquad (3)$$

$$\sin\psi \frac{d}{dz}(5nV_\parallel T - \varkappa_\parallel \sin\psi \frac{dT}{dz}) = -k_i n(\bar{n}_a^1 + \bar{n}_a^2)(R_a - \tfrac{3}{2}T) \qquad (4)$$

where the index j = 1 refers to the deuterium particles, j=2 - tritium those; k_j, k_e^j, k_e^* are the ionization constant, the constant of mutual charge-exchange between the atoms and ions of j kind, the constant of charge exchange between the particles of the different izotopes, respectively; f_i^j, n_j are distribution functions and densities of ions; $n = n_1 + n_2$; $n_a^{j,0}$ are the densities of the atom recycling from the plate, $n_a^{j,*}$ are the densities of atoms born during charge exchange; $\rho_j = m_j n_j$, $\rho = \rho_1 + \rho_2$; $\overline{\cdots}$ is averaging across the layer, R_a is an energy needed for the atom ionization, $\varkappa_\parallel$ - is the longitudinal heat conductivity of electrons, $q_\parallel = 5nV_\parallel T - \varkappa_\parallel \sin\psi \frac{dT}{dz}$. The boundary conditions for Eq -s (2)-(4) are: at the plate (z=0) $V_\parallel = V_s = \sqrt{2Tn/\rho}$, $q_\parallel = \gamma n V_\parallel T$; at the divertor chamber throat (z = L): $q_\parallel = Q_o/\sin\psi/\Delta/\delta$, $\Gamma_\parallel = nV_\parallel = 0$ as in the case of strong recycling at

the neutralizing plate the charged particle in flux into divertor from the reactor operating volume is negligible in comparison with fluxes in the divertor [3]. With the same accuracy the atom outfluxes from the plasma layer stipulated by recycling at the divertor plate is compensated by the ionization of the neutrals coming from the pumped volume:

$$\int_0^{\ell} dz \int_{-\infty}^{\infty} v_x\, dv_x \int_{-\infty}^{\infty} dv_z \; f_a^j(x = \delta/2) = \frac{n_j^o}{4}\sqrt{\frac{8T}{\pi m_j}} \int_0^{L} (1-A_j)\, dz \qquad (5)$$

where l is the distance from the plate of the order of several path lengths of the atoms; $n_j^o T_o$ are the densities and temperature of the deuterium and tritium gas at the plasma layer boundary, A_j are the plasma "allbedo" for the atoms.

Calculations have done for the parameters: Q_o=80 MW, S_o=300 m^2, Δ = 70 m, L = 0,5 m, T_o = 0,1 eV, $n_1^o + n_2^o = 2{,}2 \cdot 10^{13}$ cm^{-3}, $\mathcal{E}_i/n = 2\ m^2 s^{-1}$. The izotope compositions of the plasma and gas in the divertor are characterized by values $\xi_o = n_1^o/n_2^o$ and $\xi = n_1/n_2$.

The results of numerical solving of Eq. (1)-(4) are very surprizing at first sight: $\left|1 - \xi/\xi_o\right| \leq 0{,}03$ for all z and $0{,}5 \leq \xi_o \leq 1{,}5$. This is in contradiction with the conclusions of Ref. [2] : in the case of the plasma recycling at the first wall the difference between ξ_o and ξ may amount 60%. Qualitative explanation of this distinction is as follows. In Ref. [2] situation the flux of neutral particles from the wall is compensated by the plasma diffusion across the magnetic field. If the former depends on the izotope masses the latter doesn't depend. In our case of strong recycling of the plasma on the divertor plates the both sides of Eq.(5) depend on the particle masses. In it's left side the main contribution is due to particles born not far from the plasma layer boundary, at the distance of the order of the atom path length before ionization $l_j \approx \sqrt{\frac{T}{m_j}}\,\frac{1}{k_i n}$. The dependence of l_j on m_j compensates the mass dependence of the gas influx into the plasma layer from the pumped volume. Thus the izotope composition of the divertor plasma can't substantially differ from the gas compozition in the pumping volume.

References

1. Mukhavatov V.S. in Itogi nayki i tekniki. Fizika Plasmy. V.1, part 1, M: VINITI, 1980 (in Russian).
2. Potters J.H.H.M., Goedheer W.J., in Eur.Contr. to the INTOR Workshop (January, 1984), Vienna, 1984, Cr.A, Ap. 4.
3. Tokar M.Z. Atomnaya Energiya, 1984, v.56, p.165 (in Russian).

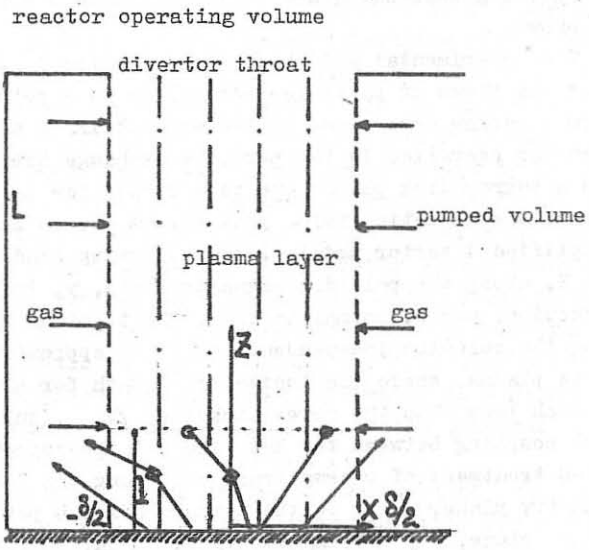


Fig.1

Geometry of the divertor chamber

——— neutral fluxes

—·—→ plasma fluxes

o - ionization

□ - charge-exchange

RELAXATIONAL OSCILLATIONS IN THE DIVERTOR PLASMA

S.I.Krasheninnikov, A.S.Kukushkin, V.I.Pistunovich, V.A.Pozharov

I.V.Kurchatov Institute of Atomic Energy, Moscow, USSR

Only a steady divertor operation attracted attention of theorists till now /1-3/. In the present paper, the possibility of exciting self-sustained oscillations in the divertor plasma is shown.

The experimental and theoretical studies /1,4/ have shown that the flows of particles and energy in a poloidal divertor form a narrow core close to the separatrix. A neutral component transfer prevailes in the particle exchange between the core and a surrounding plasma due to a rather low plasma diffusion across the magnetic field. This allows one to consider the simplified divertor model of the following kind. Let the axes be: Z, along the poloidal magnetic field, y, in the toroidal direction, and x, normal to them, the toroidal symmetry providing the solution independence of y. An approximation of a dense plasma, where the ionization length for a neutral, ℓ_N, is much less than the core thickness, Δ, justifies (due to weak coupling between the hot core and the surrounding plasma) a 1-D treatment of plasma transport along the Z-axis from a symmetry plane, S, to the target. Fix the power flux q_0 at the S plane, γ being its fraction carried by electrons. The plasma flow across the separatix is much less than that onto the target, hence it can be neglected. Then the parameters of the problem are the q_0 and γ-quantities together with an average particle (ions plus atoms) density in the core, n.

For the qualitative analysis, divide the core into two regions, D and T. The D-region is close to the target, particles recycle here and temperatures of electrons and ions are assumed to be equal, $T_e = T_i = T_d$. The neutral density in the T region is assumed to be zero. Relying on the

heat-conductive energy transport in the T-region, one can obtain the dependence of T_d on $\mathcal{N}$ from the energy and density balance equations for ions and atoms:

$$\mathcal{N} = \frac{7}{5}\left(\frac{\hat{\varkappa} T_d^{7/2}}{L q_o}\right)^{2/7} \frac{q_o}{C_d(E+\beta T_d)}\left[1 + \sin\psi\left(\frac{K_{ex}(T_d)}{2 K_i(T_d)}\right)^{1/2}\right] +$$

$$+ \frac{C_d}{L K_i(T_d)}\left[\sin\psi + \left(\frac{K_i(T_d)}{2 K_{ex}(T_d)}\right)^{1/2}\right]; \qquad (1)$$

$\hat{\varkappa} = 2/(\gamma/\hat{\varkappa}_e + (1-\gamma)/\hat{\varkappa}_i)$, $\hat{\varkappa}_j = 2\varkappa_j / 7 T_d^{5/2}$, $\psi = (\hat{B}, \hat{e}_y)$

where L is the length of the T-region ($L \gg L_D$); K_i, K_{ex} are the ionization and charge exchange rates; E is the energy per ionization; $\beta \approx 1 \div 3$ is the factor describing energy transfer to the divertor plate, it is determined by reflection coefficients; $\varkappa_j$ is the heat conductivity along the magnetic field. The dependence $T_d(\mathcal{N})$ (1) at sufficiently high q_o-values is S-shaped (see Fig.1) yielding an ambiguity in some band of $\mathcal{N}$ values. Note that this ambiguity and one found in /2,3/ are of different nature. One of stable branches in /2,3/ was related to a high temperature, low density plasma transparent for neutrals, whereas Eq.(1) describes only opaque plasmas.

The numerical solution of the 1-D problem of plasma transport along the Z-axis is also given in Fig.1. In this model, transport of both plasma and neutrals is treated in a framework of gas dynamics. One can see the reasonable agreement between this solution and an expression (1).

Now take an account of the terms of the order of ℓ_N / Δ describing a neutral gas transport across the core. The $\mathcal{N}$-dependence of the neutral gas pressure, P_N^d, near the neutralizer plate in the core, obtained from 1-D calculations, is shown in Fig.1 as well. It follows from this dependence that there is a range of P_N^d values for which no stable solution of the 1-D problem can be found. However, to provide a steady state solution of the 2-D problem allowing for a neutral gas surrounding the divertor plasma, the pressure balance between this gas and neutrals in the core must be ensured; otherwise, neutral flows causing $\mathcal{N}$ variations arise across the plasma layer. When the neutral pressure aside the core corresponds to the gap between the high-temperature and low-temperature branches

of solution (1) (see Fig.1), the self-sustained oscillations become possible. In this case, the $\sqrt{}$ value in the core at the low-temperature branch decreases, since the neutral pressure gradient is directed outwards, then the transition to the high-temperature branch takes place, the pressure gradient changes a sign, the $\sqrt{}$ value rises, the back transition occurs, etc. The period of these oscillations is apparently to exceed significantly the characteristic diffusion time, $\tau_D \sim \Delta^2 \nu_{ex} n_d / T_d$.

Similar oscillations were found in the 2-D simulation of the INTOR edge plasma with the model described in /1/. In Fig.2 the time dependence of parameters of the plasma and the neutral gas in the hot core near the target are given as obtained from the 2-D calculations. Here are also shown the profiles of the neutral atom density near the plate at two instants corresponding to different phases of an oscillation. The density profile of the neutral gas is seen to ensure both its removal from the core at the phase of density reduction and its supply during the density rise. The oscillation period exceeds the τ_D-value about an order of magnitude. This picture is in a good agreement with the qualitative description of self-excited oscillations given above.

Note in conclusion that a similar mechanism may be responsible for the oscillations at the plasma edge that have been observed in the present H-mode divertor experiments.

References

1. Yu.L.Igitkhanov et al. In: Plasma Phys. and Contr. Nucl. Fus. Res. 1984, IAEA, Vienna, 1985, v.2, p.113.
2. A.V.Nedospasov, M.Z.Tokar'. "Doklady Akademii Nauk SSSR", 270, 1376 (1983).
3. D.E.Post et al. J. of Nucl. Mat., 121, 171 (1984).
4. F.Wagner et al. J. of Nucl. Mat., 121, 103 (1984).

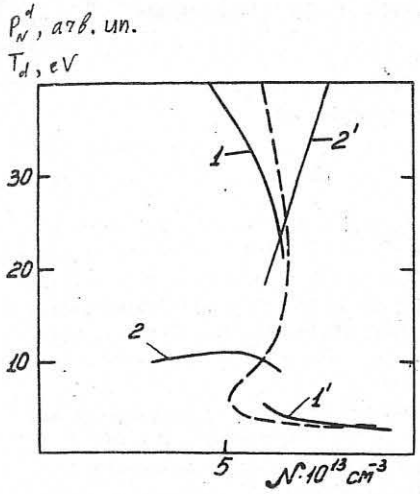


Fig. 1

Fig.1 Analytical solution, Eq.(1), (dashed line) and results of 1-D calculations (solid lines): $T_d(w)$(1) and $\rho_N^d(w)$ (2). Primed symbols 1,2 correspond to the low-temperature branch. The parameters are: the length in Z direction, L=48 cm; the (poloidal field)/ /(toroidal field) ratio is 0.08; q_o= 2.5 kW/cm^2; γ =2/3.

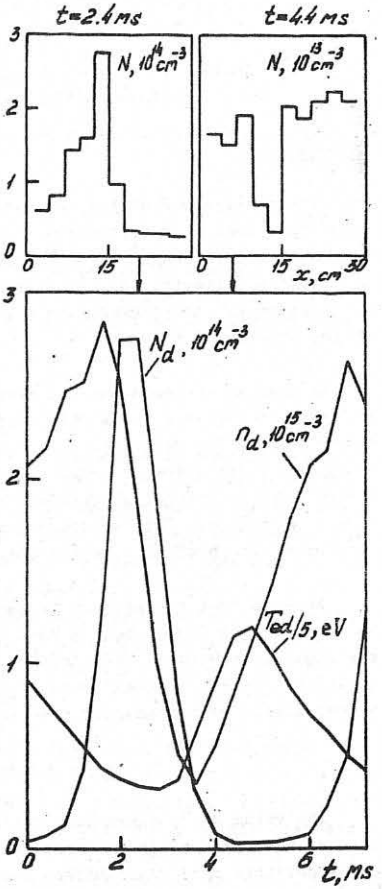


Fig. 2

Fig.2 Time evolution of the electron temperature (1), the neutral density (2) and the plasma density (3) in the hot core near the target as obtained from 2-D calculations. The neutral density profiles at the target plate corresponding to different instants are shown above.

EFFECT OF CROSS-FIELD TRANSPORT ON THE TEMPERATURE IN THE SCRAPE-OFF LAYER OF A TOKAMAK REACTOR - A CRITIQUE OF COLLISIONAL MODELS

J. Hugill
Culham Laboratory, Abingdon, Oxon, OX14 3DB, U.K.
(Euratom/UKAEA Fusion Association)

Introduction

The temperature at the boundary of a tokamak reactor is a parameter of some importance. It influences the mean energy of particles arising at the wall as charge-exchange neutrals or as ions acceleration by the electrostatic sheath, and hence the degree of damage and erosion produced by sputtering. The temperature also largely determines the collisionality of the scrape-off plasma.

A popular scenario for the next generation of ignited devices, such as INTOR, is to arrange for a scrape-off plasma with high density and low temperature. The relatively low coefficient of electron thermal conduction along the field allows a large temperature gradient, making the temperature at the divertor target plate/limiter even smaller, so that sputtering is no longer a problem. This solution looks attractive but it is questionable whether it is physically reasonable.

Suppose that the process responsible for anomalous transport in the boundary region causes both a heat flux, Q_s and a particle flux Γ_s across the separatrix between the confinement zone and the scrape-off layer. The relationship between these parameters may be discussed in terms of a perpendicular heat transport coefficient, $\gamma_\perp$ defined by:

$$\gamma_\perp = Q_s/\Gamma_s T_s. \qquad (1)$$

The value of $\gamma_\perp$ given by existing experiments is of order 10. A similar value for $\gamma_\perp$ in a device such as INTOR would yield a temperature at the separatrix many times higher than that assumed in the present design. This would make a collisional scrape-off layer impossible.

Formal expression for T_s, the temperature at the separatrix

Consider a steady-state reactor generating thermonuclear power P_{TN} in confined α-particles, of which a fraction α is conducted and convected to the separatrix. The outward current of helium ash, I_{He} (in amperes equivalent) is given by:

$$I_{He} = P_{TN}/1.76 \times 10^6. \qquad (2)$$

The total ion current across the separatrix is related to I_{He} by the fractional burn-up, f_B

$$I_s = I_{He}/f_B. \tag{3}$$

Now, substituting the mean power flux and mean particle flux across the separatrix into eq.(1) gives:

$$T_s(eV) = 1.76 \times 10^6 \, \alpha f_B/\gamma_\perp. \tag{4}$$

Evidently, T_s can be arbitrarily small if α and/or f_B are reduced sufficiently. The problems associated with such solutions are not discussed here. Attention is restricted to the effect on T_s of variations in $\gamma_\perp$, with given α and f_β.

Meaning and value of $\gamma_\perp$

If there were an adequate theory for the processes responsible for energy and particle transport, then, for given boundary conditions, Q_s, Γ_s and T_s could be calculated in a self-consistent way making this discussion, and indeed the use of the parameter $\gamma_\perp$, superfluous. Unfortunately this is not the case, so that modelling of the boundary plasma in a reactor has to rely on empirical measurements in existing tokamaks. The question is, how such measurements are to be used and how far they can be extrapolated. The parameter $\gamma_\perp$ is just one measure of the ratio of energy and particle losses. The modelling becomes suspect if it yields a value which is far outside the range obtained experimentally.

The estimation of $\gamma_\perp$ in present devices is easiest in low-density scrape-off plasmas in which power losses due to radiation and charge exchange and source terms due to ionisation can be neglected. In this case the energy and particle flows across the separatrix arrive at the limiters and can be estimated by a variety of techniques, for example using Langmuir probes. It is straightforward to show [1] that $\gamma_\perp$ is related to γ_s, the heat transport coefficient for flow parallel to the field through the sheath at the limiter, by

$$\gamma_\perp = \gamma_s \frac{r_T}{r_T + r_\Gamma} \tag{5}$$

where r_T, r_Γ are respectively the characteristic widths of the temperature and particle flux profiles in the scrape-off layer. Measurements typically obtain $r_T \gtrsim r_\Gamma$ [2,3,4] implying $\gamma_\perp \lesssim \gamma_s \sim 10$.

Experiments have been done in DIII and ASDEX with denser, collisional

scrape-off layers in which there is considerable flow amplification near the divertor target due to recycling [5,6]. These are more directly relevant to the present modelling for INTOR. However, it is difficult to obtain accurate estimates for the particle current across the separatrix in these experiments, and hence a value for $\gamma_\perp$.

Application to INTOR

The design parameters for INTOR are shown in the Table below.

INTOR parameters from ref.[7] Tables XX-2 and XX-3

Thermonuclear power (MW)	620
Total radiation + charge exchange (MW)	44
Tritium fuelling rate (A)	720
Fractional burn-up, f_β	0.05
Temp. in scrape-off layer, T_s (eV)	100
Derived parameters:	
α-particle power, P_{TN} (MW)	124
He ash generation, I_{He}(A)	71
Fraction non-radiated α-power, α	0.65

Substituting α, f_β, T_s in eq.(4) implies $\gamma_\perp = 570$. Such a large value of $\gamma_\perp$ can be obtained from a self-consistent model because of the form of the transport coefficients used. Heat fluxes are driven exclusively by temperature gradients and particle fluxes by density gradients. Thus, locally $\gamma_\perp \sim \chi\eta/D$, where $\eta = d\ln T/d\ln n$, and arbitrarily high values of $\gamma_\perp$ result by making η large enough. [The 2-D modelling actually used is, of course, more complicated.] A more realistic diffusion model would also allow heat fluxes driven by density gradients and particle fluxes driven by temperature gradients. Then it is easy to see that the ratio of the diagnonal to the cross terms in the diffusion matrix would limit the value of $\gamma_\perp$.

If $\gamma_\perp$ were of order 10, as suggested by the experimental results of the last section, the separatrix temperature obtained from eq.(4) with the design values of α and f_β would be 5.7 keV. This certainly seems unrealistically high, but a 10 × smaller value would still make a collisional scrape-off layer impossible.

Conclusion

The present combination of INTOR design parameters involving a small fraction of radiated power, a large fractional burn up and a low

temperature, collisional exhaust is a large extrapolation from existing empirical results. To justify such a model the physics data base on transport processes in the boundary needs to be considerably improved.

Acknowledgement

I thank Dr E.S. Hotston for discussion of the 2-D modelling of the scrape-off plasma in INTOR.

References

[1] J. Hugill, Nucl. Fusion 23 (1983) 331.
[2] K. Uehara, Y. Gomay, T. Yamamoto et al. Plasma Physics 21 (1979) 89
[3] T.F.R. Group, Journ. Nucl. Mater. 93&94 (1980) 272.
[4] G. Proudfoot, et al., Journ. Nucl. Mater. 128&129 (1984) 180.
[5] M.A. Mahdavi, et al. Phys. Rev. Lett. 47 (1981) 1602.
[6] M. Keilhacker, et al. Physica Scripta T2/2 (1982) 443.
[7] INTOR International Tokamak Reactor Phase I (Report of the international tokamak workshop) IAEA, Vienna (1982).

APPLICATION TO THE DITE BUNDLE DIVERTOR OF MODELS FOR PLASMA EXHAUST AND NEUTRAL PARTICLES IN THE DIVERTOR

P.C. Johnson, D.N. Edwards, S.J. Fielding,
P.J. Harbour, G.P. Maddison and J.G. Morgan
Culham Laboratory, Abingdon, Oxon., OX14 3DB, U.K.
(Euratom/UKAEA Fusion Association)

Introduction

Experimental results from the DITE Bundle Divertor Mk.II have been described elsewhere [1,2,3]. In experiments with fuelling in the divertor a complex flow pattern is observed in the exhaust plasma, with super-sonic flow into the divertor in an Inner Layer and a Middle Layer (formerly intermediate region), and sub-sonic reversed flow in an Outer Layer. The divertor magnetic mirror allows the super-sonic flow to form. In this paper, we discuss a 1-D fluid simulation of the exhaust plasma and 1-D [4] and 3-D (DEGAS code) [5] neutral-particle simulations of plasma-neutral interaction in the divertor. It will be shown that the observations on flow regimes are consistent with the predictions of the models.

The configuration of the DITE divertor experiment is shown in Fig.1. An idealised picture of the plasma cross-section in the plane of the divertor plate is shown Fig.2. In this paper we shall use the coordinate system (ξ,ψ,ζ) to describe the geometry; ξ and ψ are radial and azimuthal coordinates normal to $\underline{B}$ (Fig.2) and ζ is the coordinate along $\underline{B}$.

1-D Fluid Model

Isothermal, isotropic pressure fluid equations are used to model the plasma flow along $\underline{B}$. The variation of $|\underline{B}|$ through the mirror is included as an area change [6]. Normalizing to $L_\parallel$, $n_e(o)$ and $c_s = [(kT_e+kT_i)/m_i]^{\frac{1}{2}}$ (the length of the flow channel, the density at the symmetry point and the ion sound speed), the density and fluid speed equations become:

$$\frac{dn}{d\zeta} = \frac{(-2\alpha nu - \delta nu - nu^2\lambda_B)}{(1-u^2)}\,; \qquad \frac{du}{d\zeta} = \frac{[\alpha(1+u^2) + \delta u^2 + u\lambda_B]}{(1-u^2)}.$$

Here, $\alpha=\nu_i L_\parallel/c_s$ is a normalized particle generation frequency, $\delta=\nu_{cx} L_\parallel/c_s$ is a normalized charge-exchange collision frequency and $\lambda_B=d(\ln|B|)/d\zeta$ is the local inverse scale length of the magnetic field. Combining ionization and cross-field transport terms in ν_i allows α to be of either sign. With charge exchange collisions, the electric field in the plasma increases but the form of the solutions are not affected. The results presented below are for $\delta=0$.

Figure 3 illustrates the types of solution that are obtained. The

super-sonic solution (u=1 at $\zeta \approx \zeta_2$) has no ionisation in the divertor. This result is similar to that of Emmert's kinetic model [7]. For sub-sonic solutions (u=1 at $\zeta \approx \zeta_3$), a minimum value of α is required at $\zeta=\zeta_3$, and taking a uniform α of this value in the divertor gives the stagnant flow solution. Here the net source in the scrape-off layer is close to zero. Increasing α in the divertor results in a reversal of the flow, with $\alpha < 0$ in the scrape-off layer. These flow regimes are characteristic of those obtained in bundle divertor experiments.

The maximum value of α in the divertor for quasi-neutral solutions to exist is determined by the condition that u=-1 at $\zeta=\zeta_2$. Further increases may result in the development of a double-sheath (or a double-layer).

Neutral Particle Models

Modelling with the 3-D neutral particle code DEGAS has been extended from earlier work [2] to include a more complete description of the geometry of the divertor chamber and the baffled cryo-pump attached to it (Fig.1). More radial zones have been added to the plasma region and an optional region of private-flux plasma has been included (Fig.2). We report here mainly on the neutral particle interaction with the plasma.

Figure 4(a) shows profiles (based on experimental data) of n_e and T_e ($=T_i$) used as input to the code. The radial coordinate ξ is taken on the mid-plane of the flux bundle at the plate ($\phi=0$ in Fig.2). Except for the private-flux region, values of n_e are referred to the symmetry point in the scrape-off layer ($\zeta=0$). The fluid code is used to give $n(\zeta)$ for different flow regimes. Here, $n(\zeta)$ for the stagnant flow case was used as test for the existence of a high recycling regime in the DITE exhaust plasma.

Computed spatial profiles of ionization source in the diverted plasma are shown in Figs4(b) and 4(c) for a typical D_2 fuelling rate of 5×10^{20} s^{-1}. Recycling is not included; comparison with the slab code taking a gas pressure outside the plasma of 5×10^{-3} torr shows that $\approx$ 10 recyling generations are necessary to produce an equivalent amount of ionization. The profiles show that in the Outer Layer there is a peak of ionization arising from $e+D_2$ collisions. Without private-flux plasma there is a similar peak in the Inner Layer, but the slab code shows that this peak is confined to the first 2-3mm of the plasma near the separatrix. With plasma in the private flux region (taking similar n_e and T_e variations to those in the main body of the diverted plasma) the molecular-ionization peak is moved outside the Inner Layer and the ionization remaining is then comparable in magnitude to that in the Middle Layer.

Comparison with Experiment

Outer Layer: From the fluid model, taking a flux tube at ξ=95mm in

Fig.4, the ionization source rate in the divertor necessary for subsonic reversed flow is $S_i \approx 7.5.10^{23} m^{-3}s^{-1}$. The slab neutral particle code gives $S_i \approx 4.10^{24}\ m^{-3}s^{-1}$ in this layer for a D_2 pressure outside the flux bundle of 5.10^{-3} torr at which the plasma profiles were obtained. Thus, even allowing for some reduction through atom-molecule collisions [4], the rate of ionization at this typical pressure is sufficient to drive reversed flow. The reversed flow acts as an additional source of particles driving a radial particle flux. The added particles are small in number ($\lesssim$ 20%) by comparison with the estimated ionization source from limiter-recycled neutrals ($\gtrsim 1.10^{21}\ s^{-1}$) and are easily accommodated by a small change in the radial density gradient in front of the limiter.

Inner Layer: From the fluid model, taking a flux tube at ξ=0, a transition to subsonic flow would occur with $S_i \approx 6.10^{24}\ m^{-3}s^{-1}$ in the divertor. From Fig.4 and scaling the profile to the slab-code data, we can see that atomic-neutral ionization is insufficient to cause a transition. Molecular ions may be shielded out by the private flux plasma, but even without plasma in this region the range of molecular neutral particles is too small to affect the behaviour of the whole of the layer. Thus the flow should remain supersonic. Radial transport provides the source of particles into the layer in the tokamak boundary plasma. With $D_{BOHM} \approx 1.4\ m^2s^{-1}$ and taking the usual expression for λ_n, $\lambda_n \approx (D_\perp \tau_\parallel)^{\frac{1}{2}}$ with $\tau_\parallel = L_\parallel/0.25\ c_s$ for super-sonic flow through the magnetic mirror, a value for λ_n of 27mm is found. This value is about a factor of 2 larger than that shown in Fig.4(a), but is well within experimental uncertainty.

Middle Layer: Again, with a requirement of $S_i \approx 1.5 \times 10^{24}\ m^{-3}s^{-1}$, ionization in the divertor would appear to be insufficient to cause a transition from supersonic to subsonic flow.

Conclusions

A fluid model for plasma flow along the magnetic field predicts the flow regimes inferred from experiments with the bundle divertor.

The distribution and magnitude of ionization sources within the diverted plasma, computed with the DEGAS code and a 1-D code, is consistent with the sources required to support the observed flow pattern.

References

1. Johnson, P.C., et al., Plasma Physics and Contr Fus 26 1A (1984) 65.
2. Harbour, P.J., et al., J. Nucl. Mater. 128 & 129 (1984) 359-367.
3. Johnson, P.C., et al., Plasma Physics and Controlled Nuclear Fusion Research (Proc. 10th Int. Conf. London, 1984), Vol.I (1985) 239-247.
4. Fielding, S.J., et al., J. Nucl. Mater. 128 & 129 (1984) 390.
5. Heifetz, D., et. al., J. Comp. Phys. 46 (1982) 309.
6. Harbour, P.J. (ed) 'Tokamak Fusion Reactor Exhaust' CLM-R211 (Culham).
7. Emmert, G.A., University of Wisconsin Rep. UWFDM-343 (1980).

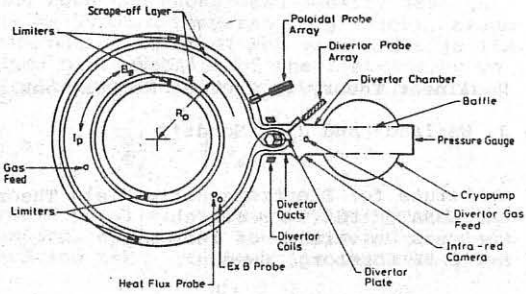


Fig.1 Schematic plan view of the DITE bundle divertor experiment. Neutral beam systems and routine diagnostics are omitted.

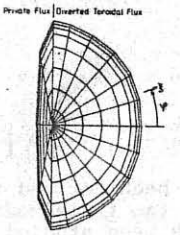


Fig.2 Plasma configuration in the plane of the divertor plate as used in DEGAS simulations.

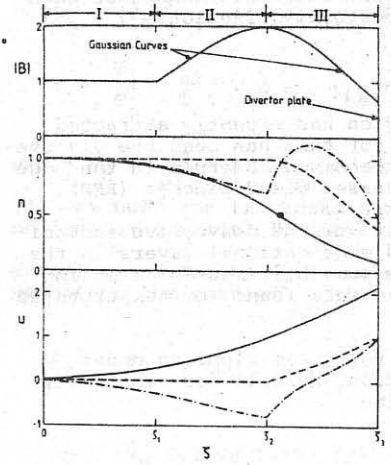


Fig.3 Fluid simulations of plasma exhaust regimes for a bundle divertor. — Super-sonic flow, —— stagnant flow, -·-·- reversed flow. I - scrape-off layer (|B| normalized to 1), II - mirror region, III - field expansion region (in divertor).

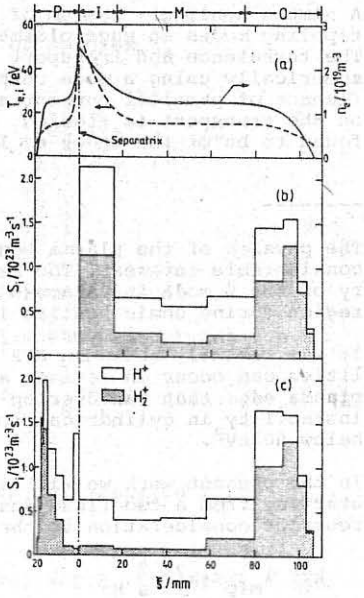


Fig.4 DEGAS code simulations of ionization sources within the diverted plasma. (a) - plasma profiles, (b) and (c) source profiles for cases with and without private-flux plasma. P - private flux layer; I - Inner Layer, M - Middle Layer, O - Outer Layer.

Nonlinear Theory of Thermal Excitations in Edge Plasmas

J. Weiland* and J.P. Mondt**

*
Institute for Electromagnetic Field Theory
and EURATOM-FUSION Research
Chalmers University of Technology
S-412 96 Göteborg, Sweden

**
Los Alamos National Laboratory
P.O.B 1663, Los Alamos, NM 87545, USA

Abstract

A simple nonlinear system of two equations has been derived for rippling modes in edge plasmas starting from a two fluid model. The turbulence and transport in this system has been studied numerically using a mode coupling code. In particular the influence of parallel current and electron thermal conductivity on the transport is studied. The convective diffusion has been found to be of the order of 16 times Bohm diffusion.

The physics of the plasma edge region has recently attracted considerable interest. The reason for this has been the discovery of the H mode in tokamaks and phenomena observed in the edge region during ohmic heating in reversed field pinches (RFP).

It was recently shown for RFP[1] that current convective instabilities can occur in regions around mode-rational layers in the plasma edge that can overlap while possibilities for rippling instability in cylindrical tokamaks were found for temperatures below 50 eV[2].

In the present work we will study nonlinear rippling modes starting from a two fluid description. We will for simplicity restrict consideration to the regime

$$k_{||}^2 \lambda_{mfp} << k_{\perp}^2 \rho_s^2$$

where λ_{mfp} is the mean free path and ρ_s is the ion Larmor radius at the electron temperature. In this regime electromagnetic terms other than the perturbed parallel current can be neglected. We will also neglect density perturbations since these are not vital for the present mode.

This can formally be done when the background density gradient is much smaller than the background temperature gradient, assuming the temperature perturbation to be of the same order as its convective part. Including perturbations of the resistivity we then obtain from the parallel equation of motion of electrons.

$$\delta j_{\parallel e} = \frac{2en}{\nu_{ei}}\left\{\frac{T_e}{m_e}\hat{e}_{\parallel}\cdot\nabla(1.71\,\frac{T_1}{T_e} - \frac{e\phi}{T_e}) - \frac{3}{4}\,\nu_{ei}\,V_{oe}\,\frac{T_1}{T_e}\right\} \qquad (1)$$

where V_{oe} is the background parallel electron velocity and the other notations are standard. Neglecting the ohmic heating rate and temperature equilibration terms we may write the energy eq. of electrons

$$\frac{\partial T_1}{\partial t} + \vec{V}_{oe}\cdot\nabla T_1 + e\vec{V}\cdot\nabla\phi + \frac{2}{3}\,T_e\vec{V}_{De}\cdot\nabla(\frac{T_1}{T_e}) + 0.47\,\vec{V}_{oe}\cdot\nabla T_1$$

$$+ \frac{2}{3}\,\hat{e}_{\parallel}\cdot\nabla V_{1e} - \frac{2}{3}\,\frac{\kappa_{\parallel}}{n}(\hat{e}_{\parallel}\cdot\nabla)^2 T_1 = -\frac{c}{B}\,(\hat{e}_{\parallel}\times\nabla\phi)\cdot\nabla T_1 \qquad (2)$$

where $\vec{V}_{*j}$ is the diamagnetic drift of species j.

The vorticity equation can be written

$$[\frac{\partial}{\partial t} + (\vec{V}_E+\vec{V}_{*i})\cdot\nabla]\Delta\,\phi - \nu_i\rho_i^2\nabla^2\phi = 2\,\frac{B\Omega_{ci}}{\nu_{ei}c}\left\{\frac{T_e}{m_e}\,(\hat{e}_{\parallel}\cdot\nabla)^2\right.$$

$$\left.[1.71\,\frac{T_1}{T_e} - \frac{e\phi}{T_e}] - \frac{3}{4}\,\nu_{ei}\,V_{oe}(\hat{e}_{\parallel}\cdot\nabla)\,\frac{T_1}{T_e}\right\} \qquad (3)$$

where $\vec{V}_E = \frac{c}{B}(\hat{e}_{\parallel}\times\nabla\phi)$ is the cross field drift and

(1) was used for the total parallel perturbed current i.e. neglecting parallel ion motion.

Normalizing time by Ω_{ci}^{-1} and space by ρ_s^{-1} and using (1) in (2) we obtain the coupled system

$$[\frac{\partial}{\partial t} + (\vec{V}_{*i} + \vec{V}_E)\cdot\nabla]\Delta_{\perp}\phi - \nu_i\Delta_{\perp}^2\phi = \Gamma(\hat{e}_{\parallel}\cdot\nabla)^2(aT-\phi) - V\,\hat{e}_{\parallel}\cdot\nabla T \qquad (4a)$$

$$[\frac{\partial}{\partial t} + (\vec{V}_E + 2.5\,V_{e\parallel})]\cdot\nabla\,(T+1.5\,\ln Te) = \Gamma(\hat{e}_{\parallel}\cdot\nabla)^2(bT-\phi) \qquad (4b)$$

where $a \approx 1.14$, $b \approx 2.14$, $v = v_{oe}/cs$, and $\Gamma = 2 \frac{m_i}{m_e} \frac{\Omega_{ci}}{\nu_{ei}}$.

The system (4) is our model system for nonlinear rippling modes. It is similar to the system for nonlinear collisional drift waves in Ref. 3, differing only due to finite V and $a \neq b$ in our system. The difference between a and b is due to parallel electron conducitivity. The system (4) has been solved numerically with a mode coupling code showing initially linear growth and subsequently stabilization by mode coupling to stable regions in k space. The behaviour and saturation levels were similar to that obtained in Ref. 3, but the scaling of saturation and transport with V and ($\nabla \ln T_e$) showed a slight nonlinearity. The thermal convective diffusion coefficient was of the order of 16 times Bohm diffusion. We also calculated the conductive thermal diffusion due to perturbation of flux surfaces and found that, due to the high resistivity in the edge the convective thermal transport was larger than the conductive.

References

1. J.P. Mondt and J. Goedert, Los Alamos National Document LA-10029-MS Los Alamos National Laboratory 1984.

2. A. Rogister, Plasma Physics 26, 1063 (1984).

3. A. Hasegawa and M. Wakatani, Phys. Rev. Lett. 50, 682 (1983).

STATIONARY PARTICLE BALANCE IN THE EDGE REGION OF A TOKAMAK PLASMA: INFLUENCE OF A DENSITY DEPENDENT DIFFUSION COEFFICIENT AND AN ANOMALOUS PINCH FLUX

K. F. Alexander, W. Hintze
Akademie der Wissenschaften der DDR, Zentralinstitut für Elektronenphysik, 1086 Berlin, GDR

1. Introduction

Recently we have considered the stationary particle balance in the edge region of a tokamak plasma within the framework of a simple one-dimensional model /1/. This theory explaines the experimental result obtained by means of double Langmuir probes in the T-10 tokamak /2/ that the plasma density n_s at the separatrix between plasma and scrape-off layer (SOL) scales approximately quadratically with the bulk plasma density. The quadratic scaling is predicted by our theory to be insensitive against model variations concerning the dynamics of neutrals and the density dependence of the particle diffusion coefficient ($D = D(n)$).

In this paper, we
(i) further extend the range of variations by including an (anomalous) pinch flux, and
(ii) compare the predictions of a particular model for $D(n)$ with experimental data.

2. Theory

A consistent nonlinear analytic treatment of the stationary interaction of neutrals and edge plasma can be given at the expense of the following drastically simplifying assumptions

(i) due to dominant charge exchange neutrals are treated in diffusion approximation and are assumed to have the same temperature as the ions

(ii) local flux balance (neglecting localized sources of recycling neutrals)

(iii) high enough plasma density prevents the neutrals to reach the centre (neglecting recombination)

(iv) impurities are neglected

(v) we work in planar geometry

(vi) complete local recycling of plasma in the SOL.

The governing equations are

(1) $\Gamma_\perp + \Gamma_P + \Gamma_N = 0$ local flux balance

(2) $\frac{d\Gamma_\perp}{dx} = -\xi_i n N + \frac{n}{\tau_\parallel}\theta(x)$ ionization and scrape-off

(3) $\Gamma_\perp = -D\frac{dn}{dx}$ diffusive plasma flux

(4) $\Gamma_p = n v_p, \quad v_p = \beta \frac{dn}{dx}$ pinch flux

(5) $\Gamma_N = -\frac{v_i^2}{\xi} \frac{1}{n} \frac{dN}{dx}$ flux of neutrals

Here x is a radial coordinate with x = 0 at the separatrix, n and N are plasma and neutral densities, resp. $\tau_{\parallel}$ is the longitudinal confinement time of an ion with velocity v_i in the SOL, $\xi = \xi_i + \xi_{cx}$ is the sum of the reaction rates for ionization and charge exchange, resp. The pinch velocity v_p has been set proportional to the plasma density gradient which ensures a qualitatively correct behaviour of the pinch flux and leads at the same time to analytically convenient expressions. The parameter ß measures the intensity of the pinch flux.

The solution to the system (1) through (5) can be easily found analytically assuming the following boundary conditions (centre and liner have been moved formally to $\mp\infty$ using assumptions (iii) and (iv).

Centre ($x = -\infty$): $n = n_{-\infty}$, $\Gamma_\perp = 0$, $N = 0$, $\Gamma_N = 0$

liner ($x = +\infty$): $n = 0$, $\Gamma_\perp = 0$, $N = N_W$, $\Gamma_N = 0$.

Integrating the flux balance (1), using (3) - (5) gives

(6) $N = \frac{\xi}{v_i^2} [G(n_{-\infty}) - G(n)]$

(7) $G(n) = \int_0^n dn' \, (n' D - \beta n'^2)$.

Inserting this into the ionization equation (2) leads to the generalized scaling for the density

(8) $G(n_s) = \Sigma^2 \tau_{\parallel} G^2(n_{-\infty})$

(9) $\Sigma = \sqrt{\xi_i \xi'} / v_i$,

the flux of neutrals

(10) $\Gamma_N = -\Sigma \frac{v_i^2}{\xi} N$,

and the density gradient in the plasma region

(11) $-\frac{dn}{dx} = \Sigma [G(n_{-\infty}) - G(n)] / (D - \beta n)$.

(A similar, but more complex, expression holds in the SOL).

Finally, (11) can be integrated immediately to yield the density profile, which completes the solution. The solution is a one-parameter family as $n_{-\infty}$ and N_W are related by (6).

Note that both plasma fluxes ($\Gamma_\perp$ and Γ_p) are treated together, mainly via the function G.

More detailed results are given for the two cases

(a) $D = \gamma n^{\alpha}$, $\beta = 0$ and (b) $D = \text{const}$, $\beta > 0$.

Figs. 1 and 2 shows the density profiles for varying parameters and $c = (2/3)\beta n_{-\infty}/D$. These solutions are valid in the plasma region only. The location of the separatrix depends on $n_{-\infty}$ and is not shown here.

The density scaling in case (a) is exactly quadratic,

(12) $n_s = \left[\frac{1}{2} \frac{\Sigma^2 \gamma \tau_{\parallel}}{\alpha + 2}\right]^{\frac{1}{2+\alpha}} \cdot n_{-\infty}^2$,

whereas it becomes weaker for high density in case (b) (of fig.3).

The density gradient scales approximately quadratically too. In case (a) we find

$$(13)\quad -\frac{dn}{dx} = \frac{1}{2}\Sigma n_{-\infty}^2\, g\left(\frac{n}{n_{-\infty}},\alpha\right), \qquad g(t,\alpha) = \frac{2}{2+\alpha}\left(t^{-\alpha} - t^2\right).$$

For case (b) figs. 4 and 5 show the gradient (together with the local decay length defined as $l = n/|dn/dx|$ in units of $\hat{n}/\lambda$ and $\lambda = \sqrt{D\tau_n}$) at $n = \frac{1}{2}n_{-\infty}$ and at $n = n_s$, resp. as a function of $n_{-\infty}$. The curves in fig. 3 to 5 are valid only up the maximum. Beyond that point there are unphysical regions of negative neutral density.

3. Comparison with experiments

Let us first mention that the density scaling found in experiment /2/ is also predicted by the more general theory presented here.

Next we make a comparison of the theoretical prediction (13) for the density gradient near the separatrix ($n = n_s$) neglecting the pinch term.

In fig. 6 we have included the few existing detailed measurements of the plasma density in the entire edge region (SOL and plasma) in a plot showing the auxiliary function $g(n_s/n_{-\infty},\alpha)$ for three values of α.

The entry numbers correspond to the references as follows: 1 - /3/, 2a,b - /4/,/5/, 3 - /6/, 4 - /2/.

The quantity Σ entering into (13) depends only weakly on the temperature in the range of interest, and was taken equal to $5\cdot10^{-19}\ m^2$.

We conclude from fig. 6 that the experiments suggest an exponent α in the range from 0 to -1.

References

/1/ K.F.Alexander, K.Günther, W.Hintze, ZIE-preprint 84-9, Berlin, GDR, 1984. 1984 International Conference on Plasma Physics, Lausanne, Switzerland
Submitted for publication in Nuclear Fusion

/2/ K.F.Alexander, M. Laux, P. Pech, H.-D. Reiner, ibid
Submitted for publication in Nuclear Fusion

/3/ M.Keilhacker et al., Plasma Physics and Controlled Fusion Vol. 26 (1984) 1A, 49-63, fig. 3

/4/ H.Murmann, MPI Garching, Jahresbericht 1981, p.32, fig.40

/5/ H.Murmann, ibid, fig. 41

/6/ H.Grote, private communication.

FIGURES

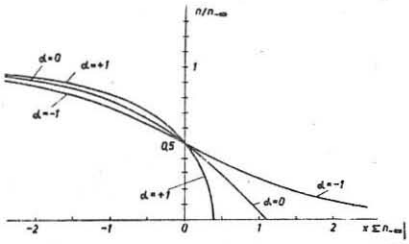


fig.1 density profiles, case (a)

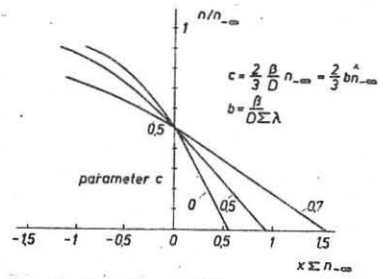


fig.2 density profiles, case (b)

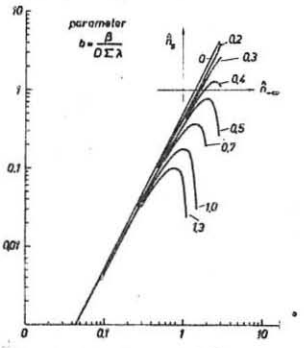


fig.3 density scaling

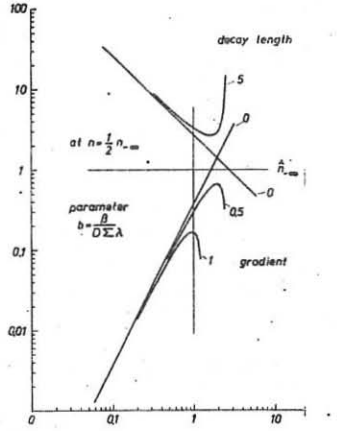


fig.4 gradient and decay length

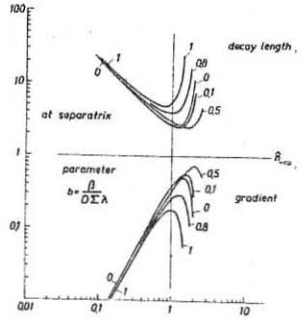


fig.5 gradient and decay length

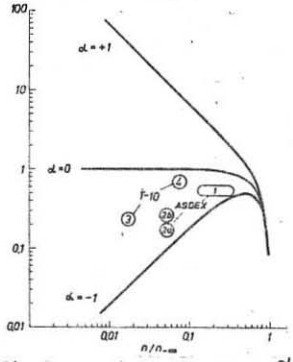


fig.6 gradients for $D \sim n^{\alpha}$

MODELLING OF THE PLASMA TRANSPORT AND PARTICLE REMOVAL CAPABILITY CHARACTERISTIC FOR THE ADVANCED PUMP LIMITER TEST FACILITY ALT I

A.Nicolai, P.Börner
Institut für Plasmaphysik der Kernforschungsanlage Jülich GmbH
Association EURATOM-KFA, P.O.B. 1913, D-5170 Jülich, FRG

1. Introduction

Centrally important to long pulse, high power tokomaks and to fusion reactors are the control of (1) particle and energy exhaust, (2) screening of the plasma core against the impurities released at the wall, (3) shielding of the wall against the hot neutrals emerging from the plasma core. Pump limiters /1/ combined with an ergodic boundary might be a simple and practical way to achieve these objectives. In the tokamak TEXTOR the pump limiter assembly consists of an actively pumped limiter chamber and an interchangeable limiter module including the head (Fig.1).
Two zone models were proposed to describe the high recycling regime possibly occurring in the throat region /2,3/. They resort to the fluid equations averaged along the field lines in the scrape off zone (SOZ) and in the throat zone (TZ). The Mach numbers in both regions are prescribed.
A two dimensional description of the divertor scrape off region /4,5/ with radial and toroidal resolution, was attempted already employing the fluid equations as well and accounting e.g. for the divertor plate and the plasma flow across the separatrix by the boundary conditions. Here ALT-I is modelled and first results of the 2d-model are presented.

2. Design of the pump limiter assembly

Two limiter modules, the "fixed geometry limiter module" (ALT-I-FG) and the more advanced "variable geometry limiter module" (ALT-I-VG) (Fig.1), to be used alternatively, can be attached to the flange of a supporting tube inside the vacuum vessel /1/. The shape of this vessel is defined by two concentric cylinders connected by a frustum. Encircling the major cylinder there is an array of getter modules with a pumping speed of v_p=18000 l/sec. The throat of ALT-I-VG has the length L_t=26 cm and entrance width L_w ($0<L_w<3$ cm). The neutralizer plate scatters the ions preferentially into the pump duct, the length of which is L_d = 83 cm.

3. Modelling of the plasma-transport in the scrape-off and throat region of ALT-I-VG

The fluid equations used here for the two zone and for the 2d-model read

$$\frac{\partial n}{\partial t} = \frac{\partial}{\partial x}(nv_x) + \frac{1}{r}\frac{\partial}{\partial r}\left(rD\frac{\partial n}{\partial r}\right) + S_0 \qquad (1)$$

$$\frac{\partial}{\partial t}(nmv_x) = -\frac{\partial}{\partial x}(nmv_x^2) - \frac{\partial}{\partial x}p + \frac{\partial}{\partial x}\left(nm\eta_{\parallel}\frac{\partial v_x}{\partial x}\right)$$

$$+\frac{1}{r}\frac{\partial}{\partial r}\left(rnm\eta_{\perp}\frac{\partial v_x}{\partial r}\right) + \frac{1}{r}\frac{\partial}{\partial r}\left(rmv_x D\frac{\partial n}{\partial r}\right) + Sp \qquad (2)$$

$$\frac{\partial}{\partial t}\left(\frac{3}{2}nkT_j + \frac{1}{2}nmv_x^2(j-1)\right) = -\frac{\partial}{\partial x}\left(\frac{5}{2}nv_x kT_j\right) + \frac{\partial}{\partial r}\left(r\frac{3}{2}kT_j D\frac{\partial n}{\partial r}\right)$$

$$-(2j-3)\,v_x\frac{\partial nT_j}{\partial x} + \frac{\partial}{\partial x}\left(\chi_{j\parallel}\frac{\partial T_j}{\partial x}\right) + \frac{1}{r}\frac{\partial}{\partial r}\left(r\chi_{j\perp}\frac{\partial T_j}{\partial r}\right) + (2j-3)\,Q_{e,i} + Q_j$$

$$+\frac{4}{3}\eta_{\parallel}\left(\frac{\partial v_x}{\partial x}\right)^2(j-1) \qquad (3)$$

Equations (1-3) are the continuity, the momentum and the energy conservation equations. In equation (3) j=1 stands for the electrons and j=2 for the ions. x, r, n, v_x, p, $\eta_\parallel$, $\eta_\perp$, $\chi_{j\parallel}$ and $\chi_{j\perp}$ are the parallel and perpendicular coordinate, the plasma density, the parallel velocity, the scalar pressure, the parallel and perpendicular viscosity, the parallel and perpendicular heat diffusivities, respectively. S_0, S_p and Q_j are the source terms due to the neutral-plasma interaction. At present state they are neglected in the 2d-model partly because there is no experimental evidence for a high recycling regime in ALT-I. The boundary conditions account for the particle and energy flux released by the core plasma and for the analogous fluxes absorbed by the walls /5/. They are modelled by source and sink terms concentrated on the mesh cells neighbouring the boundary. Differencing of equations (1-3) yields banded matrices which are inverted by means of the SIP-solver.

In a 2nd approach the averaging, already mentioned, is employed, thus reducing the system (1-3) to a set of 1d radial equations /3/. These are

coupled with a system of transcendental equations for the plasma parameters in the throat region. This system accounts approximately for the parallel transport processes and the recycling. In the SOZ the transport perpendicular (diffusion and heat conduction) and parallel to the field lines (momentum build up and parallel heat conduction) are important, whereas in the TZ the recycling processes may dominate, if the plasma flowing into the throat is dense and hot enough to reionize the neutrals coming from the deflector plate at least partly ("high recycling regime"). The equations are solved by means of a 1d-transport code, which accounts also for the core plasma.

4. Results

The calculations were based on TEXTOR data /6/: limiter radius a=50 cm, major radius R=175 cm, plasmacurrent I_p=350 kAmp, toroidal field B_t=20 kG, volume averaged density $\langle n\rangle_v = 3 \cdot 10^{13}/cm^3$. Fig.2 shows the distribution of the electron temperature computed by the 2d-model. The electron energy flux released uniformly by the core plasma is 490 kW. The figure shows that (1) the electron temperature is constant parallel to the field lines because of the large $\chi_{e\parallel}$ (2) that the temperature decays very rapidly in radial direction. The analogous Fig.3 for the ion temperature reveals that especially in the outer radial region a small temperature gradient parallel to the field lines exists; the reason is the much smaller ion heat conductivity. The maximum temperature (42 eV) agrees roughly with the experimental value (~30 eV) /6/. The Bohm value was used for $\chi_{e\perp}$ and $\chi_{i\perp}$. The maximum particle density obtained by the two zone model is $1.4 \cdot 10^{12}/cm^3$ corresponding roughly to the experimental values ($6 \cdot 10^{11}/cm^3$ - $2 \cdot 10^{12}/cm^3$). A low recycling rate (R=30%) had been assumed. Fig.4 shows the recycled fraction f_i depending on the mean density $\langle n_e\rangle$ and temperature $\langle T_e\rangle$ in the throat region. It was obtained by means of the neutral gas code EIRENE /3/ for the geometry of ALT I given in section 2 (L_t=26 cm); for $\langle n_e\rangle = 10^{12}/cm^3$ and $\langle T_e\rangle$=10 eV the recycling rate is approximately 30%, thus confirming the above assumption concerning R.

References

/1/ R.W.Conn et al., 12th SOFT (1982) 497
/2/ A.K.Prinja, R.W.Conn, J. Nucl. Mater. 128/129 (1984) 135
/3/ D.Reiter, A.Nicolai, J. Nucl. Mater. 128/129 (1984) 458
/4/ M.Petravic et al., Phys. Rev. Lett. 49 (1982) 1408
/5/ B.J.Brahms, Proc. 11th European Conf. on Controlled Fusion and and Plasma Physics, Vol 7 (1983)
/6/ A.E.Pontau et al. J. Nucl. Mater. 128/129 (1984) 434

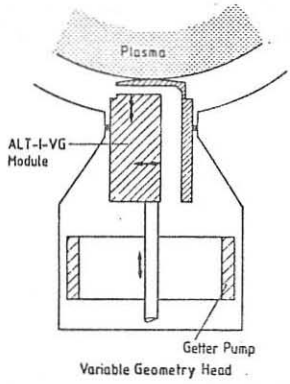


fig.1

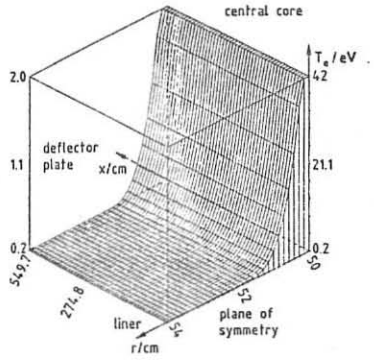


fig. 2

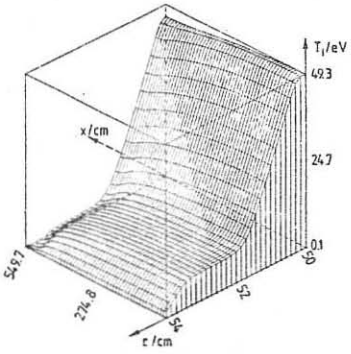


fig. 3

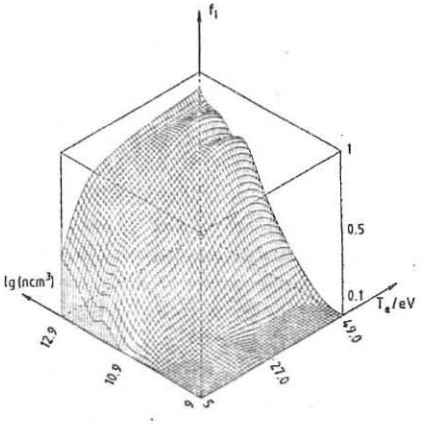


fig.4

Impurity Fluxes in TEXTOR

A. Pospieszczyk, H.L. Bay, P. Bogen, D. Rusbüldt,
U. Samm, J. Schlüter, B. Schweer
Institut für Plasmaphysik, Kernforschungsanlage Jülich GmbH
Association EURATOM-KFA

Introduction

The study of the impurity release and its relation to both the global and the edge-plasma properties is one of the major goals for the work on the TEXTOR tokamak. The excellent viewing access to its boundary and to the main limiter region allows the use of various optical diagnostic systems, which not only give general information about absolute magnitude of the impurity fluxes emitted but also detailed insight into the spatial distribution of the sources and the fluxes in the boundary layer. The very flexible limiter system allows both systematic variation of the scrape off layer and detailed investigations of the spatial and temporal changes of the flux parameters connected with it. Preliminary results have already been published in /1-3/.

Experimental arrangement

For the results reported here the TEXTOR machine parameters were: $B_T = 2$ T, $I_p = 340$ kA, $R = 1.75$ m, $40\ \text{cm} \leq a_L \leq 48$ cm and $10^{13}\ \text{cm}^{-3} \leq \overline{n}_e(o) \leq 4 \times 10^{13}\ \text{cm}^{-3}$. The following optical diagnostic methods were used for the flux measurements:

- Laser induced fluorescence was used in combination with a test limiter, the radial position of which could be varied between that of the main limiter and that of the liner. A laser system was used, which could operate with a maximum repetition rate of 100 Hz; the emission of the excited iron atoms was detected with a five channel system pointing along the minor radius. This method allows a local measurement of atom densities and, with known velocities, of fluxes near this test limiter and near the liner, where n_e is too low for emission spectroscopy. A detailed description of this system is given in /2/.
- Emission spectroscopy at the main limiter segments was performed by means of an absolutely calibrated grating spectrometer and, for spatial resolution, a combination of an interference filter and a CCD-camera connected to an image processing system, which can display the spatial distribution of the impurity sources. This system is most useful for the measurement of total atom fluxes (especially for Cr,- O- and C-atoms) from the main limiter segments, where T_e and n_e are sufficiently high. For details of the set up and the calibration procedure see /3/.

It should be briefly noted here that the penetration depth of these "natural" impurity atoms into the plasma was used to determine n_e and T_e in front of the main limiter (and liner) where so far no other method could be applied /3/.

The atom flux measurements were complemented by plasma core diagnostic techniques, which determined the corresponding ion fluxes (by optical spectroscopy) and ion concentrations (by soft x-ray pulse height-analysis).

Source distribution and penetration depth

Fig. 1 shows the emission pattern of iron atoms from a mushroom-like test limiter in the toroidal direction for two extreme limiter positions. For a) the test limiter had been moved into the same radial position as the main

limiter for b) into the liner position. Case a) demonstrates firstly that the fluxes on electron and ion drift side are approximately equal and secondly that the plasma particle fluxes, which are responsible for the emission of neutrals, follow predominantly the toroidal magnetic field lines. The radial decay is a result of the decrease of the temperature in the scrape off layer. This result is also confirmed by heat flux measurements at a similar test limiter /3,4/ and by CCD-camera recordings from the impurity release at the main limiter (Fig. 2). When the limiter is withdrawn into the liner position (case b) the pattern becomes quite flat, which indicates that the production of atoms is then due to isotropically distributed charge exchange neutrals. Simultaneously the density of the iron atoms decreases by a factor of 1000 with an exponential decay length of 6.5 mm. Assuming a ratio between the emitting area of the limiter and that of the liner of 1 to 1000 one finds about equal contributions to the impurity production from the limiter and from the liner. Due to the radial decay of the electron density the penetration depth of the neutrals increases from about 8 mm at the plasma edge to a few cm near the liner.

Fluxes, discharge parameters, and carbonization

The metal fluxes-in particular those of Cr and Fe - which are released from the limiters have been measured by emission spectroscopy and laser induced resonance fluorescence. These fluxes depend strongly on the density in the discharge (i.e. on the gas feed programme used) and drop by more than a factor of ten (for pure metal walls) when $\overline{n}_e(o)$ rises from 1×10^{13} cm^{-3} to 3×10^{13} cm^{-3} (Fig. 3). This decrease is obviously due to a strong energy dependence of the sputtering yield, which is to be expected near threshold. During this density increase a drop of the electron temperature in front of the limiter has been observed from 50 eV to 15 eV, which should be accompanied by a decrease of the sheath potential (from 180 eV - 50 eV), which then affects the ion energy and the resulting sputtering yield. It is not possible to explain the observed sputtering yields only with the proton (or deuteron) fluxes. This conclusion is confirmed by the fact that no significant change in the released metal fluxes could be observed when the filling gas was changed from hydrogen to deuterium. Therefore we have to accept a strong amount of impurity ion sputtering (C, O and/or metals).

The main light impurities - oxygen and carbon - which are released at the limiters and measured spectroscopically by their OI and CI lines in the infrared behave quite different from the metals. With increasing density $n_e(o)$ the oxygen flux increases proportional to the hydrogen flux (Fig.3) and is in general one order of magnitude larger than the metal flux. For carbon the behaviour is similar. This shows that the process of particle emission from the limiter for light impurities is closely coupled to the corresponding hydrogen fluxes and has no energy threshold.

The coating of wall and limiters with carbon by a glow discharge in a H/CH_4 mixture (carbonization) affects the metal sputtering strongly (Fig. 4). At low densities the fluxes are reduced by a factor of 10 when a fresh carbonization with about 300 monolayers of carbon is used. At high densities, when the sputtering is low in any case this reduction is less pronounced, i.e. only a factor of less than 2. At very high plasma densities (which could only be achieved with carbonization) there is no difference at all. The effect of carbonization typically holds for one day of operation (appr. 50 discharges) and gradually deteriorates during the next days. Concerning the influx of light impurities the sum of carbon and oxygen fluxes remains always approximately constant; only the ratio of carbon to oxygen is changed from 1:3 before to 3:1 after carbonization.

With carbonization a variety of lines from CH(D) radicals in front of the limiter could be detected (Fig. 5). The appearance of those lines show that a major fraction of light particles emitted at the limiter enters the plasma via molecules and demonstrates the importance of chemical processes for the particle release.

Fluxes, core concentrations and their variation with plasma radius.

The impurity concentrations in the core were measured by soft x-ray diagnostics (Fig. 6). If we compare their variation with density with that of the neutral impurity fluxes (Fig. 3) we notice that the general behaviour is quite similar, which indicates that no major changes in the particle confinement times τ_p for all species occur. We obtain τ_p about 10 ms for Cr and about 40 ms for oxygen in the case of carbonized walls. The drastic drop in the metal fluxes and concentrations during the increase of n_e leads also to a similar reduction of Z_{eff}. A metal dominated discharge with $Z_{eff} \approx 6$ at low densities changes into a light impurity governed discharge with Z_{eff} near to 1 (obtained with fresh carbonization at the density limit)

The ratios of the main metal species measured in the plasma core (Fe: Cr: Ni = 3:1:1) correspond to the composition of the limiter material and not that of the liner. Although the total fluxes from the limiter and liner are approximately equal (see above) there seems to be an effective screening of the liner material by the scrape off layer, which prevents it to enter the plasma core.

When the main limiter radius is changed from 48 cm to 40 cm the corresponding behaviour of the fluxes and core densities is shown in Fig. 7. Although there is a strong increase of atom fluxes from the limiter for smaller plasma radii the core densities remain unchanged. Obviously the impurity fluxes produced at the ICRH-antenna-shield or at the wall largely compensate for the reduction of impurity fluxes at the main limiter, when its radius is increased. This effect can also be seen in the light of H_α near the antenna shield; the intensity of which shows an inverse behaviour /5/. As the flux ratios do not change we suppose that the plasma density drop at the limiter is mainly responsible for the flux decrease; this is also confirmed by measurements of the limiter power load, which shows a similar behaviour for limiter radius variations /6/.

Conclusions

By means of various spectroscopic techniques the impurity fluxes and their dependence on plasma parameters, limiter radii and wall status could be determined from the main limiter out to the liner position. With increasing density the discharge changes from a metal to a carbon/oxygen dominated discharge. With decreasing radius the core parameters remain unchanged. Carbonization leads to a strong metal reduction, whereas the sum of the light impurities remains about constant; oxygen is largely replaced by carbon.

References:

/1/ A. Pospieszczyk, P. Bogen and U. Samm, 11th Europ. Conf. Controlled Fusion Plasma Physics, Aachen, Sept. 83 (EPS, Geneva), Vol. II, p. 417

/2/ H.L. Bay and B. Schweer, J. Nucl. Mat. 128 & 129 (1984), 257

/3/ P. Bogen, et al., J. Nucl. Mat. 128 & 129 (1984), 157

/4/ U. Samm. 11th Europ. Conf. Controlled Fusion Plasma Physics, Aachen, Sept. 83, (EPS,Geneva) Vol. II, p. 413.

/5/ L. Könen, private communication

/6/ P. Bogen et al., Properties of the TEXTOR boundary layer, paper 139. These proceedings.

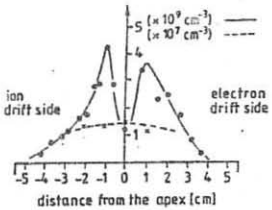


Fig. 1 Spatial distribution of the FeI density at the surface of a SS reference limiter in TEXTOR

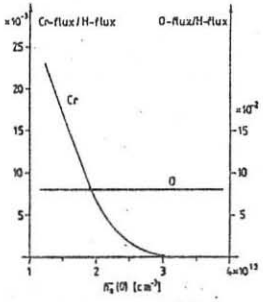


Fig. 3 Impurity fluxes from the limiter normalized to the H-flux (for uncoated walls)

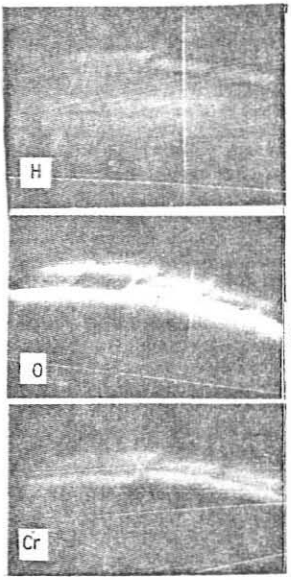


Fig. 2 CCD-camera photographs of the main upper limiter in the light of hydrogen, oxygen, and chromium atoms

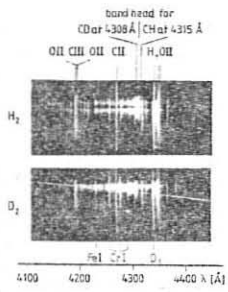


Fig. 5 Spectrum of the main limiter-plasma interaction zone in TEXTOR

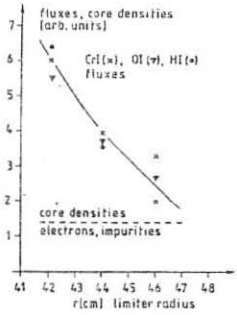
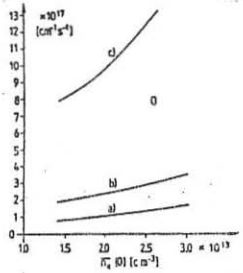


Fig. 7 Relative impurity fluxes and core densities as a function of limiter radius



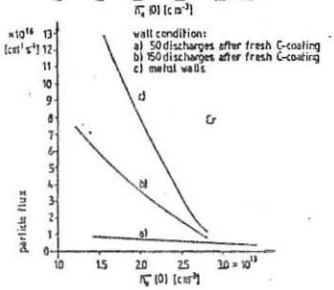


Fig. 4 Fluxes of neutral O and Cr measured at the main limiter as a function of central $\bar{n}_e$ and different wall coatings

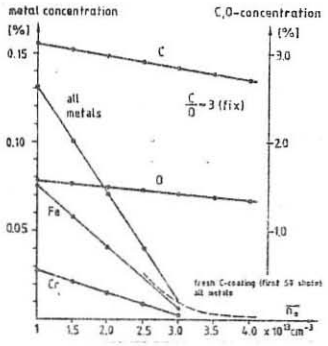


Fig. 6 Main impurity concentrations in the plasma-center as a function of central $\bar{n}_e$ (C-coated walls)

Properties of the TEXTOR boundary layer

P. Bogen, H. Hartwig, E. Hintz, K. Höthker, Y.T. Lie
A. Pospieszczyk, U. Samm, W. Bieger

Institut für Plasmaphysik, Kernforschungsanlage Jülich GmbH
Association EURATOM-KFA, P.O. BOX 1913, D-5170 Jülich

Introduction

In order to gain a better understanding of the interaction of a magnetically confined plasma with the surrounding walls and to develop further existing theoretical models /1-3/, we have to learn more about the density and temperature profiles in the boundary plasma and about the particle and energy fluxes. Up to now most of the experimental investigations have been carried out to obtain these quantities using probes as a diagnostic tool /1,2/.

In large tokamaks, probes can be applied only in the shadow of the limiter. Diagnostic methods are desirable, which are not restricted to this region. Beside Thomson scattering of lasers, limited to relatively high electron densities and to a single shot during the discharge, especially atom beam probes combined with resonance fluorescence or emission spectroscopy offer possibilities to fill this gap, and their application will be described in this paper. Additionally, probes, emission spectroscopy and infrared pyrometry at the limiter have been applied with the object to obtain data for a comparison with theoretical models of the TEXTOR boundary layer.

Experimental arrangement

The experiments have been carried out with the TEXTOR tokamak /4/ having a major radius of 175 cm, a minor radius between 48 cm and 40 cm, a toroidal field of 2 T, and a plasma current of 350 kA. With ohmic heating central temperatures of 800 eV at electron densities of $3 \times 10^{13}/cm^3$ have been obtained. The limiter system consisted of an antenna limiter at 48.5 cm and of the main limiter with one segment fixed on the inner wall at r = 48 cm, and with three limiter segments movable between r = 48 cm and r = 40 cm, as indicated in Fig. 1.

Particle fluxes from the main limiter have been derived from the emission line intensities (cf paper 138, this conference and /5/) with a calibrated spectrometer or a CCD-camera with an interference filter in front of it. Energy fluxes in the scrape-off layer have been determined by inserting an auxiliary limiter into the plasma and by observing its temperature rise and temperature profile with an IR-camera. A thermal Li-atom beam (T = 800 K) was injected radially (cf. Fig. 1), and from its emission profile, observed tangentially, the n_e-profile has been deduced. Different magnetic connection lengths between limiter segments or between limiter and Li-atom beam could be selected by introducing one or several of the three main limiter segments.

Principles

A rough description of the boundary layer is given by the following equations /2,3/: The radial particle flux density is given by

$$\Gamma = - D_{\perp} \, dn/dr \qquad (1)$$

where $D_{\perp}$ is a diffusion coefficient in the order of the Bohm diffusion coefficient /2/. The decay of the density in the shadow of the limiter is approximated by the equation

$$n = n_o \exp \left[-(r-a)/\Delta \right] \qquad (2)$$

with

$$\Delta^2 = D_{\perp} L_{\parallel}/C_s \qquad (3)$$

where $L_{\parallel}$ is the magnetic connection length between the limiters and C_s the ion sound speed.

For this result, the model assumes a constant velocity gradient along the flow to the limiter, an assumption, which appears to be questionable in view of the experimental results.

Temperature and energy flux density have characteristic scrape-off lengths which are slightly different from that of the particle densities. The power density Q arriving at the limiter is approximated by /2,3/

$$Q = \delta \, kT_e \, (n_o/2) \, C_s$$

where e.g. $\delta \approx 8$ in case that $T_e = T_i$ and that no secondary electron emission occurs.

Results

Observations have shown that the plasma parameters in the boundary as well as in the core are stationary as long as current and density are constant in time. Even after a strong perturbation of the boundary induced by shifts of the plasma position, by ICRH-heating pulses, or by impurity injection, the boundary plasma parameters normally return to their values before the perturbations. Modifications of the limiter geometry have often strong influence on the boundary plasma parameters, but the influence on the core plasma normally is low, as long as the impurity production, especially of metals, is below a certain limit.

For the recycling of the hydrogen, the fluxes emitted from the main limiter segments, the antenna limiter and the wall have to be considered . Whereas the contribution of the major part of the wall, which is sufficiently far away from the limiters, is practically independent of the radial limiter position, the contribution of the different limiters varies, when the radial position of the main limiter segments is changed. As can be seen from Fig. 2, the H_{α} -intensity at the three movable limiter segments increases by a factor of 8, when their radius is reduced from 48 cm to 42 cm. This observation may be explained in such a way that the particle load from the inner main limiter (cf. Fig. 2) and the antenna limiter is transferred to the movable limiter segments. At a plasma radius of 42 cm, we obtain a hydrogen flux of 1.2×10^{19} per centimetre limiter circumference and a particle confinement time $\tau_p \lesssim 100$ ms.

If instead of three limiter segments only one segment is used to reduce the plasma radius, this segment step by step receives the load of the others, and correspondingly the density at the limiter radius a_L increases as demonstrated in Fig. 3. It is remarkable, that the characteristic thickness of the scrape-off layer is nearly independent of a_L. This may indicate, that the diffusion constant is not much changed by the radius variation.

In order to obtain an insight into the toroidal dependence, we measured, using a single limiter segment at r = 46 cm, the density profile first near the limiter and then near the stagnation point (Fig. 4). The density decay length increases from Δ = 0.6 cm near the limiter to 1.5 cm near the stagnation point. From eq. 2 we estimate $\Delta = \sqrt{5}$ cm using $L_{\parallel}$ = 100 m, c_s = 10^7 cm/s and D = 5000 cm^2/s. The low value of Δ near the limiter may be explained by the non-linear increase of the flow velocity towards the limiter, enhanced by the recycling (cf. paper 16, this conference) at the limiter.
The density in the boundary layer normally increases about proportional to the core density (cf. Fig. 5). Density gradient and fluxes also increase by the same amount, the Δ -value decreases slightly. Depending on the preparation of the walls, also discharges have been observed, where the scrape-off layer density increases less than the core density, i.e. where the profile becomes steeper.

The characteristic decay length of the power load on the limiters is only slightly shorter than that of the density. The observed load of 300 W/cm^2 for a tpyical discharge with $\bar{n}_e = 2 \cdot 10^{13}/cm^3$ and a_L = 46 cm is in accordance with eq. 4 having a load of $4 \cdot 10^{18}$ electrons/cm^2s, kT_e = 30 eV, Δ_0 = 0.5 cm and σ = 8 assuming $T_e = T_i$. But exact values of T_e and especially of T_i have still to be measured.

Conclusions

Spectroscopic methods as H_α-spectroscopy or observation of the emission of an injected Li-atom beam give useful informations on particle flows and electron density distributions. This way poloidal and toroidal asymmetries can be investigated suggesting that a scrape-off layer model with a toroidally constant decay length is a poor approximation. Measurements show further that particle and energy load can be spread over one or many limiter segments without detectable change of the core plasma parameters.

References

/1/ P. Staib, J. Nucl. Mater. 111 & 112, (1982), 109
/2/ M.F.A. Harrison in: Applied Atomic Collision Physics, Academic Press, New York 1984
/3/ P.C. Stangeby, Phys. Fluids 28, 644 (1985)
/4/ H. Soltwisch et al., Plasma Phys. Controlled Fusion 26, 23 (1984)
/5/ P. Bogen et al., J. Nucl. Mater, 128, 157, (1984)

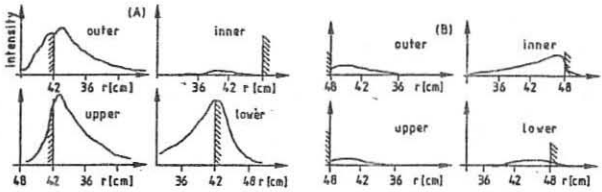


Fig. 2 Radial H_α-emission profiles at different radial positions of the main limiter segments. $n_e = 2.3 \cdot 10^{13}/cm^3$.
(A) Plasma radius 42 cm, (B) Plasma radius 48 cm.
Limiter segment positions hatched.

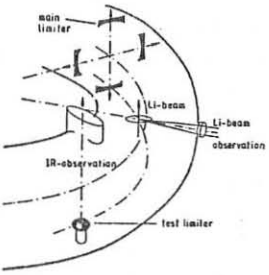


Fig. 1 Experimental arrangement

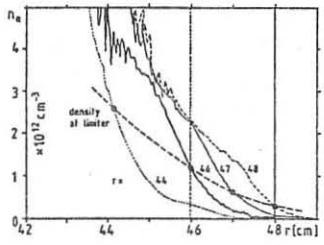


Fig. 3 Radial density profiles derived from the Li-beam emission. Inner, outer, and upper limiter segments at 48 cm, lower segment at 44, 46, 47, or 48 cm.
$n_e = 2.2 \cdot 10^{13}/cm^3$

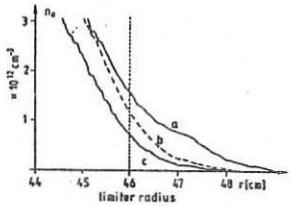


Fig. 4 Radial density profiles with one limiter segment at r = 46 cm, the others at 48 cm. a) measurement near limiter, b) measurement near stagnation point, c) all movable limiters at r = 46 cm

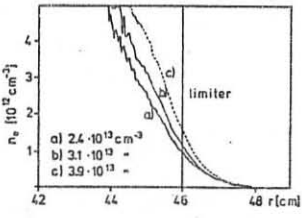


Fig. 5 Radial density profiles at different core densities

RADIAL DEPENDENCE AND MATERIAL EFFECTS WITH ALT-I PUMP LIMITER IN TEXTOR

K.H. Dippel, K.H. Finken
Institut für Plasmaphysik, Kernforschungsanlage Jülich GmbH,
Association EURATOM-KFA, D-5170 Jülich, FRG

G.J. Thomas, A.E. Pontau
Sandia National Laboratories,
Livermore, California, USA

G.A. Campbell, D.M. Goebel
University of California at Los Angeles,
Los Angeles, California, USA

ABSTRACT

ALT-I pump limiter studies were extended to smaller minor radii ($a \geq 40$ cm) using a bare graphite limiter head as well as a TiC coated graphite head. In addition to a strong radial dependence of the pump limiter pressure and power deposition, a clear drift to lower plasma densities was found in successive shots which appears to be related to material behaviour. Results of these investigations are reported and discussed.

I. INTRODUCTION

The ALT-I pump limiter has been shown to be effective in removing particles from the scrape-off layer and reducing plasma density compared to inactive limiters /1,2/. For example, particle removal rates of up to $2 \cdot 10^{20}$ particles/s had been found. In these studies, the maximum extent of the limiter position was to a minor plasma radius of 44 cm. Modifications have since been made allowing operation with the variable geometry head /2/ down to 40 cm minor radius, 8 cm from the nearest (radially) material structure. A strong radial dependence was again found for the pressure rise in the ALT-I chamber; however, in contrast to previous results, power deposition to the limiter head increased sharply at the smaller radii.

Additionally, data has now been obtained with a graphite head as well as a TiC coated graphite head at the smaller radii. Significantly greater limiter power loading was found with the graphite head compared to the TiC coated head. In addition, operation with the graphite head at the smaller radii revealed an interesting new effect - a drift in plasma density to lower values in successive shots.

In this paper we will describe some radial dependence results, differences between the graphite and TiC heads and the density drift behaviour.

II. PUMP LIMITER BEHAVIOUR

An increase in the pressure in the ALT-I vessel was observed as the limiter was moved to smaller minor radii. This is shown in Fig. 1 for the case of a graphite head and in a scoop mode of operation (i.e., no active pumping in the 700 liter ALT-I volume). The pressure can be seen to have increased by a factor of 2 to 3 when the limiter position changed from only 44 to 40 cm. The increased pressure was consistent with corresponding increases in ion saturation currents measured by Langmuir probes positioned directly in front of the

limiter throat opening.

Pressures up to 5 mTorr were attained with the TiC head in the scoop mode of operation. With pumping, the particle removal rate, $p \cdot S$ (where p is the measured pressure and S is the measured pumping speed), was as high as $6 \cdot 10^{20}$ particles/s. The exhaust efficiency, $p \cdot S/Ne/\tau_p$, was estimated using $\tau_p = \tau_E$ and found to exceed 20 %.

III. POWER LOADING TO THE LIMITER HEAD

Relative power loading on the limiter head was monitored by means of a thermocouple imbedded in the graphite at the center of the limiter surface and about 0.5 cm behind it. The temperature rise, ΔT_L, in the limiter, that is, the peak temperature after the discharge minus the temperature at the beginning of the discharge, is related to the energy deposited during the shot. It was found that there was a strong increase in ΔT_L at equal plasma densities when the limiter position changed from 44 cm to 40 cm. With the graphite head at 44 cm, temperature rises of 15-20°C were observed, whereas at 40 cm, the head temperature increased by 80-100°C.

On a limited number of discharges, infrared determinations of the limiter surface temperature were made from which the power loading could be derived. It was found that with the graphite head at 40 cm, 40-60 % of the ohmic heating power was deposited on the limiter. Considerably lower power loading to the limiter was found with the TiC head. Although ΔT_L increased with minor radius as with graphite, the maximum temperature rises (at 40 cm) were a factor of 3 to 4 lower than with the graphite head.

IV. DENSITY DRIFT IN SUCCESSIVE DISCHARGES

Fig. 2 shows the central line average plasma density for a sequence of successive discharges with the ALT-I graphite head at 40 cm. Identical conditions (e.g. gas feed) were maintained during this sequence. After opening the throat, the density decreased as expected from the pump limiter action. However, in the succeeding discharges the density continued to decrease. For initial plasma densities of the order of $3 \cdot 10^{13}/cm^3$, a steady density value would be approached after about 10 discharges. This behaviour was consistently observed during a number of different days of operation in which TEXTOR conditions were varied. The density decay was accompanied by a corresponding increase in the temperature rise of the limiter head resulting in an increasing limiter temperature as shown in Fig. 3. As discussed later, it is believed that the greater temperature rise, ΔT_L, due to the lower density in a given discharge, can then be responsible for the subsequent lowering of density in the next discharge. Similar behaviour was observed with the TiC case; however, the drift in density was markedly reduced.

A comparison of the number of particles collected in the ALT-I vessel and the observed decrease in density indicates that, after the first open throat discharge, more particles are lost from the plasma than are found in the vessel. This is shown in Fig. 4 in which is plotted the time dependence of the ratio of collected particles, N_{ALT}, to the difference in total electron number, ΔNe, compared to the closed throat condition. After the first open throat discharge, the ratio $N_{ALT}/\Delta Ne$ is less than unity at the beginning of the discharge and approaches a value of 1 or greater at later times. The initial ratio becomes smaller for each successive discharge.

V. DISCUSSION

The increase in pressure in the ALT-I chamber as the minor radius is decreased to 40 cm reflects an increased particle density in the plasma edge. This is

consistent with independent measurements using Li beam determinations of electron densities and density gradients in the range of 44 to 48 cm minor radius /3/. However, these changes in scrape-off layer density profiles are in turn likely due to temperature and density changes in the plasma boundary which are also related to the energy loss channels.

The strong increase in temperature rise, ΔT_L, on the limiter with decreasing radius for essentially equal ohmic power input indicates a reduction in radiative power loss and consequent channelling of energy to the limiter. Since there were no large reductions found in the central plasma temperature or Z_{eff} at the center (actually, Z_{eff} tends to increase with decreasing radius) for comparable plasma densities, it is suspected that low Z impurities, in particular O and C, play an important role in the observed radial dependence. Without additional diagnostic measurements in the plasma edge, however, it is not possible to uniquely determine the responsible processes. For example, the reduced radiation loss may be due to steeper temperature and density gradients producing a smaller radiative volume for the impurities, or conversely, higher densities and gradients could change the impurity concentration profile by reducing the penetration depth of recycled light impurities. Reduced wall interaction at the smaller minor radii could also result in lower light impurity levels.

It is suggested that the drift in density to lower values in successive shots is due to a varying hydrogen trapping efficiency of the graphite head during a discharge. This behaviour is intimately related to the temperature cycling of the limiter surface. Modest temperature rises occurring during closed throat operation leave the near-surface region of the graphite saturated with hydrogen. With the lower plasma density attained during pump limiter operation, higher surface temperatures are induced towards the end of the discharges which partially deplete the saturated layer. Then at the beginning of succeeding discharges, the graphite will act as a hydrogen sink until it again becomes saturated. The resultant lower density produces an even greater temperature rise which depletes the material even more, and the cycle is repeated. Detailed calculations of this behaviour have been performed and are the subject of another paper.

The reduced power loading to the TiC head is clearly due to greater radiated power loss by Ti impurities injected into the plasma from the limiter head. Soft x-ray measurements of Ti radiation indicate typical Ti concentrations in the plasma of about 0.1 %. Additional evidence for an increased power loss with TiC was found in the energy confinement time, τ_E, which was typically 40 % lower than equivalent discharges with the graphite head. The much lower density drift found with TiC could be due not only to differences in H retention, but also to the much smaller temperature rises in this case. A capability for independently heating the limiter head would aid in understanding this behaviour.

ACKNOWLEDGEMENTS

The authors wish to acknowledge useful discussions with R.W. Conn and G.H. Wolf. They would like to express their gratitude to the TEXTOR and ALT-I groups, in particular to G. Fuchs, L. Könen, H. Soltwisch, J. Schlüter, G. Waidmann (TEXTOR diagnostics), M. Korten and A.A. Ver Berkmoes (data acquisition), and B. Giesen and M. Lochter (operation of TEXTOR). They especially appreciate the expert experimental assistance of L.A. Brown and A. Hiller.

REFERENCES

/1/ Pontau, A.E. et al, Proc. 6th Int. Conf. Plasma Surface Interactions in Controlled Fusion Devices, Nagoya 1984, p. 434
/2/ Dippel, K.H. et al, Proc. 10th Int. Conf. on Plasma Physics and Controlled Nuclear Fusion Research, London 1984, Vol. 1, p. 249
/3/ Bogen, P. et al, this conference, paper no. 139

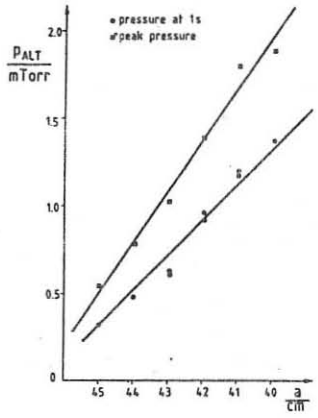


Fig. 1:

Pressure in the ALT-I vessel vs. limiter position (graphite head)

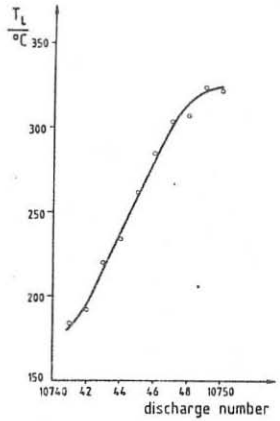


Fig. 3:

Bulk limiter temperature at the start of the discharge for the same discharges as in Fig. 2

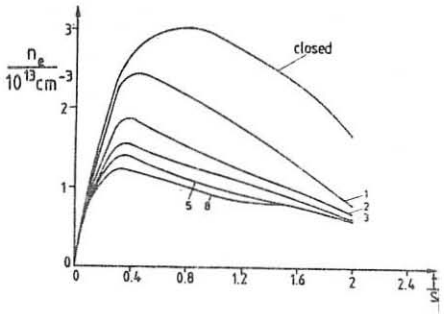


Fig. 2:

Line average density vs. time for a succession of discharges (1 to 8 after throat opening)

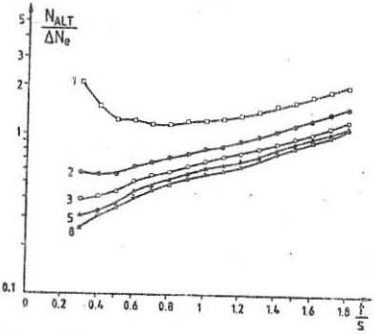


Fig. 4:

Particle balance $N_{ALT}/\Delta N_e$ vs. time (same discharges as Fig. 2)

RECYCLING, ISOTOPIC EXCHANGE AND DENSITY BEHAVIOUR IN JET DISCHARGES

P D Morgan, S Corti, J Ehrenberg*, M J Forrest+, A Gondhalekar, C W Gowers, G Magyar, J J O'Rourke, M F Stamp, D D R Summers, A Tanga, M L Watkins

JET Joint Undertaking, Abingdon, Oxon OX14 3EA, UK
* on attachment from Euratom-IPP Association, Max-Planck-Institut für Plasmaphysik, D-8046 Garching, FRG
+ on attachment from Euratom-UKAEA Association, Culham Laboratory, Abingdon, Oxon OX14 3DB, UK

INTRODUCTION

An understanding of recycling and particle confinement in tokamak discharges is an important prelude to achieving successful density control. Likewise, knowledge of isotopic-exchange processes permits a rapid and efficient changeover in the plasma hydrogenic content, when interchanging the working gas between H_2 and D_2.

The study reported is based mainly on measurements using optical spectroscopy. Details of the apparatus are to be found in /1/. Absolute H_α or D_α intensities, measured simultaneously at the graphite limiters, antennae, inner and outer walls and at upper and lower walls, yielded the neutral influxes. Other selected spectral lines were used to obtain impurity influxes. A 7-channel interferometer provided electron density profiles, while information about H or D effluxes was obtained using a neutral particle analyser (NPA).

RESULTS

The temporal behaviour of plasma current and electron line density is shown in Fig.1(a). The evolution of the line density closely follows that of the current. Also shown, as a broken line, is the evolution of $n_e.\ell$ if it were determined only by the initial torus prefill and the subsequent gas puff. To a reasonable approximation, the H_α or D_α signals from the limiters follow the current, while those from the wall, after the initial breakdown, tend to remain constant until a few seconds before the discharge ends /2/.

During current rise a substantial desorption of gas occurs. From particle balance /2/, the recycling coefficient

$$R = \Sigma S_i \,/\, (\Sigma S_i + \Phi_g - dN_e/dt)$$

is deduced to be > 1. It has the general form shown in Fig.1(b). ΣS_i is the electron production rate from ionisation of the recycled hydrogenic and impurity fluxes, Φ_g is the gas flux introduced by puffing, mostly during current rise, and N_e is the plasma electron content. The global particle confinement time $\tau_p \equiv R\, N_e/\Sigma S_i$ may also be evaluated, and permits deduction of the characteristic time for density change, $\tau^* = \tau_p/(1-R)$.

With no gas puffing, during the current plateau the plasma density is approximately constant, indicating that $R \sim 1$ (Fig.1). During this stationary phase, for sequences of shots in which the average density $\bar{n}_e$ is varied, to a good approximation the hydrogenic influxes from the limiters and wall vary quadratically with $\bar{n}_e$ (Fig.2) over the density range covered. The limiters are the main source of recycled particles. The ratio of limiter to wall flux

varies with plasma current and elongation, b/a, but is generally in the range 3-15:1, during the current plateau. Since the total limiter area is $\lesssim$ 1% of the plasma surface area, the corresponding H_α or D_α brightness ratio is in the range 300-1500:1. Fig.3 shows the variation of τ_p with $\bar{n}_e$ during the plateau, for several series of shots. Proton dilution by the impurities has been taken into account. For $\bar{n}_e \gtrsim 10^{19}$ m^{-3}, τ_p decreases with increasing density, but at lower densities the dependence is reversed /2/. The high density regime is consistent with the plasma becoming impervious to the penetrating neutrals and the recycling becoming predominantly an edge effect.

During the discharge termination phase the plasma current is ramped down to zero in $\sim$ 5s. There is a simultaneous decrease in plasma density (Fig.1(a)) indicating that $\sim 2\text{-}5\times10^{20}$ particles/s are pumped by the torus and its accessories, with concomitant decreasing influx from the limiters. A recycling coefficient < 1 is inferred during this phase (Fig.1(b)). In contrast, the H_α or D_α signal at the wall remains unchanged for several seconds following the start of current ramp-down, before steadily increasing as the discharge ends. In many discharges, particularly those at higher density, there is a sudden decrease in the influx from the limiters accompanied by a simultaneous increase in the influx from the wall and a peaking of the density profile. This is described in detail in /3/ - this conference - and is attributed to the formation of a 'marfe'.

On changing the working gas from H_2 to D_2, without conditioning the vacuum vessel, within $\sim$ 10 discharges the concentration ratio $n_D/(n_D + n_H)$ is found to be $\gtrsim$ 0.9, from measurements of the neutral influx and efflux. However, for a series of discharges following carbonisation of the vessel, by glow discharge cleaning in H_2 and $\sim$ 5% CH_4, the situation is different. The deposited carbon traps considerable amounts of H_2. On changeover, it is observed that $n_D/(n_D + n_H)$ is only $\sim$ 0.5 after 10 discharges and that it takes a further 20-30 shots to increase the ratio to $\gtrsim$0.9.

ICRH experiments have been performed on JET, using ^{3}He as a minority species. Controlled quantities of this gas are injected into the vacuum vessel towards the end of the current ramp-up. From interferometry, the increase in the plasma electron content is consistent with all of the helium entering the plasma. The increase in electron density penetrates to the plasma centre in approximately 0.5s, which is on the same time scale as the particle confinement time. Using H as minority, the application of a 2s 2.5 MW square pulse of RF power to the antenna resulted in brighter D_α signals, by a factor of $\sim$ 3 at the wall and $\sim$ 2 at the limiters. The RF power caused τ_p to drop to about half its former value of $\sim$ 0.35s, in $\sim$ 0.5s. After the pulse τ_p recovered to its previous value on the same time scale.

DISCUSSION

The gas desorbed during current rise, due to the increasing power loading and rising temperature of the graphite limiters, generally accounts for a significant fraction of the plasma density achieved during the plateau, and limits the density range over which JET can operate - typically a factor of 2 at fixed current. For mid-range densities desorption contributes $\sim$ 50% of the plasma electron content (Fig.1(a)) the amount decreasing during the course of a long series of discharges. Overnight glow discharge cleaning replenishes the source. During a discharge, additional gas is puffed in to achieve the desired density. In the case of discharges at the high end of the density range, more gas is admitted to the torus than enters the plasma, which becomes increasingly impervious to the neutral atoms.

The observed dependence of the recycled flux Φ on $\bar{n}_e^2$ during the current plateau (Fig.2) is predicted by a simple transport model /4/. In it, the inward flux of neutrals penetrating the plasma, and ionised within a short

distance of the boundary, is balanced by the diffusion of electrons at the edge with an anomalous diffusion coefficient of order 0.4 m^2/s. Since $\tau_p = V\bar{n}_e/S\Phi$, where V is the plasma volume and S the surface area, a consequence of the dependence $\Phi \propto \bar{n}_e^2$ is that $\tau_p \propto 1/\bar{n}_e$, which is in reasonable agreement with the results in Fig.3.

No clear explanation can be offered at present for the temporal variation of the recycling coefficient during a discharge. Similar behaviour has been observed on ASDEX and TFTR. Considering R to comprise two components, one possibility is that at the limiters R_L is > 1, decreasing from a high value during current rise, as the gas available for desorption becomes progressively less, whereas at the wall R_W is < 1. Under this hypothesis, during current rise the limiter recycling would dominate, while during the plateau the desorption from the limiters is approximately equal to the wall pumping. During current decay the safety factor at the edge q increases, broadening the scrape-off layer and increasing plasma-wall interaction, while the limiters cool and release less gas. In this phase, the role of the wall would dominate. However, the abrupt change in R at initiation of current ramp-down (Fig.1) is not understood. Transport code modelling /5/ indicates that in order for the ohmic power to exceed the radiated power during current decay, which is the experimental observation, a density decay is necessary. For the specific case of Pulse No.3050, using a non-coronal radiation model for carbon impurities, a decay in the electron content in the range $2\text{-}4 \times 10^{20}\ s^{-1}$ is required, which agrees well with the measured rate, $\sim 3 \times 10^{20}\ s^{-1}$.

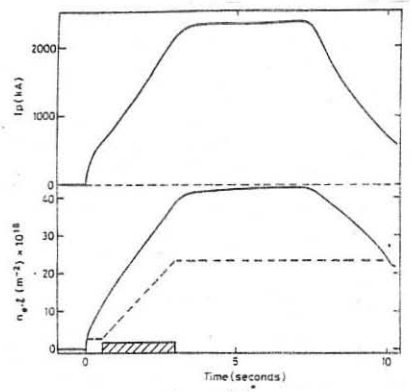
The observed behaviour on changing the working gas from H_2 to D_2 can be explained on the basis of an isotope exchange model /6/. The main assumption is that the limiters, with which the plasma mainly interacts, are saturated with hydrogen. This is then exchanged with deuterium, in accordance with the local mixing model /7/; hence, a recycling coefficient of unity is assumed. The calculated influx ratio $\Phi_H / (\Phi_H + \Phi_D)$ has been compared with measurements from the NPA and with H_α/D_α intensity ratios determined by spectroscopy /8/, for a sequence of discharges. Good agreement was obtained between theory and experiment for the temporal evolution of the ratio during a discharge and throughout the sequence. The model also describes the shot-to-shot behaviour of the flux ratio for the case of carbonised walls.

CONCLUSIONS

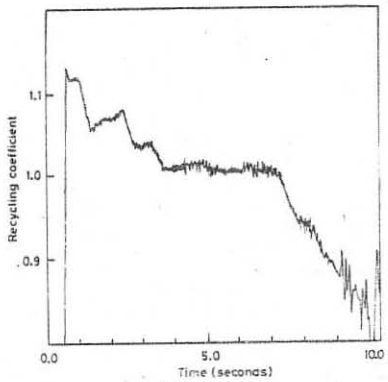
The gross recycling and particle confinement properties of JET discharges have been evaluated, from considerations of particle balance applied to spectroscopic and interferometric measurements. This has resulted in an improved understanding of the behaviour of particle fluxes from various locations in the torus, the role of fuelling and of density control. Measurements made following a change in the working gas from hydrogen to deuterium, and the results from a model of this process, have provided an insight into the mechanisms of isotopic exchange.

REFERENCES

/1/ P D Morgan et al, Rev.Sci.Instrum. 56, (5) part 2, 862, (1985).
/2/ A Tanga et al, JET Report JET-P(84) 09, (1984).
/3/ J O'Rourke et al, paper 190 this conference, (1985).
/4/ W Engelhardt and W Feneberg, J Nucl.Mat. 76 & 77, 518, (1978).
/5/ D G Muir and M L Watkins. To be published.
/6/ G M McCracken et al, Nucl.Fusion 18, 35, (1978).
/7/ B L Doyle et al, J.Nucl.Mat. 93 & 94, 551, (1980).
/8/ J Ehrenberg, JET Report JET-DN-E(84) 07, (1984).



(a)



(b)

Figure 1 (a) Plasma current I_p and electron line density $n_e \ell$ (solid line) during a discharge in H_2. Shaded area indicates waveform of gas puff. B_T = 2.5T, b/a = 1.2. Further details given in text. (b) Global recycling coefficient R versus time, for same discharge.

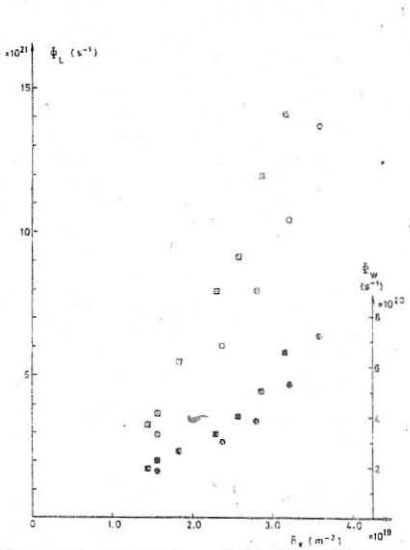


Figure 2 Variation of limiter (L) and wall (W) influx with average density during the current plateau, for 2 series of shots in D_2. Open symbols - Φ_L, solid symbols - Φ_W. O : Ip = 3.6 MA, □ : Ip = 3.0 MA. B_T = 3.4T, b/a = 1.5.

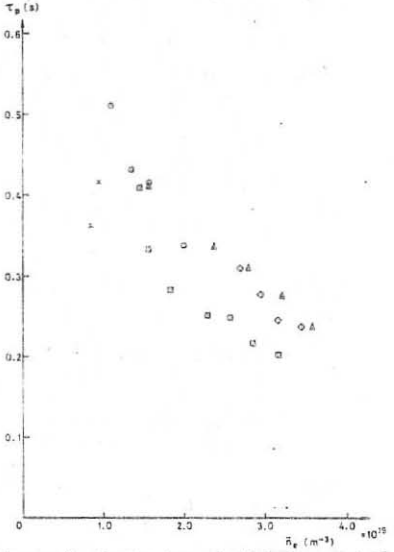


Figure 3 Variation of global particle confinement time with average density during the current plateau, for 5 series of shots in D_2. Plasma current: ◇ - 4.0 MA, Δ - 3.6 MA, □ - 3.0 MA, O - 2.0 MA and X - 1.0 MA. B_T = 3.4T, b/a = 1.5.

IMPURITY SOURCES AND IMPURITY FLUXES IN THE JET TOKAMAK

M F Stamp, K H Behringer, M J Forrest*,
P D Morgan, H P Summers

JET Joint Undertaking, Abingdon, Oxon OX14 3EA, UK
* EURATOM-UKAEA Association, Culham Laboratory, Abingdon, Oxon OX14 3DB, UK

INTRODUCTION

Spectral lines from hydrogen and low ionization stages of impurities (C, O, Cl, Cr, Ni) have been studied routinely in JET by means of visible spectroscopy. The plasma light, collected along selected chords terminating on the upper torus walls (vertical chords) or on carbon limiters or an RF antenna (horizontal chords), is relayed to spectrometers or narrow band interference filters outside the torus hall by about 100 m long optical fibres. Since the use of fibres restricts the wavelength range to $\lambda > 380$ nm, a close coupled spectrometer is mounted on the torus, viewing a carbon limiter in the extended range down to about 200 nm. Calibrated signals from these instruments are used for determining the local influxes Γ of hydrogen and impurities from walls and limiters, and for calculating the integral fluxes ϕ by multiplying by the respective areas.

METHOD OF ANALYSIS

The neutral particles are ionized in a narrow shell at the plasma periphery. Under the usual conditions of negligible recombination, the ionisation rate per unit surface area, integrated over the shell width, equals the neutral influx density Γ_o. Since ionisation and excitation rates are closely correlated, Γ_o may be derived from the line-of-sight intensities of neutral line emission, essentially by multiplying the number of photons by the ratio of ionisation coefficient S over excitation coefficient X. Within certain limitations, spectral lines from low ionisation stages can also be used for flux measurements. The results are less localised and corrections must be made for losses in lower ionisation stages. According to transport calculations, these corrections are small for limiter fluxes and about a factor of two for wall fluxes in the cases discussed here.

The majority of the observed atoms and ions have metastable levels with high statistical weights in an alternative spin system from that of the ground level. Therefore, the influxes of ground state and metastable state particles have been measured separately. This is done by analysing lines of the different spin systems, relying on the fact that excitation rates within a spin system are much larger than inter-system excitation rates. According to the present analysis, the population of metastable levels in O II, O III and C III is comparable to the ground state population, while it is much lower in C II and Cr I. In the latter cases it appears sufficient to investigate the ground state system only, in order to obtain the influx density.

The excitation rate coefficients required, mainly non-dipole transitions, were calculated by an atomic physics code. In some cases, the results are confirmed by more elaborate treatments available in the literature (eg Mann

/1/ for C II). Ionisation rate coefficients are taken from Lotz /2/. As an example, Fig.1 shows the S/X ratio for C II 657.8 mn (ground state system), C II 514.5 mn (metastable system) and Cr I (ground state system) as a function of temperature. In the analysis, temperatures for the plasma boundary have been taken from ECE and Langmuir probe measurements.

RESULTS

As demonstrated by the signals in Fig.2, the influxes of hydrogen and light impurities (C, O, Cl) scale roughly with $\bar{n}_e^2$. They are insensitive to the plasma current I_p. This means that light impurity production does not depend on temperature but on the number of recycling hydrogen particles. Throughout the JET operation period, ϕ_C was in the range 10-20% ϕ_H, with about equal contributions from walls and limiters. For oxygen, wall and limiter fluxes were also found to be about equal, but their magnitude was much more variable, ie $\phi_O \tilde{\sim} 20\% \phi_H$ after a major opening of the torus and $\phi_O \tilde{\sim} 2\% \phi_H$ after long operation and repetitive carbonisation of the vacuum vessel. During the JET start-up phase, chlorine influxes were observed, which were comparable to the hydrogen fluxes. ϕ_{Cl} decreased rapidly during operation and as a consequence of cleaning methods; it is now below 1% ϕ_H. All light impurity influxes from the top and bottom of the vessel increased substantially with reduced plasma-wall distance, ie large values of the vertical plasma dimension b. This behaviour is shown in Fig.3.

The carbon limiters have been identified as the main source of metal impurities in JET. During the first weeks of operation with new carbon tiles metal influxes from the limiters were not measurable. Later on, the graphite was coated by wall material (Inconel 600) as a consequence of tokamak operation and glow-discharge cleaning. Then, metal fluxes of 2% ϕ_H were observed for $\bar{n}_e = 2.10^{19}$ m^{-3} and $I_p = 2$ MA. This production yield can be explained by a combination of hydrogen and impurity sputtering at $T_e \tilde{\sim} 100$ eV, even if the carbon surface is only partly covered by metals. The metal influxes increased with I_p and, as shown for chromium in Fig.2, decreased with $\bar{n}_e$. The signals from the torus walls were usually below the detection limit, ie less than 10% of the limiter fluxes.

The consequences of pulse-discharge-cleaning (PDC, 12000 pulses) and of carbonisation of the vessel walls are demonstrated in Fig.4. Carbon and oxygen fluxes were lower after PDC, but higher chromium signals indicated an increased metal deposition on the limiter surface. Carbonisation lead to a substantial reduction of oxygen, chlorine and chromium signals. Although the carbon flux was higher, the resulting plasmas were cleaner as demonstrated by lower Z_{eff} values from visible bremsstrahlung and radiated power. Because of the latter fact the limiters heated up to temperatures of 1700 K and a sudden increase in metal influx was observed, which is attributed to metal evaporation. During these limiter temperature excursions the carbon influx, as derived from C II signals, followed the electron density in the usual way. There was no indication of the existence of chemical sputtering expected to occur around carbon surface temperatures of 900 K. On the other hand, the high carbon yield measured could be indicative of a temperature independent chemical release mechanism.

During ICRF heating of JET plasmas, the limiter fluxes of deuterium and light impurities behave normally, ie scale with $\bar{n}_e^2$. However, the wall fluxes increase substantially and approximately linearly with RF power, as shown in Fig.5. For $P_{RF} \tilde{\sim} 5$ MW, the deuterium wall flux is about 5 times higher and the carbon wall flux is 7 times higher than before RF. Impurity influxes from

the antennae show the same behaviour as the limiters, but with an additional small power-dependent influx when the antenna is active. From these results, an increase in light impurity content in the plasma must be expected, which may only be small due to the efficient screening of wall influxes. Metal influxes appear to be almost unaffected by RF heating. Z_{eff}, measured from bremsstrahlung, shows very little increase during RF heating.

All the results and trends of impurity influxes, discussed in this paper, are in good agreement with the impurity density behaviour in the plasma interior, as described in "Spectroscopic Measurements of the Impurity Content of JET Plasmas with Ohmic and RF Heating", B Denne et al, at this conference.

REFERENCES

/1/ J B Mann, quoted in Los Alamos Scientific Laboratory Report, LA-6691-MS (1977).

/2/ W Lotz, Lab. Reports IPP 1/62 (1967) and IPP 1/76 (1968), Garching, Germany.

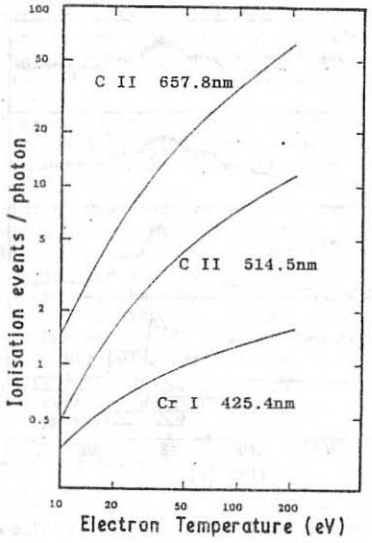


Fig.1 : S/X ratio calculated for C II (metastable system 514.5nm and ground state system 657.8nm) and for Cr I (ground state system).

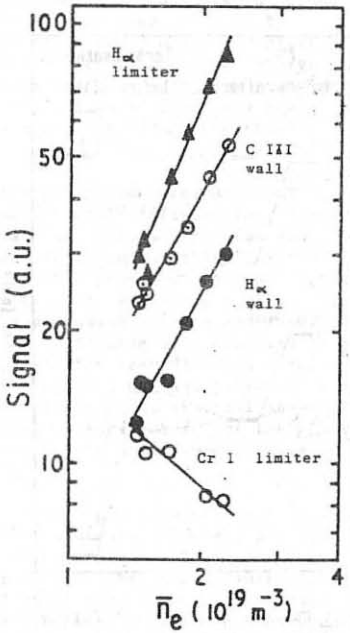


Fig.2 : Variation of hydrogen and impurity influxes with average electron density, $\bar{n}_e$. The data is from similar pulses (#1885-1895) with I_p=1.9-2.2MA, B_T=2.5T, b=1.29m, b/a=1.2.

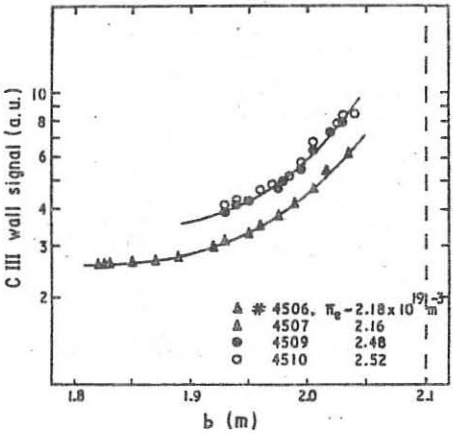


Fig.3 : Variation of carbon influx with plasma height b. The vessel wall is at 2.1m. The data was taken during the current flat-top, where I_p = 3MA, B_T = 2.6T, a =1.16m.

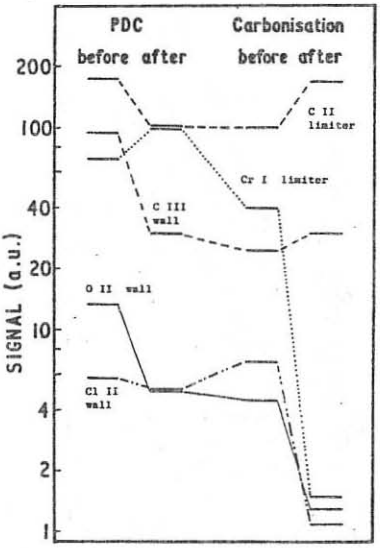


Fig.4 : Changes in impurity influx for reference discharges ($I_p \simeq$ 2.5MA, B_T = 2.6T, $\bar{n}_e$ = 2.0x10^{19} m^{-3}, $\bar{B}$ = 1.5-1.6m, b/a =1.4) as a result of PDC and carbonisation.

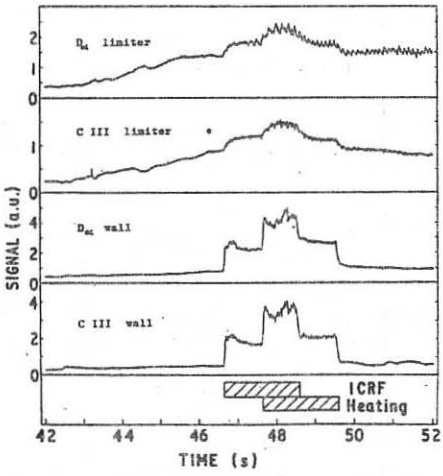


Fig.5 : Carbon and deuterium influxes during a RF heated discharge. Two antennae each couple 2.5MW for two seconds into the plasma. The RF pulses have a one second overlap.

Impurity Sources during Ohmic-heated Discharges in ASDEX

J. Roth, G. Fußmann, G. Janeschitz, H. Verbeek, F. Wagner, R. Bartiromo, G. Becker, H.S. Bosch, A. Eberhagen, K. Ertl, O. Gehre, J. Gernhardt, G. v. Gierke, E. Glock, O. Gruber, G. Haas, F. Karger, M. Keilhacker, A. Kislyakov, O. Klüber, M. Kornherr, P.B. Kotzé, K. Lackner, M. Lenoci, G. Lisitano, H.A. Mahdavi, H.-M. Mayer, K. McCormick, D. Meisel, V. Mertens, E.R. Müller, H. Murmann, H. Niedermeyer, W.Poschenrieder, H. Rapp, H. Riedler, F. Ryter, F. Schneider, G. Siller, P. Smeulders, F. Söldner, E. Speth, G. Staudenmaier, K. Steinmetz, K.-H. Steuer, E. Taglauer and O. Vollmer.

Max-Planck-Institut für Plasmaphysik
EURATOM Association, D-8064 Garching

Introduction: Impurity control, especially during auxiliary heating, is still one major issue in fusion devices. Though it has been possible to reduce considerably the heavy impurity level in the ohmic phase, either by appropriate choice of wall and limiter materials or by using divertors /1/, their origin is still under discussion /2/. The contribution of charge exchange (CX) neutral sputtering at the wall can be examined by changing the working gas from hydrogen to helium, where CX cross sections are much lower. The contribution of ion sputtering can be investigated by comparison of divertor and carbon limiter discharges.

1.Experimental: Plasma discharges with standard parameters have been performed in H_2, D_2 and He for limiter and divertor configuration. Apart from the basic plasma diagnostic special emphasis has been put to edge and impurity diagnostics. As limiter a movable air cooled graphite mushroom limiter was used. The overall temperature of the graphite block was monitored with thermocouples. A number of fixed limiters was installed further out in the scrape-off layer for protection of the microwave antenna and insulating breaks. The edge plasma temperature and densities have been measured by a Langmuir probe, Thomson scattering and the lithium beam diagonstic for comparable hydrogen discharges /2/, while they were not available for the He discharges. The CX-flux has been measured using electro-statical analysis after stripping /3/ and time of flight (TOF) measurement /4/ of the neutral particles. During these measurements especially Fe and C impurities are monitored by spectroscopy.

2.Theoretical considerations: The flux of charge exchange neutrals is well measured for hydrogen plasmas. Energetic He neutrals, however, are not stripped effectively to yield measurable charged fluxes. The TOF-system, on the other hand, did not allow mass analysis, such that the measured fluxes could well be due to the background level of CX neutral hydrogen fluxes. In order to get a criterium, the ratio of CX fluxes for helium and hydrogen discharges are theoretically estimated.
Ionization and charge exchange rate coefficients S_{ion} and S_{CX} are available from literature /5,6/. A simple balance equation for the cold and energetic neutral gas density shows that in steady stae the charge exchange fluxes are determined by the ratio of ionization to charge exchange rate coefficients. For an He^{++} plasma, which is produced by a neutral He flux Γ_{He} the charge exchange flux Γ_{He}^{CX} towards the vacuum wall is given by

$$\Gamma_{He}^{CX} = -\frac{1}{6}\left(2\langle S_{ion}/S_{CX}\rangle + 1\right)^{-1} \Gamma_{He}$$

For a hydrogen or deuterium plasma being singly ionized the same equation reads

$$\Gamma_H^{CX} = -\frac{1}{6}\left(\left\langle \frac{S_{ion}}{S_{CX}} \right\rangle + 1\right)^{-1} \Gamma_H$$

$\left\langle \frac{S_{ion}}{S_{CX}} \right\rangle$ amounts to about 0.7 for hydrogen but increases for He to about 30 for edge plasma temperatures above 20 eV. Assuming again that $\Gamma_{He} = 1/2\ \Gamma_H$ to establish the same electron density, one would expect a ratio of $\Gamma_H^{CX}/\Gamma_{He}^{CX}$ of about 72.
In this consideration only doubly charged helium ions have been taken into account. Close to the separatrix, however, also singly ionized helium ions exist, which have about 10 times higher cross sections for charge exchange with neutral helium atoms. Their contribution has been estimated by numerical transport simulations using experimental density and temperature profiles. Only small He^+ concentrations are obtained in a narrow layer close to the separatrix. But as the neutral gas density is still high at this radial position, their contribution to charge exchange fluxes is about the same as from doubly charged helium ions. Overall a reduction in charge exchange fluxes of about a factor of 30 is expected by going from hydrogen to helium discharges with equal plasma parameters.
The same transport code has been used also to calculate iron density profiles for a given flux of neutral iron atoms from the wall. Ionization and cross field diffusion are taken into account as well as losses to the wall and into the divertor.

3.Results: For the different working gases standard discharges with medium density have been examined. In total 6 different types of discharges are compared: For H_2, D_2 and He working gas both divertor and limiter discharges. As an example for H^- and He discharges fig. 1 shows the main result. The upper traces show the time dependence of the plasma current I_{pl}, the line average density $\bar{n}_e$ and the auxiliary heating power. In addition the time dependence of the Fe XVI and CIII lines are indicated. Most prominent here is the increase of the carbon density for limiter discharges in the hydrogen isotopes, while for He and all divertor discharges the CIII signal is roughly the same. In divertor discharges the Fe density is three times higher in D_2 than in H_2 discharge while for He intermediate values are found. Limiter discharges show higher iron densities than divertor discharges. The behaviour of impurities during phases of auxiliar heating will be discussed in /7/. The middle graph shows the radial profile of the plasma temperature T_e and the electron density n_e at a time of 0.9 sec. The data points are from YAG laser scattering, while the lines are results from ECE and HCN interferometer measurements. In the boundary layer the profiles are still rather uncertain and more accurate laser scattering measurements will have to be performed. The central iron densities according to spectroscopy measurements are given as well as Fe density profiles calculated from Fe fluxes due to CX sputtering. The lower graph shows the energy distribution of the CX fluxes measured by electrostatic analysis. The dashed lines are extrapolations on the basis of information from the TOF analyser. For He and D_2 discharges also the flux of neutral hydrogen atoms has been determined, which is still considerable in D_2 discharges due to HD recycling at the wall and limiter. The He fluxes estimated from theoretical considerations (section 2) are given here. By multiplying the CX flux with the known sputtering yield for stainless steel the flux of iron atoms sputtered from the wall is calculated and given in fig 1.The limiter temperatures measured at the rear surface of the graphite block rose up to 200 C after the shot, indicating that the front surface temperatur exeeded 500 C. The surface of the limiter has been examined after the experiment by ion beam analysis and was found to be covered by 2 to 8.10^{17} Fe/cm^2.

4. Discussion: -Divertor discharges: For hydrogen and deuterium discharges the total CX flux to the walls has then measured to be about a factor of 30 higher than the integrated ion fluxes parallel to the magnetic field in the shadow of the protection limiters /8/. Due to their low sputtering yield only CX sputtering is considered as impurity source. Then the calculated iron density profile as shown in fig. 1 agrees within a factor of 2 with the experimental value of $n_{Fe}(0)$. The scaling from H_2 to D_2 also yields the increase in density by factor of 3 as found experimentally. A more careful assessment of the CX sputtering /9/ shows that the iron influx is by far not homogeneous. In the vicinity of the gas valve a factor or 30 higher fluxes may be observed than away from the gas valve. The toroidal asymmetries and the poorly known angular distribution of CX neutrals and the uncertainty in the sputtering yield of the vessel wall may still contribute to an overall error of a factor of 2. For He no direct measurements of the CX fluxes exist. The fluxes expected from theoretical considerations are uncertain by more than a factor of 2. But again the calculated iron densitiy is in good agreement with the measured value. The larger sputtering yield for He atoms and the better confinement yield even higher Fe concentrations for He discharge than for H_2 discharges inspite of the much smaller CX flux. The fact that the values systematically exeed the measured densities may indicate that the sputtering yield of the oxidized vacuum wall is lower than estimated.

- Limiter discharges: In the limiter discharges the density was slightly higher leading to smaller CX fluxes. However, the measured Fe impurity concentrations are now considerable higher than the ones calculted from CX sputtering. This would be surprising for a clean graphite limiter. At the observed Fe coverage of the limiter surface ion sputtering at the limiter provides a sufficient, though quantitatively uncertain, source of Fe impurities. Ion beam sputtering experiments from an ASDEX limiter tile /10/ with similar Fe coverage showed an iron yield of about 1/10 of the yield from a pure iron sample. Especially for He discharge, now ion sputtering at the limiter may be the dominating process.

The importance of the ion-limiter interaction may be seen from the carbon signals. It increases drastically for the case of limiter discharges in hydrogen isotopes. This indicates clearly chemical interaction inspite of the considerable metal coverage on the limiter. The time dependence for the C signal shows a slow increase and passes through a maximum shortly after reaching the plateau phase. This can be explained by slowly rising carbon surface temperatures which may even slightly exceed the temperature for maximum chemical sputtering /11/. As maximum chemical sputtering yields for H ions have been found to be about 10^{-1} CH_4/atom the yield for He ions must be below $3\ 10^{-2}$ as can be seen from the comparison in fig. 1. Such low yields indicates He ion energies around and below 50 eV.

5. Conclusion: Iron impurities in ohmic divertor discharges in hydrogen isotopes can quantitatively be explained by wall sputtering of CX neutrals. For discharges in He, the expected CX flux is smaller by a factor of 30. However, the higher sputtering yield of He and the improved confinement typicall found in D_2 and He discharges /2/ lead to similar iron densities as for H_2 discharges. It is not necessary to consider other impurity sources like sputtering by ions. The precision of the measurements does not allow, however, to determine impurity sources more definitetively. As the detailed shape of the plasma edge profiles enters strongly the transport calculations but were not measured for the He discharges further experiments with improved edge diagnostic and more accurate measurements of the CX neutral fluxes are necessary. In limiter discharges the main plasma wall interaction occurs at the limiter as can be seen by the strong increase in carbon density for

hydrogen and deuterium discharges. As the carbon limiter was additionally contaminated with metal layers, the increased iron impurities also in the case of He discharges may be understood. Further measurements with a clean graphite limiter are therefore necessary.

References

/1/ M. Keilhacker et al, 8th Int. Conf. Plasma physics and Controlled Fusion Research, Brussels, Belgium (1980)
/2/ G. Fussmann et al, J. Nucl. Mat. 128&129, 641 (1984)
/3/ F. Wagner, J. Vac. Sci. Technol. 20, 1211 (1982)
/4/ H. Verbeek, these proceedings
/5/ W Lotz, Astrophys. J. Suppl. 128, 207 (1967)
/6/ C. F. Barnett et al, Atomic Data for Contr. Fusion Res. I, Rep. ORNL-5206
/7/ G. Fussmann, these proceedings
/8/ W. Poschenrieder, these proceedings
/9/ J. Roth, in "Physics of Plasma-Wall Interactions in Controlled Fusion", Plenum Press, to be published
/10/ J. Appelt, J. Bertold, J. Bohdansky, J. Roth, to be published
/11/ J. Roth, in "Sputtering by Particle Bombardment" Springer Verlag (1983)

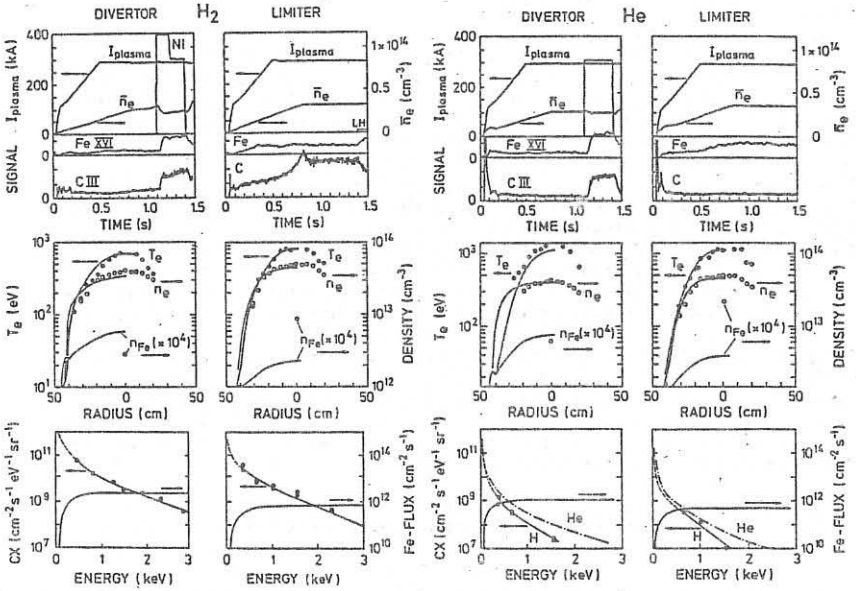


Fig. 1: Comparison of the main plasma parameters, the iron and carbon densities, the temperature and density profiles and CX fluxes for H_2 and He discharges. The iron flux from the wall calculated from CX sputtering is shown in the bottom graph integrated over the neutral particle energy. The resulting iron density profile is compared with experimental values in the middle graph.

ON THE BEHAVIOUR OF BERYLLIUM IMPURITIES IN THE PLASMA EDGE REGION OF THE TOKAMAK UNITOR

M. Bessenrodt-Weberpals, J. Hackmann, and J. Uhlenbusch
Physikalisches Institut II, Universität Düsseldorf,
D-4000 Düsseldorf, Germany

INTRODUCTION

Recently, beryllium is considered to be a promising first-wall and limiter material in fusion orientated experiments /1/. To our knowledge up to now, only two experiments have been performed to test Be as a limiter material in a tokamak /2,3/. In UNITOR the use of Be-limiters reveals an improved performance of the discharge and a reduction of the heavy metallic impurity level by approximately a factor of ten. In this contribution, the global Be release rate for UNITOR parameters is calculated taking into account sputtering by H, by Be, and by other impurities (O, C, N; Fe, Cr, Ni). Further, the spatial distribution of the different ionization states of Be is calculated using a simplified slab model.

EXPERIMENT

The experimental situation is shown in fig. 1. Two poloidal Be-limiters were exposed for a total of 1500 discharges with plasma current of 50 kA and a discharge time of 50 ms. The corresponding energy deposition on the limiters is of the order of 100 J/cm^2. After the final shut down, the limiters and a sample of the stainless steel torus wall have been removed for surface studies. The test sample of the torus wall was analyzed by AES and EMA in order to investigate the distribution of eroded limiter material on the

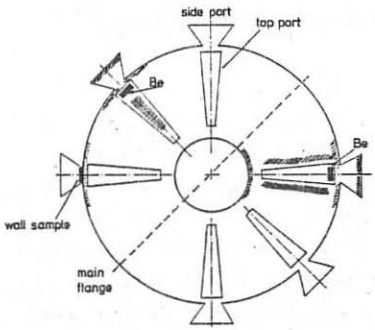


Figure 1

wall. The analysis shows a non-uniform distribution of separate islands of BeO, some of them covered with a thin layer of wall material (Fe, Cr). Together with earlier investigations /4/, which had verified that in UNITOR sputtering by O is the dominant process for metallic impurity production, this result indicates that the reduction of heavy impurities is due to effective O gettering by Be. In this contribution, the effect of Be on the plasma is studied numerically.

CALCULATIONS

To investigate the time-dependence of the release of neutral Be at the vessel wall, the global particle balance equations for H, Be, light and heavy impurities are considered. The hydrogen system is treated independently approximating the total hydrogen flux according to experiments /4/

$$Q_H(t) = Q_{Ho} \exp(-t/\tau_H) \quad \text{with} \quad Q_{Ho} = 2\times10^{21}/s \ , \ \tau_H = 10.6 \text{ ms}.$$

Be is mainly produced by self-sputtering (Y_{BeBe}), sputtering by H (Y_{HBe}), and by light impurities as C, O, and N ($Y_{lBe}=Y_{BeBe}$). Light impurities are generated by ion-induced desorption with the same rates ($Y_{Bel}=Y_{ll}=Y_{BeBe}$; $Y_{Hl}=Y_{HBe}$). Sputtering by heavy ions can be neglected at energies found in UNITOR. Hence, the balance equation takes the form

$$dN_{Be}(t)/dt = Y_{HBe}\, Q_H(t) - N_{Be}(t)/t_{Be}$$

with $t_{Be} = \tau_{Be}/(1-2Y_{BeBe})$ and τ_{Be} denoting a particle 'confinement time' of Be. The solution is given by

$$N_{Be}(t) = Y_{HBe}\, Q_{Ho} \{\exp(-t/t_{Be}) - \exp(-t/\tau_H)\}/(1/\tau_H - 1/t_{Be})$$

which reaches its maximum value at

$$t_{Be}^{Max} = \ln(t_{Be}/\tau_H) \ / \ (1/\tau_H - 1/t_{Be}) \ .$$

This time is fitted to the experimental value of 6 ms observed earlier /4/. Assuming the energy of the incoming ions to be 100 eV the distribution of Be I fits well with $\tau_{Be} = 3.0$ ms as shown in fig. 2. For comparison, the concentration of heavy impurities (Fe, Cr, Ni) is also indicated assuming equal particle confinement times of light and heavy impurities. For longer discharge times, the impurity content follows the time dependence of

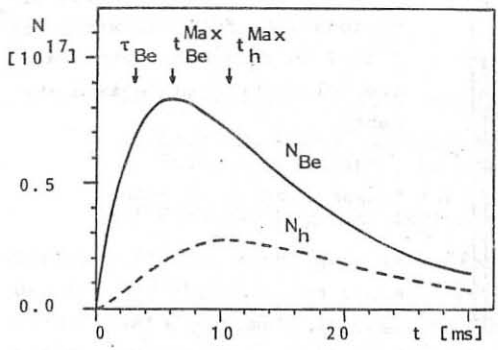


Figure 2

the hydrogen flux Q_H.

The spatial distribution of the different ionization states from Be I to fully stripped Be V is calculated with the help of one-dimensional time-independent rate equations. In our case, the dominant process is the electron ionization of Be with the rate coefficient S_q (q=1,...,4) (after /5/), whilst the recombination terms can be neglected. All particle velocities v_q (q=1,...,5) are assumed to be constant. As Be enters the plasma at the vessel wall $x = 0$ in the neutral state, the boundary conditions in this model demand $n_1(0) \neq 0$ and $n_q(0) = 0$ (q=2,...,5). This implies to normalize the densities by the incoming Be-flux $j_{Be} = n_1(0)\, v_1$ as calculated above :

$$\hat{n}_q(x) = n_q(x)\, v_q / j_{Be} \qquad (q=1,\ldots,5)$$

which fulfil $\sum_{q=1}^{5} \hat{n}_q(x) = 1$ at every position $x = a-r$ in the plasma /6/. The solution of the normalized balance equations has the form

$$\hat{n}_1(x) = \exp\{-\frac{1}{v_1}\int_0^x du\, S_1(u)\}\ ,$$

$$\hat{n}_q(x) = \frac{1}{v_{q-1}} \exp\{-\frac{1}{v_q}\int_0^x du\, S_q(u)\} \qquad ,(q=2,\ldots,4)$$

$$* \int_0^x ds\, S_{q-1}(s)\, \hat{n}_{q-1}(s) \exp\{\frac{1}{v_q}\int_0^s du\, S_q(u)\}$$

$$\hat{n}_5(x) = \frac{1}{v_4}\int_0^x ds\, S_4(s)\, \hat{n}_4(s)\ .$$

Evaluating the integrals, the radial profiles of n_e and T_e and hence S_q (q=1,...,4) are needed. Furthermore, all ions are assumed to diffuse radially inwards with the same velocity of 10 m/s, while the neutrals leave the wall with their Thompson velocity of 8 km/s. The normalized densities are shown in fig. 3. There is the characteristic exponential decay of Be I with a halfwidth of

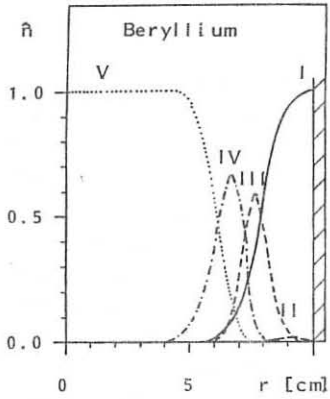


Figure 3

2 cm and the various shells of Be ions with full halfwidths of 1 to 2 cm ; beyond approx. a/2 the fully stripped Be is dominant.

SUMMARY

A global model for the transport of beryllium in the edge plasma has been presented, which together with the fit to experimental data yields the time-dependent particle source of neutral Be I at the vessel wall. Using this calculated release rate, the one-dimensional spatial distribution of the different ionization states from Be I to fully stripped Be V has been evaluated including ionization terms and inwards diffusing ions. The resulting shell structure shows that the lower ionization states of Be are rapidly run through and Be V is dominant in the plasma core.

REFERENCES

/1/ Rebut, P.H., and K.J. Dietz : Proc. 12th Symp. Fusion Technology, Jülich (1982) Vol. 1, p.85
/2/ Edmonds, P.H., P. Mioduszewski, J.B. Roberto, R.D. Watson, and M.F. Smith : J. Nucl. Mater. 128&129 (1984) 422
/3/ Hackmann, J., and J. Uhlenbusch : J. Nucl. Mater. 128&129 (1984) 418
/4/ Reinhold, G., J. Hackmann, and J. Uhlenbusch : J. Nucl. Mater. 128&129 (1984) 240
/5/ Lotz, W. : Z. Phys. 216 (1968) 241
/6/ Breton, C., C. de Michelis, and M. Mattioli : Nucl. Fusion 16 (1976) 891

PROPERTIES OF THE SOL OF T-10 INVESTIGATED BY LANGMUIR PROBES

M. Laux, H. Grote, A. Herrmann, D. Hildebrandt,
P. Pech, H.-D. Reiner, H. Wolff, G. Ziegenhagen

Academy of Sciences of the GDR, Central Institute of Electron Physics, 1086 Berlin, GDR

During different working regimes of the T-10 tokamak the ion density and the electron temperature of the SOL plasma were studied using Langmuir probes. The temporal evolution and the radial dependence as well as dependences on various discharge parameters are investigated and the following features of the SOL are observed.

In a late phase of the current rise characterized by an approximately constant loop voltage the relation $n_{SOL} \cdot T_{e,SOL}^{-1} = \text{const.}$ was found instead of $n_{SOL} \cdot T_{e,SOL}^{3/2} = \text{const}$, which was observed earlier for the stationary plateau phase /1/. Additionally the radial dependence of the SOL density during this early stage was compared with that of the plateau phase for the same inner structures and under comparable discharge conditions. An exponential radial density profile was obtained with an e-folding length $\lambda_n = 10$ mm which is about twice that of the plateau case ($\lambda_n = 6$ mm). This different behaviour suggests the influence of ionization processes. Using the very simple model of Uehara /2/ we can roughly estimate the neutral density to be $\approx 10^{19}$ m^{-3}. Therefore it seems that during the investigated early phase a SOL gas of about the chamber filling pressure is ionized.

The different temporal evolution of n_{SOL} measured at different poloidal positions is probably caused by the controlled horizontal displacement of the plasma column during the discharge. The observed relation between the density for an inner and an outer (cf. 3) Langmuir probe is in qualitative agreement with the indicated displacement of the plasma column (Fig. 1). Fig. 2 shows the plateau averaged values of n_{SOL} and $T_{e,SOL}$ measured by the outer probe versus the plateau position of the column. The observed behaviour could be understood assuming that the radial density and temperature profiles in the SOL are shifted

Fig. 1

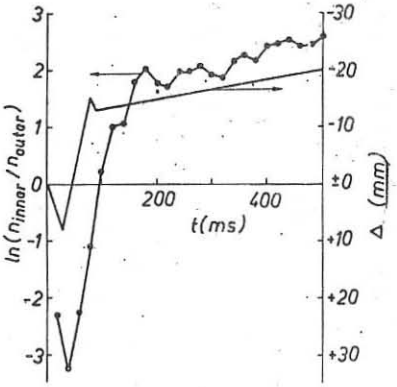


Fig. 2

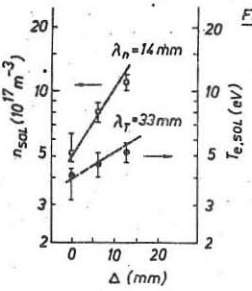
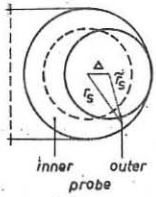


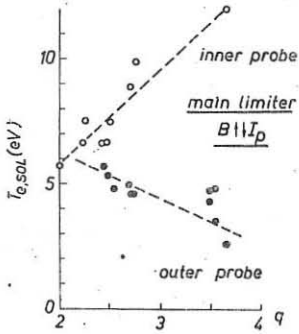
Fig. 3



together with the whole plasma column. In this case the curves can be discussed in terms of the effective radial position $\tilde{r}_s$ (Fig. 3) using the e-folding lengths λ_n and λ_T well known from earlier experiments.

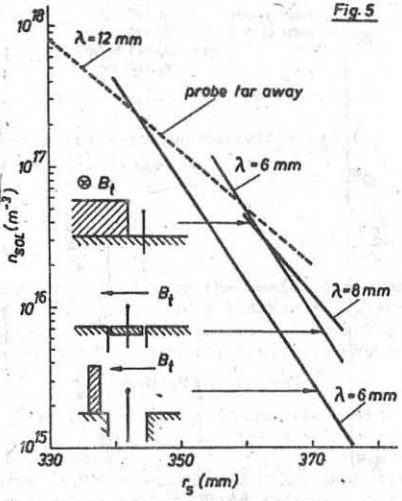
A qualitatively different influence of the safety factor q on $T_{e,SOL}$ was found for probes at different poloidal positions (Fig. 4), whereas the density does not seem to be correlated to changes of q. Further experiments revealed a simultaneous influence of the SOL structure (limiter configuration) as well as the orientation of the toroidal magnetic field on the qualitative feature of the q-dependence. This behaviour of $T_{e,SOL}$ reminds the very complex influence of SOL structure and field orientation on the anisotropic impurity fluxes measured by deposition probes in the T-10 /3/. The interpretation is not clear yet, but it seems to be obvious that drift motion or rotational transforma-

Fig. 4



tion alone cannot explain the experimental results.

The comparison of the radial profiles of the plateau averaged values of n_{SOL} and $T_{e,SOL}$ observed during different tokamak regimes demonstrates that an exponential density decay with an e-folding length of about 12 mm as well as much weaker dependence of the temperature ($\lambda_T \gtrsim 30$ mm) are rather general phenomena far away from the active main limiter. Solid surfaces (for instance the liner or a limiter) in the vicinity of the probes lead to significantly smaller decay lengths for the density (Fig. 5) independent on the orientation of the surfaces. It seems that the density reacts on the vicinity of any sink (possibly via a shortened lifetime $\tau_{\parallel}$ for the particles) and the result is a profile with a shorter decay length λ_n. This finding gives reasons for the existence of a thin (10-20 mm) near-wall region with a behaviour quite different from that of the rest of the SOL.



Langmuir single probes were used to determine plasma parameters in the pumping channel underneath the movable limiter. A relatively cold plasma ($T_e \approx 4$ eV) with a high density up to $1.5 \cdot 10^{20}$ m^{-3} could be observed. There exists a weak exponential dependence of these parameters on the distance from the limiter edge shown in Fig. 6. The decay lengths are similar for both temperature and density and are found to be in the range of the temperature decay length measured far away from the limiter (see above). The ionization of the dense neutral gas ($n_n \approx 10^{21}$ m^{-3}) observed in the limiter duct could be responsible for an enlarged λ_n. Gradients along the duct and toroidal asymmetries were not established. A peculiarity are peaks in the electron temperature during the plasma current rise. They appear at the

Fig. 6

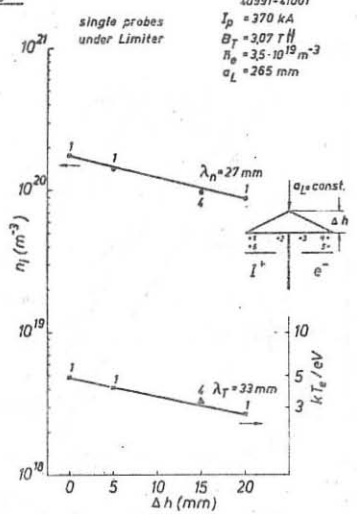
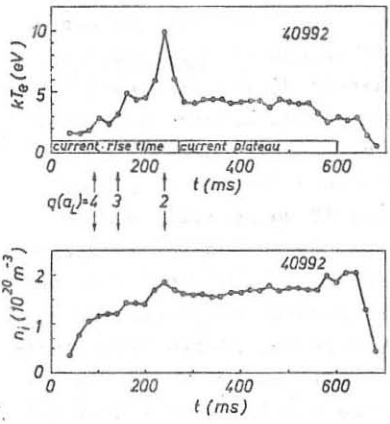


Fig. 7



moment when the safety factor $q(a_L)$ passes through rational values. An example is shown in Fig. 7. The plasma density seems to be less affected.

From a great number of Langmuir probe measurements in T-10 one can conclude that some overall features (i.e. the radial profiles) are in qualitative agreement with the simple flux-tube model and there are additional dependences of the measured values that can be explained by very simple physical properties of the SOL plasma (i.e. power balance, influence of ionization, shift of the column). But there also exists a third group of effects (like q-dependence of T_e or the influence of solid surfaces) that are in principle physically not understood yet.

Acknowledgement

The assistance of the T-10 team is gratefully acknowledged.

References

/1/ Alexander, K.F., et al., Proc. 6th Int. Conf. on Plasma Phys. Lausanne, Switzerland, 1984, Vol, II, p. 306

/2/ Uehara, K., et al., Plasma Phys. 21 (1979) 89

/3/ Wolff, H., et al., J. Nucl. Mater. 128/129 (1984) 219

EXPERIMENTAL OBSERVATIONS ON THE FT LIMITERS

C. Ferro, E. Franconi, G. Maddaluno, M. Ciotti*, A. Neri

Associazione EURATOM-ENEA sulla Fusione, Centro Ricerche Energia Frascati, C.P. 65 - 00044 Frascati, Rome, Italy

INTRODUCTION

The knowledge of the energy and particles fluxes in the boundary plasma layer is of interest for obtaining the total energy balance and for calculating the thermal loads on the limiters. This information is also necessary to estimate the impurity level due to the energy flux and for optimally design future machines.

The walls of the Frascati Tokamak (FT) (minor radius 23 cm) are protected by safety rings (radius 22.4 cm) and a main poloidal limiter which can be removed without the need to open the vacuum chamber [1]. All these items are made of stainless steel. The FT machine works routinely at high magnetic fields (between 6 T and 8 T). The average values of both iron and oxygen impurity concentration in FT discharges, as inferred from spectroscopic measurements, are reported in Table I.

TABLE I

$\bar{n}_e$ (cm^{-3})	$\bar{n}_{Fe}$ (cm^{-3})	$\bar{n}_o$ (cm^{-3})
$<5\times10^{13}$	$(0.5\div1)\times10^{11}$	2×10^{11}
$>10^{14}$	$<10^{10}$	2×10^{12}

In order to collect experimental data about energy fluxes and impurity deposition, the FT main limiter has been equipped with thermocouples and catcher-targets. They were placed in two zones of the limiter which never show large damages [2]. The positions are shown in Fig. 1.

THERMAL LOADS

The bulk temperature rise of the poloidal limiter of FT during low ($<1\cdot10^{14}cm^{-3}$) and high (up to $2.5\cdot10^{14}cm^{-3}$) density discharges was measured with chromel-alumel thermocouples brazed within two of the stainless steel mushrooms (Fig. 1).

Heat flux to the limiter was deduced by using the finite differences heat conduction code HEATING 5 [3] originally developed at Oak Ridge National Laboratory and modified to allow a radially [4] decreasing heat flux according to the well established model of exponential decay of power flowing in the scrape-off layer.

---

* Student

The thermocouples were located at the center of mushrooms head ~5mm below the surface. The output from the thermocouples was fed to transformer coupled amplifiers before input to oscilloscope and strip-chart recorder because the floating limiter can reach high potentials during the discharge [5]. The response time of the system was limited by the thickness of material below which thermocouples were buried and by electrical noise during rapid current variations, so that only at the end of the discharge significant measurements were possible. Nevertheless the temperature rise immediately after the current termination was used to have some indication about the radial distribution of the energy deposition. In fact, by code simulation, the time at which $\Delta T=\Delta Tmax/m$ $(m=2,\ldots,n)$ was found to depend on the energy scrape-off length λ_E, but not on the amount of incident power. A λ_E ranging from 0.5 to 1.5 cm was found to fit all the discharges examinated with an average value near to the lower limit, in satisfactory agreement with the value of ~1 cm as inferred from Langmuir probes [6] and molten layer thickness measurements on previous limiters [2]. Based on these λ_E values and the assumption of poloidal symmetry, a power onto the limiter ranging from 10% to at most 40% of input ohmic power was deduced, as also suggested by a simple impurity balance model [2]. Disruptive discharges were not found to cause a temperature rise higher than expected according to their duration. Because any mass loss or erosion damage was never noticed in this poloidal part of the FT limiters [2] a high surface heating only was ruled out. On the contrary during steady state high density discharges the surface temperature deduced from the bulk one reached the melting as confirmed by post-mortem analysis. A linear dependence of heat flux on bulk electron mean density was also found (Fig. 2) likewise Alcator-c results [7].

IMPURITY DEPOSITION

The Ti targets inserted under the mushroom (Fig. 1) were analyzed after 134 discharges by means of Auger Electron Spectroscopy (AES) both on the ion and on the electron side. The relative concentrations of F_e, C_r, N_i are seen to remain constant within the experimental uncertainties with a C_r-enrichment with respect to the stainless steel used in FT (AISI 316).

This enhanced Cr-deposition might be related to the depletion on Cr (and Mn) observed on the mushrooms heads by means of EDXA analysis. From the AES spectra carbon was found in the form of carbide [$(Fe, Cr, Ni)_3$ C] suggesting a deposition in a multiphase system, probably caused by high-temperature phase transformation. The total amount of iron was calculated assuming a AISI 316 SS atomic density of $8.5\cdot10^{22}$ atoms/cm^3. In Table II are reported the estimated average net deposition per discharge.

TABLE II

Fe average net deposition [atoms/cm^2 per discharge] $\cdot10^{15}$

		Ion side	Electron side
Top	$\bar{r}$ = 20.9 cm	9.17	5.23
	r = 21.1 cm	7.27	5.15
Bottom	$\bar{r}$ = 20.9 cm	2.40	9.67
	r = 21.1 cm	1.94	6.75

Experimental uncertainties does not allow a significant measure of an e-

-folding length for the Fe flux. The salient feature of these measurements is the asymmetrical deposition with respect to the equatorial plane wich is coherent with the asymmetrical damages observed on the surfaces of all FT limiters [8].

CONCLUSIONS

Power flowing to the main limiter ranges from ~ 10% to ~ 40% of the inferred input power. The energetic balance with the radiated power reveals a systematic missing power suggesting localized radiation around the limiter.

The temperature of the limiter, at the end of the discharges, increase with the density of the plasma.

The observed asymmetry in the impurity deposition as well as in the macroscopic damage could be justify on the ground of the theoretical work [9] recently carried out about the plasma flow in the shadow of a poloidal limiter.

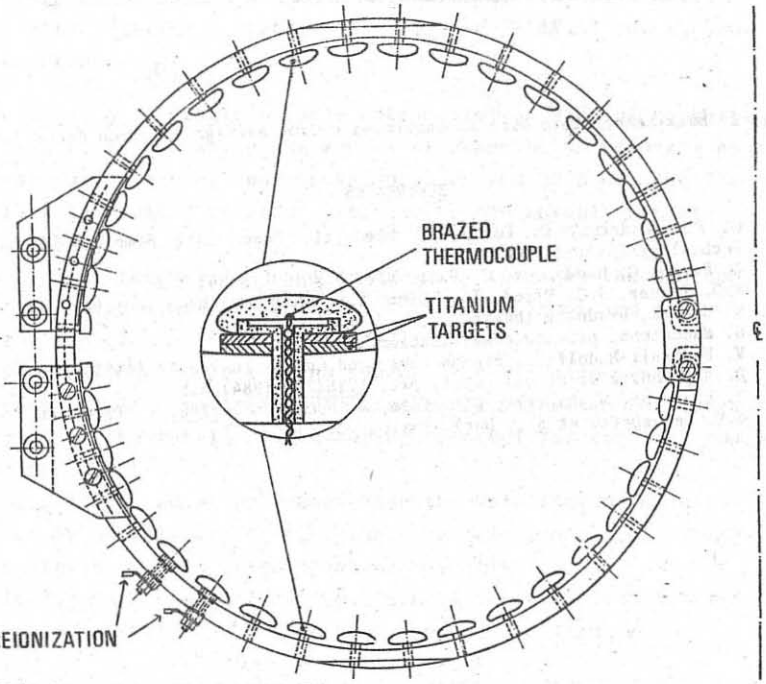


Fig. 1 Schematic view of the main poloidal FT limiter showing position of thermo couples and titanium catcher-targets.

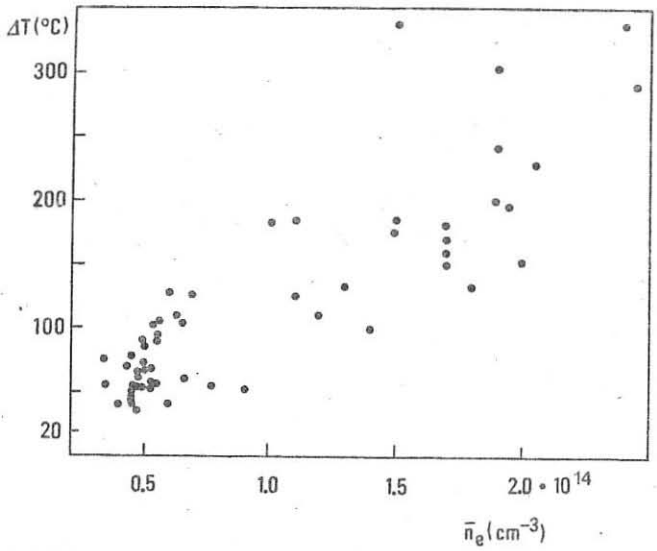


Fig. 2 Bulk temperature rise of mushrooms versus average electron density.

REFERENCES

[1] C. Alessandrini, C. Ferro, M. Samuelli, Proc. 11th Symp. on Fusion Technology (Oxford 1980)
[2] C. Ferro, G. Maddaluno, J. Nucl. Mat. 128&129 (1984) 822
[3] W.D. Turner, D.C. Elrod, I.I. Simon-Tov, ORNL/CSD/TM-15 (March 1977)
[4] M. Ciotti, Graduate thesis
[5] G. Maddaluno, private communication
[6] V. Pericoli-Ridolfini, Plasma Phys. and Contr. Fusion 27 (1985) 493
[7] B. Lipschultz et al., J. Nucl. Mat. 128&129 (1984) 555
[8] E. Franconi, M. Barteri, G.M. Ingo, J. Nucl. Mat. 128&129 (1984) 481.
[9] A.V. Nedospasov et al., Nucl. Fusion, 25 (1985) 21

LIMITER THERMOGRAPHY AND POWER BALANCE STUDIES IN THE T-10

J.Lingertat, K.F.Alexander, Ch.Grunow, K.Guenther
Akademie der Wissenschaften der DDR, Zentralinstitut für Elektronenphysik, 1086 Berlin, Hausvogteiplatz 5-7

V.M.Chicherov, S.A.Efstigneev, A.N.Vertiporokh, S.N.Zwonkov
I.V.Kurchatov Institute of Atomic Energy, Moscow, USSR

Introduction: An unsolved problem in tokamaks has been the inability to balance the energy input to the plasma with the measured losses. By investigating the dependence of one major loss channel, the power deposition onto the limiter, on discharge parameters, it should be possible to achieve a better understanding of the distribution of power flow in the various loss channels.

Experimental: A single movable bottom limiter made of graphite is used in T-10. During the series of experiments reported here it was positioned at radii between 25 cm and 32.5 cm. The fixed limiter is located in close vicinity to the movable one at r = 32.5 cm.
The limiter thermal load was measured by infrared thermography, using a AGA 750 camera. Details of the experiment and data evaluation can be found in /1/,/2/.
Power losses by radiation and charge exchange were measured at a far-from-limiter position by a wide angle bolometer and extrapolated to the total torus assuming poloidal and toroidal homogeneity.
The localized radiation losses near the main limiter were detected by a small angle bolometer, the emission of low ionization states of impurities spectroscopically /3/.
Ohmic discharges with I_p = 190...360 kA, B_t = 2.0...3.2 T and $\bar{n}_e$ = 1.9...6.6·10^{19} m^{-3} have been produced in T-10.

Results: The results are presented in terms of the quantity $\alpha = P_{lim}/(P_{in}-P_{rad})$, where P_{lim} is the power absorbed by the limiter, P_{in} is the ohmic input power ($P_{in} = I_p \cdot U$), and P_{rad} the

toroidally uniform part of bolometrically measured power loss. In all cases these quantities have been averaged over the time intervall, in which both, I_p and U were stationary.
Fig.1 shows the variation of α with the mean density $\bar{n}_e$. A step-like drop of the α-value is observed near $\bar{n}_e = 5 \cdot 10^{19}$ m^{-3}. This may be explained by assuming a cold plasma mantle to develop round the limiter. Such a phenomenon was reported from D-III /4/ and observed in a more qualitative way on T-10 /2/.
A simple model of particle balance /5/ yields the neutral density N in the edge region necessary to maintain a given plasma density $\bar{n}_e$ ($N \sim \bar{n}_e^2$). Assuming the source of recycling neutrals to be concentrated at the limiter tip, we obtain a critical density $\bar{n}_c$, for which the localized cloud of neutrals becomes opaque for ions streaming onto the limiter (self shielding of the limiter due to cx-reactions):

$$\bar{n}_c \approx \frac{1}{\Sigma} \left\{ \frac{v_i^{sol} \, \xi_i}{\pi a \, R \, D_\perp \, \xi_{cx}} \right\}^{1/3} \qquad \Sigma = \frac{\left\{ \xi_i (\xi_i + \xi_{cx}) \right\}^{1/2}}{v_i}$$

v_i^{sol} - thermal velocity of ions in the SOL, v_j - thermal velocity of ions and neutrals in the edge region, ξ_i - reaction rate for ionization, ξ_{cx} - reaction rate for charge exchange.
For our conditions we obtain $\bar{n}_c \approx 5.8 \cdot 10^{19}$ m^{-3}, which is in good agreement with the experimental findings.

The absolute α-values show that between 72 % and 94 % of the energy flowing into the SOL remains unaccounted. From the bolometer located at the limiter section we found an additional loss of about 5 % of total power, associated with line emission of carbon impurities /3/. Contrary to /6/,/7/, we did not observe a large bolometer signal peak at limiter position, which may be due to our restricted angle of view /3/.
The variation of α with the safety factor q(a) is shown in fig.2. In all experiments with $q \lesssim 2$ we found large values for α, while the peak at $q > 3$ and the 100 % at $q = 1.8$ may not be significant.
Fig.3 shows the variation of α with the plasma radius a. Two different regions can be clearly distinguished.

a > 28 cm: The effective length L, which describes the decay of α with plasma radius is about 0.8 cm. Here we usually observe deviations from the exponential law of power deposition onto the limiter. The width of this region ($\approx$4.5 cm) is in accord with results from T-11 /8/. Obviously, the fixed limiter strongly influences the power deposition onto the movable one.

a < 28 cm: The effective length L is about 6.5 cm. Here we have no distortion of the exponential power deposition profile on the movable limiter.

Conclusions: The SOL plasma in T-10 consists of at least three different regions: a near-limiter region, a near-wall region and the main part of undisturbed SOL plasma.
The parameters of the near-limiter plasma strongly depend on $\bar{n}_e$ and q(a). With $\bar{n}_e \gtrsim 5 \cdot 10^{19}$ m^{-3} and $q(a) \approx 2.5$ the limiter load is low.
Usually, between 60 % and 75 % of the input energy are missing in the power balance. With local radiation and charge exchange losses near the limiter such a deficit can not be explained. The small decay length of longitudinal energy flux observed on the limiter ($\lambda \approx 0.7$ cm /1/) prevents a significant amount of energy to reach the wall. Assuming the decay length in the undisturbed SOL region to be large, most of the missing energy should be deposited onto the wall.

References

/1/ K.Günther, et al. "Characteristics of scrape-off plasma interaction with the T-10 limiter ...", this conference
/2/ J.Lingertat, et al., Proc. 10th Int. Conf. on Plasma Phys. and Contr. Nucl. Fus. Res., London 1984, paper CN-44/A-IV-5
/3/ A.N.Vertiporokh, et al. "Power dissipation upon the limiter, radiation losses ...", this conference
/4/ D.R.Baker, et al., Nucl. Fusion 22 (1982) 807
/5/ K.F.Alexander, W.Hintze, K.Günther, submitted to Nucl. Fusion
/6/ E.R.Müller, et al., Proc. 11th Europ. Conf. on Contr. Fus. and Plasma Physics, Aachen 1983, Vol. 1,47
/7/ W.H.M.Clark, et al., Proc. 11th Europ. Conf. on Contr. Fusion and Plasma Physics, Aachen 1983, Vol. 2, 451.

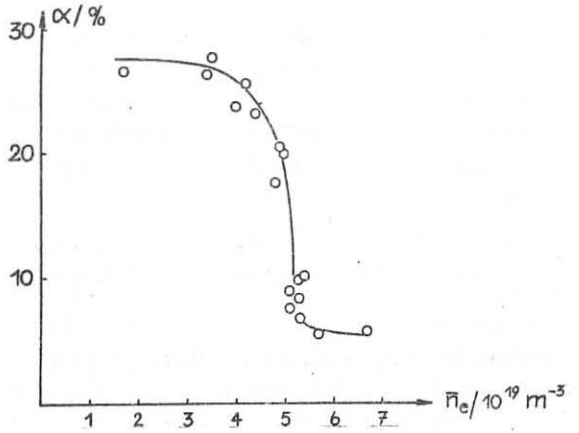


Fig.1 -value versus mean plasma density n_e for a = 28cm, q = 2.5

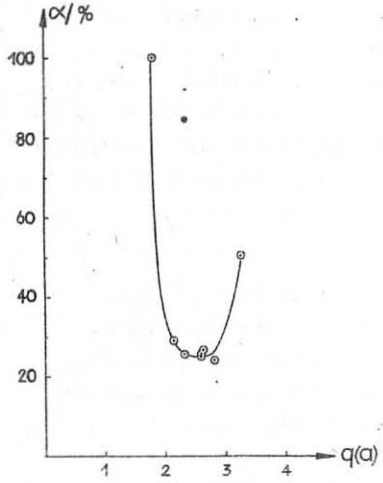


Fig.2 -value versus safety factor q(a) for a=28 cm, n_e = 4 10^{19} m^{-3}

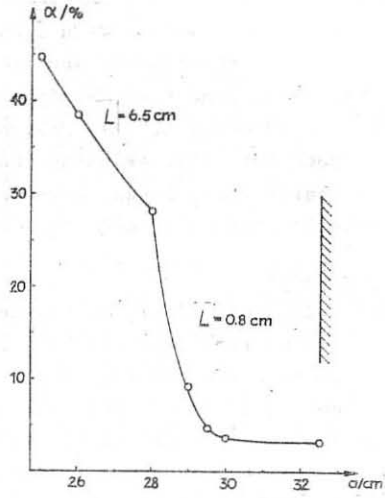


Fig.3 -value versus plasma radius a for q(a) = 2.5, n_e = 4 10^{19} m^{-3}

STUDY OF THE PLASMA INTERACTION WITH A LIMITER UNDER OHMIC HEATING IN T-10 TOKAMAK

A.N.Vertiporokh, S.A.Evstigneev, I.V.Ivanov,
Yu.S.Maksimov, K.B.Titishov, V.M.Chicherov
I.V.Kurchatov Institute of Atomic Energy, Moscow, USSR

K.Gunther, C.Crunov, W.Dreiucker, J.Lingertat
Zentralinstitut für Electronenphysic der ADW der DDR

Abstract. Experimental results on the study of impurity radiation, total radiation losses in the vicinity of a limiter, power and temperature on the limiter, the role of a limiter region in the energy balance, sources and mechanisms of contamination by impurities are given in a paper.

Introduction. The interaction between plasma and a limiter provides an enhanced influx of impurities into discharge which, affecting the plasma energy balance, results in the formation of enhanced radiation in the vicinity of the limiter [1]. Not only the value and profile of radiation losses in the toroidal direction [2], necessary for the plasma energy balance and plasma transport studies, but the factors determining the processes of impurity influx by impurities and their radiation from the limiter region are of importance in this case.

Experiment. The plasma-limiter interaction was studied on T-10 under ohmic heating. The main parameters of that regime were: $B = 15-30$ kOe, $I_p = 150-450$ kA, $a_L = 25-32.5$ cm, $q(a_L) = 1.7-8$, $\bar{n}_e = 2-5 \times 10^{13}$ cm^{-3}, $T_e(o) = 0.7-2$ keV. The movable rail limiter of graphite (30 x 5.5 x 10 cm) was introduced into the chamber through the bottom of the torus. An infra-red camera, AGA-750 type, detector of radiation losses, scanning in the toroidal direction, and the monochromator in the visible and UV regions were installed in the vicinity of the limiter, in addition to the standard diagnostic set used on T-10.

Results. The experiments have shown the enhanced radiation of the lines of light impurities and the enhanced radiation losses in the vicinity of the limiter. The magnitude and the behaviour

in time of these parameters mainly depend on the plasma current, Ip, and on a radius of the movable limiter, a_L. Comparison between the radiation losses in the vicinity of the limiter, P_{RL}, and the radiation of low-ionized impurity lines, I_L, has shown that P_{RL} and $I_L(C^{+2})$ have the best correlation in time and space (Fig.1). This shows that the main contribution into the radiation losses in the vicinity of the limiter is made by the low-ionized lines of carbon. The radiation losses, strongly-localized in the toroidal direction ($\Delta Z \simeq 6$-8 cm) and exceeding a few-times the specific radiation losses at a distance from the limiter, have been observed in the vicinity of the limiter (Fig.2).

In spite of high specific losses connected with the radiation near the limiter, their role in the total radiation losses is not great and does not exceed 20%. The behaviour in time of the plasma energy loss fractions due to radiation, P_{RO}, due to radiation in the vicinity of the limiter, P_{RL}, and the power absorbed by the limiter, P_L, in time are shown in Fig.3. The total measured energy losses are usually equal to 30-50% of the Ohmic power, that shows the presence of additional losses due to enhanced transfer in the scrape-off layer.

Discussion. Studies of radiation losses and carbon influx from the limiter parameters revealing the intensity of plasma-limiter interaction have shown that the safety factor q is the main factor determining this interaction (Fig.4). Approaching $q(a_L) \simeq 2$, a steep rise in the power incident on the limiter and in the radiation from that region is observed. In this case, the ratio P_{RL}/P_{RO} can be equal to 10-20. The critical value of q_c is varied in a range $q_c = 1.7$-2.2, and it depends on I_p and on the content of light impurities.

The comparison between P_{RL}, the intensities of carbon lines and the parameters characterizing the thermal loads on the limiter (temperature, power, scrape-off layer) has shown that the maximum temperature of the limiter surface is the most important parameter determining the plasma contamination by impurities from the limiter (Fig.5). When $T_L > 1200^{\circ}C$, a steep rise in the radiation near the limiter is observed, that

is in a good agreement with the temperature dependence of the chemical sputtering of carbon, K_c [3]. This allows to assume this mechanism to be the main technique of the plasma contamination by impurities from the limiter in our experiments.

One should note that, in spite of the fact that the limiter can be a strong local source of carbon at $q \simeq 2$ and $T_L \simeq 1500$–$2000^{\circ}C$, the radiation losses and the content of carbon in plasma rise insignificantly in comparison with weak regimes, i.e. the chamber wall, not the limiter, can provide the main atomic flux of carbon into plasma.

Conclusions. The enhanced radiation losses in the vicinity of the limiter, related to the radiation of low-ionized ions of carbon, are observed. The maximum radiation from the limiter zone 3-15-times exceeds that at a distance from it. A width of the radiation loss profile in the toroidal direction is less than 10 cm.

The magnitude of additional radiation losses in the limiter region is 5-20% of the total radiation losses, and it does not exceed 5% of the Ohmic power, the total measured losses do not exceed 50%.

The main factor determining the processes of interaction between plasma and the limiter is safety factor ($q_c \simeq 2$). The parameter affecting the intensity of contamination by impurities is the maximum temperature of the limiter, the possible mechanism of contamination is the chemical sputtering.

Figure captions.

Fig.1. Specific radiation losses and the intensities of impurity lines in the vicinity of the limiter (L) and at a distance from it (0) in time.

Fig.2. Profiles of radiation losses in the toroidal direction for different instants of time.

Fig.3. Ratios between the radiation losses, P_{RO}, radiation losses in the vicinity of the limiter, P_{RL}, the power incident on the limiter, P_L, and the ohmic power P_{OH} during the discharge.

Fig.4. Dependence of the ratio between the radiation losses in the vicinity of the limiter and the radiation losses at a

distance from it on q.

Fig.5. Radiation from the limiter area vs. maximum temperature of its surface. K_c is the coefficient of chemical sputtering for graphite [3].

References.

1. A.N.Vertiporokh et al. Fizika plasmy, 1980, 6, 14.
2. E.R.Muller et al. Proc. 11th Europ. Conf. on Contr. Fusion and Plasma Phys. Aachen, 1983, 1, 47.
3. J.Roth et al. Proc. 5th Int. Conf. on Plasma Surface Interact. in Contr. Fus. Dev., Gatlingburg, 1982.

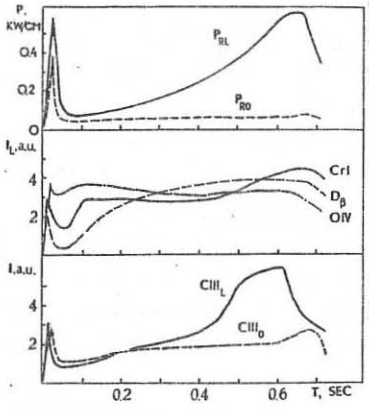


FIG.1

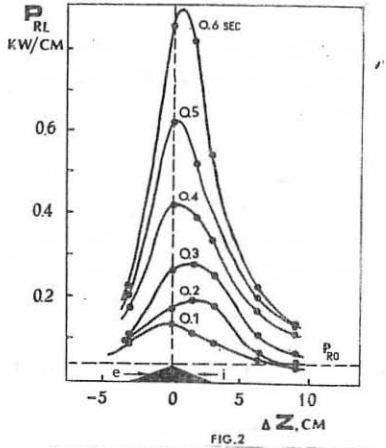


FIG.2

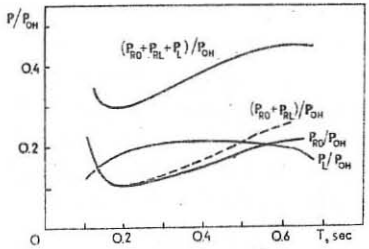


FIG.3

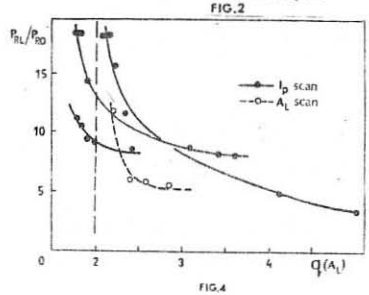


FIG.4

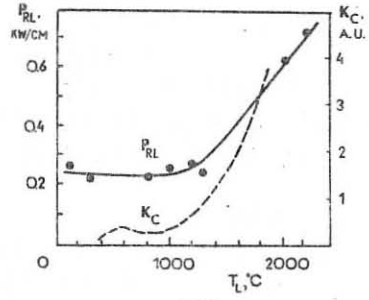


FIG.5

CHARACTERISTICS OF SCRAPE-OFF PLASMA INTERACTION WITH THE T-10 LIMITER STUDIED BY INFRA-RED THERMOGRAPHY

K. GÜNTHER, C. GRUNOW, J. LINGERTAT

Akademie der Wissenschaften der DDR, Zentralinstitut für Elektronenphysik, Berlin, German Democratic Republic

V.M. CHICHEROV, S.A. EFSTIGNEEV, S.N. ZWONKOV

I.V. Kurchatov Institute of Atomic Energy, Moscow, USSR

This paper in connection with /3/ reports results of experiments with an AGA 750 infra-red camera. It is a continuation of work described in /1, 2/, where details of the techniques used can be found. Essential differences are: symmetric form of the limiter ('span roof' surface instead of 'lean-to roof' used before) and better spatial resolution (fig. 1); variation of plasma radius a.

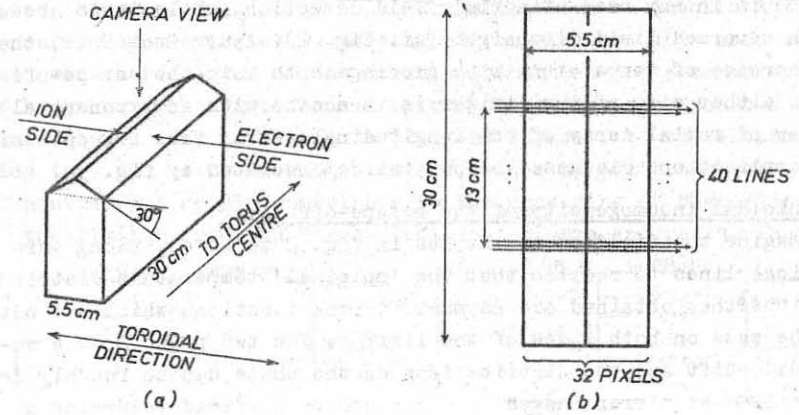


FIG. 1. (a) Form and location of the T-10 movable carbon limiter. (b) Structure of infra-red image of the limiter

Main features of the limiter surface temperature field

In general the temperature distributions (fig. 2) display the essential structure of the scrape-off layer as intersected by a rail limiter of the given form (limiter ridge rounded). The maximum temperatures reached show a wide range of variation (100 °C

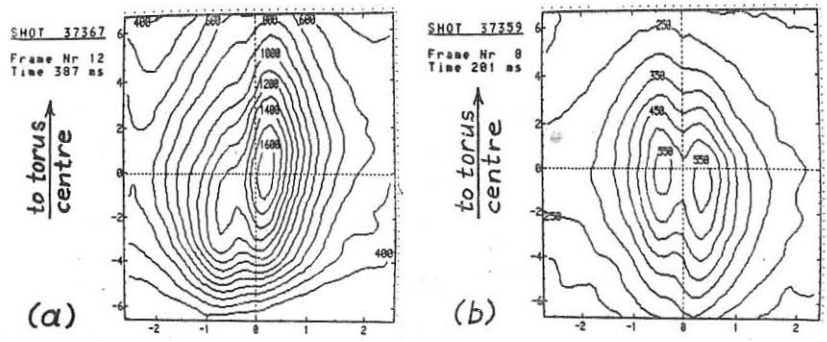


FIG. 2. Typical field of isothermes (°C) on the limiter surface at a = 25 cm for (a) normal ($B_t \downarrow\uparrow I_p$) and (b) reversed ($B_t \uparrow\uparrow I_p$) field. Crossing dotted lines indicate the middle of limiter. Axes in cm. Outside dots indicate lines and pixels.

up to >2000 °C) in dependence on the discharge parameters. For details (in terms of power flux to the limiter) see /3/.

There is no obvious explanation for the narrow peak on the electron side near the top of the limiter. For a $\lesssim$ 28 cm this peak occurs in any case of normal field direction, while it is absent in reversed field discharges (cf. fig. 2). Apart from this, the decrease of temperature with growing depth into the scrape-off on either side of the limiter is in accord with an exponential law of radial decay of the longitudinal energy flux (except for complications discussed below), as demonstrated by fig. 4a.

Poloidal inhomogeneity of the scrape-off layer

Imagine the field of isothermes in fig. 2 to be cut along vertical lines to realize that the 'poloidal' temperature distributions thus obtained are asymmetric peak functions which are not the same on both sides of the limiter. The two peaks show a mutual shift and the distributions on the whole can be roughly described as mirror images of one another. B_t-field inversion always changes the sign of this asymmetry. The effect displays a poloidal inhomogeneity of the scrape-off whose origin is likely to be the rail limiter itself (scrape-off composed of regions with open field lines differing in length). An observed influence of the safety factor q(a) corroborates this hypothesis: there is no appreciable asymmetry of this kind for q-values near 2, 2.5, 3, and for larger ones.

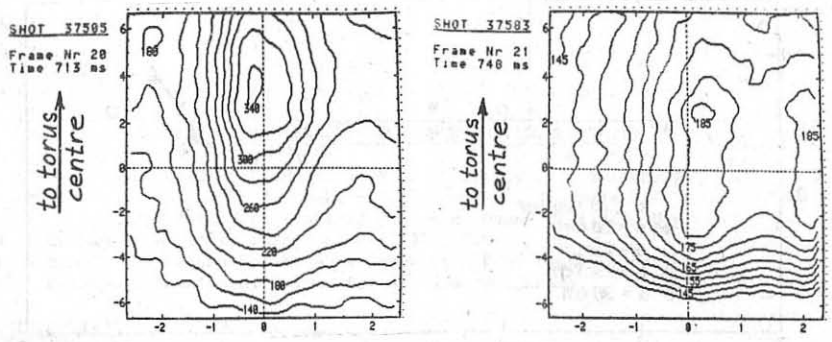


FIG. 3. Temperature distributions (°C) distorted on the electron side (a = 29 cm). See also caption of fig. 2.

Asymmetry between ion and electron sides

The decrease of temperature along the 'hottest lines' on both sides of the limiter (toroidal direction) shows good symmetry only for $a \leq 28$ cm. For $a > 28$ cm, however, the decay on the electron side typically flattens out and loses its exponential character (see fig. 3 and fig. 4b). This effect can be described as a nearly homogeneous extra heating of the electron side associated with a reduction of the normal exponential-decay component of heating. This may be caused by recycling neutrals from the fixed carbon ring limiter (r = 32.5 cm) adjacent to the electron side ($\sim$1 cm) of the movable limiter, since an additional cloud of neutral gas should contribute to the screening of that side of the limiter from the direct influx of plasma and redistribute

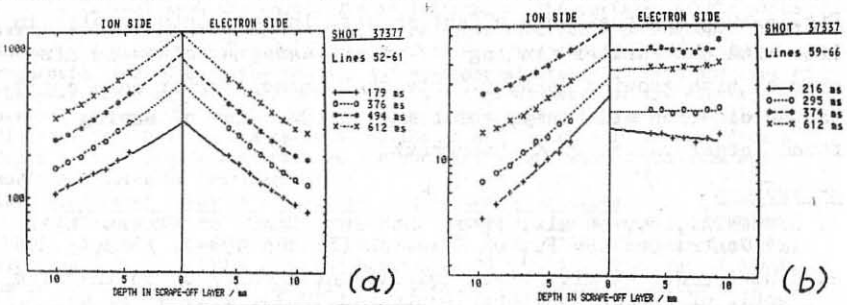


FIG. 4. Increment of temperature ($\Delta T/°C$) since beginning of discharge as a function of (r-a)/mm (ΔT values taken from the lines of maximum temperature). (a) Normal case of exponential decay (a = 28 cm). (b) Extra heat on electron side (a = 29.5 cm).

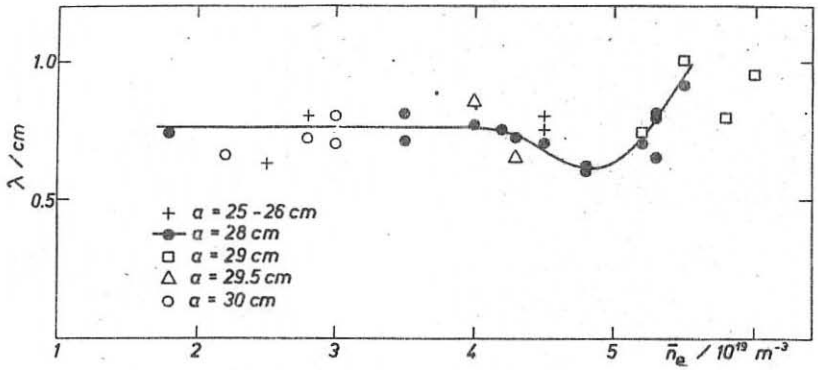


FIG. 5. Radial decay length λ (ion side only) in dependence on the line-averaged plasma density for different minor radii a.

the corresponding energy by charge exchange and radiation. Another explanation is a possible asymmetry in gas puffing (performed just through this limiter port), which would then demonstrate that the limiter could be protected by due gas puffing.

Radial decay length of energy flux

In /3/ it is argued, based on the finding that the percentage of power loss absorbed by the limiter falls steeply when the density $\bar{n}_e$ grows above 4.5×10^{19} m^{-3}, that a local 'cold gas blanket' screens the limiter at high density. If so, this should be associated with an increase of the effective decay length. This question can be reasonably studied only for the ion side where the exponential form of decay is found in any case (cf. fig. 4). Fig. 5 suggests that this effect exists, indeed. This is also in line with the earlier finding /1/ of increased λ values in discharges with growing density. Note that these earlier data apply to the electron side only, which may be the cause of having found larger values of λ throughout.

References

1. LINGERTAT, J., et al., Proc. 10th Int. Conf. on Plasma Phys. and Contr. Nuclear Fusion Research (London 1984), 1985, p.265
2. GÜNTHER, K., et al., Proc. 3rd All-Union Conf. on Engineering Probl. of Fusion Reactors (Leningrad 1984), Vol. 4, p. 86
3. LINGERTAT, J., et al., "Power Balance Studies in the T-10", this conference

IMPURITY FLUXES IN THE BOUNDARY LAYER OF JET

J.P. Coad, G.M. McCracken*, S.K. Erents*, J. Ehrenberg+, L. de Kock, P.C. Stangeby*+, T. Tagle,
JET Joint Undertaking, Abingdon, Oxon. OX14 3EA, U.K.
* Culham Laboratory, Abingdon, OX14 3DB, U.K.
\+ M.P.I. für Plasmaphysik, 8046 Garching bei München, W. Germany.
*+ Aerospace Institute, University of Toronto, Canada.

INTRODUCTION

Impurity elements are observed in the JET plasma, typically at 1 to 4% for light elements (O and C) and up to 0.2% for medium weight elements (such as Cl and Ni) leading to Z_{eff} values between 2 and 5 for most discharge conditions. For densities above $3\times10^{19}\,m^{-3}$ power is radiated from the outer regions by O and C and the contribution of metals can be neglected.

Surface analysis of the limiter tiles after operating has shown a certain spatial distribution[1] indicating migration from the wall to the limiter and erosion and redeposition during plasma discharges. However, a post-mortem analysis only gives an integrated picture of very complex sequences of operation. The information from the limiter has been supplemented by the use of collector probes which were exposed to different types of cleaning and tokamak discharges to show how these types of operation affect the impurity production. The measurements were carried out using the vertical probe drive[2] which normally operates as a Langmuir probe.

EXPERIMENTAL

(a) Method

The probe is mounted vertically near the top of the torus on a long bellows as shown in Figure 1. When operating in tokamak discharges the probe head can be inserted to within 1.5 m of the midplane, and is preset at the required distance from the predicted last closed surface. Figure 1 shows that the head can be covered over with a cap which carries small samples of various materials to act as collectors for subsequent surface analysis: this device has been used to monitor carbonisation of the vessel (see below).

On removal from the torus, the collectors, or the surfaces of the probe assembly itself, have been analysed using Auger Electron Spectroscopy (AES), Rutherford Backscattering (RBS) and Nuclear Reaction Analysis (NRA). Spatial resolution employed in the RBS and NRA was approximately 1mm (the diameter of the particle beam) and in AES was about 5μm (the diameter of the electron beam). Information on the depth distribution of the elements can be gleaned directly from RBS and NRA spectra, whilst in AES (which only samples from a depth of 1 to 2nm) depth profiles are obtained by successive analysis and surface erosion by ion bombardment.

(b) Results of Exposure to cleaning and tokamak operations

The probe has been exposed to (i) 70 hours of glow discharge cleaning (GDC) (2A at 380 V in 10^{-3} m bar of H_2), (ii) 2800 pulses of pulse discharge cleaning (PDC) (of 150 m secs and peaking at 50 KA, plus 30 pulses of ∿ 600 msecs peaking at 250 KA), and (iii) 60 tokamak discharges in September 1984. The results of RBS analysis are shown in the table below, and compared with graphite samples from the limiter and to long-term samples (LTS) from the wall.

	GDC	PDC	Tokamak Discharges	Integrated deposit Limiters	LTS
Ion Fluence m^{-2}	1.6×10^{22}	1.2×10^{23}*	-	-	
Time exposed	70 hrs	2800 pulses	~60 discharges	March - September 1984	
Ni+Cr(atoms m^{-2})	4×10^{19}	2.8×10^{21}	$0.8\text{-}1.2\times10^{21}$	3.5×10^{21}	$10^{21}\text{-}10^{22}$
Heavy species Z > 70			4×10^{19}	?	?
O (atoms m^{-2})	1×10^{20}	3×10^{20}	?	5×10^{20}	?

* From H_α at the wall.

Following the tokamak discharges (in deuterium) the deuterium content of the surface was also measured, as well as the carbon on the tungsten probe elements. The carbon on the elements was 5-8 x 10^{22} atoms m^{-2}, whilst the D was ~3 x 10^{22} on the graphite body of the probe.

(c) Carbonisation of the JET vessel

The JET vessel was 'carbonised' on occasions near the end of the 1984 operational period, by adding 3% methane to the usual GDC discharges (in hydrogen), and the impurity levels before and after treatment were monitored by VUV broadband spectroscopy.[3] Following 'carbonisation' metallic impurities such as nickel were typically reduced immediately by a factor of 5. Oxygen was reduced from 1.7 to 0.7% for reference discharges (2MA plasma current at an electron density of 2 x $10^{19}m^{-3}$) and to ~ 1% from perhaps as high as 4% for high density discharges (~ 3MA, ~ 3 x $10^{19}m^{-3}$) and chlorine was reduced by similar factors. Carbon levels increased slightly for reference discharges and decreased slightly for high density discharges. After 'carbonisation' the plasma power loss mechanisms changed markedly, with much more power going to the limiters.

The 'carbonisation' thus significantly improved the impurity situation. During the 1985 programme, the 'carbonisation' has been monitored using the surface probe, samples of Si, Ni and inconel being exposed on five occasions. Since deuterium plasmas have been used in the 1985 programme, deuterium has replaced hydrogen as the carrier gas, and the methane levels employed are either 2.15 or 12%: the wall temperature has also increased from 250 to 300°C. Figure 2 shows profiles for oxygen and carbon in inconel samples (a) as received, without any exposure in the torus, (b) after 8 hours GDC 'carbonisation' at 4A and 380V in 2.15% CH_4, and (c) after a similar exposure in 12% CH_4. For comparison (d) shows the carbon profile in nickel after 8 hours in 2.15% CH_4, and (e) shows the composition of an inconel long-term sample exposed throughout the 1984 programme. Note that the 'carbonisation' does not always produce a layer of carbon over the surface and in any case is certainly not uniform over the JET vessel due to the positioning of the discharge electrodes. Basically the treatment removes the surface oxide and carburizes the near-surface region. Tokamak operation following carbonisation is difficult for several pulses due to outgassing from the walls.

DISCUSSION

GDC and PDC each cause large amounts of metal and oxygen to move around the vessel, and some oxygen is removed from the torus by reaction to form H_2O

and CO. Nevertheless the oxygen and metal concentrations observed on the probe after the "cleaning" are also likely to arise at the limiters. They are a significant part of the equilibrium concentrations which are observed after tokamak discharges (and which clearly are soon established in the boundary layer as seen on the probe).

Similar deuterium concentrations were found on the probe after tokamak discharges to those on the limiter [1]. The carbon concentration was a factor of 3-4 greater than the deuterium. Although some of the carbon may have been displaced locally from the body of the probe, it shows that co-deposition of deuterium and carbon is the main mechanism for deuterium incorporation with important implications for recycling calculations, and eventually for the tritium inventory.

The 'carbonisation', is seen to have a marked effect on the oxygen level on the surface, and whilst significant carbon penetrates a clean inconel sample, comparison between (b) and (e) in Figure 2 suggests the carbon level on the actual wall is unlikely to be significantly affected by the process.

What happens on the limiter during carbonisation to dramatically change subsequent tokamak operation? The majority of the surface is already carbon, and the metallic deposits on it are probably also thoroughly mixed with carbon: thus the carbon content of the surface is probably little changed. However, the oxygen concentration on the surface should have been reduced and calculations of sputtering rates based on precarbonisation discharges suggest that much of the carbon entering the discharge results from sputtering by oxygen.

The combination of the lower oxygen level and the consequential reduction in sputtered carbon then leads to the immediate reduction in radiated power and increased limiter temperature observed. However, the total carbon level seen by VUV does not fall significantly, which suggests another removal mechanism for carbon from the limiter becomes significant at these high fluxes: it cannot be normal chemical sputtering as the correct behaviour with limiter temperature is not observed. The benefits of 'carbonisation' last for many tens of discharges, which is most unlikely to be due to an overlayer of carbon on the limiters (which might be ~50 monolayers thick) due to the rate of sputtering and redeposition on the surface. However, the immediate increase in limiter temperature (from $\lesssim$ 500°C to ~1500°C) due to altered sputtering coefficient caused directly by the carbonisation could cause evaporation from, or diffusion into, the limiters of the metallic impurities, resulting in medium to long-term benefits.

CONCLUSIONS

Probe measurements, allied to limiter and wall analysis and spectroscopy show that GDC and PDC cause significant contamination of the limiters without significant removal of the oxygen.

'Carbonisation' does reduce oxygen from surfaces in the torus and this may be the cause of its beneficial effect in JET in 1984, when carbon overlayers were probably not produced. (However, if carbon overlayers can be produced they might well produce further benefits).

Tokamak discharges in JET seem to produce similar levels of impurities on all parts of the torus (~10^{21} atoms m^{-2} for nickel) suggesting some form of equilibrium. Deuterium levels also reach a uniform value of ~3 x 10^{22} atoms m^{-2} [1] due to codeposition with carbon, except where significant heating occurs.

REFERENCES

(1) J. Ehrenberg et al - this conference
(2) P. Stangeby et al - this conference
(3) K. Behringer et al - JET - P(85)08

FIGURE 1

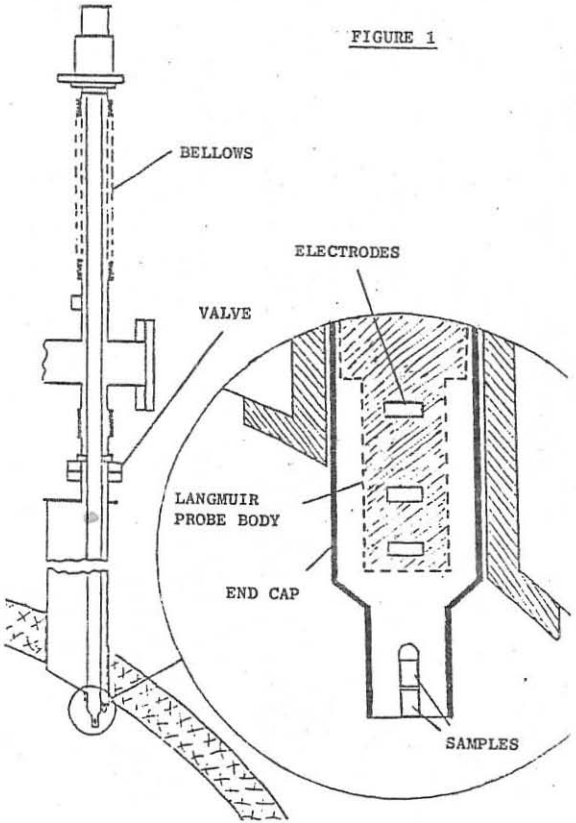
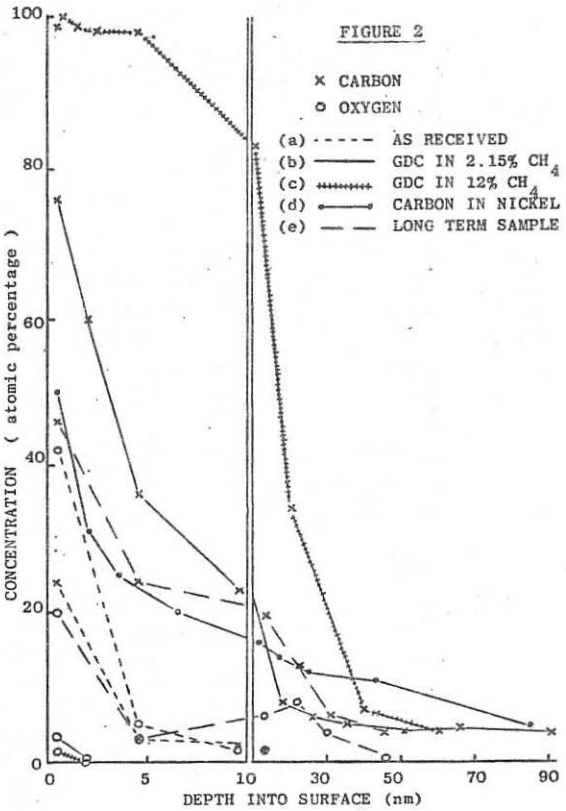


FIGURE 2



Erosion and Redeposition of Wall and Limiter Material in JET

J Ehrenberg*, R Behrisch*, P Martinelli*, H Kukral*,
G M McCracken°, J P Coad, L de Kock

JET Joint Undertaking, Abingdon, Oxon, OX14 3EA, UK
*Max-Planck - Institut für Plasmaphysik, 8046 Garching bei Munchen, FRG
°Culham Laboratory, Abingdon, OX14 3DB, UK

I Introduction

Study of walls and limiters of plasma machines by means of surface analysis techniques provides valuable information for the understanding of the causes of impurity fluxes into the plasma which is one of the most important problems in today's fusion research. Therefore, surface analyses of JET graphite limiters have been performed /1,2,3,/ after the experimental periods in 1983 as well as in 1984. In addition graphite and metal long term samples (LTS) have been analysed. They were uniformly distributed over the vessel wall and placed well in the shadow of the bellow shields . They have been exposed to all 1984 discharges, in order to monitor effective erosion and redeposition of wall material in an extended run of the machine.

II Experimental techniques

Quantitative surface analyses have been performed by means of two accelerator based techniques, namely Proton Induced X-Ray Emission (PIXE) analysis with 1.5 MeV protons and Rutherford Backscattering Spectrometry (RBS) with 2.5 MeV ^{4}He -ions. PIXE detects metallic contaminants up to depths of several µm below the surface, whereas RBS is most sensitive in more shallow regions ($\lesssim$400nm).

III Analysis Results and Discussion

All deposits found either on the limiter or on the LTS must be regarded as nett deposition, as these surfaces were also subject to erosion.

Limiters.- Fig.1 shows the toroidal distributions of metallic deposits on the 1983 and 1984 limiters as measured in both cases near the plasma midplane position. The most abundant elements are the constituents of the main wall material (Inconel 600) present in their correct ratios on the 1983 limiter and with deviations from this on the 1984 limiter. The other elements are trace elements in either inconel or carbon and have also been detected on the 1984 limiter. Not shown is oxygen, which is present with more than 10^{20}atoms/m^2. Mo was introduced into JET by an accidental contamination of the graphite limiters during manufacture. Contamination with wall materials (Ni,Fe,Cr) occurs during glow- and pulse-discharge cleaning runs [4] as well as in plasma disruptions or by runaway electrons where high power loads may hit the wall causing melting and evaporation. During normal tokamak discharges wall erosion by charge exchange neutrals may also contribute, whereas erosion by hydrogen ions may be negligable because of the low energies involved/5/. However, wall erosion by impurity impact, such as by O, C or Ni atoms cannot be excluded. Metal deposition on the limiters was found to have three different forms: firstly, between about 100mm and 350mm deposition on the centre tile (tile 4) of both limiters is mainly in the form of atomic layers,

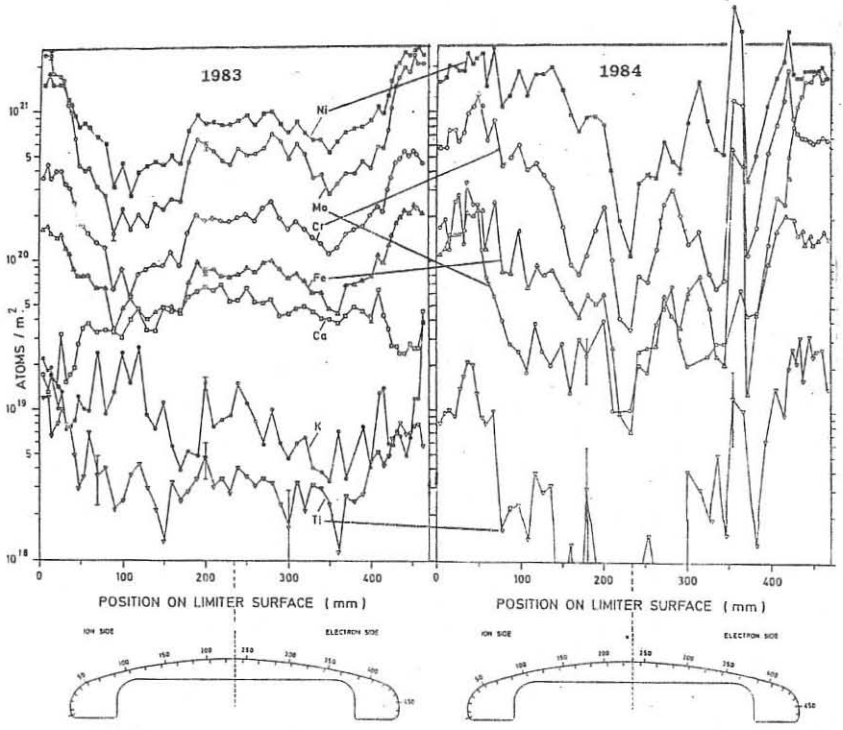


Fig. 1 Toroidal distribution of metallic contaminants on two JET graphite limiter tiles (plasma midplane) from two experimental periods.

secondly the side edges on the '83 limiter are contaminated with small metal droplets having diameters in the range of μm, and finally metal splashes of about 100 μm in diameter are present on both limiters but are much less frequent than the small droplets.

The zones on either side of the centre of the tile where the layer deposition is found correspond to the areas of plasma contact (and thus greatest heating) on the tile. The areas correlate with the "footprints" on the limiter seen by recycling light at λ = 900nm by means of a CCD video camera /6/: Maxima of intensities are in the regions 100 mm to 200 mm and 250 mm to 350 mm defined in Figure 1. Here, erosion may be larger than on more remote locations such as the limiter side edges.

The mechanism of droplet formation on the limiter side edges is not yet understood. However, they may constitute an effective source for metal erosion by evaporation as they might have poor thermal contact to the surrounding material.

During 1984 the limiter was exposed to about 400 discharges, with maximum surface temperatures towards the end of this period of 1800°C, whereas in 1983 there were only 200 discharges and the temperature was always <650°C. As the limiter is the only source of molybdenum, much more is likely to have been removed during 1984 than in 1983, as is confirmed in Fig.1. However the Ni concentrations are comparable in the two cases, with a tendency for greater Ni levels in the zones of high heat load in 1984.

Careful examination of the deposits by RBS and PIXE/7/ has shown that the Ni on the 1984 limiter is distributed to larger depths in the graphite than in the 1983 limiter. This would be expected due to the higher temperatures in that period (particularly after carbonisation of the vessel in Sept. 1984 - see reference 4). Thus, Ni is reduced at the very surface and has diffused deeper into the bulk and subsequently is less accessible for plasma erosion. This might have contributed to the conditioning of the '84 limiter.

Long term samples (LTS)

Examination of the inconel deposits on carbon LTS (Fig.2) revealed the following general trend in the distribution around the JET vessel: differences of deposited amounts are large in the poloidal direction whereas toroidally the distribution is more uniform. At the inside wall, the large deposits correlate with visible wall damage by gross melting which is also strongest there. A source-sink correlation is also observed on those LTS which have been placed closest to the Ni limiters which were retracted 9 cm behind the graphite limiters at the outer vessel wall. There, the ratio [Cr]/[Ni] (Fig.2) shows an enrichment of Ni compared to every other position. In addition, Mo was found predominantly on the outer wall samples which have been closest to the graphite limiters. From the Mo distribution on the limiter, it can be assumed that Mo erosion takes place predominantly during plasma discharges (see also Fig.1).

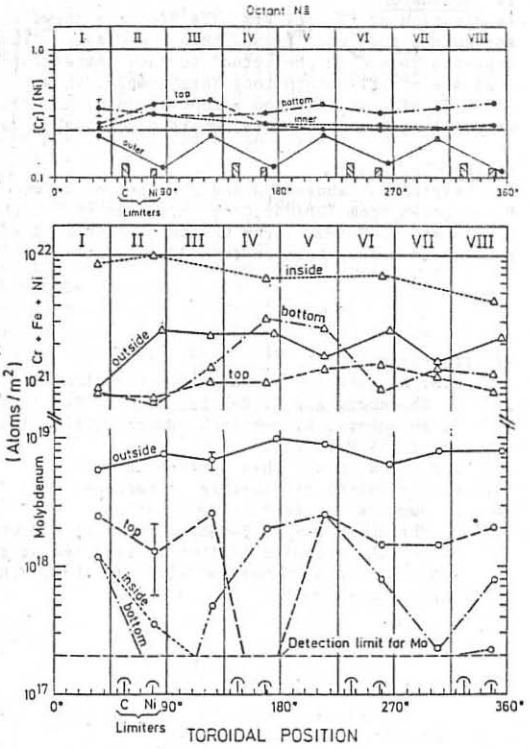


Fig. 2 Toroidal distribution of metallic contaminants as found on carbon long term samples which have been distributed around the JET vessel wall. Top, etc. denotes the position in the vessel.

However, redeposition did not occur uniformly over the torus, but is concentrated on the outer wall at the midplane. Mo from the carbon limiters appears to travel further toroidally than Ni from the Ni limiters, since the latter shows an immediate response on those LTS which have been positioned close to the Ni limiters (see the Cr:Ni ratio in Fig.2). This may reflect the different distances of the respective sources from the scrape-off layer: as stated above the Ni-limiter was retracted by ∿9cm behind the leading edge of the C-limiter. Thus the ionisation of eroded Mo is more likely than the ionisation of Ni from the Ni-limiters, and so transport of Mo would be more affected by the plasma and the magnetic field, resulting in a larger fraction of Ni being deposited as neutrals at wall positions close to this particular source.

In general it is believed that wall erosion may affect the plasma directly but also contaminates limiters with wall material thus partially losing the advantage of the carbon limiters being a low-Z material.

IV Conclusions

Examination of the JET graphite limiters shows that they constitute an important source for metal fluxes into the plasma. The amounts and distributions of deposits depend on the actual surface temperature which has been reached. Analyses of JET carbon Long Term Samples show a close correlation between metal erosion sources and redeposition sinks. Toroidally redeposition of wall material is rather uniform, whereas poloidally large differences exist.

V Acknowledgement

For helpful collaboration and discussions we would like to thank:
P. Børgesen from IPP/Garching, M. Braun and B. Emmoth from AFI Stockholm, K. Erents and D. Goodall from Culham Laboratories and C. Lowry, P.C. Stangeby, P.E. Stott and D. Summers from JET.

VI References

/1/ G.M. McCracken - private communication
/2/ J. Ehrenberg and R. Behrish IPP-JET Report No.23, May 1984
/3/ J. Ehrenberg, R. Behrisch, P. Martinelli and H. Kukral IPP-JET Report 29 May 1985.
/4/ J.P. Coad et al, this conference.
/5/ P.C. Stangeby et al, this conference.
/6/ D. Summers - private communication.
/7/ J. Ehrenberg and P. Børgesen "Effective Depth Distribution of Ni on the JET graphite limiter". presented at the 7.Int.Conf. ION BEAM ANALYSIS Berlin 7-12 July 1985, F.R.G., to be published in Nucl. Instr. Meth.B

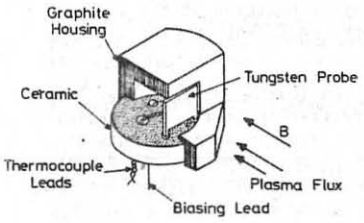
Density, Temperature and Power Measurements in the JET Edge Plasma using Heat Flux/Langmuir Probes

P.C. Stangeby+, S.K. Erents*, J.A. Tagle, G.M. McCracken*, L. de Kock
JET Joint Undertaking, Abingdon, OX14 3EA, U.K.

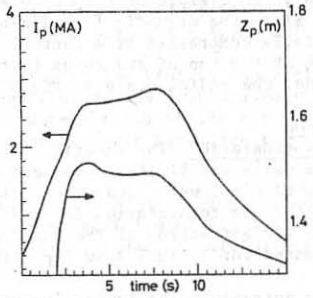
Introduction

The properties of the edge plasma in JET have been measured for ohmic discharges, with plasma currents Ip = 1-4MA, B_T = 2.6 - 3.4T, using a probe consisting of four combination Heat Flux/ Langmuir detection elements. The individual tungsten elements are as shown in Fig 1. The operation and interpretation of the probe is described further in Ref 1. Three sensing elements face the ion drift direction and are located at distances 1,4 and 8 cm from the end of the probe housing which is fabricated from a 30 mm diameter graphite rod. One sensor, 10 mm from the end, faces the electron drift direction. Each sensor was repeatedly biased with a linear voltage ramp, -100V to + 10V, every 50 ms. The power deposited on each sensor was inferred from the rate of temperature rise of a chromel-alumel thermocouple spot-welded to the back of each 1 x 5 x 10mm³ tungsten sensor plate.

A typical JET discharge current is shown in Fig 2. During the current rise the plasma vertical elongation increases, typically to b/a ≈1.5, then is roughly constant during the current flat-top before decreasing again; Fig 2 shows an example of the vertical position of the last closed flux surface (separatrix) at the probe location R_p = 3.25m. The probe was inserted from the top of the torus, and was thus sensitive to the changing probe-separatrix distance, $Z_p - Z_s$, during the discharge. The location of the separatrix is calculated for frequent time intervals during JET discharges using magnetic pick-up coil data.



1. Individual sensing element.



2. Typical time trace of plasma current I_p and vertical position of plasma edge at the probe Z_p.

+ and University of Toronto Institute for Aerospace Studies M3H 5T6
* Culham Laboratory, Abingdon OX14 3DB

The probe vertical position Z_p can be varied between one discharge and the next. Probe data was interpreted as a function of the distance between sensing element and the boundary $r=Z_p-Z_s$.

Experimental Results

Because of (a) the radial separation of the sensors on the probe housing and (b) the variation of Z_p-Z_s during a discharge, a radial profile of plasma temperature etc. could be obtained for each discharge. Fig 3 gives an example of such radial profiles. The ion saturation current density I^+_{SAT} (particle flux density), electron temperature T_e and floating potential V_f for each element were obtained by fitting each 50 ms Langmuir I-V characteristic to the function $I=I^+_{SAT}[1 - \exp(e(V-V_f)/kT_e)]$; only data points for $V \leq V_f$ were employed since it was found that the I-V characteristic departed from true exponential behaviour above V_f, giving spuriously high values of T_e. Values of ion temperature T_i were deduced from measurements of the deposited heat flux density P_d, T_e and I^+_{SAT}. Plasma density was calculated from $I^+_{SAT} = 0.5 n_e c_s e$ where $c_s = [k(T_e+T_i)/m_i]^{\frac{1}{2}}$.

The radial electric field was calculated from $E_r = -dV_f/dr + \frac{d}{dr}[(kT_e/2e) \ln[(2\pi m_e/m_i)(1+T_i/T_e)(1-\delta_s)^{-2}]$, where δ_s is the coefficient of secondary electron emission.

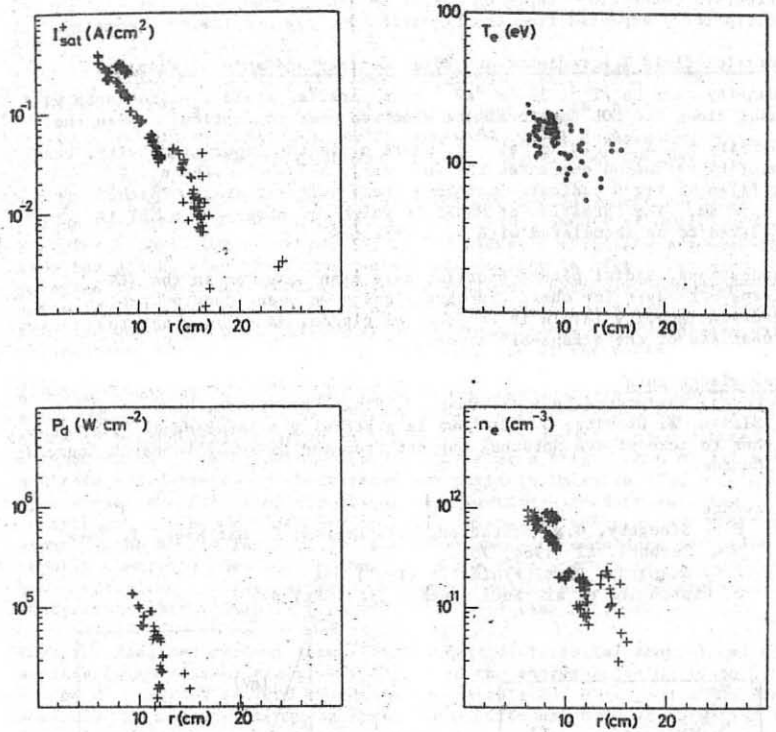
Fig 4 gives radial profiles of I^+_{SAT} for two sets of plasma current: $I_p \sim 1$MA (q_s=10-11) and ~ 3MA (q_s=3-4). As can be seen the e- folding length of the profile for lower current discharges is about double that of the higher current shots. This is evidently a direct result of the change in connection length $L=\pi R q_s$ and the relation between the scrape-off and connection lengths: $\lambda = (D_\perp/Lc_s)^{\frac{1}{2}}$. A value of $D_\perp \simeq 0.5 m^2/s$ is thus obtained which agrees with spectroscopic (impurity transport) measurements on JET.

Virtually no probe data was obtained within the last scrape-off width of the plasma boundary. Radial profiles of $n_e(r)$ and $T_e(r)$ were extended to r=0 by supplementing the probe data with spectroscopic measurements made at the limiters of heat flux (infra red camera) and particle flux (H_α emission). An example of such complete radial profiles is given in Fig.5. Since the magnetic flux lines for a typical discharge of b/a =1.5 are radially compressed by a factors of 2 in going from the probe position at the top of the torus to the limiter position at the outer mid-plane, the radial scale in Fig 5 is about half that in Fig 3.

Discussion

Impurity generation. The impurity influx rates (carbon, oxygen, metals) from the walls and limiters are measured spectroscopically. The radial profiles of Fig 5 were used to calculate the carbon sputtering rate at the limiter due to deuterium ion impact and it was found that this only accounts for a fraction of the impurity influx. The measured influx can be accounted for by including impurity (O,C), sputtering.

Impurity screening. The ionization of impurity neutrals entering the scrape-off layer, SOL, from the walls and limiters was calculated using Fig 5. Fig 5 was also used to calculate the rate of removal of impurities by convection to the limiters and diffusion into the core plasma. It was found that although impurity influxes from the walls and limiters can be comparable, the SOL effectively shields the core plasma



3. Radial profiles for a single shot (NO.3756). I_p = 3 MA, B_T = 3.4T, b/a = 1.5, $\bar{n}_e \ell = 8 \times 10^{19} m^{-2}$.

from the wall impurities. The shielding of the limiter impurities is partial. The known carbon generation rate at the limiters together with the profiles of Fig 5 give a carbon concentration in the core plasma of 2 - 4%, which is consistent with the spectroscopic estimates and measurements of Zeff (bremsstrahlung).

Hydrogen fueling efficiency. The ionization of deuterium molecules entering the SOL was calculated using the profiles of Fig 5. A fraction of the ionization occurs in the SOL itself, reducing the fueling efficiency of the core plasma.

Poloidal $\vec{E} \times \vec{B}$ drifts. The radial electric field, $\sim 10^3$V/m, causes a poloidal $\vec{E}\times\vec{B}$ drift of $\sim 10^3$m/s which greatly exceeds the radial out-drift $D_\perp/\lambda \cong 10$m/s. If this poloidal drift varies poloidally it would result in the mix of plasma between adjacent flux tubes i.e. tubes which strike one of the four small (40x80 cm) limiters on the first pass and ones

which miss. This may explain the apparent existance of a single effective connection length on JET of $L = \pi R q_s$, rather than the multiplicity expected from the magnetic topology and limiter geometry.

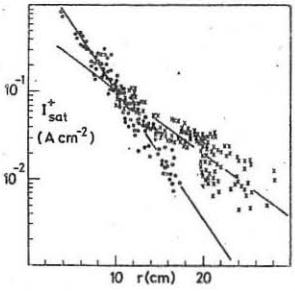
Parallel-field T_e-gradients and Edge Impurity Radiation. When the quantity $Zeff\ Ln_e/T_e^2 \gtrsim 10^{17} m^{-3} eV^{-2}$ then parallel field T_e - gradients will exist along the SOL due to finite electron heat conduction[2]. When the quantity $n_z L/T_e^{3/2} \gtrsim 10^{16} m^{-2} eV^{-3/2}$, where n_z is the impurity density, then impurity radiation dominates the SOL energy balance[2]. The n_e, T_e profiles of Fig 5 indicate that both these criteria are approached for $r \cong 50$ mm. The formation of MARFE 's which are observed in JET is believed to be associated with such effects[3].

Conclusions. Radial plasma profiles have been measured in the JET scrape-off layer for ohmic discharges and have been found to explain observed impurity levels in the central plasma, as well as several properties of the scrape-off layer.

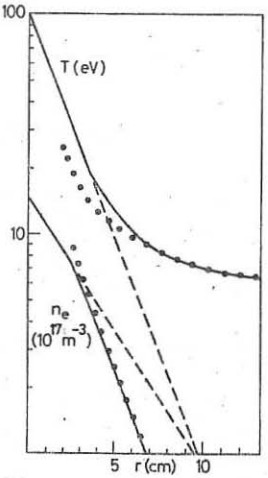
Acknowledgements
Technical assistance by A. Stevens, J. Vince, D. Wilson, J-P. Jeral, K. Slavin, W. Dearing, G. Matthews is gratefully acknowledged. PCS wishes to acknowledge personal support from the National Research Council of Canada.

Reference

1. P.C. Stangeby, G.M. McCracken, S.K. Erents, G. Matthews, J. Vac. Sci, Technol. A2 (1984) 702.
2. P.C. Stangeby, Phys. Fluids 28 (1985) 644.
3. B. Lipschultz et al, Nucl. Fusion 24 (1984) 977.



4. Radial profiles of I_{SAT}^{+}. Points for $I_p = 3$ MA, $q_s = 3$-4. Crosses for $I_p = 1.1$ MA, $q_s = 10$-11.



5. Radial profiles constructed from combined limiter and probe data. At the mid-plane. Points from probe data. Broken lines from limiter data. $\bar{n}_e \ell = 7.5 \times 10^{19} m^{-2}$, $I_p = 2.8$ MA.

Low energy neutral particle analysis at the ASDEX Tokamak

H. Verbeek and the ASDEX-Team+
Max-Planck-Institut für Plasmaphysik, EURATOM-Association
D-8046 Garching/München, Federal Republic of Germany

The neutral particle flux emitted by a Tokamak due to charge exchange of plasma ions with the neutral gas contains a large amount of neutrals with energies below 200 eV. These low energy neutrals originate predominantly from the plasma edge where the neutral gas density is high. They are not detected by the common neutral particle analyzers which are based on stripping in a gas cell followed by electromagnetic analyzers (1). However, this low energy neutral flux contributes significantly to the plasma wall interaction, i.e. impurity release and recycling at the walls.

A suitable method for the analysis of low energy neutrals is time-of-flight spectroscopy (2). In our Low Energy Neutral Analyzer (LENA) the flux from ASDEX is mechanically chopped in bunches of 1 µs duration by a slotted cylinder mounted on a modified turbopump. After a flight path of 2.2 m the neutrals are detected by their secondary particle emission from a Cu plate. In a separate calibration experiment the negative secondary emission coefficient of the Cu plate has been determined for hydrogen and deuterium atoms in the energy range of 10 to 1000 eV/amu. The secondary particles (mostly electrons, but also H^- ions) from the Cu plate are focused to an open multiplier. Single particle pulses are collected in a multichannel analyzer in the multiscaling mode with a dwell time of 1 µs.

From the measured arrival time distributions differential neutral emission spectra (number of neutrals/cm^2 s eV sr) in the energy range of 10 to 1000 eV for H^0, i.e. 20 to 2000 eV for D^0 are calculated. During an ASDEX shot every 100 ms a spectrum can be taken. In a different mode of operation the neutral flux within a preselected energy interval can be recorded over an entire discharge with a time resolution of 5 ms.

The neutral fluxes obtained with the LENA are uncertain within a factor of 2 due to the uncertainty of the multiplier detection efficiency and the errors of the secondary emission calibration. With the LENA it is impossible to distinguish between neutrals of different masses. Spectra from discharges containing H and D cannot be properly evaluated even if the mixing ratio was known.

The LENA is installed at the ASDEX WNW sector as shown in fig.1. It is in close proximity to a movable mushroom limiter and one of the neutral beam injectors. There is, however, no direct line of sight of the LENA to the plasma region where the neutral beam is absorbed. The controlled gas valve is normally at S and toroidally far away from the LENA. These major sources of neutral gas are of great influence on the neutral fluxes observed with the LENA. These fluxes have increased by an order of magnitude since the mushroom limiter was installed as a protector of the ICRH antennas. While the limiter is still 4 cm away from the separatrix due to the recycling of the edge plasma it is an intense source of neutral gas. In the region of

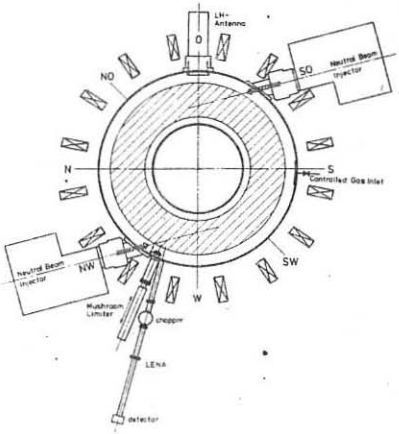


Fig. 1: Groundplan of ASDEX showing the location of LENA and major neutral gas sources.

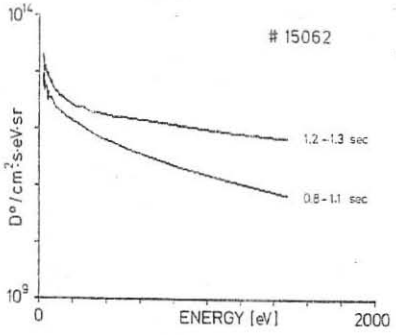


Fig. 2: Differential neutral emission spectra of a deuterium discharge before and during 2.6 MW neutral injection.

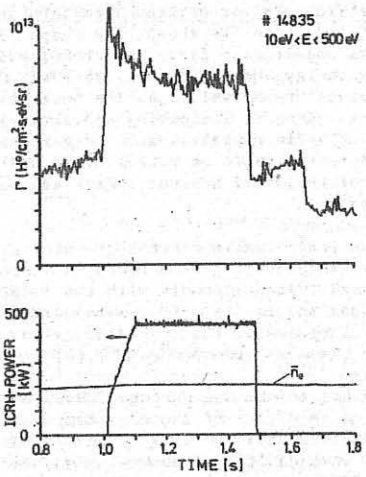


Fig. 3: Outflux of 10 - 500 eV H^o during ICRH as shown in lower fig. n_e was kept constant.

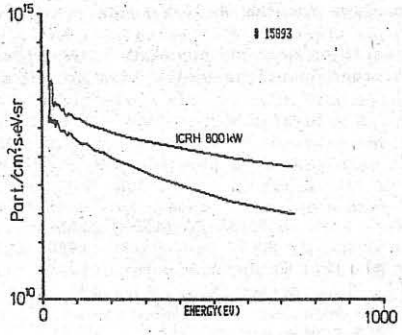


Fig. 4: Differential neutral emission spectra of a hydrogen discharge before and after 800 kW ion Cyclotron Resonance Heating.

overlap we compared our fluxes with those measured by the stripping analyzer at the NO-sector. The LENA fluxes were larger by a factor of 15. But, when the controlled gas valve was moved to NO the stripping analyzer fluxes increased and became 2 x larger than the LENA fluxes.

In fig. 2 neutral emission spectra from a divertor discharge in deuterium before and during 2.6 MW neutral H injection are shown. The shape of the curves is typically for all spectra observed so far. The intensity is steeply increasing with decreasing energy. No maximum is observed. The curves cannot be fit by single temperature Maxwellians. The neutral flux increase during NI is larger at high energies indicating an increase of the edge temprature. In some cases the flux increase was much larger when the NW injector was operated than when the SO injector was on. This can be explained by the neutral gas halo of the beam. However, there are cases when no such difference was observed.

In fig. 3 the enhancement of the neutral flux in the energy interval of 10 to 500 eV during Ion Cyclotron Resonance Heating of a hydrogen discharge is shown (3). The neutral flux increases instantaneously with the onset of ICRH (lower fig.), decreases somewhat and levels off at a value 2 x as large as before. Up to 900 keV the increase of the neutral flux is proportional to the ICRH power, as was also observed at PLT (4).

In fig. 4 the neutral emission spectra before and during ICRH with 800 kW are shown. As with NI there seems to be a rise of the edge temperature, which is in contrast to the PLT observations. The enhancement of the neutral flux appears in all cases, when additional power is injected into the plasma.

From the spectra shown in fig. 2 and 4 the impurity release due to sputtering can be estimated. More than 80 % of the sputtering is due to particles with energies below 200 eV (5,6). However, an estimate of the total impurity flux from the walls is hard to obtain from these measurements, because the flux measured at the specific location of the LENA is not representative for the whole Tokamak.

For a well grounded estimate more measurements with different limiter positions and at different locations of the LENA at ASDEX will be necessary.

References

+ See Ref. 6.
/1/ F. Wagner, J. Vac. Sci. Technol. 20 (1982) 1211
/2/ D.E. Voss, S.A. Cohen, J. Nucl. Mat. 93/94 (1980) 405
/3/ K. Steinmetz et al. this conference paper
/4/ S.A. Cohen et al. Nucl. fusion 24 (1984) 1490
/5/ G. Staudenmaier, J. Vac. Sci. A3 (1985)
/6/ J. Roth et al. this conf.

Flux Measurements with a Sniffer Probe near the Wall in ASDEX

W. Poschenrieder, G. Venus, Y.G. Wang. E.R. Müller, R. Bartiromo, G.Becker, H.S. Bosch, H. Brocken, A. Eberhagen, G. Fußmann, O. Gehre, J. Gernhardt, G. v. Gierke, E. Glock, O. Gruber, G. Haas, G. Janeschitz, F. Karger, P.B. Kotzé, M. Keilhacker, O. Klüber, M. Kornherr, K. Lackner, M. Lenoci, G. Lisitano, H.-M. Mayer, K. McCormick, D. Meisel, V. Mertens, H. Murmann, H. Niedermeyer, H. Rapp, H. Röhr, F. Ryter, F. Schneider, G. Siller, P. Smeulders, F. Söldner, E. Speth, K.H. Steuer O. Vollmer, F. Wagner.

Max-Planck-Institut für Plasmaphysik, EURATOM Association,
D-8046 Garching/München, Federal Republic of Germany

Introduction

For a detailed assessment of particle recycling in a tokamak it is necessary to know quality and quantity of the particke fluxes directed to the elements of the wall. In a divertor machine like ASDEX we have to differentiate between at least four distinct elements: main chamber wall, protective limiters, collector plates, and divertor walls. Relevant data about the divertor region are obtained from pressure and flux measurements. Earlier measurements of near wall fluxes in the main chamber were done with carbon collection probes /1/. In light of the data obtained now with the sniffer probe, fluxes which these measurements yielded turn out to be about one order of magnitude too low. This can be explained by the very low plasma temperature in this region which prevents effective collection of the majority of the protons.

In contrast, the sniffer probe is especially suited to measure proton fluxes at low energy. This probe consists of a 2 m long tube with a slit at the plasma near side and a strongly differentially pumped mass spectrometer (MS) at the downstream end. The tube can be moved longitudinally to obtain radial flux profiles, and rotated axially to sample toroidal and poloidal flux components. The probe is inserted into the edge plasma within the shadow range of the protective limiters, somewhat below the median plane.

The calibration is simple: From the pressure drop measured between plasma chamber and mass spectrometer chamber for molecular H_2, the transmission probability W_o of the tube for the flux q_o entering the slit is derived. From the known pumping speed S, and pressure p_m at the mass spectrometer we get the correlation $q_o = p_m S/W_o$ mbarl/s, e.g. for a slit area 1x1 cm^2, we obtain $W_o = 64$ %. This correlation may also be used for proton fluxes in a magnetic field based on the following assumptions:
(i) no plasma effects within the probe which is valid for plasma temperatures $T_p < 10$ eV and densities $n_p \leq 10^{12}$ cm^{-3}; (ii) diffuse scattering of H-atoms on surfaces; (iii) energy accomodation after few collisions; and (iv) that the surface at the impact zone is so saturated with H-atoms that instant recombination to molecular H_2 occurs. The conditions for assumptions (i) and (iv) are in our application well fulfilled, whereas the result is not very sensitive to the somewhat more speculative assumptions (ii) and (iii).

The time resolution of the probe, governed by the diffusive character of the gas flow to the MS, is about 100 ms but can be improved by a mathematical procedure based on the diffusion equation.

Particle Fluxes

Figure 1 shows in a 3-dimensional plot the time dependence of the flux profile in the shadow of the protection limiters in a deuterium discharge. One clearly sees the sharpening of the profile towards the plasma during the ramp-up of the plasma density until 0.4 s. A similar effect is seen during neutral injection (NI) of hydrogen from 1.1 to 1.3 s (shown is the D_2-signal of the target plasma).

Utilization of the capability of the MS to differentiate between H_2, HD, and D_2 is depicted in Fig. 2. Though more than a dozend discharges after a transition from dicharges with H_2 to D_2 had occurred, the probe still shows a majority of H-flux at the beginning of the discharge. Only in the ohmic plateau phase is the D-flux dominant. Obviously the intense wall contact at the start leads to enhanced desorption of H_2 still implanted in the wall surface layers. A drastic increase of H_2 is seen during NI. Further investigations, however, have shown this to be due not so much to injection of H-atoms directly, but to increased H-desorption during NI.

The radial dependence of the D-flux in absolute values is given in Fig.3 at the ohmic flat top phase and during neutral injection of H_2. Near the edge of the protective limiters (marked SL) a close to exponential decay with a decay length $\lambda = 1$ cm is observed. In the vicinity of the wall from $R_{SN} = 215...230$ cm the flux levels off to an almost constant value around 1×10^{16} cm^{-2} s^{-1}. Remarkable is the strong asymmetry between the toroidal flux parallel to the electron drift (ES) and the ion drift direction (IS). If the slit is positioned to look poloidally upwards (OS) a much smaller flux is observed.

The short decay length and the sensitivity to the alignment with the magnetic field is clear evidence for ionic flux close to the limiter edge, whereas the almost constant flux closer to the wall is likely to be caused by neutral atoms (Franck-Condon) originating in the edge plasma, and by molecules from the wall.

During neutral injection (coinjection of H_2) the target plasma (D_2) shows only a small flux increase on the ion drift side, but a surprisingly strong increase on the electron drift side. Also the poloidal flux component (OS) increases significantly. The reasons for the asymmetry and peculiar behaviour during NI are not yet clear.

Further investigations have shown a marked effect of a reversal of toroidal field polarity which corresponds to a topological inversion of upper and lower divertor. There is a basic asymmetry associated with the divertor fluxes which also could play a role, in here. Unfortunately, for technical reasons, it was not possible to also study the effect of a reversal of plasma current.

Data on the dependence on plasma density show a more than linear increase of the flux, which agrees with the observations made on the scrape-off flux into the divertors. In discharges with H_2 the sniffer fluxes are about 40 % above those found in D_2, reflecting the better confinement in the latter.

The results can be interpreted by a simple flux tube model which gives for the decay length $(D_\perp \cdot l/v_{//})^{1/2}$ where $D_\perp$ is the cross field diffusion constant, $v_{//}$ the parallel streaming velocity, and l the connection length of the flux tube. One can show that λ in fig. 2 is characteristic for the flux tubes undisturbed by the probe itself, whereas the flux actually measured, depends on the length of the flux tube determined by the toroidal probe position in respect to the protective limiters. One should keep in mind, however, that the near wall zone is a region of strong local gas sources, which are not accounted for in the simple model.

At the limiter edge fluxes are typically $1 \cdot 10^{18}$/cm^2 s. From our data we can estimate the total flux going to the protective limiters and the wall /4/ assuming toroidal and poloidal symmetry. For $n_e = 3 \cdot 10^{13}$/cm^3 we obtain

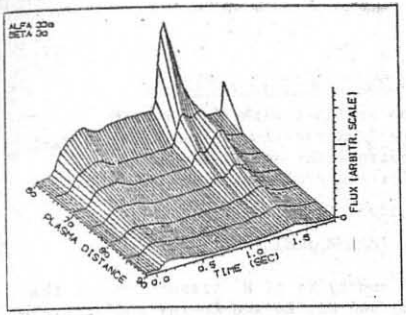


Fig.1: Time dependence of the proton flux profile. Position of protective limiter edge is at "plasma distance" 50 cm.

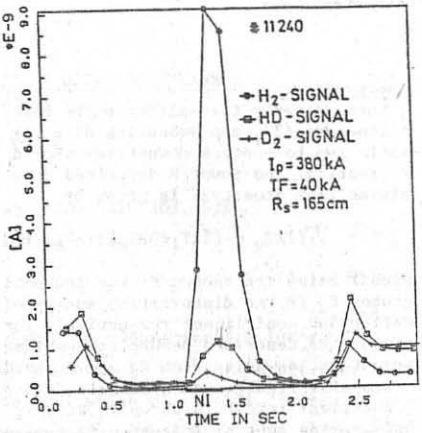


Fig.2: Isotopic composition of flux measured in a D_2-dicharge with H_2 neutral injection. Ion drift side. 1.3 cm behind protect. limiter edge.

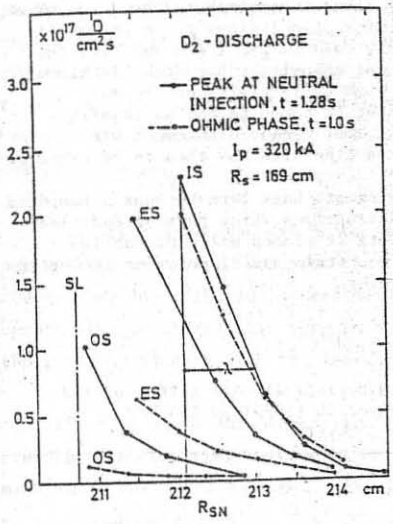


Fig.3: Radial dependence of Deuteron flux. IS: Ion drift side, ES: Electron drift side, OS: Slit in upward direction. RSN: Radial dist. from central axis. SL: position of protect. limiter edge.

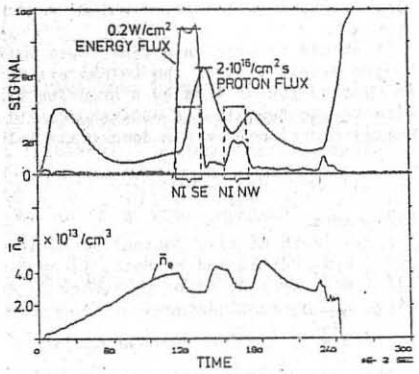


Fig.4: Proton and energy flux in a discharge with successive firing of the two NI-beamlines. Ion drift-side, 2.5 cm behind protect. limiter edge.

$5 \cdot 10^{20}/cm^2s$ and $3 \cdot 10^{21}/cm^2s$ respectively, which has to be seen in relation to the total flux of about 1 $10^{22}/cm^2s$ carried via the scrape-off layer into the divertor.

Energy Fluxes

More recently the sniffer probe has been equipped with a number of bolometers /2/, one measuring directly the flux entering through the slit, while two bolometers downstream should indicate the amount of energy reflection. The power P deposited on a floating probe surface of 1 cm^2 by a plasma flux density Γ is given by

$$P = \Gamma \cdot (2kT_e + (2kT_i + 3kT_e)(1-R_e) + \sigma E_i + (1-R_m) E_d/2)$$

with σ being the amount of the ionization energy E_i of H^+ transferred to the probe. E_d is the dissoziation energy of H_2 and R_e, R_m are energy and particle reflection coefficient respectively for the H-atoms. Since T_i is obtained by the method described before, an estimation of T_i ($= T_e$) should be possible. Uncertainties arise from R_e and R_m by lack of experimental data, but some reasonable figures are available from computer simulations /3/.

A typical result is shown in Fig. 4, taken 2.5 cm behind the limiter edge. Only during neutral injection is a significant energy deposition seen, the first peak being caused by the beam line which fires in direction of probe position. The absence of recognizeable energy deposition in the ohmic phase is surprising, since one should expect E_i alone to contribute about 100 mW at a flux of $5 \times 10^{16}/cm^2s$. There are two obvious conclusions to be drawn: (i) the plasma at this position is already very cold ($kT_e \lesssim 1$ eV) and (ii) the energy E_i of electronic recombination is not deposited, but probably almost completely radiated off, assisted by the high reflectivity of the gold surface of the bolometers. Hence: σ must not be taken as one as is often assumed. This conclusion is supported by a most recent mesurement with a black carbonized bolometer which is more in line with the then to be expected $\sigma = 0.5$.

It should be mentioned that these measurements have been seriously hampered by the sensitivity of the bolometers to disruptions which have already lead to destruction of five by a stunning variety of plasma wall interaction effects. So far, it was not yet possible to obtain useful data for reflected energy fraction from the downstream bolometer.

References

/1/ J. Roth et al., Journal of Nuclear Materials 111/112 (1982) p. 123
/2/ E.R. Müller and F. Mast, J. Appl. Phys. 55 (1984) p. 2635
/3/ W. Eckstein, to be published in Appl. Physics
/4/ W. Poschenrieder and G. Venus, Journal of Nuclear Materials 111/112 (1982) p. 29.

ION TEMPERATURE MEASUREMENTS IN DITE EDGE PLASMAS

G. F. Matthews

Culham Laboratory, Abingdon, Oxon OX14 3DB, U.K.
(Euratom/UKAEA Fusion Association)

Ion temperature plays an important rôle in plasma-surface interactions in tokamaks, yet has seldom been measured in the scrape-off layer. An innovative probe has been operated on DITE which fills this diagnostic gap[1]. The probe may be operated in the retarding field mode, ExB mode or as a single Langmuir probe. In the experiments to be described the probe was fitted with a 30 μm aperture slit. Measured electron temperatures T_e typically lie in the range 5 eV to 30 eV in the region accessible to the probe. The corresponding ion temperatures are often observed in the range $T_i = T_e$ to $T_i = 3T_e$. Generalisations about the ion temperature are however of little use divorced from details of the specific conditions in the plasma edge.

The exterior of the ExB probe is a carbon case 5 cm in diameter. It may only be considered unperturbing to the plasma in the special circumstance that the probe is located near a backstop[2]. On DITE the adjustable carbon limiter served this purpose since it was located only 45° away from the probe toroidally with its leading edge at 21 cm minor radius.

Figure 1 shows data taken with the probe operated in the retarding field mode in a rising density ohmic discharge. A constant flow of gas was maintained until 150 ms causing the line average density to rise from 10^{19} m^{-3} to a peak of 3×10^{19} m^{-3} at 200 ms. Ion and electron temperatures were recorded sequentially during each discharge by switching the probe from ion to electron mode on consecutive cycles of the probe sweep potential. During the ion mode cycle the aperture was biased to - 100 V thus drawing a current equal to the ion saturation current for $T_e \lesssim 30$ eV, from which the density was calculated.

Characteristically the radial profiles of ion temperature show a much stronger temporal dependence than do the electron temperature profiles. The T_i and T_e profiles shown in fig. 1(c) are not strongly coupled and the ion temperature appears to respond most strongly to the neutral particle refueling, indicated by the rapid ion temperature rise following the termination of the gas feed.

The Local Energy and Particle Balances

The local energy confinement time associated with any process resulting in a local loss or gain in energy per unit volume Q, will be defined as

$$\tau_E = \frac{3}{2} \frac{n_e T_i}{Q}$$

where T_i is the ion temperature (eV). Another characteristic time of importance is the parallel loss time for particles convecting to the limiter $\tau_{p\parallel} = L_\parallel / C_s$, where C_s is the ion sound speed and $L_\parallel$ the interconnection length. The particle confinement time associated with a source of ions S_p ($m^{-3}\ s^{-1}$) is defined by $\tau_p = n_e / S_p$. Table 1 lists estimates made for a variety of significant processes. The numerical evaluations were made assuming $L_\parallel \sim 28$ m, $T_i \sim 40$ eV, $T_e \sim 15$ eV, plasma density n_e over a range $10^{17} \rightarrow 10^{19}\ m^{-3}$ and atomic/molecular hydrogen density n_H from $10^{16} \rightarrow 10^{18}\ m^{-3}$.

It may be concluded from the estimates that the energy confinement times associated with electron energy loss are much shorter than the equipartition time at typical densities and so the ion and electron temperature profiles will be decoupled. It is also evident that the ion energy balance can easily be dominated by ionisation of atoms or molecules and charge exchange losses, the magnitude and sign of which depend on the atomic density and temperature. Owing to the low velocity of thermal molecules (~ 1/40 eV) it is likely that in the region accessible to the probe the molecular density will significantly exceed that of the atoms whose energy is ~ 4 eV. The experimental observations of ion temperature decoupled from the electron temperature but dependent on refuelling is thus qualitatively consistent with theoretical expectations.

TABLE 1

Summary of the local ion and electron energy confinement time estimates for plasma densities in the range 10^{17} to 10^{19} m^{-3} and neutral densities from 10^{16} to 10^{18} m^{-3}. Particle confinement times are also listed for comparison. Additional parameters used in the calculation were $T_i \sim 40$ eV, $T_e \sim 15$ eV, $L_\parallel \sim 28$ m and an oxygen impurity concentration of 10%. Sources are denoted as positive and sinks as negative.

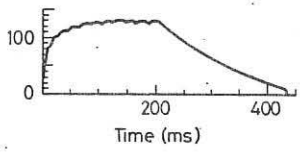
Ion Energy Confinement Times	τ_{Ei}(mS)
Cross-field ion thermal conduction	40 ($n_e=10^{17}$)→1.6 ($n_e=10^{19}$)
Ionisation of neutrals (H or H_2)	- 3 ($n_H=10^{16}$)→-0.03($n_H=10^{18}$)
Ion-electron equipartition	-50 ($n_e=10^{17}$)→-0.5($n_e=10^{19}$)
Charge exchange (H)	- 3 ($n_H=10^{16}$)→-0.3($n=10^{17}$)
Electron Energy Confinement Times	**τ_{Ee}(mS)**
Cross-field electron thermal conduction	0.2
Parallel electron convection to sheath	- 0.2
Radiation from impurities	-0.4($n_I=10^{17}$)→-0.04($n_I=10^{18}$)
Electron ionisation of neutrals (H or H_2)	- 4 ($n_H=10^{15}$)→-0.04($n_H=10^{18}$)
Electron-ion equipartition	20 ($n_e=10^{17}$)→0.2($n_e=10^{19}$)
Particle Confinement Times	**τ_p(mS)**
Parallel loss time ($\tau_{p\parallel}$)	- 0.2
Ionisation of H and H_2	5 ($n_H=10^{16}$)→0.05($n_H=10^{18}$)

References

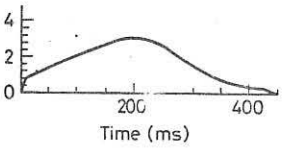
1. G.F. Matthews, J.Phys.D 17(1984) 2243-2254.
2. P.C. Stangeby, J.Nucl.Mater. 121(1984) 36-40.
3. C.S. Chang, F.L. Hinton, Phys.Fluids 25(9) (1982) 1493-1494.

FIGURE 1

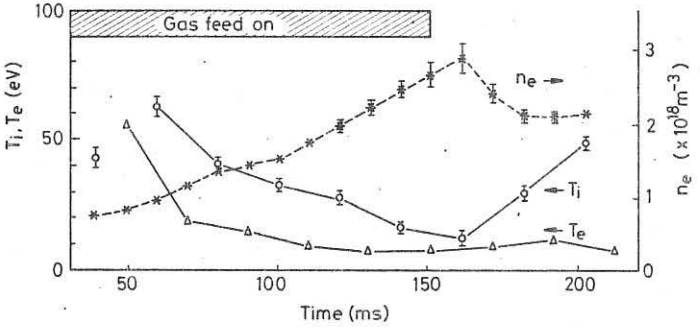
(a) Plasma Current (kA)



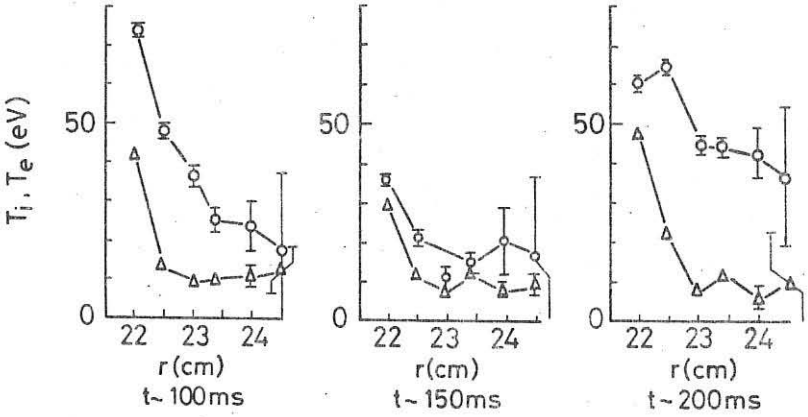
Plasma Density (x 10^{18} m^{-3})



(b) Ion and Electron Temperature, and density recorded at 23 cm radius



(c) Radial profiles of ion and electron temperature at the three times shown



PLASMA EDGE DIAGNOSTICS BY MEANS OF LITHIUM BEAM - ACTIVATED CHARGE EXCHANGE SPECTROSCOPY

F. Aumayr and H. Winter

Institut für Allgemeine Physik, Technische Universität Wien
Karlsplatz 13, A-1040 Wien, Austria

The understanding of impurity production via plasma wall interaction and related impurity ion transport is still far from being satisfactory. For further improvements toward operation of sufficiently hot, dense plasmas with stable confinement also development of advanced plasma diagnostic techniques can be useful. In recent years some new methods have been introduced, e.g. dye laser fluorescence spectroscopy /1/ and neutral beam-activated charge exchange spectroscopy ("CXS") of emitted particles /2/ or photons /3/. Fig. 1 shows the principal scheme of neutral beam-activated CXS in comparison to the usual photon spectroscopy, which until now is common for impurity ion studies, covering predominantly the vuv and xuv spectral regions. Fig. 1 demonstrates how instead of observing the characteristic line emission from particular ions excited via a complex combination of ionisation/excitation and/or recombination processes within the plasma, one can utilize production of impurity line radiation via electron capture from suitable injected atoms into excited states of impurity particles. In doing so, a much better defined excitation mechanism is given, which permits unambiguous evaluation of impurity ion transport behaviour, rather independent from otherwise necessarious plasma model assumptions.

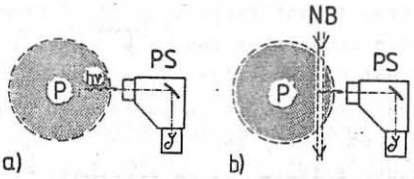


Fig 1: Comparison of conventional plasma impurity ion spectroscopy (a) with neutral beam-activated charge exchange spectroscopy (b). P..plasma, PS..photon spectrometer, NB..neutral beam

So far, hydrogen atom beams have exclusively been used to provide the electrons for CXS, and only fully stripped low-Z impurities have been studied, which mainly dwell in the inner part of magnetically confined hot plasmas /3/ - /5/. On the other hand, the properties of the plasma edge region are especially important for the plasma wall interaction processes, and modification of their parameters can be a handle to reduce impurity ion production. Therefore, investigation of impurity transport in the plasma edge region is of specific interest. However, a rather high background of neutral hydrogen in this region would cause a poor signal-to-noise ratio with H-activated CXS and, moreover, for the lower ion charge states electron capture from H^0 results in population of relatively low excited states, which are also very efficiently produced from the plasma itself. As a remedy we have proposed to apply instead neutral Li beams /6/, which not only can more efficiently excite characteristic radiation of impurities via CXS (cf. reaction (1) below), but also permit measurement of proton (via reaction (2) below) as well as electron densities /7/. Finally, Li beam injection has already been utilized to investigate poloidal magnetic field profiles of tokamak discharges /8/. To provide the data basis for Li-activated CXS of protons and impurity ions, the following reactions had to be investigated:

(1) $Z^{q+} + Li(2s) \rightarrow Z^{(q-1)+*} + Li^+$ (Z^{q+}..low-Z impurity ions as C^{3+}-C^{6+}, O^{3+}-O^{7+} /9/)

(2) $H^+ + Li(2s) \rightarrow H^*(n=3) + Li^+$ (leading to H_α emission /10/)

(3) $H^+ + Li(2s) \rightarrow H^+ + Li(2p)$ (resulting in LiI emission for electron density measurement /11/)

Reaction (3) has to be taken into account when measuring electron density via electron impact excitation of Li atoms /7/. Fig. 2 shows some emission cross sections as a comparison of the respectively strongest CIV emission lines produced by CXS with H^0 or Li, and for reaction (2). In comparison to H-activated CXS, electron capture from Li(2s) populates higher excited states and also involves larger emission cross sections. Finally, emission from higher excited states appears at larger wavelengths, the observation of which is generally more convenient.

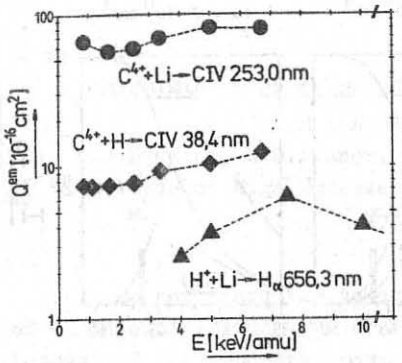


Fig 2:
Emission cross sections for the respectively strongest CIV lines produced in C^{4+}-Li /9/,/12/ or C^{4+}-H collisions /13/.
Also shown are H_α emission cross sections for H^+-Li collisions /10/.

For all measured emission cross sections the corresponding rate coefficients for given plasma temperatures have been calculated. Together with also measured cross sections for ionisation of Li by electron capture /14/ and the already known electron impact ionisation cross sections for Li, we could investigate the applicability of Li-activated CXS via numerical simulation. For this purpose, we have assumed typical ohmically heated tokamak discharges as produced e.g. by the TEXTOR facility /15/, cf. Fig. 3.

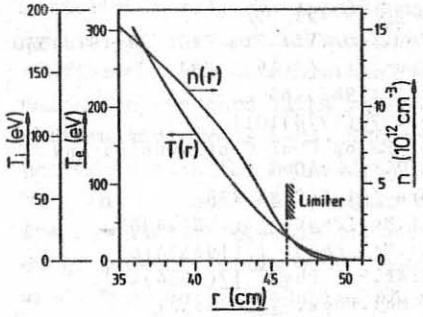


Fig. 3:
Radial profiles of plasma density, and electron and ion temperatures for TEXTOR discharges, as found in the plasma edge region /15/

Typical results of this simulation are shown in Fig. 4, for which injection of 30 keV Li atoms has been assumed into TEXTOR plasmas with profiles as shown in Fig. 3, and several central plasma densities. The results are encouraging for practical application, which is currently in preparation at the TEXTOR facility. The Li injector involves energies up to 30 keV and equivalent Li

current densities of 1 mA/cm^2 can be readily achieved /16/.

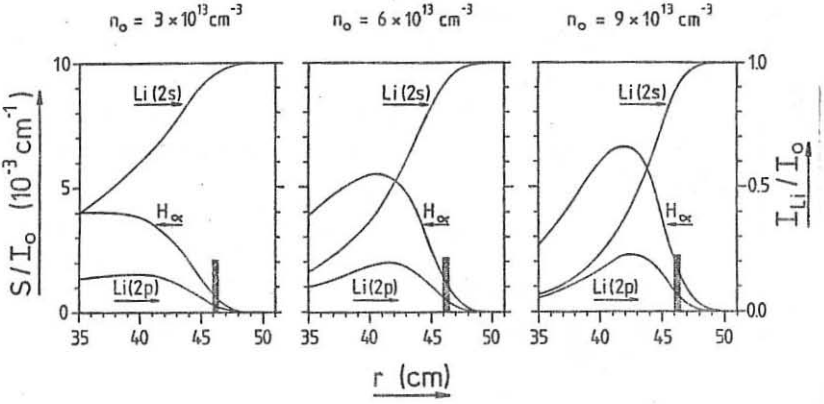


Fig. 4: Simulation of Li beam attenuation/Li(2s), LiI resonance line emission/Li(2p) and H_α emission at Li beam injection with 30 keV into plasmas with parameters as shown in Fig. 3.

Acknowledgments

This work has been supported by Kommission zur Koordination der Kernfusionsforschung in Österreich at the Austrian Academy of Sciences, and by Fonds zur Förderung der wissenschaftlichen Forschung (Projekt Nr. 5317).

References

/1/ E. Hintz, Phys.Scripta T2/2(1982)454
/2/ V.V. Afrosimov et al., Zh.Eksp.Teor.Fiz.Pis.Red. 18(1973)510
/3/ R.C. Isler, Phys.Rev.Letters 38(1977)1359
/4/ V.V. Afrosimov et al., Zh.Eksp.Teor.Fiz.Pis.Red. 28(1978)540
/5/ R.J. Fonck et al., Phys.Rev.Letters 49(1982)737
/6/ H. Winter, Comm.At.Mol.Phys. 12(1982)165
/7/ K. Kadota et al., Plasma Phys. 20(1978)1011
/8/ K. McCormick et al., Proc. 8. Europ.Conf.Contr.Fusion and Plasma Physics, Prague 1977, p. 140
/9/ A. Brazuk et al., Phys.Letters 101 A(1984)139
/10/ F. Aumayr et al., J.Phys.B:At.Mol.Phys. 17(1984)4201
/11/ F. Aumayr et al., J.Phys.B:At.Mol.Phys. 17(1985)4185
/12/ D. Dijkkamp et al., J.Phys.B:At.Mol.Phys. 17(1984)4371
/13/ D. Ciric et al., J.Phys.B:At.Mol.Phys. 18(1985)L17
/14/ F. Aumayr and H. Winter, Phys.Rev. A 31(1985)67
/15/ G. Waidmann et al., Plasma Physics and Controlled Nuclear Fusion Research 1984, vol. 1, Nucl.Fusion Suppl. 1985 IAEA Vienna 1985, p. 193
/16/ H.L. Bay et al., Verh. DPG 4/1985, p. 969

JOINT SET-UP OF LASER DIAGNOSTICS FOR DETERMINATION OF PLASMA PARAMETERS

S.S.Bychkov, R.S.Ivanov, G.V.Sergienko and G.I.Stotsky
Institute of High Temperatures, USSR Academy of Sciences,
Moscow, USSR

In recent years the tokamak edge plasma became a subject of an intensive study. Major efforts were contributed in development of the impurity control methods as well as the methods for the wall and limiter erosion reduction. However the application of laser methods in edge zone of a tokamak discharge always faced considerable difficulties caused by high level of the stray-scattered light and small admittable sampling volumes of the scattering plasma.

To supply laser measurements in a tokamak periphery a joint set-up of laser diagnostics comprising H_α resonance fluorescence and Thomson scattering systems has been developed. The set-up consisted of the TEM_{oo} Nd-glass laser (the second harmonic radiation mode), the tunable dye laser with a frequency control system and the common four-channel spectral analyzer of the scattered light. The spectral analyzer was assembled using the standard light monochromator MDR-2 and the standard photomultipliers FEU-84. Thomson scattering measurements were performed with the help of all four spectral channels, while only one of those was used in resonance fluorescence experiments. The commutation of both two probe laser beams was achieved by a single movable prizm with common light colimating elements being used. The fast commutation of both two diagnostics due to the use of common light analyzing unit enabled obtaining the data set on concentrations and temperatures of the neutral and charged plasma components (n_a, T_a, n_e, T_e) in a single set of experiments.

The extra (special) selected cut-off glass filter OS-11 positioned in front of the entrance slit of the monochromator dumped the stray-scattered background by 50 times

while the Thomson scattered light in the spectral channels being reduced by only 1,5÷4 times. The conventional special approachs of the stray-scattered light reduction have been also used in the Thomson scattering measurements.

The Raman spectrum of H_2 rotational transitions was used for the absolute calibration of the analyzer spectral channels [1] with the extra dumping of the stray-scattered light being performed. In the table I the wave lengths as well as the cross-sections for the depolarized components of anisotropic scattering for Stokes transitions J → J' of the Raman spectrum are presented, where J, J' are the corresponding rotational quantum number of the lower and the upper states. These data have been calculated after [2].

Table I

Transition J → J'	λ' , Å	$dQ_{\perp}^{JJ'}/d\Omega$ $\cdot 10^{31}$ cm^2/sr
0 → 2	5397	1,55
1 → 3	5466	4,43
2 → 4	5535	0,624
3 → 5	5603	0,410

The wave distribution of the spectral analyzing channels as well as of the Raman spectrum Stokes wing lines and the cut-off filter OS-11 wave transmission is shown in fig. 2.

The resonance fluorescence diagnostic have been performed with the help of the flash-lamp pumped dye-laser tuned to the wave of H_α transition. The laser could operate in the modes of broad- and narrow-band line generation. The generation of the broad-band line (6 Å) supplied the absolute measurements of the neutral hydrogen density, while the generation of the narrow-band line (0.1 Å) enabled the accurate successive scanning over the Doppler profile in the set of the reproducible discharges. The accurate change in the wave tuning of the laser was achieved by the slight rotation of intra-cavity Fabry-Perot etalon. The neutral hydrogen temperature was determined from the measured Doppler profile half-widths. The frequency control system supplied the crude and the accurate laser tuning using the lines of the deuterium spectral lamp for the reference and the comparison.

The passive electric band filter has been used for the extraction of the fluorescence signal from the plasma fluctuation background.

The developed set-up of laser diagnostics has been proved in various operational modes of small tokamak TV-1 ($R = 23{,}5$ cm, $a_L = 3.5$ cm, $B_T \leq 2$T, $I_p \leq 15$ kA, $U_L = 2 \div 3$ v). The neutral concentrations on plasma axis was measured to be $5 \cdot 10^9$ cm^{-3}, while at plasma edge it was $7 \cdot 10^9$ cm^{-3}. The typical H_α profile is presented in fig.3. The measured H_α profile half-width of 0.5Å corresponded to the local atom temperature of ~1 ev. The observed narrow H_α profiles demonstrated the negligible contribution of the charge-exchange neutrals in H_α radiation of TV-1 plasma. Due to the presence of 1 ev atoms in the very beginning of tokamak discharge it should be supposed that the major part of the neutrals are being generated in the processes of Franck-Condon dissociation of molecules in the vicinity of the wall and limiter surfaces. The reliable data on the electron component of plasma in the range of $T_e = 100 \div 250$ ev and $n_e = (1 \div 5) \cdot 10^{13}$ cm^{-3} have been obtained using Thomson scattering measurements.

Thus a joint set-up of laser diagnostics supplying the high spatial resolution (1 cm) for the measurement of electron and neutral components of large tokamak edge plasma has been developed and proved.

References

1. Bogomolov G.D. and Letunov A.A. Sov.J. Plasma Physics, v.5, No.6, 1380, 1979.
2. Smith J.R. and Giedt W.H. Int.J. of Heat and Mass Transfer v.20, No.9, 899, 1977.

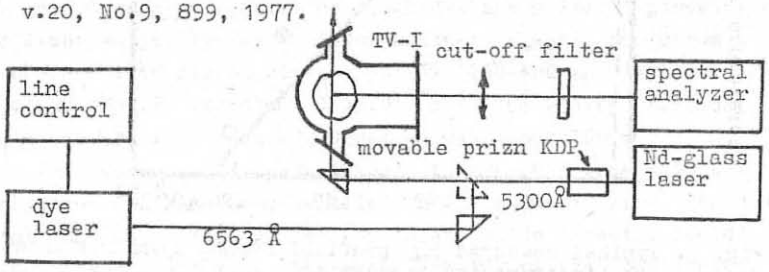


Fig. 1. Schematic diagram of experimental set-up

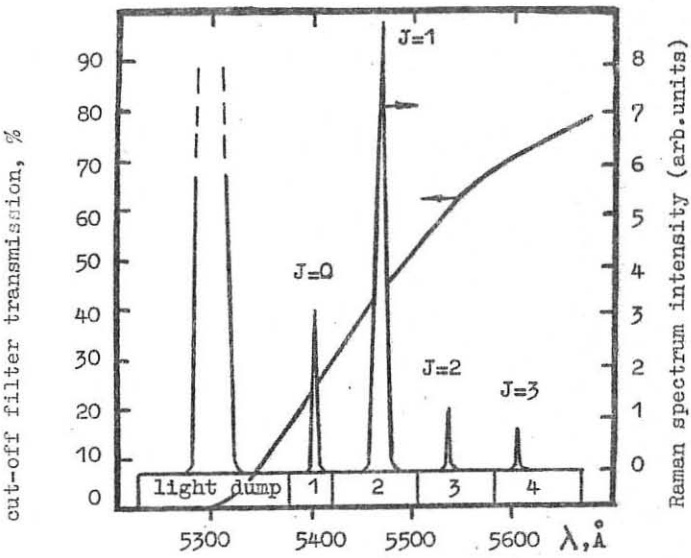


Fig. 2. Raman spectrum intensity distribution and cut-off filter transmission over channels of light detection system.

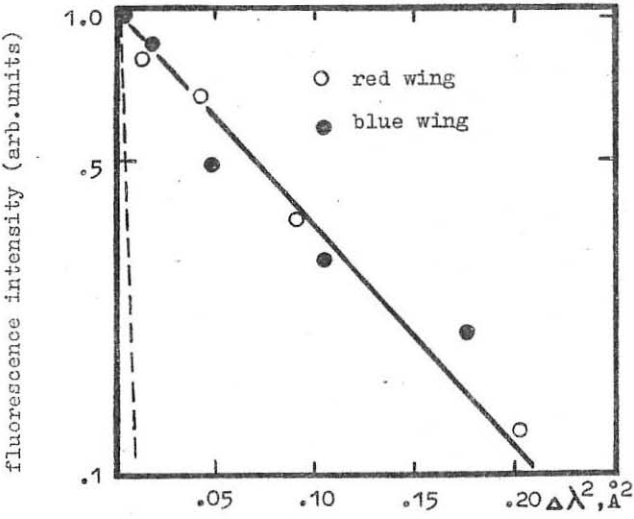


Fig. 3. Typical measured H_α profile. Dashed line indicates the instrumental broadening.

Erosion and Deposition Investigation on Time-Resolve Implanted Probes in T-10 Tokamak

G.Vízkelethy, G.Mezey, E.Kótai, A.Manuaba
Central Research Institute for Physics, Budapest, Hungary

H.Hildebrandt
Zentralinstitut für Elektronenphysik, Berlin, DDR

W.Frenstrap
Humboldt University, Berlin, DDR

Introduction

The use of special probes, either implanted or evaporated ones placed in limiter shadow could provide information not only the impurity deposition and implantation of the working gas but the detection of surface erosion might give a fuller picture about the interaction of the plasma in limiter shadow and the first wall (1,2,3). This paper deals with information that one gets a time-resolved experiment on As implanted silicon probes.

Experiments

70 keV As^+ implanted silicon was subjected to post-oxidation and oxide removal to get the arsenic distribution to the surface. This way one monolayer Si loss could easly be observed.

The samples were placed into T-10 using the WASA sample transfer system. Time resolved experiments were carried out collecting eight subsequent discharges.

Fig.1 shows both the torroidal and poloidal geometry of the experiments. The main plasma parameters were: deuterium discharges with plasma current between 200-400 kA. The average electron density was about $3\text{-}5 \times 10^{19}$ m^{-3}. The applied toroidal field was 3T. The discharge duration was about 700 ms.

The exposure to electron and ion side were made with a time resolution of 110 ms and parallel to the magnetic field line. The front side collector was perpendicular to the magnetic field without time resolution. The probe was 370 mm from the centre.

The exposed samples were investigated by RBS combining with channeling, ERD using $^{4}He^{+}$, beam and Cameca SIMS with $^{16}O^{+}$ sputtering beam. Tipical sputtering rate was about 3-4 Å/min.

Results and Discussion

Fig.2 shows the results of RBS and ERD measurements on electron, ion and front side. The dominant foreign atoms were deuterium, carbon and oxygen. Their flux is increasing during discharges and reaching a maximum at the end phase. There is an apparent asymmetry i.e. much higher fluxes were measured on the electron side. This observation is in accordance with previous ones (4) and presumably due to the limiter configuration (5).

Fig.3 shows deuterium, carbon, silicon and $SiAs^{+}$ signals obtained by SIMS on the spot marked with arrow on Fig.2. During SIMS measurements no special effort was done to determine the absolute values only the depth distributions were considered.

It is clear that approximately 30 nm thick carbon overlayer covered the sample which is not homogenious laterally as both arsenic and silicon signal is shifted but they gradually appear from 15 nm. Due to this high flux of carbon deposition no arsenic loss was detected.

The most interesting observation is the long deuterium and carbon tail which can not be explained by charge-exchange neutral deuterium implantation only, as these depths would suppose higher ion energies than 500 eV in central region of the plasma.

Besides the long deuterium tail occours together with the thick carbon overlayer. The long tail might be the consequence of electron and/or heat flux stimulated diffusion of subsequent discharges.

On the ion side however less carbon deposition was detected so it is more realistic to calculate the ion temperature from the slope of deuterium depth profile (6). This value in our case was about 60 eV.

References

(1) J.B.Roberto, R.A.Zuhr and S.P.Withrow
J.Nucl.Mater. 93/94 146 (1980)

(2) G.Mezey, J.W.Patridge and G.M.McGracken
Proc. of 9th Intern.Vacuum Congress and 5th Intern.Conf. on Solid Surfaces (Madrid 1983)

(3) J.B.Roberto, J.Roth, E.Taglauer, O.W.Holland
J.Nucl.Mater 128/129 244 (1984)

(4) H.Wolf, H.Grote, D.Hildebrandt, M.Laux, P.Pech, H.D.Reiner and H.Strusny
J.Nucl.Mater 128/129 219 (1984)

(5) D.Hildebrandt, to be published

(6) W.Eckstein, IPP 9/33, 1980.

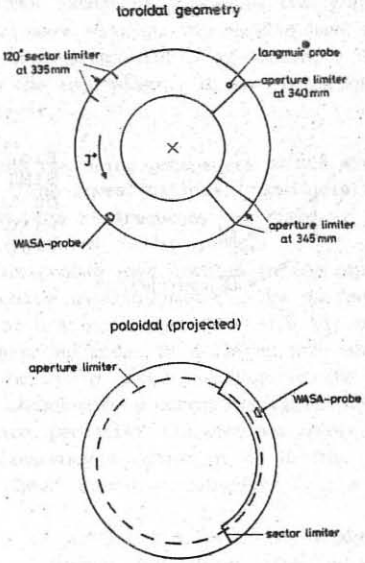


Fig. 1

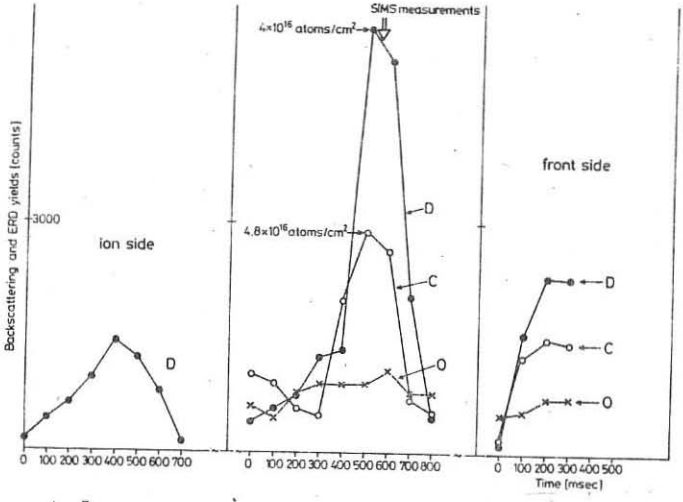


Fig. 2
Time-resolved measurement on electron side

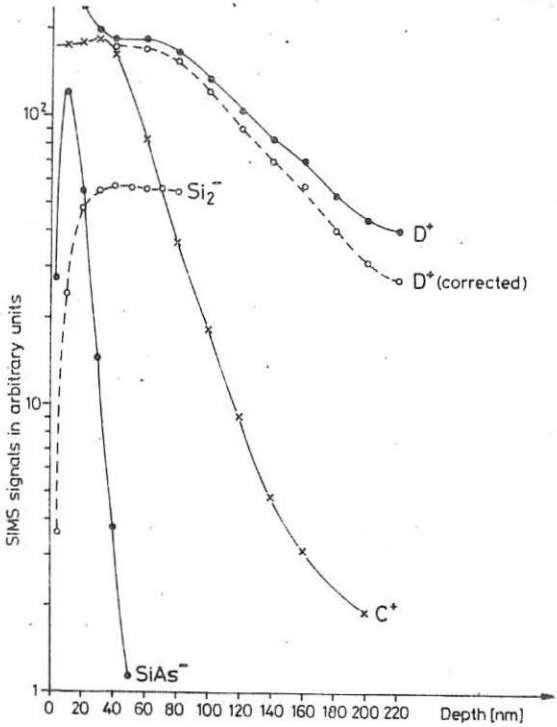


Fig. 3
SIMS measurements on the spot marked with arrow on Fig. 2

WAVE STUDIES IN THE SCRAPE-OFF LAYER OF TCA DURING ALFVEN WAVE HEATING

Ch. Hollenstein, F. Hofmann, F.B. Marcus, Y. Martin and W. Simm
Centre de Recherches en Physique des Plasmas
Association Euratom - Confédération Suisse
Ecole Polytechnique Fédérale de Lausanne
21, Av. des Bains, CH-1007 Lausanne, Switzerland

I. INTRODUCTION. In previous studies of the scrape-off layer[1] in tokamaks, the emphasis was on the measurements and interpretation of basic plasma parameters. Recent studies tried to characterise the turbulent state of the scrape-off layer[2,3]. These studies mostly apply to the ohmic heating phase only.

In the TCA tokamak extensive studies of the boundary layer have been performed during Alfvén wave heating. The results have shown that the scrape-off plasma becomes non-maxwellian during rf-heating[4]. Since the antenna is in direct contact with the edge plasma, it may excite various electrostatic waves in the scrape-off layer.

II. EXPERIMENTS. The operating parameters of TCA are $R = 0.61$ m, $a = 0.18$ m and $B \leq 15$kG. For these investigations, reproducible shots at $q \approx 3.3$ in D_2 and H_2 were studied. The rf frequency was fixed at 2.5 MHz and rf powers at around 100 kW were delivered to the plasma.

Movable Langmuir probes were located in the equitorial plane of the TCA vacuum vessel, opposite to the limiter[4]. The different probes were operated either in the ion saturation regime ($V \approx -120$ V), or the floating potential regime or in the grounded mode. This latter mode was used to minimize direct rf-pick up. The fluctuating probe currents in the ion saturation mode and grounded mode were measured by a current probe with a frequency response up to 50 MHz. The floating potential fluctuations were detected by an isolation amplifier with a frequency response up to 20 MHz. The detected signals are digitized by 8 bit CAMAC transient recorders with a sampling frequency up to 32 MHz.

Raw data of the rf current flowing in the grounded Langmuir probe and of the floating potential versus time during Alfvén wave heating are presented in Fig. 1. Beside fluctuations at the driving rf frequency and its harmonics, strong low frequency modulations occur. A typical autospectrum of the rf current is shown in Fig. 2. The floating potential data (Fig. 1b) show the appearance of large narrow spikes at the same repetition frequency as the rf. These rapid potential changes can reach several tens of Volts. The amplitudes of the rf current and of the floating potential fluctuations depend on the

probe position, the rf power and also on the particular heating scenario. A study of the radial behaviour of the potential fluctuations shows that the fluctuations are large at the antenna position. At 1 cm in front of the antenna location, the fluctuations pass through a minimum before steadily increasing towards the limiter position. The rf currents show a different behaviour. At the antenna location, the rf currents are small; they reach a local plateau 1 cm in front of the antenna before continuing to increase towards the limiter.

Correlation techniques[5] have been applied to two simple Langmuir probes spaced at 0.5 cm in the poloidal direction. The coherence obtained from these probes, operated in the grounded mode, is shown in Fig. 3. The coherence reaches nearly unity at the rf-frequency and its harmonics. An asymmetric broadening around the central lines is found. These sidebands show considerable coherence. The spread in frequency of these side bands corresponds approximately to the width in frequency of the low-frequency fluctuations. The phase difference between the two probes, obtained from correlation techniques, is presented in Fig. 4. Since the antenna excites waves at the driving frequency, and also at its harmonics, a dispersion relation may be established, supposing that the excited waves at the harmonics belong to the same type of waves. Figure 4 shows that the phase and therefore also the k values increase, within the precision of the measurements, linearly with frequency, thus indicating a dispersion relation of the form $\omega = v_{ph}k$.

The phase velocity is found to be of the order of 2×10^7 cm/sec. Figure 5 shows that this phase velocity stays constant throughout the scrape-off layer. The phase velocity of the wave in the sidebands is found to be on the order of 10^5 cm/s, the same as the phase velocity of the low-frequency fluctuations.

Correlation techniques have also been applied to the rf current and the detected potential fluctuations. Potential and rf current fluctuations were found to be out of phase at the driving frequency and its harmonics. A change in phase is observed at the antenna location.

In TCA, as in other tokamaks, high-level low-frequency fluctuations are seen in the scrape-off layer. Beside the fact that the antenna excites electrostatic waves, it is of interest whether low frequency waves are influenced by the presence of rf power. The autospectrum of a probe in the ion saturation mode is shown in Fig. 6. During the rf phase, the frequency behaviour is similar to that observed during the OH phase. In both cases the coherence can be as high as 0.8 (Fig. 7). The calculated phases are shown in Fig. 8. During the OH and rf phase, the phases increase approximately linearly with frequency. However, the direction of wave propagation reversed during Alfvén wave heating. Figure 9 shows the phase velocity as a function of the probe position within the boundary layer. The velocity during OH remains rather constant. At 5 mm behind the limiter position, measurements indicate that the phase velocity may be reversed outside the limiter position as observed in other tokamaks[3]. During Alfvén wave heating the localized reversal of the

direction of wave propagation is found to be accompanied by a broadening of the k spectrum S(k). The spectral index α ($S(k) \sim k^{-\alpha}$) drops in the region of reversal from values between 2 and 3 down to about 1.

III. CONCLUSION. The present study shows that the antenna used for auxiliary heating excites electrostatic waves in the scrape-off layer. At present state identification of the launched wave has not been possible. Also the wave excitation mechanism and possible nonlinear processes have to be studied in future. Low frequency fluctuations are strongly affected by the rf. The high level spikes found on the potential fluctuations may play a key role in antenna-plasma interaction, for example in impurity generation.

Acknowledgement. We wish to thank the whole TCA team for their excellent support. Also, the great encouragement from Professor F. Troyon is highly recognized. The present work was partially supported by the Swiss National Science Foundation.

References

[1] S.J. Zweben and R.J. Taylor, Nucl. Fusion 23 (1983) 513.
[2] S.J. Zweben and R.W. Gould, Nucl. Fusion 23 (1983) 1625.
[3] Ch. Ritz et al., Phys. Fluids 27 (1984) 2957.
[4] A. de Chambrier et al., J. Nucl. Mat. 128 & 129 (1984) 310.
[5] D.E. Smith et al., IEEE Plasma Science PS-2 (1974) 261.

Figure Captions

Fig. 1 a) Rf current fluctuations

Fig. 1 b) Floating potential fluctuations

Fig. 2 Autospectrum of rf current

Fig. 3 Coherence

Fig. 4 Phase

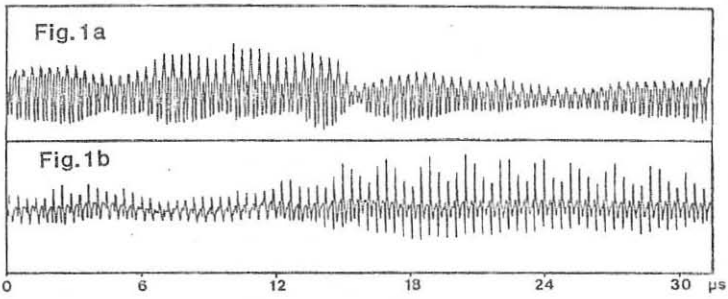
Fig. 5 Phase velocity in function of the probe position in the scrape-off layer

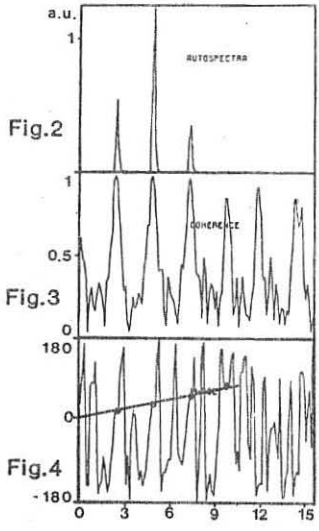
Fig. 6 Autospectrum of ion saturation current

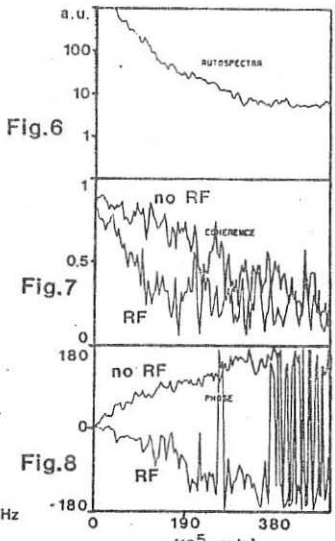
Fig. 7 Coherence during OH and rf heating

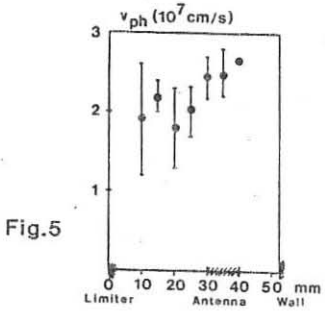
Fig. 8 Phase during OH and rf heating

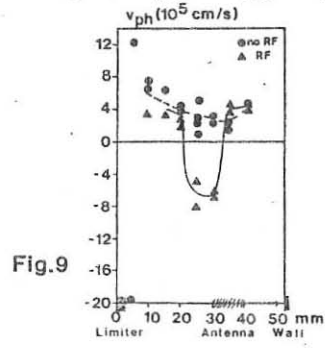
Fig. 9 Phase velocity in function of the probe position during OH and rf heating


Fig.1a
Fig.1b
0
6
12
18
24
30 µs


a.u.
1
AUTOSPECTRA
Fig.2
1
0.5
0
COHERENCE
Fig.3
180
0
-180
Fig.4
0 3 6 9 12 15 MHz


a.u.
100
10
1
AUTOSPECTRA
Fig.6
1
0.5
0
no RF
COHERENCE
RF
Fig.7
180
0
-180
no RF
PHASE
RF
Fig.8
0 190 380 kHz


v_ph (10^7 cm/s)
3
2
1
Fig.5
0 10 20 30 40 50 mm
Limiter
Antenna
Wall


v_ph (10^5 cm/s)
12
8
4
0
-4
-8
-12
-16
-20
no RF
RF
Fig.9
0 10 20 30 40 50 mm
Limiter
Antenna
Wall

CONTROL OF PLASMA IMPURITIES BY MEANS OF EXTERNAL FORCES

V.P.Sidorov, V.P.Minenko

I.N.Vekua Institute of Physics and Technology, USSR

Plasma heating with neutral beams and HF waves is accompanied by nonequal absorption of momentum by different plasma components and thus, has various effects on their diffusion. In a number of theoretical [1,2,3] and experimental [4,5] works this effect is considered as a means for cleaning the plasma from impurities. These theoretical studies are based on the concept, that no toroidal viscosity and convective diffusion are present which does not agree with recent measurements of anomalous damping of the plasma toroidal rotation [6,7] and fast penetration of impurities [9]. Existence of an anomalous toroidal viscosity of electrons has been founded theoretically in Ref.[8].

In absence of the toroidal viscosity in plasma the only cause of the toroidal rotation stopping are collisions both with trapped and neutral particles. If the collisions are rare enough, even the smallest longitudinal force applied to the one of the plasma components excites a considerable longitudinal current of this component which being combined with the toroidal drift, would change considerably its neoclassical diffusion flux. Taking into account the anomalous viscosity and convection leads to the essential revision of the energy balance.

Let us write down in conventional notations the equation of motion of the sth plasma component:

$$m_s n_s \frac{d\vec{v}_s}{dt} = -\nabla p_s - \nabla \overleftrightarrow{\pi}_s + e_s n_s (\vec{E} + \frac{1}{c}[\vec{v}_s, \vec{B}]) + \vec{R}_{Ts} + \sum m_{ss'} n_s \nu_{ss'} (\vec{v}_{s'} - \vec{v}_s) - \frac{m_s n_s \vec{v}_s}{t_s} + \vec{f}_s , \qquad (1)$$

where $\vec{R}_{Ts}$ is the thermoforce, $m_s n_s \vec{v}_s / t_s$ is the force of friction whith the trapped and neutral particles, $\vec{f}_s$ is the dragging force applied to the s-component by a beam or HF wave. Designating:

$$e_s n_s \vec{v}_s = \vec{j}_s; \quad -\nabla p_s - \nabla \overleftrightarrow{\pi}_s + e_s n_s \vec{E} + \vec{R}_{Ts} - m_s n_s d\vec{v}_s/dt + \vec{f}_s = \vec{G}_s, \tag{2}$$

one obtains

$$\frac{1}{c}[\vec{j}_s, \vec{B}] - \frac{m_s}{e_s t_s} \vec{j}_s + \sum m_{ss'} \left(\frac{\nu_{s's}}{e_{s'}} \vec{j}_{s'} - \frac{\nu_{ss'}}{e_s} \vec{j}_s \right) + \vec{G}_s = 0. \tag{3}$$

Rewriting this expression as

$$\frac{1}{c}[\vec{j}_s, \vec{B}] = \sum \alpha_{ss'} \vec{j}_{s'} - \vec{G}_s \quad , \tag{4}$$

we find that

$$\vec{j}_s = \gamma_s \vec{B} + \frac{c}{B^2}[\vec{G}_s, \vec{B}] + \frac{c^2}{B^2} \sum \alpha_{ss'} \vec{G}_{s'} - \frac{c^2}{B^2} \sum \alpha_{ss'} \alpha_{s's''} \vec{j}_{s''} \quad . \tag{5}$$

Since $(c^2/B^2)\alpha_{ss'}\alpha_{s's''} \sim (m^2c^2/e^2B^2)\nu^2 = \nu^2/\omega_B^2 \ll 1$, then

$$\vec{j}_s \approx \gamma_s \vec{B} + \frac{c}{B}\left\{ [\vec{G}_s, \vec{b}] + \frac{1}{\omega_s t_s} \vec{G}_s + \sum \left(\frac{m_{ss'}\nu_{ss'}}{m_s \omega_s} \vec{G}_s - \frac{m_{ss'}\nu_{s's}}{m_{s'}\omega_{s'}} \vec{G}_{s'} \right) \right\}, \tag{6}$$

where $\omega_s = e_s B/m_s c$. Summing up over s in Eqs. (3) and (6), we get

$$\vec{j} = \gamma \vec{B} + \frac{c}{B}\left\{ [\vec{G}, \vec{b}] + \sum \frac{\vec{G}_s}{\omega_s t_s} \right\}, \quad \frac{1}{c}[\vec{j}, \vec{B}] - \sum \frac{m_s}{e_s t_s} \vec{j}_s + \vec{G} = 0 \, . \tag{7}$$

In view of Refs. [6-8] we consider the case when the plasma motion as a whole and its total current are to a greater extent defined by its viscosity than by collisions with trapped and neutral particles. Then

$$\sum \vec{G}_s/\omega_s t_s \qquad \text{and} \qquad \sum m_s \vec{j}_s / e_s t_s \qquad (\omega_s t_s \gg 1)$$

may be omitted in Eq. (7), and the tangential to the magnetic surface component of the vector $\vec{G}$ becomes negligible: $\vec{G}_\tau \approx 0$. Summing up Eq. (2) over s, it can be easily seen that in this case

$$(\nabla \overleftrightarrow{\pi})_\tau \approx \vec{f}_\tau \, . \tag{8}$$

Since the viscosity tensor is linear in velocities, it may be devided into two parts: $\overleftrightarrow{\pi}^\circ$, corresponding to the case when external forces are absent, and $\overleftrightarrow{\pi}^* = \overleftrightarrow{\pi} - \overleftrightarrow{\pi}^\circ$, so that

$$(\nabla \overleftrightarrow{\pi}^\circ)_\tau = 0, \qquad (\nabla \overleftrightarrow{\pi}^*)_\tau = \vec{f}_\tau \, . \tag{9}$$

Let us denote

$$\frac{c}{B}\left\{ \frac{1}{\omega_s t_s} G_{s\psi} + \sum \left(\frac{m_{ss'}\nu_{ss'}}{m_s \omega_s} G_{s\psi} - \frac{m_{ss'}\nu_{s's}}{m_{s'}\omega_{s'}} G_{s'\psi} \right) \right\} = j_{s\psi}^{cl}. \tag{10}$$

It can be easily seen from Eq. (2) that the main contribu-

tion in Eq.(10) is due to the terms containing the products of the collision frequencies and the pressure gradients of plasma components; therefore, Eq.(10) is actually the classical diffusion flux. Further, let us introduce:

$$j_{s\psi}^{neo}=\left[R_{Ts\chi}+e_s n_s E_\chi-\frac{c}{B}(\nabla\overleftrightarrow{\Pi}_s^{\circ})_\chi-(m_s n_s\frac{d\vec{v}_s}{dt})_\chi\right]b_\zeta- \tag{11}$$
$$\left[R_{Ts\zeta}+e_s n_s E_\zeta-\frac{c}{B}(\nabla\overleftrightarrow{\Pi}_s^{\circ})_\zeta\right]b_\chi .$$

This expression defines the neoclassical diffusion flux, the main contribution to it being due to the term $e_s n_s E_\chi b_\zeta$.

Taking into account Eqs.(10) and (11), let us write down on the basis of Eq.(6):

$$j_{s\psi}=j_{s\psi}^{cl}+j_{s\psi}^{neo}+\frac{c}{B}\left[(\vec{f}_s-\nabla\overleftrightarrow{\Pi}_s^{*}),\vec{b}\right]_\psi . \tag{12}$$

By means of an auxiliary tensor $\overleftrightarrow{\mu}_s$ the relation between the viscosity of the sth component and the total plasma viscosity can be expressed as:

$$\nabla\overleftrightarrow{\Pi}_s^{*}=\overleftrightarrow{\mu}_s\nabla\overleftrightarrow{\Pi}^{*}=-\overleftrightarrow{\mu}_s\vec{f} . \tag{13}$$

Then, Eq.(12) takes the form:

$$j_{s\psi}=j_{s\psi}^{cl}+j_{s\psi}^{neo}+\frac{c}{B}\left[(\vec{f}_s-\overleftrightarrow{\mu}_s\vec{f}),\vec{b}\right]_\psi . \tag{14}$$

The first two terms here represent the diffusion current in the absence of external forces and we denote their sum as $j_{s\psi}^{dif}$; henceforth, the quantity $e_s^{-1}\cdot j_{s\psi}^{dif}$ will represent the real diffusion flux $\Gamma_{s\psi}$ when no external forces are present. Therefore, we can write down instead of Eq.(14):

$$j_{s\psi}=e_s\Gamma_{s\psi}+\frac{c}{B}\left[(\vec{f}_s-\overleftrightarrow{\mu}_s\vec{f}),\vec{b}\right]_\psi . \tag{15}$$

The expression obtained implies that viscosity plays an exceptional role in controlling the plasma components radial fluxes due to external forces. In particular, it follows from Eq. (15) that longitudinal forces can appreciably affect the diffusion only in the case of an essentially nondiagonal tensor $\overleftrightarrow{\mu}_s$, while for transverse forces this condition is nonsignificant. Putting in accordance with Eq.(9) $\Gamma_{s\psi}\sim n_s v_{s\psi}^{A}$, where v^A is the velocity of the anomal diffusion flux due to the turbulent con-

vection, and using the simplest relation $\vec{f} = Q/\vec{v}_{ph}$ (v_{ph} is the wave phase velocity or the beam velocity), it is not difficult to see that the impurities control requires much more energy expenses than it follows from Refs. [1,2].

REFERENCES

1. P.B.Parks, K.H.Burrell, S.K.Wong. Nucl. Fusion 20, (1980) 27.
2. K.H.Burrell. Phys. Fluids 23, No.8 (1980).
3. S.P.Hirshman, D.J.Sigmar. Neoclassical Transport of Impurities in Tokamak Plasmas. Preprint ORNL/TM-7583 (1981). Oak Ridge.
4. K.H.Burrell, J.C.Deboo, E.S,Ensberg et al. Phys. Rev. Lett. 41, 1760(E), (1978).
5. R.A.Demirkhanov, A.G.Kirov, L.F.Ruchko, A.V.Sukachov. Pis'ma v ZhETF, 37, No.8 (1983) 381.
6. S.Suckewer, H.P.Eubank, R.J.Goldstone et al. Nucl. Fusion 21, (1981) 1301.
7. K.Brau, M.Bitter, R.J.Goldstone et al. Nucl. Fusion 23, (1983) 1643.
8. B.B.Kadomtsev, D.Kh.Morokhov, O,P.Pogutse. Pis'ma v ZhETF 40, No.2 (1984) 80.
9. C.Breton, A.La Fontaine. Preprint Fontenay-aux-Roses. EUR-CEA-FC-1159 (1982).

EDGE PLASMA EFFECTS DURING RF-HEATING IN T-10 MEASURED BY ACTIVE AND PASSIVE PROBES

D. Hildebrandt, H. Grote, A. Herrmann, M. Laux, P. Pech, H.-D. Reiner, H. Strusny, H. Wolff

Academy of Sciences of the GDR, Central Institute of Electron Physics, 1086 Berlin, GDR

E. Kotai, A. Manuaba, F. Paszti

Hungarian Academy of Sciences, Central Research Institute for Physics, Budapest, Hungary

General results of effects caused by both, electron cyclotron resonance heating (ECRH) and heating in the ion cyclotron range of frequency (ICRH) in the edge plasma of T-10 are presented. The edge plasma density n_i and the electron temperature T_e were monitored by Langmuir double probes. In order to check the results from the electrical probe measurements the deposition probe technique has also been applied. This method gives further information on the ion energy and impurity fluxes in the edge plasma.

Experimental

The measurements were performed in a wide range of plasma parameters and different limiter configurations.

Main parameters were: plasma current between 200 and 400 kA, line averaged density between 1.10^{19} and 5.10^{19} m^{-3}, toroidal field between 2,4 and 2,8 T at ICRH and between 2,8 and 3,4 T at ECRH.

The general results described here have been found in all regimes.

ICRH /1/ was mainly applied in the minority regime with small additions of ^{1}H and sometimes ^{22}Ne to the bulk ions ^{2}D. An ICRH-power up to 400 kW was launched by different antennae. ECRH /2/ was done in the first harmonic regime. An ECRH-power up to 1 MW was guided to the plasma through 6 wave guides from the low field side.

Two Langmuir probes were installed at different poloidal positions, giving the possibility to detect movements of the plasma column.
Papyex and silicon collectors were used with the deposition probe.

Results

ECRH and ICRH affect the edge plasma of T-10 in different ways.

ECRH

- A general observation in discharges with ECRH is an increase of the edge plasma density n_i during the heated phase while the electron temperature T_e changes weakly.
- Two different characteristic temporal evolutions (A + B) of n_i during the heated phase were found.
  A) n_i increases as soon as the heating pulse is switched on, then the density remains approximately constant throughout the duration of the heating pulse and decreases at its end within the time resolution (10 ms) (fig. 1a).
  B) n_i increases at the beginning of the ECRH-pulse and decays already during the heating phase (fig. 1b).
- In regimes with the temporal evolution of n_i shown in fig. 1a the relative change of n_i depends on the injected heating power (fig. 2) but does not depend on the line averaged plasma density and the minor radius of the probe position (fig. 3).
- λ_n and T_e in fig. 3 indicate that diffusion processes in the edge plasma are not significantly changed by the heating pulse.
- Deposition probe measurements do neither indicate any change of the ion energy nor a significant enhanced impurity production during these ECRH-regimes /3/.

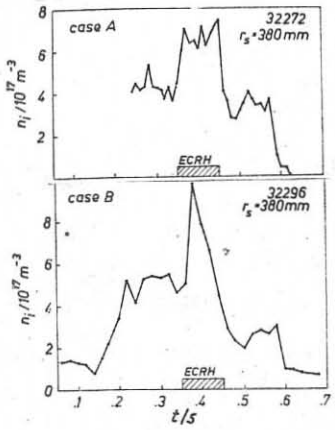


Fig. 1

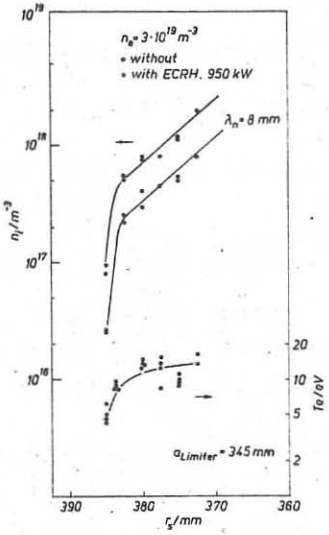


Fig. 3

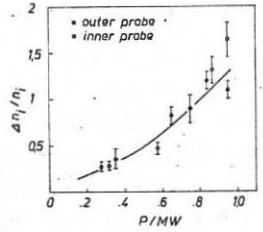


Fig. 2

ICRH

- A general observation of Langmuir probe measurements is an increase of the electron temperature T_e during ICRH-pulses while n_i does not show a definite behaviour (fig. 4).
- Deposition probe measurements indicate an increase of the impact energy of the ions of deuterium and also additional impurity fluxes of oxygen and iron during the ICR-heated phase (fig. 5). (In fig. 5 the deposited amount of deuterium is a measure of the ion energy.)
- Intensified desorption of the fueling gas (deuterium) was observed when ^{22}Ne was added and heated (fig. 6).

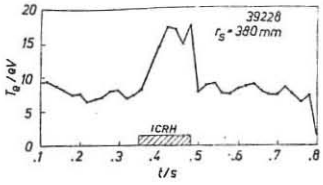


Fig. 4

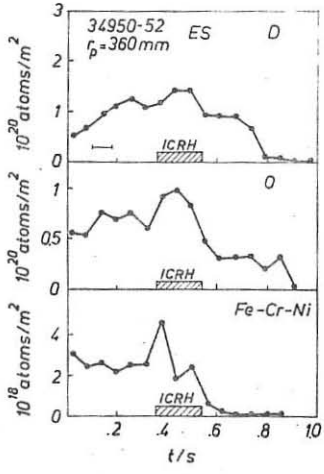


Fig. 5

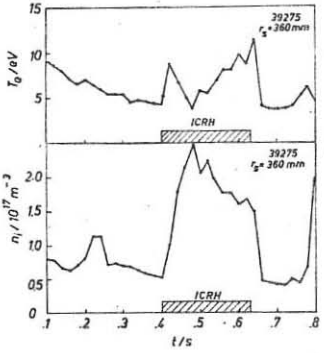


Fig. 6

Conclusions

- ECR-heating is accompanied by an increase of the edge plasma density which can be attributed to enhanced radial transport of main plasma (case A) and also to release of gas from the wall and limiters (case B) due to absorption of a part of the rf power on these structures.
  Diffusion processes in the edge plasma and impurity production seem to be hardly changed in regimes in which gas desorption during ECRH is negligible.
- During ICR-heating of the plasma of T-10 a part of the rf power is absorbed in the edge plasma. Due to an increase of the edge plasma temperature plasma surface interaction processes are intensified.

Literature

/1/ V.V. Alikajev, this conference

/2/ T-10 group, 4th Int. Symp. on Heating in Toroidal Plasmas, Rome 1984

/3/ D. Hildebrandt et al., to be published

DEPOSITION PROBE MEASUREMENTS OF IMPURITIES INJECTED INTO A TOKAMAK PLASMA

D. Hildebrandt, H. Grote, A. Herrmann, M. Laux, P. Pech, H.-D. Reiner, H. Wolff

Academy of Sciences of the GDR, Central Institute of Electron Physics, 1086 Berlin, GDR

S.M. Egorov, B.V. Kuteev, V.Y. Sergeev

M.I. Kalinin Polytechnical Institute, Leningrad, USSR

Impurity diffusion from the core plasma into the scrape-off plasma has been studied by the simultaneous application of the techniques of pellet injection /1/ and deposition probe /2/. This offers the following advantages:

- Impurities of preselectable kind and quantity can be introduced into the core plasma at a chosen time.
- The efflux of the injected impurities from the core plasma can be determined irrespective of the excitation level of the particles.

Experimental

The geometrical arrangement of the experiments done in T-10 is shown in fig. 1.

Pellets of LiH and KCl were injected with a speed of 100 ms^{-1} and ablated on their path through the plasma mainly on minor radii between 250 mm and 200 mm.

The flux of alkali metal atoms has been detected in both toroidal directions by the WASA-probe on minor radii between 340 mm and 370 mm with a time resolution of 20 ms and 80 ms. Both, the fixed aperture limiter on a small radius of 325 mm and the movable rail limiter are made of graphite. In most experiments the movable limiter was positioned on minor radii between 280 mm and 300 mm.

About 30 measurements were carried out in deuterium discharges with plasma currents between 150 kA and 370 kA.

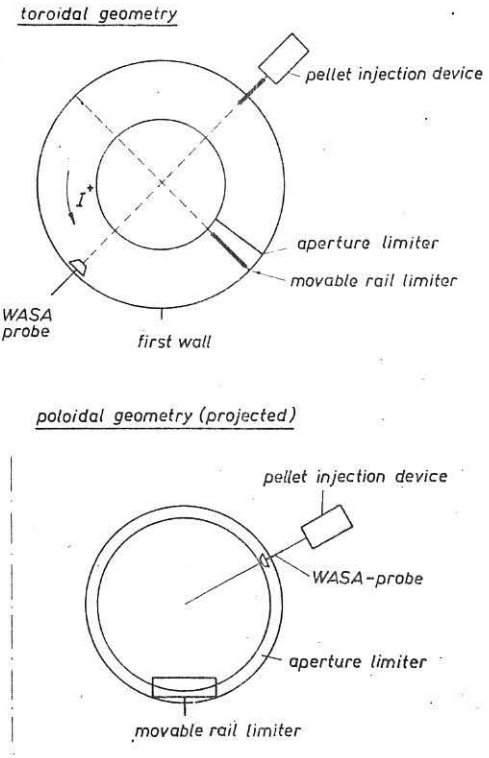


Fig. 1: Location of the limiter structures, the device for pellet injection and the WASA-probe in T-10

Results

- In contrast to earlier measurements with intrinsic impurities /3/ the flux of the injected impurities shows a similar temporal evolution in both directions parallel and antiparallel to the toroidal field in quiete plasma discharges (see fig. 2).

- In most experiments the efflux of the injected impurity from the core plasma decays exponentially (see fig. 2). The particle confinement times derived are in the order of 100 ms and are in accordance with x-ray measurements /4/.

  More systematic measurements are necessary to correlate the impurity confinement with definite discharge regimes.

- At events of strong plasma disturbance and intensified plasma wall interaction additional fluxes from the wall (recycling) can give a significant contribution to the detected particle fluxes (fig. 3).

  A characteristic feature at such events is the simultaneous occurrence of anisotropic fluxes of the injected impurity and the wall component iron (see fig. 3).

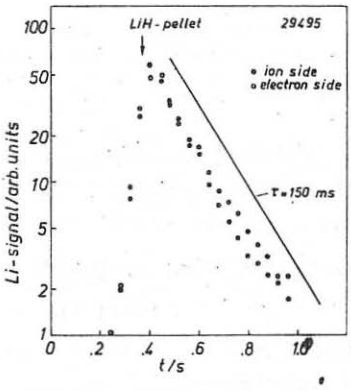


Fig. 2:
Time resolved flux of injected Li in the toroidal directions measured by the deposition probe

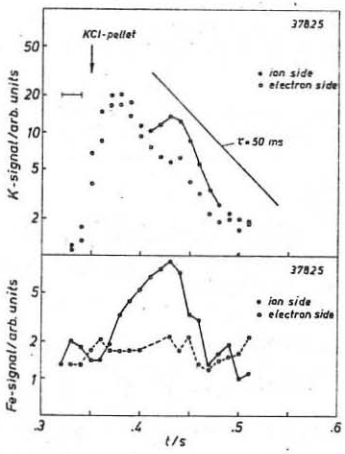


Fig. 3:
Time resolved fluxes of injected K and the intrinsic Fe showing their enhancement in ion side direction at a time of about 0.45 s

Conclusions

- The combination of both techniques pellet injection and deposition probe measurements is an appropriate method to investigate the impurity efflux from the core plasma.
- Particle fluxes from the wall (recycling) give rise to problems in these measurements only at intensive plasma wall interaction. The detection of enhanced impurity fluxes in one of the toroidal directions can be used as an indication of such events.

Acknowledgement

The authors would like to thank the T-10 team of the Kurchatov Institute, Moscow, for support and for the possibility to carry out these investigations. The authors are also grateful to Mrs. G. Ziegenhagen for helpful support in these experiments.

Literature

/1/ Egorov, S.M., et al. in: Controlled Fusion and Plasma Physics (Proc. 10th European Conf., Moscow 1981), Vol. 1, paper A-3b

/2/ Chicherov, V.M., et al., Contr. Plasma Phys. 22 (1982) 207

/3/ Wolff, H., et al., J. Nucl. Mater. 128/129 (1984) 219

/4/ Bagdasarov, A.A., et al. in: Proc. 10th Int. Conf. on Plasma Physics and Controlled Nuclear Fusion Research, London 1984, paper A III 4

Wall Material Deposition on the Limiters of Several European Tokamaks

A.P. Martinelli, R. Behrisch, and W. Englert
Max-Planck-Institut für Plasmaphysik, EURATOM Association,
D-8046 Garching/München, FRG

Abstract: On each limiter material analyzed it was found that the wall materials Fe, Ni, Cr, Ti, mostly together with D, O, Cl, and other impurities, are deposited in quantities of up to 10^{22} atoms/m^2. Their spatial distribution is analyzed and compared for the different machines.

In a collaborative effort with other European laboratories a number of small samples were cut from representative positions of the carbon limiters of TFR /1/, ASDEX /2/, and JET /3/, and of the Be limiter of UNITOR /4/ after six months to one year of exposure to plasma. They were analyzed mainly by Rutherford Backscattering Spectroscopy (RBS), Proton Induced X-Ray Emission (PIXE), and Scanning Electron Microscopy (SEM) for foreign atom deposition; and by the $^3He(D,p)^4He$ nuclear reaction to determine the deuterium content.

On the basis of the above measurements performed at Garching, any discussion and results characteristic of each single machine being left to specific reports, the following general observations can be made here.

- On all limiters investigated, foreign atoms, mainly Fe, Cr, Ni and O corresponding to the material composition of the vessel walls were found at coverages of 10^{20} to 10^{22} atoms/m^2, together with other impurities such as Ti, Mo, Sn, Cl, K, and Ca, which are specific to some machines and the cleaning procedures used.

- Only a fraction of the wall material is found to be distributed almost uniformly along the limiter surface and may reach a depth of up to a few /um.

- The greater part of materials deposited is in the form of very small droplets a few hundred nm in diameter which are mainly found at holes or grooves. They are presumably formed by agglomeration.

- In addition, large droplets with diameters of up to 100 /um are observed, which are presumably deposited during unstable plasma discharges. These large droplets appear to be partially eroded in regions of higher plasma exposure, partially covered by matrix material (C or Be) in regions of lower plasma exposure.

- The lateral distribution of the metals generally shows a maximum on the sides of the limiter, and two minima on the ion and electron drift sides close to the plasma, which indicates stronger erosion at these positions.

- The deuterium concentration measured in the surface layers of the graphite limiters shows variations of up to two orders of magnitude. This is most likely to be ascribed to temperature excursions.

- It appears that the limiters analyzed, after exposure to 500-1500 plasma discharges, are in a "quasi-steady state", where they influence the plasma with their impurities, but still behave as if made of just the matrix material (C or Be), owing to the high coverage of foreign atoms (up to 1000 atoms/cm^2) on the one hand, and to their non-uniform distribution on the other.

As an example, Fig. 1 shows results of PIXE analysis performed on the TFR limiter (analysis ion beam cross-section 1 mm^2). The sharp peak of Ni (and Cr) at position 52 mm, ion drift side, is caused by a droplet of Inconel about 200 µm in diameter (SEM analysis), coming either from the Inconel shield of the ICRH antenna or from the Inconel wall of the vacuum chamber, probably following a disruptive discharge. This droplet is visible in the center of Fig. 2 amid smaller Inconel droplets. Away from this spot, SEM analysis yields the same composition as yielded by PIXE analysis at near spots (Fig. 1), where Fe, as stainless-steel component, dominates, most probably originating from the four stainless-steel guard rings around the vacuum chamber.

As a second example, the RBS and PIXE analysis results on one of the two UNITOR Be limiters are shown in Fig. 3. Along with a uniform distribution (a few monolayers) of Fe, Ni, Cr, Sn, a particular topography in some regions is evidenced by SEM. In Fig. 4 two droplets about 30 µm in diameter are shown, the lower being of stainless steel, the higher most probably being of Be. The small droplets about 2 µm in diameter are probably of Be as well.

Acknowledgements:

The authors would like to thank the European teams concerned for providing the samples, and the PWW Group at Garching for their support, particularly H. Kukral for a number of SEM analyses.

References

/1/ TFR group (presented by A. Grosman) J. of Nucl. Mat. 128 & 129 (1984) 292-297

/2/ R. Behrisch, P. Boergesen, J. Ehrenberg, B.M.U. Scherzer, B.D. Sawicka, J.A. Sawicki, and the ASDEX-Team, J. Nucl. Mat. 128 & 129 (1984) 470.

/3/ J. Ehrenberg, R. Behrisch, IPP Report 9/47, June 1984

/4/ J. Hackmann and J. Uhlenbusch, J. Nucl. Mat., 128 & 129 (1984) 418-421.

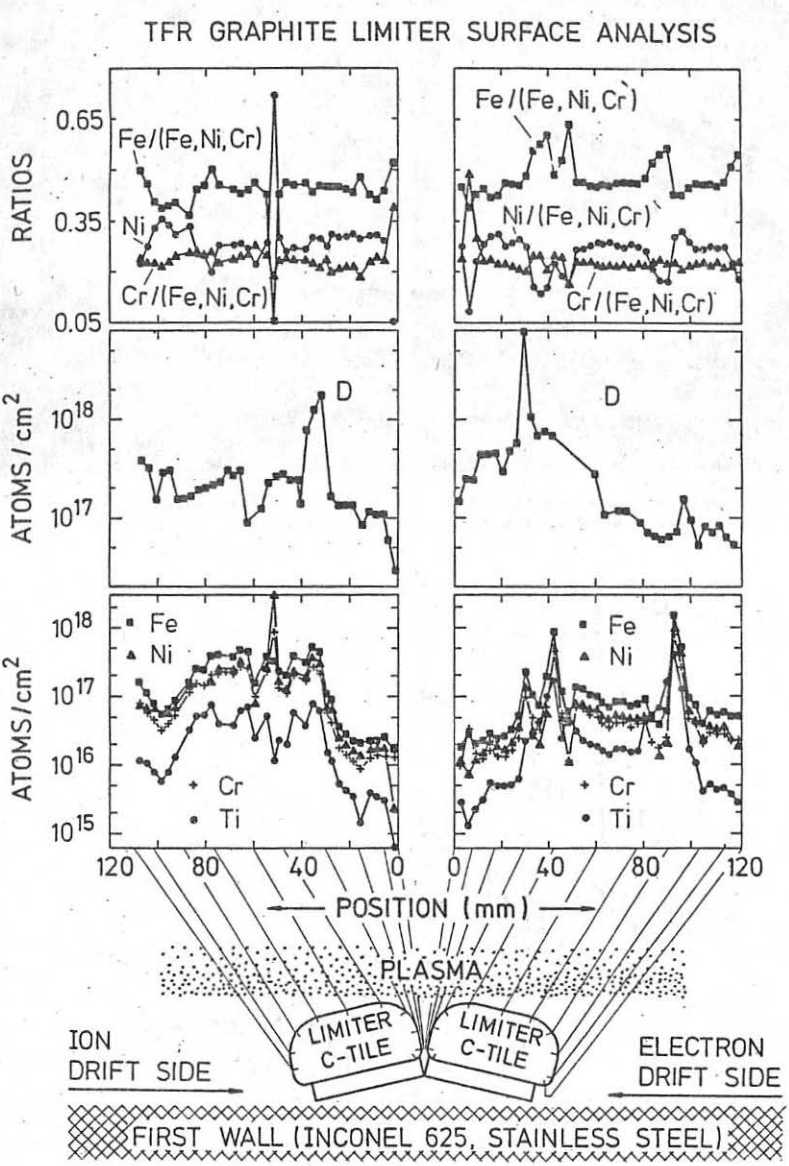


Fig.1: Surface Analysis of TFR graphite limiter

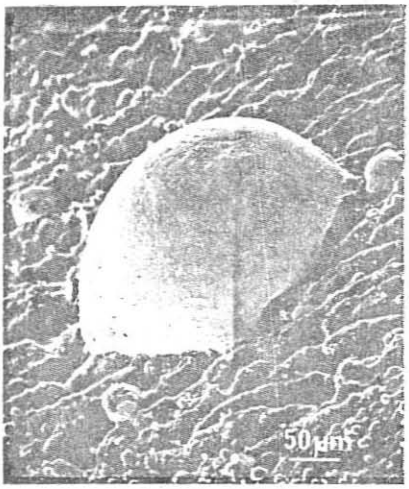


Fig.2: Surface topography of TFR limiter at position 52 mm ion side.



Fig.4: Surface topography of UNITOR Be limiter.

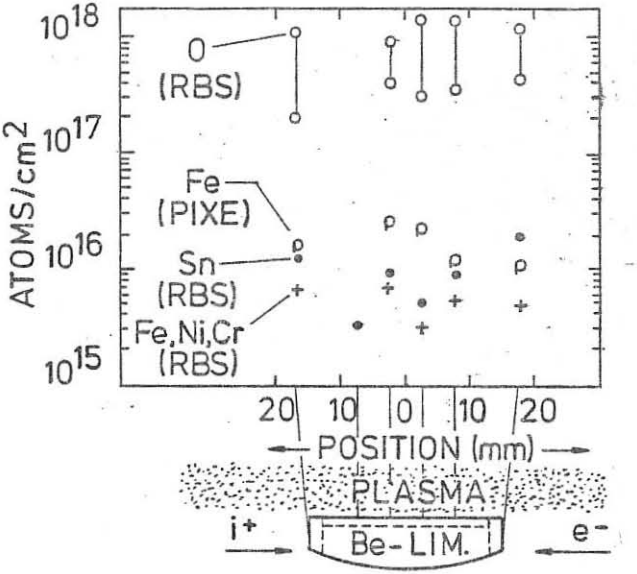


Fig.3: Surface analysis of UNITOR Be limiter.

Influence of In-Situ Carbon Deposition on the Performance of TEXTOR

J. Schlüter, E. Graffmann, L. Könen, F. Waelbroeck,
G. Waidmann, J. Winter and the TEXTOR Team

Institut für Plasmaphysik, Kernforschungsanlage Jülich GmbH,
Association EURATOM-KFA, 5170 JÜLICH, FRG

Abstract

The plasma wall interaction is strongly modified when thin layers of carbon are deposited onto all inner surfaces of the TEXTOR tokamak. Higher density limits are achievable and lower impurity levels are observed. Data demonstrating this significant change in plasma performance are presented.

Introduction

In tokamak plasmas, edge cooling by impurity radiation can reduce considerably the energy of the particles, which hit the limiter. Sputtering of high-Z material is then low and sawtoothing inside the q=1 surface stabilizes the discharge. Edge cooling is usually provided by oxygen, which is always present at the surface of the wall material and in the gaseous phase. However, the control of the oxygen concentration in the discharge is rather difficult and oxygen-dominated discharges tend often to be unstable.

With graphite limiters and first wall elements, the metal and oxygen impurities in the plasma can be substituted by carbon /1/. Another way is to deposit thin layers of carbon onto all inner metallic surfaces. This method has been developed for TEXTOR and JET /2/.

In the following, after a short description of the production of the carbon layers and their properties, the characteristics of plasmas, produced in such a carbonized surrounding, are presented.

Carbon layers

Radiofrequency assisted dc glow discharges (RG-discharge) in CH_4/D_2 mixtures are used to deposit in situ carbon layers of about .1 μ thickness onto all inner surfaces which are exposed to the tokamak plasma. The deposition process is controlled via mass spectroscopy. Typically a deposition rate of about 1 monolayer/minute (15 % CH_4 in D_2) at wall temperatures of 200 °C is used. The carbon layers produced in this way are amorphous, semitransparent, they can be extremely hard and show a good adhesion on SS and Inconel. The hydrogen content is very high. The adjustment of the H/D isotope ratio in the layer - important for Ion Cyclotron Resonance Heating (ICRH) - is achieved by isotope exchange of energetic H or D particles from RG-discharges in H_2 or D_2 or by using CD_4/D_2 mixtures. These properties have been confirmed by the investigation of samples from TEXTOR with surface analytic techniques. More details may be found in /3/.

Plasma performance

A striking result, the shift of the density limit to higher values, is demonstrated in fig. 1. Here the $\bar{n}_e$- and q-limits are compared for the cases of a (metallic) wall after careful cleaning by glow discharges and after a surface carbonization, respectively. The Murakami parameter $(\bar{n}_e R/B_T)_{max}$ was raised from 3.2 to 4.5x 10^{19} m^{-2} T^{-1}, which is at least equal to the highest

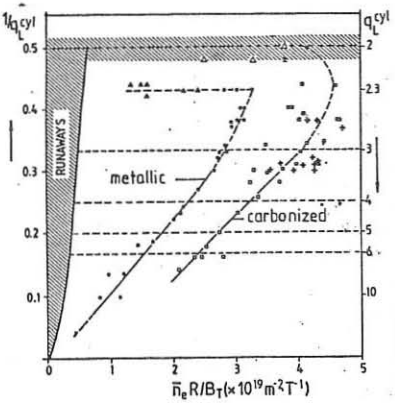


fig. 1 Operation range of TEXTOR for Ohmic heating
(R=1.75 m, a=.46 m, B_T=2T)

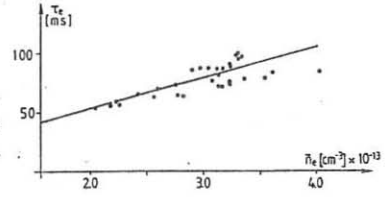


fig. 2 Global energy confinement time
• TEXTOR data
—— Goldston scaling

values obtained in well Ti-gettered devices /4/. The operational regime of TEXTOR was extended also to lower q-values down to $q_{cyl}(a) = 2$. The larger scattering of data for the carbonized wall probably reflects slightly different surface conditioning states encountered during various experimental runs.

The linear increase of the global energy confinement time τ_E with $\bar{n}_e$ continues in the high density regime which is now accessible. Values of τ_E=100 ms were registered as shown in fig. 2. The measurements agree well with Goldstons scaling law /5/.

Only after application of this conditioning technique we succeeded to launch ICRH power in the MJ level to the plasma. More than 1.3 MW ICRH power for 1 s were recently coupled without substantial increase in the impurity level /6/.

With wall carbonization, the discharges can be terminated without disruptions (soft landing), if the dI/dt-value of the current ramp-down is

wall surface	metallic	carbonized
n_e/cm^{-3}	$3x10^{13}$	$3x10^{13}$
n_C/n_e	$<.3x10^{-2}$	$1\text{-}3x10^{-2}$
n_O/n_e	$1\text{-}3x10^{-2}$	$<.25x10^{-2}$
n_{met}/n_e	$3x10^{-5}$	$<10^{-5}$

tab.1 Concentrations of carbon, oxygen and metals (Cr, Fe, Ni) measured with metallic and carbonized surfaces.

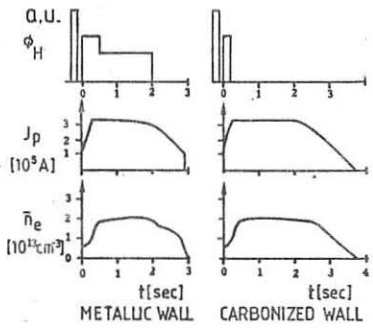


fig. 3 $\bar{n}_e$, I_p and gas feed rate ϕ_H vs time

programmed to values of about -200 kA/s. No feedback-control of the gas-feeding system is needed for this soft-landing. In fact, due to the strongly increased hydrogen recycling of carbonized walls no external gas feeding is required during the density flat-top and ramp-down phases. Fig. 3 shows the deuterium feed rates Φ_H, n_e and I_p for discharges with metallic and carbonized walls, respectively.

Impurity concentrations

Typical impurity concentrations derived from spectroscopic measurements are compared in tab. 1 for the two surface conditions. A comparison is possible only at $\bar{n}_e$ around 3 x 10^{13} cm^{-3}, because the density limit has been shown to be rather low with metallic surfaces, whereas with freshly carbonized walls the strong recycling does not allow to operate at low densities.

In general, by depositing carbon on liner and limiter, O is replaced by C as the main low-Z impurity. As long as the carbon layer persists on the limiter, metal impurities are below the detection limit of n_{met}/n_e = 1x10^{-5}. Under these conditions, $Z_{eff} \approx 1$ has been observed by conductivity measurements. From the enhancement of the continuum in the soft x-ray region, carbon concentrations even lower than 1 % or oxygen concentrations lower than .25 % have been derived, assuming only one species of low-Z impurities to be present. These numbers correspond to values of $Z_{eff} \leq 1.3$.

Parallel to the reduction of Z_{eff}, the loop voltage decreases typically from 1.3 to 1 V and the central electron temperatur from 850 to 600 eV at $\bar{n}_e$ = 3x10^{13} cm^{-3} and I_p = 330 kA.

Profile studies

Fig. 4 shows, that for a given central electron density $n_e(o)$, the n_e-profiles are broader in discharges of the C-type than in those of the O-type. T_e is reduced in the former case, but the half width of the Te-profile remains nearly unchanged.

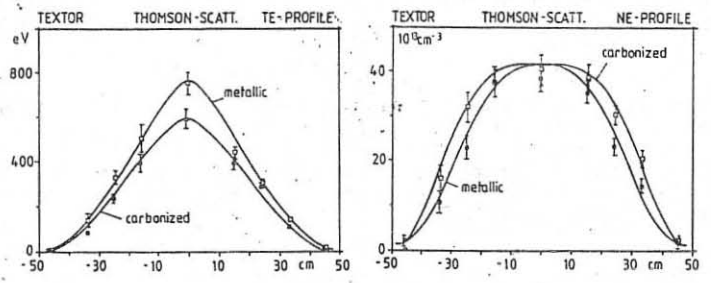


fig. 4 Radial profiles of T_e and n_e.

In C-dominated discharges (with n_O/n_e < .4 %), the T_e-profiles are practically constant during the flat-top phase of the current of about 2s, even when the C-concentration approaches 10 % (by operating in pure methane). In contrast to that, T_e-profiles contract, when the O-concentration exceeds a critical value of about 2 %. In fig. 5a, this "thermal collapse" is demonstrated by repeated radial scans of a OV-line. T_e at the maxima of the OV-intensity plots is about 45 eV. During the contraction of the plasma column the n_O/n_e rises from about 2 to 8 %, as confirmed by soft x-ray measurements. On the uppermost trace at 2 s, the disruptive termination of the discharge is recognizable. Fig. 5b

shows the stable behaviour in a C-type discharge by a similar scanning of a CV- line occurring at T_e= 130 eV.

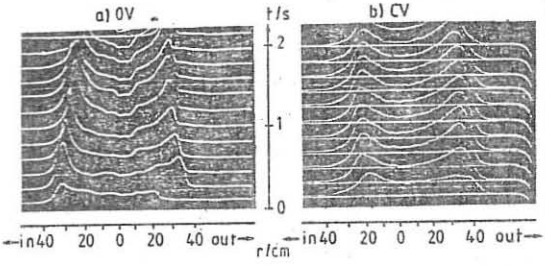


fig. 5
Radial scans of spectral lines
a) OV (2781Å) in an O-type discharge
b) CV (2271Å) in a C-type discharge.

Persistency of the carbon layer

During a series of shots following a carbonization procedure, it is observed, that the operational regime is gradually extended to lower densities, and, after a certain number of shots, the metal concentrations also gradually rise to about half the values obtained with clean metallic surfaces. We explain the first effect by a hydrogen loss from the carbon layer on the liner, the second one might result from a decarbonization of the limiters. The carbon would then be removed from the limiters with estimated rates of 10 monolayers/shot at $\bar{n}_e < 2 \times 10^{13}$ cm^{-3} and 1 monolayer/shot at $\bar{n}_e > 3 \times 10^{13}$ cm^{-3}. We cannot exclude the possibility, that at very high densities this removal rate is zero or even negative (redeposition of C). If operation at lower densities is avoided, the impurity concentration remains constant for about 100 shots (depending on the thickness of the carbon layer) at the low level measured immedeately after a carbonization. In contrast to metal film gettering, the carbon layers can be removed by prolonged RG-discharges in pure hydrogen. Uncontrolled build-up of thick deposits is avoided.

CONCLUSION

The method of depositing carbon layers on the inner surface of a tokamak device proved to be as effective as Ti-gettering in achieving low Z_{eff} values in Tokamak plasmas. The residual carbon concentration provides an efficient edge-cooling. A supression of sawtoothing, as often observed in gettered devices, is avoided. The new method facilitates tokamak operation at high densities, at low q-values, and with ICRH-heating.

References

/1/ G.J. Dobrokhotov et al., Proc. 11th European Conf. on Controlled Fusion and Plasma Physics, Aachen 1983, Vol. 2, p. 369
/2/ R.F. Clausing et al., Proc. Symp. on Energy Removal and Particle Control in Fusion Devices, Princeton 1983, North-Holland Physics Publ., Amsterdam 1984, p. 249
/3/ J. Winter et al., J. of Nucl. Materials 128 & 129, (1984)841
/4/ J. Hugill, et al., Report CLM-R 239(1983)
/5/ R.J. Goldston, Plasma Physics and Contr. Fusion 26(1984)87
/6/ R.R. Weynants et al., Proc. 6th Top. Conf. on Radio Frequency Plasma Heating, Atlanta 1985

INVESTIGATION OF FILM PROTECTION ICF REACTOR FIRST WALL.

Berendeev S.A.,Kagan D.N.,Shpilrain E.E.
Institute for High Temperatures USSR Academy of Sciences
Lebo I.G., Rozanov V.B., Sklizkov G.V.
P.N.Lebedev Physical Institute USSR Academy of Sciences

In order to create thermonuclear power unit it's necessary to designe practical and competitiveness ICF reactor, which can resist the poweful influence of pulsing microexplosions products/1/. The repeated microexplosions are able to destroy unprotected walls of the reactor causing their ablation, fatique defectc and neutron damage. One of the ways to prolong lifetime of the first wall of the reactor is to cover it the liquid metai film protection /2,3/. The film of liquid lithium make it possible to protect the wall from the flow of x-rays, alpha particles and pellet debris. Appoximately 20% of the microexplosion energy is absorbed in the first wall in a layer about 50 μm thick during 1μs.

After the begining of the burning in ICF reactor the first wall is being irradiated by reflected laser light, then x-rays, then 14,1 MeV neutrons and at last by alpha particles and charged pellet debris. Irradiation by reflected laser light leads to partial evaporation of the lithium from the wall, the steam screens the surface of the film and so diminishes force of subsequent flow of alpha particles and pellet debris. The spectrum of the radiation, falling on the first wall, to a considerable extent depends on the target design and the degree of its compression ρR .

We think that a pulse of energy is deposited in the lithium with the energy attenuation coefficient μ in the form:

$$Q(x) = Q_0 \exp(-\mu x)$$

where Q_0 is the energy deposition in the surface layer of the lithium, x-axis is directed from the surface acros the lithium. We define the characteristic thermal and mechanical responce time of the energy deposition in the metal as:

$$\tau_T = (\mu^2 a)^{-1} \qquad \tau_M = (\mu c)^{-1}$$

where a is the thermal diffusivity and c is the wave velocity in the metal /2/. Deposition time τ , time τ_T and τ_M, deposition depth and energy attenuation coefficient μ are given in Table 1 for different products of microexplosion.

Because of considerable deposition depth in lithium neutrons will not exercise their influence on the thin, less 1 cm, protection film. The main influence on the film is produced by x-rays with the energy 1-10 keV and by energetic alpha particles. The shock wave of the pellet debris in the chamber may be reduced /3/.

Table 1

Products	τ, s	dep.dep., cm	τ_T, s	τ_M, s	μ, m^{-1}	Correlation
Photons	10^{-10}	10^{-5}	10^{-11}	10^{-11}	10^{8}	$\tau \simeq \tau_T \simeq \tau_M$
X-rays	10^{-11}	$(1-100)\cdot10^{-5}$	$10^{-7}-10^{-5}$	$10^{-9}-10^{-8}$	$10^{5}-10^{6}$	$\tau < \tau_M \ll \tau_T$
Neutrons	10^{-11}	~50	10^{3}	10^{-4}	~8	$\tau \ll \tau_M \ll \tau_T$
Charged particles	10^{-6}	$(2-200)\cdot10^{-5}$	$10^{-7}-10^{-5}$	$10^{-9}-10^{-8}$	$10^{5}-10^{6}$	$\tau_M \ll \tau_T < \tau$

Generally, the amplitude of the pressure pulse can be diminished by minimization of the product of the Grüneisen constant and the energy attenuation coefficient $\Gamma \cdot \mu$. The amplitude of the temperature pulse be diminished by minimization of the ratio of the energy attenuation coefficient to the specific heat at constant volume μ/c_v . For example, computer simulations show that peak tensile in the Li-film is ten times less, than such in the K -film.

From the table 1 we can see that component of microexplosion products interaction with the lithium protection film may be simulated in our installation. The laser sistems with λ_1=1,06 and λ_2 = =0,69 μm are used, hence $\tau_M \simeq \tau_T \simeq 10^{-11}+10^{-10}$ s. If the duration of the laser impuls can be varied from 10^{-8} to $5\cdot10^{-6}$ s with the output energy from 4 to 600J respectively, then the qualitative simulation is possible only for photons and charged particles. For more comlete correspondence of the influence on the film of the charged particles we propose to use the laser plasma, see fig.1. Ion composition is defined by the target material, the duration of impuls of the jet ion current depends on the duration of laser impuls and can be chosen from the time corellation in the table 1.

When the duration of the ion current is 10^{-8} – 10^{-6} s and electron density is about 10^{19} cm^{-3} on the experimental installation the speed of laser plasma front as much as 10^{7} $cm\cdot s^{-1}$ is reached, which is in a good agreement with the expected influence on the film.

For simulating of the processes on the first wall of the ICF reactor, a special stand was built in IVTAN, see fig.2. Two different regimes of functioning are possible: with a steady film of liquid lithium, and with a pouring down film. For the pumping of lithium there is designed MGD-pump, the volume of Li is controlled by MGD-spend. There are the following main components: the working vacuum chamber with a system for preparation of Li-film(1), the laser system (2), and the system of diagnostics (3-13). The vacuum chamber is designed from stainless steel in the form of cylinder 400 mm long and 300 mm in diameter, and has a system of windows for the entrance of coming radiation, thermocouples (7) and electric heater (8) of the Li-cell (9), diagnostical windows (10). The laser system consists of three glass laser: Ruby- and Nd -laser. The R.- laser has a modulated regym, the duration of impuls can be varied step by step from 10^{-8} to 10^{-6} s.

It may be use film thickness to 2 cm at various initial temperatures up to 1000°K. Stainless steel, molibden, niobium and its alloys are used for structural wall.

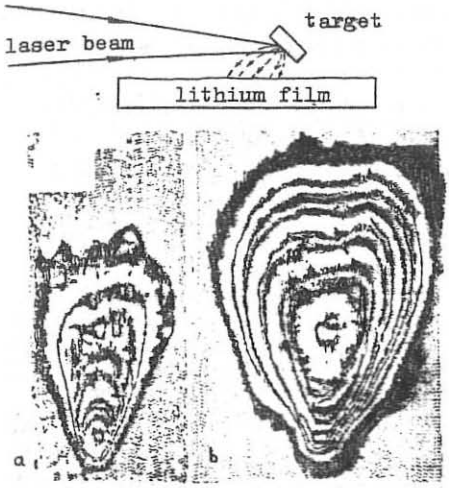


Fig.1 The simulation of charged particles interection with Li-film by laser plasma. With 200 ns delay (b after a) isodensity photo of the laser plasma

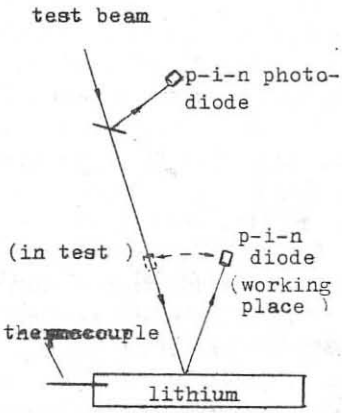


Fig.3 The scheme of the measurement of the lithium reflection coefficient.

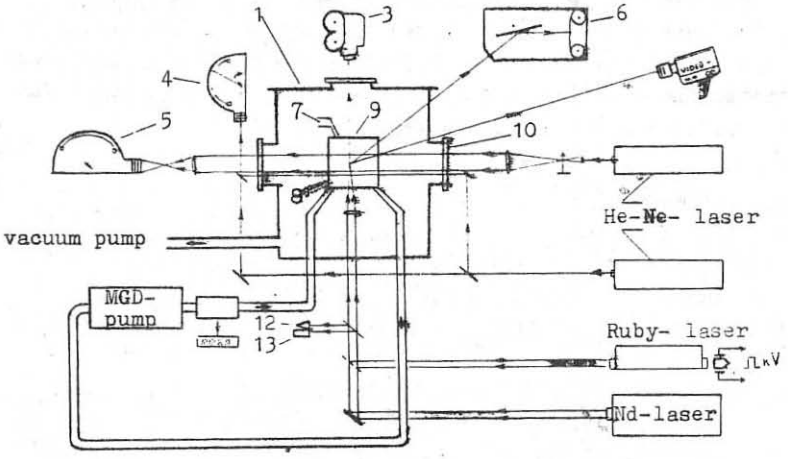


Fig.2 The scheme of the experimental installation.

The diagnostic system including Mach-Zehnder laser interferometer (5), spectroscope (6), Shliren (4) and high rapid photography (3), the laser control (12-13), video and temperature control systems. This set permits to investigate Li-plasma to density $N_e \sim 10^{20} cm^{-3}$; to determine Li-vapor expansion speed to $10^8 cm \cdot s^{-1}$, peak temperature in the heated layer and lithium reflective characteristic at different temperatures; to carry out high rapid film photography. The spatial resolution of photo system is to 10 μm. Video and high speed camera (3) allow to observe the whole picture of the film reply on the impuls of action. The working with ns-impulses was possible due the EO"Agat", with time resolution to 10 ps.

At fig.3 there is the scheme of the measurement of the reflection coefficient. So, for λ=0,63 μm and Li-temperature of 573°K, the r.c. is 94%, the angle of incidence is 30°. Such a big r.c. causes numerous photon rereflection, that is eqivalent to the increase of the impuls duration and leads to the diminishing of the amplitude of shock wave in the heated layer of the film.

The quality of the wall surface preparation is of vital importance and strongly influences the behaviour of the lithium film.

The goal of IVTAN experimental work is investigation of impulse energy influence on a liquid Li-film and the behaviour of the Li-film on various metal. Lithium flow controlled by the magnetic field is examined both theoretically and by computer simulation in addition to the experiment.

REFERENCES

1. Yu.V. Afanasiev, N.G. Basov, V.B. Rozanov et al, "Conditions in the laser fusion reactor compartment produced as a result of target microexpl", Quantum Electronics, Vol.2, N.6, p.1190-1196.

2. M.J. Monsler, J. Hovingh, D.L. Cook, T.G. Frank, G.A. Moses, " An Overview of Inertial Fusion Reactor Design", Nuclear Technology/ Fusion, 1, 302 (1981).

3. L.P. Feoctistov, G.V. Sklizkov, V.B. Rozanov, E.E. Shpilrain, D.N. Kagan, S.A. Berendeev, "State of Ingineer Problem of Laser Fusion", 2nd Ull-Union Conf. of Fusion Reactor Ing. Problem, Leningrad, 1981, vol.1, p.59-66, Leningrad, (1982).

EFFECTIVE PLASMA CHARGE IN THE TOKAMAK WITH GRAPHITE WALLS AND WITH A GRAPHITE LIMITER (TM-G)

Yu.D.Pavlov, D.P.Petrov, A.M.Solntsev, A.M.Stefanovskij, A.L.Terebkov, A.F.Shcherbak

I.V.Kurchatov Institute of Atomic Energe, Moscow, USSR

The experimentally measured values of an effective plasma charge in different discharges on TM-G /1,2/ are given in the paper. A value of Z_{eff} has been obtained by a few methods: 1) by the plasma conductivity with the account for the measured electron temperature profile, 2) by the magnitude of bremsstrahlung in a visible spectrum range, 3) by the plasma conductivity in the presence of saw-tooth oscillations, 4) by estimation of the concentration of highly-ionised carbon ions in the experiments with the laser injection of carbon, 5) by the enhancement factor of soft X-ray intensity with the use of the experimental results of laser injection.

1) and 2). The Z_{eff}-determination in TM-G by the first two methods has already been described in /1,2/. The value of Z_{eff} obtained by the first method for the regime with $I_p = 40$ kA, $\bar{n}_e = 2.4 \times 10^{13} cm^{-3}$ is within the range $1 \leq Z_{eff} \leq 1.35$. We have succeeded in the estimation of Z_{eff} by the second method only for the regime with $I_p = 60$ kA and $\bar{n}_e = 7 \times 10^{13} cm^{-3}$ due to a low Z_{eff}, small size of plasma and due to the presence of a some background. $Z_{eff} \leq 1.5$ in this regime.

3). Saw-tooth oscillations are usually connected with the development of internal MHD-instability in plasma at $q(r_s) = 1$ /3/. If $q(o) = 5B_T/\hbar R\, \sigma_o E_o \cong 1$, one can find $Z_{eff}(o)$, knowing E_o and $T_e(o)$. At the emergence of rather intensive saw-tooth oscillations in plasma, the electromagnetic probes have registered the plasma column displacements sinchronous with sawteeth. These displacements could be measured only at high densities ($\bar{n}_e \geq 6 \times 10^{13} cm^{-3}$ for $I_p = 40$ kA). For fast displacements, $\delta(\Delta r)$, of the plasma column ($\tau \sim 0.3$-0.4 ms), one can use the formulae for the plasma column displacement, Δr, within an ideal shield /4/.

Using the measured value $\delta(\Delta r)$, one can determine the contribution of the term $\Delta V_o = 10^{-9} I_p 2\pi R \delta l_i/\tau$ into the loop voltage at the axis (l_i is the internal inductance). Thus, for the regime mentioned above (in which $T_e(o) = 600 \pm 50$ eV, $V_o = 2$ V, $\delta(\Delta r) = 0.2$ mm) $\Delta V_o = 0.8$ V and $Z_{eff}(o)$ is equal to $1.12 \leq Z_{eff}(o) \leq 1.45$.

4). A run of the experiments with the injection of carbon into plasma under laser irradiation of the graphite wall has been done on TM-G /2/. At a low level of the carbon injection, the main discharge parameters (I_p, $\bar{n}_e$, V_o, P_{rad}) have not been changed. The typical oscillograms of intensity for the CV-line (2271 Å, I_{cv1} in the port through which the injection was done, I_{cv2} in opposite one along the torus) and the intensity of soft X-rays, I_{sxr}, are given in Fig.1. From these oscillograms one can determine an ionization rate (averaged over the volume) τ_{i4} for C^{+4} (from a decay time of an additional intensity ΔI_{cv} of CV-line) and life time τ_p of C^{+5} and C^{+6} ions in the central core of the plasma column (from a decay time of an additional intensity of soft X-rays, ΔI_{sxr}). One should note that only the highly-ionized ions of carbon made a contribution into the intensity of soft X-rays because a signal ΔI_{sxr} starts only after the beginning of decay ΔI_{cv} (see Fig.2 where the additional intensities of lines H_β, CII, CIII, CV, I_{sxr} are given respective to a time of injection). The concentrations, n_k, of ions C^{+k} averaged over the volume, are connected with each other by evident relationships (recombination and charge exchange are neglected): $n_4/\tau_{i4} = n_5(\tau_{i5}^{-1} + \tau_{p5}^{-1})$; $n_5/\tau_{i5} = n_6/\tau_{p6}$, where τ_{ik} is the average ionization time for the ion C^{+k} and τ_{pk} is its average life time. It has been assumed, for rough estimations, that $\tau_{p5} = \tau_{p6} = \tau_{sxr} = \tau_p$. Hence, $n_5 + n_6 = n_4\tau_p/\tau_{i4}$. The measurements show that $n_4 = 2.5\times10^{-3}\bar{n}_e$; $\tau_{i4} = 0.55$ ms; $\tau_p = 1.5$ ms in the regime with $I_p = 40$ kA and $\bar{n}_e = 2\times10^{13}$ cm^{-3}. Thus, $Z_{eff} \simeq 1.2$. The laser injection of carbon into plasma has been performed only at low plasma density. Therefore, the relationships $\tau_{i4} \sim \bar{n}_e^{-1}$ and $\tau_p \sim \bar{n}_e$ (observed in the density range at which the laser injection was performed) have been used to obtain similar estimations for a plasma with "medium" density about 7×10^{13} cm^{-3}. Thus, $Z_{eff}(o) \leq 1.4$ for this regime.

5). As carbon is practically the only impurity in the TM-G

plasma, the enhancement factor in the soft X-ray intensity can be interpreted as radiation due to carbon ions. If the main plasma parameters are not changed, it will be evident that:

$$I_{cv} = n_4 \bar{n}_e \langle \sigma v \rangle_{exc} B$$

$$\Delta I_{cv} = \Delta n_4 \bar{n}_e \langle \sigma v \rangle_{exc} B$$

$$I_{sxr} = I^p_{sxr} + I^c_{sxr} = \bar{n}_e \left[n_p f_p(T_e) + \sum_{\xi\delta} n_{ck} Z_k^2 (f_b(T_e) + f_r(T_e)) \right] \mu(T_e, \delta) A$$

$$I_{sxr} = \bar{n}_e \sum_{\xi\delta} \Delta n_{ck} Z_k^2 (f_b(T_e) + f_r(T_e)) \mu(T_e, \delta) A$$

where $\mu(T_e, \delta)$ is the characteristic function of the radiation passage through a foil with thickness δ ; I^p_{sxr}, I^c_{sxr} are the intensities of X-ray radiation for the hydrogen and carbon ions, respectively; $f_p(T_e)$ is the bremsstrahlung function for hydrogen; $f_b(T_e)$, $f_r(T_e)$ are the bremsstrahlung and recombination radiation function for carbon; Z_k is the ion charge of the k-fold ionization; B, A are some coefficients. As it has been shown in 4) $\Delta n_4/n_4 = \Delta(n_5+n_6)/(n_5+n_6)$. Then $I^c_{sxr} = \Delta I_{sxr} I_{cv} / \Delta I_{cv}$. Hence, the enhancement factor, F, is equal to: $F = (1 - \Delta I_{sxr} I^{-1}_{sxr} I_{cv} \Delta I^{-1}_{cv})^{-1}$. An average value of F in the experiments with injection (I_p = 40 kA; $\bar{n}_e$ = 2-3x10^{13}cm^{-3})has been found to be equal to $\simeq$ 1.67, that gives Z_{eff} near the axis: $1.15 \leq Z_{eff} \leq 1.2$. The intensity of a "hydrogen" part in the X-ray radiation, I^p_{sxr}, at the transition to other regimes of operation (I_p, $\bar{n}_e$) can be calculated when the electron density and temperature profiles near the plasma axis are weakly changed: $I^p_{sxr} \sim \bar{n}_e f_p(T_e) \mu(T_e, \delta)$. The values I^p_{sxr} and $Z_{eff}(o)$ have been calculated by the method given above for four discharges with the measured $T_e(o)$. The values obtained in such a way are shown in Fig.3. The dashed lines show the error bars connected with the measurements of $T_e(o)$. Z_{eff} obtained by other methods are also given in the same figure.

Thus, Z_{eff} didn't exceed 1.5 in all the TM-G discharges with the currents up to 60 kA and at $\bar{n}_e$ up to 7-8x10^{13}cm^{-3}. One should note that assumptions made in the calculations of Z_{eff} by all the methods should result in an increase in Z_{eff}. One should also emphasize that the plasma parameters have no time to reach their stationary values (especially, at high plasma density) during the discharge, that follows from the line intensity of the ions of carbon and from the power of radiation loss. Therefore, the value of Z_{eff} should probably be somewhat higher than

that given in the paper at a longer discharge duration.

REFERENCES

1. Dobrokhotov, E.I., et al. Proc. of 9th Int. Conf. on Pl. Ph. Cont. Nuc. Fus., Baltimore, 1982, v.3, p.229.
2. Dobrokhotov, E.I., et al. 11th Europ. Conf. on Contr. Fus. and Pl. Phys., Aachen, 1983, v.7D, part 2, p.369.
3. Kadomtsev, B.B. Fizika plasy, 1975, v.1, p.710.
4. Shafranov, V.D. Voprosy teorii plazmy, Moscow, 1963, Issue 2.

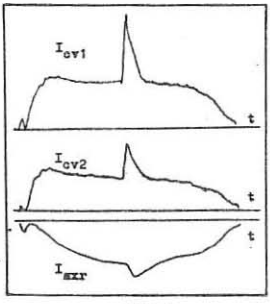


Fig. 1

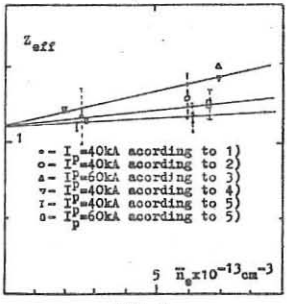


Fig. 3

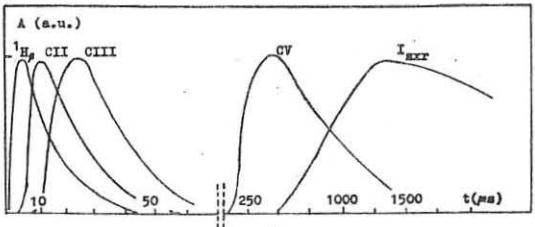


Fig. 2

Effects of Heavy Ion Bombardment Induced Damage on Surface Deformation and Re-emission Characteristics of Aluminium under High Energetic He Irradiation

N.T.My, G.Mezey, A.Manuaba, F.Pászti, L.Pogány, E.Kótai, M.Fried
L.Pócs

Central Research Institut for Physics
H-1525 Budapest, P.O.Box 49, Hungary

Introduction

The (d,t) reactions in future controlled thermonuclear reactors will produce 14,1 MeV neutrons and 3.52 MeV He. The neutrons and a small fraction of α particles will leave the plasma with their full energy and impact directly the wall of vacuum vessel. These α particles can cause surface modification such as blistering, exfoliation and plaking. The neutrons, on the other hand, produce heavy cascade damage in the bulk material. The simultaneous irradiation of these particles can be expected to give synergetic effects [1]. The effect of neutron impact can be simulated by heavy ion bombardment [2]. This paper presents the results on the effects of Ne^+ bombardment to surface modification and gas re-emission behaviour of Al under high dose He^+ bombardment.

Experimental

Al foil of thickness 21 μm (Goodfellow Metals) was first implanted with 1000 keV Ne^+ ions to a dose 1.1×10^{17} ion/cm^2 in the vacuum chamber of $\sim 7 \times 10^{-5}$ pa. In the same chamber the virgin sample as well as the pre-implanted one were bombarded with 3385 keV He^+ beam through an Al foil of 12.26 μm put very close to the sample. The He energy and the thickness of the foil were chosen so that the He profile overlapped the damaged region induced by Ne implantation at depth of 1.3 μm. During irradiation the current density was kept at $\sim 1.0 \times 10^{13}$ ions cm^{-2}sec^{-1} to prevent the beam heat effect. While the helium depth profiles for different implanted doses were measured in situ by 3 MeV proton RBS analysis. After irradiation the implanted spot was subjected to JEOL-JSM 35 type scanning electronmicroscope.

Results

Helium depth profiles in the virgin and pre-implanted samples for different doses are shown in fig.1. It can be seen that up to a dose of 6×10^{17} ion/cm^2 there is no observable re-emission on both samples. At higher doses significant difference between the virgin and the pre-implanted samples is noted. In the pre-implanted sample the re-emission increases radiply and the He concentration soon saturates at a dose of 7×10^{17} ions/cm^2 (21 at%). For further bombardment a considerable depletion takes place at a depth of 1 μm forming two peaks. Above 7.5×10^{17} ions/cm^2 the He profiles decrease gradually and at a dose of 1.0×10^{18} He/cm^2 nearly all helium are blowed out from the sample. On the virgin sample no such phenomenon was observed. The re-emission remains low up to dose of 9.2×10^{17} He/cm^2. Above this dose the He profile

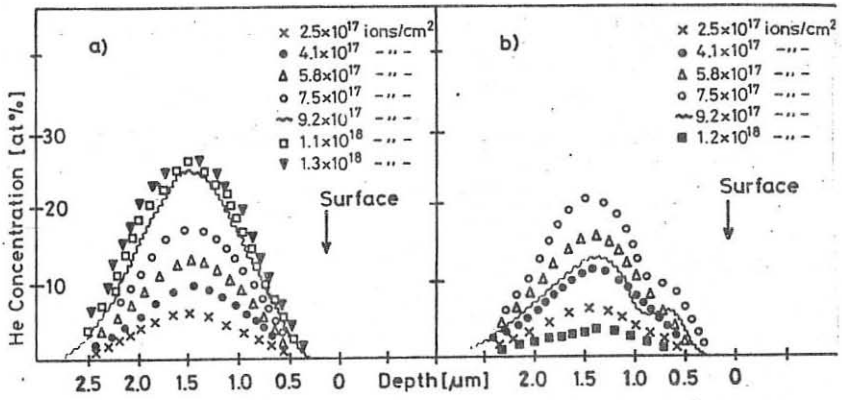


Fig.1. He depth profiles for various doses in virgin (a) and pre-implanted (b) sample.

saturates at 28 at% concentration. The SEM investigations show further differences (fig.2-4). On the pre-implanted sample a layer of 1.6 ± 0.2 μm thickness flaked off from nearly all the implanted spot (fig.2). Taking into account the swelling effect this thickness well coincides with the He implanted range. The remaining part of the bombarded spot clearly shows that before the flaking blistering took place (fig.3). On the virgin sample just the beginning of blister coalescence was observed (fig.4). The blister size in both cases varies between 5-20 μm.

Conclusion

From depth profiles and SEM micrographs together we can conclude as the following. The Ne pre-implantation of 1.1×10^{17} Ne/cm^2 dose lowering the critical dose for the onset of blistering from $10 \pm 1 \times 10^{17}$ He/cm^2 to $8 \pm 1 \times 10^{17}$ He/cm^2 and the maximum concentration of retained He from 28 at% to 22 at%. From the Ne pre-implanted depth the He easily escape when blistering takes place (double peaks).

References

[1] S.K.Das et al.
Paper presented at the Intern.Conf. on Low Energy Ion Beams, Salford, England 1977.
[2] T.Leffers et al., Rad.Eff. 83(1984)1
[3] D.K.Brice, SAND 75-06 22

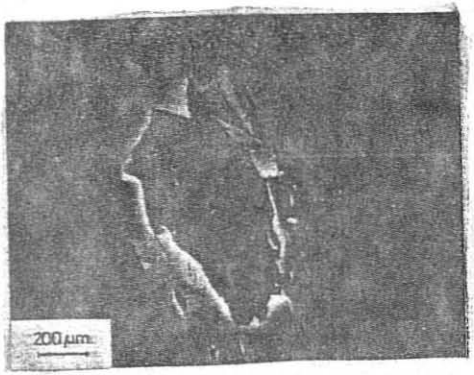


Fig.2.

SEM micrograph of bombarded area of Ne pre-implanted Al taken at a dose of 1.2×10^{18} He cm^{-2}. From nearly the whole implanted spot a layer flaked off.

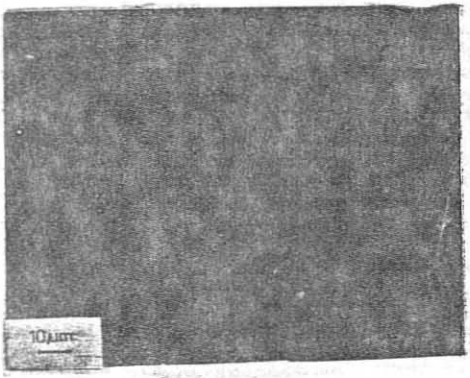


Fig.3.

Close looking of fig. 2 at the remaining area. It is clearly seen the blisters developed before flaking.

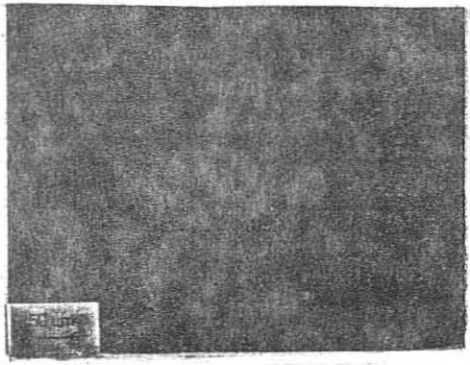


Fig.4.

SEM micrograph of bombarded spot of virgin Al taken at a dose of 1.3×10^{18} He cm^{-2} and the blisters just begin to coalesce forming exfoliation.

Surface Modification and Gas Re-emission Behaviour of Aluminium under Quasi-simultaneous Multiple Energy Helium Bombardment

N.T. My, A. Manuaba, G. Mezey, F. Pászti, E. Kótai, L. Pócs, E. Klopfer, P. Kostka, M. Fried

Central Research Institute for Physics
H-1525 Budapest, P.O.Box 49, Hungary

Introduction

First wall components in fusion reactor will be exposed to He projectiles having a broad energy spectrum. The high-dose impact of helium ions can couse serious surface modification such as blistering, exfoliation and flaking. However, most of the studies on helium bombardment of candidate first wall materials were conducted with monoenergetic He^+ beams. Only a few studies have dealt with helium irradiation of a broad energy spectrum. In most of these studies, the helium spectrum was simulated by irradiating the materials sequentially with monoenergetic helium ions at different energies [1]. Recently a simple method was developed to produce practically simultaneous multiple-energy irradiation [2]. Using that method of implantation surface modification and gas re-emission in Al were studied and the result is reported in this paper.

Experimental

Polycrystalline Al sample of high purity (99.999 %) were first mechanically polished and then cleaned in ultrasonic baths of ethanol and destilled water. The samples were bombarded at ambient temperature by 3500 keV $^4He^+$ beam through an Al absorber foil of 5 μm. During irradiation the foil was tilted periodically between 17^o and 60^o angles in such a way that its effective thickness varied linearly with time. The corresponding helium energies after leaving the foil swept so quickly on the target that the implantation could be considered as a simultaneous multiple energy implantation. The ion flux was kept at 10^{13} ions cm^{-2} sec^{-1} and the vacuum in the target chamber was maintained at $5x10^{-5}$ pa. During implantation the evolution of helium profiles was studied in situ by RBS using 3000 keV protons. At a dose of $19x10^{18}$ He cm^{-2} the irradiation was ended and the irradiated surface were examined in JEOL-JSM 35 type Scanning Electron Microscope.

Results and discussion

Typical RBS spectrum taken at dose of $5x10^{18}$ He/cm^2 is shown in Fig. 1. As can be seen the He profile extending from

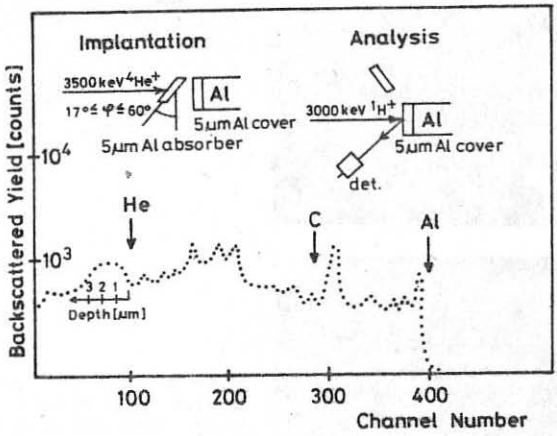


Fig. 1. 3 MeV proton RBS energy spectrum taken at implanted dose of $5x10^{18}$ He cm^{-2}

the surface to a depth of 3 μm is nearly flat with a little depletion at the surface. Integrating the amount of retained He it is found that at low doses nearly all implanted heliums are trapped within the sample. Up to dose $9.5x10^{18}$ He/cm^2 the re-emission increases slowly. Above this dose the re-emission increases rapidly (accelerated re-emission) and at a dose of $15x10^{18}$ He/cm^2 (which corresponds to ~30 at% He concentration) sudden release of helium initiates. Further bombardment the He concentration decreases continuously.

SEM investigation of the sample shows serious flaking as well as multiple flaking on nearly all irradiated area (Fig. 2). Flaking of 3 or more generations with some craters and porous structure bottom can be seen in Fig. 3. The accelerated re-emission is due to the migration of heliums through interconnecting porosity grain boundaries to the surface [3]. Microcracks and porous structure on the bottom of the flaked surface confirmed this consideration. The sudden release of implanted helium is caused by a structural changes of the materials as it is shown in Fig. 4. For further bombardment more flakes are formed thus more heliums leak out from the sample.

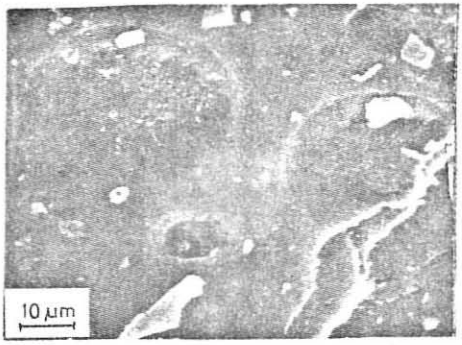


Fig. 2. SEM micrograph of the bombarded Al surface with multiple energy helium taken at dose 1.9×10^{19} He cm^{-2}. Grain boundaries on the bottom of craters created by multiple flaking are clearly seen.

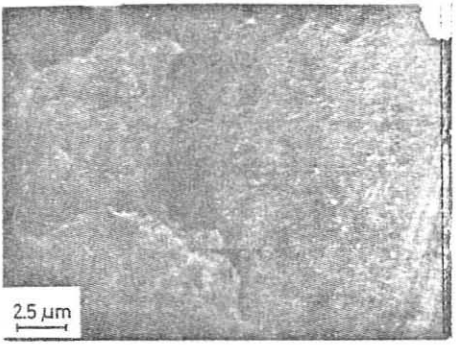


Fig. 3. Insight into the bottom of a crater. Porous structures exist both on the bottom as well as on the wall of the crater.

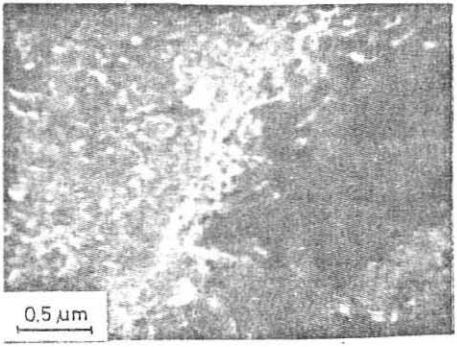


Fig. 4. Magnified view of typical porosity covering nearly the whole area of the implanted spot.

References

[1] M.I. Guseva et al., J. Nucl. Mater. 63 (1976) 245
[2] F. Pászti et al., J. Nucl. Mater. 114 (1983) 330
[3] J.B. Holt, Rad. Eff. 7 (1971) 269

I

other related topics

Injection of solid deuterium pellets as a diagnostic tool

V. Andersen
Association Euratom-Risø National Laboratory
DK-4000 Roskilde, Denmark

1. Introduction

Injection of frozen pellets into a hot plasma has been a subject of increasing interest, mainly from the viewpoint of refuelling the plasma. In consequence, the required velocity of such pellets has been discussed at a number of meetings. It has been claimed that the previously believed high velocities are unnecessary, because the pellet needs only to be well inside the area of the actual divertor arrangement. From this position the ablated material will be drawn inwardly into the plasma by the same effect that makes gas-puffing possible. Another point of view is to consider the pellets as small diagnostic probes in order to study the parameters of the hot plasma, dealing with runaway electrons or localized heating, for instance. In this case it will be necessary for the pellet to survive, until it reaches the area of interest in the plasma. Furthermore, it will be advantageous to use relatively small pellets to avoid disturbing the original parameters too much. The use of this technique in larger tokamaks will therefore demand further development in pellet-injection high-velocity technique. Small pellets of frozen deuterium have been injected into Dante (DANish Tokamak Experiment) to study the profile of runway electrons in the plasma.

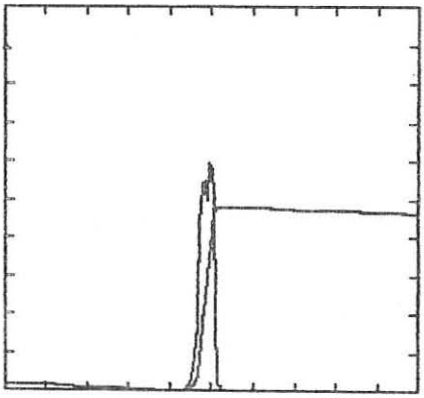


Fig. 1. The light output and the integrated amount of light from the ablating pellet versus time. The time scale is 1 ms/div, the scale for the integrated light is 0.01 mVs/div.

2. Pellet ablation.

2.1. Ablation rate.

Investigations on pellet ablation in the plasma are made by detecting the emitted D_α light. The corre-

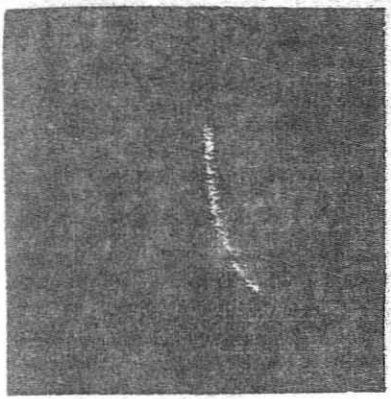


Fig. 2. Photograph of the pellet orbit, bent by the fast electrons.

spondence between the ablated material and emitted light has been found by measuring the integrated amount of light for a known amount of ablated material. For this purpose a solid state photodetector with a D_α filter has been used. A typical signal from a totally ablated pellet is shown versus time in Fig. 1. On comparing the integrated amount of light and the known amount of ablated material, we found $(N_{D\alpha}/N_i) = 0.02$ in agreement with the result of Milora et al. (Ref. 1).

2.2. Pellet orbit.

In Dante, the pellets are injected vertically downwards into the plasma along the minor radius. The normal experience is that the pellet orbit is bent. The bending has been photographed looking in the radial direction of the tokamak. This is shown in Fig. 2, where a strong toroidal component of the deflection is seen. It has also been photographed vertically, showing that the radial component is negligible.

A curved motion has also been seen of pellets injected into the plasma of Ormak (Ref. 2). In this case the pellets were injected tangentially into the tokamak. Therefore, they were influenced by a temperature gradient, perpendicular to the direction of movement, that could account for the deflection. The same explanation could be valid for the downward deflection seen in ASX-B (Ref. 1), and the negligible radial component of the deflection in Dante, if the pellets are not injected precisely towards the center of the plasma.

One explanation of the toroidal deflection might be that the pellet is influenced by runaway electrons that give an unsymmetrical ablation of the pellet. In this case the pellet orbit should be influenced by the direction of the plasma current in the tokamak. Experiments in Dante have shown that the deflection is opposite to the direction of the plasma current. Furthermore, it has been seen in those cases, where it has been possible to avoid runaway, that the pellet orbit has been straight. As the direct momentum transfer from the impact of electrons is negligible, this indicates that it is the recoil process from the extra ablation, caused by the runaway electrons, that is responsible for the bending. Therefore, it is possible to use the bending to find the distribution of the runaway electrons in the plasma. To calculate the influence of the extra ablation, momentum conservation in the

direction perpendicular to the direction of the initial velocity is used. At a given time the pellet will have a mass M, and velocity v in the perpendicular direction. In time dt, the mass dM_o has been ablated from the pellet surface as dM_1, coming from the fast electrons, and $dM_o - dM_1$, coming from the thermal ones. The latter is equally dispersed around the pellet and will contribute nothing to the momentum of the pellet. Taking the pellet as a plane disc, the following momentum relation is given:

$$M \cdot dv = dM_1 \cdot u_s$$

where u_s is the velocity of the particles emitted in the extra ablation from the fast electrons. Taking the spherical shape of the pellet into consideration and asssuming that the particles are ablated perpendicularly to the pellet surface, a correction factor of 2/3 will be found. Therefore, the velocity increase in the perpendicular direction is given by:

$$dv = 2/3 \cdot u_s \cdot dM_1/M.$$

dM_1 may be calculated when the total amount of energy received from the flux, G, of fast electrons is known. The pellet is assumed to be unshielded against the fast electrons, because the thickness of the protecting cloud around the pellet corresponds to the energy of the thermal electrons. Therefore, we have:

$$dM_1 = G \cdot \rho \cdot \pi \cdot r_p^2 \cdot dt/(h_s \cdot n_s)$$

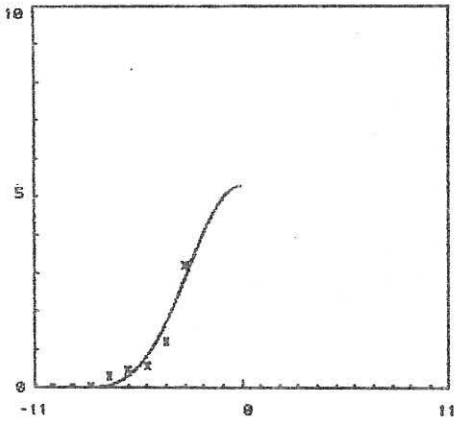


Fig. 3. Calculated fast flux responsible for the deflection of the pellet orbit. Solid curve is an approximated profile. Vertical scale is 1.10^{21} eV/($cm^2 \cdot s$) per div.

with ρ the mass density, r_p the actual pellet radius, h_s the sublimation energy and n_s the molecular density.

The ablated material caused by the thermal electrons $dM_o - dM_1$, is calculated by use of the neutral shielding model by Parks and Turnbull (Ref. 3). The velocity, u_s, of the ablated particles is taken from $u_s = \sqrt{\gamma \cdot kT/M_D}$, with the ratio of specific heats, γ, taken as 7/5 and the temperature, T, taken as the electron cloud temperature near the pellet. As this is expected to be about

0.02-01 eV (Ref. 4), 0.05 eV has been used, giving u_s = $1.3 \cdot 10^5$ cm/sec. The other parameters used to calculate the amount of ablated material are taken from other diagnostic equipments combined with the normally accepted profiles used for a tokamak:

$$T_e = T_{eo}\,(1-(r/a)^2)^2 \text{ and } n_e = n_{eo}\,(1-(r/a)^2).$$

A soft X-ray measurement has been used to give the energy of the thermal electrons, and the total density is known from the CO_2-interferometer. As dv can be found from the vertical velocity v_I, and the actual deflection of the pellet orbit, a connection between the fast flux and the deflection is established. The deflection is measured on the photograph in Fig. 2, and v_I is expected to be constant throughout the lifetime of the pellet. For dv we have:

$$dv = (x_{i+1} - 2 \cdot x_i + x_{i-1})/dt \text{ where } dt = \Delta y/v_I$$

with Δy the radial steplength used for measuring the deflection. When the deflection in the pellet orbit versus the entrance into the plasma is measured, the necessary fast flux responsible for this deflection can be calculated. The result is shown by crosses in Fig. 3. To approximate these crosses to a profile of fast flux, the form:

$$G = G_o(1-(r/a)^2)^{Gp}$$

has been used. The continuous curve shown in Fig. 3 corresponds to $G_o = 5.3 \cdot 10^{21}$ eV/(cm^2·s) and $G_p = 8$.

Discussion

In this example the flux of fast electrons is calculated only from the edge of the plasma to 3 cm from the axis, because this corresponds to the penetration depth of the pellet. In the actual case the pellet used was a 5 μg deuterium pellet with velocity 160 m/s. We will try to increase the velocity to be able to investigate the total profile of the plasma.

In the near future we plan to inject microwave energy into Dante to heat the plasma by ECRH. In this case the heat is delivered locally in the plasma, and this will be another example where pellet injection will be used to diagnose the process. As the ablation rate depends strongly on the temperature of the plasma, we expect a clear increase in the D_α emission, when the pellet penetrates the heated area.

References

1) MILORA, S.L. et al., Nuclear Fusion 20, 12 (1980), 1491-1514.
2) FOSTER, C.A. et al., Nuclear Fusion 17, 5 (1977), 1067-1075.
3) PARKS, P.N. and TURNBULL, R.J., Phys. Fluids 21, 10, (1978), 1735-1741.
4) PARKS, P.B. et al., Nuclear Fusion 17, 3 (1977) 539-556.

D_2 pellet injector work at Risø

H. Sørensen, S.A. Andersen, A. Nordskov Nielsen,
B. Sass and K.-V. Weisberg.

Association Euratom-Risø National Laboratory,
DK-4000 Roskilde, Denmark.

Introduction. The possibility of fuelling plasma experiments and planned fusion reactors by injecting high-velocity pellets of hydrogen isotopes into them has been discussed for several years. A number of injection experiments have now been made at various laboratories, and the interest in pellet injection is sharply increasing.

At Risø National Laboratory we have worked for several years on the design and construction of pellet injectors and related problems.

Our work has resulted in the development of a versatile extrusion-type pneumatic gun (1,2,3). This gun has been tested with pellets in the diameter range 0.4 to 3.2 mm, and a change of pellet diameter may be made rather easily. Velocities in the range 0.1 to 1.4 km/s have been obtained by varying the propeller gas pressure. The gun is designed for accelerating deuterium pellets, but it has also been used as well for those of hydrogen and neon. Only one pellet is fired per firing cycle; but it may be possible, however, to fire 3-4 pellets with time intervals of some milliseconds.

Injecting pellets into an experiment involves more than their formation and acceleration, however. The pellets should be transferred to the experiment, and the gun should be operated automatically in a manner such that the arrival of the pellet at the experiment is timed to coincide precisely with the appearance of the plasma. Information on the velocity and size of a pellet should be obtainable from suitable pellet diagnostics placed between the gun and the experiment.

From the plasma experiment demands will be made on the size, shape, composition, velocity and repetition rate of each pellet; the aiming and timing with respect to the experiment should be precise. There will be further requirements caused by environmental conditions at the experiment and the access through the vacuum wall.

Here, we shall discuss how to build a pellet injector based on the above-mentioned pneumatic gun.

The gun. A pellet must be made at the temperature of liquid helium where deuterium is solid. A schematic drawing of a gun is shown in Fig. 1. The pellets are made from solid deuterium extruded from a cylinder placed below the bottom of a liquid helium cryostat and then loaded into a gun barrel. The procedure is described in detail elsewhere (1,2,3). The extrusion

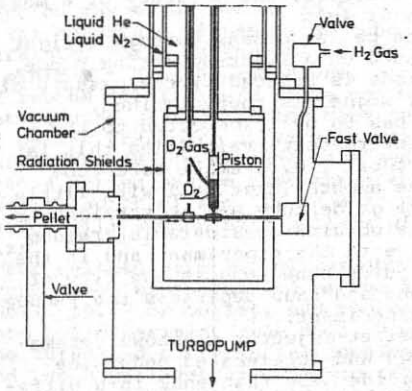


Fig. 1. Schematic drawing of pellet gun.

nozzle and the gun barrel is an integrated unit which is exchangeble. The pellet is blown out through the gun barrel with a burst of hydrogen propeller gas let in through a fast valve, i.e. an electromagnetic valve opened briefly by discharging a condenser bank through the coil. The pellet size depends on the type of nozzle and barrel used, while the velocity depends on the propeller gas pressure and the barrel length (2,3). In principle, the velocity should be proportional to the square root of both the accelerating force and the acceleration length; in reality, the variation with gas pressure and barrel length is weakened by poor flow conditions for the propeller gas. A limit for the velocity is also found; for pellets of diameter 1.4 mm and larger it is around 1400 m/s at present, while for smaller pellets it may be lower.

The firing of a pellet is made stepwise. One should first heat the solid deuterium to make it sufficiently plastic, and then extrude some of it by applying pressure to the piston. Thereafter, one should fabricate a pellet and then fire it by means of a trigger pulse. To facilitate the mutual timing of pellet gun and experiment one may let the pellet wait in the loaded position for several seconds. The valve on the propeller gas line outside the vacuum system is a safety valve that is open only during firing. The time delay between the firing pulse and the appearance of the pellet outside the barrel is typically 1 to 5 ms with a scatter of around 0.5 ms. The scatter in pellet size and velocity may be as small as ±2-3%. During firing the barrel is heated and the vacuum is destroyed by the propeller gas. A new firing can be started only when the temperature and vacuum have recovered. The preparation for a firing usually takes 60 seconds, while the recovery time takes twice as long.

Diagnostics. Two diagnostic methods are used for a pellet injector. One should measure and control the pellet size with a microwave pellet detector and use photodiode detectors for time-of-flight measurements for triggering of events at the

experiment and controlling the pellet condition.

The microwave detector consists of a tuned microwave cavity through which the pellet passes (1,4). The resonance frequency of the cavity changes when the pellet passes through it, and this change may be transformed into an electrical signal of amplitude proportional to the pellet mass. The microwave cavity should be calibrated; the accuracy of a mass determination is in the range of 4-6%.

In a photodiode detector the pellet passes through a light beam or a light carpet, focussed on a light-detecting diode. The amount of light to the diode is reduced by the passage of the pellet, and an electrical signal is then obtained.

The guide tube. The pellet has to be transported to the experiment, and for low and intermediate velocities this is accomplished through a guide tube, i.e. a small bore tube where the pellet slides on the smooth inner wall with little loss of mass and velocity. The guide tube may be straight or curved; in the latter case one obtains considerable freedom in positioning the gun relative to the experiment and in the choice of entrance port. The guide tube reduces the flow of propeller gas to the experiment and thus separates the vacuum of the gun from that of the experiment.

The injector. In Fig. 2 a pellet injector is shown schematically. The pellet is produced and accelerated under the cryostat. It is fired into a guide tube that ends in a differential pumping chamber at the experiment. A valve is situated between this chamber and the experiment; the valve may be an automatic one open only during firing. There may still be a considerable distance between the end of the guide tube

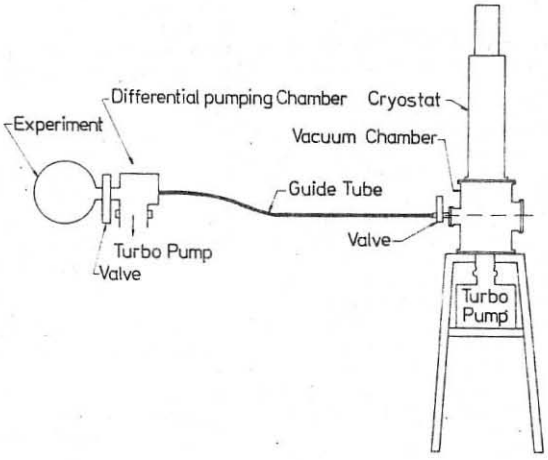


Fig. 2. Schematic drawing of pellet injector set-up.

and the plasma, and a small scatter in direction is required for the pellet. The last part of the guide tube system must be made in in such a manner that the pellet is constrained to follow a well-defined trajectory. All pellets then leave the guide tube system in the same manner and the scatter in direction may be as low as ±0.5°.

The curvature of the guide tube provides a centripetal constraining force on the pellet. For a given velocity there is a minimum radius of curvature, and there is also a velocity of around 1.2-1.3 km/s above which the guide tube method cannot be used (2,3,5) as too many pellets are damaged. A study of pellet transport at varying velocities through a given guide tube system has not been made; it is, however, unlikely that a system may be used where the velocity varies by more than a factor of two. It is also possible that a guide tube system will accept only pellets within a limited interval of size.

For pellets with velocities above 1.2 km/s of diameter equal to or exceeding 1.4 mm the scatter in direction may be small, ±0.1° or better, and the pellets are fired directly into the experiment. One does, however, need a number of apertures and differential pumping chambers between the gun and the experiment in order to remove the propeller gas.

The pellet detectors may be placed in the differential pumping chamber; alternatively with a plastic guide tube, where they can act through the wall, they may be placed anywhere along the tube.

The pellet injector is operated automatically by means of a programable logical controller, and the operation should be timed together with that of the experiment. Here one should remember that it takes around 60 seconds to fabricate a pellet, and that a pellet must be fired within a few seconds after being made. Providing simultaneity between the experiment and pellet arrival may present difficulties. With an experiment of long plasma lifetime and with fast pellets having short transport time, the final triggering of the firing of a pellet may be made from the experiment. In the very opposite case with a very slow pellet and a short plasma life one must measure the pellet velocity and calculate when the plasma should be triggered.

The mutual operation of the injector and the experiment requires careful design work with respect to mutual timing, and some of the trickier problems may be related to the transfer of the pellet and the timing of the pellet arrival.

In conclusion we want to emphasize that a complete pellet injector set-up may vary much from one experiment to another and that an injector in general must be tailored to the task.

References

1) H. SØRENSEN et al. Fusion Technology 6, part 2, 378 (1984).
2) S.A. ANDERSEN et al. 13th Symposium on Fusion Technology, Varese, September 1984.
3) H. SØRENSEN et al., American Vacuum Society, 31st National Symposium, Reno, December 1984.
4) P.B. JENSEN et al., J. Phys. D: Appl. Phys. 15, 785 (1982).
5) K. BÜCHL et al., 12th Symposium on Fusion Technology, Jülich, September 1982, Proceedings pp. 1507.

Scaling Law of the Pellet Ablation Rate

C.T.Chang and K. Thomsen
Risø National Laboratory-Association Euratom
DK-4000 Roskilde, Denmark

Abstract. The scaling law of the particle ablation rate $\dot{N}_p$ of a hydrogen (or its isotope) pellet in a homogeneous, time-independent plasma is derived both for a frozen and for an equilibrium state of the ablated flow.

General Consideration. Irrespective of the ablated flow is in a frozen or in an equilibrium state, the particle ablation rate $\dot{N}_p$ can be deduced from the consideration of mass conservation and the definiteness of the kinetic energy gradient, dw/dr, of the ablated flow at the singular point, r*.

Frozen Flow. When the expansion rate of the ablatant is much faster than the average reaction rate of the dissociation and ionization process, the ablated flow can be considered in a frozen molecular state. The mass ablation rate G at r* reads

$$G = 4\pi r_* \frac{m\lambda_*}{\Lambda_*} \left(\frac{\gamma k T_*}{m}\right)^{1/2} \qquad (1)$$

where $m\lambda_* = \rho_* \Lambda_* r_*$, $m = m_{H_2}$ or m_{D_2}, etc., Λ_* is the total energy attenuation cross section. Meanings of other symbols are given in reference [3]. The condition of $(dw/dr)_{r=r_*}$ being definite requires that

$$G = 4\pi r_*^2 \left(\frac{\gamma-1}{2}\right) \lambda_* q_* \left(\frac{m}{\gamma k T_o}\right) \tag{2}$$

Eliminating $(\gamma k T_o/m)$ and using the definitions of

$$r_* = r_p/\hat{r}\ , \quad q_* = q_o/\tilde{q} = \frac{n_o (2kT_o)^{3/2}}{(4\pi m_e)^{1/2}}/\tilde{q}\ , \tag{3}$$

we can write the particle ablation rate, $\dot{N}_p = G/m$, as

$$\dot{N}_p = \left[\frac{4\pi}{(2\pi m_e)^{1/6}} \left(\frac{\gamma-1}{m}\right)^{1/3}\right] \frac{\lambda_*}{(\hat{r}^4 \tilde{q} \Lambda_*^2)^{1/3}} (r_p^4 n_o)^{1/3} (kT_o)^{1/2} \tag{4}$$

Since there is no atomic effect, γ and m are constants, the expression within the square bracket can be viewed as a material constant, i.e. $\gamma = 1.4$, $m = m_{H_2}$ or m_{D_2}, etc. The factor $\lambda_*/(\hat{r}^4 \tilde{q} \Lambda_*^2)^{1/2}$ depends only on the plasma temperature, kT_o, thus, the scaling law can be written as

$$N_p/(r_p^4 n_o)^{1/3} = f(T_o) \tag{5}$$

To determine the function $f(T_o)$, we have solved the system of the governing equations of the neutral-shielding model [1] with various boundary conditions at the pellet surface. A difference in the boundary condition used does give a marked difference of the state of the ablatant within the subsonic region [2]. As shown in Fig. 1, it gives no noticeable influence on the pellet ablation rate. In the plasma temperature range, 10^2–10^4 eV, the function $f(T_o)$ can be fitted with a nth degree polynominal. For the practical purpose, a power law approximation will be sufficient, thus for an H_2-pellet

$$\begin{aligned} f(T_o) &= 1.724\times10^{16}\ T_o^{1.439} && 600 > T_o > 100 \text{ eV} \\ &= 3.830\times10^{15}\ T_o^{1.673} && 10 > T_o > 0.6 \text{ keV} \end{aligned} \tag{6}$$

Equilibrium Flow. When dissociation and ionization are present, the governing equations must be modified to include the energy loss corresponding to these effects, the change of the specific heat ratio, γ, and the average molecular weight m. When

thermodynamic equilibrium exists, the system of equations is to be supplemented by the degree of dissociation $\alpha_d(p,T)$ and $\alpha_i(p,T)$.

The mass ablation rate G at the singular point, where $(dw/dr)_{r=r_*} = o/o$, becomes

$$G = 4\pi r_*^2 \rho_* v_* = 4\pi r_* \left(\frac{\lambda_* m_{H_2}}{\Lambda_*}\right)\left(\frac{\gamma_* kT_*}{m_*}\right)^{1/2} M_* \tag{7}$$

where $$\lambda_* m_{H_2} = \rho_* r_* \Lambda_* \tag{8}$$

The requirement of $\frac{dw}{dr}|_{r=r_*}$ being definite reads

$$G = 4\pi r_*^2 \left(\frac{\gamma_*-1}{2C_*}\right)\lambda_* g_* \left(\frac{m_*}{\gamma_* kT_*}\right) \tag{9}$$

where C_* is a numerical constant to be determined by the specified value of α_d^* and α_i^* at r_*.

Eliminating $\left(\frac{\gamma_* kT_*}{m_*}\right)$ between Eqs. (7) and (9) and using the definitions of r_* and q_*, the particle ablation rate $\dot{N}_p$, finally can be written as

$$\dot{N}_p = \left[\frac{4\pi}{(2\pi m_e)^{1/6}}\left(\frac{\gamma_*-1}{C_* m_{H_2}}\right)^{1/3} M_*^{2/3}\right] \frac{\lambda_*}{(\tilde{r}^4 \tilde{q} \Lambda_*^2)^{1/3}} (r_p^4 n_o)^{1/3} (kT_o)^{1/2} \tag{10}$$

Comparing Eq. (10) with Eq. (4), we observe that they are essentially of the similar expression except that the factor $(\gamma-1)$ being replaced by $(\gamma_*-1)M_*^2/C_*$.

To derive the scaling law, we have considered the restricted case of $\alpha_d^* = 1$ and $\alpha_i^* = 0$,

$$N_p/(r_p 4 n_o)^{1/3} = f(T_o)$$

As shown in Fig. 2 apart from the difference of a numerical constant factor, $f(T_o)$ has the same power index of T_o independent on the state of the ablatant.

References:

[1] P.B. Parks and R.J. Turnbull, Phys. Fluids 21 (1978), 1735.
[2] C.T. Chang, Phys. Fluids 26 (1983), 805.
[3] C.T. Chang, (1982), Risø Report, Risø-R-460.

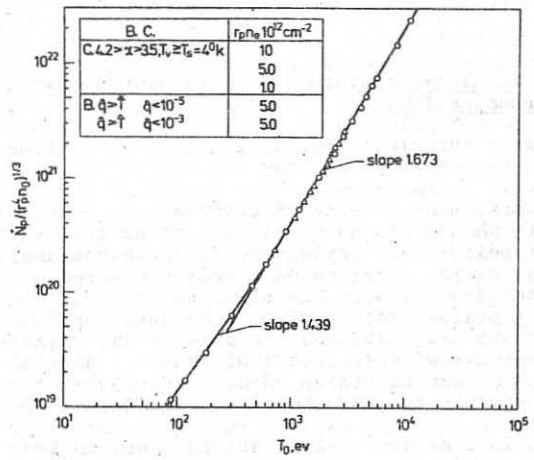


Fig. 1. Variation of $\dot{N}_p/(r_p^4 n_o)^{1/3}$ vs. plasma temperature, T_o. Condition (B) corresponds to a sublimation and (C) corresponds to a dynamic phase transition process, [3].

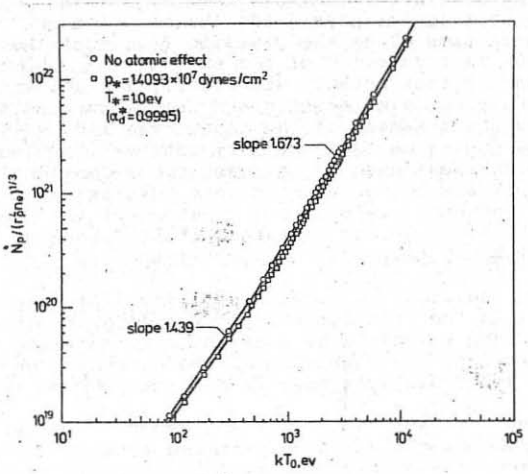


Fig. 2. Variation of $\dot{N}_p((r_p^4 n_o)^{1/3}$ vs. plasma temperature, T_o. The upper curve corresponds to a frozen, the lower one, an equilibrium ablated flow. Boundary condition $\hat{q} > \hat{T}$, $\hat{q} < 1 \times 10^{-5}$.

Pellet Ablation in High-Temperature Plasmas with Allowance for Magnetic Confinement Effects

P.Lalousis* and L. Lengyel
Max-Planck-Institut für Plasmaphysik, EURATOM Association,
D-8046 Garching, Fed. Rep. of Germany

In the present work, some results of computations pertaining to magnetogasdynamic phenomena and atomic processes that affect the ablation rate of pellets are presented. Two problems shall be considered: (a) the initial ablation of a pellet exposed to a hot plasma and the build-up of a relatively low-temperature gas layer shield around the pellet because of the magnetic confinement of the ablated substance; and (b) the increase of the ablation rate caused by the presence of energetic (non-thermal) particles in fusion plasmas. The results presented here are parts of a comprehensive study performed for NET (Next European Torus) /1/.

Pellets injected into magnetically confined thermonuclear plasmas are subject to bombardment by thermal and non-thermal species present in the recipient medium. As a result of energy transfer to the pellet (surface or volume heating, depending on the energies and the respective penetration depths of the energy carriers considered), the pellet material vaporizes, expands, and becomes ionized at some distance from the pellet surface. The ionized pellet material is decelerated and confined by the magnetic field and the initially spherical expansion of the ablatant becomes a funneled channel flow along the magnetic flux surfaces. Since the ablatation rate is a function of the energy flux reaching the pellet surface and is thus notably affected by the evolution of the flow characteristics (e.g. density and temperature distributions), information on the dynamics of the transverse and axial expansions of the ionized substance is of primary interest. Obviously, the physical problem considered is at least two-dimensional. Recalling that the pellets are being injected into tokamaks in a direction normal to the magnetic field, the 3-D nature of the problem becomes apparent. Nevertheless, an attempt shall be made to analyze the problem with the help of 1-D approximations.

For estimating the order to magnitude of the ionization and confinement radii in the transverse direction (i.e. the radius of the magnetic flux tube in which the ablatant expands along the magnetic field lines) and the magnitude of the component velocities to be expected a 1-D radially symmetric Eulerian MGD model has been developed /2/.
The two-temperature two-velocity three-component model is based on the usual conservation equations (particle density, momentum, energy) and takes fully into account the ionization dynamics (collisional ionization and three-body recombination), the collisions between the components, and the interaction of the ionized sub-

*Euratom NET Post-Doc Fellow, c/o IPP Garching, on leave from Div. Appl. Phys., CSIRO, Sydney, Australia

stance with the magnetic field. It has been assumed that $T_i = T_a \neq T_e$ and $v_i = v_e \neq v_a$ (subscripts a, i, and e denote neutrals, ions, and electrons, respectively). It was assumed that energy is transferred from the ambient hot plasma to the ablatant by classical thermal conduction (electron, ion, and neutral conductions). The initial conditions assumed are as follows: ablatant temperature and density $T_e \approx 10^{-2}$ eV, $n_a = 2.5 \times 10^{26}$ m^{-3}; ablatant radius $r_a = 2.5$ mm, plasma temperature and density $T_e = 500$ eV and $n_e = 10^{20}$ m^{-3}, respectively. The general expansion dynamics observed in the calculations can be described as follows: after being exposed to the hot plasma, there is a sudden increase of the ablatant pressure at the front of the heat conduction wave (because of inertia effects, the energy input rate is higher than the convective removal of the deposited heat). As a result of this, the center of the ablatant undergoes compression while, at the same time, the plasma layers outside of the heat deposition zone rapidly expand. Since an axially symmetric geometry is assumed (i.e. the fluid cannot escape from the domain considered) and heat deposition by conduction is continuous as long as temperature gradients exist, a quasi-continuous expansion results. However, at the radius at which the neutrals become ionized a sudden drop of the expansion velocity (of the ionized component) and a pile-up of the ablatant are observable. As of this moment (at latest), the results of 1-D approximations are of limited value: in reality the ionized substance may continuously escape along the field lines, i.e. the flow becomes at least two-dimensional. (A further limitation of the present model is associated with the heat input mechanism assumed: while thermal conduction in transverse direction is assumed, in reality the pellets are heated primarily by plasma particles moving along the m.f. lines. To model this rather large heat flux, we have assumed transverse thermal conductivities equal to the parallel conductivity values.)

The radial distribution of the pellet particles $\Delta N = (n_a + n_i) \cdot \Delta V$, where ΔV denotes volume differential, in the end phase of its deceleration and the associated confinement radii are shown in Fig. 1a to 1c for three magnetic field strengths: 1T, 2T, and 4T,

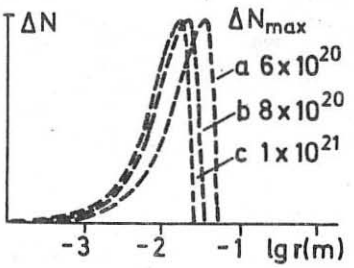


Fig. 1: Radial distribution of the ablated material for three m.f. strengths: 1T (a), 2T (b), 4T (c).

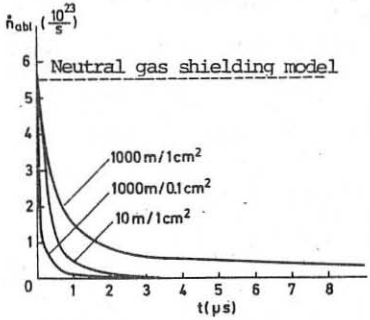


Fig. 2: Reduction of the ablation rate for different flux tube length/cross-section ratios.

respectively. (The hollowness of the ΔN distributions is caused by the log (r) scale used: the respective density distributions have their maxima in the center of the coordinate system).

The major results corresponding to the three magnetic field strengths cited are summarized in Table 1 where the confinement time t_c, the associated confinement radius r_c (given by the right-side boundaries of the curves in Fig. 1) and the location of the maximum ΔN value r_m at $t = t_c$ are given. Confinement time is defined here as the time at which the rapid expansion of the ablatant boundary can be considered to be completed.

Table 1: Deceleration and confinement of pellet substance by magnetic field

Magn.field strength (Tesla)	Confinment time t_c (μs)	Confinement radius r_c (cm)	Mass radius r_m (cm)	Max. velocity during expan. phase (m/s)
1	15	5.5	3.5	3.62×10^3
2	16	3.2	2.1	2.97×10^3
4	17	2.7	1.7	0.79×10^3

Note that the confinement radii and confinement times tabulated represent limit values corresponding to vanishing axial expansion.

In a realistic case, axial expansion sets on long before these values are reached. Nevertheless, the information obtained is rather useful for defining the order of magnitude of the physical quantities to be used in further analyses. For example, calculations performed for fixed flux tube cross-section flux tube length combinations with the help of a 1-D channel flow model /3/ supplemented by the so-called neutral gas shielding ablation model /4/ have shown a drastic reduction (in time) of the ablation rate as compared with the results of the commonly used neutral gas shielding model. Figure 2 shows the time variation of the ablation rate for three flux tube length/cross-section combinations. The cause of the notable ablation rate reduction is the pile-up of the cold ablatant in the flux tube around the pellet.

An effect not taken into account in the above calculations that may drastically increase the ablation rate is the presence of non-thermal particles in fusion plasma. Neutral-beam-produced ions, runaway electrons, and alpha particles may penetrate, or even traverse, the pellet thus transferring, partially or totally their energy to it. In a series of calculations /5/, the effect of these particles has been estimated on the basis of a simple ablation model /6/. As an example Figures 3a and 3b show the ratios of the ablation rates caused by non-thermal particles to that caused by thermal electrons as a function of the thermal electron energy for different beta (i.e. energy content) ratios. As can be seen, if the non-thermal particles reside in low-temperature plasma regions, their effect may be quite substantial. Their relative importance decreases in the high-temperature regions.

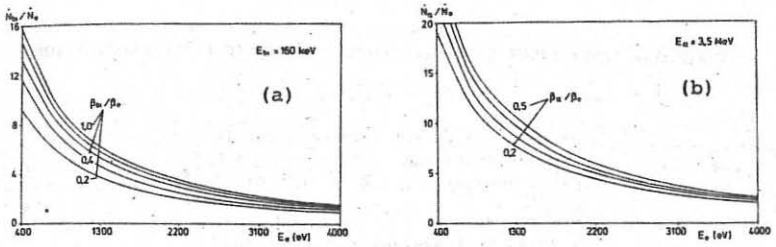


Fig. 3: Ratio of ablation rates caused by non-thermal particles and thermal electrons as a function of the energy of the thermal electrons for different beta ratios.
(a) NB ions of 160 keV energy; (b) Alpha particles of 3.5 MeV energy.

In summary, the results of these calculations show that pellet ablation in high-temperature magnetically confined fusion plasmas is a rather complex phenomenon. Reliable ablation models should take into account the retardation of the ablated substance by the confining magnetic field and the simultaneous action of the different energy carriers. The problem thus defined calls for more sophisticated approximations.

References

/1/ L.L.Lengyel, Assessment of Pellet Injection for NET, Pt. I to Pt. V: IPP Repts. 1/231 to 1/233 (1984) and IPP Rept. 1/236 (1985)
/2/ P. Lalousis, Numerical calculations on the Transverse Expansion of Pellet Plasmas in Linear Magnetic Fields, Rept. NET/IN/85-052 (1985)
/3/ M. Kaufmann, K. Lackner, L. Lengyel and W. Schneider, Verhandl. DPG (Bull. Germa. Phys. Soc.) VI, 19 (1984) 1210
/4/ P.B. Parks, R.J. Turnbull and C.A. Foster, Nucl. Fusion 17 (1977), 539
/5/ L.L. Lengyel, IPP Rept. 1/233 (1984)
/6/ D.F. Vaslow, IEEE Trans. Pl. Sci., PS-5 (1977), p. 12

PLASMA SCATTERED LIGHT DEPOLARIZATION BY MAGNETIC FIELD FLUCTUATIONS

T. Lehner, D. Grésillon, X.L. Zou, B. De Gentile*

Laboratoire de Physique des milieux Ionisés
Groupe de recherche n° 29 du C.N.R.S
Ecole Polytechnique, 91128 Palaiseau Cedex, France.

* Association Euratom-CEA pour la fusion, DFRC, B.P. n° 6,
92160 Fontenay-aux-Roses, France.

Abstract

The energy transport in magnetically confined plasmas involves transversal electromagnetic field fluctuations. To detect these fluctuations, we propose to use the tensorial polarizability of magnetized electrons. A pump em wave is scattered with a polarization component perpendicular to the "normal" (density fluctuation induced) scattered radiation. Detection of this cross-polarized scattered field is possible via heterodyne techniques, and yields the B_φ field fluctuation.

The depolarizing effect

Let us consider a single cold particule in a static magnetic field B_o (gyrofrequency ω_c) and pump field (E_i, B_i) of high frequency $\omega_i >> \omega_c$. The Lorentz equation reads:

$$m \frac{d\bar{v}}{dt} = q_e(\bar{E}_i + \bar{v} \wedge (\bar{B}_o + \bar{B}_i)) \qquad (1)$$

We can solve eq. (1) by iteration and get the quiver velocity to lowest order in pump field strenght :

$$\bar{v}_i = q_e \bar{E}_i \exp(-i\omega_i t)/-im\omega_i + cc \qquad (2)$$

If we substitute (2) in (1), the next term is a correction of order ω_c/ω_i proportional to $E_i \wedge B_o$: this acceleration radiates a field perpendicular to E_i (depolarized) : its forward scattering "fs" is the source of the Faraday rotation. Now if we add the fluctuating fields (E_φ, B_φ) with a typical low frequency $\omega_\varphi << \omega_c$, the Lorentz equation contains a new term $v_i \wedge B_\varphi$ which is also depolarizing, since perpendicular to E_i and proportional to the magnetic field fluctuation B_φ : this is a modulated Faraday like effect on which we shall focus on the following.

Second order current

We start with the electric pump field equation of propagation in the a rarefied medium :

$$-\Delta\bar{E} + 1/c^2 \, \partial^2\bar{E}/\partial t^2 = -\mu_o \, \partial\bar{J}^{(2)}/\partial t - \nabla\rho^{(2)}/e_o \qquad (3)$$

A multiple amplitude order expansion of the fluctuations <1>, restricts to second order terms. Variations in permittivity ε can be neglected here. For transverse far field radiation $J^{(2)}$ contributes by :

$$(J^{(2)} \wedge s) \wedge s \qquad (4)$$

where s is the observation unit vector direction. We shall use a fluid

current description in which $J^{(2)}$ is built up of three terms :

$$\bar{J}^{(2)} = q(n\bar{v})^{(2)} = q(n_o\bar{v}^{(2)} + n^{(1)}\bar{v}^{(1)} + n^{(2)}\bar{v}_o) \qquad (5)$$

If we look for radiation at the beating frequency $(\omega_i-\omega_\varphi)$, there are no source density fluctuations. We split, to first order, terms between fluctuations and pump contibutions : $n=n_\varphi+n_i$, $v=v_\varphi+v_i$, $B=B_o+B_\varphi+B_i$, $E=E_\varphi+E_i$ where v_φ is the first order source quiver velocity in the fluctuating fields (E_φ,B_φ), $v^{(2)}$ is solution of the fluid cold plasma equation :

$$\partial\bar{v}^{(2)}/\partial t - q/m\,(\bar{v}^{(2)}\wedge\bar{B}_o) = [-(\bar{v}^{(1)}.\bar{\nabla})\bar{v}^{(1)} + q/m(\bar{v}^{(1)}\wedge\bar{B}^{(1)}] \qquad (6)$$

Thus the current expression :

$$\bar{j}^{(2)}(\bar{r},t) = q(n_i\bar{v}_\varphi + n_\varphi\bar{v}_i) + n_o\mu(-(\bar{v}_\varphi.\bar{\nabla})\bar{v}_i-(\bar{v}_i.\bar{\nabla})\bar{v}_\varphi + q/m \ldots$$

$$\ldots(\bar{v}_i \wedge \bar{B}_\varphi + \bar{v}_\varphi \wedge \bar{B}_i)) \qquad (7)$$

Where μ is the cold magneto mobility. One can show <2>, solving for v_φ in the guiding center approximation, that the leading polarized term in $j^{(2)}$ is the $n_\varphi v_i$ one in (7) whereas the leading depolarizing term is $n_o\mu(v_i\wedge B_\varphi)$. The scattered electric field can be obtained from eq. (3),(4) :

$$\bar{E}s(\bar{r},\omega) = i\omega\mu_o \int \Phi(\bar{r}-\bar{r}',\omega)(\bar{j}(\bar{r}',\omega)^{(2)}\wedge s)\wedge s\, d^3r' \qquad (8)$$

Where Φ is the spherical wave function.

$$\Phi(r-r',\omega) = e^{ik|r-r'|}/4\pi|r-r'| \qquad (9)$$

If $j^{(2)}$ is nearly harmonic around a typical $(k_\varphi,\omega_\varphi)$ the integration in eq. (9) will asymptotically satisfies the selection rules for three mode coupling. We can say that the far field approximation amounts to make a Fourier transform, the probed wave vector and frequency being related by : $k_\varphi=ks-k_i$, $\omega_\varphi=\omega s-\omega_i$.

Antenna beam field

The detection method should be sensitive to the scattered field polarization. For the heterodyne technique, the polarization reference is provided by the antenna beam one. The heterodyne current on a detector of specific constant C and efficient area A_d is :

$$I(t) = C \int_{A_d} \bar{E}_{OL}^*(\bar{r},t).\bar{E}s(\bar{r},t)\eta(r)d^2r + cc \qquad (10)$$

Where E_{OL} is the local oscillator field and η the detector efficiency. The antenna beam is defined as, using merely the scalar Kirchhoff-Sommerfeld diffraction formula <3,4> :

$$\bar{E}a(\bar{r}',\omega) = 1/i\lambda_i \int_{A_d} \bar{E}_{OL}(\bar{r},t)\Phi(r)\eta(r)d^2r \qquad (11)$$

By eq. (11) this antenna beam field is the local oscillator beam diffracted by the aperture A_a of the detector, and traced back toward the source. Hence the current expression using Ea in (10) :

$$i(t) \sim \int \bar{E}a^{*}(r',\omega).(\bar{j}'^{a})(r',\omega)\wedge s)\wedge s)\ d^{3}r' \qquad (12)$$

Different component of the radiating current can be probed by chosing the proper Ea direction or lo polarization.

Polarized and depolarized terms

The polarized "p" terms are defined as those parallel to $(E_i \wedge s)\wedge s$, while depolarized "dp" terms are perpendicular to this one. Such is our term proportional to $((E_i \wedge B_\varphi)\wedge s)\wedge s$. Restricting to the main terms (in a ω_c/ω_i small parameter expansion) of second order, in eq. (7),

$$\bar{A}_1 = q(n_\varphi \bar{v}_i) \text{ is a p + dp term since } \bar{v}_i = \bar{\bar{\mu}}\,\bar{E}_i \sim \bar{E}_i - i\omega_c/\omega_i (b_o \wedge \bar{E}_i)$$

$$\bar{A}_a = n_o \bar{\bar{\mu}} q / m\ (\bar{v}_i \wedge \bar{B}_\varphi) \text{ is a dp term (to order one in } \omega_c / \omega_i) \text{ plus p term.}$$

We have to consider $(A_1\wedge s)\wedge s = A_1'$ and $(A_a\wedge s)\wedge s = A_a'$. Fig. 1 shows the geometry of the scattering : k_i is along the z axis, ks lies in the x0z plane with an angle θ to the z axis, E_i is tranverse to k_i with angle α to the x axis. The projection of A_a' along c, be c a direction of Ea perpendicular to E_i in the scattering region ("dp" detection set-up), contains the following components of B_φ :

$$c.A_a' \sim \cos(\theta)B_{\varphi,z} - \sin(\theta)\sin\alpha(\cos(\alpha)B_{\varphi,y} - \sin(\alpha)B_{\varphi,x})$$

For the "fs" case (θ=0), the "dp" set up detects the component $B_{\varphi,z}$ parallel to k_i. Note that the direction of B_o is arbitrary with respect to k_i. Fig. 2 specializes to the case of perpendicular propagation for k_i, with an ordinary wave or an extraordinary wave (electric field in dotted line). In the case of an ordinary wave, A_1 is purely polarized, while A_a is purely depolarized. For the extraordinary mode there can be spurious competiting terms such as

$$\tilde{n}(\omega_c \wedge \bar{E}_i) \text{ in the direction of } n_o(\bar{E}_i \wedge \bar{B}_\varphi)$$

and a careful analysis is required. Note that convection depolarizing terms such as

$$-n_o(\bar{v}_i.\nabla)\,\tilde{v} \text{ can be shown <2> negligible even for large angle scattering.}$$

According to the classical space Fourier analysis performed by the scattering geometry, the probed wavenumber k_φ lies in the z0x plane with B_φ transverse. If one choose the antenna field Ea parallel to $E_i\wedge s\wedge s$, we shall select the n_φ density fluctuation term, while if Ea perpendicular, it selects the B_φ fluctuations.

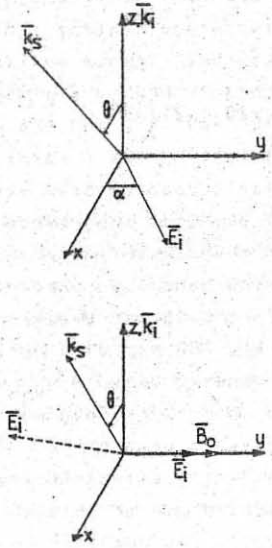
Sensitivity

Thus by changing the lo polarization, it is possible to detect a current eq. (12) that is either a p term A_1' proportional to density fluctuations, or a dp term A_a' proportional to B_φ fluctuations. The ratio $\rho = A_a'/A_1'$ yields the relative sensitivity of the measurement. We find,

$\rho=\omega_c/\omega_i\ n_\varphi/n_o\ B_\varphi/B_o$ for $\omega_i>>\omega_c$. Thus $\rho=1$ means we are detecting a n_φ or B_φ signal with the same amplitude. For $\omega_i \sim \omega_c$ the theory is more complex, but one can show <2> that ρ is given by the same ratio multiply by an enhancement factor, which in a cold theory is $Q=(1-\omega_i^2/\omega_c^2)^{-1}$.

Numerical application

The value of the rms density fluctuation in k space in a non uniform plasma is of order ρ_i/L, where ρ_i is the ion Larmor radius, L the mean density gradient lenght. It is of order 10^{-3} in large machines. Phenomenological arguments for B_φ lead to a rms value of B_φ/B_o of order 10^{-4}. Besides the n_φ spectrum is peaked at $k_\varphi\rho_i \sim 1$, whereas the B_φ spectrum is expected to be peaked at higher k_φ values. In the TFR Tokamak we observed a value $n_\varphi/n_o \sim 10^{-6}$ in a given spectral experimental Δk window around ρ_i^{-1} <4> while we are able to detect 10^{-6}. Using a CO_2 laser beam in a 4T B_o field would allow a minimum detectable $B_\varphi/B_o = 3.10^{-6}$ in the same Δk window. A better sensitivity could be expected using a lower frequency probing beam.



References

<1> A.G. Sitenko, Fluctuations and non linear wave interactions in plasmas, Pergamon Press (1982).

<2> T. Lehner, B. de Gentile, D. Grésillon, submitted to Plasma Physics, and to be published.

<3> E. Holzauer, J.M. Massig, Plasma Physics, 20, 1867 (1978).

<4> D. Grésillon and al, Physica Scripta, tome 2, Goteborg ICPP (1982).

CONTROLLED REB ENERGY DEPOSITION IN AN INHOMOGENEOUS PLASMA

P.Šunka, V.Babický, V.Boháček, M.Člupek, K.Koláček, I.Kováč, A.Krejčí, V.Piffl, J.Rauš, M.Řípa, J.Ullschmied

Institute of Plasma Physics, Czechoslovak Academy of Sciences
Pod vodárenskou věží 4, 182 11 Prague 8

The heating of an inhomogeneous /localized/ plasma by using REBs reflected at the virtual cathode created spontaneously near the plasma-vacuum boundary represents, in some respect, an alternative to the two-stage heating scheme proposed for Budker's reactor [1,2]. As shown in our earlier experiments [3,4], the reflected-beam method is highly efficient in plasmas with the maximum density of 10^{20}-10^{21} m^{-3} and the maximum value of the energy deposition efficiency / 30% / seems to be only little sensitive to the angular spread of beam electrons. This obvious advantage could be of decisive importance at heating of higher density plasmas. In the present experiment the method is tested for the maximum plasma densities exceeding 10^{21} m^{-3}.

According to Fig.1, in the latest version of the REBEX machine the REB / 500 kV, 50 kA, 100 ns, Ø 45 mm / is injected along an almost homogeneous magnetic field / B_{max} = 0,5 T / into a plasma column formed by two cooperating plasma guns. This doubling of plasma sources makes it possible to increase the average plasma density in the first part of interaction chamber up to 5.10^{21} m^{-3}. Behind the second gun the plasma density drops rapidly by an order of magnitude. The position of plasma-vacuum boundary is either determined by a free plasma expansion, or fixed at z=1,7 m by a terminating foil. A large variety of axial profiles of plasma density can be formed in this arrangement. Besides the plasma diagnostics used earlier /diamagnetic coils, magnetic probes, Thomson scattering, microwave interferometers, vacuum photodiodes etc/ optical and infrared interferometers /3,39 μm, 0,6328 μm/ and surface-barrier X-ray detectors /SBD/ were introduced.

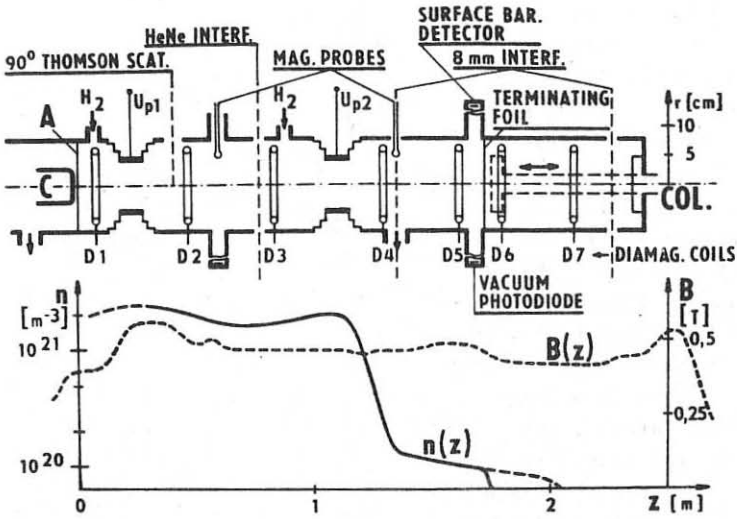


Fig.1

In Fig.2 several distributions of the plasma energy content along the system, as reconstructed from the diamagnetic measurements, are shown. The numbers denote profiles corresponding to various free-expanding plasmas produced by: the first gun only /1,2/, two guns /3-5/. The dashed line /6/ marks the energy deposited by non-reflected beam. The maximum energy deposition rate /200-300 Jm^{-1}/ is always observed in the region with the plasma density of 5.10^{19}-$2.10^{20} m^{-3}$, which can be easily shifted at will along the interaction chamber by appropriate choice of the initial plasma parameters.

The indispensable role of the reflected beam in achieving high energy deposition rates was confirmed by special experiments with a foil-terminated plasma and a movable collector /cf Fig.3/. The beam can be reflected back into the plasma only with the collector removed at least 20 cm off the terminating foil /pos.B/. Then, the energy deposition rate is equal to that in the free-expanding plasma, about 80% of the deposited energy being found in the lower density region. In the single-transit beam regime /pos.A/ the plasma energy content decreases more

than two times.

At constructing the profiles in Fig.3 the finite conductivity of the plasma surrounding the directly heated plasma core was taken into account. The data on magnetic field diffusion were obtained from the time-resolved radial profiles monitored by magnetic probe in the cross-section close to a corresponding diamagnetic coil. Two examples showing the magnetic field variations ΔB outside the hot plasma core are chosen in Fig.4. The nonlinear character of the magnetic field diffusion is apparent /cf [5]/. While the correction factor is as high as 1,5 in the lower density region, it increases to 2-3 in the high density one.

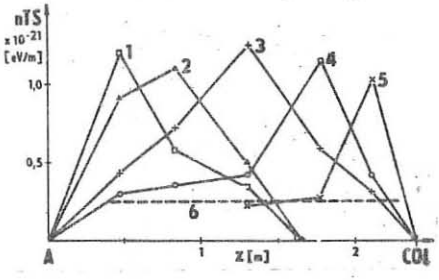


Fig.2

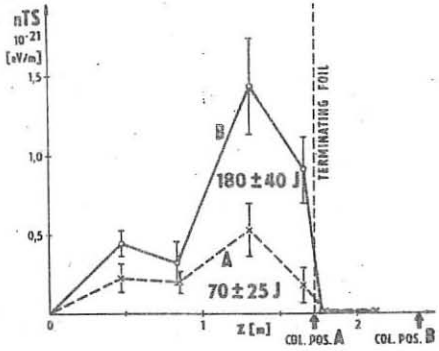


Fig.3

Two kinds of soft X-ray detectors were exploited to obtain data on the electron distribution /see Fig.1/. While the vacuum photodiodes /together with the Thomson scattering/ provide information on the plasma bulk, the solid-state detectors monitoring X-radiation from the terminating foil or from a solid target immersed in the dense plasma are used to analyze high-energy tails. Unfortunately, till now we have too little data to reconstruct the electron distribution. However, a hot component /E_{max}= 10-30 keV/ has been found not only in the lower density region but also in the high-density one. The former is demonstrated by the signal of solid-state detector viewing the terminating foil /Fig.5/. The high-energy electrons are confined

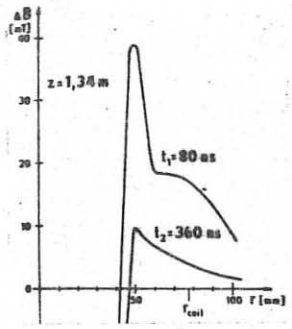


Fig.4

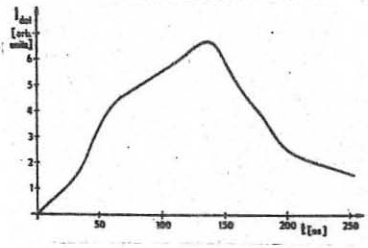


Fig.5

in the system much longer /100-200 ns/ than it would correspond to their free escape. The estimated number of electrons in this group is at least 10% of all particles in the lower density region. Their energy is available for heating a sufficiently long dense plasma. In our machine, the resulting temperature of the dense plasma is several times the initial one.

Although the role of the reflected electrons in energy deposition was fully demonstrated and the high-power rf radiation from the virtual cathode in the frequency range of 3-12 GHz was really observed, a consistent model of plasma heating by the reflected beam is still missing. Nevertheless, as an efficient means for conversion of REB energy into lower energy electrons, this heating mechanism deserves further investigation.

REFERENCES

[1] Budker G.I., Proc. 6th Europ.Conf. on Contr.Fus. and Plasma Phys.,Moscow 1973,Vol.II,p.136.

[2] Arzhannikov A.V. et al., Nucl.Fus.Suppl.1979,Vol.II,p.623

[3] Šunka P. et al., Proc. 3rd Int.Top.Conf. on High-Power El. and Ion-Beam Res.and Techn.,Novosibirsk 1979,Vol.I,p.103

[4] Šunka P. et al., Proc. 4th Int.Top.Conf. on High-Power El. and Ion-Beam Res. and Techn.,Palaiseau 1981,Vol.II,p.583

[5] Gorev V.V., Zakharov S.V., Voprosi atomnoi nauki i tekhniki, seria Termoiadernyi sintez,1980,Vol.1/5/,p.106

J

late papers

PRODUCTION OF HIGH DENSITY PLASMA BY PELLET INJECTION IN TFTR

G.L. Schmidt, S.L. Milora[a], M.G. Bell, M. Bitter, C.E. Bush, R.J. Colchin[a], S.K. Combs[a], A. England[a], E. Fredrickson, R.J. Goldston, B. Grek, L. Grisham, R.J. Hawryluk, W. Heidebrink, H.W. Hendel, D. Johnson, P. LaMarche, R. Little, D. Mansfield, D.C. McCune, K. McGuire, D.M. Meade, D. Mueller, M. Murakami[a], E.B. Nieschmidt[c], H. Park, A.T. Ramsey, D. Rasmussen[a], J.F. Schivell, S. Sesnic, M. Shimada[a], F. Staurfer[b], B.L. Stratton, G. Taylor

Plasma Physics Laboratory, Princeton University, Princeton, New Jersey 08544, U.S.A.

INTRODUCTION Experiments on various tokamaks, most recently on PDX [1], ALCATOR [2], and DIII [3], have shown that high electron densities, in particular central densities, can be achieved by high speed injection of solid hydrogen or deuterium (pellet injection). The injection of fuel by this means is efficient as to the fraction of mass retained by the plasma, and can be accompanied by an improvement in the global confinement time of the discharge.

Experiments on TFTR extend these results to the larger volumes and higher electron temperatures present in the TFTR device. The size and speed of the solid deuterium pellets used also represent an extension of previous experiments. Both ohmic and neutral beam heated plasmas have been studied. In the case of neutral beam injection, pellets have been used primarily to prepare a target plasma.

INJECTOR DESCRIPTION A Repeating Pneumatic Injector (RPI) [4] developed by Oak Ridge National Laboratory was used in these experiments. When triggered, the injector produces a continuous extrusion of solid hydrogen or deuterium permitting the injection of single or multiple pellets. Pellets are accelerated by a pulse of high pressure hydrogen gas through a single reciprocating gun barrel. The amount of propellant gas injected into the tokamak is limited to 0.04 torr liters/pellet by the use of conductance limiting guide tubes and a fast acting valve. The injector was operated in deuterium to produce single 4 mm diameter (2.1×10^{21} D_o) pellets at 1300 m/s, and multiple 2.67 mm diameter (7×10^{20} D_o) pellets at up to 1350 m/s. The injector is capable of producing 4 mm pellets at 1900 m/s when operated in hydrogen.

SINGLE 4 MM PELLETS Single 4 mm deuterium pellets were injected into 1.4 MA TFTR ohmic plasmas. The best results achieved are illustrated in Fig. 1. Line average density of 8.1×10^{13} cm^{-3}, near triangular shape, and central density of 1.6×10^{14} cm^{-13} are obtained. The central particle replacement time obtained from the decay rates of the multichord interferometer channels in this discharge was ~ 2 sec. A strong reduction in central electron temperature occurs at the instant of pellet injection followed by a reheat of the plasma. The plasma energy content rises due to an immediate increase in ohmic input power accompanied by an increase in global confinement from ~ 290 ms to ~ 430 ms (kinetic analysis).

For TFTR, the parameter $n_e R/B_T$ (10^{13} cm^{-2} T^{-1}) obtained with pellets (5.6) exceeds that which has been achieved by deuterium gas fueling (3.2) and is approached only by operation in helium (5.3). In the case of helium however, broader density profiles are observed with a peak to line average ratio of 1.3.

Operation of TFTR with 4 mm pellets at plasma parameters then available was extremely difficult during this series of experiments. High radiated power could not be controlled and disruptions followed within 200 to 500ms after pellet injection. The use of deuterium neutral beam injection at the 3-4 MW level did sustain the plasma for the 500ms injection time. Central density approaching 2 x 10^{14} cm^{-3} and reheat temperatures of ~ 1500 eV were achieved under these conditions, but strong central radiation was observed and a disruption followed termination of the beam pulse.

MULTIPLE 2.67 MM PELLETS Using multiple 2.67 mm pellets spaced from 200 to 500 ms apart, the total particle content of the plasma could be raised to the level reached with single 4 mm pellets without disruption. In the best cases, radiated power, excluding localized edge radiation, was maintained at a level from 30 to 50% of the input power, comparable to gas fueled TFTR discharges. Typically, one to three pellets were injected; but five pellets have been injected using staggered neutral beams to supplement ohmic input power. Pellet injection has produced higher neutron source strength than gas fueling in ohmically heated plasmas.

Evolution of the line integral density and the density profile at 2.8 s are illustrated in Fig. 2 for a three pellet case. The line integral density in this case is sustained following the third pellet, by deuterium neutral beam injection at 5.7 MW. Pellet penetration in these discharges is approximately 45 cm, leading to hollow density profiles immediately following pellet ablation. The resulting inverted density gradient relaxes in 20 to 100 ms. The electron temperature profile following each of the three sequential pellet events evolves on a similar time scale as shown in Fig. 3. The measured density rise accounts for essentially all the pellet mass.

The strong reheating of the central plasma observed during neutral beam injection is illustrated in Fig. 4. Large sawtooth oscillations, as shown in Fig. (4b), are observed in gas fueled discharges at this power level, but for the case of pellet injection (4a) the sawtooth oscillations are suppressed for at least the 500 ms of the neutral beam pulse. The q=1 radius as determined approximately from the sawtooth inversion radius before and after neutral beam injection is not significantly perturbed by pellet injection. A central Z_{eff} of 1.3 is measured by X-ray pulse height analysis. At the end of the neutral beam pulse, neutron levels due to Maxwellian thermal reactions of up to 1 x 10^{14} N/sec are observed. Central electron pressure is as great or greater than obtained in gas fueled discharges despite the strong reduction in central input power caused by beam attenuation at this high density. Sixty percent of the injected power and fifty percent of the total input power is deposited outside the q=2 surface. Global confinement in these discharges is between 200 and 250 ms at 2.2 MA, comparable to that obtained with gas fueling; however, confinement within the plasma core is appreciable longer.

SUMMARY Central density > 1.6 x 10^{14} cm^{-3}, and $n_e R/B_T$ = 5.6 x 10^{13} cm^{-2} T^{-1} have been produced in TFTR by injection of 4 mm deuterium pellets.

Injection of multiple 2.67 mm pellets produces hollow density profiles which relax in 20 to 100 ms. When neutral beam injection follows pellets injection, a strong reheating of the plasma core is observed, and sawtooth oscillations can be suppressed. Global confinement time is between 200 and 250 ms, comparable to that obtained with gas fueling. Confinement within the plasma core can be appreciably longer.

ACKNOWLEDGMENTS The authors wish to acknowledge the many other TFTR physicists and engineers and technicians who together as a group have enabled us to carry out these experiments. In addition, we express our thanks to the engineers and technicians both from ORNL and Princeton whose long hours of extraordinary effort provided us with the pellet injector facility used in these experiments. We also appreciate the support and continuing interest of H.P. Furth and D. Grove. This work was supported by U.S. Department of Energy Contract No. DE-AC02-76-CHO-3073.

REFERENCES

[1] R.J. Fonck et al., J. Nucl. Mater. 128 and 129 (1984) 330.
[2] M. Greenwald et al., Proc. of the 10th IAEA Conf. (London 1984), Vol. 1, p. 45.
[3] S. Sengoku et al., Proc. of the 10th IAEA Conf. (London 1984), Post deadline paper.
[4] S.K. Combs, S.L. Milora, C.R. Foust, C.A. Foster, D.D. Schuresko, Rev. Sci. Instrum. 56 (1985) 1173.

[a]Oak Ridge National Laboratory, [b]University of Maryland, [c]EG&G Idaho, [d]JAERI

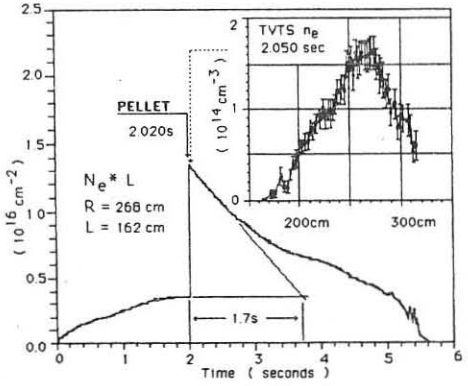


FIG. 1. Density evolution and profile shape - single 4 mm pellet.

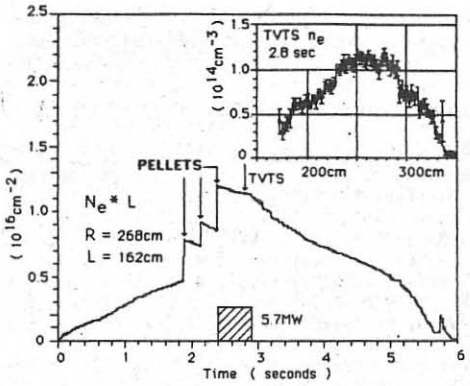


FIG. 2 Density evolution and profile shape - three 2.67 mm pellets at 1.88, 2.13, and 2.38 seconds.

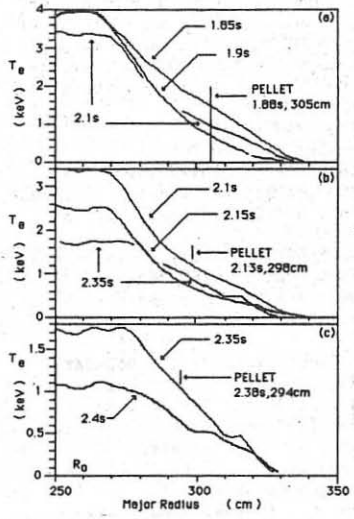


FIG. 3 Electron temperature profiles following pellet injection at 1.88, 2.13, and 2.38 seconds.

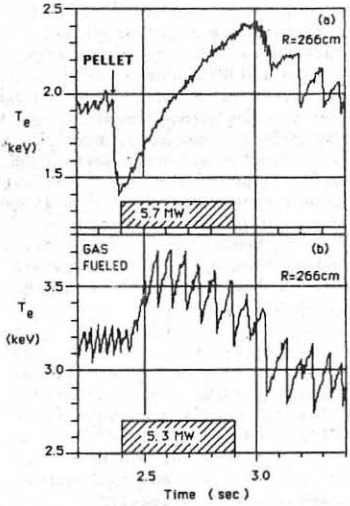


FIG. 4 Central electron temperature during beam heating pellet fueled (a) and gas fueled (b) discharges. At 2.8 seconds $\bar{n}_e$ equals: (a) 7 x 10^{13} cm^{-3}, (b) 4.1 x 10^{13} cm^{-3}.

LOWER HYBRID HEATING EFFECTS IN THE ASDEX TOKAMAK

D. Eckhartt, F. Leuterer, F. Söldner, A. Eberhagen, A. Giuliana[1], V. Mertens, H. Murmann, F. Ryter[2], R. Bartiromo[1], G. Becker, H.S. Bosch, M. Brambilla, H. Brocken, R. Burhenn, H. Derfler, G. Fußmann, O. Gehre, J. Gernhardt, G. v. Gierke, E. Glock, O. Gruber, G. Haas, M. Hesse[2], G. Janeschitz, F. Karger, M. Keilhacker, O. Klüber, M. Kornherr, P. B. Kotzé[3], M. Lenoci[1], G. Lisitano, H.M. Mayer, K. McCormick, D. Meisel, E. R. Müller, M. Münich, H. Niedermeyer, W. Poschenrieder, H. Rapp, H. Röhr, N. Ruhs, K.H. Schmitter, F. Schneider, G. Siller, P. Smeulders, K.-H. Steuer, T. Vien, G. Vlases[4], F. Wagner, F. v. Woyna, M. Zouhar

Max-Planck-Institut für Plasmaphysik
EURATOM Association, D-8046 Garching

1. During Lower Hybrid experiments in ASDEX significant bulk plasma heating was observed inside regions of the parameter space where none of the quasi-linear theories would predict coupling to any of the thermal plasma constituents. Launching of 400 kW of LH power at 1300 Mhz during 1 s in a deuterium plasma, generated by Ohmic heating, produced a maximum increase of the central electron temperature $\Delta T_e(0)$ of about 600 eV at an average plasma density $\bar{n}_e = 0{,}8 \cdot 10^{13}$ cm^{-3}, while the maximum ion temperature increase $\Delta T_i(0) = 150$ eV occurred at $\bar{n}_e = 3 \cdot 10^{13}$ cm^{-3}. These heating effects have been investigated in more detail by varying:
- the average plasma density, $\bar{n}_e$, between 0,4 and $4 \cdot 10^{13}$ cm^{-3}
- the relative composition of the working gases, H_2 and D_2
- the symmetric power spectra launched from the eight-waveguide grill coupler: by proper phasing between adjacent waveguides spectra centered around $\bar{N}_{\parallel} = 2$ and $\bar{N}_{\parallel} = 4$ were used with all other parameters kept as constant as possible.

The Ohmic heating currrent of 300 kA through the ASDEX target plasma produced central electron temperatures slowly decreasing with density, $T_e(0) = 0{,}9 \ldots 0{,}6$ keV whereas the central ion temperature stayed roughly constant, $T_i(0) = 0{,}5 \ldots 0{,}6$ keV.

2. The density range under consideration is determined by two boundary situations. At the high density end the LH-waves were found to generate energetic ions in the outer plasma regions /1/. At the lowest densities a non-thermal electron energy distribution develops, and with asymmetric power spectra from the grill launcher a net plasma current was driven by the LH-waves alone /2/. The plasmas thus formed have many features in common with those produced by Ohmic suprathermal discharges in ASDEX /3/. Upon increasing the density the plasma becomes more and more thermal, and a high heating efficiency for the LH-waves is observed /4/.

---

[1]ENEA Frascati, Italy
[2]CEN Grenoble, France
[3]Nuclear Development Corp. of South Africa, Pretoria
[4]University of Washington, Seattle, USA

3. Stochastic ion acceleration has been modelled /5/ and combined with numerical codes to calculate the power spectrum emitted by the grill and subsequent ray tracing through the ASDEX target plasmas. The validity of this approach was checked by comparing the results of similar calculations for WEGA III with the experimental data /6/, good agreement was found. For the $\bar{N}_{\parallel} = 4$-grill in ASDEX it was predicted that wave absorption by ions should start around $\bar{n}_e = 4 \cdot 10^{13}$ cm^{-3} in a H_2-plasma with $T_i(0) = 0{,}55$ keV, and should reach 40 % at $\bar{n}_e = 5 \cdot 10^{13}$cm^{-3}. The deposition was located in a wide zone around half minor radius. In experiments aimed to find this heating energetic ions started to appear at about half the predicted threshold density but no bulk heating was observed /1/. At a density of $3.6 \cdot 10^{13}$ cm^{-3} their place of birth was determined at $r \geq 0.7 \cdot a$ /7/. Absorption of LH-wave power by electrons via parallel Landau damping was predicted in a cylindrical two-fluid plasma of ASDEX properties to occur at higher $\bar{N}_{\parallel}$-numbers and much lower densities than quoted above for stochastic ion heating /8/. At such low densities ray tracing calculations did not show up any large modifications of the $\bar{N}_{\parallel}$-numbers when the waves propagate inwards. The calculations showed that different grill spectra produced different $T_e(0)$-increases in a given target plasma, revealing a "window" along the $\bar{N}_{\parallel}$-axis similar to the one found during ion heating in PETULA /9/. A certain minimum number $N_{\parallel}$ at the upper end of the power spectrum had to be surpassed in order to get the electron heating started, at too high $N_{\parallel}$-numbers the deposition zone lied close to the plasma edge and the additional heat was quickly lost to the outside.

4. In the density range foreseen for electron Landau damping bulk plasma heating has been observed in ASDEX, as mentioned in the beginning /4/, but with much lower $N_{\parallel}$-spectra. In Figs. 1 and 2 the measured increases in central electron and ion temperature are plotted as a function of mean plasma density. The electron heating was found to be concentrated in the central plasma region. With increasing density the heating zone broadens. Remarkably better electron heating was achieved when the LH-power was launched at lower $N_{\parallel}$-numbers - quite opposite to what one would expect from Landau damping. The ECE-signals of Fig. 3 which are due to the perpendiuclar velocity component of the high energy electrons (tail temperature around 50 keV) generated by the RF in the electron energy distribution, show an analogous dependence. This high energy electron population disappears at densities above $2 \cdot 10^{13}$ cm^{-3} (in H_2) and the electron energy distribution becomes thermal. Electron heating in deuterium persists to higher densities than in hydrogen plasmas. A similar trend was found in the current drive experiments /2/ for densities above $2 \cdot 10^{13}$ cm^{-3} as depicted by the $\Delta\dot{I}$-curves ($\Delta\dot{I} = (\dot{I}_{RF} - \dot{I}_{NORF})$ where $\dot{I}$ is the rate of plasma current change when the primary current I_{OH} is clamped. (During Ohmic discharges global energy confinement in D_2 is better than in H_2). The electron heating improves continuously with rising deuterium content. The central ion temperature increases (Fig. 2) show a common feature: a maximum increase around $\bar{n}_e = 3 \cdot 10^{13}$ cm^{-3}. At first sight this might be explained as a result of collisional coupling (increasing with density) and falling electron temperatures. The good agreement between neutron temperatures and parallel CX-temperatures as well as the absence of high energy tails in the parallel CX-spectra would also be compatible with collisional heat transfer from the electrons.

5. However, upon closer examination a number of discrepancies become evident: when comparing matching temperature increases of electrons and ions at a given density it is seen that higher electron temperature increases belong

to lower temperature increases of the ions, and vice versa In other words, higher $N_{\parallel}$-values generate higher ion temperature increases (Fig. 4) but lower electron temperature increases (Fig. 1). This behaviour leads one to consider heating effects other than collisional transfer from the electrons. In fact, the charge exchange detector viewing in the direction perpendicular to the main magnetic field starts to register the appearance of high energy ions above a threshold density of about $2 \cdot 10^{13}$ cm^{-3}. These fast ion fluxes continue to increase with density in the range considered here. They form a high energy tail in the perpendicular energy distribution of the ions thus indicating their direct interaction with LH-waves (which was expected to occur at about double the density as mentioned before). Subsequent collisions can transfer this energy gain into the parallel velocity component provided the ions stay long enough inside the plasma which implies that they are generated well inside the plasma volume where ripple diffusion becomes less and less important. As described above, this is not the case at higher plasma densities /7/. Thus one would have to speculate about the reasons which makes the ion interaction zone shift from the plasma centre to its periphery in the density range $\bar{n}_e = 1{,}5 \ldots 4 \cdot 10^{13}$ cm^{-3}. Such an outward shift would cause a decrease in the life times of the energetic ions thus explaining the observed maxima of the ion parallel temperature increases in this density range. At present, the available charge exhcange data is insufficient to support or discard such a possibility.

References

/1/ D. Eckhartt, et al., 4th Int. Symp. Heating in Toroidal Plasmas, Rome, Vol. I, 501 (1984)
/2/ F. Leuterer, et al., 10th Int. Conf. Plasma Physics and Contr. Fusion, London, IAEA Vienna 1985, Vol. I, p. 597. See also this conference
/3/ G. Fußmann et al., Phys. Rev. Letts. 47, 1004 (1981)
/4/ F. Söldner, et al., this conference
/5/ M. Brambilla, Chen Yan Ping, Proc. 3rd Int Symp. Heating in Toroidal Plasmas, Grenoble, 1982, EUR 7979 EN, Vol. II, p. 565
/6/ C. Gormezano, et al., Ibid., Vol. II, p. 439
/7/ F. Ryter, e al., Verh. Deutsch. Phys. Gesellsch. Frühjahrstagung Bayreuth 1985, paper P5
/8/ D. Eckhartt, A. McKenney, IPP-Report IV/197, March 1981 (unpubl.)
/9/ C. Gormezano, et al., Invited Paper, 6th Top. Conf. Radio Freq. Plasma Heating, Pine Mountain, Ga. (U.S.A.) 1985

Figure Captions

Fig. 1: Increase in peak electron temperature $\Delta T_e(0)$ vs. mean electron density $\bar{n}_e$. Electron temperatures are measured by Thomson scattering of laser light and by electron cyclotron radiation.
Fig. 2: Increase in peak ion temperature $\Delta T_i(0)$ vs. mean electron density $\bar{n}_e$. Ion temperatures are measured from the energy spectrum of charge exchange neutrals leaving the plasma in direction parallel to the main magnetic field, and from neutron radiation in deuterium plasmas.
Fig. 3: Plotted vs. mean electron density are: ECE-radiation at $2{,}5 \cdot \omega_{ce}$, and the changes in plasma current decay rate $\dot{I} = (\dot{I}_{RF} - \dot{I}_{NORF})$ when I_{OH} is set to zero.
Fig. 4: Ion temperature increase vs. rf-power from neutron flux increases in a deuterium plasma.

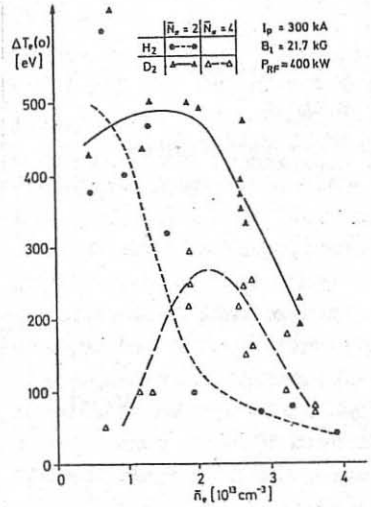


Fig. 1

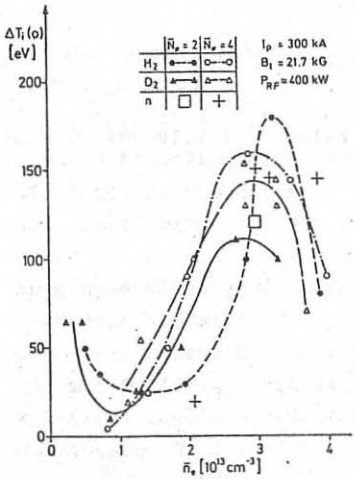


Fig. 2

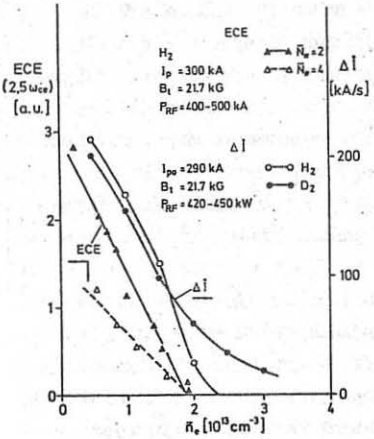


Fig. 3

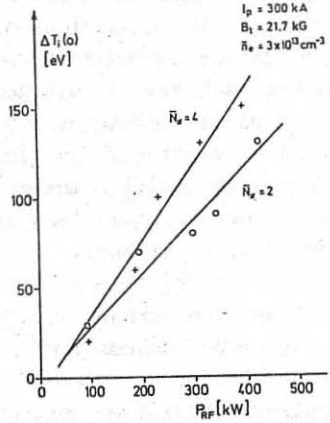


Fig. 4

PERIPHERAL PLASMA BEHAVIOUR AND LIMITER EROSION STUDIES IN T-3M TOKAMAK

D.G.Baratov, A.A.Vasiliev, V.N.Demyanenko, L.E.Demyanenko, E.V.Zelenov, I.V.Ivanov, S.B.Leonov, S.N.Luzganov, S.V.Mirnov*, V.V.Myalton, A.M.Runov, I.B.Semenov*, V.P.Fokin

NPO "Energiya", 109507 Moscow, USSR

* Kurchatov Atomic Energy Institute, Moscow, USSR

The study of erosion processes and plasma-wall interaction was continued in a T-3M tokamak facility. Experiments were conducted in the discharge with the following parameters: R=0,95 m; a - chamber radius - 0,2 m; $B_T \leqslant 1T$; $I_p \leqslant 45$ kA; $n_e \lesssim 3 \cdot 10^{19} m^{-3}$; $T_e(0) \leqslant 400$ ev; $Z_{eff} = 1.5 \div 2.5$, pulse length 50 msec., the plasma column is formed by three stationary circular graphite (УСБ-15) limiters with $a_L = 0,16$ m.

The specimens to be studied, made of graphite and boron nitride were placed on a rotating disc in one of the ports from the outside of the torus and could be alternately inserted into the discharge to the depth of2÷2.5 cm. The specimens represented a plate-shaped poloidal limiter with effective area of 7 x 2.5 cm^2. The dimensions of the specimens are 7 x 4 cm. In the section deflected to 135° along the torus, a vertical molybdenum bar (d = 1.4 cm) could be inserted into the plasma.

The plasma parameters in the limiter's shadow were studied by means of electrical probes-thermocouples suggested by A.P.Popryadukhin [1] . The relative degree of erosion was determined by the radiation from carbon and boron lines of low ionization (CII; CIII; BII).

Fig. 1 presents a profile T_e, obtained by means of X-ray, optical and probe measurements. The central "bell-shaped" part and a wider peripheral part of the profile are distinguished. The insertion of the specimen into the plasma within the wider peripheral part 2÷3 cm deep did not result in sharp changes in the discharge, although was accompanied by a certain decrease in the discharge current (in the T-3M facility, the supply system is programming a $V_p(t)$ change).

Depending on n_e, two types of modes were found.

Experiments with $n_e < 1.5 \cdot 10^{19}$ m^{-3} revealed strong heating of limiter surface corresponding to local power load of 5 kW/cm^2. The study of the boron nitride specimens [2] revealed erosion of the electron side of the limiter to the depth of 2÷3 mm. One could suggest that the reason was the runaway electrons. Fig. 2 shows the boron spectral line BII intensity as a function of n_e. Also shown is the X-radiation intensity from the studied specimen in the range of 20÷100 kev. Apparent correlation in their behaviour is observed. Such modes can be eliminated increasing the concentration $n_e > 1.5 \cdot 10^{19}$ m^{-3} or by imposing with multipole windings external perturbations $m = 1$, $n = 1$ (or $m = 2$, $n = 2$) at the level of 3÷5% B_φ, which do not affect significantly the column's macroscopic stability but suppress the accelerated electrons maybe due to destruction of magnetic surfaces in the acceleration zone.

In the case of modes with $n_e > 1.5 \cdot 10^{19}$ m^{-3}, the measurements of the radial distribution of thermal fluxes dropping on the surface of the moving limiter has been made. At first the measuring limiter was placed at the radius, equal to the radius of the stationary limiter. The following results were obtained:

a) heat release in the limiter's shadow decreases exponentially, $P = P_o \exp.(-x/\lambda_p)$;

b) the maximum discharge-averaged P_o value at the limiter's edge reached 0.5÷1 kW/cm^2. The heat release on the electron side of the plate exceeds the heat release on the ion side by a factor of 2;

c) n_e density in the limiter's shadow was also proportional to $\exp(-x/\lambda_n)$ decreasing from $1 \cdot 10^{18}$ m^{-3} near the edge to $3 \cdot 10^{16}$ m^{-3} near the wall;

d) typical $\lambda_p \approx \lambda_n$ values are 5 - 8 mm;

e) assuming that plasma penetration into the limiter's shadow is described by diffusion model (penetration time is determined by ion transit along the torus at a speed of $V_s = 10^6 \sqrt{T_e}$), diffusion coefficient near the T-3M wall will be of the order of Bohm value and $\lambda_p \propto R^{\frac{1}{2}}$, which is typical for tokamaks. Note that for T-10 facility (R=1.5 m) λ_p=0.7÷1 cm and for JET facility (R=3 m) λ_p = 1.2÷2 cm;

f) giving the energy flux P as $P = \gamma I_s T_e$, where I_s is the density of the ion saturation current, we found the γ value corresponding to actual heat transfer on the T-3M limiter. The expected γ value may vary from 8 to 30 [3] being dependent on emission properties of the surface. In our case γ value was 10÷20.

Then the moving limiter was inserted deep into the plasma. It was to be expected that in course of plate insertion deeper into the plasma column λ_p would increase at least by the factor of $q^2 \approx 2$ ($q = B_T a^2 / 0.2 I_p \cdot R$) together with exponential increase of energy release onto the plate surface up to the total flux carried away from the column by charged particles. However, even when inserting the plate 2 cm deep ($\approx 3\lambda_p$), energy release onto the limiter was no more than 0.2 ($\overline{P}_{OH} - \overline{P}_{rad}$) ($\overline{P}_{OH}$ - average ohmic energy contribution during the discharge; $\overline{P}_{rad}$ - the power of radiation losses). Fig.3 presents the value of energy release in the limiter's point at the distance of 8 mm from the limiter's edge depending on the depth of the moving limiter insertion into the column from ion and electron side. The total heat flux not only has no exponential increase but rather reveals saturation at the level 0.2 ($\overline{P}_{OH} - \overline{P}_{rad}$) which is 5 times lower than the expected value. This suggests the presence of the plate's self-shielding effect when the plate is inserted into the plasma. To determine the reason of self-shielding, a molybdenum bar was inserted into the plasma. Fig.4 presents the results of interaction of the two limiters - the moving limiter and the bar-limiter. The calculation shows that at the point rapid decrease P the bar starts to overlap the surface $q = 3$. The local overlapping of the resonance surfaces is equivalent to introducing $I_p(r,\varphi)$ current modulation [4], and this should cause the formation of stationary magnetic islands (in our case $m=3$, $n=1$). The formation of the islands will lead to the increase in particle transfer onto the wall and stationary limiter. Of course, the above interpretation is only one of those possible. Erosion experiments using different specimens show that insertion of the specimen into the plasma entails the increase in background radiation from chamber walls with deposited impurities (namely, carbon). This may be the result of plate's self-shielding. The measurements of CII background when inserting the

tantalum plate showed that his background was comparable with CII radiation induced by УС6-15. This make erosion experiment more difficult. In conclusion, the following results were obtained during experiments at the T-3M facility:

1. At $n_e < 10^{19} m^{-3}$ the high heat release on the limiter may be due to the hitting of accelerated electrons on the limiter. 2. In the range of average and high n_e values, heat release near the edge of stationary limiters can be well described by diffusion model with a diffusion coefficient close to D_B. 3. The plateshaped limiter, when inserted into the plasma, reveals the effect of self-shielding in relation to the heat fluxes. The possible reason may be the formation of stationary magnetic islands near the integer q zone.

References

1. L.A.Artyomenkov et al. Pervie experimenti na tokamake s divertorom TO-2. Preprint IAE-3515/7, 1981.
2. D.G.Baratov et al. Voprosi atomnoi nauki i techniki. Ser. Termoyaderniy sintez, vip.2, 1985, p.27.
3. S.J.Zweben, R.J.Taylor, Nucl.Fus., v.23, No.4, 1983, p.513.
4. S.V.Mirnov, Fizika Plasmi, vol.7, N.4, 1981, p.795.

FIG.1

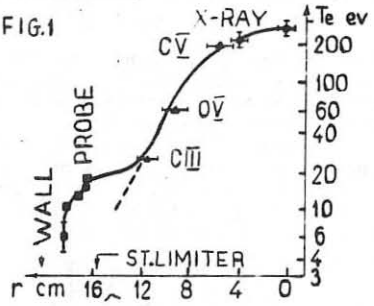


FIG.2

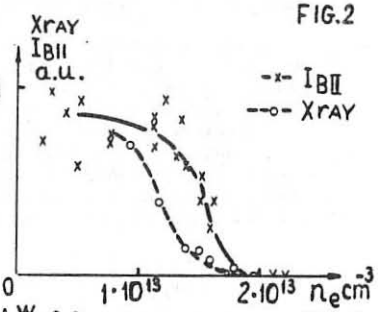


FIG.3

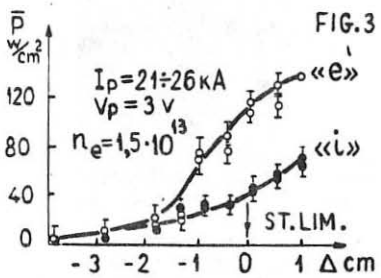
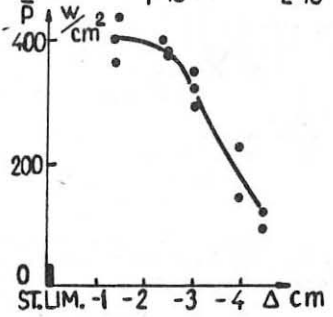


FIG.4



EXPERIMENTAL STUDY OF STIMULATED RAMAN STATTERING IN LASER-PLASMA INTERACTION AT 0.26 μm

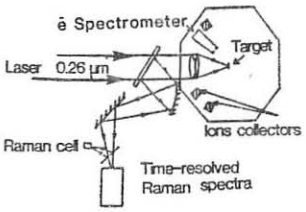
GRECO INTERACTION LASER-MATIERE - ECOLE POLYTECHNIQUE

C. LABAUNE, E. FABRE, F. BRIAND (PMI Ecole Polytechnique
91128 Palaiseau France)
H. BALDIS (NRC, Ottawa K1A OR6 Canada))

In stimulated Raman scattering (SRS) the incident e.m. wave decays into a scattered e.m. wave and an electron plasma wave. This instability is of concern for laser fusion experiments because very energetic electrons can be generated by damping of the electron plasma wave and lead to target preheat.

Past experiments [1] have shown that short laser wavelengths are very favourable for interaction processes because they produce high absorption rate by enhancing inverse Bremsstrahlung. Future experiments will use smoother density gradient plasmas, so that the thresholds of most of the parametric instabilities in the corona could be exceeded even for short laser wavelengths. We present here some new results on the observation of stimulated Raman backscattering in thin plastic foils interaction with 0.26 μm laser light.

Experiments are conducted with the neodymium laser of the GRECO ILM. Its frequency is doubled and quadrupled by the use of KDP crystals with a total efficiency of about 35%. Pulses are 450 ps F.W.H.M. The beam is focused with a f/2.5 aperture lens and the focal spot diameter is 45 μm at half energy : maximum intensity on target is 2×10^{15} W/cm^2. Targets are thin plastic ($C_{10}H_8O_4$) foils of 1.5 μm initial thickness ; the latter is chosen so that the foil is completely ablated during the laser pulse ; a quasi-parabolic density profile along the laser axis is thus produced. The useful length for Raman instability, which corresponds to plasma densities going from ~ 0.05 to 0.25 n_c (n_c is the



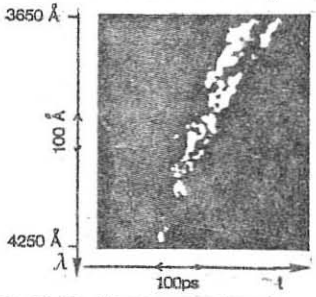


Figure 1 : Experimental set-up of the Raman experiment
Figure 2 : Exemple of time-resolved spectrum of backscattered Raman light emitted during the interaction of 0.26 μm laser and a thin plastic foil.

critical density), is about 50 μm ; this value is obtained from 2D hydrodynamic simulations [2] which also yield a local electronic temperature in the corona of 600 eV. The experimental set-up is shown on figure 1. Main diagnostics of Raman instability are based on the analysis of scattered light and hot electron generation. Time-resolved spectra are recorded on a streak camera with temporal and spectral resolutions of respectively 30 ps and 90 Å at the output of the system ; the full spectral range is 3000-5000 Å. Electron energy distribution is analysed with a magnetic spectrometer in the range 20 to 250 keV. Energies of incident, transmitted, scattered light are also monitored with properly filters on calorimeters.

Figure 2 shows an example of Raman spectrum versus time recorded for an intensity of 1.2×10^{15} W/cm^2. Some characteristics are common to all the observed spectra :

- For all the shots the spectral emission lies between 3600 and 4400 Å.
- As time increases, wavelength decreases. Emission for a given wavelength is very short in time : 10 to 120 ps ; total emission lasts about 300 ps, so, it is shorter than the laser pulse.
- Many spectra show temporal and spectral sturctures.
- Polarizations of the scattered light and of the laser are parallel.

Intensity of the Raman light versus incident intensity is shown on Figure 3 ; for all these points the focal spot diameter is kept constant:

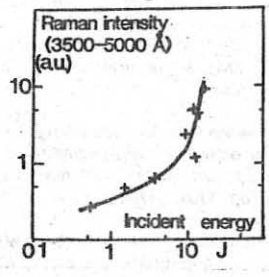


Figure 3 : Raman intensity versus incident intensity

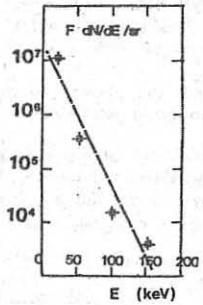


Figure 4 : energy distribution of hot electrons.

From this curve we can define a threshold for the emission at about 5J, that is an intensity of 7×10^{14} W/cm^2 on the target. Behond this, Raman intensity grows very fast with laser intensity. Nevertheless maximum Raman rate over incident energy is 10^{-7} for light collected in the focusing optics.

Figure 4 shows an example of the spectrum of energy of hot electrons. Assuming it is a Maxwellian distribution, we obtain a hot temperature of (17-21 keV). Total number of electrons collected is very low ~ (5×10^7 - 5×10^8)/sr, and their emission is connected with Raman light.

All these results are consistent with the occurence of SRS in the underdense plasma. If (ω_o, $\underline{k}_o$), (ω_s, $\underline{k}_s$), (ω_p, $\underline{k}_p$) are the pulsations and wave-vectors respectively of the incident, backscattered e.m. wave and plasma

wave, the linear dispersion relations and conservation laws for Raman backscattering are : $\omega_o = \omega_s + \omega_p$; $k_o = k_p - k_s$; $\omega_o^2 = \omega_{pe}^2 + k_o^2 c^2$; $\omega_s^2 = \omega_{pe}^2 + k_s^2 c^2$; $\omega_p^2 = \omega_{pe}^2 + 3\, k_p^2 v_{Te}^2$, where $\omega_{pe} = (n_e e^2/m_e \epsilon_o)^{1/2}$ is the plasma frequency, n_e the electron density and $v_{Te} = (Te/m_e)^{1/2}$ the thermal velocity. When the electronic temperature is not too high, that means if $3\, k_p^2 v_{Te}^2 \ll \omega_{pe}^2$ which is valid for Te < 7 keV at $n_e = 0.1\, n_c$ and Te < 20 keV at $n_e = 0.2\, n_c$, and can be used for our conditions, there is a relationship between the scattered wavelength (λ_s) and the electronic density :

$$\omega_s = \omega_o - \omega_p \simeq \omega_o \left[1 - \left[\frac{n_e}{n_c}\right]^{1/2}\right] \Longleftrightarrow \lambda_s = \lambda_o \left[1 - \left[\frac{n_e}{n_c}\right]^{1/2}\right]^{-1} \qquad (1)$$

If we apply this formula to the measured spectral limits, we can see that SRS takes place for densities between 0.26 µm and 0.16 n_c, going to lower densities as time increases.

With same hypothesis as above, we can establish a relationship between the hot electron temperature (n_h) and the electronic density by assuming, as suggested by numerical simulations [3], that electrons are accelerated up to the phase velocity of the plasma wave :

$$T_h \simeq \frac{1}{2} m_e \left[\frac{\omega_p}{k_p}\right]^2 \Longrightarrow T_h \simeq \frac{1}{2} m_e c^2 \frac{n_e}{n_c} \left[\left[1 - \frac{n_e}{n_c}\right]^{1/2} + \left[1 - 2\left[\frac{n_e}{n_c}\right]^{1/2}\right]^{1/2}\right]^{-2} \qquad (2)$$

For the above densities this formula provides a hot temperature of 4 to 17 keV, in good agreement with the measured values.

Number of hot electrons (n_h) can be estimated by assuming [4] that the energy flux in hot electron due to the damping of the plasma wave is equal to the energy flux carried away by hot electons with a half Maxwellian distribution : $0.6\, n_n T_h v_n \simeq r I\, \omega_p/\omega_s$ when r is the Raman rate. This gives :

$$n_{h(m-3)} \simeq 1.4 \times 10^5 r I_{(W/cm^2)} \frac{n_c}{n_e} \left[1 - \left[\frac{n_e}{n_c}\right]^{1/2}\right]^{-1} \left[\left[1 - \frac{n_e}{n_c}\right]^{1/2} + \left[1 - 2\left[\frac{n_e}{n_c}\right]^{1/2}\right]^{1/2}\right]^3$$

So, the very low level of Raman rate can explain the small number of hot electrons measured.

Comparison between experimental threshold and theory must take into account the density profile shape. In a linear density profile reference [5] provides :

$$I_{th} = \frac{4.3\ 10^{17}}{\lambda L} \qquad (3)$$

when I_{th} is in W/cm^2, L the gradient density scale length and λ are in µm. With L = 50 µm and λ = 0.26 µm, we obtain $I_{th} = 3 \times 10^{16}$ W/cm^2 which is higher than the measured value.

If we use a parabolic density profile, the threshold formula at the top of the parabola $n_e = n_o (1 - x^2/L^2)$ can be achieved [6] :

$$I_{th} = 5 \times 10^{15} \frac{T_e^{1/3}}{\lambda^{2/3} L^{4/3}} \left[\frac{n_c}{n_o}\right]^{1/3} \qquad (4)$$

with the same units as above and T_e in eV. For L = 50 μm and T_e = 1 keV we obtain $I_{th} = 6 \times 10^{14}$ W/cm² very close to the experimental results. This could explain that SRS can occur at relatively low intensities.

Some other effects may also happen, as profile steepening at $n_c/4$ due to two-plasmons decay or absolute Raman scattering ; consequently a smoother density gradient, or a plateau, is generated below, which locally lowers the SRS threshold in formula (3). Propagation of this plateau downwards the density gradient [7] could explain the spectral behaviour as observed on figure 2. The latter could also be correlated with the decrease of the maximum density of the thin foil during the laser pulse. Spectral and temporal structures correspond to more or less intense emission area which are not reproducible from one shot to another. More work is needed to better understand all the physical processes involved.

In conclusion, stimulated Raman backscattering has been evidenced in 0.26 μm experiments with aspect ratio (L/λ) of about 200 and intensities up to 2×10^{15} W/cm². SRS occurs for laser flux higher than 7×10^{14} W/cm² at densities between 0.06 n_c and 0.16 n_c ; hot electrons temperature and number are consistent with simple model. One important result is the very low level of Raman light (~ 10^{-7} I_o) which indicates that collisional damping may severely reduce SRS at short laser wavelength.

REFERENCES

[1] C. LABAUNE, E. FABRE, C. MAX, F. AMIRANOFF, R. FABBRO, A. MICHARD
Phys. Rev. Lett., 48, 1018 (1982)

[2] These simulations were provided by K. ESTABROOK that we thank here for his helpful collaboration.

[3] K. ESTABROOK and W.L. KRUER
Phys. Fluids, 26, 1892 (1983)

[4] K. ESTABROOK, W.L. KRUER and B.F. LASINSKI
Phys. Rev. Letter, 45, 1399 (1980)

[5] C. LIU, M.N. ROSENBLUTH and R. ROSCOE, B. WHITE
Phys. Fluids, 17, 1211 (1974)

[6] C. LABAUNE, E. FABRE, J. BRIAND, F. BRIAND, G. BONNAUD, A. MICHARD
GRECO ILM Annual Report (1984)

[7] A.B. LANGDON, B.F. LASINSKI and W.L. KRUER
Phys. Rev. Letter, 43, 133 (1979)

BEHAVIOUR OF RECYCLING AND IMPURITY RADIATION DURING LH HEATING IN FT DISCHARGES

R. De Angelis, G. Tonini

Associazione EURATOM-ENEA sulla Fusione, Centro Ricerche Energia Frascati, C.P. 65 - 00044 Frascati, Rome, Italy

INTRODUCTION

To obtain a better understanding from auxiliary heating experiments in a Tokamak plasma it is necessary to monitor either the heating efficiencies and other related effects such as profile modifications, power emission, impurity influxes, partial confinement times etc..

We report here measurements of bolometric, spectroscopic and H_α brightnesses in FT discharges in which LH waves at 2.45 GHz with a power up to 450 kW were injected through two 2x2 coupling structures.

1. INSTRUMENTATION AND MAIN CHARACTERISTICS OF THE DISCHARGES

i) Bolometric data were obtained from a tiltable, collimated pyroelectric detector looking at various chords with 1 cm spatial resolution. Radiation distributions were then estimated by Abel inversion methods.

A calibrated V.U.V. monochromator allowed detection of impurity lines in the 200÷1200 Å wavelength range along a central chord, located near one of the launching structures. The most important lines observed were OVI-(1032 Å), FeXVI-(335 Å), FeXXIV-(192 Å). Other atomic species are hardly detectable on FT, which has stainless steel limiter and liner and has usually $Z_{eff} \sim 1\div2$.

Recycling was monitored by several H_α detectors at different toroidal locations, in particular H_α radiation at the limiter port plays the major role for the global recycling in our machine.

ii) We examined discharges (mainly in the electron heating mode) with $B_T = 60\div80$ kG, $n_e = 3\div6\times10^{13}$ cm^{-3}, $I_p = 300$ kA, $P_{RF} = 200\div450$ kW. In all the shots the RF pulse started at 400 msec (during current plateau) and lasted 100÷120 msec. P_{RF} was always an appreciable amount of ohmic input power (50-100%).

2. EFFECTS OF IMPURITIES

The Z_{eff} of the discharge is only slightly affected by the RF pulse, the variation of the impurity signals being due mainly to the density increase rather than to real flux increments.

The iron contribution (as determined by the FeXVI line brightness) is the most important; the flux increase during RF is 20÷30% and the normal level for absolute concentration is between .5-1×10^{11} cm^{-3}. The brightness of oxygen lines (the only important light impurity in FT) may even vary by factors 3 during RF but the absolute concentration, which is initially ~ 5×10^{10} cm^{-3} does not contribute much to Z_{eff}.

3. RADIATED POWER

During RF a general increase of emitted power detected bolometrically was observed in the whole discharge. Although the absolute radiative emission is strongly influenced by plasma parameters and RF level, the fraction of total input power (ohmic + RF) lost by radiation increases only slightly in the heating phase. For all discharges P_{rad} was 140÷210 kW before RF i.e. 30÷40% of ohmic power, while during heating P_{rad} = 240÷360 kW: about 35÷45% of ohmic + RF power.

No significant profile variation is generally seen during RF: indeed for $P_{RF} \leq 300$ kW the central plasma emission does not increase within the data errors.

Radiation behaviour seems to agree qualitatively with numerical simulations of Fe line brightness (which strongly affects P_{rad}) showing an increase of FeXVI line (located mainly at about 3/4 of minor radius) but no increase of FeXVIV line (located at the plasma core).

4. BEHAVIOUR OF DENSITY AND RECYCLING

A regular feature of all discharges below the critical density for electron heating was a significant increase of the electron density during LH. The value of $\Delta n/n$ ranged between ~20% at P_{RF} = 300 kW and ~50% at P_{RF} 450 kW in discharges without sawtooth activity. At P_{RF} = 300 kW discharges in which sawteeth were present showed $\Delta n/n$ of the order of 50%.

The density variation was correlated to a sudden decrease of radiation at the limiter port, while no significant variations were observed in other toroidal locations.

Estimates of gross particle confinement time were carried out from the mass conservation equation. The neutral gas flux into the plasma was derived from gas puffing flux (actually no gas was injected during RF) while recycling was determined from H_α data; a correction term for the iron flux, which constitute an extra n_e source, was also included.

The particle confinement time derived from this model improves by 50÷100% during RF, even when the variation of iron flux, which reduces this increment, is considered in the most pessimistic way (i.e. maximized by over estimating its ionization degree).

In the figure the B_{lim}/B_{wall} ratio is plotted against n_e. The figure suggests that recycling changes suddenly before n_e rises, so that the density increase and the τ_p improvement seem to be a result of better plasma wall interaction.

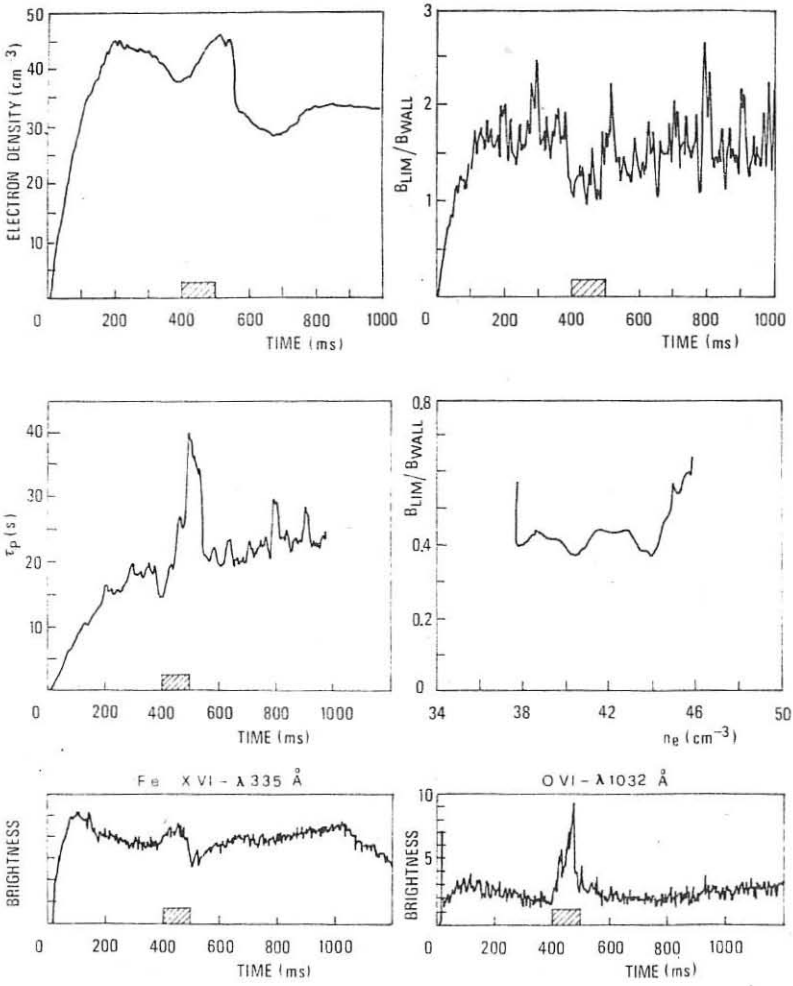


Fig. 1 - Electron density, H_α brightness ratio vs time, τ_p, B_{ratio} vs n_e during RF, FeXVI and OVI brightness.

At densities well above the threshold for electron heating mode no change is observed either in the electron density or in the H_α brightness.

In some discharges in the electron heating mode we had some evidence that the τ_p improvement ended when the density, during rise, crossed the threshold for electron heating.

CONCLUSIONS

The behaviour of bolometric and line radiation in FT discharges during LH heating has been investigated.

No dramatic impurity flux increment was detected spectroscopically in accordance with the modest increase of bolometric signals.

When operating in the electron heating mode a sharp decrease of the recycling process was deduced by the H_α measurements, this can be interpreted as an improvement of particle confinement time and is confirmed by the significant increment in the observed density.

REFERENCES

[1] S.C. Luckhardt et al., AFC/JA 84-42, MIT Int. Report (December 1984)

TURBULENT CONDUCTIVITY OF A MAGNETIZED PLASMA

V.N.Pavlenko, V.G.Panchenko
Institute for Physics of the Ukrainian Academy of Sciences, Kiev - 28, USSR

and S.M.Revenchuk
Institute for Nuclear Research of the Ukrainian Academy of Sciences, Kiev - 28, USSR

The investigation of a magnetized plasma heating by r.f. waves is carried out mostly for the frequency ranges where the effective mechanisms of r.f. power absorption exist. One of them is lower hybrid frequency range for which the frequencies of order GHz are typical in the fusion plasmas. The effect of parametric resonance is widely used for the anomalous plasma heating. In this case r.f. wave energy dissipation is determined by effective collision frequency or r.f. turbulent conductivity since $\sigma_{turb} \propto \nu_{eff}$ [1].

In the present report the anomalous plasma heating is investigated for the case when the pump intensity exceeds the threshold value for the excitation of three-wave parametric instability, i.e. decay of the pump wave into lower hybrid and ion-acoustic waves. It is shown that scattering of the charged particles by the suprathermal plasma fluctuations which are expressed in the form of effective collision frequency provides a nonlinear mechanism of the instability saturation. The magnitude of σ_{turb} is calculated and is shown to be proportional to the pump wave intensity in this case while the linear theory [2,3] predicts unlimited increasing of plasma conductivity near the parametric instability threshold. The value of σ_{turb} may exceed considerably the conductivity due to Coulomb collisions.

Let us determine the effective collision frequency ν_{eff} for the magnetized plasma ($\vec{B}_0 = B_0\hat{z}$) immersed into the homogeneous pump field $\vec{E}(t) = E_0\hat{y}\cos\omega_0 t$. Assuming that ν_{eff} is determined by the level of the fluctuation fields we have to find the

relationship between these quantities. Following [4] we shall consider the pump wave frequency $\omega_0 \geq 3\omega_{LH}$, where $\omega_{LH} = \omega_{pi}(1 + \omega_{pe}^2/\Omega_e^2)^{-1/2}$, $\omega_{p\alpha}^2 = 4\pi e^2 n_\alpha/m_\alpha$ and $\Omega_\alpha = e_\alpha B_0/m_\alpha c$. In this case the resonant excitation of the lower hybrid and ion-acoustic waves by the pump wave is possible. The threshold of such instability is [4]

$$E_{th}^2 = \frac{\omega_0^2 B_0^2}{k^2 c^2} \frac{16 \gamma_0 \gamma_{-1}}{\omega_s \omega_{lk}} \left(k r_{De}\right)^2$$

Here ω_s and ω_{lk} are the frequencies and γ_0 and γ_{-1} are the damping rates of the ion-acoustic and lower hybrid waves, respectively, and r_{De} is the Debye radius of electrons. An idia of the obtaining of the equation for ν_{eff} is based on the analogy between the effects of Coulomb collisions and particles scattering by the fluctuations [5,6]. We can express ν_{eff} through the turbulent conductivity σ_{turb} as

$$\nu_{eff} = \frac{m_e \omega_0^2}{e^2 n_e} \sigma_{turb} \qquad (1)$$

The conductivity σ_{turb} caused by r.f. pump field is determined by the energy balance equation

$$\frac{1}{2} \sigma_{turb} E_0^2 = \sum_\alpha n_\alpha \int \frac{p^2}{2m_\alpha} I_\alpha(\vec{p}) d\vec{p}$$

where $I_\alpha(\vec{p})$ is the collision integral of the charged particles in plasma. When the parametric instability may be excited, i.e. $E_0 > E_{th}$, the intensity of the fluctuation fields becomes sufficiently large and the velocity space diffusion coefficient gives the main contribution to the collision integral [2,3]. Then we obtain the following expression for the effective collision frequency

$$\nu_{eff} = \frac{2m_e \omega_0^2}{e^2 n_0 E_0^2} \int \frac{d\vec{k}}{(2\pi)^3} \int \frac{d\omega}{2\pi} \langle \delta\vec{E} \cdot \delta\vec{E} \rangle_{\omega,\vec{k}} \frac{\omega}{4\pi} \sum_\alpha \mathrm{Im}\, \chi_\alpha^0 \qquad (2)$$

Here $\langle \delta\vec{E} \cdot \delta\vec{E} \rangle_{\omega,\vec{k}}$ is the spectral fluctuation density of the

electric field and $\chi_\alpha^n \equiv \chi_\alpha(\omega + n\omega_0, \vec{k})$ is the linear susceptibility of the magnetized plasma.

We can write the spectral distribution of the electric field fluctuations near the eigenfrequencies in the form

$$\langle \delta\vec{E} \cdot \delta\vec{E} \rangle_{\omega,\vec{k}} = \pi \sum_i I_{\vec{k}_i} \delta(\omega - \tilde{\omega}_{\vec{k}_i}) \qquad (3)$$

where $I_{\vec{k}_i}$ is the intensity of the fluctuations at the eigenfrequencies $\omega_{\vec{k}_i}$ and ν_{eff} is taken into account so that $\tilde{\omega}_{\vec{k}_i} = \omega_{\vec{k}_i} + i\nu_{eff}$.

The form of the obtained equation for the intensity of the fluctuations $I_{\vec{k}_i}$ is analogous to the linear theory equation (see Eq. (44) in [3]), but now the oscillation frequency $\tilde{\omega}_{\vec{k}_i}$ is a function of the fluctuation intensity $I_{\vec{k}_i}$. Integrating this equation over k we find the effective collision frequency since ν_{eff} is determined by the fluctuation intensity as it follows from Eqs. (2) and (3). The existence of the solution of this equation means that the interaction between the perturbations of the unstable plasma leads to the establishment of the stationary level of turbulence [7]. Comparing the scattering of charged particles by ion-acoustic and lower hybrid fluctuations we see that ν_{eff} is determined mostly by the level of ion-acoustic fluctuations.

When the pump intensity exceeds the threshold value considerably we have developed level of turbulent fluctuations. Then ν_{eff} exceeds the damping rates of the resonant Landau damping of the decay waves. The expression for ν_{eff} takes a form ($\nu_{eff} < \omega_s$)

$$\nu_{eff} = 16\sqrt{8\pi}\,\frac{m_i}{m_e}\left(k_0 r_{De}\right)^4 \left(\frac{\gamma_0}{\omega_s}\right)\left(\frac{\gamma_{-1}}{\omega_{lk}}\right)^2 \frac{E_0^2}{E_{th}^2}\,\omega_s \qquad (4)$$

Eq. (4) is valid for the pump fields which satisfy the conditions

$$10^{-2}\,\frac{m_e}{m_i}\left(k_0 r_{De}\right)^{-4}\left(\frac{\omega_{lk}}{\gamma_{-1}}\right)^2 < \frac{E_0^2}{E_{th}^2} < \left(\frac{m_e}{m_i}\right)^{5/6}\left(n r_{e De}\right)^{-1/3}\left(\frac{\omega_{lk}}{\gamma_{-1}}\right)^{5/3}\left(\frac{\omega_s}{\gamma_0}\right)\left(k_0 r_{De}\right)^{-10/3}\left(\frac{\omega_{pe}}{\Sigma_e}\right)^{2/3} \qquad (5)$$

The turbulent conductivity caused by ν_{eff} may exceeds the classical one $\sigma_0 \propto \nu_{ei}$ (ν_{ei} is the electron-ion collision frequency) by several order of magnitude for the pump fields satisfying inequalities (5). Thus, an effective mechanism of r.f. power dissipation in plasma is provided and it explains qualitatively the process of lower hybrid plasma heating.

It has been noted in [8,9] that it is impossible to explain the observed r.f. plasma heating by Coulomb collisions and Cherenkov damping only and that the charged particles scattering by turbulent pulsations of electric field described by effective collision frequency may be a cause of the anomalous plasma heating.

Referencies

1. V.P.Silin. Parametric Effects of High Power Radiation on a Plasma, Nauka Press, Moscow, 1973.
2. V.Yu.Bychenkov, V.P.Silin. JETP 67, 134 (1974).
3. V.N.Pavlenko, V.G.Panchenko, S.M.Revenchuk. Plasma Phys. and Contr. Fusion 26, 1221 (1984).
4. M.Porkolab. Phys. Fluids 17, 1432 (1974).
5. C.T.Dum, T.H.Dupree. Phys. Fluids 13, 2064 (1970).
6. A.A.Galeev, D.G.Lominadze, A.D.Pataraya, R.Z.Sagdeev, K.N. Stepanov. JETP Lett. 15, 417 (1972).
7. A.G.Sitenko. Fluctuations and Non-Linear Wave Interaction in Plasmas, Pergamon Press, Oxford, 1982.
8. V.F.Tarasenko, A.B.Kitsenko, V.I. Panchenko, K.N.Stepanov. JTP 42, 1996 (1972).
9. G.M.Batanov, L.M.Kovrizhnykh, A.E.Petrov, A.V.Sapozhnikov, K.A.Sarksyan et al. JETP 85, 1209 (1983).

SIMULATION OF THE PLASMA RESPONSE TO MODULATED POWER IN LOWER HYBRID ELECTRON HEATING EXPERIMENTS

E. Barbato, R. Giannella

Associazione EURATOM-ENEA sulla Fusione, Centro Ricerche Energia Frascati, C.P. 65 - 00044 Frascati, Rome, Italy

It has been recently suggested [1] to measure the energy deposition profile in plasma heating experiments by modulating, at an appropriate frequency, a fraction of the additional power. In fact, if the modulation time is less than the time employed by the heat diffusion to cover the resolution length, the temperature oscillations occur, with appreciable amplitude, only where the energy is directly deposited. This clearly emerges from the high frequency analysis of the diffusion equation for the plasma temperature, in which an oscillating source term is included:

$$\partial/\partial t\ [\langle T\rangle + \tilde{T}] = 3/2\ \chi\ \nabla^2 T + 2/3n\ [\langle P\rangle + \tilde{P}] \qquad (1)$$

here $\langle T\rangle$ and $\tilde{T}$ and ($\langle P\rangle$ and $\tilde{P}$) are the mean part and the oscillating part of the temperature (of the power density) respectively, n is the density and χ the thermal conductivity which is allowed to be a function of the spatial position of the type $\chi \sim 1/n$.

Once the deposition profile is obtained, operations at lower frequency permit to study plasma transport properties, this can be done by measuring the phase delay of the temperature oscillations outside the deposition region by means of the synchronous detection [2].

In this paper we study the possibility of applying this technique to the Lower Hybrid Electron Heating (LHEH) scheme having in mind the parameter of the Frascati Tokamak experiment [3,4].

To establish the working modulation frequency for a medium size tokamak like FT we refer the reader to the discussion of Ref. [1] where the adimensional parameter $\gamma=(\omega/D)^{1/2}$ (Δr) was introduced and a γ value of the order of 4 was judged to be adequate. Assuming a resolution length $\Delta r \cong 3$ cm (FT has a minor radius of 20 cm) and a diffusion coefficient $D = (2/3)\ \chi \cong 8000\ cm^2/sec$ at the plasma center, a modulation time $\tau = \pi/\omega = 250\ \mu sec$ results.

As shown in Ref. [1], for this value of γ a 6% is expected for the ratio $\tilde{T}/\langle T\rangle$, if all the injected power is modulated. Since in the FT experiment 300 kW of unmodulated power give an electron temperature increase of ~ 1 keV [4], at the plasma center, a temperature oscillation amplitude of some tenth of eV is expected if a train of square pulses of 600 kW power is injected into the plasma.

In order to establish what is expected in such a kind of experiment we try to simulate the plasma response to a modulation of the RF power through a very simple model. In the LHEH scheme the RF power couples to the supra-

thermal electrons and the plasma temperature increase results from the relaxation of these fast electrons.

The time evolution of the power density collisionally released to the bulk electrons is calculated by numerically solving the one dimensional Fokker-Planck equation for the tail electrons [5] in the presence of a modulated quasilinear term due to the RF waves.

$$\partial f/\partial \tau = \partial/\partial w\ D_o\ \partial/\partial w\ f + (\partial f/\partial t)_c \qquad (2)$$

when w is the velocity parallel to the magnetic field, D_o the RF quasilinear diffusion coefficient and $(\partial f/\partial t)_c$ the Fokker-Planck term. Here the time and the velocity are normalized to $\nu^{-1}=(\ell n\Lambda \omega_{pe}^4 /2\pi n v_{the}^3)^{-1}$ and to $v_{th}=\sqrt{T/m}$ respectively, so that D_o is the diffusion coefficient normalized to $\nu_o v_{th}^2$. The Fig. 1 shows the assumed temporal behaviour of the RF power [1a] and the corresponding time evolution [1b] of the power density gained by the bulk electrons at different radial positions. To obtain these results same hypothesis were made:

i) All the power was assumed to be absorbed inside the flux surface of radius r/a = 0.4, according to a deposition profile consistent with a power balance performed on FT [6].
ii) The space velocity diffusion coefficient D_o was assumed constant between the minimum and the maximum phase velocities and equal to the lowest value (D_o = 1.5) giving in the steady state a dissipated power level independent from D_o.
iii) The maximum $n_{//}$ value was adjusted ($n_{//max}$ = 6) to give the expected level for the mean power density at the plasma center (~ 6 W/cm^3 for P_{RF} ~ 300 kW); while to take into account the effect of the DC electric field, the minimum $n_{//}$ value was chosen to give a maximum resonant velocity equal to the Dreicer critical velocity (since the electrons with $v_{//} > v_c$ play a minor role in releasing collisional power).
iv) The density profile was of parabolic type with a peak density $\hat{n} = 4\times10^{13}$ cm^{-3}.
v) The peak temperature was $\hat{T}$ = 1.5 keV.

A peculiar feature of the power density shown in Fig. (1b) is the phase displacement, on a very short time scale, with respect to the input power (Fig. 1a). (This effect has already been referred and accounted for in Ref. [5]).

The power density so calculated, constitutes the source term in the diffusion equation (1) for the electron temperature which has been in turn numerically solved. The time behaviour of the temperature increase ΔT_e (with respect to the ohmic phase) is shown in Fig. 2, at seven radial position. As it is expected, the temperature oscillations occur only where the energy is directly deposited (that is inside the flux surface of radius r/a = 0.4) with oscillation amplitudes ranging from 10 to 60 eV.

These amplitudes can be detected by means of the synchronous detection of the signals which allows to achieve very high signal to noise ratio.

Diagnostics for the electron temperature measurement with high time resolution are required to follow the temperature oscillations. The measurement of the ratio of soft X-ray fluxes transmitted by different absorbers [7] can provide an adequate time resolution.

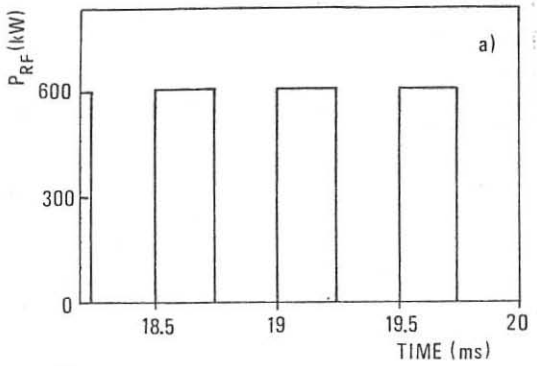


Fig. 1a - Assumed RF input power

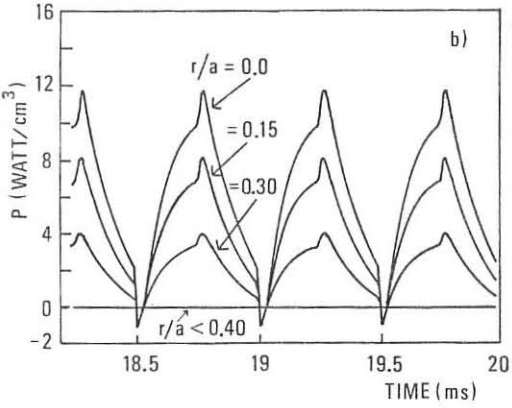


Fig. 1b - Corresponding time evolution of the collisional power gained by the bulk electrons, at different radial posions.

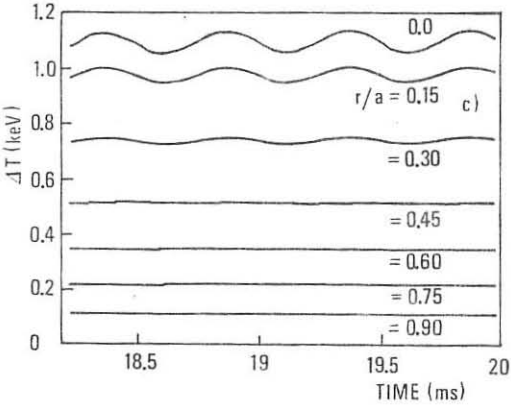


Fig. 1c - Steady state temperature oscillations at different radial positions, the same as b).

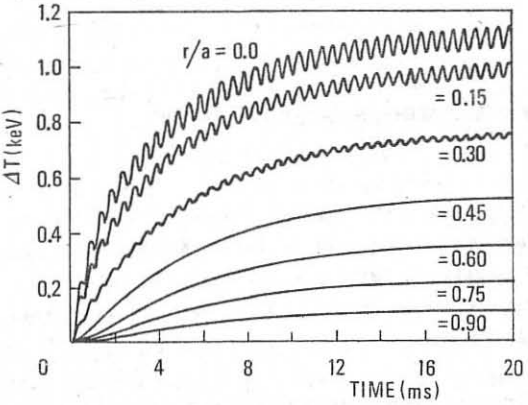


Fig. 2 - Temporal behaviour of the temperature increments ΔT_e (with respect to the ohmic phase) at different radial positions, as they result by solving Eq. 1 and by using (1b) as source term.

Figure 1c shows the steady state temperature oscillations and allows, together with Fig. 1a and 1b to observe the expected phase relation between the RF power, the collisional power and the temperature. A phase displacement of the order of π results between the input power and the temperature.

Operations at lower frequency (typically τ = 3 msec) allow the temperature to oscillate also outside the deposition region. The measure of the phase delay of the temperature oscillations at different radial position permit to determine the thermal diffusion coefficient D outside the deposition region [1], provided that the latter is narrow enough. In fact the model is adequate only where the radiative losses are not important, i.e. not too for from the plasma center.

CONCLUSIONS

The plasma response to a modulation of the RF power, in LHEH scheme has been calculated, by means of a very simple model. On this basis it seem possible to get information about the energy deposition profile by modulating the input RF power, since both the modulation time and the temperature oscillation amplitudes result to be detectable through soft X-ray diagnostic.

REFERENCES

[1] E. Barbato, R. Giannella, Phys. Lett. A (to be published)
[2] G.L. Jahns, S.K. Wong, R. Prater, S.H. Lin, S.E. Jima, GA-A17858 Report (1985)
[3] F. Alladio et al., Nucl. Fusion 24 (1984) 725
[4] F. Alladio et al., Proc. of the 10th Int. Conf. on Plasma Phys. and Controlled Nucl. Fusion Res. (London, 1984) IAEA-Vienna Vol. 1 (1985) 481
[5] F.F. Karney, N.J. Fisch, Phys. Fluids 22 (1979) 1817
[6] FT Group: Invited Paper at this Conference
[7] J. Kyraly et al., Rev. of Scient. Instrum. 56 (1985) 827.

HIGH POWER ICRF HEATING IN JIPP T-IIU TOKAMAK

J. Fujita, T. Watari, K. Toi, T. Amano, R. Ando, Y. Hamada, S. Hirokura, E. Kako, K. Kawahata, Y. Kawasumi, S. Kitagawa, K. Masai, K. Matsuoka, K. Matsuura, Y. Midzuno, S. Morita, H. Naitou, A. Nishizawa, N. Noda, I. Ogawa, Y. Ogawa, K. Ohkubo, M. Sasao, K. Sato, K. N. Sato, S. Tanahashi, Y. Taniguchi, T. Tetsuka, K. Yamazaki

Institute of Plasma Physics, Nagoya University, Nagoya 464, Japan

Abstract : A fast wave heating of D-plasma with H-minority at an injection power up to 1.3 MW has been attained by means of a strong gas puffing and an additional current rise. A new mechanism of ion Bernstein wave heating is suggested from the mass-resolved energy analysis of fast neutral particles.

Introduction : The ICRF heating experiments by the use of JIPP T-IIU tokamak have been carried out on the following two subjects: The first is a high power ICRF heating in two-ion hybrid heating regime with H-minority putting an emphasis on the impurity control. The second is an ion Bernstein wave (IBW) heating. We reported [1] previously that the heating was achieved, under the injection power of about 0.5MW, without major disruptions by mea. of a combined application of a strong gas puffing (GP) and an additional plasma current rise (CR) synchronized with the ICRF heating pulse, and that impurity influx was reduced by this technique. A proper choice of limiter materials and a careful conditioning of the first wall, limiters and ICRF antennae have made it possible to achieve an injection power of 1.3 MW and produce an ICRF-heated plasma of $T_{eo} \sim 1.8$ keV, $T_{io} \sim 1$ keV, and $\bar{n}_e \sim 7 \cdot 10^{13}$ cm^{-3} in recent experiments. Useful data for the analysis of heating processes, such as the behavior of impurities and the evolution of radiation losses during the heating have also been obtained by utilizing calibrated bolometers and visible, VUV, and X-ray spectrometers.

As for the IBW heating, We reported [1,2] that this new heating scheme had high heating efficiency but further studies were needed to make the heating mechanism clear. Recent experiments of analyzing the energy distribution of deuterium and hydrogen ions separately have brought an

information related to the heating mechanism.

Fast Wave Heating : The JIPP T-IIU is a tokamak with circular plasma cross section (R = 91 cm, a = 23 cm, $B_t \leq 3T$). Specifications of the ICRF heating systems are listed on Table 1. Typical time evolutions of plasma parameters, the intensity of impurity lines and total radiated power are shown in Fig. 1. A strong GP and an additional CR are applied just prior to the ICRF heating pulse. Favorable radial profiles of plasma parameters and plasma current density are established for suppressing the major disruptions by this combined application of GP and CR. The previous conclusion [1] of the impurity reduction by this technique which was obtained from the VUV spectroscopy has been confirmed until about 0.5 MW rf power by the X-ray crystal spectroscopy. [4] Spectra of highly ionized iron before and during the ICRF heating are shown in Fig. 2. It is seen from the figure that no significant ionization from FeXXIV to FeXXV takes place during the heating so that the reduction of impurity line intensities associated with the strong GP and CR means the amount of iron impurity is actually reduced.

An effort has been made to apply this technique to a high power heating above 1 MW. The use of graphite for both main and guard limiters definitely reduces the amount of high-Z impurity ions, and a higher power can be injected even when only GP is applied. The application of CR upon GP certainly decreases the probability for the occurrence of major disruption.

The role of the strong gas puffing is regarded first to cool down the edge part of the plasma which faces directly to the limiters and the first wall. This in turn reduces the sputtering yield especially for the high-Z impurities. The reduction of the impurity influx will prevent the cooling of electrons at a little inside from the edge, which suppresses the current shrinkage so that the disruption can be prevented even when the electron density is increased. The application of the additional CR will heat up that part and assist the suppression of the disruptions. [5] In Fig. 3 the stored energy in the ICRF-heated plasma is plotted against the total power injected into the plasma to see the overall heating efficiency. Here the stored energy is deduced from the magnetics assuming the self inductance of the plasma remains unchanged during the heating. The plots deviate from a linear dependence at the injection rf power of around 0.5 MW and show a tendency of saturation, but the most of the plasma energy is lost through intense radiations which originate from the impurities, as is shown in the same figure. If we take this fact into consideration, no significant deterioration of the confinement seems to occur.

A space-resolved analysis of the radiation loss and the comparison with spectroscopic measurements reveal that the dominant radiation loss in the early phase of the heating is from the peripheral region, but in the later phase, it is likely from high-Z impurities around the central part. A fairly high fraction of the injected power is estimated to be lost through the radiations from the impurities in the later phase. Therefore, if we could improve the structure of the antenna, especially about the materials of protection plate and Faraday shield to suppress the impurity release, the saturation of stored energy against the injected power would be avoided and a stable ICRF-heated plasma would be realized with high heating efficiency.

Ion Bernstein Wave Heating : In the previous Ion Bernstein Wave Heating, we suggested the existence of subharmonic resonance as a wave absorption mechanism. In the experiment with ^{4}He-H gas mixture this result was derived from the fact that the high energy tail was observed in the perpendicular energy spectrum for hydrogen, while only mild ion temperautre rise was observed in the parallel direction. In the recent experiment ^{2}D-H gas mixture was used instead of ^{4}He-H. The ion energy distributions for each species are separately measured and shown in Fig. 4. We observe in the figure, that a high energy tail is clearly seen both for hydrogen and deuterium. Thus this experiment provides further evidence for the previously suggested presence of subharmonic heating as well as the third harmonic damping predicted in a linear theory.

References

[1] K. Toi et al., in Plasma Phys. and Cont. Nucl. Fusion Res., vol. 1, IAEA, Vienna (1985) 523

[2] M. Ono et al., Phys. Rev. Lett. 54 (1985) 2339

[3] T. Watari et al., Phys. Fluids 21 (1978) 2076
T. Watari et al., Nucl. Fusion 22 (1983) 1359

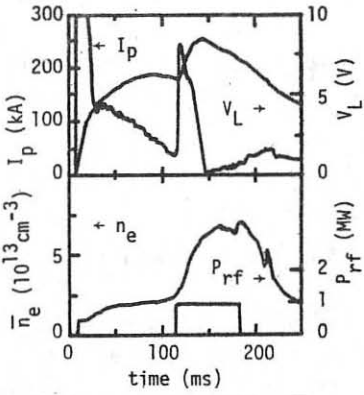
[4] S. Morita and J. Fujita, J. Phys. Soc. Jpn., 52 (1983) 1957

[5] K. Toi et al., Nucl. Fusion, 19 (1979) 1643

Table 1. ICRF heating systems

Fast Wave Heating
$n_H/n_D \sim 10\%$, $B_t \sim 3$T, $f \sim 40$ MHz, 3 sets of high-field-side antennas

Ion Bernstein Wave Heating
$n_D/n_H \sim 40\%$, $B_t \sim 1.8$T, $f \sim 40$ MHz, Nagoya Type III coil.[3]



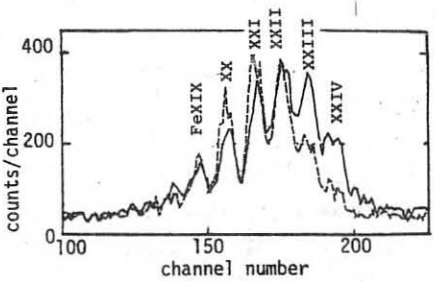
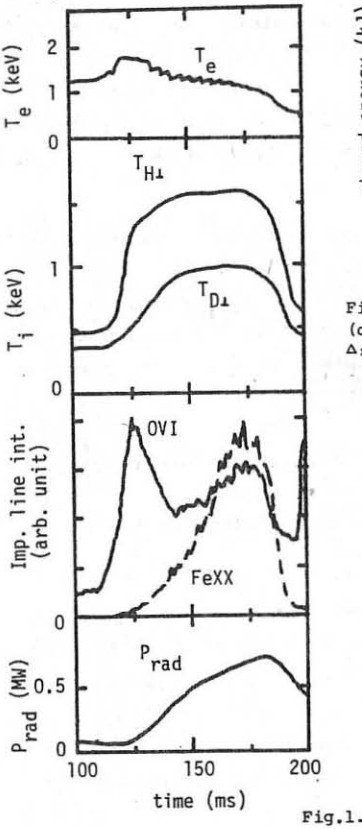


Fig.2. X-ray spectra of iron impurity before (--) and during (—) the ICRF heating.



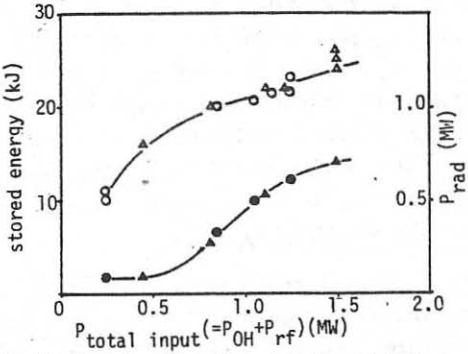


Fig.3. Stored energy (open) and radiated power (closed) versus total power input (○: GP only, △: GP+CR).

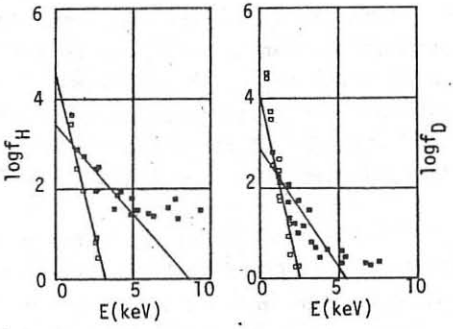


Fig.4. Energy spectra of H and D in perpendicular direction before (□) and during (■) the heating.

Fig.1.Time evolutions of typical plasma parameters.

INVESTIGATION OF DISRUPTIVE INSTABILITY OF TOKAMAK "LIBTOR"

Alabyad,A., Almagri,A., Letuchii,A., Mabruk,E., Nagornii,A., Poznyak,V., Sannikov,V., Sokolov,Yu., Zanati, F.

Plasma Physics Department, T.N.R.C., TAJOURA (TRIPOLI) LIBYA

The results of experiments carried out during the unstable hydrogen discharges on "LIBTOR" (R=53 cm, a_ℓ=10 cm) with B_t=1.1-1.8T, I_p=34-42kA, $\bar{n}_e=(0.6\text{-}4.5)10^{13}cm^{-3}$ are described here. Discharges with major disruptions (loop voltage spikes ~100V) were investigated. The appearance and growth of the helical disturbances in the poloidal magnetic field with amplitude up to $\delta H_\varphi/H_\varphi \simeq 0.01$ were characteristics of the discharge. The excitation of m/n=2/1 mode was observed on Mirnov coils prior to the spike as a precursor for disruption.

Fig. 1 shows the behaviour of some diagnostics signals during the discharge with a major disruption. Charge-exchange neutrals were detected using a 5-channel scanning analyzer for neutral particles [1]. The time dependence study of atom fluxes with resolution t=30μs showed that after the spike, ions of high energies are created in plasma column. The distorting of the ion distribution function can be explained by the generation of a strong toroidal electric field in the plasma due to the structure rearrangement of the magnetic field at the disruption moment. The magnitude of this assumed field was E = 0.7 V/cm according to the corpuscular diagnostic data analysis.

Application of Thomson scattering technique showed that the electron temperature in the plasma core was monotonously increasing between the spikes (Fig. 2). T_e - profile measurements before and after the spike disclosed drastic decrease of the plasma temperature during the disruption. Based upon the change of the poloidal magnetic flux and assuming the Spitzer electric conductivity the value E of electric field was determined to be (0,8-1,2)V/ cm.

Such a strong electric field should cause an enrichment of the superthermal region in the electron distribution function.

Before and after the spike the spectra of the soft X-rays ($2 < \mathcal{E}_\gamma < 20$ KeV) measured along the chords r=0 and r=4 cm were obtained with time resolution t=0.2ms. The soft X-ray spectrum within the spike was selected using a special algorithm of the data acquisition program. After the spike, T_e was found to decrease drastically and the distortion of the distribution function, however, did not take place. The intensity time dependence of the impurity K-lines disclosed an increase of the superthermal electron losses some tens of microseconds prior to the spike but did not show a generation of the runaway electrons with energy $5 \leq \mathcal{E}_e < 50$ KeV.

Measurements of the electron cyclotron radiation were fullfilled in a wide range of frequencies f=26 - 43 GHz including the region of high energy electrons $\mathcal{E}_e > 100$ KeV where the Coulomb colligions are negligible. At the ratio $W/W_{Ce} \sim 1$ the ECE behaviour is similar to that of the soft X-ray emission and T_e change character measured by the laser. Fig. 4 shows the ECE spectra for high energy electrons. Using a programmed gas puffing at the initial stage one can obtain a beam of the accelerated electrons up to $\bar{n}_e = 4.10^{13}$ cm^{-3}. This was proved by the emission flashes at the beginning of the discharge. Curve "a" depics their spectrum. The spike radiation spectra are shown by the curves: "b" - when $\bar{n}_e = 2.10^{13}$cm^{-3} and interspike interval 't' was 2.5 ms; "c" - the same but t ~1 ms. The radiation maximum of "b" and "c" curves corresponds to $\mathcal{E}_e \sim 250$ KeV according to the relativistic Doppler effect. An appearance of the ECE flashes at the spike, only when the accelerated electrons are present, proves the electric field generation and indicates that that there is no particle transport from the bulk to the tail of the distribution function. The hard X-ray emission proves losses of the electrons with $\mathcal{E}_e \geq 500$ KeV during the spike.

In the discharges which have an accelerated electron beam at the start of the current, one can see HF oscillation flashes (f = 400 - 750 MHz) during the spike that points out a kinetic instability. This is a consequence of the amplification of acceleration process which takes place during the spike. This instability can be one of the reasons for appearing of fast ions.

The behaviour of the soft X-ray emission shows a relatively weak acceleration process in the plasma core $r \leq 4$ cm. A strong acceleration of the high energy electrons confirmed by the ECE behaviour demonstrates the generation of the accelerating electrical field to be in a relatively narrow zone $r > 4$ cm and seems to coincide with the location of m=2/1 mode. According to the laser measurement data the width of the magnetic island is $\Delta r \sim 1$ cm for the given mode.

Our data indicate the forming of a strong toroidal electric field in the plasma column during the spike and support the assumtion of the magnetic island overlapping during the disruptive instability [2].

ACKNOWLEDGEMENT

We wish to thank Dr. V. Leonov for the fruitful discussions which were of much help in the experiments and preparation of this paper.

REFERENCES

[1] Alabyad, A.M., Ivanov, N.V., Hudoleev, A.V., Sov, J. "Plasma Phys". 1 (1984), 199.

[2] Kadomtzev, B.B. Plasma Phys. 26 (1984), 217.

INSCRIPTIONS TO THE FIGURES.

Fig. 1 The diagnostic signal correlation with the loop voltage spikes; A-neutral atoms and soft X-rays; B-$W/W_{Ce} \sim 1$; C-$W/W_{Ce} \sim 0.6$, D-HF oscillations.

Fig. 2 T_e behaviour for $r \sim 0$ and r=6 cm between the spikes.

Fig. 3 T_e and q distributions before (0.5 ms) and after (0.2 ms) the spike.

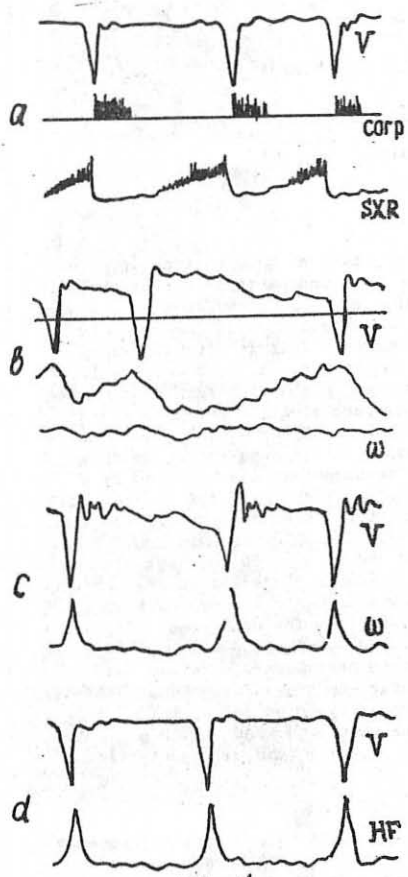


Fig. 1.

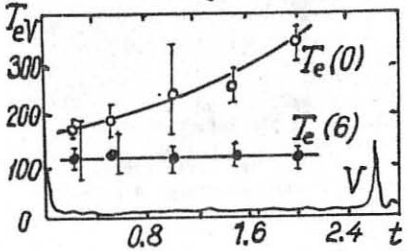


Fig. 2.

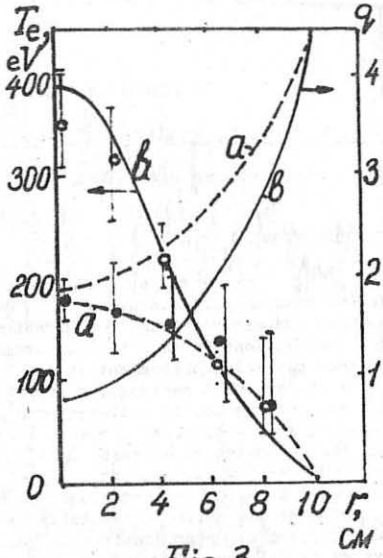


Fig. 3.

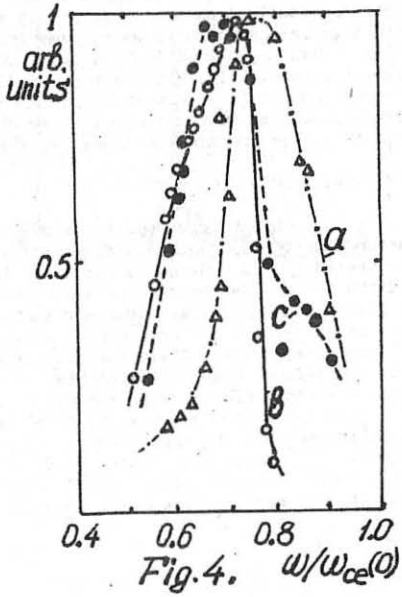


Fig. 4.

FLUCTUATION STUDIES IN THE TJ-I TOKAMAK

A.P. Navarro, M. Aguilar, E. Romero and TJ-I Group.

División de Fusión, JEN, 28040 Madrid, Spain.

INTRODUCTION

Due to the suggested relationship between fluctuations in different tokamak parameters (n_e, Te, φ , B_θ ,...) and particle diffusion |1|, we have addressed a programme to measure the level of those fluctuations and the correlations between them in order to understand and, if possible, to control particle confinement in the TJ-I tokamak. This is a small device, (R_o = 30 cm), with rectangular cross-section chamber, (a = 9.5 cm, b = 12 cm), and no limiters so, in well-centered discharges, chambers itself at the mid-plane acts as a toroidal limiter. The shots generated for our measurements had the following parameters: B_T = 1T, I_p = 45 KA, T_{eo} = 400 eV, $\bar{n}_e = 3x10^{13}$ cm^{-3} and density kept almost constant by gas puffing along the 20 ms discharges. Experimental setup used in these measurements was composed by a set of 8 Mirnov coils horizontally located along the top of the plasma, at 12 cm from the center, inside the vacuum chamber. Frecuency cutoff for this system is well above 100 KHz. Also there were 3 double Langmuir probes, installed in top of the machine at the center and at 95 $\pm$ 20 mm, that can be moved vertically to scan the plasma edge. A fourth probe was located at the botton and 60° toroidally apart from the previous one. Mirnov coils were 180° toroidally from the three probes and 120° from the other one. Signals are digitized and stored using camac-controlled modules, LC8210 and LC8800/10, with a total number of 8 channels, 8 Kb memory per channel, and 250 KHz sampling rate. Fig. 1 shows typical discharges oscilograms including, a) plasma current (I_p), magnetic loop and probe at fixed potential (n_e); b) I_p, probe potential fluctuations (φ), and c) probe waveforms, and Fig. 2 presents the frecuency spectra for those signals: a) n_e, b) φ and c) magnetic loop.

MHD MODE STRUCTURE ANALYSIS

Loop signal spectra show along the distance a dominant frequency, around 30-40 KHz (see Fig. 2c) with a long coherence length that can be interpreted as MHD mode perturbations. Tokamaks with rectangular cross-section of the vacuum chamber require a similar shape for any poloidal array of magnetic pick-up coils. Standard techniques for determining MHD mode structure |2| are not applicable, so we have developed a technique using |3| the component of the field that is parallel to the wall and taking into account effects due to toroidicity, plasma displacement and eddy currents in the walls. Fig. 3 shows the phase and poloidal amplitude variation of the parallel component obtained from the simulation of a m=2 perturbation. Superimposed are the experimental values obtained with the array of Mirnov coils. Data agree with the m=2 mode structure but there are some discrepances that could be due to other modes. To infer a mixed-mode structure is possible but it will require more loops around the plasma.

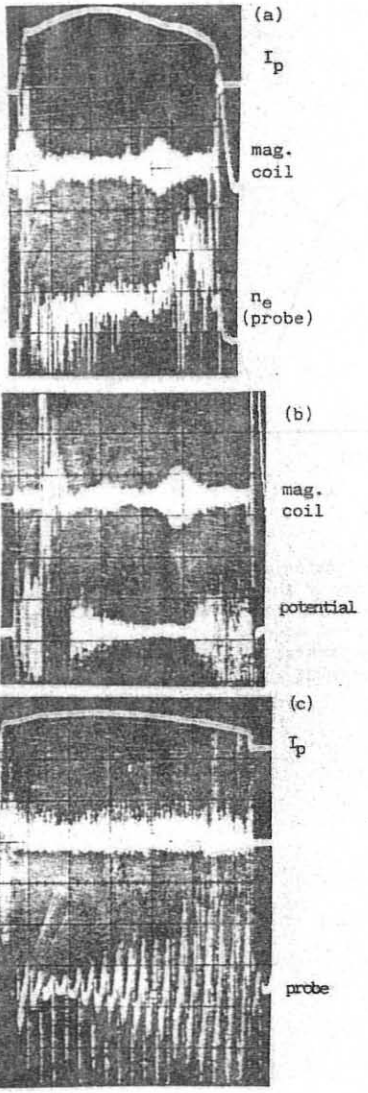


Fig. 1: Typical shot of TJ-I (3 msec/div)

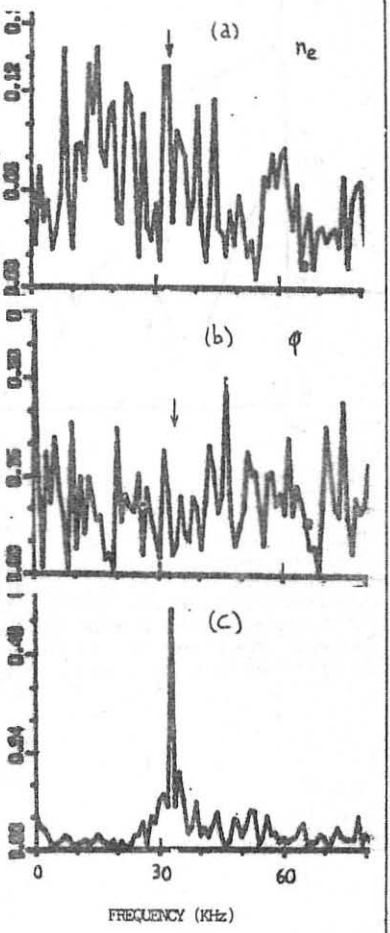


Fig. 2: Frequency spectra (Fast Fourier Transform) of a): n_e, b) φ and c) magnetic coils.

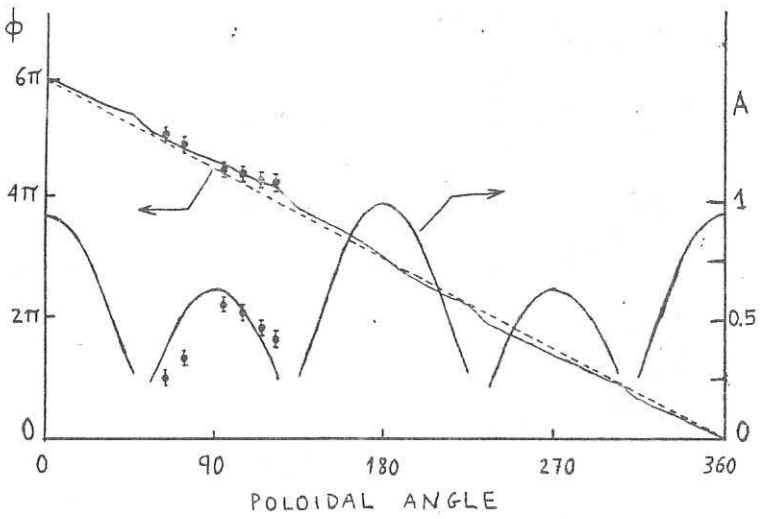


Figure 3: Amplitud (A) and phase (ϕ) variation with poloidal angle of the dominant frequency in the Fourier spectrum of the signal detected by Mirnov coils. It is also included theoretical simulation of both A and ϕ. The continuous line has been obtained for an m=2 mode by including the effects of toroidicity, eddy current and 1 cm horizontal displacement of the plasma current. The broken line was obtained without including these effects. Experimental data are represented by ‡.

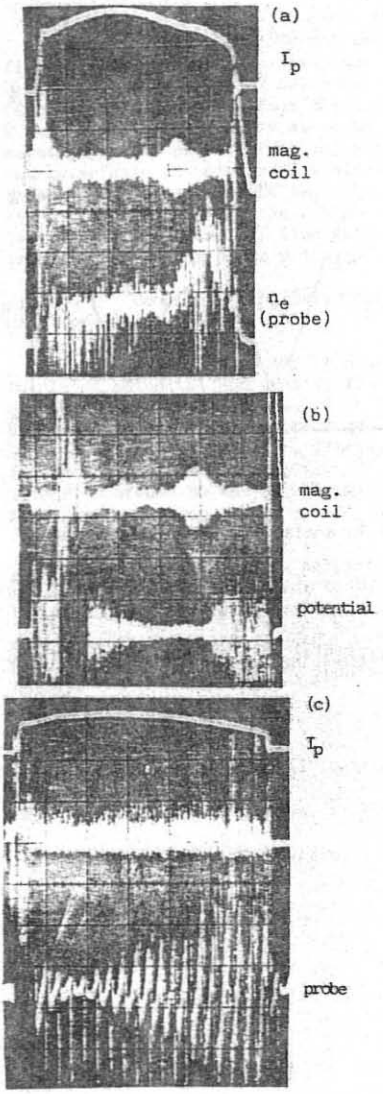


Fig. 1: Typical shot of TJ-I (3 msec/div)

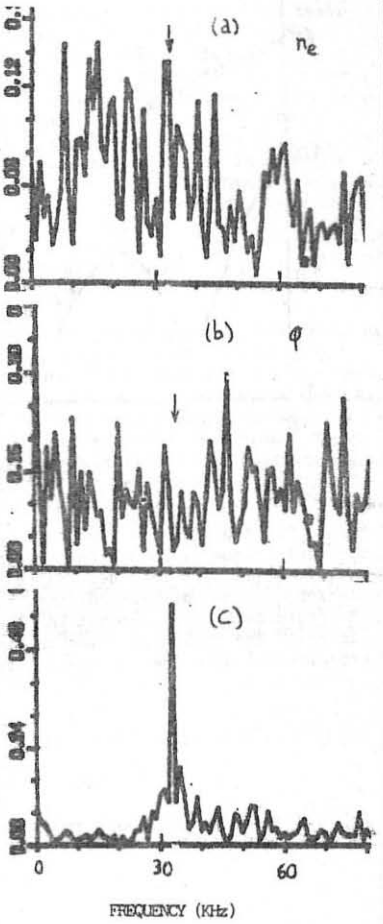


Fig. 2: Frequency spectra (Fast Fourier Transform) of a): n_e, b) φ and c) magnetic coils.

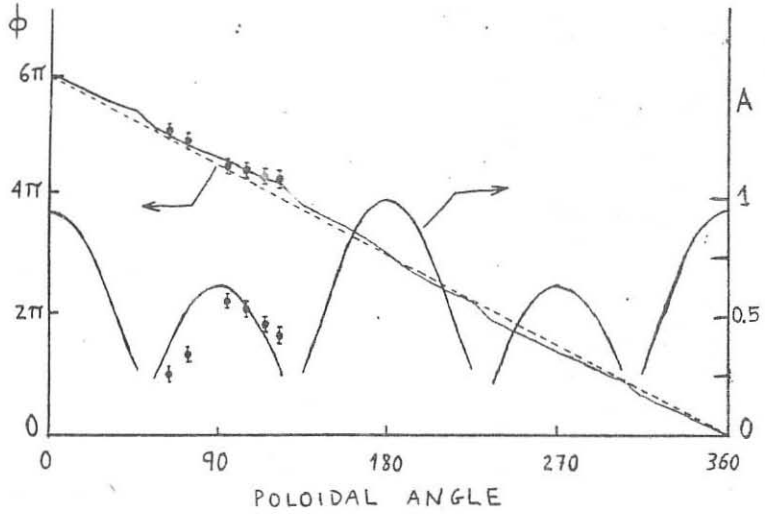


Figure 3: Amplitud (A) and phase (ϕ) variation with poloidal angle of the dominant frequency in the Fourier spectrum of the signal detected by Mirnov coils. It is also included theoretical simulation of both A and ϕ. The continuous line has been obtained for an m=2 mode by including the effects of toroidicity, eddy current and 1 cm horizontal displacement of the plasma current. The broken line was obtained without including these effects. Experimental data are represented by ⧗.

PROBE-MEASUREMENTS

Electron density and temperature, plasma potential, and their fluctuations, along the plasma edge can be deduced from signals obtained with the probes when they are inserted along the plasma. Electron temperature is obtained from the slope at V=0 of the characteristic curve V versus I, i.e., from the slope in Fig. 1c obtained by feeding a triangular waveform on the probe. From the maximum value of the current in the characteristic is obtained the electronic density, n_e. If potential applied to the probe is a constant one, then the signal obtained give information on the n_e fluctuation (Fig. 1a). Finally, when the probe is connected to ground through a resistance, the fluctuation on the voltage in this resistor is proportional to the probe voltage fluctuations (Fig. 1b).

Density in the neighbouring of probe is between 1 and $5 \times 10^{12} cm^{-3}$ and temperature between 3 and 15 eV.

In Fig. 2 it may be observed the frequency spectra corresponding to plasma potential and density fluctuation, together with the one from magnetic field fluctuations. From this figure it is clear that no dominant frequency is present in probe signal, both n_e and ϕ. However, in general, the frequency spectrum of n_e fluctuation has a broad envelope centered at around 15 KHz. On the contrary, as previously mentioned, a dominant frequency at around 30 KHz has been found in the magnetic field fluctuations. Then, as conclusion, there is no correlation between the magnetic field fluctuations and the variations of density and potential in the plasma edge.

ACKNOWLEDGMENT

Thanks are due to A.J. Wootton for many clarifying discussions and the design for the Langmuir probes. One of the authors (M.A.) was supported by Spain - U.S. Joint Committee on Cooperation in Science and Technology.

References:

|1| P.C. Liewer, California Institute of Technology, 1984, and references there in.

|2| K. Odajima et al. Phys. Fluids 21, 846 (1978).

|3| E. Romero and A.P. Navarro, Bull. Am. Phys. Soc. 29, 1338 (1984).

OBSERVATION OF SMALL-SCALE TURBULENCE IN THE "FT-2" TOKAMAK VIA CO_2 LASER SCATTERING

V.V.Bulanin, *L.A.Esipov, D.O.Korneev, *A.Yu.Stepanov, S.N.Ushakov
M.I.Kalinin Polytechnical Institute, Leningrad, USSR
*A.F.Ioffe Physico-Technical Institute, Leningrad, USSR

Investigation of small-scale fluctuations of magnetically confined plasmas seem to be of significant importance. Some theories predict that such fluctuations can be responsible for anomalous energy transport[1] . It was reported already[2]of observations of small-angle CO_2 laser scattering from plasma density fluctuations in the FT-2 tokamak. This report presents new data on small-scale fluctuations in this machine.

The FT-2 tokamak has major radius of 55 cm and minor radius of 8 cm[3]. The investigations were performed in the ohmic heating regime, the toroidal magnetic field being 2,4T, plasma current plateau of 43...48 kA and discharge duration of 40 ms. The central chord averaged plasma density was $(0.5...2)\cdot10^{13}cm^{-3}$, and the electron and ion temperatures in the flat phase of the discharge were estimated to be respectively 400... 600 eV and 100...150 eV. The probing laser beam was directed along chords shifted by X=+1,+5 and +7 cm outside of the plasma column axis. Scattering was observed at small angles $\theta = 3...12$ mrad. That corresponds to plasma wavelengths $\lambda_0/\theta = 0.7...5$ mm (λ_0=10.6 um is laser wavelength). The frequencies of the observed fluctuations were found to be 3 to 15 MHz.

A single-mode hybrid pulsed CO_2 laser oscillator [4]was used as probing beam source providing peak power of 30 kW and pulse duration of 5 us. An optical mixing homodyne technique was used for detection of the scattered radiation. The amplified output of the detector was fed to a dispersive delay frequency analyser. The frequency scan of the analyser was equal to 10 MHz with the spectral resolution of 0.5 MHz. The reference laser beam was formed broad enough to cover all the scattering angles of interest.

At small scattering angles $\theta \ll 1$ the detector conductivity response power spectrum $S_g(\omega)$ can be conviniently regarded as an integral of local power spectrum of plasma densit, fluctuations $S(K_\perp, K_z, \omega, z)$ along the probing direction (the Z-axis)

$$S_g(\omega) = \iint H(K_\perp, z) S(K_\perp, -\frac{K_\perp^2}{2K_0}, \omega, z) dK_\perp dz \qquad (1)$$

We denote here $K_0 = 2\pi/\lambda_0$, $K_\perp$ and K_z are the components of the density, fluctuations wave vector with regard to the Z-direction, $H(K_\perp, z)$ is the resolution function, which was determined for the general homodyne detection conditions. In case of small chord lengths $L_z < \frac{2w_0}{\theta}$, where w_0 is the probing beam waist characteristic radius, a chord integral of the density fluctuations power spectrum is measured:

$$\bar{S} = \int S(\theta K_0, -\frac{\theta^2 K_0}{2}, \omega, z) dz \simeq S_g(\omega) / \int H(K_\perp, 0) dK_\perp \qquad (2)$$

This is valid under condition of broad K -spectrum of the fluctuations as compared to the resolution function $\Delta K = 5.3$ cm^{-1}.

Wave vectors of the fluctuations were confined to the minor cross section of the torus. The toroidal wavelenghts of the fluctuations were estimated to be greater than 1.5 cm. A typical single-shot spectrogram of the detector signal presented a number of peaks filling frequency band depending on the scattering angle. The spectrograms obtained under similar experimental conditions were averaged over 6...10 tokamak shots. A time dependence of the fluctuations intensity throughout the plasma currents pulse was examined for $K_\perp = 26$ cm^{-1} at X=+7 cm by means of changing the moment of laser excitation. The most intensive fluctuations were found in the current rise phase at delays of 2... 3 ms (Fig.1). The averaged spectrograms for different scattering angles at X=+1 cm are presented at Fig.2 as $\sqrt{S}$ against ω and $K_\perp$ plots. The results were obtained in the current rise phase. The peaked nature of the spectra remained quite appreciable even after the averaging procedure. For the chord close to the center of the plasma column (X=+1 cm) the body of the spectrum shifted towards high frequencies with higher values of $K_\perp$. For most frequency intervals a dominating $K_\perp$ value could be found. The poloidal phase velocity was estimated as $(1...2) \cdot 10^6$ cm/s. At other chords (X=+5 cm and X=+7 cm) the ω and K -spectra were transformed significantly. The peaked structure and the

frequency band remained the same in general, but the spectra were broadened towards greater $K_\perp$. In order to clarify such transformations an additional averaging procedure over different frequency bands of ± 1 MHz width was performed. In Fig.3 the isolines of $\overline{S}$ plotted against ω and $K_\perp$ are compared for chords X=+1cm and X=+5 cm. The spectra broadenings, significant in Fig.3 for X=5 cm, increased further at X=+7 cm chord. On approaching the plasma edge a rise in the detector output was obtained, in spite of the chord length decrease. For X=+7 cm the ω -and K -spectra of the fluctuations in the flat current phase of the discharge (20 ms after ignition) were measured.

Occasionally, the spectra evolution with chord displacements, could be qualitatively described by a simple model of the "frozen" turbulence with the power spectrum

$$S \sim S(K_r)\,\delta[K_\vartheta v(r) - \omega]\,A(r) \qquad (3)$$

where δ is Dirac delty function, K_ϑ and K_r are the fluctuations wave vector poloidal and radial components, $v(r)$ is the frozen wave's phase velocity. It's radial dependence was assumed to be $v(r) \sim \frac{r}{a}\left(1-\left(\frac{r}{a}\right)^2\right)^{-\alpha}$. The function $A(r) \sim (1-r^2)\exp[-((1-r^2)/\Delta r)^\gamma]$ presents a model of the fluctuations peaked near the limiter (see [5]). It was assumed also that $S(K_r)$ is peaked at $K_r \simeq 0$ (see [6]). It occurred that for satisfactory description of the spectra $\overline{S}$ broadening behaviour with chord displacement a broad spectrum is needed: $\Delta K_r \simeq (2 \ldots 4) K_\vartheta$, ($\alpha = 0.7$, $\gamma = 2$, maximum intensity radius 7.5 cm). Such broad a spectrum seems likely to be formed by some MHD instability (perhaps of micro-tearing mode type).

The proposed model cannot, however, describe the peaked structure of the frequency spectra. The coincidence of the frequency band of the fluctuations with the girofrequencies of the impurity ions allows us to suppose also that the observed peaks are associated with some kind of impurity instability.

References:

1. Kadomtsev B.B., Pogutse O.P., Pis'ma Zh.Eksp.Teor.Fiz., 39, 225 (1984).
2. Askinazy L.G. et al, Pis'ma Zh.Teh.Fiz., 10, 1517 (1984)
3. Budnikov V.N. et al. Fizika Plazmy, 10, 485 (1984)

4. Bulanin V.V., Petrov A.V. Optika i spectrosc. 45, 582 (1978)
5. Budaev V.P. et al. Preprint No.7-143. Inst.High Temp. USSR Acad.Sci., (1984)
6. Brower D.L. et al. Proc.Tenth Int.Conf. on Plasma Phys. and Contr.Nucl.Fusion Res., London, 1984, IAEA-CN-44/A-IV-6.

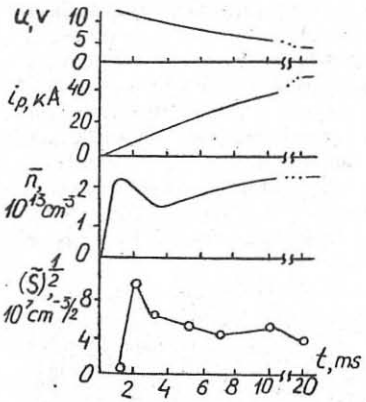


Fig.1

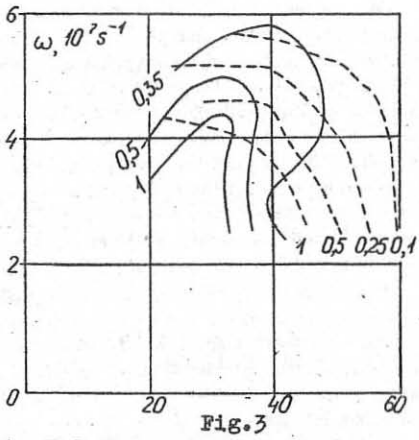


Fig.3

F.1.The evolution of plasma parameters and the value of $\tilde{S}=\int \bar{S}\, d\omega$ during the plasma current pulse k =26cm x=+7cm,u-loop voltage,i_p-the plasma current,$\bar{n}$-central chord averaged density.

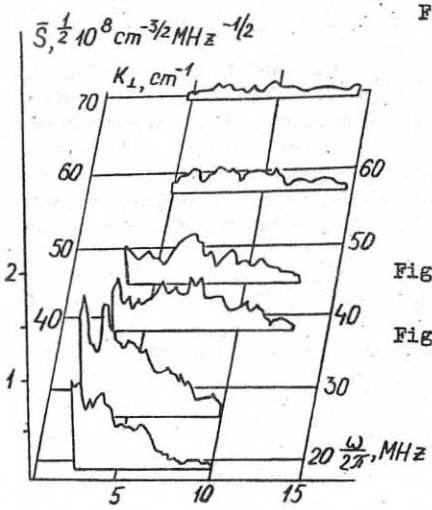


Fig.2

Fig.2.Dependence of $\bar{S}$ on ω and $k_\perp$ x=+1cm

Fig.3.Isolines of frequency smoothed value of $\bar{S}$ solid curve-x=+1cm, dashed curve- x=+5cm

Toroidal Equilibrium and Stability for Steep Pressure Profile Stellarators

H.L. Berk, J.P. Friedberg, X. Llobet, P.J. Morrison, M.N. Rosenbluth, J.A. Tataronis***
Institute for Fusion Studies
The University of Texas at Austin
Austin, Texas 78712

We consider the ideal MHD equilibrium and stability of sharp and steep boundary stellarators. We can show that the solution to the sharp boundary, finite pressure equilibrium problem exists, and approximate methods for its evaluation are developed using that the sharp pressure solution is the lowest order solution to the steep pressure profile. This solution exhibits both nested toroidal flux surfaces as well as islands. By carrying the solution to higher order, the finite width of the interface can be resolved, and details such as the "radial" B fields and the spatial island widths can be determined. For the stability of the system we consider the ballooning modes of a steep pressure profile equilibrium in which the perturbation is localized to a "radial" width smaller than the equilibrium width. This model, though, apparently artificial, gives a deep insight into understanding "second stability" of toroidal systems, as will be discussed below.

If one has an equilibrium vacuum magnetic field in a region A with no currents in A, bounded by an exact flux surface that is generated by a magnetic field line with a rotational transform ι (such a field exists as can be seen by the formulation of an appropriate Neumann problem), then one can imagine the same region A, containing a constant pressure p_o. The vacuum field $\mathbf{B}_v$ can be expressed in the following covariant and contravariant forms,

$$\mathbf{B}_v = \nabla\Phi_v = \nabla\alpha_v \times \nabla\beta_v \tag{1}$$

and $(\Phi_v, \alpha_v, \beta_v)$ is a triad determining every point in space and Φ_v changes by $2\pi g$ (the total enclosed poloidal current) for one toroidal transit to the same point. Where surfaces exist, let α_v represent the enclosed flux divided by 2π, and β_v then varies by 2π when circulating in the poloidal direction at fixed Φ_v.

Now let us attempt to construct an equilibrium solution when p_o is the pressure in A, and $2\pi g$ is the total enclosed poloidal current. We note that the field $\mathbf{B} = \lambda\mathbf{B}_v$ with λ a constant is a solution in A as $\nabla \times \mathbf{B} = 0$. The solution for $\mathbf{B}$ just outside A, must satisfy that the equation,

$$\frac{B_{out}^2}{2} = \frac{\lambda^2 B_v^2}{2} + p_o \tag{2}$$

where $\mathbf{B}_{out}$ is the magnetic field just outside the region A. If we represent $\mathbf{B}_{out}$ in the

---

* *Permanent address, M.I.T.*
** *Permanent address, University of Wisconsin*

covariant representation,

$$\mathbf{B}_{\text{out}} = \frac{\partial \Phi_o}{\partial \Phi_v}\mathbf{B}_v + \frac{\partial \Phi_o}{\partial \alpha_v}\nabla\alpha_v + \frac{\partial \Phi_o}{\partial \beta_v}\nabla\beta_v, \tag{3}$$

it follows from $\mathbf{B}_{\text{out}} \cdot \nabla\alpha_v = 0$, that

$$\frac{\partial \Phi_o}{\partial \alpha_v} = -\frac{\partial \Phi_o}{\partial \beta_v}\nabla\alpha_v \cdot \nabla\beta_v / |\nabla\alpha_v|^2, \tag{4}$$

and Eq. (3) can be written as

$$H \equiv 1 + \frac{p}{B_o^2} = \left(\frac{\partial \Phi}{\partial \Phi_v}\right)^2 + \left(\frac{\partial \Phi}{\partial \beta_v}\right)^2 \frac{1}{|\nabla\alpha|^2} - \sum_{n,m} \frac{p_o \delta_{n,m}}{B_o^2} \cos\left[\frac{(n - mx)\Phi_v}{g} - m\beta_v\right] = 0 \tag{5}$$

where $\Phi = \Phi_o/\lambda$, $p = p_o/\lambda^2$

$$\frac{1}{B_v^2} = \frac{1}{B_o^2} + \sum_{n,m} \frac{\delta_{n,m}}{B_o^2} \cos\left[\frac{(n - mx)\Phi_v}{g} - m\beta_v\right] \tag{6}$$

$$\frac{1}{|\nabla\alpha|^2} = \frac{1}{|\nabla\alpha|_o^2} + \sum \frac{\alpha_{n,m}}{|\nabla\alpha|_o^2} \cos\left[\frac{(n - mx)/\Phi_v}{g} - m\beta_v\right]. \tag{7}$$

Equation (5) is in Hamiltonian form with $P_{\phi_v} \equiv \frac{\partial \Phi}{\partial \Phi_v}$ and $P_{\beta_v} \equiv \frac{\partial \Phi}{\partial \beta_v}$ the canonical momenta conjugate to Φ_v and β_v respectively, and Φ the action integral of Hamilton-Jacobi theory. The equations governing P_{ϕ_v}, P_{β_v}, Φ_v, β_v are then

$$\frac{dP_{\Phi_v}}{d\tau} = -\frac{\partial H}{\partial \Phi_v}, \quad \frac{dP_{\beta_v}}{d\tau} = -\frac{\partial H}{\partial \beta_v}, \quad \frac{d\Phi_v}{d\tau} = \frac{\partial H}{\partial P_{\Phi_v}}, \quad \frac{dP}{d\tau} = \frac{\partial H}{\partial P_{\beta_v}}$$
$$\frac{d\Phi}{d\tau} = -\frac{\partial H}{\partial \Phi_v}\frac{\partial H}{\partial P_{\phi_v}} - \frac{\partial H}{\partial \beta_v}\frac{\partial H}{\partial P_{\beta_v}}. \tag{8}$$

An equilibrium exists if Eq. (8) is integrable, i.e., for a given P_{Φ_v} and P_{β_v} at an initial point Φ_{v_o} and β_{v_o}, P_{Φ_v} is a single-valued function of Φ_v and β_v. In general P_{Φ_v} can be a multi-valued function or an ergodic function of Φ_v and β_v and then the sharp boundary equilibrium does not exist. However, it follows from the KAM theorem that for sufficiently small $P\delta_{m,n}$ and $P\alpha_{n,m}$, solutions must exist. We also note that the "action" function Φ, which has no particular relevance in a mechanics problem, has an important physical significance in this problem, viz. the currents enclosed in one toroidal and poloidal transit is directly related to the jump in Φ in one poloidal and toroidal transit respectively.

Analytic solutions can be generated when $p\delta_{n,m}$ and $p\alpha_{n,m}$ are sufficiently small. When double valued solutions arise, the solutions represent a magnetic island. As an example, for a system with zero net toroidal current, the change of rotational transform, $\Delta x(p)$ from just outside the plasma to just inside is (when $x + \Delta x \neq n/m$)

$$\Delta x(p) = \sum_{m,n} \frac{g^3 p^2 \delta_{m,n}^2}{2B_o^4\left(\frac{n}{m} - x\right)^3}\left[g + |\nabla\alpha|^2\left(\frac{n}{m} - x\right)^2\right]\frac{1}{|\nabla\alpha|^2\left(1 + 2p_o^2/B_o^2\right)^2}. \tag{9}$$

If the profile is considered sharp but finite, the sharp boundary problem is the lowest order solution for each pressure surface p. Higher order perturbation theory that uses $\nabla \cdot \mathbf{B} = 0$, determines $\mathbf{B} \cdot \nabla \alpha$ and corrections to $\nabla \alpha$.

When we consider the ballooning mode equation for the steep profile equilibrium, we note that the possibility of ballooning is strongly determined by whether the local shear, which is the sum of the mean vacuum shear $(\partial \iota / \partial \alpha)/\iota$ and an oscillating component with an amplitude $\frac{2}{B_o^2} \frac{\partial p}{\partial \alpha} \frac{1}{\iota^2} \frac{R_o}{r}$ due to Pfirsch-Schluter currents (with R_o the major radius of the torus) will vanish and whether the normal component of curvature $\kappa_n \equiv (\mathbf{b} \cdot \nabla)\mathbf{b} \cdot \nabla \alpha$ ($\mathbf{b} = \mathbf{B}/|B|$) is positive (favorable for stability) or negative (unfavorable for stability), at the point of vanishing shear. For sufficiently high beta one can show that the stability condition is

$$-\kappa_n < .471|\kappa_g| \tag{10}$$

where $\kappa_g = (\mathbf{b} \cdot \nabla)\mathbf{b} \cdot \nabla \alpha \times \mathbf{b}$. In tokamaks the local shear first vanishes with increasing pressure on the outer part of the torus where $\kappa_n < 0$, and ballooning instability sets in. As the pressure increases further, the zero local shear point approaches the top (and bottom)regions of the tokamak, where κ_n is becoming small and $\kappa_g \to 1/R_o$. Thus, when roughly Eq. (10) is satisfied, where $\left|\frac{1}{\iota^2} \frac{\partial p}{\partial \alpha B_o^2} \frac{R_o}{r}\right| \gtrsim \left|\frac{1}{\iota} \frac{\partial \iota}{\partial \alpha}\right|$, second stability is reached. For stellarators, the zero shear point is inside the torus, where κ_n is positive and therefore favorable for stability and ballooning modes do not arise. As $\left|\frac{\partial p}{\partial \alpha}\right|$ increases the zero shear point moves to the top and bottom, where if one is close enough to the magnetic axis, Eq. (10) would be satisfied and the system would still be ballooning mode stable. However, when one is sufficiently far from the magnetic axis, the helical contributions to κ_n become important, even when the local shear vanishes near the top (or bottom) of the cross section, and it is possible for Eq. (10) to be violated. In that case we can observe ballooning mode instability even in a stellarator. Numerical examples will be exhibited illustrating this effect.

Study of T-10 tokamak plasma by low-Z impurity pellet injection

Egorov S.M., Kuteev B.V., Sergeev V.Yu.
Kalinin Polytechnikal Institute, Leningrad, USSR

Pellet injection into tokamak plasma presents numerous diagnostical possibilities [1]. It is now used for impurity transport studies [2,3], for measurement of effective plasma charge [4] and poloidal plasma rotation [5]. We present here the results of our investigations of electron density transport and heat perturbations evolution after injection of C and LiH pellets. In the experiment we have determined diffusional and convective particle flows and estimated heat conductivity coefficient χ_e. The fine structure on the carbon pellet evaporation curves $\dot{N}(r)$ was studied as well.

Pellets with diameter d_p=300-400 μm and velocity V_p =100-150 m/s were injected into T-10 plasma by gas dynamic accelerator [6]. The seven-channel microwave interferometer [4] was used to observe the electron density perturbation $\Delta n_e(t)$. The perturbation of electron temperature $T_e(t)$ in central region after injection were observed using the second cyclotron harmonic emission [3]. The initial density perturbation was usually located nearly half of limiter radius a_1 where particle sources of another origin were negligible. This allows to simplify the particle balance equation used to simulate the density transport in tokamak:

$$\frac{\partial n_e}{\partial t} = \frac{1}{r}\frac{\partial}{\partial r}\left(D\frac{\partial n_e}{\partial r} - V n_e\right) + \hat{Q}_{mix}$$

The recycling of carbon and litium was neglected. So the zero boundary conditions for density perturbations were imposed. Diffusion coefficient D and pinch velocity V were supposed to be following functions: D=const(r), $V=V(a_1)(r/a_1)$. The mixture process (Q_{mix}) was included into simulation according to obtained experimental data. It formed flat density profile in the region $r \leq \sqrt{2}\, r_s$ (where r_s is sawteeth radius) with sawteeth oscillations frequency without changing of total particle number in this re-

gion. Fig.1 presents experimental signals of line density measured by interferometer $\langle n_e l \rangle$ and the simulated ones for D=5000 cm^2/s and $a_l V(a_l)/D=2$. Deviations of D or $a_l V(a_l)/D$ with 20-30% from the values mentioned above were clearly visible. This circumstance characterizes the accuracy of our estimations. The data obtained for C, LiH and also He injection (100% recycling) are summarised in the table:

sort impurity	shot number	a_l cm	I_p kA	B_t kGs	q_l a.u.	$T_e^{SXR}(0)$ kev	n_e $10^{13}cm^{-3}$	D $10^3 cm^2/s$	$a_l V/D$ a.u.
LiH	28508	34.7	251	32.0	5.10	1.45	2.8	4	4.5
LiH	28499	34.7	244	14.9	2.45	0.95	2.0	7	4
C	23654	32.5	495	30.1	2.20	1.00	5.0	4	4
C	27543	32.0	211	25.6	4.15	0.80	2.5	5	2
He	28498	34.7	244	14.9	2.45	0.95	2.0	7	4
He	27516	32.0	221	25.7	4.00	0.80	2.8	5	4

The data present the weak dependence of D and V on the impurity sort. There is some decrease of D values with magnetic field. The absolute values of D and V are of Alcator-C data order [7] and correspond to confinement time for heavy impurities at T~10 in regime with small τ [3]. They exceed neoclassical values essentially.

The heat conductivity χ_e was estimated using time evolution of ECE-signal after injection of carbon pellets $\chi_e = 3\, r'^2/8\, t$ (r' is the distance between ablation curve maximum and observation point of ECE, t is time interval between maximum of $\dot{N}(t)$ and minimum of $T_e(t)$). Typical signals of $T_e(t)$ and $\dot{N}(t)$ are shown on Fig.2. The signals of two different types were observed. The diffusion type signal is presented on Fig.2a. The signals of second type (Fig.2b) are similar to ones observed in hydrogen pellet injection experiments [7] and apparently correspond to initiation of inner disruption. The greater pellet size and q_l the more probable the last type becames. Fig.3 shows χ_e data obtained in diffusion type discharge. It is seen decreasing of χ_e with drowth of n_e and q_l which is in qualitive agreement with Mukhovatov-Merezhkin scaling low. Numerical values of χ_e are approximately twice greater than the ones calculated from stationary energy

balance. It is possible that this discrepancy is connected with ohmic power variation due to plasma cooling and increase of effective ion charge after injection. The mechanism which determines fast profile evolution is not clear yet.

A fine radial structure has been observed on carbon ablation curves $\dot{N}(r)$ (Fig.4). Decrease of the $\dot{N}(r)$ in the region r=2-3 cm varied from 20% to 0, but the positions of peculiarities were usually reproduced. The origin of these peculiarities may be connected with pellet transversing the rational magnetic surfaces with low values q=m/n=1, 3/2,2,5/2,3. Ablation rate should decrease because of plasma cooling when $d_p/2V_p > 2\ Rm/V_{Te}$. The absence of peculiarities in some shots could be explained by island structure of magnetic surfaces. For two types of peculiarities we have plotted the dependence of their positions r_q/a_1 on safety factor (see circlies on Fig.5). The first type peculiarity position coincides with the location of q=3/2 surface position calculated from Spitzer formula (the data obtained by Yu.V.Yesiptchuk) or q=2 surface position according to [8]. The second one corresponds to Spitzer q=2 surface position or tearing mode q=3 position. It is difficult now to make final choice between these possibilities and thus to determine the magnetic surface position by pellet injection. Were this problem solved one could obtain the additional possibilities for current profile diagnostic.

References

1 . Golant V.E. et al., Pis'ma Zh. Tech. Fiz., 3, 1035, 1977.
2 . Kuteev B.V. et al., Pis'ma Zh. Tech. Fiz., 9, 529, 1983.
3 . Bagdasarov A.A. et al., in 10th Int.Conf. on Plasma Phys. and Contr.Nucl.Fus.Res.,London,1984,IAEA-CN-44/A-III-4.
4 . Vasin N.L. et al., Fizika Plasmy,10,1133,1984.
5 . Bulyginsky D.G. et al., ibid [3], v.1, p.491.
6 . Egorov S.M. et al., Zh.Tech.Fiz., 55, 692, 1985.
7 . Greenwals M. et al., ibid [3], IAEA-CN-44/A-1-3.
8 . Ivanov N.V., Fizika Plasmy, 9. 703, 1983.

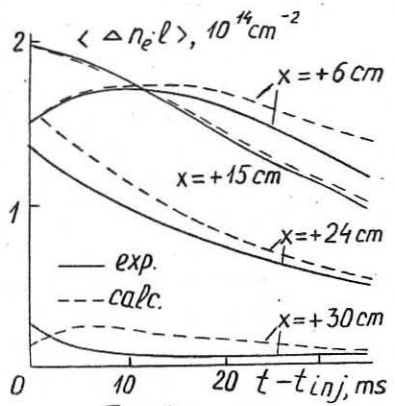


Fig. 1

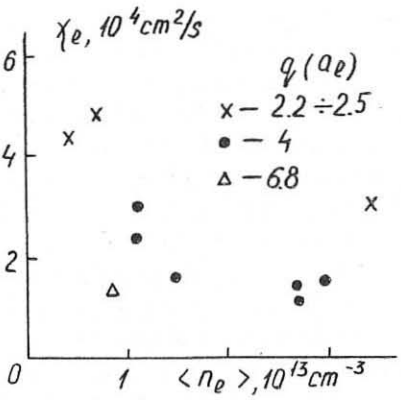
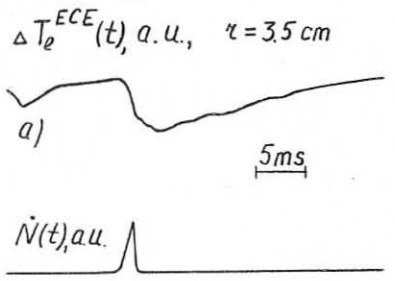


Fig. 3



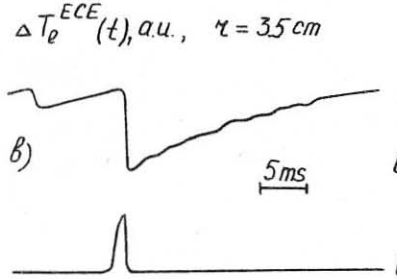


Fig. 2

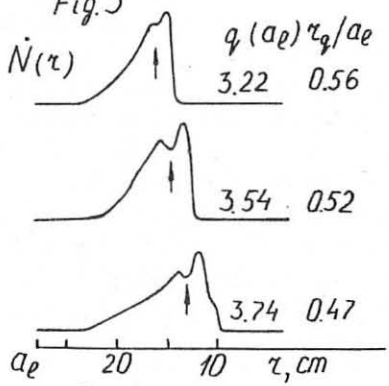


Fig. 4

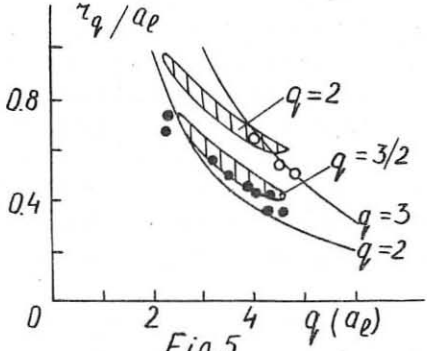


Fig. 5

author index

Abe, M I 6
Abels van-Maanen, A E P M I 22
Adachi, S I 528
Adam, J II 108
Adati, K I 504
Ag, A I 663
Agarici, G II 168, II 172
Aguilar, M II 710
Ainsworth, N R II 80
Airoldi, A II 84
Akulina, D K I 413
Alabyad, A II 706
Alexander, K F II 515, II 559
Alikaev, V V II 156, II 160
Alladio, F I 138, I 151, I 171, I 319
Allgeier, C I 655, I 659
Almagri, A II 706
Alper, A I 578
Alper, B II 80
Alvarez Rivas, J L I 433, I 441
Amano, T II 702
Andersen, S A II 652
Andersen, V II 648
Anderson, D T I 465
Anderson, F S B I 465
Andersson, P II 394
Ando, R II 702
Andryukhina, E D I 421, I 481
Angel, T I 6
Antoni, V I 578, I 582
Aoki, T I 504
Appert, K II 124
Arendzikowski, R II 2
Argenti, L II 300
Armstrong, W T I 590
Arter, W II 442
Asakura, N I 602, I 626
ASDEX Team I 78, II 583
Askinasi, L G I 363
Atkinson, D II 80
Aumayr, F II 595
Axon, K B I 371
Azumi, M I 179
Babicky, V II 668
Badalec, J I 275
Baetzner, R I 231
Bagdasarov, A A I 207, II 160
Baker, D A I 570
Baker, E A M I 227
Bakhst, R B II 26
Bakos, J S I 271
Baldis, H II 686
Baratov, D G II 682
Barbato, E II 196, II 698
Barbian, E I 215
Barbotko, V M I 239
Barnes, C W I 643
Barth, C J II 272
Bartiromo, R I 159, I 195, I 199, I 299, I 331, I 335, II 240, II 244, II 284, II 543, II 587, II 678
Bartlett, D V I 26, I 130, I 227, II 152
Bassan, M I 578
Batanov, G M I 421
Batenyuk, A A I 562
Bay, H L II 523
Becker, G I 159, I 299, I 331, I 335, II 240, II 244, II 284, II 454, II 543, II 587, II 678
Behnel, J II 468
Behringer, K H I 267, I 379, II 539
Behrisch, R II 575, II 623
Beidler, C D I 461
Beklemishev, A D II 413
Belikov, V S II 208
Bell, M G II 674
Bell, R II 120, II 192
Bender, S E I 363
Berendeev, S A II 631
Berezhetskij, M S I 421
Berezovskij, E L I 235, II 156, II 160
Berge, G I 487
Berk, H L II 718
Bernabei, S II 192
Bernhardi, K I 18, II 240
Bertschinger, G I 251
Besedin, N T II 417
Bessenrodt-Weberpals, M II 547
Besshou, S I 401, I 405
Best, C I 130
Bickerton, R J I 26
Bieger, W II 527
Biermayer, W I 542
Bishop, C M II 401
Bitter, M I 343, II 120, II 674
Bittoni, E I 211
Blackwell, B D I 429
Blanc, P II 168, II 172
Blewett, S G F II 80
Blokh, M A I 421, I 424
Bobeldijk, C I 594
Bobrovskii, G A I 142
Boeckle, G I 659
Boerner, P I 187

Bogen, P II 523, II 527
Bohacek, V II 668
Bol, K I 58
Bondarenko, S P I 247
Bonoli, P II 232
Boody, F P I 339
Boozer, A H II 425
Bornatici, M II 52
Borowiecki, M I 546
Borshchegovskij, A A I 307
Bosch, H S I 159, I 195, I 199, I 299, I 331, I 335, II 240, II 244, II 284, II 543, II 587, II 678
Botcharov, V N I 516
Botija, J I 433
Bottollier, H II 164, II 168
Bottollier-Curtet, H II 172
Braams, B J I 163, I 167, II 480
Bracco, G I 219, II 196
Bral, L II 48
Brambilla, M I 199, II 240, II 244, II 678
Breizman, B N I 516, II 338
Briand, F II 686
Briand, P II 164, II 168, II 172
Briffod, G II 164, II 168, II 172
Briguglio, S I 630
Brocken, H I 159, I 299, II 240, II 244, II 587, II 678
Bruhns, H I 655, I 659
Brusati, M I 26, I 34, I 130, I 219, I 227
Buchenauer, C J I 570, I 643
Buchenauer, D I 58
Budaev, V P I 303
Buechl, K I 78
Buffa, A I 578
Bugarya, V I I 207
Bulanin, V V II 714
Bunting, CC A I 634
Bures, M II 148, II 152
Burhenn, R II 244, II 678
Burkhardt, L C I 570
Burrell, K I 6
Bush, C E I 339, II 674
Buzankin, V V II 160
Bychkov, S S I 239, II 599
Cabrera, J A I 10
Callen, J D I 134, II 64, II 397
Campbell, D J I 26, I 70, I 130, I 151, I 155, I 215, I 227, I 327, II 152
Campbell, G A II 531
Canobbio, E II 314
Cantrell, J L I 441
Cap, F F II 276
Cardinali, A II 228
Carolan, P G I 253, I 267, I 634
Carreras, B A I 433, I 441
Cattanei, G I 385
Cavallo, A II 120, II 192
Cayton, T E I 570
Cenacchi, G II 84
Cepero, J R I 10, I 433
Cesario, R II 220
Chabert, P II 164, II 168, II 172
Chance, M S II 421
Chang, C T II 656
Checkin, V V II 128
Chen, K I II 232
Chen, Sh I 520
Cheng, C Z II 421
Chernyshev, S E I 363
Chesnokov, A V II 156
Chicherov, V M II 559, II 563, II 567
Chikunov, V V I 508
Chipley, K K I 433
Chmyga, A A II 156
Cho, T I 528
Chodura, R II 472
Choe, W H I 487
Chrien, R E I 590
Christiansen, J P I 26, I 130, I 283, I 327
Chu, T K II 192
Chuyanov, V A I 347
Cima, G II 300
Ciotti, M II 555
Cirant, S II 300
Claassen, H A II 460, II 464
Clement, M II 164, II 168, II 172
Clupek, M II 668
Coad, J P II 571, II 575
Coda, S I 130
Cohen, S II 120, II 192
Colchin, R J I 134, II 674
Colestock, P II 120, II 192
Collins, G A II 248, II 264
Collins, P R II 80
Combs, S K II 674
Consoli, T II 92
Coppi, B II 322
Cordey, J G I 26, I 34, I 130, I 327
Core, W I 22, II 124
Corti, S I 26, I 219, II 535
Costa, S I 578

Costley, A E I 26, I 130, I 227
Cote, A I 311, II 450
Cotruta, D I 558
Cottet, F II 10
Cottrell, G A I 130, II 152
Couture,P I 58
Cox, M II 76, II 140
Crisanti, F I 151, I 171, I 319
Croci, R II 314
Crunov, C II 563
Czekaj, S I 546, I 550
D'yakov, V E I 473
Danilkin, I S I 481
Datsko, I M II 26
David, C II 172
De Angelis, R II 690
de Chambrier, A II 264
De Gentile, B II 664
de Groot, B II 272
de Kluiver, H II 272
de Kock, L I 26, I 130, I 151, II 571, II 575, II 579
De Luca, F II 300
De Menna, L I 110
De Michaelis, C I 379
De Simone, P I 259
de Zeeuw, W A II 272
DeBoo, J C I 2
Decker, G I 227, I 566
Degtyarev, L M I 106, I 347
Dellis, A N II 80
Demyanenko, L E II 682
Demyanenko, V N II 682
Dendy, R II 140
Denne, B I 70, I 155, I 379
Denus, S I 546, I 550, II 2, II 6
Derfler, H I 199, II 240, II 244, II 678
Detragiache, P II 322
Dietrich, J II 334
DiMarco, J N I 570
Dimitrescu-Zoita, C I 558
Ding, H C II 429
Ding, N II 252
Dippel, K H II 531
Dnestrovskij, Yu N I 102, I 235, II 200
Doerner, R P I 465
Donskaya, N P I 421, I 424
Dorokhov, V V II 260
Dorst, D I 385
Doublet III Group I 2, I 6
Downing, J N I 570
Doyle, E J I 311
Dreiucker, W II 563
Drozdov, V V I 106
Dubois, M II 386
Duechs, D F I 22
Duperrex, P A I 126, I 130
Duval, B P I 203, I 267
Dyabilin, K S I 421, I 481
Dyachenko, V V I 363
Eberhagen, A I 18, I 159, I 195, I 199, I 231, I 299, I 331, I 335, II 240, II 244, II 284, II 543, II 587, II 678
Eckhartt, D I 199, II 240, II 244, II 678
ECRH Group I 384, I 393
Edenstrasser, J W II 374
Edlington, T II 80
Edwards, A I 26, I 130
Edwards, D N II 442, II 508
Efremov, S L I 207, I 235, II 156, II 160
Efstigneev, S A II 559, II 567
Efthimion, P C I 134
Eggen, J B M M II 370
Egorov, S M I 207, II 619, II 721
Ehrenberg, J II 535, II 571, II 575
Ehrhardt, A B I 183
Ejima, S I 26, I 283, I 327, II 40
Elfimov, A G II 256, II 260
Elsner, A I 385
Engelhardt, W I 379
England, A C I 343, II 674
Englert, W II 623
Equipe TFR II 108
Erckmann, V I 385
Erents, S K II 571, II 579
Erickson, R M I 570
Eriksson, G I 618
Ertl, K II 543
Esipov, L A II 714
Esypchuk, Yu V I 142, II 160
Evans, D E I 311, I 614
Evrard, M P II 148
Evstigneev, S A II 563
Fabbro, R II 10
Fabre, E II 686
Fabregas, J A I 433, I 437, I 441
Fang, Y I 520
Faral, B II 10
Faulconer, D W II 48
Fedorenko, S I I 413
Fedushchak, V F II 26

Fedyanin, O I I 413, I 421, I 481
Feneberg, W I 299, II 484
Ferro, C II 555
Fessey, J A I 26, I 130
Fiedorowicz, H II 2, II 6
Field, A R I 267, I 634
Fielding, S J I 203, I 267, II 508
Finken, K H II 531
Fiore, C II 232
Flor, G I 578
Fokin, V P II 682
FOM-ECRH Team II 60
Fonck, R I 58
Forman, P R I 570
Forrest, M J I 263, II 535, II 539
Fraiman, A A I 417, I 421
Franconi, E II 555
Fredrickson, E I 134, I 343, II 674
Freidberg, J P I 487
Freisinger, J II 292
Fried, Burton II 116
Fried, M II 603
Friedberg, J P II 718
Frigione, D I 259
Fubini, A I 211
Fujii, M I 457
Fujita, H I 504
Fujita, J II 702
Fujiwara, M I 491
Fukuyama, A I 477, I 524, II 72, II 104
Funahashi, A I 62, II 184
Furth, H P Ii 358
Furutani, Y I 524
Fussmann, G I 18, I 159, I 195, I 199, I 267, I 299, I 331, I 335, II 240, II 244, II 284, II 543, II 587, II 678
Gabellieri, L I 586
Gadeberg, M I 26, I 227
Galvao, R M O I 54
Gambier, D J I 130, II 152
Gammel, G I 58, II 192
Garner, H R I 504
Gee, S J II 446
Gegechkory, N M I 207, II 160
Gehre, O I 18, I 159, I 195, I 199, I 231, I 299, I 331, I 335, II 240, II 244, II 284, II 543, II 587, II 678
Gell, Y II 236
Gerhauser, H II 460, II 464
Gernhardt, J I 18, I 159, I 195, I 199, I 299, I 331, I 335, II 240, II 244, II 284, II 543, II 587, II 678
Giannella, R II 698
Gibson, A I 26, I 70
Gierke, G v. I 18, I 159, I 195, I 199, I 299, I 331, I 335, II 240, II 244, II 284, II 543, II 587, II 678
Gill, R D I 26, I 130, I 227, I 379
Gippius, E F I 421, I 424
Girard, A II 164, II 168, II 172
Giruzzi, G II 96
Giudicotti, L I 578
Giuliana, A I 159, I 199, I 299, II 240, II 244, II 678
Gladushchak, V I I 359
Glasser, A H II 358
Glock, E I 18, I 159, I 195, I 199, I 299, I 331, I 335, II 240, II 244, II 284, II 543, II 587, II 678
Goebel, D M II 531
Goedbloed, J P I 54
Goedheer, W J I 122
Goeler, S von I 343
Golant, V E I 247, I 363
Goldston, R J I 343, II 674
Goloborod'ko, V Ya I 90
Golota, V I II 18
Goncharov, S G I 363
Gondhalekar, A I 26, I 130, I 155, I 219, II 535
Gorbunov, E P II 160
Gorini, G I 223
Gormezano, C II 164, II 168, II 172
Gorshkov, A V II 160
Goto, A I 477, I 524, II 72
Gott, Yu, V I 94
Gottardi, N I 26, I 30, I 70, I 155
Gowers, C W I 26, I 130, I 147, II 535
Graffmann, E II 627
Grashin, S A I 207
Greene, G J II 120
Grek, B I 58, I 339, II 674
Grekov, D L I 473
Grelot, P II 168, II 172

Gresillon, D II 664
Gribble, R F I 570
Grieger, G I 385
Grigor'eva, L I II 128
Grigull, P I 385
Grisham, L II 674
Groebner, R J I 2, I 6
Grosso, G I 219
Grote, H II 551, II 615, II 619
Gruber, O I 18, I 66, I 78, I 159, I 195, I 199, I 279, I 299, I 331, I 335, II 240, II 244, II 284, II 543, II 587, II 678
Grunow, C II 567
Grunow, Ch II 559, II 567
Gryaznevich, M P I 247, I 363
Guasp, J I 433, I 437, I 441
Guenther, K II 559
Guharay, S II 192
Gulyaev, V A I 355
Gunther, K II 563
Gusev, V K I 363
Guty, V I 606
Haas, F A II 362
Haas, G I 18, I 78, I 159, I 195, I 199, I 299, I 331, I 335, II 240, II 284, II 543, II 587, II 678
Haberstich, A I 570
Hacker, H I 385
Hackmann, J II 547
Haegi, M I 211
Hamada, Y II 702
Hamberger, S M I 429
Hamett, G W II 120
Hammett, G II 192
Hammett, G W I 343
Hamnen, H II 124, II 140
Han, W I 147
Hanatani, K I 401
Hansen, F R II 36
Harbour, P J I 323, II 508
Harmeyer, E I 449
Harris, J H I 441
Hartfuss, H J I 385
Hartwig, H II 527
Hasegawa, K I 62
Hasegawa, M I 62, II 184
Hatori, T I 504
Hattori, K I 504, I 602
Hawkes, N C I 203, I 263, I 267, I 371, I 379
Hawryluk, R J I 339, I 343, II 674
Hayashi, K I 375
Haynes, P S I 315, II 450
Heidbrink, W I 58, II 674
Heifetz, D B I 183, I 339
Heikkinen, J A II 56
Heindler, M II 330
Hellsten, T I 22, II 124
Hendel, H W I 339, I 343, II 674
Hender, T C I 433, I 441
Hendriks, F I 26, I 219
Henins, I I 643
Herold, H I 542
Herrmann, A II 551, II 615, II 619
Herrnegger, F I 408
Hershkowitz, N II 64
Hess, W II 164, II 168, II 172
Hesse, M I 199, II 240, II 244, II 678
Hickok, R L I 255
Hicks, H R I 441
Hidekuma, S I 504
Hildebrandt, D II 551, II 603, II 615, II 619
Hill, K W I 134, I 339, I 343
Hinnov, E II 120
Hinsch, H I 231
Hintz, E II 527
Hintze, W II 515
Hirayama, T I 6, I 179, I 375
Hirokura, S II 702
Hitchon, W N G I 461
Hoang, G T II 164, II 168, II 172
Hoekzema, J A I 594
Hofmann, F I 50, II 607
Hogeweij, G M D I 54
Hoida, H W I 643
Hollenstein, Ch II 607
Honda, A I 62
Hone, M I 223
Hooke, W II 192
Hosea, J II 120, II 192
Hoshino, K I 62, II 184
Hosogane, N I 375
Hosokawa, M I 491
Hothker, K II 527
Houtman, H II 14
Howell, R B I 570
Howling, A I 311, II 450
Hrehuss, G I 118
Hsuan, H II 120
Huang, Ch I 520

Huang, L II 252
Hubbard, A I 130
Huebner, K I 231
Hugenholtz, C A J I 215
Hugill, J I 130, I 203, I 371, II 504
Hugrass, W N I 590
Huo, Y P II 224
Hutter, T II 308
Hwang, D II 120
Ichimura, M I 528
Ichtchenko, G II 164, II 168, II 172
Ida, K I 58
Igitkhanov, Yu L II 488
Iguchi, H I 491
Iiyoshi, A I 401, I 405
Ikegami, H I 491
Illyukhin, B N I 421
Ilyukhin, B I I 424
Inaba, N II 280
Ingraham, J C I 570
Innocente, P I 578
Inoue, N I 602, I 626
Inutake, M I 528
Ipatov, V A I 359
Irisov, G S I 243
Ishibori, I I 62
Ishida, S I 602
Ishii, K I 528
Itakura, A I 528
Itami, K I 58
Itoh, K I 477, II 72, II 104
Itoh, S-I I 477, II 72, II 104
Ivanov, I V I 207, II 563, II 682
Ivanov, N V I 207
Ivanov, R S I 239, I 303, II 599
Ivascu, M I 558
Izvozchikov, A B I 363
Jacchia, A II 300
Jacquinot, J I 130, II 140, II 144, II 148, II 152
Jaeckel, H I 385
Jaeger, U I 542
Jaenicke, R I 385
Jahns, G I 58, II 40
Jakubka, K I 275
Jakubowski, L I 538
Janeschitz, G I 18, I 159, I 195, I 199, I 267, I 299, I 331, I 335, II 240, II 244, II 284, II 543, II 587, II 678
Janzen, G I 385
Jarboe, T R I 643
Jarvis, O N I 26, I 130, I 223
Jennings, W C I 255
Jernigan, T C I 433, I 441
Jeziak, K II 2
Jiang, H Y II 44
Jilge, W I 18, I 163
Jobes, F II 192
Johnson, D W I 339, II 674
Johnson, J L I 408
Johnson, P C I 323, I 371, II 508
Jones, I R I 647, I 651
Joye, B I 14, II 248, II 264, II 268
Jungwirth, K II 338
Junker, J I 385
Kaczmarczyk, B II 2
Kaellne, E I 26, I 227, I 379
Kaellne, J I 26, I 223
Kaeppeler, H J I 542
Kagan, D N II 631
Kaita, R I 58, I 343, II 120
Kako, E II 702
Kaleck, A I 187
Kalmykov, S G I 46, I 359
Kameari, A I 6
Kamelander, G II 30
Kaminura, T I 491
Kaminskij, A O I 247
Kammash, T I 496
Kaneko, H I 401
Kaneko, K I 405
Karas, V I II 18
Karger, F I 18, I 159, I 195, I 199, I 299, I 331, I 335, II 240, II 244, II 284, II 543, II 587, II 678
Kariya, T I 528
Karlson, E T II 405
Karttunen, S J II 56
Karzhavin, Yu Yu I 207
Kasai, S I 62, II 184
Kashimura, T I 62
Kashiwa, Y I 62
Kasparek, W I 385
Kasperczuk, A I 550
Katanuma, I I 528
Katsumori, H I 457
Katzenstein, J II 304
Kaufmann, M I 78, II 292
Kawahata, K II 702
Kawakami, T I 62, II 184
Kawamoto, T I 504
Kawashima, H I 62, II 184

Kawasumi, Y II 702
Kawata, S II 22
Kaye, S I 58
Kaye, S M I 343
Kazawa, M I 62
Keilhacker, M I 18, I 159, I 195, I 199, I 299, I 331, I 335, II 240, II 244, II 284, II 543, II 587, II 678
Keller, R I 126, I 291
Kellman, A I 70, I 287
Khalilov, M A I 363
Khautiev, E Yu I 562
Kholnov, Yu, V I 421
Kick, M I 385
Kies, W I 566
Kikuchi, K I 62
Kikuchi, M I 375
Kirolous, H I 651
Kirov, A G II 260
Kiselev, A V I 516
Kishimoto, S I 491
Kislov, A Yu II 160
Kislyakov, A I 195, I 335, II 284, II 543
Kissel, S E I 26, I 130, I 227, II 152
Kisslinger, J I 449, I 453
Kitagawa, S II 702
Kitagawa, Y I 554
Kitsunezaki, A I 6
Kiwamoto, Y I 528
Kladov, S V I 421, I 424
Kleibergen, R I 54
Klima, R II 188
Klopfer, E II 642
Klueber, O I 18, I 159, I 195, I 199, I 299, I 331, I 335, II 240, II 244, II 284, II 543, II 587, II 678
Knight, A I 647
Knowlton, S II 232
Knox, S O I 643
Knyazev, B A I 508
Koenen, L I 251, II 627
Koidan, V S I 508
Koide, Y I 375
Kolacek, K II 668
Kolesnichenko, Ya I I 90, II 208
Kolesnikov, V N I 421, I 424
Kolik, L V I 421
Komoshvili, K G II 260
Kondo, K I 401, I 405
Kondo, T I 528
Konoshima, S I 6, I 375
Konstantinov, S G I 516
Kopecky, V I 275
Korneev, D O II 714
Kornherr, M I 18, I 159, I 195, I 199, I 299, I 331, I 335, II 240, II 244, II 284, II 543, II 587, II 678
Kostecki, J II 6
Kostka, P II 642
Kostomarov, D P I 102, I 235, II 200
Kotai, E II 615, II 639, II 642
Kotze, P B I 159, I 195, I 199, I 299, I 331, I 335, II 240, II 244, II 284, II 543, II 587, II 678
Kovac, I II 668
Kovrizhnykh, L M I 421
Kovrov, P E I 207
Kovsharov, N F II 26
Koziarkiewicz, W I 546
Kraemer, M II 334
Kramskoj, E D II 156
Krasheninnikov, S I II 216, II 500
Kraus, V I I 562
Kraus, W II 292
Krause, H I 26, I 30, I 151, I 155, I 379
Krejci, A II 668
Krikunov, S V I 363
Krivenski, V II 96
Kroiss, H I 385
Krupin, V A I 207
Kudryavtsev, A M I 516
Kuehner, G I 385
Kugel, H I 58
Kukral, H II 575
Kukushkin, A S II 488, II 500
Kulaga, A E I 469
Kuleshov, I E I 469
Kumazawa, R I 504
Kusama, Y I 528
Kuteev, B V I 207, II 619, II 721
Kuznetsov, Yu K I 247
Labaune, C II 686
Lacina, J II 342
Lackner, K I 18, I 66, I 159, I 279, I 299, I 331, I 335, II 284, II 543, II 587

Lallia, P P I 130, II 140, II 144, II 148, II 152
Lalousis, P II 660
LaMarche, P II 674
Lang, R S I 78
Langer, W D I 183
Lappus, G I 66
Lapshin, V I I 413
Larionova, N F I 421, I 424
Lasarev, V B I 413
Lashkul, S I I 46, I 359
Laux, M II 551, II 615, II 619
Lazzaro, E I 26, I 70, I 130, I 287, I 319, I 327
Lebedev, S V I 247, I 363, I 508
LeBlanck, B I 58
Lebo, I G II 631
Lehner, T II 664
Lengyel, L I 82, II 660
Lenoci, M I 159, I 195, I 199, I 299, I 331, I 335, II 240, II 244, II 284, II 543, II 587, II 678
Leonov, S B II 682
Leonov, V N I 413
Letuchii, A II 706
Leuterer, F I 199, II 240, II 244, II 678
Levkov, B S I 355
Li, D F II 224
Li, R II 304
Liberman, M A I 622
Lie, Y T II 527
Lietti, A II 264
Lin, S H II 40
Lingertat, J II 559, II 563, II 567
Lipin, B M I 363
Lisitano, G I 18, I 159, I 195, I 199, I 299, I 331, I 335, II 240, II 244, II 284, II 543, II 587, II 678
Lister, J B I 14, II 248, II 264, II 268
Little, R II 674
Litunovskij, R N I 363
Litvak, A G I 421, II 346
Litwin, C II 64
Liobet, X II 718
Lloyd, B II 80
Loeb, H W II 292
Lok, J I 594
Lomas, P J I 26, I 151, I 287
Longinov, A V II 132, II 156
Lopes Cardozo, N J II 272
Lopes Fraguas, J A I 433
Lopez Fraguas, J A I 441
Loskutov, V V II 26
Lozovskij, S N II 260
Luchinsky, A V II 26
Luckhardt, S C II 232
Ludu, A I 558
Luk'yanitsa, A A II 200
Lukjanov, S Yu II 160
Luzganov, S N II 682
Lynch, V E I 441
Lynov, J P II 36
Lyon, J F I 433, I 441
Ma, F II 80
Maassberg, H I 384, I 385
Mabruk, E II 706
Maddaluno, G II 555
Maddison, G P II 508
Maelzig, M I 566
Maeno, M II 184
Maerlo, V I 223
Magyar, G I 155, I 379, II 535
Mahdavi, M A I 159, I 195, II 543
Mahn, C I 385
Maksimov, Yu S II 156, II 563
Malacarne, M I 126, I 151, I 155
Mandache, N I 558
Maneo, M I 62
Mansfield, D II 674
Mansfield, M I 379
Mantica, P II 300
Manuaba, A II 603, II 615, II 639, II 642
Marcus, F B I 50, II 268, II 607
Marinucci, M I 171
Marklin, G J I 643
Marlier, S I 385
Marmillod, Ph I 14
Maroli, C II 36
Martin, P I 163
Martin, R I 433
Martin, Y II 607
Martinelli, A P II 623
Martinelli, P II 575
Martini, S I 578, I 638
Martynov, A A I 106
Masai, K II 702
Masamune, S I 570
Mase, A I 528
Massey, R S I 570
Mast, K F I 26, I 30, I 70, I 147, I 151, I 155, I 379

Matoba, T I 62, II 184
Matsuda, T I 62, II 184
Matsumoto, H I 62, II 184
Matsuoka, K II 702
Matsuura, K II 702
Matsuzaki, Y I 62
Matsuzuka, S I 602
Matthews, G F II 591
Maximov, Yu S II 160
Mayberry, M II 232
Mayer, H M II 678
Mayer, H-M I 18, I 159, I 195, I 199, I 299, I 331, I 335, II 240, II 244, II 284, II 543, II 587
Mazzitelli, G I 138
Mazzucato, E II 120, II 192
McCool, S II 232
McCormick, K I 18, I 159, I 195, I 199, I 299, I 331, I 335, II 240, II 244, II 284, II 543, II 587, II 678
McCracken, G M I 70, II 571, II 575, II 579
McCune, D C II 674
McDermott, S II 232
McGuire, K I 58, I 134, I 343, II 674
McIntosh, G II 14
McKenna, K F I 590
McNeill, D II 120
McVey, B D II 296
Meade, D M I 343, II 674
Medley, S S I 343
Medvedev, A A I 235, II 160
Medvedev, S Yu I 106, I 347
Meisel, D I 18, I 159, I 195, I 199, I 299, I 331, I 335, II 240, II 244, II 284, II 543, II 587, II 678
Melin, G II 164, II 168, II 172
Merlin, D I 578
Mertens, V I 18, I 159, I 195, I 199, I 231, I 299, I 331, I 335, II 240, II 244, II 284, II 543, II 587, II 678
Meservey, E II 192
Meshcheryakov, A I I 421
Mesyats, G A II 26
Meyer, J II 14
Mezey, G II 603, II 639, II 642
Miano, G I 110
Midzuno, Y II 702
Miklaszewski, R I 550
Miley, G H II 288
Millar, W I 371
Miller, G I 570
Milora, S L II 674
Milovich, J L II 116
Minardi, E II 378
Minenko, V P II 611
Ming lun, Xue I 74
Minyaev, O A I 363
Mirnov, S V II 682
Mirnov, V V I 512
Miroshnichenko, G A II 156
Miura, Y I 62, II 184
Miyajima, S I 457
Miyamoto, K I 602, I 626
Miyoshi, S I 528
Mizuuchi, T I 401, I 405
Moeller, C P II 40
Mond, M I 485
Mondt, J P II 512
Montvai, A I 146, II 441
Morales, G J II 116
Moret, J-M I 14, II 248, II 264
Morgan, J G II 508
Morgan, P D I 26, I 130, I 155, I 379, II 535, II 539
Mori, M I 62, II 184
Morikawa, J I 602
Morimoto, S I 401
Morita, S II 702
Moroz, P E II 351
Morris, A W I 315, II 450
Morrison, P J II 718
Motley, R II 192
Motojima, O I 401, I 405
Moulin, B II 164, II 168, II 172
Mueller, D II 674
Mueller, E R I 18, I 159, I 195, I 199, I 299, I 331, I 335, II 240, II 244, II 284, II 543, II 587, II 678
Mueller, G I 385
Mueller, G A I 385
Muenich, M I 199, II 240, II 244, II 678
Muir, D G I 22
Munson, C P I 570
Murakami, M I 343, II 674

Murmann, H I 159, I 195, I 199, I 299, I 331, I 335, II 240, II 244, II 284, II 543, II 587, II 678
Mutoh, T I 401, I 405
My, N T II 639, II 642
Myatlov, V V II 682
Mynick, H E I 461
Myskin, O K I 516
Nagami, M I 6, I 375
Nagao, S I 457
Nagayama, Y I 602, I 626
Nagornii, A II 706
Nagraba, S II 2, II 6
Naitou, H II 702
Nakach, R II 236
Nakamura, H I 375
Nakashima, Y I 528
Nakasuga, M I 401
Nalesso, G F I 598
Nassri, A II 330
Navarro, A P I 441, II 710
Nave, M F I 147, I 151, I 155
Nedospasov, A V II 492
Nelson, B E I 433
Nemeth, G I 663
Neri, A II 555
Nesterova, M V I 235
Neudachin, S V II 212
Neuhauser, J I 82, II 476
NI Team I 384, I 393
Nicolai, A II 519
Niedermeyer, H I 18, I 159, I 195, I 199, I 299, I 331, I 335, II 244, II 284, II 543, II 587, II 678
Nielsen, P I 26, I 227
Nieschmidt, E B I 343, II 674
Niestadt, R M I 130, I 151, I 215, II 152
Nihei, H I 602
Niikura, S I 375
Ninimiya, H I 375
Nishikawa, K II 104
Nishimura, K I 504
Nishizawa, A II 702
Niu, K II 22
Nocentini, A I 367, II 180
Noda, N II 702
Nogi, Y II 280
Noll, P I 70, I 151
Nordskov Nielsen, A II 652
Noterdaeme, J-M II 100
Notkin, G E I 142, I 355, II 156, II 160
Novac, B I 558
Novikova, A V I 421
Nowak, S I 14, II 268
Nuehrenberg, J I 445
O'Brien, M R II 76, II 140
O'Rourke, J I 26, I 130, I 155, II 535
Obiki, T I 401, I 405
Ochiai, I II 184
Odajima, K I 62, II 184
Oepts, D I 594
Ogawa, H I 62, II 184
Ogawa, I II 702
Ogawa, T I 62, II 184
Ogawa, Y II 702
Ohkubo, K II 702
Ohlendorf, W I 385
Ohta, K I 62, II 184
Ohtake, I I 401, I 405
Ohtsuka, H I 62, II 184
Ohuchi, K I 62
Ohyabu, N I 58
Okabayashi, M I 58
Okada, H I 401, I 405
Okamura, S I 504
Okano, H I 62
Okazaki, N I 477
Okubo, Y I 504
Olivares, A G I 114
Omeltchenko, A Y II 342
Ono, M II 120
Oomens, A A M I 594
Orefice, A II 84
Orsitto, F I 259
Ortolani, S I 578, I 582, I 586, I 638
Osanai, Y II 280
Osipov, M V II 6
Ott, W I 397
Oyevaar, Th I 130, I 215
Paccagnella, R I 578
Paduch, M I 550
Pan, C H II 429
Panarella, E I 606
Panasyuk, V M I 516
Panchenko, V G II 694
Pankratov, I M II 417
Panzarella, A II 168, II 172
Parail, V V I 98, II 200, II 212, II 409
Paramonov, A V I 421, I 424
Pardo, C I 10

Pare, V I 134
Parham, B II 80
Park, H II 674
Park, W I 134, II 358
Parlange, F II 164, II 168, II 172
Parys, P II 2
Pashchenko, A V II 128
Pasini, D I 227, I 379
Paszti, F II 603, II 615, II 642
Patron, Z II 2
Pavlenko, V N II 694
Pavlo, P II 188
Pavlov, I P I 363
Pavlov, S S II 132, II 156
Pavlov, Yu D II 635
Pawlowicz, W II 2, II 6
Peacock, N J I 203, I 263, I 267, I 371, I 379
Pech, P II 551, II 615, II 619
Pedorenko, A V I 102
Pedretti, E I 211
Pegoraro, F II 318, II 322, II 366
Penningsfeld, F P I 397
Pepin, H II 10
Perea, A I 433, I 441
Perepelkin, N F I 469
Pereverzev, G V II 212
Perez Navarro, A I 433
Pericoli-Ridolfini, V II 220
Pesic, S II 88
Petrillo, V II 36
Petrov, A E I 421
Petrov, D P II 635
Petrov, V G II 492
Petrov, Yu V I 46, I 359
Petrova, T A II 346
Petviashvili, V I II 350
Phillips, J A I 570
Phillips, M W I 500
Pickrell, M M I 570
Piekaar, H W I 130, I 151, I 215, I 287
Piffl, V II 668
Pillon, M I 211
Pimenov, A B I 207, I 235, II 160
Pisarczyk, T I 550
Pistunovich, V I II 488, II 500
Plotnik, I S II 208
Pochelon, A I 126, I 130, I 291
Pocs, L II 603, II 639, II 642
Podda, S II 196
Pogany, L II 639
Pogutse, O P II 409
Pontau, A E II 531
Popov, A M I 102
Popov, I A I 307
Popov, S N I 421
Porcelli, F II 318
Porkolab, M II 232, II 232
Portnov, D V I 142
Poschenrieder, W I 18, I 159, I 195, I 199, I 299, I 331, I 335, II 240, II 244, II 284, II 543, II 587, II 678
Pospieszczyk, A II 523, II 527
Pozharov, V A II 488, II 500
Poznyak, V II 706
Prater, R II 40
Preinhaelter, J II 342
Preis, H I 66
Prentice, R I 26, I 130, I 227
Price, H D I 504
Pritchard, J I 371
Probert, P H I 465
Pueblas, A I 433
Puiatti, M E I 578, I 586
Puik, E J II 272
Putvinskij, S V I 347
Pyatov, V N I 247
Qiu, X II 252
Qu, W X II 397
Ramponi, G II 84, II 300
Ramsey, A T I 339, II 674
Rantzev-Kartinov, V A II 160
Rapp, H I 18, I 159, I 195, I 199, I 231, I 299, I 331, I 335, II 240, II 244, II 284, II 543, II 587, II 678
Rasmussen, D II 674
Ratakhin, N A II 26
Rau, F I 385, I 449
Raupp, G I 655, I 659
Raus, J II 668
Razdobarin, G T I 359, I 363
Reiner, H-D II 551, II 615, II 619
Reiter, D I 251, II 519
Rej, D J I 590
Rem, J I 54
Ren, Z I 520
Renner, H I 385
Reusch, M I 58
Reuschling, R II 292
Revenchuk, S M II 694
Rice, J E I 401
Riedler, H I 335, II 284, II 543
Ringler, H I 385

Ripa, M II 668
Riviere, A C II 80
Robinson, D C I 311, I 315, II 80, II 450
Rodriguez Solano, E I 433
Roehr, H I 159, I 299, II 244, II 587, II 678
Rohatgi, R II 232
Romain, J P II 10
Romanelli, F I 630, II 228
Rome, J A I 441
Romero, E II 710
Roquemore, A KL I 343
Rosbueldt, D II 523
Rosenbluth, M N II 718
Ross, R T I 26, I 130
Rostoker, N II 304
Roth, J I 18, I 195, I 335, II 284, II 543
Roubin, J P II 308
Rozanov, V B II 631
Rozhdestvenskij, V V I 363
Rubinacci, G I 110
Ruchko, L F II 260
Ruffina, U II 52
Ruhs, N II 244, II 678
Runov, A M II 682
Rupasov, A A II 6
Rutherford, P II 358
Rydygier, E I 538
Ryter, F I 18, I 159, I 195, I 199, I 299, I 331, I 335, II 240, II 244, II 284, II 543, II 587, II 678
Saadatmand, K I 255
Sadler, G I 26, I 130, I 223
Sadowski, M I 538
Saito, K II 280
Saito, T I 457, I 528
Sakanaka, P H I 54
Sakharov, N V I 247, I 363
Salukvadze, R G I 562
Samain, A II 386
Samm, U II 523, II 527
Sand, F II 144, II 148, II 152
Sandmann, W I 78
Sannikov, V II 706
Sano, F I 401, I 405
Saoutic, B I 191, II 112
Sapozhnikov, A V I 421
Sardei, F I 385
Sarksyan, K A I 421
Sasao, M II 702
Sass, B II 652
Sato, K II 702
Sato, K N II 702
Sato, M I 401, I 405
Sato, T I 504
Sauthoff, N I 134
Savrukhin, P V I 142
Sawada, K I 528
Sawley, M L I 291
Sbitnikova, I S I 421
Scarin, P I 578, I 586
Scharer, J E II 144, II 296
Scheglov, D A II 160
Schep, T J II 366
Schivell, J F I 339, II 674
Schlueter, J II 523, II 627
Schmidt, G L I 58, II 674
Schmidt, H I 542
Schmidt, R I 542
Schmitter, K H I 199, II 240, II 244, II 678
Schneider, F I 18, I 159, I 195, I 199, I 299, I 331, I 335, II 240, II 244, II 543, II 587, II 678
Schneider, J II 284
Schneider, W II 476
Schoenberg, K F I 570
Schofield, A E I 570
Schueller, F C I 26, I 70, I 151, I 155, I 287
Schueller, P G I 385
Schuresco, D II 120
Schuurman, W II 370, II 374, II 382
Schweer, B II 523
Schwoerer, K I 385
Scott, S D I 343
Sedlacek, Z II 338
Segre, S I 219
Seidel, U I 66
Seki, S I 375
Selberg, H II 358
Semenov, I B II 682
Sengoku, S I 6, I 62, II 184
Sergeev, A M II 346
Sergeev, V Yu I 207, II 619, II 721
Sergienko, G V II 599
Sesnic, S I 58, I 339, II 674
Sestero, A I 367
Shaing, K C II 397
Shakhatre, M I 542
Shakhovetz, K G I 247, I 363
Shapotkovskij, N V II 156, II 160
Sharp, L E I 429

Shats, M G I 421
Shcerbak, A F II 635
Shcheglov, M A I 508
Shcherbinin, O N I 363
Shi, S X I 429
Shibata, T I 62
Shibuya, T I 62
Shiina, S II 280
Shiina, T I 62
Shikanov, A S II 6
Shimada, M I 6, I 339, II 674
Shimizu, K I 179, I 375
Shimomura, Y I 375
Shinohara, S I 602, I 626
Shirai, H I 179
Shissel, D P I 6
Shohet, J L I 461, I 465
Shoji, T I 62, I 491, II 184
Shpilrain, E E II 631
Shprits, I D I 46, I 359
Shtan', A F I 469
Shukla, P K II 326
Shurygin, R V II 136, II 212
Shyam, A I 542
Sidorov, V P II 260, II 611
Siemon, R E I 590
Sigmar, D J II 288, II 390
Siller, G I 18, I 159, I 195, I 199, I 299, I 331, I 335, II 240, II 244, II 284, II 543, II 587, II 678
Simm, W II 607
Simonetto, A II 300
Simonini, R II 484
Sinman, A I 534, I 642
Sinman, S I 534, I 642
Skinner, C II 120
Sklizkov, G V II 631
Skrzeczanowski, W I 546
Smerdov, B I II 128
Smeulders, P I 18, I 159, I 195, I 199, I 299, I 331, I 335, II 240, II 244, II 284, II 543, II 587, II 678
Smirnov, A P I 235, II 200
Smirnova, A D I 421, I 424
Smolyakova, O B I 417, I 421
Snider, R II 40
Soboleva, T K II 216
Socha, R I 546
Soeldner, F I 18, I 159, I 195, I 199, I 267, I 299, I 331, I 335, II 240, II 244, II 284, II 543, II 587, II 678
Soell, M II 100
Sokolov, Yu II 706
Solano, E R I 441
Soler, Mario I 114
Sollich, N II 334
Solnetsev, A M II 635
Solodovchenko, S I I 469
Sorensen, H II 652
Sorlei, Zs I 271
Sorokhin, S A II 26
Spatschek, K H II 326
Speth, E I 18, I 159, I 195, I 299, I 331, I 335, I 397, II 284, II 543, II 587
Spigel, I S I 421, I 424
Spineanu, F I 175
Stacey, W M II 390
Staebler, A I 18, II 284
Stamp, M F I 26, I 130, I 155, II 535, II 539
Stangeby, P C I 70, II 571, II 579
Start, D F H II 76, II 140
Stas'ev, V P II 26
Staudenmaier, G II 543
Stauffer, F II 674
Stavinoha, P II 338
Stefanovskij, A M II 635
Steiger, J I 655, I 659
Steinmetz, K I 195, I 335, II 284, II 543
Stepanenko, M M I 307, II 160
Stepanov, A Yu II 714
Stepanov, K N II 132, II 156, II 204
Steuer, K-H I 18, I 159, I 195, I 199, I 299, I 331, I 335, II 240, II 244, II 284, II 543, II 587, II 678
Stevens, J E II 192
Stoeckel, J I 275
Storey, D P I 614
Stotsky, G J I 239, II 599
Stott, P E I 26
Strachan, J D I 339, I 343
Stratton, B L II 674
Strelkov, V S II 160
Stringer, T E I 86, I 130
Strizhov, V F I 207

Strusny, H II 603, II 615
Stubberfield, P M I 22
Succi, S II 124
Suckever, S II 120
Sudo, S I 401, I 405
Sukhodolskii, V N I 421
Summers, D D R I 26, I 70, I 130, I 155, II 535
Summers, H P I 379, II 539
Sund, R S II 296
Sunka, P II 668
Sutton, W R II 288
Suvorov, E V I 417, I 421
Suzuki, K I 62
Suzuki, N I 62, II 184
T-10 Group I 38, I 42
Taglauer, E II 543
Tagle, A J I 70
Tagle, J A II 579
Tagle, T II 571
Tait, G D I 343
Takada, S I 62, II 184
Takahashi, C I 491
Takahashi, H I 58
Takase, Y II 232
Takasugi, K I 491
Takeda, T II 433
Takeiri, Y I 401, I 405
Takita, Y I 491
Takizuka, T I 179
Talmadge, J N I 465
Tamai, H I 62, II 184
Tanahashi, S II 702
Tanaka, Y I 62, II 184
Tanga, A I 26, I 70, I 287, II 535
Tani, K I 179
Tani, T I 62
Taniguchi, Y II 702
Taroni, A I 22, II 484
Tartari, U II 300
Tataronis, J A II 718
Taylor, G I 134, I 339, II 674
Taylor, J B II 401, II 446
Tenney, F I 58
Teplov, P P I 363
Terebkov, A L II 635
Tetsuka, T II 702
Texter, S II 232
TEXTOR Team II 627
TFR Group I 191, I 295, II 60, II 112, II 308
Thomas, C E I 343
Thomas, G J II 531
Thomas, P R I 26, I 70, I 151, I 283, I 287
Thompson, J I 151
Thomsen, K II 152, II 656
Thumm, M I 385
Thyagaraja, A II 362
Tibone, F I 22
Titishov, K B II 563
TJ-I Group I 10, II 710
Todd, A M M I 500
Todd, T N II 80
Toi, K II 702
Tokar', M Z II 496
Tokuda, S II 433
Tomaszewski, K I 546
Tondello, G I 586
Tonetti, G I 26, I 130, I 151
Tonini, G II 690
Toschi, V II 378
Toyama, H I 602, I 626
Truc, A I 295
Trukhin, V M I 287, II 160
Tsel'nik, F A I 516
Tsubot, F I 491
Tsuchidate, T I 491
Tsuji, S I 375
Tsunematsu, T II 433
Tsurikov, V A II 156
Tsypin, V S II 437
Tubbing, B J D I 130, I 151, I 215, II 152
Tuccillo, A A I 138
Turnbull, A D I 50
Turner, M I 147
Tuszewski, M I 590
Tutter, M I 385
Ueda, Y I 602, I 626
Uesugi, Y I 62, II 184
Uhlenbusch, J II 547
Ullschmied, J II 668
Uo, K I 401, I 405
Ursu, I I 558
Ushakov, S N II 714
Ushigusa, K I 375
Valisa, M I 70, I 130
Vallet, J C II 168, II 172
Valovic, M I 275
van Belle, P I 130, I 223
Van Calker, C I 566
van der Laan, H A II 272
van der Meer, A F G I 594
van der Meiden, H J II 272
van Houten, M A II 382
Van Houtte, D II 164, II 168, II 172

van Toledo, W II 272
Vannucci, A I 211
Vasil'ev, M P I 469
Vasiliev, A A II 682
Vasin, N A II 156, II 160
Vasin, N L I 207, I 351, II 68
Vdovin, V L II 156, II 160
Velikovich, A L I 622
Venus, G II 587
Verbeek, H II 543, II 583
Vershkov, V A I 207
Vertiporokh, A N I 207, II 156, II 160, II 559, II 563
Vien, T I 199, II 240, II 244, II 678
Virmont, J II 10
Vizkelethy, Gy II 603
Vlad, G I 138, I 630
Vlad, M I 175
Vlases, G I 78, I 159, I 199, I 299, II 244, II 678
Vojtsenya, V S I 469
Volkov, V V I 207
Vollmer, O I 18, I 159, I 195, I 299, I 331, I 335, II 284, II 543, II 587
Voloshko, A Yu I 469
von Goeler, S II 192
Voronov, G S I 421, I 424
Voropajev, S G I 508
Voytsekhovich, I A II 409
W VII-A Team I 384, I 393
Waelbroeck, F II 627
Wagner, F I 18, I 159, I 195, I 199, I 299, I 331, I 335, II 240, II 244, II 284, II 543, II 587, II 678
Wahlberg, C I 574
Waidmann, G I 118, II 627
Wakatani, M I 401
Wan, B I 520
Wang, Y G II 587
Wang, Z II 355
Wang, Zh I 520
Washizu, M I 6
Watari, T II 702
Watkins, M L I 22, I 26, I 147, II 535
Watt, R G I 570
Weber, P G I 570
Weenink, M P H II 382
Wegrowe, J-G II 176
Weichelt, A I 655, I 659
Weiland, J II 394, II 512
Weisberg, K-V II 652
Weldon, D M I 570
Weller, A I 385
Wereszczynski, Z I 550
Wesner, F I 195
Wesson, J A I 130, I 147, I 151
Westerhof, E I 122, II 52
White, R B I 134, II 358
Wilcock, P D I 614
Wilczynski, A II 2, II 6
Wilhelm, R I 385
Wilson, J R II 120, II 192
Winter, H II 595
Winter, J II 627
Wintermeyer, G I 659
Witalis, E A I 610
Wobig, H I 385, I 449, I 453
Wolff, H II 551, II 615, II 619
Wolowski, J II 2, II 6
Wong, K-L I 343
Woyke, H I 66
Woyna, F v. I 199, II 240, II 244, II 678
Wu, L Q II 429
Wuersching, E I 385
Wunderlich, R I 279, II 476
Wurden, G A I 570
Wurz, H I 231
Xiao, Li I 74
Yamada, H I 58, I 134
Yamada, K I 375
Yamada, Y I 554
Yamagishi, K I 602
Yamaguchi, N I 528
Yamamoto, S I 62, II 184
Yamamoto, T I 6, I 62, II 184
Yamamoto, Y I 554
Yamanaka, M I 554
Yamauchi, T I 62, II 184
Yamazaki, K II 702
Yanagisawa, I I 62, II 184
Yang, W H II 224
Yasin, I V I 247
Yatsu, K I 528
Yavorskij, V A I 90
Yegorenkov, V D II 204
Yokoyama, K I 62
Yokoyama, M I 554
Yoshida, H I 375
Yoshida, Z I 602, I 626
Yoshino, R I 375
Young, K M I 343
Yousef, N II 272

Yunakovsky, A D II 346
Yurchenko, E I I 94, II 413
Yushmanov, P N I 98, I 243, II 136
Zacek, F I 275
Zadrozny, M I 546
Zambreanu, V I 558
Zanati, F II 706
Zanza, V I 219, II 196
Zarnstorff, M C I 339, I 343
Zavadsky, N A I 516
Zavala, G I 496
Zaveryaev, V S I 235, II 156, II 160
Zebrowski, J I 538
Zehrfeld, H P I 66
Zelenov, E V II 682
Zhang, G I 520
Zhang, Z X II 44
Zharova, N A II 346
Zhuravlev, V A I 207
Ziebell, L F II 96
Ziegenhagen, II 551
Ziethen, G I 566
Zille, R I 445
Zippe, M I 385
Zoita, V I 558
Zoletnik, S I 146
Zou, X L II 664
Zouhar, M I 199, II 240, II 244
Zurro, B I 10
Zushi, H I 401, I 405
Zwonkov, S N II 559, II 567